

Anders Lund · Masaru Shiotani *Editors*

Applications of EPR in Radiation Research

 Springer

Applications of EPR in Radiation Research

Anders Lund • Masaru Shiotani
Editors

Applications of EPR in Radiation Research

 Springer

Editors

Anders Lund
Linköping University
Linköping
Sweden

Masaru Shiotani
Hiroshima University
Higashi-Hiroshima
Japan

ISBN 978-3-319-09215-7 ISBN 978-3-319-09216-4 (eBook)

DOI 10.1007/978-3-319-09216-4

Springer Cham Heidelberg New York Dordrecht London

Library of Congress Control Number: 2014951335

© Springer International Publishing 2014

This work is subject to copyright. All rights are reserved by the Publisher, whether the whole or part of the material is concerned, specifically the rights of translation, reprinting, reuse of illustrations, recitation, broadcasting, reproduction on microfilms or in any other physical way, and transmission or information storage and retrieval, electronic adaptation, computer software, or by similar or dissimilar methodology now known or hereafter developed. Exempted from this legal reservation are brief excerpts in connection with reviews or scholarly analysis or material supplied specifically for the purpose of being entered and executed on a computer system, for exclusive use by the purchaser of the work. Duplication of this publication or parts thereof is permitted only under the provisions of the Copyright Law of the Publisher's location, in its current version, and permission for use must always be obtained from Springer. Permissions for use may be obtained through RightsLink at the Copyright Clearance Center. Violations are liable to prosecution under the respective Copyright Law.

The use of general descriptive names, registered names, trademarks, service marks, etc. in this publication does not imply, even in the absence of a specific statement, that such names are exempt from the relevant protective laws and regulations and therefore free for general use.

While the advice and information in this book are believed to be true and accurate at the date of publication, neither the authors nor the editors nor the publisher can accept any legal responsibility for any errors or omissions that may be made. The publisher makes no warranty, express or implied, with respect to the material contained herein.

Printed on acid-free paper

Springer is part of Springer Science+Business Media (www.springer.com)

Preface

Electron Paramagnetic Resonance, EPR, has been widely used for nearly 60 years in studies of intermediate products like free radicals, triplet state molecules and other paramagnetic species, formed by irradiation. The applications of EPR (ESR) in radiation research have since then been reviewed in several monographs and edited works. The progress made during the last two decades has so far not been treated in a single volume, however, in spite of the significant progress reached by applying modern continuous wave (CW) and pulsed EPR, development of detection methods with high resolution and sensitivity, application of sophisticated matrix isolation techniques and by the advancement in quantitative EPR to mention a few recent experimental trends. On the theoretical side methods based on first principles have been developed and applied for the calculation of hyperfine couplings, zero-field splittings and g-factors as well as in spectral simulations. In the present work an effort was made to present developments of particular interest for radiation research in 19 chapters written by invited specialists.

Elementary radiation processes is treated in the first four chapters. The subject is introduced in Chap. 1 and is illustrated by recent applications in radiation chemistry employing steady-state and pulse radiolysis. Experimental EPR studies of the radicals and radical ions formed by radiolysis of crystalline organophosphorus compounds, metal complexes, and halocarbons are reviewed in the following two chapters, with assignments supported by state-of-the-art quantum chemistry calculations. Recent progress in studies of hydrogen molecular ions is reviewed in Chap. 4. EPR studies in solid para-hydrogen matrices at cryogenic temperatures were reported. Several applications of EPR in solid state radiation chemistry are considered in the three following chapters. A combination of EPR and IR methods was used in Chap. 5 to obtain information on the structure and dynamics of radicals and radical ions produced by *in situ* irradiation with fast electrons. A rigorous matrix isolation approach using solid noble gases was applied. Research towards identification of radiation-induced radicals in solid state sugars and sugar phosphates is treated in Chap. 6. EPR and ENDOR single crystal measurements combined with DFT calculations were utilized to obtain information of initial radiation damages and thermally induced transformation mechanisms. Structures of radiation-induced defects in silica (SiO_2) were investigated by pulsed ENDOR and ESEEM as well

as EPR in Chap. 7. Recent progress made on selected radiation-induced defects in crystalline SiO_2 and amorphous SiO_2 doped (and undoped) with diamagnetic impurities is reviewed. Direct and indirect radiation effects are considered in two chapters devoted to biochemistry, biophysics, and biology applications. In Chap. 8 EPR studies of radical formation by direct ionization of DNA are reviewed. Mechanisms that lead to production of stable damage, such as strand breaks were considered. A method presented in Chap. 9 combining EPR, spin trapping and chromatographic separation made it possible to identify free radicals in nucleic-acid and protein-related compounds. Applications in material science are treated in three chapters. As explained in Chap. 10 EPR studies of polymers have been closely related to the research and development of polymer modification by radiation processing. EPR in combination with theoretical modeling and optical and electrical characterizations were used in Chap. 11 for studies of radiation-induced defects in SiC and III-nitrides. The use of intrinsic defects in controlling properties of materials for power electronics was discussed. The radiation induced reactions and fragmentation in room temperature ionic liquids using EPR spectroscopy are reviewed in Chap. 12 with particular emphasis on applications in nuclear fuel cycle separations. Radiation metrology is treated in two chapters concerned with EPR dosimetry. In Chap. 13 the alanine-EPR metrology system for high-dose radiation dosimetry at NIST is presented. The use of EPR dosimetry in medicine, predominantly within radiotherapy, is reviewed in Chap. 14. Most applications have employed polycrystalline alanine, but the use of other materials is also discussed. The utilization of CW and pulsed EPR measurements as a tool for astrobiology in search of primitive organic matter is considered in Chap. 15. Materials originating from meteorites and terrestrial substances could for example be distinguished. Studies involving pulsed EPR and optical detection are treated in two chapters presenting advanced methods. EPR methods to determine the distribution of radiation damage products in solids are reviewed in Chap. 16. The emphasis is on pulsed EPR methods that measure weak dipolar interactions between paramagnetic centers. Radical ion pairs in irradiated solutions were investigated by optically detected EPR and related techniques in Chap. 17. A brief history, a theoretical background, methodological details, as well as the unique experimental results obtained with these sensitive techniques are discussed. Quantum chemistry calculations and spectrum simulation tools applied to irradiated systems are presented in the last two chapters. Periodic density-functional calculations were employed for confrontation with experimental results in Chap. 18. Software for EPR and ENDOR simulations by exact and perturbation methods are presented in Chap. 19.

Contents

Part I Elementary Radiation Processes

- 1 Fundamental Reaction Mechanisms in Radiation Chemistry and Recent Examples**..... 3
Mamoru Fujitsuka and Tetsuro Majima
- 2 Single Crystal EPR Studies of Radicals Produced by Radiolysis of Organophosphorus Compounds**..... 33
Michel Geoffroy
- 3 EPR Studies of Radical Ions Produced by Radiolysis of Fluorinated Hydrocarbons and Related Compounds in Solid Media**..... 67
Masaru Shiotani and Kenji Komaguchi
- 4 Hydrogen Molecular Ions in Solid Parahydrogen: EPR Studies at Cryogenic Temperatures**..... 117
Jun Kumagai

Part II Solid State Radiation Chemistry

- 5 EPR and IR Spectroscopy of Free Radicals and Radical Ions Produced by Radiation in Solid Systems** 151
Vladimir I. Feldman
- 6 Radiation Chemistry of Solid-State Carbohydrates Using EMR**..... 189
Henk Vrielinck, Hendrik De Cooman, Freddy Callens and Einar Sagstuen
- 7 EPR on Radiation-Induced Defects in SiO₂** 255
Antonino Alessi, Simonpietro Agnello, Gianpiero Buscarino, Yuanming Pan and Rudolf I. Mashkovtsev

Part III Biochemistry, Biophysics, and Biology Applications

- 8 Electron Spin Resonance of Radicals in Irradiated DNA** 299
Amitava Adhikary, David Becker and Michael D. Sevilla
- 9 Applications of the Spin-Trapping Method in Radiation Biology** 353
Mikinori Kuwabara, Wakako Hiraoka and Osamu Inanami

Part IV Materials Science

- 10 EPR Application to Polymers: Radiation Induced Crosslinking and Graft Polymerization** 387
Tadao Seguchi
- 11 Electronic Defects in Electron-Irradiated Silicon Carbide and III-Nitrides** 417
Nguyen Tien Son and Erik Janzén
- 12 Radiation Induced Reactions and Fragmentation in Room Temperature Ionic Liquids** 453
Ilya A. Shkrob, Timothy W. Marin and James F. Wishart

Part V Radiation Metrology

- 13 Alanine-EPR High-Dose Radiation Metrology** 489
Marc F. Desrosiers
- 14 EPR Dosimetry in Clinical Applications** 509
Eirik Malinen

Part VI Geological Applications

- 15 EPR of Primitive Organic Matter: A Tool for Astrobiology** 541
Didier Gourier, Laurent Binet and Hervé Vezin

Part VII Advanced EPR Techniques

- 16 EPR Measurement of the Spatial Distribution of Radiation Damage** 581
Michael K. Bowman, Alexander G. Maryasov and Yuri D. Tsvetkov
- 17 Study of Spin-Correlated Radical Ion Pairs in Irradiated Solutions by Optically Detected EPR and Related Techniques** 629
Vsevolod Borovkov, Dmitri Stass, Victor Bagryansky and Yuriy Molin

Part VIII Theoretical Tools

18 Uncovering Radiation Chemistry in the Solid State Through Periodic Density-Functional Calculations: Confrontation with Experimental Results and Beyond	667
Ewald Pauwels	
19 Applications of EPR and ENDOR Spectrum Simulations in Radiation Research	703
Roland Erickson and Anders Lund	
General Appendices	751
Index	763

Contributors

Amitava Adhikary Department of Chemistry, Oakland University, Rochester, MI, USA

Simonpietro Agnello Department of Physics and Chemistry, University of Palermo, Palermo, Italy

Antonino Alessi Department of Physics and Chemistry, University of Palermo, Palermo, Italy

Victor Bagryansky V. V. Voevodsky Institute of Chemical Kinetics and Combustion, SB RAS, Novosibirsk, Russia

Novosibirsk State University, Novosibirsk, Russia

David Becker Department of Chemistry, Oakland University, Rochester, MI, USA

Laurent Binet Institut de Recherche de Chimie-Paris, CNRS, Chimie-ParisTech, Paris, France

Vsevolod Borovkov V. V. Voevodsky Institute of Chemical Kinetics and Combustion, SB RAS, Novosibirsk, Russia

Novosibirsk State University, Novosibirsk, Russia

Michael K. Bowman Department of Chemistry, The University of Alabama, Tuscaloosa, USA

Gianpiero Buscarino Department of Physics and Chemistry, University of Palermo, Palermo, Italy

Freddy Callens Department of Solid State Sciences, Ghent University, Ghent, Belgium

Hendrik De Cooman Department of Solid State Sciences, Ghent University, Ghent, Belgium

Marc F. Desrosiers Radiation Physics Division, National Institute of Standards and Technology, Gaithersburg, USA

Roland Erickson Department of Physics, Chemistry and Biology, Linköping University, Linköping, Sweden

Systems Development, SAAB Aeronautics, SAAB AB, Linköping, Sweden

Vladimir I. Feldman Department of Chemistry, Lomonosov Moscow State University, Moscow, Russia

Mamoru Fujitsuka The Institute of Scientific and Industrial Research (SANKEN), Osaka University, Ibaraki, Osaka, Japan

Michel Geoffroy Department of Physical Chemistry, University of Geneva, Geneva, Switzerland

Didier Gourier Institut de Recherche de Chimie-Paris, CNRS, Chimie-ParisTech, Paris, France

Wakako Hiraoka Laboratory of Biophysics, School of Science and Technology, Meiji University, Kawasaki, Japan

Osamu Inanami Laboratory of Radiation Biology, Graduate School of Veterinary Medicine, Hokkaido University, Sapporo, Japan

Erik Janzén Semiconductor Materials, IFM, Linköping University, Linköping, Sweden

Kenji Komaguchi Department of Applied Chemistry, Graduate School of Engineering, Hiroshima University, Hihashi-Hiroshima, Japan

Jun Kumagai Eco-Topia Science Institute, Nagoya University, Nagoya, Japan

Mikinori Kuwabara Laboratory of Radiation Biology, Graduate School of Veterinary Medicine, Hokkaido University, Sapporo, Japan

Anders Lund Department of Physics, Chemistry and Biology, Linköping University, Linköping, Sweden

Tetsuro Majima The Institute of Scientific and Industrial Research (SANKEN), Osaka University, Ibaraki, Osaka, Japan

Eirik Malinen Department of Physics, University of Oslo, Oslo, Norway

Department of Medical Physics, Oslo University Hospital, Oslo, Norway

Timothy W. Marin Chemical Sciences and Engineering Division, Argonne National Laboratory, Illinois, USA

Alexander G. Maryasov V. V. Voevodsky Institute of Chemical Kinetics and Combustion, Siberian Branch, Russian Academy of Science, Novosibirsk, Russia

Rudolf I. Mashkovtsev V.S. Sobolev Institute of Geology and Mineralogy, SB RAS, Novosibirsk, Russia

Yuriy Molin V. V. Voevodsky Institute of Chemical Kinetics and Combustion, SB RAS, Novosibirsk, Russia

Yuanming Pan Department of Geological Sciences, University of Saskatchewan, Saskatoon, Canada

Ewald Pauwels Center for Molecular Modeling, Ghent University, Zwijnaarde, Belgium

UGent HPC, Ghent University, Gent, Belgium

Einar Sagstuen Department of Physics, University of Oslo, Oslo, Norway

Tadao Seguchi Takasaki Advanced Radiation Research Institute, Japan Atomic Energy Agency, Takasaki, Japan

Michael D. Sevilla Department of Chemistry, Oakland University, Rochester, MI, USA

Masaru Shiotani Department of Applied Chemistry, Graduate School of Engineering, Hiroshima University, Hihashi-Hiroshima, Japan

Ilya A. Shkrob Chemical Sciences and Engineering Division, Argonne National Laboratory, Argonne, Illinois, USA

Nguyen Tien Son Semiconductor Materials, IFM, Linköping University, Linköping, Sweden

Dmitri Stass V. V. Voevodsky Institute of Chemical Kinetics and Combustion, SB RAS, Novosibirsk, Russia

Novosibirsk State University, Novosibirsk, Russia

Yuri D. Tsvetkov V. V. Voevodsky Institute of Chemical Kinetics and Combustion, Siberian Branch, Russian Academy of Science, Novosibirsk, Russia

Hervé Vezin Laboratoire Spectrochimie Infrarouge et Raman, CNRS, University of Lille 1, Villeneuve d'Ascq, France

Henk Vrielinck Department of Solid State Sciences, Ghent University, Ghent, Belgium

James F. Wishart Department of Chemistry, Brookhaven National Laboratory, Upton, New York, USA

Part I
Elementary Radiation Processes

Chapter 1

Fundamental Reaction Mechanisms in Radiation Chemistry and Recent Examples

Mamoru Fujitsuka and Tetsuro Majima

Abstract By using radiation chemical methods, such as γ -ray radiolysis and pulse radiolysis, powerful oxidative and reductive reagents, which are not available with other methods, can be generated to promote various reactions. The reaction pathways caused by these oxidative and reductive reagents can be followed by various spectroscopic methods, such as transient absorption and EPR. Therefore, radiation chemical methods are applicable to various systems in a wide variety of fields. For example, our research group has studied the mechanisms of various phenomena by means of radiation chemical methods. In the present chapter, fundamental reaction mechanisms of radiation chemistry are introduced in the initial part. Additionally, our radiation chemical investigations on charge delocalization process, radical ions in the excited state, photocatalytic systems, emitting device, and biological systems are introduced as examples of wide applicability of radiation chemical methods.

1.1 Introduction

For many years, radiation chemical methods, such as γ -ray radiolysis and pulse radiolysis, have been employed by a variety of researchers as a well-established chemical method [1–5]. Generation of powerful oxidative and reductive reagents, which cannot be obtained by other methods, should be the most important characteristic of radiation chemical methods: these species can be used to initiate redox reactions of various molecules and materials. Therefore, radiation chemistry provides powerful techniques for investigating intermediate species such as radicals and radical ions. It is known that the radical ion species can be generated by other methods such as chemical and electrochemical reactions and photoinduced electron transfer. However, in the cases of chemical and electrochemical reactions, control of the oxidation or reduction states is a rather difficult task for the molecules with similar first

T. Majima (✉) · M. Fujitsuka
The Institute of Scientific and Industrial Research (SANKEN),
Osaka University, Ibaraki, Osaka 567-0047, Japan
e-mail: majima@sanken.osaka-u.ac.jp

M. Fujitsuka
e-mail: fuji@sanken.osaka-u.ac.jp

© Springer International Publishing 2014
A. Lund, M. Shiotani (eds.), *Applications of EPR in Radiation Research*,
DOI 10.1007/978-3-319-09216-4_1

and second oxidation or reduction potentials. In addition, heterogeneous generation of radical ion species by electrochemical reaction causes difficulty in the analysis of the reactions. Furthermore, radical ion generation by photoinduced electron transfer means formation of radical ion pair. Thus, contribution of the counter ion species cannot be neglected. On the other hand, radiation chemistry retains many advantages over these methods including high oxidation or reduction ability. Furthermore, the performance of radiation chemistry facilities has been significantly improved by continuous efforts by scientists in this field. These improvements made radiation chemical study more reliable and reproducible.

Our research group has continuously carried out mechanistic investigations of chemical reactions by means of radiation chemical methods [6, 7]. From these studies, we have reported reaction mechanisms of redox reactions of fundamental molecules, excited states, mechanisms of devices that are close to practical application, and biological processes caused by redox reactions. In the present chapter, fundamental reaction mechanisms of radiation chemistry are summarized in the initial part. In addition, our recent researches based on the radiation chemistry were summarized as examples of such studies to show the wide applicability of radiation chemical methods. In the later section, four topics are summarized. The first topic is charge delocalization over stacked or expanded chromophores. By employing structurally well-defined molecules, detailed insight into charge delocalization was obtained. Negative charge delocalization over organic chromophores was also revealed. Charge delocalization in two-dimensionally expanded oligomer is also introduced. The second topic involves the properties of radical ions in the excited state, which can be generated by a combination of pulse radiolysis and laser flash photolysis. The third topic is the investigation of reaction mechanisms of systems related to practical applications such as the photocatalysts and light emitting devices. The fourth topic concerns the effect of radiation to biological materials. In particular, studies on oxidation processes in DNA and structural change of proteins upon irradiation are summarized.

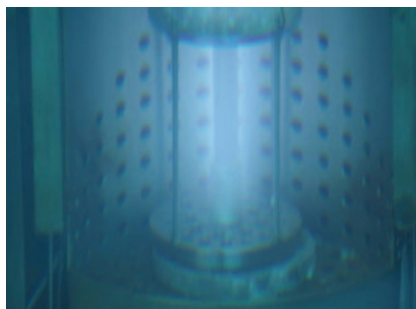
1.2 Fundamental Reaction Mechanisms in Radiation Chemistry

In this section, fundamental reaction mechanisms during γ -ray irradiation and pulse radiolysis are provided as a representative in radiation chemistry.

1.2.1 *Generation of Radical Ion of Substrate by γ -Ray Irradiation*

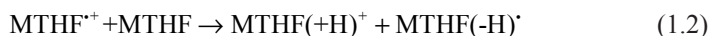
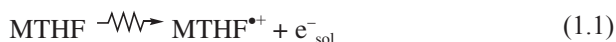
Generation of radical ions of solute molecule is normally carried out by γ -ray irradiation to low temperature (77 K or lower) glassy matrix of appropriate solvent, which has to be selected on the basis of preferred ion species, i.e., radical cation or

Fig. 1.1 γ -Ray source (^{60}Co , 265.7 TBq) emitting Cerenkov light at Osaka University



radical anion. By employing rigid matrices, conventional steady-state spectroscopic measurements including absorption, fluorescence, and EPR become possible, because chemical reactions of generated intermediates are inhibited in the rigid matrices where translational and rotational motions of solute are highly restricted. As γ -ray source, ^{60}Co and ^{137}Cs are often employed (Fig. 1.1). ^{60}Co disintegrates by emitting two cascade γ -rays of 1.17 and 1.33 MeV, generating ^{60}Ni . The half-life of ^{60}Co is 5.27 years. ^{137}Cs emits γ -ray of 0.66 MeV to generate ^{137}Ba with half-life of 30 years. Because of the high energy, the γ -ray irradiation causes inner-shell ionization, the Compton effect, and electron-positron pair formation, generating electron ejection. Although these processes are possible with both solvent and solute, direct ionization of solute molecules is usually negligible due to quite small population compared to solvent molecule. This point is quite different from photochemistry using UV or visible excitation light (1–4 eV), which excites only solute. After ionization of solvent due to radiolysis, ionized molecule and ejected electrons are deactivated by various energy dissipation processes and thermalized within picoseconds. The thermalized species can generate radical ion species as indicated in what follows.

For the formation of solute radical anion, 2-methyltetrahydrofuran (MTHF) is often used as a solvent. In MTHF, reduction of solute (S) by solvated electron (e_{sol}^-) occurs to form S radical anion ($\text{S}^{\cdot-}$) according to the following scheme:



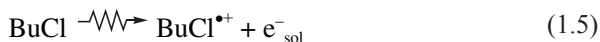
Reduction of S yielding $\text{S}^{\cdot-}$ by the similar reaction mechanism occurs in alkaline solutions such as ethers, amines, and alcohols.

Concentration of $\text{S}^{\cdot-}$ ($[\text{S}^{\cdot-}]$ (M)) generated by the γ -ray radiolysis can be estimated by the following equation:

$$[\text{S}^{\cdot-}] = (G_{\text{Itd}}/N)(1000/100) \quad (1.4)$$

where G is so-called G -value and defined as the total number of e^-_{sol} applicable to reduction of solute per 100 eV energy absorbed by the system, I is the radiation dose rate ($\text{eV g}^{-1} \text{min}^{-1}$), t is the irradiation time (min), d is the density of solvent at the temperature or frozen matrix at 77 K (g cm^{-3}), and N is the Avogadro number. In the case of the reduction of solute forming $S^{\bullet-}$ in MTHF, $G=2.55$ can be applied.

For generation of solute radical cation ($S^{\bullet+}$), saturated alkylhalides (RX) such as CCl_4 and buthylchloride (BuCl) are employed as a solvent. The oxidation reactions in BuCl are summarized as follows:



The concentration of the resulted radical cation [$S^{\bullet+}$] can be calculated on the basis of Eq. (1.4). G -value of s -BuCl is reported to be 3.25.

As indicated above, the employment of the glassy matrices realizes steady-state spectroscopic measurements of reactive intermediates due to restriction of molecular motion. Slight warming of the rigid glass causes softening of the matrices to start chemical reactions, and such processes can be also followed by various spectroscopic methods.

1.2.2 Generation of Radical Ions of Substrate by Pulse Radiolysis

In the pulse radiolysis, reactions are initiated by an electron pulse. The electron pulse can be generated by various types of radiation sources such as linear accelerator (linac) and Van de Graaf accelerator. The performance of accelerators depends on the facilities. For example, in the case of the L-band electron linac of Osaka University (Fig. 1.2), electrons injected from the gun (up to 91 nC) are bunched to 20–30 ps and accelerated up to 40 MeV through the acceleration tube. These values can be changed according to the condition of experiments. Furthermore, the laser-photocathode RF electron linear accelerator of Osaka University generates single bunch electron beam shorter than 100 fs. These electron pulses have been employed to follow the reactions in the time domain from sub-picosecond to millisecond.

Fast electrons generated by an accelerator lose its kinetic energy during the passing through the sample by scattering due to atoms or molecules, which causes either electronic excitation or ionization initially. The excited states or ionized species generated initially produce secondary products such as ions and radicals. For example, pulse radiolysis of water caused following ionization (1.8) and electronic excitation (1.9) as the primary processes:



Fig. 1.2 L-band linac of Osaka University



The ionized water undergoes rapid reaction with another water molecule to produce hydronium ion (H_3O^+) and hydroxyl radical (OH) in 10^{-11} s:



Ejected electrons are trapped by water after being thermalized to form thermalized electrons (e^-_{thermal}) and then hydrated electrons (e^-_{aq}).



The excited water (H_2O^*) dissociates in 10^{-13} s to give a hydrogen atom and a hydroxyl radical.



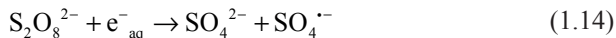
H_2O_2 is also a reactive intermediate generated from coupling of OH during the pulse radiolysis of water.



These primary species are localized in the track, called as spur, in which the electron pulse passed through. The generated primary species can escape from the spur with time by diffusion to react with other primary species or solute in water. The G -values are $G(e^-_{\text{aq}})=2.7$, $G(\text{H})=0.55$, $G(\text{OH})=2.75$, $G(\text{H}_2)=0.45$, $G(\text{H}_2\text{O}_2)=0.7$, $G(\text{H}^+)=2.9$, and $G(\text{OH}^-)=0.2$ [5].

As indicated above, various species are generated by the initial processes. Thus, for the selective generation of reaction intermediate of the solute, so-called

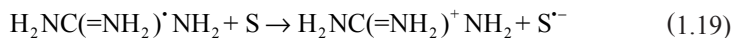
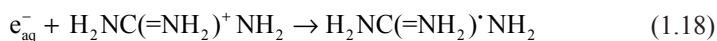
scavengers, which trap un-desirable intermediates, have to be included in the reaction system. For example, in order to achieve oxidation of DNA in water media, we employed a buffer solution including $S_2O_8^{2-}$ and *t*-BuOH ($(CH_3)_3COH$), since *t*-BuOH traps hydroxyl radical and $S_2O_8^{2-}$ generates oxidant $SO_4^{\cdot-}$ upon reaction with e_{aq}^- as summarized in (1.14, 1.15 and 1.16) [8].



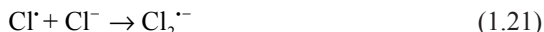
On the other hand, reduction of substrate can be achieved by e_{aq}^- as indicated by (1.17) in the presence of *t*-BuOH which traps hydroxyl radical according to (1.15).



Recently, we reported that guanidine HCl ($H_2NC(=NH_2)^+NH_2 \cdot Cl^-$), which is well known denaturant of protein, is effective to reduce solutes such as protein in solution according to the following scheme [9].

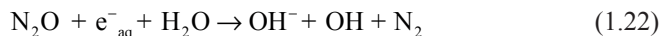


During the reduction process, Cl^- is used to trap hydroxyl radical according to the following scheme.



Although $Cl_2^{\cdot-}$ is a possible oxidizing reagent, it was confirmed that its effect was negligible in the study of reduction of cytochrome *c*.

For the oxidation reaction by hydroxyl radical, e_{aq}^- should be trapped. For this purpose, N_2O is often employed due to the reaction indicated in (1.22). In the pulse radiolysis study on the TiO_2 reaction mechanism, we employed N_2O -saturated water to generate hydroxyl radical according to following equation [10].

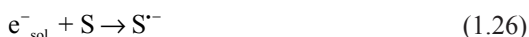


For reduction and oxidation of organic substrate in organic solvent, reactions similar to those indicated in the section above are applicable. For oxidation, alkyl halides such as 1,2-dichloroethane (DCE) and dichloromethane and benzonitrile are employed as solvents. On the other hand, MTHF and dimethylformamide are used as solvents for the generation of radical anions.

When the excitation energy level of solvent in the singlet and triplet excited states ($\text{RH}_{\text{S,T}}^*$) is higher than that of solute (S), it can be transferred to solute to generate solute in the singlet or triplet excited states ($\text{S}_{\text{S,T}}^*$),



where RH is hydrocarbon solvent such as cyclohexane and benzene and subscripts S and T indicate singlet and triplet, respectively. In addition to the energy transfer (1.23), recombination of the solute ions provides the solute in the excited states ($\text{S}_{\text{S,T}}^*$) according to the following mechanisms (1.24–1.29):



It should be noted that the formation of $\text{S}_{\text{S,T}}^*$ by the recombination mechanisms (1.24–1.29) is proposed by the observation of radical ion species of the solute based on the highly time-resolved experiments [4].

As summarized in this section, various reactive intermediates can be generated during the pulse radiolysis. Since the reactive intermediates are generated instantaneously, deactivation or reaction pathways of intermediates can be followed by various experimental methods with better time resolution. Characteristics of the experimental methods are summarized briefly [4].

Electronic transition of intermediates can be measured with transient absorption spectroscopy. In order to follow the reactions of oxidized or reduced solute in solution, measurements in nanosecond to millisecond time scale are essential, because generation of the oxidized or reduced solute by initially generated solvent-related species takes a few tens nanoseconds due to limitation of diffusion in solution. Transient absorption measurements in nanosecond to millisecond time scale can be achieved by using instruments similar to nanosecond laser flash photolysis. That is, combination of steady state or pulsed Xe lamps and gated CCD or photodetectors such as photodiode and photomultiplier realizes the measurements. It is notable that employment of near-IR sensitive photodiode such as InGaAs detector is effective to expand the spectral region. Relatively better signal to noise ratio can be achieved with smaller number of accumulation when compared with other spectroscopic methods.

For the detection of kinetic processes faster than nanosecond such as reactions of the initial species generated by radiolysis like hydrated electron, techniques similar to femtosecond pump & probe, i.e. stroboscopic method, are often employed. In such systems, duration of probe light has to be short and delay time with respect to the electron pulse is controlled by an optical delay. Thus, white continuum or output of an optical parametric amplifier is often employed as a probe light. For determination of kinetics of the intermediate, a number of events have to be accumulated, which causes longer estimation time as well as damage of the sample, usually. In order to diminish these problems, a streak scope can be used as a detector for these measurements, although time resolution is not so high when compared to above pump & probe type measurement.

If intermediate generated during pulse radiolysis is emissive, its emission can be detected by CCD or photodetector. By employment of a streak scope, better time resolution can be expected.

Vibrational spectra of intermediate can be also measured. Raman spectrum of the intermediate generated during pulse radiolysis can be measured by synchronization of the accelerator and pulse laser, which is used as Raman probe. Raman signal can be detected by a gated CCD and the time resolution is determined by the laser pulse duration. For Raman spectrum measurement with better signal to noise ratio, accumulation of substantial number of events is required.

EPR measurement of the intermediate during the pulse radiolysis is also achieved by averaging a number of events. To take a spectrum at a certain delay with respect to an electron pulse, the EPR signals are sampled and averaged by using a box-car averager, under slow sweep of the magnetic field. Time profiles of the intermediate can be obtained by a transient digitizer. Thus, the time resolution is not better than other methods, while the information on the electronic population is quite informative as summarized in this book.

1.3 Recent Examples of Radical Chemical Works

In this section, some of our works are introduced as examples of the wide applicability of radiation chemical methods.

1.3.1 *Charge Delocalization over Well-Defined Oligomer Systems*

1.3.1.1 **Positive and Negative Charge Delocalization on Stacked Benzene Rings**

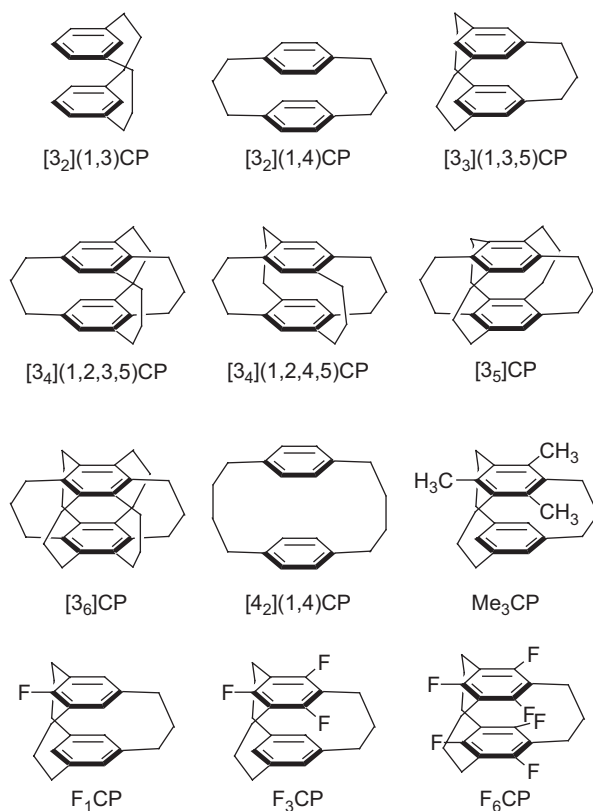
For years, charge transport in organic materials has been an attracting subject for a wide variety of researchers [11]. Recently, Miller et al. and Shanze et al. reported charge transport in conjugated polymers in the picosecond time scale using radiation

chemical methods [12, 13]. In these studies, well-defined polymeric structures and high time resolution are indispensable. It should be noted that the charge carrier in organic molecular materials is always stabilized by surrounding molecules [11]. Furthermore, the charge stabilized in the molecular solid exhibits behaviors different from charged molecules isolated in solution or in the gas phase. For understanding the effect of the stabilization in molecular solids, dimer of molecules can be regarded as the simplest model. The charge resonance (CR) band, which manifests an interaction between the radical ion and neutral molecule in a dimeric molecule, is a characteristic property of the charge stabilized over chromophores. Dimer radical cations of aromatic molecules have been extensively studied since the initial observation of the CR band by γ -ray radiolysis of aromatic compounds by Badger and Brocklehurst in the 1960s [14]. It is well recognized from numerous studies that the stabilization energy of the dimer radical cation, which can be evaluated from the peak position of the CR band, is closely related to the conformations of chromophores that form the dimer radical cation [15]. That is, a larger molecular overlap and shorter distance between chromophores generate highly stabilized dimer radical cations, which show CR band at shorter wavelength side. In spite of this simple relation, quantitative analysis on the relation between the structure and amount of stabilization energy was difficult to obtain, because the structure of chromophores in solution was difficult to determine or be fixed. To clarify the relationship between conformation of chromophores and stabilization energy, a molecular system with fixed conformation has to be employed.

Cyclophanes, which possess two benzene rings connected by alkyl chains (Fig. 1.3), will be ideal molecules for studies on charge delocalization because of well-defined face-to-face structure. X-ray crystallographic studies revealed that the distance between the two benzene rings in cyclophanes depends on the number of bridging alkyl chains. In addition, the face-to-face structure is kept even in the oxidized state [16]. It was also confirmed that their molecular structure could be estimated adequately using theoretical calculations based on the density functional theory. In order to elucidate the relationship between structure and stabilization energy, we studied the dimer radical cation of cyclophanes using the radiation chemical methods [17–21].

Among cyclophanes in the study, $[3_6]$ CP is expected to have the shortest transannular distance. The absorption spectrum of the $[3_6]$ CP radical cation, which was generated by pulse radiolysis using DCE as a solvent, showed a CR band at 667 nm, corresponding to 89.7 kJ mol⁻¹ of the stabilization energy [17]. The observed peak was located at a shorter wavelength than the commonly reported peak positions of the CR band (around 1–3 μ m), indicating the formation of highly stabilized dimer radical cation. Similarly stable dimer radical cation was confirmed with $[3_5]$ CP and $[3_3](1,3,5)$ CP, although the peak position varied with the number of linker: CP with many linkers gave CR band at shorter wavelength. In order to explain this finding quantitatively, we measured the CR bands of 12 cyclophanes by means of pulse radiolysis [18]. A series of data indicated that the peak position of the CR band tends to shift to longer wavelength side with an increase in the distance between the two benzene rings. The exchange interaction is expected to be important in the

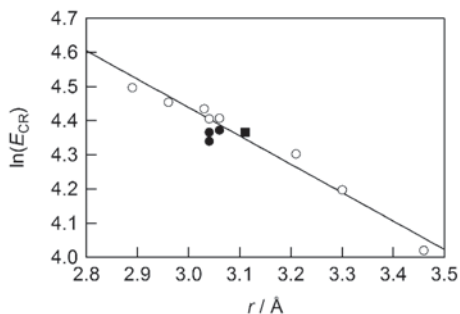
Fig. 1.3 Molecular structures of cyclophanes (CP). (Reprinted with permission from [18]. Copyright (2006) American Chemical Society)



interactions between the two benzene rings of $[3_n]CPs$. Therefore, the stabilization energy (E_{CR}) should be a function of the distance (r) between the two chromophores, i.e., $E_{CR} \propto \exp(-\beta r)$, where β is a constant. The estimated stabilization energy was plotted against the transannular distance in Fig. 1.4. The resultant linear relation indicates the importance of the exchange interaction in charge delocalization. The β value was estimated to be 0.83 \AA^{-1} . It was also confirmed that the electron-donating or electron-withdrawing nature of substituents does not significantly affect the stabilization energy.

For further understanding of charge delocalization over chromophores, the investigation of chromophore arrays with multi-layers is desirable. For cyclophanes, a series of multilayered cyclophanes were successfully synthesized. Therefore, we investigated the transient absorption spectra of three- and four-layered meta- and para-cyclophanes during the pulse radiolysis [19]. Local excitation (LE) and CR bands were successfully observed. It was revealed that the CR band shifted to longer wavelength side with the number of benzene rings. The stabilization energy estimated from the peak position of the CR band implied efficient charge delocalization over the multilayers of cyclophanes. Furthermore, the CR bands showed a slight peak position change attributable to change in the distribution of conformers.

Fig. 1.4 Distance (r) dependence on the stabilization energy (E_{CR}) for $[3_n]\text{CP}$ and $[4_2](1,4)\text{CP}$ (open circle), M_3CP (solid square), and F_nCPs (solid circle). Solid line is a fitted line for $[3_n]\text{CP}$ and $[4_2](1,4)\text{CP}$. (Reprinted with permission from [18]. Copyright (2006) American Chemical Society)



The CR band also exhibited a substantially long lifetime, which is due to the smaller charge distribution on the outer layers of multi-layered cyclophanes as expected from the theoretical calculation.

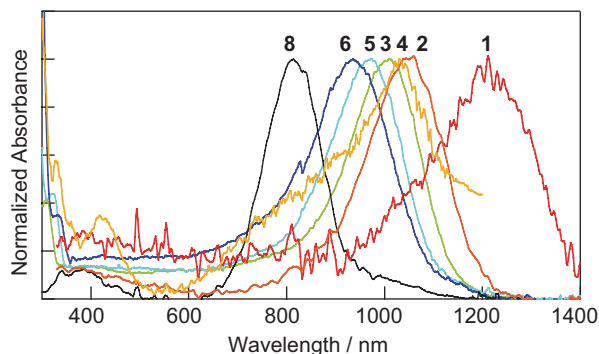
Although there are numerous studies on the delocalization of positive charge over chromophore arrays, the number of reports on delocalization of negative charge is quite small. In the case of the intermolecular dimer radical anions, Kochi et al. reported the CR band of some molecules with electron acceptor nature [22]. For cyclophane, in the 1960s, Ishitani and Nagakura reported an absorption spectrum of the radical anion of $[2_2]$ paracyclophane generated by chemical reduction at low temperature; $[2_2]$ paracyclophane showed a peak due to the dimer radical anion at 760 nm [23]. Despite these studies, a quantitative relation between structure and the stabilization energy of delocalized negative charge has not been estimated. Thus, we carried out γ -ray radiolysis of several cyclophanes and successfully observed the CR band due to the dimer radical anion (Fig. 1.5) [20]. It was confirmed that the peak position of the CR band shifts to longer wavelength side with an increase in the distance between the two benzene rings. This finding was also analyzed in terms of the exchange interaction indicated above. The β value of the dimer radical anion was estimated to be 0.62 \AA^{-1} , which is slightly smaller than that of the dimer radical cation (0.83 \AA^{-1}). This result indicates that negative charge delocalizes in stacked chromophores similarly to the positive charge; therefore, the negative charge is potentially an effective carrier in organic assemblies like positive charge.

The dimer radical anion was also observed with cyclophanes of benzothiadiazole, electron acceptor molecule [21]. In this case, two structural isomers, i.e., the *syn*- and *anti*-forms, were investigated. It was revealed that their stabilization energy depends largely on the overlap. These findings indicate that negative charge delocalization is possible in a variety of compounds when the two chromophores are held close to each other by alkyl chains.

1.3.1.2 Charge Delocalization on Two Dimensional Oligomers

As indicated in the above section, charge delocalized materials can be obtained by stacking of aromatic molecules. Connection of aromatic molecules by adequate

Fig. 1.5 Absorption spectra of γ -ray irradiated cyclophanes in MTHF glassy matrix. 1: $[3_2](1,3)$ CP, 2: $[3_2](1,4)$ CP, 3: $[3_3](1,3,5)$ CP, 4: $[3_4](1,2,4,5)$ CP, 5: $[3_4](1,2,3,5)$ CP, 6: $[3_3]$ CP, and 8: $[22](1,4)$ CP. (Reproduced from [20] with permission from The Royal Society of Chemistry)



covalent bond so as to expand the π -conjugation system is also effective to construct charge delocalized materials. To date various kinds of conjugated materials have been synthesized. Polyacetylene and polythiophene are well known polymeric materials with expanded π -conjugation systems. Among them, polyfluorenes have attracted wide attention due to their excellent optical and electric properties useful in various applications. To reveal their properties, an understanding of the charge states is important. From this viewpoint, radical ion species of oligofluorenes, which can be regarded as a model of polymers due to their well-defined structure, have been examined by means of radiation chemical methods [24].

These linear polymers and oligomers can be regarded as a conjugated material with a one-dimensional π -electron system. On the other hand, conjugated materials with a two-dimensional π -electron system have been realized by recent synthetic efforts. Among them, star-shaped oligofluorenes having a truxene (T) or isotruxene (IT) core are interesting (Fig. 1.6). Because T and IT can be regarded as three overlapping fluorene units, the conjugation pathway will be maintained through the core. To date various interesting optical and electronic properties have been reported for these star-shaped oligofluorenes. In order to understand these properties, we investigated radical ions species of these star-shaped oligofluorenes by means of γ -ray radiolysis to the glassy matrix [25].

The observed absorption spectra of radical ion species were in the range from the UV to near-IR regions. By using theoretical calculations, the observed peaks were assigned to electronic transitions. In the cases of radical cations, the near-IR bands were assigned to transitions from HOMO- n ($n \geq 1$) to HOMO, while the major visible band was assigned to transition from HOMO to LUMO (Fig. 1.7). In the cases of radical anions, on the other hand, the near-IR bands were assigned to transitions from HOMO to LUMO + n ($n \geq 0$), while the major visible band was assigned to transition from HOMO-1 to HOMO, which corresponds to HOMO to LUMO of the neutral molecules. Thus, it is indicated that the transition between HOMO and LUMO of the original neutral molecule is significant in the visible region both for radical cation and radical anion. Furthermore, structural changes generating more planar structure upon oxidation and reduction were indicated from the theoretical calculations. It is indicated that the charge is delocalized on the whole molecules. In addition, it is also indicated that the reduction induced larger structural change than oxidation.

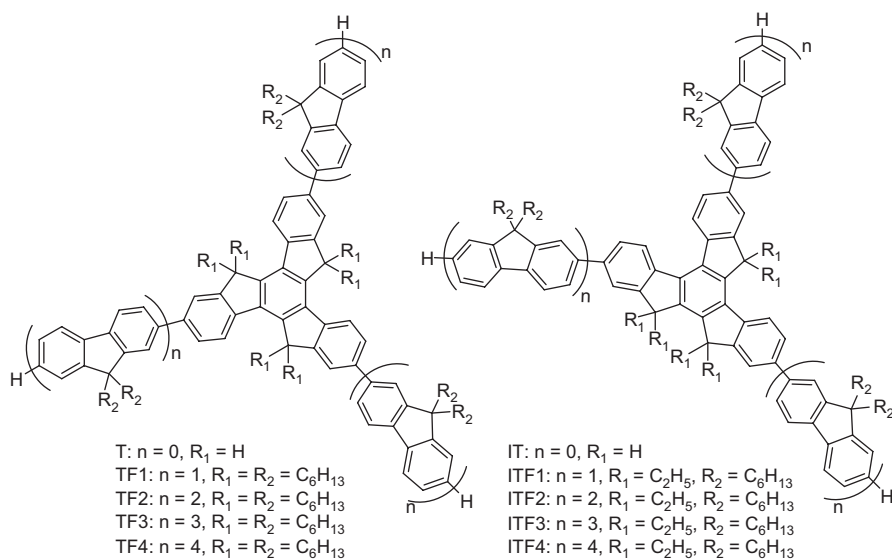
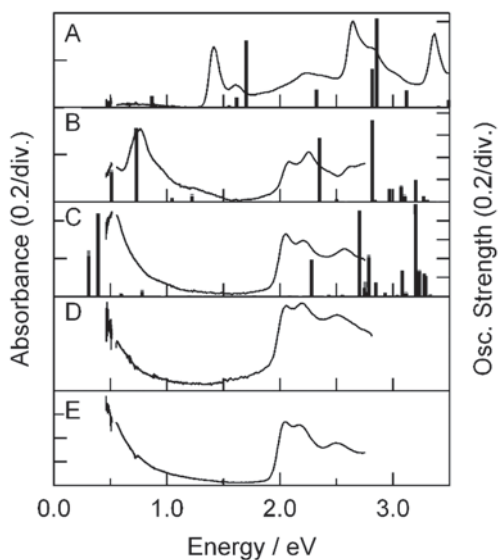


Fig. 1.6 Molecular structures of star-shaped oligofluorenes having T or IT as a core. (Reprinted from [25] with permission from Elsevier)

Fig. 1.7 Absorption spectra of ITF n in BuCl (A: IT, B: ITF1, C: ITF2, D: ITF3, E: ITF4) at 77 K after γ -ray irradiation. Bar indicates oscillator strength evaluated using TDDFT at UB3LYP/6-31G(d) level. Oscillator strengths for *syn*- and *anti*-conformers were indicated by gray and black, respectively. (Reprinted from [25] with permission from Elsevier)



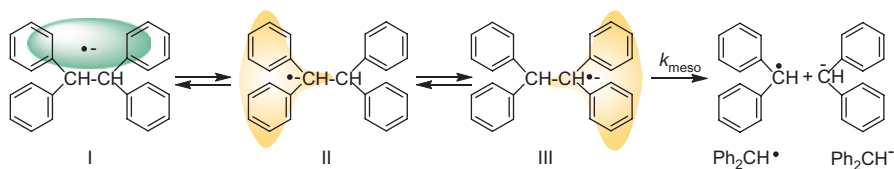


Fig. 1.8 Intramolecular negative charge delocalization and mesolysis of 1,1,2,2-tetraphenylethane. *I* denotes 1,2 dimer. *II* and *III* are 1,1-dimer. (Reprinted with permission from [26]. Copyright (2013) American Chemical Society)

1.3.1.3 Dissociation Reactions of Charge Delocalized Phenyl-Substituted Ethanes

As indicated in the above section, application of structural constraint to a molecular assembly realizes intramolecular negative charge delocalization. To confirm this issue with more simple organic compounds, we have examined intramolecular negative charge delocalization on phenyl-substituted ethanes: The number of the phenyl rings was varied from three to six [26]. Upon γ -ray irradiation, these phenyl-substituted ethanes showed absorption bands attributable to two kinds of intramolecular charge delocalization, i. e., delocalization over phenyls on the same carbon or that on different carbon atoms of the ethane molecule (namely, 1,1-dimer or 1,2-dimer, respectively. Figure 1.8). It is notable that the peak position of the CR band of the 1,2-dimer is located at longer wavelength side than that of 1,1-dimer, because of weak interaction due to longer distance: In the case of radical anion of 1,1,2,2-tetraphenylethane at 77 K, CR bands due to 1,1- and 1,2-dimer appeared at ~ 1500 and >2000 nm, respectively. It was revealed from the transient absorption measurements during the pulse radiolysis and absorption measurement of warmed glassy matrix sample after γ -ray irradiation that radical anion of polyphenyl-substituted ethanes undergoes mesolysis generating phenyl-substituted methyl anion and phenyl-substituted methyl radical. Since no mesolysis occurred with disappearance of 1,2-dimer radical anion, the importance of an interaction between π^* delocalized over 1,1-diphenyl and σ^* of C-C of the ethane backbone was indicated.

1.3.2 Dimer Radical Cation in the Excited State and Its Dissociation Reaction

During the pulse radiolysis, various intermediates are generated transiently. Since these transient species exhibit characteristic absorption bands different from the original molecule, selective excitation of intermediates to generate intermediates in the excited states is possible by using laser flash photolysis synchronized with pulse radiolysis. The excited intermediates are expected to possess various characteristic properties different from the ground state. The most important one should

be electron donor- or acceptor-ability higher than those in the ground state. In addition, by combination of pulse radiolysis and laser flash photolysis, reactions can be caused site-selectively, because the excited intermediate can be generated at the intersection of the electron beam and laser pulse. Furthermore, the amount of the excited intermediate can be controlled by radiation timing of these pulses. We already reported numerous reports on hole and electron transfer from radical cations and anions in the excited states, respectively [6, 27, 28]. For example, hole transfer from stilbene radical cation in the excited state to anisole was reported [27]. By assuming a diffusion-controlled reaction, the lifetime of the radical cation in the excited state was determined. Additionally, we reported that the fluorescence intensity from an radical cation in the excited state depends on the irradiation timing of the laser pulse with respect to the electron pulse [29], indicating that the amount of excited intermediate can be controlled by the radiation timing.

Higher reactivities of the excited intermediate were also observed with other reactions [30]. For example, it was revealed that excitation of the radical ion species induced bond cleavage, even when such cleavage did not occur from the ground state radical ions.

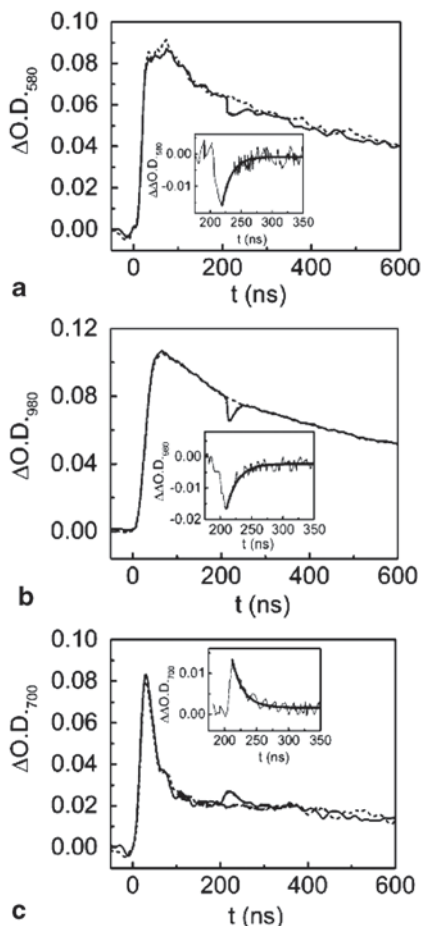
Although the properties of dimer radical cations have been well investigated, those in the excited states have not been reported. This topic is informative, because charge injected to organic materials is expected to be a “hot” carrier corresponding to the excited state in many cases. From this viewpoint, we studied the properties of dimer radical cations in the excited state using the pulse radiolysis-laser flash photolysis combined method [31]. In order to study the excited dimer radical cation, the dimer radical cation of naphthalene ($\text{Np}_2^{+\cdot}$) was selected, because $\text{Np}_2^{+\cdot}$ shows a CR band around 1000 nm, which can be selectively excited by the fundamental pulse of Nd:YAG laser (1064 nm).

$\text{Np}_2^{+\cdot}$ was generated by the pulse radiolysis of Np in DCE. When the CR band of $\text{Np}_2^{+\cdot}$ was excited by the 1064 nm laser flash, the bleaching and recovery of $\Delta\text{O.D.}$ at 580 and 980 nm were observed with the concomitant growth and decay of $\Delta\text{O.D.}$ at 700 nm (Fig. 1.9). The immediate decay of the CR (980 nm) and LE (580 nm) bands of $\text{Np}_2^{+\cdot}$ and the rise of the $\text{Np}^{+\cdot}$ band (700 nm) indicate dissociation of $\text{Np}_2^{+\cdot}$ from $\text{Np}_2^{+\cdot*}$ to generate $\text{Np}^{+\cdot}$ and Np. On the other hand, recovery of these bands indicates quantitative regeneration of $\text{Np}_2^{+\cdot}$ by the dimerization of $\text{Np}^{+\cdot}$ and Np.

It should be noted that the yield of the dissociation of $\text{Np}_2^{+\cdot*}$ is quite low (3.2×10^{-3}), indicating that the main deactivation pathway of $\text{Np}_2^{+\cdot*}$ is internal conversion to generate the ground state. In addition, the recombination of the radical cation and neutral molecule in the solvent cage should be efficient and finished within laser duration. These findings indicate that the energy imparted to $\text{Np}_2^{+\cdot}$ is only partly used for dissociation to Np and $\text{Np}^{+\cdot}$; the majority of the excitation energy is dissipated by rapid internal conversion, which should be the important process when the fate of the “hot” carrier in the organic materials is considered.

Photodissociation of dimer radical cations was also examined by using pyrene (Py) [32]. In the case of $\text{Py}_2^{+\cdot}$, the excitation pulse at 532 nm was absorbed by the LE band of the dimer radical cation, indicating the formation of dimer radical cation in the higher excited state. The quantum yield of photodissociation of

Fig. 1.9 Kinetic traces of $\Delta O.D.$ during the pulse radiolysis-laser flash photolysis of naphthalene in DCE at **a** 580, **b** 980, and **c** 700 nm. (Reprinted with permission from [31]. Copyright (2006) American Chemical Society)

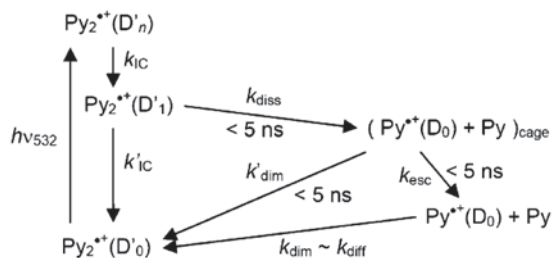


Py_2^{++} was estimated to be 2.9×10^{-3} and the regeneration of Py_2^{++} occurred at the rate constant of $4.8 \times 10^9 \text{ M}^{-1} \text{ s}^{-1}$ in DCE which is almost equal to k_{diff} ($8.5 \times 10^9 \text{ M}^{-1} \text{ s}^{-1}$). From the comparison with dissociation of Np_2^{++*} , it was suggested that the photodissociation of Py_2^{++} occurred from the lowest-excited state $Py_2^{++}(D'_1)$, even though Py_2^{++} was initially excited to the higher-excited $Py_2^{++}(D'_n)$, due to the rapid internal conversion from $Py_2^{++}(D'_n)$ to $Py_2^{++}(D'_1)$ (Fig. 1.10). Consequently, the internal conversion rate is one of the major factors which govern the yield of the dissociation of Py_2^{++} .

1.3.3 Clarification of Photocatalytic Reaction by Radiation Chemistry

Titanium dioxide (TiO_2) has been widely used as a photocatalyst and charge transport material in dye-sensitized solar cells because of high photo-activity and preferable

Fig. 1.10 Schematic diagram of dissociation process of Py dimer radical cation ($\text{Py}_2^{+\bullet}$) via higher excited state. (Reprinted from [32], with permission from Springer)

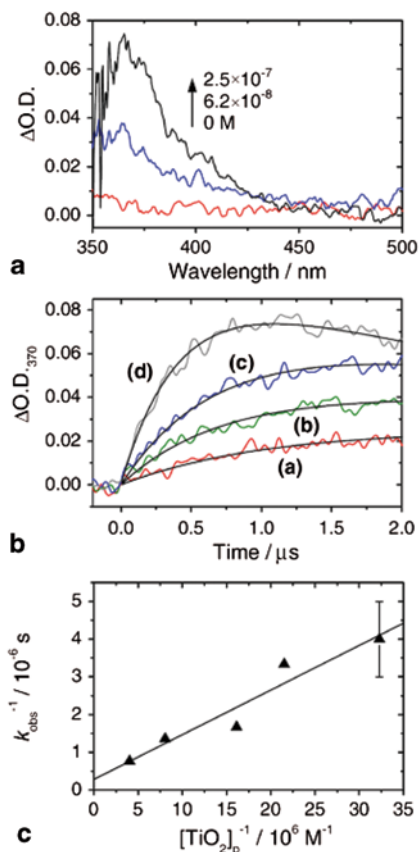


electric characteristics as well as high stability under various conditions. In the applications to photocatalysts, generation of the electron/hole pair upon absorption of a photon with a greater energy than the band gap (3.2 eV) is an initial important process. The electron/hole pair generates a trapped hole and surface-bound OH radicals, which are responsible for the initiation of a wide variety of photocatalytic one-electron redox reactions. However, information about the oxidizing ability of the surface-bound OH radicals is scarce. In order to clarify its oxidizing ability in physical chemical manner, pulse radiolysis was applied [10], since the generation of OH radicals is well established in the field of radiation chemistry as summarized in (1.8–1.13). The pulse radiolysis of N_2O -saturated colloidal TiO_2 aqueous solution generated OH radicals according to (1.22) which were strongly adsorbed on the TiO_2 particles with an apparent association constant of $\sim 10^6 \text{ M}^{-1}$. The OH radicals trapped on the TiO_2 surface exhibited an absorption with a maximum at 370 nm (Fig. 1.11). To clarify the oxidation ability of this species, the oxidation processes of 4-methylthiophenylmethanol (MTPM) and 2-phenylthioethanol (PTE) in an aqueous solution of the colloidal TiO_2 were studied on the basis of a kinetic analysis of the transient absorption. It was revealed that the oxidation ability of the surface-bound OH radical is high but still lower than that of free OH radicals in solution. On the basis of the oxidation potentials of MTPM and PET, it was proposed that the redox potential of surface-bound OH radicals is higher than 1.6 V vs. NHE. Therefore, using the pulse radiolysis method, the nature of surface-bound OH radicals was elucidated.

1.3.4 Emission Process by Recombination of Radical Ion Species Generated during Pulse Radiolysis

Electrochemical luminescence (ECL) devices utilize the emission from excited molecules generated by the recombination process of radical cation and radical anion, which were formed by electrochemical oxidation and reduction, respectively. The emission is primarily resulted from the singlet excited state generated by recombination, while contribution of excimer and/or exciplex is also possible. In addition, the singlet excited state generated by triplet-triplet annihilation will be included in emission mechanisms. However, the mechanism for the formation of the singlet excited state and/or excimer as the emissive species was not fully un-

Fig. 1.11 **a** Transient absorption spectra at 1 μs after an electron pulse during the pulse radiolysis of colloidal TiO_2 aqueous solution (TiO_2 concentration: 0, 6.2×10^{-8} and 1.2×10^{-7} M). **b** Time profile of $\Delta\text{O.D.}$ at 370 nm (TiO_2 concentration: *a* 0, *b* 6.2×10^{-8} , *c* 1.2×10^{-7} , and 2.5×10^{-7} M). **c** The Benesi–Hildebrand plot for the $[\text{TiO}_2]_{\text{p}}^{-1}$ vs k_{obs}^{-1} , where $[\text{TiO}_2]_{\text{p}}$ denotes concentration of TiO_2 particle. (Reprinted from [10], with permission from Elsevier)



derstood. Especially, its kinetics is not known. As summarized in Eqs. (1.24–1.29), pulse radiolysis of nonpolar solvents such as benzene (Bz) generates the hole and electron pair, which undergoes fast geminate charge recombination to mainly produce solvent molecules in the excited states. In addition, a small fraction of the holes and electrons escape to generate radical cations and radical anions of the solute, respectively. Since the recombination of radical cation and radical anion of the solute generates the solute in the excited state, emission from the solute in the excited state is expected. These reactions are similar to the ECL mechanisms. Therefore, the kinetic aspects can be obtained from the study of the pulse radiolysis of the solute in nonpolar solvents [33–40].

We measured emission spectra of various aromatic hydrocarbons (AHs) in Bz during pulse radiolysis [33]. Generation of an emissive molecule can be attributed to charge recombination of radical cation and radical anion as indicated above. This emission mechanism is supported by the relationship between the annihilation enthalpy change ($-H^\circ$) for charge recombination and the excitation energies of $^1\text{AH}^*$ (E_{S1}): It was confirmed that the ratio of fluorescence intensity (I) and fluorescence

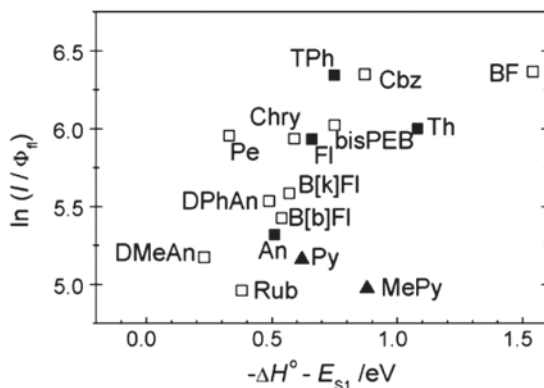


Fig. 1.12 Relation between $\ln(I/\phi_{fl})$ and $-\Delta H^\circ - E_{S_1}$, where I and ϕ_{fl} are emission intensity and fluorescence quantum yield, respectively. Characters close to marks indicate compounds name: *An*: anthracene, *BF*: 2,3-benzofluorene, *bisPEB*: 1,4-bis(phenylethynyl)benzene, *B[b]Fl*: benzo[b]fluoranthrene, *B[k]Fl*: benzo[k]fluoranthrene, *Chry*: chrysene, *Cz*: carbazole, *DMeAn*: 9,10-dimethylanthracene, *DPhAn*: 9,10-diphenylanthracene, *Fl*: fluoranthene, *MePy*: 1-methylpyrene, *Pe*: perylene, *Py*: pyrene, *Te*: tetracene, *Th*: thianthrene, *TPh*: triphenylene, *Rub*: rubrene. (Reprinted from [33], with permission from Elsevier)

quantum yield (ϕ_{fl}), which relates to the rate constant of the charge recombination of AH^{*+} and AH^{*-} , increases with an increase of the energy difference between $-H^\circ$ and E_{S_1} (Fig. 1.12), which corresponds to the driving force for charge recombination. Therefore, the observed tendency accords with the electron transfer theory, supporting the emission mechanisms based on the charge recombination between radical cation and radical anion generated by the pulse radiolysis.

Furthermore, we applied the pulse radiolysis technique to a variety of donor-acceptor compounds including compounds that were developed for ECL applications (Fig. 1.13) [34–37]. These molecules showed emission attributable to formation of the singlet excited state and excimer/excplex. It was shown that both quantitative and qualitative explanations of the emission intensity can be given on the basis of the redox and structural properties. In the case of donor-acceptor quinolones with an ethynyl linkage (PnQ in Fig. 1.13), the emission due to the charge recombination was explained on the basis of positive and negative charge localization on donor and acceptor moieties, respectively, in the radical ion state, in accordance with the ECL mechanisms [34]. The localization of the charge in the radical ion state was also indicated for phenylethynyl substituted cyanoanthracenes (PEA etc. in Fig. 1.13) [35, 36]. In the case of PEA, which takes a planar structure, both monomer and excimer emission occurred upon charge recombination. On the other hand, DEA with twisted structure showed strong charge transfer emission. Excimer emission was also confirmed with arylethynyl substituted pyrenes [37].

During the pulse radiolysis of the benzene solution of donor-acceptor substituted tetrakis(phenylethynyl)benzenes (TAEB, Fig. 1.14), emission with a peak, which largely depends on the CT character induced by substituents as well as its

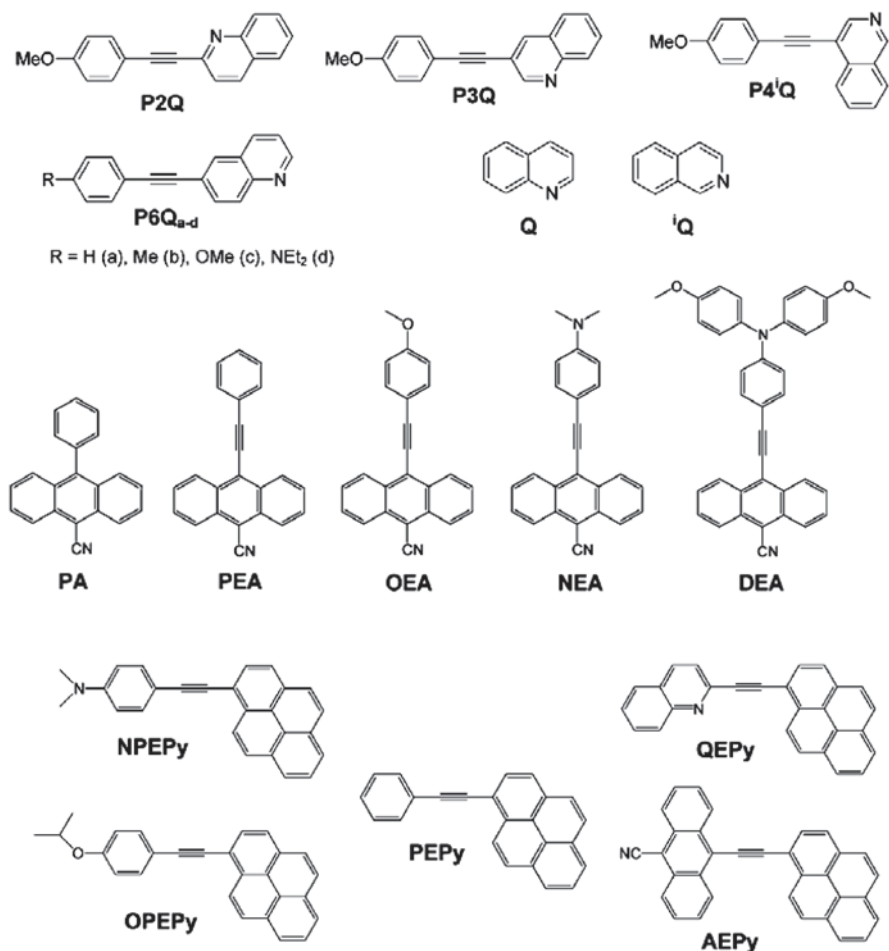


Fig. 1.13 Structure of donor-acceptor molecules investigated using pulse radiolysis. (Reprinted with permission from [34–37]. Copyright (2005, 2006) American Chemical Society)

conjugation pathway, was observed [38, 39]. Because donor/acceptor substituted TAEBs possess three types of conjugation pathways (linear conjugated, cross-conjugated, and bent conjugated pathways between donor and acceptor substituents through ethynyl linkage), CT interaction largely depends on the substitution patterns. It was revealed that the emission peak varied from 405 to 640 nm depending on the substitution pattern [38, 39]. These results will be interesting examples showing that the substitution pattern allows one to control the emission peak precisely.

It is interesting to note that a dimerization reaction of the radical anions of bis(phenylethynyl)benzenes was found during the study of their radical ion species [41] similar to that of the radical anion of biphenylacetylene [6].

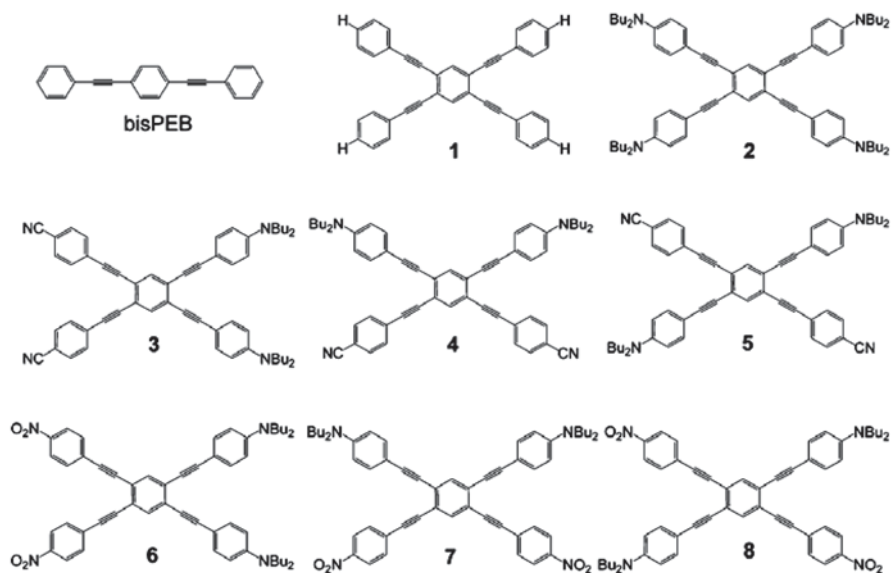


Fig. 1.14 Molecular structures of donor-acceptor substituted tetrakis(phenylethynyl)benzenes. (Reprinted with permission from [38, 39]. Copyright (2007, 2008) American Chemical Society)

1.3.5 Application to Biological Systems

1.3.5.1 Charge Transfer in DNA

For years, biological systems have been important subjects for radiation chemistry because of the significant interests on the effects of radiation to biological systems. One of the well investigated materials from the viewpoints of the radiation effects is DNA, because it is well known that the oxidation and reduction of DNA are closely related to DNA damage and repair, respectively [42–44]. To understand DNA damage or repair at a site apart from the initially oxidized or reduced sites, respectively, charge transfer along DNA has to be taken into account. Thus, charge transfer in DNA has been investigated by many researchers. Our research group has also investigated charge transfer in DNA using various methods including pulse radiolysis.

Nowadays, it is widely accepted that both tunneling and hopping mechanisms are included in hole transfer in DNA [45]. For the tunneling mechanism, the hole transfer rate (k_{HT}) can be expressed by a β factor of $0.6\text{--}0.7 \text{ \AA}^{-1}$ in $k_{HT} \propto \exp(-\beta r)$, where r is the distance between the donor and acceptor [46, 47], while the hopping mechanism provides a smaller β value [48]. In order to estimate the β value, our research group applied pulse radiolysis to pyrene (Py)-conjugated oligodeoxynucleotides (ODNs) in the presence of $\text{K}_2\text{S}_2\text{O}_8$, which generates oxidant $\text{SO}_4^{\cdot-}$ upon reaction with e_{aq}^- to realize oxidation of DNA and/or Py according to (1.14, 1.15 and 1.16). Upon oxidation of ODN, hole transfer from G moiety in ODN to Py or from Py to 8-oxo-7,8-dihydroguanine (oxG) was expected [49]. From transient

absorption measurements during the pulse radiolysis, both hole transfers were confirmed. From the distance dependence of the observed hole transfer rate from Py to oxG, the β value was estimated to be 0.6 \AA^{-1} in accordance with the reports by other research groups.

It is well known that multistep hopping mechanism makes long range hole transfer in DNA possible. In order to clarify the factors that govern the hopping rate, we employed Py-modified DNA in the pulse radiolysis study. By analyzing the kinetic trace of the transient absorption band of a Py radical cation ($\text{Py}^{+\bullet}$) formed by hole transfer from DNA to Py, the rate constants for hole transfer in various sequences of DNA were determined [8]. It was revealed that the rate constants of the hole transfer from the nearest G to Py were weakly dependent on the distance between them, indicating the hole transfer in DNA by the multistep hopping mechanism. In contrast, in the hole transfer where the rate-determining step was the single-step hole transfer between guanines (Gs), the rate was strongly dependent on the distance. By comparing the intervening nucleobases between Gs, it was revealed that the rate constants of multistep hole transfer were in the order of $\text{G}^{+\bullet}\text{AG} > \text{G}^{+\bullet}\text{AC} > \text{G}^{+\bullet}\text{TG}$. These results showed that A can mediate hole transfer between Gs effectively. The effect of multiple Gs (GGG) on multistep hole transfer was also examined. It was indicated that the hole transfer from DNA to Py became slow when the GGG site is located at a distant position from Py. The hole transfer rate in ODN with seven base pairs between Py and GGG decreased by one order when compared to that of ODN with one base pair between Py and GGG. The present finding indicates that the multiple G acts as an efficient hole trap site, which decreases the hole transfer rate in ODN.

In addition to the GGG consecutive site, we investigated the possibility of the planar G quartet in G quadruplex as a hole trapping site by means of the transient absorption measurement during the pulse radiolysis (Fig. 1.15) [50]. It was revealed that the spectrum of G+C observed from the G-quadruplex is red-shifted compared to the spectra with two or three consecutive G bases (Fig. 1.16), supporting that the hole trapping in the planar G quartet of the G-quadruplex is favored because of the delocalized positive charge along the more extended π orbitals. Meanwhile, the spectra with absorption maxima at 390 and 550 nm observed at longer delay times are due to the neutral radical of G [$\text{G}+\text{C}(-\text{H})$], which is the deprotonated species of G+C. The rate constant for the formation of $\text{G}+\text{C}(-\text{H})$ was determined to be $4.0 \times 10^6 \text{ s}^{-1}$. Therefore hole trapping process in DNA was reasonably investigated by the radiation chemical method.

As indicated above, mechanisms of hole transfer are well established. On the other hand, the report on excess electron transfer is rather limited, probably because reduction of nucleobases is rather difficult due to their low reduction potentials. Thus, application of radiation chemical methods is effective in the study of the excess electron transfer in DNA. By applying EPR to the γ -ray-irradiated DNA at low temperature, Sevilla et al. reported the contribution of tunneling and hopping mechanisms in excess electron transfer in DNA [51]. Kobayashi et al. revealed the delocalization of the excess electron over nucleobases using pulse radiolysis [52]. Our research group investigated excess electron transfer in DNA conjugated with naphthalimide (NI) using the pulse radiolysis method [53]. Reduction of DNA was

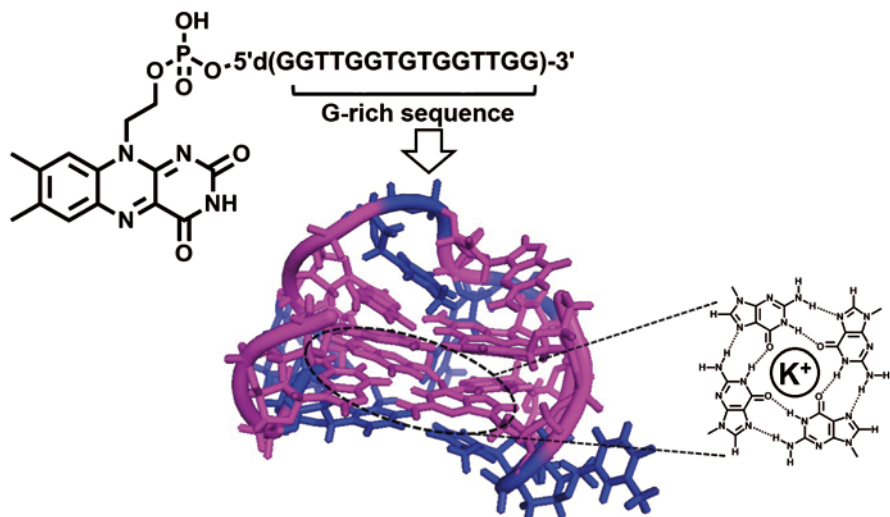


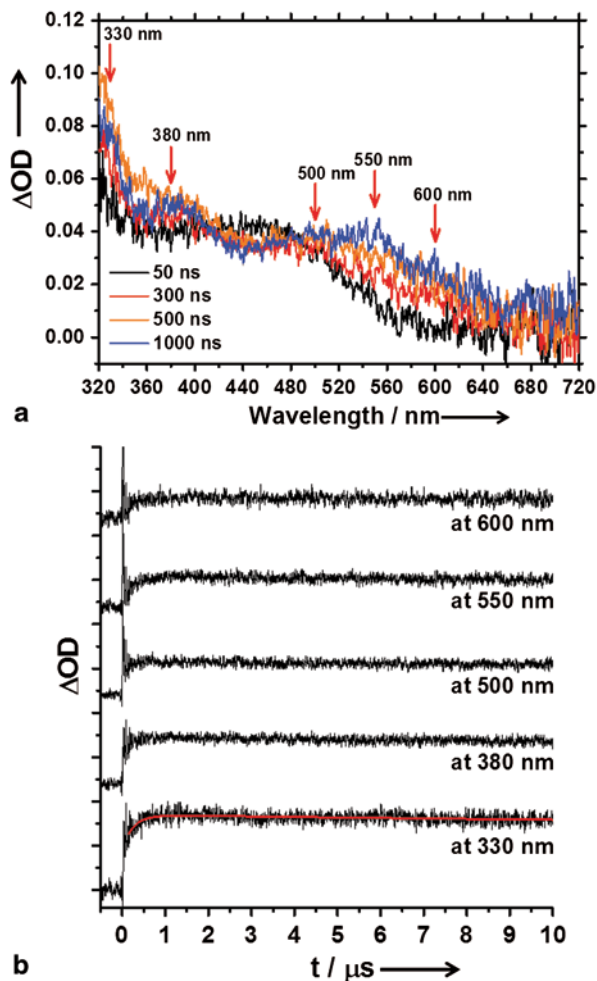
Fig. 1.15 Molecular structure of riboflavin labeled oligonucleotide and G-quadruplex. (Reprinted from [50], with permission from Wiley)

achieved according to (1.17). Although the formation of radical anion of NI ($\text{NI}^{\cdot-}$) due to excess electron transfer from DNA to NI was expected, the component due to excess electron transfer was not confirmed in the time profile of $\text{NI}^{\cdot-}$, indicating that excess electron transfer in DNA occurs very quickly. This assumption was confirmed by our recent laser flash photolysis studies on oligothiophene or *N, N*-dimethylaminopyrene conjugated DNA [54, 55].

1.3.5.2 DNA Motion

Conformational change of DNA is also an important subject in biological science because DNA is known to take a variety of structures, which relate to its biological functions. To reveal such DNA structures, various structural probes have been developed. For this purpose, the FRET system using fluorescence probes has been often employed. It should be noted that a probe which can monitor DNA structure in a long time domain is preferable. From this viewpoint, we examined to utilize the CR band which can be generated during the pulse radiolysis as a structure probe of DNA [56]. For this purpose, the formation of a Py dimer radical cation ($\text{Py}_2^{\cdot+}$) in doubly Py-conjugated ODNs upon one-electron oxidation during the pulse radiolysis was investigated (Fig. 1.17). The formation of $\text{Py}^{\cdot+}$ within 5 μs was confirmed by the observation of a 470 nm-band during the pulse radiolysis of doubly Py-conjugated ODN in D_2O in the presence of $\text{K}_2\text{S}_2\text{O}_8$. With the decay of $\text{Py}^{\cdot+}$, the concomitant formation of $\text{Py}_2^{\cdot+}$, which has an absorption peak at 1500 nm (CR band), was confirmed in the time range of $\sim 100 \mu\text{s}$. The rate of formation of $\text{Py}_2^{\cdot+}$ in DNA reflects the dynamics of DNA, which allows the interaction between $\text{Py}^{\cdot+}$ and Py, since the transient DNA structure is trapped by the attractive CR interaction to

Fig. 1.16 **a** Transient absorption spectra during the pulse radiolysis of G-quadruplex (5'-TAGGG(TTAGGG)₃TT-3') in potassium buffer. **b** Kinetic profiles of $\Delta O.D.$ at indicated wavelengths. *Red curve* indicates fitted curve obtained by global analysis. (Reprinted from [50], with permission from Wiley)



produce Py_2^{+} . The formation rate of Py_2^{+} , which has a characteristic CR absorption band in the near-IR region, is useful to obtain structural and dynamic information on transient DNA structures in the time range of 1 μs to 1 ms. Application of the CR band is also beneficial, because the CR bands usually appear at a wavelength region where other species do not exhibit absorption. These results indicate that pulse radiolysis is also useful for investigating the various dynamic aspects of DNA such as charge transfer and conformational motions.

1.3.5.3 Protein Dynamics

Since the oxidation and reduction processes promote various biological process, pulse radiolysis will be one of the promising methods for these studies although examples of pulse radiolysis work on the biological systems are rather limited.

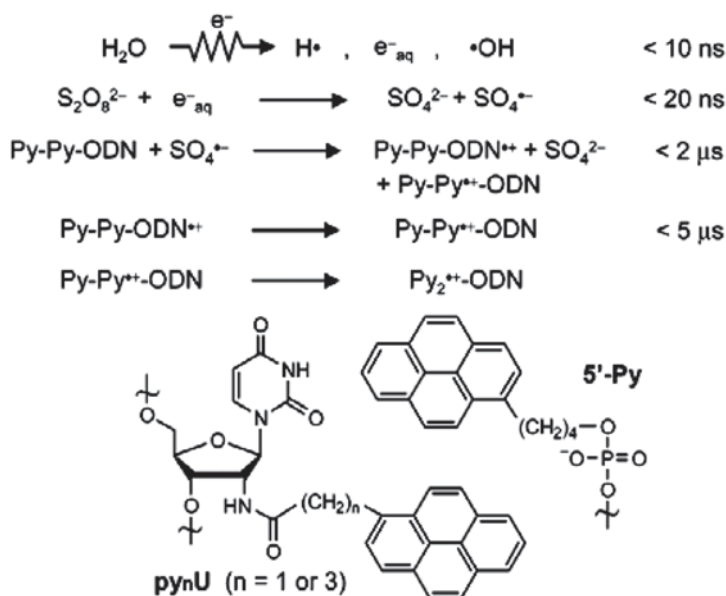


Fig. 1.17 Formation of Py dimer radical cation ($\text{Py}_2^{\bullet+}$) in Py-modified DNA (Py-Py-ODN) during the pulse radiolysis. (Reprinted with permission from [56]. Copyright (2003) American Chemical Society)

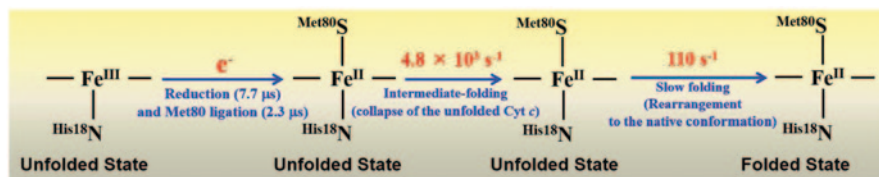


Fig. 1.18 Folding dynamics of oxidized Cyt c upon reduction during the pulse radiolysis. (Reprinted with permission from [9]. Copyright (2012) American Chemical Society)

We applied the pulse radiolysis to reveal the folding process of cytochrome c (Cyt c) [9]. In order to realize selective reduction of oxidized Cyt c, we applied high concentration of the denaturant, guanidine HCl (GdHCl , $\text{H}_2\text{NC}(=\text{NH}_2)^+\text{NH}_2\cdot\text{Cl}^-$), which generates guanidine radical as a reducing reagent from the reaction between the solvated electron and guanidine as indicated in (1.18, 1.19, 1.20 and 1.21). From the kinetic profile of $\Delta\text{O.D.}$ at Q-band region during the pulse radiolysis of Cyt c, it was confirmed that ligation of Met80 and reduction of oxidized Cyt c occurred with time constants of 2.3 and 7.7 μs (Fig. 1.18). We also suggested that the dynamics which is characterized by 204 μs of the time constant is due to the intermediate-folding kinetics corresponding to the collapse of the unfolded Cyt c into a compact denatured structure. In addition, the slow dynamics (110 s^{-1}) attributable to the rearrangement to the native conformation was observed. These results indicate that application of pulse radiolysis is also effective to investigate the dynamics of proteins upon oxidation and reduction processes.

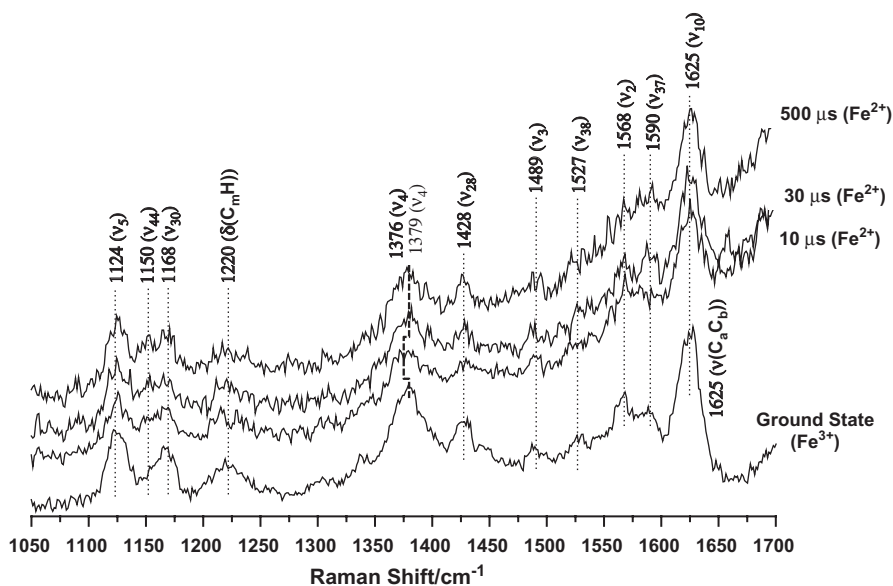


Fig. 1.19 Time-resolved resonance Raman spectra of metMb in the presence of GdHCl during the pulse radiolysis in buffer solution [57]

By employing the reduction agent generated by the pulse radiolysis, we also investigated folding dynamics of myoglobin (Mb) upon reduction [57]. To obtain structural information, we combined pulse radiolysis and time-resolved resonance Raman spectroscopy. Upon reduction, the folded metmyoglobin (metMb), which has a six-coordinated heme geometry linked with a water molecule as a distal ligand, is structurally relaxed to the deoxymyoglobin (deoxyMb) form with a five-coordination heme geometry without water ligand. Meanwhile, the Raman spectrum of an unfolded metMb is almost identical to those of the unfolded deoxyMb formed by the reduction (Fig. 1.19), indicating that both unfolded metMb and deoxyMb have similar heme geometries. The results provided herein show that upon reduction, the folded metMb with a six-coordinated heme geometry is structurally relaxed to deoxyMb with a five-coordination heme geometry, while both unfolded metMb and deoxyMb have a six-coordinated heme geometry linked with a water molecule or histidine as a distal ligand (Fig. 1.20).

1.4 Summary

In the initial part of the present chapter, fundamental reaction mechanisms in radiation chemistry are introduced. Because radiation chemical methods provide powerful oxidative and reductive species, radiation chemical methods can be applied to a variety of systems where oxidation and reduction processes play important roles.

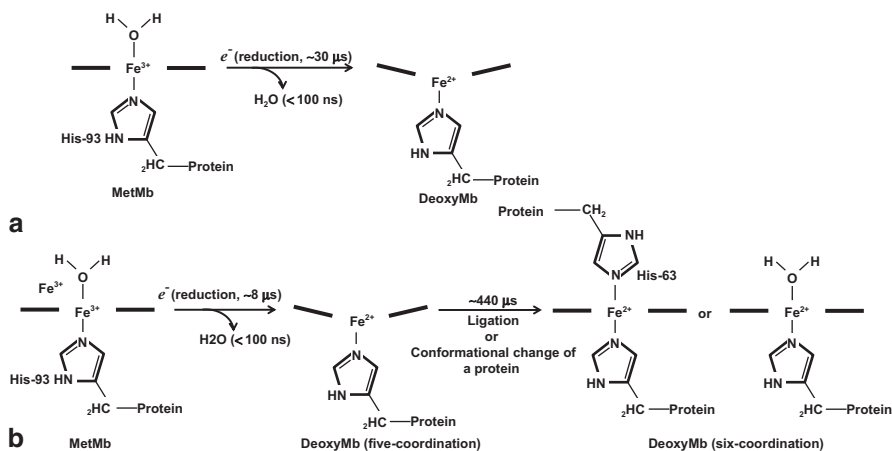


Fig. 1.20 Proposed structural change in the heme moiety of both folded (a) and unfolded (b) metMb followed by one-electron reduction [57]

The time resolution of these systems is much improved nowadays. Furthermore, the application of various time-resolved spectroscopic techniques, such as IR, Raman, EPR, and so on, will enhance the availability of radiation chemical methods for researchers. Actually, we have been engaged to the studies on the variety of subjects as introduced in this section. Thus, the continuous contribution of the radiation chemical methods to a wide variety of research fields is expected.

Acknowledgments We thank the members of the Research Laboratory for Quantum Beam Science of SANKEN, Osaka University, for running the linear accelerator. This work has been partly supported by a Grant-in-Aid for Scientific Research (Projects 25220806, 25288035, and others) from the Ministry of Education, Culture, Sports, Science and Technology (MEXT) of Japanese Government.

References

1. Kaiser ET, Kevan L (eds) (1968) Radical ions. Wiley, New York
2. Shida T (1988) Electronic absorption spectra of radical ions. Elsevier, New York
3. Lund A, Shiotani M (eds) (1991) Radical ionic systems: properties in condensed phases. Kluwer Academic, Dordrecht
4. Tabata Y, Ito Y, Tagawa S (eds) (1991) CRC handbook of radiation chemistry. CRC Press, Boston
5. Tabata Y (eds) (1991) Pulse radiolysis. CRC Press, Boca Raton
6. Majima T (2004) Application to reaction mechanism studies of organic systems. In: Mozumder A, Hatano Y (eds), Charged particle and photon interaction with matter, Marcel Dekker, New York, pp 645–696
7. Fujitsuka M, Majima T (2011) Recent approach in radiation chemistry toward material and biological science. J Phys Chem Lett 2:2965–2971

8. Takada T, Kawai K, Tojo S, Majima T (2003) Kinetics of multistep hole transfer in DNA by monitoring the transient absorption of the pyrene radical cation. *J Phys Chem B* 107:14052–14057
9. Choi J, Fujitsuka M, Tojo S, Majima T (2012) Folding dynamics of cytochrome c using pulse radiolysis. *J Am Chem Soc* 134:13430–13435
10. Tojo S, Tachikawa T, Fujitsuka M, Majima T (2004) Oxidation processes of aromatic sulfides by hydroxyl radicals in colloidal solution of TiO₂ during pulse radiolysis. *Chem Phys Lett* 384:312–316
11. Pope M, Swenberg CE (1999) *Electronic processes in organic crystals and polymers*. Oxford University Press, New York
12. Asaoka S, Takeda N, Iyoda T, Cook AR, Miller JR (2008) Electron and hole transport to trap groups at the ends of conjugated polyfluorenes. *J Am Chem Soc* 130:11912–11920
13. Keller JM, Glusac KD, Danilov EO, McIlroy S, Sreearuothai P, R. Cook A, Jiang H, Miller JR, Schanze KS (2011) Negative polaron and triplet exciton diffusion in organometallic “molecular wires”. *J Am Chem Soc* 133:11289–11298
14. Badger B, Brocklehurst B (1968) Formation of dimer cations of aromatic hydrocarbons. *Nature* 219:263–263
15. Yamamoto M, Tsujii Y, Tsuchida A (1989) Near-infrared charge resonance band of intramolecular carbazole dimer radical cations studied by nanosecond laser photolysis. *Chem Phys Lett* 154: 559–562
16. Yasutake M, Koga T, Sakamoto Y, Komatsu S, Zhou M, Sako K, Tatemitsu H, Onaka S, Aso Y, Inoue S, Shinmyozu T (2002) An alternative synthetic route of [3_n](1,2,3,4,5)Cyclophane, and structural properties of multibridged [3_n]Cyclophanes and their charge-transfer complexes in the solid state. *J Am Chem Soc* 124:10136–10145
17. Fujitsuka M, Samori S, Hara M, Tojo S, Yamashiro S, Shinmyozu T, Majima T (2005) Formation of highly stabilized intramolecular dimer radical cation and π -Complex of [3_n]Cyclophanes (n = 3, 5, 6) during pulse radiolysis. *J Phys Chem A* 109:3531–3534
18. Fujitsuka M, Cho DW, Tojo S, Yamashiro S, Shinmyozu T, Majima T (2006) Transannular distance dependence of stabilization energy of the intramolecular dimer radical cation of cyclophanes. *J Phys Chem A* 110:5735–5739
19. Fujitsuka M, Tojo S, Shibahara M, Watanabe M, Shinmyozu T, Majima T (2011) Delocalization of positive charge in π -stacked multi-benzene rings in multilayered cyclophanes. *J Phys Chem A* 115:741–746
20. Fujitsuka M, Tojo S, Shinmyozu T, Majima T (2009) Intramolecular dimer radical anions of [3_n] cyclophanes: transannular distance dependent stabilization energy. *Chem Commun*: 1553–1555
21. Watanabe M, Goto K, Fujitsuka M, Tojo S, Majima T, Shinmyozu T (2010) 2,1,3-benzothiadiazole dimers: preparation, structure, and transannular electronic interactions of syn- and anti-[2.2](4,7)benzothiadiazolophanes. *Bull Chem Soc Jpn* 83:1155–1161
22. Ganesan V, Rosokha SV, Kochi JK (2003) Isolation of the latent precursor complex in electron-transfer dynamics. Intermolecular association and self-exchange with acceptor anion radicals. *J Am Chem Soc* 125: 2559–2571
23. Ishitani A, Nagakura S (1967) Electronic absorption and E.S.R. spectra of the benzene and paracyclophane anions. *Mol Phys* 12: 1–12
24. Fratiloiu S, Grozema FC, Koizumi Y, Seki S, Saeki A, Tagawa S, Dudek SP, Siebbeles LDA (2006) Electronic structure and optical properties of charged oligofluorenes studied by VIS/NIR spectroscopy and time-dependent density functional theory. *J Phys Chem B* 110: 5984–5993
25. Fujitsuka M, Tojo S, Yang J-S, Majima T (2013) γ -Ray radiolysis and theoretical study on radical ions of star-shaped oligofluorenes having a truxene or isotruxene as a core. *Chem Phys* 419: 118–123
26. Tojo S, Fujitsuka M, Majima T (2013) Mesolysis of radical anions of tetra-, penta-, and hexaphenylethanes. *J Org Chem* 78: 1887–1893

27. Ishida A, Fukui M, Ogawa H, Tojo S, Majima T, Takamuku S (1995) Lifetimes and transient phenomena of stilbene radical cations in the second excited doublet state. *J Phys Chem* 99: 10808–10814
28. Majima T, Fukui M, Ishida A, Takamuku S (1996) Stilbene radical anions in the excited doublet state. *J Phys Chem* 100: 8913–8919
29. Ichinose N, Majima T (2000) Transient absorption and fluorescence measurements of free radical cation and radical ion pair during pulse radiolysis of 1,3,5-trimethoxybenzene in chlorinated solvents. *Chem Phys Lett* 322: 15–20
30. Yamaji M, Tojo S, Takehira K, Tobita S, Fujitsuka M, Majima T (2006) S-S bond mesolysis in α , α' -Dinaphthyl Disulfide radical anion generated during γ -radiolysis and pulse radiolysis in organic solution. *J Phys Chem A* 110: 13487–13491
31. Cai X, Tojo S, Fujitsuka M, Majima T (2006) Photodissociation of naphthalene dimer radical cation during the two-color two-laser flash photolysis and pulse radiolysis-laser flash photolysis. *J Phys Chem A* 110: 9319–9324
32. Samori S, Fujitsuka M, Majima T (2013) Photodissociation of pyrene dimer radical cation during the pulse radiolysis–laser flash photolysis combined method. *Res Chem Intermed* 39:449–461
33. Samori S, Tojo S, Fujitsuka M, Majima T (2009) Important factors for the radiolysis-induced emission intensity of aromatic hydrocarbons. *J Photochem Photobiol, A* 205:179–185
34. Samori S, Hara M, Tojo S, Fujitsuka M, Yang S-W, Elangovan A, Ho T-I, Majima T (2005) Efficient emission from charge recombination during the pulse radiolysis of electrochemical luminescent substituted quinolines with donor-acceptor character. *J Phys Chem B* 109:11735–11742
35. Samori S, Tojo S, Fujitsuka M, Yang S-W, Elangovan A, Ho T-I, Majima T (2005) Efficient emission from charge recombination during the pulse radiolysis of electrochemical luminescent donor-acceptor molecules with an ethynyl linkage. *J Org Chem* 70: 6661–6668
36. Samori S, Tojo S, Fujitsuka M, Liang H-J, Ho T-I, Yang J-S, Majima T (2006) Emission from charge recombination during the pulse radiolysis of 9-cyano-10-phenylethynylanthracenes with donor and acceptor substituents. *J Org Chem* 71: 8732–8739
37. Samori S, Tojo S, Fujitsuka M, Yang S-W, Ho T-I, Yang J-S, Majima T (2006) Emission from charge recombination during the pulse radiolysis of arylolethynylpyrenes. *J Phys Chem B* 110: 13296–13303
38. Samori S, Tojo S, Fujitsuka M, Spittler EL, Haley MM, Majima T (2007) Donor-acceptor-substituted tetrakis(phenylethynyl)benzenes as emissive molecules during pulse radiolysis in benzene. *J Org Chem* 72:2785–2793
39. Samori S, Tojo S, Fujitsuka M, Spittler EL, Haley MM, Majima T (2008) Fine-tuning of radiolysis induced emission by variable substitution of donor-/acceptor-substituted tetrakis(arylolethynyl)benzenes. *J Org Chem* 73:3551–3558
40. Samori S, Tojo S, Fujitsuka M, Ryhding T, Fix AG, Armstrong BM, Haley MM, Majima T (2009) Emission from regioisomeric bis(phenylethynyl)benzenes during pulse radiolysis. *J Org Chem* 74:3776–3782
41. Fujitsuka M, Samori S, Tojo S, Haley MM, Majima T (2012) Dimerization reaction of regioisomeric bis(phenylethynyl)benzene radical anions during pulse radiolysis. *ChemPlusChem* 77: 682–687
42. Burrows CJ, Muller JG (1998) Oxidative nucleobase modifications leading to strand scission. *Chem Rev* 98:1109–1152
43. Armitage B (1998) Photocleavage of nucleic acids. *Chem Rev* 98:1171–1200
44. Carell T (1995) Sunlight-damaged DNA repaired with sunlight. *Angew Chem Int Ed Engl* 34:2491–2494
45. Fujitsuka M, Majima T (2012) Hole and excess electron transfer dynamics in DNA. *Phys Chem Chem Phys* 14:11234–11244
46. Lewis FD, Wu T, Zhang Y, Letsinger RL, Greenfield SR, Wasielewski MR (1997) Distance-dependent electron transfer in DNA hairpins. *Science* 277: 673–676

47. Meggers E, Michel-Beyerle ME, Giese B (1998) Sequence dependent long range hole transport in DNA. *J Am Chem Soc* 120:12950–12955
48. Giese B, Amaudrut J, Kohler A-K, Spormann M, Wessely S (2001) Direct observation of hole transfer through DNA between adenine bases and by tunneling. *Nature* 412:318–320
49. Kawai K, Takada T, Tojo S, Ichinose N, Majima T (2001) Observation of hole transfer through DNA by monitoring the transient absorption of pyrene radical cation. *J Am Chem Soc* 123:12688–12689
50. Choi J, Park J, Tanaka A, Park MJ, Jang YJ, Fujitsuka M, Kim SK, Majima T (2013) Hole trapping of G-quartets in a G-quadruplex. *Angew Chem Int Ed Engl* 52:1134–1138
51. Messer A, Carpenter K, Forzley K, Buchanan J, Yang S, Razskazovskii Y, Cai Z, Sevilla MD (2000) Electron spin resonance study of electron transfer rates in DNA: determination of the tunneling constant β for single-step excess electron transfer. *J Phys Chem B* 104: 1128–1136
52. Yamagami R, Kobayashi K, Tagawa S (2009) Dynamics of the delocalized charges of a radical anion in AT DNA duplexes. *Chem Eur J* 15: 12201–12203
53. Kawai K, Kimura T, Kawabata K, Tojo S, Majima T (2003) Excess electron transfer in dna studied by pulse radiolysis and γ -Radiolysis of naphthalimide and iodouridine modified ODN. *J Phys Chem B* 107: 12838–12841
54. Park MJ, Fujitsuka M, Kawai K, Majima T (2011) Direct measurement of the dynamics of excess electron transfer through consecutive thymine sequence in DNA. *J Am Chem Soc* 133: 15320–15323
55. Park MJ, Fujitsuka M, Nishitera H, Kawai K, Majima T (2012) Excess electron transfer dynamics in DNA hairpins conjugated with N, N-dimethylaminopyrene as a photosensitizing electron donor. *Chem Commun* 48: 11008–11010
56. Kawai K, Miyamoto K, Tojo S, Majima T (2003) Formation of pyrene dimer radical cation in dna reflecting dna dynamics in the time range of 1 μ s to 1 ms. *J Am Chem Soc* 125: 912–915
57. Choi J, Tojo S, Fujitsuka M, Majima T (2014) Dynamics in the heme geometry of myoglobin induced by the one-electron reduction. *Int J Radiat Biol* 90:459–467

Chapter 2

Single Crystal EPR Studies of Radicals Produced by Radiolysis of Organophosphorus Compounds

Michel Geoffroy

Abstract The main radical species produced by radiolysis of organophosphorus compounds are described in this chapter. Their identification is generally based on an analysis of the g and hyperfine tensors obtained from EPR experiments performed on irradiated single crystals. Special emphasis is placed on the properties of the ^{31}P hyperfine tensor, which is often decisive in determining the structure of these radicals. Radiogenic species mentioned in the beginning of this review correspond to simple phosphorus-centered radicals (PR_2 , PR_3^- , PR_4 , PR_3^+ , and R_2PO). Then, more delocalized systems are reported (allylic structures, captodatively stabilized radicals, symmetrical radical ions containing a P–P bond). The effects of radiolysis on compounds containing low-coordinate phosphorus atoms (e.g. phosphalkenes) are also described as well as the formation of radical pairs in irradiated phosphated sugars. The last part of the chapter deals with metallated radicals formed by radiolysis of metallic complexes $\text{M}(\text{CO})_5\text{P}(\text{H})\text{Ph}_2$ (with $\text{M} = \text{Mo}, \text{Cr}, \text{W}$). In some cases, phosphorus-centered radicals are compared with their arsenic analogues. For several systems the focus lies on dynamical effects; this is the case, for example, for the triptycenesphosphinyl radical, which undergoes internal rotation around a P–C bond. Molecular rearrangements after radiolysis of some organophosphorus compounds (e.g. diphosphenes) are also reported.

2.1 Introduction

Phosphorus, the 11th most abundant element in the Earth's crust, plays a crucial role in almost all fields of chemistry. It participates in a multitude of industrial processes, is a key element in the life sciences and is involved in the structure of numerous reactants useful in organic synthesis [1]. The ability of phosphorus to adopt several oxidation states and various coordination numbers is the source of its rich and diversified chemistry. This property is especially important for explaining

M. Geoffroy (✉)

Department of Physical Chemistry, University of Geneva, 30 quai Ernest Ansermet,
1211 Geneva, Switzerland
e-mail: michel.geoffroy@unige.ch

© Springer International Publishing 2014

A. Lund, M. Shiotani (eds.), *Applications of EPR in Radiation Research*,
DOI 10.1007/978-3-319-09216-4_2

the huge variety of reaction intermediates encountered in the radical chemistry of organophosphorus compounds. Without any doubt, EPR is one of the most efficient methods to detect these radicals. A great number of phosphorus-centered radicals, formed by photolysis, chemical reaction or electrochemistry, have been identified by liquid phase EPR [2, 3]. In these experiments, however, due to rapid motion of the radicals, only the average g value and the isotropic component of the hyperfine interactions can be measured. More complete information about the structure of these species is provided by solid state EPR [4]. In most cases, these spectra are recorded after rapid freezing of the reaction medium or by direct radiolysis of a solid sample containing the randomly oriented precursor. All the tensors that participate in the spin Hamiltonian of the radical contribute to the resulting "powder" spectra and, in principle, this technique is well suited for structural interpretation. However, due to frequent overlapping signals, the analysis of these spectra is often quite tedious, especially when several paramagnetic species are simultaneously produced in the sample. Moreover, it cannot be entirely excluded, when line-widths are rather large, that various sets of tensors can lead to similar spectra. All these difficulties are overcome when the radiogenic radical is trapped in a single crystal matrix. The angular dependences of the signals lead to an unambiguous determination of all the tensors of the system and, in favorable cases, additional valuable information can be obtained. As mentioned in this chapter, when the crystal structure of the sample is known, it is possible to directly determine the orientation of the orbital containing the unpaired electron with respect to the undamaged molecule. It is also possible to get a clear description of molecular motion when, after radiolysis, the radical undergoes internal rotation or rearrangement. Contributions of the matrix to stabilizing the trapped radical can be revealed by comparing the principal directions of the EPR tensors with the bond directions given by the crystal structure of the precursor; this approach is particularly pertinent when hydrogen bonds are involved. Specific information about radiation mechanism can also be provided by single crystal EPR in the case of pair wise trapping; for these systems the vector linking the two radicals of the pair can be determined and discussed in relation to the crystallographic data.

Analysis of EPR spectra obtained with radiolyzed single crystals of organophosphorus compounds is greatly facilitated by the magnetic properties of the ^{31}P nucleus. The natural abundance of this nucleus is equal to 100% and its spin is equal to $\frac{1}{2}$. Moreover, the isotropic coupling constant associated with an electron localized in a phosphorus 3s orbital is large ($^{31}\text{P}-A_{\text{iso}}^* = 13306$ MHz) and the dipolar tensor associated with an electron lying in a phosphorus 3p orbital ($2B_o = 733$ MHz) leads to rather anisotropic hyperfine splittings. The angular variation of signals due to radicals exhibiting hyperfine interactions with ^{31}P is therefore easy to follow, even when several species are simultaneously trapped in the crystal. Many programs have been written in order to extract the g and hyperfine tensors from the angular dependence of signals recorded in a single crystal EPR study or from powder spectra [5, 6]; some of them are commercially available [7]. For some organophosphorus radicals presenting a small ^{31}P hyperfine interaction, assignment of the couplings to the various spin $\frac{1}{2}$ nuclei present in the molecule is not straightforward but can be performed by running single crystal ENDOR spectra.

Interpretation of ^{31}P hyperfine tensors in terms of radical structure is generally performed by comparing the experimental isotropic and anisotropic coupling constants with the expectation values of the Fermi contact and dipolar interactions obtained from *ab initio* calculations or Density Functional Theory (DFT). It is then possible to check if the measured isotropic (A_{iso}) and anisotropic (τ) coupling constants are consistent with the calculated s and p contributions to the SOMO of the postulated radical. A rapid but rather rough method for estimating the phosphorus s and p characters of the SOMO of a radiogenic radical is to merely compare the experimental A_{iso} and τ values with the atomic constants A_{iso}^* and $2B_0$. Several sets of atomic constants have been tabulated in the literature [8, 9]; in the present chapter, for sake of consistency, only the values published by Morton and Preston [10] will be used. The hybridization ratio λ^2 , equal to the ratio of the p character ρ_p over the s character ρ_s has frequently been used to get information about the geometry of a radical. For an AB_3 radical with local C_{3v} symmetry, λ^2 allows calculation of the interbonding angle and the pyramidalty (out-of-plane angle) of the radical [9, 11].

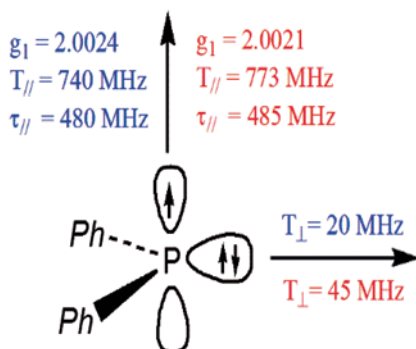
From a chemical point of view it can be interesting to compare phosphorus-centered radicals with other species centered on a heavy atom in group 15. Although considerably less numerous than their phosphorus homologues, some arsenic and antimony radicals will be mentioned in this chapter. For these radicals, structural information is provided not only by the magnetic hyperfine interaction but also by the quadrupolar coupling: ^{75}As : natural abundance = 100%, $I=3/2$, $A_{\text{iso}}^*=14660$ MHz, $2B_0=667$ MHz, ^{121}Sb : natural abundance: 57.2%, $I=5/2$, $A_{\text{iso}}^*=35100$ MHz, $2B_0=1257$ MHz [10].

The present chapter deals with radicals produced by radiolysis of organic compounds containing a phosphorus atom. However, for historical reasons, pure inorganic radicals, such as PO_3^{2-} or PF_4 , will also be mentioned.

2.2 Phosphinyl Radicals

The first EPR study of a phosphinyl radical was reported almost 50 years ago [12]. It concerned the formation of PH_2 produced by γ -irradiation of PH_3 in a diluted solution in a Kr matrix at low temperature. Due to the rapid motion of this small radical, only the isotropic part of the ^{31}P hyperfine tensor could be measured ($A_{\text{iso}}=224$ MHz). A few years later, the anisotropic part of the phosphorus coupling could be estimated for PF_2 [13] ($\tau=626$ MHz) and PCl_2 [14] ($\tau=605$ MHz) after trapping these species at 4 K in Xe matrices. As shown by Symons et al. [15, 16], powder spectra recorded after γ -radiolysis at 77 K of several trivalent phosphorus derivatives (e.g. $\text{P}(\text{SMe})_3$, $\text{P}(\text{OMe})_3$, Pr_2PCl) revealed the formation of phosphinyl radicals. A full determination of both the g and ^{31}P hyperfine tensors could be obtained for the diphenylphosphinyl radical Ph_2P after trapping of this radical in X-irradiated single crystals of triphenyl phosphine oxide and diphenyl phosphine sulfide at room temperature [17]. The ^{31}P hyperfine tensor presents axial symmetry and is moderately sensitive to the host matrix: (740, 20, 20 MHz in Ph_3PO ; 773,

Fig. 2.1 ^{31}P hyperfine values for Ph_2P trapped in an X-irradiated single crystal of Ph_3PO (data in blue) and in an X-irradiated single crystal of $\text{Ph}_2\text{P}(\text{S})\text{H}$ (data in red)



55, 35 MHz in $\text{Ph}_2\text{P}(\text{S})\text{H}$). Similarly, the g -tensor is not very affected by the nature of the crystal: (2.0024, 2.0052, 2.0124) in Ph_3PO and (2.0021, 2.0039, 2.0094) in $\text{Ph}_2\text{P}(\text{S})\text{H}$. As shown in Fig. 2.1, drawn in the approximation of a perfect cylindrical symmetry of ^{31}P -T, the ^{31}P -T $_{//}$ direction is oriented along the g -eigenvector corresponding to the g value close to that of the free electron. This relative orientation of the g and phosphorus hyperfine tensors agrees with properties predicted by Atkins and Symons for this type of radical with C_{2v} symmetry [9].

Assuming a positive sign for the three ^{31}P coupling eigenvalues leads to isotropic coupling constants of 260 MHz in Ph_3PO and 287 MHz in $\text{Ph}_2\text{P}(\text{S})\text{H}$, respectively. The corresponding s -spin densities are small ($\rho_s = 0.020$ and 0.022) and are mainly due to inner shell polarization. The anisotropic coupling constants $\tau_{//}$ shown in Fig. 2.1 are consistent with a rather large localization of the unpaired electron in the phosphorus $\text{P}\pi$ -orbital ($\rho_p = 0.65$ in Ph_3PO , $\rho_p = 0.66$ in $\text{Ph}_2\text{P}(\text{S})\text{H}$). This identification of the Ph_2P radical was confirmed by uv-photolysis of frozen Ph_2PH at -100°C ; the resulting spectrum could be simulated using the tensors obtained from the Ph_3PO single crystal study. In order to assess the sensitivity of the structure of R_2P to the nature of R, the radical $(\text{PhNH})_2\text{P}$ was trapped in an X-irradiated single crystal of $(\text{PhNH})_2\text{P}(\text{O})\text{H}$; a marked axially of the ^{31}P coupling tensor was still observed but a variation in the anisotropic components revealed a decrease of $\sim 15\%$ in the phosphorus spin density [18].

Lately, renewed interest has focused on phosphinyl radicals in organic and organometallic chemistry. Due to the use of sterically encumbering substituents, very persistent phosphinyl radicals have been synthesized [19, 20]. A dialkylphosphinyl radical was even obtained as thermally stable crystals [21] and an X-ray diffraction study was performed on a phosphinyl radical bearing a cationic substituent [22].

2.2.1 Arsenic and Antimony Homologues of Phosphinyl Radicals

It is interesting to compare the structures of phosphinyl radicals with those of arsinyl and stibinyl radicals. This is possible for the diphenyl phosphinyl radical since Ph_2As could be produced in an X-irradiated single crystal of triphenylarsine oxid [23], while Ph_2Sb was trapped, after radiolysis or uv-photolysis, in a single crystal

of triphenylantimony [24, 25]. For Ph_2As , both magnetic ($^{75}\text{As-T}$) and quadrupolar ($^{75}\text{As-P}$) hyperfine coupling tensors exhibit cylindrical symmetry. As expected, the direction of T_{\parallel} , (628 MHz) aligned along the arsenic p-orbital containing the unpaired electron is perpendicular to the quadrupolar interaction eigenvector P_{\parallel} (-19 MHz), which is oriented along the direction of the lone pair. The tensors g , $^{121/123}\text{Sb-T}$ and $^{121/123}\text{Sb-P}$ obtained for Ph_2Sb are also consistent with this model. Measurements of both the magnetic and quadrupolar interactions with the central atom allow an estimation of the bonding angle: the C-As-C as well as the C-Sb-C angle are close to 98° .

2.2.2 Internal Rotation in Phosphinyl Radicals

During the last two decades considerable efforts have been devoted to the development of molecular rotors and motors [26]. For example, Kelly et al. took advantage of the C_3 symmetry in the triptycene moiety to design a diamagnetic molecular brake in solution [27]. In a similar approach, secondary phosphines containing a barrelene moiety were synthesized and crystallized. In these systems, after radiolysis, a paramagnetic PH bond can rotate around an immobilized phosphorus-barrelene bond [28, 29, 30]. These radicals are shown in Fig. 2.2.

X-irradiation of a single crystal of 9-phosphinotriptycene at room temperature gives rise to a radical characterized by hyperfine couplings with a ^{31}P nucleus and a proton [28]. As shown by experiments performed with deuterated crystals of triptycene- PD_2 [29], the ^1H -coupling is due to a hydrogen atom bound to the phosphorus. Angular variations of the spectrum show that at room temperature, the radical is trapped along a single orientation. The hyperfine eigenvalues for ^1H and ^{31}P are

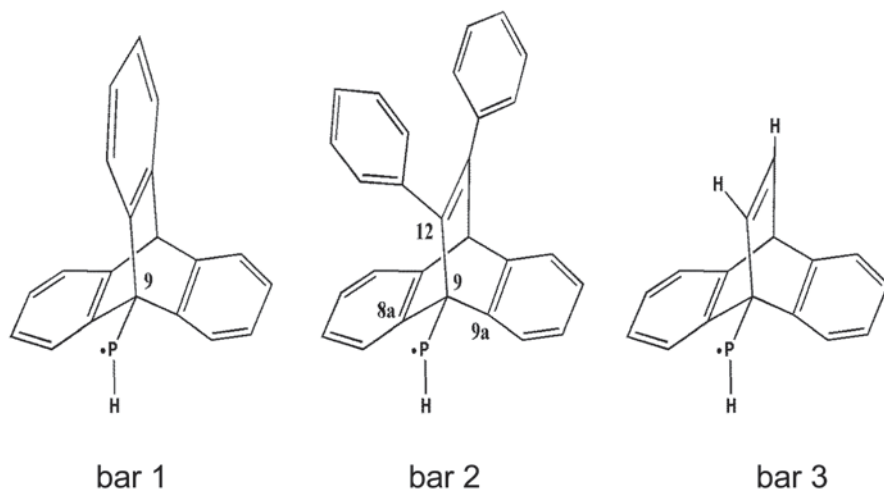


Fig. 2.2 Phosphinyl radicals formed in an x-irradiated single crystal of 9-phosphinotriptycene (bar 1), diphenyldibenzobarrelenephosphine (bar 2), dibenzobarrelenephosphine (bar 3)

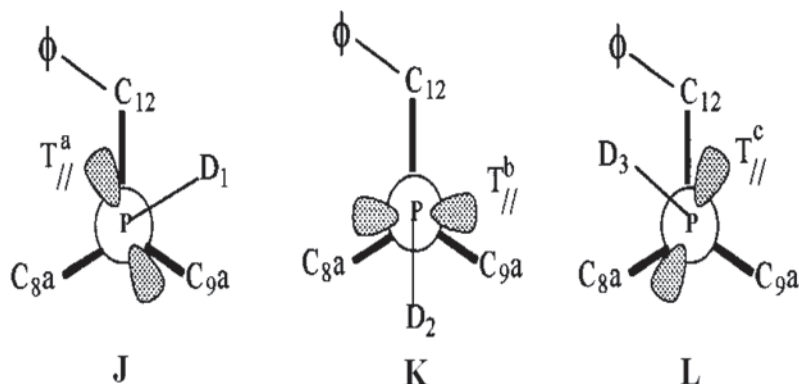


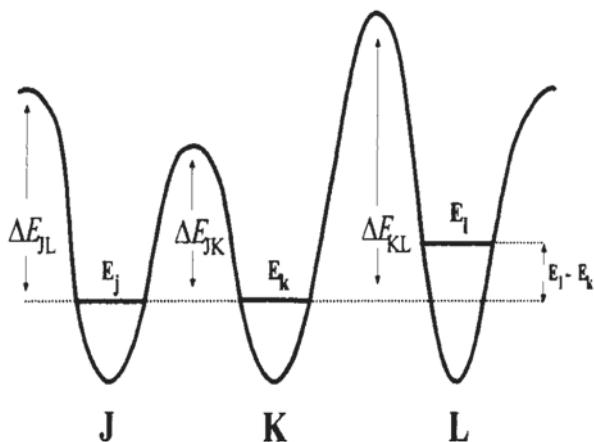
Fig. 2.3 The three staggered configurations of the phosphinyl radical (bar 2) trapped in an irradiated crystal of diphenyldibenzobarrelenephosphine. The figure is adapted from [29] by permission of the American Chemical Society

equal to (38, 39, 61 MHz) and (23, 409, 413 MHz), respectively. Decreasing temperature drastically modifies the spectrum. At 77 K, the radical is trapped along three magnetically non-equivalent sites with new sets of eigenvalues: (37, 42, 67 MHz) for ^1H and (4, 74, 848 MHz) for ^{31}P . The phosphorus isotropic coupling constant is therefore rather small ($A_{\text{iso}} = 308$ MHz) and the anisotropic constant $\tau_{\parallel} = 540$ MHz $_z$ implies a spin density of 0.73 in a phosphorus p orbital. The component of the g-tensor (2.0036, 2.0102, 2.0134) close to the free electron value is aligned along $^{31}\text{P}-T_{\parallel}$. The angle between the three new $^{31}\text{P}-T_{\parallel}$ eigenvectors is equal to 120° and these three directions are perpendicular to the C–P crystallographic direction. All these features demonstrate that the phosphinyl radical resulting from homolytic scission of a P–H bond is trapped in the crystal and that this radical, immobilized at 77 K, is freely rotating at 300 K around the triptycene-phosphorus bond. In accordance with *ab initio* calculations, the three sites observed at low temperature correspond to the three most stable staggered conformations of the phosphinyl radical (bar 1 in Fig. 2.2). The dynamical process occurring between 77 and 300 K was studied by recording the temperature dependence of the spectrum and analyzing this temperature dependence with density matrix formalism. From the Arrhenius plot $\ln(1/\tau_c) = f(1/T)$, the energy barrier to the rotation of the P–D bond around the P–C bond was found to be about 2.75 kcal mol $^{-1}$ [29].

In order to assess the factors that influence the motion of the P–H bond in this type of phosphinyl radical, single crystals of deuterated and non-deuterated diphenyldibenzobarrelenephosphine were X-irradiated at 300 K and their EPR spectra studied at various temperatures [29]. As with bar 1, the radical due to the homolytic scission of a P–H bond is trapped in the crystal. Three staggered conformations, denoted **J**, **K**, and **L** in Fig. 2.3, are possible for this phosphinyl radical (bar 2, Fig. 2.2), whose internal rotation of the P–H bond is hindered by the presence of the phenyl ring linked to the ethylenic bond.

However, at 77 K, only conformations **J** and **K** contribute to the EPR spectrum; steric constraints between the phosphinyl deuterium and the phenyl group bound

Fig. 2.4 Variation in the potential energy of the phosphinyl radical bar 2 as a function of the $C_{12}C_9PH$ torsion angle. The figure is reproduced from [29] by permission of the American Chemical Society



to C_{12} preclude occupation of site L. A schematic representation of the energy for the three rotamers is shown in Fig. 2.4. At 100 K, site L begins to be populated and to exchange with site J, while exchange with site K starts only at 130 K. Exchange between J and K begins at 110 K.

The temperature dependence of the EPR spectrum indicates that steric interactions with the phenyl ring bound to the ethylenic carbon C_9 give rise to three different potential wells: $\Delta E_{JL} = 2.46 \text{ kcal mol}^{-1}$, $\Delta E_{JK} = 2.37 \text{ kcal mol}^{-1}$, $\Delta E_{KL} = 2.74 \text{ kcal mol}^{-1}$ and $E_L - E_K = 0.5 \text{ kcal mol}^{-1}$. The role of the environment of the phosphinyl group on the motion of the P-H bond was confirmed by studying the temperature dependence of the EPR spectrum obtained after x-irradiation of a single crystal of dibenzobarrelenephosphine [31]. In the resulting phosphinyl radical (bar 3, Fig. 2.2), there is no group linked to C_{12} and it was necessary to decrease the temperature to 40 K to stop the motion of the P-H bond. The phosphinyl radical was blocked in only two conformations and the motion observed between 45 and 200 K was attributed to jumps between the two corresponding rotamers. The energy barrier associated with this hopping of the phosphinyl proton between two sites was found to be equal to $0.5 \text{ kcal mol}^{-1}$.

The triptycengermany radical (Triptycene- GeH_2) is another example of a radiogenic radical located on a heteroatom bound to triptycene [32]. In this radical, the rotation of the GeH_2 moiety is blocked at 90 K and is free above 110 K. The corresponding rotation barrier is equal to $1.3 \text{ kcal mol}^{-1}$.

2.3 Radical Anion PR_3^-

Earlier studies on non-oriented samples have shown that radiolysis of trivalent tri-coordinated phosphorus compounds leads to a large variety of radical species. The resulting EPR spectra are strongly dependent upon the experimental conditions: polycrystalline or dilute frozen solutions, nature of the solvent (protic or aprotic),

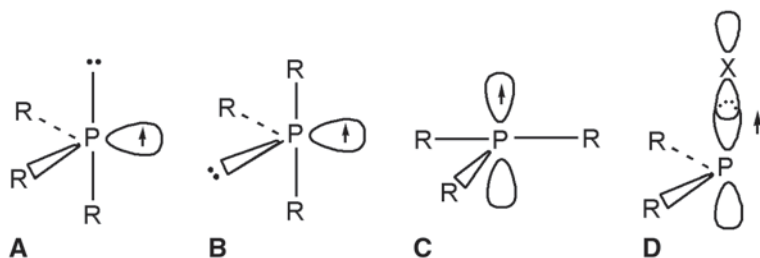


Fig. 2.5 Examples of structures adopted by a radical monoanion centered on a tricoordinated phosphorus atom. The figure is adapted from [33] by permission of Elsevier

temperature of irradiation, and annealing temperature of the irradiated sample [33]. This sensitivity to experimental conditions has been attributed, in part, to the various conformations that the primary radical anion can adopt and to the secondary reactions that this anion can undergo. Trimethylphosphite has been widely studied in this context. Three structures have been proposed for this radical anion. Both structures **A** and **B** are derived from a trigonal bipyramid structure, with a lone pair of electrons in the axial position for **A** and a lone pair of electrons in equatorial position for **B**. Structure **C** corresponds to a planar T-shape structure with the unpaired electron located in a phosphorus p_{π} orbital (see Fig. 2.5).

One of the first species (called species **1**) formed by γ -irradiation of polycrystalline $\text{P}(\text{OMe})_3$ at 77 K is characterized by ^{31}P hyperfine splittings equal to $T_{\parallel}=1792$ MHz and $T_{\perp}=1464$ MHz. By annealing, this species transforms into a new radical (called species **2**) characterized by $T_{\parallel}=2274$ MHz and $T_{\perp}=1870$ MHz. Hudson and Williams [34] proposed that species **1** corresponds to the radical anion $\text{P}(\text{OMe})_3$ in conformation **A** and that species **2** results from the rearrangement of structure **A** into structure **B**. However, as shown by Symons et al. [33], the species trapped after radiolysis of polycrystalline $\text{P}(\text{OMe})_3$ are different from those formed by radiolysis of frozen solutions. In MeTHF, a species (called species **1'**) with a hyperfine splitting $T_{\parallel}=748$ MHz is observed immediately after irradiation at 77 K. A slight increase in temperature transforms this species into species **2'** with $T_{\parallel}=812$ MHz. Symons et al. identified species **1'** as being the planar radical anion $\text{P}(\text{OMe})_3$ with structure **C** and proposed that species **2'** results from a dissociative reaction which gives rise to the phosphinyl radical $\text{P}(\text{OMe})_2$. In this interpretation, signals observed for species **1** and **2** in polycrystalline samples are attributed to phosphoranyl radicals (*vide infra*).

Phosphorus-centered radical anions resulting from the reduction of a phosphine are rarely observed. The $(\text{PhPMe}_2)^{\cdot-}$ species formed from phenyldimethylphosphine by electrolysis or by reaction with metal alkali exhibits a $^{31}\text{P}-A_{\text{iso}}$ coupling of 5 G, and corresponds, in fact, to a phenyl radical anion bearing a dimethylphosphino group [35].

Electron capture by a R_2PCl compound and subsequent dissociation into a chlorine anion and a phosphinyl radical were clearly observed with an irradiated single crystal of 1,2-phenylenephosphorochloridite (**I**) [36]. The crystal structure of **I** is

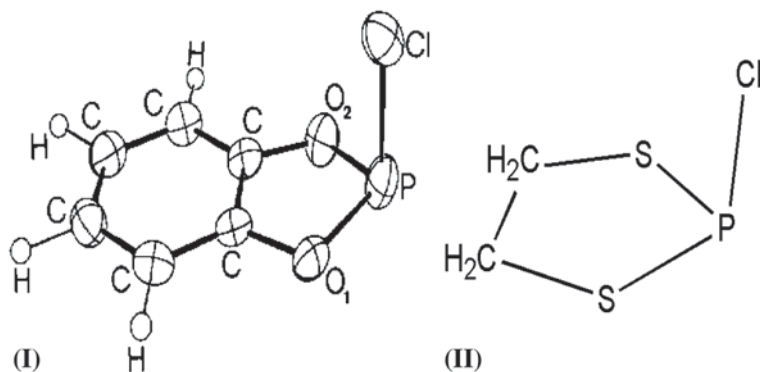


Fig. 2.6 (I) perspective view of 1,2-phenylenephosphorochloridite (from the crystal structure given in [36]. (II) molecule of 2-chloro-1,3,2-dithiaphospholane. The figure is adapted from [36] by permission of the American Chemical society

known (see Fig. 2.6) and confirms the pyramidity of the phosphorus coordination ($\text{OPO} = 95.5^\circ$ and $\text{OPCl} = 99^\circ$). X-irradiation of such a single crystal at 77 K leads to a radical exhibiting hyperfine coupling with both a ^{31}P nucleus (868, 56, 44 MHz) and a ^{35}Cl nucleus (41, (-)20, (-)19 MHz). This radical disappears by annealing or photolysis; it is replaced by a new species without ^{35}Cl coupling whose ^{31}P coupling eigenvalues are equal to 755, 111, 93 MHz.

As indicated by the hyperfine interactions, in the first species the unpaired electron is mainly located in a phosphorus p-orbital ($\sim 74\%$) and a chlorine p orbital ($\sim 10\%$, by assuming negative signs for “perpendicular” ^{35}Cl hyperfine eigenvalues). The angle between the two “parallel” eigenvectors is rather small (26°). These properties are consistent with the formation of a radical anion I^- in which the unpaired electron belongs to a phosphorus-chlorine σ^* orbital (Fig. 2.5, structure D). This type of structure has also been observed with selenium-centered radicals [37]. This is also the structure predicted by former *ab initio* calculations for H_2PCl^- whereas a planar T-shape structure was predicted for PCl_3^- .

The ^{31}P coupling of the radical observed after annealing is very anisotropic and indicates a spin density of $\sim 60\%$ in a phosphorus p-orbital. Moreover, its T_{\parallel} eigenvector is oriented along a direction corresponding to g near 2.0023. These properties agree with those expected for phosphinyl radicals and show that a slight increase in temperature causes the dissociation reaction of $(\text{RO})_2\text{PCl}^-$ into $(\text{RO})_2\text{P}$ to occur. Similar results have been obtained with a radiolyzed single crystal of chlorodithiaphospholane (see Fig. 2.6) [38]. The resulting radical anion II^- , trapped at 77 K, also adopts a pyramidal conformation with the unpaired electron localized in a P-Cl σ^* orbital. This is confirmed by the small angle formed by the $^{31}\text{P-T}_{\parallel}$ and $^{35}\text{Cl-T}_{\parallel}$ directions (11°). The presence of the sulfur atoms linked to the phosphorus atoms does not appreciably affect the spin density in the P-Cl bond ($\rho \sim 0.80$). Similar to (I), the phosphinyl radical is observed after annealing. As shown by *ab initio* calculations, the dissociation energy of H_2PCl^- into Cl^- and the phosphinyl radical

is rather low ($\Delta E = 29.3 \text{ kJ mol}^{-1}$). This is probably why the radical anion resulting from electron capture by a chlorophosphine is rarely observed.

It is worthwhile noting that electron addition to compounds containing a pentacoordinated phosphorus has also been reported. PF_5^- has been formed by γ -irradiation of solid solution of PF_5 in neopentane [39] and a $(\text{RO})_4\text{PCl}^-$ radical has been trapped in X-irradiated crystals of a derivative of chlorobenzodioxaphosphole [40]. The structure of this latter species is octahedral with the unpaired electron and the chlorine atom in axial position. In this context, irradiation of a single crystal of Ph_3AsF_2 led to the formation of $\text{Ph}_3\text{AsF}_2^-$ adopting a square base pyramidal structure [41].

2.4 Phosphoranyl Radicals

Formally, in phosphoranyl radicals the unpaired electron is mainly localized on a neutral tetracoordinated phosphorus atom. The exact electronic configuration and the conformation of these radicals have been shown to be very dependent upon the nature of the chemical groups bound to phosphorus [42, 43]. A large number of EPR studies has been devoted to the various structures of these radicals [44] and this species is now well documented. Here, we will focus our attention on results obtained after radiolysis of single crystals.

Early investigations, carried out in liquid solution, concluded that phosphoranyl radicals adopt a trigonal bipyramid structure. Single crystal EPR studies on two halogen-containing phosphoranyls (PF_4 [45] and POCl_3^- [46]) showed, however, that the angular dependences of the spectra were not in accord with a traditional valence bond description, which expects the unpaired electron to occupy one of the five sp^3d -hybridized orbitals. The low anisotropy of the ^{31}P coupling together with the rather large anisotropic coupling with two equivalent halogens were interpreted in terms of a Rundle three-center non-bonding orbital [47]. In this model the two axial ligand p_z -orbitals mix with the phosphorus s and p_x orbitals in an antibonding combination. In this structure most of the *phosphorus* spin density lies in the equatorial plane of a trigonal bipyramid (*structure TBP-e*). As shown by Buck et al., phosphoranyl can also adopt a second type of TBP structure in which the unpaired electron lies in an apical position (*structure TBP-a*) [48]. A third limiting structure was found for some R_3PX phosphoranyls [49]; in this C_{3v} structure, the unpaired electron lies in a σ^* P–X bond as shown in Fig. 2.7.

A simple way to trap a phosphoranyl radical in an oriented matrix is to irradiate a crystalline pentacoordinated phosphorus compound containing a P–H bond. This method was used by Buck et al. to generate phosphoranyl radicals **A** [50, 51], **B** [51] and **C** [52] (see Fig. 2.8). As shown by X-ray diffraction analysis, the conformation of the precursor of **A** corresponds to a trigonal bipyramid with the hydrogen atom in the equatorial position. The resulting EPR parameters are given in Table 2.1. The ^{31}P - T_{\parallel} eigenvector—found to be oriented along the crystallographic P–H direction of the precursor—confirms that this radical adopts a *TBP-e* structure.

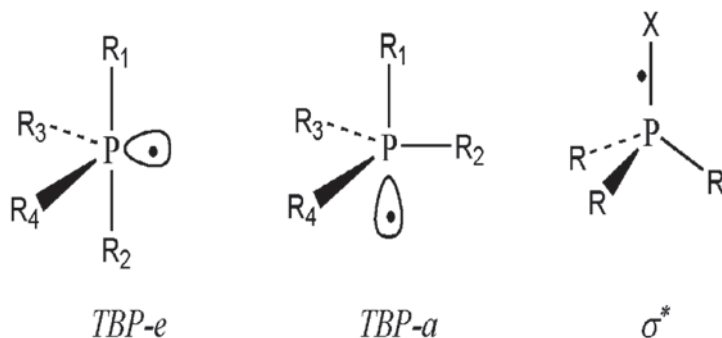


Fig. 2.7 Trigonal bipyramidal and σ^* structures adopted by phosphoranyl radicals. The figure is adapted from [53] by permission of the American Chemical Society

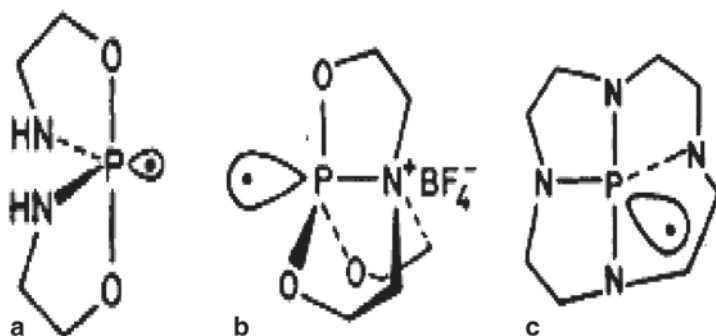


Fig. 2.8 Phosphoranyl radicals trapped in irradiated single crystals of $\text{HP}(\text{OCH}_2\text{CH}_2\text{NH})_2$ (structure a), $\text{HP}(\text{OCH}_2\text{CH}_2)_3\text{N}^+\text{BF}_4^-$ (structure b), $\text{HP}(\text{NCH}_2\text{CH}_2)_4$ (structure c). The figure is adapted from [50] and [51] by permission of the Royal Society of Chemistry

In contrast with $\text{HP}(\text{OCH}_2\text{CH}_2\text{NH})_2$, the crystal structure of the precursor of **b** indicates that the initial P–H bond is aligned along an apical direction of the TBP formed by the five ligands. The species trapped at 77 K (radical **b_e**) is characterized by “parallel” and “perpendicular” phosphorus splittings equal to 1120 and 930 G respectively. Radical **b_e** is irreversibly replaced above 193 K by radical **b_a** whose “parallel” and “perpendicular” phosphorus splittings are equal to 888 and 753 G. By comparing the orientations of the ^{31}P - T_{\parallel} directions with the crystallographic bond directions of the precursor, Buck et al. concluded that **b_e** and **b_a** correspond to the *TBP-e* and the *TBP-a* structure, respectively, and that stereoisomerization occurs in the crystal. Another dynamical effect was reported by the same authors for phosphoranyl **c** [52]. At 258 K, this radical adopts a *TBP-e* conformation **c_e** with large hyperfine splittings for the two nitrogens in apical positions ($T_{\parallel}=26.3$ G, $T_{\perp}=24.0$ G) and a splitting less than 5 G for the two nitrogens in equatorial positions. At 295 K a coupling with four equivalent nitrogens ($T_{\parallel}=14.4$ G, $T_{\perp}=12.7$ G) is observed due to a rapid pairwise interconversion between the ligands. This exchange mechanism

Table 2.1 ^{31}P hyperfine interactions (MHz) for some phosphoranyl radicals

Radical	Ref	$^{31}\text{P-T}_1$	$^{31}\text{P-T}_2$	$^{31}\text{P-T}_3$	$^{31}\text{P-A}_{\text{iso}}$	$^{31}\text{P-}\tau_{\text{max}}$
$(\text{NHCH}_2\text{CH}_2\text{O})_2\text{P}^{\text{a}}$	[50]	2485	2062	2062	2203	282
$(\text{morph})_2\text{P}(\text{S}^-)\text{F}^{\text{b}}$	[53]	2535	2214	2140	2296	239
Ph_3PCl	[54]	2016	1545	1512	1691	325
Ph_3PBr	[57]	1876	1439	1408	1574	302
$\text{C}_6\text{H}_4\text{O}_2\text{P}(\text{O}^-)\text{Cl}$	[55]	3230	3017	2924	3057	173

^a Radical a shown in Fig. 2.8

^b morph: morpholino group $\text{O}(\text{CH}_2\text{CH}_2)_2\text{N}$

does not affect the phosphorus couplings ($T_{\parallel} = 715\text{G}$, $T_{\perp} = 606\text{G}$) and was described as a Berry pseudorotation with the unpaired electron acting as a pivot.

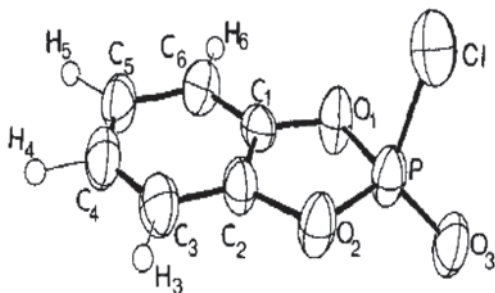
Although radicals **a** and **b** adopt a *TBP-e* and a *TBP-a* structure, respectively, their ^{31}P hyperfine tensors are quite similar; it seems therefore that structural assignment to one type of *TBP* cannot be made on the basis of hyperfine couplings with phosphorus alone. Couplings with the ligands are more informative since the value of $A_{\text{iso}}(^{14}\text{N})$ passes from $\sim 25\text{G}$ for a nitrogen in the axial position to a value $< 5\text{G}$ for a nitrogen in the equatorial position.

Electron capture by a crystalline four-coordinated phosphorus compound containing a $\text{P} = \text{X}$ bond ($\text{X} = \text{O}$, S or Se) is also an efficient method to generate phosphoranyl radicals in oriented matrices. Irradiation of single crystals of dimorpholinofluorophosphine sulfide produces a phosphoranyl radical $(\text{morph})_2\text{P}(\text{S}^-)\text{F}$ whose ^{31}P hyperfine couplings are given in Table 2.1. The principal directions of phosphorus and fluorine anisotropies are almost perpendicular. This implies for this phosphoranyl radical $\text{R}_2\text{P}(\text{S}^-)\text{F}$ a *TBP-e* structure with fluorine and sulfur in apical positions [53].

Ph_3PCl , the first phosphoranyl radical trapped in a C_{3v} conformation, was observed after irradiation of a crystal of Ph_3PBCl_3 [54]. Its mechanism of formation in this matrix is not straightforward and was not described. The measured ^{31}P hyperfine tensor together with its decomposition into isotropic and anisotropic constants are given in Table 2.1. They lead to phosphorus spin densities, ρ_s and ρ_p , equal to 0.13 and 0.44, respectively. The chlorine spin densities obtained from the ^{35}Cl coupling tensor ($T_{\parallel} = 229\text{MHz}$, $T_{\perp} = 95\text{MHz}$) are equal to $\rho_s = 0.02$ and $\rho_p = 0.25$. The major part of the spin lies on the two magnetic atoms and the density on chlorine, the more electronegative atom, is less than on phosphorus as expected for an antibonding orbital. The angle formed by the $^{31}\text{P-T}_{\parallel}$ and $^{35}\text{Cl-T}_{\parallel}$ eigenvectors is very small (10°) in good accord with an electron localized in a P-Cl σ^* orbital.

Another phosphoranyl radical with a σ^* structure was trapped in a single crystal of 1,2 phenylene phosphorochloridate (Fig. 2.9) irradiated at 77 K. This structure was confirmed by the small angle (12°) formed by the $^{31}\text{P-T}_{\text{max}}$ and $^{35}\text{Cl-T}_{\text{max}}$ eigenvectors [55]. Some departure from cylindrical symmetry occurs for both the ^{31}P anisotropic interaction (173 MHz, -40MHz , -133MHz) and the ^{35}Cl anisotropic coupling (58, -13 , -45MHz). This departure indicates some distortion from the idealized local C_3 conformation. In the phosphoranyl radical resulting from the electron capture by dipyrrolidinochloro phosphine sulfide [53], the directions of the

Fig. 2.9 Perspective view of 1,2-phenylenephosphorochloridate (from the crystal structure given in [55]. The figure is adapted from [55] by permission of John Wiley and Sons



phosphorus and chlorine tensors are inclined by an angle of 29° . A near σ^* structure was attributed to this radical with the unpaired electron located in an antibonding orbital between phosphorus and chlorine.

A detailed description of the structure of phosphoranyls generated by electron capture of $R_3P=Se$ (R is an alkyl group) has been obtained by analyzing the hyperfine interaction with ^{77}Se ($I = 1/2$) [56]. For these species 40% of the spin lies in a Se 4p orbital. The phosphorus and selenium anisotropic couplings were found to be parallel and oriented along the P-Se bond direction of the precursor in good accord with a σ^* structure for the R_3PSe^- species. The same structure has also been shown to be valid for sulfur analogues.

As discussed above, the alignment of the $^{31}P-T_{//}$ and $X-T_{//}$ eigenvectors in R_3PX constitutes a powerful argument in favor of a σ^* -structure. For Ph_3PBr trapped in an X-irradiated single crystal of triphenyliminophosphonium bromide [57], the eigenvalues found for ^{31}P and Br couplings were quite consistent with those found for Ph_3PCl . For this radical, however, the $^{31}P-T_{//}$ direction makes an angle of 35° with the direction of $Br-T_{//}$ and implies an appreciable distortion of the C_{3v} structure. Such a distortion is not too surprising. The P-X bond is weakened by the antibonding character of the extra electron, an elongation of the P-X distance occurs and the geometry of the trapped phosphoranyl radical can be appreciably affected by crystal matrix effects and by small interactions with neighboring molecules. As reported for the phosphoranyl radical trapped in an irradiated crystal of dipyrrolochlorophosphine sulfide, an increase in temperature can even cause cleavage of the phosphorus-halogen bond leading, in this case, to the formation of a thiophosphonyl radical [53].

2.4.1 Arsenic Homologues

The arsoranyl radicals Ph_3AsCl and Ph_3AsBr were trapped in single crystals of triphenylmethylarsonium chloride and of triphenylmethylarsonium bromide, respectively [58, 59]. Analysis of ^{75}As , ^{35}Cl and ^{79}Br hyperfine tensors leads to spin repartitions for Ph_3AsCl (As: $\rho_s = 0.13$, $\rho_p = 0.51$; Cl: $\rho_s = 0.02$, $\rho_p = 0.26$) and for Ph_3AsBr (As: $\rho_s = 0.11$, $\rho_p = 0.53$, ^{79}Br $\rho_s = 0.02$, $\rho_p = 0.24$) that are very similar to

Table 2.2 Hyperfine coupling constants (MHz) for some radical species produced by radiolysis of triphenylmethyl arsonium iodide

Radical	Ref	$^{75}\text{As}-A_{\text{iso}}$	$^{75}\text{As}-\tau_{\text{max}}$	Ligand- A_{iso}^a	Ligand- τ_{max}^a
$\text{Ph}_3\text{As}\dots\text{CH}_3$	[63]	253	20	108	134
Ph_3AsCH_3	[66]	1514	118		
Ph_3AsI	[65]	1440	320	800	490

^a For $\text{Ph}_3\text{As}\dots\text{CH}_3$, ligand: ^{13}C (CH_3); for Ph_3AsI , ligand: ^{127}I

the repartition found for Ph_3PCl . However, in contrast to this radical where the $^{31}\text{P}-T_{\parallel}$ and $^{35}\text{Cl}-T_{\parallel}$ eigenvectors are practically aligned, the arsenic- T_{\parallel} and halogen- T_{\parallel} directions make an angle of 25° in Ph_3AsCl and 35° in Ph_3AsBr . Clearly, as for Ph_3PBr , these two arsoranyl radicals adopt a structure that is intermediate between the local C_{3v} structure found for Ph_3PCl and the C_{2v} structure reported for PF_4 . An EPR study of arsoranyl radicals trapped in X-irradiated single crystals of triphenylarsine chalcogenides led to the same conclusions for Ph_3AsO^- , Ph_3AsS^- , and Ph_3AsSe^- [60].

An interesting property of some arsoranyl radicals concerns their ability to produce an arsine-radical adduct during their dissociation process. A similar mechanism had been reported for some alkyl halides which, after γ -irradiation in CD_3CN at 77 K, give rise to a weak alkyl radical-halide ion adduct such as $\text{Me}\dots\text{I}^-$ and $\text{Et}\dots\text{Br}^-$ [61, 62]. Identification of radiogenic radical species produced in single crystals of triphenylmethyl arsonium iodide was performed by analyzing spectra obtained after various isotopic enrichments of the arsonium cation: Ph_3AsCH_3 , Ph_3AsCD_3 and $\text{Ph}_3\text{As}^{13}\text{CH}_3$ [63]. The ^{75}As magnetic coupling tensor, measured at 77 K after X-irradiation of the crystal in liquid nitrogen (see Table 2.2), indicates a small spin density on the arsenic atom ($\rho_s=0.02$, $\rho_p=0.03$), while the largest component of the quadrupolar tensor ($e^2Qq_{zz}=186$ MHz) remains very close to the value measured on pure triphenylarsine [64]. Hyperfine interactions with three equivalent protons indicate the presence of a methyl group and the ^{13}C coupling tensor (see Table 2.2) shows that more than 63 % of the spin is localized in a carbon p-orbital of the methyl radical. This adduct is not stable with increasing temperature. Above -170°C its signals decrease in intensity and irreversibly disappear above -140°C . They are replaced by a spectrum exhibiting hyperfine couplings with ^{75}As and ^{127}I that are in good accordance with those expected for the arsoranyl radical Ph_3AsI [65]. Symons and McConnachie have shown that, in contrast with the results obtained with crystalline $\text{Ph}_3\text{As}^+\text{CH}_3\text{I}^-$, radiolysis of solutions of this arsonium salt in CD_3OD at 77 K generates the arsoranyl radical Ph_3AsCH_3 which, by annealing, leads to the trapping of free methyl radicals [66]. These studies on irradiated $\text{Ph}_3\text{AsCH}_3^+\text{I}^-$ point to the importance of the experimental conditions on the nature of the arsenic-containing radical formed by radiolysis of arsonium compounds. Fortunately, as shown in Table 2.2, the great sensitivity of the isotropic and anisotropic ^{75}As couplings to the molecular structure allows easy differentiation between these radicals. Nevertheless, controversy regarding possible structures of reaction intermediates can occur. This is the case for $\text{Ph}_3\text{As}\dots\text{CH}_3$ which was not considered by Symons et al. as a real adduct but as a pure methyl radical undergoing a very weak charge-transfer interaction with the Ph_3As molecule.

2.5 Phosphoniumyl Radical Cation PR_3^+

Phosphoniumyl radical cations are frequently invoked as reaction intermediates in the chemistry of phosphorus-containing compounds. They are, for example, involved in the design of photoinitiating systems [67] and in models capable of predicting the air stability of phosphines [68]. Moreover, their participation in electron transfer reactions has been frequently mentioned [2, 69].

The earliest EPR detections of phosphoniumyl radicals were carried out at 77 K after γ -radiolysis of solutions of phosphonium ions in H_2SO_4 [70, 71, 72] or CFCl_3 [73]. The first single crystal EPR study was performed on Ph_3P^+ trapped, at room temperature, in X-irradiated crystals of Ph_3PBCl_3 and Ph_3PBF_3 [74]. In addition to the phosphoranyl radical $\text{Ph}_3\text{P}\cdot$, irradiation of a single crystal of Ph_3PBCl_3 produces the phosphoniumyl radical cation, whose ^{31}P hyperfine parameters are given in Table 2.3. The principal g -values of Ph_3P^+ are rather close to the free electron value and the phosphorus hyperfine tensor exhibits axial symmetry. The ^{31}P isotropic and anisotropic couplings clearly indicate, after comparison with atomic constants, that the unpaired electron is mainly localized on the phosphorus atom $\rho_s=0.08$, $\rho_p=0.60$. It is worth remarking that in the irradiated crystal of Ph_3PBCl_3 , the $^{31}\text{P}-\tau_{\text{max}}$ eigenvector of Ph_3P^+ is aligned along the direction found for $^{31}\text{P}-\tau_{\text{max}}$ and $^{35}\text{Cl}-\tau_{\text{max}}$ in the phosphoranyl radical $\text{Ph}_3\text{P}\cdot$. Clearly, this common direction corresponds to the P–Cl bond of $\text{Ph}_3\text{P}\cdot$ and to the phosphorus magnetic p -orbital in Ph_3P^+ . The ^{31}P couplings measured for Ph_3P^+ produced in a solid solution of FCCl_3 [73] lead to spin densities ($\rho_s=0.06$, $\rho_p=0.60$) quite similar to those obtained in the single crystal studies. As shown by the results obtained for Me_3P^+ formed in FCCl_3 ($\rho_s=0.08$, $\rho_p=0.76$), this spin repartition is moderately affected by substitution of the phenyl ligands with alkyl groups.

X-irradiation of phosphoalkenes, $\text{RP}=\text{CR}'_2$, was reported to generate phosphoniumyl radical cations [75]. These compounds, which contain a two-coordinated phosphorus atom, are very reactive but they can be stabilized by binding the phosphorus atom to a cumbersome ligand such as the supermesityl group $^t\text{Bu}_3\text{C}_6\text{H}_2$ (hereinafter Mes*). EPR spectra obtained with irradiated single crystals of $\text{Mes}^*\text{P}=\text{C}(\text{H})\text{Ph}$ were analyzed after ^{13}C and ^2D enrichment of the phosphoalkene moiety. They showed that a rearrangement occurs inside the electron-deficient center and leads to incorporation of the phosphorus atom inside a five-membered ring (Fig. 2.10). Consistent

Table 2.3 ^{31}P hyperfine interactions (MHz) for some phosphoniumyl radical cations

Radical	$^{31}\text{P}-T_1$	$^{31}\text{P}-T_2$	$^{31}\text{P}-T_3$	$^{31}\text{P}-A_{\text{iso}}$	$^{31}\text{P}-\tau_{\text{max}}$
$\text{Ph}_3\text{P}^{+\text{a}}$	1554	888	882	1108	446
$\text{Ph}_3\text{P}^{+\text{b}}$	1397	750	731	959	438
$\text{Ph}_3\text{P}^{+\text{c}}$	1274	605	605	828	446
$(\text{R}_1(\text{R}_2)\text{PCH}_2\text{Ph})^{+\text{d}}$	1534	992	984	1171	364
$\text{Me}_3\text{P}^{+\text{c}}$	1635	798	798	1077	558

^a In a single crystal of Ph_3PBCl_3 [74]

^b In a single crystal of Ph_3PBF_3 [74]

^c In FCCl_3 [73]

^d In a single crystal of $\text{Mes}^*\text{P}=\text{C}(\text{H})\text{Ph}$ [75], (see Fig. 2.10)

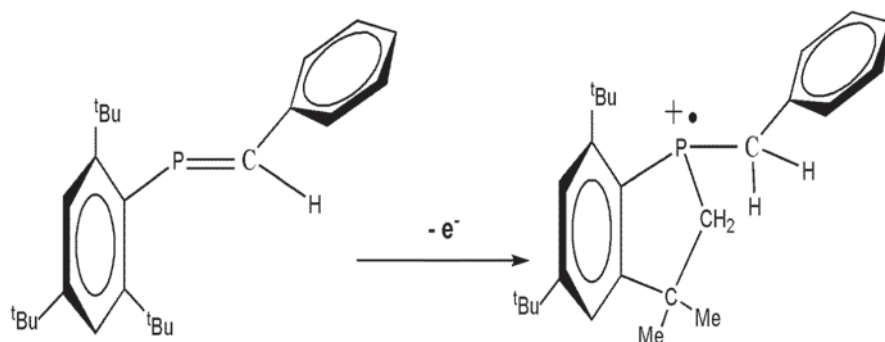


Fig. 2.10 Formation of a phosphoniumyl radical cation in an irradiated single crystal of $\text{Mes}^*\text{P}=\text{CHPh}$. The figure is adapted from [75] by permission of the American Chemical society

with the fact that two *ortho tert*-butyl groups can participate in the intramolecular cyclization, two slightly different conformations of the resulting phosphoniumyl radical were observed. Besides the ^{31}P coupling parameters given in Table 2.3, hyperfine interactions with protons and with the phosphaaalkenic ^{13}C nucleus (42, 48, 51 MHz) are convergent with this identification.

In contrast with the phosphorus s-character ($\rho_s=0.08$), the phosphorus p-character ($\rho_p=0.50$) found for this phosphoniumyl radical is slightly less than that measured for Ph_3P^+ or Me_3P^+ . It cannot be excluded that the constraints caused by the formation of the five-membered ring induce a change in the spin repartition.

2.6 Phosponyl and Phosphinoyl Radicals

Phosponyl and phosphinoyl radicals (formally $(\text{RO})_2\text{PO}$ and R_2PO species, respectively) have attracted attention in recent years because of their applications in various areas of chemistry: photochemistry [76, 77], stereoselective synthesis [78], chemically induced electron spin polarization in low magnetic fields [79], and synthesis of fullerene derivatives [80].

Phosphinoyl radicals are phosphorus analogues of the well-known nitroxide radicals extensively used for spin labeling experiments [81, 82]. However, in contrast with R_2NO species, R_2PO radicals are not stable and the determination of their electronic structure by EPR has required trapping them in irradiated solid precursors. The first single crystal EPR study of a phosphinoyl radical was reported for Ph_2PO . This radical was trapped after X-irradiation of a crystal of diphenyl phosphine oxide, $\text{Ph}_2\text{P}(\text{H})\text{O}$, under argon atmosphere at room temperature [83]. The phosphorus hyperfine tensor of Ph_2PO is almost axial ($T_{\perp 1}=929$ MHz, $T_{\perp 2}=908$ MHz) and, as shown in Table 2.4, its decomposition into isotropic and anisotropic components indicates that more than half of the spin is located on the phosphorus atom. Radiolysis of a single crystal of phenylphosphinic acid at room temperature under argon atmosphere [84] produced the radical $\text{PhP}(\text{O})\text{OH}$, whose hyperfine couplings

Table 2.4 ^{31}P hyperfine constants (MHz), phosphorus spin densities and hybridization ratios for some phosphinoyl and phosphonyl radicals

Radical	Ref	$^{31}\text{P}-A_{\text{iso}}$	$^{31}\text{P}-\tau_{\parallel}$	ρ_s	ρ_p	λ^2
Ph_2PO	[83]	1092	347	0.08	0.47	5.77
$\text{PhP}(\text{O})\text{OH}$	[84]	1510	355	0.11	0.48	4.26
$\text{PhP}(\text{O})\text{O}^-$	[84]	1397	327	0.10	0.44	4.28
$(\text{MeO})_2\text{PO}$	[85]	1918	308	0.14	0.42	2.92

(Calculations in the axial symmetry approximation)

are reported in Table 2.4 together with those of $\text{PhP}(\text{O})\text{O}^-$ and $(\text{MeO})_2\text{PO}$. For the last two radicals, EPR analyses were performed on powder spectra obtained with irradiated samples of $\text{PhP}(\text{O})\text{O}^- \text{K}^+$ [84] and dimethylphosphite, respectively [85].

It is interesting to compare these parameters with those of the inorganic radical PO_3^{2-} [86], which has been exhaustively studied ($A_{\text{iso}} = 1680$ MHz, $\tau_{\parallel} = 283$ MHz, $\rho_s = 0.12$, $\rho_p = 0.38$, $\lambda^2 = 3.16$), and those of the above mentioned phosphoniumyl cation Ph_3P^+ . Starting from Ph_3P^+ , subsequent substitutions of a phenyl by an oxygen leads to Ph_2PO , $\text{PhP}(\text{O})\text{O}^-$ and PO_3^{2-} . In the crude approximation of a local C_3 symmetry, the variation in the hybridization ratio λ^2 shows that this substitution is accompanied by a progressive pyramidalisation of the radical with an out-of-plane angle θ which passes from $\sim 14^\circ$ for Ph_3P^+ , to $\sim 15^\circ$ for Ph_2PO , $\sim 17^\circ$ for $\text{PhP}(\text{O})\text{O}^-$ and 19° for PO_3^{2-} . This evolution is the result of several factors such as the difference in electronegativity between O^- and a phenyl group and steric interactions between bulky phenyl groups. As expected, in contrast with its nitroxide homologue, Ph_2PO is not a planar radical. For $(\text{MeO})_2\text{PO}$ the θ angle is equal to $\sim 19.5^\circ$. The fact that phosphinoyl (R_2PO) radicals are generally flatter than the phosphonyl radical $(\text{RO})_2\text{PO}$ has often been invoked to explain the greater reactivity of phosphinoyl radicals towards olefins [1, 78].

2.6.1 Thiophosphonyl Species

Ph_2PS has been trapped in X-irradiated single crystals of diphenylthiosulfide [87] and tetraphenyldiphosphine disulfide [88], while Et_2PS and radical $[\text{N}(\text{C}_4\text{H}_8)]_2\text{PS}$ (shown in Fig. 2.11) have been studied in irradiated single crystals of tetraethyldiphosphine disulfide [88] and dipyrrolidinochloro phosphine sulfide [53], respectively.

Fig. 2.11 Thiophosphonyl radical trapped in an irradiated single crystal of dipyrrolidinochlorophosphine sulfide [53]. The figure is adapted from [53] by permission of the American Chemical Society

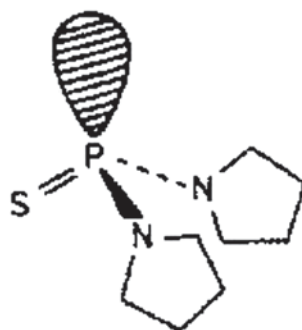


Table 2.5 ^{31}P coupling constants (MHz), spin densities, hybridization ratios and out-of-plane angles for some thiophosphonyl radicals

Radical	Ref	$^{31}\text{P}\text{-}A_{\text{iso}}$	$^{31}\text{P}\text{-}\tau_{\parallel}$	ρ_s	ρ_p	λ^2	θ
Ph_2PS	[87]	989	332	0.074	0.453	6.09	14.9
Ph_2PS	[88]	841	289	0.063	0.39	6.23	14.7
$[\text{N}(\text{C}_4\text{H}_8)]_2\text{PS}^a$	[53]	1153	299	0.087	0.408	4.71	16.5
Et_2PS	[88]	975	348	0.073	0.474	6.46	14.5

^a See Fig. 2.11

The values reported in Tables 2.4 and 2.5 for Ph_2PO and Ph_2PS show that replacement of the oxygen atom by a sulfur atom in R_2PO does not lead to drastic structural modifications. For both radicals the out-of-plane value is close to 15° . The effects of the host matrix on the parameters of the trapped radical are revealed by the values found for Ph_2PS . While the thiophosphonyl radical results from the simple homolytic scission of a P–H bond in an irradiated crystal of $\text{Ph}_2\text{P}(\text{S})\text{H}$, in $\text{Ph}_2(\text{S})\text{P}\text{-P}(\text{S})\text{Ph}_2$ it necessitates the dissociation of a P–P bond and a displacement of the resulting fragments to avoid any recombination. The pyramidality of the radical does not seem to be affected by these constraints ($\theta = 14.8 \pm 0.1^\circ$), but the total spin density on the phosphorus atom is reduced from 0.53 to 0.45.

2.6.2 Arsenic Homologues

Irradiation of a single crystal of $\text{Me}_2\text{AsO}_2^- \text{Na}^+$ at 77 K gave rise to two radicals identified as MeAsO_2^- ($^{75}\text{As}\text{-}A_{\text{iso}} = 1309$ MHz, $^{75}\text{As}\text{-}\tau_{\parallel} = 315$ MHz, $\rho_s = 0.089$, $\rho_p = 0.472$, $\lambda^2 = 5.30$, $\theta = 15.7^\circ$) and Me_2AsO ($^{75}\text{As}\text{-}A_{\text{iso}} = 1169$ MHz, $^{75}\text{As}\text{-}\tau_{\parallel} = 296$ MHz, $\rho_s = 0.080$, $\rho_p = 0.447$, $\lambda^2 = 5.65$, $\theta = 15.3^\circ$) [89]. These parameters are quite similar to those obtained from powder spectra by Lyons and Symons [90] for PrAsO_2^- ($^{75}\text{As}\text{-}A_{\text{iso}} = 1294$ MHz, $^{75}\text{As}\text{-}\tau_{\parallel} = 344$ MHz, $\rho_s = 0.088$, $\rho_p = 0.516$, $\lambda^2 = 5.85$, $\theta = 15.12^\circ$); they show that arsonyl radicals adopt a pyramidal structure with an out-of-plane angle quite similar to the angle for phosphinoyl radicals.

2.7 Radicals Centered on an Atom Adjacent to a Phosphorus Atom

It is well known that the cage effect for hydrogen atoms is very weak, so it is likely that, when an A–H bond is located adjacent to a phosphorus atom (e.g. phosphonium $\text{R}_3\text{P}^+\text{-AH}_3$), radiolysis gives rise to a radical centered in α position to the phosphorus. Such radicals are well documented and we will briefly mention only two examples corresponding to a radical formed on a carbon atom and on a boron atom, respectively.

The radical $\text{Ph}_3\text{P}^{+13}\text{CH}_2$ was trapped in an X-irradiated single crystal of $\text{Ph}_3(^{13}\text{CH}_3)\text{P}^+ \text{Cl}^-$ [91]. Hyperfine tensors with ^{13}C , ^{31}P and two protons were measured at 77 K and at room temperature. They showed that the unpaired electron remains localized on the carbon atom. Variable temperature experiments indicated that the barrier to rotation of the CH_2 group around the P–C bond presents a strong two-fold component located 5.5 kJ below two intermediate minima. X-irradiation at 3 K in the dark of a single crystal of $\text{Ph}_2\text{P}(\text{O})\text{CH}_2\text{Cl}$ showed that electron capture occurs to produce $\text{Ph}_2\text{P}(\text{O})\text{CH}_2\text{Cl}^-$ and does not give rise to the phosphoranyl radical $\text{Ph}_2\text{P}(\text{O}^-)\text{CH}_2\text{Cl}$ [92].

Radicals $\text{Ph}_3\text{P-BH}_2$ and $\text{Ph}_3\text{P-BD}_2$ were trapped in an X-irradiated single crystal of triphenylphosphineborane [93]. The ^1H , ^{11}B and ^{31}P hyperfine tensors show that the radical is planar with a strong localization of the unpaired electron on the boron atom. These tensors are consistent with the mesomeric structure $\text{Ph}_3\text{P}^+-\text{BH}_2^-$. Rotation of the BH_2 group around the P–B bond occurs at room temperature and could not be blocked at -130 C .

2.8 Delocalized Systems

2.8.1 Allylic Structures

Due to potential applications in molecular electronics, considerable efforts have been made in recent years to design new systems able to delocalize an unpaired electron along several atoms. In this context, an elementary system could consist of a phosphonium moiety insuring the electron capture and an allylic chain insuring electron delocalization. After reduction, such a system can be seen as an allylic radical in which a terminal carbon group has been replaced by a phosphoranyl fragment (2.1).



Roberts et al. showed that this type of radical can be produced in solution by adding butoxy radicals to phosphorus in vinylic phosphines $\text{CH}_2=\text{C}(\text{H})\text{PX}_2$ ($\text{X}=\text{MeO}$, EtO) [94]. However, the isotropic ^{31}P coupling constants measured for these radicals were very small (~ 40 MHz) and clearly indicated that the unpaired electron remained localized on the terminal carbon, consistent with the mesomeric formula $^t\text{BuO}(\text{MeO})_2\text{P}=\text{C}(\text{H})-\text{CH}_2$. In contrast with these results, X-irradiation, at room temperature of a single crystal of the phosphoranylidene $\text{Ph}_3\text{P}=\text{CH}-\text{C}(\text{H})\text{O}$ revealed trapping of a radical exhibiting a large ^{31}P hyperfine interaction [95]. Phosphorus and proton coupling constants for this radical are given in Table 2.6 together with those measured in solution for $^t\text{BuO}(\text{MeO})_2\text{P}=\text{C}(\text{H})\text{CH}_2$.

Comparison with phosphorus atomic coupling constants indicates that for the radical formed by radiolysis of phosphoranylidene $\sim 30\%$ of the spin is located on the phosphorus atom ($\rho_s=0.045$, $\rho_p=0.30$). The proton coupling tensor is consistent with a proton attached to a sp^2 hybridized carbon bearing $\sim 35\%$ of the spin in

Table 2.6 ^{31}P and ^1H hyperfine interactions (MHz) for $\text{Ph}_3\text{PCHC}(\text{H})\text{O}^-$ and ${}^t\text{BuO}(\text{MeO})_2\text{PCHCH}_2$

Species	$^{31}\text{P}-A_{\text{iso}}$	$^{31}\text{P}-\tau^c$	$^1\text{H}-A_{\text{iso}}$	$^1\text{H}-\tau^c$
$\text{Ph}_3\text{PCHC}(\text{H})\text{O}^-^a$	654	225	(-20.3	(+)16.3
		-116		(-)1.7
		-108		(-)14.7
${}^t\text{BuO}(\text{MeO})_2\text{PCHCH}_2^b$	39		42 ^d	
			5	

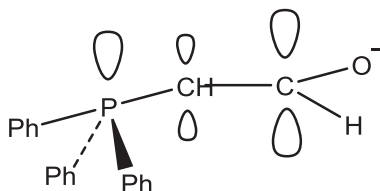
^a Trapped in a single crystal matrix [95]

^b Measured in liquid solution [94]

^c Principal values for the hyperfine dipolar tensor

^d Two equivalent protons

Fig. 2.12 Radical formed in an irradiated single crystal of (triphenylphosphoranylidene) acetaldehyde. The figure is adapted from [95] by permission of the American Chemical Society



a p_π orbital. The relative orientations of the phosphorus and proton coupling tensors ($^{31}\text{P}-\tau_{\parallel}$, $^1\text{H}-\tau_2 = 10^\circ$) show that the overlap between this carbon p_π orbital and the p component of the phosphorus magnetic orbital allows conjugation between the phosphorus and the carbon part of the radical, in good accordance with the structure shown in Fig. 2.12. This result agrees with *ab initio* calculations run for $(\text{H}_3\text{PCHC}(\text{O})\text{H})^-$; moreover, these calculations indicate that in this allylic structure the phosphoranyl adopts a TBP structure with the electron in an equatorial position (Fig. 2.12)

This difference in the structures of $\text{CH}_2\text{CHP}(\text{OMe})_2\text{O}^t\text{Bu}$ and $\text{Ph}_3\text{PCHC}(\text{H})\text{O}^-$ is due to stabilization of the ylid form $\text{H}_2\text{C}^--\text{PR}_3$ in $\text{CH}_2\text{CHP}(\text{OMe})_2\text{O}^t\text{Bu}$. This structure of the corresponding “phosphoranyl” radical is reminiscent of $\text{PhP}(\text{OEt})_2\text{O}^t\text{Bu}$ [96], which exhibits a small hyperfine ^{31}P coupling (27 MHz) that can be viewed as a phenyl radical anion substituted by a phosphonium group.

Stabilized structures of radicals trapped in irradiated phosphinylidene often require drastic changes in the geometry of the original molecules. Such is the case, for instance, when relaxation of the radical requires the rearrangement of a cumbersome PPh_3 moiety. In $\text{Ph}_3\text{P}=\text{CH}-\text{C}(\text{O})\text{CH}_3$, intramolecular and intermolecular hydrogen bonds, identified from the crystal structure, produce considerable constraints on the relaxation mechanism of the molecule after ionisation [97]. The EPR/ENDOR spectra obtained with an irradiated single crystal of this compound show that the radiogenic species presents a small ^{31}P -coupling indicating a small phosphorus spin density ($\rho_s = 0.002$, $\rho_p = 0.002$) incompatible with a phosphoranyl participating in the SOMO. Discussion of the ^{31}P and ^1H hyperfine tensors in light of the crystal structure and of *ab initio* calculations suggest the trapping of $\text{Ph}_3\text{P}^+-\text{CH}=\text{C}(\text{OH})\text{CH}_2^-$ as shown in Fig. 2.13.

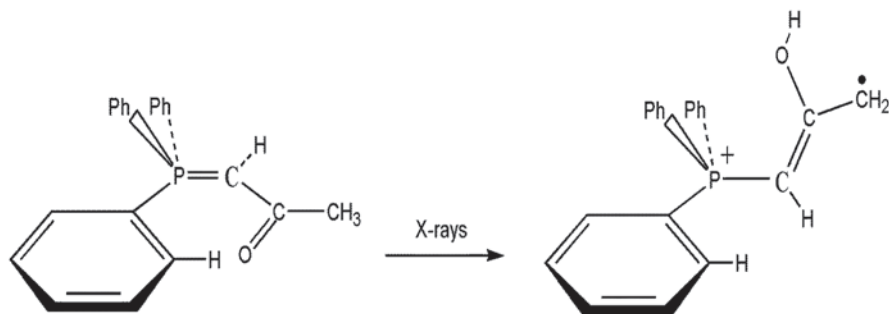


Fig. 2.13 Radiation damage in a single crystal of 1-triphenylphosphoranylidene-2-propanone. The figure is adapted from [97] by permission of Elsevier

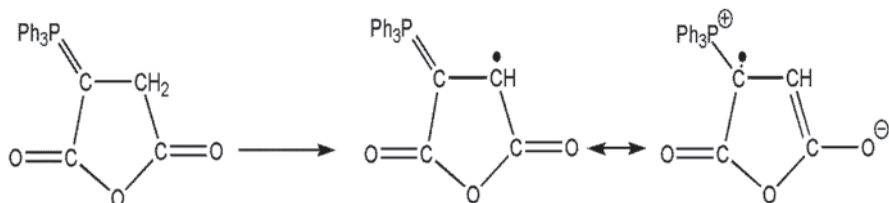


Fig. 2.14 Radical formation in an X-irradiated single crystal of 2-(triphenylphosphoranylidene)succinic anhydride

2.8.2 Captodatively Stabilized Radicals

Electron delocalization and charge separation play a crucial role in radical stabilization. These properties are at the basis of “captodative” effects observed in radicals containing electron donor and electron acceptor groups adjacent to the atoms bearing the unpaired electron [98]. These effects are currently invoked in biochemistry to explain, among other phenomena, reactivity modulation and proton-coupled electron transfer [99, 100, 101].

Irradiation of a single crystal of 2-(triphenylphosphoranylidene)succinic anhydride leads to EPR/ENDOR spectra that exhibit hyperfine coupling with a ^{31}P nucleus and a proton [102]. This radical is stable at room temperature during several weeks and can be generated in liquid solution by photolysis. The phosphorus coupling ($A_{\text{iso}} = (-)29.8$ MHz, $\tau_{\text{max}} = 5$ MHz) is too weak to be attributed to a phosphoranyl radical, while the ^1H coupling is consistent with a hydrogen in a position to an sp^2 carbon. Clearly the radical results from the homolytic scission of a CH bond in the methylene group. Among the numerous limit formulas that can describe this radical, the zwitterionic structure shown in Fig. 2.14 points out the phosphonium and enolate mesomeric forms and is expected to give rise to captodative stabilization.

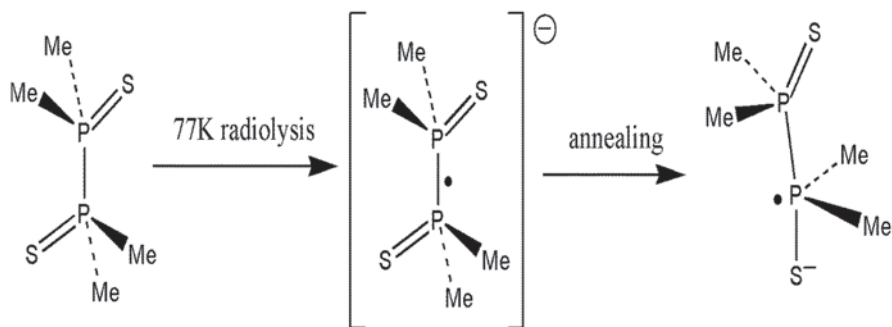


Fig. 2.15 Formation of phosphoranyl radical in an irradiated single crystal of tetramethyldiphosphine disulfide. The figure is adapted from [107] by permission of the American Institute of Physics

Using *ab initio* calculations together with the method of Katritzky [103] to assess this stabilization energy (call merostabilization ΔE_M), it was shown that, indeed, ΔE_M is equal to $-12.4 \text{ kcal mol}^{-1}$ for $\text{PH}_3=\text{CHCHC}(\text{H})\text{O}$; this value is slightly less ($-9.5 \text{ kcal mol}^{-1}$) for $\text{PH}_2\text{CH}_2\text{CHC}(\text{H})\text{O}$, which cannot adopt a phosphonium-enolate structure. Similar results were obtained when the method of Pasto [104] was used to estimate the captodative stabilization energy.

2.9 Symmetrical Radical Ions Containing a P–P Bond

As shown by Williams et al. [105], the radical cation $[(\text{MeO})_3\text{P-P}(\text{OMe})_3]^+$ is produced by γ -irradiation at 77 K of single crystals of trimethylphosphite; similarly, Lyons and Symons reported the formation of the dimer cation $[\text{Me}_3\text{P-PMe}_3]^+$ by γ -irradiation of Me_3P at low temperature [106]. The tendency for R_3P^+ to react with a nearby phosphine was clearly shown by exposing dilute solutions of phosphine in freon [73]. These species exhibit a large phosphorus hyperfine splitting and are described as σ^* radicals with a three electron P–P bond. For $[\text{Me}_3\text{P-PMe}_3]^+$ the phosphorus coupling constants ($A_{\text{iso}} = 1407 \text{ MHz}$, $\tau_{\parallel} = 251 \text{ MHz}$) lead to a hybridization ratio $\lambda^2 = 3.2$, indicating a bending of the R_3P moiety when passing from Me_3P^+ (see Table 2.3) to the dimeric radical cation.

In their work on tetramethyldiphosphine disulfide, Buck et al. [107] showed that the radical anion $[(\text{Me}_2(\text{S})\text{P-P}(\text{S})\text{Me}_2)]^-$ was formed by X-irradiation of single crystals of this compound at 77 K. This species is characterized by a symmetrical distribution of the unpaired electron over the two phosphorus atoms. This is not the case for a second radical, formed after annealing of the sample, which was identified as the phosphoranyl radical $\text{Me}_2(\text{S})\text{P-P}(\text{S}^-)\text{Me}_2$ adopting a TBP-e structure with the second phosphorus in apical position (see Fig. 2.15). The radical anion $[(\text{Me}_2(\text{S})\text{P-P}(\text{S})\text{Me}_2)]^-$ is a three-electron bond radical in which 65% of the unpaired electron lies on the phosphorus atoms.

2.10 Radicals Produced by Radiolysis of Diphosphenes

ArP = PAr

As phosphalkenes, diphosphenes are highly reactive compounds containing di-coordinated trivalent phosphorus atoms. They are often stabilized by linking the phosphorus atom to a bulky group such as the supermesityl moiety (Mes*). Initial EPR experiments on diphosphenes were carried out by photolysis in liquid solution; they showed that in the presence of di-*t*-butylperoxide the spectrum was mainly due to addition of ¹Bu on the P=P bond [108]. The electronic structure of this type of radical was obtained from single crystal EPR studies performed on X-irradiated bis(2,4,6-tri-*tert*-butylphenyl) diphosphene [109, 110]. Immediately after irradiation at 77 K, the spectra are composed of a broad intense signal, probably due to numerous orientations of RCH₂ radicals located on the supermesityl moieties and of signals due to a radical **R1** exhibiting hyperfine interactions with two non-equivalent ³¹P nuclei and a proton. One of these phosphorus coupling tensors ($A_{\text{iso}} = 316.5$ MHz, $\tau_{//} = 524.1$ MHz, $\rho_s = 0.02$, $\rho_p = 0.71$) reveals the trapping of a phosphinyl radical while the second ³¹P coupling ($A_{\text{iso}} = 118.9$ MHz, $\tau_{//} = 43.7$ MHz, $\rho_s = 0.01$, $\rho_p = 0.06$) is consistent with a phosphorus nucleus linked to a phosphorus atom bearing the unpaired electron in a p_π orbital. As shown by its hyperfine interaction ($A_{\text{iso}} = 68.8$ MHz, $\tau_1 = 6.7$ MHz, $\tau_2 = -1.2$ MHz, $\tau_3 = -5.4$ MHz), a proton is also located in β -position to the magnetic phosphorus atom. This species **R1** was therefore identified as the Mes*P(H)-PMes* radical produced by intermolecular addition of a H atom on the diphosphene P=P bond (Fig. 2.17).

At 170 K, the broad intense signal disappears and a new species (**R2**) is formed. The coupling tensors for this species are given in Table 2.7. The spin density ρ_p on phosphorus P₁ ($A_{\text{iso}} = 227.6$, $\tau_{\text{max}} = 425.4$ MHz, $\rho_s = 0.017$, $\rho_p = 0.58$) is smaller than for (**R1**) but is not in conflict with the spin densities expected for a phosphinyl radical of the ArP(X)-PAr type. For both species, **R1** and **R2**, the direction of the phosphorus p_π orbital, as given by the P₁- $\tau_{//}$ eigenvector, is found to be oriented perpendicular to the crystallographic C1P1P2 plane. Hyperfine interaction with P₂ ($A_{\text{iso}} = 378.3$, $\tau_{\text{max}} = 104.7$ MHz, $\rho_s = 0.028$, $\rho_p = 0.14$) indicates, however, a larger delocalization of the spin on this second phosphorus atom. Moreover, the additional ¹H coupling is very small, consistent with a proton in γ -position to the radical phosphorus. These changes in the coupling constants suggest that radical **R2**

Table 2.7 Principal values (MHz) of the ³¹P and ¹H coupling tensors for radicals derived from diphosphene

Radical	³¹ P ₁ -coupling			³¹ P ₂ -coupling			¹ H-coupling		
	T ₁	T ₂	T ₃	T ₁	T ₂	T ₃	T ₁	T ₂	T ₃
R1 ^a	840.6	89.3	19.7	162.6	105.3	89.0	75.5	67.6	63.3
R2 ^a	653.0	29.0	1.0	483.0	337.0	315.0	<15	<15	<15
Mes*(Me)P-PMes*	708	36	5	504	326	342			

^a See Fig. 2.17

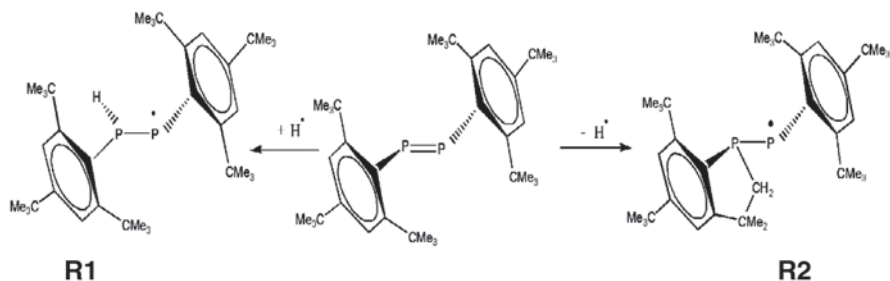


Fig. 2.16 Phosphinyl-type radicals formed in irradiated single crystals of bis(2,4,6-tri-tert-butylphenyl) diphosphene

results from an intramolecular cyclisation caused by the addition of a CH_2 group to a nearby phosphorus atom (see Fig. 2.16). The constraints caused by this rearrangement lead to a small internal rotation around the P-P bond and to a better overlap between the p orbitals of the two phosphorus atoms.

At higher temperature, the spectra due to **R1** and **R2** species disappear and are replaced by lines due to radicals that exhibit hyperfine coupling with a single ^{31}P nucleus and which likely result from scission of the P-P bond.

More attention can be paid to the structure of radical **R1**. Although detection of this radiolytic radical is possible owing to stabilization by the crystalline matrix, simple replacement of the hydrogen atom bound to phosphorus by a methyl group leads to a radical that can be observed in solution at room temperature [111]. Reaction of the phosphonium salt $[\text{Mes}^*\text{MeP}=\text{PMes}^*]^+ (\text{O}_3\text{SCF}_3)^-$ with the electron donor tetrakis(dimethylamino)ethylene gives rise to yellow-orange crystals of $[\text{Mes}^*\text{MeP}=\text{PMes}^*]$. The EPR tensors of this radical were obtained by doping a single crystal of diphosphane $\text{Mes}^*\text{MeP}=\text{PMes}^*\text{Me}$ with traces of $[\text{Mes}^*\text{MeP}=\text{PMes}^*]$. The resulting EPR parameters are given in Table 2.7. They agree with those measured for the radiogenic radicals **R1** and **R2**. It is interesting to compare the structure of this diphosphanyl radical $\text{R}_2\text{P}=\text{PR}$ with that of 1,2-diphenyl picrylhydrazyl (DPPH), the most popular EPR marker, which is also a nitrogen homologue of phospholanes. In $[\text{Mes}^*\text{MeP}=\text{PMes}^*]$ 62% of the spin is localized in a p orbital of the dicoordinated phosphorus atom P_1 and less than 15% lies on the other phosphorus atom P_2 . As shown by DFT calculations, the distance between the two phosphorus atoms is close to that of a P-P single bond and the environment of P_2 is pyramidal. In DPPH, the unpaired electron is almost equally shared between the two nitrogen atoms, the coordination of N_2 is planar and the N-N bond length is intermediate between a single and a double bond. It is worthwhile remarking that the large anisotropy of the hyperfine coupling with P_1 in $[\text{Mes}^*\text{MeP}=\text{PMes}^*]$ makes its EPR spectrum particularly sensitive to molecular motion. This is the fundamental property required for spin labels. The temperature dependence of the liquid phase EPR spectrum as well as the simulation of the spectrum as a function of the tumbling correlation time has been reported [112].

2.11 Radical Pair Formation

Radical pairs involving phosphorus-centered radicals have been detected after radiolysis of some phosphated sugars. Identification of radiogenic radicals produced on the sugar phosphate moiety is important for understanding mechanisms related to radiolysis of nucleic acids and many studies have been devoted to this subject [113, 114, 115]. Consistent with results obtained with various phosphates, X-irradiation of a single crystal of a phenoxyphosphoryl xylofuranose derivative [116] and a single crystal of a diphenoxyphosphoryl ribofuranose derivative [117] led to the trapping of phosphoranyl and phosphonyl radicals. In addition to the signals of these isolated radicals, the spectrum exhibits anisotropic lines due to the formation of a radical pair. Analysis of the angular variation of signals due to a radical pair is well known. The Hamiltonian takes into account the electron-electron dipolar interaction (*SDS*), which leads to the zero-field splitting parameters *D* and *E*. The hyperfine tensor corresponds to half the values that would have been measured with an isolated radical. Irradiation temperature is a very critical parameter for the formation of the pairs detected in these two crystals. The good temperature range comprises between 90 and 100 K; moreover, a rather short irradiation time (30 min) is sufficient to observe these pairs, which are stable till 160K. The zero-field splitting parameters (*D* = 500 MHz, *E* = 15 MHz) suggest that the unpaired electrons are strongly localized on each member of the pair; a point-dipole approximation leads to an interspin distance of $\sim 5 \text{ \AA}$. As shown by hyperfine coupling with a single ^{31}P nucleus, the pair is composed of two different species and one of these species is consistent with a phosphoryl radical $\text{P}(\text{O})(\text{OR})_2$. The observation of this pair agrees with a mechanism proposed by Nelson and Symons for organic phosphates [118]: in this mechanism the main step is an electron capture by the cationic species $[(\text{RO})_3\text{PO}]^+$ to give $[(\text{RO})_3\text{PO}]^*$, which undergoes a homolytic scission of a P–O bond. Formation of the $\text{RO}\dots(\text{RO})_2\text{PO}$ pair results from diffusion of the phosphoryl radical 5 \AA from the sugar moiety. In this process the crystal packing and the size of the radical are determinant.

2.12 Metallated Radicals

The role of metal-containing radicals is increasingly invoked in modern organic synthesis and in biochemistry. The presence of the metal is meant to participate in stabilization of the radical; a dialkylaminyl radical, for example, was stabilized by coordination to a cationic Rh center and the corresponding radical metal complex could be isolated [119]. Complexation of a PR_2 moiety by a transition metal containing *n* electrons can, a priori, give rise to one of three structures: (1) a phosphido-type ligand PR_2^- linked to a d^{n-1} metal; (2) a phosphinyl radical PR_2 linked to a d^n metal; (3) a phosphonium-type ligand $^+\text{PR}_2$ linked to a d^{n+1} metal. The first type has been used for enantioselective catalysis [120] and the third is involved in the

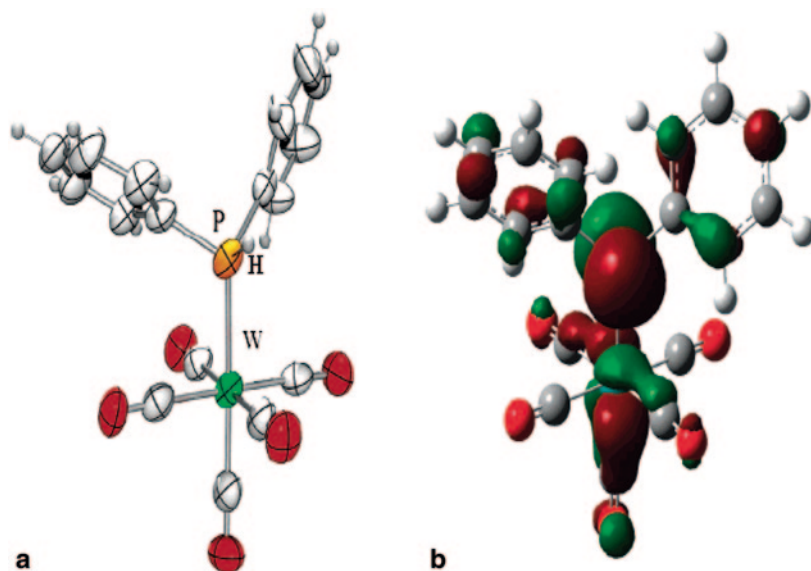


Fig. 2.17 **a** ORTEP view of the crystal structure of $\text{W}(\text{CO})_5\text{P}(\text{H})\text{Ph}_2$. **b** SOMO for $\text{Mo}(\text{CO})_5\text{PPh}_2$. The figure is adapted from [122] by permission of the American Chemical Society

stabilization of electrophilic complexes with late metal atoms [121]. A single crystal of diphenyl phosphine complexed by a transition metal constitutes an excellent system to assess the structure of one of these species [122]. Exposure of $\text{W}(\text{CO})_5\text{P}(\text{H})\text{Ph}_2$ (see Fig. 2.17a) to X-rays at room temperature provokes homolytic scission of a P–H bond and the trapping of $\text{W}(\text{CO})_5\text{PPh}_2$. The EPR spectrum of this species is characterized by a large and anisotropic ^{31}P coupling. Similar results are obtained by irradiating $\text{Cr}(\text{CO})_5\text{P}(\text{H})\text{Ph}_2$ as well as the two complexes of triphenylphosphine $\text{W}(\text{CO})_5\text{PPh}_3$ and $\text{Mo}(\text{CO})_5\text{PPh}_3$. For these latter two complexes the radicals result from scission of a P–C bond and three orientations are observed for each radical site.

The ^{31}P hyperfine interactions reported in Table 2.8 are quite reminiscent of the values reported for the diphenylphosphinyl radical (*vide supra*). As for Ph_2P , the direction of $\tau_{//}$ is almost aligned along the direction of g close to 2.0023. A notable difference lies, however, in the isotropic coupling constant, which is appreciably larger for the metallated radical.

DFT calculations on $\text{M}(\text{CO})_5\text{PPh}_2$ (with $\text{M} = \text{Mo}, \text{Cr}, \text{W}$) correctly reproduce the experimental hyperfine tensors as well as the relative orientations of the g and ^{31}P coupling eigenvectors. They confirm the increase in the isotropic coupling when passing from Ph_2P to $\text{M}(\text{CO})_5\text{PPh}_2$. As shown by the SOMO (Fig. 2.17b), in $\text{M}(\text{CO})_5\text{PPh}_2$ a σ bond is formed between the lone pair of the sp^2 -hybridized phosphorus of the phosphinyl group and the empty metal d_{z^2} orbital. Clearly, scission of a P–H bond in $\text{M}(\text{CO})_5\text{P}(\text{H})\text{Ph}_2$ leads to a species that maintains the principal features of the phosphinyl radical even if a small delocalization of the spin from the phosphorus p-orbital to the metal d_{xz} orbital occurs.

Table 2.8 EPR parameters and phosphorus spin densities for the radical species $M(\text{CO})_5\text{PPh}_2$

Single crystal	g-tensor	$^{31}\text{P}-A_{\text{iso}}^b$	$^{31}\text{P}-\tau^b$	ρ_s	ρ_p
$\text{W}(\text{CO})_5\text{P}(\text{H})\text{Ph}_2^a$	2.007, 2.025, 2.016	499	433, -239, -194	0.04	0.59
$\text{Cr}(\text{CO})_5\text{P}(\text{H})\text{Ph}_2^a$	2.002, 2.007, 2.011	500	434, -226, -208	0.04	0.59
$\text{W}(\text{CO})_5\text{PPh}_3^a$	1.994, 2.018, 2.030	423	426, -219, -207	0.03	0.58
$\text{Mo}(\text{CO})_5\text{PPh}_3^a$	2.003, 2.009, 2.016	419	411, -232, -179	0.03	0.56

^a From [122]^b In MHz

$M(\text{CO})_5\text{PPh}_2$ is not the single species observed by EPR after radiolysis of $M(\text{CO})_5\text{PPh}_3$. Irradiation at 77 K leads to a radical characterized by a very strong g anisotropy, a small ^{31}P hyperfine interaction ($A_{\text{iso}} \sim -30$ MHz, $\tau \sim 10$ MHz) and, in the case of $\text{W}(\text{CO})_5\text{PPh}_3$, by a coupling of ~ 30 MHz with ^{183}W (natural abundance: 14.3 %, $I = 1/2$) [123]. This species, identified as $[\text{M}(\text{CO})_4\text{PPh}_3]^-$, results from the departure of a CO group after electron capture by the precursor. As shown by DFT calculations, the electron-excess center $[\text{M}(\text{CO})_5\text{PPh}_3]^-$ tends to dissociate; within the crystal matrix the cage effect likely precludes the PPh_3 group from escaping and scission of a M–C bond occurs. This mechanism is reminiscent of observations on some polycarbonyl complexes that lose a carbonyl by reduction [124]. A more direct method to produce this type of radical anion by radiolysis is to start from the diamagnetic stable host anion $[\text{W}(\text{CO})_4(\text{H})\text{P}(\text{OMe})_3]^-$ [125]. Irradiation of a crystal of $[\text{N}(\text{PPh}_3)_2][\text{W}(\text{CO})_4\text{H}\{\text{P}(\text{OMe})_3\}]$ causes departure of the hydrogen atom directly linked to the tungsten atom and leads to ^{31}P hyperfine interaction quite similar to those reported for $[\text{M}(\text{CO})_4\text{PPh}_3]^-$. The EPR tensors measured for $[\text{M}(\text{CO})_4\text{PPh}_3]^-$ agree with those calculated by DFT, showing that this complex adopts a square pyramidal structure with PPh_3 in basal position. The phosphorus spin density is very small, the unpaired electron being mainly delocalized in the p_z and d_z^2 orbitals of the transition metal and in the carbon p_z orbitals of the three basal carbonyl groups. As shown by EPR measurements at variable temperature, $[\text{M}(\text{CO})_4\text{PPh}_3]^-$ undergoes irreversible small structural distortions and reorientations in the crystal matrix between 77 and 300 K.

While the neutral $M(\text{CO})_5\text{PPh}_2$ and anionic $[\text{M}(\text{CO})_4\text{PPh}_3]^-$ radicals could be detected after radiolysis at room temperature, a third species, corresponding to the electron-deficient center, could be detected only after irradiation at 77 K [126]. This radical cation, formed by X-irradiation of a single crystal of $\text{Mo}(\text{CO})_5\text{PPh}_3$, irreversibly disappears above 180 K. Experimental g-tensor and hyperfine couplings with phosphorus and molybdenum (^{95}Mo , $I = 5/2$, natural abundance: 15.9 %; ^{97}Mo , $I = 5/2$, natural abundance: 9.6 %) indicate a large localization of the spin on the metal (~ 60 %) and a low phosphorus spin density (~ 4 %). The coupling tensors are in good accordance with DFT predictions for $[\text{Mo}(\text{CO})_5\text{PPh}_3]^+$. These DFT calculations indicate that ionization of $\text{Mo}(\text{CO})_5\text{PPh}_3$ causes a shortening and a small tilt of the Mo–P bond. This geometrical change induces an interaction between one of the phenyl rings and the region containing the unpaired electron. Such rearrangements are likely partly hindered by nearby complexes; this could explain the difference

Table 2.9 EPR parameters for $[\text{Mo}(\text{CO})_4\text{PPh}_3]^{-\text{a}}$ and $[\text{Mo}(\text{CO})_5\text{PPh}_3]^{+\text{b}}$

	g-tensor	$^{31}\text{P-A}_{\text{iso}}^{\text{c}}$	$^{31}\text{P-}\tau^{\text{c}}$	$(g_{\text{min}}, T_{\text{max}})_{\text{exp}}$	$(g_{\text{min}}, T_{\text{max}})_{\text{DFT}}$
$[\text{Mo}(\text{CO})_4\text{PPh}_3]^{-}$	2.001, 2.022, 2.024	-43	9, -7, -2	15°	8°
$[\text{Mo}(\text{CO})_5\text{PPh}_3]^{+}$	1.961, 2.080, 2.116	72	31, -12.5, -18.5	66°	88°

^a From [123]^b From [126]^c In MHz

in the $(g_{\text{min}}, ^{31}\text{P-T}_{\text{max}})$ angle, whose measured value is equal to 66°, while the DFT value is equal to 88°. It can be remarked that in the radical anion $[\text{Mo}(\text{CO})_4\text{PPh}_3]^{-}$ experiment and DFT calculations lead to a much smaller angle (see Table 2.9).

2.13 Conclusion

A considerable number of studies have been devoted to phosphorus containing radicals. Although numerous methods are able to generate such species, only the radicals produced by radiolysis of solid precursors have been considered in this chapter. In contrast with EPR experiments, which use chemical reactants or electrochemistry to generate organophosphorus radicals in solution, trapping of radiogenic radicals inside an oriented matrix yields all components of the EPR tensors and leads to an accurate description of the SOMO and confident identification of the radical species. As mentioned in this review, radiolysis of organophosphorus compounds can give rise to numerous radical species and each type of radical can often adopt several conformations. Moreover, an increase in temperature often causes a change in structure or a molecular rearrangement. Phosphoranyl radicals are a good example of this problem. This complexity, due to the various types of valency and coordination that phosphorus can adopt, can lead to different interpretations. A careful analysis of the spectra obtained after irradiation of the crystal at very low temperature followed by variable temperature measurements is therefore required to get accurate information on radiation mechanism. This information is especially precious because of the participation of phosphorus in the structures of numerous important biological molecules.

References

1. Leca D, Fensterbank L, Lacote E, Malacria M (2005) Recent advances in the use of phosphorus-centered radicals in organic chemistry. *Chem Soc Rev* 34:858–865
2. Tordo P (2005) Reactivity of phosphorus centered radicals. *Topics Current Chem* 250:43–76
3. Benstrude WG (1990) Free radicals reactions of organophosphorus (III). *Chem Organophosphorus Compd* 1:531–566

4. Lund A, Shiotani M (eds) (2003) EPR of free radicals in solids: trends in methods and applications. Prog Theor Chem Phys 10 Springer US
5. Soulié E, Berclaz T (2005) Electron paramagnetic resonance: nonlinear least-squares fitting of the Hamiltonian parameters from powder spectra with the Levenberg–Marquardt algorithm. Appl Magn Reson 29:401–416
6. Hanson GR, Noble CJ, Benson S (2003) X-Sophe- XeprView and Molecular Sophe: computer simulation software suites for the analysis of continuous wave and pulsed EPR spectra (in Prog Theor Chem Phys, Lund A, Shiotani M Edts Springer 223–284)
7. Thiele H, Erstling J, Such P, Höfer P (1992) WIN-EPR: EPR Software Suites from Bruker Corporation. Germany; Hanson GR (2007) XSophe simulation Package. Bruker Biospin, Rheinstetten/Karlsruhe, Germany
8. Watson RE, Freeman AJ (1961) Hartree-Fock wave functions for the 4p-shell atoms. Phys Rev 124:1117–1123
9. Atkins PW, Symons MCR (1967) The structure of inorganic radicals. Elsevier Publishing Company, London
10. Morton JR, Preston KF (1978) Atomic parameters for magnetic resonance data. J Magn Reson 30:577–582
11. Coulson CA (1948) Contribution to the study of molecular structure. Volume commémoratif Victor Henri, Desoer, Liège, pp 15–31
12. Morehouse RL, Christiansen JJ, Gordy W (1966) E.S.R. of free radicals trapped in inert matrices at low temperature: P, PH₂, and As. J Chem Phys 45:1747–1751
13. Nelson W, Jackel G, Gordy W (1970) Electron spin resonance of trapped PF₂ and PF₄ radicals. J Chem Phys 52:4572–4578
14. Wei MS, Current JH, Gendell J (1972) Anisotropic electron spin resonance spectra of phosphorus dichloride and nitrogen dichloride in low temperature matrixes. J Chem Phys 57:2431–2442
15. Fullam BW, Mishra SP, Symons MCR (1974) Unstable intermediates. Electron spin resonance study of phosphinyl radicals formed by solid-state radiolysis. J Chem Soc DaltonTrans 20:2145–2148
16. Fullam BW, Symons MCR (1975) Radiation mechanisms. Electron spin resonance studies of the mechanism of radiation processes in trivalent phosphorus derivatives. J Chem Soc Dalton Trans Inorg Chem 10:861–866
17. Geoffroy M, Lucken EAC, Mazeline C (1974) Diphenylphosphino radical Ph₂P. Mol Phys 28:839–845
18. Ginet L, Geoffroy M (1974) Electron paramagnetic resonance study of the φ-diamino phosphine radical trapped in x-irradiated diphenylaminophosphine oxide single crystals. Helv Chim Acta 57:1761–1765
19. Hill NJ, Reeske G, Cowley AH (2010) Reaction of persistent phosphinyl radical P[CH(SiMe₃)₂]₂ with elemental chalcogens. Main group. Chemistry 9:5–10
20. Giffin NA, Hendsbee AD, Roemmele TL, Lumsden MD, Pye CC, Masuda JD (2012) Preparation of a diphosphine with persistent phosphinylradical character in solution: characterization, reactivity with O₂, S₈, Se, Te and P₄, and electronic structure calculations. Inorg Chem 51:11837–11850
21. Ishida S, Hirakawa F, Iwamoto T (2011) A stable dialkylphosphinyl radical. J Am Chem Soc 133:12968–12971
22. Back O, Celik MA, Frenking G, Melaimi M, Donnadiou B, Bertrand G (2010) A crystalline phosphinyl radical cation. J Am Chem Soc 132:10262–10263
23. Geoffroy M, Ginet L, Lucken EAC (1976) Electron spin resonance study of the diphenylarsino radical (C₆H₅)₂ as produced in a single crystal matrix. J Chem Phys 65:729–732
24. Geoffroy M, Ginet L, Lucken EAC (1977) Electron spin resonance study of the radical diphenylantimony trapped in a single crystal matrix. J Chem Phys 66:5292–5295
25. Cook WT, Vincent JS (1977) ESR of diphenylantimony radical in a triphenylantimony single crystal. J Chem Phys 67:5766–5769

26. Colin J-P, Heitz V, Sauvage J-P (2005) Transition-metal complexed catenanes and rotaxanes in motion: towards molecular machines. *Top Curr Chem* 262:29–62
27. Kelly TR, Bowyer MC, Bhaskar KV, Bebbington D, Garcia A, Lang F, Kim M, Jette MP (1994) A molecular brake. *J Am Chem Soc* 116:3657–3658
28. Ramakrishnan G, Jouaiti A, Geoffroy M, Bernardinelli G (1996) 9-Substituted triptycene as a probe for the study of internal rotation around a C–PH Bond in the solid state: a single crystal EPR study at variable temperature. *J Phys Chem* 100:10861–10868
29. Brynda M, Berclaz T, Geoffroy M, Ramakrishnan G (1998) Hindered rotation around a C–•PH bond: a single-crystal EPR study of the diphenyldibenzobarrelenephosphinyl radical. *J Phys Chem A* 102:8245–8250
30. Brynda M, Dutan C, Berclaz T, Geoffroy M (2002) Dynamic phenomena in barrelenephosphinyl radicals: a complementary approach by density matrix analysis of EPR spectra and DFT calculations. *Current Topics in Biophysics* 26:35–42
31. Brynda M, Berclaz T, Geoffroy M (2000) Intramolecular motion in dibenzobarrelenephosphinyl radical: a single crystal EPR study at variable temperature. *Chem Phys Lett* 323:474–481
32. Brynda M, Dutan C, Berclaz T, Geoffroy M, Bernardinelli G (2003) Intramolecular motion in the triptycengermany radical: single crystal EPR study at variable temperature and DFT calculations. *J Phys Chem Solids* 64:939–946
33. McConnachie GDG, Rai US, Symons MCR (1993) Electron addition to trimethyl phosphite induced by ionizing radiation: an electron spin resonance study. *J Mol Struct* 300:527–537
34. Hudson RL, Williams F (1979) The radical anion of trimethyl phosphate. *J Chem Soc Chem Commun* 24:1125–1126
35. Gerson F, Plattner G, Bock H (1970) ESR spectra of the radical anion of dimethylphenylphosphine. *Helv Chim Acta* 53:1629–1636
36. Cattani-Lorente M, Geoffroy M, Mishra SP, Weber J, Bernardinelli G (1986) Theoretical and single-crystal ESR study of the structure and dissociation of a R_2PCl radical anion. *J Am Chem Soc* 108:7148–7153
37. Franzi R, Geoffroy M, Ginet L, Leray N (1979) Structure of selenium-centered radicals. An electron spin resonance study of $R_2 SeHal$ trapped in single crystals. *J Phys Chem* 83:2898–2902
38. Cattani-Lorente M, Geoffroy M (1990) Electron capture by trivalent phosphorus compounds: a single crystal ESR study of the chlorodithiaphospholane anion. *Chem Phys Lett* 167:460–466
39. Boate AR, Colussi AJ, Morton JR, Preston KF (1976) ESR spectra of fluorine-containing radicals of phosphorus and arsenic. *Chem Phys Lett* 37:135–137
40. Hamerlinck JHM, Schipper P, Buck HM (1981) Single crystal ESR study of x-irradiated 2-chloro-2,2'-spirobis(1,3,2-benzodioxaphosphole): phosphorus in an octahedral geometry with the unpaired and chlorine in axial positions. *Chem Phys Lett* 80:358–360
41. Geoffroy M, Hwang J, Llinares A (1982) An ESR study of an x-ray irradiated Ph_3AsF_2 single crystal. *J Chem Phys* 76:5191–5194
42. Hodgson JL, Coote ML (2005) Effects of substituents on the stability of phosphoranyl radicals. *J Phys Chem* 109:10013–10021
43. Giles JRM, Roberts BP (1981) Electron spin Resonance studies of thiophosphoranyl radicals. The mechanism of ligand permutation in phosphoranyl radicals. *J Chem Soc Perkin Trans* 2:1211–1220
44. Krusic PJ, Mahler W, Kochi JK (1972) Electron spin resonance spectra and structures of phosphoranyl radicals in solution. *J Am Chem Soc* 94:6033–6041
45. Hasegawa A, Ohnishi K, Sogabe K, Miura M (1975) ESR spectra of phosphorus tetrafluoride radicals produced in a single crystal of phosphorus trifluoride. *Mol Phys* 30:1367–1375
46. Gillbro T, Williams F (1974) Electronic structure of phosphoranyl radicals. *J Am Chem Soc* 96:5032–5038
47. Rundle RE (1963) Implications of some recent structures for chemical valence theory. *Surv Progr Chem* 1:81–131

48. Hamerlinck JHH, Schipper P, Buck HM (1980) ESR study of X-irradiated [HP(OCH₂CH₂)₃N]BF₄: phosphorus in a trigonal bipyramidal configuration with the unpaired electron in apical position. *J Am Chem Soc* 102:5679–5680
49. Berclaz T, Geoffroy M, Lucken EAC (1975) An electron spin resonance study of x-irradiated single crystals of the triphenylphosphine-boron trichloride adduct: the triphenylchloro phosphorane radical. *Chem Phys Lett* 36:677–679
50. Hamerlinck JHH, Schipper P, Buck HM (1981a) Single crystal ESR study of the 1,6-dioxo-4,9-diaza-5-phospha(V)spiro[4.4]nonan-5-yl and the 1,6-dioxo-4,9-diaza-2,3,7,8-dibenzo-5-phospha(V)spiro[4.4]nona-2,7-dien-5-yl radicals. *J Chem Soc Chem Commun* 3:104–106
51. Hamerlinck JHH, Schipper P, Buck HM (1981b) Stereoisomerization of the tricyclotrioxaa-zoniaphosphaundecane tetrafluoroborate phosphoranyl radical: a single crystal ESR study. *J Chem Soc Chem Commun* 21:1148–1149
52. Hamerlinck JHH, Hermkens PHH, Schipper P, Buck HM (1981c) Single crystal ESR study of the octahydro-2a,4a,6a,8a-tetraaza-8b-phospha(V)pentaleno[1,6-cd]pentalen-8b-yl radical. Evidence of ligand exchange via a Berry pseudorotation mechanism. *J Chem Soc Chem Commun* 8:358–360
53. Janssen RAJ, Sonnemans MHW, Buck HM (1986) σ^* and TBP-e radicals obtained by electron capture of four-coordinated phosphorus compounds. A single-crystal ESR study. *J Am Chem Soc* 108:6145–6149
54. Berclaz T, Geoffroy M, Lucken EAC (1975) An electron spin resonance study of x-irradiated single crystals of the triphenylphosphine-boron trichloride adduct: the triphenylchloro phosphorane radical. *Chem Phys Lett* 36:677–679
55. Cattani-Lorente M, Bernardinelli G, Geoffroy M (1987) Formation and structure of the phosphoranyl radical derived from 1,2-phenylene phosphorochloridate: a solid-state ESR study. *Helv Chim Acta* 70:1897–1904
56. Janssen RAJ, Kingma JAJM, Buck HM (1988) A single-crystal ESR and quantum chemical study of electron-capture trialkylphosphine sulfide and selenide radical anions with a three-electron bond. *J Am Chem Soc* 110:3018–3026
57. Berclaz T, Geoffroy M, Ginet L, Lucken EAC (1979) Phosphoranyl radicals: an ESR study of triphenylbromophosphoranyl radical trapped in a single crystal. *Chem Phys Lett* 62:515–518
58. Berclaz T, Geoffroy M, Lucken EAC (1979) The EPR spectrum of the triphenylchloroarsanyl radical, Ph₃AsCl, trapped in a single crystal of triphenylmethylarsonium chloride. *J Magn Reson* 33:577–583
59. Geoffroy M, Llinares A (1983) ESR study of the Ph₃AsBr-radical trapped in an x-irradiated single crystal of Ph₃As⁺CH₃Br⁻. *Helv Chim Acta* 66:76–81
60. Geoffroy M, Llinares A, Krzywanska E (1984) ESR study of chalcogenotriphenylarsoranyl radicals Ph₃AsX⁻ trapped in single crystal matrices. *J Magn Reson* 58:389–400
61. Mishra SP, Symons MCR (1973) Unstable intermediates. Alkyl radical-halide ion adducts. *J Chem Soc Perkin Trans* 2:391–396
62. Fujita Y, Katsu T, Sato M, Takahashi K (1974) Carbon-13 hyperfine splittings of normal and abnormal methyl radicals trapped on the porous Vycor glass surface. *J Chem Phys* 61:4307–4311
63. Geoffroy M, Llinares A (1980) Identification and structure of a novel adduct: an ESR study of triphenylarsine-methyl radical trapped in a single crystal matrix. *Mol Phys* 41:55–62
64. Barnes RG, Bray PJ (1955) Nuclear quadrupole resonances of arsenic⁷⁵. *J Chem Phys* 23:407
65. Geoffroy M, Llinares A, Mishra SP (1986) Electron capture in single crystals of triphenylmethylarsonium iodide. Electron spin resonance detection of iodotriphenylarsoranyl radical. *J Chem Soc Faraday Trans* 1(82):521–525
66. Symons MCR, McConnachie GDS (1984) Electron addition to triphenylmethyl arsonium iodide. *J Chem Soc Faraday Trans* 1(80):211–216
67. Stewart B, Harriman A, Higham LJ (2011) Predicting the air stability of phosphines. *Organometallics* 30:5338–5343

68. Lalevee J, Morlet-Savary F, Tehfe MA, Graff B, Fouassier JP (2012) Photosensitized formation of phosphorus-centered radicals: application to the design of photoinitiating systems. *Macromolecules* 45:5032–5039
69. Merzougui B, Berchadsky Y, Tordo P, Gronchi G (1997) Trimesityl phosphoniumyl cation radical: electrogeneration and evolution. *Electrochim Acta* 42:2445–2453
70. Begum A, Lyons AR, Symons MCR (1971) Unstable intermediates. Radicals AlR_3^- , SiR_3^- , PR_3^+ . Their electron spin resonance spectra and pyramidal character. *J Chem Soc A* 971:2290–2293
71. Lyons AR, Symons MCR (1973) Electron spin resonance spectra of γ -irradiated or photolyzed arsines. *J Am Chem Soc* 95:3483–3485
72. Eastland GW, Symons MCR (1977) Unstable intermediates. Triphenyl-phosphonium and -arsonium cations and various phosphoranyl and arsoranyl radicals derived from triphenylphosphine and its oxide, sulfide, and selenide and triphenylarsine and its oxide by the action of ionizing radiation. *J Chem Soc Perkin Trans 2*:833–838
73. Hasegawa A, McConnachie GDG, Symons MCR (1984) Preparation and structure of certain phosphorus-centered radical cations. An electron spin resonance study. *J Chem Soc Faraday Trans 1*(80):1005–1016
74. Berclaz T, Geoffroy M (1975) Triphenylphosphinium radical cation. *Mol Phys* 30:549–555
75. Bhat SN, Berclaz T, Geoffroy M, Jouaiti A (1995) Radical reactions in a single crystal of phosphalkene: EPR and *ab initio* calculations of phosphoniumyl radical cations. *J Phys Chem* 99:15864–15869
76. Sheberla D, Tumanskii B, Tomasik AC, Mitra A, Hill NJ, West R, Apeloig Y (2010) Different electronic structure of phosphonyl radical adducts of N-heterocyclic carbenes, silylenes and germylenes: EPR spectroscopic study and DFT calculations. *Chem Science* 1:234–241
77. Jockusch S, Turro NJ (1998) Phosphinoyl radicals: structure and reactivity. A laser flash photolysis and time-resolved ESR investigation. *J Am Chem Soc* 120:11773–11777
78. Pan XQ, Wang L, Zou JP, Zhang W (2011) Manganese(III)-mediated phosphinoyl radical reactions for stereoselective synthesis of phosphinoylated tetrahydronaphthalenes. *J Chem Soc Chemical Commun* 47:7875–7877
79. Bagryanskaya E, Fedin M, Forbes MDE (2005) CIDEP of micellized radical pairs in low magnetic fields. *J Phys Chem A* 109:5064–5069
80. Tumanskii BL, Bashilov VV, Bubnov NN, Solodovnikov SP, Sokolov VI (1996) EPR study of spin-adducts of dialkylphosphonyl radicals with fullerenes and [60] fullerene-metallocomplexes. *Mol Cryst Liq Cryst Sci Technol* 8:61–64
81. Lawrence JB. (doi:10.5772/45779) in “Nitroxides. Theory, Experiment and Applications” edited by Alexander I. Kokorin
82. Rassat A (1971) Application of electron spin resonance to conformational analysis. *Pure Appl Chem* 25:623–634
83. Geoffroy M, Lucken EAC (1971) Electron spin resonance spectrum of x-irradiated single crystals of diphenylphosphine oxide. *Mol Phys* 22(2):257–262
84. Geoffroy M, Lucken EAC (1972) Electron spin resonance spectrum of x-irradiated phenylphosphinic acid and its salts. *Mol Phys* 24:335–340
85. Kerr CML, Webster K, Williams F (1975) Electron spin resonance studies of γ -irradiated phosphite and phosphate esters. Identification of phosphinyl, phosphonyl, phosphoranyl, and phosphine dimer cation radicals. *J Phys Chem* 79:2650–2662
86. Schlick S, Silver BL, Luz Z (1970) ESR of oxygen-17 labeled PO_3^{2-} ion trapped in a single crystal of $\text{Na}_2\text{DPO}_3 \cdot 5\text{D}_2\text{O}$. *J Chem Phys* 52:1232–1237
87. Geoffroy M (1973) Electronic paramagnetic resonance spectra of x-ray irradiated crystalline diphenylphosphine sulfide. *Helv Chim Acta* 56:1552–1557
88. Janssen RAJ, Sonnemans MHW, Buck HM (1986) Electron capture phosphoranyl radicals in x-irradiated diphosphine disulfides. A single crystal ESR and *ab initio* quantum chemical study. *J Chem Phys* 84:3694–3708
89. Geoffroy M, Llinares A (1979) Electron paramagnetic resonance study of trapped radicals in an x-ray irradiated sodium dimethylarsinate single crystal. *Helv Chim Acta* 62:1605–1613

90. Lyons AR, Symons MCR (1974) Effect of high-energy radiation on sodium methylarsenate and propylarsenic acid studied by electron spin resonance spectroscopy. *J Chem Phys* 60:164–169
91. Geoffroy M, Ginet L, Lucken EAC (1977) Electron spin resonance of $\text{Ph}_3\text{P}^+-13\text{CH}_2$ trapped in a single crystal matrix. *Mol Phys* 34:1175–1183
92. Samskog P-O, Lee S-h, Arroyo CM, Kispert LD, Geoffroy M (1984) Electron paramagnetic resonance study of $\text{Ph}_2\text{P}(\text{O})\text{CH}_2\text{Cl}^-$ trapped in x-ray irradiated (chloromethyl) diphenylphosphine oxide crystals at 3 K and $\text{Ph}_2\text{P}(\text{O})\text{CH}_2$ at 77 K. *J Phys Chem* 88:1804–1807
93. Berclaz T, Geoffroy M (1976) Electron spin study of the radical $(\text{C}_6\text{H}_5)_3\text{P}-\text{BH}_2$ trapped in an irradiated single crystal of triphenylphosphineborane. *Mol Phys* 32:815–821
94. Baban JA, Cooksey CJ, Roberts BP (1979) An electron spin resonance study of radical addition to vinylphosphines. *J Chem Soc Perkin Trans 2*:781–787
95. Geoffroy M, Rao G, Tancic Z, Bernardinelli G (1990) Trapping and ESR study of an allylic radical involving the participation of a phosphoranyl moiety: $\text{R}_3\text{PC}^*\text{HCR}_2$. *J Am Chem Soc* 112:2826–2827
96. Boekestein G, Jansen EHJM, Buck HM (1974) Phosphoranyl radical in a tetrahedral configuration. *J Chem Soc Chem Commun* 1974:118–119
97. Berclaz T, Bernardinelli G, Geoffroy M, Rao G, Tancic Z (1999) EPR/ENDOR study of an X-irradiated single crystal of 1-triphenylphosphoranylidene-2-propanone: the role of hydrogen bonds in the trapping of radiogenic radicals. *Rad Phys Chem* 56:539–545
98. Viehe HG, Janousek Z, Merenyi R, Stella L (1985) The captodative effect. *Accounts Chem Res* 18:148–154
99. Wood ME, Bissiriou S, Lowe C, Windeatt KM (2013) Synthetic use of the primary kinetic isotope effect in hydrogen atom transfer 2: generation of captodatively stabilized radicals. *Org Biomol Chem* 11:2712–2723
100. Khalaf AI (2010) Photochemistry and free radical stabilisation of the captodative centre. *Trends Photochem Photobiol* 12:7–15
101. Steill J, Zhao J, Siu CK, Ke Y, Verkerk UH, Oomens J, Dunbar RC, Hopkinson AC, Siu KWM (2008) Structure of the observable histidine radical cation in the gas phase: a captodative alpha-radical ion. *Angew Chem (International ed.)* 47:9666–9668
102. Geoffroy M, Rao G, Tancic Z, Bernardinelli G (1993) Radicals containing both a phosphoranylidene and a ketone group: an electron paramagnetic resonance/electron nuclear double resonance study of their structure and *ab initio* investigations on the captodative effects. *J Chem Soc Faraday Trans* 89:2391–2396
103. Katritzky AR, Zerner MC, Karelson MM (1986) A quantitative assessment of the merostabilization energy of carbon-centered radicals. *J Am Chem Soc* 108:7213–7214
104. Pasto DJ (1988) Radical stabilization energies of disubstituted methyl radicals. A detailed theoretical analysis of the captodative effect. *J Am Chem Soc* 110:8164–8175
105. Gillbro T, Kerr CMR, Williams F (1974) Electron spin resonance identification of the dimer cation $(\text{MeO})_3\text{PP}(\text{OMe})_3^+$ in γ -irradiated trimethyl phosphate from second-order hyperfine structure. *Mol Phys* 28:1225–1232
106. Lyons AR, Symons MCR (1972) Electron spin resonance of dimeric (σ^*) radicals of type $(\text{R}_3\text{X}-\text{XR}_3)$ with a three electron X-X bond, when X is phosphorus or arsenic. *J Chem Soc Faraday Trans* 2(68):1589–1594
107. Janssen RAJ, Sonnemans MHW, Buck HM (1986) Electron capture phosphoranyl radicals in x-irradiated diphosphine disulfides. A single crystal ESR and *ab initio* quantum chemical study. *J Chem Phys* 84:3694–3708
108. Cetinkaya B, Hudson A, Lappert MF, Goldwhite H (1982) Generation and ESR spectra of some new phosphorus-centered radicals $\bullet\text{P}_2\text{Ar}_2\text{X}$, $\bullet\text{P}(\text{Ar})\text{X}$, $\bullet\text{P}(\text{OAr})_2$, $\bullet\text{PAr}_2(\text{:O})$, $\bullet\text{PAR}[\text{N}(\text{SiMe}_3)_2](\text{:NSiMe}_3)$, and $[\text{P}_2\text{Ar}_2]^*$ - derived from the bulky group $\text{C}_6\text{H}_2(\text{CMe}_3)_3-2,4,6$ (= Ar). *J Chem Soc Chem Commun* 1982:609–610
109. Cattani-Lorente M, Geoffroy M (1989) Structure of the radical resulting from the addition of hydrogen on a phosphorus:phosphorus bond: a theoretical and single crystal electron spin resonance study. *J Chem Phys* 91:1498–1503

110. Geoffroy M, Cattani-Lorente M (1991) Radical reactions in an x-ray irradiated single crystal of diphosphene: an ESR study. *Journal de Chimie Physique et de Physico-Chimie Biologique* 88:1159–1166
111. Loss S, Magistrato A, Cataldo L, Hoffmann S, Geoffroy M, Rothlisberger U, Grutzmacher H (2001) Isolation of a highly persistent diphosphanyl radical: the phosphorus analogue of a hydrazyl. *Angew Chem (International ed)* 40:723–726
112. Cataldo L, Dutan C, Misra SK, Loss S, Gruetzmacher H, Geoffroy M (2005) Using the diphosphanyl radical as a potential spin label: Effect of motion on the EPR spectrum of an R1(R2)P-PR1 radical. *Chem Eur J* 11:3463–3468
113. Close D, Bernhard W (1979) ESR and ENDOR study of 5⁺dCMP at 6 K. *J Chem Phys* 70:210–215
114. Radons G, Oloff H, Hüttermann J (1981) Free radicals from x-irradiated single crystals of uridine-5⁺-phosphate disodium salt. *Int J Rad Biol* 40:245–263
115. Stelter L, Von Sonntag C, Schulte-Frolinde D (1976) Phosphate ester cleavage in ribose-5-phosphate induced by OH radicals in deoxygenated aqueous solution. The effect of Fe(II) and Fe(III) ions. *Int J Radiat Biol* 29:255–269
116. Celalyan-Bertier A, Berclaz T, Geoffroy M (1987) An electron spin resonance study of phosphorus-centered radicals trapped in an x-irradiated single crystal of phenoxyphosphoryl xylofuran derivative. *J Chem Soc Faraday Trans1* 83:401–409
117. Berclaz T, Bernardinelli G, Celalyan-Berthier A, Geoffroy M (1988) Radiation Damage in Organic Phosphates. Crystal structure of 3-O-Diphenoxyphosphoryl-1,2-O-isopropylidene 5-O-Trityl- α -D-ribofuranose and an ESR study of the X-irradiated single crystal. *J Chem Soc Faraday Trans* 84:4105–4113
118. Nelson D, Symons MCR (1977) Electron capture processes in organic phosphates: an electron spin resonance study. *J Chem Soc Perkin II* 1977:286–293
119. Büttner T, Geier J, Frison G, Harmer J, Calle C, Schweiger A, Schönberg H, Grützmacher H (2005) A stable aminyl radical metal complex. *Science* 307:235–238
120. Planas JG, Hampel F, Gladysz JA (2005) Generation and reactions of ruthenium phosphide complexes $[\eta^5\text{-C}_5\text{H}_5]_2\text{Ru}(\text{PR}'_3)_2(\text{PR}_2)$: remarkably high phosphorus basicities and applications as ligands for palladium-catalyzed Suzuki cross-coupling reactions. *Chem Eur J* 11:1402–1416
121. Burck S, Daniels J, Gans-Eichler T, Gudat D, Nättinen K, Nieger MZ (2005) N-heterocyclic phosphonium, arsenium, and stibonium ions as ligands in transition metal complexes: a comparative experimental and computational study. *Anorg Allg Chem* 631:1403–1412
122. Ndiaye B, Bhat S, Jouaiti A, Berclaz T, Bernardinelli G, Geoffroy M (2006) EPR and DFT studies of the structure of phosphinyl radicals complexed by a pentacarbonyl transition metal. *J Phys Chem A* 110:9736–9742
123. Berclaz T, Ndiaye B, Bhat S, Jouaiti A, Geoffroy M (2007) $[\text{M}(\text{CO})_4\text{PPh}_3]^-$ radicals (M = Cr, Mo, W): DFT and single crystal EPR investigations. *Chem Phys Lett* 440:224–228
124. Zalis S, Daniel C, Vleeck A Jr (1999) Structural and electronic changes accompanying reduction of $\text{Cr}(\text{CO})_4(\text{bpy})$ to its radical anion: a quantum chemical interpretation of spectrochemical experiments. *J Chem Soc Dalton Trans* 1999:3081–3086
125. Hynes RC, Preston KF, Springs JJ, Williams AJ (1990) EPR study of the $[\text{W}(\text{CO})_4\text{P}(\text{OMe})_3]^-$ radical anion trapped in a single crystal of $[\text{N}(\text{PPh}_3)_2][\text{W}(\text{CO})_4\text{H}\{\text{P}(\text{OMe})_3\}]$. *Organometallics J Chem Soc Dalton Trans* 1990:3655–3661
126. Sidorenkova H, Berclaz T, Ndiaye B, Jouaiti A, Geoffroy M (2009) Single crystal EPR study and DFT structure of the $[\text{Mo}(\text{CO})_5\text{PPh}_3]^+$ radical cation. *J Phys Chem Solids* 70:713–718

Chapter 3

EPR Studies of Radical Ions Produced by Radiolysis of Fluorinated Hydrocarbons and Related Compounds in Solid Media

Masaru Shiotani and Kenji Komaguchi

Abstract CW-EPR spectroscopic studies on the radical ions of small fluorinated hydrocarbons and related compounds are reviewed. The radical ions were generated and stabilized in low temperature solid media by ionizing radiation. Structures, dynamics and reactions are discussed based on the EPR hyperfine (*hf*) and *g*-tensors compared with the quantum chemical computations for the radical anions of perfluorocycloalkanes $c\text{-C}_n\text{F}_{2n}^-$ ($n: 3\text{--}5$), perfluoroalkenes $\text{C}_n\text{F}_{2n-2}^-$ ($n: 2\text{--}5$), and related compounds, and for the radical cations of mono- and di-haloalkanes, $\text{H}(\text{CH}_2)_n\text{X}^+$ and $\text{X}(\text{CH}_2)_n\text{X}^+$ ($\text{X}: \text{Cl}, \text{Br}; n < 10$), fluorinated ethylenes and benzenes, and halogen-substituted dimethylethers.

3.1 Introduction

Electron and hole transfer is one of the most important fundamental chemical processes that contribute to the detailed mechanism of radiation effects in condensed phase. Radical anions are formed by the addition of one electron to the lowest unoccupied molecular orbital (LUMO) of parent molecules, while molecular radical cations are formed by the loss of one electron from the highest occupied molecular orbital (HOMO). Both the radical anions and cations are in a doublet electronic state with one unpaired electron ($S=1/2$) in a singly occupied molecular orbital (SOMO). The radical ions in condensed media are of interest as the reaction intermediates in radiation chemistry but also are important in the context of molecular science and technology (e.g. electron transfer processes, photoconductivity of polymers, etc.). The publication of comprehensive monographs and book chapters of radical ions well reflect the interest [1–8].

M. Shiotani (✉)

Department of Applied Chemistry, Graduate School of Engineering, Hiroshima University,
Takamigaoka 4-26-8, Takaya, Higashi-Hiroshima 739-2115, Japan
e-mail: mshiota@hiroshima-u.ac.jp

K. Komaguchi

Department of Applied Chemistry, Graduate School of Engineering, Hiroshima University,
Kagamiyama 1-4-1, Higashi-Hiroshima 739-8527, Japan
e-mail: okoma@hiroshima-u.ac.jp

© Springer International Publishing 2014

A. Lund, M. Shiotani (eds.), *Applications of EPR in Radiation Research*,
DOI 10.1007/978-3-319-09216-4_3

Electron Paramagnetic Resonance (EPR) or Electron Spin Resonance (ESR) spectroscopy is one of the best experimental methods to characterize the radical ions because of its high specificity and sensitivity; the method can provide direct information on the electronic structure of the radical ions as well as information on their participation in elementary chemical reactions. That is, EPR parameters, especially hyperfine (hf) and g -tensors, can provide detailed information about geometrical and electronic structures of radicals [5, 9, 10]. The hf tensor provides information about the interactions between electronic spin density and certain nuclei within a given radical, whereas the g -tensor reflects properties of the entire molecule, i.e. a general spin density distribution and bonding features, and interactions with the environment, etc. Quantum chemical computations have now become an indispensable tool for the experimentalists to correctly correlate the hf and g tensors to the structures and bonding of the radicals.

Matrix-isolation is an experimental technique used in chemistry and physics for stabilizing a material in a large excess of an unreactive host matrix at low temperature [11, 12]. Originally this technique has been developed to study unstable reactive chemical species and is nowadays widely used for various types of research problems. The matrix-isolation method combined with ionizing radiation (by γ -ray, X-ray, UV-light, etc.) at low temperature has been extensively developed for EPR study of radical ions [1–8, 13–21]. The procedure consists of dissolution of the solute molecules of interest in an appropriate matrix (solvent), freezing at low temperature, irradiation, and EPR measurements before and after thermal treatment. The matrix molecules (atoms) are ionized by the irradiation to yield an electron (e^-) and a positive hole (h^+). The electron is transferred in general to a solute molecule with higher electron affinity than that of the matrix molecule to form a solute molecular radical anion. On the other hand, the positive hole is transferred to a solute molecule with first ionization energy (potential) lower than that of the matrix molecule, resulting in the formation of a solute molecular radical cation. Thus formed molecular radical anions and cations can undergo a wide variety of reactions by illuminating the samples with visible or UV-light, or by annealing them at elevated temperatures.

Since applications of EPR to free radical chemistry started in the middle of the 1950s a large number of radical ions were subjected to EPR studies. They were in general prepared in the liquid phase by reduction-oxidation (redox) reactions, electrolysis or photolysis, and rather stable radical ions possessing a conjugation system such as aromatics have been studied. The results have been summarized, for example, in a book “Radical Ions” by Kaiser and Kevan [1] and in “Magnetic Properties of Free Radicals” in the Landolt-Börnstein series [22]. Since the middle of the 1960s a number of radical anions were successfully generated by ionizing radiation combined with the matrix-isolation method and their structures and reactions have been extensively studied by the EPR method. Selected radical anions reported until the end of the 1980s have been listed in CRC Handbook of Radiation Chemistry [3] and book chapters [2, 13, 19, 23]. On the other hand, chemically important radical cations of alkanes, alkenes and other small organic and inorganic molecules have never been observed by EPR until the development of new

matrix-isolation methods. In 1978 Shida et al. [24] first demonstrated the usefulness of halocarbon matrices, especially CFCl_3 , for the EPR studies of solute radical cations generated by ionizing radiation. Since then a variety of halocarbon matrices have been developed for the studies of radical cations and a large number of radical cations have been subjected to EPR studies which include some *n*-alkane cations, *c*-alkane cations, branched-alkane cations, alkene and alkyne cations, aromatic and hetero-aromatic cations, ester cations, ether and some other cations [2–8, 15–18, 20–22, 24, 25]. For highly reactive small radical cations, however, lower temperatures available by using liquid helium cryostats are essential. In 1982 Knight et al. reported another method for the EPR observation of radical cations in an inert-gas matrix at cryogenic temperatures [26]. The method involves radical generation techniques such as fast atom bombardment, electron bombardment or photoionization from discharged neon gas during deposition on a cold finger surface at 4 K in an ESR matrix-isolation apparatus [26–30]. By employing this method a variety of small radical cations were successfully generated and were subjected to EPR studies, which include H_2O^+ [27] and CH_4^+ [28–30].

Fluorine-substitution in organic molecules has received considerable attention because of remarkable changes in chemical and physical properties of the parent molecules. For examples, it is known that some fluorocarbons and chlorofluorocarbons capture very effectively the electrons released in the radiolysis of liquid cyclohexane [31–34] and possess extremely large rate constants for thermal electron attachment in the gas phase [35–41]. Furthermore, fluorocarbons have remarkable properties such as chemical inertness, thermal stability, high hydrophobicity, low dielectric constant, and large electronegativity and have gained much attention [42–47]. A deeper understanding of the electronic structure, dynamics, and reactivity of the fluorocarbons has been demanded for their widespread applications. From the view point of the EPR spectroscopist fluorine has ideal characteristics. Fluorine is isotopically pure (^{19}F) and has a large magnetic moment, and a nuclear spin of one-half ($I=1/2$); the properties of various nuclei being summarized in General Appendix (Table 7). Thus, since the beginning of the 1960s a number of fluorine-containing organic radicals have been generated by ionizing radiation and subjected to EPR studies, for example see [48–58]. In 1971 a comprehensive review article of ‘Halogen Hyperfine Interactions’ in organic and inorganic radicals was reported by Hudson and Root [10]. Since the middle 1970s a number of EPR studies were carried out on the radical anions and cations of fluorinated hydrocarbons and related compounds, which were generated in irradiated solid matrices. The EPR studies on ‘Electron Attachment to Fluorocarbons (1978)’ [13], ‘Radical Ions (1991)’ [3] and ‘Radical Anions (1991)’ [19] were reviewed by Hasegawa, Shiotani, Williams, et al. Since then comprehensive reviews in the field have not been published as far as we know. In this chapter we deal with CW-EPR studies combined with quantum chemical computations to investigate structures, dynamics and reactions of fluorocarbon and related radical ions generated by ionizing radiation in low temperature solid media. We do not intend to give a full coverage of the EPR studies of fluorinated organic radical ions reported so far, but to show some typical examples and to demonstrate general trends.

3.2 Fluorinated Alkanes and Related Molecules

We start with our recent EPR studies combined with quantum chemical computations on electronic structure of perfluorocycloalkane radical anions, $c\text{-C}_n\text{F}_{2n}^-$ ($n: 3\text{--}5$) in which the unpaired electron delocalization over the entire molecular framework is emphasized. Then we move on to the EPR of trifluoromethyl halide radical anions and mono- and di-halogen substituted n -alkane radical cations, $\text{H}(\text{CH}_2)_n\text{X}^+$ and $\text{X}(\text{CH}_2)_n\text{X}^+$ ($\text{X}: \text{F}, \text{Cl}, \text{Br}$).

3.2.1 Cyclic-Perfluoroalkane Radical Anions: Electron Delocalization

Radical anions of $c\text{-C}_n\text{F}_{2n}^-$ ($n=3\text{--}5$) were generated in γ -irradiated (plastically crystalline) tetramethylsilane (TMS), neopentane (NEP) and hexamethylethane (HME) matrices, and (rigid) 2-methyltetrahydrofuran (2-MTHF) matrix, and subjected to EPR studies. The temperature-dependent EPR spectra of $c\text{-C}_3\text{F}_6^-$ are shown in Fig. 3.1 as an example. The identification of the radical anions was confirmed by generating the identical EPR spectra in photoionization experiments using N,N,N',N' -tetramethyl- p -phenylenediamine (TMPD) [13, 59, 60]. The isotropic EPR spectra of $c\text{-C}_3\text{F}_6^-$, $c\text{-C}_4\text{F}_8^-$, and $c\text{-C}_5\text{F}_{10}^-$ in the TMS matrix show second-order hyperfine structures [5, 6, 48–50] characteristic of six, eight and ten equivalent ^{19}F atoms with the isotropic hf -splittings of 19.8, 14.85, and 11.6 mT, respectively (see Table 3.1). The values of the isotropic ^{19}F hf -splittings are in inverse ratio to the total number of fluorine atoms per anion; the total splitting being approximately the same value (117.0 ± 2.0 mT) in each case. This indicates that the unpaired electron is delocalized over the entire molecular framework in a SOMO of high symmetry. Furthermore, the isotropic ^{19}F hf -splittings observed for the radical anions in the TMS matrix are in excellent agreement with the values obtained for those in the NEP and HME matrices. This suggests a negligible influence of matrix effects on the electronic structure of these radical anions and made it possible to compare the experimental ^{19}F hf -splittings with the theoretical ones computed on the basis of the isolated molecule approximation.

A comparison between the experimental and theoretical data was carried out for both the isotropic and anisotropic ^{19}F hf -splittings to elucidate the geometrical and electronic structures of the anions [60]. The UHF MO computations with 6–311+G(d, p) basis set resulted in a planar geometrical structure for all the three radical anions in which the respective six, eight, and ten ^{19}F atoms are magnetically equivalent; the resulted molecular symmetries and electronic ground states being illustrated in Fig. 3.2 and listed in Table 3.1. The computations predict geometrical structures that are significantly altered by the electron attachment. For example, the electron attachment to $c\text{-C}_4\text{F}_8$ results in a geometrical change from the puckered D_{2d} to the planar D_{4h} symmetrical structure so as to stabilize the radical anion by the complete delocalization of the added electron in the planar D_{4h} ring structure. The computations further predict that, relative to the values in neutral $c\text{-C}_4\text{F}_8$, the

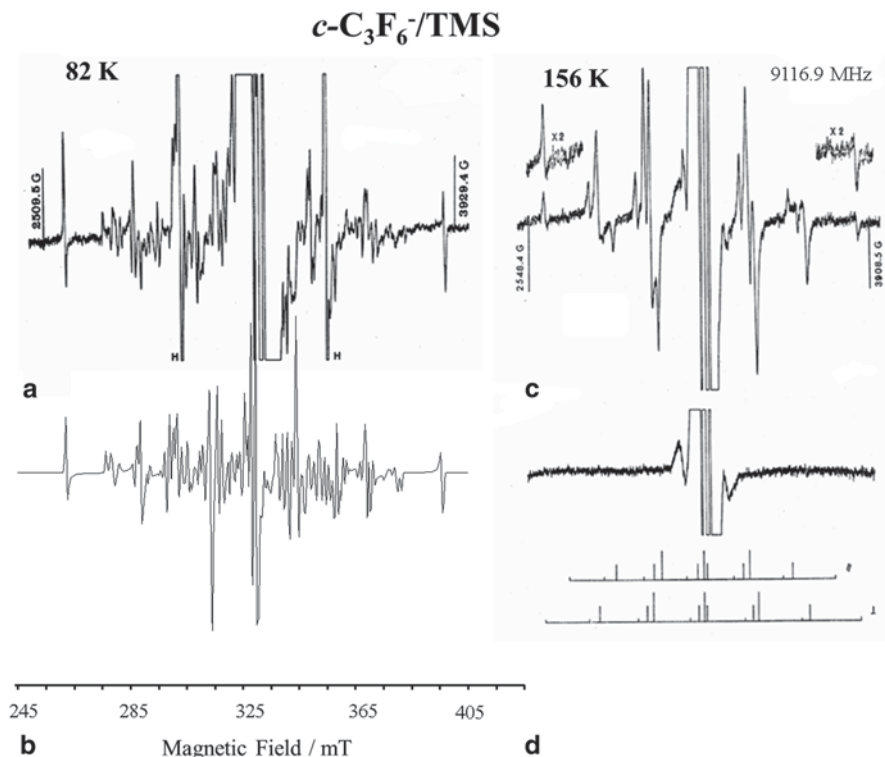
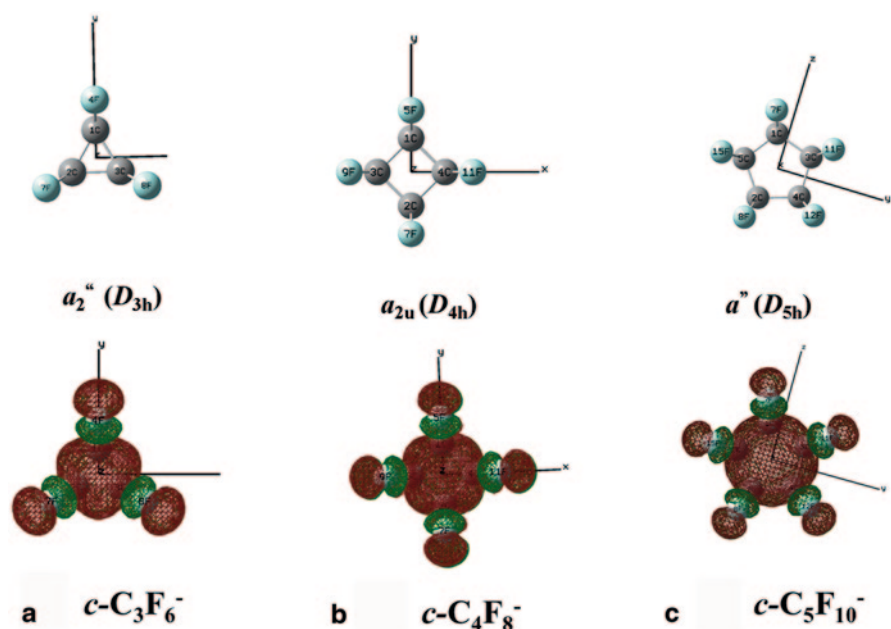


Fig. 3.1 **a** and **c** CW X-band EPR spectra of $c\text{-C}_3\text{F}_6^-$ generated by γ -ray irradiation of a solid solution of $c\text{-C}_3\text{F}_6$ in TMS at 77 K, and recorded at 82 K and 156 K, respectively. **b** Theoretical spectrum of $c\text{-C}_3\text{F}_6^-$ calculated using the computed principal values and principal directions of ^{19}F ($I=1/2$) hf -splittings. The vertical bars correspond to the outermost anisotropic doublet ($M_I, I=\pm 3, 3$). **d** Experimental spectrum recorded at 156 K after exposing the sample to unfiltered light from a tungsten lamp, and the line diagram at the bottom of this panel shows the expected positions of the second-order ^{19}F hf lines of $c\text{-C}_3\text{F}_6^-$ calculated from the parameters listed in Table 3.1 (10 G = 1 mT). The figure is adapted from [60] by permission of American Chemical Society (2007)

C–C bond length decreases by ca. 0.1 Å, while the C–F bond increases by 0.1 Å. The changes in the bond lengths arise from the nature of the high-symmetric SOMO (a_{2u} symmetric orbital) with its C–C bonding and C–F anti-bonding characteristics. Similar changes in the bond lengths have been found to occur on the electron attachment to $c\text{-C}_3\text{F}_6$ and $c\text{-C}_5\text{F}_{10}$. The isotropic ^{19}F hf -splittings computed by the DFT B3LYP method with the 6–311+G(2df, p) basis set for the optimized geometries are in almost perfect agreement with the experimental values. Furthermore the overall ESR spectral features in the anisotropic powder spectra of $c\text{-C}_n\text{F}_{2n}^-$ ($n=3\text{--}5$) were reproduced quite well by simulations using the anisotropic ^{19}F hf -splittings together with their direction cosines computed as shown for $c\text{-C}_3\text{F}_6^-$ in Fig. 3.1b as an example. The readers can refer to Sect. 19.3.1 for more details on the EPR spectrum simulations of $c\text{-C}_3\text{F}_6^-$ and $c\text{-C}_4\text{F}_8^-$ in frozen matrices.

Table 3.1 Hyperfine (*hf*) splittings for perfluorocycloalkane $c\text{-C}_n\text{F}_{2n}^-$ ($n=3-5$) radical anions from matrix EPR studies [60]. (The *g*-values are omitted in this table)

Radical anion	Matrix ^a	<i>T</i> /K	Nucleus (assignment)	Hyperfine (<i>hf</i>) splitting/mT				Symmetry ^d (state)
				<i>A</i> _{aa}	<i>A</i> _{bb}	<i>A</i> _{cc}	<i>A</i> _{iso} ^b (computed value) ^c	
$c\text{-C}_3\text{F}_6^-$	TMS	147	6 ¹⁹ F	20.8	20.8	17.6	19.8 (19.78)	D_{3h} (2A_2)
$c\text{-C}_4\text{F}_8^-$	TMS	113	8 ¹⁹ F	15.05	15.05	14.45	14.85 (14.84)	D_{4h} (${}^2A_{2u}$)
$c\text{-C}_5\text{F}_{10}^-$	TMS	167	10 ¹⁹ F	11.3	11.3	12.2	11.6 (11.65)	D_{5h} (2A_2)

^a TMS: Tetramethylsilane, Si(Me)₄^b The experimental isotropic ¹⁹F *hf*-splittings (*A*_{iso}) were evaluated by averaging the measured parameters for a spectrum showing residual anisotropy^c Isotropic *hf*-splitting computed by the DFT method. For the details of the computed ¹⁹F *hf* tensors the readers can refer to [60]^d Molecular symmetry (electronic ground state)**Fig. 3.2** Singly occupied molecular orbitals (SOMOs) computed for $c\text{-C}_3\text{F}_6^-$, $c\text{-C}_4\text{F}_8^-$, and $c\text{-C}_5\text{F}_{10}^-$ radical anions with point group symmetries (in parentheses). The computations were carried out using the B3LYP/6-311+G(2df, p)//UHF/6-31+G(d, p) method

The EPR spectrum of $c\text{-C}_3\text{F}_6^-$ radical anion in TMS at 156 K is characteristic of an axial symmetric line shape with a partially averaged ¹⁹F *hf* and *g*-anisotropy as seen in Fig. 3.1c. Other radical anions such as $c\text{-C}_4\text{F}_8^-$ and CF_3X^- (X: Cl, Br, I; see below) have also showed a similar residual anisotropy in crystalline TMS or NEP matrices. Precession [61, 62] may be a possible motion responsible for the observed partially averaged axial symmetric line shape; see Sect. 4.3.3.

The EPR spectra of $c\text{-C}_n\text{F}_{2n}^-$ (n : 3–5) radical anions were decayed out by exposure of the sample to visible light [13, 59, 60]. Furthermore, a photo-induced electron transfer reaction from the $c\text{-C}_n\text{F}_{2n}^-$ anions to SF_6 molecules was observed by visible light illumination of γ -irradiated TMS solutions containing both $c\text{-C}_4\text{F}_8$ and SF_6 :



The observations provide direct experimental evidence that the $c\text{-C}_n\text{F}_{2n}^-$ anion can undergo a simple electron detachment, i.e. an alternative decay process by the C–F bond dissociation to give an associated perfluorocycloalkyl radical and a fluoride anion (F^-) is considered less likely in view of the highly delocalized and non-bonding characters of the excess electron in the excited states. The electronic transitions in $c\text{-C}_n\text{F}_{2n}^-$ have been discussed based on the computations by the TD (Time-Dependent) – DFT/ Gaussian method in [60].

3.2.2 Trifluoromethyl Halide Radical Anions

There is some experimental evidence to suggest that the electron attachment to a halogen substituted saturated carbon is followed immediately by dissociation into a neutral carbon-centered radical and a halide anion, the intermediate molecular anion having only a transitory existence [13, 63–65]. An intermediate stage in the process of dissociative electron attachment at a saturated carbon atom has been revealed by the EPR observation of weakly-bound radical-anion pairs or adducts such as $\text{CH}_3 \cdots \text{Br}^-$ and $\text{CH}_3 \cdots \text{I}^-$ derived from methyl halides in a crystalline matrix [66–68]. It has been justifiably argued that the shallow minimum in the potential energy curves of the species derives principally from the constrictive cage effect of the rigid crystalline lattice.

On the other hand, in addition to the perfluorocycloalkane radical anions the EPR spectra of CF_3X^- (X: Cl, Br or I) radical anions were observed in irradiated solid TMS or NEP matrix [13, 19, 69]. Confirmation of the CF_3X^- identifications was achieved by parallel photoionization experiments using TMPD and by observing that the thermal decay of CF_3X^- was accompanied by a concomitant growth of the CF_3 radical. The experimental EPR spectra of CF_3X^- were analyzed in terms of axially symmetric hf tensors due to three magnetically equivalent ^{19}F -nuclei and one X-nucleus based on the assumption that the principal directions of all nuclei concerned are co-axial; the hyperfine splittings are summarized in Table 3.2.

Our recent DFT computations (B3LYP/6–311+G(d, p) level) suggest that the C–X bond length of CF_3X is largely elongated by an electron attachment. For example, in CF_3Cl^- the C–Cl bond increases by as much as 49%, i.e. 2.641 Å (CF_3Cl^-) vs 1.772 Å (CF_3Cl), whereas the C–F bond lengths remain almost constant. Figure 3.3 shows plots of the a_1 SOMO and spin density (SD) of the CF_3Cl^- anion in C_{3v}

Table 3.2 Hyperfine (*hf*) splittings of CF_3X^- (X: Cl, Br, I) anions in solid TMS matrix [13, 69]. The ^{19}F and ^{35}Cl *hf* tensors of CF_3Cl^- are compared with the calculated ones for the 2A_1 state in C_{3v} symmetry

Radical anion	Nucleus (assignment)	Hyperfine (<i>hf</i>) splitting/mT			
		A_{iso}	B_{aa}	B_{bb}	B_{cc}
CF_3Cl^- <i>Exp.</i> ^a <i>Cal.</i> ^b	3 ^{19}F	12.40	-3.66	-3.66	7.33
	1 ^{35}Cl	2.62	-0.85	-0.85	1.70
	3 ^{19}F	9.93	-3.84 (-0.3251, 0.9457, 0.0000)	-3.66 (0.0000, 0.0000, 1.0000)	7.50 (0.9457, 0.3251, 0.0000)
	1 ^{35}Cl	2.93	-1.77 (0.0000, 0.0000, 1.0000)	-1.77 (-0.0002, 1.0000, 0.0000)	3.55 (1.0000, 0.0002, 0.0000)
CF_3Br^- <i>Exp.</i> ^a	3 ^{19}F	11.64	-3.24	-3.24	6.48
	1 ^{81}Br	16.40	-4.98	-4.98	9.96
CF_3I^- <i>Exp.</i> ^a	3 ^{19}F	9.30	-2.58	-2.58	5.16
	1 ^{127}I	24.36	-6.48	-6.48	12.96

^a The experimental isotropic (A_{iso}) and anisotropic (B_{xx}) *hf*-splittings were derived from the partially averaged EPR spectra. The *hf*-splittings of ^{37}Cl and ^{79}Br nuclei and the *g*-values are omitted in this table

^b The calculations were carried out by DFT [B3LYP/6-311+G(2df, p)//B3LYP/6-31+G(d, p)] method. The direction cosines computed for the anisotropic *hf*-splittings of the ^{35}Cl and the ^{19}F nucleus at position 3 are given in parenthesis: those for the ^{19}F nuclei at positions 4 and 5 are obtained by taking into account the C_{3v} symmetry (C_3 symmetry operation about the x-axis). See Fig. 3.3 for the x, y, z-coordinate system.

symmetry. Consistent with the experimental results a large portion of the unpaired electron resides in the C–Cl anti-bonding orbital and the spin densities in the *s* and *p* orbitals of the unique halogen increase along the series Cl, Br, I, the order expected due to the effect of decreasing halogen electronegativity. The computed anisotropic ^{35}Cl and ^{19}F *hf* values of CF_3Cl^- have almost axial symmetry, but the principal directions of the three ^{19}F *hf*-splittings are not co-axial to each other and the principal directions of Cl-nucleus also differ from those of the three ^{19}F -nuclei. The result suggests that the experimentally determined anisotropic *hf* values do not correspond to a rigid limit state, but a motional state. A possible motion is a rotational motion about the unique axis along the C–Cl bond, which was suggested in previous works [13, 19, 69], or a procession motion [61].

Assuming rotational motion about the C–Cl bond and using the computed *hf*-splittings and direction cosines in Table 3.2 the axial symmetric *hf* values of $B_{\parallel}^{\text{rot}}$ and B_{\perp}^{rot} are evaluated for the three equivalent ^{19}F nuclei. The obtained theoretical values are comparable with the experimental ones: $B_{\parallel}^{\text{rot}} = 6.33$ (cal) vs 7.33 (exp) and $B_{\perp}^{\text{rot}} = -3.17$ (cal) vs -3.65 (exp) mT. The $^{35,37}\text{Cl}$ *hf* anisotropy, however, remained unchanged by this rotation and was about twice larger than the experimental value. The possibility of a procession motion cannot be completely ruled out.

The EPR spectra of CF_2Cl_2^- [13], CFCl_3^- [13], and CCl_4^- [70] radical anions were also observed. Furthermore congenic radical anions such as SiF_4^- , SiF_3Cl^- ,

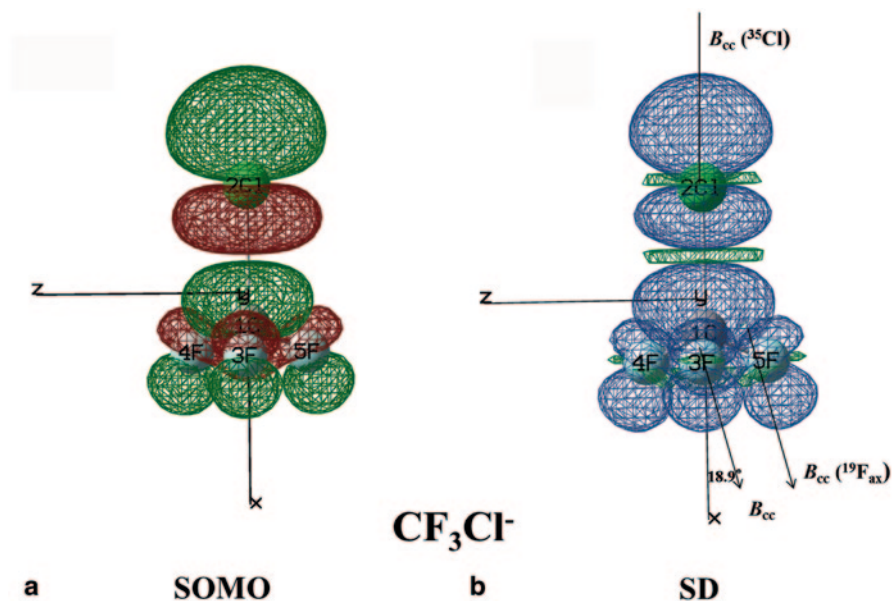


Fig. 3.3 Plots of **a** the SOMO (singly occupied molecular orbital) and **b** the spin density (SD) projected to the xz -plane of the CF_3Cl^- anion with 2A_1 electronic state in C_{3v} symmetry computed by DFT [B3LYP/6-311+G(2df, p)//B3LYP/6-31+G(d, p)] method. The computed direction cosines of the hf principal directions resulted in the maximum ^{35}Cl anisotropic splittings (B_{cc} of ^{35}Cl) along the x -axis, and that of $^{19}\text{F}_{ax}$ (3F) lying in the x - y plane with an angle of *ca.* 19° from the x -axis

$\text{SiF}_2\text{Cl}_2^-$, SiFCl_3^- and SiCl_4^- were studied by Morton and Preston [71] and Hasegawa [72, 73].

3.2.3 Mono- and Di-Halogen Substituted n -Alkane Radical Cations

A series of linear alkane radical cations, $\text{H}(\text{CH}_2)_n\text{H}^+$ have been radiolytically generated in low temperature solid halocarbon matrices and subjected to EPR studies [8, 74, 75]. The observed major hf -splitting to a 1:2:1 triplet was assigned to the two ^1H -protons, one in each terminal CH_3 group. The splitting steadily decreases with increasing carbon number of the alkyl chain, which strongly suggests the two end protons being connected through σ -delocalization over the chain.

The EPR spectra of alkyl halide radical cations generated in halocarbon matrices were first reported in the beginning of the 1980s and since then a number of EPR studies were reported so far. They include the radical cations of alkyl halide dimers [76], di-, tri-, and tetra-bromomethane [77], di-chloroalkane [78], di-bromoalkane [79], and tetra-chloromethane [80]. Here we focus on the radical cations of mono- and di-haloalkanes, $\text{H}(\text{CH}_2)_n\text{X}^+$ and $\text{X}(\text{CH}_2)_n\text{X}^+$ with $\text{X}=\text{F}, \text{Cl}, \text{Br}$ and $n=1, 2$.

3.2.3.1 CH_3F^+ vs CH_4^+ Cations: Structural Distortion

Methane (CH_4), the most simple alkane, has a doubly degenerate HOMO in a high symmetrical structure of T_d and the associated radical cation has been specially interesting from the viewpoint of static and dynamic Jahn-Teller (J - T) effects. Knight et al. reported a detailed EPR study of a series of selectively deuterated methane radical cations, CH_4^+ , CDH_3^+ , CD_2H_2^+ , CD_3H^+ and CD_4^+ , generated and stabilized in solid neon matrix at cryogenic temperatures [30]. Some of the experimental isotropic hf coupling constants (A_{iso}) are summarized in Table 3.3. Based on the D isotope effects of the hf -splittings and their temperature dependences it was concluded that the methane radical cation possesses a C_{2v} type geometrical structure with two distinctly different electronic sites, a co-planar site “ a ” and a nodal plane site “ e ” (Fig. 3.4) where the lighter ^1H -atom prefers the former site and the heavier D-atom the latter site.

Fluorinated methane (CH_3F) has a doubly degenerate HOMO like CH_4 . It is of interest to know how the geometric and electronic structures are changed with substitution of a fluorine for one H-atom of CH_4^+ . Knight et al. reported an EPR study on CH_3F^+ generated in the neon matrix [81]. The EPR spectrum at 4 K shows magnetically equivalent three ^1H -atoms with an averaged large hf -splitting of 11.3 mT, see Table 3.3. The experimental values of the ^{19}F and ^{13}C hf tensors suggest that a considerably large amount of unpaired electron density is in the fluorine $2p$ orbital, but significant spin density also resides in the carbon $2p$ -orbital (Fig. 3.4). The results were explained in terms of a static C_s conformation with a $^2A''$ state in which the unique H-atom (in CH_2DF^+ the D-atom occupies this site) located in the nodal plane of the fluorine $2p$ orbital should have a very small or negative A_{iso} value. The presence of a single D-atom in the methylfluoride radical cation drastically changed the EPR hf pattern and confirmed the averaging conformation of CH_3F^+ . That is, the D-atom in CH_2DF^+ acts to prevent the averaging process and yields two ^1H -atoms with an unusually large $A_{\text{iso}}(^1\text{H})$ value of 17.1 mT and one D-atom with a small $A_{\text{iso}}(\text{D})$ value of -0.2 mT (-1.3 mT on the ^1H -atom scale). A weighted average of the $A_{\text{iso}}(^1\text{H})$ values is very close to the value of $A_{\text{iso}} = 11.3$ mT observed for CH_3F^+ . A suggested mechanism for this averaging is a combination of dynamic J - T distortion and tunnelling interchange of the H-atoms [81].

We studied the radical cations of $\text{CH}_3\text{CH}_2\text{F}^+$ and its partially deuterated derivatives generated in irradiated SF_6 matrix at 77 K [82]. The spectra consisted of two hf lines typical of an axially symmetric anisotropic hf -splitting to a ^{19}F nucleus, the ^1H hf -splittings being too small to be resolved, *i.e.* less than *ca.* 0.5 mT. Referring to the DFT computations it is concluded that the SOMO of $\text{CH}_3\text{CH}_2\text{F}^+$ was composed of the $2p$ -orbitals of two C-atoms and one F-atom in the molecular plane, and has an elongated C–C bond with a similar structure as the CH_3F^+ cation.

3.2.3.2 $\text{H}(\text{CH}_2)_n\text{X}^+$ (X: Cl, Br) Cations: Interactions with Matrix

When dilute solid solutions (less than 2–3 mol%) of mono-alkyl halide, $\text{H}(\text{CH}_2)_n\text{X}$ (X=Cl, Br; $n=1, 2$) in halocarbon (CFCl_3 or $\text{CFCl}_2\text{CF}_2\text{Cl}$) matrix were exposed

Table 3.3 Hyperfine (*hf*) splittings for the radical cations of some halogenated alkanes from matrix EPR studies

Radical cation	Matrix	T/K	Nucleus (assignment) ^a	Hyperfine (<i>hf</i>) splitting/mT				Ref.
				A_1	A_2	A_3	A_{iso}	
CH ₄ ⁺	Ne	4	4 ¹ H				5.43	[30]
CD ₂ H ₂ ⁺	Ne	4	2 ¹ H 2 D				12.2 -0.22	[30]
CH ₃ F ⁺	Ne	4	¹ H ^b ¹⁹ F ^b	11.3 32.8	11.5 -4.51	11.1 -5.54	11.3 7.51	[81]
CH ₂ DF ⁺	Ne	4	¹ H ^b D ^{b,c} ¹⁹ F ^b	17.2 A_X : 0.18 34.2	16.9 A_Y < 0.1 -4.62	17.2 A_Z : 0.25 -5.89	17.1 0.2 7.93	[81]
Cl(CH ₂) ₃ Cl ⁺	CCl ₂ FC- ClF ₂	77	2 ³⁵ Cl 2 ³⁷ Cl 2 ¹ H _a	~1.5 ~1.2 ~2.2	~1.5 ~1.2 ~2.2	9.5 7.9 2.23		[78]
[H(CH ₂) ₂ Br- -ClCCl ₂ F] ⁺	CCl ₃ F	4, 77	1 ³⁵ Cl 1 ⁸¹ Br	1.8 17.2	1.8 17.2	5.3 53.8		[8]
H(CH ₂) ₄ Br ⁺	CCl ₂ FC- ClF ₂	77	1 ⁸¹ Br 1 ¹ H _a	-	-	43.2	~8.0	[79]
H(CH ₂) ₃ Br ⁺	CCl ₂ FC- ClF ₂	77	1 ⁸¹ Br 1 ¹ H _a 1 ¹ H _b	9.0	9.0	39.0	11.1 41.4	[79]
H(CH ₂) _n Br ⁺ (n=8-10)	CCl ₂ FC- ClF ₂	77	1 ⁸¹ Br 1 ¹ H _a 1 ¹ H _b 1 ¹ H _c	9.5	9.5	37.3	11.1 4.2 4.2	[79]
Br(CH ₂) _n Br ⁺ (n=1-3)	CCl ₂ FC- ClF ₂	77	2 ⁸¹ Br	8.6	8.6	46.5		[79]
Br(CH ₂) _n Br ⁺ (n=4-7)	CCl ₂ FC- ClF ₂	77	2 ⁸¹ Br	8.0	8.0	48.6		[79]
Br(CH ₂) _n Br ⁺ (n=8-10)	CCl ₂ FC- ClF ₂	77	1 ⁸¹ Br 1 ¹ H _a 1 ¹ H _b	9.5	9.5	3.80	11.1 4.14	[79]

^a Hyperfine splittings for ³⁷Cl and ⁷⁹Br and *g*-values are omitted in this table

^b The experimental *hf*-splittings in MHz unit were converted to the mT unit using the following relation: A_i (mT) = 0.07144771 A_i (MHz)/ g_i ($i=X, Y, Z$)

^c The signs of A_{iso} (D) cannot be determined from the experimental results alone but theory predicts a negative value

to ionizing radiation at 77 K, the radical cation H(CH₂)_nX⁺ interacting with one Cl atom of the matrix molecule was observed [76]. That is, the EPR spectrum of the H(CH₂)_nCl⁺ cation showed a *hf* pattern due to two ³⁵Cl (³⁷Cl) nuclei with almost the same *hf*-splittings, whereas the spectrum of H(CH₂)_nBr⁺ consisted of a dominant quartet due to ⁷⁹Br (and ⁸¹Br) and an additional quartet due to ³⁵Cl (and ³⁷Cl); see General Appendix (Table 7) for the magnetic properties. The results suggest an anti-bonding weak σ^* bond formation between the halogen (X) of H(CH₂)_nX⁺ and one matrix Cl atom, *i.e.* [H(CH₂)_nX---ClCFCl₂]⁺, see Table 3.3.

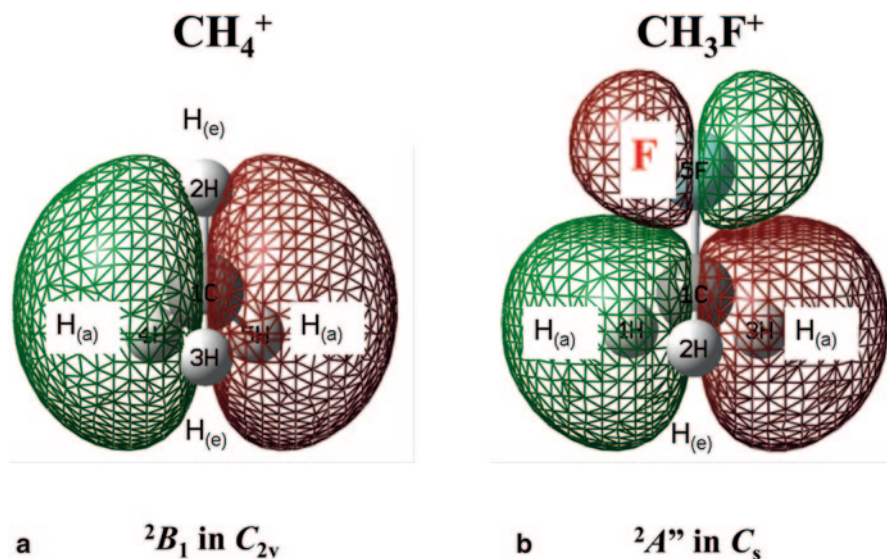


Fig. 3.4 Singly occupied molecular orbitals (SOMOs) of **a** the CH_4^+ cation with a 2B_1 state in C_{2v} symmetrical structure and **b** the CH_3F^+ cation with a ${}^2A''$ state in C_s symmetrical structure computed by DFT [B3LYP/6-311+G(2df, p)//B3LYP/6-31+G(d, p)] method. The sites marked as “a” in **a** are coplanar with the carbon $2p$ -orbital with an unpaired electron and sites “e” lie in the nodal plane of the $2p$ -orbital (the molecular symmetry plane). The ${}^1\text{H}$ -atom prefers the co-planar “a” site and the D-atom occupies the nodal plane site “e”.

For more concentrated solutions of $\text{H}(\text{CH}_2)_n\text{X}$ ($\text{X}=\text{Cl}, \text{Br}$) the EPR spectra show septet hyperfine patterns arising from the splitting due to two equivalent halogen (X) nuclei, indicating the formation of dimer radical cations, $[\text{H}(\text{CH}_2)_n\text{X}---\text{X}(\text{CH}_2)_n\text{H}]_2^+$ similar to those in the irradiated pure alkyl halide systems containing P or S nuclei such as $[\text{R}_3\text{P}---\text{PR}_3]^+$ ($\text{R}=\text{alkyl group}$) [83, 84], $[\text{R}_2\text{S}---\text{SR}_2]^+$ [85–88], and $[\text{RS}---\text{SR}]^-$ [89, 90].

Strong solute cation–matrix chlorine interactions (complex cation) similar to the $[\text{H}(\text{CH}_2)_n\text{X}---\text{ClCFCl}_2]^+$ radical cation have been reported for other solute cations with the SOMO localized on atoms such as Cl, O and S in the cations of alkyl-halide $(\text{RX})^+$ [76], $\text{CH}_3\text{CO}_2\text{H}^+$ [91, 92], CH_3COH^+ [93] and $(\text{CH}_3)_2\text{S}^+$ [94]. It was suggested in early EPR and quantum computational studies that the value of $A_\square(^{35}\text{Cl})$ linearly increases with the ionization potential (I_p) of the solute molecules, and the complex cations are formed when the difference between the values of I_p of the solute and matrix CFCl_3 molecules is less than *ca.* 3 eV [94, 95].

On the other hand weak matrix fluorine–solute cation interactions (*super-hyperfine*) have been observed for π -type solute radical cations such as $\text{CF}_2=\text{CF}_2^+$ [96], $(\text{CH}_3)_2\text{C}=\text{CH}_2^+$ [97], and dimethylketene $^+$ [98] in which the SOMO is delocalized over the entire molecule. A dilute solution of halogenobenzenes ($\text{C}_6\text{H}_5\text{X}$ with $\text{X}=\text{Cl}, \text{Br}$ and I) in irradiated CFCl_3 matrix gave isolated radical cations of $\text{C}_6\text{H}_5\text{X}^+$, which showed no such *super-hf*-splitting due to Cl nuclei of the matrix

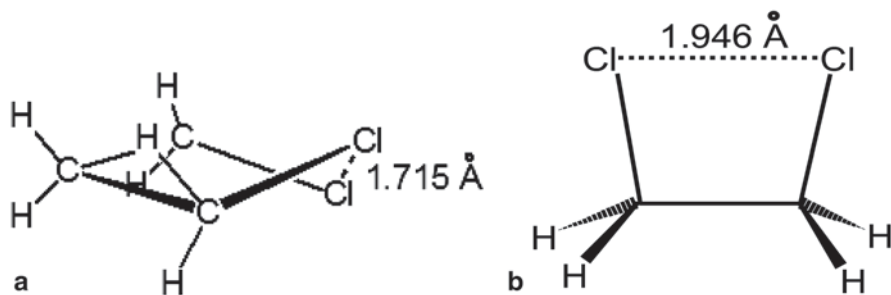


Fig. 3.5 **a** A non-planar five-membered structure and **b** a planar four-membered structure proposed for the radical cations of $\text{Cl}(\text{CH}_2)_3\text{Cl}^+$ and $\text{Cl}(\text{CH}_2)_2\text{Cl}^+$, respectively: the Cl...Cl bond length was derived from the CNDO/2 calculations. The structures are adapted from [78, 79] by permission of Royal Chemical Society (1989)

[99, 100]. For example the anisotropic hf value of ^{81}Br in $\text{C}_6\text{H}_5\text{Br}^+$ was 18.5 mT, which corresponds to a spin density of only *ca.* 0.30 in the p_z -orbital of the Br atom: an extensive delocalization of the unpaired electron onto the benzene ring seems to oppose the formation of a σ^* -bonding with the matrix Cl atom.

3.2.3.3 $\text{X}(\text{CH}_2)_n\text{X}^+$ ($\text{X}=\text{Cl}, \text{Br}$) Cations: Ring Formation

The radical cations of dihaloalkanes containing two chlorines or bromines separated by an alkyl chain, $\text{X}(\text{CH}_2)_n\text{X}^+$ ($\text{X}=\text{Cl}, \text{Br}$) were generated by exposing dilute solutions of the $\text{X}(\text{CH}_2)_n\text{X}$ molecule in halocarbon matrices to γ -rays at 77 K and subjected to EPR studies combined with MO calculations [78, 79].

$\text{Cl}(\text{CH}_2)_n\text{Cl}^+$ cations The EPR spectrum of the $\text{Cl}(\text{CH}_2)_2\text{Cl}^+$ cation consists of the hf pattern attributable to two equivalent ^{35}Cl (and ^{37}Cl) nuclei alone [78], whereas that of the $\text{Cl}(\text{CH}_2)_3\text{Cl}^+$ cation showed hf lines due to two equivalent protons in addition to the two equivalent Cl nuclei [78]. According to *semi-empirical* CNDO/2 calculations the $\text{Cl}(\text{CH}_2)_3\text{Cl}^+$ cation was concluded to have a non-planar cyclic structure, structure (a) in Fig. 3.5, with a three electron Cl-Cl bond ($\sigma_1^2\sigma_2^1$) and with two coupled protons, one on each terminal CH_2Cl group. In contrast, the EPR spectrum of the $\text{Cl}(\text{CH}_2)_2\text{Cl}^+$ cation was attributed to a planar four-membered ring structure, structure (b) in Fig. 3.5, in which the two CH_2Cl groups are tilted by *ca.* 10° from the *cis*-conformation so as to reduce the Cl-Cl distance to *ca.* 1.95 Å, and stabilize the unpaired electron in the Cl-Cl bond.

A similar spectrum, indicating that the unpaired electron is on two equivalent Cl nuclei, was obtained for $\text{Cl}(\text{CH}_2)_n\text{Cl}^+$ cations with $n=1, 4$ and 5 , whereas a different spectrum was obtained for dichloroalkane cations with $n=8$ and 10 [78]. The results suggest that the matrix molecules prevent such cyclizations of the longer dichloroalkanes. In Sect. 3.5 the EPR results of halogenated dimethyl ether radical cations are compared with the halogenated alkane radical cations.

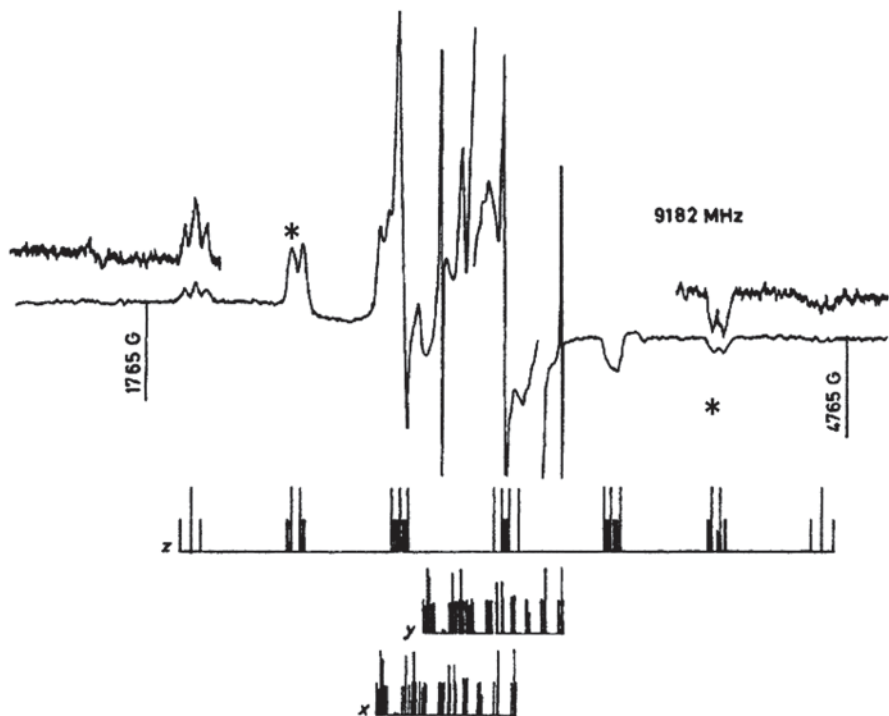


Fig. 3.6 First-derivative X-band EPR spectrum of a solution containing *ca.* 1 vol. % $\text{Br}(\text{CH}_2)_3\text{Br}$ in $\text{CCl}_2\text{FCClF}_2$ after exposure to X-rays at 77 K, showing features assigned to $\text{Br}(\text{CH}_2)_3\text{Br}^+$ and stick diagrams for the cation calculated using the EPR parameters listed in Table 3.3. The doublets at $M_1 = \pm 2$ components are marked with a star (*) in the figure (see the text). The figure is adapted from [79] by permission of Royal Chemical Society (1989)

$\text{Br}(\text{CH}_2)_n\text{Br}^+$ with $n = 1 - 7$ The EPR spectra of $\text{Br}(\text{CH}_2)_n\text{Br}^+$ with $n = 1 - 7$ show septet features characteristic of two equivalent Br nuclei: the spectrum of $\text{Br}(\text{CH}_2)_3\text{Br}^+$ in $\text{CCl}_2\text{FCClF}_2$ at 77 K is illustrated in Fig. 3.6. Clear doublet *hf*-splittings appeared for the components corresponding to $M_1 = m_1(1) + m_1(2) = \pm 2$ for the two equivalent Br nuclei. The *hf* line separation between the centres of the doublets in the two components increases with the number of carbon atoms (*n*), but reaches a plateau for *n* larger than 3. The results suggest that the unpaired electron in these cations is shared, not only by the two Br atoms connected through σ -delocalization over the chain, but also by the same two Br atoms weakly bonded to each other. According to CNDO/2 calculations the $\text{Br}(\text{CH}_2)_2\text{Br}^+$ cation was concluded to have a planar four-membered ring structure containing the two Br atoms bonded to each other similar to structure (b) of $\text{Cl}(\text{CH}_2)_2\text{Cl}^+$ in Fig. 3.5 and $\text{Br}(\text{CH}_2)_3\text{Br}^+$ has a non-planar five-membered ring similar to structure (a) of $\text{Cl}(\text{CH}_2)_3\text{Cl}^+$ in the same figure. The smaller Br *hf*-splittings observed for the cations with $n < 4$ are attributable to spin density in the p_z orbitals on the two Br atoms sharing the unpaired electron. The principal axes are not parallel to each other because of the strain in the cyclic structure of the cation with the shorter alkyl chains.

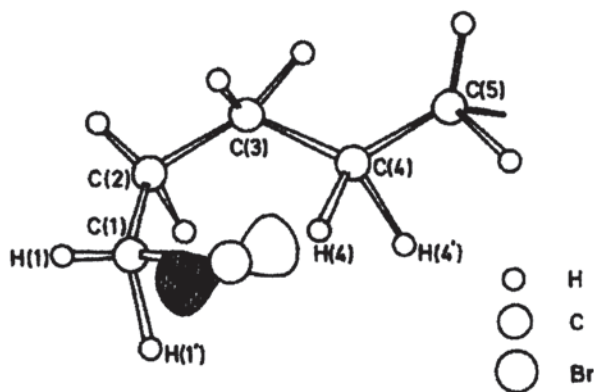


Fig. 3.7 The structure proposed for the radical cations of $\text{Br}(\text{CH}_2)_n\text{Br}^+$, $n > 7$, and $\text{H}(\text{CH}_2)_n\text{Br}^+$, $n > 3$, comprising a six-membered ring resulting from partial cyclization by four C-atoms, one Br-atom, and one H-atom bonded to the C-atom (four atoms away from the Br atom). H(4) and H(1) nuclei are assigned to the doublets with the splittings of 11.1 and 4.14 mT, respectively. The figure is adapted from [79] by permission of Royal Chemical Society (1989)

$\text{Br}(\text{CH}_2)_n\text{Br}^+$ with $n > 7$ A different type of EPR spectrum was observed for the radical cations of dibromoalkanes with $n > 7$ [79]. The spectrum consisted of a ^{79}Br (^{81}Br) quartet (see Table 3.3 for the hf coupling) and a ^1H doublet with a large hf coupling of 11.1 mT. The result suggests that the unpaired electron mainly occupies the p -orbital of the Br atom with which one H atom interacts to give the hf doublet. When a similar experiment was carried out with monobromoalkane cations, $\text{H}(\text{CH}_2)_n\text{Br}^+$ with $n > 3$, an analogous spectrum was observed. The results, considered together with the spectral changes observed for the $\text{Br}(\text{CH}_2)_n\text{Br}$ and $\text{H}(\text{CH}_2)_n\text{Br}$ cations in different halocarbon matrices ($\text{CCl}_2\text{FCClF}_2$, CCl_3F , and CCl_4), suggest that $\text{Br}(\text{CH}_2)_n\text{Br}^+$ ($n > 7$) forms a six-membered ring made by four C-atoms, one Br-atom, and one H-atom bonded to the C-atom (four atoms away from the Br atom), the unpaired electron being located in a three-centre bond comprising the Br nucleus, see Fig. 3.7.

3.3 Perfluoroalkenes and Related Compounds

3.3.1 Perfluoroalkene Radical Anions: Structural Distortion

Tetrafluoroethylene radical anion, $\text{CF}_2=\text{CF}_2^-$ is an important basic constituent of the family of perfluoroalkene radical anions and serves as a prototype of such anions. In an early contribution [101, 102] we reported the isotropic and anisotropic EPR spectra of $\text{CF}_2=\text{CF}_2^-$, see Table 3.4 for the ^{19}F hf -splittings. Subsequently Paddon-Row et al. computed the geometrical structure of $\text{CF}_2=\text{CF}_2^-$ by an *ab initio* UHF method (3–21G basis set) and suggested that the radical anion has a distorted *anti-bent*

Table 3.4 Hyperfine (hf) splittings for perfluorocycloalkenes $c\text{-C}_n\text{F}_{2n-2}^-$ ($n = 3-5$), and related radical anions from matrix EPR studies. (The g -values and the hf -splittings of ^{37}Cl and ^{79}Br are omitted in this table)

Radical anion	Matrix ^a	T/K	Nucleus (assignment)	Hyperfine (hf) splitting/mT				Symmetry ^d (state)	Ref.
				A_{aa}	A_{bb}	A_{cc}	A_{iso} (computed value) ^c		
$c\text{-C}_3\text{F}_4^-$	TMS- d_{12}	142	2 $^{19}\text{F}_a$ (CF)	18.4	18.4	20.1	18.9 (18.3)	C_2 (2A)	[106]
$c\text{-C}_4\text{F}_6^-$	TMS- d_{12}	167	2 $^{19}\text{F}_a$ (CF) 2 $^{19}\text{F}_b$ (CF ₂) 2 $^{19}\text{F}_c$ (CF ₂)				15.2 (15.07) 6.5 (6.32) (-1.1 (-1.50)	C_1 (2A)	[106]
$c\text{-C}_5\text{F}_8^-$	TMS- d_{12}	168	2 $^{19}\text{F}_a$ (CF) 2 $^{19}\text{F}_b$ (CF ₂) 2 $^{19}\text{F}_c$ (CF ₂)				14.7 (13.6) 7.4, (6.6) 1.0 (0.8)	C_1 (2A)	[106]
$\text{CF}_2=\text{CF}_2^-$	TMS- d_{12}	120	4 ^{19}F (CF) 2 ^{13}C				9.43 (9.71) 4.87 (4.29)	C_{2h} (2A_g)	[101, 102, 106]
$\text{CF}_3\text{CF}=\text{CFCF}_3^-$	TMS	134	2 $^{19}\text{F}_a$ (CF) 6 $^{19}\text{F}_b$ (CF ₃)				16.93 (15.98) 2.56 (1.95)	C_2 (2B)	[106]
$\text{CF}_2=\text{CFCl}^-$	TMS- d_{12}	98	1 ^{35}Cl (CFCl) 1 $^{19}\text{F}_a$ 1 $^{19}\text{F}_b$ 1 $^{19}\text{F}_c$	3.76 7.72 0.73 0.45	3.76 7.72 0.73 0.45	8.40 13.23 6.48 ~0	5.31 9.56 2.65 0.3		[107]
$\text{CF}_2=\text{CFBr}^-$	TMS- d_{12}	98	1 ^{81}Br (CFBr) 1 $^{19}\text{F}_a$ 1 $^{19}\text{F}_b$ 1 $^{19}\text{F}_c$	2.120 3.54 3.02 1.01	21.20 3.54 3.02 1.01	46.53 13.06 6.53 ~0	29.64 6.71 4.19 0.67		[107]

^a TMS: Tetramethylsilane, Si(Me)₄; TMS- d_{12} : Si(Me- d_3)₄

^b The experimental isotropic ^{19}F hf -splittings (A_{iso}) were evaluated by averaging the measured parameters for a spectrum showing residual anisotropy

^c Isotropic hf -splitting computed by DFT method. For the details of the computed ^{19}F hf -tensors the readers can refer to [106]

^d Molecular symmetry (electronic ground state)

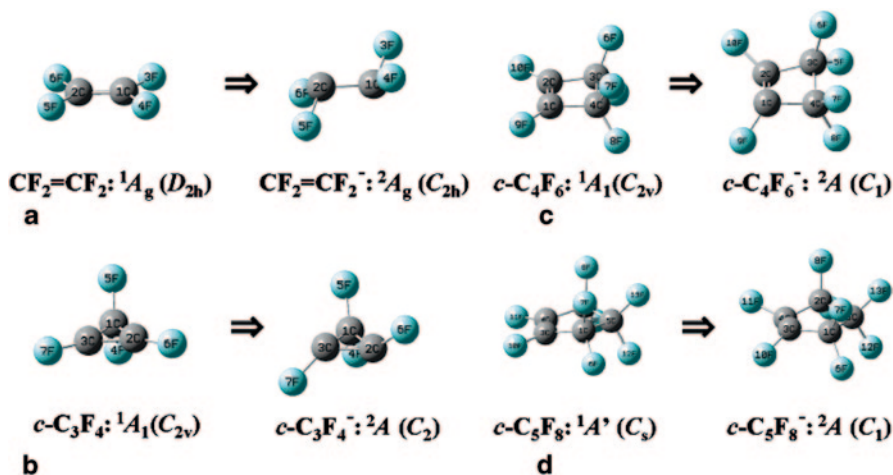


Fig. 3.8 Geometrical structure distortions of the perfluoroalkene radical anions. **a** C_2F_4 , **b** $c\text{-C}_3\text{F}_4$, **c** $c\text{-C}_4\text{F}_6$, **d** $c\text{-C}_5\text{F}_8$ before and after one electron reduction together with ground electronic states and point group symmetries (in *parentheses*). The diagram is adapted from [106] by permission of the American Chemical Society (2006)

structure with C_{2h} symmetry [103]. Furthermore, Shchegoleva et al. showed that *semi-empirical* INDO calculations of the ^{19}F *hf*-splittings support a chair (C_{2h}) structure [104]. The anisotropic EPR line shape of $\text{CF}_2=\text{CF}_2^-$ has been discussed on the basis of INDO computations [105]. However, the latter calculations lacked sufficient precision to predict the geometrical parameters as well as the anisotropic ^{19}F *hf*-splittings. Thus we have recently carried out systematic EPR studies combined with DFT computations for a series of perfluoroalkene radical anions [106].

In addition to the $\text{CF}_2=\text{CF}_2^-$ anion the EPR spectra were observed for the radical anions of tetrafluorocyclopropene ($c\text{-C}_3\text{F}_4^-$), hexafluorocyclobutene ($c\text{-C}_4\text{F}_6^-$), octafluorocyclopentene ($c\text{-C}_5\text{F}_8^-$) and perfluoro-2-butene ($\text{CF}_3\text{CF}=\text{CFCF}_3^-$), which were generated in neopentane (NEP), TMS, TMS- d_{12} , or 2-MTHF matrix by γ -irradiation [106]. For example, the isotropic spectra of $c\text{-C}_4\text{F}_6^-$ and $c\text{-C}_5\text{F}_8^-$ were characterized by three different sets of pairs of ^{19}F nuclei with the following isotropic *hf*-splittings: 15.2 (2F), 6.5 (2F) and 1.1 (2F) mT for $c\text{-C}_4\text{F}_6^-$, and 14.7 (2F), 7.4 (2F) and 1.0 (2F) mT for $c\text{-C}_5\text{F}_8^-$. By comparison with the DFT computations, the large triplet ^{19}F *hf*-splittings of *ca.* 15 mT were assigned to the two ^{19}F -nuclei attached to the C=C bond, one to each carbon; see Table 3.4 for the ^{19}F *hf*-splittings of the other perfluoroalkene radical anions.

The computations further predicted that the geometrical structures of the perfluoroalkenes were strongly distorted by one electron reduction to form their radical anions: for C_2F_4^- D_{2h} symmetry (1A_g electronic ground state) $\Rightarrow C_{2h}$ (2A_g), for $c\text{-C}_3\text{F}_4^-$ C_{2v} (1A_1) $\Rightarrow C_2$ (2A), for $c\text{-C}_4\text{F}_6^-$ C_{2v} (1A_1) $\Rightarrow C_1$ (2A) and for $c\text{-C}_5\text{F}_8^-$ C_s (${}^1A'$) $\Rightarrow C_1$ (2A), see Fig. 3.8. The structural distortion arises from a mixing of the ground π^* -orbital and higher-lying σ^* -orbitals so as to give a pyramidal structure at the

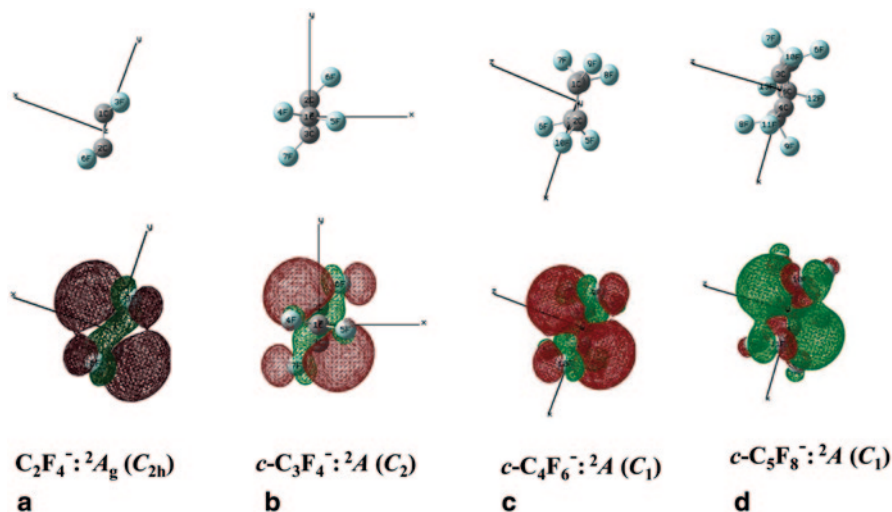


Fig. 3.9 SOMOs computed for $\text{CF}_2=\text{CF}_2^-$, $c\text{-C}_3\text{F}_4^-$, $c\text{-C}_4\text{F}_6^-$ and $c\text{-C}_5\text{F}_8^-$ radical anions with ground electronic states and point group symmetries (in parentheses). The computations were carried out using the B3LYP/6-311+G(2df, p)//UHF/6-31+G(d, p) method. The figure is adapted from [106] by permission of the American Chemical Society (2006)

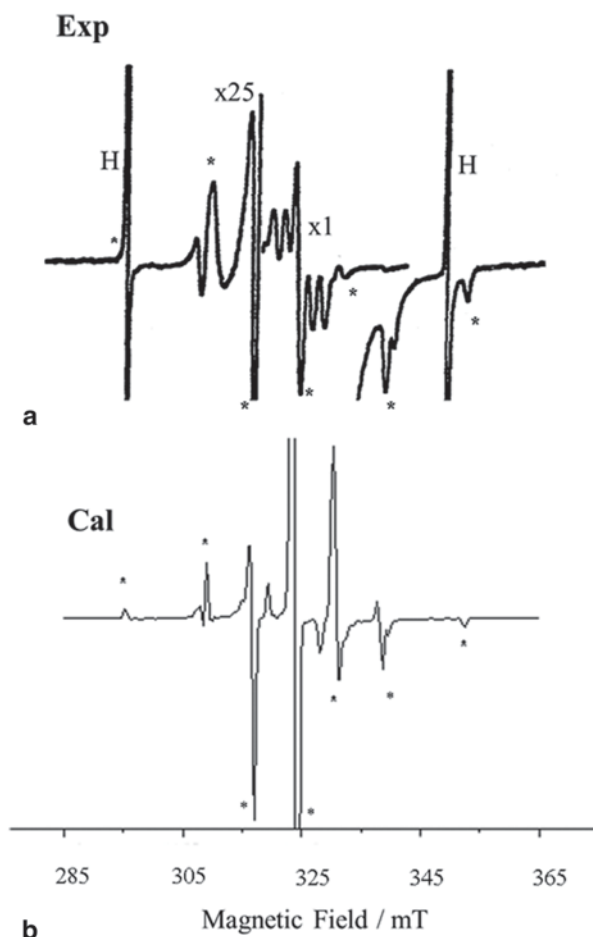
C=C carbons similar to that for unsaturated alkyne and alkene radical anions such as acetylene and ethylene radical anions [103, 104, 108, 109]. The singly occupied molecular orbitals (SOMOs) for C_2F_4^- , $c\text{-C}_3\text{F}_4^-$, $c\text{-C}_4\text{F}_6^-$ and $c\text{-C}_5\text{F}_8^-$ are illustrated in Fig. 3.9. In each case the unpaired electron is primarily localized in the sp^3 -like hybrid orbitals formed by the π^* and σ^* orbital mixing and is transferred to the fluorine orbitals so as to give large hf -splittings by hyper-conjugation mechanism for the two (or four) ^{19}F nuclei at the original C=C bond.

The experimental anisotropic spectra of $\text{CF}_2=\text{CF}_2^-$, $c\text{-C}_4\text{F}_6^-$ and $c\text{-C}_5\text{F}_8^-$ were satisfactorily reproduced by the EPR spectral simulation method using the computed hf principal values and principal directions of the ^{19}F nuclei. The spectrum of C_2F_4^- in the 2-MTHF matrix is compared with the computed anisotropic spectrum in Fig. 3.10 as an example, refer to [106] for the ^{19}F hf tensors used. The electronic excitation energies and oscillator strengths of some typical perfluoroalkene radical anions were also computed by the TD-DFT method and well compared with the photo-bleaching experiments of the radical anions [106].

An EPR study of halogeno-trifluoroethylene radical anions, $\text{CF}_2=\text{CFX}^-$ (X: Cl, Br, I) was reported by Williams et al. [107]. Our recent DFT computations suggest that these radical anions have also a non-planar distorted structure similar to the $\text{CF}_2=\text{CF}_2^-$ radical anion. The experimental hf values of ^{19}F , ^{35}Cl (^{37}Cl) and ^{81}Br (^{79}Br) (Table 3.4), however, are not principal values as they were obtained from partially oriented samples, and cannot be directly compared with the theoretical ones. The readers can refer to the *ab-initio* calculations on the geometries of the radical anions of ethylene, fluoroethylene, 1,1-difluoroethylene, and tetrafluoroethylene by Paddon-Row et al. [103].

Fig. 3.10 The anisotropic (first derivative) EPR spectra of $\text{CF}_2=\text{CF}_2^-$ radical anion.

a Experimental spectrum recorded at 83 K for the $\text{CF}_2=\text{CF}_2^-$ anion generated by γ -ray irradiation in 2-MTHF at 77 K. **b** Theoretical spectrum calculated for the $\text{CF}_2=\text{CF}_2^-$ anion with 2A_g state in C_{2h} symmetry by the B3LYP/6-311+G(2df, p)//UHF/6-311+G(d, p) method. The principal hf values for four equivalent ${}^{19}\text{F}$ nuclei used in the spectral calculations are: $A_{\text{iso}}=9.71$ mT; $B_{\text{aa}}, B_{\text{bb}}, B_{\text{cc}}=-2.78, -2.37, 5.15$ mT. See [106] for the principal directions of the anisotropic ${}^{19}\text{F}$ hf -splittings used for the spectrum calculation. The figure is adapted from [106] by permission of the American Chemical Society (2006)



3.3.2 Fluoroethylene Related Radical Cations

We summarize here the EPR results on tetrafluoro ethylene ($\text{CF}_2=\text{CF}_2^+$) and related radical cations such as $\text{CF}_2=\text{CFX}^+$ (X: Cl, Br, I). The EPR spectrum of the $\text{CF}_2=\text{CF}_2^+$ cation was first reported in 1983 by Hasegawa and Symons [110]. Then, we carried out EPR studies of halogeno-trifluoroethylene cations, $\text{CF}_2=\text{CFCl}^+$ and $\text{CF}_2=\text{CFBr}^+$ [111]. All the three radical cations of $\text{CF}_2=\text{CFX}^+$ showed an anisotropic spectral feature in halocarbon matrices at 77 K and were successfully analyzed in terms of the axially symmetric A - and g -tensors of ${}^{19}\text{F}$ - and X-nuclei with common principal axes (Table 3.5). The EPR parameters strongly suggest that the $\text{CF}_2=\text{CFX}^+$ cations have a planar structure with delocalized spin density in the p_z - π orbitals of ${}^{19}\text{F}$ - and X-nuclei. In this case, the g -factor parallel to the p_z orbital (i.e. g_{\parallel}) is expected not to be significantly shifted from the free-electron value of $g_e=2.0023$ [112] as observed. Furthermore, the observed ${}^{19}\text{F}$ hf -splittings with

Table 3.5 Hyperfine splittings for the radical cations of fluorinated ethylenes, propylenes and related radical cations from matrix EPR studies. (^{37}Cl and ^{79}Br hf values and g -values were omitted in this table)

Radical cation	Matrix	T/K	Nucleus (assignment)	Hyperfine (hf) splitting/mT		Ref.
				A_{\perp}	A_{iso}	
$\text{CH}_2=\text{CH}_2^+ \text{ Cal}^b$	CCl_3F	93	2 ^{19}F (=CF ₂) 2 ^1H (=CH ₂)	10.0	-0.3	[115]
					3.7 2.1	[113]
$\text{CF}_2=\text{CFH}^{+c}$	CCl_3F	105	1 ^{19}F 2 ^{19}F 1 ^1H (=CHF) 1 $^{19}\text{F}^d$	22.3	8.3	[113]
				12.1	4.5	
				1.6	0.4	
				1.0	8.4	
				22.6	4.4	
$\text{CF}_2=\text{CF}_2^+$	SF_6	77	2 ^{19}F 1 ^1H (=CHF) 1 $^{19}\text{F}^d$	11.9	1.6	[111]
				1.6	1.0	
				1.6	0.6	
				14.63	~5.46	
				1.39		
$\text{CF}_2=\text{CFCl}^+$	CCl_3F	77	4 ^{19}F (=CF ₂) 1 $^{19}\text{F}^d$	16.32	3.50	Present work ^e
				-2.91		
$\text{CF}_2=\text{CFCl}^+$	CCl_3F	77	2 ^{19}F 1 ^{19}F 1 ^{35}Cl (=CFCl) 1 ^{37}Cl (=CFCl) 1 $^{19}\text{F}^d$	13.5	-	[111]
				13.1	-	
				3.03	-	
				2.57	-	
				1.83	1.17	

Table 3.5 (continued)

Radical cation	Matrix	T/K	Nucleus (assignment)	Hyperfine (<i>hf</i>) splitting/mT		Ref.
				A_I	A_{iso}	
<i>Cal</i>			1 ¹⁹ F (=CF ₂ : F1) 1 ¹⁹ F (=CF ₂ : F2) 1 ¹⁹ F (=CFCl: F3) 1 ³⁵ Cl (=CFCl)	13.73	-3.72	Present work ^e
				13.94	-3.69	
				14.37	-3.99	
				2.66	-1.0	
CF ₂ =CFBr ⁺	CCl ₃ CF ₃	77	2 ¹⁹ F 1 ¹⁹ F 1 ⁸¹ Br (=CFBr)	-		[111]
				12.46		
				16.01		
<i>Cal</i>			1 ¹⁹ F (=CF2: F1) 1 ¹⁹ F (=CF2: F2) 1 ¹⁹ F (=CFBr: F3) 1 ⁸¹ Br (=CFBr)	13.01	-3.31	Present work ^e
				13.50	-3.36	
				12.38	-3.40	
				16.07	-7.59	
				2.3		
				1.2		
CH ₂ =CHCH ₃ ⁺	CCl ₃ F	77	1 ¹ H _a (CH ₂) 1 ¹ H _b (CH) 3 ¹ H(CH ₃) 1 ¹ H(CH)			[97]
CH ₂ =CFCH ₃ ⁺	CCl ₃ F	93	2 ¹ H(CH ₂) 3 ¹ H(CH ₃) 1 ¹⁹ F(CF)			[113]
				1.7		
				1.4		
CF ₂ =CFCF ₃ ⁺	CCl ₃ F	77	1 ¹⁹ F(CF) 2 ¹⁹ F(CF ₂)	13.8	5.1	[113]
				22.9	8.6	
				11.5	4.3	
<i>s-trans</i> -CF ₂ =CF- CF=CF ₂ ⁺	CF ₂ ClCF ₂ Cl	77	2 ¹⁹ F _a (2CF ₂) 2 ¹⁹ F _b (2CF ₂) 2 ¹⁹ F(CF)			[116, 117]
				10.64	-	
				10.64	-	
				4.22	-	

Table 3.5 (continued)

Radical cation	Matrix	T/K	Nucleus (assignment)	Hyperfine (<i>hf</i>) splitting/mT		Ref.
				A_{\parallel}^a	A_{iso}	
<i>s-cis</i> -CF ₂ =CF- CF=CF ₂ ⁺	CF ₂ ClCF ₂ Cl	77	2 ¹⁹ F _a (2CF ₂)	10.62	—	[116, 117]
			2 ¹⁹ F _b (2CF ₂)	9.70	—	
			2 ¹⁹ F (CF)	6.09	—	

^aThe mark, “_a”, stands for unresolved *hf*-splittings

^bValue computed by DFT method

^cApproximate isotropic *hf* values of A_{iso} for ¹⁹F were evaluated using the relations $3A_{\text{iso}} = (A_{\parallel} + 2A_{\perp})$ and $A_{\perp} = 0.660A_{\parallel}$, see [113] for details

^dSuper-*hf*-splitting due to one ¹⁹F-nucleus of matrix CFC₁ or SF₆ molecule

^eCalculated with B3LYP/6-311+G(2df, p)//B3LYP/6-311+G(d, p)

large A_{\parallel} , but negligibly small A_{\perp} are also characteristic of planar π -type radicals containing ^{19}F -nuclei [13, 51–56, 59, 110–112]. The planar π -type structure of the $\text{CF}_2=\text{CFX}^+$ cations was further confirmed theoretically by DFT computations, see Table 3.5.

The EPR studies on the related fluorinated radical cations such as $\text{CF}_2=\text{CH}_2^+$, $\text{CF}_2=\text{CFH}^+$, $\text{CF}_2=\text{CFCF}_3^+$ were also carried out [113] and the *hf*-splittings are summarized in Table 3.5. The geometrical structures and hyperfine parameters of some fluorinated hydrocarbon radical cations were computed by Huang et al. [114].

3.3.3 Hexafluoro-1,3-Butadiene Radical Cation: Photo-isomerization

Fluorinated radical ions, generated and stabilized in low temperature solid matrices can undergo a variety of reactions, as in the case of their hydrocarbon analogues [2, 3, 8, 19–21, 118], by illuminating light to the samples or annealing them at elevated temperatures. For example, in early papers we reported an EPR study on a thermal cyclization reaction of the $\text{CF}_2=\text{CF}_2^-$ radical anion with neutral $\text{CF}_2=\text{CF}_2$ to form *c*- C_4F_8 [101, 102]. Here we present our recent study on a photo-isomerization reaction of the hexafluoro-1,3-butadiene radical cation (HFBD $^+$) [116, 117].

Two distinctly different EPR spectra were observed for the HFBD $^+$ cation generated in a γ -irradiated solid solution of HFBD in the $\text{CF}_2\text{ClCF}_2\text{Cl}$ matrix [116, 117]. The two spectra were analyzed in terms of axially symmetric ^{19}F *hf*- and *g*-tensors with common principal axes. The principal values determined by the simulation method are given in Table 3.5. Comparing the experimental ^{19}F *hf*-splittings with the theoretical ones, the two spectra were attributed to *s-cis*-HFBD $^+$ and *s-trans*-HFBD $^+$ cations with a planar structure: the ground electronic states are 2A_2 (in C_{2v} symmetry) and 2B_g (in C_{2h}), respectively. Neutral HFBD has a non-planar structure (in C_2) with a carbon skeleton dihedral angle of *ca.* 47° [119], which is in contrast to 1,3-butadiene with *s-trans* planar structure [120]. It was concluded that, when PFBD loses one electron to form PFBD $^+$, the geometrical structure is changed from non-planar C_2 to planar C_{2v} or C_{2h} structure, see Fig. 3.11.

Immediately after γ -irradiation at 77 K the EPR spectrum was predominated by *s-cis*-HFBD $^+$ cation; the relative concentration of $[\textit{s-cis-HFBD}^+]/[\textit{s-trans-HFBD}^+]$ being *ca.* 4.0. By subsequent visible-light illumination (500–600 nm) a large part of *s-cis*-HFBD $^+$ was found to be isomerized to *s-trans*-HFBD $^+$: $[\textit{s-cis-HFBD}^+]/[\textit{s-trans-HFBD}^+] \approx 0.5$. The processes of non-planar neutral HFBD ionizing to form planar *s-cis*- and *s-trans*-HFBD $^+$ cations and the reaction mechanism of the *cis*-to-*trans* photo-isomerization have been discussed based on the vertical excitation energies (T_v) and torsional potential energy curves (TPEC) of HFBD and HFBD $^+$ [117]. That is, the computed T_v value of the first excited state $1^{-2}B_1$ in *s-cis*-HFBD $^+$ is 2.5 eV (=495 nm): the value corresponding well to the experimental result of the *cis*-to-*trans* isomerization initiated by visible-light illumination. Once the ground state $1^{-2}A_2$ of *s-cis*-HFBD $^+$ is excited by light to form the first excited state $1^{-2}B_1$, the state may slide down to the ground state of *s-trans*-HFBD $^+$, $1^{-2}B_g$, via the TPEC crossing point of the $1^{-2}A$ and $1^{-2}B$ states of HFBD $^+$ cation (Fig. 3.12). The

Fig. 3.11 When non-planar neutral HFBD with C_2 symmetry is ionized to form HFBD⁺ cation the original geometrical structure is initially maintained and then is relaxed into *s-cis*- and *s-trans*-planar structure with C_{2v} and C_{2h} symmetry, respectively. The figure is adapted from [117] by permission of the American Chemical Society (2007)

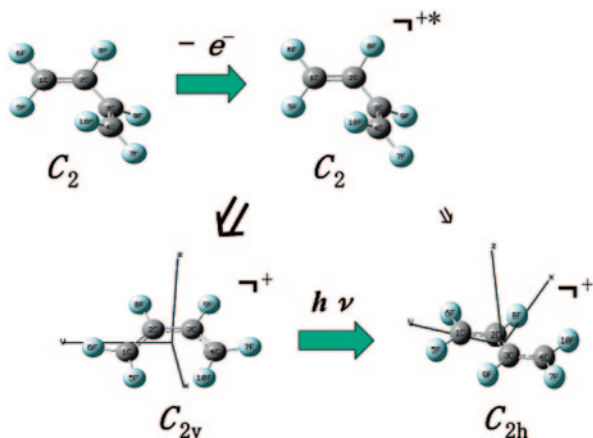
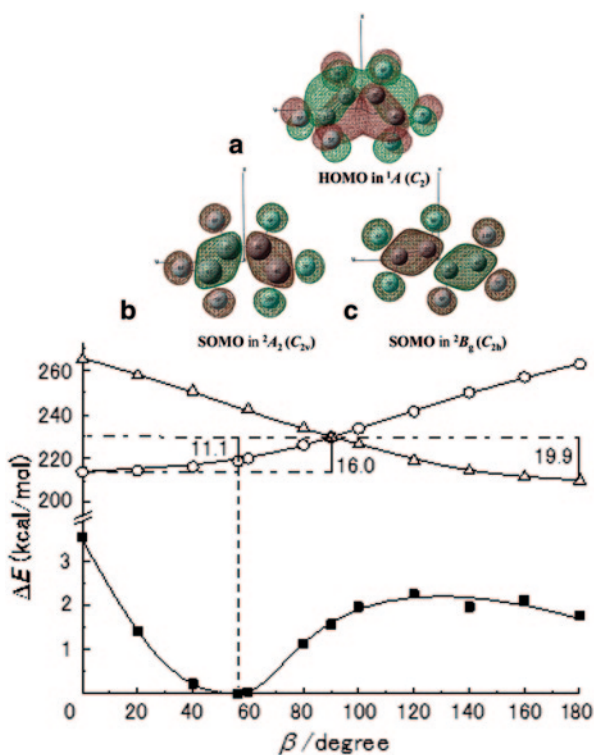


Fig. 3.12 (Upper) HOMO and SOMO plots of a neutral HFBD with 1A (in C_2 symmetry), **b** *s-cis*-HFBD⁺ with 2A_2 (in C_{2v}), and **c** *s-trans*-HFBD⁺ with 2B_g (in C_{2h}) ground electronic state. The computations were carried out by B3LYP/AUG-cc-pVDZ method. (Lower) ASPT2//CASSCF calculated ground-state torsional potential energy curve (TPEC) of HFBD and TPECs of the first two states of HFBD⁺ cation in C_2 symmetry. The lines marked with (■), (○) and (Δ) stand for HFBD ($S_0^{-1}A$), HFBD⁺ ($1^{-2}A$), and HFBD⁺ ($1^{-2}B$) state, respectively. The figure is adapted from [117] by permission of the American Chemical Society (2007)



calculated potential barrier from the *cis*- to the *trans*-form is 16.0 kcal/mol, whereas it is 19.9 kcal/mol from the *trans*- to the *cis*-form. Thus, the *cis*-to-*trans* isomerization is much more favorable.

The readers can refer to the original papers for other reactions of fluorinated organic radical ions such as dissociations [8, 19, 63, 64], dimer formation ([8, 121] and references cited therein), solute-matrix interactions (see Sect. 3.2.3.2) and photo-induced electron transfer [60, 106].

3.4 Fluorinated Benzenes

Benzene (C_6H_6) radical ions have been employed as a probe of redox reactions in catalytic systems [122–125]. The EPR studies of C_6H_6 ions have been interesting from a basic view point because they can provide experimental information about how the two fold degeneracy of e_{1g} orbitals (HOMO) of neutral C_6H_6 (D_{6h} symmetry) is removed so as to give rise to a lowering of the molecular symmetry due to the *Jahn-Teller* (*J-T*) effect [5, 21, 126].

In this section we deal with EPR studies on the electronic structure of fluorine-substituted benzenes (F-benzene) radical cations and anions which were radiolytically generated in low temperature solid matrices. The radical ions of F-benzenes have attracted much attention in a number of experimental and theoretical investigations [59, 104, 121, 127–146]. The interest in these ions is due to the peculiarities of their electronic and geometrical structures. The ^{19}F *hf*-splittings are very sensitive to the spin density distribution and the substituted fluorines can play a role as spin probe in examining their structures.

3.4.1 Benzene Radical Ions

Before going into the F-benzenes we shortly summarize the EPR studies of (*non*-fluorinated) benzene radical anions and cations as references. The EPR studies of the benzene radical ions were initiated by investigations of the radical anions generated by chemical reduction with alkali metals [147–149] and then the radical cations generated on a benzene/silica-gel system by γ -irradiation [150–152]. In both systems structural distortions due to the *J-T* effect [126] were expected, but only a dynamically averaged structure was observed with the *hf*-splittings due to the six equivalent protons. This is because the energy barrier for *pseudo*-rotation of the benzene ring is extremely small [153, 154], while strongly or weakly perturbing substituents have been introduced in the benzene ions to artificially remove the orbital degeneracy [155–158].

The first clear EPR evidence on statically *J-T* distorted structure was observed for the $C_6H_6^+$ cation generated in irradiated $CFCl_3$ matrix at 4 K by Iwasaki et al.

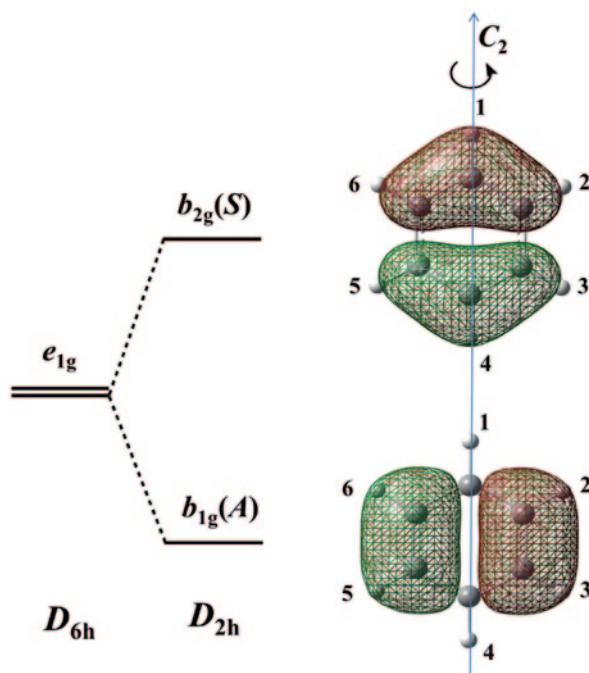


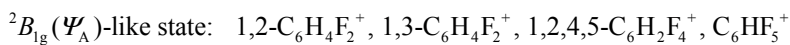
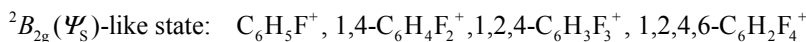
Fig. 3.13 Schematic representation for the electronic states of $C_6H_6^+$ cation. When the D_{6h} benzene ring is distorted into a D_{2h} structure by the static J - T effect, the doubly degenerated e_{1g} HOMO splits into b_{1g} and b_{2g} orbitals. The SOMO of $C_6H_6^+$ is either the b_{1g} orbital in a compressed D_{2h} geometry or the b_{2g} orbital in an elongated D_{2h} geometry, which are anti-symmetric (A) or symmetric (S) with respect to the C_2 operation about the z -axis, respectively.

[159]. They concluded that the radical cation has ${}^2B_{2g}$ ground state in a distorted D_{2h} structure in which C(1) and C(4) carbons have major spin densities, see Fig. 3.13: the ${}^2B_{2g}$ ground state has been theoretically supported for the radical cation [160]. Feldman et al. have reported, by contrast, the $C_6H_6^+$ radical cation with ${}^2B_{1g}$ state in an Ar matrix at 4 K [161, 162]. The results suggest that the electronic structure of $C_6H_6^+$ cation is strongly affected by the interactions with matrix molecules because of the small energy separation between the two states. ENDOR studies of $C_6H_6^+$ in $CFCl_3$ matrix have confirmed that the unpaired electron preferentially occupies the b_{2g} orbital rather than the b_{1g} orbital [163–166]. In the ${}^2B_{2g}$ state the six protons can be classified into two groups in terms of the 1H hf -splittings. One is two protons of H(1,4) with a larger splitting (A_{iso} : $|-0.9|$ mT), the other four protons of H(2,3,5,6) with a smaller splitting (A_{iso} : $|-0.19|$ mT) [164]. The readers can refer to [137, 138, 159, 164, 165] for details on the anisotropic 1H hf -splittings.

3.4.2 Fluorinated Benzene Radical Cations

A series of selectively fluorinated benzene (F-benzene) radical cations were radiolytically generated in either $CFCl_3$ (IP₁: 11.8 eV [8]) or perfluorocyclohexane

(*c*-C₆F₁₂; IP₁: 12.9 eV [8]) matrix and subjected to EPR studies; the latter matrix was found more preferable to generate F-benzene cations with more than three fluorines [137]. Some typical EPR spectra are shown in Fig. 3.14 together with the theoretical spectra calculated using the EPR parameters given in [137]. The *g* and ¹⁹F (and ¹H) *hf* tensors with an axial symmetry were observed for all the F-benzene cations studied, suggesting that they are planar π -type radicals. For example, the isotropic *hf*-splittings observed for C₆H₅F⁺ cation are: $A_{\text{iso}} = 5.7, 1.1$ and ca. 0 mT for ¹⁹F(1), ¹H(4) and ¹H(2,3,5,6) nuclei, respectively. The A_{iso} value of ¹H(4) is very close to that of C₆H₆⁺ (0.9 mT) in the B_{2g} state [166]. The results suggest that the C₆H₅F⁺ cation has a ${}^2B_{2g}(\Psi_S)$ -like ground state in which larger spin density resides on the C(1,4) carbons with smaller density on the C(2,3,5,6) carbons. By contrast, the isotropic *hf*-splittings for the 1,2-C₆H₄F₂⁺ cation are: $A_{\text{iso}} = 4.2, 0.5$ and 0 mT for the ¹⁹F(1,2), ¹H(4,5) and ¹H(3,6) nuclei, respectively. The A_{iso} value of H(4,5) is smaller than that of H(4) in C₆H₅F⁺ and close to the value of the ${}^2B_{1g}$ benzene cation (0.64 mT [161, 162]). Thus, it is suggested that the 1,2-C₆H₄F₂⁺ cation has a ${}^2B_{1g}(\Psi_A)$ -like ground state in which larger spin density resides on the four C(1,2,4,5) carbons and smaller ones on the two C(3,6) carbons. In a similar manner a series of fluorinated benzene radical cations studied are classified into the ${}^2B_{2g}(\Psi_S)$ -like or the ${}^2B_{1g}(\Psi_A)$ -like state:



The results are interpreted as follows. When the degeneracy of the two fold e_{1g} orbitals is lifted in the F-benzene cations, the orbital in which larger spin density is distributed on the carbons bonded to F-atoms gains higher energy due to their electron repelling property and becomes the SOMO. Recently we have computed the isotropic and anisotropic ¹⁹F and ¹H *hf*-splittings of a series of fluorinated benzene radical cations by a DFT B3LYP//MP2 method and confirmed that most of the calculated results are in reasonable agreement with the experimental values [167]. Furthermore, consistent with the EPR results the photoelectron spectroscopic studies of neutral F-benzenes have indicated that the HOMOs have the same symmetry as the SOMOs of the cations [132–135].

C₆F₆⁺ Cation The EPR spectra of C₆F₆⁺ radical cation generated in *c*-C₆F₁₂ matrix show a strong temperature dependence similar to the case of the C₆H₆⁺ cation [136]. The spectrum at 10 K exhibited a triple quintet *hf* structure due to two and four magnetically equivalent ¹⁹F nuclei: ¹⁹F(1,4) ($A_{\parallel} = 1.35$ mT) and ¹⁹F(2,3,5,6) ($A_{\parallel} = 9.85$ mT). At 170 K the spectrum due to six equivalent ¹⁹F nuclei was observed with the axially symmetric parameters: $A_{\parallel} = 6.77$ mT, $A_{\perp} \approx 0$ mT, $g_{\parallel} = 2.0020$, and $g_{\perp} = 2.0060$. The observed relation of $A_{\parallel} > A_{\perp} \approx 0$ mT and $g_{\parallel} < g_{\perp}$ is characteristic of a planar π -type radical. DFT B3LYP//MP2 computations resulted in a ${}^2B_{2g}$ electronic ground state with an elongated D_{2h} ring structure [167]. However, the calculated *hf*-splittings for the ${}^2B_{1g}$ state (with a compressed D_{2h} structure) are in better agreement with the experimental ones, see Table 3.6. The presence of the ${}^2B_{1g}$ state can be rationalized by taking the very small energy separation (0.11 eV by the computations) between the two electronic states, and matrix effects into consideration. An averaging of the A_{\parallel} values calculated for the ${}^2B_{1g}$ state gives 7.94 mT, which is compatible to the

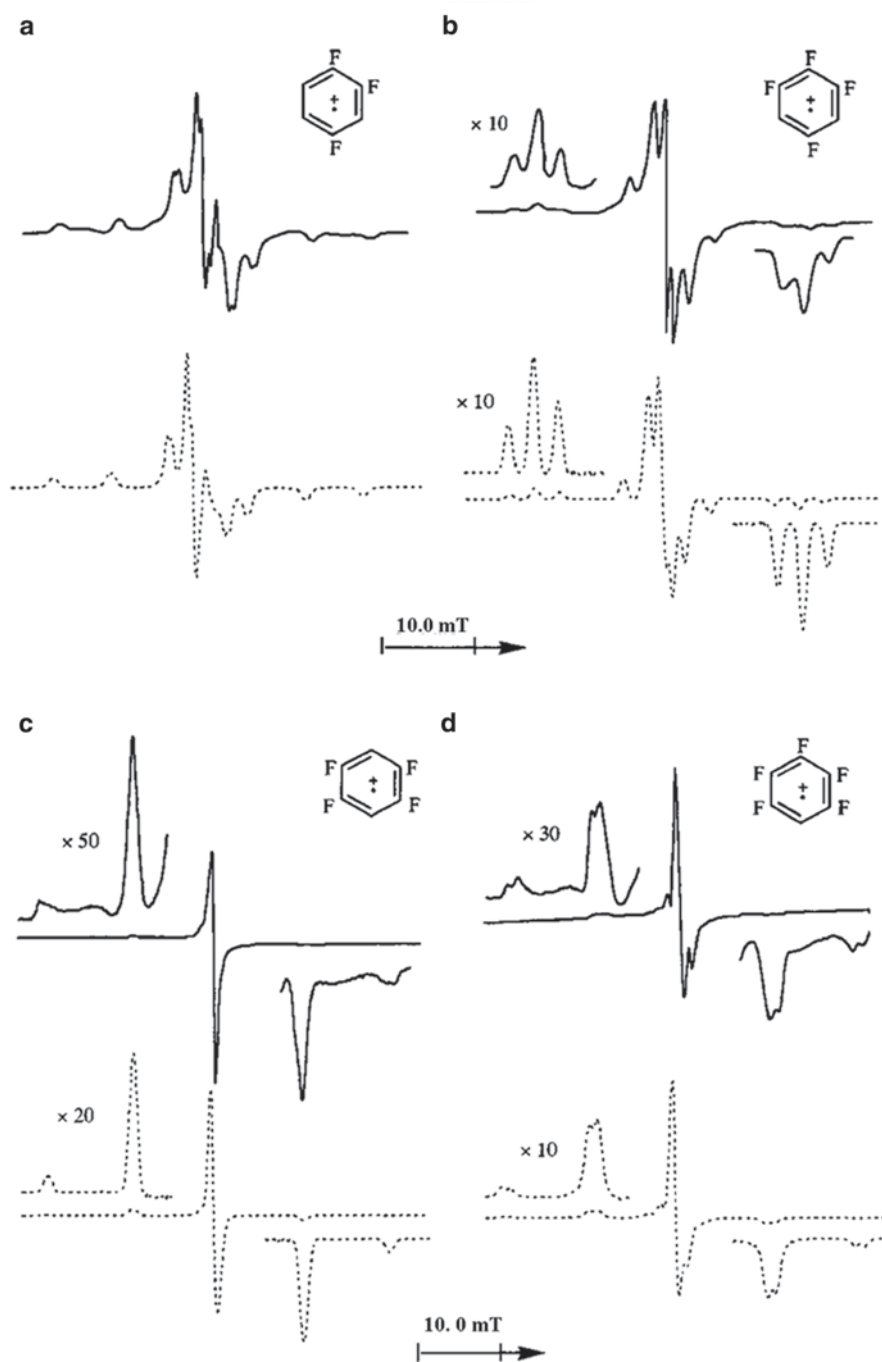


Fig. 3.14 First derivative X-band EPR spectra for solid solutions of **a** 1,2,4-trifluorobenzene, **b** 1,2,4,6-tetrafluorobenzene, **c** 2,3,5,6-tetrafluorobenzene, and **d** pentafluorobenzene in $c\text{-C}_6\text{F}_{12}$ matrix γ -irradiated at 77 K, and observed at 84 K, 77 K, 77 K and 93 K, respectively. The spectra with dashed lines are the simulated ones using the EPR parameters given in [137]. The spectra are adapted from [137] by permission of Royal Chemical Society (1997)

Table 3.6 Hyperfine (*hf*) splittings of hexafluorobenzene radical cation and anion. The experimental ^{19}F and ^{13}C *hf* values are compared with the calculated ones

Radical cation	State (symmetry) ^a	Nucleus (assignment) ^b	Hyperfine (<i>hf</i>) splitting (<i>A</i>) ^c /mT			
			A_{aa}	A_{bb}	A_{cc}	A_{iso}
C_6F_6^+ <i>Exp</i> [136]		2 ^{19}F	–	–	1.35	–
		4 ^{19}F	–	–	9.85	–
		6 $<^{19}\text{F}>_{\text{av}}$	–	–	6.77	–
<i>Cal 1</i>	${}^2B_{2g}(D_{2h})$	2 ^{19}F (1,4)	–1.95	0.63	0.44	1.03
		4 ^{19}F (2,3,5,6)	(1.00,0.00,0.00)	(0.00,1.00,0.00)	(0.00, 0.00, 1.00)	1.04
		6 $<^{19}\text{F}>_{\text{av}}$	–3.27 (0.00,0.948,0.318)	–3.09 (0.00, –0.32,0.95)	11.72 (1.00,0.00,0.00)	–
<i>Cal 2</i>	${}^2B_{1g}(D_{2h})$	2 ^{19}F (1,4)	–4.44	–4.05	8.00	–
		4 ^{19}F (2,3,5,6)	(0.00,0.00,1.00)	(0.00,1.00,0.00)	16.26	–
		6 $<^{19}\text{F}>_{\text{av}}$	–0.96 (0.00, –0.37,0.93)	–0.78 (0.00,0.93,0.37)	2.51 (1.00,0.00,0.00)	–
C_6F_6^- <i>Exp</i> [139, 142]		6 $<^{19}\text{F}>_{\text{av}}$	–	–	–	13.7
		6 $<^{13}\text{C}>_{\text{av}}$	–	–	–	1.21
			–	–	–	–
<i>Cal 1</i>	${}^2A_1(C_{2v})$	2 ^{19}F (1,4)	12.23 (0.00,0.89,0.46)	12.94 (1.00,0.00,0.00)	22.66 (0.00, –0.46,0.89)	14.16
		4 ^{19}F (2,3,5,6)	11.10 (–0.36, –0.38, 0.85)	11.63 (–0.54,0.83, 0.14)	17.06 (0.76, 0.41, 0.50)	1.15
		6 $<^{19}\text{F}>_{\text{av}}$	–	–	–	–
<i>Cal 2</i>	${}^2A(D^2)$	2 ^{19}F (1,4)	11.69 (0.99, –0.11,0.00)	12.50 (0.112,0.99,0.00)	17.54 (0.00,0.00,1.00)	14.85
		4 ^{19}F (2,3,5,6)	12.34 (0.59,0.76, –0.29)	12.79 (–0.09,0.42,0.90)	20.85 (0.80, –0.50, 0.32)	1.10
		6 $<^{19}\text{F}>_{\text{av}}$	–	–	–	–
		6 $<^{13}\text{C}>_{\text{av}}$	–	–	–	–

^aCalculations were carried out by DFT B3LYP/6–311 + G(2df, p)/MP2/6–311 + G(d, p) method.^b6 $<^{19}\text{F}>_{\text{av}}$ and 6 $<^{13}\text{C}>_{\text{av}}$ stand for the averaged isotropic (or anisotropic) *hf*-splittings expected for the six equivalent ^{19}F and ^{13}C nuclei, respectively. See Fig. 3.13 for the numbering of the ^{19}F -atoms.^cThe direction cosines computed for the anisotropic *hf*-splittings of the ^{19}F nuclei at positions 1 and 2 are given in parenthesis: those for the other ^{19}F nuclei are obtained by taking the molecular symmetries adopted into account. See Fig. 3.15 for the coordinate system

experimental one ($A_{\parallel} = 6.77$ mT). This suggests that three-site exchange motion (or *pseudo-rotation*) takes place among the three equivalent distorted D_{2h} structures so as to average the six ^{19}F splittings of the C_6F_6^+ cation in the $c\text{-C}_6\text{F}_{12}$ matrix at 170 K.

Related Radical Cations An EPR study was carried out for the radical cations of fluorinated pyridines such as 2-fluoropyridine, 2,6-difluoropyridine, and pentafluoropyridine radiolytically generated in $c\text{-C}_6\text{F}_{12}$ or CCl_3F matrix [168]. All the EPR spectra observed were successfully analyzed in terms of axially symmetric ^{19}F *hf*- and *g*-tensors similar to the F-benzene radical cations. A planar π -type SOMO was concluded from the experimentally evaluated spin density distribution in these radical cations; the result being supported by the *semi-empirical* INDO MO calculations of the respective cation. In contrast an EPR study of the (*non*-fluorinated) pyridine radical cation has indicated a σ -type SOMO in which the unpaired electron resided mostly in the nitrogen lone-pair orbital [169].

Similar to the case of the fluorine substitution the methyl group substitution can strongly perturb the electronic structure of the benzene ring. The readers can refer to a review paper on the EPR studies of the radical cations of methyl-substituted benzenes such as toluene and xylene [138]. The ENDOR spectroscopy facilitated investigations of the anisotropic ring ^1H *hf* tensors in disordered solid matrices at low temperatures [163, 170, 171]. The EPR studies of other halogen substituted benzene cations such as $\text{C}_6\text{H}_5\text{X}^+$ (X: Cl, Br, I) and $\text{C}_6\text{H}_4\text{Br}_2^+$ have been reported in early contributions [99, 100].

3.4.3 Fluorinated Benzene Radical Anions

Fluorinated benzene (F-benzene) radical anions were investigated using the EPR method combined with quantum chemical computations by several groups [139–146]. The radical anions have been especially interesting in view of their structural distortions from the original planar structure arising from a mixing of the ground π^* -orbital and higher-lying σ^* -orbitals, which is similar to the case of the fluorinated alkene radical anions discussed in Sect. 3.3. For example, Barlukova et al. reported optically detected EPR (ODEPR) studies of 1,2,3-trifluorobenzene radical anion in liquid solution: a doublet of triplets with isotropic ^{19}F *hf* splittings, 29 mT (F(2)) and 7.6 mT (F(1,3)), being observed at 243 K [146]. The experimental *hf*-splittings are temperature-dependent and the results were discussed in terms of a pseudo rotation (*intra*-molecular rotation) surface formed by nonplanar stationary structures, see Sect. 17.6.2.

C_6F_6^- Anion Since the ESR spectra of C_6F_6^- radical anion generated in an adamantane matrix were reported by Yim et al. [139, 140], many discussions have been provoked on the structure of the radical anion. A large isotropic *hf* coupling of 13.7 mT was observed for the six equivalent ^{19}F nuclei of C_6F_6^- and interpreted in terms of a $\sigma^*-\pi^*$ orbital crossover in a D_{6h} planar structure [140]. On the other hand, a nonplanar chair structure with a puckered ring has been postulated by Symons et al. [141]. Williams et al. observed an isotropic ^{13}C coupling (1.21 mT) for the radical anion [142]. The ODEPR study by Anisimov et al. confirmed the large isotropic *hf*-splitting of ^{19}F in the spectra of C_6F_6^- in solution [143]. Based on

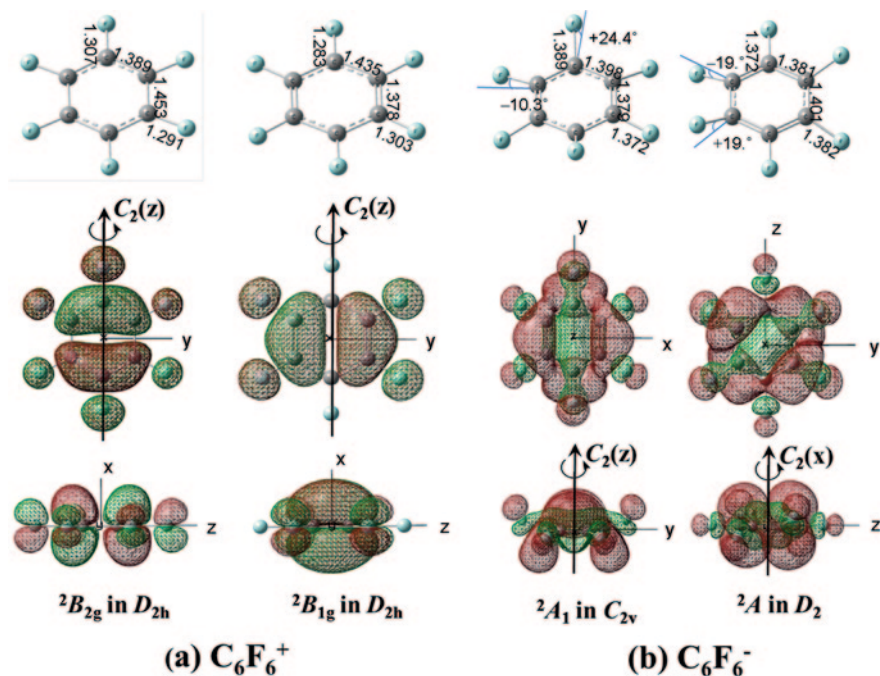


Fig. 3.15 Plots of the SOMOs computed for **a** $C_6F_6^+$ cation with either ${}^2B_{2g}$ or ${}^2B_{1g}$ ground electronic state in a distorted D_{2h} symmetrical structure and for **b** $C_6F_6^-$ anion with either 2A_1 state (in C_{2v} structure) or 2A (in D_2 structure). The upper row shows the associated geometrical structures with the bond length (in Å) and the out-of-plane C–F bond angle (in degree). The computations were carried out using DFT B3LYP/6–311+G(2df, p)//MP2/6–311+G(d, p) method

semi-empirical INDO calculations Shchegoleva et al. [144] proposed two possible distorted structures of C_{2v} (2A_1 state) and D_2 (2A state) due to the J - T effect and the observed isotropic ${}^{19}\text{F}$ and ${}^{13}\text{C}$ *hf*-splittings were interpreted in terms of averaging over the two structures. We observed anisotropic EPR spectra of $C_6F_6^-$ in NEP matrix and suggested that the former state (2A_1) is the electronic ground state by comparing the experimental spectra with the theoretical ones simulated using the INDO results although the agreement was not perfect [136].

As mentioned in Sects 3.2.1 and 3.3.1, an excellent agreement was obtained between the experimental EPR spectra and the theoretical ones simulated using the DFT computational results for the perfluoroalkane and perfluoroalkene radical anions [60, 106]. This encouraged us to recalculate the ${}^{19}\text{F}$ (and ${}^{13}\text{C}$) *hf*-splittings by the DFT method and to simulate an anisotropic “powder” spectrum that involved anisotropic *hf*-splittings of $C_6F_6^-$ using the computed *hf* principal values and directions of the ${}^{19}\text{F}$ nuclei. Consistent with a previous report by Huang [145] the B3LYP/6–311+G(d, p)//MP2/6–311+G(d, p) computations resulted in the 2A_1 electronic ground state in C_{2v} structure which is only by 0.08 eV more stable than the 2A state (D_2). The geometrical parameters computed for the two structures are shown together with plots of the associated SOMOs in Fig 3.15: the ${}^{19}\text{F}$ and ${}^{13}\text{C}$ *hf*-splittings being summarized in Table 3.6. In Fig. 3.16 the EPR spectra simulated

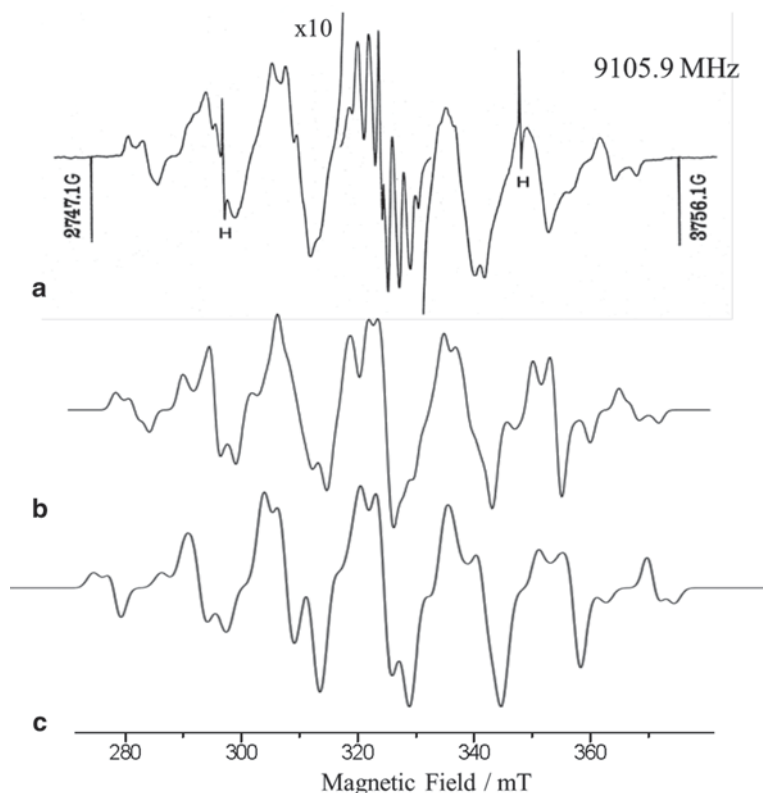


Fig. 3.16 **a** EPR spectrum of $C_6F_6^-$ generated by γ -ray irradiation of C_6F_6 in 2-MTHF at 77 K. **b** and **c** Simulated spectra calculated for the $C_6F_6^-$ anions with C_{2v} (2A_1) and D_2 (2A) structure, respectively. The spectra were simulated using the computed principal values and principal directions of ${}^{19}F$ hf tensors in Table 3.6 and using the g -tensor of (g_{xx} , g_{yy} , g_{zz} : 2.0015, 2.0015, 1.9994): The EasySpin MATLAB toolbox in Windows 7 [172] was employed for the simulation

using the computed ${}^{19}F$ hf tensors are compared with the experimental one observed for the $C_6F_6^-$ anion in a ‘rigid’ 2-MTHF matrix. The simulated spectrum of 2A_1 (C_{2v}) agrees with the experimental one slightly better than that of 2A (D_2) in overall spectral features as seen in Fig. 3.16. The results suggest that the C_{2v} structure can be stabilized in the low temperature rigid matrix although the energy difference between the two distorted C_{2v} and D_2 structures is very small.

3.4.4 Dimer Radical Cations of Fluorinated Benzenes

Dimer radical cations are of interest because they can be intermediate species of ion–molecular reactions and potentially provide basic knowledge of cluster chem-

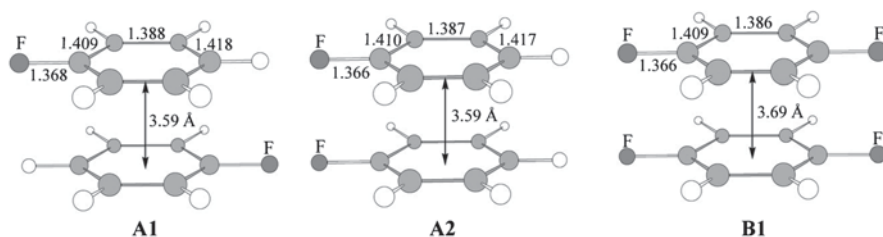


Fig. 3.17 Optimized geometries calculated for A1 and A2 structures of $(C_6H_5F)_2^+$ and B1 structure of $(1,4-C_6H_4F_2)_2^+$ at the B3LYP/6-31G(d, p) level of theory. Dissociation energies of 17.06, 17.09 and 14.92 kcal/mol were evaluated for A1, A2 and B1 structures, respectively, from the energy difference between the dimer cation and the sum of the monomer cation and the corresponding neutral molecule. The figure is adapted from [121] by permission of the PCCP Owner Societies (2002)

istry [3, 8, 25]. A variety of dimer radical cations of polycyclic aromatic compounds have been generated in the liquid phase by chemical or electrochemical oxidation methods [173–176]. Using an irradiation method, Edlund et al. [151, 177] first reported a well resolved EPR spectrum of benzene dimer cations, $(C_6H_6)_2^+$ in silica gel. Later, Iwasaki et al. [159] observed an EPR spectrum of $(C_6H_6)_2^+$ in the $CFCl_2CF_2Cl$ matrix.

Electronic and geometric structures of dimer radical cations of fluorinated benzenes such as $(C_6H_5F^+)_2$ and $(1,4-C_6H_4F_2^+)_2$ formed by γ -irradiation in solid $CF_2ClCFCl_2$ and CF_3CCl_3 matrices were investigated in detail by the EPR method combined with DFT calculations [121]. For example, the monomer cation $1,4-C_6H_4F_2^+$ was transformed to the dimer cation $(1,4-C_6H_4F_2)_2^+$ upon annealing the sample at 110 K in the $CF_2ClCFCl_2$ matrix. It was found that the dimer cation formation strongly depended on both the matrix and the concentration of solute molecules, which suggests molecular diffusion in the matrix being an important factor for the dimerization.

Both the dimer cations of $(C_6H_5F)_2^+$ and $(1,4-C_6H_4F_2)_2^+$ were concluded to have an overlapped sandwich type of structure with the two planar benzene rings parallel to each other, see Fig. 3.17. Two conformational isomers, A1 and A2, are possible for the $(C_6H_5F)_2^+$ dimer cation. The DFT calculations resulted in essentially the same energy and hf -splittings for the two conformations. The ^{19}F anisotropic hf -splitting (B) was found to be a good indicator for evaluating the distance between the two benzene rings. Furthermore the anisotropic splittings of the dimer cation were smaller than half that of the corresponding monomer cation. The result was explained in terms of the anti-bonding feature of the C–C bond between the two benzene rings and of the C–F bond [121].

Here we add to note that the anisotropic 1H hf -splittings of the ring protons of $(C_6H_6)_2^+$ were investigated by the ENDOR method, the results allowed to precisely evaluate the intra-molecular distance [178, 179]. For the dimer radical cations of toluene the 1H hf -splittings of the methyl protons were observed to be considerably smaller than half that of the monomeric cations, due to the interaction between the two equivalent partners as observed for the fluorinated benzene dimer radical cations.

3.5 Halogenated Dimethyl Ethers

3.5.1 $\text{CH}_3\text{OCH}_3^+$ Radical Cations

We start by considering the (non-halogenated) dimethyl ether radical cation ($\text{CH}_3\text{OCH}_3^+$: DME⁺). The EPR spectrum of $\text{CH}_3\text{OCH}_3^+$ cation generated in irradiated CCl_3F matrix was reported in the early 1980s by Williams [180] and Shida [181]. The spectrum consists of a septet with an averaged isotropic hf -splitting of 4.3 mT and an approximately binominal intensity ratio at 97 K, which was attributed to six equivalent protons of the two methyl groups in the DME⁺ cation. The result suggests that the methyl groups are subjected to a rotation rapid enough on the EPR time scale and the unpaired electron mainly resides in the oxygen nonbonding orbital of the radical cation. The DFT calculations of DME⁺ resulted in a symmetric structure with the two methyl groups occupying an eclipsed position relative to each other [182].

Strong deuterium(D)-isotope effects were observed on the conformation and rotation of the methyl group in selectively D-labelled DME⁺ cations [182]. The hf -splitting of the CH_3 protons in $\text{CH}_3\text{OCH}_3^+$ and $\text{CD}_3\text{OCH}_3^+$ showed no significant temperature dependence in the temperature range of 4.2 K to 100 K, but the EPR spectral line shape became complicated, especially below 30 K, by overlapping with lines due to the tunneling rotation of the methyl protons with a low rotational barrier. On the other hand, temperature dependent ^1H hf -splittings were observed for the CH_2D and CHD_2 protons in $\text{CD}_3\text{OCH}_2\text{D}^+$ and $\text{CD}_3\text{OCHD}_2^+$, respectively. The observed D-isotope effects were interpreted in terms of the difference in the zero-point vibrational energy due to the mass difference of the two hydrogen isotopes (^1H and D) in addition to their magnetic properties. Furthermore, it was revealed that the light hydrogen-atom (^1H) preferentially occupied a position closely parallel to the unpaired p -orbital of the oxygen atom in the selectively D-labelled DME⁺ cations.

3.5.2 $\text{CH}_3\text{OCH}_2\text{F}^+$ and $\text{CH}_3\text{OCH}_2\text{Cl}^+$ Radical Cations

The radical cations of mono-halogen substituted DMEs, $\text{CH}_3\text{OCH}_2\text{X}^+$ (X: F, Cl), were generated in irradiated low temperature solid matrix, and their electronic and geometrical structures were studied by EPR [183]. The experimental EPR spectra were unambiguously identified with the help of partially D-labelled compounds, $\text{CD}_3\text{OCH}_2\text{X}$, see the hf -splittings in Table 3.7.

The EPR spectra of $\text{CH}_3\text{OCH}_2\text{F}^+$ and $\text{CD}_3\text{OCH}_2\text{F}^+$ in CF_3CCl_3 matrix are shown in Fig. 3.18. Interestingly, the hf -splittings due to only two of the protons in the CH_3 group were observed in addition to the two protons in the CH_2F group of the $\text{CF}_3\text{OCH}_2\text{F}^+$ cation in the temperature range between 4.2 and 100 K. The result suggests that the rotation of the CH_3 group is largely hindered even at 100 K in the matrix. Furthermore, regardless of the fact that the ^{19}F nucleus has a large atomic hf -splitting [10, 185], no appreciable ^{19}F hf -splitting was observed for both

Table 3.7 Isotropic hyperfine (*hf*) splittings for the radical cations of halogenated dimethylethers (DME) and related radical cations from matrix EPR studies.

Radical cation	Matrix	T/K	Nucleus (<i>assignment</i>)	A_{iso}/mT (<i>calculations</i>) ^b	Ref.
$\text{CH}_3\text{OCH}_3^+$	CCl_3F	77	6 ^1H (2 CH_3)	4.3	[180, 181]
$\text{CD}_3\text{OCH}_3^+$		10, 77	3 ^1H (CH_3) 3 D (CD_3)	4.3 0.6	[182]
$\text{CD}_3\text{OCHD}_2^+$	CCl_3F	10	1 ^1H (CHD_2) 5 D (CD_3 and CHD_2)	8.8 0.6	[182]
		77	1 ^1H (CHD_2) 5 D (CD_3 and CHD_2)	6.2 0.6	
$\text{CD}_3\text{OCH}_2\text{D}^+$	CCl_3F	10	1 $^1\text{H}_a$ (CH_2D) 1 $^1\text{H}_b$ (CH_2D) 4 D (CD_3 and CH_2D)	8.4 4.2 0.6	[182]
		77	2 ^1H (CH_2D) 4 D (CD_3 and CH_2D)	5.2 0.6	
$\text{CH}_3\text{OCH}_2\text{F}^{+a}$	CF_3CCl_3	4.2, 77	2 $^1\text{H}_a$ (CH_2F) 2 ^1H (CH_3) 1 ^1H (CH_3) 1 ^{35}Cl	14.0 (8.43) 3.2 (6.34) ≈ 0 (-0.14) ≈ 0 (0.71)	[183]
		4.2, 77	2 $^1\text{H}_a$ (CH_2F) 3 D (CD_3)	14.0 ≈ 0	
$\text{CH}_3\text{OCH}_2\text{Cl}^{+a}$	CF_3CCl_3	4.2	1 $^1\text{H}_a$ (CH_2Cl) 1 $^1\text{H}_b$ (CH_2Cl) 2 ^1H (CH_3) 1 ^1H (CH_3) 1 ^{35}Cl	10.2 (8.73) 8.7 (8.73) 5.1 (5.26) ≈ 0 (-0.10) ≈ 0 (0.75)	[183]
		77	2 $^1\text{H}_a$ (CH_2Cl) 3 ^1H (CH_3)	9.5 3.4	
$\text{CD}_3\text{OCH}_2\text{Cl}^+$	CF_3CCl_3	4.2, 77	1 $^1\text{H}_a$ (CH_2Cl) 3 D (CD_3)	9.5 ≈ 0	
$\text{ClCH}_2\text{O}-\text{CH}_2\text{Cl}^+$	CF_3CCl_3	77	2 ^{35}Cl (CH_2Cl) ^a 2 $^1\text{H}_a$ (CH_2Cl) 2 $^1\text{H}_b$ (CH_2Cl)	$\sim 3.7^c$ 0.8 ≈ 0	[184]

^a Hyperfine splitting for ^{37}Cl and *g*-values are omitted in this table

^b Theoretical isotropic *hf* values calculated by the B3LYP/6-31G(d, p)//B3LYP/6-31G(d, p) method

^c Averaged value of $A_{iso} = (A_{aa} + A_{bb} + A_{cc})/3$ in which $(A_{aa}, A_{bb}, A_{cc}) = (\sim 0.7, \sim 0.7, 9.6)$ mT

the $\text{CH}_3\text{OCH}_2\text{F}^+$ and $\text{CD}_3\text{OCH}_2\text{F}^+$ cations. To verify the assignment of $\text{CH}_3\text{OCH}_2\text{F}^+$ the $\text{CD}_3\text{OCH}_2\text{Cl}^+$ cation was investigated. The spectrum of $\text{CD}_3\text{OCH}_2\text{Cl}^+$ consists of only a triplet split by 9.5 mT due to the two protons of the CH_2Cl group, but not of a quartet due to ^{35}Cl (and ^{37}Cl) splitting. Thus, it is a common phenomenon for $\text{CD}_3\text{OCH}_2\text{Cl}^+$ and $\text{CD}_3\text{OCH}_2\text{F}^+$ that no splitting was caused by the halogen atom in the two cations.

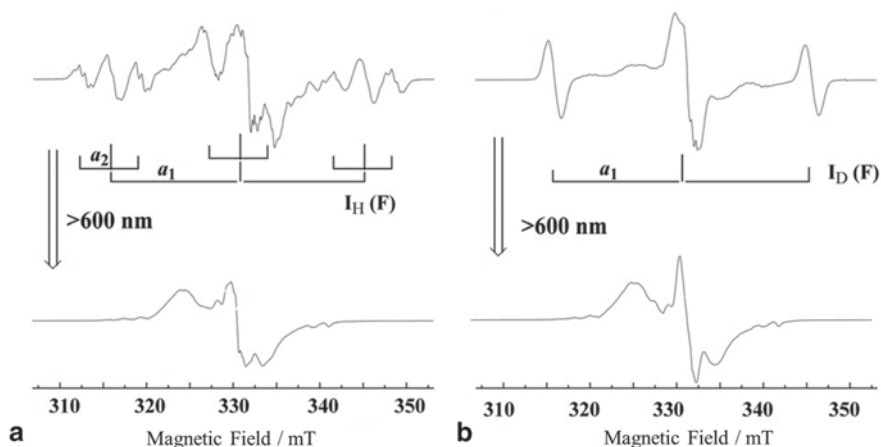


Fig. 3.18 EPR spectra for **a** $\text{CH}_2\text{OCH}_2\text{F}$ and **b** $\text{CD}_3\text{OCH}_2\text{F}$ formed by exposure to γ -rays in CF_3CCl_3 matrices, observed at 77 K (*top*), and those observed after photo-illumination with $\lambda > 600$ nm at 77 K (*bottom*). The figure is adapted from [183] by permission of the PCCP Owner Society (2002)

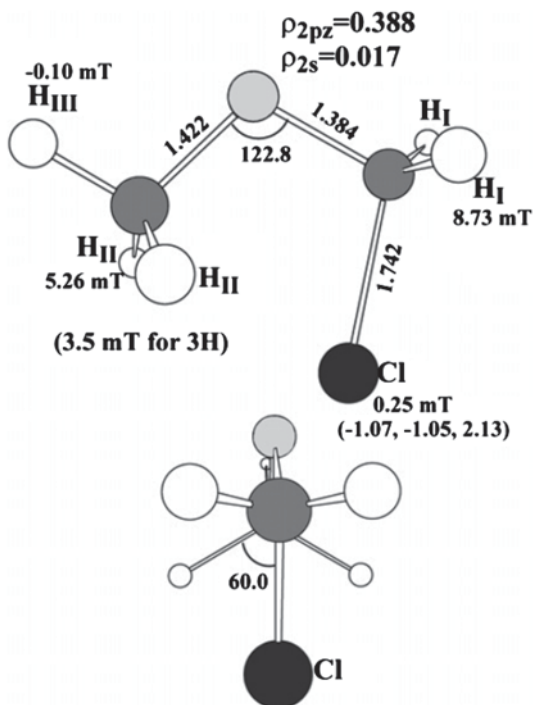
According to DFT calculations the above EPR result was explained as follows. The C-O-C-X framework takes a *cis*-conformation in which the halogen atom (X) preferentially occupies a position in the molecular C-O-C plane. The $2p_z$ orbital (nonbonding) on the oxygen atom possesses a major spin density and is perpendicular to the the molecular plane, see Fig. 3.19 for the $\text{CH}_3\text{OCH}_2\text{Cl}^+$ cation [183].

Temperature Dependent EPR Spectra of $\text{CH}_3\text{OCH}_2\text{Cl}^+$ Strong temperature dependent EPR spectra were observed for $\text{CH}_3\text{OCH}_2\text{Cl}^+$ in the CF_3CCl_3 matrix [183]. Based on a three-site chemical exchange model the spectral line-shapes were simulated as a function of rate constants, k (s^{-1}), for the rotation of the CH_3 protons as shown in Fig. 3.20. Assuming a linear Arrhenius plot between k (s^{-1}) and T^{-1} (K^{-1}) an activation energy of 3.3 ± 0.5 (kJ mol^{-1}) was evaluated for the rotation. The value corresponds to the theoretical one of 2.0 (kJ mol^{-1}) calculated for the potential barrier of the internal rotation of the methyl group.

3.5.3 $\text{ClCH}_2\text{OCH}_2\text{Cl}^+$ Cation

The EPR spectrum of bis-chlorinated DME^+ , $\text{ClCH}_2\text{OCH}_2\text{Cl}^+$, generated in irradiated CF_3CCl_3 matrix consisted of a major anisotropic septet due to two equivalent Cl atoms and an additional triplet (0.8 mT) due to two protons in each terminal CH_2Cl group [184]. The spectrum was unambiguously identified using a fully D-labelled compound, $\text{ClCD}_2\text{OCD}_2\text{Cl}$, as seen in Fig. 3.21. The observed anisotropic ^{35}Cl *hf*-splitting of 9.6 mT (see Table 3.7) suggests that the unpaired electron is largely and

Fig. 3.19 The optimized geometry with bond lengths (in Å), and bond angles (in degrees), and isotropic hf -splittings (in mT) of $\text{CH}_3\text{OCH}_2\text{Cl}^+$, calculated by B3LYP/6-31G(d, p)//B3LYP/6-31G(d, p) method. The values in parentheses are the anisotropic terms of the hf tensor (in mT) due to the ^{35}Cl nucleus. The $2p_z$ orbital of the oxygen atom is perpendicular to the molecular plane. The figure is adapted from [183] by permission of the PCCP Owner Society (2002)



equally shared by the $3p$ -orbitals of the two Cl nuclei with a weak Cl---Cl bond so as to form a five-membered ring. A similar structure with an X---X bond (X: halogen) has been observed for $\text{Cl}(\text{CH}_2)_3\text{Cl}^+$ [78] and $\text{Br}(\text{CH}_2)_n\text{Br}^+$ with $n = 1-7$ [79] as mentioned in Sect. 3.2.3.2.

Based on the EPR results combined with the DFT calculations two non-planar structures of C_s and C_2 symmetries were discussed for the $\text{ClCH}_2\text{OCH}_2\text{Cl}^+$ cation in which the two Cl-atoms, two C-atoms and one O-atom make a five-membered ring (Fig. 3.22). The calculations predicted that the C_s symmetry (Structure I) is 15.7 kJ/mol more stable than the C_2 symmetry (Structure II). Furthermore, the isotropic ^1H hf -splitting calculated for one of the CH_2 protons in the C_s structure is 0.99 mT, which is very close to the experimental value of 0.8 mT. Thus, the C_s structure was concluded to be the most plausible for the $\text{ClCH}_2\text{OCH}_2\text{Cl}^+$ cation.

$\text{ClCH}_2\text{OCH}_2\text{Cl}^+$ vs $\text{Cl}(\text{CH}_2)_3\text{Cl}^+$ It is of interest to compare the results of $\text{ClCH}_2\text{OCH}_2\text{Cl}^+$ [184] with those of $\text{Cl}(\text{CH}_2)_3\text{Cl}^+$ [78]. Similar to the $\text{ClCH}_2\text{OCH}_2\text{Cl}^+$ cation the $\text{Cl}(\text{CH}_2)_3\text{Cl}^+$ cation shows an hf pattern due to two equivalent Cl nuclei as mentioned in Sect. 3.2.3.3. In addition two equivalent protons of $\text{Cl}(\text{CH}_2)_3\text{Cl}^+$ gave an isotropic hf -splitting of 2.23 mT, which is slightly larger than that of $\text{ClCH}_2\text{OCH}_2\text{Cl}^+$ and attributable to one of the protons in each terminal CH_2Cl group. For the $\text{Cl}(\text{CH}_2)_3\text{Cl}^+$ cation a C_2 symmetrical structure has been suggested based on the *semi-empirical* CNDO/2 calculations in a previous study [78]. Recently we re-

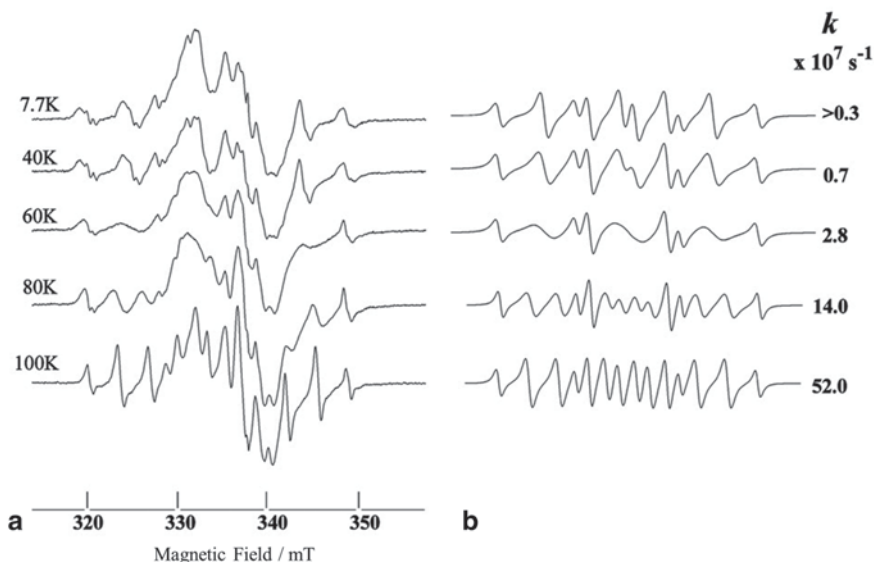


Fig. 3.20 The temperature-dependent EPR spectra of $\text{CH}_3\text{OCH}_2\text{Cl}^+$ in CF_3CCl_3 in a temperature range from 7.7 K to 100 K (a) and the spectra simulated (b) by applying a three-site exchange parameter for the rotation of the CH_3 protons with the exchange rate constant, k (s^{-1}), as an adjustable parameter. The figure is adapted from [183] by permission of the PCCP Owner Society (2002)

examined the electronic structure of $\text{Cl}(\text{CH}_2)_3\text{Cl}^+$ based on DFT calculations and reached the conclusion that the $\text{Cl}(\text{CH}_2)_3\text{Cl}^+$ cation prefers to take a structure similar to $\text{ClCH}_2\text{OCH}_2\text{Cl}^+$, Structure III (C_s symmetry) in Fig. 3.22 [184]. An early IR spectroscopic study has revealed that neutral $\text{Cl}(\text{CH}_2)_3\text{Cl}$ molecule prefers the *gauche-gauche* conformation in the crystalline solid state [185]. The EPR results suggest that the conformation in the neutral molecule is retained for the corresponding radical cation in solid matrices.

3.6 Summary

CW-EPR spectroscopic studies combined with quantum chemical calculations were applied to investigate structure, reactions and dynamics of the radical ions generated by radiolysis of fluorinated hydrocarbons and related compounds in low temperature solid matrices. Isotropic and anisotropic EPR spectra of perfluorocycloalkane radical anions, $c\text{-C}_n\text{F}_{2n}^-$ ($n=3-5$) were observed. The hyperfine (*hf*) splittings were attributed to a planar structure with an entirely delocalized singly occupied MO, whereas the spectra of perfluoroalkene radical anions, $c\text{-C}_n\text{F}_{2n-2}^-$ were attributed to a distorted pyramidal structure occurring at the $\text{C}=\text{C}$ carbons by a mixing of the ground π^* -orbital and higher-lying σ^* -orbitals. The EPR parameters of these radical anions were reproduced with considerable precision by quantum chemical

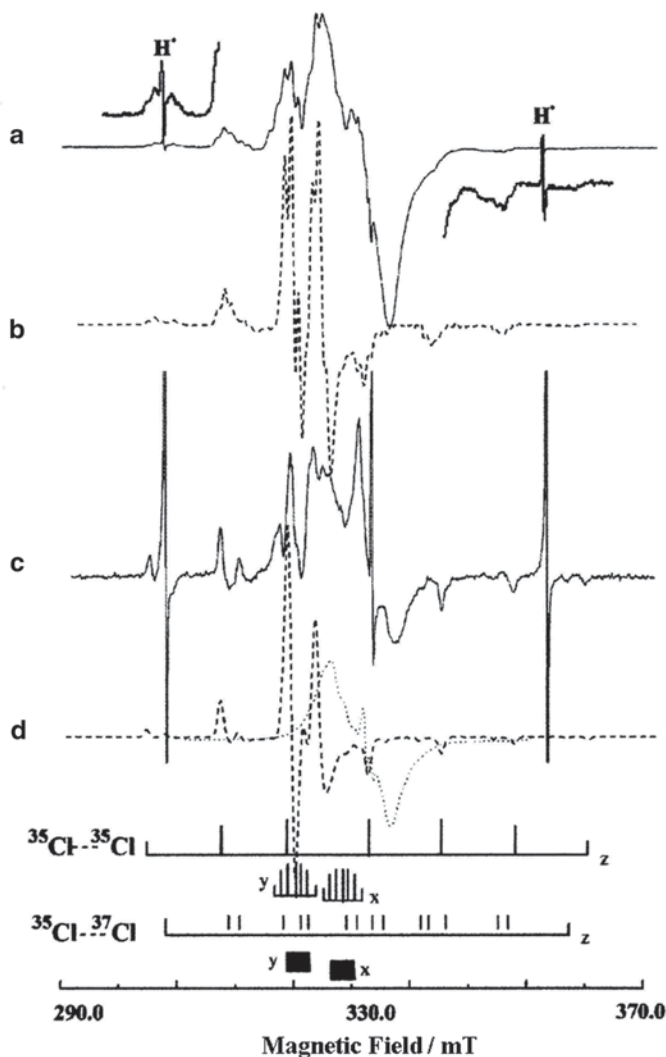


Fig. 3.21 The EPR spectra of **a** $\text{ClCH}_2\text{OCH}_2\text{Cl}^+$ and **c** $\text{ClCD}_2\text{OCD}_2\text{Cl}^+$ generated in CF_3CCl_3 by γ -ray irradiation and observed at 77 K after annealing at 130 K. **b** and **d** The spectra simulated for $\text{ClCH}_2\text{OCH}_2\text{Cl}^+$ and $\text{ClCD}_2\text{OCD}_2\text{Cl}^+$ were calculated using the g -value and hf -splittings in Table 3.7 for two magnetically equivalent Cl-nuclei and two equivalent protons. The EPR signal of irradiated pure matrix CF_3CCl_3 is denoted by the dotted lines (.....) in **d**. Stick diagrams for the spectral assignment are shown at the bottom. The figure is adapted from [184] by permission of the PCCP Owner Society (2001)

computations, affording a valuable bridge between experiment and theory. The EPR studies of the radical cations of mono- and di-haloalkanes, $\text{H}(\text{CH}_2)_n\text{X}^+$ and $\text{X}(\text{CH}_2)_n\text{X}^+$, with $\text{X}=\text{Cl}$ and Br in halocarbon matrices were reviewed. The EPR results of di-haloalkane radical cations suggested a σ^* -bond formation between two

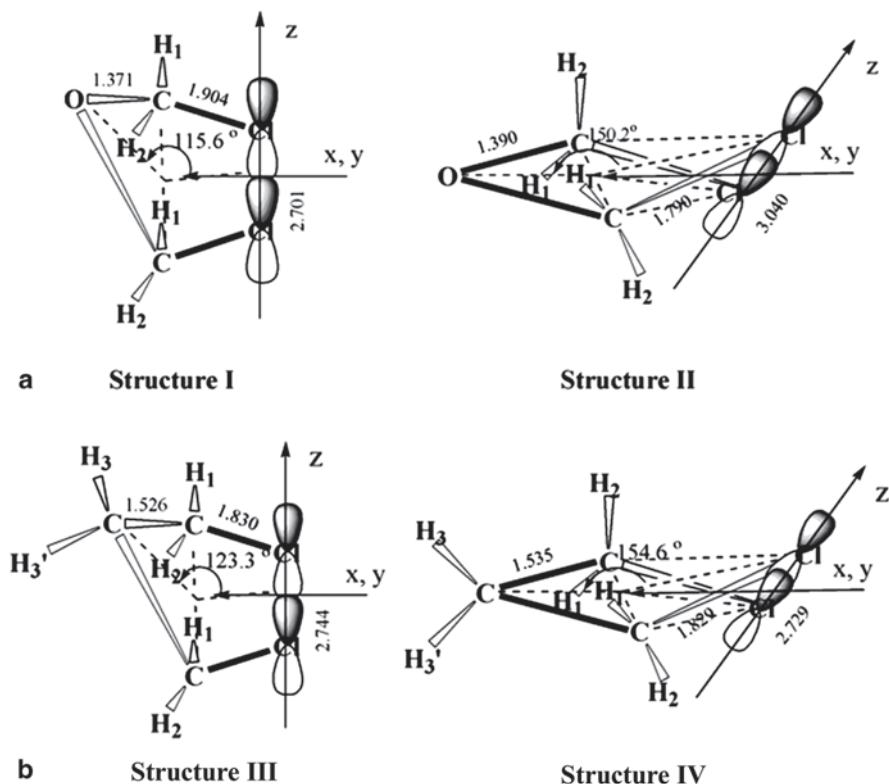


Fig. 3.22 Two possible structures optimized for $\text{ClCH}_2\text{OCH}_2\text{Cl}^+$ and $\text{Cl}(\text{CH}_2)_3\text{Cl}^+$ with the DFT B3LYP/6-31G(d, p) level of theory. The length of the bonds is in Å unit. **a** $\text{ClCH}_2\text{OCH}_2\text{Cl}^+$: Structure I (C_s symmetry), in the lowest energy, has the C–O–C plane intersecting the C–Cl–Cl–C plane, while Structure II (C_2 symmetry) has the C–O–C plane intersecting the two C–Cl–C planes in the opposite phase. **b** $\text{Cl}(\text{CH}_2)_3\text{Cl}^+$: Structure III (C_s), with the lowest energy, has the C–C(central)–C plane intersecting the C–Cl–Cl–C plane, while Structure IV (C_2) has the C–C–C plane intersecting the two C–Cl–C planes in the opposite phase. The figure is adapted from [184] by permission of the PCCP Owner Society (2001)

halides in the cations as a result of cyclization in the matrix. The *g*- and ^{19}F *hf*-tensors with an axial symmetry were observed for a series of selectively fluorinated (F-) benzene radical cations, suggesting that they are planar π -type radicals. The radical cations were classified into a symmetric $^2B_{2g}(\Psi_S)$ like (with an elongated carbon ring) or an anti-symmetric $^2B_{1g}(\Psi_A)$ like (with a compressed ring) electronic ground state. The EPR studies on the dimer cations of F-benzenes in solid matrices were reviewed. Moreover, the anisotropic EPR spectrum of C_6F_6^- radical anion in MTHF matrix was simulated using the ^{19}F *hf* tensors computed by DFT method. Static and dynamic structures of halogen-substituted dimethyl ether radical cations such as $\text{CH}_3\text{OCH}_2\text{F}^+$ and $\text{CH}_3\text{OCH}_2\text{Cl}^+$ were studied by EPR combined with MO calculations. For the $\text{ClCH}_2\text{OCH}_2\text{Cl}^+$ cation it was suggested that the two Cl,

two C and one O atoms make a non-planar five-membered ring structure with C_s symmetry similar to the $X(CH_2)_3X^+$ cation. Furthermore, EPR studies on fluoroethylene related radical cations were reviewed. A photo-isomerization reaction of perfluoro1,3-butadiene radical cation was presented.

References

1. Kaiser ET, Kevan L (eds) (1968) Radical ions. Interscience Publishers, New York
2. Lund A, Shiotani M (eds) (1991) Radical ionic systems: properties in condensed phases. Kluwer, Dordrecht
3. Shiotani M, Yoshida H (1991) ESR of radical ions. In: Tabata Y (ed) CRC handbook of radiation chemistry. CRC, Boca Raton, pp 440–467
4. Lund A, Shiotani M (eds) (2003) EPR of free radicals in solids. Kluwer, Dordrecht
5. Lund A, Shiotani M, Shimada (2011) Principles and applications of ESR spectroscopy. Springer, Dordrecht, pp 211–271
6. Lund A, Shiotani M (eds) (2013) EPR of Free radicals in solids I: trends in method and applications, 2nd ed. Springer, Dordrecht
7. Lund A, Shiotani M (eds) (2013) EPR of Free radicals in solids II: trends in method and applications, 2nd ed. Springer, Dordrecht
8. Shiotani M (1987) ESR studies of radical cations in solid matrixes. *Magn Reson Rev* 12:333–381
9. Atkins PW, Symons MCR (1967) The structure of inorganic radicals. Elsevier, Amsterdam
10. Hudson A, Root K (1971) Halogen hyperfine interactions. In: Waugh J (ed) Advances in magnetic resonance, vol 5. Academic Press, New York, pp 1–63
11. Barnes AJ (ed) (1981) Matrix-isolation spectroscopy. NATO advanced study institutes series. C 76, Reidel, Dordrecht
12. Dunkin IR (1989) Matrix-isolation techniques: a practical approach. Oxford University Press, Oxford
13. Hasegawa A, Shiotani M, Williams F (1978) Electron spin resonance studies of electron attachment to fluorocarbons and related compounds. *Faraday Discuss Chem Soc* 63 (Radiation effects on liquids and solids):157–174
14. Lund A, Lindgren M, Lunell S, Maruani J (1989) Hydrocarbon radical cations in condensed phases. In: Maruani J (ed) Molecules in physics, chemistry and biology. Topics in molecular organization and engineering, vol 3. Springer, New York, pp 259–300
15. Shiotani M (1991) ESR detection of radicals trapped in solid. In: Tabata Y (ed) CRC handbook of radiation chemistry. CRC, Boca Raton, pp 139–144
16. Shiotani M (1991) ESR spectra of free radicals generated by ionizing radiations. In: Tabata Y (ed) CRC Handbook of radiation chemistry. CRC, Boca Raton, pp 544–567
17. Lindgren M, Shiotani M (1991) ESR studies of radical cations of cycloalkanes and saturated heterocycles. In: Lund A, Shiotani M (eds) Radical ionic systems: properties in condensed phases. Kluwer, Dordrecht, pp 125–150
18. Shiotani M, Lund A (1991) Deuterium labeling studies of cation radicals. In: Lund A, Shiotani M (eds) Radical ionic systems: properties in condensed phases. Kluwer, Dordrecht, pp 151–176
19. Hasegawa A (1991) Radical anions in disordered matrices. In: Lund A, Shiotani M (eds) Radical ionic systems: properties in condensed phases. Kluwer, Dordrecht
20. Shiotani M, Komaguchi K (2003) Quantum effects in isotopically labeled radicals at low temperatures. In: Lund A, Shiotani M (eds) EPR of free radicals in solids. Kluwer, Dordrecht, pp 153–195

21. Shiotani M, Komaguchi K (2012) Deuterium labeling studies and quantum effects of radicals in solids. In: Lund A, Shiotani M (eds) *EPR of free radicals in solids I*, 2nd ed. Springer, Dordrecht, pp 171–221
22. Morton JR, Preston KF (1977) Magnetic properties of free radicals. In: Landolt-Börnstein, Group II molecules and radicals. vol 9, Part a–d. Springer, Berlin
23. Muto H (1991) Trapped anions on organic crystals. In: Lund A, Shiotani M (eds) *Radical ionic systems: properties in condensed phases*. Kluwer, Dordrecht, pp 337–360
24. Shida T, Nosaka Y, Kato T (1978) Electronic absorption spectra of some cation radicals as compared with ultraviolet photoelectron spectra. *J Phys Chem* 82:695–698
25. Shiotani M, Lindgren M (1994) Radicals on surfaces formed by ionizing radiation. In: Lund A, Rhodes CJ (eds) *Radicals on surfaces*. Kluwer, Dordrecht, pp 179–199
26. Knight LB Jr, Steadman J (1982) An experimental procedure for ESR studies of rare gas matrix isolated molecular cation radicals: $^{12}\text{CO}^+$, $^{13}\text{CO}^+$, $^{14}\text{NH}_3^+$, and $^{15}\text{NH}_3^+$. *J Chem Phys* 77:1750–1756
27. Knight LB Jr, Steadman J (1983) ESR investigations of H_2O^+ , HDO^+ , D_2O^+ , and $\text{H}_2^{17}\text{O}^+$ isolated in neon matrices at 4 K. *J Chem Phys* 78:5940–5945
28. Knight LB Jr, Steadman J, Feller D, Davidson ER (1984) Experimental evidence for a C_{2v} ($^2\text{B}_1$) ground-state structure of the methane cation radical: ESR and ab initio CI investigations of methane cation radicals (CH_4^+ and CD_2H_2^+) in neon matrixes at 4 K. *J Am Chem Soc* 106:3700–3701
29. Knight LB Jr (1991) Generation and study of inorganic cations in rare gas matrices by electron spin resonance. In Lund A, Shiotani M (eds) *Radical ionic systems: properties in condensed phases*. Kluwer, Dordrecht, Chapter I.3
30. Knight LB Jr, King GM, Petty JT, Matsushita M, Momose T, Shida T (1995) Electron spin resonance studies of the methane radical cations ($^{12,13}\text{CH}_4^+$, $^{12,13}\text{CDH}_3^+$, $^{12}\text{CD}_2\text{H}_2^+$, $^{12}\text{CD}_3\text{H}^+$, $^{12}\text{CD}_4^+$) in solid neon matrices between 2.5 and 11 K: analysis of tunneling. *J Chem Phys* 103:3377–3385
31. Rajbenbach LA (1966) Nondissociative electron attachment reactions in γ -radiolysis of solutions of cyclic perfluorocarbons in alkanes. *J Am Chem Soc* 88:4275–4277
32. Rajbenbach LA, Kaldor U (1967) Yield of scavengeable hydrogen atoms, electrons, and positive charges in the radiolysis of liquid hexane. *J Chem Phys* 47:242–247
33. Sagert NH (1968) γ -Radiolysis of cyclohexane with electron scavengers. III. Perfluorocarbons as electron scavengers. *Canad J Chem* 46:95–99
34. Rajbenbach LA (1969) Radiolysis of solutions of perfluorocarbons in hexane. *J Phys Chem* 73:356–360
35. Asundi RK, Craggs JD (1964) Electron capture and ionization phenomena in SF_6 and C_7F_{14} . *Proc Phys Soc* 83:611–618
36. Mahan BH, Yong CE (1966) Electron capture and ionization phenomena in SF_6 and C_7F_{14} . *J Chem Phys* 44:2192–2196
37. Fessenden RW, Bansal KM (1970) Direct observation of electron disappearance in pulse irradiated fluorocarbon gases. *J Chem Phys* 53:3468–3473
38. Bansal KM, Fessenden RW (1973) Electron disappearance in pulse irradiated fluorocarbon gases. *J Chem Phys* 59:1760–1768
39. Naff WT, Cooper CD, Compton RN (1968) Transient negative-ion states in alicyclic and aromatic fluorocarbon molecules. *J Chem Phys* 49:2784–2788
40. Davis FJ, Compton RN, Nelson DR (1973) Thermal energy electron attachment rate constants for some polyatomic molecules. *J Chem Phys* 59:2324–2329
41. Christophorou LG, McCorkle DL, Pittman D (1974) Attachment of slow (<1 eV) electron to molecular oxygen in very high pressures of nitrogen, ethylene, and ethane. *J Chem Phys* 60:1183–1184
42. Green SW, Slinn DSL, Simpson RNF, Woytek AJ (1994) In: Banks RE, Smart BE, Tatlow JC (eds) *Organofluorine chemistry: principles and commercial applications*. Plenum, NY, pp 1–89

43. Barthe-Rosa LP, Gladysz JA (1999) Chemistry in fluorous media: a user's guide to practical considerations in the application of fluorous catalysts and reagents. *Coord Chem Rev* 190:587–605
44. Takahashi K, Ithoh A, Nakamura T, Tachibana K (2000) Radical kinetics for polymer film deposition in fluorocarbon (C_4F_8 , C_3F_6 and C_5F_8) plasmas. *Thin Solid Films* 374:303–310
45. Tachi S (2003) Impact of plasma processing on integrated circuit technology migration: from 1 μm to 100 nm and beyond. *J Vac Sci Technol A* 21:S131–S138
46. Hiraoka K, Takao K, Iino T, Nakagawa F, Suyama H, Mizuno T, Yamabe S (2002) Gas-phase ion-molecule reactions in C_3F_6 . *J Phys Chem A* 106:603–611
47. Hiraoka K, Fujita K, Ishida M, Okada K, Hizumi A, Wada A, Yamabe S, Tsuchida N (2005) Gas-phase ion/molecule reactions in C_5F_8 . *J Phys Chem A* 109:1049–1056
48. Fessenden RW (1962) Second-order splittings in the electron spin resonance (E.S.R) spectra of organic radicals. *J Chem Phys* 37:747–750
49. Fessenden RW, Schuler RH (1965) E.S.R. spectra and structure of the fluorinated methyl radicals. *J Chem Phys* 43:2704–2714
50. Fessenden RW, Schuler RH (1963) Electron spin resonance studies of transient alkyl radicals. *J Chem Phys* 39:2147–2195
51. Iwasaki M (1971) Electron spin resonance of irradiated organic fluorine compounds. *Fluorine Chem Rev* 5:1–56
52. Iwasaki M (1971) Origin of the ESR hyperfine anisotropy and the $\cos^2\theta$ rule of the β -fluorine couplings. *Mol Phys* 20:503–512
53. Chachaty C, Forchioni A, Shiotani M (1969) Résonance paramagnétique électronique de radicaux cycliques perfluorés. *C R Acad Sci Paris Ser C* 268:1181–1184
54. Chachaty C, Forchioni A, Shiotani M (1970) Etude par résonance paramagnétique électronique de la radiolyse en phase solide composé cyclique perfluorés. *Can J Chem* 48:435–446
55. Chachaty C, Shiotani M (1971) Résonance paramagnétique électronique de radicaux aliphatiques fluorés. *J Chim Phys* 66:300–310
56. Edlund O, Lund A, Shiotani M, Sohma J, Thuomas KA (1976) Theory for the anisotropic hyperfine coupling with fluorine: the perfluoromethyl radical. *Mol Phys* 32:49–69
57. Maruani J, McDowell CA, Nakajima H, Raghunathan P (1968) The electron spin resonance spectra of randomly oriented trifluoromethyl radicals in rare-gas matrixes at low temperatures. *Mol Phys* 14:349–366
58. Maruani J, Coope JAR, McDowell CA (1970) Detailed analysis of the singularities and origin of the 'extra' lines in the ESR spectrum of the CF_3 radical in a polycrystalline matrix. *Mol Phys* 18:165–176
59. Shiotani M, Williams F (1976) Electron spin resonance spectrum of the perfluorocyclobutane radical anion. *J Am Chem Soc* 98:4006–4008
60. Shiotani M, Lund A, Lunell S, Williams F (2007) Structures of the hexafluorocyclopropane, octafluorocyclobutane and decafluorocyclopentane radical anions probed by experimental and computational studies of anisotropic ESR spectra. *J Phys Chem A* 111:321–338
61. Aguirregabiria J (2013) Ejs Symmetric Top Model. <http://www.opensourcephysics.org/items/detail.cfm?ID=7872>
62. Shimizu Y, Kumada T, Kumagai J (2008) Electron spin resonance spectroscopy of molecules in large precessional motion: a case of H_6^+ and $H_4D_2^+$ in solid parahydrogen. *J Mag Res* 19:76–80
63. Shiotani M, Imura D, Murabayashi S, Sohma J (1975) Dissociative electron capture of fluorinated acetic acids. *Int J Radiat Phys Chem* 7:265–274
64. Shiotani M, Sohma J (1975) Dissociative electron capture in low temperature solid phase. *Kagaku (Chemistry)* 30:161–163
65. Wentworth WE, George R, Keith H (1969) Dissociative thermal electron attachment to some aliphatic chloro, bromo, iodo compounds. *J Chem Phys* 51:1791–1801
66. Sprague ED, Williams F (1971) ESR observation of methyl radical-halide ion pairs produced by dissociative electron capture in a crystalline matrix. *J Chem Phys* 54:5425–5427
67. Mishra SP, Symons MCR (1973) Unstable intermediates. Part CXXIV. Alkyl radical-halide ion adducts. *J Chem Soc Perkin Trans II*:391–394

68. Fujita Y, Katsu T, Sato M, Takahashi K (1974) Carbon-13 hyperfine splittings of normal and abnormal methyl radicals trapped on the porous Vycor glass surface. *J Chem Phys* 61:4307–4311
69. Hasegawa A, Williams F (1977) ESR spectra and structure of the CF_3Cl^- , CF_3Br^- , and CF_3I^- radical anions. *Chem Phys Lett* 46:66–68
70. Muto H, Nunome K (1991) Electron spin resonance and optical studies on the radiolysis of carbon tetrachloride. II. Structure and reaction of CCl_4^- radical anion in tetramethylsilane low temperature solids. *J Chem Phys* 94:4741–4748
71. Morton JR, Preston KF (1975) Etude R.P.E. des anions paramagnétiques SnH_4^- et SiF_4^- . *Mol Phys* 30:1213–1215
72. Hasegawa A, Uchimura S, Koseki K, Hayashi M (1978) ESR spectrum and structure of the SiF_3Cl^- radical anion. *Chem Phys Lett* 53:337–340
73. Hasegawa A, Uchimura S, Hayashi M (1980) Electron paramagnetic resonance spectra of SiF_3X^- (X=Cl, Br, I) and $\text{SiF}_n\text{Cl}_{4-n}^-$ ($n=0-2$) radical anions. *J Mag Res* 38:391–400
74. Toriyama K, Nunome K, Iwasaki M (1982) Structures and reactions of radical cations of some prototype alkanes in low temperature solids as studied by ESR spectroscopy. *J Chem Phys* 77:5891–5912
75. Toriyama K (1991) ESR studies of radical cations of saturated hydrocarbons: structure, orbital degeneracy, dynamics, and Reactions. In: Lund A, Shiotani M (eds) *Radical ionic systems: properties in condensed phases*. Kluwer, Dordrecht, pp 99–124
76. Eastland GW, Maj SP, Symons MCR, Hasegawa A, Glidewell C, Hayashi M, Wakabayashi T (1984) Radiation chemical formation of radical cations of halo alkanes and their electron spin resonance spectra and structure. *J Chem Soc Perkin Trans 2*:1439–1447
77. Symons MCR (1985) Radical cations of di-, tri-, and tetra-bromomethane formed by radiolysis: an electron spin resonance study. *J Chem Res* 8:256–257
78. Hasegawa A, Symons MCR, Shiotani M (1989) Electron spin resonance spectra and structure of the radical cations of 1,3-dichloropropane and other dichloroalkanes. *J Chem Soc Perkin Trans II*:147–151
79. Hasegawa A, Symons MCR, Shiotani M (1989) Electron spin resonance spectra and structure of the radical cations of dibromoalkanes and monobromoalkanes. *J Chem Soc Perkin Trans II*:657–665
80. Muto H, Nunome K, Iwasaki M (1989) An electron spin resonance study of the structure of the tetrachloromethane radical cation (CCl_4^+) in carbon tetrachloride γ -irradiated at low temperatures by powder and single crystal analyses. *J Chem Phys* 90:6827–6832
81. Knight LB Jr, Gregory BW, Hill DW, Arrington CA, Momose T, Shida T (1991) Electron spin resonance studies of $^{12}\text{CH}_3\text{F}^+$, $^{13}\text{CH}_3\text{F}^+$, and $^{12}\text{CH}_2\text{DF}^+$ in neon matrices at 4 K: comparison with theoretical calculations. *J Chem Phys* 94:67–79
82. Komaguchi K, Sakurai H, Shiotani M, Hasegawa A (2001) The ESR spectra, electronic structure, and thermal reactivity of fluoroethane cations. *Bull Chem Soc Jap* 74:2319–2324
83. Gillbro T, Kerr CML, Williams F (1974) Electron spin resonance identification of the dimer radical cation $(\text{MeO})_3\text{PP}(\text{OMe})_3^+$ in γ -irradiated trimethyl phosphite from second-order hyperfine structure. *Mol Phys* 28:1225–1232
84. Hasegawa A, McConnachie GD, Symons MCR (1984) Preparation and structure of certain phosphorus-centred radical cations: an electron spin resonance study. *J Chem Soc Faraday Trans I* 80:1005–1016
85. Nelson DJ, Petersen RL, Symons MCR (1977) Unstable intermediates. Part 178. The structure of intermediates formed in the radiolysis of thiols. *J Chem Soc Perkin Trans II*:2005–2015
86. Petersen RL, Nelson DJ, Symons MCR (1978) Unstable intermediates. Part 179. Electron spin resonance studies of radicals formed in irradiated organic sulphides and disulphides. *J Chem Soc Perkin Trans II*:225–231
87. Rao DNO, Symons MCR, Wren BW (1984) Radical cations of organic sulphides and disulphides formed by radiolysis: an electron spin resonance study. *J Chem Soc Perkin Trans II*:1681–1687

88. Qin XZ, Meng O, Williams F (1987) ESR studies of the thietane and thiirane radical cations in freon matrixes. Evidence for ethylene molecule extrusion from a σ^* thiirane dimer radical cation $[\text{C}_2\text{H}_4\text{S}-\text{SC}_2\text{H}_4^+]$. *J Am Chem Soc* 109:6778–6788
89. Symons MCR (1979) Electron spin resonance studies of radicals derived from dithionate, tetrathionate, and thiosulphate anions. *J Chem Soc Dalton Trans* 1979:1468–1472
90. Mishra SP, Symons MCR (1975) Unstable intermediates. Part CLIX. Dihalide anions and related species as products in the radiolysis of organic halides. *J Chem Soc Perkin Trans II*:1492–1498
91. Sevilla MD, Becker D, Sevilla CL, Swarts S (1984) An ESR investigation of ester π -cation radicals in a Freon matrix at low temperatures: evidence for unusual barriers to methyl group rotation and intramolecular bonding. *J Phys Chem* 88:1701–1706
92. Sevilla MD, Becker D, Sevilla CL, Swarts S (1985) Reactions of the methyl and ethyl formate cation radicals: deuterium isotope effects. *J Phys Chem* 89:633–636
93. Snow LD, Williams F (1983) An ESR study of the acetaldehyde radical cation in freon matrixes: evidence for halogen superhyperfine interaction. *Chem Phys Lett* 100:198–202
94. Clark T, Hasegawa A, Symons MCR (1985) Matrix interactions for radical cations: theoretical and experimental results for the trichlorofluoromethane matrix illustrated by ^{19}F coupling for Me_2Se^+ radical cations. *Chem Phys Lett* 116:79–82
95. Becker D, Plante K, Sevilla MD (1983) Methyl formate cation radical: electron spin resonance evidence for a σ^* radical formed by strong matrix-solute cation interaction in frozen fluorotrichloromethane solutions. *J Phys Chem* 87:1648–1652
96. Hasegawa A, Symons MCR (1983) Electron spin resonance spectra of tetrafluoroethylene radical cation. *J Chem Soc Faraday Trans 1*(79):93–97
97. Shiotani M, Nagata Y, Sohma J (1984) Electron spin resonance studies on propylene radical cation. *J Phys Chem* 88:4078–4082
98. Fujisawa J, Sato S, Shimokoshi K, Shida T (1985) Environment effects on the ESR spectrum of the cation radical of dimethylketene in low temperature matrixes. *Bull Chem Soc Jap* 58:1267–1272
99. Maj P, Hasegawa A, Symons MCR (1983) Radical cations of halobenzenes: an electron spin resonance study. *J Chem Soc Faraday Trans 1*(79):1931–1938
100. Symons MCR, Hasegawa A, Maj P (1982) ESR spectra of matrix-isolated bromobenzene cations formed by radiolysis. *Chem Phys Lett* 8:254–257
101. McNeil RI, Shiotani M, Williams F, Yim MB (1977) The isotropic and anisotropic ESR spectra of the tetrafluoroethylene radical anion. *Chem Phys Lett* 51:433–437
102. McNeil RI, Shiotani M, Williams F, Yim MB (1977) Novel cycloaddition of tetrafluoroethylene to the tetrafluoroethylene radical anion at 95 K: direct observation by EPR studies. *Chem Phys Lett* 51:438–441
103. Paddon-Row MN, Rondon NG, Houk KN, Jordan KD (1982) Geometries of the radical anions of ethylene, fluoroethylene, 1,1-difluoroethylene, and tetrafluoroethylene. *J Am Chem Soc* 104:1143–1145
104. Schastnev PV, Shchegoleva LN (1995) Molecular distortions in ions and excited states. CRC, Boca Raton, Chapter 3
105. Hasegawa A, Symons MCR (1983) Structure of the tetrafluoroethylene radical anion and interpretations of its electron spin resonance spectra. *J Chem Soc Faraday Trans 1* 79:1565–1571
106. Shiotani M, Person P, Lunell S, Lund A, Williams F (2006) Structures of tetrafluorocyclopropene, hexafluorocyclobutene, octafluorocyclopentene and related perfluoroalkene radical anions revealed by ESR spectroscopic and computational studies. *J Phys Chem A* 110:6307–6323
107. McNeil RI, Williams F, Yim MB (1979) EPR Spectra and structure of the chlorotrifluoroethylene and bromotrifluoroethylene radical anions. *Chem Phys Lett* 61:293–298
108. Itagaki Y, Shiotani M (1999) Photoinduced isomerization of trans-acetylene radical anion to vinylidene radical anion in 2-methyltetrahydrofuran. *J Phys Chem A* 103:5189–5195

109. Matsuura K, Muto H (1993) Electronic structure of acetylene radical anion with a trans-bent form. *J Phys Chem* 97:8842–8844
110. Hasegawa A, Symons MCR (1983) Electron spin resonance spectra of tetrafluoroethylene radical cation. *J Chem Soc Faraday Trans I* 79:93–97
111. Ohta K, Shiotani M, Sohma J (1987) ESR spectra and structures of radical cations of chlorotrifluoroethylene and bromotrifluoroethylene. *Chem Phys Lett* 140:148–153
112. Carrington A, McLachlan (1967) *Introduction to magnetic resonance*. Harper & Row, New York
113. Itagaki Y, Shiotani M, Hasegawa A, Kawazoe H (1998) EPR spectra and structure of the radical cations of fluorinated ethylenes and propenes. *Bull Chem Soc Jpn* 71:2547–2554
114. Li WZ, Huang MB (2003) Equilibrium structures and hyperfine parameters of some fluorinated hydrocarbon radical cations: a DFT BLYP and MP2 study. *J Mol Struct (Theochem)* 639:71–79
115. Lunell S, Huang MB (1990) The hyperfine structure in the ethylene radical cation: an accurate CI study. *Chem Phys Lett* 168:63–68
116. Shiotani M, Kawazoe H, Sohma J (1984) The radical cation of hexafluoro-1,3-butadiene: an ESR study. *Chem Phys Lett* 111:254–257
117. Xiao HY, Cao J, Liu YJ, Fang WH, Tachikawa H, Shiotani M (2007) Structures and cis-to-trans photoisomerization of hexafluoro-1,3-butadiene radical cation: electron spin resonance (ESR) and computational studies. *J Phys Chem A* 111:5192–5200
118. Shiotani M, Ohta K, Nagata Y, Sohma J (1985) Novel cycloaddition of dimethylacetylene to the dimethylacetylene radical cation: direct observation by ESR. *J Am Chem Soc* 107:2562–2564
119. Chang CH, Andreassen AL, Hbaiter SHS (1971) Molecular structure of perfluoro-2-butyne and perfluoro-1,3-butadiene as studied by gas phase electron diffraction. *J Org Chem* 36:920–923
120. Aston JG, Sasz G, Woolley HW, Brickwedde FG (1946) Thermodynamic properties of gaseous 1,3-butadiene and the normal butenes above 25 °C equilibria in the system 1,3-butadiene, n-butenes, and n-butane. *J Chem Phys* 14:67–79
121. Itagaki Y, Yanagida N, Shiotani M (2002) Formation and structure of dimer radical cations of fluorinated benzenes in solid matrices. *Phys Chem Chem Phys* 4:5982–5987
122. Slinkin AA, Kucherov AV, Kondrat'ev DA, Bondarenko TN, Rubinstein AM, Minachev KM (1986) Formation of radicals and catalytic activity of pentasil-type zeolites in unsaturated hydrocarbon conversions: part 1. Radical formation upon olefin adsorption. *J Mole Cat* 35:97–105
123. Kucherov AV, Slinkin AA, Kondratyev DA, Bondarenko TN, Rubinstein AM, Minachev KM (1986) Formation of radicals and catalytic activity of H-ZSM-5-type zeolites in unsaturated hydrocarbon conversions: part 2. Radical formation upon adsorption of aromatic compounds. *J Mol Cat* 37:107–115
124. Volodin AM, Bolshov VA, Panov GI (1994) The Role of Surface α -Oxygen in Formation of Cation Radicals at Benzene Adsorption on ZSM-5 Zeolite. *J Phys Chem* 98:7548–7550
125. Bolshov VA, Volodin AM, Zhidomirov GM, Shubin AA, Bedilo AF (1994) Radical intermediates in the photoinduced formation of benzene cation-radicals over H-ZSM-5 zeolites. *J Phys Chem* 98:7551–7554
126. Jahn HA, Teller E (1937) Stability of polyatomic molecules in degenerate electronic states I: orbital degeneracy. *Proc R Soc Lond A* 161:220–235
127. Dewar MJS, Yamaguchi Y, Doraisways S, Sharma SD, Such SH (1979) Structures and properties of fluorinated pyridines; assignment of the two homo's of pyridine. *Chem Phys* 41:21–33 (and references cited therein)
128. von Nissen W, Diercksen GHF, Cederbaum S (1975) The electronic structure of molecules by a many-body approach: II. Ionization potentials one-electron properties of pyridine and phosphoridine. *Chem Phys* 10:345–360
129. Berg JO, Parker DH, El-Sayed MA (1978) Assignment of the lowest ionization potentials in pyridine and pyrazine by multiphoton ionization spectroscopy. *Chem Phys Lett* 56:411–416

130. Duke CB, Yip KL, Ceaser GP, Potts AW, Streets DG (1977) Electronic structure of the fluorobenzenes, ethylene, and tetrafluoroethylene. *J Chem Phys* 66:256–268
131. Frazier JR, Christophorou LG, Carter JG, Schweinler HC (1978) Low-energy electron interactions with organic molecules: negative ion states of fluorobenzenes. *J Chem Phys* 69:3807–3818
132. Rabalais JW (1977) Principles of ultraviolet photoelectron spectroscopy. Wiley, New York
133. Turner DW, Baker C, Baker AD, Brundle CR (1970) Molecular photoelectron spectroscopy. Wiley, New York
134. Brundle CR, Robin MB, Kuebler NA, Basch H (1972) Perfluoro effect in photoelectron spectroscopy I: nonaromatic molecules. *J Am Chem Soc* 94:1451–1465
135. Brundle CR, Robin MB, Kuebler NA (1972) Perfluoro effect in photoelectron spectroscopy II: aromatic molecules. *J Am Chem Soc* 94:1466–1475
136. Hasegawa A, Shiotani M, Hama Y (1994) ESR Studies of Jahn-Teller distortion in the radical anions and cations of hexafluorobenzene. *J Phys Chem* 98:1834–1839
137. Hasegawa A, Itagaki Y, Shiotani M (1997) EPR spectra and structure of the radical cations of fluorinated benzenes. *J Chem Soc Perkin Trans 2*:1625–1631
138. Itagaki Y, Lund A, Shiotani M, Hasegawa A (1999) Substitution effects on the structure of benzene radical cations. *Trends Chem Phys* 7:277–300
139. Williams LF, Yim MB, Wood DE (1973) Electron paramagnetic resonance of free radicals in adamantane matrix. VI. Hexafluorobenzene anion radical. *J Am Chem Soc* 95:6475–6477
140. Yim MB, Wood DE (1976) Free radicals in an adamantane matrix. XII. EPR and INDO study of $\sigma^*-\pi^*$ crossover in fluorinated benzene anions. *J Amer Chem Soc* 98:2053–2059
141. Symons MCR, Selby RC, Simth IG, Bratt SW (1977) ESR studies on the structure of $C_6F_6^-$ anions. *Chem Phys Lett* 48:100–102
142. Wang JT, Williams F (1980) Carbon-13 hyperfine interaction in the hexafluorobenzene radical anion. *Chem Phys Lett* 71:471–475
143. Anisimov OA, Grigoryants VM, Molin YN (1980) Optical detection of the ESR spectrum of hexafluorobenzene anion radicals in squalane at room temperature. *Chem Phys Lett* 74:15–18
144. Shchegoleva LN, Bilkis II, Schastnev PV (1983) Geometrical and electronic structure of fluoro-substituted benzene radical anions based on quantum chemical analysis of hyperfine interactions. *Chem Phys* 82:343–353
145. Hou XJ, Huang MB (2003) Structure of the hexafluorobenzene anion. *J Mol Struct (Theochem)* 638:209–214
146. Barlukova MM, Beregovaya IV, Vysotsky VP, Shchegoleva LN, Bagryansky VA, Molin YN (2005) Intramolecular dynamics of 1,2,3-trifluorobenzene radical anions as studied by OD ESR and quantum-chemical methods. *J Phys Chem A* 109:4404–4409
147. Tuttle TR Jr, Weissmn SI (1958) Electron spin resonance spectra of the anions of benzene, toluene and the xylenes. *J Am Chem Soc* 80:5342–5344
148. Lawler RG, Bolton JR, Fraenkel GK, Brown TH (1964) Orbital degeneracy and the electron spin resonance spectrum of the benzene-1-d negative ion. *J Am Chem Soc* 86:520–521
149. Lawler RG, Fraenkel (1968) Effects of deuterium substitution on the ESR spectrum of the benzene negative ion. *J Chem Phys* 49:1126–1139
150. Edlund O, Kinell PO, Lund A, Shimizu A (1967) Electron spin resonance spectra of monomeric and dimeric cations of benzene. *J Chem Phys* 46:3679–3680
151. Edlund O, Kinell PO, Lund A, Shimizu A (1968) Electron spin resonance study of energy transfer in the γ -irradiated system benzene-silica gel. In: Gould RF (ed) *Advances in chemistry series*. American Chemical Society Publications 82:311–326
152. Nagai S, Ohnishi S, Nitta I (1971) ESR study of adsorbed monomer and dimer cation radicals of benzene and its methyl derivatives. *Bull Chem Soc Jpn* 44:1230–1233
153. Raghavachari K, Haddon RC, Miller TA, Bondybey VE (1983) Theoretical study of Jahn-Teller distortions in $C_6H_6^+$ and $C_6F_6^+$. *J Chem Phys* 79:1387–1395
154. Lindner R, Müller-Dethlefs K, Wedum E, Haber K, Grant ER (1996) On the shape of $C_6H_6^+$. *Science* 271:1698–1702

155. Bowers KW (1968) Orbital degeneracy in benzene and substituent effects. In: Kaiser ET, Kevan L (eds) *Radical ions*. Interscience Publishers, New York, pp 211–244
156. Komatsu T, Lund A, Kinell PO (1972) Electron spin resonance studies on irradiated heterogeneous systems VIII: radical cation formation from toluene. *J Phys Chem* 76:1721–1726
157. Komatsu T, Lund A (1972) Electron spin resonance studies on irradiated heterogeneous systems IX: anisotropy of the g factor and the hyperfine coupling constant of the benzene cation in the adsorbed state. *J Phys Chem* 76:1727–1728
158. Tabata M, Lund A (1983) ESR of cation radicals of methyl-substituted benzenes in a trichlorotrifluoroethane matrix. *Zeitschrift fuer Naturforschung, Teil A: Physik, Physikalische Chemie. Kosmophysi* 38A:428–433
159. Iwasaki M, Toriyama K, Nunome K (1983) ESR evidence for the static distortion of ${}^2E_{1g}$ benzene cations giving ${}^2B_{2g}$ with D_{2h} symmetry in low temperature matrixes. *J Chem Soc Chem Commun* 1983:320–322
160. Huang MB, Lunell S (1990) Accurate configuration interaction calculations of the hyperfine interactions in the benzene cation. *J Chem Phys* 92:6081–6083
161. Feldman VI, Suknov FF, Orlov AY (1999) An ESR study of benzene radical cation in an argon matrix: evidence for favourable stabilization of ${}^2B_{1g}$ rather than ${}^2B_{2g}$ state. *Chem Phys Lett* 300:713–718
162. Feldman VI, Suknov FF, Orlov AY, Kadam RM, Itagaki Y, Lund A (2000) Effect of matrix and substituent on the electronic structure of trapped benzene radical cations. *Phys Chem Chem Phys* 2(1):29–35
163. Erickson R, Lund A, Lindgren M (1995) Analysis of powder EPR and ENDOR spectra of the biphenyl radical cation on H-ZSM-5 zeolite, silica gel and in $CFCl_3$. *Chem Phys* 193:89–99
164. Kadam RM, Erickson R, Komaguchi K, Shiotani M, Lund A (1998) ENDOR and EPR studies of benzene radical cations in halocarbon matrices: the Jahn-Teller distortion of the monomer and geometry of the dimer cation. *Chem Phys Lett* 290:371–378
165. Kadam RM, Itagaki Y, Benetis NP, Lund A, Erickson R, Hubar M, Hilczer W (1999) An EPR, ENDOR and ESEEM study of the benzene radical cation in $CFCl_3$ matrix: isotopic substitution effects on structure and dynamics. *Phys Chem Chem Phys* 1:4967–4973
166. Toriyama K, Okazaki M (1999) Benzene cation radical in mesoporous silicate: EPR detection of unusually stabilized Jahn-Teller distortion. *Phys Chem Chem Phys* 1:2607–2612
167. Xiao HY, Cao J, Liu YJ, Fang WH, Liu RZ, Shiotani M (2008) Hyperfine coupling constants of fluorinated benzene radical cations: a DFT B3LYP and MP2 study. *J Theo Comp Chem* 7:879–887
168. Shiotani M, Kawazoe H, Sohma J (1984) ESR studies of fluorinated pyridine radical cations. *J Phys Chem* 88:2220–2224
169. Shida T, Kato T (1979) ESR and optical studies on the cation radical of pyridine in a γ -irradiated rigid matrix at low temperatures. *Chem Phys Lett* 68:106–110
170. Erickson R, Benetis NP, Lund A, Lindgren M (1997) Radical cation of naphthalene on H-ZSM-5 zeolite and in $CFCl_3$ Matrix. A theoretical and experimental EPR, ENDOR, and ESEEM Study. *J Phys Chem* 101:2390–2396
171. Kadam RM, Itagaki Y, Erickson R, Lund A (1999) ENDOR and ESR studies of radical cations of methyl-substituted benzene in halocarbon matrixes. *J Phys Chem A* 103:1480–1486
172. Stoll S, Schweiger A (2006) EasySpin, a comprehensive software package for spectral simulation and analysis in EPR. *J Magn Reson* 178:42–55
173. Shiotani M, Nagata Y, Tasaki M, Sohma J, Shida T (1983) Electron spin resonance studies on radical cations of five-membered heteroaromatics: furan, thiophene, pyrrole, and related compounds. *J Phys Chem* 87:1170–1174
174. Shiotani M, Ohta K, Nagata Y, Sohma J (1985) Novel cycloaddition of dimethylacetylene to the dimethylacetylene radical cation: direct observation by ESR. *J Am Chem Soc* 107:2562–2564

175. Ohta K, Shiotani M, Sohma J, Hasegawa A, Symons MCR (1987) Formation of methyl-propargyl radicals from tetramethylcyclobutadiene radical cations: an ESR study. *Chem Phys Lett* 136:465–470
176. Komaguchi K, Nomura N, Shiotani M, Lund A, Jansson M, Lunell S (2006) ESR and theoretical studies of trimer radical cations of coronene. *Spectrochimica Acta A* 63:76–84
177. Edlund O, Kinell PO, Lund A, Shimizu A (1967) Electron spin resonance spectra of monomeric and dimeric cations of benzene. *J Chem Phys* 46:3679–3680
178. Itagaki Y, Lund A, Shiotani M, Hasegawa A (1999) Substitution effects on the structure of benzene radical cations. *Trends Chem Phys* 7:277–300
179. Itagaki Y, Benetis NP, Kadam RM, Lund A (2000) Structure of dimeric radical cations of benzene and toluene in halocarbon matrices: an EPR, ENDOR and MO study. *Phys Chem Chem Phys* 2:2683–2689
180. Tzong J, Williams F (1981) ESR detection of the dimethyl ether radical cation. *J Am Chem Soc* 103:6994–6996
181. Kubodera H, Shida T, Shimokoshi K (1981) ESR evidence for the cation radicals of tetrahydrofurans and dimethyl ether produced in a gamma-irradiated frozen matrix of trichlorofluoromethane. *J Phys Chem* 85:2583–2586
182. Shiotani M, Isamoto N, Hayashi M, Fångström T, Lunell S (2000) Deuterium isotope effects on rotation of methyl hydrogens: a study of the dimethyl ether radical cation by ESR spectroscopy and ab initio and density functional theory. *J Am Chem Soc* 122:12281–12288
183. Itagaki Y, Wang P, Isamoto N, Shiotani M, Hasegawa A, Jansson M, Lunell S (2002) Static and dynamic structures of halogenated dimethyl ether radical cations: an ESR and MO study. *Phys Chem Chem Phys* 4:2524–2529
184. Itagaki Y, Wang P, Shiotani M, Hasegawa A (2002) ESR spectra and structure of bis-chlorinated dimethyl ether radical cation, $\text{ClCH}_2\text{OCH}_2\text{Cl}^+$. *Phys Chem Chem Phys* 4:2530–2533
185. Brown JK, Sheppard N (1955) Infra-red spectroscopic studies of rotational isomerism in the polymethylene halides. *Proc R Soc Lond A* 231:555–574

Chapter 4

Hydrogen Molecular Ions in Solid Parahydrogen: EPR Studies at Cryogenic Temperatures

Jun Kumagai

Abstract Electron paramagnetic resonance (EPR) spectroscopy for the assignment of H_6^+ and its isotopomers, analysis of large precessional motion of them, and isotope condensation of H_6^+ in solid parahydrogen at cryogenic temperature is treated in this chapter. The structure of H_6^+ consisting of an H_2^+ -core sandwiched with two side-on H_2 s is confirmed to have D_2 symmetry by the comparison of the experimental hyperfine coupling constants (HFCC) with the theoretical ones. The substitution of one side-on H_2 with D_2 induced distortion of the spin density and nonequivalent HFCCs on the H_2^+ -core indicating that the quantum effect due to nuclear motion cannot be ignored in this system. Rotational states of side-on D_2 and H_2 are attributable to $J=0$ from the corresponding nuclear spin states of $I=0$ and 0, 2 for H_2 and D_2 , respectively. The H_6^+ ion migrates via hole hopping diffusion of H_2^+ -core in solid parahydrogen, and turns into more stable $H_4D_2^+$ or $H_2D_4^+$ ion when it meets D_2 molecules. During the diffusion, H_6^+ and $H_4D_2^+$ are in large precessional motion as indicated by an analysis of the anisotropic HFCCs.

4.1 Properties of Solid Parahydrogen

Many properties of solid hydrogen are summarized by Silvera and Kranendonk as a review [1] and a book [2], respectively, and important facts for the understanding of this chapter are extracted here from these sources. Solid parahydrogen ($p-H_2$) has various quantum effect features. Because of the small mass and the weak interactions, the rotational angular momentum J of each hydrogen molecule is still a good quantum number in the solid [3]. The largest of the orientation-dependent interactions is the electric quadrupole-quadrupole (EQQ) interaction, which is in the order of magnitude of ~ 4 K. Because the EQQ interaction is much smaller than the rotational constant of H_2 ($B=85.2$ K), the rotational states of H_2 are almost undistorted by neighbors [1].

J. Kumagai (✉)

Eco-Topia Science Institute, Nagoya University, Furo-cho, Chikusa-ku, Nagoya 464-8601, Japan
e-mail: kumagai@apchem.nagoya-u.ac.jp

© Springer International Publishing 2014

A. Lund, M. Shiotani (eds.), *Applications of EPR in Radiation Research*,
DOI 10.1007/978-3-319-09216-4_4

117

Table 4.1 Allowed combinations of I and J for H_2 and D_2 [1]

Molecule	I	J	Designation
H_2 ($I_N=1/2$)	0	even	Para
	1	odd	Ortho
D_2 ($I_N=1$)	1	odd	Ortho
	0, 2	even	Para

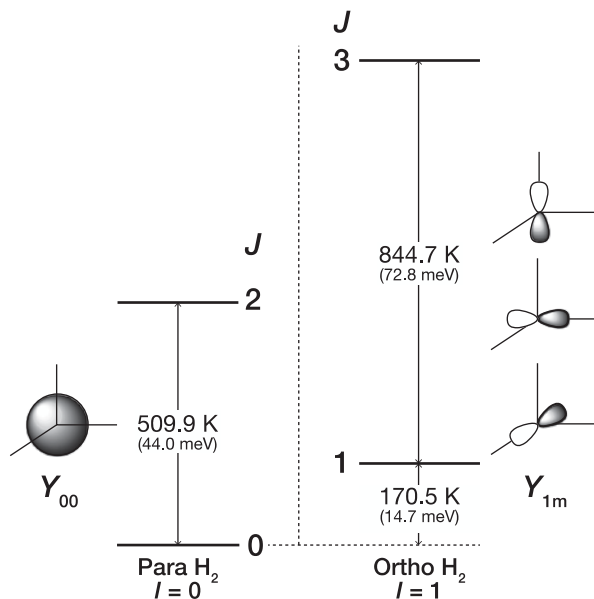
The Pauli exclusion principle requires that the rotational states having even quantum numbers couple with the $I=0$ nuclear spin states where I is the total nuclear spin number, while those having odd quantum numbers couple with $I=1$ nuclear spin state, exclusively (Table 4.1) [1]. The former is called parahydrogen (p- H_2), and the latter orthohydrogen (o- H_2). At very low temperatures, p- H_2 occupies only the $J=0$ rotational state, while o- H_2 the $J=1$ state. Relaxation from the $J=1$ to the $J=0$ rotational state is extremely slow, so that p- H_2 and o- H_2 can be treated as almost different molecules. Since the $J=0$ rotational wavefunction has a spherical shape, p- H_2 at liquid helium (LHe) temperatures have no permanent electric moments of any order. Thus, the p- H_2 crystal provides a homogeneous environment for a solute embedded in it. On the other hand, o- H_2 occupying the $J=1$ rotational quantum number have a small permanent electric quadrupole moment. The quadrupole moment of the o- H_2 in $J=1$ state provides slightly stronger interaction with its surroundings than the p- H_2 in $J=0$ state. The concentration of o- H_2 , therefore, needs to be as low as possible in order that solute molecules may have least electric and magnetic perturbation in solid hydrogen matrices. Since the o- H_2 in $J=1$ state has 170.5 K higher energy than the p- H_2 in $J=0$ state (Fig. 4.1), the concentration of o- H_2 can be reduced to less than 0.05% by immersing FeO(OH) into liquid H_2 at just above the melting point of 13.8 K.

Another important feature is the large amplitude of zero-point vibration. The root-mean-square width of the single particle distribution function is about 18% of the nearest neighbor distance (3.793 Å; *cf.* Table 4.2). This large zero-point motion is a result of the weak isotropic intermolecular potential and the light mass. As a result, the intermolecular distance in solid p- H_2 is considerably larger than the interatomic distance in solid Ne, although the Lennard-Jones type of pair potentials between H_2 molecules is similar to the potential between Ne atoms [1, 4].

The crystal structure of solid p- H_2 was firstly determined by Keesom et al. in 1930 [5, 6]. Their seven X-ray reflections could be fit to the hexagonal closest packed lattice. It is known that the crystal structures of Ne and Ar matrices consist both of hexagonal-close-packed (*hcp*) and face-centered-cubic (*fcc*) structures as listed in Table 4.2. The mixtures of different crystal structures in Ne and Ar matrices cause additional complexity and broadening in their optical spectra that makes the spectral analysis impossible in some cases. On the other hand, the crystal structure of solid p- H_2 is a pure *hcp*, which has provided highly resolved spectra of IR, EPR, and other types of spectroscopy [4, 7–36].

Solid p- H_2 is one of the most feasible and ideal media for the study of matrix isolation spectroscopy. Thanks to the quantum nature, solid p- H_2 has a self-annealing

Fig. 4.1 The molecular rotational energy levels for an isolated H_2 molecule [1]. The same diagram applies to D_2 but scaled down by about a factor of 2 due to the larger moment of inertia. The angular distribution of the two lowest rotational states is also indicated (Y_{10} and $Y_{11} \pm Y_{1-1}$ are actually shown). I is the total nuclear spin composed of the nuclear spins of two protons with $I_N = 1/2$ aligned in antiparallel ($I=0$) or in parallel ($I=1$). The figure is adapted from [1] by permission of American Physical Society (1980)



character, in which defects and imperfections of the solid p- H_2 crystal produced during both the crystal growth and the harsh irradiation are eliminated [9, 21, 22, 34, 37]. Unlike in other molecular crystals, spectroscopic data measured in solid p- H_2 are highly reproducible and independent on scheme of sample preparation. Secondly, the EPR lines of solute molecules becomes highly resolved due to the narrow spectral linewidth [9, 21, 22, 25]. Third, solute molecules are almost free from the cage effect because of the softness of p- H_2 as a quantum crystal. A variety of chemical reactions can take place in solid p- H_2 at LHe temperature by light or ionizing radiation [19, 30, 33, 35, 36, 38–40]. Availing these unique properties, solid p- H_2 matrix has been applied to the spectroscopic studies for physical and chemical processes of solute molecules.

Table 4.2 Physical properties of molecular crystals [1, 4]

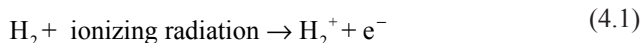
Properties	p- H_2	Ne	Ar
Triple point (K)	13.80	24.56	83.81
Boiling point ^a (K)	20.28	27.07	87.29
Lattice constant (Å)	3.793	3.16	3.76
Crystal structure	<i>hcp</i>	<i>fcc/hcp</i>	<i>fcc/hcp</i>
Lennard-Jones parameter ϵ^b (K)	37	35.6	119.3
σ^b (Å)	2.92	2.74	3.45

^a At a pressure of 0.1 MPa

^b The Lennard-Jones potential is defined as $V(r) = 4\epsilon[(\sigma/r)^{12} - (\sigma/r)^6]$

4.2 H_2^+ and H_3^+ Molecular Ions

The initial products by ionizing radiation in gas or condensed hydrogen are simply H_2^+ and electrons by ionization of H_2 as in Eq. (4.1) [41]. When the ejected electrons return to the parent H_2^+ ions in geminate recombination, part of them recombine to H_2 in their ground state while another part become electronically excited states which decompose by neutral elimination to produce H atoms as in Eq. (4.2). If H_2^+ reacts with another H_2 before the recombination with electrons, H_2^+ may convert to H_3^+ by ion-neutral molecule reaction as shown in reaction (4.3) [42].



H_3^+ was discovered in 1911 by J. J. Thomson by the method of mass spectrometry in discharged gaseous H_2 [43]. There had been no spectroscopic observation of H_3^+ for 69 years until Oka found the spectrum of vibration-rotation band of H_3^+ in the laboratory in 1980 [44]. This breakthrough led to the discovery of the infrared spectrum of interstellar H_3^+ after 16 years of searching since laboratory detection [45]. H_3^+ is highly reactive donating a proton to almost every atom and molecule it encounters to produce many chemicals in interstellar space. It is also a good astrophysical probe in cold and warm clouds as thermometer and densitometer. Recent details of interstellar H_3^+ are summarized in the review written by Oka [46].

H_2^+ might be present in condensed phase of H_2 exposed to ionizing radiation in very short time but has never been detected by any spectroscopic measurements even at cryogenic temperature. It is probably because the reaction (4.3) is really dominant in solid hydrogen although many trials of measurements of H_3^+ have not been succeeded [37, 47–56]. Very recently EPR spectra of H_2^+ , HD^+ , D_2^+ in ground vibrational state have been firstly measured by Correnti et al. in X-ray irradiated Ne matrices at 2 K [57]. They also found that H_2^+ turned into H_4^+ , which, according to *ab initio* calculation, is expected to be a complex of H_3^+ and H atom when the temperature is increased from 2 to 4 K.

4.3 H_6^+ Molecular Ions

The H_6^+ ion was firstly observed in H_2 gas phase with electron beam irradiation using mass spectroscopy by Kirchner and Bowers [58]. Although odd-membered hydrogen ions are mainly observed from H_2 gas irradiated by electron beam, the yield of H_6^+ ions was the largest by far among even-membered hydrogen ions

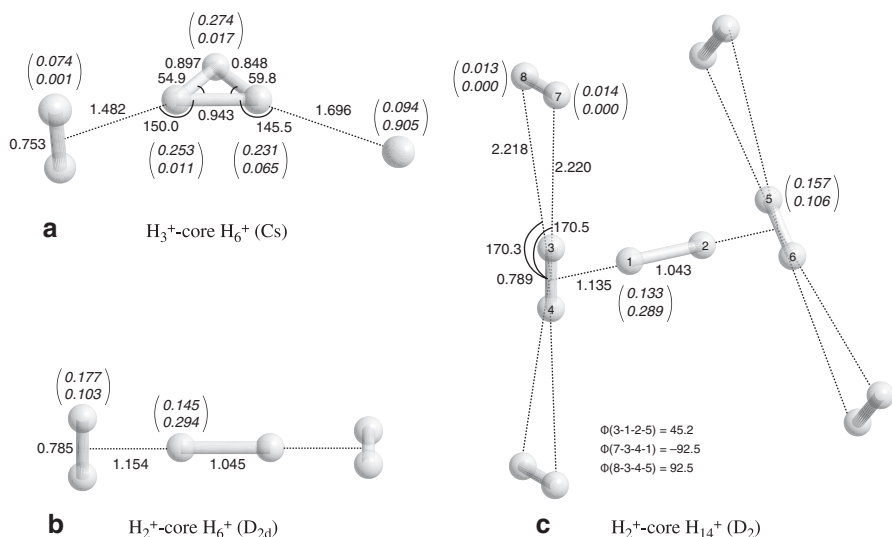


Fig. 4.2 Optimized geometries of **a** H_3^+ -core H_6^+ , **b** H_2^+ -core H_6^+ , and **c** H_2^+ -core H_{14}^+ at MP2/cc-pVTZ level. Bond lengths in Å and angles in degrees. In parentheses are shown atomic net charge and spin density in the upper and lower lines, respectively. The figure is adapted from [62] by permission of American Institute of Physics (1998)

($H_6^+ \gg H_8^+ > H_{10}^+ > H_4^+$). Fiegele et al. have reproduced the results by using deuterium ions [59]. Although the mass and charge of H_6^+ were clear from the mass spectroscopy, chemical structural information has been unknown due to the lack of spectroscopic measurement. Kirchner and Bowers expected that H_6^+ was a cluster composed of H_3^+ , H, and H_2 because H_3^+ was the major radiolysis product of H_2 gas. In the same year, Montgomery and Michels proposed that H_6^+ has two isomers, a H_3^+ -core type with C_s symmetry and a H_2^+ -core type with D_{2d} symmetry (cf. Fig. 4.2), and that the H_2^+ -core isomer is about 0.1 eV lower in energy than the H_3^+ [60]. This prediction is surprising because it has been widely accepted that all H_n^+ cluster geometries are composed of a H_3^+ -core and surrounding H_2 molecules weakly bound to it.

In 1998, Kurosaki and Takayanagi did an extensive theoretical treatment of the H_2^+ -core H_6^+ ion [61, 62]. They found a reaction path connecting the two H_6^+ isomers. They also pointed out that “six” is the magic number for even-membered H_n^+ . Their calculations predict that the central H_6^+ is almost unperturbed in all even-membered H_n^+ ($n \geq 6$), and outer H_2 's are very weakly bound to its corners.

As shown in Fig. 4.2c, the structure of central H_6^+ in H_{14}^+ is found to be almost the same as that in Fig. 4.2b, and charge and spin densities on outer four H_2 's are negligible. The total binding energy of the four H_2 's to H_6^+ in H_{14}^+ is only 0.05 eV, which is negligible compared to the exothermic $H_2^+ + 2H_2 \rightarrow H_6^+$ reaction of 2.12 eV. It means that, when H_6^+ is generated in solid H_2 , the positive charge remains localized on unperturbed H_6^+ . Although theoretical approaches on H_2^+ -core H_6^+ ions have been accumulated for over a decade from 1987, no experimental results, which

support the chemical structure of H_2^+ -core H_6^+ ions, has appeared until we have published EPR spectroscopic results on $\text{H}_{6-n}\text{D}_n^+$ ions in γ -ray irradiated solid p- H_2 - D_2 or HD mixtures in 2007 [28].

4.3.1 Experimental Assignment of H_6^+ and Its Isotopomers in γ -Ray Irradiated Solid p- H_2 by EPR Spectroscopy

Experimental procedures for detecting H_6^+ and its isotopomers are as follows. p- H_2 samples were obtained and purified by immersing iron hydroxide $\text{FeO}(\text{OH})$ into liquid normal H_2 (>99.99999%; Taiyo Nippon Sanso Co.) for 10 h at 14 K in a cryocooler (Daikin UV204SCL). o- D_2 specimens were obtained from normal D_2 (n- D_2) (99.999%; 99.96 atom % D; Isotec Inc.) in a similar manner at 18 K. All hydrogen gases, p- H_2 , o- D_2 , and HD (99.6%; 96 atom % D; Isotec Inc.) were purified through seven condensation/vaporization cycles at condensation and vaporization temperatures of 10 and 25 K, respectively. The gases were recovered at 25 K. Five p- H_2 samples, namely, p- H_2 , p- H_2 -o- D_2 (1 and 8 mol%), and p- H_2 -HD (1 and 8 mol%) were prepared using different isotopic hydrogen molecule contents. All samples contained 0.1 mol% of He gas (99.9999%; Taiyo Nippon Sanso Co.) for thermal contact. The samples were sealed in quartz cells and immersed in a quartz Dewar filled with LHe to prepare the solids. Solid samples were irradiated with γ -rays for *ca.* 1 h to a total dose of 2.88 kGy at the ^{60}Co γ -ray irradiation facility (Nagoya University). The irradiated samples were placed in an X-band EPR spectrometer (JEOL JES-RE1X) to measure the time course of EPR lines at 4.2 K. Microwave frequency and magnetic field of the spectrometer were monitored using a microwave frequency counter (Hewlett-Packard, 53150A) and an NMR field meter (Echo Electronics Co. Ltd., EFM-2000AX), respectively. Microwave powers of 1.0 mW and 0.1–1 nW were used to measure the H_6^+ and e_t^- lines, respectively.

Figure 4.3a shows the EPR spectrum of γ -ray irradiated solid p- H_2 . The lines named B1–B4 are the quartet lines assigned to be H_2^+ -core H_6^+ . Yield of the ion of the B1–B4 series of lines is $\sim 10^{-4}$ ppm, which is 10^4 times smaller than that of H atoms. Figure 4.3c is the spectrum obtained by subtracting (b) from (a), such that only B1–B4 are present in the difference spectrum. All EPR spectra from solid p- H_2 -o- D_2 and p- H_2 -HD mixtures shown in this subsection are the difference spectra after subtraction of the background. The B1–B4 series of lines are composed of sharp doublet lines, B1 and B2, separated by 1.25 mT near $g \approx 2.002$, and broad B3 and B4 lines with uniaxial asymmetry whose resonance magnetic fields are lower and higher than the center of B1 and B2 by 20.4 mT, respectively. Precise EPR parameters of B1–B4 lines are determined as $g = 2.00212$, nuclear spin quantum numbers $I = 0$ and 1, and isotropic hyperfine coupling constant $A_{\text{iso}} = 20.441$ mT [32]. B1, B3, and B4 are the lines corresponding to the total nuclear magnetic spin $I = 1$ with projections $I_z = 0, 1,$ and -1 , respectively, and B2 corresponds to $I = I_z = 0$. The splitting between B1 and B2 is due to the second-order hyperfine term A^2/H_0 [63]. As shown in a stick diagram in Fig. 4.3, resonance magnetic fields of B1–B4 lines coincide with

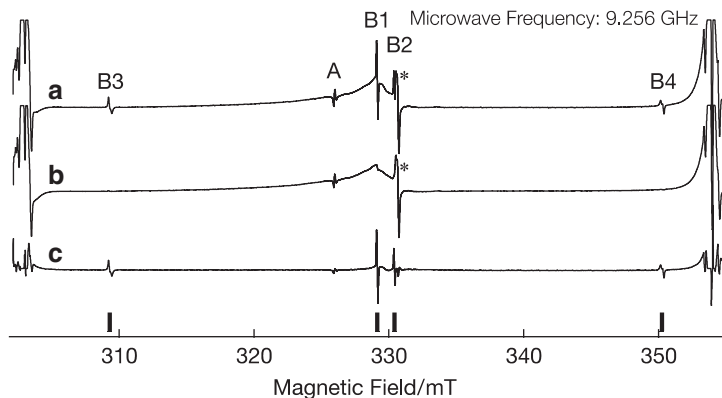


Fig. 4.3 **a** EPR spectra of γ -ray irradiated solid p-H₂ measured at 4.2 K. **b** Same as **(a)** but 5 min illumination of the sample with an infrared lamp. **c** Difference spectrum generated by subtracting **(b)** from **(a)**. Stick diagram shows line positions obtained by Eq. 2.7 with $g=2.0020$, $I_{12}=1$ and 0, and $A_{\text{cr}}=20.44$ mT. Note that B1–B4 lines in spectrum are broadened due to over-modulation and that intensity of B2 is saturated due to the high microwave power. Intense doublet lines at the magnetic fields $H_0=304$ and 355 mT belong to hydrogen atoms. The lines at 332 mT marked by “*” are due to radicals produced in the irradiated quartz sample cells and Dewar. The singlet line at 327 mT named A line results from a forbidden transition of H atoms. The figure is adapted from [28] by permission of American Institute of Physics (2007)

those calculated by these EPR parameters. Microwave power-saturation behavior among $I=1$ species B1, B3, and B4 were almost the same, whereas $I=0$ species B2 saturates at lower microwave power probably due to the absence of relaxation paths via hyperfine interaction. Although B3 and B4 lines are much broader and then look weaker than B1 and B2, integrated intensities among B1–B4 lines are the same within experimental accuracy [28, 32]. These results indicate that the quartet lines are a set of lines assigned to one chemical species.

Figure 4.4 shows an EPR spectrum of irradiated solid p-H₂-o-D₂ (1 mol%). Except for the B1–B4 lines, three series of lines named C1–C16 were also observed at around 310 mT (C1–C5), 330 mT (C6–C12), and 350 mT (C13–C16). At lower magnetic field, the quintet lines C1–C5 are equally separated by 1.44 mT with an intensity ratio of roughly 1:1:2:1:1. The center C3 line is very close to the position of the B3 one. At higher magnetic field, only four lines, C13–C16, equally separated by 1.44 mT are detected. Since the ratio in intensity is 1:1:2:1 and C15 is very close to B4, C13–C16 are expected to be parts of a quintet of lines. The fifth line could not be measured due to overlapping with an intense line of the H atom spectrum. Figure 4.5a shows the enlarged portion of the same spectrum at around 330 mT. All of the C8, C9, and C10 lines appear as doublets and are more intense than C6, C7, C11, and C12, suggesting that each of C8–C10 is composed of two superimposed lines. Although it is less clear due to the overlap in C8–C10, an asymmetry of EPR line shape is observed in C6, C7, C10, and C11: the lower (upper) peak is higher than the upper (lower) one in C6 and C7 (C10 and C11) by ~50%. Since the asymmetry is

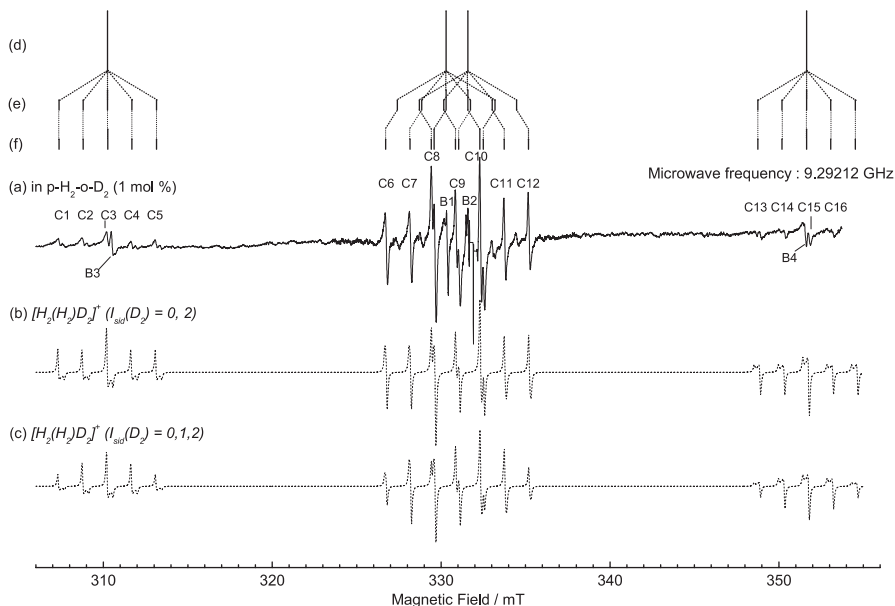


Fig. 4.4 **a** An EPR spectrum of γ -ray irradiated solid $p\text{-H}_2$ (1 mol%) at 4.2 K. **b** A simulated spectrum of $[\text{H}_2(\text{H}_2)\text{D}_2]^+$ with $I_{\text{sid}}(\text{D}_2)=0$ and 2 and Lorentzian full linewidth of $\Delta H_{\text{FWHM}}=0.12$ mT. **c** A simulated spectrum of $[\text{H}_2(\text{H}_2)\text{D}_2]^+$ with $I_{\text{sid}}(\text{D}_2)=0, 1$, and 2. Stick diagram shows line positions of $[\text{H}_2(\text{H}_2)\text{D}_2]^+$. The spectrum below 305 mT and above 353 mT could not be measured because of the overlapping with very intense signal of H atoms. The figure is adapted from [28] by permission of American Institute of Physics (2007)

bilateral against the field at $g=2.0020$ ($H_0 \approx 332$ mT), it should be due to the asymmetry in hyperfine coupling constants. A set of lines that becomes pronounced in Fig. 4.5c is marked as D1–D8. Although some of them such as D1, D2, D5, and D6 are also observed in (a), the ratio in intensity of D to C lines in (c) is much higher than that in (a). No line is detected below 324 and above 340 mT in solid $p\text{-H}_2\text{-o-D}_2$ (8 mol%) except for very small C lines and intense H atom lines (not shown).

Figure 4.6a compares the decay behaviors of B1, B2, and C6–C12 lines in solid $p\text{-H}_2\text{-D}_2$ (1 mol%), whereas B3, B4, C1–C5, and C13–C16 are too weak to measure the decay. C6–C12 lines decay in a similar manner but slower than B1 and B2 lines. This result indicates that the C lines are a set of lines assigned to a single chemical species different from that of the B lines. In Fig. 4.6b the decay of C and D lines in solid $p\text{-H}_2\text{-D}_2$ (8 mol%) is compared. D lines decay slower than C. These results indicate that C and D series of lines belong to two distinct species.

Figure 4.7 shows an EPR spectrum of irradiated solid $p\text{-H}_2\text{-HD}$ (1 mol%). Except for the B lines, about 30 sharp lines named E and F were observed, whereas C and D lines were negligible. Figures 4.8a and c compare spectra in irradiated solid $p\text{-H}_2\text{-HD}$ (1 and 8 mol%). The ratio in intensity of F to E lines in $p\text{-H}_2\text{-HD}$ (8 mol%) is larger than that in $p\text{-H}_2\text{-HD}$ (1 mol%).

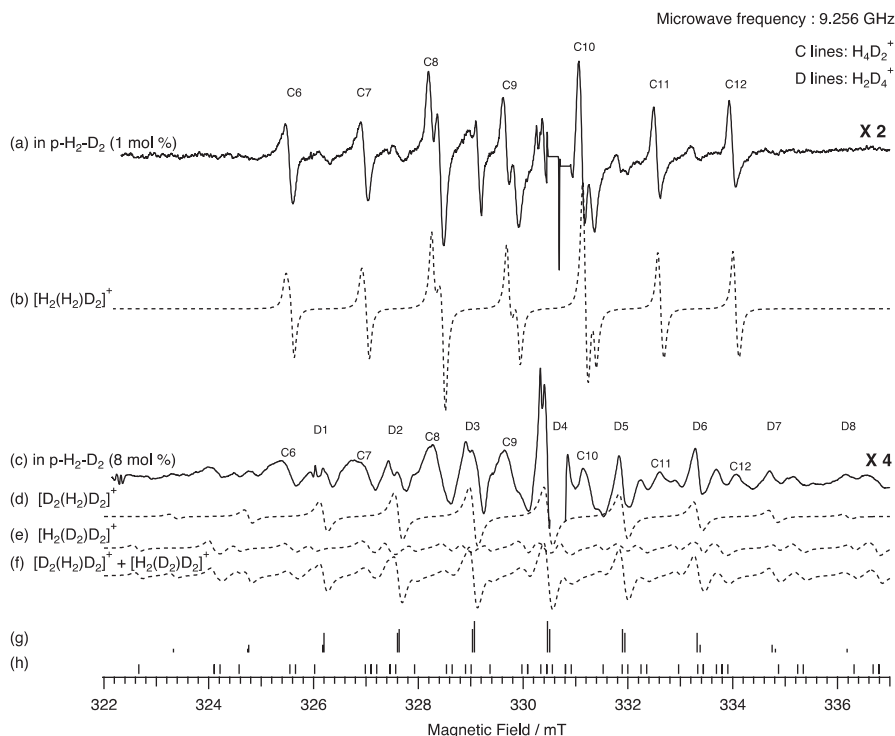


Fig. 4.5 **a** An EPR spectrum of γ -ray irradiated solid p-H₂-o-D₂ (1 mol%) at 4.2 K. **b** A simulated spectrum of H₂⁺-core H₄D₂⁺ with $\Delta H_{\text{FWHM}}=0.12$ mT. **c** An EPR spectrum of irradiated p-H₂-o-H₂ (8 mol%) at 4.2 K. **d** A simulated spectrum of H₂⁺-core H₂D₄⁺ for $[I_{\text{ctr}}(\text{H}_2), I_{\text{ctrz}}(\text{H}_2)]=[0, 1]$ and $[0, 0]$ with $\Delta H_{\text{FWHM}}=0.24$ mT. Stick diagram shows line positions of H₂⁺-core H₂D₄⁺ for $[I_{\text{ctr}}(\text{H}_2), I_{\text{ctrz}}(\text{H}_2)]=[0, 1]$ and $[0, 0]$

4.3.2 Assignment of H₆⁺, H₅D⁺, H₄D₂⁺ and H₂D₄⁺

4.3.2.1 B Lines Belonging to H₆⁺

For the purpose of understanding EPR parameters of H₆⁺ and its isotopomers, the optimized geometry of H₆⁺ is given in Fig. 4.9.

The spin Hamiltonian for H₆⁺ is given by

$$\hat{H} = g\mu_B S H_0 + \sum_i (-g_{ni}\mu_N I_i H_0 + g\mu_B A_i I_i H_0) \quad (4.4)$$

where μ_B and μ_N are the Bohr and nuclear magnetons, $S=1/2$ is the electron spin quantum number, H_0/z is the magnetic field, g_{ni} , I_i , and A_i are the g value, the spin quantum number, and the hyperfine coupling constant of the i th nucleus of H₆⁺ in Fig. 4.9, respectively. Because of $A_i < H_0$ in our experimental condition, the

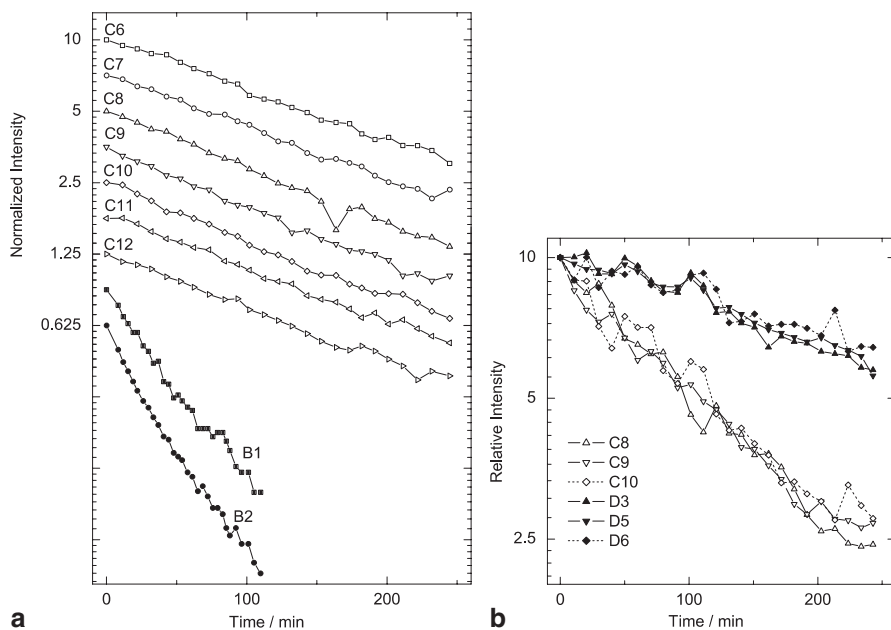


Fig. 4.6 **a** Time course of intensity of B and C lines in γ -ray irradiated solid $p\text{-H}_2\text{-o-D}_2$ (1 mol %) at 4.2 K. Intensities of all lines are normalized at $t=0$. The vertical scale is the same for all signals but offset to facilitate comparison of the decay; **b** Time course of intensity of C and D lines in γ -ray irradiated solid $p\text{-H}_2\text{-o-D}_2$ (8 mol %) at 4.2 K. The figure is adapted from [28] by permission of American Institute of Physics (2007)

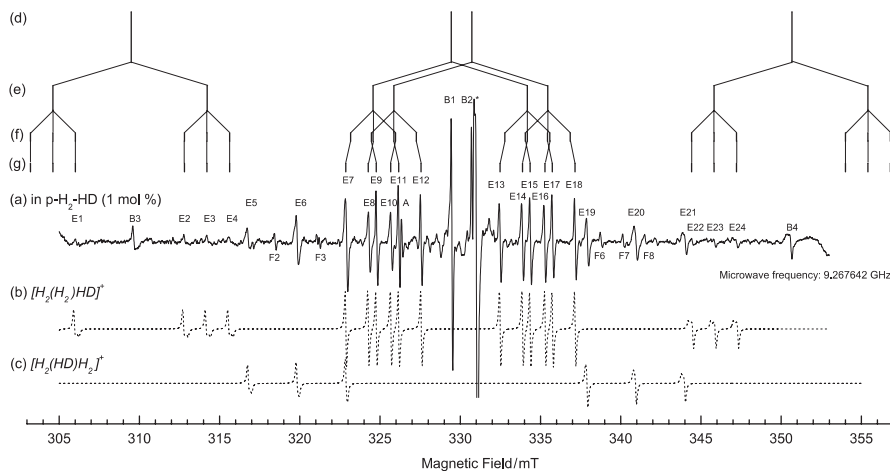


Fig. 4.7 **a** An EPR spectrum of γ -ray irradiated solid $p\text{-H}_2\text{-HD}$ (1 mol %) at 4.2 K. **b** A simulated spectrum of H_2^+ -core H_3D^+ and HD^+ -core H_3D^+ with $\Delta H_{\text{FWHM}} = 0.15$ mT. **c** An EPR spectrum of irradiated $p\text{-H}_2\text{-HD}$ (8 mol %) at 4.2 K. **(d)** A simulated spectrum of H_2^+ -core H_4D^+ (HD-sub.) for $[I_{\text{ctr}}(\text{H}_2), I_{\text{ctr}}(\text{H}_2)] = [0, 1]$ and $[0, 0]$ and $\Delta H_{\text{FWHM}} = 0.15$ mT. Microwave frequency in (c) is normalized to 9.267642 GHz. Stick diagram shows line positions of H_2^+ -core H_4D^+ (HD-sub.) for $[I_{\text{ctr}}(\text{H}_2), I_{\text{ctr}}(\text{H}_2)] = [0, 1]$ and $[0, 0]$. The figure is adapted from [28] by permission of American Institute of Physics (2007)

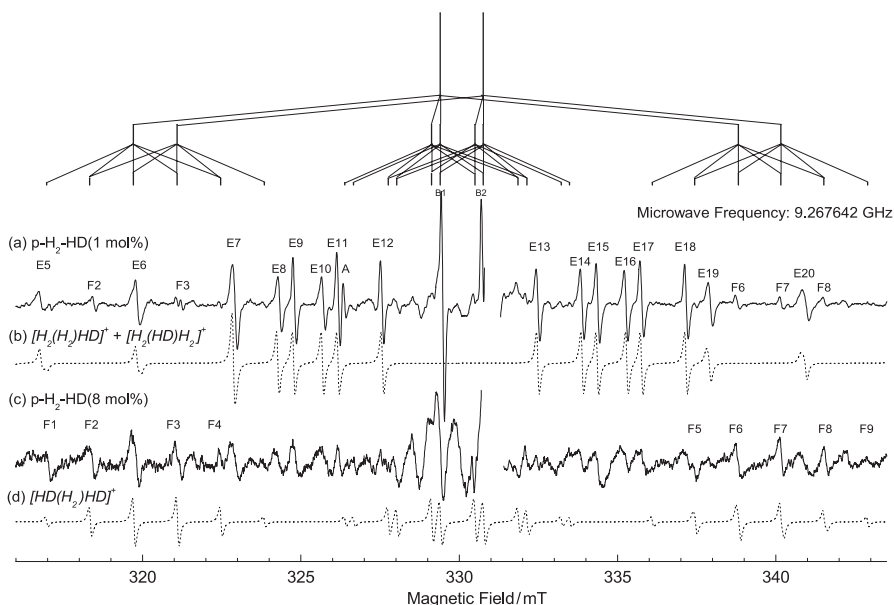


Fig. 4.8 **a** An EPR spectrum of γ -ray irradiated solid $p\text{-H}_2\text{-HD}$ (1 mol%) at 4.2 K. **b** A simulated spectrum of H_2^+ -core H_2D^+ and HD^+ -core H_2D^+ with $\Delta H_{\text{FWHM}} = 0.15$ mT. **c** An EPR spectrum of irradiated $p\text{-H}_2\text{-HD}$ (8 mol%) at 4.2 K. **d** A simulated spectrum of H_2^+ -core H_4D^+ (HD-sub.) for $[I_{\text{ctr}}(\text{H}_2), I_{\text{ctrz}}(\text{H}_2)] = [0, 1]$ and $[0, 0]$ and $\Delta H_{\text{FWHM}} = 0.15$ mT. Microwave frequency in (c) is normalized to 9.267642 GHz. Stick diagram shows line positions of H_2^+ -core H_4D^+ (HD-sub.) for $[I_{\text{ctr}}(\text{H}_2), I_{\text{ctrz}}(\text{H}_2)] = [0, 1]$ and $[0, 0]$. The figure is adapted from [28] by permission of American Institute of Physics (2007)

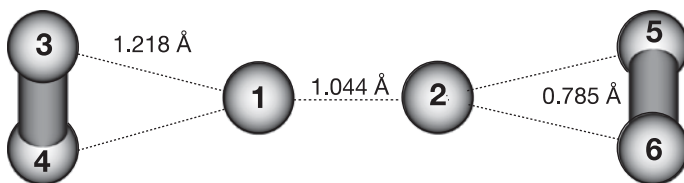


Fig. 4.9 Optimized structure of H_6^+ calculated by MP2/cc-pVQZ basis set. H_6^+ is composed of H_2^+ -core numbered as 1 and 2 and two side-on H_2 s

hyperfine terms can be referred to as a perturbation of the Zeeman term. Because of D_{2d} symmetry with $A_{\text{ctr}}(\text{H}) = A_1 = A_2$ and $A_{\text{sid}}(\text{H}) = A_3 = A_4 = A_5 = A_6$, $I_{12} = I_1 + I_2$ and $I_{34} + I_{56} = I_3 + I_4 + I_5 + I_6$ should be good quantum numbers for H_6^+ . Allowed EPR conditions are given as

$$\frac{h\nu}{g\mu_B} = H_0 + A_{\text{ctr}}(\text{H})I_{12z} + \frac{A_{\text{ctr}}(\text{H})^2 \{I_{12}(I_{12} + 1) - I_{12z}^2\}}{2H_0} + A_{\text{sid}}(\text{H})(I_{34z} + I_{56z}) + \frac{A_{\text{sid}}(\text{H})^2 \{(I_{34} + I_{56})(I_{34} + I_{56} + 1) - (I_{34z} + I_{56z})^2\}}{2H_0} \quad (4.5)$$

Table 4.3 Comparison of experimental and theoretical values of g -factor and HFCC (A) of H_6^+

	g -value	$A_{\text{ctr}}/\text{mT}^b$		$A_{\text{sid}}/\text{mT}^c$	
		Iso.	Ani.	Iso.	Ani.
Exp.	2.002120	20.441	-0.061	N.D.	N. D.
Calc. ^a	2.002238	20.231 (3.106) ^d	1.25	9.007 (1.383) ^d	0.46

^a MP2/cc-pVQZ^b A_{ctr} : HFCC for center H_2^+ -core numbered as 1 and 2 in Fig. 4.9^c A_{sid} : HFCC for side-on H_2 s numbered as 3, 4, 5 and 6 in Fig. 4.9^d HFCC values in parentheses are for D atoms multiplied by $\gamma_p/\gamma_d=6.514$

where h is the Planck constant and ν is the microwave frequency [28]. Theoretical calculation summarized in Table 4.3 predicted $A_{\text{ctr}}(\text{iso.})=20.2$ mT for the H_2^+ -core and $A_{\text{sid}}(\text{iso.})=9$ mT for side-on H_2 . Observation of 36 EPR lines can be expected from Eq. (4.5), but as shown in Fig. 4.3 only four lines have been detected experimentally. This can be interpreted assuming that the nuclear spins of side-on H_2 s, I_{34} and I_{56} , are both zero. The resonance condition can then be written as

$$\frac{h\nu}{g\mu_B} = H_0 + A_{\text{ctr}}(\text{H})I_{12z} + \frac{A_{\text{ctr}}(\text{H})^2 \{I_{12}(I_{12}+1) - I_{12z}^2\}}{2H_0} \quad (4.6)$$

showing hyperfine structure of the H_2^+ -core only. The positions of the experimental lines of B1–B4 are reproduced with $I_{12}=0$ for B2 and $I_{12}=1$ with $I_{12z}=0, -1$ and 1 for B1, B3, B4 lines, respectively, with the parameters of $g=2.002120$ and $A_{\text{ctr}}(\text{iso.})=20.441$ mT. The experimental $A_{\text{ctr}}(\text{iso.})$ is almost the same as the calculated one although there is a large difference in the value (and sign) of $A_{\text{ctr}}(\text{ani.})$ between experiment and the calculation. The difference in $A_{\text{ctr}}(\text{ani.})$ will be discussed in Sect. 4.3.3 by considering a large processional motion of H_6^+ in solid p- H_2 . It should be noted that the experimental g -value of 2.002,120 is smaller than that of the free electron (2.002,319), which is probably due to the effect of spin-Zeeman relativistic mass correction term [32, 64]. It is also consistent with the results of theoretical calculations (2.002,238).

Double integrated values of B1–B4 lines are almost equal. It means that the para/ortho ratio for the H_2^+ -core of H_6^+ is 1/3 although the concentration of o- H_2 in the p- H_2 sample is below 0.2%. We speculate that the para-ortho conversion could proceed by the effects of the unpaired electron of H_6^+ so that the para/ortho ratio of the H_2^+ -core obeys the Boltzmann distribution as shown in Eq. (4.7), where J and B are the rotational quantum number and the rotational constant, respectively. The rotational constant of H_6^+ around an axis perpendicular to the main axis was calculated at the MP2/cc-pVQZ level to be 1.97 K, which is lower than the experimental temperature of 4.2 K. By using Eq. (4.7) with the constant B equal to 1.97 K, a para/ortho ratio of the H_2^+ -core is calculated as 1/2.8 at 4.2 K. It is almost equal to the experimental ratio of 1/3. However, suspicion that the species is not H_6^+ but another radical is still remaining due to the lacking hyperfine structure of the side-on H_2 s. This suspicion will be resolved by the effect of the addition of D_2 molecules to p- H_2 explained in the next section.

$$\frac{para}{ortho} = \frac{\sum_{even} (2J+1) \exp\{-BJ(J+1)/T\}}{\sum_{odd} 3(2J+1) \exp\{-BJ(J+1)/T\}} \quad (4.7)$$

4.3.2.2 C Lines Belonging to $H_4D_2^+$

The C lines shown in Figs. 4.4 and 4.5 were observed from a γ -ray irradiated solid p- H_2 - D_2 mixture. As shown in Table 4.1 the Pauli exclusion principle requires that the rotational states of D_2 having even quantum numbers couple with the $I=0$ and 2 nuclear spin states (ortho- D_2), while those having odd quantum numbers interact with $I=1$ nuclear spin state (para- D_2), exclusively. Although H_2 lacks nuclear spin when it is in the para state, D_2 has a nuclear spin both in the para and ortho states. When the protons of H_6^+ at positions 5 and 6 in Fig. 4.9 are replaced by deuterons to obtain $[H_2(H_2)D_2]^+$, it is expected that side-on D_2 should show hyperfine structures.

The simulation with equivalent nuclei of the center H_2^+ -core having $I=0$ and 1 as assumed for H_6^+ reproduced the C1–C5 and C13–C16 lines but did not account for the C6–C12 lines. This conflict arose from the assumption that the H_2^+ -core is in $I=0$ and 1 states. The mismatch for the C6–C12 is due to the lowering of D_{2d} symmetry of the electronic wave function, so that $\Delta A(H)=[A_1(H)-A_2(H)]/2 \neq 0$. In this case, the resonance condition [28] is expressed by

$$\frac{h\nu}{g\mu_B} = H_0 + A_{ctr}(H)(I_{1z} + I_{2z}) + \frac{A_{ctr}(H)^2}{2H_0} + (I_{1z} - I_{2z}) \sqrt{\Delta A(H)^2 + \left(\frac{A_{ctr}(H)^2}{2H_0}\right)^2} + A_{sid}(D)I_{56z}. \quad (4.8)$$

The stick diagram in Fig. 4.4f shows resonance fields obtained by Eq. (4.8) with $g=2.0020$. By using Eq. (4.8) the two simulated spectra plotted in Fig. 4.4b and c were obtained. A single g value and three HFCCs, with $g=2.0020$; $A_1(H)=A_{ctr}(H)+\Delta A(H)=21.83$ mT; $A_2(H)=A_{ctr}(H)-\Delta A(H)=19.43$ mT, and $A_{sid}(D)=A_{56}(D)=1.44$ mT, reproduce the positions of all sixteen C lines within an error of 0.03 mT as shown in Fig. 4.4f. Not only $A_{ctr}(H)$ itself but also the quantity $A_{sid}(D)=\gamma_d/\gamma_p \times A_{sid}(H)$, with γ_p and γ_d equal to the magnetomechanical ratios for the proton and deuteron, is very close to that calculated for H_6^+ (cf. Table 4.3). The second-order perturbation term for $A_{sid}(D)$ ($\approx A_{sid}(D)^2/H_0$) is neglected in Eq. (4.8) because its magnitude (≈ 0.01 mT) is much smaller than the EPR linewidth of C-lines (≈ 0.1 mT).

The nonequivalence of the HFCCs with $A_1(H) > A_2(H)$ indicates that this is a typical system in which quantum effects due to nuclear motion cannot be ignored. In order to predict the nonequivalent HFCCs, solving the Schrödinger equation without the Born-Oppenheimer approximation is required [65, 66]. The dotted lines in Figs. 4.4b and 4.5b show spectra of $[H_2(H_2)D_2]^+$ fitted to the C lines using a Lorentzian line shape function with full width at half maximum $\Delta H_{FWHM}=0.12$ mT, and

uniaxial anisotropy $A_1^{\text{ani}} = -0.08$ mT and $A_2^{\text{ani}} = -0.16$ mT. Not only line positions but also the line shapes of C lines are reproduced. That allows the unique assignment of the C lines to $[\text{H}_2(\text{H}_2)\text{D}_2]^+$.

The appearance of hyperfine structure by $A_{\text{sid}}(\text{D})$ provides strong evidence that the side-on H_2 s should exist, but still no hyperfine structure appeared from a side-on H_2 in $[\text{H}_2(\text{H}_2)\text{D}_2]^+$. The solution of this inconsistency came from the ratio of line intensities of C1–C5 as 1:1:2:1:1 shown in Fig. 4.10. This ratio of quintet lines is due to the two nuclear magnetic states of a side-on D_2 with $I_{\text{sid}}(\text{D}_2) = 0$ and 2; the B3 line of H_6^+ splits into a quintet of lines at $I_{\text{sidz}} = 2, 1, 0, -1,$ and -2 with an intensity ratio of 1:1:2:1:1. The doubled intensity at the center is due to the overlap of lines of $[I_{\text{sid}}(\text{D}_2), I_{\text{sidz}}(\text{D}_2)] = [0, 2]$ and $[0, 0]$ states. The $I_{\text{sid}}(\text{D}_2) = 0$ and 2 states directly prove that the side-on D_2 in $[\text{H}_2(\text{H}_2)\text{D}_2]^+$ is in $J=0$ rotational states at 4.2 K due to free rotation along the H–H bond axis of the H_2^+ -core. It can be concluded that the rotational states of the side-on H_2 in $[\text{H}_2(\text{H}_2)\text{H}_2]^+$ and $[\text{H}_2(\text{H}_2)\text{D}_2]^+$ must be $J=0$ associated with $I=0$. The reason why no hyperfine structure appears in the EPR spectra due to side-on H_2 is clearly explained here. If rotation of side-on D_2 is strongly hindered, side-on D_2 should be populated in $I_{\text{sid}}(\text{D}_2) = 0, 1,$ and 2 states proportional to their spin degeneracy, $2I_{\text{sid}} + 1 = 1:3:5$, respectively, to split the B3 line of H_6^+ to quintet lines with an intensity ratio of 1:2:3:2:1 as in the simulated spectrum shown at the bottom of Fig. 4.10. Since the rotational constant for H_2 (~ 8 meV) is much larger than the calculated rotational barrier for side-on H_2 along the main axis of H_6^+ (1.4 meV) and the thermal energy at 4.2 K (0.4 meV), almost all side-on H_2 should be nearly free rotating, and be in the $J_{\text{sid}}(\text{H}_2) = 0$ rotational state. Like a p- H_2 molecule, H_6^+ at $J_{\text{sid}}(\text{H}_2) = 0$ is exclusively at the $I_{\text{sid}}(\text{H}_2) = I_{34} = I_{56} = 0$ state due to the parity conservation rule on exchanging the proton fermion species [1, 50]. Kakizaki et al. have carried out path integral molecular dynamics simulations for H_6^+ and D_6^+ at 4 K and found that the side-on $\text{H}_2(\text{D}_2)$ nuclei rotate almost freely [67] (cf. Fig. 4.10 right).

4.3.2.3 D Lines Belonging to $[\text{D}_2(\text{H}_2)\text{D}_2]^+$ and $[\text{H}_2(\text{D}_2)\text{D}_2]^+$

Since the intensity ratio of D to C lines in solid p- H_2 - D_2 (8 mol%) is higher than that in p- H_2 -o- D_2 (1 mol%), D lines should be assigned to the species which contain a larger number of D_2 than $[\text{H}_2(\text{H}_2)\text{D}_2]^+$. The resonance condition for $[\text{D}_2(\text{H}_2)\text{D}_2]^+$ is given by

$$\frac{h\nu}{g\mu_B} = H_0 + A_{\text{ctr}}(H)I_{12z} + \frac{A_{\text{ctr}}(H)^2 \{I_{12}(I_{12} + 1) - I_{12z}^2\}}{2H_0} + A_{\text{sid}}(\text{D})(I_{34z} + I_{56z}), \quad (4.9)$$

with equivalent nuclei of center H_2^+ -core having $I_{12} = 0, 1$ and side-on D_2 s with $I_{34}, I_{56} = 0, 2$. Figure 4.5g shows line positions of $[\text{D}_2(\text{H}_2)\text{D}_2]^+$ obtained by Eq. (4.9) with $g = 2.0020$, $A_{\text{ctr}}(H) = 21$ mT, and $A_{\text{sid}}(\text{D}) = 1.44$ mT. The positions of lines for $[\text{D}_2(\text{H}_2)\text{D}_2]^+$ coincide well with the experimental lines shown in Fig. 4.5c, however, the

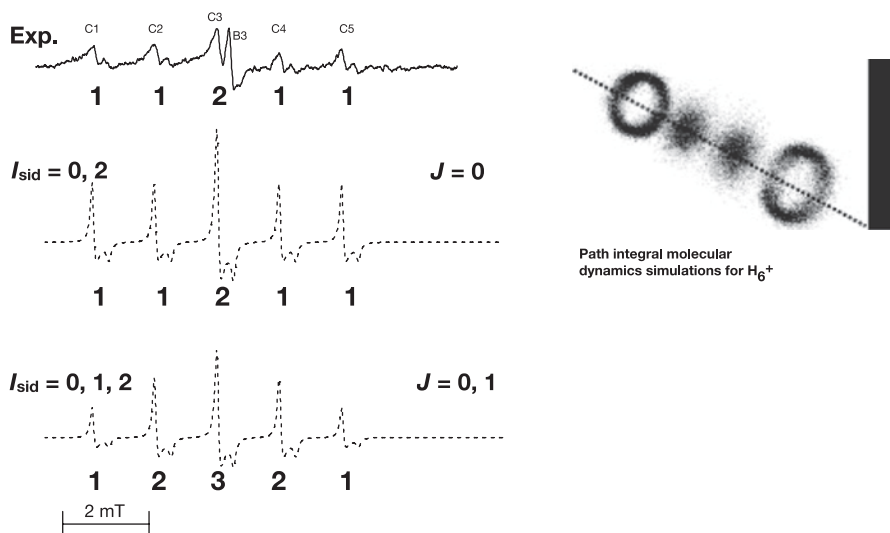


Fig. 4.10 EPR spectra at 4.2 K of γ -ray irradiated p-H₂-D₂ (1%) mixture enlarged near and around C1–C5 lines (cf. Fig. 4.4). Two simulated spectra having $I_{\text{sid}} = 0, 2$ and $0, 1, 2$ are plotted in *dotted lines* at the *middle* and the *bottom*, respectively. Three-dimensional perspective plots of probability distribution functions of the H₆⁺ nuclei obtained by path-integral molecular dynamics simulation at $T=4$ K calculated by Kakizaki et al. [67] are schematically shown in the right side

experimental spectrum has small broadened lines in addition to those positions. This is because broadened lines due to $[\text{H}_2(\text{D}_2)\text{D}_2]^+$, having nonequivalent A_1 and A_2 , are overlapped. The resonance condition for $[\text{H}_2(\text{D}_2)\text{D}_2]^+$ applying nonequivalent nuclei of center D₂⁺-core is given as Eq. (4.10). Figure 4.4h shows line positions of $[\text{H}_2(\text{D}_2)\text{D}_2]^+$ obtained by Eq. (4.10) with $g=2.0020$, $A_1(\text{D})=A_{\text{ctr}}+\Delta A(\text{D})=3.35$ mT, and $A_2(\text{D})=A_{\text{ctr}}-\Delta A(\text{D})=2.98$ mT, and $A_{\text{sid}}(\text{D})=1.44$ mT. The dotted line in Figs. 4.4d, e, and f shows the simulated spectra of

$$\frac{h\nu}{g\mu_B} = H_0 + A_{\text{ctr}}(\text{D})(I_{1z} + I_{2z}) + \frac{A_{\text{ctr}}(\text{D})^2}{2H_0} + (I_{1z} - I_{2z})\sqrt{\Delta A(\text{D})^2 + \left(\frac{A_{\text{ctr}}(\text{D})}{2H_0}\right)^2} + A_{\text{sid}}(\text{D})I_{56z}. \quad (4.10)$$

$[\text{D}_2(\text{H}_2)\text{D}_2]^+$, $[\text{H}_2(\text{D}_2)\text{D}_2]^+$, and superposition of them ($[\text{D}_2(\text{H}_2)\text{D}_2]^+ : [\text{H}_2(\text{D}_2)\text{D}_2]^+ = 1:1$), respectively, with $\Delta H_{\text{FWHM}}=0.24$ mT. The simulated spectrum of (f) coincides very precisely with that of (c) including the small broadened lines, demonstrating that the D lines are assigned to $[\text{D}_2(\text{H}_2)\text{D}_2]^+$ and $[\text{H}_2(\text{D}_2)\text{D}_2]^+$.

4.3.2.4 E lines Belonging to $[\text{H}_2(\text{H}_2)\text{HD}]^+$ and $[\text{H}_2(\text{HD})\text{H}_2]^+$

When the proton of H_6^+ at position 6 in Fig. 4.9 is replaced by D to form $[\text{H}_2(\text{H}_2)\text{HD}]^+$, asymmetric A_{ctr} of A_1 and A_2 and independent A_{sid} for A_5 and A_6 can be expected. The resonance condition is given by

$$\frac{h\nu}{g\mu_B} = H_0 + A_{\text{ctr}}(\text{H})(I_{1z} + I_{2z}) + \frac{A_{\text{ctr}}(\text{H})^2}{2H_0} + (I_{1z} - I_{2z})\sqrt{\Delta A(\text{H})^2 + \left(\frac{A_{\text{ctr}}(\text{H})^2}{2H_0}\right)^2} + A_{\text{sid}}(\text{H})I_{5z} + \frac{A_{\text{sid}}(\text{H})^2}{4H_0} + A_{\text{sid}}(\text{D})I_{6z}, \quad (4.11)$$

where I_5 is the spin quantum number of the proton and I_6 is that of the deuteron in side-on HD. The second-order correction for $A_{\text{sid}}(\text{H})$ is kept in Eq. (4.11) since it is not negligible compared with the linewidth of the E lines (cf. Fig. 4.8a). Figure 4.7g shows the stick diagram of the positions using EPR parameters of $g=2.0020$, $A_1(\text{H})=A_{\text{ctr}}(\text{H})+\Delta A(\text{H})=21.24$ mT, $A_2(\text{H})=A_{\text{ctr}}(\text{H})-\Delta A(\text{H})=19.86$ mT, $A_{\text{sid}}(\text{H})=9.58$ mT, and $A_{\text{sid}}(\text{D})=1.40$ mT. Figure 4.7b shows the simulated spectrum of $[\text{H}_2(\text{H}_2)\text{HD}]^+$ with $A_1^{\text{ani}}(\text{H})=A_2^{\text{ani}}(\text{H})=-0.13$ mT and $\Delta H_{\text{FWHM}}=0.15$ mT. The simulated spectrum coincides with both positions and shape of E1–E4, E7–E18, and E22–E24 lines but does not account for the positions of E5, E6, and E19–E21 lines. These lines could be assigned to $[\text{H}_2(\text{HD})\text{H}_2]^+$. When the proton of H_6^+ at position 2 in Fig. 4.9 is replaced by a deuteron to form $[\text{H}_2(\text{HD})\text{H}_2]^+$, the resonance condition is given by

$$\frac{h\nu}{g\mu_B} = H_0 + A_{\text{ctr}}(\text{H})I_{1z} + A_{\text{ctr}}(\text{D})I_{2z} + \frac{A_{\text{ctr}}(\text{H})^2/2 + A_{\text{ctr}}(\text{D})^2\{2 - I_{2z}^2\}}{2H_0} \quad (4.12)$$

The dotted line in Fig. 4.7c shows the simulated spectrum of $[\text{H}_2(\text{HD})\text{H}_2]^+$ with $A_{\text{ctr}}(\text{H})=21.02$ mT, $A_{\text{ctr}}(\text{D})=3.02$ mT, $A_1^{\text{ani}}(\text{H})=-0.12$ mT, and $A_2^{\text{ani}}(\text{D})=-0.02$ mT. The simulated spectrum coincides with both line positions and shape of E5–E7, and E19–E21 lines. Addition of the two spectra in Figs. 4.7b and c gives the spectrum shown in Fig. 4.8b which precisely coincides with all of the E lines shown in Fig. 4.8a, indicating that the E lines are attributable to both $[\text{H}_2(\text{H}_2)\text{HD}]^+$ and $[\text{H}_2(\text{HD})\text{H}_2]^+$.

4.3.2.5 F Lines Belonging to $[\text{HD}(\text{H}_2)\text{HD}]^+$

In addition to the E lines in Fig. 4.8a, F lines coexist in the spectrum, and the relative intensity of the F lines increased when the concentration of HD increased from 1 to 8 mol% as shown in Fig. 4.8c. The resonance condition of $[\text{HD}(\text{H}_2)\text{HD}]^+$ as an expected species in this system is given by

Table 4.4 HFCC of H_6^+ and its isotope substituents in mT determined by the analysis of B-F lines. Italic values show HFCC for D atoms

Lines	Species	g-value	A_1		A_2		A_5	A_6	Remarks
			Iso.	Ani.	Iso.	Ani.			
B	$[H_2(H_2)H_2]^+$	2.00,212	20.440	-0.061	20.440	-0.061			[32]
C	$[H_2(H_2)D_2]^+$	2.0020	21.83	-0.08	19.43	-0.16	<i>1.44</i> (9.38)	<i>1.44</i> (9.38)	
D	$[D_2(H_2)D_2]^+$	2.0020	21		21		<i>1.44</i> (9.38)	<i>1.44</i> (9.38)	$A_3=A_4=$ $A_5=A_6$
D	$[H_2(D_2)D_2]^+$	2.0020	3.35 (21.8)		2.98 (19.4)		<i>1.44</i> (9.38)	<i>1.44</i> (9.38)	
E	$[H_2(H_2)HD]^+$	2.0020	21.24	-0.13	19.86	-0.13	9.58	<i>1.40</i> (9.12)	
E	$[H_2(HD)H_2]^+$	2.0020	21.02	-0.12	3.02 (19.7)	-0.02 (-0.12)			
F	$[HD(H_2)HD]^+$	2.0020	21		21		9.52	<i>1.37</i> (8.92)	$A_3=A_5,$ $A_4=A_6$

$$\frac{h\nu}{g\mu_B} = g\mu_B H_0 + A_{ctr}(H)I_{12z} + \frac{A_{ctr}(H)^2 \{I_{12}(I_{12}+1) - I_{12z}^2\}}{2H_0} \quad (4.13)$$

$$+ A_{sid}(H)I_{35z} + \frac{A_{sid}(H)^2 \{I_{35}(I_{35}+1) - I_{35z}^2\}}{2H_0} + A_{sid}(D)I_{46z}$$

with $I_{35} = I_3 + I_5$, $I_{35z} = I_{3z} + I_{5z}$, $I_{46} = I_4 + I_6$, and $I_{46z} = I_{4z} + I_{6z}$. Since H_6^+ does not rotate about its main axis in solid p- H_2 [27], I_{35} and I_{46} are not coupled to the rotational states but have 0 and 1 for I_{35} and 0, 1, and 2 for I_{46} even at 4 K. The stick diagram and simulated spectrum (d) in Fig. 4.8 shows line positions and spectral shapes of $[HD(H_2)HD]^+$ at $[I_{12z}, I_{12z}] = [0, 1]$ and $[0, 0]$ with $g=2.0020$, $A_{ctr}(H)=21$ mT, $A_{sid}(H)=9.52$ mT, and $A_{sid}(D)=1.37$ mT. The simulated spectrum satisfactorily fits the positions and intensities of F1 to F8 lines. The other lines of $[HD(H_2)HD]^+$ at $I_{12z} = \pm 1$ are not recognized probably due to broadened line shapes.

HFCCs obtained by the fittings are summarized in Table 4.4. $A_{ctr}(H) \approx 20$ and $A_{sid}(H) \approx 9.5$ mT obtained for all series of lines, B–F, are very close to those of H_6^+ calculated in Table 4.2. These results indicate that totally more than 50 B–F lines observed in this study are uniquely assigned to H_6^+ and its isotopomers.

4.3.3 Large Precessional Motion of H_6^+ and $H_2D_4^+$

The isotropic hyperfine-coupling constants (HFCCs) A_{iso} obtained theoretically coincide with the experimental ones with excellent accuracy, indicating that the theo-

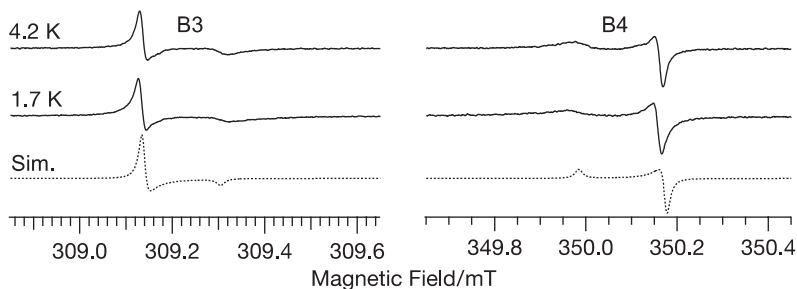


Fig. 4.11 EPR lines of H_6^+ at $I_{12z} = \pm 1$ (B3 and B4) in γ -ray irradiated solid p- H_2 measured with field-modulation frequency of 50 kHz, its amplitude of 0.01 mT, and microwave power of 1 mW for (a) and 0.4 mW for (b). The dashed line is a simulated spectrum of H_6^+ with $A^{\text{ani}} = -0.06$ mT. The figure is adapted from [29] by permission of Elsevier Inc. (2008)

retical calculation properly optimized the geometry of H_6^+ , however, anisotropic HFCCs, A^{ani} are quite different from the theoretical ones as shown in Table 4.3.

Figure 4.11 shows EPR lines at 4.2 and 1.7 K of H_6^+ at $I_{12z} = \pm 1$ named B3 and B4, respectively. The lineshape is almost the same at 4.2 and 1.7 K and is a typical powder-pattern shape with an uniaxial asymmetric hyperfine interaction. HFCC A is composed of an isotropic Fermi contact term A^{iso} and an anisotropic dipolar-dipolar interaction A^{ani} expressed as

$$\begin{aligned} A &= A^{\text{iso}} + A^{\text{ani}}(\Theta) \\ &= A^{\text{iso}} + A^{\text{ani}}(3\cos^2\Theta - 1) \end{aligned} \quad (4.14)$$

where Θ is the angle between the main axis of the H_2^+ -core of H_6^+ and the direction of magnetic field. A^{iso} determines line positions, and A^{ani} gives lineshape. The simulated powder-pattern spectrum of H_6^+ with a negative sign of $A^{\text{ani}} = -0.06$ mT shown in the dotted lines in Fig. 4.11c coincides with the experimental B3 and B4 lines shapes very well. The larger peaks in B3 and B4 are for $\Theta = 90^\circ$ in Eq. (4.14), while the smaller ones are for $\Theta = 0^\circ$. However, as shown in Table 4.3, theory has predicted $A^{\text{ani}} = 1.25$ mT, as positive and much larger than that experimentally determined by a factor of -20 .

Figure 4.12 shows C1–C5 and C13–C16 lines of $H_4D_2^+$ at 4.2 and 1.7 K for $I_{12z} = I_{1z} + I_{2z} = \pm 1$. The experimental lines at 4.2 K are well reproduced by using $A^{\text{ani}} = -0.12$ mT. Although this value is twice that for H_6^+ , it is still much less than the theoretical result by a factor of -10 . Unlike H_6^+ , $H_4D_2^+$ was remarkably changed both in line-positions and shapes by the decrease in temperature from 4.2 to 1.7 K. The C1–C5 (C13–C17) lines were shifted to upper (lower) fields by 1.2 mT. In addition, although upper (lower) peaks were more intense than the lower (upper) in the C1–C5 (C13–C17) lines at 4.2 K, the lower (upper) ones became more intense at 1.7 K. The change in lineshape of C1–C5 and C13–C17 can be reproduced by a change in A^{ani} . The simulated spectrum with $A^{\text{ani}} = 1.17$ mT for 1.7 K coincides with the experimental one. The value of $A^{\text{ani}} = 1.17$ mT is positive and close to the theo-

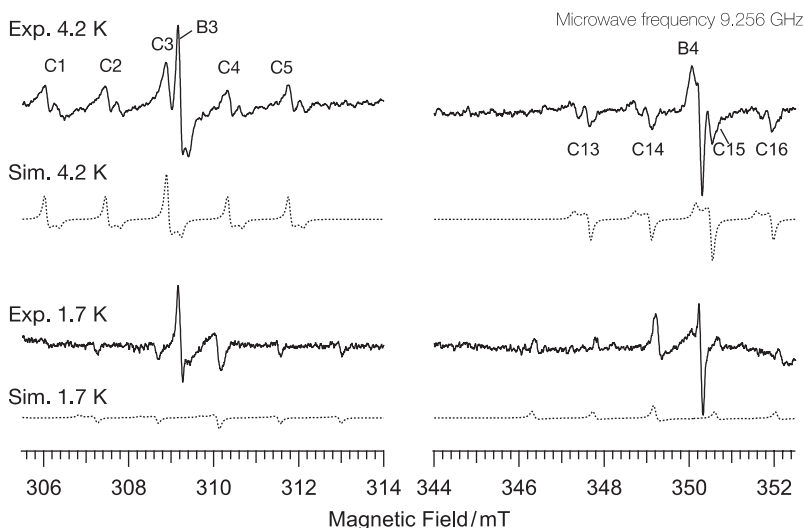


Fig. 4.12 EPR lines of H_4D_2^+ at $I_{12z} = \pm 1$ (C1–C5 and C13–C17) in γ -ray irradiated solid p- H_2 containing o- D_2 at 1 mol% with field-modulation frequency of 50 kHz, its amplitude of 0.1 mT, and microwave power of 1 mW for (a) and 0.4 mW for (b). The dashed lines are simulated spectra of H_4D_2^+ with $A^{\text{ani}} = -0.12$ mT for (a) and 1.17 mT for (b). The figure is adapted from [29] by permission of Elsevier Inc. (2008)

retical value of 1.25 mT. The smaller peaks of C1–C5 and C13–C17 lines of H_4D_2^+ for $\Theta = 0^\circ$ in Eq. (4.14) disappeared at 1.7 K probably due to poor signal-to-noise ratio. The inversion of the sign and the change in absolute value of A^{ani} at decreased temperature is a novel and unexpected observation.

We propose that the discrepancy in A^{ani} between experiment and theory is due to the local motion of H_6^+ and H_4D_2^+ in the cage of solid p- H_2 . Although theory calculates A_0^{ani} , (the anisotropic HFCC) against the molecular axes system, A^{ani} determined by EPR is the projection of A_0^{ani} on the crystalline axes as shown in the left part of Fig. 4.13. Theoretical values of A_0^{ani} can be compared with experimental ones only when the H_6^+ or H_4D_2^+ molecules are completely fixed in the solids. The A^{ani} values should decrease with the increase in amplitude of libration or rotation due to the motional narrowing effect.

As shown in Fig. 4.13a, suppose that a radical has a precessional motion around a crystalline axis of a solid with the precession angle θ with the phase of precession ϕ . The anisotropic HFCC $A^{\text{ani}}(\theta, \phi, \Theta)$, at Θ , θ , and phase ϕ , is given by

$$A^{\text{ani}}(\theta, \phi, \Theta) = (3r_z^2 - 1)A_0^{\text{ani}} \quad (4.15)$$

where r_z is the z -component of the unit vector \mathbf{r} along the main axis of the H_6^+ or H_4D_2^+ radical ion (cf. Fig. 4.13, left part), A_0^{ani} is the value when the H_6^+ is completely immobile ($\theta = 0^\circ$ and $\phi = 0^\circ$) [29]. A_0^{ani} is calculated to be 1.25 mT (Table 4.3).

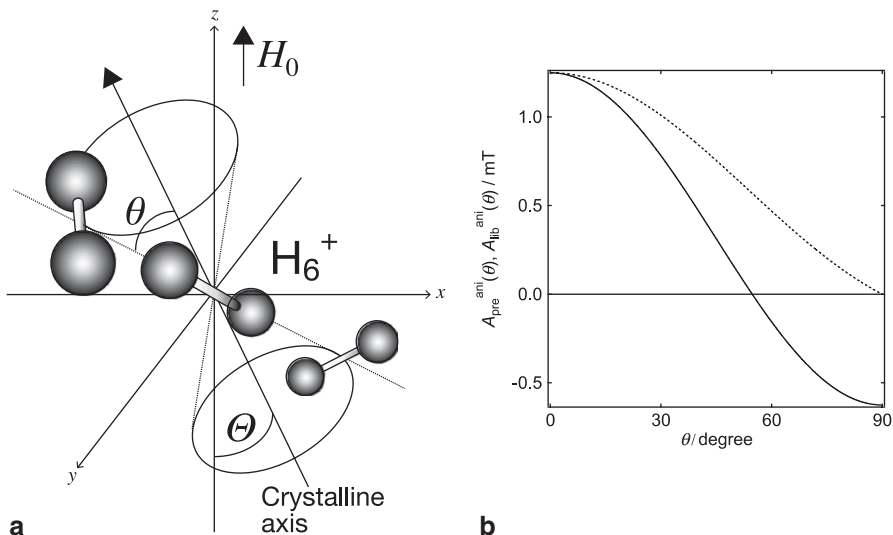


Fig. 4.13 **a** Schematic representation of H_6^+ in a precession motion against crystalline axis. θ is the angle between the main axis of H_6^+ and crystalline axis, and Θ the angle between the crystalline axis and vector of static magnetic field (H_0). **b** $A_{pre}^{ani}(\theta)$ and $A_{lib}^{ani}(\theta)$ plotted against θ . Solid line and dotted line shows $A_{pre}^{ani}(\theta)/A_0^{ani}$ and $A_{lib}^{ani}(\theta)/A_0^{ani}$, respectively

The expected value for $A^{ani}(\theta, \phi, \Theta)$ in the precessional motion, is given in Eq. (4.16) by averaging $A^{ani}(\theta, \phi, \Theta)$ around ϕ . In Eq. (4.16), $\theta=0^\circ$ corresponds to the situation that radicals are completely fixed to crystalline axes, and $\theta=90^\circ$ corresponds to the situation that each radical rotates in a plane. The anisotropy measured by EPR is $A_{pre}^{ani}(\theta)$ derived from A_0^{ani} as shown in Eq. (4.17). $A_{pre}^{ani}(\theta)$ decreases with increasing θ from 0° , crosses 0 at the magic angle of 54.74° , and then reaches $-A_0^{ani}/2$ at $\theta=90^\circ$ as shown in Fig. 4.13b. The sign of $A_{pre}^{ani}(\theta)$ inverses at the magic angle.

$$A_{pre}^{ani}(\theta, \Theta) = \frac{\int_0^{2\pi} (3r_z^2 - 1) A^{ani}(\theta, \phi, \Theta) d\phi}{\int_0^{2\pi} d\phi} = \frac{3\cos^2\theta - 1}{2} (3\cos^2\Theta - 1) A_0^{ani}$$

$$\equiv (3\cos^2\Theta - 1) A_{pre}^{ani}(\theta), \quad (4.16)$$

$$A_{pre}^{ani}(\theta) = (3\cos^2\theta - 1) A_0^{ani} / 2 \quad (4.17)$$

On the other hand, when the radical is in librational motion with the maximum libration angle θ , the expected value, $A_{lib}^{ani}(\theta, \Theta)$, is given by,

$$A_{lib}^{ani}(\theta, \Theta) = \frac{\int_0^\theta \int_0^{2\pi} A^{ani}(3r_z^2 - 1) d\phi \sin\theta d\theta}{\int_0^\theta \int_0^{2\pi} d\phi \sin\theta d\theta} = A_0^{ani} \frac{\cos\theta(1 + \cos\theta)}{2} (3\cos^2\Theta - 1)$$

$$\equiv A_{lib}^{ani}(\theta) (3\cos^2\Theta - 1) \quad (4.18)$$

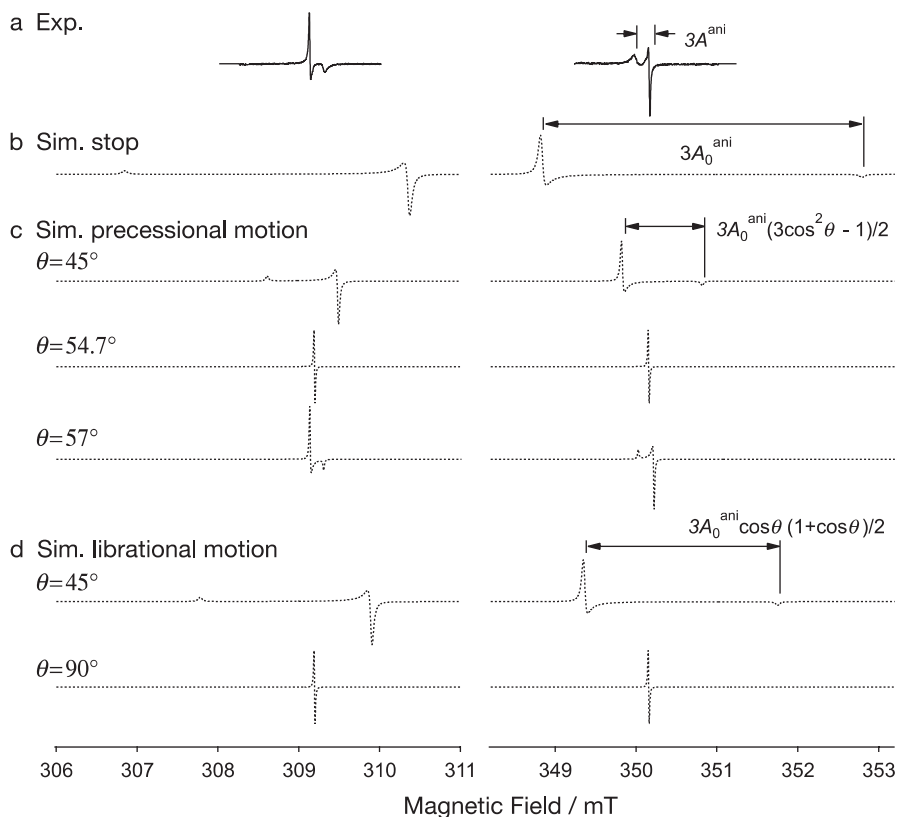


Fig. 4.14 Simulated B3 and B4 lines according to the precessional and librational models written in Eqs. (4.16) and (4.18), respectively, as a function of $A^{\text{ani}}(\theta, \phi, \Theta)$ (**b–d**) with theoretical A_0^{ani} value of 1.25 mT by MP2/cc-pVQZ. The simulations correspond to the motions of H_6^+ as **a** B3 and B4 lines in experiment; **b** stopped ($\theta=0$ in Eq. (4.17)); **c** in precessional motion (Eq. (4.17)) **d** in librational motion (Eq. (4.18))

$A_{\text{lib}}^{\text{ani}}(\theta)$ decreases with increasing θ from 0° to 90° . The radicals are in free rotational state at $\theta=0^\circ$. Unlike $A_{\text{pre}}^{\text{ani}}(\theta)$, the sign of $A_{\text{lib}}^{\text{ani}}(\theta)$ cannot be negative for $0^\circ \leq \theta \leq 90^\circ$ as shown in Fig. 4.13b.

Figure 4.14 shows simulated EPR spectra of B3 and B4 lines depending on the rotational motions of H_6^+ as a function of $A^{\text{ani}}(\theta, \phi, \Theta)$. The outer peaks of the experimental B3 and B4 lines were more intense than the corresponding inner peaks. The splitting of the outer and the inner peaks is 0.018 mT, which corresponds to $3 \times A^{\text{ani}}$. However, simulated lines of immobile H_6^+ have completely opposite symmetry, as the inner peaks were more intense than the outer ones. The splitting $3 \times A_0^{\text{ani}} = 3.75$ mT is 20 times larger than the experimental value. As is mentioned above, the expected value for $A^{\text{ani}}(\theta, \phi, \Theta)$ in the precessional motion is given by averaging $A^{\text{ani}}(\theta, \phi, \Theta)$ around ϕ , and that in the librational motion by averaging $A^{\text{ani}}(\theta, \phi, \Theta)$ around θ and ϕ . These averaging motions can be observed by EPR when

Table 4.5 A^{ani} of H_2^+ -core of H_6^+ and H_4D_2^+ determined by the analysis of ESR lineshape of H_6^+ and H_4D_2^+

	Temperature/K	A^{ani}/mT	precession angle θ / degree
H_6^+	4.2	-0.06	57
	1.7	-0.06	57
H_4D_2^+	4.2	-0.12	59
	1.7	1.17	—
Theory ^a		1.25	—

^a MP2/cc-pVQZ level

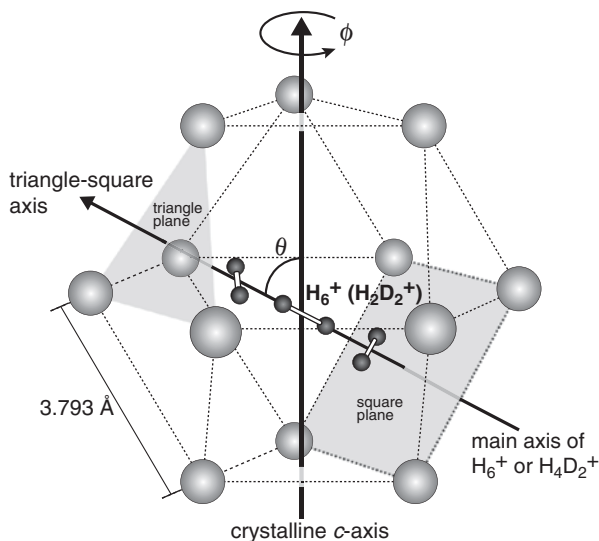
the precessional or librational frequency is faster than ~ 100 MHz because the splitting due to A_0^{ani} is 3.75 mT (~ 100 MHz).

When H_6^+ is in precessional motion at $\theta < 54.7^\circ$, the symmetry of simulated lines was opposite from experimental ones. When H_6^+ is in precessional motion at $\theta > 54.7^\circ$, the symmetry of simulated lines can be reproduced to that of the experimental ones. The splitting width increased with increasing θ above 54.7° and agreed with the experimental value at $\theta = 57^\circ$ (cf. Table 4.5). It is concluded that the H_6^+ ions are not in libration motion. The negative value of experimental A^{ani} in H_6^+ at 4.2 and 1.7 K, and H_4D_2^+ at 4.2 K should be due to a large precessional motion of them with $\theta > 54.74^\circ$.

We determined θ by substituting the experimental value of A^{ani} for $A_{\text{pre}}^{\text{ani}}(\theta)$, and the theoretical one for A_0^{ani} in Eq. (4.17), respectively. $\theta = 57^\circ$ is obtained for H_6^+ at 4.2 and 1.7 K, and 59° for H_4D_2^+ at 4.2 K, indicating that H_6^+ at 4.2 and 1.7 K and H_4D_2^+ at 4.2 K are in a large precessional motion faster than 100 MHz. The positive and large A^{ani} for H_4D_2^+ (1.17 mT) at 1.7 K, which is close to theoretical value, indicates that the precessional motion of H_4D_2^+ at 1.7 K is quenched or much slower than 100 MHz.

Figure 4.15 shows a model of H_6^+ trapped in a single substitutional *hcp* cage of solid p- H_2 . The cage has 8 triangular and 6 square planes. All triangular planes at the side diagonally face to the square ones, but the triangular plane at the top faces to the triangular one at the bottom. We propose that the main axis of H_6^+ should be along the axis passing through centers of a pair of diagonally faced square and triangle planes (triangle-square axis) in order to avoid overlap of electronic orbital between H_6^+ and p- H_2 s. When a position of H_6^+ molecule moved to the square plane by 0.3 Å along the main axis, the distances between side-on H_2 of H_6^+ to each lattice p- H_2 molecule at the apexes of the triangle and square are calculated to be equally 2.8 Å. Distance between a side-on H_2 of H_6^+ and an outer H_2 in Fig. 4.2c is 2.2 Å. These values indicate that H_6^+ can be trapped along the triangle-square axis with little distortion of the *hcp* cage of solid p- H_2 . H_6^+ ions are probably in precessional motion along the *c*-axis by jumping among the six equivalent triangle-square axes in solid p- H_2 . When the cage is not distorted, the angle between the *c*-axis and triangle-square axis in the *hcp* cage is calculated to be $\theta_{\text{min}} = 63.2^\circ$, which is very close to the precession angle of H_6^+ at 4.2 K and 1.7 K (57°), and H_4D_2^+ at 4.2 K (59°).

Fig. 4.15 Schematic representation of H_6^+ in a precession motion against crystalline axis. θ is the angle between the main axis of H_6^+ and crystalline axis. The figure is adapted from [29] by permission of Elsevier Inc. (2008)



The similar values of A^{ani} between experiment and theory in $H_4D_2^+$ at 1.7 K indicate that the precessional motion is stopped. We propose two possible reasons as follows: First, the moment of inertia for $H_4D_2^+$ is larger than that for H_6^+ . $H_4D_2^+$ is heavier than H_6^+ , and the center of mass does not coincide with the center of geometry in $H_4D_2^+$. Second, not only the nuclear configuration but also the electronic wave function of $H_4D_2^+$ no longer has D_{2d} symmetry but has C_{2v} . This means that the energy $E(\theta_{\text{min}}, \phi)$ of $H_4D_2^+$ in the *hcp* cage of solid p- H_2 does not have 6-fold but has 3-fold symmetry around ϕ . $H_4D_2^+$ should be localized in one of three deeper potential wells at 1.7 K.

4.3.4 Isotope Condensation of H_6^+ in p- H_2 - D_2 Mixture at 4.2 K

Table 4.6 shows the relative yields of radical ions detected 30 min after irradiation in p- H_2 and p- H_2 -o- D_2 mixture. The yields were obtained by double integration of the corresponding EPR lines. Compared to the H_6^+ yield in p- H_2 , the total yields of H_6^+ , $H_4D_2^+$, and $H_2D_4^+$ displayed 2.8- and 9-fold increases upon addition of 1 and

Table 4.6 Relative yields of e_t^- , H_6^+ , $H_4D_2^+$, $H_2D_4^+$, and H atoms produced in p- H_2 and p- H_2 -o- D_2 mixtures measured 30 min after irradiation

	Negative		Positive			Neutral
	e_t^-	H_6^+	$H_4D_2^+$	$H_2D_4^+$	Total	H atoms
p- H_2	~7	1	–	–	1	$6 \pm 1 \times 10^3$
p- H_2 - D_2 (1 mol%)	70	0.5	1.9	0.4	2.8	$6 \pm 1 \times 10^3$
p- H_2 - D_2 (8 mol%)	170	–	4 ± 1	5 ± 2	9 ± 3	n.d.

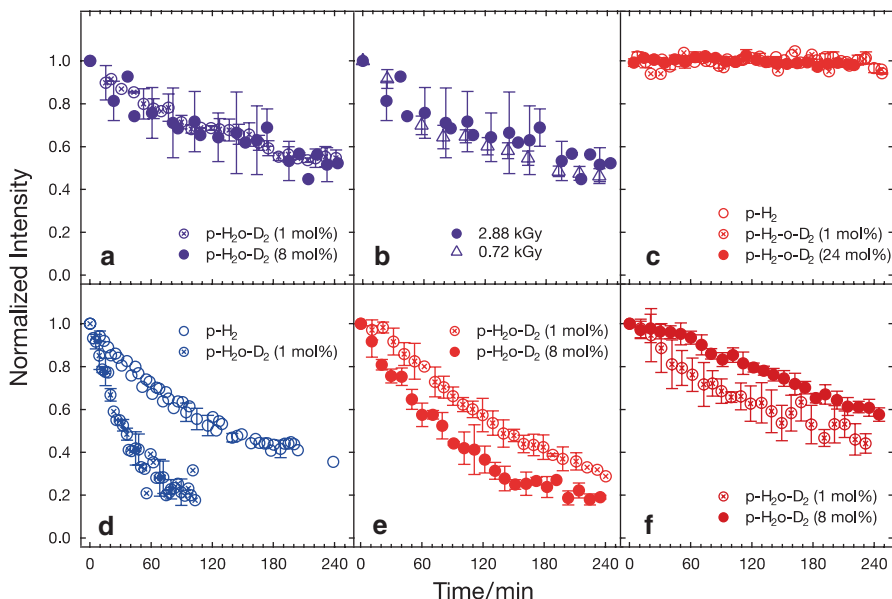


Fig. 4.16 Decay behaviors of **a** e_t^- , **b** e_t^- at different γ -ray irradiation doses, **c** H atoms **d** H_6^+ , **e** $H_4D_2^+$, and **f** $H_2D_4^+$ in p- H_2 and p- H_2 -o- D_2 mixtures. Decay of e_t^- in **(b)** were measured in a p- H_2 -o- D_2 (8 mol%) mixture. The figure is adapted from [30] by permission of American Institute of Physics (2010)

8 mol% o- D_2 to p- H_2 , respectively. The ratios of the $H_6^+ : H_4D_2^+ : H_2D_4^+$ yields would be 97:3:0.03 for p- H_2 -o- D_2 (1 mol%) and 74:23:1.9 for p- H_2 -o- D_2 (8 mol%) if H_6^+ , $H_4D_2^+$, and $H_2D_4^+$ were produced statistically with respect to p- H_2 and o- D_2 concentrations. However, the experimental ratios were 18:68:14 and 0:44:56, respectively. These results clearly show that the $H_{6-n}D_n^+$ ($4 \geq n \geq 1$) species were preferentially produced in solid p- H_2 mixtures.

Figure 4.16 shows the decay behavior of trapped electrons (e_t^-), H_6^+ , $H_4D_2^+$, $H_2D_4^+$, and H atoms produced in p- H_2 and p- H_2 -o- D_2 mixtures. The decay behavior of e_t^- in p- H_2 -o- D_2 was found to be independent of o- D_2 concentration and γ -ray dose ((a), (b)). H_6^+ decayed much faster in p- H_2 -o- D_2 (1 mol%) than in p- H_2 . On the other hand, $H_4D_2^+$ and $H_2D_4^+$ decayed in a similar manner in both p- H_2 -o- D_2 mixtures ((d)–(f)). The H atoms did not decay in p- H_2 [21] and p- H_2 -o- D_2 mixtures ((c)).

4.3.4.1 Trapping Mechanism of Free Electrons by Heavier Hydrogen Isotope Molecules

Large increases in e_t^- yields caused by increases in o- D_2 concentrations in irradiated solid p- H_2 strongly suggest that isotopic hydrogen molecules play an important role in trapping electrons in p- H_2 crystals. We would like to propose the new trapping mechanism of o- D_2 -mediated electron. The isotope effect on electron trapping

was derived from the difference in rotational constants between these isotopes as follows. Long-range charge-induced dipole and quadrupole interactions between e_t^- with H_2 or with D_2 were calculated by assuming a point-charge model [50]. The Hamiltonian (H_s) of the interactions is thus given by:

$$H_s = -\alpha e^2 / 2R^4 + (eQ / R^3 - \gamma e^2 / 3R^4) P_2(\cos\theta) \quad (4.19)$$

where R is the separation between a point charge and H_2 or D_2 . θ denotes the orientation of the hydrogen molecule with respect to R and $P_2(\cos\theta)$ is the Legendre polynomial. α and γ are the mean polarizability and its corresponding anisotropy, respectively. Q is the quadrupole moment of the hydrogen molecule in a molecule fixed frame. The first and second terms describe the charge-induced dipole interaction and the quadrupole interactions, respectively. Because both p- H_2 and o- D_2 exclusively have a $J=0$ rotational state at about 4.2 K, the interaction ($W_{J=0}$) is

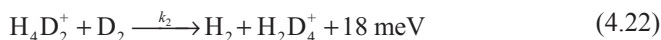
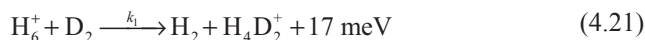
$$W_{J=0} = \langle \psi_{J=0} | H_s | \psi_{J=0} \rangle + \frac{|\langle \psi_{J=0} | H_s | \psi_{J=2} \rangle|^2}{E_0 - E_2} = \frac{-\alpha e^2}{2R^4} + \frac{M |eQ / R^3 - \gamma e^2 / 3R^4|^2}{15\hbar^2} \quad (4.20)$$

Here, Ψ_J and E_J are the rotational wave function of hydrogen nuclei and the rotational energy for J , respectively. M is the moment of inertia of the molecule. Although the first term is common to o- D_2 and p- H_2 , the second term for o- D_2 is twice as large as that for p- H_2 due to the difference in M .

Brooks et al. calculated that electrons produced in solid hydrogen were stabilized to form trapped electrons called electron bubbles having a radius of 5 Å because of the zero-point energy. At $R=5$ Å, $|W_{J=0}|$ was 1.4 meV higher for o- D_2 (12.3 meV) than for p- H_2 (10.9 meV). The difference is larger than the thermal energy at 4.2 K of 0.4 meV. The relative e_t^- yields in irradiated p- H_2 and p- H_2 -o- D_2 (1 mol%) of 1:10 are in the same order as the $|W_{J=0}|$ for e^- -p- H_2 and e^- -o- D_2 , respectively. These results strongly suggest that the existence of o- D_2 molecules assisted the trapping of electrons qualitatively at 4.2 K.

4.3.4.2 Isotope Condensation of H_6^+ via Hole Hopping Diffusion in Solid p- H_2

As shown in Fig. 4.16d, addition of o- D_2 in p- H_2 induced a faster decay behavior of H_6^+ . We propose that the following three reactions can proceed in solid p- H_2 -o- D_2 mixture at 4.2 K as



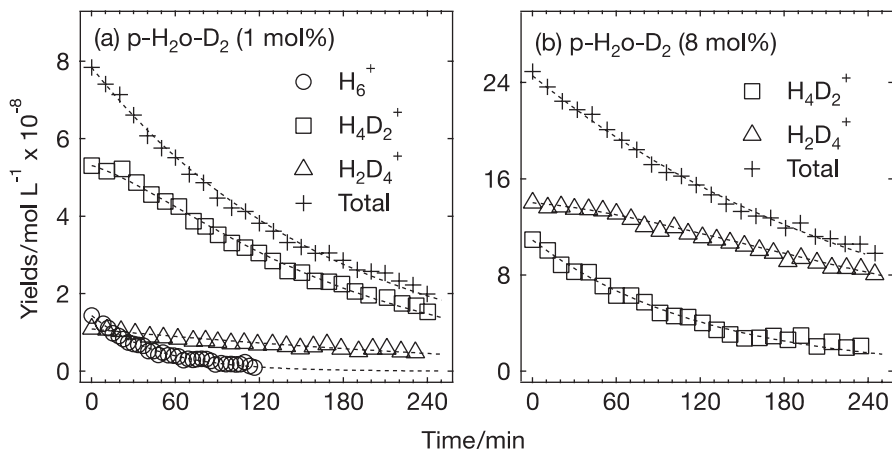
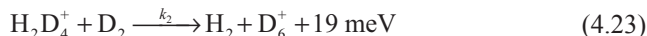


Fig. 4.17 Time course of the yields of H₆⁺ (open circles), H₄D₂⁺ (open squares), and H₂D₄⁺ (open triangles) and the total yield (crosses) in p-H₂-o-D₂ **a** 1 mol%, **b** 8 mol%. Broken lines are simulated decays obtained using K_e , k_1 , k_2 , and k_3 in Eqs. (4.24)–(4.26). The figure is adapted from [30] by permission of American Institute of Physics (2010)



Because these three substitution reactions are exothermic by 17~19 meV (~210 K) due to the difference in the zero-point vibrational energy estimated from theoretical calculation at the MP2/cc-pVQZ level, no reverse reactions proceeded in solid p-H₂ at 4.2 K. To examine the quantitative validity of the proposed condensation reactions, chemical kinetic analysis was performed. The rate equations for H₆⁺, H₄D₂⁺, and H₂D₄⁺ can be described by

$$-\frac{d[\text{H}_6^+]}{dt} = k_1[\text{D}_2][\text{H}_6^+] + K_e'[\text{H}_6^+], \quad (4.24)$$

$$-\frac{d[\text{H}_4\text{D}_2^+]}{dt} = -k_1[\text{D}_2][\text{H}_6^+] + k_2[\text{D}_2][\text{H}_4\text{D}_2^+] + K_e'[\text{H}_4\text{D}_2^+], \quad (4.25)$$

$$-\frac{d[\text{H}_2\text{D}_4^+]}{dt} = -k_2[\text{D}_2][\text{H}_4\text{D}_2^+] + k_3[\text{D}_2][\text{H}_2\text{D}_4^+] + K_e'[\text{H}_2\text{D}_4^+], \quad (4.26)$$

where k_1 , k_2 , and k_3 are the rate constants for reactions (4.21)–(4.23), respectively, and K_e' is the rate constant for the recombination involving e_t⁻. The decay mechanism of e_t⁻ is estimated to be geminate recombination reaction with H₆⁺ or H₃⁺ in solid p-H₂, so that K_e' is independent on the concentrations of the ions [30]. Figure 4.17 shows the experimental decay curves of H₆⁺, H₄D₂⁺, and H₂D₄⁺ in p-H₂-

o-D_2 mixtures, along with the total decay curve. The simulated decay curves coincide with experimental ones very well by using k_1 of $0.045 \text{ L mol}^{-1} \text{ min}^{-1}$, k_2 of $0.0015 \text{ L mol}^{-1} \text{ min}^{-1}$, and k_3 of $0 \text{ L mol}^{-1} \text{ min}^{-1}$ for both $\text{p-H}_2\text{-o-D}_2$ samples (1 and 8 mol%). The K_c' values were determined to be 0.0058 min^{-1} for $\text{p-H}_2\text{-o-D}_2$ (1 mol%) and 0.0039 min^{-1} for $\text{p-H}_2\text{-o-D}_2$ (8 mol%) from the simulated decay curves shown in the figure. Noticeable differences between k_1 , k_2 , and k_3 thus reflect differences in mobility between H_6^+ , H_4D_2^+ , and H_2D_4^+ by hole hopping diffusion.

4.4 Summary

Totally more than fifty ESR lines in γ -ray irradiated solid p-H_2 , $\text{p-H}_2\text{-o-D}_2$, and $\text{p-H}_2\text{-HD}$ mixtures were assigned to H_2^+ -core H_6^+ and its isotopomers such as H_5D^+ , H_4D_2^+ , H_2D_4^+ [26, 28]. All experimental spectra were reproduced by a small number of parameters such as nuclear spin quantum numbers, hyperfine coupling constants (HFCCs), and g -values for these lines. Theoretical calculations of the HFCC and g -value of H_6^+ show good agreement with the experimental ones. The observation of H_2^+ -core H_6^+ denies the widely accepted idea that even membered H_n^+ ions ($n \geq 6$) exclusively have H_3^+ -cored structure.

Direct detection and assignment of H_6^+ boosted up variety of this field. H_6^+ is also confirmed in ultracold helium nanodroplets by electron-impact ionization as icosahedral shell closures of $\text{H}_6^+(\text{H}_2)_{12}$ and $\text{H}_6^+(\text{H}_2)_{54}$ [68]. Hao et al. systematically investigated six isomers of the H_6^+ ions and concluded that the H_2^+ -core cluster with D_{2d} symmetry has been confirmed to be the global minimum on the H_6^+ potential energy surface [69]. Lin et al. also performed very precise theoretical calculations for the purpose of estimating the strength of vibrational transitions of H_6^+ and its isotopomers [70], and predicted the frequencies of the fundamental bands for five modes of vibration. $(\text{HD})_3^+$ is a good candidate for the detection due to its asymmetric structure by IR transition. For $(\text{HD})_3^+$ all of these are found to lie close to some of the strongest of the pervasive mid-infrared astronomical emission bands. It must be very interesting if the existence of H_6^+ and its isotopomers are revealed in galaxy or in some clouds in a near future.

Our experimental results for H_6^+ and its isotopomers revealed that distribution of unpaired electron was distorted by substituting deuterons for protons [28, 71]. This is a typical system where the quantum effect of nuclear motion cannot be ignored. Solving the non-Born-Oppenheimer Schrödinger equation was applied for H_2^+ , HD^+ , HT^+ very recently [65, 66]

Isotope condensation reactions of H_6^+ such as $\text{H}_6^+ + \text{D}_2 \rightarrow \text{H}_2 + \text{H}_4\text{D}_2^+$ in solid p-H_2 were found, and the dynamics of the reactions were elucidated quantitatively. H_6^+ diffused via repeated hole hopping in solid p-H_2 [30]. The hole is moving to the next lattice H_2 to produce a H_2^+ but simultaneous approaching of two lattice H_2 s makes H_6^+ , and they start precessional motion. Stopping of the precessional motion of H_4D_2^+ at 1.7 K was firstly detected by inversion of anisotropic hyperfine structure.

In general trapped electrons cannot be detected in crystalline phase [72] but were observed in the solid p-H₂ crystal with D₂. This new isotope effect is probably due to induced dipole and quadrupole moments between the trapped electrons acting by making local potential minima available. Previous reports on the enhancement of yields or electron lifetime in several irradiated deuterated molecular crystals may be partly explained by our proposed mechanisms [30].

Owing to the homogeneous property of solid p-H₂ and the low temperature, we can reveal a lot of physical and chemical properties on H₆⁺, which are hidden in complicated interactions at room temperature. I am very excited of the development of H₆⁺ studies in cryogenic physics, chemistry, and astrophysics.

Acknowledgments The author would like to express great appreciation to editors of Profs. M. Shiotani and A. Lund for giving me a chance to introduce our study. The author also would like to appreciate to Drs. T. Kumada (Japan Atomic Energy Agency) and Y. Shimizu (Nippon Light Metal Company, Ltd) for many experiments and discussions on this H₆⁺ study.

References

1. Silvera I (1980) The solid molecular hydrogens in the condensed phase—fundamentals and static properties. *Rev Mod Phys* 52:393–452
2. Kranendonk JV (1982) *Solid Hydrogen: theory of the properties of solid H₂, HD, and D₂*. Plenum, New York
3. McLennan JC, McLeod JH (1929) The Raman effect with liquid oxygen, nitrogen, and hydrogen. *Nature* 123:160–160
4. Momose T, Hoshina H, Fushitani M et al (2004) High-resolution spectroscopy and the analysis of ro-vibrational transitions of molecules in solid parahydrogen. *Vib Spectr* 34:95–108
5. Keesom WH, De Smedt J, Mooy HH (1930) Crystal structure of parahydrogen. *Nature* 126:757–757
6. Keesom WH, de Smedt J, Mooy HH (1930) On the crystal structure of para-hydrogen at liquid helium temperatures. *Proc Konink Akad Van Wetenschappen Te Amsterdam* 33:814–819
7. Momose T, Shida T (1998) Matrix-isolation spectroscopy using solid parahydrogen as the matrix: application to high-resolution spectroscopy, photochemistry, and cryochemistry. *Bull Chem Soc Jpn* 71:1–15
8. Fajardo ME, Tam S (1998) Rapid vapor deposition of millimeters thick optically transparent parahydrogen solids for matrix isolation spectroscopy. *J Chem Phys* 108:4237–4241
9. Tam S, Fajardo ME, Katsuki H et al (1999) High resolution infrared absorption spectra of methane molecules isolated in solid parahydrogen matrices. *J Chem Phys* 111:4191–4198
10. Sogoshi N, Kato Y, Wakabayashi T et al (2000) High-resolution infrared absorption spectroscopy of C60 molecules and clusters in parahydrogen solids. *J Phys Chem A* 104:3733–3742
11. Fajardo ME, Tam S (2001) Observation of the cyclic water hexamer in solid parahydrogen. *J Chem Phys* 115:6807–6810
12. Tam S, Fajardo ME (2001) Single and double infrared transitions in rapid-vapor-deposited parahydrogen solids: application to sample thickness determination and quantitative infrared absorption spectroscopy. *Appl Spectro* 55:1634–1644
13. Anderson DT, Hinde RJ, Tam S et al (2002) High-resolution spectroscopy of HCl and DCl isolated in solid parahydrogen: direct, induced, and cooperative infrared transitions in a molecular quantum solid. *J Chem Phys* 116:594–607

14. Hinde RJ, Anderson DT, Tam S et al (2002) Probing quantum solvation with infrared spectroscopy: infrared activity induced in solid parahydrogen by N₂ and Ar dopants. *Chem Phys Lett* 356:355–360. Pii s0009-2614(02)00346-9
15. Yoshioka K, Anderson DT (2003) Infrared spectra of CH₃F(ortho-H₂)_n clusters in solid parahydrogen. *J Chem Phys* 119:4731–4742
16. Wang XF, Andrews L, Tam S et al (2003) Infrared spectra of aluminum hydrides in solid hydrogen: Al₂H₄ and Al₂H₆. *J Am Chem Soc* 125:9218–9228
17. Fajardo ME, Tam S, DeRose ME (2004) Matrix isolation spectroscopy of H₂O, D₂O, and HDO in solid parahydrogen. *J Mol Struct* 695:111–127
18. Wu YJ, Yang XM, Lee YP (2004) Infrared matrix-isolation spectroscopy using pulsed deposition of p-H₂. *J Chem Phys* 120:1168–1171
19. Hoshina H, Fushitani M, Momose T et al (2004) Tunneling chemical reactions in solid parahydrogen: Direct measurement of the rate constants of R+H₂ → RH+H (R=CD₃, CD₂H, CDH₂, CH₃) at 5 K. *J Chem Phys* 120:3706–3715
20. Hoshina H, Kato Y, Morisawa Y et al (2004) UV and IR absorption spectra of C₃ embedded in solid para-hydrogen. *Chem Phys* 300:69–77
21. Kumada T, Sakakibara M, Nagasaka T et al (2002) Absence of recombination of neighboring H atoms in highly purified solid parahydrogen: electron spin resonance, electron-nuclear double resonance, and electron spin echo studies. *J Chem Phys* 116:1109–1119
22. Kumada T, Kumagai J, Miyazaki T (2001) High-resolution electron spin resonance spectroscopy of ethyl radicals in solid parahydrogen. *J Chem Phys* 114:10024–10030
23. Kumada T, Mori S, Kumagai J et al (1999) Observation of electron bubbles in para-H₂-D₂ (HD) mixtures by high-resolution ESR spectroscopy. *J Phys Chem A* 103:8966–8968
24. Kumada T (2002) Rotation of O₂ molecules in solid D₂ and HD: an electron spin resonance study. *J Chem Phys* 117:10133–10138
25. Miyazaki T, Yamamoto K, Arai J (1994) Effect of rotational quantum states (*J*=0, 1) of matrix H₂-molecules on esr-spectra of radicals at 4.2-K. *Chem Phys Lett* 219:405–408
26. Kumada T, Shimizu Y, Ushida T et al (2008) H atom, e⁻, and H₆⁺ ions produced in irradiated solid hydrogens: an electron spin resonance study. *Radiat Phys Chem* 77:1318–1322
27. Kumada T, Tachikawa H, Takayanagi T (2005) H₆⁺ in irradiated solid para-hydrogen and its decay dynamics: reinvestigation of quartet electron paramagnetic resonance lines assigned to H₂⁻. *Phys Chem Chem Phys* 7:776–784
28. Kumagai J, Inagaki H, Kariya S et al (2007) Electron spin resonance study on H₆⁺, H₃D⁺, H₄D₂⁺, and H₂D₄⁺ in solid parahydrogen. *J Chem Phys* 127:024505
29. Shimizu Y, Kumada T, Kumagai J (2008) Electron spin resonance spectroscopy of molecules in large precessional motion: a case of H₆⁺ and H₄D₂⁺ in solid parahydrogen. *J Mag Reson* 194:76–80
30. Shimizu Y, Inagaki M, Kumada T et al (2010) Negative and positive ion trapping by isotopic molecules in cryocrystals in case of solid parahydrogen containing electrons and H₆⁺ radical cations. *J Chem Phys* 132:244503
31. Kumada T, Takayanagi T, Kumagai J (2006) ESR study of H₆⁺ and H₄D₂⁺ produced in irradiated solid hydrogens. *J Mol Struct* 786:130–133
32. Kumagai J, Hanabusa M, Inagaki H et al (2004) Is the ESR spectrum attributable to H₂ or H₂⁺ (H₃)₂? Precise measurement of the *g*-value and anisotropic hyperfine structure in gamma-irradiated solid parahydrogen. *Phys Chem Chem Phys* 6:4363–4368
33. Momose T, Fushitani M, Hoshina H (2005) Chemical reactions in quantum crystals. *Int Rev Phys Chem* 24:533–552
34. Kumada T, Kitagawa N, Noda T et al (1998) An ENDOR spectrum of H atoms in solid H₂. *Chem Phys Lett* 288:755–759
35. Fushitani M, Sogoshi N, Wakabayashi T et al (1998) Photoinduced reactions of methyl radical in solid parahydrogen. *J Chem Phys* 109:6346–6350
36. Momose T, Hoshina H, Sogoshi N et al (1998) Tunneling chemical reactions in solid parahydrogen: a case of CD₃+H₂ → CD₃H+H at 5 K. *J Chem Phys* 108:7334–7338

37. Oka T (1993) High-resolution spectroscopy of solid hydrogen. *Ann Rev Phys Chem* 44:299–333
38. Sogoshi N, Wakabayashi T, Momose T et al (2001) Infrared spectroscopic study on photolysis of ethyl iodide in solid parahydrogen: perdeuterated iodide system. *J Phys Chem A* 105:3077–3086
39. Fushitani M, Momose T (2003) A study on diffusion of H atoms in solid parahydrogen. *Low Temp Phys* 29:740–743
40. Tam S, Macler M, Fajardo ME (1997) Matrix isolation spectroscopy of laser ablated carbon species in Ne, D₂, and H₂ matrices. *J Chem Phys* 106:8955–8963
41. Hogness TR, Lunn EG (1925) The ionization of hydrogen by electron impact as interpreted by positive ray analysis. *Phys Rev* 26:0044–0055
42. Smyth HD (1925) Primary and secondary products of ionization in hydrogen. *Phys Rev* 25:452–468
43. Thomson JJ (1911) Rays of positive electricity. *Philos Mag* 21:225–249
44. Oka T (1980) Observation of the infrared-spectrum of H₃⁺. *Phys Rev Lett* 45:531–534
45. Geballe TR, Oka T (1996) Detection of H₃⁺ in interstellar space. *Nature* 384:334–335
46. Oka T (2013) Interstellar H₃⁺. *Chem Rev* 113:8738–8761
47. Souers PC, Fearon D, Garza R et al (1979) Infrared-spectra of liquid and solid DT and T₂. *J Chem Phys* 70:1581–1584
48. Souers PC, Fearon EM, Roberts PE et al (1980) Collision-induced infrared lines in solid hydrogens caused by tritium radioactivity. *Phys Lett A* 77:277–280
49. Souers PC, Fearon EM, Stark RL et al (1981) Radiation-induced infrared lines in solid hydrogens containing tritium. *Can J Phys* 59:1408–1417
50. Poll JD, Hunt JL, Souers PC et al (1983) Broad infrared-absorption feature in solid D₂ and H₂ containing tritium. *Phys Rev A* 28:3147–3148
51. Souers PC (1986) Hydrogen properties for fusion energy. University of California, Berkeley
52. Brooks RL, Bose SK, Hunt JL et al (1985) Electron bubbles, small-polaron holes, and charge-induced effects in solid deuterium. *Phys Rev B* 32:2478–2488
53. Brooks RL, Hunt JL, Macdonald JR et al (1985) Interference effects in the charge-induced spectrum of H₂ at 4.2 K. *Can J Phys* 63:937–940
54. Miller JJ, Brooks RL, Hunt JL et al (1988) Charge-induced absorption in proton-beam-irradiated solid hydrogen deuteride. *Can J Phys* 66:1025–1030
55. Chan MC, Okumura M, Oka T (2000) Infrared spectrum of p-hydrogen crystals ionized by 3 MeV electrons: cluster ions of hydrogen in condensed phase. *J Phys Chem A* 104:3775–3779
56. Momose T, Lindsay CM, Zhang Y et al (2001) Sharp spectral lines observed in gamma-ray ionized parahydrogen crystals. *Phys Rev Lett* 86:4795–4798
57. Correnti MD, Dickert KP, Pittman MA et al (2012) Electron spin resonance investigation of H₂⁺, HD⁺, and D₂⁺ isolated in neon matrices at 2 K. *J Chem Phys* 137:7204308
58. Kirchner NJ, Bowers MT (1987) An experimental-study of the formation and reactivity of ionic hydrogen clusters—the 1st observation and characterization of the even clusters H₄⁺, H₆⁺, H₈⁺, and H₁₀⁺. *J Chem Phys* 86:1301–1310
59. Fiegele T, Hanel G, Echt O et al (2004) Appearance energies of hydrogen and deuterium cluster ions. *J Phys B At Mol Opt Phys* 37:4167–4175
60. Montgomery JA, Michels HH (1987) On the structure of the ground-state of H₆⁺. *J Chem Phys* 87:771–773
61. Kurosaki Y, Takayanagi T (1998) A direct isomerization path for the H₆⁺ cluster: an ab initio molecular orbital study. *Chem Phys Lett* 293:59–64
62. Kurosaki Y, Takayanagi T (1998) An ab initio molecular orbital study of even-membered hydrogen cluster cations: H₆⁺, H₈⁺, H₁₀⁺, H₁₂⁺, and H₁₄⁺. *J Chem Phys* 109:4327–4334
63. Symons MCR (1995) Possible identification of the dihydrogen radical anion in irradiated solid hydrogen. *Chem Phys Lett* 247:607–610
64. Neese F (2001) Prediction of electron paramagnetic resonance g values using coupled perturbed Hartree-Fock and Kohn-Sham theory. *J Chem Phys* 115:11080–11096

65. Nakashima H, Nakatsuji H (2013) Non-born-oppenheimer potential energy curve: hydrogen molecular ion with highly accurate free complement method. *J Chem Phys* 139:074105
66. Nakashima H, Hijikata Y, Nakatsuji H (2013) Solving the non-born-oppenheimer schrodinger equation for the hydrogen molecular ion with the free complement method. II. Highly accurate electronic, vibrational, and rotational excited states. *Astrophys J* 770:144
67. Kakizaki A, Takayanagi T, Shiga M (2007) Path integral molecular dynamics calculations of the H_6^+ and D_6^+ clusters on an ab initio potential energy surface. *Chem Phys Lett* 449:28–32
68. Jaksch S, Mauracher A, Bacher A et al (2008) Formation of even-numbered hydrogen cluster cations in ultracold helium droplets. *J Chem Phys* 129:224306
69. Hao Q, Simmonett AC, Yamaguchi Y et al (2009) Structures and energetics of H_6^+ clusters. *J Phys Chem A* 113:13608–13620
70. Lin CY, Gilbert ATB, Walker MA (2011) Interstellar solid hydrogen. *Astrophys J* 736:91
71. Kurosaki Y, Shimizu Y, Kumagai J (2008) Isotope effects on the spin-density distribution in the H_6^+ clusters: direct ab initio molecular dynamics study. *Chem Phys Lett* 455:59–63
72. Tabata Y, Ito Y, Tagawa S (1991) *CRC handbook of radiation chemistry*. CRC Press, Boca Raton

Part II
Solid State Radiation Chemistry

Chapter 5

EPR and IR Spectroscopy of Free Radicals and Radical Ions Produced by Radiation in Solid Systems

Vladimir I. Feldman

Abstract EPR spectroscopy was extensively used for characterization of highly reactive paramagnetic species produced by ionizing radiation in low-temperature solids for 60 years. The present chapter outlines experimental approaches in this field and presents a review of recent development using a combination of EPR and IR spectroscopy. This approach made it possible to get a new insight in the radiation-induced chemistry of molecules in solids and to provide more detailed information on the structure and dynamics of radiation-induced radicals.

5.1 Introduction

EPR spectroscopy is probably the most powerful and versatile tool for investigations of the radiation effects in different types of solid materials. Indeed, the key primary events upon interaction of radiation with condensed matter are ionization and electronic excitation. The former process leads to charge and spin separation, that is, direct formation of charged paramagnetic species detectable by EPR. The relaxation of electronically excited states often yields neutral atoms and free radicals, which can be trapped in solid matter. The first observation of the radiation-induced paramagnetic defects in inorganic solids was reported in 1949 [1], just 5 years after the discovery of the EPR phenomenon. Two years later, Schneider et al. recorded the EPR spectrum of an organic radical resulting from irradiation of poly(methyl metacrylate) with X-rays [2]. During the next six decades, EPR spectroscopy was extensively used to investigate the structure of radiation-induced intermediates, their spatial distribution and kinetics. These studies provided very important (and often unique) information on the mechanisms of radiation effects in both inorganic and organic solids, including polymers. They also played significant role in basic

V. I. Feldman (✉)

Department of Chemistry, Lomonosov Moscow State University,
Leninskie Gory 1/3, Moscow 119991, Russia
e-mail: vladimir.feldman@rad.chem.msu.ru

© Springer International Publishing 2014

A. Lund, M. Shiotani (eds.), *Applications of EPR in Radiation Research*,
DOI 10.1007/978-3-319-09216-4_5

development of the EPR theory [3]. A comprehensive review of the early work can be found in the book by Pshchetskii et al. [4].

An important contribution of EPR spectroscopy to understanding the primary events in the radiation chemistry of organic substances is concerned with the application of a specific approach for selective stabilization of highly reactive radical cations known as the Freon matrix technique introduced in 1979 [5]. Extensive work on structure and reactivity of the radiation-induced radical cations through the next decade was the topic of several reviews [6–8]. More recently, a rigorous matrix isolation approach using solid noble gases was applied to the studies of the primary radiation-induced radical cations [9–18]. As a whole, the present knowledge on electronic structure, geometry, and properties of the reactive radical cations relies essentially on the data obtained in matrix EPR studies. From the viewpoint of basic radiation chemistry, a main impact of these studies was concerned with a new concept of selectivity and fine tuning at early stages of the radiation-induced processes in molecular solids and polymers [19–22]. An outline of the results obtained in the EPR spectroscopic studies of the radiation-induced organic radical cations and neutral radicals in low-temperature matrices during the past two decades is given in a recent review [23].

It is worth noting that, in addition to identification of radiation induced paramagnetic species and quantification of their yields, EPR spectroscopy may provide information concerning fine details of their dynamics and interaction with solid environment. These data are very important for different aspect of solid-state chemistry and chemical physics, including better understanding of dynamics of defects and impurities in solids, chemical reactions in constrained environment, and peculiarities of radiation damage in organized molecular materials.

Beyond any doubts, the EPR spectroscopy provides many opportunities for getting structural and kinetic information on different aspects of the radiation chemistry and physics of solids. Nevertheless, this method certainly has its own limitations, and it is important to use some complementary techniques. The most common choice is using electronic absorption (UV/Vis) spectroscopy. In the case of good absorbers, the sensitivity of UV/Vis spectroscopy is comparable to EPR. A combination of these two methods has been applied extensively to identification of radical ions [24] and investigation of the photochemical reactions of the radiation-induced radicals (both neutral and charged) [25, 26]. Meanwhile, it should be noted that the electronic absorption spectra of radical ions in solid matrices usually show broad bands, which give no detailed structural information. Furthermore, the absorptions of neutral aliphatic radicals are often not characteristic. Another possibility is to combine EPR with IR (vibrational) spectroscopy, which is highly informative from the structural point of view. In addition to direct information on the vibrational spectra of paramagnetic intermediates, IR spectroscopy may be very useful for indirect monitoring of their formation and reactions since it makes it possible to detect virtually all kinds of diamagnetic species, invisible by EPR (parent and product molecules, diamagnetic ions and complexes, etc.). However, up to now, this combination is not widely used in radiation chemistry because of experimental problems. Possible solutions are discussed below.

This chapter will describe mainly the results of recent model studies on structure and reactivity of the radiation-induced radicals and radical ions in low-temperature matrices carried out in our laboratory. Particularly, it will focus on the following aspects: (i) experimental approach and design for combined EPR/IR spectroscopic studies; (ii) application of the combined approach to the studies of radiation-induced intermediates and their reactions in the noble gas matrices; (iii) EPR studies of the matrix effects in the radiation chemistry of solids.

5.2 Experimental Approaches

5.2.1 *Low-Temperature Stabilization and Matrix Isolation*

5.2.1.1 General Overview

Generally speaking, the radiation-induced paramagnetic defects (including atoms, charged species, and neutral radicals) may be trapped in crystals and glasses at ambient temperatures, because their decay due to diffusion and chemical reactions is often suppressed in rigid media. Nevertheless, in the case of molecular solids and polymers, low temperatures are often used to prevent secondary reactions, which may occur due to local relaxation processes. This approach can be described as *low-temperature stabilization*. Most commonly, the low-temperature EPR studies of radiation-induced radicals in solids are carried out at 77 K using standard equipment for irradiation and measurements, which is commercially available for tens of years. Using “helium-range” temperatures (below 77 K) may be significant for both trapping of highly reactive intermediates and visualisation of spatial distribution of the primary chemical events [19–21, 27–32].

The method of low-temperature stabilization may be applied to the “common” solids irradiated at low temperatures. Meanwhile, the term *low temperature solids* often has a somewhat different meaning. It implies the substances, which are liquids or gases under ambient conditions, but can become solids at a certain low temperature. Actually, it applies to any kind of substance. This is just the question, how low the temperature should be in each case. Again, a moderately low temperature (77 K) is usually sufficient for molecular substances, which are liquids at room temperature. Helium-range temperatures are needed to make solids from simple gases (e.g., hydrogen, nitrogen, methane, carbon monoxide). The most important use of such solidified gases is *matrix isolation*.

The matrix isolation method introduced 60 years ago [33] is a widely used experimental approach for the studies of highly reactive intermediates. In general, it implies trapping of a reactive species (e.g., atom, radical, or radical ion) in a rigid, chemically inert environment at low temperature. Classic procedure makes use of deposited matrices obtained mainly from noble gases; however, “compromise” techniques using dilute frozen solutions are also often referred to as matrix isolation methods. The matrices used for the EPR studies of radiation-induced intermediates should meet a num-

Table 5.1 Physical characteristics of solid noble gas matrices significant for EPR and IR studies of the radiation-induced radicals

Matrix	Melting point, K	Operating temperature range, K	IP, eV	Polarizability, nm ³	Magnetic nuclei
Ne	24.6	Up to 11	21.56	4×10^{-4}	²¹ Ne (<i>I</i> =3/2, 0.27%)
Ar	84	Up to 39–42	15.75	1.64×10^{-3}	–
Kr	116	Up to 60	14	2.48×10^{-3}	⁸³ Kr (<i>I</i> =9/2)
Xe	164	Up to 90–100	12.13	4.16×10^{-3}	¹²⁹ Xe (<i>I</i> =1/2, 26.44%); ¹³¹ Xe (<i>I</i> =3/2, 21.18%)
N ₂	63	Up to 35	14.53	1.76×10^{-3}	¹⁴ N (<i>I</i> =1, 99.6%)

ber of specific requirements. First, the matrix substance should have relatively high ionization and/or excitation potential. Indeed, the high-energy radiation is absorbed primarily by the matrix, and the species from guest molecules are produced only by positive hole or excitation transfer. Second, the EPR spectra of paramagnetic species produced from matrix radiolysis should not overlap with the spectra of radicals under study (ideally, the matrix should yield no paramagnetic species under irradiation). Third, the matrix should have weak interactions with the trapped species. In the case of EPR studies, it implies primarily that magnetic interactions of trapped radical with matrix nuclei should be negligible (the best choice is matrix without magnetic nuclei). Another important characteristic is low polarizability of matrix atoms or molecules. Although the polarizability has no direct effect on the EPR spectra, it may result in significant disturbance of the electronic structure of the trapped species, in particular, for radical ions. This property becomes even more crucial, if one considers IR spectroscopy as a complementary tool (see Sect. 5.2.3).

Essential characteristics of inert matrices typically used for matrix isolation are shown in Table 5.1.

5.2.1.2 Noble Gas Matrices

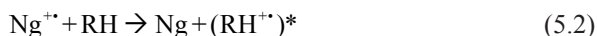
Solid noble gases are classical media for matrix isolation studies used during several decades. Meanwhile, up to recently, the application of solid noble gas matrices to the EPR investigations of paramagnetic species produced by the solid-state radiolysis was limited. First EPR studies of methane radiolysis in solid argon, krypton and xenon at 4.2 K reported by Bouldin and Gordy [34] used frozen solution technique (“ampoule method”) rather than the classical matrix isolation procedure. Several other groups applied similar technique to radiolysis of larger hydrocarbons in solid noble gases [35–37] and Qin and Trifunac reported the EPR spectrum of 1,1,2,2-tetramethylcyclopropane radical cation in a frozen xenon solution containing an electron scavenger at 77 K [38]. Obvious limitations of the “ampoule” method are concerned with aggregation of solute molecules since the solute–solute interactions are much stronger than the solute–matrix interactions.

Classical matrix isolation procedure was applied by Knight and co-workers for the studies of inorganic and small organic radical cations in neon matrices [9, 39]. Early studies of this group used a number of different techniques for generation of

radical ions, including in-situ photoionization, electron bombardment, pulsed laser and discharge treatment during the matrix deposition. It was found that the X-ray radiolysis of solid deposited matrices was quite effective for producing organic radical cations in high concentrations [11, 40]. However the matrix isolation studies of organic radical cations in neon were restricted to a few small species.

Somewhat surprisingly, the use of solid argon for the EPR studies of the radiation-induced radicals and radical ions was rather limited. An example of application of this matrix for obtaining high-resolution EPR spectra using X-ray radiolysis of isolated methane and its isotopomers was presented by Yamada et al. [41].

During the last two decades we carried out extensive studies aimed at characterization of intermediates resulting from irradiation of various organic molecules in different solid noble gas matrices. Experimental technique and apparatus used in these studies are described in Sect. 5.2.3. In order to get additional structural and mechanistic information, EPR spectroscopy was complemented by the IR spectroscopic studies, when it was practicable (see Sect. 5.2.3). The results of these studies are discussed in Sects. 5.3 and 5.4 below; more details can also be found in several reviews [12, 13, 23]. Our findings suggest the following basic scheme of the radiation-induced transformations of isolated molecules:



Here Ng denotes a noble gas atom, and RH is an organic molecule. An important feature of this mechanism is that the positive hole transfer (5.2) generally leads to formation of *unrelaxed* (“hot”) radical cation marked as $(\text{RH}^{\bullet+})^*$. This effect is due to excess energy resulting from highly exothermic nature of the positive hole transfer from noble gas to RH. The excess energy can be estimated roughly from the difference in ionization potentials of the Ng atom and RH molecule (ΔIP). The typical ΔIP values are 2–3, 4–5 and 5.5–7 eV for Ng = Xe, Kr, and Ar, respectively. Formal meaning of reaction (5.3) is stabilization (relaxation) of the radical cation in matrix, which competes with “hot” reaction channels (5.4), namely, fragmentation or isomerization. The significance of the “hot” reactions (in particular, in solid argon) and their dependence on molecular structure have been demonstrated in our studies [12–18, 42, 43] as well as in some earlier works of other groups [37, 44].

Recombination of radical cations with electrons yields neutral excited states, which may dissociate yielding either hydrogen atoms (5.6) or other kinds of products (5.7). It is worth noting that the hydrogen atoms can possess sufficient kinetic energy to escape from the matrix cage, whereas the skeleton bond rupture is suppressed due to the cage effect. Thus, in most cases, reaction (5.7) represents formation of molecular products rather than heavy radicals [45].

In the presence of an electron scavenger S, the ion–electron recombination (5.5) is ceased due to electron capture:



As a result, the radical cation may be trapped in the matrix and detected by EPR spectroscopy. A strong effect of electron scavenger [12, 46] clearly suggests that the main primary process is positive hole transfer rather than excitation transfer for most kinds of organic molecules. Indeed, in the absence of an electron scavenger, the yields of trapped radicals and hydrogen atoms were nearly balanced (in the case of xenon) or, at least, comparable (for argon and krypton matrices). In all the cases, addition of electron scavengers resulted in drastic decrease in the yield of trapped H atoms (by one or two orders of magnitude). This effect may be used as criterion of electron scavenging (with Freons, high efficiency was achieved at low scavenger concentration, typically 0.1–0.2 mol%). Meanwhile, the exciton transfer mechanism cannot be excluded in the case of small molecules with high IP, in particular, inorganic species.

Comparing different noble gas matrices from the spectroscopic point of view, one may conclude that argon appears to be the most suitable matrix for the EPR studies of moderate-size radicals and radical ions, because natural argon contains no isotopes with magnetic nuclei ($I \neq 0$). As a result, the EPR spectra in solid argon are often well resolved and exhibit sharp lines. A common shortcoming of the argon matrix is the limited range of its thermal stability (see Table 5.1). On the other hand, xenon offers a much wider temperature range, which makes it possible to study dynamics and reactions of the trapped radical species. The problem is that natural xenon contains large amounts of magnetic isotopes: ^{129}Xe ($I=1/2$) and ^{131}Xe ($I=3/2$). This often leads to severe broadening of the EPR signals from trapped radicals, which means significant loss in resolution and sensitivity. In order to overcome this limitation, recently we suggested to use a specific isotopically pure non-magnetic xenon matrix of ^{136}Xe ($I=0$) [47, 48]. In fact, this matrix can be described as an “*argon-like xenon*” for the EPR spectroscopy. Indeed, its magnetic properties are similar to those of argon, but it is still xenon in terms of other properties. The use of monoisotopic and isotopically enriched xenon matrices will be illustrated in Sect. 5.3.1.

In summary, matrix isolation in solid noble gases can be very useful for basic studies of the primary radiation-induced processes in solids. It is worthwhile noting that physical characteristics of the noble gas matrices (IP, polarizability, rigidity) vary over a wide range when turning from neon to argon, krypton and xenon, which allows one to follow the most general matrix effects. The main disadvantage of this

method is concerned with a rather complex experimental procedure and relatively high cost of the equipment for matrix isolation studies.

5.2.1.3 Low-Temperature Molecular Matrices

Simple molecular hosts (e.g., N₂, CH₄, or CO) can be used for matrix isolation studies in the frame of the classical approach described above for noble gases. However, the application of such media to the studies of radiation-induced species is not practicable, because they have virtually no advantages in comparison with noble gases and may give radiolysis products. An alternative way is using a compromise approach based on irradiation of dilute frozen solutions. A common advantage of such method is the very simple experimental design, because most solutions are quite rigid at 77 K and may be studied with “ampoule” technique in liquid nitrogen. One should bear in mind that the frozen solutions definitely fail to meet basic criteria of matrix isolation outlined above. Indeed, the “matrices” (solvents) are not inert, they give radiolysis products and may strongly interact with the radiation-induced species. Furthermore, even the assumption of “isolation” is often questionable, because the solute concentrations used in these studies are sometimes rather high (ca. 1 mol. %) and the microstructure of frozen solutions is unknown. Nevertheless, the frozen solutions may be very useful for some specific purposes, in particular for selective stabilization and characterization of the radiation-induced radical ions. Here we will briefly outline two main approaches of this kind, developed for the studies of hole and electron species by EPR spectroscopy.

As mentioned in the Introduction, the information on the structure of unstable radiation-induced cations is essentially available due to the so-called Freon matrix technique. In fact, it is a modification of the halocarbon method for optical spectroscopic studies of radical cations introduced by Shida and Hamill [49]. Freons are chemically inert fluorinated halocarbons widely used in various technologies. A general scheme of the method for Freon-11 may be represented as follows:



Reaction (5.9) implies that the positive hole is mobile in the matrix and may be transferred to the solute molecule with lower IP. The problem of background EPR signal from matrix radicals is not crucial, because fluorinated radicals yield very broad and weak signals in macroscopically disordered media due to very large anisotropy of the ¹⁹F hyperfine coupling. Other popular freons for such studies are the isomers of trifluorotrchloroethane (Freon-113), CFCl₂CF₂Cl and CF₃CCl₃. The former matrix is especially useful for the studies of ion–molecule reactions, whereas the latter one

may be helpful for investigation of unimolecular transformations of the radical cations. The mixture of $\text{CF}_2\text{BrCF}_2\text{Br}$ (Freon-114B2) and Freon-11 yielding transparent glasses of good optical quality [50] was also used for combined EPR/UV-Vis studies. In addition to freons, some other fluorinated compounds (in particular, perfluoroalkanes and SF_6) were applied for the EPR studies of radical cations.

The most important progress in the studies of organic radical cations using the Freon matrix technique was achieved in the 1980ths [6–8] and later work in this field is outlined briefly in a recent review [23].

In contrast to freons, the matrices used for stabilization of the radiation-induced excess electrons and radical anions should basically trap the hole and not react with electrons. In this case, the scheme of the radiation-induced processes may be written in the following form:



Here RH denotes matrix and X is a solute molecule, which may yield radical anions. The hole is supposed to convert to neutral matrix radical due to fast deprotonation reaction (5.13), whereas the excess electron be either physically trapped in matrix (5.14) or react with solute X (5.15). Actually, reaction (5.15) is similar to (5.7) and different symbols (S and X) are used just to mark different role of scavengers in specific experiments (S is used to prevent the recombination and, thus, to isolate radical cation, while $\text{X}^{\cdot-}$ is the target species). The above-given scheme works well for the low temperature aqueous or organic glasses, where RH may be water, alcohol, ether, or hydrocarbon [8]. A significant complication in using EPR spectroscopy for the studies of radical anions produced by radiolysis in molecular glasses results from the interference of intense signal from the matrix radicals. In certain cases, combination with other spectroscopic methods may be helpful.

It is worth noting that freons and low-temperature molecular glasses as matrices have one important common feature. In both cases, the matrix itself plays an active role reacting either with excess electrons or with positive holes produced by irradiation. It is different from noble gas matrices, which are supposed to serve only as “transport systems” for holes, electrons, and excitons (see above). Furthermore, the matrix interactions with radical cations and radical anions are not negligible and, in the latter case, they may be quite crucial for stabilization of the trapped species (this aspect and its importance for basic radiation chemistry will be discussed in view of our recent related studies in Sect. 5.5). Thus the methods using molecular media as described above should be referred to as *matrix stabilization* rather than matrix isolation technique.

5.2.2 Fast Electron and X-ray Irradiation

In many cases, early EPR studies on the EPR spectroscopy of radiation-induced paramagnetic specie in the low-temperature matrices were carried out using γ -irradiation (typically, with a ^{60}Co source). This was a practical solution for irradiation of the samples in ampoules immersed in liquid nitrogen, in view of high homogeneity of dose rate and appropriate irradiation time to reach the doses of 1–10 kGy. However, this method is not good for more complex configurations, when local irradiation of the sample is preferable and, in particular, for matrix isolation studies using the classical approach. Furthermore, rapidly increasing cost of isotope irradiators and rigid safety regulations for their use in most countries make these sources less attractive for basic research carried out in university laboratories.

The most common alternatives are fast electrons or X-rays. Generation of these types of radiation does not imply using any radioactive materials and, in both cases, the irradiation configuration may be arranged to produce local effect on the studied samples. Both fast electrons and X-rays were used in the studies carried out in our laboratory. Regarding the comparison of different irradiation sources, first, it is worth noting that the chemical effects induced by fast electrons and high-energy photons (γ -rays and X-rays) are basically similar. In all these cases, the ionization and excitation in solid matter results mainly from secondary electrons. Moreover, all these types of radiation are characterized by relatively low linear energy transfer (LET) values, so the spatial distribution of primary events is qualitative similar, and, in first approximation, one should not expect any specific “track effects”, which may occur for the high LET radiations. Nevertheless, there are important physical and technical differences between fast electrons and X-rays, which should be considered.

From a physical point of view, one should bear in mind a basic difference in the energy absorption mechanisms. In the case of fast electron irradiation, the absorption is mainly determined by inelastic collisions with the electrons of the medium (ionization losses) and typically there is a rather weak effect of the chemical nature of absorber. In other words, the absorbed dose is roughly similar for different substances irradiated under the same conditions. The same conclusion is valid for irradiation with γ -rays ($E \sim 1$ MeV), because the basic mechanism of photon interaction with matter in this energy range is Compton scattering, and the mass absorption coefficients for different substances are rather similar. Meanwhile, in the case of X-rays with typical energy of 20–50 keV, the principal mechanism is photoelectric absorption, which implies dramatic effect of the absorber nature on the absorption cross-section. If the photon energy is above the K-edge, the atomic absorption cross-section for photoelectric effect is roughly proportional to Z^4/E_p^3 [51] and the mass absorption coefficient increases approximately as Z^3 (Z is atomic number of the absorber and E_p is photon energy). The effect of element composition of the matrix on absorption of photons with the energy of 20 to 40 keV is illustrated by Table 5.2 (the data for different elements and photon energies may be found elsewhere [52]).

Table 5.2 Mass absorption coefficients (in cm²/g) for some typical matrix media (calculated from the data presented in Ref. [52])

E_p , keV	H ₂ O	C ₆ H ₁₄	C ₂ H ₅ OH	MTHF	CFCl ₃	SF ₆	Ne	Ar	Kr	Xe
20	0.550	0.189	0.333	0.273	5.74	2.05	1.32	8.97	35.1	24.7
30	0.156	0.0583	0.0971	0.0804	1.68	0.588	0.368	2.31	13.65	7.97
40	0.0695	0.0317	0.0466	0.0400	0.695	0.245	0.153	0.991	6.54	9.32

The peculiarities for xenon at $E=20$ and 30 keV are explained by the fact that the K-edge for xenon lies above 30 keV. In all other cases, the mass-absorption coefficients increase drastically with increasing effective atomic number of absorber and decreasing photon energy. In practice, it means that the absorbed dose rate in different matrices may differ by more than two orders of magnitude, when the samples are irradiated with X-rays in the same geometry. This effect is often ignored in qualitative structural studies. However, it should be definitely taken into account for proper planning of the experiment. Indeed, the half attenuation length for the photons with $E=20$ keV is 0.9 cm for water and only 120 μm for krypton. It implies that aqueous (or organic) substances may be used in the form of massive samples, which should be irradiated for a rather long time to produce sufficient amount of the trapped radicals. On the other hand, the noble gas matrices should be prepared as thin deposited films (up to 100 μm) and irradiated for a rather short time. This difference justifies effective use of X-rays for the studies of both molecular glasses (frozen solutions) and solid noble gas matrices.

From technical point of view, there are two possible arrangements for fast electron irradiation. The sources of accelerated electrons with relatively low energy (below 100 keV) can be used for irradiation of thin solid films, including polymers and deposited matrices. In this case, the source may be mounted in the cryostat. A few examples of such experimental set-ups used for IR spectroscopic studies can be found in the literature [53, 54]. However, to my knowledge, they were not applied for EPR spectroscopy of irradiated low-temperature solids. It should be mentioned that low-energy electron accelerators cannot be used for irradiation of frozen solutions in liquid nitrogen because of very low penetration depth of radiation. Another configuration implies use of relatively large commercial electron accelerators producing fast electrons with the energy of ca. 1 MeV or above. In this case, the task is to make proper arrangement of the sample and the cryostat in respect to the electron beam. Such design has been developed at the Karpov Institute using an EG-2.5 Van-de-Graaf accelerator (typical electron energy 1 – 1.2 MeV) [12, 55]. A common advantage of using electron accelerators is easy tunability of the beam parameters, that is, electron energy and beam current. Thus, it is possible to vary the penetration depth and the dose rate over a relatively wide range. On the other hand, there are significant limitations due to high cost of equipment and demand for a special radiation protection system. Furthermore, even the 1 -MeV electrons are not really suitable for irradiation of the frozen solutions in ampoules.

Using commercial X-ray tubes as radiation sources appears to be a very reasonable solution for university laboratories, which may be applied to irradiation of both standard ampoules in liquid nitrogen and thin solid films in the specific cryostat

configurations. As mentioned above, a practicable range of photon energy used for these purposes is 20–50 keV. It is worth noting that the X-ray tubes emit continuous (“white”) spectrum of radiation with maximum of spectral distribution at $E' = 2E_0/3$ (E_0 is the maximum photon energy determined by the applied voltage U_0). Thus, the U_0 value should be typically between 30 and 75 kV. A tube with tungsten anode (operating voltage up to 50 kV, anode current 70–100 mA) was found to be quite useful for different-type experiments in our laboratory. In the case of irradiation of ampoule samples in liquid nitrogen (frozen solutions), the Dewar with the studied sample can be positioned very close to the tube outlet window. Typical absorbed dose rate for this arrangement was estimated as ca. 3 Gy/s for aqueous samples and ca. 30 Gy/s for freons. This range is quite reasonable in terms of irradiation time to produce sufficient concentration of trapped paramagnetic species (typically, from several minutes to 1 h). A different situation occurs for irradiation of deposited samples in the cryostats, because the distance r between the sample and the outlet tube window cannot be small. As a result, the dose rate decreases significantly since the intensity of radiation decreases as r^2 . The estimations in our experimental configuration have shown that the dose rate in water is below 1 Gy/s. At first glance, it may require very long irradiation time to get reasonable absorbed dose. However, due to very strong dependence of absorption cross-section on atomic number of the absorber (see Table 5.2), the dose rate in noble gas matrices is much higher under similar conditions (up to 10–50 Gy/s, depending on the noble gas nature). Thus, the required irradiation time is again reasonable (it is also the case for deposited freons, Table 5.2). It should be noted that for krypton, typical irradiation time (5–10 min) was even shorter than that used with electron accelerator.

Generally, we can conclude that there is no qualitative difference between the results obtained with fast electrons and X-rays. From a practical point of view, using X-rays may be even preferable for EPR and combined EPR/IR studies outlined in this chapter. More experimental details will be given in the next sub-section.

5.2.3 Combination of EPR and IR Spectroscopy

5.2.3.1 Motivation and Problems

As mentioned in the Introduction, the combination of EPR and UV/Vis spectroscopy was often used for characterization of the radiation-induced intermediates, in particular, radical ions. This approach is rather straightforward from the experimental viewpoint, because both methods can be applied to the same sample. However, as stated above, the structural information available from such combination is relatively limited. The combination of EPR with IR (vibrational) spectroscopy looks attractive for several reasons:

1. IR spectroscopy is a universal tool to study different kinds of species, independent of their charge and spin. Indeed, only isolated atoms and homonuclear diatomic molecules are invisible by this method, and all the other species have,

at least, one IR-active vibration. Furthermore, the vibrational spectra of molecules and radicals may exhibit a unique characteristic set of absorptions and the corresponding features may be relatively narrow and resolved even in the solid phase.

2. The experimental information on vibrational spectra of radicals and radical ions is still rather limited. These data can be useful for different areas beyond radiation chemistry (e.g., atmospheric chemistry and astrochemistry, combustion, catalysis). Comparison with the EPR results obtained under similar conditions is crucial for unambiguous assignment of the observed IR absorptions to radicals.
3. Although EPR spectroscopy is usually the most informative method for characterization of free radicals in solids, it may fail to detect some species of this kind. For instance, the radicals and radical ions with nearly degenerate orbital states may give very broad and weak EPR signals in macroscopically disordered solids due to extremely large anisotropy of the g -factor. In such cases, the IR spectroscopy can be helpful.
4. The combination of EPR and IR spectroscopy is especially useful for detailed, step-by-step characterization of the radiation-induced transformations in solids. IR spectroscopy makes it possible to monitor consumption of the parent molecules and formation of diamagnetic final products, while EPR spectroscopy provides direct information on the behaviour of paramagnetic intermediates. It is worth noting that using only EPR spectroscopy may lead to missing significant reaction channels and wrong estimation of overall radiation stability.

In spite of obvious potential benefits of the combined approach, in fact, its application to the studies of radiation effects in molecular solids was quite limited due to serious experimental problems, both general and technical.

First, the sensitivity of these two methods is often supposed to be quite different. Indeed, the detection limit for conventional IR spectroscopy based on direct spectrophotometric scheme is typically higher than that of EPR spectroscopy by, at least, two orders of magnitude. It suggests using much higher doses for the IR spectroscopic studies of the radiation effects in solids that, in turn, may lead to involvement of secondary processes. The situation has changed with the development of the Fourier Transform IR (FTIR) spectroscopy, which has higher sensitivity and much shorter measurement time. Meanwhile, even in this case, comparable sensitivity of the two methods is achieved only for intense and relatively narrow IR absorptions. Thus, in most cases, only a few vibrational features can be observed in the experiment, which may be insufficient for unequivocal assignment.

Second, the IR absorption of the initial sample may present a serious problem. It is the back side of universality of IR spectroscopy mentioned above. Indeed, if the solid matrix has intense absorption bands, the sample becomes virtually non-transparent in some regions of the IR spectrum, even for relatively thin layers (several tens of microns). On the other hand, using very thin films again turns us to the problem of detection limit at moderate absorbed doses.

Finally, the experimental arrangement for EPR and IR spectroscopy at low temperatures is typically quite different. The EPR spectra are usually measured in the ampoules made from high-purity quartz or special radiation-resistant glass, which

are transparent in UV and visible regions, but not in the mid-IR region. In fact, there are no commercially available cells, which would be suitable for irradiation, EPR and IR measurements of the solid samples at low-temperatures.

Taking into account the above mentioned complications, one may conclude that combined studies of radiation effects in frozen molecular liquids or solutions by EPR and IR spectroscopy are usually not practicable. However, this is somewhat different, if we consider matrix isolation, particularly, in solid noble gas matrices. In this case, the matrix itself does not absorb in the IR region and the bands from parent isolated molecules are not so strong to prevent the observation of the radiation-induced species. Furthermore, the IR absorptions in matrices are often narrow enough. In addition, using deposited samples instead of frozen solutions may provide more similar conditions for EPR and IR spectroscopic measurements, if they are carried out in special cryostats, as described below.

5.2.3.2 Experimental Cryostats for Combined Studies

Generally speaking, the studies of radiation-induced effects under the conditions of matrix isolation are not routine experiments and they are carried out with custom-made equipment. In order to use combination of EPR and IR spectroscopy for these purposes, we have designed two versions of complexes of cryostats. An early version made at the Karpov Institute was based on a continuous-flow scheme with the lowest attainable temperatures of 8–12 K (the details can be found elsewhere [12]). These cryostats were designed for irradiation with fast electrons using a Van-de-Graaf accelerator ($E \sim 1$ MeV). The latest version of complex of portable cryostats in our laboratory at Moscow State University is based on closed-cycle cryocoolers (sample temperature down to ca. 6 K). The cryostats can be applied for both X-ray and fast electron irradiation. Currently they are used with an X-ray tube with a tungsten anode, typically operated at anode voltage of 32–33 kV and anode current of 70–80 mA.

The scheme of cryostats for EPR and IR spectroscopic studies is shown in Fig. 5.1. As stated above, it is virtually impossible to make EPR and IR measurements in the same cryostat in a single experiment, so the complex includes two separate cryostats. In this case, the term “combination” implies close similarity of all experimental procedures used in the two separate experiments for EPR and IR spectroscopy, namely, similar deposition conditions with the same line and same source mixture, similar irradiation geometry and dose rate, and similar sample temperature, strictly controlled at all stages. This is important because of strong effect of the experimental details on the sample microstructure and kinetic behaviour of isolated species under the conditions of matrix isolation experiment.

The EPR cryostat (Fig. 5.1, top) contains an original cylindrical (H_{011} mode) vacuum resonator cavity. A sample is obtained by slow controlled deposition of gaseous mixture onto the tip of a 4-mm cylindrical sapphire rod inserted into the cavity. There are two options: (a) a truncated conical tip, which corresponds to the symmetry of the resonator cavity and (b) a cut-off at 45° (shown in Fig. 5.1).

The latter geometry is more suitable for photobleaching, which can be carried out through the quartz window. If the deposition is slow enough and the nozzle comes close to the tip, the shape of the growing sample follows the tip shape. In this case, the radiation-induced radicals exhibit random orientation in macroscopic scale. For this reason, the effect of preferential orientation often observed in the spot-like samples obtained on a flat rod [9] is of minor importance, especially for the samples prepared on the truncated conical tip. After the deposition is complete, the sample is irradiated with X-rays through a thin aluminium foil window, and then the cavity is matched to the microwave bridge of spectrometer.

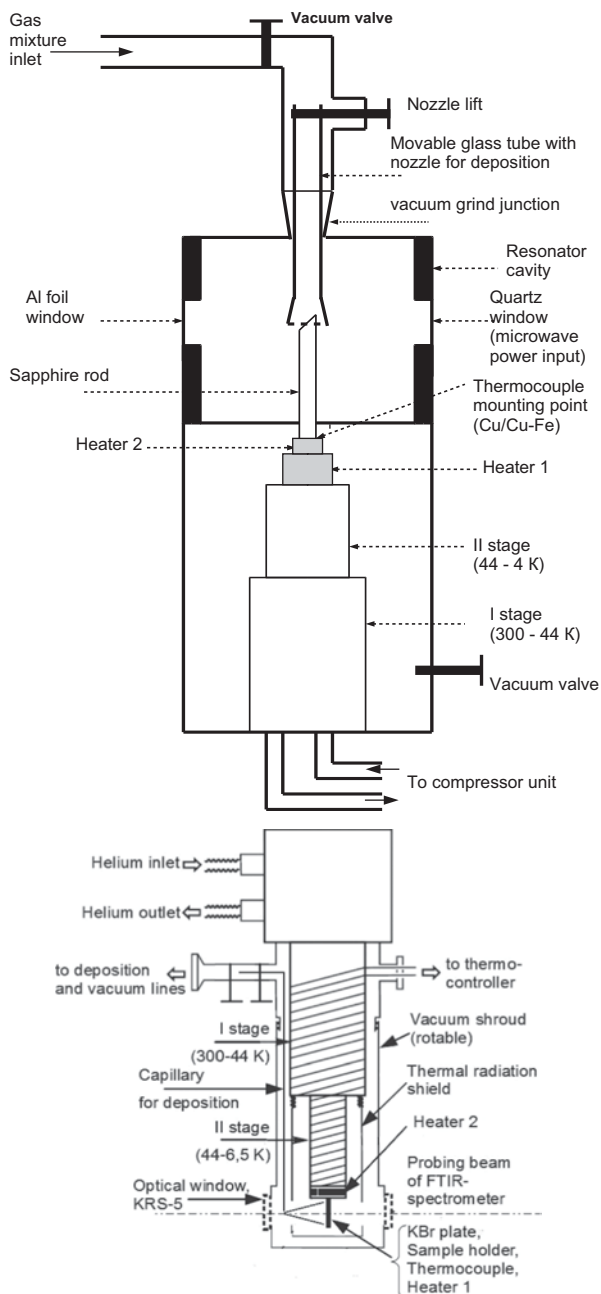
The cryostat for IR studies (Fig. 5.1, bottom) designed under similar basic principles contains a cooled KBr plate for sample deposition and optical windows for IR spectra measurements made from KRS-5 (mixed TlI/TlBr). The foil window for irradiation is the same as that in the EPR cryostat. In addition, there are two quartz windows, which can be used for photolysis, or for UV/Vis spectral measurements in the same experiment.

5.3 Formation and Reactions of Hydrogen Atoms in Low-Temperature Solids

The hydrogen atom is the simplest and, probably, the most common radiation-induced intermediate, which can be produced from many kinds of different molecules, both organic and inorganic. As mentioned above, the hydrogen atoms resulting from dissociation of excited molecules may have significant kinetic energy to escape from the matrix cage, even in rigid solids. For this reason, production of hydrogen atoms often predominates over the skeleton bond cleavage yielding heavy radical fragments in the solid phase. The studies on trapping and dynamics of hydrogen atoms in solid hosts present considerable interest for general modeling of the behaviour of guest atoms in solid hosts. Due to extremely high hyperfine coupling constant, these species can be used as very sensitive EPR probes for the environment effects. On the other hand, chemical reactions of H atoms in rigid media are of basic importance for the radiation chemistry of molecules in solids.

Hydrogen atoms generated by radiolysis can be trapped in different media at cryogenic temperatures (e. g., in water ice, glassy aqueous acids and salt solutions, solid CH_4 , NH_3 , HF, etc.), whereas in most organic solids and polymers they are not observed due to chemical reactions, possibly involving tunnelling mechanism. The results of early EPR studies on radiolytically produced H and D atoms were summarized by Pshchetskii et al. [4]. Later, several groups investigated production and reactions of hydrogen atoms upon radiolysis of some hydrogenated molecules (mainly, hydrocarbons) in solid noble gas matrices using EPR spectroscopy [35–37]. Nevertheless, these studies still left a number of unresolved issues concerning the trapping, distribution, dynamics and reactivity of hydrogen atoms in solid noble gases. An important limitation of EPR studies, particularly, in the assessment of lost channels for H atoms results from the fact that the diamagnetic reaction products are

Fig. 5.1 Scheme of a custom-made complex for spectroscopic matrix isolation studies of the radiation-induced species (Laboratory of radiation chemistry, Lomonosov Moscow State University, 2010) (Adapted from Ref. [23] with kind permission of © Springer, 2013)



invisible by EPR. Here we will focus on the recent studies of production, distribution and reactions of H atoms in solid noble gases in our laboratory as monitored by a combination of EPR and IR spectroscopy.

5.3.1 *Trapping and Spatial Distribution of Radiolytic H Atoms*

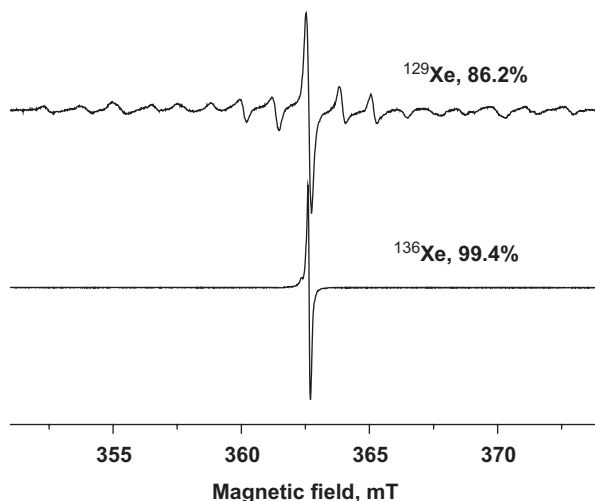
Generally speaking, the radiolytic hydrogen atoms can be stabilized in solid noble gases due to their trapping in specific sites of the matrix lattice, namely, interstitial sites of various symmetry and substitutional sites. The atoms trapped in different sites are distinguishable by EPR spectroscopy because of the difference in both g -value and hyperfine coupling constant [56]. On the basis of comparative studies of the EPR spectra of H atoms produced by photolysis and radiolysis in solid argon at 4.2 K, it was suggested that the relative population of interstitial traps increased with increasing kinetic energy of H atoms [37]. This finding might be of common interest for an understanding of the dynamics of the radiation-induced species in solids. However, this effect could depend strongly on the sample morphology.

Another basic issue, which may be probed by EPR spectroscopy, is the spatial distribution of radiolytic H atoms relative to their counterparts (radicals). Actually, it is a matter of long-term discussion, based mainly on indirect arguments. An important direct finding for the radiolysis of the CH_4/Ar system was reported by Komaguchi et al. [57]. The results of this study suggest mainly distant distribution of fragments with minor contribution from close radical pairs, which was interpreted as an evidence for two different mechanisms. The role of precursor nature and the applicability of this conclusion to other noble gas hosts were unclear.

As mentioned above, the argon matrix is particularly good for structural studies, whereas solid xenon is a more suitable host, if we are interested mainly in dynamics and chemistry [58]. Meanwhile, the interpretation of the EPR spectra of H atoms trapped in solid xenon remained controversial for a long time. In the case of xenon, the main problem is a very complicated spectral pattern due to extended super-hyperfine structure resulting from strong anisotropic magnetic interaction of the unpaired electron with surrounding magnetic matrix nuclei abundant in natural xenon (see Table 5.1). In order to overcome this difficulty, we have used a series of monoisotopic and isotopically enriched xenon matrices [47, 48]. The effect of matrix isotopic composition on the EPR spectra of radiolytically produced H atoms in solid xenon is illustrated by Fig. 5.2.

The analysis of these results [48] revealed clearly that more than 99% of H atoms generated by radiolysis from various precursors (H_2O , C_2H_2 , alkanes, etc.) was trapped in octahedral (O_h) interstitial sites of the xenon lattice. Using controlled doping of non-magnetic ^{136}Xe matrix with a small amount of magnetic isotope (^{129}Xe , $I=1/2$), it was possible to determine the parameters of the super-hyperfine coupling with ^{129}Xe nuclei for interstitially trapped H atoms: $|A_{\parallel}(^{129}\text{Xe})| = 136$ MHz; $|A_{\perp}(^{129}\text{Xe})| = 70.2$ MHz [48]. The population of other-type traps (presumably, substitutional) is quite minor (less than 1%).

Fig. 5.2 Effect of matrix isotopic composition on the high-field component of the EPR spectra of trapped H atoms produced by radiolysis of the C_2H_2/Xe system (1/2000) at 16 K (see Ref. [48] for details)



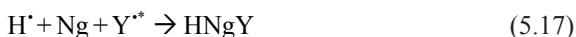
An important implication of this finding is concerned with different dynamics and reactivity of H atoms trapped in different sites. Indeed, it is known that the interstitially trapped H atoms in solid xenon can be thermally mobilized at ca. 40 K [48, 59] and they may react with different molecules and radicals stabilized in the matrix. On the other hand, the atoms trapped in substitutional sites decay gradually at higher temperatures and their reactivity is unclear. Thus, the radiolysis of different hydrogenated molecules in solid xenon is a very good source of potentially reactive trapped H atoms, which are “stored” in the O_h sites at low temperatures. Selective thermally induced mobilization of such atoms makes it possible to study chemical reactions in solid matrix and to prepare new radicals and molecules (see Sect. 5.3.2 and 5.4). It is worth noting that no difference in this aspect was found for the H atoms produced by fast electrons and X-rays. Furthermore, the spectral pattern reported for H atoms generated in solid xenon by photolysis [60] and radiolysis is rather similar, which suggest similarity of trapping site nature, independent of the generation method and initial excess energy of H atoms.

Using monoisotopic ^{136}Xe matrix also provides some information on the spatial distribution of the radiolytic fragments. Judging from the observed EPR linewidth, it was concluded that most part of the H atoms are trapped at a long distance from their counterparts (ca. 4 nm, or more) [48]. This is consistent with the previous finding for the radiolysis of the CH_4/Ar system [57]. In any case, no evidence for close radical pairs was found for the radiolytic production of H atoms in solid xenon. Meanwhile, the previous studies on photolysis of matrix isolated molecules suggest that photodissociation is rather a local process, giving close pairs, both in argon [61] and, probably, in xenon [62]. If this difference between photolysis and radiolysis is real, it may imply basic difference in the formation mechanism.

5.3.2 Formation of Noble Gas Hydrides

Although IR spectroscopy cannot be used directly for detection of radiolytic H atoms, it is very useful as a complementary tool for detailed characterization of their reaction channels. Some of the reactions of mobilized hydrogen atoms result in formation of radicals due to hydrogen abstraction from saturated molecules (e.g., alkanes) or hydrogen addition to unsaturated molecules (e.g. C₂H₂ or CO), which can be observed by EPR [35, 36, 63]. The application of IR spectroscopy to characterization of such radicals will be considered in more detail in Sect. 5.4. Meanwhile, all the experimental studies indicate significance of “loss channels”, that is, the total number of paramagnetic species is reduced substantially upon decay of H atoms. This implies formation of diamagnetic products, invisible by EPR spectroscopy. The most common explanation is recombination yielding either initial parent molecules or molecular hydrogen. Meanwhile, recent works have revealed a very unusual additional reaction channel in xenon and krypton matrices leading to formation of novel-type molecules—noble gas hydrides.

The noble gas hydrides of general formula HNgY (Ng=Xe or Kr, Y—an electronegative fragment) were first discovered in 1995 in the IR spectroscopic studies of UV-photolysis of hydrogen halides in solid xenon and krypton [64, 65]. These species were characterized by intense characteristic absorptions in the IR spectra corresponding to the H–Ng stretching vibrations, which appeared after annealing of the photolyzed samples at 30–50 K. Very soon after this finding, it was demonstrated that the simplest molecule of this kind, xenon dihydride HXeH (Ng=Xe, Y=H) can be obtained with high yield using radiolysis of different hydrogenated precursors (organic molecules of RH type) in solid xenon [66]. The characteristic IR bands of HXeH appear at 1181 and 1166 cm⁻¹ (doublet is due to matrix site splitting [65, 66]). Initially, it was supposed that noble gas hydrides resulted from some ionic processes [64]. However, the effect of electron scavengers on the formation of HXeH made us suggest that this molecule could be produced from neutral hydrogen atoms mobilized upon annealing at 30–40 K [66]. This suggestion was confirmed by combined studies using EPR and IR spectroscopy, which showed good correlation between the thermal decay of H atoms observed by EPR and formation of xenon dihydride monitored by IR spectroscopy [46]. Furthermore, the quantitative analysis revealed that formation of HXeH represents one of the major channels of thermal reactions of H atoms in the studied systems, which was completely ignored in early works. An independent proof of the dominating role of the reactions of neutral H atoms in the formation of different HNgY compounds was obtained in the studies on HXeI [67]. These findings suggest the following common scheme of formation of noble gas hydrides:



It should be noted that reaction (5.17) represents an interaction of mobile H atoms with the Y' fragment trapped in a xenon lattice, so it is not a trimolecular process as

Table 5.3 Radiation-induced formation of noble gas hydrides as monitored by a combination of EPR and IR spectroscopy

Precursor molecule	Matrix	Radiation-induced radicals observed by EPR	Noble gas hydrides observed by IR spectroscopy	Reference
RH	Xenon	R \cdot , H \cdot	HXeH	[66]
H ₂ O	Xenon	H \cdot , OH \cdot	HXeH, HXeOH, HXeO \cdot	[71, 72]
C ₂ H ₂	Xenon	H \cdot , C ₂ H \cdot	HXeH, HXeCCH, HXeCC \cdot , HXeCCXeH	[73, 74]
H ₂ S	Xenon	H \cdot	HXeH, HXeSH	[72, 75]
C ₂ H ₂	Krypton	H \cdot , C ₂ H \cdot	HKrCCH	[72]

might be suggested from the formal description. The stability of HNgY (local minimum at the potential surface) is explained by a substantial kinetic barrier preventing it from conversion to global minimum corresponding to HY.

During the past two decades, the experimental and theoretical studies on formation and properties of noble gas xenon hydrides became a fascinating area of low-temperature chemistry and chemical physics. Most of these species were prepared by UV photolysis and characterized by IR spectroscopy. The results are covered in a number of reviews [68–70] and their detailed consideration is out of the scope of this book. Here we will briefly consider the use of combination of EPR and IR spectroscopy for monitoring of the radiation-induced formation of xenon and krypton hydrides in solid matrices. In fact, radiolysis is generally more universal tool for this purpose than photolysis, because it is not limited by the optical absorption spectrum of HY. The combined approach works well in this case, because the sensitivity of the two methods (EPR and IR spectroscopy) is really comparable due to extremely high intensity of the absorptions corresponding to the H–Ng stretching. Table 5.3 summarizes the results obtained with this approach.

The most important benefit of the combination is that, in certain cases, it allows complete monitoring of all the species produced in primary and secondary processes and quantitative evaluation of different competing channels. The studies on the C₂H₂/Xe system represent an illustrative example of such approach, where virtually all the products can be characterized by one or both methods. This case is of particular interest since the reactions of H atoms may yield four different xenon hydrides [74, 76]. Detailed studies of the radiolysis of this system with fast electrons (C₂H₂/Xe = 1/1000–1/2000, absorbed dose 10–80 kGy) led to the following reaction scheme [74]:





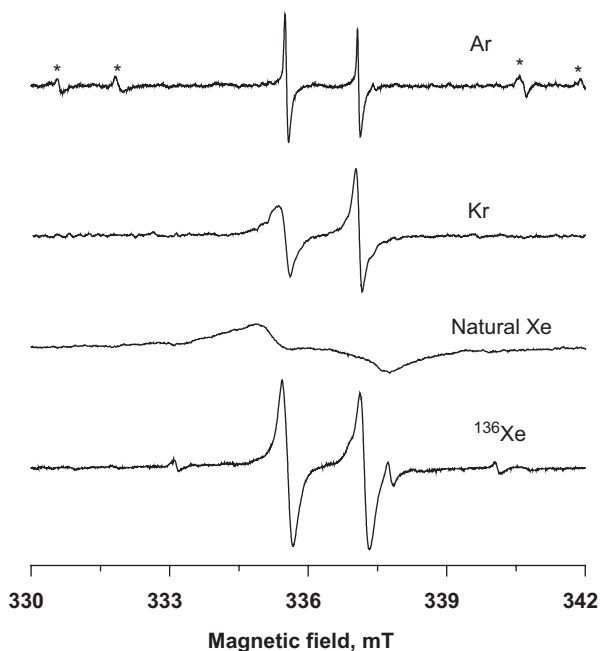
Reactions (5.18) and (5.19) occur upon radiolysis at low temperature, whereas reactions (5.20)–(5.23) take place upon annealing the sample at ca. 40 K. EPR spectroscopy makes it possible to monitor the behaviour of H atoms (in fact, the principal reagents), ethynyl and vinyl radicals. IR spectroscopy basically detects all the species, except for hydrogen atoms. As mentioned above, this method is the unique tool to observe xenon hydrides, all of which can be distinguished due to specific characteristic frequencies of H–Xe stretching vibrations (in the range of 1100–1500 cm^{-1} in this case). Meanwhile, both ethynyl and vinyl radicals also yield observable absorptions in the IR spectra (more details on vibrational spectroscopy of the radiation-induced radicals will be given in Sect. 5.4). The main qualitative conclusion derived from these studies is the lack of specific selectivity in the reactions of H atoms. In other words, it means that the reactions of thermally mobilized H atoms are diffusion-controlled and the relative yield of the products of reactions (5.20)–(5.23) is determined by the concentration of the corresponding species in the xenon lattice. It was found that a major part of radiolytic H atoms could be used for synthesis of xenon hydrides. In the case of $\text{C}_2\text{H}_2/\text{Kr}$ system, only one krypton hydride (HKrCCH) is formed, so the reaction scheme is simplified. On the other hand, it is an indirect evidence for prompt recombination of H atoms giving molecular hydrogen [72]. For more complex molecules the scheme of radiolysis becomes more complicated, and a combination of EPR and IR spectroscopy makes it possible to determine multiple reaction channels [43, 72].

In general, the studies of formation and dissociation of noble gas hydrides provide important insight in the dynamics and reactivity of radiolytic H atoms in solid hosts. In this sense, the HN_gY molecules may be considered as a very sensitive IR probe due to their huge molar absorption coefficients and high sensitivity to local environment. This aspect may be illustrated by the determination of the isotopic effect in thermal mobility of H(D) atoms in solid xenon based on the monitoring of different isotopomers of xenon hydrides [71].

5.4 Characterization of the Radiation-Induced Radicals by a Combination of EPR and IR Spectroscopy

The EPR spectra of radicals in matrices were essentially obtained by solid-state radiolysis, whereas vibrational spectroscopic characteristics of matrix isolated radicals are mainly available from the experiments using other generation methods (gas-phase pyrolysis, glow discharge, or photolysis). A combined spectroscopic approach provides new information concerning the mechanism of radiolysis, structure and dynamics of radicals and matrix effects.

Fig. 5.3 Effect of matrix on the EPR spectra of ethynyl (C_2H) radical obtained by irradiation of acetylene in solid noble gas matrices at 7–16 K (asterisks show the signals from vinyl radical)



5.4.1 Radicals Produced by Dissociation of Excited Molecules

5.4.1.1 Ethynyl and Propargyl Radicals

The ethynyl (C_2H) radical is effectively produced under radiolysis of acetylene in solid argon, krypton, and xenon according to reaction (5.18). Comparison of the data obtained in different noble gas media reveals manifestations of specific matrix effects on these species. The EPR spectra (Fig. 5.3) represent an anisotropic doublet due to ethynyl proton coupling.

The spectrum in natural xenon is severely broadened due to interaction with magnetic matrix nuclei. Meanwhile, in the case of monoisotopic ^{136}Xe [47], the spectral pattern is very close to that observed in argon [77] (more isotropic shape in xenon possibly suggests rotation of the small C_2H radical in a xenon lattice even at low temperature). Somewhat surprisingly, the EPR spectrum obtained in krypton demonstrates marked difference from the spectra obtained in argon and xenon. The case of krypton clearly reveals anisotropy of both g and hyperfine coupling. A possible explanation is that the ethynyl radical in krypton occupies a “tight” low-symmetry trap, which results in an asymmetric distortion. IR spectra show an absorption band corresponding to the $C\equiv C$ stretching, known from other sources [78]. Again, the matrix effect does not show an expected monotonous frequency shift following the changes in matrix polarizability ($Ar > Kr > Xe$), but reveals a peculiarity

for krypton (1846, 1842, and 1852 cm^{-1} for Ar, Kr, and Xe, respectively). Thus, both EPR and IR data make us suggest that the matrix effects on ethynyl radical are determined by specific trapping site structure rather than macroscopic properties of matrix. This is an interesting probe, which could be compared with calculations of local configuration.

Propargyl radical ($\text{C}_3\text{H}_3\dot{\text{C}}$) is produced from propyne by a similar mechanism



It was also found in all the three noble gas matrices [43, 72]. The EPR spectra of this radical obtained by radiolysis of propyne are in agreement with those reported previously under photolysis of propargyl bromide in argon [79], taking into account significant line broadening in krypton and xenon. IR spectra demonstrate two bands, which can be assigned to the propargyl radical corresponding to the C–H stretching (3308.5, 3300.5, and 3296 cm^{-1} in Ar, Kr, and Xe, respectively) and CH_2 wagging mode (686–687 cm^{-1} in all the matrices) [43, 72]. The data for argon matrix agree with known values [78]. In this case, the observed matrix effect on the stretching band is “normal” (correlating with polarizability).

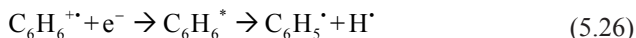
An interesting issue is concerned with possible formation of another isomer of $\text{C}_3\text{H}_3\dot{\text{C}}$, the propynyl radical $\text{CH}_3\text{C}\equiv\text{C}\dot{\text{C}}$. This poorly studied species is of basic interest and it can be considered as a potential precursor of new xenon and krypton hydrides (still unknown). The experiments in xenon and krypton gave no clear evidence for stabilization of propynyl radical under radiolysis. Possibly, it undergoes rearrangement to a more stable propargyl radical even at low temperature.

5.4.1.2 Phenyl Radical

Phenyl radical ($\text{C}_6\text{H}_5\dot{\text{C}}$), a fundamentally important species, can be generated from different benzene derivatives and its IR and EPR spectra in argon matrices are well known [4, 78]. Nevertheless, in the early studies, this radical was never produced by direct radiolysis or photolysis of benzene molecules in solid matrices. It is known that photolysis of benzene result mainly in its isomerisation. Furthermore, the radiation-chemical yield of phenyl radicals in the radiolysis of benzene in condensed phases is supposed to be very low [80], which is usually attributed to high efficiency of radiationless deactivation for excited benzene molecules and competing reaction channels. In contrast with this expectation, we have found [81] that radiolysis of benzene in a solid xenon matrix produces phenyl radicals and trapped hydrogen atoms with reasonably high yield (comparable to the decomposition yield of saturated molecules in solid xenon). The phenyl radicals were characterized by both EPR (a broadened, poorly resolved triplet signal) and IR spectra (a strong characteristic absorption at 703 cm^{-1} and weaker bands at 3056, 1437, 1429, 1023 and 655 cm^{-1} [81]). All the IR bands exhibit “normal” small red shifts (by 3–4 cm^{-1}), in comparison with the known data for argon matrix [78]. It is worth noting that, in this case,

IR spectroscopy provides more conclusive data than EPR, because the EPR signal is poorly resolved and may overlap with the signals from other species.

Regarding the mechanistic aspects, it was concluded that phenyl radical was produced from dissociation of the benzene excited states resulting from the ion-electron recombination:



In line with this scheme, addition of an electron scavenger to the studied system resulted in stabilization of benzene radical cation and a dramatic drop in the yield of trapped H atoms [15]. An obvious difference between direct photoexcitation of benzene and reaction (5.26) occurring under radiolysis in solid xenon should be attributed to a different nature of the excited states. Most probably, the ion-electron recombination leads to population of high-lying triplet states, which are not attainable by direct excitation. This result has two important implications. First, the radiolysis of benzene in solid noble gas matrices provides a good source of isolated phenyl radicals, which may be used for model studies. Second, from the point of view of basic radiation chemistry, it makes us to reconsider the common intuitive concept of radiation resistance of aromatic molecules due to effective dissipation of excitation energy. Indeed, it turns out that isolated aromatic molecules in solids are not so stable to indirect action of radiation and intermolecular interactions leading to formation of dimer radical cations and excimers may be crucial.

5.4.1.3 OH and SH Radicals

Simple and basically important diatomic inorganic radicals ($\text{OH}\cdot$ and $\text{SH}\cdot$) are rather problematic species for matrix isolation studies by EPR and IR spectroscopy. Because of orbital degeneracy, the EPR signals of these species in weakly interacting matrices are severely broadened, so they become virtually undetectable. On the other hand, these radicals are known as poor IR absorbers due to relatively low intensity of the corresponding vibrational stretching bands. In this case, however, molecular interactions provide some help in the detection of radicals. The studies of radiolysis of water [71] in a xenon matrix made it possible to assign a broad anisotropic doublet in the EPR spectrum to the $\text{OH}\cdot$ radical. A tentative explanation is that the orbital degeneracy is lifted due to relatively strong interaction with xenon matrix (it is not the case for a low-polarizable argon). It is also possible that the observed signal results from the $\text{OH}\cdot \dots \text{H}_2\text{O}$ complex. It is worth noting that the EPR spectrum of the $\text{OH}\cdot$ radical in a strongly interacting environment (water ice) is well known [4]. The IR spectrum of the $\text{Xe}/\text{H}_2\text{O}$ system after radiolysis reveals a moderately weak absorption at 3402 cm^{-1} assigned to the $\text{OH}\cdot \dots \text{H}_2\text{O}$ complex and a very weak feature at 3531 cm^{-1} ascribed to isolated $\text{OH}\cdot$ radical (both species were identified previously in photochemical studies [82]). It may be noted that complex is a better absorber than an isolated radical because of higher intensity of the corresponding vibrational mode.

In the case of the $\text{H}_2\text{S}/\text{Xe}$ system, the EPR spectrum did not reveal definite proof of formation of the SH^\cdot radical, whereas the IR spectrum showed a radiation-induced absorption at 2550 cm^{-1} assigned to the $\text{SH}^\cdot \cdots \text{H}_2\text{S}$ complex [75] (the identification relies on the data obtained in earlier photochemical studies [83]). The formation of OH^\cdot and SH^\cdot radicals upon radiolysis of H_2O and H_2S in a solid xenon matrix is supported indirectly by a high yield of trapped hydrogen atoms observed by EPR and effective annealing-induced formation of the corresponding xenon hydrides (HXeOH and HXeSH , respectively) characterized by IR spectroscopy (see Section 5.3.2).

5.4.2 Radicals Produced by Reactions of the Radiation-Induced Hydrogen Atoms

5.4.2.1 Vinyl Radical

Vinyl ($\text{C}_2\text{H}_3^\cdot$) radical is a widely occurring intermediate, which was a subject of many spectroscopic studies using both EPR and IR spectroscopy. This radical can be easily produced by reaction (5.24) of mobile hydrogen atoms generated in solid noble gas matrices with acetylene molecules. The EPR spectrum of vinyl radical obtained in solid argon at low temperature represents a rigid structure, where all the three protons are magnetically non-equivalent and exhibit isotropic hyperfine coupling constants of 3.96, 6.59, and 1.38 mT, respectively [79]. The reported spectral pattern is rather complicated due to significant anisotropy and manifestations of forbidden transitions. However, the EPR spectrum obtained in solid xenon at 16 K exhibits a triplet of doublets with $a_1 \approx 5.1$ mT and $a_2 = 1.38$ mT and non-binomial intensity ratio [84]. This result (also confirmed by experiments in a ^{136}Xe matrix [47]) can be interpreted as an evidence of interconversion between the two tautomeric forms of vinyl radical (*cis-trans* inversion). Low intensity of the central doublet implies intermediate frequency of inversion (between 10^8 and 10^9 s^{-1}). One should note that the inversion rate does not show significant temperature dependence in the range of 16 to 60 K [47], which may imply involvement of tunneling. The quantitative model of this phenomenon is lacking.

The IR spectra of vinyl radicals obtained by reactions of radiolytic and photolytic hydrogen atoms with acetylene in different matrices [84] show a well-defined absorption band corresponding to out-of-plane bending, which appears at 900.8, 896.6, and 891 cm^{-1} in Ar, Kr, and Xe, respectively. The data obtained in argon are in agreement with previous reports [78] and the red shift in more polarizable matrices is reasonable. In addition to this previously known feature, the combined spectroscopic studies revealed a new band (maximum at 1379 cm^{-1} in xenon) also assigned to vinyl radical. This assignment was confirmed by correlation with EPR data, isotopic substitution and quantum-chemical calculations [84].

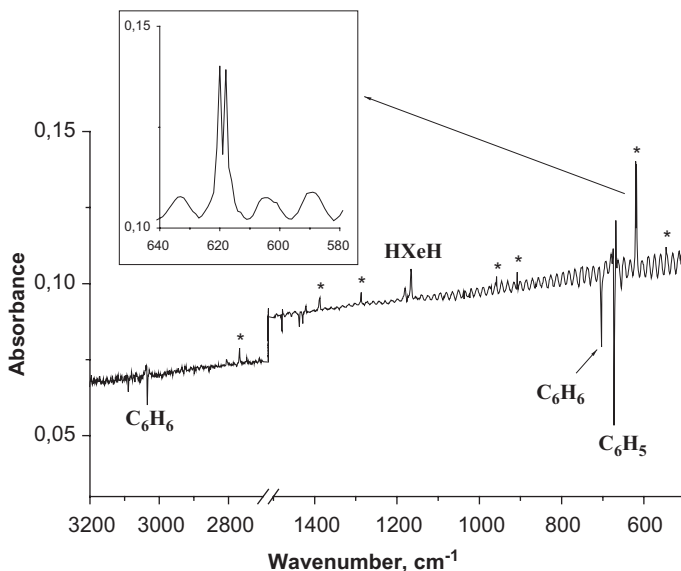


Fig. 5.4 Effect of annealing at 45 K on the IR spectra of irradiated system $C_6H_6/Xe=1/1500$ (difference spectrum). Asterisks show the annealing-induced absorptions assigned to the cyclohexadienyl radical. (Adapted from Ref. [81] with kind permission of © Elsevier, 2007)

5.4.2.2 Cyclohexadienyl Radical

The cyclohexadienyl ($C_6H_7^{\cdot}$) radical is produced by hydrogen atom addition to benzene molecules. Its EPR spectrum is well known from the early EPR studies of benzene radiolysis at 77 K (see Ref. [4] for review). A characteristic feature of this species is very large hyperfine coupling with the protons of the CH_2 group: $a_1(2H)=4.7-5.0$ mT, which makes it easily distinguishable from other radicals produced from aromatic hydrocarbons. Meanwhile, the vibrational spectrum of this radical was unavailable before recently. The application of combined spectroscopic approach to the radiolysis of C_6H_6/Xe system allowed us to identify the IR spectrum of the cyclohexadienyl radical resulting from the reactions of thermally mobilized H atoms with benzene molecules in solid xenon [81]. In this case, the EPR spectrum of $C_6H_7^{\cdot}$ is characterized by the hyperfine coupling constants of $a_1(2H)=4.85$ mT and $a_2(3H)=1.05$ mT, in basic agreement with previous findings in other matrices [4]. The IR spectrum recorded after annealing the irradiated sample at 45 K (Fig. 5.4) shows a number of new absorption bands ascribed to the cyclohexadienyl radical on the basis of their correlation with the EPR signal of $C_6H_7^{\cdot}$ and quantum-chemical calculations.

The most prominent absorption is the doublet at $620/618$ cm^{-1} and it may serve as a “marker” of this radical in complex systems. Weaker features appear at 2786, 1387, 1287, 958, 908, and 546 cm^{-1} [81]. This example is a remarkable

demonstration of the feasibility of the combined spectroscopic approach, which made it possible to identify seven vibration bands of the $C_6H_7\cdot$ radical. The assignment was fully confirmed in a recent study of Bahou et al. [85] in the *para*-hydrogen matrix using a quite different generation method.

5.4.2.3 HXeCC and HXeO Radicals

The family of noble gas hydrides resulting from hydrogen atom reactions in xenon and krypton matrices (see Sect. 5.3.2) includes two open-shell species, HXeCC \cdot and HXeO \cdot , which were identified by IR spectroscopy in the experiments with photochemical dissociation of precursors [76, 86]. The characteristic absorptions corresponding to H–Xe stretching were found at 1478 and 1466 cm^{-1} for HXeCC \cdot and HXeO \cdot , respectively. It is worth noting that the latter species actually results from mobility of O atoms rather than H atoms, because the oxygen atoms become mobile at lower temperature (below 35 K [86]). It was found that both species could be produced with good yield also using radiolysis of C_2H_2 and H_2O in a xenon matrix [72, 74]. The radiolysis to sufficiently high doses is practicable in this case since the direct precursors of xenon containing radicals (C_2 and oxygen atoms) result from secondary processes. In this case, IR spectroscopy serves as “primary” identification method, and a challenge for combined spectroscopic studies is to obtain the EPR spectra of these very unusual species, which are still unknown. Efforts were made to assign the EPR signal of HXeCC \cdot on the basis of correlation with IR spectra and quantum chemical calculations [74]; however, conclusive evidence is still missing. In the case of HXeO \cdot , no sign of the EPR signal which might be attributed to this radical was found. Possibly, the problem is orbital degeneracy. It should be noted that reliable calculations of magnetic resonance parameters for such species are very demanding. More experimental and computational work is necessary to resolve this issue.

5.5 Matrix Effects on the Primary Radiation-Induced Effects in Solids as Probed by EPR and Combined Spectroscopic Approach

The previous sections of this review were mainly concerned with using radiolysis for generation and characterization of reactive intermediates and novel species in low-temperature matrices (a common approach defined as “*radiation chemistry for matrix isolation*”). Meanwhile, the radiation-induced effects in solids are essentially controlled by physical properties of matrix, which may be described either in terms of macroscopic properties or in terms of local configurational interactions. These effects are particularly important in consideration of the fate of primary radical ions and excess electrons, the principal primary intermediates of the radiation-induced

processes. The approach defined as “*matrix isolation for radiation chemistry*” is based on using inert low-temperature matrices with variable physical characteristics (IP, polarizability, rigidity) for simulation of the basic matrix effects at the early stages of solid-state radiolysis at molecular level. Extensive studies in this direction using both solid noble gases and molecular matrices revealed important features of such effects, which may provide a key for understanding the nature of selectivity and fine tuning in the radiation chemistry of molecular solids and polymers. The experimental findings and their implications were summarized in recent reviews [22, 23, 87]. Here we will briefly outline some results, which demonstrate effective use of EPR spectroscopy and combined spectroscopic approach for these purposes.

5.5.1 Radical Cations

5.5.1.1 Simulation of the Effects of Excess Energy: “Hot” Fragmentation and Rearrangements in the Solid Phase

As mentioned in Sect. 5.2.2.2, the positive hole transfer from solid noble gas matrices to organic molecules is strongly exothermic because of substantial difference in the IP values. This IP gap can be tuned in a rather wide range changing the matrix IP (switching from xenon to argon) and argon represents an “extreme case”, which results in significant excess energy of the radical cation. This may provide an opportunity for experimental simulation of the effect of excess energy and elucidation the role of “hot” ionic reaction channels in solids.

Typical IP values for simple organic molecules are ca. 9–10 eV, so, in the case of argon, the IP gap is around 6 eV. This value definitely exceeds the energy of chemical bonds in the resulting radical cations. Taking into account inefficient dissipation of excess energy to the argon lattice, one can conclude that the “hot” fragmentation should be highly probable. In fact, an indication of such process was obtained in early studies of the radiolysis of alkanes in argon and krypton [37]. In addition to fragmentation, excess energy may also result in rearrangement of the primary radical cations in a solid argon matrix. Table 5.4 summarizes the results of the studies on this issue by a combination of EPR and IR spectroscopy.

It is worth noting that, in all the studied cases, the estimated excess energy (>5.5 eV) is high enough for bond cleavage or rearrangement of the primary radical cations (the corresponding processes always have lower threshold under the conditions of mass-spectrometry). However, as seen from Table 5.4, the efficiency of “hot” fragmentation of the radical cations in solid argon varies strongly, depending on the molecular structure of the guest species, even for rather similar electronic structure of radical cations (e. g., to compare dimethyl ether and methylal, or acetone and diacetyl). Furthermore, it was shown that radical cations of 2-butene isomers retained not only molecular structure, but also spatial configuration (*cis/trans*) without any fragmentation or rearrangement, even though excess energy was ca 6.5 eV. These findings clearly suggest the crucial role of intramolecular relaxation

Table 5.4 Radical and molecular products resulting from “hot” reactions of the primary radical cations upon irradiation of organic molecules in an argon matrix at 7–16 K

Parent radical cation	Observed products of “hot” reactions	Relative yield of fragmentation/rearrangement	Reference
$\text{CH}_3\text{OCH}_3^{+\bullet}$	$\text{CH}_3\cdot$	Low	[13]
$\text{CH}_3\text{OCH}_2\text{OCH}_3^{+\bullet}$	$\text{CH}_3\cdot, \text{CH}_3\text{O}\cdot$	High	[13, 14]
$n\text{-C}_7\text{H}_{16}^{+\bullet}, n\text{-C}_5\text{H}_{12}^{+\bullet}$	$\text{CH}_3\cdot, \text{CH}_4, \text{RCH}=\text{CH}_2$	Moderate high	[12]
$(\text{CH}_3)_3\text{CC}\equiv\text{CH}^{+\bullet}$	$\text{CH}_3\cdot, \text{CH}_4$	Moderate	[43]
$\text{CH}_3\text{CHO}^{+\bullet}$	$\text{CH}_3\cdot$	Moderate high	[17]
$\text{CH}_3\text{COCH}_3^{+\bullet}$	$\text{CH}_3\cdot$	Very low	[17]
$(\text{CH}_3)_3\text{COCH}_3^{+\bullet}$	$\text{CH}_3\cdot$	Very high	[17]
$\text{CH}_3\text{CH}_2\text{OCH}=\text{CH}_2^{+\bullet}$	$\text{CH}_3\cdot$	Low	[18]
$\text{CH}_3\text{CH}_2\text{CH}=\text{CH}_2^{+\bullet}$	<i>cis</i> - $\text{CH}_3\text{CH}=\text{CHCH}_3^{+\bullet}$	Very high	[18]
$\text{CH}_3\text{COCOCH}_3^{+\bullet}$	$\text{CH}_3\cdot$	Very high	[43]
$\text{CH}_3\text{COCH}_2\text{CH}_2\text{COCH}_3^{+\bullet}$	$\text{CH}_3\cdot$	Moderate high	[42, 43]
$\text{CH}_3\text{OCH}_2\text{COCH}_3^{+\bullet}$	$\text{CH}_3\cdot$	Moderate high	[42]

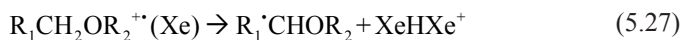
of excess energy followed by its dissipation to the matrix lattice. In general, the relaxation processes are determined by vibronic interactions, coupling between different vibrational modes, and cation–matrix interactions. This may imply an important role of molecular symmetry and cage structure, which can be considered as another illustrative example for fine tuning in the high-energy chemistry in solids. In any case, it should be noted that the reactivity of “hot” radical cations generated in argon is different from the behaviour of electronically excited cations resulting from photoexcitation in halocarbon matrices [26]. Apparently, indirect ionization in argon leads to population of high vibrational levels, which cannot be reached in photoprocesses. If it is the case, using argon matrices may provide unique information on the properties of vibrationally excited radical cations; however, further work is necessary to prove this assumption.

5.5.1.2 Matrix-Assisted Deprotonation and Matrix Switching Between Reaction Channels

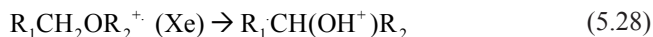
The probability of “hot” reactions (fragmentation and rearrangements) decreases with decreasing excess energy determined by the IP gap and such processes are less common in krypton and virtually do not occur in xenon. However, in certain cases, the yields of the primary organic radical cations produced by irradiation in a xenon matrix in the presence of electron scavengers are quite low (or even zero). Instead of this, the EPR spectroscopy reveals formation of radicals resulting from specific C–H bond rupture, which corresponds formally to proton loss in the primary radical cations. In particular, such behavior was observed for a number of oxygen containing species, including dimethyl ether, methylal, 1,3-dioxolane, THF, and acetaldehyde

and [13, 16, 88]. It is worth noting that, in all the cases studied, only one specific radical was produced for each parent cation. This means that deprotonation of the primary radical cations is a *regioselective* process (in contrast with the C–H bond cleavage in excited molecules observed in the absence of electron scavengers). The selectivity of this process correlates with spin density distribution in the radical cation (proton loss occurs at the maximum spin density position).

Concerning the mechanism of proton transfer, the main problem is assignment of the proton acceptor site in a xenon matrix. At first glance, deprotonation might occur in dimers or larger molecular aggregates. However, such a possibility was ruled out, because this process occurs in very dilute matrices, where the matrix isolation is guaranteed. Thus, one may conclude that the xenon matrix plays an active role. Indeed, the proton affinity of a xenon atom is rather high (5.2 eV), that is, comparable to proton affinities of simple organic molecules and neutral radicals [78]. Furthermore, in the case of solid xenon matrix, additional stabilization of proton results from specific collective solvation (formation of protonated xenon clusters of the Xe_nH^+ type) and long-range medium polarisation. In particular, the IR spectroscopic studies show formation of linear centrosymmetrical cation XeHXe^+ , which is characterized by a progression of vibration bands with the most intense feature at 731 cm^{-1} [89, 90]. Thus, direct deprotonation of radical cations to matrix may be justified reasonably (at least, from qualitative viewpoint). The reaction scheme for ether-type radical cations can be written as follows:



However, the correlation between the formation of deprotonation products and the amount of produced XeHXe^+ is not straightforward. An alternative explanation can be based on a theoretical finding [91], which shows that relatively polarizable rare gas atoms (in particular, xenon) may facilitate intramolecular rearrangement (H transfer to oxygen atom) due to formation of transition-state complex. In this case, the role of xenon is lowering the reaction barrier, which may be described as *matrix catalysis*. If such a model is applicable to the studied radical cations, the observed transformation may be represented by the scheme:



At the moment, it is not possible to make a definite choice between these two possibilities.

One of the most interesting findings is concerned with observation of both reaction channels for the same species, when the yields of the primary radical cations are low for both xenon and argon matrices, but the observed products are quite different. An illustrative example of such effect of nearly complete “*matrix switching*” between reaction channels (deprotonation to fragmentation) is given by methylal radical cation [16]. In the case of xenon, the EPR spectra show dominating contribution from the $\text{CH}_3\text{O}\cdot\text{CHOCH}_3$ radicals (anisotropic doublet), which corresponds to selective deprotonation of the primary cation. Mainly fragmentation products ($\text{CH}_3\cdot$ and $\text{CH}_3\text{O}\cdot$, probably in the form of complex with $\text{CH}_2\text{OCH}_3^+$ ion) were

found in argon [16], whereas both processes occur in krypton. This is a prominent illustration of the interplay between different matrix characteristics.

5.5.2 Radical Anions

Radical anions are formed from the reactions of the radiation-induced excess electrons with molecules. Basically, these species are often less reactive than radical cations and many of them were characterized by EPR spectroscopy in the early period [4]. Meanwhile, a closer look reveals that the radical anions observed in solid matrices often result from the molecules, which have no intrinsic electron affinity in the gas phase. It means that the stabilization of radical anions in such cases is a matter of matrix effects and the matrix interactions often control reactions of excess electrons in condensed phase. This aspect was still not investigated in detail from experimental and theoretical points of view. In order to shed a bit of light on this issue, recently we studied some model carbonyl compounds in matrices of various polarity and polarizability.

The simplest molecule of this kind is acetone, which is known to be a “good electron scavenger” in radiation chemistry. The acetone molecule has definitely negative intrinsic electron affinity [92], so the stabilization of radical anions may occur only due to intermolecular interactions. Our experiments did not reveal any sign of the formation of acetone radical anion under radiolysis of isolated acetone molecules in solid argon or non-polar molecular matrices. At first glance, it seems to be in conflict with that an earlier finding reported the EPR spectrum of this radical anion in solid argon generated by photolysis of Na/CH₃COCH₃/Ar co-deposited mixture [93]. However, one should bear in mind that the photogeneration may produce the ion pairs stabilized by strong coulombic interaction rather than isolated radical anions. Indeed, preliminary calculations do not support stabilization of radical anions, even in the large argon clusters.

A prominent example of the dominating role of matrix in stabilization of radical anions is presented by diacetyl [94]. According to calculations, this diketone also has virtually zero intrinsic electron affinity. The EPR study reveals that irradiation of diacetyl solutions in hydrocarbon glassy matrices does not result in appearance of any new signal, although the formation of trapped electrons is strongly suppressed in the presence of diacetyl. This may be interpreted as an evidence of “intermediate trapping”, that is, formation of metastable radical anions, which transfer an electron to a deeper trap (presumably, neutral radicals). Meanwhile, in the case of weakly polar ether matrices, experiment shows formation of a new EPR signal (Fig. 5.5, top), which was attributed to a delocalized diacetyl radical anion of C₂ symmetry with the following set of hyperfine coupling constants: $a_1(2H)=2.05$ mT, $a_2(2H)=0.76$ mT, $a_3(2H)=0.53$ mT). This signal correlates with the radiation-induced optical absorption band with maximum at ca. 600 nm, assigned to the same species. From computational point of view, the stabilization of the radical anion

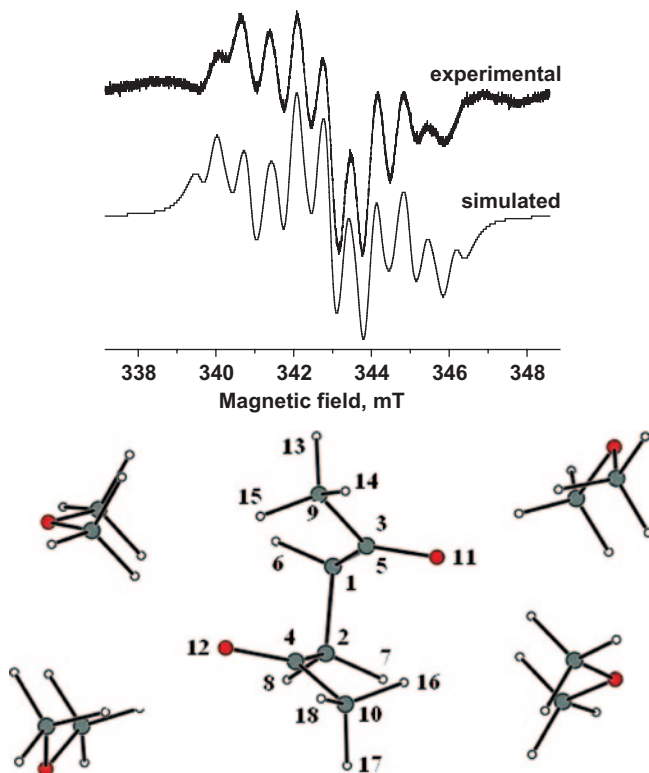


Fig. 5.5 Experimental and simulated EPR spectra of diacetyl radical anion observed in a glassy diethyl ether at 77 K; computed geometrical structure of the C_2 conformer of diacetyl radical anion solvated by four dimethyl ether molecules (adapted from Ref. [94] with kind permission of The American Institute of Physics, 2011)

can be explained in the frame of the microsolvation model with explicit account of local configuration. Indeed, the computed electron affinity of a microsolvate containing four dimethyl ether molecules (Fig. 5.5, bottom) is essentially positive, and the calculated hyperfine coupling constants for the C_2 conformer are in reasonable agreement with the experimental values.

Generally, it should be noted that the matrix effects on stability of radical anions can be realized on the basis of local configurational models rather than macroscopic properties of the medium. This leads to the concept of *microscopically tunable* excess electron capture in low-temperature media, which may have very interesting implications, particularly, for organized systems and nanostructures. Direct probe of the environment interactions for such cases is still lacking. In principle, this information might be obtained from ENDOR and IR spectroscopy, however, the application of both techniques to the radical anions in molecular matrices is still questionable because of their limited sensitivity.

5.6 Conclusions and Outlook

In summary, it is not doubts that EPR spectroscopy remains the most informative method for detailed studies of the mechanism of the radiation effects in a wide variety of solids. Meanwhile, using IR spectroscopy as a complementary tool to EPR may provide essential new information in structural and mechanistic aspects. The application of such approach to model studies in low-temperature matrices was illustrated in this chapter. An important point is that both methods were applied under similar experimental conditions, which justifies direct comparison. The outlined approach reveals hidden (sometimes, rather unusual) features of the radiation-induced chemistry in matrices and the nature of matrix effects. Furthermore, it provides more detailed understanding on the electronic and vibrational properties of the radiation-induced radicals and radical ions. Typically, EPR spectroscopy can be used as a reference method for unequivocal assignment of the IR absorptions. Meanwhile, in certain cases, IR spectroscopy may detect radicals, “invisible” by EPR due to the peculiarities of their electronic structure.

The investigations of radiation-induced effects in solid matrices using combined spectroscopic approach are still restricted to relatively simple systems and definitely there is room for future studies. One challenge is concerned with characterization of the vibrational spectra of highly reactive primary radical ions in both inert media and molecular matrices using EPR as a reference method. Also, the combination of EPR and IR spectroscopy may bring better understanding of matrix interactions and their role in the radiation chemistry in solids. However, more experimental and computational efforts are needed to clarify these issues.

Acknowledgments I am indebted to all my collaborators and students, who took part in our research of the radiation-induced radicals and radical ions in low-temperature matrices during the past two decades, in particular, Dr. F.F. Sukhov, Dr. A.V. Kobzarenko, Dr. A.Yu. Orlov, Dr. D.A. Tyurin, Dr. D.N. Laikov, Dr. I.A. Baranova, I.V. Tyulpina, E.V. Saenko, S.V. Ryazantsev, and S.V. Kameneva. The studies described in this chapter were supported by The Division of Chemistry of The Russian Academy of Sciences (program no. 1) and by The Russian Foundation for Basic Research (projects no. 06-03-33104-a, 09-03-00848-a and 12-03-01009-a).

References

1. Hutchison CA (1949) Paramagnetic resonance absorption in crystals colored by irradiation. *Phys Rev* 75:1769
2. Schneider EE, Day MJ, Stein G (1951) Effects of X-rays upon plastics: paramagnetic resonance. *Nature* 168:645–664
3. Morton JR (1964) Electron spin resonance spectra of oriented radicals. *Chem Rev* 64:453–471
4. Pshchetskii SYa, Kotov AG, Milinchuk VK, Roginskii VAT (1974) EPR of free radicals in radiation chemistry. Wiley, NY
5. Shida T, Kato T (1979) ESR and optical studies on the cation-radical of pyridine in a gamma-irradiated rigid matrix at low-temperatures. *Chem Phys Lett* 68:106–111
6. Symons MCR (1984) Radical cations in condensed phases. *Chem Soc Rev* 13:393–439

7. Shiotani M (1987) ESR studies of radical cations in solid matrices. *Magn Reson Rev* 12:333–381
8. Lund A, Shiotani M (eds) (1991) *Radical ionic systems. Properties in condensed phases.* Kluwer, Dordrecht
9. Knight LB (1986) ESR investigations of molecular cation radicals in neon matrices at 4 K: generation, trapping, and ion-neutral reactions. *Acc Chem Res* 19:313–321
10. Knight LB, Gregory BW, Cobranchi ST, Williams F, Qin X-Z (1988) High-resolution electron-spin-resonance spectroscopy and structure of the acetaldehyde radical cation (CH_3CHO^+) in neon matrices at 4 K-comparison with results in freon matrices. *J Am Chem Soc* 110:327–342
11. Knight LB, Kerr K, Villanueva M, McKinley AJ, Feller D (1992) Theoretical and neon matrix electron-spin-resonance studies of the methanol cation- CH_3OH^+ , CH_3OD^+ , CH_2DOH^+ , and $(\text{CH}_3\text{OH}^+)\text{C}^{13}$. *J Chem Phys* 97:5363–5376
12. Feldman VI (1997) Structure and properties of hydrocarbon radical cations in low-temperature matrices as studied by a combination of EPR and IR spectroscopy. *Acta Chem Scand* 51:181–192
13. Feldman VI (1999) Radiation-induced transformations of isolated organic molecules in solid rare gas matrices. *Radiat Phys Chem* 55:565–571
14. Feldman VI, Sukhov FF, Orlov AYu (1999) An ESR study of benzene radical cation in an argon matrix: evidence for favourable stabilization of $^2\text{B}_{1g}$ rather than $^2\text{B}_{2g}$ state. *Chem Phys Lett* 300:713–718
15. Feldman VI, Sukhov FF, Orlov AYu, Kadam R, Itagaki Y, Lund A (2000) Effect of matrix and substituent on the electronic structure of trapped benzene radical cations. *Phys Chem Chem Phys* 2:29–35
16. Feldman VI, Sukhov FF, Orlov AYu, Shmakova NA (2000) Effect of matrix electronic characteristics on trapping and degradation of organic radical cations in solid rare gases: a case study of methylal radical cation. *J Phys Chem A* 104:3792–3799
17. Feldman V, Sukhov F, Orlov A, Tyulpina I (2003) Stabilization and reactions of aliphatic radical cations produced by fast electron irradiation in solid argon matrices. *Phys Chem Chem Phys* 5:1769–1774
18. Feldman VI, Sukhov FF, Orlov AYu, Tyulpina IV, Ivanchenko VK (2006) Stabilization and isomerization of radical cations generated by fast electron irradiation of unsaturated organic molecules in a solid argon matrix. *Radiat Phys Chem* 75:106–114
19. Iwasaki M, Toriyama K, Fukaya M, Muto H, Nunome K (1985) 4 K radiolysis of linear alkanes as studied by electron-spin resonance spectroscopy-selective formation of terminal alkyl radicals in the primary process. *J Phys Chem* 89:5278–5284
20. Feldman VI, Sukhov FF, Slovokhotova NA (1994) Selectivity of radiation-induced chemical processes in low-molecular-mass and high-molecular-mass hydrocarbons. *Vysokomolek soedin B* 36:519–543
21. Feldman VI (1996) Selective localization of primary radiation-chemical events in solid aliphatic hydrocarbons and related polymers as evidenced by ESR. *Appl Radiat Isot* 47:1497–1501
22. Feldman VI (2011) Selective and long-range effects in the radiation chemistry of molecular solids and polymers. In: Stass DV, Feldman VI (eds) *Selectivity, control, and fine tuning in high-energy chemistry.* Research Signpost, Trivandrum
23. Feldman VI (2013) Organic radical cations and neutral radicals produced by radiation in low-temperature matrices. In: Lund A, Shiotani M (eds) *EPR of free radicals in solids II. Trends in applications and methods* (2nd edn). Springer, Dordrecht
24. Shida T (1988) *Electronic absorption spectra of radical ions.* Elsevier, Amsterdam
25. Mel'nikov MYa, Smirnov VA (1996) *Handbook of photochemistry of organic radicals.* Begell House Inc Publishers, NY
26. Feldman VI, Mel'nikov MYa (2000) Matrix effects in the reactions of organic radical cations in ground and excited states in solid phase. *High Energy Chem* 34:236–245

27. Gillbro T, Lund A (1975) High-yield of radical pairs in deuterated normal-alkane single-crystals gamma-irradiated at 4.2 K. *Chem Phys Lett* 34:375–377
28. Gillbro T, Lund A (1976) Deposition of radiation energy in solids as visualized by distribution, structure and properties of alkyl radicals in gamma-irradiated normal-alkane single-crystals. *Int J Radiat Phys Chem* 8:625–641
29. Iwasaki M, Toriyama K, Muto H, Nunome K (1976) Pairwise trapping of radicals in single-crystals of normal-decane irradiated at 1.5 and 4.2 degrees K. *J Chem Phys* 65:596–606
30. Toriyama K, Muto H, Nunome K, Fukaya M, Iwasaki M (1981) Radiation damages of organic materials at 4 K—an electron spin resonance study of polyethylene and related hydrocarbons. *Radiat Phys Chem* 18:1041–1052
31. Toriyama K, Iwasaki M (1979) Electron spin resonance studies on radiolysis of crystalline methanol at 4.2 K. *J Am Chem Soc* 101:2516–2523
32. Feldman VI, Borzov SM, Sukhov FF, Slovokhotova NA (1987) Radical processes in polyethylene, irradiated at 10–100 K. *Khimicheskaya fizika* 6:477–483
33. Whittle E, Dows DA, Pimentel GC (1954) Matrix isolation method for the experimental study of unstable species. *J Chem Phys* 22:1943
34. Bouldin WV, Gordy W (1964) Energy migration + isotopic effects in irradiated solids at low temperature. *Phys Rev* 135:A806–A814
35. Bhattacharya D, Willard JE (1981) Radiolytic production of trapped hydrogen atoms from organic compounds in Xe, Kr, and Ar at 10 K. *J Phys Chem* 85:154–159
36. Muto H, Toriyama K, Nunome K, Iwasaki M (1982) Radiolysis of alkanes and olefins in xenon matrices at 4.2 K as studied by electron spin resonance-formation and trapping of hydrogen atoms and their subsequent reactions at cryogenic temperatures. *Radiat Phys Chem* 19:201–208
37. Gotoh K, Miyazaki T, Fueki K, Lee K-P (1987) Electron spin resonance study of radiolysis of solid rare-gas alkane mixtures at 4.2 K—ionic fragmentation and initial energy of hot H-atoms. *Radiat Phys Chem* 30:89–89
38. Qin X-Z, Trifunac AD (1990) Radiolytic generation of radical cations in xenon matrices—tetramethylcyclopropane radical cation and its transformations. *J Phys Chem* 94:3188–3192
39. Knight LB (1991) Generation and study of inorganic cations on rare gas matrices. In: Lund A, Shiotani M (eds) *Radical ionic*. Kluwer, Dordrecht
40. Knight LB, King GM, Petty JT, Matsushita M, Momose T, Shida T (1995) Electron-spin-resonance studies of the methane radical cations ($(\text{CH}_4^+) \text{C}^{12,13}$, $(\text{CDH}_3^+) \text{C}^{12,13}$, $(\text{CD}_2\text{H}_2^+) \text{C}^{12}$, $(\text{CD}_3\text{H}^+) \text{C}^{12}$, $(\text{CD}_4^+) \text{C}^{12}$) in solid neon matrices between 2.5 and 11 K—analysis of tunnelling. *J Chem Phys* 103:3377–3386
41. Yamada S, Komaguchi K, Shiotani M, Benetis NP, Sornes AR (1999) High-resolution EPR and quantum effects on CH_3 , CH_2D , CHD_2 , and CD_3 radicals under argon matrix isolation conditions. *J Phys Chem A* 103:4823–4829
42. Feldman VI, Baranova IA, Kobzareno AV, Tyulpina IV (2011) Fragmentation of the primary radical cations of methoxyacetone and diacetylonyl in a solid argon matrix. *High Energy Chem* 45:351–352
43. Kobzareno AV, Sukhov FF, Orlov AY, Kovalev GV, Baranova IA, Feldman VI (2012) Effect of molecular structure on fragmentation of organic molecules in solid rare gas matrices. *Radiat Phys Chem* 81:1434–1439
44. Bally T (1991) Electronic structure, spectroscopy, and photochemistry of organic radical cations. In: Lund A, Shiotani M (eds) *Radical ionic systems. Properties in condensed phases*. Kluwer, Dordrecht
45. Feldman VI, Sukhov FF, Slovokhotova NA, Bazov VP (1996) Radiation-induced degradation of alkane molecules in solid rare gas matrices. *Radiat Phys Chem* 48:261–269
46. Feldman VI, Sukhov FF, Orlov AY (1997) Further evidence for formation of xenon dihydride from neutral hydrogen atoms: a comparison of ESR and IR spectroscopic results. *Chem Phys Lett* 280:507–512
47. Feldman VI, Sukhov FF, Orlov AY, Tyulpina IV (2008) High-resolution EPR spectroscopy of small radicals in a solid ^{136}Xe matrix. *Mendelev Commun* 18:121–122

48. Feldman VI, Orlov AYu, Sukhov FF (2008) Hydrogen atoms in solid xenon: trapping site structure, distribution, and stability as revealed by EPR studies in monoisotopic and isotopically enriched xenon matrices. *J Chem Phys* 128:214511
49. Shida T, Hamill WH (1966) Molecular ions in radiation chemistry I. Formation of aromatic-amine cations in CCl_4 by resonance charge transfer at 77 K. *J Chem Phys* 44:2369–2374
50. Grimpson A, Simpson GA (1968) Spectrophotometric identification of gamma-radiolytic intermediates in a new halogenic glassy matrix. *J Phys Chem* 72:1776–1779
51. Henly E, Johnson E (1969) *The chemistry and physics of high energy reactions*. University Press, Cambridge
52. Hubbell JH, Seltzer SM (1996) Tables of X-ray mass attenuation coefficients and mass energy-absorption coefficients from 1 keV to 20 MeV for elements $Z=1$ to 92 and 48 additional substances of dosimetric interest. <http://www.nist.gov/pml/data/xraycoef>. Accessed 28 Feb 2014
53. Pacansky J, Maier M (1990) Irradiation of small molecules isolated in rare-gas matrices by high-energy electron-beams. *J Molec Struct* 222:33–75
54. Ennis CP, Kaiser RI (2010) Mechanistical studies on the electron-induced degradation of polymers: polyethylene, polytetrafluoroethylene, and polystyrene. *Phys Chem Chem Phys* 12:14884–14901
55. Sukhov FF (1988) Low-temperature radiation-chemical processes in polymers and their low-molecular-weight analogues (in Russian). Dissertation, Karpov Institute of Physical Chemistry
56. Foner SN, Cochran EL, Bowers VA, Jen CK (1960) Multiple trapping sites for hydrogen atoms in rare gas matrices. *J Chem Phys* 32:963–971
57. Komaguchi K, Nomura K, Shiotani M (2007) High-resolution ESR study of the H center dot center dot center dot CH_3 , H center dot center dot center dot CHD_2 , D center dot center dot center dot CH_2D , and D center dot center dot center dot CD_3 radical pairs in solid argon. *J Phys Chem A* 111:726–733
58. Feldman VI, Kobzareno AV, Orlov AY, Sukhov FF (2012) The radiation-induced chemistry in solid xenon matrices. *Low Temp Phys* 38:766–773
59. Eberlein J, Creuzburg M (1997) Mobility of atomic hydrogen in solid krypton and xenon. *J Chem Phys* 106:2188–2194
60. Kinugawa K, Miyazaki T, Hase H (1978) Trapping and reaction of hydrogen atoms produced by ultraviolet photolysis of xenon-isobutane mixtures at 4 and 77 K. *J Phys Chem* 82(15):1697–1700
61. Apkarian VA, Schwentner N (1999) Molecular photodynamics in rare gas solids. *Chem Rev* 99:1481–1514
62. Pettresson M, Kriachnchev L, Roozeman RJ, Räsänen M (2000) Photolysis of HI in solid Xe: production and distribution of hydrogen atoms. *Chem Phys Lett* 323:506–513
63. Muto H, Nunome K, Iwasaki M (1980) Reactions of thermal H atoms at cryogenic temperature below 77 K as studied by ESR. Competitive H abstraction from C_2H_6 and HI in rare-gas Matrices. *J Phys Chem* 84:3402–3408
64. Pettersson M, Lundell J, Räsänen M (1995) Neutral rare-gas containing charge-transfer molecules in solid matrices. I. HXeCl , HXeBr , HXeI , and HKrCl in Kr and Xe. *J Chem. Phys* 102:6423–6431
65. Pettersson M, Lundell J, Räsänen M (1995) Neutral rare gas containing charge transfer molecules in solid matrices. II. HXeH , HXeD , and DXeD in Xe. *J Chem Phys* 103:205–210
66. Feldman VI, Sukhov FF (1996) Formation and decay of transient xenon dihydride resulting from hydrocarbon radiolysis in a xenon matrix. *Chem Phys Lett* 255:425–430
67. Pettersson M, Nieminen J, Kriachnchev L, Räsänen M (1997) The mechanism of formation and infrared-induced decomposition of HXeI in solid Xe. *J Chem Phys* 107:8423–8431
68. Pettersson M, Lundell J, Räsänen M (1999) New rare-gas-containing neutral molecules. *Eur J Inorg Chem* 1999:729–737
69. Kriachtchev L, Räsänen M, Gerber RB (2009) New chemistry at low temperatures. *Acc Chem Res* 42:183–191

70. Grochala L, Khriachtchev L, Räsänen M (2011) Noble-gas chemistry. In: Khriachtchev F (ed) *Physics and chemistry at low temperatures*. Pan Stanford Publishing, Singapore
71. Khriachtchev L, Tanskanen H, Pettersson M, Räsänen M, Feldman V, Sukhov F, Orlov A, Shestakov AF (2002) Isotopic effect in thermal mobility of atomic hydrogen in solid xenon. *J Chem Phys* 116:5708–5716
72. Kobzareno AV (2013) Mechanism of the radiation-chemical synthesis and properties of some xenon and krypton hydrides (in Russian). Dissertation, Lomonosov Mocsow State University
73. Feldman VI, Sukhov FF, Orlov AYu, Tyulpina IV (2003) Experimental evidence for the formation of HXeCCH: the first hydrocarbon with an inserted rare-gas atom. *J Am Chem Soc* 125:4698–4699
74. Feldman VI, Sukhov FF, Orlov AYu, Tyulpina IV, Logacheva ES, Tyurin DA (2005) Chemical reactions in the xenon-acetylene systems irradiated with fast electrons at 16 K: formation of xenon-containing molecules and radicals. *Russ Chem Bull* 54:1458–1466
75. Ryazantsev SV, Kobzareno AV, Feldman VI (2013) Photolabile xenon hydrides: a case study of HXeSH and HXeH. *J Chem Phys* 129:124315 (1–7)
76. Khriachtchev L, Tanskanen H, Lundell J, Pettersson M, Kiljunen T, Räsänen M (2003) Fluorine-free organoxenon chemistry: HXeCCH, HXeCC, and HXeCCXeH. *J Am Chem Soc* 125:4696–4697
77. Cochran EL, Adrian FJ, Bowers VA (1964) ESR study of ethynyl and vinyl free radicals. *J Chem Phys* 40:213–220
78. Chemistry Webbook NIST. NIST Standard Reference Database Number 69 (2011). <http://webbook.nist.gov/chemistry/>. Accessed 28 Feb 2013
79. Kasai PH (1972) Electron spin resonance studies of vinyl, propargyl, and butatrienyl radicals isolated in argon matrices. *J Am Chem Soc* 94:5950–5956
80. Földiák G (ed) (1981) *Radiation chemistry of hydrocarbons*. Akademiai Kiado, Budapest
81. Feldman VI, Sukhov FF, Logacheva EA, Orlov AYu, Tyulpina IV, Tyurin DA (2007) Reactions of H atoms produced by electron irradiation of benzene in solid xenon: IR spectrum of cyclohexadienyl radical and possible involvement of HXeC₆H₅. *Chem Phys Lett* 437:207–211
82. Pettersson MA, Khriachtchev L, Lundell J, Räsänen M (1999) Chemical compound formed from water and xenon: HXeOH. *J Am Chem Soc* 121:11904–11905
83. Isoniemi E, Pettersson M, Khriachtchev L, Lundell J, Räsänen M (1999) Infrared spectroscopy of H₂S and SH in rare-gas matrixes. *J Phys Chem A* 103:679–685
84. Tanskanen H, Khriachtchev L, Räsänen M, Feldman VI, Sukhov FF, Orlov AY, Tyurin DA (2005) Infrared absorption and electron paramagnetic resonance studies of vinyl radical in noble-gas matrices. *J Chem Phys* 123:064318
85. Bahou M, Wu Y-J, Lee Y-P (2012) A new method for investigating infrared spectra of protonated benzene (C₆H₇⁺) and cyclohexadienyl radical (c-C₆H₇) using para-hydrogen. *J Chem Phys* 2012:154304
86. Khriachtchev L, Pettersson M, Lundell J, Tanskanen H, Kiviniemi T, Runeberg N, Räsänen M (2003) A neutral xenon-containing radical, HXeO. *J Am Chem Soc* 125:1454–1455
87. Feldman V (2014) Structure and reactions of aliphatic “Bridged” bifunctional radical ions: exploring fine tuning in radiation chemistry. *Isr J Chem* 2014 (in press)
88. Feldman VI, Sukhov FF, Orlov AYu, Shmakova NA (2001) Radiation chemistry of organic molecules in solid rare gas matrices: 2 selective deprotonation of the primary radical cations upon irradiation of oxygen-containing molecules in xenon matrices. *High Energy Chem* 35:319–327
89. Karatun AA, Sukhov FF, Slovokhotova NA (1981) Stabilization of HAR_n⁺, HKR_n⁺, and HXe_n⁺ in solid inert-gases on irradiation of 2-chloropropane in them by fast electrons. *Khim Vys Energ* 156:371–372
90. Kunttu H, Seetula J, Rasanen M, Apkarian A (1992) Photogeneration of ions via delocalized charge-transfer states 1 xe₂h⁺ and xe₂d⁺ in solid xe. *J Chem Phys* 96:5630–5635

91. Fridgen TD, Parnis JM (1999) A density functional theory study of the catalytic role of Ar, Kr, Xe, and N₂ in the CH₃OH center dot + to CH₂OH₂ center dot + isomerization reaction. *Int J Mass Spectrom Ion Process* 190-191:181–194
92. Fourre I, Silvi B, Chaquin P, Sevin A (1999) Electron localization function comparative study of ground state, triplet state, radical anion, and cation in model carbonyl and imine compounds. *J Comput Chem* 20:897–910
93. Köppe R, Kasai PH (1994) Aliphatic ketone anion radicals: a matrix isolation ESR study. *J Phys Chem* 98:12904–12910
94. Saenko EV, Laikov DN, Baranova IA, Feldman VI (2011) Communication: stabilization of radical anions with weakly bound electron in condensed media: a case study of diacetyl radical anion. *J Chem Phys* 135:101103 (1–4)

Chapter 6

Radiation Chemistry of Solid-State Carbohydrates Using EMR

Henk Vrielinck, Hendrik De Cooman, Freddy Callens and Einar Sagstuen

Abstract We review our research of the past decade towards identification of radiation-induced radicals in solid state sugars and sugar phosphates. Detailed models of the radical structures are obtained by combining EPR and ENDOR experiments with DFT calculations of g and proton HF tensors, with agreement in their anisotropy serving as most important criterion. Symmetry-related and Schonland ambiguities, which may hamper such identification, are reviewed. Thermally induced transformations of initial radiation damage into more stable radicals can also be monitored in the EPR (and ENDOR) experiments and in principle provide information on stable radical formation mechanisms. Thermal annealing experiments reveal, however, that radical recombination and/or diamagnetic radiation damage is also quite important. Analysis strategies are illustrated with research on sucrose. Results on dipotassium glucose-1-phosphate and trehalose dihydrate, fructose and sorbose are also briefly discussed. Our study demonstrates that radiation damage is strongly regio-selective and that certain general principles govern the stable radical formation.

6.1 Introduction and Motivation of the Study

The structure of radiation-induced radicals in solid state sucrose has been studied with electron magnetic resonance (EMR) techniques since the early 1960's [1–7]. However, only some 5 years ago the identity of three radicals, dominating the room temperature (RT) stable electron paramagnetic resonance (EPR) spectrum, was convincingly established [8, 9]. This resulted primarily from a detailed comparison of proton hyperfine (HF) interactions, determined from single crystal electron nuclear double resonance (ENDOR) experiments, with the results of high-level

H. Vrielinck (✉) · H. De Cooman · F. Callens
Department of Solid State Sciences, Ghent University,
Krijgslaan 281-S1, 9000 Ghent, Belgium
e-mail: Henk.Vrielinck@UGent.be

E. Sagstuen
Department of Physics, University of Oslo, Blindern,
P.O.Box 1048, 0316 Oslo, Norway

© Springer International Publishing 2014

A. Lund, M. Shiotani (eds.), *Applications of EPR in Radiation Research*,
DOI 10.1007/978-3-319-09216-4_6

density functional theory (DFT) calculations. The situation for other sugars and related carbohydrates is similar: although stable radical production has been reported for several decades, reliable identifications of their structures are in general much more recent [10–12] or has to date not yet been achieved [13, 14]. A first important reason for this is that stable radical structures in organic solids very often differ substantially from the pristine molecule (crystal) structures and are the result of a complex reaction chain after the initial ionization or electron capture process [15]. The radicals stabilized after irradiation at low temperatures (\sim liquid He or N₂) are, however, more directly structurally related to those of the pristine molecules, and although such studies are experimentally far more challenging, the identification of the radical species is therefore in principle simpler [16–21]. Following the evolution of the EPR and ENDOR spectra towards the RT stable stage via thermal annealing is one approach to elucidate the structures of the stable species and to unveil their formation mechanisms. Irradiation in general, however, produces several distinct radical species whose EPR spectra, all characterized by HF interactions with several protons, strongly overlap. This is the second main reason why EPR spectra of irradiated sugars are often difficult to interpret, even when studied in single crystal form. In this chapter, techniques for spectrum decomposition and strategies for identification of structure and formation pathways for (stable) radicals are illustrated using our studies on solid state sucrose and related carbohydrates.

The main goal of this research is fundamental: improving the understanding of the radiation chemistry in solid carbohydrates. Important research objectives include uncovering general principles in the radiation-induced reactions and understanding the selectivity of radical formation in these materials. First and foremost, this requires reliable identification of the radicals in a sufficiently large number of materials and at different stages of the post-radiation chemistry. The results of this study may furthermore help to elucidate the direct radiation effect in the sugar units of the DNA helix [22, 23]. The latter is of considerable importance as sugar radicals are the main precursors for double strand breaks, the most harmful form of DNA damage with respect to biological consequences. Although not *a priori* obvious, solid state sugars may present a good model for studying direct effect radiation-induced damage in DNA as there are no radical interactions with a solvent. Moreover, the crystal structure to some extent mimics the tight, rigid packing of DNA in chromatin, and the role of hydrogen bonds in both systems is expected to be similar. As the similarity between DNA and solid state sugars may include both the initial radiation damage and the stable products, information on structures and processes at all stages after irradiation is relevant.

A second motivation is more applied and mostly related with the final stable radicals. The EPR signal intensity of such radicals may be used to determine radiation doses. Since the beginning of the 1980s the potential of sucrose in radiation dosimetry has been recognized [24, 25] and has been the subject of many EPR studies [26–32]. When samples are properly stored, the EPR spectrum of irradiated sucrose has long term stability and, after a short initial period of strong changes, shows only limited fading. Table sugar consists for over 90% of sucrose and the radiation-induced EPR spectra of table sugar and sucrose resemble each other very

closely. Therefore, the ubiquitous table sugar is of particular interest for accident and emergency dosimetry. The composite nature of the stable EPR spectrum of irradiated sucrose, as a result of the presence of various types of radicals, along with the complex transformations of this spectrum in a short time span after irradiation, are issues of concern. Sucrose is not the only sugar interesting from a dosimetric point of view. One can also apply EPR spectrometry for detection and control of irradiated sugar-containing foodstuffs [33–42]. Here, however, an additional complication arises. In foodstuffs very often a mixture of sugars is present, all giving rise to distinct radiation-induced EPR spectra. In this respect achieving a detailed understanding of the spectral shape of various common sugars, e.g. glucose, fructose and sorbose, is very relevant.

6.2 Materials and Experimental Methods

6.2.1 Solid State Carbohydrates

Table 6.1 gives an overview of the carbohydrates that have been covered by our studies. Most of the experiments were performed on single crystals, grown from aqueous solution by slow evaporation of the solvent at constant temperature. When possible, partially deuterated crystals were also grown from D₂O solutions. Crystallization from D₂O, redissolution in D₂O and recrystallization is expected to replace all the crystal water by D₂O and 95% of the OH groups by OD. For fructose, crystallization proved very difficult, rendering deuteration unfeasible.

Selected experiments were also performed on irradiated powders of carbohydrates. These were used as purchased, without further refinement. In the case of fructose, selectively ¹³C and ²H labeled carbohydrate powders (Sigma Aldrich, Omicron Chemicals) were included in the study.

Crystals were oriented for rotation around a crystallographic axis, either by Laue diffraction or by inspection of the X-ray diffraction pole figures and then transferred to sample holders (quartz rods or copper pedestals) or fixed in quartz tubes with minimal loss of orientation (<5°). For the crystals with orthorhombic symmetry these rotation axes are usually $\langle a \rangle$, $\langle b \rangle$ and $\langle c \rangle$. For sugars (sugar phosphates) with monoclinic symmetry crystals were at some occasions oriented for rotation around the $\langle a^* \rangle$ (perpendicular to $\langle b \rangle$ and $\langle c \rangle$) or $\langle c^* \rangle$ axes. In order to resolve the Schonland ambiguity [43, 44], the angular dependence of the EPR and ENDOR spectra was also recorded for rotations around axes deviating from those mentioned above. These rotation planes will be referred to as skewed planes.

6.2.2 Irradiation for Radical Production

Irradiations either at RT or at 273 K (water-ice cooled sample) occurred *ex situ*, using X-rays from a Philips W-anode X-ray tube operated at 60 kV and 40 mA,

Table 6.1 Overview of carbohydrates investigated in this work, labeling the C-atoms. β indicates the angle between the $\langle a \rangle$ and the $\langle c \rangle$ direction for monoclinic lattices

Chemical name	Short name	Molecular structure	Space group
α -D-glucopyranosyl-(1 \leftrightarrow 2)- β -D-fructofuranoside	Sucrose		$P2_1$, monoclinic, $\beta=102.97^\circ$
Dipotassium glucopyranose-1-phosphate	K2G1P		$P2_1$, monoclinic, $\beta=110.39^\circ$
α -D-glucopyranosyl-(1 \leftrightarrow 1)- α -D-glucopyranoside	Trehalose		$P2_12_12_1$, orthorhombic
β -D-fructopyranose	Fructose		$P2_12_12_1$, orthorhombic
α -L-sorbopyranose	Sorbose		$P2_12_12_1$, orthorhombic

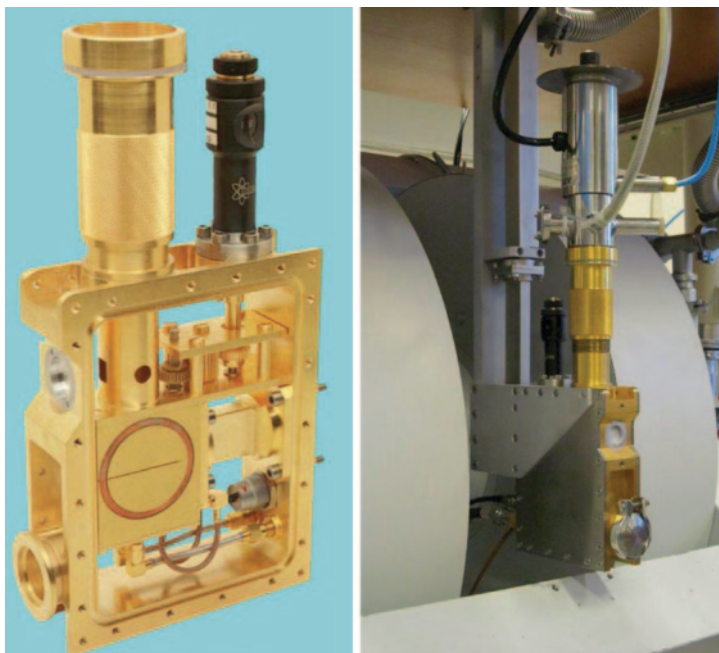


Fig. 6.1 X-band EPR/ENDOR cavity for *in situ* X-irradiation of crystals at low temperature. *Left:* detail of the cavity design with the vacuum-sealed side-walls of the system removed for showing the EPR modulation coils, the iris adjustment system, optical and X-ray irradiation windows, electrical connections for the EPR modulation and the (internal) 4-turn ENDOR coils, the waveguide connection and a vacuum pump-out port, *right:* cavity in the setup—microwave bridge and cavity can be slid between and outside of the poles of the electromagnet, for measurement and X- or UV irradiation, respectively

resulting in a radiation dose rate of approximately 1.3 kGy/min. For most ENDOR experiments the samples needed to be irradiated for at least 1 h. In the study of stable radicals, crystals were irradiated before orienting and mounting onto quartz sample holders. In the study of less stable species samples had to be irradiated after mounting in quartz holders and EPR spectra sometimes contained contributions from irradiated quartz. After irradiation, crystals or powders were transferred into a temperature-controlled (by Oxford He flow cryostats) microwave cavity, stabilized at the measurement temperature.

For studying primary radical species and/or intermediate steps in the evolution towards RT stable radiation products, crystals were irradiated *in situ* at 6–8 K using liquid helium or at 77 K using liquid nitrogen. For this purpose, a special microwave cavity assembly originally devised by W.H. Nelson was constructed [45]. The setup for X-band (9.8 GHz) is shown in Fig. 6.1.

A copper sample rod to which the crystal is mounted with conducting epoxy glue is fixed to the Joule-Thompson end of a cold-finger cryostat (Air Products He-liTran). This is inserted into a telescoping cryostat holder at the top of an evacuated

titanium/brass enclosure. The enclosure is equipped with a thin Al and a quartz window to allow for X-ray and optical irradiation, respectively. These windows are situated above the microwave cavity. The cavities used are home-made X (TM_{110}) or Q-band (34 GHz, TE_{011}) cavities equipped with EPR modulation- and ENDOR coils as well as externally accessible variable iris control. The cryostat with sample is lowered to the irradiation position, and after evacuation of the assembly, the crystal is cooled to the desired temperature and irradiated. The temperature is monitored and controlled using an Oxford ITC 503 temperature controller connected to a heater assembly and thermocouple at the cryostat cold end. As X-ray source, a Philips Cr-anode X-ray tube operated at 60 kV and 40 mA was used, providing a radiation dose rate of approximately 0.16 kGy/min. For the results presented here, doses between 10 and 40 kGy were used. After irradiation, the sample is lowered into the center of the microwave cavity for EMR measurements. Oxygen-free high conductivity copper sample posts and conducting epoxy glue are used to avoid EPR signals from radiation-induced radicals in the crystal mounting system.

6.2.3 EPR, ENDOR and ENDOR-Induced EPR Experiments

The EMR experiments were performed using commercial Bruker CW spectrometers (ER200, Elexsys 500/560) at the microwave X- and Q-bands. For g factor determinations, accurate measurements of the microwave frequency and magnetic field are indispensable. The frequency measurements were achieved using external X and Q-band frequency counters.

For the EMR measurements after RT irradiation, the magnetic field at the beginning and at the end of each field sweep was measured using an ER035M NMR Teslameter. Subsequently a calibration of the field measurements was performed by determining the g value of a field marker (DPPH at 2.0036 [46] in X-band, g_{\perp} of CO_3^{3-} in $CaCO_3$ at 2.0031 [47] in Q-band). For the EMR measurements after *in situ* low temperature (LT) irradiation, the magnetic field was calibrated using a BRUKER ER036 TM Teslameter in combination with a DPPH field marker.

All EPR spectra presented here are recorded using magnetic field modulation (100 kHz, 0.1 mT, unless otherwise mentioned) and all ENDOR spectra using frequency modulation (modulated at 10, 12.5 or 25 kHz with a few 100 kHz depth). As a result their shape resembles the first derivative of an absorption spectrum. Occasionally, pulsed EPR experiments at X-band (Hyperfine Sublevel Correlation Spectroscopy=HYSCORE [48]) were performed in collaboration with other research groups: we refer to the relevant paper for experimental details [9].

ENDOR normally requires partial saturation of the EPR spectrum. Although EPR spectra of radiation-induced radicals in carbohydrates readily saturate at any temperature for microwave powers above 1 mW, for ENDOR experiments very often temperatures are required that only are attainable using liquid helium (50 K or 20 K). For sucrose at X-band, however, ENDOR spectra can be recorded at any temperature from 4 to 300 K.

ENDOR measurements for carbohydrates in general only reveal HF interactions with protons, the larger of which are resolved in the EPR spectra. Yet, a detailed ENDOR analysis is necessary as the EPR spectra are very complex. The simultaneous observation of spectra from several symmetry-related orientations—with respect to the magnetic field—of the same radical species [49], and this for several different radicals present, makes an EPR-only analysis practically impossible. ENDOR is usually performed by saturating the EPR spectrum at a fixed magnetic field position, sweeping the radiofrequency. In order to obtain the transitions for all dominant radical species and all sites, for each magnetic field orientation, the ENDOR spectrum has to be recorded at several (very often 2–3) field positions for each orientation. Nonetheless, certain (probably less dominant) radical species may escape from detection in this way. In order to avoid this, one can record the ENDOR spectrum as a function of magnetic field over the complete range where EPR intensity is observed [50, 51].

As an example of such an ENDOR experiment carried out in the field-frequency space (also called Field-Frequency ENDOR, FF-ENDOR), a FF-ENDOR spectrum of sucrose, recorded at 110 K several days after X-ray irradiation at RT, is shown in Fig. 6.2. This spectrum is obtained with the magnetic field oriented close to the $\langle b \rangle$ axis. Along with the FF-spectrum, corresponding ENDOR, EPR and ENDOR-induced EPR (EIE) traces are shown. The signal height is represented in color scale in the FF-ENDOR spectrum, with red and blue indicating high and low (negative) values, respectively. The intensity of the spectra is increased in order to enhance the contrast for the signals of the more informative larger proton HF couplings, and as a result in the proton Larmor frequency range (50–52 MHz at Q-band) only one broad, intense line can be discerned. The horizontal dashed line in Fig. 6.2 corresponds to an ENDOR spectrum recorded at one magnetic field position (1212.5 mT) which is shown at the top of the figure. Combinations of ENDOR transitions at particular radiofrequencies (ν_{ENDOR}) are repeated at several magnetic field positions, although the transition frequencies exhibit a slight shift with magnetic field (B). This shift may be predicted to first order as (see also Sect. 6.2.4, spin Hamiltonian = SH) [49]

$$\frac{\partial \nu_{\text{ENDOR}}}{\partial B} = \pm g_H \mu_N \quad (6.1)$$

with g_H the proton nuclear g factor and μ_N the nuclear magneton. For nuclei with $I=1/2$ all ENDOR transitions can be recorded at each EPR transition of a particular radical, hence one can in principle reconstruct the EPR spectrum corresponding to a particular ENDOR transition by measuring its signal height at a maximum of the (first derivative) signal as a function of magnetic field while simultaneously correcting the transition frequency according to Eq. (6.1). Such spectra are referred to as EIE spectra [52–54]. In the bottom of the figure, examples of the EIE spectra are shown, recorded by monitoring the height of the ENDOR lines marked in the top spectrum of Fig. 6.2 while sweeping the magnetic field. As we follow the positive peak position, the EIE spectrum is expected to have an absorption-like shape, as opposed to the first-derivative shape for the EPR spectrum. Although EPR and EIE

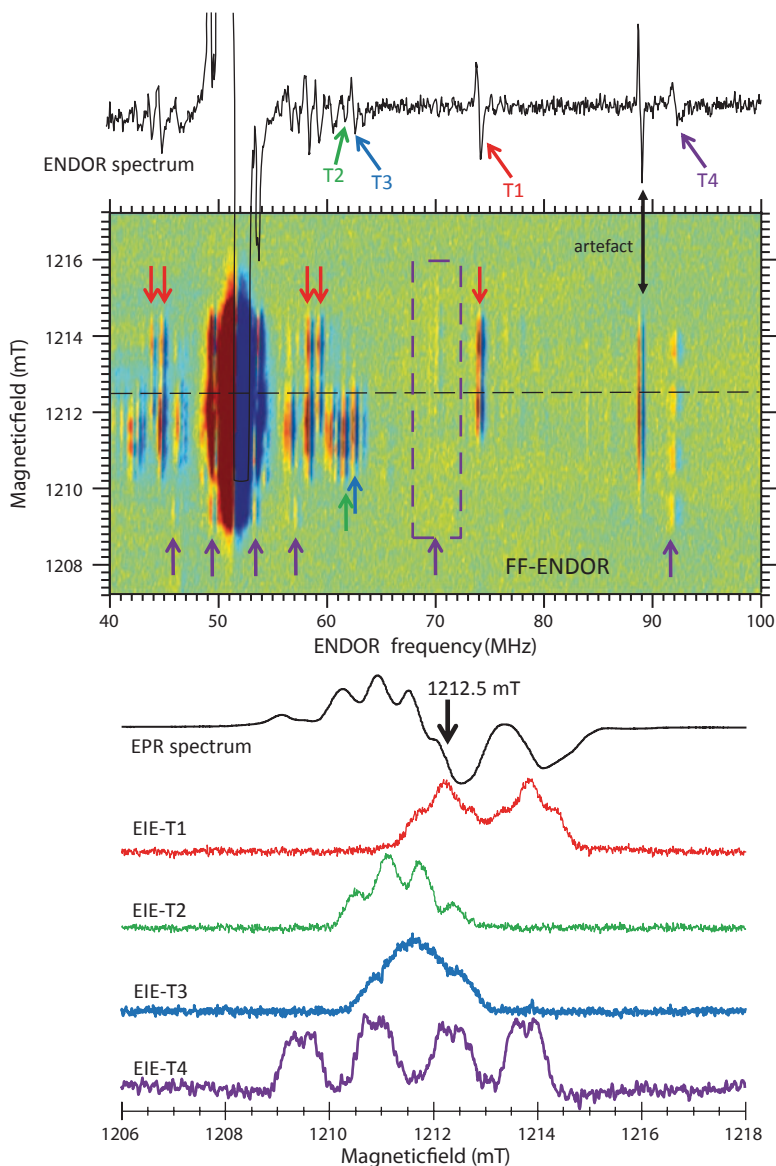


Fig. 6.2 ENDOR, FF-ENDOR, EPR and EIE spectra of stable radical species in sucrose X-irradiated at RT and recorded at 110 K with the magnetic field parallel to the $\langle b \rangle$ axis, several days after irradiation. The ENDOR spectrum is recorded at the magnetic field position marked with an *arrow* in the EPR spectrum and corresponds to the horizontal cut in the FF-ENDOR spectrum indicated by the *dashed line*. The ENDOR transitions whose intensity is monitored in the EIE experiments (*bottom traces*) are marked by *colored arrows*. $\nu_{\text{MW}} = 34.00$ GHz

spectra of a radical should carry the same SH information, an EIE spectrum cannot be expected to perfectly match the integrated EPR spectrum of the corresponding radical component. Indeed, this would imply that (i) there are no higher order field corrections to the ENDOR frequencies, (ii) the width (shape) of the ENDOR line remains constant throughout the complete EPR field range and (iii) the EPR and ENDOR spectra are by no means distorted by the electron and/or nuclear spin relaxation. In particular, it should be remembered that the EIE is recorded under EPR microwave saturation conditions commonly resulting in significant line broadening. Nevertheless, EIE is very effective in decomposing multi-composite EPR spectra and is less time-consuming than recording the FF-ENDOR spectrum over the complete EPR field range.

As for the interpretation of Fig. 6.2, in the FF-ENDOR spectrum four dominant contributions can be discerned. A first clear contribution, labeled T1 (red arrows), has its largest ENDOR frequency around 73 MHz, due to a β -proton HF interaction. The corresponding EIE spectrum exhibits in addition two smaller ^1H interactions, clearly visible with high-frequency transitions slightly below 60 MHz and low-frequency transitions around 45 MHz. In the 60–65 MHz range, the two overlapping transitions of the strongest, α -type HF interactions of radicals T2 and T3 are seen. Also these two radicals have two more pronounced HF interactions, which are strongly overlapping at this particular field orientation and for this reason are not indicated in the FF-ENDOR spectrum. The T1-T3 radicals have been thoroughly characterized through angular dependent EPR and ENDOR measurements [55] and detailed molecular models were found for them, based on DFT calculations (see Sect. 6.3.4) [8, 9]. They constitute the dominant contribution to the central part of the powder EPR spectrum of irradiated sucrose (see Sect. 6.4.5).

Above 90 MHz, another interesting contribution to the spectrum is discerned. It is labeled here as T4 [56] and its ENDOR transitions are marked by purple arrows in the FF-ENDOR spectrum. The corresponding EPR (EIE) spectrum exhibits three resolved HF interactions. The largest splitting (2.9 mT, ~ 81 MHz) corresponds to the ENDOR transition at 92–93 MHz. The ENDOR transition of the intermediate splitting (1.4 mT, ~ 37 MHz) is not clearly observed (area bordered by purple dashed line), probably as a result of line broadening. For the smallest HF interaction, only barely resolved in the EIE spectrum (0.3 mT, ~ 10 MHz), the ENDOR transitions are found at 46 and 57 MHz. The HF splitting corresponding to the transitions at 49 and 53 MHz (~ 4 MHz, 1.3 mT) is not resolved in the EIE spectrum. The as yet unidentified T4 radical very probably constitutes the dominant contribution to the “wing parts” of the EPR spectrum of irradiated sucrose powder [57, 58] (see Sect. 6.4).

6.2.4 Spin Hamiltonian Analysis: Extraction of g and HF Tensors

The SH relevant to the analysis of radicals in carbohydrates is that for a paramagnetic center with spin $S=1/2$, interacting with various nuclei—mostly protons—with spin $I_i=1/2$ [49]

$$\hat{H}_S = \mu_B \vec{B} \cdot \vec{g} \cdot \hat{S} + \sum_i \left(\hat{S} \cdot \vec{A}_i \cdot \hat{I}_i - \mu_N g_H \vec{B} \cdot \hat{I}_i \right) \quad (6.2)$$

in which μ_B represents the Bohr magneton. \vec{g} and the proton HF tensors \vec{A}_i are to be determined by fitting the experimental angular dependence of the EPR and ENDOR spectra. In this chapter we follow the convention of labeling the principal values of these tensors ($g_x, g_y, g_z; A_x, A_y, A_z$) in ascending order and the corresponding principal directions are specified via their direction cosines with respect to the $\langle a^* \rangle$, $\langle b \rangle$ and $\langle c \rangle$ crystal axes. For radicals, which exhibit three appreciable HF interactions, like the stable radicals in sucrose (see Sect. 6.4.5), the SH already involves 16 states, rendering the time for computing transition frequencies (or fields) very long, especially in the context of fitting. For this reason, simplifications are used that are justified *a posteriori* by comparison between the experimental data and simulations based on the diagonalization of the full SH. These approximations yield sufficiently high accuracy as long as high-field conditions are satisfied, that is, as long as the first term in the SH is at least two orders of magnitude larger than all other terms. Under these circumstances it is justified to determine the g tensor for a single radical species from the center of the EPR pattern recorded at each magnetic field orientation, and thus effectively only consider the first term of the SH. The same can be done for multi-composite spectra after separating the different contributions by EIE measurements. For ENDOR experiments the high-field condition implies that coupling between the different nuclei via the electron spin is practically absent. As a result, one can analyze the HF coupling for an individual nucleus as if this is the only nuclear interaction with the unpaired electron. The sum over nuclear interactions in the SH reduces to just two terms (HF and nuclear Zeeman interaction for this one nucleus). However, it also implies that if ENDOR transitions of different symmetry-related crystal sites of the same radical are recorded in the same spectrum, e.g. as a result of insufficient g resolution, it may not be evident to link HF tensors for interactions from the same site of the radical correctly. This has implications for simulations of the EPR spectra, especially for powders [57, 58].

The fitting of angular dependent ENDOR data was mostly performed using the MAGRES program [59]; simulations of EPR, ENDOR and EIE spectra and fitting of angular dependent EIE data were based on the EasySpin routines [60] in MATLAB. In some cases, the KVASAT program was used [61, 62]. For extracting a HF or a g tensor from angular dependent ENDOR or EIE spectra, respectively, data in at least three independent planes have to be available. As mentioned in Sect. 6.2.1, for orthorhombic crystals very often the $\{ab\}$, $\{bc\}$ and $\{ca\}$ planes are selected, and for monoclinic either $\{a^*b\}$, $\{bc\}$ and $\{ca^*\}$, or $\{ab\}$, $\{bc^*\}$ and $\{c^*a\}$. Indeed, using

crystallographic rotation axes is practical, as they most often are easily recognized from the crystal morphology. In addition, a considerable advantage of taking these planes is that the magnetic field may be aligned quite easily to specific (crystallographic) orientations where different symmetry-related sites of the radicals become magnetically equivalent. At these orientations their EPR/ENDOR spectra coincide: the site-related branches in the angular variations cross. At such coincidences EPR and ENDOR spectra can be recorded with higher signal/noise ratio and they usually exhibit an easier substructure. However, an analysis in these three planes in general yields two g or HF tensors that fit the available data equally well. This phenomenon, that has been labeled as the “Schonland ambiguity” [43, 44], is well-established in literature but still not widely recognized among experimental and computational researchers. Only one of the two fitting results corresponds to the actual tensor to be determined, and also fits the data that may be obtained outside of these three planes. The second tensor (labeled “Schonland conjugate”) is merely a fitting result without further physical meaning. For the principles of this ambiguity in g and HF tensor analysis, as well as for practical ways of avoiding it, we refer to our recent paper on this subject [44]. In the next subsection, the Schonland ambiguity is illustrated in the analysis procedure for a particular example.

6.2.5 Example of Schonland Ambiguity in Data Analysis

The Schonland ambiguity finds its origin in an ambiguity in the choice of rotation sense when analyzing angular dependent data. We illustrate the principles here using the SH data for the stable radical T1 in irradiated sucrose. This is not because it would be the best example, but rather in order to demonstrate that the Schonland ambiguity may pop up in any g or HF tensor analysis when data are restricted to three orthogonal planes defined by the unit cell axes. As already mentioned, sucrose has monoclinic symmetry. The analysis is presented for data in the $\{a^*b\}$, $\{bc\}$ and $\{ca^*\}$ planes, and the SH parameters (tensors) are represented in the a^*bc reference frame. Implications of having data in other (non-orthogonal) rotation planes for calculating Schonland conjugate tensors and/or lifting Schonland ambiguity may be found in our basic article on this subject [44].

For most of the radicals discussed here, the HF tensors were analyzed before the g tensors, which were extracted from EIE measurements and relied on the knowledge of the HF tensors [13, 57, 63]. It is more instructive, however, to start the discussion with the problem of extracting a g tensor from angular dependent resonance field positions. In Fig. 6.3 simulated angular dependences of the central field position of the EPR (or EIE) spectrum of T1 are shown in four rotation planes [57]. These make use of the g tensor data in Table 6.2: the g tensors for the two (monoclinic) symmetry-related radicals (Tensors 1 and 2) and the two tensors Schonland conjugated to these (Tensors 3 and 4). In Ref. [44] it is shown that the latter can be calculated by changing either the (1,2) and (2,1), or the (2,3) and (3,2) elements of the symmetric tensor $\tilde{g}^2 = \tilde{g} \cdot \tilde{g}^T$. Symmetry-related tensors only differ with respect

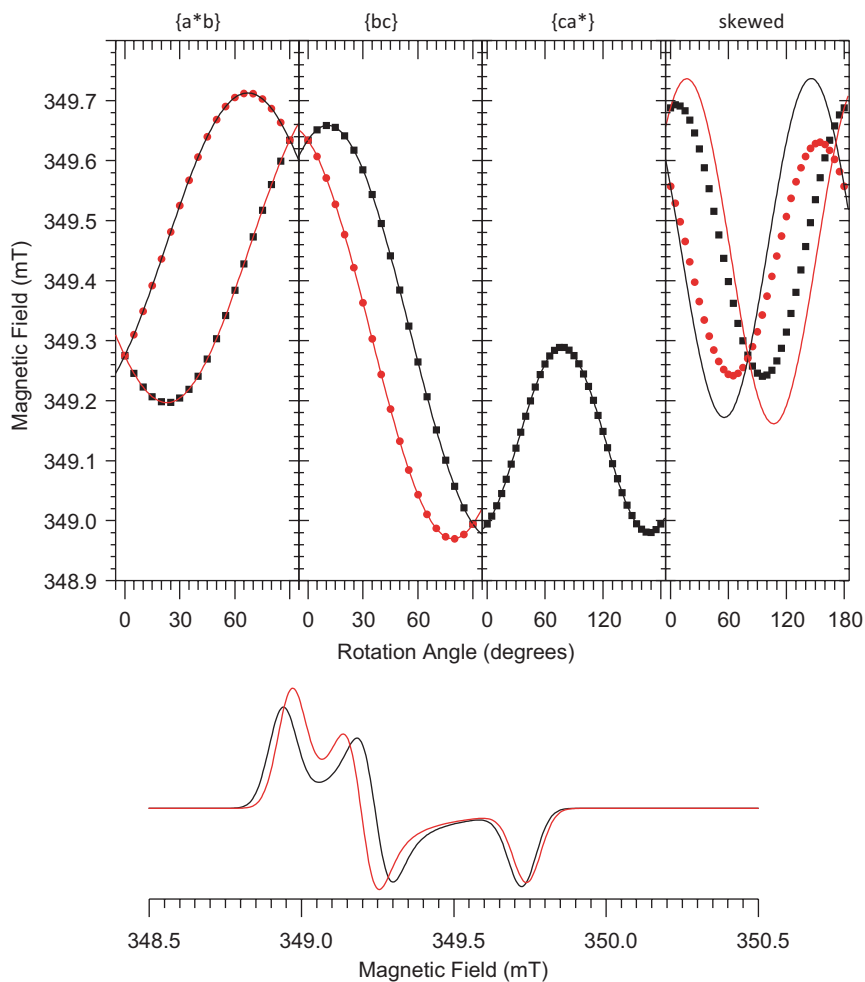


Fig. 6.3 Illustration of Schonland ambiguity for the g tensor for data analysis in three orthogonal ($\{a^*b\}$, $\{bc\}$ and $\{ca^*\}$) and one skewed plane (polar angles $\theta=26.1^\circ$, $\phi=190.3^\circ$). The g tensors used in the simulations are listed in Table 6.2: *filled black squares*—tensor 1; *filled red circles*—tensor 2; *full black line*—tensor 3; *full red line*—tensor 4. In the *bottom* part of the figure the simulated powder EPR spectra are shown, assuming that no HF interactions are resolved, using the original g tensor (tensor 1 or tensor 2—*black line*) and its Schonland conjugate (tensor 3 or tensor 4). The polar angles are defined such that $\langle c \rangle$ corresponds with $\theta=0^\circ$ and $\langle a^* \rangle$ with $\theta=90^\circ$, $\phi=0^\circ$. $\nu_{\text{MW}}=9.8$ GHz

to their principal directions, whereas Schonland conjugate tensors also differ with respect to the principal values. In Table 6.2 one may verify that in the chosen example this difference in principal g values is subtle (yet not negligible), but that the differences in principal directions may be quite substantial.

Table 6.2 g tensor for the T1 stable radical in irradiated sucrose [57]: tensor 1—original tensor as obtained from fitting angular dependent EIE data; tensor 2—monoclinic symmetry-related tensor to 1; tensor 3—Schonland conjugate of tensor 1 by inverting the $g^2(1,2)$ and $g^2(2,1)$ matrix elements of tensor 1; tensor 4—monoclinic symmetry-related tensor to 3. In the last two columns, the difference in principal values and directions (smallest angle between the directions, in degrees) with tensor 1 are given

Tensor #	g_i	$\langle a^* \rangle$	$\langle b \rangle$	$\langle c \rangle$	Δg_i	$\Delta \theta$
1	2.0021	0.3619	-0.9232	-0.1295		
	2.0049	0.8781	0.2991	0.3798		
	2.0066	-0.3130	-0.2512	0.9160		
2	2.0021	-0.3619	-0.9232	0.1295	0	45
	2.0049	0.8781	-0.2991	0.3798	0	34
	2.0066	-0.3130	0.2512	0.9160	0	29
3	2.0020	-0.3862	-0.9030	-0.1884	-0.0001	44
	2.0051	0.9156	-0.4001	0.0405	0.0002	45
	2.0065	-0.1120	-0.1569	0.9813	-0.0001	13
4	2.0020	0.3862	-0.9030	0.1884	-0.0001	18
	2.0051	0.9156	0.4001	0.0405	0.0002	21
	2.0065	-0.1120	0.1569	0.9813	-0.0001	27

Carbon-centered radicals in carbohydrates often exhibit close to axial g tensor symmetry ($g_x < g_y \approx g_z$). The g tensor of the T1 radical is, however, clearly rhombic, with three clearly different principal values, two of which exhibit a considerable positive shift from the free electron g value. The implications of these characteristics for the radical model will be discussed in Sect. 6.3.4.

In Fig. 6.3 X-band simulations using Tensors 1 and 2 are represented with symbols and could be considered as experimental data. The simulations with the other two tensors are shown as full lines.

The example nicely illustrates that when restricting measurements to the first three planes, one can find two tensors, not related by symmetry, which fit the data equally well. The Schonland ambiguity springs from the fact that one cannot *a priori* know which symmetry-related branches in the different rotation planes to connect with one another. It is, however, also immediately clear that in the fourth skewed plane the degeneracy of the Schonland conjugate tensors is lifted, presenting an obvious method to select the right set of tensors among the two possibilities.

The simulations at the bottom of Fig. 6.3 suggest that inspection of the powder spectrum may also be used for resolving the Schonland ambiguity. This may in particular be so if line widths are narrow and if the spectra are not complicated by resolved HF interactions. Powder spectra are particularly sensitive to changes in the rhombicity of g tensors. This results in a considerable difference in the low field part of the simulated powder EPR spectra for the two Schonland conjugate tensors, in spite of only very subtle changes in the absolute g values.

We now move on to the analysis of HF tensors from angular dependent ENDOR measurements. The three HF tensors determined for the T1 radical in irradiated

Table 6.3 Principal A values and directions for the three resolved proton HF interactions of the T1 stable radical in irradiated sucrose, as determined from angular dependent ENDOR measurements in four rotation planes (HF1, HF2, HF3) [9] and the Schonland conjugate tensors (HF1S, HF2S and HF3S) which fit the data for the high-frequency X-band ENDOR branches in the $\{a^*b\}$, $\{bc\}$ and $\{ca^*\}$ planes equally well. The last two columns present the differences in principal values and directions (angles in degrees) between Schonland conjugate and original tensors

A tensor	A_i	$\langle a^* \rangle$	$\langle b \rangle$	$\langle c \rangle$	ΔA_i	$\Delta \theta$
HF1	42.81	0.616	0.121	-0.778		
	44.42	0.072	0.975	0.209		
	53.17	0.784	-0.185	0.592		
HF1S	41.90	0.547	0.499	-0.673	-0.91	23
	45.56	-0.246	0.863	0.441	1.14	24
	52.92	0.800	-0.075	0.595	-0.24	7
HF2	13.19	0.106	0.825	0.555		
	13.57	0.989	-0.144	0.025		
	20.87	0.101	0.546	-0.832		
HF2S	12.66	0.595	0.658	0.461	-0.53	30
	14.15	0.803	-0.519	-0.294	0.58	31
	20.81	0.046	0.545	-0.837	-0.06	3
HF3	-17.48	-0.711	-0.241	0.660		
	-14.80	-0.38	0.922	-0.073		
	-0.93	-0.591	-0.302	-0.748		
HF3S	-19.12	-0.633	-0.516	0.577	-1.64	17
	-12.07	-0.492	0.844	0.215	2.73	18
	-2.18	-0.598	-0.148	-0.788	-1.25	9

sucrose [55], along with their Schonland conjugates, are taken as an example. Their principal values and directions are given in Table 6.3, for only one of the symmetry-related sites. The calculation of a Schonland conjugate A tensor requires more care than in the case of the g tensor, however. The result does not only depend on the rotation planes in which experimental data were analyzed (as for the g tensor), but also on the microwave frequency (magnetic field B_0 at which the ENDOR spectrum is recorded) and in which of the M_S electron spin multiplets the ENDOR transitions take place. Very often only the high-frequency branches (with $M_S = -1/2$ ($1/2$) for $A > 0$ ($A < 0$)) of ENDOR transitions are considered for extracting the HF tensor. The low-frequency transitions are in many cases not (well) observed and for that reason sometimes simply not recorded. In Ref. [44] it is demonstrated that in this particular case one can find the tensor Schonland conjugate to a given tensor \vec{A} by making a similar sign change in the off-diagonal elements (as for the g tensor) of the symmetric tensor \vec{K}_{high}^2

$$\vec{K}_{high} = -\text{sign}(A_{iso}) \frac{\vec{A}}{2} - g_N \mu_N B_0 \vec{1} \quad (6.3)$$

with $A_{iso} = \text{trace}(\vec{A})/3$, the isotropic HF coupling.

Figure 6.4 is organized in a similar way as Fig. 6.3: symbols represent simulations (\sim experimental data points) for the original tensor and full lines for its Schonland conjugate. The simulations are again performed at X-band. Exactly as in the discussion for the g tensor, for the high frequency branches the simulation for the two Schonland conjugate tensors coincide perfectly in the first three (orthogonal) planes, but in the fourth (skewed) plane a clear mismatch is observed [64]. However, Fig. 6.4 and Eq. (6.3) illustrate that the Schonland ambiguity for HF tensors is not as essential as in the case of the g tensor. The B_0 dependence suggests that a comparison of spectra recorded in different microwave frequency bands may also resolve the ambiguity, and if one manages to record transitions in both M_S multiplets, the ambiguity *in principle* does not exist [65].

The simulations for the HF1 and HF2 tensors (and their Schonland conjugates) demonstrate that in practice, the differences may be quite subtle and even lie within experimental accuracy. The differences are clearest for interaction HF3, which exhibits the largest anisotropy. In addition, in Ref. [44] we have shown that in the limiting cases for very low and very high microwave frequencies (when one of the terms in Eq. (6.3) clearly dominates), the ambiguity may also not be resolved by analyzing the data for both M_S multiplets.

Finally, the comparison of the Schonland conjugate forms of the tensors in Tables 6.2 and 6.3 deserves some further comments. The Schonland ambiguity may hamper radical identification if the two possible fitting results may lead to different interpretations of the type of interaction. In the example elaborated in Ref. [44] it is shown how the Schonland conjugate of a particular HF tensor, typical of an α -proton, may have the symmetry typical of a β -proton coupling with large anisotropy, as expected for e.g. a β -hydroxyl proton coupling (see Sect. 6.3.1).

For none of the T1 HF tensors such drastic changes in interpretation occurs, although finding the correct form for the HF3 tensor (assisted by X-band HYSORE [9]) proved to be the key for finding the correct radical model. One may consider the differences in principal directions in Tables 6.2 and 6.3 not to be very large. However, in Sect. 6.3 it will be shown that the model identification strongly relies on the comparison between experimental and DFT calculated HF (and g) tensors. For accurate radical models, in particular the principal directions of calculated tensors are expected to reproduce the experimental results very well. Hence, it is important to determine these principal directions as precisely as possible and differences of the order of ~ 10 – 20° may indeed be very relevant.

As a conclusion of this subsection, we want to emphasize that both experimental and computational scientists involved in the identification of paramagnetic centers in low-symmetry (orthorhombic, monoclinic, triclinic) crystals should be aware of the Schonland ambiguity and its implications. Very often, having experimental data in three orthogonal planes is not sufficient to obtain an unambiguous result for the SH tensors. The discussion in this section and in Ref. [44] should enable computational scientists, aiming to find models for radicals characterized using EPR and ENDOR by others, to recognize situations where Schonland ambiguity may be an issue. Ref. [44] also provides details how to calculate the Schonland conjugate of

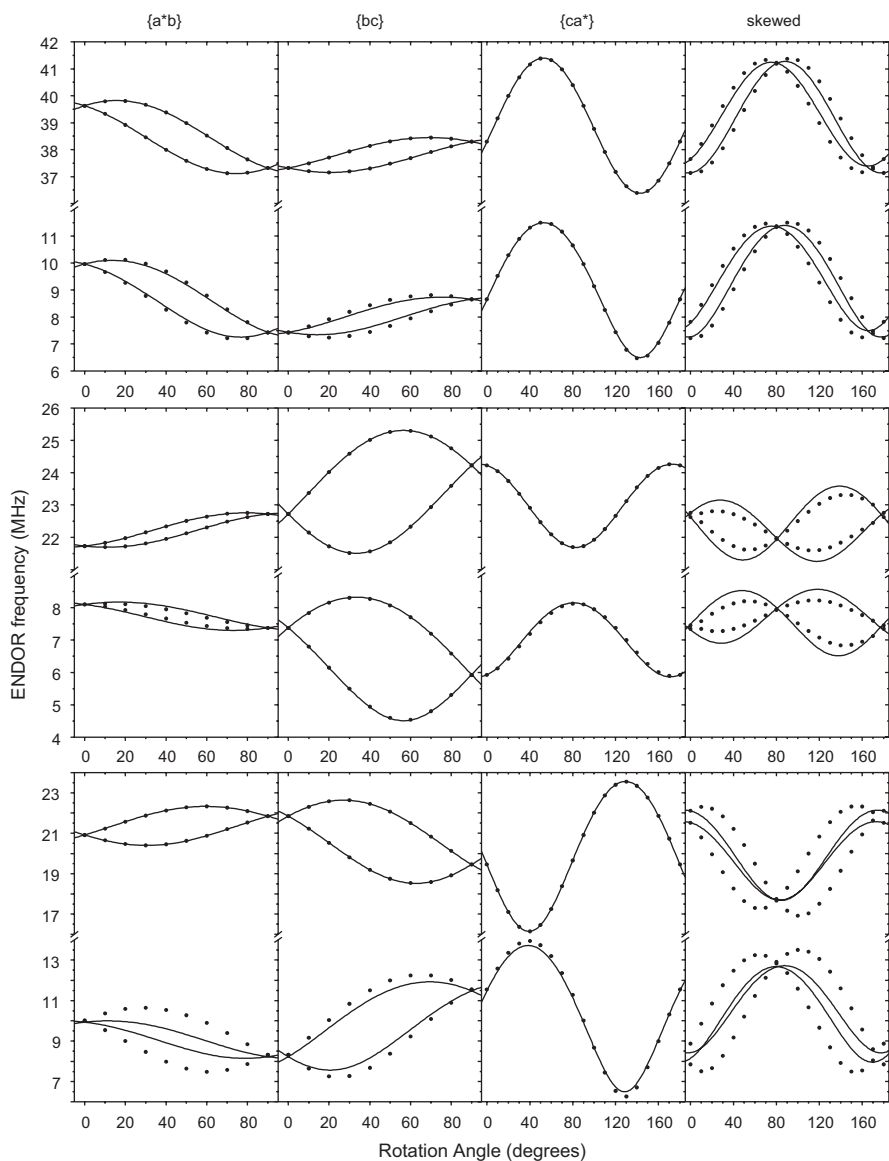


Fig. 6.4 Illustration of Schonland ambiguity for HF tensors for data analysis in three orthogonal ($\{a^*b\}$, $\{bc\}$ and $\{ca^*\}$) and one skewed plane (polar angles $\theta=26.1^\circ$, $\phi=190.3^\circ$). The HF tensors selected for simulation are those of the three resolved interactions for the stable radical T1 in irradiated sucrose (original—*filled circles*, and Schonland conjugate tensors—*full lines*), listed in Table 6.3

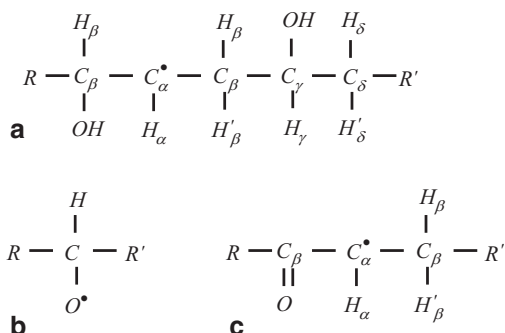
g and A tensors, for cases where the wrong tensor may have been reported in the literature. Finally, it is interesting to note that similar ambiguities may arise in the analysis of EPR/ENDOR data for high-symmetry crystals. A well-known example is the ambiguity in fitting the angular dependence of the EPR spectrum for a center with trigonal symmetry in a cubic crystal in a $\{100\}$ plane: two g tensors are found that fit the data equally well [66]. The ambiguity is lifted, however, if the angular dependence in a $\{110\}$ plane is analyzed.

6.3 Radical Model Identification: From Semi-empirical Theory to DFT Calculations

Even when created by low temperature irradiations, bond distances and angles in the relaxed radical structures may differ significantly from those in the undamaged molecule in the crystal. This may render radical identifications based on comparisons between the experimentally determined SH parameters and the undamaged molecular structure highly uncertain. For this reason, comparison of experimental SH parameters with those calculated using relaxed radical geometries in many cases represent the most reliable method for identifying radical species in irradiated carbohydrates. With increasing processor power and developments in DFT methodology, such calculations have undergone a tremendous evolution in the past decades. As this chapter focuses on the experimental aspects of the study, the technical details of the calculations will not be discussed here. We will only highlight the key points in the computational evolution. For more details, we refer to our papers and to Chap. 18 of this book, devoted to this issue.

In spite of this progress, the calculations have not evolved that far that they can predict which radicals will be formed and are stable (although progress in this direction is currently being pursued). In addition, our studies have shown that stable radical structures may differ very strongly from the undamaged structure, involving not only H-abstraction, but possibly also H_2O elimination, opening of the sugar ring, glycosidic bond rupture, etc. Considering that all these events may occur at several positions in the molecule, the number of radical structures to consider in the calculations becomes very large. Fortunately, the SH parameters carry key information on the radical structure, that can be used to obtain an initial guess of the radical structure and to restrict the number of physically realistic candidates via a set of semi-empirical theoretical rules [15]. Most of the theory that relates g and HF tensors of organic radicals to their electronic and geometrical structure was developed in the period 1950–1970, as experimental data became available. Very often, theoretical relations were developed for radicals with an essentially planar C-structure (sp^2 hybridization), where the radical's unpaired electron (spin density) is mainly localized in the $2p_z$ orbital of one of the C-atoms, directed perpendicular to the plane of C atoms. There is also very useful information available for non-planar radicals, though [67–73].

Fig. 6.5 Radical fragments that may be expected in carbohydrates. **a** Pure hydroxyalkyl radical **b** alkoxy radical **c** hydroxyalkyl radical with a carbonyl group in a β position



6.3.1 Semi-empirical Theory: Information Obtained from HF Interactions

Most of the radicals discussed in this chapter are carbon-centered with a planar bonding structure. Figure 6.5a shows a hypothetical hydroxyalkyl radical fragment that may be produced after irradiation of a carbohydrate, in which the nomenclature for proton HF couplings is defined. The proton bound directly to the carbon atom carrying the main spin density (C_α) is called an α -proton, a proton bound to a carbon atom adjacent to that (C_β) is called β -proton, on a next-nearest carbon atom γ , etc. The HF tensors of α -protons are characterized by a negative isotropic value, A_{iso}^α , due to spin polarization, and a strong anisotropy with a characteristic rhombic pattern [74]

$$\vec{A}_{iso}^\alpha = \begin{pmatrix} -a^\alpha & 0 & 0 \\ 0 & 0 & 0 \\ 0 & 0 & +a^\alpha \end{pmatrix} \quad (6.4)$$

where the positive principal value is found along the $H_\alpha-C_\alpha$ bond axis and the 0 principal value indicates the direction parallel to the carbon lone electron $2p_z$ orbital. Both A_{iso}^α and a^α have been found to be proportional to the spin density on the C_α atom ρ^π

$$A_{iso}^\alpha = \rho^\pi Q_{iso}^\alpha \quad a^\alpha = \rho^\pi Q_{aniso}^\alpha \quad (6.5)$$

known as the McConnell [75] and Gordy-Bernhard [68] relations, respectively. Common values are $Q_{iso}^\alpha = -72$ MHz and $Q_{aniso}^\alpha = 38.7$ MHz, and from actually measured α -proton HF couplings the spin density on the C_α can be estimated.

The isotropic HF coupling of a β -proton, due to hyperconjugation, is given by the Heller-McConnell relation [76]

$$A_{iso}^\beta = \rho^\pi (B_0 + B_2 \cos^2 \theta) \quad (6.6)$$

where θ is the dihedral angle between the p_z lone electron orbital axis and the C_β -H $_\beta$ bond, viewed along the C_α -C $_\beta$ bond. B_0 and B_2 are empirical constants. B_0 is often assumed to be close to 0 MHz and for alkyl, hydroxyalkyl and alkoxy radicals typical B_2 values of ~ 126 , ~ 73 and ~ 336 MHz are commonly taken [77, 78]. Based on estimations for the spin density, relation (6.6) is regularly used to estimate dihedral angles for β -protons. The isotropic HF couplings for protons in γ , δ , etc. positions are in general considerably smaller than those expected for β -protons. For all these proton couplings, the anisotropic HF interaction is dominated by the point dipole contribution and is therefore essentially axial around the $H \cdots C_\alpha$ axis [49]

$$\vec{A}_{aniso}^{\beta, \gamma, \delta} = \begin{pmatrix} -b & 0 & 0 \\ 0 & -b & 0 \\ 0 & 0 & +2b \end{pmatrix} \quad (6.7)$$

with, in frequency units (MHz)

$$b = \frac{\mu_0}{4\pi h} \frac{(g_e \mu_B)(g_N \mu_N)}{R^3} \rho^\pi \quad (6.8)$$

where μ_0 is the vacuum permeability and R the distance between the C_α carbon and the interacting H. For β -protons, the deviation from these axial formula may be considerable and an appreciable rhombicity is often found (principal values in Eq. (6.7) being $-b-d$, $-b+d$, and $2b$). For C-bound protons further away the point-dipole approximation works quite well and allows estimating $H \cdots C_\alpha$ distances and directions [79]. Comparison of these distances and directions with values for the intact molecule in the undamaged lattice, along with the number of α - and β -type interactions observed, usually strongly limits the number of possible locations for the radical center. It is also interesting to note that hydroxyl β -proton HF tensors usually exhibit a larger anisotropic and a smaller isotropic part than those of C-bound protons in a similar position [80]. Studies on crystals grown from D_2O solutions, where the exchangeable oxygen-bound protons have been replaced by deuterium, are of course the most effective way for distinguishing hydroxyl from carbon-bound proton interactions.

^{13}C isotopic substitution is also a very powerful, but expensive, tool for identifying the center of spin density of radicals. It is hardly affordable to grow single crystals 100% enriched in ^{13}C for angular dependent EPR and ENDOR studies, but for systems in which the radicals have been thoroughly characterized on crystals with natural C isotopic distribution, powder EPR (if possible complemented with powder ENDOR) measurements may provide unambiguous information [13, 81].

6.3.2 Semi-empirical Theory: Information Obtained from g Tensors

C- and O-centered radicals may easily be distinguished from each other via their g tensors. As typical example of g tensor for a C-centered radical without spin

delocalization on oxygen, one can take the radical in malonic acid, for which $g_x=2.0026$, $g_y=2.0033$ and $g_z=2.0035$ have been measured with EPR [82] and $g_x=2.0023$, $g_y=2.0033$ and $g_z=2.0037$, using EIE [62]. The smallest principal value, which nearly coincides with the free electron value g_e , marks the direction of the lone-electron orbital. For the other principal values only small positive shifts $\Delta g=0.0010$ – 0.0020 are expected [83] and observed. For pure alkyl and hydroxy-alkyl radicals (Fig. 6.5a), with a high spin density at the radical C-center, similar g tensors are expected.

Alkoxy radicals, on the other hand, obtained by H-abstraction from a sugar OH group (Fig. 6.5b), have their spin density mainly localized on an oxygen atom. They exhibit a more pronounced g anisotropy mainly due to the much larger spin-orbit coupling constant of O with respect to that of C [15, 84]. They are easily recognized in angular dependent EPR spectra, because their transitions move strongly with the magnetic field orientation. At certain orientations their resonances move far outside the spectral range of the (usually more prominent) C-centered radicals, whose spectral center hardly moves when the magnetic field is rotated (at least at X-band) and whose range and anisotropy are dominated by HF splitting. For alkoxy radicals $1.970 < g_x < 2.0023$; $2.005 < g_y < 2.009$ and $2.021 < g_z < 2.11$ have been reported [84–88]. Again, the smallest g value (closest to g_e) indicates the lone-electron orbital direction, while the largest g value is found along the C–O• bond.

C-centered radicals have been reported with considerably larger g shifts (and anisotropy) than simple alkyl and hydroxyalkyl radicals. The T1 radical with principal g values presented in Table 6.2 is an example of this type, R–(C=O)–•C–R'R". These enhanced g shifts are attributed to spin delocalization onto oxygen: ring oxygen and/or C=O (carbonyl) groups close to the C_α , usually in β positions (resonance contribution of structures like R–(C–O•)=C–R'R", see Fig. 6.5c). g_x , found along the lone-electron orbital, remains close to g_e , but g_y and g_z undergo larger positive shifts. In the case of spin delocalization onto a β -carbonyl, g_z is found (close to) parallel with the C=O bond axis, often in the range 2.0055–2.0080.

6.3.3 DFT Calculations: Evolving Methodology

Very early in our research of radiation-induced radicals in nucleic acid constituents, amino acids and carbohydrates, it was realized that isotropic HF couplings alone, as one would determine from solution or powder EPR experiments, are not sufficiently discriminative with respect to the radical model. Angular dependent ENDOR experiments provide detailed information about anisotropy of the HF interactions, and this information should also be fully exploited in the comparison with DFT calculations of SH parameters. The DFT modeling of g and HF tensors generally proceeds in two steps. First a geometry optimization is performed and next the SH parameters are calculated for the optimized radical geometry. The reliability of the results depends critically on how accurately the environment of the radical is taken into account in these two steps.

In our very first computational studies on radicals in carbohydrates, only single molecule calculations were computationally feasible [89]. For the geometry optimization this implied that constraints needed to be imposed and that only part of the molecular radical was allowed to relax. For taking the directional information into account, angles between principal directions of the various experimental HF tensors were compared with the DFT calculated counterparts. Such comparisons later on proved insufficient for credible radical model assignments. In a better approach, the orientation of the molecule in the crystal was properly taken into account, which allowed more complete comparisons between experimental and calculated HF tensors and already proved quite successful in radical model identification [10, 90].

An obvious improvement consisted in embedding of the molecular radical in neighboring intact molecules for the geometry optimization, while the HF tensor calculations still were performed on single molecules [91]. This allowed for more realistic atomic relaxations around the radical center. In the subsequent step in the modeling refinement, the embedding was also applied for the tensor calculations [16, 92]. The molecules hydrogen-bound close to the radical center appeared to have the largest influence, both on the geometry and on the calculated HF parameters. In all geometry optimizations, Gaussian type orbitals and gradient corrected exchange correlation functionals were employed; for calculations of HF and g tensors, hybrid functionals were often used.

The most natural way of taking the crystalline environment of the radical into account is, however, via periodic boundary conditions. A potential draw-back of this method is that interactions between the periodic images of the radical have to be avoided. This may be accomplished by taking a unit cell in the periodic calculations which is larger than the crystallographic unit cell (the supercell approach). In the past 5 years in all our studies the geometry optimizations were performed in periodic schemes based on Car-Parrinello Molecular Dynamics using plane wave and pseudopotential basis sets (CPMD [93, 94]) and variants employing Gaussian and plane wave, and Gaussian and augmented plane wave basis sets (CP2K [95–97]). Supercells doubled or quadrupled in size with respect to the crystallographic unit cell along the shortest lattice parameters proved sufficient, although this choice still implies a high radical concentration of 5–25%. It was verified that periodic cell sizes larger than about 1 nm along each crystal axis do no longer demonstrate influences of interactions between radicals in periodic images (see e.g. [8]). As opposed to single molecule and cluster calculations, no constraints on atomic relaxations have to be imposed in this type of calculations.

In these first attempts to properly take into account the full lattice environment of the radical, SH parameter calculations were still performed on clusters cut out of the periodically optimized structure, because g and HF tensors reflect local properties, which are known not to be well reproduced by plane wave basis sets [8, 9, 14, 17–19, 55]. A further major improvement in the calculations came from the implementation of HF [98] and g tensor calculations [99, 100] in periodic codes (CP2K) using Gaussian and augmented plane wave basis sets. This allowed to perform the SH parameter calculations directly on the periodically optimized structure. Our latest computational results for neutral carbohydrate radicals are all performed in this

way [12, 20, 21, 57, 101]. In the case of charged radicals, the periodic boundary conditions induce an infinite charge on the lattice, which would have to be balanced by a background countercharge density.

A common problem in this context—not only for the periodic boundary calculations, but also for cluster modeling—is that of localization of charge and spin. Adding or subtracting an electron to/from a model system, mimicking the formation of a reduced or an oxidized radical species, quite often results in the charge and spin becoming distributed over several molecules, or even over the entire system. There are not many remedies to this problem. Possibly the implementation and use of other functionals, containing a higher degree of exact Hartree-Fock exchange, might be helpful [102]. Sometimes, it is sufficient to make slight changes to the geometry of one molecule in the lattice to make the spin (and/or charge) localized at that particular molecule.

6.3.4 *Practical Example of Radical Identification*

We return to the example of the T1 stable radical in irradiated sucrose, whose g (see Table 6.2) and proton A tensors (see Table 6.3) have already been discussed in the context of Schonland ambiguity (Sect. 6.2.4). This ambiguity has been solved for all tensors, however, and we only consider the first tensor in Table 6.2 and the 1st, 3rd and 5th tensor in Table 6.3 for semi-empirical theoretical analysis and comparison with DFT calculations. Experiments on crystals grown from D_2O solutions yielded the same three HF couplings, demonstrating that none of the A tensors correspond to OH proton couplings. The main purpose here is to illustrate the principles of identification based on comparison between experimental and DFT computed SH parameters, for models constructed using the semi-empirical theoretical considerations discussed in Sects. 6.3.1 and 6.3.2. A more elaborate discussion is found in Ref. [9].

The negative isotropic HF value and the rather large and fairly axial anisotropic interaction, make HF3 quite atypical and for that reason less straightforward to be used in a semi-empirical analysis. The tensors HF1 and HF2, on the other hand, exhibit a positive isotropic HF value and close to axial anisotropy. These properties are typical of regular β - or γ -type couplings. From Eqs. (6.7) and (6.8) the H \cdots C distances between the radical's central carbon and the interacting proton are estimated at 2.0 and 2.2 Å for HF1 and HF2, respectively. These values are close to those expected for protons in β -positions (2.1–2.2 Å). The weaker HF2 interaction could, however, also come from a γ -proton whose coupling is atypically large because it is next to a ring oxygen or a carbonyl group, onto which a considerable amount of spin density is delocalized. The enhanced g tensor anisotropy for this radical, indeed, suggests a significant spin delocalization onto oxygen for this center.

In order to narrow down the possibilities for the location of the radical center, the C \cdots H directions in the intact sucrose molecule (in the crystal) are compared with the principal directions corresponding to the largest principal A value for HF1 and

Table 6.4 Atomic distance D (in Å) and angle δ (in degrees) between C–H directions (see Table 6.1 and Fig. 6.6a for atom numbering) in the crystalline sucrose molecule and principal directions of the largest principal value for the HF1 and HF2 A tensors (Table 6.3) [9]

Direction	H-position	D	$\langle a^* \rangle$	$\langle b \rangle$	$\langle c \rangle$	$\delta(\text{HF1})$	$\delta(\text{HF2})$
C1–H2	β	2.14	0.556	−0.454	0.696	21.3	
C1–H5	γ	2.74	−0.139	0.647	−0.750		15.7
C4–H5	β	2.15	0.542	0.443	0.714	21.6	
C4–H2	γ	2.69	−0.148	0.652	−0.744		16.4
C2′–H3′	β	2.16	0.854	0.420	0.307	21.7	
C2′–H5′	γ	3.01	0.077	0.731	−0.678		13.9

HF2 for both symmetry-related sites. The smallest deviation angles δ are listed in Table 6.4. The comparison yields C1, C4 and C2′ as possible radical centers, with similar deviations in the order of 20°.

In Fig. 6.6, the intact sucrose molecule is presented along with five radical models that can be obtained at the three sites found plausible for T1, and for which spin density delocalization onto neighboring oxygen atoms is expected. The first four models (M(C1), M(C4), M(C2′)a and M(C2′)b) are the simplest radicals one can obtain at these positions with the given specifications, the fifth (M(C2′)c) is a further modification of the fourth model (M(C2′)b). An overview of the computed principal HF values for these models is given in Table 6.5, along with the differences in principal values and directions with the HF1 and HF2 tensors. The couplings with only small and rather isotropic HF values, expected to contribute mainly to the ^1H matrix ENDOR line, are omitted. For the angles between principal directions, both symmetry-related sites of the experimental tensor are considered and the results are presented for the site yielding the smallest angles. The radical geometry was optimized in a periodic scheme using a supercell consisting of two crystallographic unit cells along the $\langle c \rangle$ direction. HF tensor calculations were performed in a single molecule approach (radical molecule cut out from the periodically optimized structure) using Gaussian03, with a B3LYP hybrid functional and a 6-311G(d,p) basis set.

M(C1) is obtained by simple hydrogen abstraction at the C1 atom. For neither of the HF interactions, the isotropic and anisotropic HF values seem in good agreement with experiment. The principal directions of the β -proton appear to be in fair agreement with those of HF1 (deviations smaller than 20°), but for the γ -proton a more severe discrepancy is observed. In addition, this model does not account for the third HF coupling experimentally observed.

M(C4) is obtained by hydrogen abstraction at C4 and carbonyl group formation at C3. This model does yield three HF tensors with isotropic couplings in the right order of magnitude, one having a negative isotropic value, as observed experimentally. The latter interaction, however, is due to a hydroxyl proton, in contradiction with the experiments on deuterated crystals. In addition, the principal directions of the calculated HF tensors deviate very strongly from those of HF1 and HF2. Hence, also this model should not be further considered.

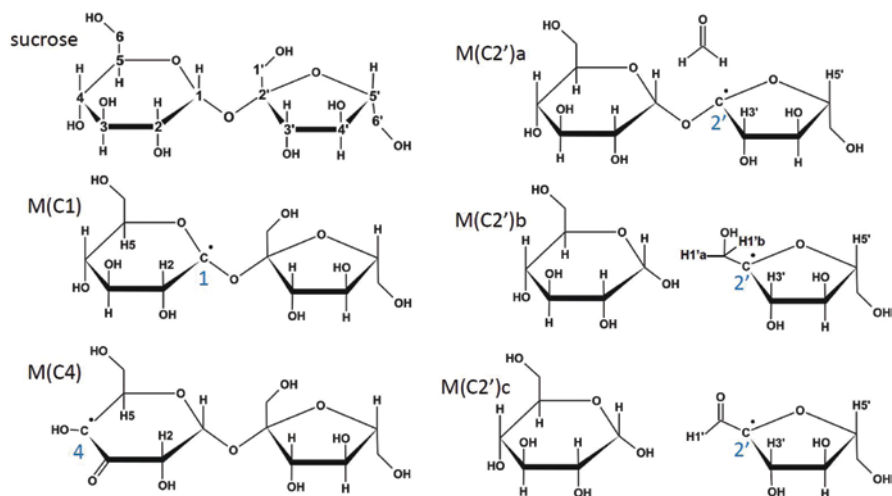


Fig. 6.6 Intact sucrose molecule, defining the labeling of the carbon atoms, and radical models for T1 in sucrose, compatible with the location determined by comparison of the principal directions of tensors HF1 and HF2 (Table 6.3) with crystal directions (Table 6.4) and with the observed large g -shifts (considerable spin delocalization onto oxygen) [9]. The central carbon of the radicals and the hydrogen nuclei exhibiting appreciable HF interaction (DFT calculated values in Table 6.5) are numbered

Model M(C2')a is obtained by splitting off a formaldehyde molecule at C2'. Additional constraints had to be imposed in the periodic geometry optimization in order to prevent spontaneous reattachment of the formaldehyde and formation of the O1'-centered alkoxy radical. In the HF tensor calculations, the formaldehyde molecule was left out. The model again yields only two appreciable HF couplings: one β -coupling and one γ -coupling with negative A_{iso} . The very strong deviations in principal directions with the experimental tensors suggest that also this model may be eliminated.

M(C2')b is obtained by cleaving the glycosidic bond in the sucrose molecule at the fructose side. The calculations yield three considerable HF couplings. For two of them, the anisotropy and principal directions are in acceptable agreement with HF1 and HF2, but the deviation in A_{iso} for both tensors is quite large. In particular, A_{iso} for the interaction with the β -proton H3' is strongly overestimated. The most important flaw of the model is, however, the large β -proton interaction with H1'a, not observed in experiment. A modification of this model eliminates these two problems: carbonyl formation (by H₂ elimination) on the C1' position is expected to decrease the spin density on the central C2' atom and hence also A_{iso} for the H3' proton. At the same time, the remaining H1' is expected to lie in the $\bullet\text{C}2-\text{C}1=\text{O}$ plane (perpendicular to the lone electron p_z orbital), which should, according to Eq. (6.6), result in a relatively small HF coupling. The results of the HF tensor calculations on this model, labeled M(C2')c in Fig. 6.6, even in this rather simple computational scheme, lead to very good quantitative agreement with experiment for HF1 and

Table 6.5 Calculated principal HF values (MHz) for five radical models for T1 (Fig. 6.6) and deviations in values and directions (δ , in degrees) with HF1 and HF2 (see Table 6.3) [9]

Model	Proton	A_{iso}	ΔA_{iso}	$A_{aniso,i}$	$\Delta A_{aniso,i}$	δ
M(C1)				-6.08	-2.09	15.9
	β -H2	32.85	-13.95	-4.78	-2.40	12.4
				10.86	4.49	19.8
				-4.44	-1.75	23.3
	γ -H5	-2.60	-18.48	-1.33	0.98	29.0
			5.77	0.77	24.2	
M(C4)				-3.65	0.34	43.4
	β -H5	56.60	9.8	-2.62	-0.24	44.7
				6.27	-0.10	34.2
				-2.65	0.04	56.3
	γ -H2	10.86	-5.02	-1.40	0.91	64.0
				4.05	-0.95	33.3
			-8.38			
	HO4	-10.12		-7.37		
				15.74		
M(C2')a				-5.82	-1.83	63.2
	β -H3'	32.15	-14.65	-5.23	-2.85	67.7
				11.05	4.68	21.7
				-3.31	-0.62	67.8
	γ -H5'	-3.01	-18.89	-2.29	0.02	69.9
			5.60	0.60	22.8	
M(C2')b				-5.22	-1.23	16.3
	β -H3'	66.83	20.03	-2.70	-0.32	17.3
				7.91	1.55	6.8
				-4.24	-1.55	6.1
	γ -H5'	6.95	-8.93	-2.90	-0.59	11.7
				7.14	2.14	10.3
			-5.96			
	β -H1'a	56.66		-2.77		
				8.73		
M(C2')c				-3.79	0.20	3.9
	β -H3'	44.40	-2.20	-2.52	-0.14	4.1
				6.31	-0.06	1.5
				-2.60	0.09	8.0
	γ -H5'	12.90	-2.98	-2.20	0.11	8.2
				4.80	-0.20	2.5
				-5.08		
	β -H1'	-6.50		-3.30		
				8.37		

Table 6.6 DFT calculated proton principal HF (in MHz [9]) and g [57] values for the M(C2')c model for T1, depicted in Fig. 6.6, and deviations in values (Δg values in parts per thousand) and directions (δ , in degrees) with experimental data for this radical (Tables 6.2 and 6.3). In order to illustrate the problem of Schonland ambiguity, the final three columns give the differences in principal values and directions with the Schonland conjugate tensors, although in this particular case the ambiguity was solved by measurements in a fourth rotation plane [9]

Proton	A_{iso}	$A_{aniso, i}$	ΔA_{iso}	$\Delta A_{aniso, i}$	δ	ΔA_{iso}	$\Delta A_{aniso, i}$	δ
$B-H3'$		-3.74		0.25	4.7		1.16	18.5
	41.90	-2.33	-4.90	0.05	4.7	-4.90	-1.10	19.2
		6.07		-0.30	1.1		-0.06	7.1
$\gamma-H5'$		-2.40		0.29	9.0		0.81	21.3
	16.30	-2.26	0.42	0.05	9.2	0.43	-0.54	21.8
		4.67		-0.33	1.6		-0.27	4.5
$\beta-H1'$		-6.92		-0.51	5.9		1.07	22.7
	-11.47	-4.64	-0.40	-0.91	5.8	-0.35	-3.69	23.7
		11.56		1.42	4.6		2.62	13.5
g		-0.0020		0.2	7.4		0.3	14.7
	2.0043	0.0003	-0.21	-0.3	7.3	-0.22	-0.5	21.1
		0.0018		-0.5	1.4		-0.4	25.8

HF2. Moreover, the HF interaction with the remaining H1' proton appears to exhibit the characteristics of HF3. Improvements of the calculation scheme lead to an even better agreement, especially for the latter coupling.

In Table 6.6 the results of HF and g tensor calculations on the periodically optimized model M(C2')c are shown, using a supercell comprising eight crystallographic unit cells. The HF tensor calculations, which came earlier [9], were performed on a cluster containing the radical molecule and ten sucrose molecules hydrogen-bound to it. The more recent g tensor calculations [57] are all-periodic. The agreement between the four experimental tensors and their calculated counterparts is very good on all accounts. In particular we want to emphasize here that the agreement in principal directions for g and A tensors is excellent. It is also important to note that all other HF couplings calculated for this model are much smaller than those listed in Table 6.3. These are expected to contribute in the ENDOR spectra to the multitude of ENDOR lines near the ^1H Larmor frequency and to be hidden in the EPR line width.

To further exemplify the issue about Schonland conjugates and radical identification, in the final three columns of Table 6.6 the DFT calculated tensors are also compared with the Schonland conjugates of the experimental tensors. It is clear that Schonland ambiguity may blur or even hamper the identification of radicals based on DFT calculations of SH parameters. Not surprisingly, the differences between DFT calculated and Schonland conjugate experimental tensors are largest for HF3 and for the g tensor for which also the largest differences between the Schonland conjugate forms of the experimental tensors were found. Even having only one

tensor in the Schonland conjugate form would render the identification considerably less convincing.

The results presented here illustrate the importance of an accurate SH analysis of experimental data: having the right model at hand and performing calculations of sufficiently high level (taking the molecular environment into account in a correct way), the agreement between experiment and calculations may be impressive. Our experience tells us that in convincing identifications, for large isotropic HF values (in particular α -protons) deviations of 10–15 MHz may still occur, though. For anisotropic g and A values, however, deviations should not be larger than 10–20%. All SH tensors should have at least one principal direction (and very often all) for which the deviation between experiment and calculation is well below 10°. Furthermore, all calculated HF couplings of significant magnitude (> 10–20 MHz) should have an experimental counterpart, either determined from ENDOR angular variation results or inferred from the EPR/EIE spectra, when the corresponding ENDOR transitions are experimentally not detected.

In the following sections, explicit comparisons between experimental and DFT calculated g and HF tensors will be limited. Based on the comparison criteria set out above, we will label identifications as “*certain*” if all criteria are met, comparable to the situation for T1. Structures are labeled “*plausible*” if for certain tensors the criteria are not fully met, and “*suggested*” if only qualitative agreement is obtained, e.g. because certain experimental couplings are not predicted by the calculations or vice versa. The label “*proposed*” is used when models are derived from experimental studies only, without explicit verification by DFT calculations.

6.4 Radical Stability and Evolution vs. Radiation Chemistry

In this section, we review the results of radical identification studies on sucrose after irradiation at various temperatures, immediately after irradiation or after annealing to temperatures higher than the irradiation temperature. Irradiation and annealing temperatures range between ~6–8 K and RT. The ultimate aim of such studies is to unravel the radiation chemistry that leads to the production of the final stable radicals. The structures of these radicals (see e.g. T1, Sect. 6.3.4) suggest complex, multistep formation mechanisms, wherein the primary ionization or electron capture event is followed by various thermally activated structural relaxations and chemical reactions. At lower temperatures, (some of) these subsequent reactions may be frozen out, leaving the radical in a metastable state that is closer to its primary form. As large structural rearrangements are not expected at low temperatures, these metastable radicals often are the result of breaking of a bond or abstraction of a small fragment in the molecule (H, OH). Adequate structures are in general more easily found than for radicals with higher thermal stability. Knowledge of the structure of these (close to) primary radicals, and understanding why exactly these radicals and not others are produced, is important in the context of understanding and/or

controlling the (initial) radiation damage to more complex biomolecules, like DNA. In addition, following the subsequent transformations upon thermal annealing may help in unraveling the structure of the more complex RT stable radicals. We take sucrose as an example for explaining the methodology in this section, because for this carbohydrate the most comprehensive experimental data set is available. Moreover, it illustrates very well all pitfalls of this type of analyses. Some of the results presented in this Section have not been published before [56, 103–106]. In Sect. 6.5, the results for the sugar phosphate K2G1P, the disaccharide trehalose dihydrate, and the monosaccharides fructose and sorbose are reviewed.

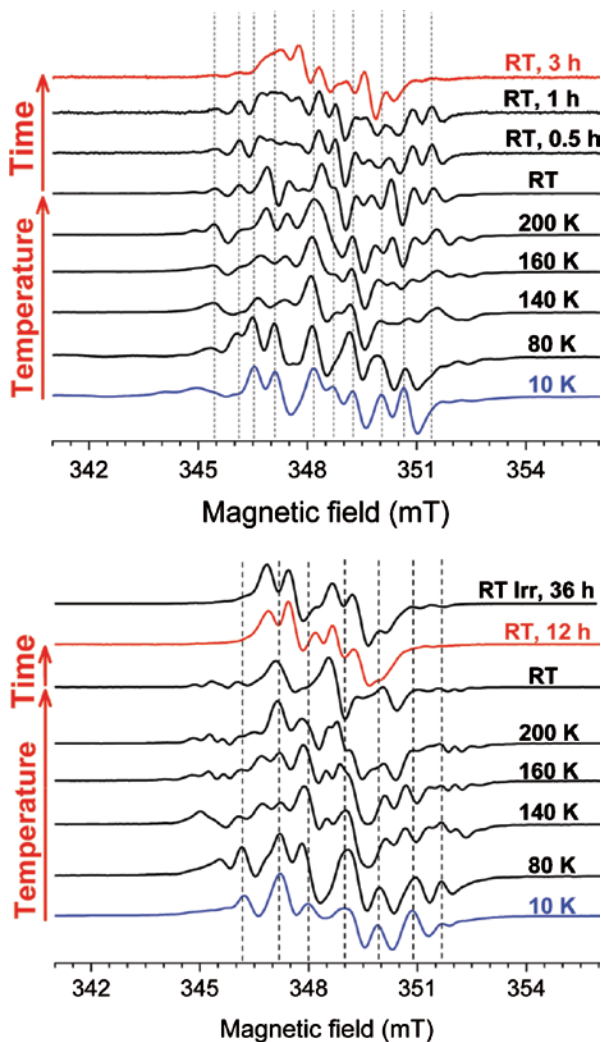
Before embarking on the discussion of the available experimental results, a remark about the methodology is in order. It is not *a priori* evident that low temperature irradiation followed by thermal annealing to RT is equivalent to RT irradiation in terms of radical products. In our studies of carbohydrates we have checked by monitoring EPR and ENDOR spectra, that the radical composition after low temperature irradiation and annealing to a certain temperature (up to RT) is the same as that after irradiation at the latter temperature: the same types of dominant radical species are present in approximately the same relative concentrations. This confirms that irradiation at low temperature and gradual anneal to RT may elucidate the complex radical formation processes at RT. The total EPR intensity after low temperature irradiation and annealing is, however, considerably lower than that after RT irradiation to similar doses. This suggests that radical recombination is more important in the former process than in the latter. It should further be born in mind that in most analyses (see further in Sects. 6.4 and 6.5), radical components with low EPR (and ENDOR) intensities have remained unidentified. Furthermore and perhaps more importantly, EPR is only sensitive to the paramagnetic forms of radiation damage, not to diamagnetic radiation products.

6.4.1 Types of Annealing Experiments

In order to follow the radical evolution after the formation of the primary radiation products, one may decide to monitor changes in the EPR spectrum of crystals initially irradiated at low temperature and then annealed for a long time (typically > 10 min) to increasing temperatures, recording EPR spectra at the annealing temperature. The results of such experiments at X-band for two orientations of a sucrose single crystal, initially irradiated at 10 K, are presented in Fig. 6.7. In addition to the temperature evolution, isothermal evolution after RT irradiation is also included in the top few spectra of both figure parts (arrow labeled “Time”). All spectra were normalized in height. These experiments indicate that

1. the primary and finally stable radicals are substantially different and transformation between these two states goes through various steps. The stages at 10 K [19, 104], 80 K [105] and RT (metastable [51, 106] and fully stable [8, 9, 55–58]) have been investigated in more detail and will be discussed in the following subsections.

Fig. 6.7 EPR spectra of sucrose irradiated *in situ* at 10 K for $B//\langle b \rangle$ (top) and $B//\langle c^* \rangle$ (bottom) [103]. Annealing and recording temperatures are indicated on the right. The top spectrum with $B//\langle c^* \rangle$ was recorded at RT, 36 h after irradiation at RT. $\nu_{\text{MW}} = 9.78$ GHz



2. the component(s) dominating the spectrum at 10 K is (are) still present and fairly dominant in the 80 K spectrum.
3. the component(s) dominating the spectrum immediately after RT irradiation is (are) very probably already seen in the spectra after annealing to 200 K.

The interpretation of experiments, such as shown in Fig. 6.7, presents two complications. First, this type of experiments does not allow distinguishing irreversible from reversible temperature-induced spectrum transformations. Second, the combined thermal population and paramagnetic relaxation effects [49] render a direct comparison of intensities of spectra recorded at different temperatures difficult. Pulse annealing experiments in which all EPR spectra are recorded at the same temperature after annealing (usually during constant annealing times, i.e. isochronal

annealing) to increasing temperatures, eliminate these problems. Their drawback is, however, that they are very time-consuming: each step comprises heating, stabilization and cooling times. Results of selected pulse annealing experiments are presented in Sects. 6.4.2 and 6.4.6. For following the kinetics of radical transformations, isothermal annealing is most appropriate, in which EPR spectra are recorded at a constant temperature with fixed time intervals. Such experiments have so far only been performed sporadically in our studies of carbohydrates (see Sect. 6.4.4 and [51]).

6.4.2 *Close-to-Primary Radiation Products (Irradiation at 6–10 K)*

The X-band EPR and ENDOR spectra of sucrose recorded at 10 K after X-ray irradiation at 10 K contain contributions of at least six radical components, four of which dominate the first derivative EPR spectra [19]. Two of these were identified (certain) as H-abstracted C5- and C1-centered radicals in the glucose unit (C5(-H) and C1(-H), respectively). A third C-centered radical was suggested to be produced by H-abstraction at C6 (C6(-H)). Among all H-abstracted radicals at C-atoms, the HF tensors calculated for the C6(-H) species matched the experimental tensors best. Still, considerable discrepancies, both in principal values and directions, were found for the two resolved HF interactions observed, whereas a third interaction predicted by the calculations was not found in experiment. The fourth identified (certain) species (O3'(-e⁻)) is O-centered and was previously studied by Box and Budzinski [107]. Excellent agreement between experimental and calculated HF tensors was found for six proton interactions. The calculations explicitly confirmed the radical model that Box and Budzinski had proposed for this O3' centered alkoxy radical in the fructose unit, where the HO3' proton has migrated to the O4' oxygen of a neighboring molecule. The DFT calculations, however, showed that some of the HF tensor assignments made by Box and Budzinski needed correction. The models for these four radical species are shown in Fig. 6.8.

Two minor radicals remained unidentified in the spectra, both are C-centered.

In previous investigations of sucrose irradiated at liquid helium temperature, an inter-molecularly trapped electron (IMTE) center had been detected and found to be stable in the dark up to ~60 K [108, 109]. Like in other carbohydrates, this IMTE was characterized by large and anisotropic HF interactions with exchangeable protons and by a nearly isotropic *g* value, slightly smaller than the free-electron value. In the X-band spectra after 10 K irradiation, this type of radical was not detected, neither with EPR nor with ENDOR. K-band (24 GHz) ENDOR experiments after 6 K X-ray irradiation, however, did reveal the presence of this IMTE [104].

Figure 6.9 shows EPR spectra after irradiation at 6 K and subsequent UV-bleaching at 6 K or after thermal pulse anneal to 50 K (up to 40 K the EPR and ENDOR spectra remained unchanged). Both treatments appear to have similar effects: while the total double integrated intensity of the spectrum remains nearly unchanged

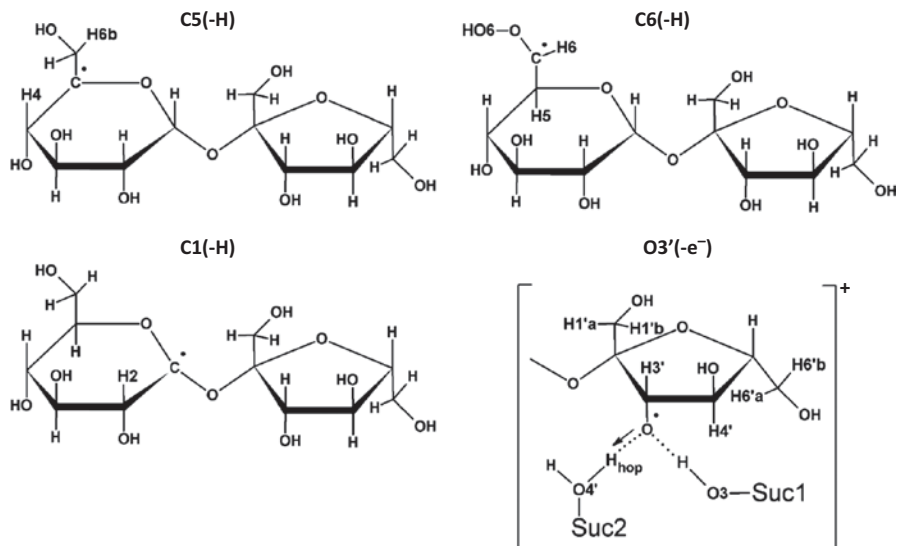


Fig. 6.8 Models for the four radical species dominating the EPR spectra of sucrose after X-ray irradiation at 10 K. Protons with significant calculated HF interactions are labeled in the models [19]

(inset in Fig. 6.9 for the pulse annealing experiments) the EPR transitions of the C5(-H) radical (corresponding EIE spectrum in Fig. 6.9d), characterized by a four-line HF structure and already present immediately after irradiation, apparently increase strongly at the expense of a broad-line EPR component (EIE spectrum in Fig. 6.9e). The ENDOR and EIE spectra recorded for the broad-line EPR spectrum correspond to the IMTE as reported by Budzinski et al. [108]. In particular, the slightly lower g value of the IMTE triplet contribution is clearly recognizable. The slight discrepancy in annealing temperature (50 K in our experiments vs. 60 K according to Budzinski et al.) is most likely only instrumental. Spectrum simulations show that the broad-line IMTE component easily remains undetected in EPR, whereas its relaxation properties may be unfavorable for ENDOR at X-band.

Closer inspection of Fig. 6.9 reveals that the effects of optical and thermal bleaching are not identical, though. The intensity increase of the C5(-H) radical appears larger after thermal anneal than after UV-illumination. ENDOR experiments reveal that in both cases the IMTE signal has completely bleached out, while the total spectrum intensity remains practically identical. However, in the ENDOR spectra of annealed samples the presumed C6(-H) radical appears to be missing, while after UV-bleaching at 6 K it was clearly observed.

These results suggest a transformation of the IMTE into the C5-centered radical as main reason for the spectral changes. Molecular modeling of the IMTE is far from obvious, not in the least because it requires electron orbitals (basis sets) that are not centered on lattice atoms, which comes at strongly increased computational cost and requires extensive testing of basis sets. Consequently, it has so far not been

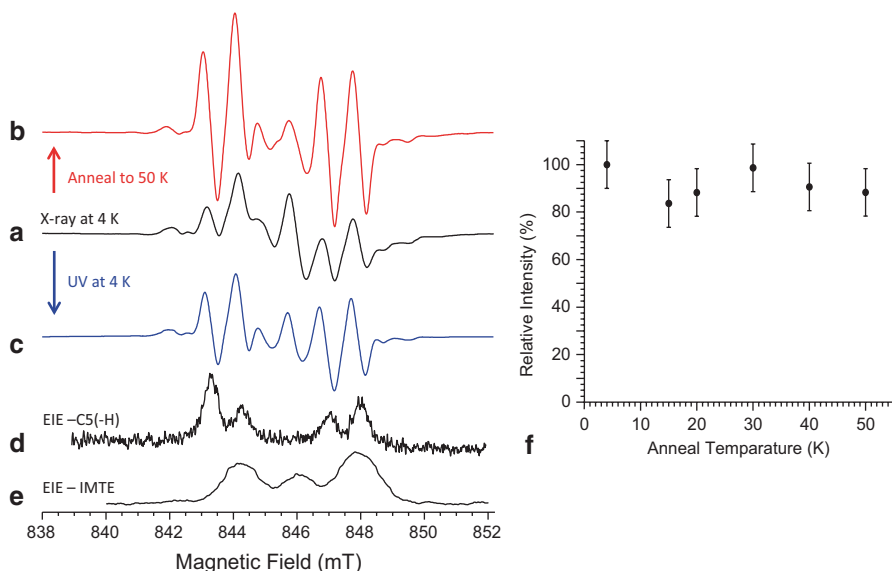
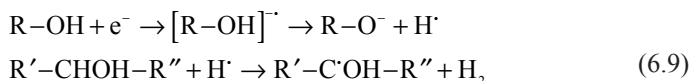


Fig. 6.9 K-band spectra ($\nu_{\text{MW}} = 23.69$ GHz) recorded at 6 K with $B// \langle b \rangle$ of **a** a sucrose single crystal irradiated at 4 K, **b** after irradiation at 6 K and subsequent thermal anneal to 50 K, **c** after irradiation at 4 K and UV-bleaching at 6 K. EIE spectra of **d** the C5(-H) radical and **e** the IMTE. **f** Total double integrated EPR intensity as a function of annealing temperature in the pulse annealing experiment (measurements at 6 K) [104]

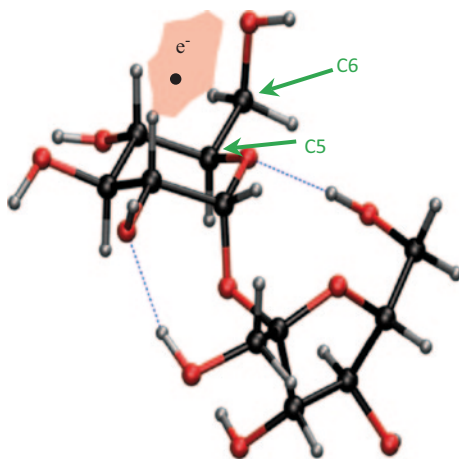
possible to determine the location of the IMTE by direct comparison of calculated and experimental HF tensors. It may however be anticipated that the electron will be trapped in the dipolar field between at least two OH-dipoles in carbohydrate crystals [108–112]. Plausible sites for inter-molecular electron trapping in carbohydrates have been calculated applying the semi-continuum potential model [110], and considerable rearrangements of OH-dipoles, even at 4 K, have been suggested. In the particular case of sucrose, the most plausible site for the observed IMTE was determined by analysis of the anisotropy of non-exchangeable proton interactions, observed with ENDOR [108]. This site is shown in Fig. 6.10. It is situated close to the C5 and C6 atoms in the glucose unit.

Considering this site assignment for the IMTE, the following scheme for the production of the C5(-H) radical can be devised [19], in agreement with mechanisms proposed by Samskog et al. for trehalose [111] and rhamnose [112]



A similar formation mechanism (with $\text{R}''=\text{H}$) could, in principle, also be valid for the radical assigned as C6(-H). The mechanism outlined in Eq. (6.9) in itself does not allow to identify the actual site for the initial electron trapping on the sucrose molecule. The fact that UV-illumination after X-ray irradiation increases the

Fig. 6.10 Plausible site for the IMTE center in the sucrose lattice [108]



C5(-H) concentration appears to support the site assignment by Budzinski et al., although it seems strange then that UV-exposure does not lead to a similar increase of the C6(-H) concentration. The difference between UV-bleaching and thermal annealing experiments, on the other hand, might be a result of a thermally activated transformation of C6(-H) to C5(-H). It seems in any case very plausible that these two radical types are both reduction radiation products. The alkoxy radical, which still has the H3' proton in its vicinity, is most likely an oxidation product. EPR spectrum simulations allowed to estimate the relative contributions of the various radical types to the spectra: C5(-H)—15%, C1(-H)—20%, C6(-H)—30%, O3'(-H)—25%, unidentified C-centered components < 10% [19]. Assuming a balance between oxidation and reduction products at low temperature, and taking also a finite concentration of IMTE centers into account, that is difficult to quantify, one may expect the C1(-H) radical to be an oxidation product.

6.4.3 Intermediate Temperature Stage (Irradiation at 80 K)

Annealing from 6–10 K up to RT, the EPR spectra of X-ray irradiated sucrose undergo many complex transformations (see Fig. 6.7), which all bear information on the radical chemistry. Transformations between 6 and 50 K have been discussed in Sect. 6.4.2. The only notable event in the 50–80 K range is the disappearance of the O3'(-H) alkoxy radical: all radicals stable at $T > 80$ K are C-centered. This section is confined to the species stable at 80 K (~liquid N₂ temperature), which have been studied quite thoroughly [105]. The annealing (and irradiation) stages between 80 K and RT are still largely unexplored.

Figure. 6.11a shows the EPR spectrum of sucrose after X-ray irradiation at 80 K and recorded at 80 K for a magnetic field orientation in the $\{ac\}$ plane close to $\langle c^* \rangle$. It contains contributions of at least 5 distinct radical species, as is clear from the EIE decomposition. The two most prominent components were already produced

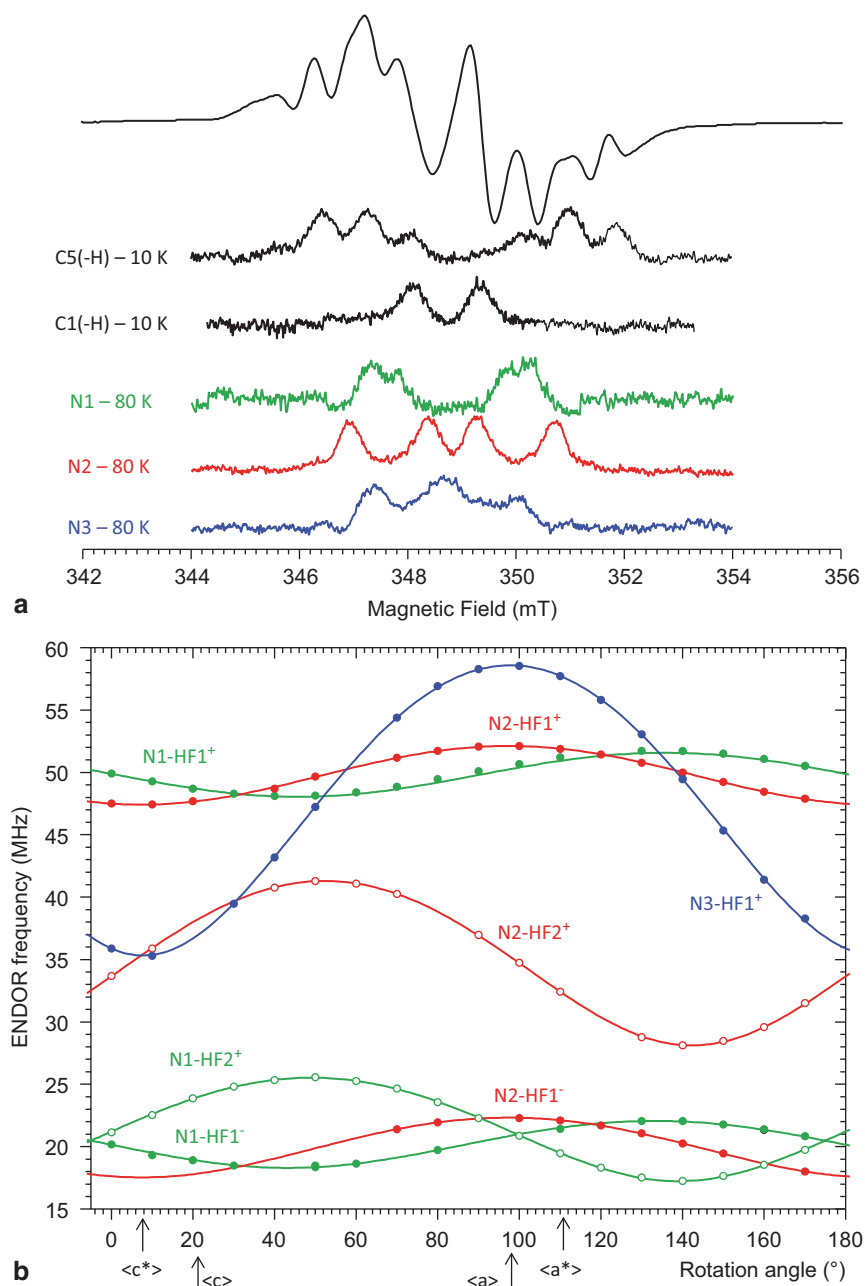


Fig. 6.11 **a** EPR spectrum and its EIE decomposition, recorded at 80 K, of a sucrose single crystal irradiated at 80 K. The magnetic field is oriented in the $\{ac\}$ plane, 8° from $\langle c^* \rangle$ and 21° from $\langle c \rangle$ (0° -point of the ENDOR angular dependence). $\nu_{\text{MW}} = 9.77$ GHz. **b** Angular variation of the ENDOR transitions assigned to species not detected by irradiation at 10 K. *Filled* (largest HF interaction, observed in two M_S multiplets for N1 and N2) and *open circles* (smaller interaction for N1 and N2) represent experimental transition frequencies, *full lines* are simulations assuming an angular dependence of transition frequencies of the form $A = ((A_{\text{max}})^2 \cos^2(\theta - \theta_0) + (A_{\text{min}})^2 \sin^2(\theta - \theta_0))^{1/2} \pm g_{\text{H}\mu\text{N}} B$ [105]

by irradiation at 10 K: C5(-H), which is stable up to ~ 100 K, and C1(-H), that remains prominently present in the spectra up to ~ 200 K (structures, see Fig. 6.8). These radicals very probably correspond with these reported in an earlier study by Ueda et al. [113]. Three additional radical species have not been detected after 10 K irradiation and are labeled N1, N2 and N3 in Fig. 6.11a.

The ENDOR angular dependence in the $\{ac\}$ plane for these “new” radicals is shown in Fig. 6.11b. Most of these ENDOR transitions could not be followed in other rotation planes. Only for the largest HF coupling of N1 (N1-HF1⁺ and N1-HF1⁻, + and - refer to the two M_S multiplets in which ENDOR transitions were observed) and N2 (N2-HF1⁺ and N2-HF1⁻) A tensors could be reliably determined and the Schonland ambiguity was resolved by measurements in a fourth rotation plane. These tensors are listed in Table 6.7. Both interactions are β -type. The anisotropy of the second HF interaction of N2 (N2-HF2⁺) and of the HF coupling observed for N3 (N3-HF1⁺) suggests that these interactions are α -type (or, less likely, β -hydroxyl type).

The DFT modeling of these radicals has to date not been exhaustively investigated, but the experimentally determined HF tensors were compared with those calculated (HF tensor calculation on single molecule cut from periodically optimized structures) for all possible C-centered H-abstraction radicals in sucrose.

The β -interaction of N1 is found to correspond very well with the largest interaction calculated for the C5'(-H) model, as can be seen in Table 6.8. Two more appreciable HF interactions are predicted for this radical. One of these, (probably β -H6'a) can account for the second coupling observed in the ENDOR angular dependence in the $\{ac\}$ plane (N1-HF2⁺, Fig. 6.11b) and for the small splitting in the EIE spectrum (Fig. 6.11a). Although further experimental and computational confirmation is desirable, the proposed model for N1 is already convincing. It should also be noted that even after irradiation at 10 K, very faint transitions of the largest HF interaction of N1 have been detected in the X-band ENDOR spectra.

For N2, none of the H-abstraction models yield reasonable agreement with the characterized β -coupling. Very probably, the model for this radical is more complex than a simple H-abstraction. Insufficient data are available for N3 to allow even a guess of its radical model.

6.4.4 Immediately After RT Irradiation

In Fig. 6.7, one can see that the spectrum of sucrose irradiated at low temperature, after anneal to RT differs strongly from that of the final stable radiation products. The latter spectra are only obtained after keeping the irradiated crystal for several hours at RT. An initial characterization of the metastable stage immediately after RT irradiation [51], in which EPR and FF-ENDOR were combined with statistical EPR spectrum decomposition based on Maximum Likelihood Common Factor Analysis (MLCFA [6, 114]), revealed that

Table 6.7 Principal A values (MHz) and direction cosines for the HF couplings determined for the N1 and N2 radicals in sucrose, produced by X-ray irradiation at 80 K and not prominently present after 10 K irradiation, from angular dependent ENDOR measurements in four rotation planes at 80 K [105]

A tensor	A_i	A_{iso}	$A_{aniso, i}$	$\langle a^* \rangle$	$\langle b \rangle$	$\langle c \rangle$
N1–HF1	66.38		–5.16	–0.226	0.223	0.948
	69.12	71.54	–2.42	0.756	0.654	0.026
	79.13		7.59	–0.615	0.723	–0.316
N2–HF1	62.95		–4.83	0.103	0.915	0.389
	65.74	67.68	–2.04	0.213	–0.403	0.890
	74.64		6.86	0.972	–0.009	–0.236

Table 6.8 Principal A values (MHz) and direction cosines calculated for the radical produced by H-abstraction at the C5' carbon atom of sucrose. Angles between experimental and calculated directions are given in degrees [105]

C5'(–H)	A_{iso}	$A_{aniso, i}$	$\langle a^* \rangle$	$\langle b \rangle$	$\langle c \rangle$	ΔA_{iso}	$\Delta A_{aniso, i}$	δ
β -H4'	64.55	–5.11	–0.237	0.198	0.951	–6.99	0.05	1.6
		–2.67	0.725	0.687	0.038		–0.25	2.6
		7.78	–0.646	0.699	–0.307		0.19	2.3
β -H6'a	9.40	–6.12	0.103	0.915	0.389			
		–3.65	0.213	–0.403	0.890			
		9.77	0.972	–0.009	–0.236			
β -H6'b	7.04	–6.50	0.836	–0.345	0.427			
		–3.59	0.348	0.935	0.073			
		10.09	–0.424	0.088	0.901			

1. the final stable radicals (see Sect. 6.4.5) are already present immediately after irradiation at RT or 273 K.
2. the spectra immediately after irradiation are dominated, however, by two other radical components, labeled U1 and U2 in Ref. [51].
3. the U1 and U2 radicals decay at RT, with characteristic double exponential decays having time constants $\tau_1=850$ s and $\tau_2=4700$ s, and apparently without production of stable radical components. This conclusion was obtained by MLCFA decomposition of the Q-band EPR spectra recorded while monitoring the spectral transformation during isothermal annealing at RT. This, at least in part, explains why, for reliable dose estimations, irradiated sucrose EPR spectra can only be recorded after a sufficiently long waiting time (typically 2–3 days) [30].
4. the stable radical concentration is about half the total concentration of paramagnetic centers measured immediately (within 5 min) after irradiation at RT or 273 K.

A thorough characterization of the U1 and U2 radicals combining ENDOR and EIE with DFT calculations is presently ongoing [56]. The EPR and EIE spectra for the two radicals in three perpendicular magnetic field orientations are shown in

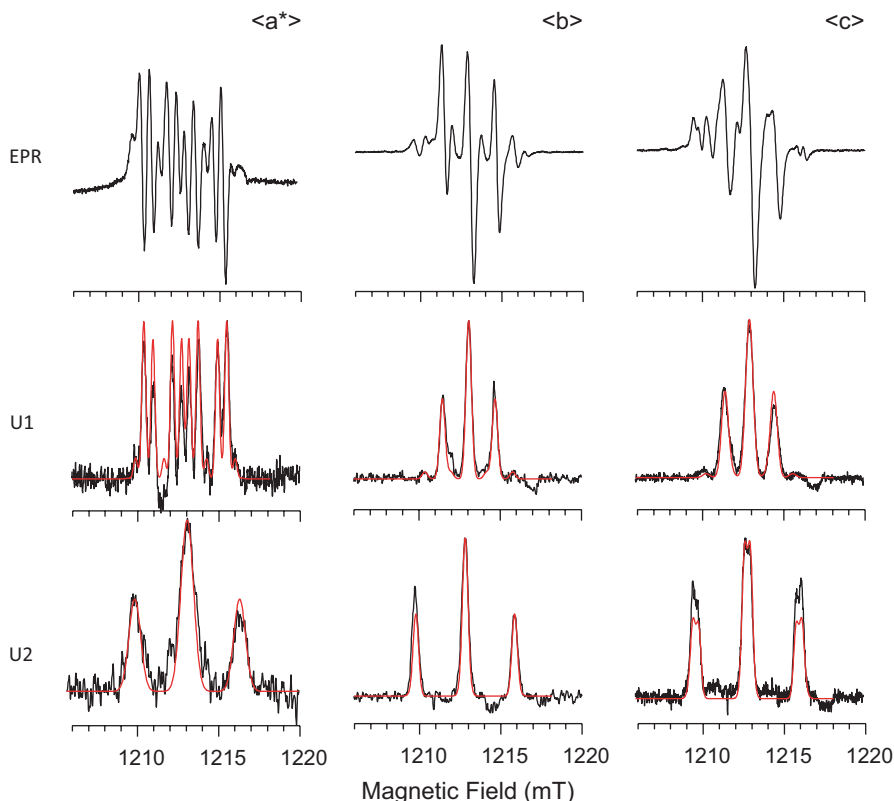


Fig. 6.12 Q-band EPR and EIE spectra (50 K, *black*—experimental and *red*—simulation) of sucrose, short time after irradiation at ice-water temperature. $\nu_{\text{MW}} = 34.00$ GHz [56, 106]. SH parameters for U1— $\langle a^* \rangle$: $g = 2.0027$, $A_1 = 2.72$ mT, $A_2 = 1.66$ mT, $A_3 = 0.57$ mT; $\langle b \rangle$: $g = 2.0026$, $A_1 = 1.59$ mT, $A_2 = 1.55$ mT; $\langle c \rangle$: $g = 2.0027$, $A_1 = 1.46$ mT, $A_2 = 1.66$ mT. SH parameters for U2— $\langle a^* \rangle$: $g = 2.0022$, $A_1 = 3.36$ mT, $A_2 = 3.03$ mT; $\langle b \rangle$: $g = 2.0029$, $A_1 = 3.04$ mT, $A_2 = 2.99$ mT; $\langle c \rangle$: $g = 2.0029$, $A_1 = 3.14$ mT, $A_2 = 2.89$ mT, $A_3 = 0.40$ mT

Fig. 6.12. U1 exhibits three resolved HF interactions: one α -type interaction ($A_{\text{iso}} \sim 1.8$ mT), one β -type of intermediate magnitude ($A_{\text{iso}} \sim 1.5$ mT) and a smaller coupling that is only resolved in the EPR spectra at magnetic field orientations near the $\langle a \rangle$ and $\langle a^* \rangle$ axes (0.5–0.6 mT). The U2 radical exhibits two strong β -type HF interactions ($A_{\text{iso},1} \sim 3.1$ mT and $A_{\text{iso},2} \sim 2.9$ mT). In the EIE spectrum with $B // \langle c \rangle$ a barely resolved additional splitting of ~ 0.4 mT is observed. It is noteworthy that for all measured U1 and U2 EIE spectra g factors in the 2.002–2.003 range are found (see simulation parameters in the caption). This result suggests that the g tensors for these radicals are fairly isotropic, and that these EPR components most probably are due to (hydroxy)alkyl radicals, without significant spin delocalization onto oxygen (see Sect. 6.3.2). Preliminary comparisons between DFT calculated and experimental HF tensors suggest that neither of these radicals correspond to simple H-abstraction radicals on C-atoms.

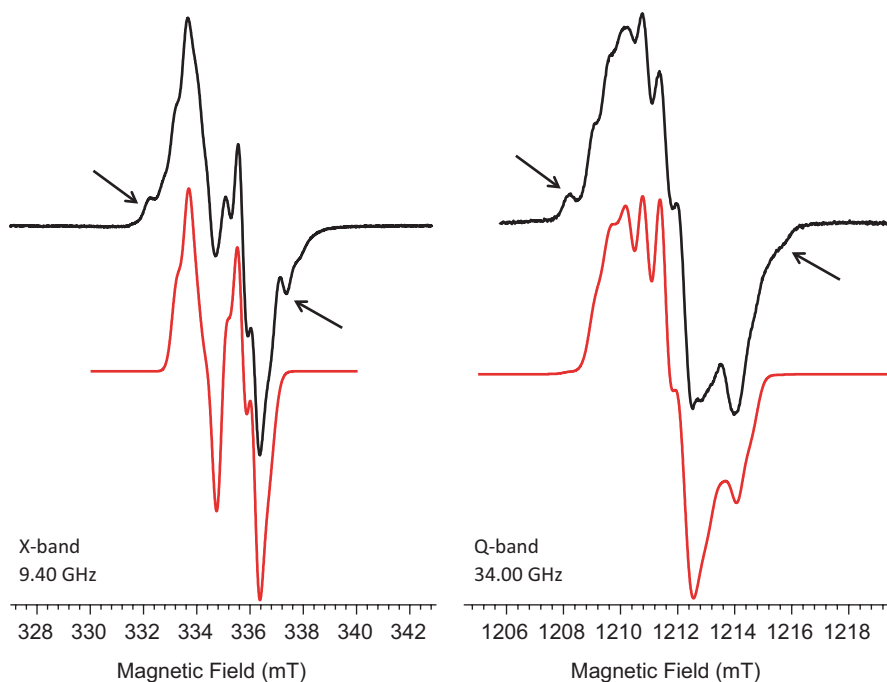


Fig. 6.13 Stable RT X- and Q-band powder EPR spectrum of irradiated sucrose (~ 40 kGy). *Black*—experiment; *red*—simulations, assuming a radical composition T1:T2:T3 of 1:0.72:0.48. $\nu_{\text{MW}} = 34.00$ GHz

6.4.5 Final Stable Stage

The X-band RT EPR spectrum of irradiated sucrose powder, long time after irradiation (typically 3 days), is shown in Fig. 6.13. This spectrum looks deceptively simple: it appears to be dominated by a component exhibiting a doublet HF splitting with a weaker triplet structure on both components, very likely due to two additional smaller HF interactions. The asymmetry between the low and high-field HF lines and the occurrence of side-lines (indicated with arrows), however, suggest that the radical composition may be more complicated. This is confirmed when recording the spectrum at higher microwave frequencies, as shown in Fig. 6.13 at Q-band.

Using ENDOR at RT, Sagstuen et al. were able to characterize two distinct radical types [5]. MLCFA decomposition of RT X-band powder EPR spectra in a dose series, on the other hand, revealed three dominant contributions with distinct dose responses [6]. ENDOR studies at low temperature (55 K [6] and 110 K [55]) of crystals irradiated at RT allowed to distinguish, indeed, three types of radicals, labeled T1–T3, all exhibiting one large and two small proton HF couplings. Comparison between experimental and calculated HF tensors for these couplings allowed to identify the two radical models, depicted in Fig. 6.14.

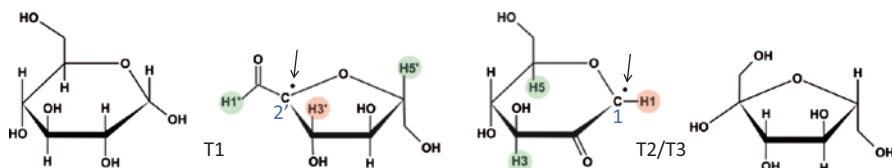


Fig. 6.14 Models for the T1 (*left*) and T2/T3 (*right*) stable radicals in sucrose [8, 9]. The central carbon on which the unpaired electron is mainly localized, is numbered and indicated with an *arrow*. The proton exhibiting the strongest HF interaction with the unpaired electron is indicated with a *red circle*, the protons yielding the two resolved γ -couplings with *green circles*

The model for T1 was already shown in Fig. 6.6 (M(C2')c). It exhibits one β -type and two γ -type HF couplings. T2 and T3 have very similar HF couplings (one α and two γ -types) and are two slightly different conformations of the same C1-centered radical, formed by rupture of the glucose-fructose glycosidic bond [8]. The DFT calculations for the common T2/T3-model in Fig. 6.14 agree significantly better with the results for T2, suggesting that T3 has basically the same structure but with a perturbation in its environment.

It is interesting to note that these two models, and hence also the three stable radical types in sucrose, have very similar characteristics, almost like mirror images in the fructose (T1) and glucose (T2/T3) units. They are both formed by glycosidic bond cleavage and have their unpaired electron mainly localized on a C-atom next to the ring oxygen, with carbonyl formation in a β -position. These features are indicative of a formation process involving β -elimination (see Sect. 6.6). The resulting strong delocalization of the unpaired electron is evidenced by the atypically small HF couplings with α - or β -protons, and by the atypically large interaction with distant γ -protons. In addition, the g tensors (experiment and calculations) that were recently reported for these radicals [57] reveal an enhanced anisotropy, with principal g shifts from the free-electron value up to 0.0045.

In order to understand the difference between the low temperature (50 K [6], 110 K [55]) and RT ENDOR results, the temperature dependence of the ENDOR spectra at certain magnetic field orientations was recorded [55]. This indicated that all determined HF tensors are only slightly temperature-dependent and that near RT the difference between the T2 and T3 radicals appears to vanish. As a consequence, the three radical types detected with ENDOR at low temperature do not necessarily correspond to the three components deduced from the MLCFA decomposition of the RT powder EPR spectra of a dose series. Moreover, if certain radical types exhibit the same dose response, MLCFA would not be able to distinguish between them. Spectrum simulations using the 110 K ENDOR data for the T1–T3 (also shown in Fig. 6.13) reproduce the central parts of the RT powder EPR spectra fairly well, but fail in reproducing the wing-lines (indicated by arrows in the spectra), even though transitions often regarded as forbidden were included in the simulations [57, 58]. This was also noticed by Georgieva et al. [7] in the high-frequency powder EPR spectra. For most magnetic field orientations such wing-lines are also seen in the X

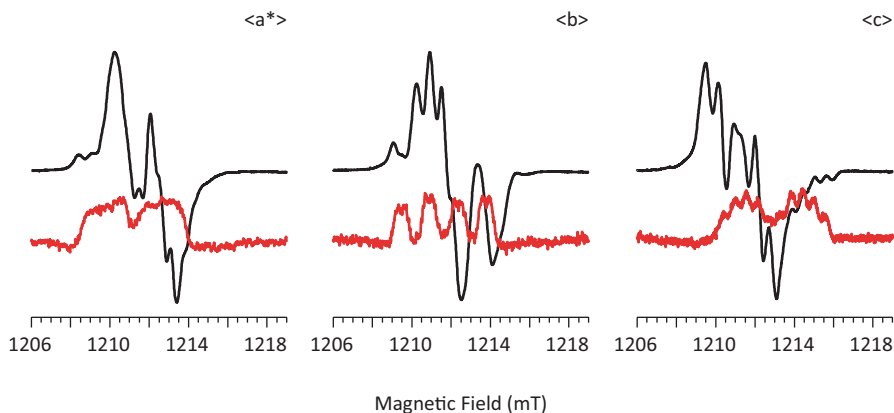


Fig. 6.15 EPR (black) and EIE spectra (red, recorded on the ENDOR line above 90 MHz at ~ 1210 mT static field) of RT irradiated sucrose (long time after irradiation) for magnetic field orientations along $\langle a^* \rangle$, $\langle b \rangle$ and $\langle c \rangle$; $T = 110$ K, $\nu_{MW} = 34.00$ GHz

and Q-band single crystal EPR spectra. Hence, certain (essential) contributions to the spectra to date still remain unidentified.

The metastable U1 and U2 components (see Sect. 6.4.4) might in principle be considered as responsible for these wing-lines. FF-ENDOR and statistical decomposition studies, however, suggest that these components decay completely at RT [51], whereas the missing spectral component has a rather low, but stable intensity. On the other hand, the single crystal ENDOR spectra of irradiated sucrose in the stable stage reveal the presence of at least one additional radical component exhibiting 3 or 4 resolved proton HF interactions. This is clearly seen in the FF-ENDOR spectra in Fig. 6.2. EPR and EIE spectra for this component are shown in Fig. 6.15 [56]. These indicate that the corresponding radical exhibits one large β -type HF interaction and several smaller couplings, one of which probably has intermediate magnitude (~ 30 – 40 MHz). The EIE spectra also show that, similar to T1–T3, this radical has an appreciable g anisotropy, indicating spin delocalization onto ring and/or carbonyl oxygen. A complete characterization of this radical is presently ongoing [56]. Comparison of the powder EPR (and possibly also ENDOR) spectra with spectrum simulations will allow to verify if this radical actually corresponds to the presently unknown components in the powder spectra.

6.4.6 Pulse Annealing Results—Pitfalls in the Analysis

In addition to the shape (radical composition), the intensity of the EPR spectra provides relevant information on the radiation chemistry of carbohydrates. In the introduction to this section, it is explained that for reliable comparison of intensities, EPR spectra have to be recorded at the same temperature. Pulse annealing experiments (although very time consuming) are most appropriate for this. For sucrose a pulse annealing experiment covering the complete ~ 6 K to RT temperature range

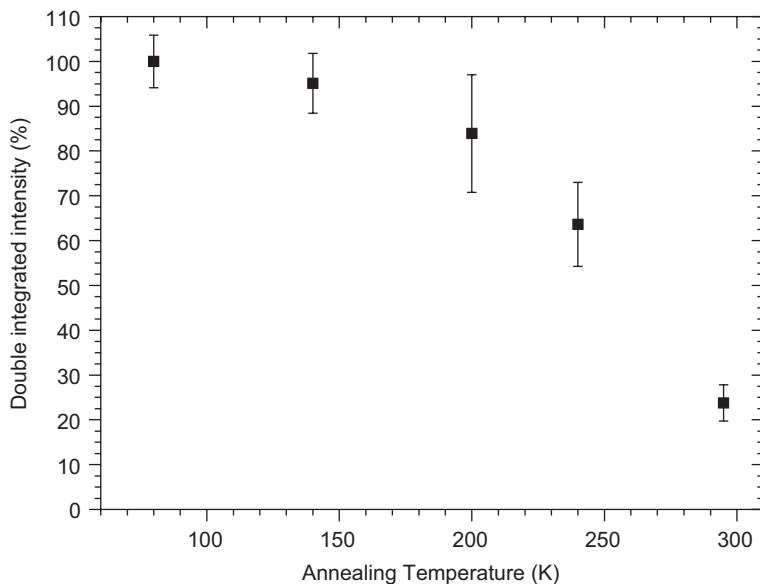


Fig. 6.16 Double integrated total intensity of the EPR spectrum of sucrose irradiated at 80 K, measured at 80 K (9.78 GHz) as a function of annealing temperature in pulse annealing experiments [105]. In each step the sample was heated to the annealing temperature, kept there for ~ 10 min after stabilization, and quenched to 80 K. EPR spectra were then recorded after a stabilization time of ~ 10 min. *Filled squares* indicate averages of data points collected for magnetic field alignments along $\langle a \rangle$, $\langle a^* \rangle$, $\langle c \rangle$ and $\langle c^* \rangle$. *Error bars* indicate 2 times the experimental standard deviation

has not been performed yet. The results of pulse annealing experiments up to RT after 80 K irradiation [105] are summarized in Fig. 6.16. The total double intensity data points are averages over pulse annealing experiments performed for four different magnetic field orientations in the $\{ac\}$ plane at X-band. In order to get a more complete picture of the evolution of the radical concentration, results from the previous sections should also be taken into account.

In Sect. 6.4.2 it was shown that in the 6–50 K range the total EPR intensity remains essentially constant and in the 50–80 K range the O3'(-H) alkoxy radical is annealed out. Finally, when keeping the crystal for a prolonged time at RT a further decrease in the total intensity by about 50% is expected (Sect. 6.4.4). One may conclude that only about 10% of the original radical concentration created at 6K “survives” to the RT stable stage. This implies that identifying radicals with low concentrations at low temperatures may be important, as they may be involved in the formation mechanisms of the stable radicals. On the other hand, certain (majority) radical components at low temperature may not be precursor to any of the radicals stable at higher temperatures. In addition, for a complete understanding of the radiation chemistry, recombination processes and diamagnetic radiation products should also be properly identified.

The discussion in Sect. 6.4 clearly demonstrates that, in spite of the very detailed investigation of the paramagnetic radiation products, even for sucrose several features are still not properly understood. Hence, the detailed reaction sequences leading to the stable radicals cannot be elucidated yet. Nevertheless, the results of our investigations allow proposing certain very likely reaction schemes for some of the stable radicals, as will be discussed in Sect. 6.6.

Table 6.9 summarizes the results of the radical identification studies on sucrose, listing for each irradiation stage the species characterized by EMR, along with models, wherever these are available, and references to the appropriate literature. In the models, the protons are labeled whose HF interactions have been characterized in the EMR studies. In Sect. 6.5 similar tables are presented for the other carbohydrates taken up in our studies (see Table 6.1 for atom labeling). For each carbohydrate, a discussion of the results is also given.

6.5 Results for Other Carbohydrates

6.5.1 *Dipotassium Glucose-1-Phosphate*

Table 6.10 is a particularly interesting model system for studying radiation damage to DNA, because it also contains sugar-phosphate bonds and strand breaks in DNA involve rupture of this bond. The primary radiation-induced radicals in K2G1P after exposure at 4 K were studied by Locher and Box [88], who reported 3 different alkoxy radicals (A1–A3, A1=O6(–H)), an IMTE and a C6(–H) hydroxyalkyl radical (IV) [88]. The assignment of the latter was explicitly confirmed by DFT calculations [11]. A meta-analysis of the data, including new crystal structure determinations [117], and considering the Schonland ambiguity [115, 118], showed that the assignment of A1 is reasonable and that A2 and A3 most probably correspond to alkoxy radicals at O4 and O2, respectively. In partially deuterated crystals, only A3 was observed together with the IMTE and C6(–H) [88]. Several other radicals were formed at LT, but not further analyzed. Also, no thermal annealing or light bleaching studies were reported. Interestingly, no P-centered radicals were produced by irradiation at this temperature.

Bungum et al. [118] and Sanderud and Sagstuen [119] studied the structures of P-centered radicals in this compound. They found that such radicals are not produced by irradiation at 77 K, but do appear after subsequent anneal to RT or when irradiating crystals at (close to) RT. Hence, sugar radicals very probably act as precursors for the P-centered radicals. This was one of the motivations for the elaborate study of C-centered radicals after X-ray irradiation at 77 K by De Cooman et al. [116] and Pauwels et al. [11]. Four C-centered radicals were identified in these studies. Other C-centered radicals were detected in the EPR spectra but could, for technical reasons, not be studied with ENDOR. The R2 radical, with the most prominent

Table 6.9 Radiation-induced radicals in sucrose

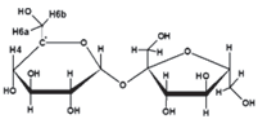
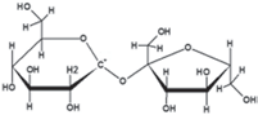
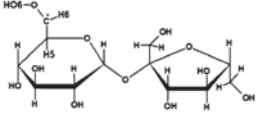
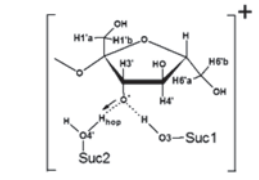
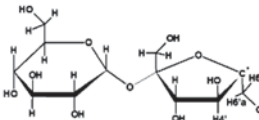
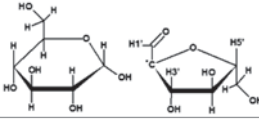
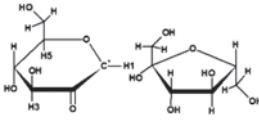
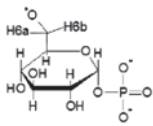
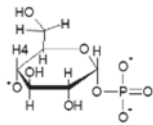
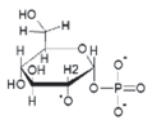
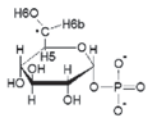
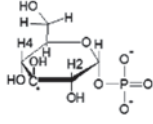
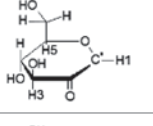
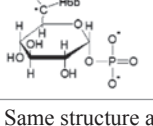
T_{irr}	Label	Structure	Confidence	Ref.
6–10 K	R1		Certain	[19]
	R2		Certain	[19]
	R3		Suggested	[19]
	R4	C-centered, location?	N/A	[19]
	R5	C-centered, location?	N/A	[19]
	R6		Certain	[17, 107]
	IMTE	OH dipole field near C5 and C6	Proposed	[104, 108]
80 K	R1	Same structure as R1 at 6–10 K, see above	Certain	[19, 105]
	R2	Same structure as R2 at 6–10 K, see above	Certain	[19, 105]
	N1		Plausible	[105]
	N2	C-centered, location?	N/A	[105]
	N3	C-centered, location?	N/A	[105]
295 K, limited stability	U1	C-centered, location?	N/A	[51, 106]
	U2	C-centered, location?	N/A	[51, 106]
295 K, stable	T1		Certain	[9, 55]
	T2/T3		Certain	[8, 55]
	T4	C-centered, location?	N/A	[56]

Table 6.10 Radiation-induced radicals in K2G1P

T_{irr}	Label	Structure	Confidence	Ref.
4.2 K	A1		Proposed	[88]
	A2		Proposed	[88, 115]
	A3		Proposed	[88, 115]
	Trapped electron	Location?	n/a	[88]
77 K	IV		Certain	[11, 88]
	R1		Certain	[11, 116]
	R2		Certain	[11, 116]
	R3		Certain	[11, 116]
	R4	Same structure as IV at 4.2 K, see above	Certain	[11, 116]

contribution to the EPR spectrum, has a structure very similar to that of T2/T3 in sucrose. It is also interesting to note that a C5-centered radical, that had been proposed as precursor for the phosphoryl radical detected at RT in K2G1P [119], was not identified in these studies.

6.5.2 *Trehalose Dihydrate*

To evaluate to which extent the findings of the sucrose studies can be generalized, we have undertaken an analogous study on the structurally similar trehalose (see Table 6.11). The first EPR spectra from RT irradiated trehalose crystals had already been investigated at 77 K by Gräslund and Löfroth in the 1970s [4]. A 1:2:1 triplet with a 3 mT HF splitting was assigned to a C3 or C3'-centered radical.

Samskog and Kispert extended this EPR work to radicals formed after irradiation at 3 K [111] and 77 K [120]. Irradiation at 3K led to three (close to) primary radicals, proposed to be an IMTE (radical I), an O4' alkoxy radical (radical III) and again a 1:2:1 triplet (radical II), also found after irradiation at 77 K and assumed to be the same as found previously [4]. After irradiation at 10 K (Tarpan et al. [20]), the trapped electron could no longer be detected at variance with the radicals II and III, relabeled as R1 and R4 respectively. A thorough ENDOR and DFT analysis convincingly modified the identification of the 1:2:1 triplet II/R1 to a C5'-centered radical, whereas the III/R4 assignment to the O4' alkoxy radical appeared plausible but still not conclusive. Two more radicals, R2 and R3, were convincingly identified as C5 and O2-centered radicals, respectively [20].

Tarpan et al. [101] also extended the EPR investigations of Samskog and Kispert after irradiation at 77 K [120] with ENDOR and DFT. Not surprisingly, the strongly composite EPR spectrum was for a major part interpreted in terms of the same (at least) 7 components, albeit again with a different labeling. Apart from the O2 alkoxy radical mentioned above, all assignments by Samskog and Kispert have been questioned and/or corrected by the combined ENDOR/DFT investigations [101]. Again a 1:2:1 triplet was prominently present and convincingly assigned to two slightly different conformations of a C4(-H) hydrogen-abstracted radical (VII or T1/T1*). In spite of its similar appearance, the triplet has another origin than the one mentioned in the lower temperature studies (both different from the radical after RT-irradiation, see also [4]). In addition, mainly based on their characteristic *g* tensors, the formation of 4 different alkoxy type radicals is quite certain, although their location remains mostly unknown or speculative (III, IV or T5, T6). Radicals T3 and T4 (or I) have been tentatively identified as O2' and O4-centered respectively. The stronger *g* anisotropy of T5,T6 as compared with T3 and T4 could not be explained by calculations yet. Finally, the T2 radical was only reported by Tarpan et al. [101] and is probably due to a C1(-H) radical.

In another combined ENDOR/DFT study, De Cooman et al. [12] provided firm proof for two H-abstracted radicals with limited stability, created by RT-irradiation. The I1 and I2 spectra have been assigned to C3' and C2-centered radicals respectively, the latter with additional formation of a carbonyl group at C3. Similar H-abstracted radicals occur in irradiated glucose [16]. The stable radicals S1 and S2 could only be tentatively identified. Like for I2, C2 seems to be the most likely site for the radical center of S1 and S2.

Table 6.11 Radiation-induced radicals in trehalose dihydrate

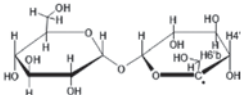
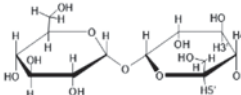
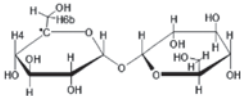
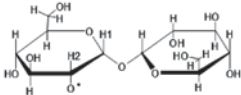
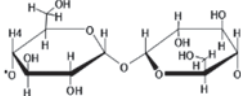
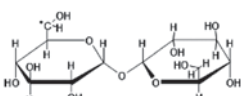
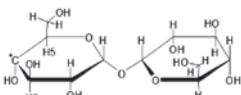
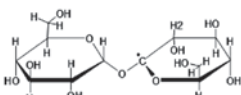
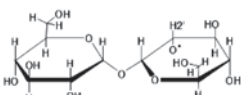
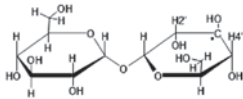
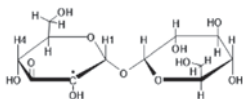
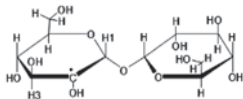
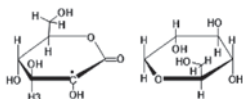
T_{HT}	Label	Structure	Confidence	Ref.
3 K	I ^{3K}	IMTE, location?	N/A	[111]
	II ^{3K}		Certain	[20, 111]
	III ^{3K}		Suggested	[20, 111]
10 K	R1	Same model as II ^{3K} , see above	Certain	[20]
	R2		Certain	[20]
	R3		Plausible	[20]
	R4	Same model as III ^{3K} , see above	Suggested	[20]
80 K	I ^{77K} =T4		Suggested	[101, 120]
	II ^{77K}	Same model as R3, see above	Plausible	[101, 120]
	III ^{77K} =T5	O-centered, location?	N/A	[101, 120]
	IV ^{77K} =T6	O-centered, location?	N/A	[101, 120]
	V ^{77K}		Proposed	[120]
	VI ^{77K}	C-centered, same as R2?	N/A	[20, 120]
	VI ^{77K} =T1/ T1*		Certain	[101, 120]
	T2		Plausible	[101]
	T3		Plausible	[101]
R2	See above, 10 K	Certain	[101]	

Table 6.11 (Continued)

T_{irr}	Label	Structure	Confidence	Ref.
RT, limited stability	I1		Certain	[4, 12]
	I2		Certain	[12]
	I3	C-centered, location? Less stable than I1 and I2	N/A	[12]
RT, long term stable	S1		Suggested	[4, 12]
	S2		Suggested	[4, 12]

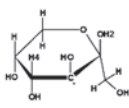
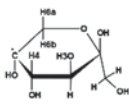
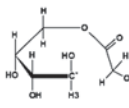
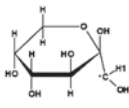
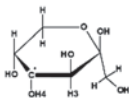
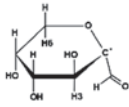
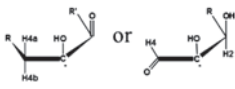
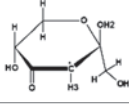
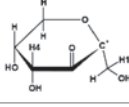
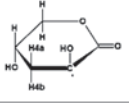
6.5.3 Fructose

It could *a priori* be expected that monosaccharides as, e.g., fructose, glucose and sorbose, would lead to EMR spectra that are simpler and easier to interpret than the disaccharides sucrose and trehalose. Therefore, about one decade ago, our group started an extensive EMR investigation on β -D-fructopyranose. This was also the first sugar for which a combined ENDOR/DFT approach was applied. It appeared that, contrary to expectations, a realm of radicals are detected in fructose and as a consequence, several identification problems are still unsolved (see Table 6.12).

Fructose and sorbose are structurally very similar and Ueda [121] was the first to systematically compare the EPR spectra of these materials both on powders and single crystals, after irradiation at 77 K and at RT. These authors found that irradiating fructose and sorbose at 77 K indeed leads to similar spectra whereas RT irradiation gives rise to significantly different spectra. Heating sorbose to 100 °C for 10 min. however, makes the spectra of both sugars similar again. Without having access to ENDOR or DFT methods and undoubtedly underestimating the complexity of the spectra, these authors proposed a C5-centered model for one of the radicals formed after 77 K irradiation [121]. In the remainder of this section, only fructose radicals will be discussed.

In their first study on fructose, Vanhaelewyn et al. [122] confined themselves to stable radicals in RT irradiated powders and single crystals. From a statistical MLCFA study on EPR powder spectra, it became clear that at least four stable radicals contributed to the spectra. This finding was confirmed later by ENDOR and EIE investigations [14, 81]. Two dominant radicals, labeled F1/F2, were found

Table 6.12 Radiation-induced radicals in β -D-fructose

T_{HT}	Label	Structure	Confidence	Ref.
10 K	T1/T1*		Certain	[18]
	T2		Plausible	[18]
80 K	R1/R1*	Same model as T1/T1* at 10 K, see above	Certain	[91]
	R2/R3		Certain	[91]
160 K	Q1		Plausible	[81]
	Q2	Same model as R2/R3 at 80 K, see above	Certain	[81]
RT, unstable	Im1		Plausible	[81]
	Im3	C5-centered, broken ring?	Proposed	[81]
	Im4		Plausible	[81]
	Im5	C2-centered, broken ring?	Proposed	[81]
	RT, stable	F1/F2 = Im2		Proposed
F3			Plausible	[14, 81]
F4/F5 = Im6			Plausible	[14, 81]
F6			Plausible	[14, 81]

to exhibit quite comparable HF interactions and, based on single molecule DFT calculations, a C2-centered model was proposed for both of them [89, 122] (an alternative labeling of the fructose atoms was used in that work). Although Tarpan et al. in later work also determined the g tensors of F1/F2 and applied selective ^{13}C enrichment in fructose powders [13, 14, 81], the identity of these main stable radicals remains uncertain. Using the most advanced DFT methods presently available, a C3(-H) model, featuring a neighboring carbonyl group and possibly also ring opening, seems the most plausible. Still, overall good agreement between experimental and computational data has not been reached [14, 81]. Also radicals F3 and F6 were proposed to be C3-centered. F6 is H-abstracted with a carbonyl group at C2, whereas a C3(-OH) model seems plausible for radical F3 [14, 81]. Another pair F4/F5 has been assigned to C2(-OH) radicals in slightly different conformations, accompanied by carbonyl formation at C3. The radicals F1/F2, F4/F5 were demonstrated to be present immediately after RT-irradiation (Im2, Im6) [14, 81]. Plausible models were found by Tarpan et al. for two unstable radicals: Im1 and Im4 have been assigned to C4(-H) and C2(-OH), respectively. The identifications of Im3 and Im5 remain far more speculative (broken-ring radicals centered at C5 and C2) [81].

In search of (close to) primary radicals, Tarpan et al. [18] and Vanhaelewyn et al. [91] also investigated fructose single crystals after X-irradiation at 10, 80 K and annealing to 160 K. All proposed models for these radicals can be considered to be highly reliable if not certain. Both after irradiation at 10 K and 80 K a prominent pair (labeled T1/T1* and R1/R1* respectively) has been identified (again) as the C3(-H) species. After 10 K irradiation, a second simple H-abstracted radical, C5 (-H) was reported (T2). Another C3-centered radical (two conformations) that was discovered after irradiation at 80 K (R2/R3), remained stable up to at least 160 K (Q2). Ring opening and formation of a carbonyl group appeared essential to reach excellent agreement between experimental and computational data. It is clear that the convincing identification of these radicals puts severe constraints on the precise identity of the F1/F2 C3-centered radicals (also assumed to have a broken ring) mentioned above. The C3-centered F3 and F6 radicals were proposed to have an intact ring [81, 91]. Finally the last fructose radical with a probable identification (Q1), stable up to at least 160 K, is a C1(-H) radical species [81].

6.5.4 Sorbose

The chemical structure of sorbose is nearly identical to that of fructose and *a priori* many similarities in radical formation could be expected, as were also discovered by Ueda [121] (see Sect. 6.5.5). However, the EMR study of this material appeared experimentally extremely complex and lack of complete g and HF data for most of the components prohibits detailed comparison with DFT modeling. Extensive MLCFA analyses, exploiting differential radical annealing between RT and 435 K, revealed more than 10 stable radicals after RT irradiation. In spite of considerable efforts hardly any complete HF tensor could be determined even using ENDOR.

Table 6.13 Radiation-induced radicals in α -L-Sorbose

T_{irr}	Label	Structure	Confidence	Ref.
295	R1/R1'		Plausible	[10]

The models, very tentatively proposed for the stable radicals, usually involve ring-openings and the formation of a carbonyl group adjacent to the radical center [123, 124]. As a result of these studies, however, excellent simulations of the RT EPR spectra became possible.

So far, the best characterized and identified radicals are R1/R1' (see Table 6.13), which dominate the EPR spectrum after RT irradiation. They are very probably C3(-H) species. The difference between R1 and R1' has been ascribed to the structural α/β disorder in the sorbose lattice, which may in part be responsible for the problems encountered in characterizing the other radical species in the EMR analyses [10].

In view of the very limited information on radical structures, no attempts are made to interpret the radical chemistry of sorbose in Sect. 6.6.

6.6 Radical Formation Mechanisms and Radiation Chemistry

In Sects. 6.4 and 6.5, the structures of free radicals formed after irradiation at very low temperatures (6–10 K, LT), intermediate temperatures (typically 80 K) and at RT have been presented. For the interpretation of these results it is important to keep in mind that the radical products formed by irradiation at a given intermediate or high temperature are the same as those obtained after irradiation at 6–10 K followed by warming to this temperature. This strongly suggests an internal connection between the radicals produced at LT and those observed at a higher temperature, to be described by chemical conversion processes. In Sects. 6.1 and 6.4 we mentioned this as a motivation for studying radiation products after irradiation at various temperatures.

The structures depicted in Tables 6.9, 6.10, 6.11, 6.12, 6.13 may be considered as dots in a complex drawing of the entire radiation processes picture, dots which remain to be connected by lines to obtain the full picture. The tools for completing the scheme are presented by radiation chemistry [125, 126]. Once hypotheses on actual processes connecting two or more structures are formulated, they should be probed by kinetic studies or quantum chemical modeling. However, constructing schemes that connect species stable at different temperatures, solely based on their structure assignments, presents several pitfalls. First, EMR techniques only detect

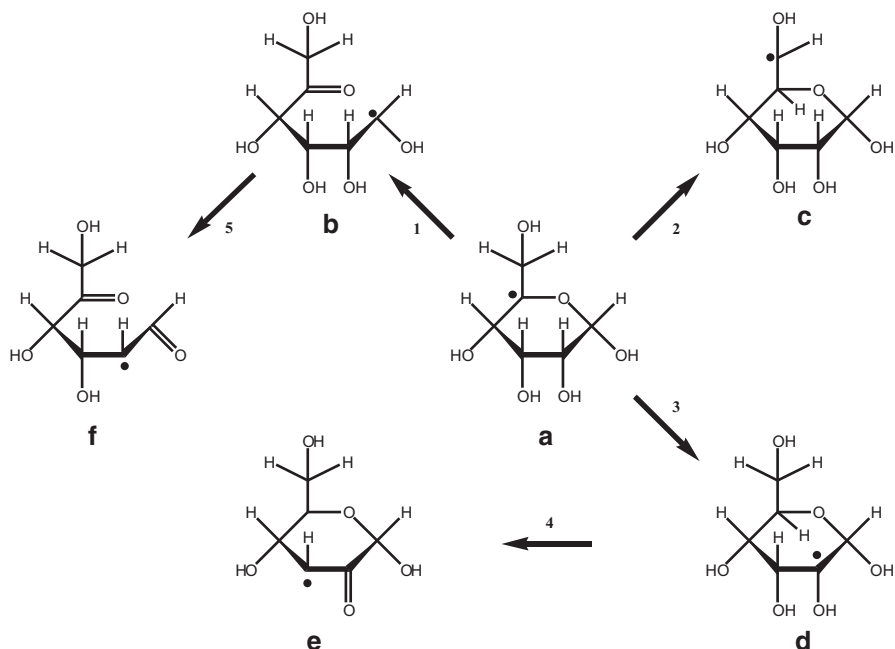


Fig. 6.17 Starting from a given primary radical structure A, processes 1–5 illustrate electronic reorganization (1), 1,2 H-atom shift (2) 1,4 H-atom shift (3), and β -OH elimination (4 and 5) processes, the latter with the release of a H_2O molecule

paramagnetic species: diamagnetic products from a given reaction are not observable. Secondly, when only starting and end-point in a reaction chain are known, there may be several possible routes between them. EMR spectroscopy alone will not allow deciding which route is actually followed. Recent results obtained for the amino acid alanine illustrate the important role of quantum chemical modeling in this: the entire sequence of processes in the reduction chain could finally be mapped by using advanced DFT calculations [127] even if the basic radical structures have been known for many years [128]. Another example is the recent advances made using mass spectroscopy and high-performance liquid chromatography to understand the early radiation-induced processes in DNA [129, 130]. Thirdly, depending on the temperature (thermal energy), a given primary product may proceed along different reaction paths, sometimes leading to different end products. Finally, in too many instances there are no experimental indications available showing which radical observed at higher temperature is connected to which LT radical species.

The exposure of organic matter to ionizing radiation (photons, electrons) initiates a number of processes in the material. The field of radiation physics describes these processes in great detail [131], far beyond the scope of this chapter. It is sufficient to state that the deposition of radiation energy in organic matter mainly results in ionizations and excitations. An ionization event creates a hole and a secondary electron with a mean kinetic energy below 30 eV, the vast majority of the secondary

electrons being below 70 eV. For each MeV of energy absorbed, about 3×10^4 low-energy electrons are created [132]. Secondary electrons travel further into the matter losing energy by scattering and new ionizations. The scattering events may sometimes be resonant, resulting in significant dissociative damage through the formation of transient negative ions (TNI) [133]. Each interaction reduces the electron kinetic energy, and eventually the electron will be trapped by thermalization, either in an empty non-dissociative molecular orbital creating a relatively stable molecular anion, or in some cases 'solvated' in a shallow intermolecular potential well, created by molecular dipoles (IMTE, see Sects. 6.4 and 6.5). In solid state carbohydrates this will be two or more OH dipoles [134]. Both the oxidation products and the reduction products will normally be left in vibrationally and sometimes also electronically excited states. Relaxation of these states often provides the activation energy necessary for subsequent processes.

Solid state organic materials usually are very good insulators [135]: extensive charge transfer processes will not take place. This is the main reason why charge recombination is prohibited, radicals become trapped and detectable with EMR. Solid state carbohydrates often give a high yield of radicals at low temperatures, indicating that charge transfer reactions are rare. Of course charge transfer does take place under given conditions [21, 136], but its range is limited and it enters in strong competition with radical trapping and subsequent secondary reactions.

6.6.1 Primary Processes

Reduction The one-electron reduced radical species (radical anion) will either protonate, most often through a hydrogen bond, or the additional charge becomes eliminated by expelling a negatively charged fragment like H^- or OH^- (typically from TNI's by dissociative electron attachment). Such mechanisms physically separate charge and spin, thereby reducing the possibility for charge combination processes. H^- and OH^- are reactive and may readily capture a proton, forming H_2 or H_2O .

Hydrogen bonding is associated with the hydroxyl substituents in carbohydrates and the initial reduction and protonation may be followed by dissociation of H atoms or OH radicals, which in turn may attack neighboring undamaged molecules, most often abstracting a hydrogen atom from these neighbors. High yields of hydrogen gas have been measured upon irradiation of carbohydrates [137].

The major results of the primary reductive trapping reactions in carbohydrates are hence neutral C-centered radicals. The most common products identified, as evident from the Tables in Sect. 6.5, are neutral C-centered hydroxyalkyl radicals apparently formed by net H-abstraction. It is experimentally not possible to distinguish between such initially reduced species and radicals formed by prompt H-abstraction from molecules left in highly excited (superexcited) states. Due to the lack of thermal energy, usually only simple processes requiring a minimum of energy are considered as relevant for explaining the neutral C-centered hydroxyalkyl radicals observed at low temperatures.

Carbohydrates form a group of compounds in which electrons may become intermolecularly trapped, due to the large number of OH groups exhibiting large dipolar moments. These IMTE centers may be compared with solvated electrons in frozen solutions [138]. The IMTE may also be compared with a polaron [139], as the trapping of the electrons probably results in a reorientation of OH fragments due to the excess electronic charge, enhancing the propensity for temporary trapping and consequent screening of the excess charge. The electron wave function is spread over a number of hydroxyl protons (in the vicinity of the trapping site), which in turn are somewhat displaced from their equilibrium positions. Upon thermal activation or exposure to visible light, the IMTE is excited and transfers to a neighboring OH group initiating the formation of a C-centered hydroxyalkyl radical as described by Eq. (6.9). It has been observed that optical and thermal bleaching can result in different products [140]. Lund and co-workers [134] have characterized the optical properties of trapped electrons for several carbohydrates and nicely demonstrated a well-developed absorption band in the 450–550 nm region.

The tables in Sect. 6.5 illustrate that radical formation is selective: only a few specific radicals appear to be formed from the vast number of possible species. The origin of this specificity is in principle unknown, but the observations indicate that primary radical formation is governed by overall energetic considerations, tightly associated with structural features of the compounds in question [21].

Oxidation The one-electron oxidized species (radical cation) will, in analogy with the radical anion, eliminate the excess positive charge by expelling a proton. It appears likely that the $R-OH^+$ is a general oxidation product [84]. This product deprotonates immediately, most often by way of the hydrogen bonding system. Under favorable conditions a proton will be transferred from an OH^+ group of the cation to a neighboring molecule, leaving behind an O-centered neutral alkoxy radical. As the hydrogen bonding scheme often is a continuous chain of O-bonded protons (C-OH and/or H_2O) throughout the lattice, the deprotonation has in some cases been shown to initiate a proton shuffle covering several molecules in the lattice [20, 21]. The driving force for the deprotonation may partly result from a change in the acid-base equilibrium for the cation as compared with the neutral molecule [141] and the excitation energy available by vibrational relaxation of the initial oxidation product. This, in combination with the structural features of the environment is expected to explain the selectivity of the alkoxy radical formation.

If deprotonation at an OH-group is not feasible (or back-protonation is immediate), it may rather occur at the neighboring carbon atom, resulting in a neutral C-centered species [84]. Highly excited oxidative states created by the ionization event may in addition produce a number of other radical or non-radical fragments [142].

The species formed by one-electron oxidation/reduction or from super-excited states, as described here, are those commonly observed at the lowest irradiation temperatures. The mechanisms are based mainly on radiation physical/chemical principles, and the diversity of species from each of the compounds investigated illustrates the delicate overall energy balance of the system, whose structural properties are essential. It is therefore not surprising to observe several reduction and

oxidation products simultaneously, even at the lowest irradiation temperatures. It is remarkable that in spite of the tremendous progress made in the field of molecular modeling, to date no modeling routines have been presented yet for reliably predicting the outcomes of radiation action at low temperatures.

6.6.2 Secondary Processes

Once the primary neutral radicals have been formed and trapped in the solid lattice, and thermal energy is supplied to the system, secondary processes take over the radical formation development. Here, thermally activated electronic reorganization processes and bond scissions dominate. Consequently, understanding the processes critically relies on the possibility to follow the transitions which occur in detail. Radiation chemists have investigated radical chemistry for years, but almost exclusively in solution, and occasionally in frozen solutions and glasses [125]. In crystalline solids, however, the conditions are basically different. Generally, only few mechanistic approaches are available for these systems, and intramolecular conversions are the most probable ones. Experimentally, each conversion between radical species must be followed sufficiently closely to convincingly argue for their interrelationship.

In carbohydrates, there are generally no prominent leaving groups present, as one finds in e.g. amino acids (amino group, carboxyl group). Starting from the neutral reduction and oxidation products, Fig. 6.17 schematically illustrates the following possible processes that have been argued to occur in the solid state (among a few others): 1—thermally induced electronic reorganization; 2 and 3—common 1,2- and 1,4 H-atom shifts; 4 and 5—elimination reactions like β -OH elimination. Reactions 1+5 ($A \rightarrow B \rightarrow F$) demonstrate how relatively simple processes may severely alter the molecular structure.

6.6.3 Radical Reactions

Sucrose After LT irradiation 4 major radicals were observed: the C1(-H), C5(-H), C6(-H) and the O3' alkoxy radical (Sect. 6.4.2). An IMTE was identified, shown to transfer to the C5(-H) radical by optical excitation or careful warming in the dark [104, 109]. A C6(-H) \rightarrow C5(-H) transformation was very probably observed upon annealing [104], which may be explained as a (C5,C6) H-shift reaction in the opposite direction of process 2 in Fig. 6.17. The neutral C6(-H) may either be a primary oxidation product formed by deprotonation at C6 of the RCH_2OH^+ species [84], or alternatively be formed by a net H-abstraction in a reductive process. The C1(-H) radical was tentatively ascribed to oxidative deprotonation, based on stoichiometric considerations that assume C6(-H) to be a reduction species.

The O3' alkoxy radical decays in the 50–80 K range. Again, a (C3',O3') H-shift (or back-protonation followed by a deprotonation from C3') will create a C3'

centered intermediate, which by a β -OH elimination may yield a radical centered at C4'. From here it is possible to speculate that a C5'(-H) radical species may become stabilized, the most probable site for the intermediate radical N1. More detailed EMR and DFT characterization of N1 and the two as yet unidentified species at 80 K (N2 and N3, not formed by simple H-abstractions) is necessary to elucidate the fate of the alkoxy species. C5(-H) and C1(-H) also remain as dominant paramagnetic species at 80 K. The precursors for the RT radicals are expected to be among these five species.

Above 100 K, the C5(-H) radical disappears, and above 200 K also C1(-H). The RT stable radicals T1 and T2/T3 are also present immediately after irradiation at RT, along with U1 and U2. It was proposed that the C1(-H) radical may be the precursor for the stable radical T2/T3, proceeding through a (C2,C1) H-shift followed by an elimination reaction. With regard to the C5(-H) radical, an electronic reorganization may be suggested that leaves the spin at C1, and a subsequent elimination reaction could lead to the T1 radical. However, the RT unstable U1 and U2 species, which have not been identified yet and seem to evolve in diamagnetic radiation products, may also result from the decay of C5(-H) and/or C1(-H). Therefore, the picture is still confusing with regard to processes between 100 K and RT. Work in progress towards identification of U1 and U2 will hopefully clear out this situation.

The present discussion clearly shows that, even if a vast amount of information on the radiation responses of sucrose is available (more than for any other carbohydrate to date), mapping specific radical reaction mechanisms remains to some extent speculative. Time-consuming and tedious monitoring the conversion of each component into its successor is necessary. This is work mostly remains to be done.

K2G1P Glucose-phosphate is an interesting substituted carbohydrate: a phosphate group is linked to a carbohydrate unit, mimicking the (deoxy)ribonucleotide ester bond in nucleic acids. A number of studies on K2G1P crystals have been summarized in Sect. 6.5.2 (Table 6.10, [11, 88, 103, 115, 118, 119]).

The LT irradiation study demonstrated that 3 different alkoxy radicals (A1–A3), an IMTE and a C6(-H) (labeled IV) hydroxyalkyl radical are trapped [88]. As no thermal or optical bleaching studies were reported, details on the processes connecting these radicals to those stable at elevated temperatures are not available from experiment. No P-centered radicals were observed after LT irradiation.

At 80 K, the four dominating radicals were all hydroxyalkyl radicals, labeled R1–R4 in Table 6.10. R3 and R4 are two distinct geometrical conformations of the C6(-H) radical, also detected after LT irradiation (IV=R4). Conformationally different C6(-H) radicals may be formed from the O6 alkoxy radical A1, e.g. by back-transfer of the proton and consecutive deprotonation at C6 [84], or by a H-shift process. Similarly, H-atoms released by the decay of other LT-trapped radicals may lead to C6(-H) radicals.

R1 is the C3(-H) radical species and good agreement with experimental data in the DFT modeling was only obtained if one assumes that the abstracted proton is transferred to a neighboring phosphate group [11]. This was hypothesized to be the 'missing' oxidation product at C3: rather than an O3(-H) alkoxy, the C3(-H)

radical is produced [84]. This model remains to be confirmed by analyzing hereto non-analyzed components of the spectra obtained after LT irradiation [88].

R2 is a C1-centered species formed by the net scission of the phosphate ester bond. Its structure is similar to that of T2/T3 in sucrose. A model for the formation of R2 was proposed [11], starting from a tentative C2(-H) hydroxyalkyl radical and proceeding by β -phosphate elimination, leaving the unpaired spin at C1, in addition to a non-radical HOPO_2^{2-} species. The C2(-H) species may be formed from the O2 alkoxy radical (A3) by a (C2,O2) H-atom shift.

Other radicals were detected at 80 K but not identified [103, 116]. None of these appeared to be alkoxy radicals, IMTE's or phosphate-centered radicals. At RT, the only well-identified species is a phosphoryl PO_3^{2-} radical [119]. A proposed mechanism for the formation of this radical [119] was however questioned in ref. [11] on basis of its large endothermicity. Other processes, e.g. electronic reorganization from a C1(-H) species, may be envisioned for the formation of a phosphoryl radical, but without more detailed investigation of the $g=2$ products at RT and the connections between radical products occurring between 80 K and RT, any suggestion remains highly speculative.

Trehalose Dihydrate Table 6.11 reveals a very complex and in part confusing array of radicals formed by irradiation at various temperatures. Based on our recent EMR/DFT work [12, 20, 101] many early radical assignments [4, 111, 120] needed to be corrected. However, it was not always evident to establish the correspondence with these earlier publications unambiguously. A considerable number of proposed radical models are based on few data, leaving some identifications rather uncertain.

The situation after LT irradiation appears rather clear, with the formation of an IMTE center (not seen by Tarpan et al. [20]), two alkoxy radicals (probably at O2 and O4', Samskog and Kispert report only the latter [111]) and two hydroxyalkyl radicals (identified as C5(-H) and C5'(-H), Samskog and Kispert report only the latter [111]). Furthermore, it was noted [111] that the intensity of C-centered radical(s) increased after thermal annealing to 50 K and was stable at 77 K. The fact that Tarpan et al. did not observe the IMTE at slightly higher irradiation temperature, but did detect an extra C5-centered radical, might imply a thermal transformation from the former to the latter radical at a relatively low temperature. On the other hand, the reasons for not detecting the IMTE at X-band [20] may be similar as for sucrose (see Sect. 6.4.2). Ref. [20] reports another interesting feature of the O4' alkoxy radical: in order to reproduce the experimental data in the DFT modeling, the abstracted proton needed to be shuffled through three hydrogen bonds and trapped as a hydronium ion. A similar observation was made for an alkoxy radical in crystals of rhamnose [17, 21].

After 77 K (80 K) irradiation, the situation looks considerably more complicated. Both Samskog et al. [120] and Tarpan et al. [101] reported four alkoxy and three hydroxyalkyl radicals, but two radicals in each study ($V^{77\text{K}}$, $VI^{77\text{K}}$ /T2,T3) have no clear counterpart in the other. In addition, only for two radicals DFT modeling allowed convincing (certain) identification, and one of these, C5(-H) (R2) is

already present after 10 K irradiation. Also one of the alkoxy species created at 10 K remains stable up to 80 K (O2(-H)). The other alkoxy, the IMTE and the C5'(-H) radical decay in the in the 10–80 K temperature range [101] and may be expected to transform into 6 new paramagnetic species. Indeed, pulse annealing in the 10–80 K range [101] showed (almost perfect) equivalence between LT irradiation followed by annealing to 80 K and irradiation at the latter temperature.

The fact that irradiation at 77 K yields a larger variety of alkoxy species than irradiation at LT is remarkable. It is possible that the larger thermal energy available at 77 K would allow for a larger diversity in alkoxy formation from the primary cation radical. Studying the thermal annealing [101] of samples irradiated at LT in further detail may bring answers to this question. Concerning the hydroxyalkyl radicals, for T1, dominant at 80 K and identified as C4(-H) (certain), it is not evident to construct a reasonable reaction chain starting from the radicals identified after LT irradiation. Furthermore it is not straightforward to link the unstable alkoxy (O4'(-H)) to any of the hydroxyalkyl radicals at 80 K. Tarpan et al. [101] argue that in spite of the structural information available, it is still premature to speculate on mechanisms, as the actual conversions have not been followed in detail. Indeed, it is possible that the decay of LT radicals results in diamagnetic molecules and H-atoms (or other mobile radical fragments), and that the action of the latter is to a large extent unpredictable without further experimental information. The large decrease in EPR intensity observed in the 10–80 K pulse annealing experiments [81], indeed, points to formation of diamagnetic radiation damage.

The RT studies [4, 12] agree on the presence of a dominant EPR triplet contribution immediately after irradiation, I1, identified as C3'(-H), and two contributions to the final stable spectrum (S1 and S2, only suggested models, no convincing identification). Tarpan et al. [12] detected two more species immediately after irradiation: one was identified as C2(-H) with a β -carbonyl at C3, the other only has very limited stability and remained unidentified. Pulse annealing experiments between 80 K and RT have only been performed coarsely. From 150 K onwards, no strong changes seem to occur in the EPR spectrum (dominant triplet contribution). However, this may be deceiving as ENDOR analyses at 10 K, 80 K and RT have shown that three very similar EPR triplets correspond to hydroxyalkyl radicals centered at different C-atoms [12] (Table 6.11, II^{3K}=R1, VII^{77K}=T1/T1*, I1). Pulse annealing experiments evidenced a further decrease in the total EPR intensity, suggesting formation of diamagnetic species [81]. This hampers devising chemical links between the species observed immediately after RT irradiation and radicals stable at 80 K. Gräslund and Löfroth [4] proposed β -elimination reactions to explain the transformations at RT to the final stable stage. The model suggested for S2 (C2(-H) with β -carbonyl at C1) seems compatible with such hypothesis. The role of crystal water in this carbohydrate also deserves further investigation.

Fructose The LT study (10 K irradiation) by Tarpan et al. [18] gave evidence for two hydroxyalkyl radicals: a C3(-H) (certain) and a C5(-H) species (plausible). Trapped electrons were not detected and no attempts were made to analyze weak features, probably due to alkoxy radicals. After irradiation at 80 K, C3(-H) species

was still observed [91], but C5(-H) was not. At this temperature, however, another radical was seen, identified (certain) as a ring-opened species with the spin localized at C3 (R2/R3). It was originally proposed that this ring-opened species originated from an O2(-H) alkoxy radical [81]. Because at 10 K no alkoxy radical was observed as a dominant radiation defect, and the C5(-H) hydroxyalkyl radical decayed between 10 and 80 K, a link between C5(-H) and the ring-opened species seems more reasonable. However, if both structure assignments are correct, there is no straightforward reaction pathway between them. It may be speculated that C5(-H) decays by releasing a H-atom, which abstracts the O2 hydroxyl proton at a neighboring molecule, yielding the ring-opened species R2/R3 by a subsequent electronic reorganization.

Thermal annealing at 160 K of crystals irradiated at 77 K resulted in two major radicals only. There is an apparent transformation of the C3(-H) radical into a new species assigned to a C1(-H) radical (plausible) [81]. The ring-opened species remained present at this temperature. Again, there is no obvious reaction pathway between the C3(-H) and the C1(-H) species, except for a H-transfer process.

Upon irradiation of fructose crystals at RT followed by immediate cooling, unstable species were stabilized for a sufficiently long time to allow a detailed analysis [81]. Six distinct species (Im1–Im6, see Table 6.12) were detected and analyzed. Two of these remained stable upon storage at RT (Im2=F1/F2 and Im6=F4/F5). The other 4 either decayed or developed into further stable radicals F3 and F6 (Table 6.12). None of these species had been observed in the studies at lower temperatures. Hence, a considerable number of reactions and rearrangements must occur between 160 K and RT and there is by far insufficient information presently available to provide direct links between these species. A few speculations can, nonetheless, be made. Indeed, e.g., the Im4 radical (plausible) can be formed from the C1(-H) radical (plausible) by a simple β -OH elimination. The ring-opened species Q2, stable at least to 160 K, most probably dehydrogenates, yielding one or several of the still unidentified RT radicals with limited stability, or even the stable radicals F1/F2, whose structure could not be completely elucidated. More firm conclusions will only be possible after closely monitoring which species are formed at stages between 160 K and RT.

6.6.4 Final Remarks

In addition to the carbohydrates discussed above, a variety of other solid-state sugars have been investigated for different purposes. Box and co-workers have characterized IMTEs in a number of compounds, as nicely summarized in the review by Lund and Schlick [134]. The group of Box has characterized an even larger number of primary alkoxy radicals in carbohydrates [107–109, 144]. These authors, however, seldom discussed secondary radicals and radical reactions. Lund and coworkers have analyzed many different solid-state carbohydrates using both pulse radiolysis and EMR techniques. Some of these studies have been discussed above [85, 111,

112, 120]. They elucidated several of the most important secondary reactions for IMTE and alkoxy radicals. Bernhard and co-workers [22, 143] investigated some carbohydrate derivatives in large detail, and also in some cases they provided possible reaction sequences. The carbohydrate rhamnose has been studied by several groups, both for characterizing IMTE and alkoxy radicals, and for discussing reaction sequences ([140] and references therein). Advanced DFT calculations for this compound have yielded important information on oxidative proton shuffling at low temperatures ([17, 21], see also Chap. 18 of this book). Presently, theoretical and experimental work, predicting the initial radical products after ionizing radiation as well as providing detailed understanding of the nature and reactions of the IMTE and alkoxy radicals, is ongoing [145]. This also includes mapping of radical reactions from C-centered low temperature precursors into RT stable radicals.

6.7 Summary and Conclusions

In this chapter, we have outlined the strategy and reviewed the results of our EMR studies of radiation-induced radicals in solid-state sucrose, dipotassium glucose-1-phosphate, trehalose dihydrate, fructose and sorbose. This work has been primarily directed towards identification of radical structures. We have shown that single crystal EPR, ENDOR and EIE measurements, together with DFT modeling, present a winning combination for radical identification. Comparing SH parameters resulting from carefully analyzed experiments (e.g. eliminating the Schonland ambiguity) with high-level DFT calculations on correct radical models can lead to remarkably good agreement. This holds particularly true for the g and A tensor principal directions and the anisotropy in the principal values, but also isotropic values are fairly well predicted by calculations.

For most carbohydrates discussed here, radicals have been identified after irradiation at various temperatures, in order to follow the reaction pathways between the primary radiation products and the final stable radicals. Low-temperature irradiation (4–10 K), as expected, produces IMTE centers along with net H-abstracted alkoxy and hydroxyalkyl radicals. The stable radiation-induced radicals are C-centered and often feature carbonyl formation close to the radical center, evidenced by an increased anisotropy of the g tensor. The multi-compositeness of the spectra, that in addition considerably lose intensity upon annealing after irradiation at low temperature, renders direct monitoring of inter-conversions between radical species difficult. Hence, despite the experimental and modeling efforts, for none of the carbohydrates discussed here, the radiation chemistry could be elucidated. Nonetheless, certain plausible reaction paths have been presented and considerable progress is currently being made for other carbohydrates.

In the context of applying the EPR spectra of sugars for dosimetry and detection of irradiated foodstuffs, we recently made significant progress in understanding the EPR spectrum of irradiated sucrose powder. Our studies provide a mechanistic understanding of the common practice to wait at least 48 hours (allowing for the U1 and U2 components to decay) before using the spectrum of irradiated sucrose for

dosimetric purposes. Simulations taking into account the contributions of the three stable radicals, that were thoroughly characterized using single crystal EMR measurements and identified via DFT modeling, reproduce the central part of this spectrum very well. The stable radicals responsible for the remaining discrepancies are currently being characterized. Somewhat surprisingly, the knowledge of the radical models also appears helpful for powder EPR spectrum simulations.

Acknowledgments The authors thank the many PhD and Master students whose experimental work has contributed to this chapter, which we dedicate to the memories of Profs. W.H. Nelson and W.A. Bernhard.

References

1. Ueda H, Kuri Z, Shida S (1961) Electron spin resonance studies of gamma-irradiated single crystals of sucrose. *J Chem Phys* 35:2145
2. Shields H, Hamrick P (1962) X-Irradiation damage of sucrose single crystal. *J Chem Phys* 37:202–203
3. Lomaglio G (1967) Résonance Paramagnétique Electronique et Susceptibilité Paramagnétique d'un Monocristal de Saccharose Irradié. *C R Séances Acad Sci Ser B* 264:1637
4. Gräslund A, Löfroth G (1975) Free-radicals in gamma-irradiated single-crystals of trehalose dihydrate and sucrose studied by electron-paramagnetic resonance. *Acta Chem Scand Ser B* 29:475–482
5. Sagstuen E, Lund A, Awadelkarim O, Lindgren M, Westerling J (1986) Free-radicals in X-irradiated single-crystals of sucrose—a reexamination. *J Phys Chem* 90:5584–5588
6. Vanhaelewyn G, Sadlo J, Callens F, Mondelaers W, De Frenne D, Matthys P (2000) A decomposition study of the EPR spectrum of irradiated sucrose. *Appl Radiat Isot* 52:1221–1227
7. Georgieva ER, Pardi L, Jeschke G, Gatteschi D, Sorace L, Yordanov ND (2006) High-field/high-frequency EPR study on stable free radicals formed in sucrose by gamma-irradiation. *Free Radic Res* 40:553–563
8. De Cooman H, Pauwels E, Vrielinck H, Sagstuen E, Callens F, Waroquier M (2008) Identification and conformational study of stable radiation-induced defects in sucrose single crystals using density functional theory calculations of electron magnetic resonance parameters. *J Phys Chem B* 112:7298–7307
9. De Cooman H, Pauwels E, Vrielinck H, Sagstuen E, Van Doorslaer S, Callens F, Waroquier M (2009) ENDOR and HYSCORE analysis and DFT-assisted identification of the third major stable radical in sucrose single crystals X-irradiated at room temperature. *Phys Chem Chem Phys* 11:1105–1114
10. Vanhaelewyn GCAM, Jansen B, Pauwels E, Sagstuen E, Waroquier M, Callens FJ (2004) Experimental and theoretical electron magnetic resonance study on radiation-induced radicals in alpha-L-sorbose single crystals. *J Phys Chem A* 108:3308–3314
11. Pauwels E, De Cooman H, Vanhaelewyn G, Sagstuen E, Callens F, Waroquier M (2008) Radiation-induced radicals in glucose-1-phosphate. II. DFT analysis of structures and possible formation mechanisms. *J Phys Chem B* 112:15054–15063
12. De Cooman H, Tarpan MA, Vrielinck H, Waroquier M, Callens F (2013) Room temperature radiation products in trehalose single crystals: EMR and DFT analysis. *Radiat Res* 179:313–322
13. Tarpan MA, Vrielinck H, De Cooman H, Callens F (2009) Determination of the *g* tensors for the dominant stable radicals in X-irradiated beta-D-fructose single crystals. *J Phys Chem A* 113:7994–8000

14. Tarpan MA, Pauwels E, Vrielinck H, Waroquier M, Callens F (2010) Electron magnetic resonance and density functional theory study of room temperature X-irradiated beta-D-fructose single crystals. *J Phys Chem A* 114:12417–12426
15. Box HC (1977) Radiation effects: ESR and ENDOR analysis. Academic, New York
16. Pauwels E, Van Speybroeck V, Waroquier M (2006) Radiation-induced radicals in alpha-D-glucose: comparing DFT cluster calculations with magnetic resonance experiments. *Spectrochim Acta A* 63:795–801
17. Pauwels E, Declerck R, Van Speybroeck V, Waroquier M (2008) Evidence for a grotthuss-like mechanism in the formation of the rhamnose alkoxy radical based on periodic DFT calculations. *Radiat Res* 169:8–18
18. Tarpan M, Sagstuen E, Pauwels E, Vrielinck H, Waroquier M, Callens F (2008) Combined electron magnetic resonance and density functional theory study of 10 K X-irradiated beta-D-fructose single crystals. *J Phys Chem A* 112:3898–3905
19. De Cooman H, Pauwels E, Vrielinck H, Sagstuen E, Waroquier M, Callens F (2010) Oxidation and reduction products of X irradiation at 10 K in sucrose single crystals: radical identification by EPR, ENDOR, and DFT. *J Phys Chem B* 114:666–674
20. Tarpan MA, De Cooman H, Sagstuen E, Waroquier M, Callens F (2011) Identification of primary free radicals in trehalose dihydrate single crystals X-irradiated at 10 K. *Phys Chem Chem Phys* 13:11294–11302
21. Aalbergsjö SG, Pauwels E, De Cooman H, Hole EO, Sagstuen E (2013) Structural specificity of alkoxy radical formation in crystalline carbohydrates. *Phys Chem Chem Phys* 15:9615–9619
22. Madden KP, Bernhard WA (1979) ESR-ENDOR study of α -D-glucopyranose single crystals X irradiated at 12 and 77 K. *J Phys Chem* 83:2643–2649
23. Von Sonntag C (2006) Free-radical-induced DNA damage and its repair—A chemical perspective. Springer, Berlin
24. Nakajima T (1988) Sugar as an emergency populace dosimeter for radiation accidents. *Health Phys* 55:951–955
25. Nakajima T (1989) Possibility of retrospective dosimetry for persons accidentally exposed to ionizing-radiation using electron-spin resonance of sugar and mother-of-pearl. *Br J Radiol* 62:148–153
26. Silveira FAM, Baffa O (1995) Lyoluminescence and ESR measurements on alanine and sucrose dosimeters. *Appl Radiat Isot* 46:827–830
27. Son PK, Ok CI, Kim JW (2001) EPR study of sugar irradiated with X-Rays. *J Korean Phys Soc* 38:315–317
28. Yordanov ND, Gancheva V, Georgieva E (2002) EPR and UV spectroscopic study of table sugar as a high-dose dosimeter. *Radiat Phys Chem* 65:269–276
29. Yordanov ND, Georgieva E (2004) EPR and UV spectral study of gamma-irradiated white and burned sugar, fructose and glucose. *Spectrochim Acta A* 60:1307–1314
30. Desrosiers M, Wadley S (2006) Time dependence of the radiation-induced EPR signal in sucrose. *Radiat Prot Dosim* 118:479–481
31. Trompier F, Bassinet C, Wieser A, De Angelis C, Viscomi D, Fattibene P (2009) Radiation-induced signals analysed by epr spectrometry applied to fortuitous dosimetry. *Ann Ist Super Sanita* 45:287–296
32. Karakirova Y, Yordanov ND, De Cooman H, Vrielinck H, Callens F (2010) dosimetric characteristics of different types of saccharides: an EPR and UV spectrometric study. *Radiat Phys Chem* 79:654–659
33. Desrosiers MF (1996) Current status of the EPR method to detect irradiated food. *Appl Radiat Isot* 47:1621–1628
34. European Committee for Standardisation (2001) EN 13708:2001 E: foodstuffs-detection of irradiated food containing crystalline sugar by ESR spectroscopy. CEN, Brussels
35. Malec-Czechowska K, Strzelczak G, Dancewicz AM, Stachowicz W, Delincée H (2002) Detection of irradiation treatment in dried mushrooms by photostimulated luminescence, EPR spectroscopy and thermoluminescence measurements. *Eur Food Res Technol* 216:157–165

36. Yordanov ND, Pachova Z (2006) Gamma-irradiated dry fruits—an example of a wide variety of long-time dependent EPR spectra. *Spectrochim Acta A* 63:891–895
37. Guzik GP, Stachowicz W, Michalik J (2008) Study on stable radicals produced by ionizing radiation in dried fruits and related sugars by electron paramagnetic resonance spectro-metry and photostimulated luminescence method-I. D-fructose. *Nukleonika* 53:S89–S94
38. Guzik GP, Stachowicz W, Michalik J (2012) EPR study on sugar radicals utilized for detection of radiation treatment of food. *Nukleonika* 57:545–549
39. Ahn JJ, Akram K, Kwon JH (2012) Electron spin resonance analyses of grinding- and radiation-induced signals in raw and refined sugars. *Food Anal Methods* 5:1196–1204
40. Son PK, Choi S-W, Kim SS, Gwag JS (2012) Dosimetry Application of Irradiated D-fructose using the electron paramagnetic resonance. *J Magnetics* 17:271–274
41. Ahn J-J, Akram K, Kim H-K, Kwon J-H (2013) Electron spin resonance spectroscopy for the identification of irradiated foods with complex ESR Signals. *Food Anal Methods* 6:301–308
42. Mangiacotti M, Marchesani G, Floridi F, Siragusa G, Chiaravalle AE (2013) Official checks by an accredited laboratory on irradiated foods at an Italian market. *Food Control* 33:307–312
43. Schonland DS (1959) On the determination of the principal g-values in electron spin resonance. *Proc Phys Soc Lond* 73:788–792
44. Vrielinck H, De Cooman H, Tarpan MA, Sagstuen E, Waroquier M, Callens F (2008) Schonland ambiguity in the electron nuclear double resonance analysis of hyperfine interactions: principles and practice. *J Magn Reson* 195:196–205
45. Nelson WH (1980) Quick-access sample system for low-temperature ESR-ENDOR at K-band. *J Magn Reson* 37:205–207
46. Krzystek J, Sienkiewicz A, Pardi L, Brunel LC (1996) DPPH as a standard for high-field EPR. *J Magn Reson* 125:207–211
47. Serway RA, Marshall SA (1967) Electron spin resonance absorption spectra of CO_3^- and CO_3^{3-} molecule-ions in irradiated single-crystal calcite. *J Chem Phys* 46:1949–1952
48. Schweiger A, Jeschke G (2001) Principles of pulsed electron paramagnetic resonance. Oxford University Press, Oxford
49. Weil JA, Bolton JR, Wertz JE (1994) Electron paramagnetic resonance-elementary theory and practical applications. Wiley, New York
50. Loncke F, De Cooman H, Khaidukov NM, Vrielinck H, Goovaerts E, Matthys P, Callens F (2007) EPR and ENDOR analysis of Fe^{3+} impurity centers in fluoroelpasolite lattices. *Phys Chem Chem Phys* 9:5320–5329
51. Vrielinck H, De Cooman H, Karakirova Y, Yordanov ND, Callens F (2009) Early-stage evolution of the EPR spectrum of crystalline sucrose at room temperature after high-dose X irradiation. *Radiat Res* 172:226–233
52. Hyde JS (1965) ENDOR of free radicals in solution. *J Chem Phys* 43:1806
53. Robinson BH, Dalton LA, Beth AH, Dalton RL (1976) ENDOR induced electron paramagnetic resonance: application to the resolution of overlapping spectra. *Chem Phys* 18:321–332
54. Andersen MF, Sagstuen E, Henriksen T (1987) Radiation damage to steroids. An ENDOR study to cholest-4-en-3-one. *J Magn Reson* 71:461–475
55. De Cooman H, Pauwels E, Vrielinck H, Dimitrova A, Yordanov ND, Sagstuen E, Waroquier M, Callens F (2008) Radiation-induced defects in sucrose single crystals, revisited: a combined electron magnetic resonance and density functional theory study. *Spectrochim Acta A* 69:1372–1383
56. Kusakovskij J, Vrielinck H, Callens F, work in progress
57. De Cooman H, Keysabyl J, Kusakovskij J, Van Yperen-DeDA, Waroquier M, Callens F, Vrielinck H (2013) Dominant stable radicals in irradiated sucrose: g tensors and contribution to the powder electron paramagnetic resonance spectrum. *J Phys Chem B* 117:7169–7178
58. Vrielinck H, Kusakovskij J, Vanhaelewyn G, Matthys P, Callens F (2014) Understanding the dosimetric powder EPR spectrum of sucrose by identification of the stable radiation-induced radicals. *Radiat Prot Dosim* 157:118–124
59. Nelson WH (1980) Estimation of errors in eigenvalues and eigenvectors from magnetic resonance results by use of linear data-fitting techniques. *J Magn Reson* 38:71–78

60. Stoll S, Schweiger A (2006) EasySpin, a comprehensive software package for spectral simulation and analysis in EPR. *J Magn Reson* 178:42–55
61. Lund A, Thuomas KA, Maruani J (1978) Calculation of powder ESR-spectra of radicals with hyperfine and quadrupolar interactions-application to monochloroalkyl and dichloroalkyl radicals. *J Magn Reson* 30:505–514
62. Sagstuen E, Lund A, Itagaki Y, Maruani J (2000) Weakly coupled proton interactions in the malonic acid radical: single crystal ENDOR Analysis and EPR Simulation at Microwave Saturation. *J Phys Chem A* 104:6362–6371
63. Kang J, Tokdemir S, Shao J, Nelson WH (2003) Electronic *g*-factor measurement from ENDOR-induced EPR patterns: malonic acid and guanine hydrochloride dihydrate. *J Magn Reson* 165:128–136
64. Theisen H, Sagstuen E (1981) The indole H-adduct radical in single crystals of tryptamine-HCl: an ESR-ENDOR study. *J Chem Phys* 74:2319–2324
65. Sagstuen E, Awadalkarim O, Lund A, Masiakowski J (1986) Trapping site geometry of $N_2H_4^+$ radical ion in X-irradiated single-crystals of $N_2H_5HC_2O_4$: an ENDOR study. *J Chem Phys* 85:3223–3228
66. Maes F (1996) Electron paramagnetic resonance and electron nuclear double resonance of chalcogen ions in alkali halide single crystals. PhD thesis, Ghent University (in Dutch)
67. Dobbs AJ, Gilbert BC, Norman ROC (1971) Electron spin resonance studies. XXVII. Geometry of oxygen-substituted alkyl radicals. *J Chem Soc A* 1:24–135
68. Bernhard WA (1984) The use of alpha hyperfine coupling tensors as a measure of unpaired spin density and free radical geometry. *J Chem Phys* 81:5928–5936
69. Muto H (1991) Trapped anions in organic systems. In: Lund A, Shiotani M (eds) *Radical ionic systems. Properties in condensed phases*. Kluwer, Dordrecht, pp 337–360
70. Sørnes AR, Sagstuen E (1995) ENDOR study of 1H couplings in single crystals of 2-aminoethyl hydrogen sulfate X-irradiated at 295 K. Radical geometry analysis using effective dipole center approximations and UHF-INDO calculations. *J Phys Chem* 99:16857–16866
71. Colson AO, Sevilla MD (1995) Structure and relative stability of deoxyribose radicals in a model DNA backbone: Ab initio molecular orbital calculations. *J Phys Chem* 99:3867–3874
72. Erling PA, Nelson WH (2004) Dependence of alpha-proton hyperfine couplings on free radical geometry. *J Phys Chem A* 108:7591–7595
73. Øhman KT, Sanderud A, Hole EO, Sagstuen E (2006) Single crystals of L-O-serine phosphate X-irradiated at low temperatures: EPR, ENDOR, EIE, and DFT studies. *J Phys Chem A* 110:8585–9596
74. McConnell HM, Strathdee J (1959) Theory of anisotropic hyperfine interactions in Pi-electron radicals. *Mol Phys* 2:129–138
75. McConnell HM, Chesnut DB (1958) Theory of isotropic hyperfine interactions in Pi-electron radicals. *J Chem Phys* 28:107–117
76. Heller C, McConnell HM (1960) Radiation damage in organic crystals. 2. Electron spin resonance of $(CO_2H)CH_2CH(CO_2H)$ in beta-succinic acid. *J Chem Phys* 32:1535–1539
77. Morton JR (1964) Electron spin resonance of oriented radicals. *Chem Rev* 64:453–471
78. Bernhard WA, Close DM, Mercer KR, Corelli JC (1976) ESR of X-irradiated single-crystals of 3'-cytidylic acid-hydrogen abstraction from C5' of sugar moiety. *Radiat Res* 66:19–32
79. Vestad TA, Gustafsson H, Lund A, Hole EO, Sagstuen E (2004) Radiation-induced radicals in lithium formate monohydrate ($LiHCO_2 \cdot H_2O$). EPR and ENDOR studies of X-irradiated crystal and polycrystalline samples. *Phys Chem Chem Phys* 6:3017–3022
80. Ko CL, Box HC (1978) Exchangeable proton couplings in free-radicals-radiation products of hydroxyproline HCl. *J Chem Phys* 68:5357–5362
81. Tarpan MA (2011) Electron magnetic resonance study of the structure and thermal stability of radiation-induced radicals in fructose and trehalose. PhD thesis, Ghent University
82. McConnell HM, Heller C, Cole T, Fessenden RW (1960) Radiation damage in organic crystals I. $CH(COOH)_2$ in malonic acid. *J Am Chem Soc* 82:766–775
83. McConnell HM, Robertson RE (1957) Spectroscopic splitting factors in aromatic radicals. *J Phys Chem* 61:1018

84. Bernhard WA, Close DM, Hüttermann J, Zehner H (1977) Alkoxy radical, RCH_2O , as a free-radical product in X-irradiated single crystals of nucleosides and nucleotides. *J Chem Phys* 67:1211–1219
85. Samskog PO, Lund A (1980) The Alkoxy radical RCHO formed in irradiated single-crystals of rhamnose. *Chem Phys Lett* 75:525–527
86. Lee JY, Box HC (1973) ESR and ENDOR studies of DL-serine irradiated at 4.2 K. *J Chem Phys* 59:2509–2512
87. Box HC, Budzinski EE (1975) Primary radiation damage in thymidine. *J Chem Phys* 62:197–199
88. Locher SE, Box HC (1980) ESR-ENDOR studies of X-irradiated glucose-1-phosphate dipotassium salt. *J Chem Phys* 72:828–832
89. Pauwels E, Lahorte P, Vanhaelewyn G, Callens F, De Proft F, Geerlings P, Waroquier M (2002) Tentative structures for the radiation-induced radicals in crystalline beta-D-fructose using density functional theory. *J Phys Chem A* 105:12340–12348
90. Pauwels E, Van Speybroeck V, Vanhaelewyn G, Callens F, Waroquier M (2004) DFT-EPR study of radiation-induced radicals in alpha-D-glucose. *Int J Quantum Chem* 99:102–108
91. Vanhaelewyn GCAM, Pauwels E, Callens FJ, Waroquier M, Sagstuen E, Matthys PFAE (2006) Q-band EPR and ENDOR of low temperature X-irradiated beta-D-fructose single crystals. *J Phys Chem A* 110:2147–2156
92. Pauwels E, Van Speybroeck V, Waroquier M (2006) Study of rhamnose radicals in the solid state adopting a density functional theory cluster approach. *J Phys Chem A* 110:6504–6513
93. Car R, Parrinello M (1985) Unified approach for molecular-dynamics and density-functional theory. *Phys Rev Lett* 55:2472–2474
94. CPMD V3.11, Copyright IBM Corp., 1990–2006, Copyright MPI für Festkörperforschung, Stuttgart, 1997–2001
95. Lippert G, Hutter J, Parrinello M (1997) A hybrid gaussian and plane wave density functional scheme. *Mol Phys* 92:477–487
96. Lippert G, Hutter J, Parrinello M (1999) The gaussian and augmented-plane-wave density functional method for Ab initio molecular dynamics simulations. *Theo Chem Acc* 103:124–140
97. <http://www.cp2k.org/>
98. Declerck R, Pauwels E, Van Speybroeck V, Waroquier M (2006) First-principles calculations of hyperfine parameters with the Gaussian and augmented-plane-wave method: application to radicals embedded in a crystalline environment. *Phys Rev B* 74:art. no. 245103
99. Declerck R, Van Speybroeck V, Waroquier M (2006) First-principles calculation of the EPR g tensor in extended periodic systems. *Phys Rev B* 73:art. no. 115113
100. Weber V, Iannuzzi M, Giani S, Hutter J, Declerck R, Waroquier M (2009) Magnetic linear response properties calculations with the gaussian and augmented-plane-wave method. *J Chem Phys* 131:art. no. 014106
101. Tarpan MA, De Cooman H, Hole EO, Waroquier M, Callens F (2012) Radiation products at 77 K in trehalose single crystals: EMR and DFT analysis. *J Phys Chem A* 116:3377–3387
102. Kevorkyants R, Wang X, Close DM, Pavanello M (2013) Calculating hyperfine couplings in large ionic crystals containing hundreds of QM atoms: subsystem DFT is the key. *J Phys Chem B* 117:13967–13974
103. De Cooman H (2009) A combined EMR and DFT study of radiation-induced defects in sucrose and glucose 1-Phosphate. PhD thesis, Ghent University
104. De Cooman H et al. Unpublished Results (K-band EMR Study of 6 K Irradiated Sucrose)
105. De Cooman H et al. Unpublished Results (X-band EMR Study of 80K Irradiated Sucrose)
106. Kusakovskij J (2013). Exploring the possibilities of EPR methods for identifying radiation damage to solids: application to sucrose and silicon. Master thesis, Vilnius University [in Lithuanian]
107. Box HC, Budzinski EE (1983) A variation of the alkoxy radical. *J Chem Phys* 79:4142–4145

108. Budzinski EE, Potter WR, Potienko G, Box HC (1979) Characteristics of trapped electrons and electron traps in single crystals. *J Chem Phys* 70:5040–5044
109. Box HC, Budzinski EE, Freund HG (1990) Studies of electrons trapped in X-irradiated rhamnose crystals. *J Chem Phys* 93:262–266
110. Kevan L, Schlick S, Narayana PA, Feng DF (1981) Application of the semicontinuum potential model to deduce localized electron trapping sites in single crystals of D-sorbitol. *J Chem Phys* 75:1980–1983
111. Samskog PO, Kispert LD, Lund A (1983) Geometric model of trapped electrons in trehalose single crystals X ray irradiated at 3 K. An EPR study. *J Chem Phys* 78:5790–5794
112. Samskog PO, Kispert LD, Lund A (1983) Geometric model of trapped electrons in X-ray-irradiated single-crystals of rhamnose. *J Chem Phys* 79:635–638
113. Ueda H (1963) Electron spin resonance studies of irradiated single crystals of sugars. *J Phys Chem* 67:2185–2190
114. Moens P, Devolder P, Hoogewijs R, Callens F, Verbeeck R (1993) Maximum-likelihood common-factor analysis as a powerful tool in decomposing multicomponent EPR powder spectra. *J Magn Reson Ser A* 101:1–15
115. Bungum B (1992) Radiation-induced radicals in glucose-1-phosphate studied with ESR and ENDOR techniques. Master thesis, University of Oslo (in Norwegian)
116. De Cooman H, Vanhaelewyn G, Pauwels E, Sagstuen E, Waroquier M, Callens F (2008) Radiation-induced radicals in glucose-1-phosphate. I. Electron paramagnetic resonance and electron nuclear double resonance analysis of in situ X-irradiated single crystals at 77 K. *J Phys Chem B* 112:15045–15053
117. Narendra N, Visvamitra MA (1984) Structure of the dipotassium glucose 1-phosphate dihydrate $C_6H_{11}O_9P^{2-} \cdot 2K^+ \cdot 2H_2O$. *Curr Sci* 53:1018–1020
118. Bungum B, Hole EO, Sagstuen E, Lindgren M (1994) Electron-paramagnetic-resonance of X-irradiated sodium and potassium-salts of glucose-1-phosphate-identification of PO_3^{2-} radicals at room-temperature. *Radiat Res* 139:194–202
119. Sanderud A, Sagstuen E (1996) EPR study of X-irradiated hydroxyalkyl phosphate esters-phosphate radical formation in polycrystalline glucose phosphate, ribose phosphate and glycerol phosphate salts at 77 and 295 K. *J Chem Soc Faraday Trans* 92:995–999
120. Samskog PO, Kispert LD, Lund A (1982) An electron-spin-resonance study of 77 K alkoxo and hydroxyalkyl radicals in X-ray-irradiated trehalose single-crystals. *J Chem Phys* 77:2330–2335
121. Ueda H (1963) Electron spin resonance studies of irradiated single crystals of D-fructose and L-sorbose. *J Phys Chem* 67:966–968
122. Vanhaelewyn G, Lahorte P, De Proft F, Mondelaers W, Geerlings P, Callens F (2001) Electron magnetic resonance study of stable radicals in irradiated D-fructose single crystals. *Phys Chem Chem Phys* 3:1729–1735
123. Vanhaelewyn GCAM, Jansen B, Callens FJ, Sagstuen E (2004) ENDOR-assisted study of the stable EPR spectrum of X-irradiated α ; -L-sorbose single crystals: MLCFA and simulation decomposition analyses. *Radiat Res* 162:96–104
124. Jansen B (1992) Radiation induced radicals in single crystals of α ; -L-sorbose. ESR-, ENDOR, and pulse radiolysis studies at room temperature. Master thesis, University of Oslo [in Norwegian]
125. von Sonntag C (1987) The chemical basis of radiation biology. Taylor & Francis, London
126. Chatgililogly C (2009) Reactivity of nucleic acid sugar radicals. In: Greenberg MM (ed) *Radical and radical ion reactivity in nucleic acid chemistry*. Chapter 4. Wiley, New York
127. Pauwels E, De Cooman H, Waroquier M, Hole EO, Sagstuen E (2014) Solved? The reductive radiation chemistry of alanine. *Phys Chem Chem Phys* 16:2475–2481
128. Sagstuen E, Hole EO, Sanderud A (2004) The solid state radiation chemistry of simple amino acids, revisited. *Radiat Res* 162:112–119
129. Bernhard WA (2009) Radical reaction pathways initiated by direct energy deposition in DNA by ionizing radiation. In: Greenberg MM (ed) *Radical and radical ion reactivity in nucleic acid chemistry*. Chapter 2. Wiley, New York

130. Bernhard WA, Close DM (2004) DNA damage dictates the biological consequences of ionizing radiation: the chemical pathways. In: Mozumder A, Hatano Y (eds) *Charged particle and photon interactions with matter*. Chapter 15. Marcel Dekker, New York
131. Attix FH (1986) *Introduction to radiological physics and radiation dosimetry*. Wiley, New York
132. Sanche L (2009) Low-energy electron interaction with DNA: bond dissociations and formation of transient anion, radicals and radical ions. In: Greenberg MM (ed) *Radical and radical ion reactivity in nucleic acid chemistry*. Chapter 8. Wiley, New York
133. Bass AD, Sanche L (2004) Interactions of Low Energy Electrons with Atomic and Molecular Solids. In: Mozumder A, Hatano Y (eds) *Charged particle and photon interactions with matter*. Chapter 9. Marcel Dekker, New York
134. Lund A, Schlick S (1989) Trapped electrons in crystalline media. *Res Chem Intermed* 11:37–66
135. Debije MG, Milano MT, Bernhard WA (1999) DNA responds to ionizing radiation as an insulator, not as a ‘Molecular Wire’. *Angew Chem Int Ed* 38:2752–2756
136. Krivokapic A, Herak JN, Sagstuen E (2008) Proton-coupled hole transfer in X-irradiated doped crystalline cytosine.H₂O. *J Phys Chem A* 112:3597–3606
137. Löfroth G, Gejvall T (1974) Radiation induced effects on exchangeable hydrogens in crystalline solids. *Acta Chem Scand B* 28:777–780
138. Hart EJ, Anbar M (1970) *The hydrated electron*. Wiley, New York
139. Kuper GC, Whitfield GD (1963) *Polarons and excitons*. Oliver and Boyd, Edinburgh
140. Sagstuen E, Lindgren M, Lund A (1991) Electron trapping and reactions in rhamnose by ESR and ENDOR. *Radiat Res* 128:235–242
141. Steenken S (1989) Purine bases, nucleosides, and nucleotides: aqueous solution redox chemistry and transformation reactions of their radical cations and e⁻ and OH adducts. *Chem Rev* 89:503–520
142. Grigoriev EI, Trakhtenberg LI (1996) *Radiation chemical processes in solid phase-theory and applications*. CRC, Boca Raton
143. Madden KP, Bernhard WA (1980) A 1,2 hydrogen shift and other thermally induced free radical reactions in X-irradiated methyl-alpha-d-glucopyranoside single crystals. An ESR-ENDOR study. *J Phys Chem* 84:1712–1717
144. Box HC, Budzinski EE, Freund HG (1984) The gamut of alkoxy radicals. *J Chem Phys* 81:4898–4900
145. Aalbergsjø SG, Pauwels E, Van Yperen-De Deyne A, Van Speybroeck V, Sagstuen E (2014) Automated generation of radical species in crystalline carbohydrate using ab initio MD simulations. *Phys Chem Chem Phys* 16:17196–17205

Chapter 7

EPR on Radiation-Induced Defects in SiO₂

Antonino Alessi, Simonpietro Agnello, Gianpiero Buscarino,
Yuanming Pan and Rudolf I. Mashkovtsev

Abstract Continuous-wave electron paramagnetic resonance (EPR) spectroscopy has been the technique of choice for the studies of radiation-induced defects in silica (SiO₂) for 60 years, and has recently been expanded to include more sophisticated techniques such as high-frequency EPR, pulse electron nuclear double resonance (ENDOR), and pulse electron spin echo envelope modulation (ESEEM) spectroscopy. Structural models of radiation-induced defects obtained from single-crystal EPR analyses of crystalline SiO₂ (α -quartz) are often applicable to their respective analogues in amorphous silica (a-SiO₂), although significant differences are common.

7.1 Introduction

Electron paramagnetic resonance (EPR) spectroscopic studies of radiation-induced defects in quartz and a-SiO₂ dated back to the early 1950s [1–2] and has been continued today, including the use of related but more sophisticated techniques such

Antonino Alessi, Yuanming Pan Principal Investigators

A. Alessi (✉) · S. Agnello · G. Buscarino
Department of Physics and Chemistry, University of Palermo,
Via Archirafi 36, 90123 Palermo, Italy
e-mail: antonino.alessi@unipa.it

S. Agnello
e-mail: simonpietro.agnello@unipa.it

G. Buscarino
e-mail: gianpiero.buscarino@unipa.it

Y. Pan (✉)
Department of Geological Sciences, University of Saskatchewan,
Saskatoon, SK S7N 5E2, Canada
e-mail: yuanming.pan@usask.ca

R. I. Mashkovtsev
V.S. Sobolev Institute of Geology and Mineralogy,
SB RAS, 630090 Novosibirsk, Russia
e-mail: rim@igm.nsc.ru

© Springer International Publishing 2014

A. Lund, M. Shiotani (eds.), *Applications of EPR in Radiation Research*,
DOI 10.1007/978-3-319-09216-4_7

as pulse electron nuclear double resonance spectroscopy (ENDOR) and electron spin echo-envelope modulation spectroscopy (ESEEM) [3–5]. EPR remains a fundamental technique for the studies of radiation-induced defects in SiO_2 , because they are usually too dilute to be investigated by other structural techniques. For example, EPR techniques with superior sensitivities coupled with the fact that quartz is one of the best diamagnetic hosts, resulting in usually very narrow resonance lines (i.e., $< \sim 0.02$ mT), make possible of detailed studies of dilute defects, including common identification and characterization of more distant nuclei on the basis of well-resolved superhyperfine structures [6–9]. Other principal motivations include the fact that paramagnetic defects in SiO_2 are known to profoundly impact on the application and performance of this important material for high-tech electronics, fiber optics, solar energy and quantum computers [10]. Also, radiation-induced defects in quartz have long been shown to be useful as dosimeters and geochronometers with diverse applications from the dating of archeological and anthropological artifacts to tracing dust provenance, dating of seismic activities, and mineral exploration [11–18].

Radiation-induced defects in SiO_2 can be classified into two broad types: (1) intrinsic and (2) extrinsic. The former involves the trapping of an unpaired spin(s) related to oxygen or silicon vacancies, whereas the latter are those derived from diamagnetic impurities that trap an unpaired spin(s) during artificial or natural irradiation. Structural models and dynamic properties of defects in quartz determined from the single-crystal EPR techniques often serve as the prototypes or test cases for analogous defects in $\alpha\text{-SiO}_2$ and other materials (e.g. nanoparticles, gel, thin films, etc.). This chapter starts with a section on recent progresses made on selected radiation-induced defects in quartz by using the single-crystal EPR techniques written by Y. Pan and R. Mashkovtsev and continues with a detailed synthesis on defects in silica redacted by A. Alessi, S. Agnello and G. Buscarino.

7.2 Radiation-Induced Defects in Quartz

Single-crystal EPR studies of radiation-induced defects in crystalline SiO_2 are not restricted to α -quartz but have recently been extended to the high pressure polymorph stishovite [19, 20].

7.2.1 *Coordinate System for Reporting EPR Data of Quartz*

Single-crystal EPR studies of radiation-induced defects in quartz are possible owing to the readily available high-quality crystals of this material both in nature and from laboratory syntheses. Single-crystal EPR studies are often preferred over powder experiments, because they provide information about the orientations of the spin Hamiltonian parameters (e.g., principal-axes directions) of defects. These principal-axes directions are not only useful for placing the defects in the quartz structure but also locating the neighboring nuclei when superhyperfine structures are resolved and determined. However, the confusing history in the description of

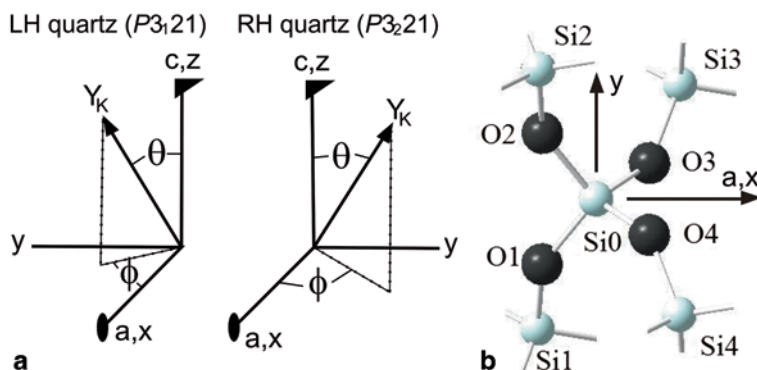


Fig. 7.1 **a** Coordinate systems for *left-handed* and *right-handed* quartz after [23], and **b** projection of *right-handed* quartz structure perpendicular to the crystallographic *c* axis (i.e., the experimental *z* axis) showing a unit of SiO₄ and its neighboring Si atoms

the quartz structure [21, 22] has been a significant obstacle in the communication of experimental data, including EPR results. Following Heaney [22], morphologically left-handed (LH) quartz has space group $P3_121$, and right-handed (RH) quartz belongs to space group $P3_221$. Feigl and Anderson [23] advocated a unified coordinate system for reporting single-crystal EPR data of quartz (Fig. 7.1a).

In this age of computer programs that often use a default RH coordinate system, however, the principal-axis directions determined from LH crystals are best converted to those in the RH coordinate system, provided that the choice of the coordinate system is clearly stated. Conversions can be done by (1) changing θ to $180^\circ - \theta$, if ϕ is kept the same and (2) reversing the sign of ϕ , if θ is fixed.

Therefore, any single-crystal EPR study of quartz must start with determinations of (1) crystal handedness and (2) the polarity of one two-fold symmetry axis. The handedness of quartz crystals can be determined by either morphologies or optical observations, while other techniques such as X-ray diffraction [24–26] have also been shown to be useful. The signs of the two-fold symmetry axes are usually determined by the piezoelectric effects. An alternative approach that has been proven to be successful in the authors' labs is the use of the crystal orientation and coordinate system determined from the spectra of the E'_1 center with its well-established spin Hamiltonian parameters from Jani et al. [27]. The common presence of the E'_1 center makes this approach applicable to most quartz crystals, irrespective of natural or synthetic varieties. One additional complication in EPR measurements of quartz is that crystals are often twinned, resulting in doubling of resonant signals that can be analyzed by using the effective rotation group D_6 [28].

7.2.2 Intrinsic Oxygen-Vacancy Electron Centers in Quartz

The most common radiation-induced defects in natural and synthetic quartz are those associated with oxygen vacancies (i.e., the so-called E defects that are commonly divided into E' and E'' to denote the presence of one and two trapped

electrons, respectively [29–31]). Following the nomenclature of Weeks and Nelson [30], the various E' centers are designated as E'_i with a subscript number ($i=1$ to 10) to indicate different electron trapping [9, 27, 32–35]. The E'_1 center, which is the most common defect in quartz and has close analogs in other SiO_2 -based materials, has been the subject of numerous experimental and theoretical studies [36] and has recently seen significant progresses towards the most complete spin Hamilton parameters [37]. The E'_2 center, which is one of the first radiation-induced defects discovered in quartz [30, 31], was studied in detail only recently [5, 34].

Only the g anisotropy and a spectrum measured at the applied magnetic field direction parallel to the crystallographic c -axis (\mathbf{B}/\mathbf{c}) are available for the E'_3 and E'_5 centers, respectively [5, 32, 34]. The E'_4 center, which is one of the best known defects and is characterized by four lines of similar intensities and two strong ^{29}Si couplings in X-band EPR spectra, has been proposed to represent electron trapping on two Si atoms next to an oxygen vacancy and having one hydrogen atom bonding weakly to one Si and residing close to the oxygen vacancy [33]. Mashkovtsev and Pan [9] noted that the previously proposed E'_{6-8} centers arise from the hyperfine lines of the E'_7 triplet center. The E'_9 center observed in fast-electron-irradiated quartz [35] is known to convert to the E'_{10} center after annealing at 210 °C for 5 min. Mashkovtsev and Pan [9], on the basis of DFT theoretical results [38], raised the possibility that the E'_{10} center may represent the less stable state of E'_1 .

The E'_1 Centers Silsbee [39] made the first detailed angular dependence study of the E'_1 center by measuring single-crystal EPR spectra of a fast-neutron-irradiated LH quartz, and reported its g matrix and three ^{29}Si (one strong and two weak) hyperfine couplings. Jani et al. [27] performed a detailed EPR study on the formation and thermal decay properties of the E'_1 center created by fast electron irradiation and re-determined its spin Hamiltonian parameters in a RH crystal, including high-precision data for the two weak ^{29}Si hyperfine couplings determined by the ENDOR technique. Jani et al. [27] did not compare their principal-axes directions with those reported by Silsbee [39], citing a lack of knowledge about the coordinate system and the $+x$ -axis choice in the latter. Table 7.1 shows the principal-axes directions of the E'_1 center in LH quartz [39], after transforming to one of the six symmetrically related sites $[(\theta, \phi), (\theta, \phi \pm 120^\circ), (180^\circ - \theta, -\phi), (180^\circ - \theta, -\phi \pm 120^\circ)]$, can be compared with those determined from RH crystals [27].

These EPR data for the E'_1 center have led to lengthy discussions and debates about its structural model. The substantial spin density observed in one Si sp^3 non-bonding orbital is not in accord with the presence of a single oxygen vacancy. An agreement with the experimental result is possible provided a sufficiently large asymmetric relaxation of the two Si atoms facing the vacancy is involved. In quartz, the asymmetry for a positively charged oxygen vacancy, $V(\text{O})^+$, was originally proposed and supported with semi-empirical calculations by Feigl et al. [40].

Further theoretical efforts have improved this assumption [41–43]. The positive charge state yields a minimum energy configuration with a large relaxation of Si1 on the long-bond side of the vacancy (Fig. 7.1b). This silicon is thought to move through its basal oxygen plane to form a puckered configuration and to bond with an oxygen atom, making that O atom threefold coordinated, and the spin is

Table 7.1 Spin Hamiltonian parameters of the E'_1 center in quartz

Parameters		LH quartz [39]			RH quartz [27]		
Y		Y_k	θ_k (°)	ϕ_k (°)	Y_k	θ_k (°)	ϕ_k (°)
	g_1	2.00176	66	230	2.00179	114.5	227.7
g	g_2	2.00049	52	339	2.00053	134.5	344.4
	g_3	2.00029	45	114	2.00030	125.4	118.7
²⁹ Si0	$A_1/g_e\beta_e$	45.3	67	230	-45.32	114.1	229.7
$A/g_e\beta_e$	$A_2/g_e\beta_e$	38.9			-39.08	128.3	340.4
(mT)	$A_3/g_e\beta_e$	38.9			-39.07	132.1	115.9
²⁹ Si1	$A_1/g_e\beta_e$	0.979	39	286	-0.983	140.7	284.5
$A/g_e\beta_e$	$A_2/g_e\beta_e$	0.785			-0.795	125.5	133.9
(mT)	$A_3/g_e\beta_e$	0.785			-0.790	104.6	33.1
²⁹ Si2	$A_1/g_e\beta_e$	0.921	125	263	-0.928	58.9	260.9
$A/g_e\beta_e$	$A_2/g_e\beta_e$	0.737			-0.751	104.4	179.9
(mT)	$A_3/g_e\beta_e$	0.737			-0.746	35	111.4

localized on the other silicon Si0, moved towards the oxygen vacancy (e.g., O1 in Fig. 7.1b). The puckered configuration was adopted and supported by several subsequent studies using larger clusters [43], including the embedded-cluster treatment [44]. Several calculations [45–47] yielded accurate theoretical estimates of the ²⁹Si hyperfine coupling parameters for E'_1 in quartz [27] and the equivalent center E'_γ in vitreous silica.

Li and Pan [48] conducted first-principles calculations for the E'_1 center in quartz by using the supercell approach with Gaussian-type all-electron basis sets and hybrid functionals as implemented in the *ab initio* code CRYSTAL06/09. Their calculations featured both the traditional single-oxygen-vacancy model and a new tri-vacancy with an Al impurity model with one silicon and two oxygen vacancies. The latter model was motivated by the close association between the E'_1 center and the aluminum-associated oxygen hole center $[AlO_4]^0$ [27, 49, 50]. Their calculated hyperfine coupling constants for the strong and two weak ²⁹Si hyperfine structures from the new tri-vacancy model are all within 5% of the experimental values, and the calculated directions of the principal hyperfine axes are in agreement with the experimental results as well. Moreover, the tri-vacancy with an Al impurity model can account for the common association of the E'_1 center with the $[AlO_4]^0$ center and superoxide O_2^- radicals in quartz.

The debates about the structural model for the E'_1 center in quartz (and its analogous defects in other silica-based materials as well) arised largely from incomplete spin Hamiltonian parameters from previous single-crystal EPR studies [27, 39]. In particular, ¹⁷O hyperfine couplings, which would provide definitive information about the number and geometry of the nearest-neighbor oxygen atoms, were not detected owing to the exceedingly low abundance of this nucleus (nuclear spin $I=5/2$ and natural isotope abundance=0.038%). This deficiency in previous EPR studies has recently been overcome by the detection of ¹⁷O hyperfine splittings arising from

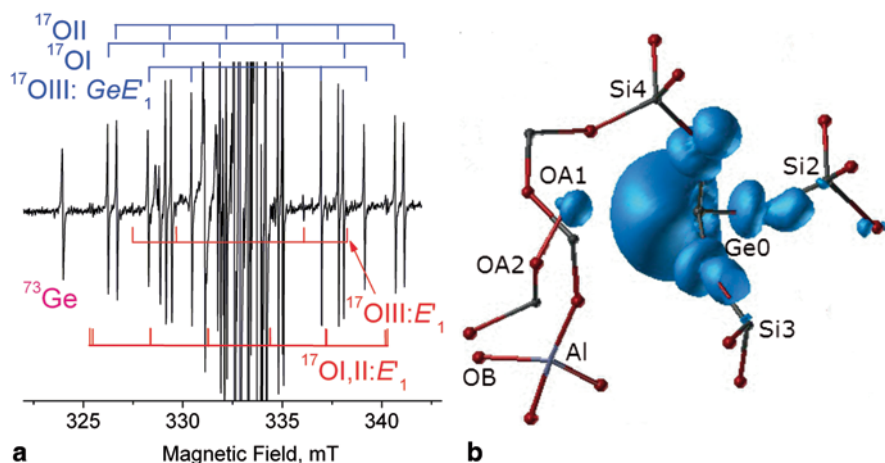


Fig. 7.2 **a** X-band single-crystal EPR spectrum of ^{17}O -enriched quartz (JC324) at \mathbf{B}/\mathbf{c} , illustrating three ^{17}O hyperfine hexets and one ^{73}Ge hyperfine line of the $\text{Ge } E'_1$ center. Also marked are three ^{17}O hyperfine hexets of the E'_1 center; and **b** 3D spin density of the $\text{Ge } E'_1$ center calculated from the $V(\text{SiO}_2)^{\text{Al}}$ model. The figure is modified from [37] by permission of Academic Press (2013)

three nonequivalent oxygen nuclei of the E'_1 center (Fig. 7.2a) and quantitative analysis of ^{17}O hyperfine couplings arising from three nonequivalent oxygen nuclei of the $\text{Ge } E'_1$ center in an ^{17}O -enriched crystal [37].

Feigl and Anderson [23] first reported two E'_1 -type centers with the unpaired electron trapped largely on a substitutional Ge atom at the Si site in Ge doped LH quartz after X-ray irradiation. These two E'_1 -type centers, originally denoted as $[\text{Ge}(\text{III})e^-]$ and $[\text{Ge}(\text{IV})e^-]$, are both produced by X-ray irradiation at room temperature but have contrasting thermal stabilities. The former is stable above 600 K and is bleached out completely after annealing at 700 K, whereas the latter is not stable at room temperature and bleaches out after annealing at 400 K. Feigl and Anderson [23] suggested that the $[\text{Ge}(\text{III})e^-]$ center is the Ge analog of the E'_1 center ($\text{Ge } E'_1$; Table 7.2). The $[\text{Ge}(\text{IV})e^-]$ center is closely comparable to the E'_{10} center (Table 7.3) and may also represent the less stable state of the $\text{Ge } E'_1$ center.

Mashkovtsev et al. [37] re-investigated the $\text{Ge } E'_1$ center in two Ge doped RH quartz crystals, including one (JC324) enriched at 4.4 at% ^{17}O [51–53]. The EPR spectra of these crystals after fast electron irradiation, even at the canonical orientation \mathbf{B}/\mathbf{c} , are complex with the presence of not only the $\text{Ge } E'_1$ and E'_1 centers but also several hole type radicals [3, 15, 28, 54, 55]. With knowledge about the thermal properties of the $\text{Ge } E'_1$ and E'_1 centers as well as the hole type radicals [56], annealing of the quartz crystals up to 573 K led to enhanced intensities of the former but bleaching of the latter (Fig. 7.2a). The intensity ratio of the $\text{Ge } E'_1$ and E'_1 centers in JC324 annealed to 573 K is ~ 8 , with an estimated concentration of the former at $\sim 3 \times 10^{17} \text{ cm}^{-3}$. Figure 7.2a shows that the $\text{Ge } E'_1$ center is characterized by three sets of six approximately equal intensity lines, which are attributable to ^{17}O hyperfine structures arising from interactions with three nonequivalent oxygen nuclei.

Table 7.2 Spin Hamiltonian parameters of the Ge E'₁ center in quartz

Parameters		LH quartz [23]			RH quartz [37]		
Y		Y _k	θ _k (°)	φ _k (°)	Y _k	θ _k (°)	φ _k (°)
	g ₁	2.0011	113	50	2.00111	66.8	51.0
g	g ₂	1.9950	52	340	1.99501	129.7	341.8
	g ₃	1.9939	47	116	1.99399	131.3	118.8
⁷³ Ge	A ₁ /g _e β _e				-22.293	132	119
A/g _e β _e	A ₂ /g _e β _e				-22.337	129	341
(mT)	A ₃ /g _e β _e				-25.214	67.55	50.81
²⁹ Si1	A ₁ /g _e β _e	0.818			-0.829	34	125
A/g _e β _e	A ₂ /g _e β _e	0.818			-0.851	70	2
(mT)	A ₃ /g _e β _e	1.054	66	83	-1.057	115.9	81.3
²⁹ Si2	A ₁ /g _e β _e	0.750			-0.755	63	239
A/g _e β _e	A ₂ /g _e β _e	0.750			-0.768	108	159
(mT)	A ₃ /g _e β _e	0.979	146	97	-0.987	33.3	98
¹⁷ OI	A ₁ /g _e β _e				-2.8963	13.7	61
A/g _e β _e	A ₂ /g _e β _e				-2.9129	96	124
(mT)	A ₃ /g _e β _e				-4.1894	77.89	212.59
¹⁷ OII	A ₁ /g _e β _e				-2.6517	90	1
A/g _e β _e	A ₂ /g _e β _e				-2.6619	17.6	272
(mT)	A ₃ /g _e β _e				-3.8068	72.42	90.67
¹⁷ OIII	A ₁ /g _e β _e				-0.932	84	285
A/g _e β _e	A ₂ /g _e β _e				-0.968	44.1	189
(mT)	A ₃ /g _e β _e				-2.979	133.50	200.84

Table 7.3 Spin Hamiltonian parameters of the [Ge(IV)e⁻] and E'₁₀ centers in quartz

Parameters		[Ge(IV)e ⁻] in LH quartz [23]			E' ₁₀ in RH quartz [9]		
Y		Y _k	θ _k (°)	φ _k (°)	Y _k	θ _k (°)	φ _k (°)
	g ₁	2.0010	114	49	2.00169	64.3	46.9
g	g ₂	1.9942	53	339	2.00041	142	335
	g ₃	1.9935	47	114	2.00021	116	124
⁷³ Ge/ ²⁹ Si	A ₁ /g _e β _e	25.78			-40.931	48	163
A/g _e β _e	A ₂ /g _e β _e	25.78			-40.910	52	298
(mT)	A ₃ /g _e β _e	28.67	113	50	-47.289	65.66	48.82
²⁹ Si1	A ₁ /g _e β _e	0.808					
A/g _e β _e	A ₂ /g _e β _e	0.808					
(mT)	A ₃ /g _e β _e	1.028	67	85			
²⁹ Si2	A ₁ /g _e β _e	0.878					
A/g _e β _e	A ₂ /g _e β _e	0.878					
(mT)	A ₃ /g _e β _e	1.132	146	96			

Two pairs of the weak ^{29}Si superhyperfine lines with $A_c = 0.91$ and 0.86 mT and another pair with a very small and isotropic ^{29}Si superhyperfine splitting of 0.15 mT are clearly observable in the spectra of the other quartz crystal without artificial ^{17}O enrichment (JC206), especially after annealing to 573 K.

Analyses of the single-crystal EPR spectra measured on JC206 and JC324 have resulted in the most complete set of spin Hamiltonian matrices, including \mathbf{g} , $\mathbf{A}(^{73}\text{Ge})$, $\mathbf{P}(^{73}\text{Ge})$, three $\mathbf{A}(^{17}\text{O})$, and two $\mathbf{A}(^{29}\text{Si})$, for the Ge E'_1 center [37]. Table 7.2 shows the spin Hamiltonian parameters determined from these RH crystals are directly (i.e., with conversions) comparable to those for the LH quartz [23].

These spin Hamiltonian parameters, particularly the three distinct matrices $\mathbf{A}(^{17}\text{O})$, not only confirm the Ge E'_1 center to represent spin trapping on a substitutional Ge atom coordinated to three nonequivalent nearest-neighbor O atoms (i.e., the $\bullet\text{Ge}=\text{O}$ moiety involving an oxygen vacancy) and two next-nearest-neighbor Si atoms but also permit determination of the spin population on all of these atoms. Periodic DFT calculations using the popular $V(\text{O})^+$ model, even with the puckered configuration, cannot account for experimental $\mathbf{A}(^{17}\text{O})$ arising from three nonequivalent O atoms. Recent calculations showed that the tri-vacancy with an Al impurity model $V(\text{SiO}_2)^{\text{Al}}$ [37] can reproduce the spin population determined from EPR experiments (Fig. 7.2b) and match experimental hyperfine matrices. Moreover, the $V(\text{SiO}_2)^{\text{Al}}$ model could explain the common associations of the E'_1 centers with both Al related defects and superoxide/peroxy radicals in quartz [37].

The E'_2 Centers The preliminary EPR spectra of the E'_2 center in gamma-ray irradiated quartz had long been known [29–31]. Feigl and Anderson [23] reported the Ge analogue of the E'_2 center (i.e., Ge E'_2) in Ge doped LH quartz after X-ray irradiation at room temperature and determined the spin Hamiltonian parameter matrices \mathbf{g} and $\mathbf{A}(^1\text{H})$ for both the E'_2 and Ge E'_2 centers (Table 7.4). Here, the spin Hamiltonian parameters of the E'_2 center [23] were recalculated from Weeks' [31] spectra, who did not determine the handedness of the crystals investigated. Perlson and Weil [34] re-determined the spin Hamiltonian parameters, including the strong $\mathbf{A}(^{29}\text{Si})$ hyperfine coupling, of the E'_2 center in one of Weeks' [31] crystals after X-ray and gamma-ray irradiations and showed that crystal to be right handed (Table 7.4).

In addition to the previously reported E'_2 center, Perlson and Weil [34] found and characterized a new variant of this defect and re-labeled them as $E'_2(\text{I})$ and $E'_2(\text{II})$ (Table 7.4). The $E'_2(\text{II})$ center is unstable at room temperature and decays by first-order kinetics with a half-life of ~ 4.2 h to $E'_2(\text{I})$. By analogy with the E'_1 centers, it is tempting to postulate that the $E'_2(\text{I})$ and $E'_2(\text{II})$ centers may also represent a similar defect at the ground and excited states, respectively.

The E'_2 centers have been interpreted to arise from attack on a diamagnetic oxygen vacancy by an electron and a proton during the irradiation process. Perlson and Weil [34] noted that the concentration of E'_2 rapidly reaches a maximum with dose, suggesting its diamagnetic precursor to have a limited concentration in quartz. Perlson and Weil [34] also noted that E'_2 is rapidly bleached out at room temperature when exposed to ultraviolet light, which is accompanied by an increase in the intensity of the E'_1 center and the formation of other uncharacterized paramagnetic

Table 7.4 Spin Hamiltonian parameters of the E'_2 centers in quartz

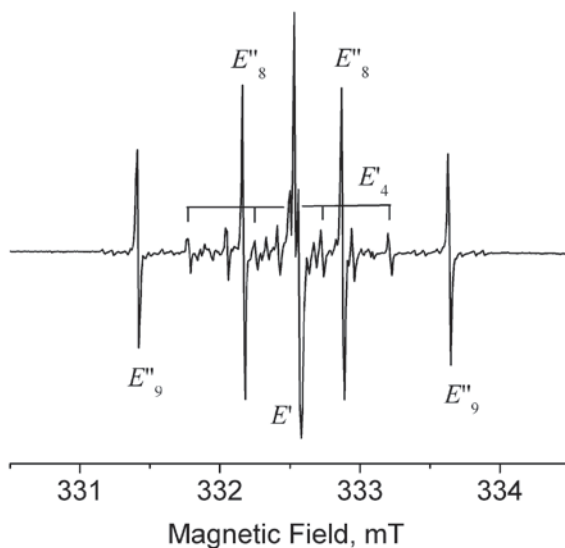
Parameters							
Y		Y_k	θ_k (°)	ϕ_k (°)	Y_k	θ_k (°)	ϕ_k (°)
		E'_2 in quartz [23]			Ge E'_2 in LH quartz [23]		
	g_1	2.0020	120	208	2.0009	131	208
g	g_2	2.0007	67	133	1.9952	49	167
	g_3	2.0005	39	253	1.9943	68	277
⁷³ Ge/ ²⁹ Si	$A_1/g_e\beta_e$	Only c-axis orientation data			Only c-axis orientation data		
$A/g_e\beta_e$	$A_2/g_e\beta_e$						
(mT)	$A_3/g_e\beta_e$						
¹ H	$A_1/g_e\beta_e$	0.17	126	215	0.114	130	203
$A/g_e\beta_e$	$A_2/g_e\beta_e$	-0.01	44	257	-0.036	57	145
(mT)	$A_3/g_e\beta_e$	-0.02	70	140	-0.062	57	260
		E'_2 (I) in RH quartz [34]			E'_2 (II) in RH quartz [34]		
	g_1	2.0020	120.1	206.4	2.00161	45.7	72.2
g	g_2	2.0007	67.2	132.5	2.00051	129.1	109.8
	g_3	2.0005	39.3	253.3	1.99994	109.8	2.7
²⁹ Si	$A_1/g_e\beta_e$	-45.857	121.2	267.7	-49.6016	48.8	70.7
$A/g_e\beta_e$	$A_2/g_e\beta_e$	-40.539	132.9	143.4	-43.3413	132.8	106.4
(mT)	$A_3/g_e\beta_e$	-40.490	121.1	19.1	-43.2862	71.2	178.1
¹ H	$A_1/g_e\beta_e$	0.16	125.7	214.9	0.0249	44.9	10.6
$A/g_e\beta_e$	$A_2/g_e\beta_e$	-0.01	43.2	254.7	-0.0096	83.2	107.5
(mT)	$A_3/g_e\beta_e$	-0.02	69.2	140.8	-0.0112	134.2	24.2

defects. The E'_2 center after the photo-bleaching treatment can be restored by X-ray irradiation. Perlson and Weil [34] interpreted the apparent transformation from E'_1 to E'_2 to either hydride-ion attack on the former or a process involving trapping of an electron and a proton in discrete steps.

Feng et al. [5] investigated the E'_2 (I) center in gamma-ray-irradiated RH quartz by using pulse ENDOR and determined its spin-lattice relaxation T_1 and transverse relaxation time T_2 from 20 K to room temperature. Their pulse ENDOR results showed that the E'_2 (I) center possesses a long T_2 of over 260 μ s at 60 K. This T_2 along with the well-separated energy levels arising from the proton-coupled electron-nuclear structure makes E'_2 (I) a potential candidate for quantum memory in quantum computing [5].

The E'' Centers Three oxygen-vacancy defects in triplet states (i.e., the E'' centers) have long been observed in irradiated quartz [32, 57, 58] but their spin Hamiltonian parameters have quantitatively been determined only recently [59–61]. After a synthetic quartz subjected to electron irradiation (3 MeV and a fluence of 10^{17} cm⁻²) at room temperature, the E''_{1-7} centers were observed. The intensities of the E''_{1-5} centers diminish but those of the $E''_{6,7}$ centers remain unchanged after the sample was kept at room temperature for about half year [59, 60]. Mashkovtsev and Pan [61]

Fig. 7.3 Single-crystal EPR spectrum of fast-electron-irradiated quartz (**B**//**c**) after annealing at 200 °C for 15 min, illustrating the $E''_{8,9}$ centers as well as the E'_4 center [61]



studied another piece of this crystal using isochronal annealing treatments (5 min each step) immediately after electron irradiation at room temperature. They noted that only the $E''_{6,7}$ centers remain after annealing at 100 °C, which are accompanied by a new E''_8 center. The $E''_{6,7}$ centers do not show any visible change in intensity after annealing at 120 °C but are both bleached out at 150 °C. The intensity of the E''_8 center is enhanced with annealing above 100 °C and reaches a maximum after annealing at 200 °C, when the E''_9 center also appears. The intensities of the $E''_{8,9}$ centers become comparable after annealing at 200 °C for 15 min (Fig. 7.3). Further annealing at 200 °C diminish the intensities of the $E''_{8,9}$ centers, which are bleached out after annealing at 220 °C for 15 min.

Mashkovtsev and Pan [61] noted that the $E'_{1,9}$ centers are also resolved in the electron irradiated quartz and both grew in intensity after annealing at 200 °C. After annealing at 210 °C for 5 min, the intensity of the E'_9 center diminished but that of the E'_1 center continued to grow. Also resolved after annealing at 210 °C for 5 min is the E'_{10} center [9], which remains stable after annealing to 300 °C for 15 min when the intensity of the E'_1 center reaches its maximum.

Among the nine observed E'' centers, E''_1 and E''_{7-9} have two $A(^{29}\text{Si})$ matrices each determined by using the triplet state model, but those of E''_3 were obtained from the biradical model (Table 7.5). The E''_1 and E''_9 centers with large D values have the ^{29}Si hyperfine values at approximately half of those of the E' centers; whereas the E''_3 , E''_7 and E''_8 centers with small D values have similar ^{29}Si hyperfine constants to the E' centers.

The biradical state ($S=1$) of two similar defects is characterized by one-half hyperfine value in comparison to the single defect state ($S=1/2$) when the exchange energy is far greater than the hyperfine constant [62]. Therefore, the $E''_{1,9}$ centers are two interacting E' defects forming biradicals with large exchange terms that

Table 7.5 Spin Hamiltonian parameters of the E'' centers in quartz [9]

g	D			²⁹ Si HF (1)			²⁹ Si HF (2)		
	mT	θ°	φ°	mT	θ°	φ°	mT	θ°	φ°
E''_1									
2.00156	8.13	56.1	63.5	22.64	62.3	86.1	21.99	119	215
2.00081	-3.93	145.8	55.9	19.49	114	163	18.76	32	241
2.00052	-4.19	86.5	331.1	19.48	142	38	18.75	79	132
E''_3									
2.00148	1.793	42	46	47.99	142	155	44.01	119	215
2.00069	-0.894	52	196	41.6	126	318	37.53	32	240
2.00066	-0.899	75	298	41.48	198	54	37.51	79	131
E''_7									
2.00151	0.794	48.5	58.28	45.35	61	87	43.88	120	215
2.00079	-0.394	48	200	39.12	30	283	37.48	86	303
2.00045	-0.399	70	310	39.08	97	1	37.41	150	26
E''_8									
2.00178	1.318	132.3	244.3	47.55	131	211	43.92	60	85
2.00097	-0.662	64	308	41.26	66	278	37.45	69	188
2.0006	-0.656	53	197	41.24	129	346	37.43	38	308
E''_9									
2.00189	2.664	136.1	239.2	24.04	131	210	23.97	65.4	71.5
2.00084	-1.325	99.8	339.5	20.95	100	309	20.84	112	151
2.00051	-1.339	132.2	78.5	20.93	137	51	20.82	34	204

cannot be determined directly from the EPR spectra [59]. With the increase of distance between interacting E' centers the exchange term decreases and becomes comparable with the strong ²⁹Si hyperfine values, resulting in hyperfine lines shift to the normal magnetic field positions (i.e. the splitting between the pair of lines at ~40 mT) of the usual E' centers [61]. It makes possible to determine the exchange terms by computer optimization. We note that one of the ²⁹Si hyperfine couplings of the E''_1 center matches closely in both principal values and the unique-axis direction to the E''_9 center. Similarly, these of the other ²⁹Si hyperfine couplings of the five E'' centers match reasonably well with those of the E''_1 , E''_9 or E''_{10} centers.

The E defects are induced with particles irradiation and associated with oxygen vacancies formed in the process of atom displacements. The neutral oxygen vacancy leaves two unpaired electrons on the Si dangling bonds. The model proposed for the E''_1 center consists of two Si atoms relaxed from the oxygen vacancy, resulting in a puckered configuration [59, 60]. The set of E'' centers is related to the biradicals formed by two interacting E' centers located at various distances from each other.

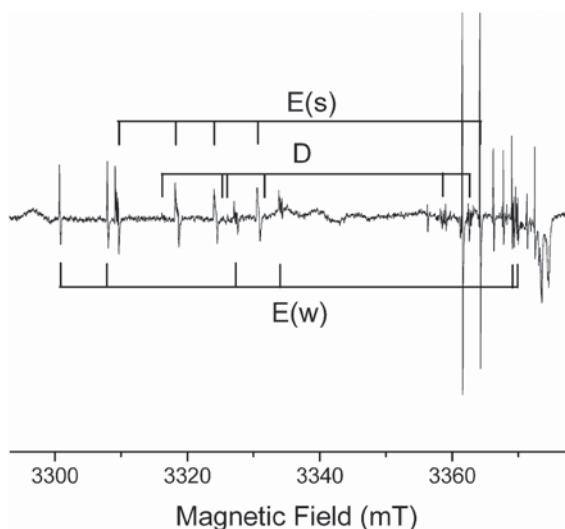
7.2.3 Intrinsic Silicon-Vacancy Hole Centers in Quartz

The removal of a Si atom in the quartz structure is expected to lead to hole trapping by two or three oxygen ions with the formation of various O_2^{3-} , superoxide (O_2^-), ozonide (O_3^-), and peroxide ($\equiv Si-O-O\bullet$, where \equiv denotes three Si-O bonds and \bullet represents an unpaired electron) radicals. However, previous studies of silicon-vacancy hole centers in quartz [63–65] were mired in experimental difficulties, including incompletely resolved magnetic site splittings and/or superhyperfine structures in X- and Q-band EPR spectra. Consequently, all proposed silicon-vacancy hole centers were poorly understood owing to (1) uncertainty in the localization of the unpaired electron and (2) misidentification or incomplete characterization of associated superhyperfine structures. Recently, single-crystal EPR at W-band frequencies and pulse ENDOR and ESEEM experiments together with first-principles theoretical calculations established a series of O_2^- , O_2^{3-} and O_3^- radicals in natural and artificially irradiated quartz (Table 7.6).

One example is provided by a group of defects with the g_{\max} values of ~ 2.050 , which showed considerable discrepancies in the literature. Mashkovtsev et al. [63] first reported such a center (denoted #4) in the X-band EPR spectra of electron- and neutron-irradiated natural quartz and interpreted its incompletely resolved multiplets as representing a hyperfine structure arising from interaction with either a 7Li or ^{23}Na nucleus. Maschmeyer and Lehmann [64], on the basis of a Q-band (~ 36 GHz) EPR study, distinguished two similar centers (D and E) and showed them each to possess a ^{27}Al hyperfine structure. Azzoni et al. [65] measured X-band EPR spectra of a neutron-irradiated synthetic quartz and recognized a center I with comparable principal g values but somewhat different g -axis directions to D and E. They also noted that the center I possessed an incompletely resolved ^{27}Al hyperfine structure. Pan et al. [28] noted that spectral simulations using any one, or combination, of these literature data did not reproduce the single-crystal EPR spectra of natural quartz from uranium deposits.

Single-crystal EPR spectra measured at W-band frequencies and 115 K (Fig. 7.4) revealed that the electron-irradiated RH quartz investigated in Mashkovtsev et al. [63] contains two sets of signals (with an intensity ratio of $\sim 6:1$) similar to the center E of Maschmeyer and Lehmann [64]. Fittings of spin Hamiltonian parameters and spectral simulations confirmed that the two sets belong to the same center related by a reflection, suggesting crystal twinning. Similarly, other centers such as #1, $[AlO_4]^0$ and E'_1 in this crystal also occur in pairs and can be analyzed by the effective rotation group D_6 , further supporting crystal twinning. The ^{27}Al hyperfine structure of the center E is highly anisotropic, with both well-resolved ^{27}Al hyperfine splittings up to 0.5 mT and singlets as narrow as 0.02 mT observed in the same spectra. The W-band spectra show that the narrowest peaks (i.e., those with almost zero ^{27}Al hyperfine splitting) of the center E are accompanied by well-resolved satellites with a total splitting of ~ 0.4 mT, which are attributable to a ^{29}Si superhyperfine structure arising from interaction with two equivalent or nearly equivalent Si atoms. The 115 K W-band spectra measured at one plane also resolve the presence of the center

Fig. 7.4 W-band single-crystal EPR spectrum of fast-electron-irradiated quartz measured at 115 K and ($\theta=68.9^\circ$, $\phi=326.1$), illustrating two sets (strong and weak) of the center E as well as the center D. The figure is modified from [28] by permission of Mineralogical Society (2009)



D [64], which has an intensity of only 1/10 of the center E. Therefore, the center #4 originally described from X-band spectra [63] is a mixture of two defects with similar g tensors. Also the center I described in Azzoni et al. [65] is probably a mixture of the centers D and E, because they occur together in both natural and synthetic quartz that we investigated [28].

The g_{\max} direction and value of the center I [65] are intermediate between those of the centers D and E, also suggesting that the former is a mixture of the latter two. The g tensors of the centers D and E reported by Maschmeyer and Lehmann [64] are closely comparable to those determined from the W-band spectra, except that the g_{\max} and g_{int} values of Maschmeyer and Lehmann [64] are too large, probably due to a lack of appropriate field calibration in their study. Spectral simulations showed that peak overlapping between the centers D and E is a significant problem in Q-band spectra, which may explain the large A_{\max} value of the ²⁷Al hyperfine structure of the center E in Maschmeyer and Lehmann [64]. The difference in the principal A -axes directions of the center D (e.g., the unique A axis differs by reflection) may be attributed to either incompletely resolved Q-band spectra or a typographic error. Therefore, the W-band spectra have not only removed the discrepancies in the literature but also improved substantially the spin Hamiltonian parameters of the centers D and E.

An isolated O₂⁻ is expected to have a degenerate $p\pi_g^*$ ground state, but this degeneracy can be lifted in a crystal field arising from surrounding ions. The g factor along the O–O bond (g_z) is inversely proportional to the crystal field splitting Δ that lifts the degeneracy of the two $p\pi_g^*$ orbitals [66]. Typical g_z values for O₂⁻ bound to a trivalent ion range from 2.036 to 2.044, whereas those to a tetravalent ion vary from 2.018 to 2.030 [67]. The g_{\max} values of Centers #1, B, B', D, E, G and G' in quartz are all in these ranges (Table 7.6).

Table 7.6 Spin Hamiltonian parameters of silicon-vacancy hole centers in quartz

Center	Electron Zeeman g			Hyperfine coupling constants				Ref.	Label
T (K)	g_k	θ (°)	ϕ (°)	nuclei	A_k (mT)	θ (°)	ϕ (°)		
#1 (O ₂ ⁻)	2.02945	26	266.2	²⁷ Al	0.024	79	352	[3]	H' ₁
110	2.00765	64	91.2		-0.025	63	87		
	2.00210	88	0.3		-0.027	29	242		
				²⁹ Si	0.432	73	261		
					0.457	69	358		
					0.460	27	136		
B (O ₂ ⁻)	2.03505	22.1	172.6	²⁷ Al	-0.222	65	156	[55]	H' ₂ (I)
298	2.00773	71.1	319.3		-0.292	42	36		
	2.00234	78.6	5.32		-0.30	58	263		
B' (O ₂ ⁻)	2.03555	22.5	165.5	²⁷ Al	-0.27	62	156	[55]	H' ₂ (II)
298	2.00771	69.5	319.5		-0.35	107	237		
	2.00231	80.9	52.9		-0.36	33	300		
D (O ₂ ⁻)	2.04953	73.6	248.9		-0.038	73	28	[28]	H' ₃ (I)
115	2.00701	50.1	353	²⁷ Al	-0.14	77	122		
	2.00206	44.4	141.5		-0.146	20	248		
E (O ₂ ⁻)	2.05175	76.4	244.1		-0.020	51	302	[28]	H' ₃ (II)
115	2.00682	51.7	345.1	²⁷ Al	-0.092	38	128		
	2.00213	41.5	138.2		-0.101	92	214		
G (O ₂ ⁻)	2.03079	46.3	1.5		-0.306	57	303	[54]	H' ₄ (I)
110	2.00816	84.2	266	²⁷ Al	-0.402	39	158		
	2.00226	44.2	170.1		-0.421	72	45		
G' (O ₂ ⁻)	2.02918	46.7	1.2		-0.41	54	309	[55]	H' ₄ (II)
110	2.00828	84.6	266.1	²⁷ Al	-0.51	39	159		
	2.00229	43.7	170.5		-0.54	74	50		
#6 (O ₂ ³⁻)	2.06807	57.6	276.7					[55]	H' ₅
77	2.00732	69.5	173.1						
	2.00187	39.7	56.5						
#7 (O ₂ ³⁻)	2.05960	76	278.9					[55]	H' ₆
77	2.00759	22.1	46.4						
	2.00179	73	184.6						
C (O ₃ ⁻)	2.0183	26.7	270		0.15	33	90	[64]	H' ₇ (I)
RT	2.0090	90	0	²⁷ Al	0.12				
	2.0033	63.3	90		0.12				
C' (O ₃ ⁻)	2.01698	30.7	274.9		-0.1	53	309	[55]	H' ₇ (II)
298	2.00823	75.2	158.6	²⁷ Al	-0.21	57	191		
	2.00248	63.7	61.1		-0.22	52	72		
X (O ₃ ⁻)	2.0177	39.6	269.8					[15]	H' ₇ (III)
RT	2.0076	89	0.4						
	2.0029	50.3	90.8						

All of these hole centers possess characteristic ²⁷Al hyperfine structures of various sizes (Table 7.6), resulting in broad line-widths or complex multiplets in powder EPR spectra. For example, the multiplet centered at $g \approx 2.034$ has a width of ~ 2.0 mT and is attributable to the ²⁷Al hyperfine structures of B and B' [55]. Among similar defects, Centers G and G' have the largest ²⁷Al hyperfine constants ($A/g\beta_e$) of ~ 0.4 and ~ 0.5 mT, respectively, hence well-resolved ²⁷Al hyperfine structures [54, 55]. Centers D and E have ²⁷Al hyperfine constants ($A/g\beta_e$) of ≤ 0.15 mT [28], responsible for a ~ 0.75 -mT-wide multiplet at $g \approx 2.049$. Center #1 has $A/g\beta_e \leq 0.015$ mT, hence a narrow peak at $g \approx 2.030$ [3].

The basic theory of the g factors for the O₂³⁻ centers predicts that g along the O–O direction is g_e and ($g_{\perp} - g_e$) is proportional to the ratio of the spin-orbital coupling for oxygen and the energy difference between the $p\pi_u$ and $p\sigma_u^*$ orbitals. Scaling the value of ($g_{\perp} - g_e$) observed for isostructural F₂⁻ by the ratio of the spin-orbital coupling from F to O yields $g_{\perp} \approx 2.014$ and $g_{\parallel} \approx g_e = 2.0023$ for the isolated O₂³⁻ center. The ordering of the g factors for O₂³⁻ is expected to be $g_x > g_y > g_z \approx g_e$, which is reversed in comparison with that for O₂⁻ ($g_z > g_y > g_x \approx g_e$). New spin Hamiltonian parameters determined from W-band spectra of a natural citrine [55], together with observed thermal properties and microwave power dependence, suggest that Centers #6 and #7 (Table 7.6) are probably the O₂³⁻ type [55]. However, the g_{\perp} values of Centers #6 and #7 (Table 7.6) are significantly higher than that predicted for the isolated O₂³⁻. Also, the O₂³⁻ centers are commonly stabilized by a neighboring trivalent cation [20, 68–70], whereas Centers #6 and #7 do not have any detectable ²⁷Al hyperfine structures. Therefore, the proposed structural models for Centers #6 and #7 remain tentative.

The basic model of the g factors for the ozonide radical predicts the g_{\min} axis perpendicular to the molecular plane and the g_{\max} along an O–O direction [71]. The W-band spectra of a natural citrine [55] reveal Center C', which has similar principal g values but a larger ²⁷Al superhyperfine structure in comparison with Center C [64]. The direction of the g_{\max} axis of center C' is only 5° away from the O3-O4 edge of the SiO₄ tetrahedron. The average g values of centers C and C' (Table 7.6) are similar to those of the classic ozonide radicals [71, 72]. The orientation of the unique A axis of center C' approximately along the Si4–Si0 direction suggests that C' is linked to a substitutional Al³⁺ ion at the neighboring Si4 site [55]. Another proposed ozonide radical [15] does not have any detectable ²⁷Al superhyperfine structure, suggesting no Al³⁺ at the immediate neighboring Si sites.

The previous usage of mixed labels for the silicon-vacancy hole centers (Table 7.6) is obviously not satisfactory. By analogy with Weeks and Nelson's [30] nomenclature, we herein propose a unified label (H'_i) for the silicon-vacancy hole centers, where H' denotes all these defects of the hole type with a single unpaired spin ($S = 1/2$) and the number in subscript ($i = 1$ to 7) is used to distinguish different centers. Similar to the E'_2 centers, it is advantageous to group similar centers together (e.g., H'_2 (I) and H'_2 (II) for B and B'). Hopefully, this new nomenclature will facilitate the communication of the silicon-vacancy hole centers in quartz.

7.2.4 Extrinsic Radiation-Induced Defects in Quartz

Extrinsic radiation-induced defects derived from diamagnetic impurities by trapping unpaired spin(s) include those associated with substitutional Al^{3+} , Ge^{4+} , Ti^{4+} , and P^{5+} at the Si site, with or without charge compensators such as H^+ , Li^+ , Na^+ and Ag^+ in the c-axis channels. Among them, several Al- and Ge-associated centers have been investigated by single-crystal EPR techniques to great details. In particular, their ^{17}O hyperfine structures arising from interaction with the nearest-neighbor oxygen atoms have been determined quantitatively from crystals containing either natural or artificially enriched ^{17}O abundances [51–53, 73–75].

For example, the well-established $[\text{AlO}_4]_0^0$ center has the nuclear hyperfine and nuclear quadruple parameters of the central ^{27}Al nucleus as well as those of one ^{17}O nucleus determined, where the ^{17}O hyperfine coupling constants were first determined from a crystal with natural isotope abundance and were confirmed by subsequent measurements on a ^{17}O -enriched crystal [73]. Similarly, several $[\text{AlO}_4/\text{Li}]^+$ centers have not only ^{27}Al and ^{17}O hyperfine coupling constants but also their ^7Li superhyperfine coupling constants quantitatively determined [53, 75]. These aluminum centers and their well determined EPR parameters including ^{17}O hyperfine matrices have stimulated theoretical works [76–79], resulting in excellent agreements between theory and experiments. Howarth et al. [53] noted that the EPR linewidths of the $[\text{AlO}_4/\text{Li}]^+$ center show little or no thermal broadening below 75 K and interpreted it to be dynamically inactive in that region. They also observed a marked increase in the individual peak-to-peak linewidth from 75 to 130 K, at which point the lines become too broad to measure adequately and possible loss of Li^+ to form the $[\text{AlO}_4]_0^0$ center as well. Fitting of the 100–130 K data yielded an average activation energy $E_a = 52$ meV, in comparison with the value of 70 ± 10 meV for the E'_1 center [80]. Another interesting aluminum-related defect in an X-ray irradiated quartz is the $[\text{AlO}_4]^+$ center [74], which is characterized by the presence of two unpaired electrons.

Similarly, irradiation of substitutional Ge^{4+} ions results in diverse paramagnetic Ge centers without or with compensating H^+ , Li^+ and Na^+ ions [6–9]. Among them, ^{17}O hyperfine coupling constants of two uncompensated $[\text{GeO}_4]_{\text{I,II}}^-$ and two compensated $[\text{GeO}_4/\text{Li}]_{\text{A,C}}^0$ have been determined from single-crystal EPR spectra of an isotopically enriched quartz crystal [51, 52]. These data demonstrated that the majority of the unpaired spin in these centers is localized in the $2p$ orbitals of only two of the four oxygen atoms. Also, the GeO_4 tetrahedron in $[\text{GeO}_4]_{\text{I}}^-$ and $[\text{GeO}_4/\text{Li}]_{\text{A}}^0$ is distorted to result in four symmetrically distinct oxygen atoms, whereas that in $[\text{GeO}_4]_{\text{II}}^-$ and $[\text{GeO}_4/\text{Li}]_{\text{C}}^0$ retains the local symmetry (C_2) and has only two types of oxygen atoms. These ^{17}O hyperfine coupling constants provide conclusive proof for an isomorphic relationship between $[\text{GeO}_4]_{\text{I}}^-$ and $[\text{GeO}_4/\text{Li}]_{\text{A}}^0$ and also between $[\text{GeO}_4]_{\text{II}}^-$ and $[\text{GeO}_4/\text{Li}]_{\text{C}}^0$. The compensated centers have essentially the same electronic structures as their respective uncompensated counterparts, with the charge compensator Li^+ causing only a minimal perturbation [52]. Interestingly, Griscom [81] suggested that the Ge(1) and Ge(2) centers in SiO_2 glass are two energetically inequivalent configurations of a single trapped-electron defect, similar to the $[\text{GeO}_4]_{\text{I,II}}^-$ centers in quartz.

Finally, the family of defects involving several small monovalent cations at the Si site can be classified as either the silicon-vacancy hole centers [9, 82, 83] or the extrinsic type. The best examples of this family include the two hydrogenic [H₄O₄]⁺ and [H₃O₄]⁰ centers involving four and three protons, respectively [82]. The [H₄O₄]⁺ center is most likely formed from the neutral diamagnetic “hydrogarnet” defect [H₄O₄]⁰ by the loss of an electron. Lees et al. [83] described a new hydrogarnet-like center [HLi₂O₄]⁰ in a gamma-ray-irradiated, synthetic quartz and suggested, on the basis of the principal directions of the **g** matrix, that hole trapping on the oxygen ion long-bonded to the missing silicon atom. Lees et al. [83] evaluated the locations of the three monovalent cations by modeling the experimentally determined proton and lithium superhyperfine matrices. Their results showed that the proton position can be assigned with reasonable confidence and is closely associated with O4, adjacent to the main c-axis channel, with an O–H bond distance of ~1 Å. However, the two lithium nuclei could not be assigned with as much confidence and are probably located roughly equidistant from two oxygen anions surrounding the silicon vacancy, close to the tetrahedral edges formed by the four oxygen anions. Lees et al. [83] recommended further evaluation of the electronic structures and magnetic properties of the [HLi₂O₄]⁰ center and other hydrogarnet-like paramagnetic defects in quartz by use of first-principles calculations.

7.3 Radiation-Induced Defects in Silica

The E'_γ center is the most commonly observed point defect induced in a-SiO₂ (amorphous silicon dioxide or silica) by UV, X, γ and neutrons irradiation. This defect was first observed by Weeks [2] and successively characterized by Griscom [84–88]. The E'_γ center exhibits an almost axially symmetric EPR line shape with principal **g** values $g_1 = 2.0018$, $g_2 = 2.0006$ and $g_3 = 2.0003$. In order to obtain a good fit of its EPR line shape a distribution of the latter two principal **g** values has to be considered in the simulated line [86]. A strong hyperfine structure, constituted by a pair of lines with splitting of ~42 mT and due to the interaction of the unpaired electron with a ²⁹Si nucleus, has been definitively attributed to the E'_γ center [84, 85]. In the 1978 [89], studying a γ-ray irradiated sample, Shendrik and Yudin found that a pair of lines split by 1.3 mT appeared together with the E'_γ signal, they also noted that treatment in hydrogen atmosphere favored its appearance. The relation between this weak hyperfine structure and the E'_γ has been debated as reported in the following of this chapter.

The E'_β center was first observed and characterized by Griscom [86, 87]. Its main EPR line shape possesses a marked axial symmetry [86], as testified by its principal **g** values that are $g_{||} = 2.0018$ and $g_{\perp} = 2.0004$, this latter was statistically distributed to simulate the EPR line shape [86]. A pair of lines splitted by 42 mT has been considered as an hyperfine structure related to the E'_β center. This experimental finding suggested that in the E'_β center an O≡Si• moiety similar to that of the E'_γ center is involved [86, 87]. Basing on experimental data it was suggested that the E' center could originate from the interaction of H atoms with some precursor site

in a-SiO₂ [86, 87]. The most reasonable hypothesis on the microscopic structure of the E'_β center is that it represents the equivalent defect in a-SiO₂ of the E'₂ center of α-quartz. Basing on the supposition that these two point defects could have similar microscopic structures, an OA band peaked at 5.4 eV was tentatively attributed to the E'_β center in a-SiO₂, [88].

In Ref. [86] Griscom defined the E'_{α1} and E'_{α2}. However, since the EPR features of the latter were found to be indistinguishable with respect to those of the E'_{γ2} in successive papers [87, 88] Griscom has renamed the E'_{α1} as E'_α and the E'_{α2} as E'_γ. The principal g values of E'_α defect are g₁=2.0018, g₂=2.0013 and g₃=1.9998 [86, 87]. The latter two g values have been distributed to simulate the EPR signal.

The E'_δ center was first observed and characterized by Griscom [90]. It possesses an highly symmetric EPR line shape with principal g values g_{||}=2.0018 and g_⊥=2.0021 [90]. In the following we will discuss the various structural models that have been proposed for this defect. In Fig. 7.5, we report an experimental spectrum composed by the EPR signals of the E'_δ, E'_α, E'_γ together with the isolated spectra of these three E' typologies.

Another class of intrinsic point defects in silica is constituted by the Non Bridging Oxygen Hole Centres (NBOHC) and Peroxy Radicals (POR) [91, 92]. As reported in [91], the NBOHC signal is characterized by g values g₁=2.0010, g₂=2.0095, g₃=2.078, whereas for the POR they are: 2.0014, 2.0074, 2.067, respectively. Their microscopic structures were proposed by the study of their ²⁹Si and ¹⁷O EPR hyperfine structures [91, 93]. Experimental supports in determining the spectral features of the two signals of these defects arise from annealing studies; in [93] Griscom evidenced that annealing temperature of POR is higher than that of NBOHC [93]. It was suggested that NBOHC is created by breaking of strained Si–O–Si linkages, by the rupture of a SiOH group or of a peroxy linkage [94, 95]. On the other side the reaction of interstitial oxygen molecules or atoms with an E' centre or with a NBOHC [96, 97] can create POR. They can also be generated, simultaneously with an E', through the breakage of a Si–O bond in a Peroxy linkage [98].

For the relevant and historical role covered by the Ge doped silica in optical fiber technology in the following we will report various data and models of point defects obtained for this material. In the first structural models proposed the irradiation induced Ge related defects have been named Ge(n), with n=0, 1, 2, 3. The different thermal stability and dose dependence were used to distinguish these defects. These latter were considered to have an E'_γ-like structure and the structural differences were related to the number, indicated as n, of Ge atoms present in the first neighbours tetrahedron [99].

The authors of Ref. [99] established the g values of each defect from the experimental EPR spectra, acquired for irradiated Ge doped SiO₂ fibers, using the dissimilar thermal stability and simulations. These g values are summarized in Table 7.7. In Fig. 7.6a, we illustrate an experimental spectrum recorded on a 1% Ge doped sample; in Fig. 7.6b we report the reference signals of the Ge(1), Ge(2) and E'Ge used to decompose the experimental spectrum. These first structural models have been modified by the successive investigations; the ones that are nowadays considered will be reported in the following. Finally we only remark that the structural model of the Ge(2) is still the most debated.

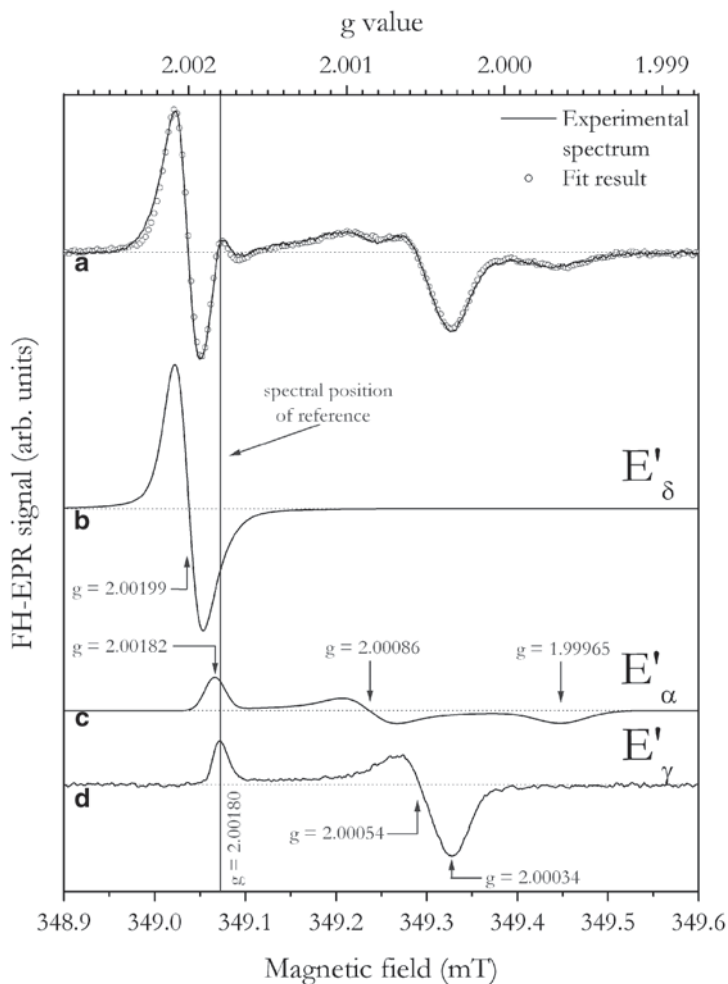


Fig. 7.5 a First harmonic EPR experimental spectrum of an irradiated silica sample containing E'_α , E'_γ and E'_δ (continuous line) compared to the line obtained as a weighted sum (circles) of the reference lines for b E'_δ , c E'_α and d E'_γ centers

Table 7.7 g_i values of the Ge(n) paramagnetic point defects in Ge doped SiO₂ [99]

Paramagnetic defects	g_1	g_2	g_3
Ge(0)	2.0009 ± 0.0002	1.9943	1.9943
Ge(1)	2.0007 ± 0.0001	1.9994	1.993
Ge(2)	2.0010 ± 0.0001	1.9978	1.9868
Ge(3) or (E'Ge)	2.0011 ± 0.0001	1.9945	1.9945

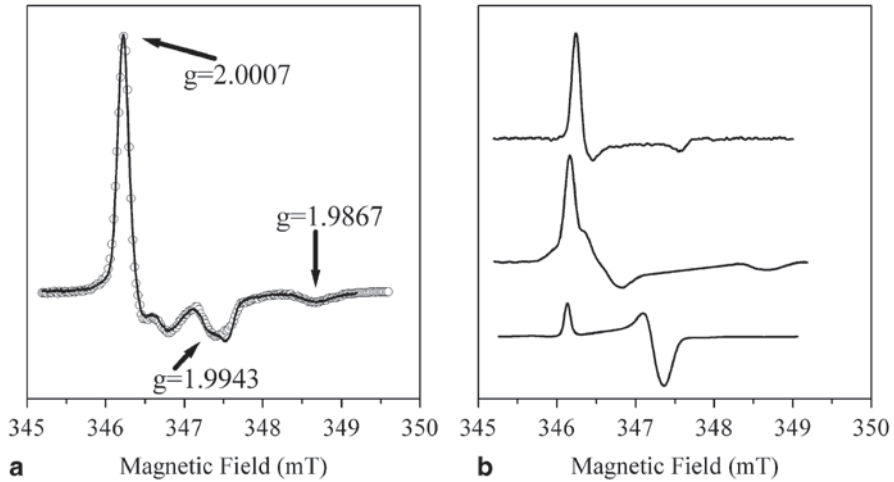


Fig. 7.6 **a** First harmonic EPR spectrum recorded in a Ge doped silica sample (Ge content 1%), *full line*, and signal obtained by summing Ge(1), Ge(2) and E'Ge signals, *open circles*, **b** from top to bottom, signals of Ge(1), Ge(2) and E'Ge used for experimental spectrum decomposition. The figure is modified from [100] with kind permission of The European Physical Journal (EPJ) (2008)

7.3.1 Intrinsic Defects

The structural similarity between the E'_γ center in a-SiO₂ and the E'_1 in α quartz was debated because, in analogy with E'_1 center, the E'_γ center was expected to possess a weak hyperfine doublet split by about $0.8 \text{ mT} \div 0.9 \text{ mT}$, but the doublet of lines with a peak-to-peak separation of $\sim 1.26 \text{ mT}$ observed in irradiated a-SiO₂, attributable by computer simulations to an isotropic hyperfine splitting constant of $\sim 0.8 \text{ mT}$ [101], was assigned to the hyperfine interaction of an unpaired electron with a proton [101–105]. In contrast Boero et al. [45], on the basis of a first principles study, and Agnello et al. [106, 107], on the basis of experimental strong correlation between the 1.26 mT doublet EPR signal and the E'_γ center main EPR line and on hydrogen/deuterium exchange studies, supported the attribution of the 1.26 mT doublet to the hyperfine interaction of the unpaired electron involved in the E'_γ center with a second nearest neighbor ^{29}Si atom. This hyperfine structure was also studied by Griscom and Cook [108] performing an EPR study of γ -ray irradiated ^{29}Si enriched a-SiO₂ samples. In this experiment the hyperfine interaction strength of the unpaired electron of the E'_γ centers with a second nearest neighbor ^{29}Si atom agrees with that of the E'_1 center only in few cases, whereas in most cases it is negligible [108, 109]. In order to account for this experimental evidence, it was proposed that in the majority of E'_γ centers the Si on which the unpaired electron is localized relaxes through the plan of its basal O atoms in a back projected configuration [108, 109], the weak hyperfine interaction being reduced in this configuration. Theoretical studies [110–111] supported this previous suggestion.

The attribution of a specific microscopic structure to the E'_γ center was complicated by some experimental evidences found in a-SiO₂ films on crystalline Si [112–

116]. In fact, capacitance-voltage measurements and charge injection experiments suggested the existence of two types of E'_γ [113, 115], differing in the charge state which can be neutral or positive [112–115]. It is worth to note that the positively charged E'_γ could be considered the equivalent in a-SiO₂ of the E'_1 , but the neutral E'_γ is not consistent with an oxygen vacancy model. It was proposed that the latter defect could possess a structure similar to the former but for the lack of the positively charged group of atoms facing the unpaired electron [115, 116].

Recent simulative studies proposed various structural models for the E'_γ . Uchino et al. [117–119] suggested that the E'_γ could originate from an “edgesharing” oxygen vacancy (triangular oxygen-deficient center); Lu et al. [120] reconsidered the simple oxygen vacancy as a precursor of the E'_γ , whereas theoretical study with the Embedded-Cluster-Method [110, 111] suggested that many microscopic structures can stabilize in a-SiO₂ after ionization of an oxygen vacancy. Basing on recent experimental investigations two structures of the E'_γ center can be distinguished by EPR and optical absorption spectroscopic parameters [121–124]. In the following, for convenience, we will refer to the two E'_γ as $E'_\gamma(1)$ and $E'_\gamma(2)$, respectively. They were observed in natural dry and wet and in synthetic dry materials for γ -ray irradiation doses lower than ~ 10 kGy and higher than $\sim 10^3$ kGy, respectively, whereas in the synthetic wet materials the $E'_\gamma(2)$ is detected for all the irradiation doses [121, 122]. During thermal treatments in the range 370–460 K, the $E'_\gamma(2)$ center undergoes to a structural conversion leading its spectral features to coincide with those of the $E'_\gamma(1)$ in all the materials [121, 123]. Basing on these results the existence of two different precursors of the E'_γ center can be supposed [121–123]. Since the $E'_\gamma(1)$ center is observed in correspondence to lower γ -ray doses than the $E'_\gamma(2)$, then the precursor site of the latter should possess a radiation activation energy higher than that of the former. Furthermore, since the signal of the $E'_\gamma(2)$ is observed in all the materials irradiated at doses higher than 10^3 kGy, it follows that the concentration of the precursors of the $E'_\gamma(2)$ center is higher than that of the $E'_\gamma(1)$ center in all the materials investigated. A thermally induced shift of the optical absorption (OA) band of the $E'_\gamma(2)$ center was observed and was correlated to the variation reported in both the main EPR line and hyperfine doublet of the same center permitting to gain information on the nature of the electronic levels transition involved in the OA band of the E'_γ [123, 124]. Making use of the broken tetrahedron structural model it was proposed that the thermally induced conversion from $E'_\gamma(2)$ to $E'_\gamma(1)$ should involve a change of the perturbative effect of the structure facing the $O\equiv Si^\bullet$ moiety [124]. This conclusion also agrees with the similarity of the main hyperfine splittings before and after thermal treatment approximately equal to 41.8 mT which indicates that the mean value of the angle between the unpaired electron wave function and the three Si–O back bonds is nearly the same in the two cases. In this context, the $E'_\gamma(2)$ center could be a positively charged oxygen vacancy, which comprises a structure facing the unpaired electron wave function constituted by the $^+Si\equiv O$ group (see Fig. 7.7a) and the thermally induced change could be connected with the relaxation of the $^+Si\equiv O$ group (see Fig. 7.7b), which reduces its perturbative effect on the unpaired electron wave function.

Considering that the EPR and OA features of the $E'_\gamma(1)$ and of the $E'_\gamma(2)$ center are virtually indistinguishable after isochronal thermal treatment up to 460 K, it

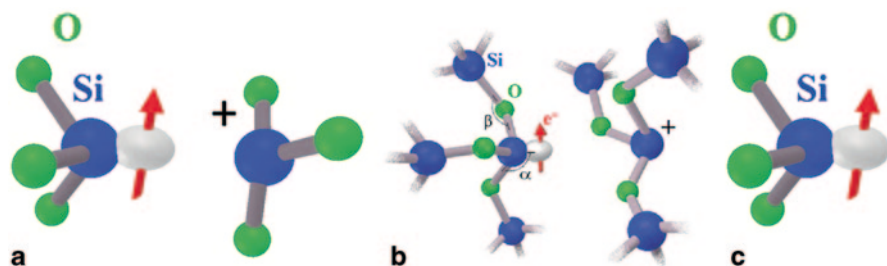


Fig. 7.7 **a** Structural model of $E'_{\gamma}(2)$ before thermal treatment, **b** $E'_{\gamma}(2)$ structural model thermally converted in $E'_{\gamma}(1)$, **c** structural model of the radiation induced $E'_{\gamma}(1)$ from Si–H groups. The figure is modified from [132] and [133] by permission of the American Physical Society (2008 and 2009)

was proposed that this facing $^+Si\equiv O$ structure is absent in the $E'_{\gamma}(1)$ center. As a consequence it was supposed that the $E'_{\gamma}(1)$ center originates from an $O\equiv Si-H$ (see Fig. 7.7c) group embedded in the matrix, following the radiation induced breaking of the Si–H bond and the subsequent diffusion of the H atom away from its initial site. The occurrence of this E'_{γ} centers generation process in a-SiO₂ was previously suggested on the basis of UV laser irradiation [125–129]. It is worth to note that the attribution of the $E'_{\gamma}(2)$ center to the positively charged oxygen vacancy model is also supported by the data obtained upon thermal treatment of Al-containing oxygen-deficient a-SiO₂ materials [130, 131]. At present, the specific structures attributed to the $E'_{\gamma}(1)$ and $E'_{\gamma}(2)$ centers reported in Fig. 7.7 have to be considered as tentative, and require new experiments for their validation.

It is important to note that since the EPR signal of the E'_{γ} and its strong hyperfine structure with separation of 42.0 mT depend on the surrounding matrix such signals have been widely used to characterize different a-SiO₂ materials [134], the pressure-densified [135, 137], the irradiation-densified [133, 135–141] ones and the nanoparticles [142–147]. For these latter systems the investigation of the E'_{γ} supported, together with other data [148–150], the so called shell like model.

In 2000, Griscom proposed [109] that the ^{29}Si hyperfine structure of the E'_{α} center should consist in a pair of lines split by ~ 14 mT. On the basis of this latter attribution, as illustrated in Fig. 7.8b, a model consisting in a twofold coordinated Si ($O=Si\cdot$, where: represents an electron lone pair) having trapped an electron was put forward [109]. Successively, Uchino et al. [118, 151] on the basis of quantum-chemical calculations suggested that the E'_{α} center could originate from a hole trapped in a twofold coordinated Si. As reported in Fig. 7.8a, it has been experimentally established that the E'_{α} possesses a strong hyperfine structure consisting in a pair of lines split by 49 mT. The ratio between the concentration of defects responsible for the 49 mT doublet and that of defects responsible for the main resonance line of the E'_{α} center is about 0.05, suggesting that the unpaired electron wave function involved in the defect is localized on a single Si atom. Such data disagree with the structural models in which the E'_{α} center consists in a twofold coordinated Si having trapped [109] or lost an electron [118, 151]. Furthermore, the concentration of E'_{α}

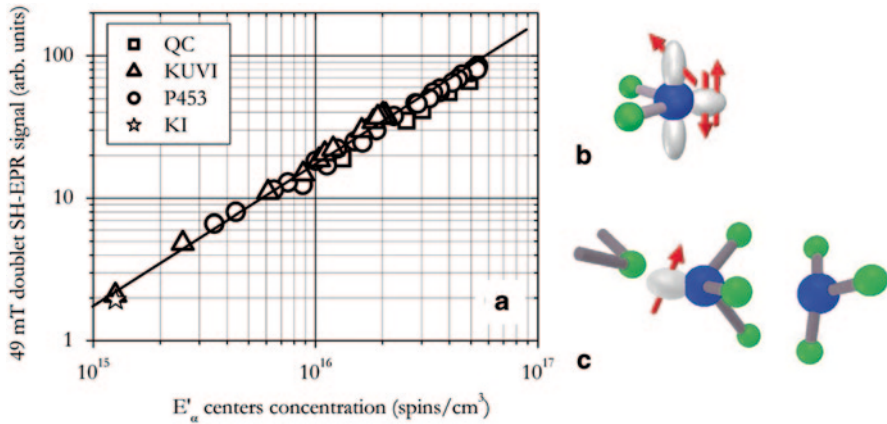


Fig. 7.8 **a** Second Harmonic EPR signal of the 49 mT doublet as a function of the concentration of the E'_α obtained from their main resonance in KI [154], KUVI [152], P453 (Purosil 453 [155]) and QC [156] samples γ -ray irradiated at 10² kGy and isothermally treated at $T=580$ K and $T=630$ K [153]. The *straight line*, with slope 1, is superimposed for comparison; microscopic structure proposed for the E'_α **b** by Griscom [109] and **c** by Buscarino et al. [152]. The figure is modified from [152] and [132] by permission of the American Physical Society (2006 and 2008)

centers induced in all the materials considered in [152, 153] was found to be larger than the concentration of twofold coordinated Si estimated in the as-grown materials and it was suggested that the E'_α could originate from an oxygen vacancy. The similarities in the strong hyperfine structures of the E'_α and E'_γ together with the orthorhombic symmetry of the E'_α center g matrix [152, 153] permitted to hypothesize that this latter defect could consist in a hole trapped in an oxygen vacancy with the unpaired electron Si sp^3 orbital pointing away from the vacancy in a back-projected configuration and interacting with an extra O atom of the matrix [132, 152, 153]. This model, illustrated in Fig. 7.8c, is consistent with a previous work, based on embedded cluster calculations [110], where an hyperfine constant of ~ 48.9 mT was obtained for this structure.

The E'_δ point defect was revealed in bulk silica [90, 157–159], in thermally grown a-SiO₂ films on Si [113, 160–167], and in buried oxide layer of separation by implantation of oxygen (SIMOX) materials [160, 164, 168–171]. In these experimental works it was shown that this defect can be induced in a-SiO₂ by X- and γ -ray irradiation, hole injection and by bombardment with Ar⁺ ions. Although E'_δ centers are induced by the above treatments the experimental data indicates that holes injection is able to originate E'_δ centers in many a-SiO₂ on Si systems, whereas this cannot be accomplished by an equal number of injected electrons [113, 162, 169]. Such results suggest an hole trapped nature of the E'_δ center [113, 162, 169]. Furthermore, experimental data show that the ²⁹Si hyperfine splitting of the E'_δ center (~ 10 mT [90]) is ~ 4 times smaller than that of the E'_γ (~ 42 mT), and that the g tensor of the E'_δ center is almost isotropic. A model suggesting that the unpaired electron of the E'_δ center is delocalized over four symmetrically disposed Si sp^3 orbitals [90]

was used to explain the above data. Furthermore, the concentration of E'_{δ} center was found to correlate with the Cl content of the materials, even if, the absence of EPR lines due to the hyperfine interaction of the unpaired electron with the nuclei of ^{35}Cl and ^{37}Cl represented a limit of a structural model involving Cl atoms. The presence of F and Cl atoms in the microscopic structure of the E'_{δ} center was also suggested by Tohmon et al. [157]. Successive studies showed that the E'_{δ} defect can be generated in Cl- and F-free samples too, ruling out the direct involvement of these element in the structure of the E'_{δ} center [113, 162, 170]. Tohmon et al. [157] have shown that the oxygen deficiency of the material is a necessary condition for the formation of the E'_{δ} center and it was proposed that the E'_{δ} center consists in an ionized single oxygen vacancy with the unpaired electron nearly similarly shared by the two Si atoms (2-Si model) [157]. Vanheusden and Stesmans [170] studying the centers induced in SIMOX systems proposed a different microscopic model in which the unpaired electron of the defect was considered to be delocalized over the four sp^3 hybrid orbitals of an Si atom located at the center of a five Si cluster (5-Si model) [170].

Zhang and Leisure [158] experimentally studied the EPR intensity ratio between the 10 mT doublet and the E'_{δ} main line and suggested the delocalization of the unpaired electron over four equivalent Si atoms [158]. Basing on this estimation, the authors proposed a microscopic model for the E'_{δ} center consisting in a pairs of nearby oxygen vacancies with the unpaired electron delocalized over the four sp^3 hybrid orbitals of the Si atoms (4-Si model) [158].

The effects on E'_{γ} and E'_{δ} centers of a room temperature treatment in hydrogen atmosphere were studied by Conley and Lenahan [171] and they proposed that the E'_{δ} center could possess a microscopic structure consisting in an unpaired electron strongly localized on a single Si atom, as for the E'_{γ} center (1-Si model).

The E'_{δ} center was studied in many simulative calculations using Density Functional (DFT) [46, 117, 120, 172–174], Hartree-Fock (HF) [175–177], and Embedded Cluster [110, 111, 178, 179] methods. The electronic structure of 2-Si, 4-Si and 5-Si models of the E'_{δ} have been studied in [175] and [180] showing that the unpaired spin preferentially localizes on a single pair of Si, supporting the 2-Si model. However in these simulations the atoms were not allowed to relax after ionization.

Successively the electronic properties of the ionized single oxygen vacancy (2-Si model) were considered in [46, 110, 111, 117, 120, 172, 173, 176–179]. It has been so shown that an ionized single oxygen vacancy in a-SiO₂ could stabilize in a configuration with the unpaired electron nearly equally shared by the two Si atoms (2-Si model). This structure does not coincide with the E'_{γ} because of the lack of puckering. We remark that the hyperfine structure [46, 110, 111, 117, 174, 175, 178, 180] and the principal g values [111, 178] were calculated. The hyperfine structure has been found to consist of a doublet of lines split by 8 mT–13.5 mT, in good agreement with the experimental findings [90, 157, 158]. By contrast, the calculated principal g values are significantly different from those obtained by EPR measurements [90, 113, 162, 168–170]. It is important to note that a triplet state center was observed in the same irradiated a-SiO₂ materials in which the E'_{δ} center was induced [90, 157, 158]. This signal consists of a pair of lines with peak-to-peak split

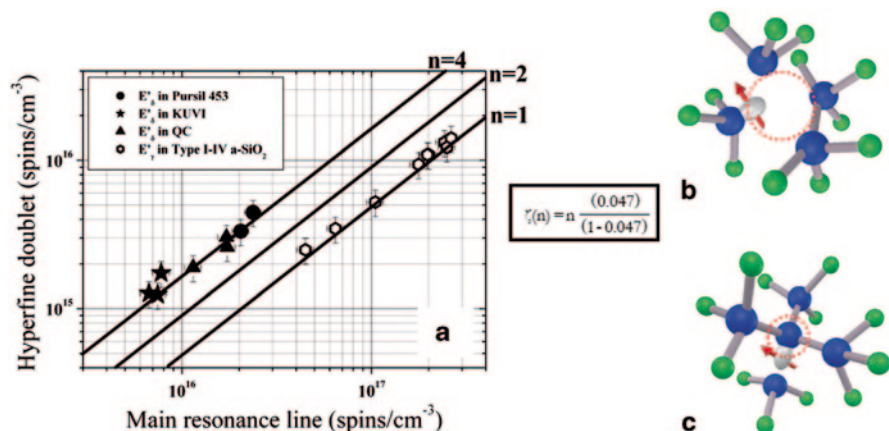


Fig. 7.9 a Concentration of defects responsible for the 10 mT doublet as a function of the concentration of the main resonance line of the E'_{δ} center in Pursil 453 (●) [155], KUVI (★) [154] and QC (▲) [156] samples γ -ray irradiated at 10² kGy and isothermally treated at $T=630$ K [184] (and at $T=580$ K in ref [153]). Similar data, but obtained for the E'_{γ} center and its 42 mT hyperfine doublet, are also reported (○) [184] for comparison. The *straight lines* indicate the dependences expected when the number (n) of ²⁹Si atoms, present in the defect structure, is 1, 2 or 4. The equation obtained for parameter ζ , defined as the ratio between the intensity of the hyperfine doublet and that of the main resonance, [153] is reported too; **b** 4-Si model for the E'_{δ} center **c** 5-Si model for the E'_{δ} center. Panel **a** is reprinted from [184] with permission from Elsevier (2007); modified from [131] by permission of the American Physical Society (2006)

of ~ 13.4 mT and center of gravity at $g \approx 2$ correlated to a characteristic weak EPR line with $g \approx 4$. Although an exact model has not been established, it is believed that this center represents the equivalent in α -SiO₂ of one of the triplet centers observed in α -quartz. On the basis of their co-presence, it was proposed also that the triplet center and the E'_{δ} share the same precursor site [90, 157, 158]. Data indicating that the E'_{δ} center is related to the oxygen deficiency of the material and that it is positively charged has been reported in [131, 181, 182].

Recent data, as those reported in Fig. 7.9a, confirmed that the strong hyperfine structure of the E'_{δ} center consists in a pair of lines split by 10 mT and enabled to determine the concentration ratio of hyperfine structure and main line [137, 181–184]. These data and the ones reported in [185, 186] disagree with the models as those in which this defect consists in an unpaired electron localized on a single Si [172] or nearly equally shared between the two Si atoms of a single oxygen vacancy [46, 110, 111, 117, 157, 175, 178, 180]. At variance, they indicate that the E'_{δ} consists in an unpaired electron delocalized over four symmetrically disposed Si-sp³ orbitals of a pair of nearby oxygen vacancies (see Fig. 7.9b) or of a 5-Si cluster [182–186] having a structure as the one showed in Fig. 7.9c.

Furthermore, it was tentatively suggested [181, 182] that the triplet state center consists in two weakly interacting unpaired electrons localized in two different Si-sp³ orbitals of a pair of nearby oxygen vacancies [158] or of a 5-Si cluster. So, a

single and a double ionization of the same precursor site could be the processes responsible for the generation of the E'_δ and the triplet center, respectively.

The microscopic structures of the E'_δ [182–186] center reported in Figs. 7.9b and 7.5c agree with the main experimental evidences described in the following. The g tensor is nearly isotropic, as expected for a delocalized highly symmetric electronic wave function. The hyperfine splitting of the E'_δ center is ~ 4 times smaller than that of E'_γ center ($10\text{ mT} \approx \frac{1}{4} \cdot 42\text{ mT}$), due to delocalization of the unpaired electron over four Si-sp³ orbitals each one similar to that involved in the E'_γ center. The ratio between the concentration of defects responsible for the 10 mT and that of the defects responsible for the main resonance line of the E'_δ center is near the one expected for $n=4$ or 5.

Among the E' like defects reported in the last two decades we remind the E' (Sn) detected in Sn doped silica [36, 187] and a doublet with separation 0.08 mT tentatively attributed to E' (OH) in F_2 laser low temperature irradiated silica [36, 188]. In this defect the Si atom is bonded with two normal bridging O, whereas the third is substituted by an OH group, this defect should be comparable to centers observed on SiO₂ surfaces and its signal overlaps with the one of the other E' Si.

Non Bridging Oxygen Hole Centres (NBOHC) and Peroxy Radicals (POR) can be considered oxygen-excess related defects. These two defects originate extended EPR signals that overlap [111, 189]. The NBOHC gives also important contributions to the optical absorption spectra since they are responsible for bands at 2.0 eV, 4.8 eV and 6.8 eV; furthermore these defects are responsible for a luminescence activity peaked at ~ 1.9 eV [189–191]. The exact features of the OA band peaked at about 5.3 eV related to the bulk PORs is not yet definitively established, since they are commonly induced together with NBOHC. Even if both the defects were identified by EPR data [109, 189], the detailed study of the NBOHC is difficult because of some of its properties [189]. Recent experiments reported that the NBOHC EPR signal shows non-Curie temperature dependence at lower temperatures and that a part of NBOHC is EPR silent [189]. Moreover, the emission of the NBOHCs, with a local environment similar to that in glass, was detected in neutron-irradiated α -quartz [189], and it was suggested that NBOHCs could be attached to ordered parts of the α -quartz, as a consequence one should expect that the orientation of these NBOHCs could be correlated to the direction of Si–O bonds. In the same study an EPR signal was attributed to the NBOHC. Such attribution was based on the following considerations: temperature dependence of the signal, its fast relaxation times, its large g-shift for the g_3 , similarity of the values of the g_1 and g_2 to the free electron g, and the expectation of the g_3 principal axis with direction close to ones of Si–O bonds in α -quartz. Using the g_{zz} value 2.062 ($g_{xx} = 2.0016$, $g_{yy} = 2.0070$) these defects were considered the ones originated by NBOHCs oriented along the “short” Si–O bond. Another less resolved signal was tentatively attributed to NBOHCs oriented along the “long” Si–O bond [189].

7.3.2 Ge Related Paramagnetic Centers in Ge-Doped Silica

The production of various silica based devices requires the doping with other chemical elements [109, 136]. The Ge doped silica attracted a great attention since the Ge doping increases the refractive index and since photosensitivity and the second harmonic generation were observed in the Ge doped silica [109, 136]. The relation between these phenomena and the Ge related defects was widely studied as well as the structures and the physical properties of the defects [192, 193]. Several experimental studies pointed out that the exposition of the Ge doped silica to ionizing radiation (UV, X, γ or β ray) induces the generation of optical absorption (OA) bands and of different EPR signals [193]. In details, the EPR signals were attributed to three Ge related defects named Ge(1), Ge(2) and E'Ge [193].

Studying the hyperfine structure generated by the ⁷³Ge atoms [194, 195] it was suggested that the Ge(1) defect is constituted by an electron trapped by a tetra-coordinated Ge atom. Figure 7.10a illustrates the Ge(1) structure. The experiments performed on Ce and Ge doped samples [196] confirmed such model. In these experiments, the samples were irradiated with light inside the 3.9 eV OA band due to the Ce³⁺ inducing the conversion Ce³⁺ \rightarrow Ce⁴⁺ and the trapping of an electron on a substitutional Ge atom. For short exposures the authors did not detect signals originated by other Ge related defects. An essential experimental datum regarding the Ge(1) is that in pure GeO₂ its EPR signal was not detected [193, 197]. This finding agrees with the fact that the electron should be localized on a Ge atom and that this condition occurs when a Ge atom is surrounded by Si and O atoms.

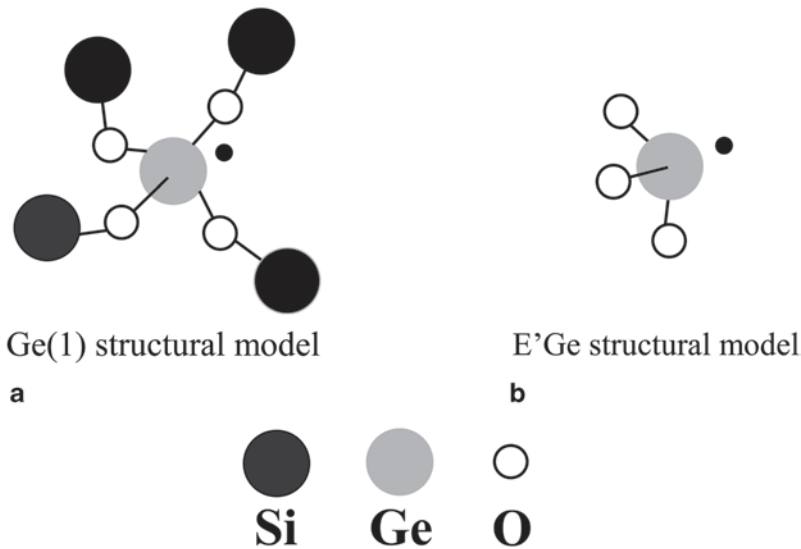
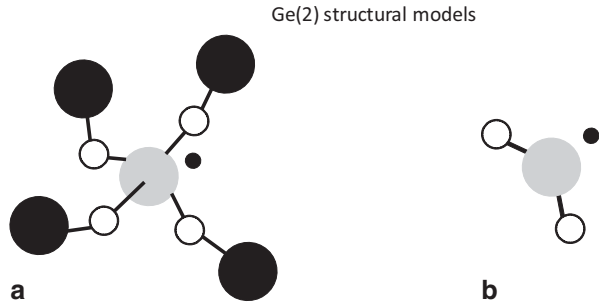


Fig. 7.10 **a** Structural model of Ge(1) defects; **b** structural model of the E'Ge defects. The figure is modified from [192] with permission from Nova Science Publishers (2012)

Fig. 7.11 Structural models of Ge(2) defects: **a** structure similar to the Ge(1); **b** ionized GLPC. The figure is modified from [192] with permission from Nova Science Publishers (2012)



Quanto-mechanic computations have shown that in silica the substitutional Ge atoms can be electron traps and that the electron trapping is followed by a structural re-organization [198]. This distortion makes the structure stable and it originates the orthorhombic features of the EPR signal [199, 200]. Another simulative investigation proposed that the Ge(1) is originated by a substitutional Ge atom with a near alkaline atom ($[\text{GeO}_4^-/\text{Na}^+]^0$, $[\text{GeO}_4^-/\text{Li}^+]^0$) or with a near STH (Self Trapped Hole) $[\text{GeO}_4^-/\text{STH}]^0$ [201]. Recently, it was underlined that the principal g values of the Ge(1) are similar to the one of the Ge(II) defects in Ge-doped crystalline SiO_2 supporting the attribution of the Ge(1) to an electron trapped in a fourfold coordinated Ge atom [81]. A different structure for the Ge(1) was proposed by Chiodini et al. [202], they studying the features of the EPR signal, the generation and thermal properties, suggested a similarity between the Ge(1) and the E'_α .

The defects initially named Ge(0) and Ge(3) basing on their different thermal stabilities, were successively considered as two variants of the same center since they had similar g values. This point defect was named $E'Ge$ because of the similarity of its EPR line with that of $E'Si_\gamma$ and of the existence of an analogous resonance in pure GeO_2 [203]. In analogy with the $E'Si_\gamma$, the $E'Ge$ was suggested to consist in a three-coordinated Ge atom, forming three covalent bonds with three O atoms, and maintaining an unpaired electron in a sp^3 orbital [195, 200]. We remark (i) that this structural model was enforced by the EPR study of the hyperfine structures recorded on samples containing ^{73}Ge [194] and (ii) that $\Delta g_3(E'Ge) / \Delta g_3(E'Si) \approx \lambda(Ge) / \lambda(Si)$ [203] ($\Delta g_3 = g_e - g_3$, $g_e = 2.0023$ free-electron g value, $\lambda(Ge)$ and $\lambda(Si)$ are the spin-orbit coupling constants of the Ge and Si atom, respectively).

By contrast various models have been proposed for describing the Ge(2) and its structural model is still debated. Recently, Griscom proposed that the Ge(2) has a structure similar to Ge(1) (see Fig. 7.11a); in details, they are considered the analogous in glass of the Ge(I) (Ge(2)) and Ge(II) (Ge(1)) in α quartz [81, 204]. Such attributions were proposed considering the g values, the ^{73}Ge hyperfine lines of Ge doped glass and Ge and Na containing crystals, and the temperature dependencies of the Ge(1) and Ge(2) in comparison with the ones of the Ge(I) and Ge(II). However, it is important to remind that, differing from the Ge(1), a Ge(2) like signal was observed in pure GeO_2 [197]. In 1998, Fujimaki et al. [205], proposed that the Ge(2) is, as illustrated in Fig. 7.11b, a positively ionized GLPC (Germanium Lone Pair

Center) [206]), which is a Ge atom, bonded to two oxygen atoms, with two non-bonding electrons forming a lone pair (=Ge•• where = indicates the bonds with two oxygen atoms and • stands for an electron) [206, 207].

This model was based on the following considerations: (1) the proportionality between the Ge(1) and Ge(2) concentrations induced by irradiation and the decrease of the B_{2p} OA band, associated to the GLPC [206, 207], interpreted as the indication that by laser irradiation the electrons are released from the GLPC and then trapped in other centers; (2) the absence of EPR signal different from the ones of the Ge(1) and Ge(2), and attributable to the GLPC⁺; (3) the similarity in the overall number of induced Ge(1) and Ge(2); (4) the absence of the Ge(2) signal in H₂ loaded samples [205, 208]. This latter finding can be explained by the fact that in samples with high hydrogen content the generation of another defect could be favoured. This defect, called H(II), originates a 11.9 mT hyperfine structure [207].

In addition, Fujimaki et al. recorded thermally stimulated luminescence data. They detected a band peaked at ~3.1 eV that was considered the 3.1 eV band attributed to the GLPC emission activity [207]. On these basis it was suggested that the electrons can be de-trapped from Ge(1) and re-captured by the GLPC⁺.

Another well known effect of the irradiation of the Ge doped silica is the appearance of OA bands in the range 3–6 eV. Nowadays there is a widely agreement in considering the Ge(1) the origin of a 4.5 eV band [195, 202, 204, 208, 209] and the E'Ge the defect responsible for a 6.3 eV band [193, 195]. At variance it is still debated the origin of a 5.8 eV band usually induced in Ge doped silica by irradiation. This band was attributed to the Ge(2) [195, 204], or to the Ge(1) [202, 208, 209] being detected in samples in which the Ge(2) signal was not observed.

Recent experimental investigations on sol-gel and PCVD samples with Ge contents up to 20% by weight showed a relevant property of the EPR signal of the Ge(1) and Ge(2) [210]. In particular, it was evidenced that the EPR line shapes of the Ge(1) and the Ge(2) centers are progressively modified for doping levels higher than 1%, whereas the line shape of the E'Ge defect appears independent from the doping [210]. The invariance of the E'Ge signal in samples doped with different amounts of Ge seems less surprising if one considers that its g values in pure GeO₂ (~2.0012 and ~1.9945) [203] are close to those determined in [210]. By contrast, even if in [210] a tentative explanation is given, the changes of the signal of the Ge(1) and the Ge(2) requires to be more deeply considered.

The debates on the structures of the Ge related defects and their relation with absorption bands have been accompanied by that concerning their generation mechanisms [211–215]. In agreement with data published in the past, in [100, 192, 209, 216] a complex scenario regarding the Ge(1) generation process was highlighted. The authors observed very different ratios between the Ge(1) and Ge(2) (this latter being absent in some cases) concentrations. These data could be explained by the presence of additional electron donors and/or electron traps, with concentrations dependent on the sample production process. Furthermore, for low radiation doses, the Ge(1) concentrations measured in many samples were approximately independent from the Ge content [100, 192, 216] and a limit value of the induced concentration was always measured [100, 192, 216–218], apart from one sample. The different

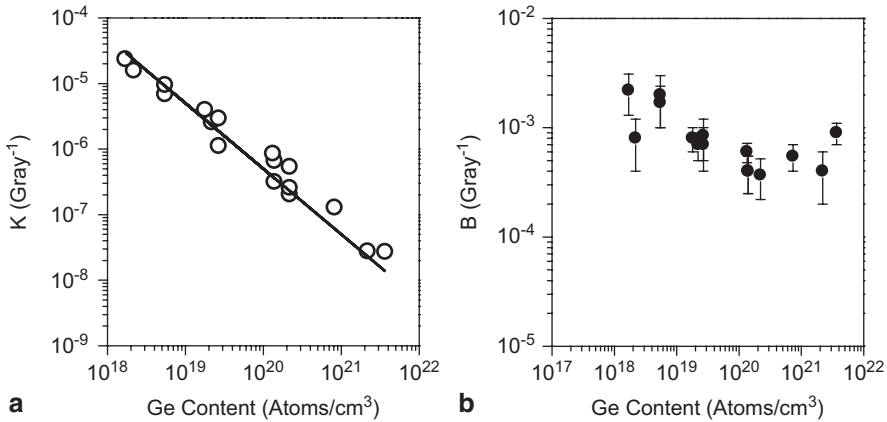


Fig. 7.12 **a** K values (\circ) calculated in [192, 216] the *black line* is the law $[\text{Ge}]^{-1}$; **b** B factors obtained by the fits of the experimental data [192, 216], see text for the definitions of K and B . The figure is modified from [192] with permission from Nova Science Publishers (2012)

behavior was attributed to the fact that for high doses in this sample the GLPC, which are electron donors as reported in the following, are induced by radiation [192, 216] in agreement with [219, 220] and to the related increase of the content of electron donors which was very low in the starting sample.

Basing on these data, recorded in a large dose range, the Ge(1) growth with dose was described with the law: $A(1 - e^{-Bx})$, and the observed concentration kinetics of the Ge(1) defects were considered the result of a competition between defect generation and destruction processes. In this context, we note that from literature data and from the data of [192], the amount of the Ge related defects is usually at least one order of magnitude lower than the doping level.

Even if the exact processes cannot be evidenced, one can use the equation $d[\text{Ge}(1)]/dx \approx K[\text{Ge}] - b[\text{Ge}(1)]$ to interpret the data, where K and b are the generation and destruction probabilities (see reference [192, 216] for further explanation). Considering that the solution of this latter equation is:

$$[\text{Ge}(1)] \approx \frac{K[\text{Ge}]}{b} (1 - e^{-bx}) \tag{7.1}$$

the similarity in the Ge(1) saturation concentrations and behavior at low doses induced in samples with different Ge content, suggested that K should depend on Ge as $[\text{Ge}]^{-\alpha}$ with $\alpha \sim 1$. This suggestion was enforced by fitting the Ge(1) concentration kinetic as a function of the dose with the law $A(1 - e^{-Bx})$ and by calculating $AB/[\text{Ge}]$ to obtain the K values reported in Fig. 7.12a. It is important to remind that this behavior was observed in samples differently produced, with dissimilar GLPC contents, and in which the Ge(2) and E/Ge concentrations follow different kinetics as a function of the dose. So it was suggested that the dependence of K on the Ge doping level is related to a general characteristic of the electron trapping mechanism

of the substitutional Ge atoms [192, 216]. The other parameter that influences the dependence on dose of [Ge(1)] is B that is the probability to destroy the Ge(1). As illustrated in Fig. 7.12b within the concentration range 10^{18} – 10^{20} Ge atoms/cm³, this parameter tends to decrease with the Ge doping level, then it seems to be independent from it. In the range 10^{18} – 10^{20} Ge atoms/cm³, one could interpret the data of Fig. 7.12b assuming that enhancing the Ge doping level the probability that an electron released by the destruction of a Ge(1) is re-trapped by another substitutional Ge atom raises. In simpler words, the larger is the Ge content the lower is the relevance of the existence of other alternative traps. To give a possible explanation of the B values determined for higher Ge content, it is relevant to remind that in pure GeO₂ the Ge(1) was not detected [193, 197]. Under the hypothesis that the electron cannot be trapped by a Ge atom with four other neighboring Ge, raising the Ge doping level one could imagine a decrease of *K* and/or an increase of the B. Nevertheless, the study of samples doped with $> 10^{20}$ Ge atoms/cm³ is essential for a profounder understanding of this topic. If we assume that the precursor of the Ge(1) is a Ge atom with a quartz-like coordination sphere ($[Ge]^*$) as recently proposed by Griscom [204] we obtain the equation $d[Ge(1)]/dx = K([Ge]^* - [Ge(1)]) - b[Ge(1)]$, where *K* and *b* have the same meaning as above. For low doses this equation can be approximated by $[Ge(1)] \approx K[Ge]^* x$ (a similar law is obtained also for the above reported model), then the fact that for low doses the growth kinetics are similar leads to the result that the generation probability *K* of the Ge(1) is inversely proportional to $[Ge]^*$ which is not established and which could be proportional to the Ge content or not. These considerations indicate that the Ge(1) kinetics can hardly distinguish between the Griscom or the Fujimaki models.

Further investigation is required even because a recent study on preforms and on the drawn fibers revealed further aspects on the Ge(1) generation and on the role of the GLPC [221] in determining radiation induced effects. Moreover, even if the GLPC are considered single electron donors [205, 221] or able to trap holes in pairs [204] it was proposed that oxygen deficiency ($[GLPC]/[Ge]$) does not ensure an increase of the Ge(1) generation which seems to be enhanced only in samples with high (from 1%) Ge content [100, 192].

The Ge(2) in [192, 216] were observed only in samples containing GLPC and by contrast, they were absent in a sample with $\sim 3.7 \times 10^{21}$ Ge atoms/cm³ but without the GLPCs, and that by irradiation presented the Ge(1). Moreover, the Ge(2) EPR signal was observed in samples with a low Ge content but with a GLPC content of $\sim 4.5 \times 10^{17}$ defects/cm³. It is also important to note that in the samples studied in [192, 216] the concentrations of the radiation induced Ge(2) were fitted by the law $C_{\max} (1 - e^{-hx})$. Using this analysis it was evidenced that the ratio $C_{\max}/GLPC$ assumed values inside the range 0.1–0.2 in the majority of the samples. These findings support the model in which the Ge(2) is related to an ionized GLPC more than the one that assigns the Ge(2) EPR signal to a Ge(1)-like structure. However, the model that considers the Ge(2) as ionized GLPC should be improved to explain some results summarized by Griscom [204] before to be indicated as the real structural model. As a conclusion it appears that even after many efforts devoted to solve this problem further experimental and theoretical investigations are necessary to definitively understand the structure of this defect.

A more complex generation mechanisms of E'Ge was observed. The data of Ref. [192, 216] suggest the existence of a generation process approximately independent on the Ge content. In many of the samples investigated in [192, 216] the dose dependences of the E'Ge concentrations were not described by a law: $V_{\max}(1-e^{-Rx})$. By contrast, the E'Ge growths appear to be the sum of the law $V_{\max}(1-e^{-Rx})$ (low doses) and of a sub-linear one (high doses), suggesting the presence of a generation channel from precursors and of a more complex process that originates the sub-linear growth.

Acknowledgments We thank Drs. David Griscom, Anders Lund and Masaru Shiotani for invitation to participate in this review. YMP and RIM also wish to thank the Natural Science and Engineering Research Council of Canada and the Russian Foundation for Basic Research, respectively, for financial support. AA, SA and GB thank the University of Palermo for financial support and the people of the LAMP group (<http://www.fisica.unipa.it/amorphous/>)

References

1. Griffiths JHE, Owen J, Ward EM (1954) Paramagnetic resonance in neutron irradiated diamond and smoky quartz. *Nature* 174:439–440
2. Weeks RA (1956) Paramagnetic resonance of lattice defects in irradiated quartz. *J Appl Phys* 27:1376–1381
3. Nilges MJ, Pan YM, Mashkovtsev RI (2009) Radiation-induced defects in quartz. III. Single-crystal EPR, ENDOR and ESEEM study of a peroxy radical. *Phys Chem Miner* 36:61–73
4. Romanelli M, Di Benedetto F, Bartali L, Innocenti M, Fornaciai G, Montegrossi G, Pardi LA, Zoleo A, Capacci F (2012) ESEEM of industrial quartz powders: insights into crystal chemistry of Al defects. *Phys Chem Miner* 39:479–490
5. Feng PB, Wang Y, Rong X, Su JH, Ju CY, Du JF (2012) Characterization of the electronic structure of E'₂ defect in quartz by pulsed EPR spectroscopy. *Phys Lett A* 376:2195–2199
6. Weil JA (1984) A review of electron-spin spectroscopy and its application to the study of paramagnetic defects in crystalline quartz. *Phys Chem Miner* 10:149–165
7. Weil JA (1993) A review of the EPR spectroscopy of the point-defects in alpha-quartz—the decade 1982–1992. In: Helms CR, Deal BE (eds) *Physics and chemistry of SiO₂ and the Si–SiO₂ interface*. Plenum Press, New York, pp 131–144
8. Weil JA 2000 A demi-century of magnetic defects in alpha-quartz. In: Pacchioni G, Skuja L, Griscom DL (eds) *Defects in SiO₂ and related dielectrics: science and technology*. Kluwer Academic, Dordrecht, pp 197–212
9. Mashkovtsev RI, Pan Y (2013) Nature of paramagnetic defects in quartz: progresses in the first decade of the 21st century. In: Novak B, Marek P (eds) *New developments in quartz research: varieties, crystal chemistry and uses in technology*. Nova Science Publisher, New York, pp 65–104.
10. Han D, West D, Li XB, Xie SY, Sun HB, Zhang SB (2010) Impurity doping in SiO₂: formation energies and defect levels from first-principles calculations. *Phys Rev B* 82:155132
11. Garrison EG, Rowlett RM, Cowan DL, Holroyd LV (1981) Electron-spin-resonance dating of ancient flints. *Nature* 290:44–45
12. Ikeya M (1993) *New applications of electron paramagnetic resonance: ESR dating, dosimetry, and spectroscopy*. World Scientific, Singapore
13. Botis S, Nokhrin SM, Pan Y, Xu Y, Bonli T, Sopuck V (2005) Natural radiation-induced damage in quartz. I. Correlations between cathodoluminescence colors and paramagnetic defects. *Can Mineral* 43:1565–1580

14. Botis S, Pan Y, Bonli T, Xu Y, Zhang A, Nokhrin S, Sopuck V (2006) Natural radiation-induced damage in quartz. II. Distribution and implications for uranium mineralization in the Athabasca basin, Saskatchewan, Canada. *Can Mineral* 44:1387–1402
15. Botis S, Pan Y, Nokhrin S, Nilges MJ (2008) Natural radiation-induced damage in quartz. III. A new ozonide radical in drusy quartz from the Athabasca Basin, Saskatchewan. *Can Mineral* 46:125–138
16. Hu B, Pan Y, Botis S, Rogers B, Kotzer T, Yeo G (2008) Radiation-induced defects in drusy quartz, Athabasca basin, Canada: a new aid to exploration of uranium deposits. *Econ Geol* 103:1571–1580
17. Sun Y, Chen H, Tada R, Weiss D, Lin M, Toyoda S, Yan Y, Isozaki Y (2013) ESR signal intensity and crystallinity of quartz from Gobi and sandy deserts in East Asia and implications for tracing Asian dust provenance. *Geochem Geophys Geosys* 14:2615–2627
18. Pan Y, Nilges MJ (2014) Electron paramagnetic resonance spectroscopy: basic principles, experimental techniques and applications to Earth and planetary sciences. *Rev Mineral Gechem* 78:655–690
19. Pan Y, Mashkovtsev RI, Huang D, Mao M, Shatskiy A (2011) Mechanisms of Cr and H incorporation in stishovite determined by single-crystal EPR spectroscopy and DFT calculations. *Am Mineral* 96:1331–1342
20. Pan Y, Mao M, Li Z, Botis SM, Mashkovtsev RI, Shatskiy A (2012) Single-crystal EPR study of three radiation-induced defects (Al-O₂³⁻, Ti³⁺ and W⁵⁺) in stishovite. *Phys Chem Miner* 39:627–637
21. Donnay JDH, Le Page Y (1978) The vicissitudes of the low-quartz crystal setting or the pitfalls of enantiomorphism. *Acta Crystallogr* A34:584–594
22. Heaney PJ (1994) Structure and chemistry of the low-pressure silica polymorphs. *Rev Mineral* 29:1–40
23. Feigl FJ, Anderson JH (1970) Defects in crystalline quartz: electron paramagnetic resonance of E' vacancy centers associated with germanium impurities. *J Phys Chem Solids* 31:575–596
24. Glazer AM, Stadnicka K (1986) On the origin of optical-activity in crystal structures. *J Appl Crystallogr* 19:108–122
25. Tanaka Y, Takeuchi T, Lovesey SW (2008) Right handed or left handed? Forbidden X-ray diffraction reveals chirality. *Phys Rev Lett* 100:145502
26. Tanaka Y, Lovesey SW (2012) Determination of absolute chirality using resonant X-ray diffraction. *Eur Phys J Special Topics* 208:67–74
27. Jani MG, Bossoli RB, Halliburton LE (1983) Further characterization of the E'₁ center in crystalline SiO₂. *Phys Rev B* 27:2285–2293
28. Pan Y, Nilges MJ, Mashkovtsev RI (2009) Radiation-induced defects in quartz: a multifrequency EPR study and DFT modeling of new peroxy radicals. *Mineral Mag* 73:519–535
29. Nelson CM, Weeks RA (1960) Trapped electrons in irradiated quartz and silica: I. Optical absorption. *J Am Ceramic Soc* 43:396–399
30. Weeks RA, Nelson CM (1960) Trapped electrons in irradiated quartz and silica: II. Electron spin resonance. *J Am Ceramic Soc* 43:399–404
31. Weeks RA (1963) Paramagnetic spectra of E'₂ centers in crystalline quartz. *Phys Rev* 130:570–576
32. Solntsev VP, Mashkovtsev RI, Shcherbakova MY (1977) Electron paramagnetic resonance of the radiation centers in quartz. *J Struct Chem* 18:578–583
33. Isoya J, Weil JA, Halliburton LE (1981) Electron-paramagnetic-res and ab initio SCF-MO studies of the Si–H–Si system in the E'₄ center of alpha-quartz. *J Chem Phys* 74:5436–5448
34. Perlson BD, Weil JA (2008) Electron paramagnetic resonance studies of the E' centers in alpha-quartz. *Can J Phys* 86:871–881
35. Mashkovtsev RI, Pan Y (2012) Five new E' centers and their Si-29 hyperfine structures in electron-irradiated alpha-quartz. *Phys Chem Miner* 39:79–85
36. Weeks RA, Magruder RH, Stesmans A (2008) Review of some experiments in the 50 year saga of the E' center and suggestions for future research. *J Non-Cryst Solids* 354:208–216

37. Mashkovtsev RI, Li Z, Mao M, Pan Y (2013) ^{73}Ge , ^{17}O and ^{29}Si hyperfine interactions of the $\text{Ge } E'_1$ center in crystalline SiO_2 . *J Magn Reson* 233:7–16
38. Laino T, Donadio D, Kuo IFW (2007) Migration of positively charged defects in alpha-quartz. *Phys Rev B* 76:195210
39. Silsbee RH (1961) Electron spin resonance in neutron-irradiated quartz. *J Appl Phys* 32:1459–1462
40. Feigl FJ, Fowler WB, Yip KL (1974) Oxygen vacancy model for the E'_1 center in SiO_2 . *Solid State Commun* 14:225–229
41. Rudra JK, Fowler WB (1987) Oxygen vacancy and the E'_1 center in crystalline SiO_2 . *Phys Rev B* 35:8223–8230
42. Edwards AH, Fowler WB, Feigl FJ (1988) Asymmetrical relaxation of simple E' centers in silicon dioxide isomorphs. *Phys Rev B* 37:9000–9005
43. Snyder KC, Fowler WB (1993) Oxygen vacancy in alpha-quartz—a possible bistable and metastable defect. *Phys Rev B* 48:13238–13243
44. Giordano L, Sushko PV, Pacchioni G, Shluger AL (2007) Optical and EPR properties of point defects at a crystalline silica surface: Ab initio embedded-cluster calculations. *Phys Rev B* 75:024109
45. Boero M, Pasquarello A, Sarnthein J, Car R (1997) Structure and hyperfine parameters of $E'(1)$ centers in α -quartz and in vitreous SiO_2 . *Phys Rev Lett* 78:887–890
46. Blöchl PE (2000) First-principles calculations of defects in oxygen-deficient silica exposed to hydrogen. *Phys Rev B* 62:6158–6179
47. Mysovsky AS, Sushko PV, Mukhopadhyay S, Edwards AH, Shluger AL (2004) Calibration of embedded-cluster method for defect studies in amorphous silica. *Phys Rev B* 69:085202
48. Li Z, Pan Y (2012) First-principles calculations of the E'_1 center in quartz: structural models, ^{29}Si hyperfine parameters and association with Al impurity. In: Götze J, Möckel R (eds) *Quartz, deposits, mineralogy and analytics*. Springer, Berlin, pp 161–175
49. Toyoda S, Hattori W (2000) Formation and decay of the E'_1 center and of its precursor. *Appl Rad Isotop* 52:1351–1356
50. Usami T, Toyoda S, Bahadur H, Srivastava AK, Nishido H (2009) Characterization of the E'_1 center in quartz: role of aluminum hole centers and oxygen vacancies. *Physica B Condens Matter* 404:3819–3823
51. McEachern RJ, Weil JA, Sawyer B (1992) Distortion and ^{17}O hyperfine interactions in the centers $[\text{GeO}_4]_{\text{I,II}}^-$ in alpha-quartz. *Solid State Commun* 81:207–209
52. McEachern RJ, Weil JA (1994) ^{17}O hyperfine interaction for the $[\text{GeO}_4]_{\text{I,II}}^-$ and $[\text{GeO}_4/\text{Li}]_{\text{A,C}}^0$ centers in an enriched crystal of alpha-quartz. *Phys Rev B* 49:6698–6709
53. Howarth DF, Mombourquette MJ, Weil JA (1997) The magnetic properties of the oxygen-hole aluminum centres in crystalline $\text{SiO}_2 \cdot 5$. ^{17}O -enriched $[\text{AlO}_4/\text{Li}]^+$ and dynamics thereof. *Can J Phys* 75:99–115
54. Nilges MJ, Pan Y, Mashkovtsev RI (2008) Radiation-damage-induced defects in quartz. I. Single-crystal W-band EPR study of hole centers in an electron-irradiated quartz. *Phys Chem Miner* 35:103–115
55. Pan Y, Nilges MJ, Mashkovtsev RI (2008) Radiation-induced defects in quartz. II. Single-crystal W-band EPR study of a natural citrine quartz. *Phys Chem Miner* 35:387–397
56. Pan Y, Hu B (2009) Radiation-induced defects in quartz. IV. Thermal properties and implications. *Phys Chem Miner* 36:421–430
57. Weeks RA, Abraham MM (1965) Spin-one states of defects in quartz. *Bull Am Phys Soc* 10:374
58. Bossoli RB, Jani MG, Halliburton LE (1982) Radiation-induced E'' centers in crystalline SiO_2 . *Solid State Commun* 44:213–217
59. Mashkovtsev RI, Howarth DF, Weil JA (2007) Biradical states of oxygen-vacancy defects in alpha-quartz. *Phys Rev B* 76:214114
60. Mashkovtsev RI, Pan Y (2011) Biradical states of oxygen-vacancy defects in alpha-quartz: centers $E''(2)$ and $E''(4)$. *Phys Chem Minerals* 38:647–654
61. Mashkovtsev RI, Pan Y (2012) Stable states of E'' defects in α -quartz. *EPL* 98:56005

62. Weil JA, Bolton JR (2007) *Electron Paramagnetic Resonance*. Wiley, New York
63. Mashkovtsev RI, Shcherbakova MY, Solntsev VP (1978) *Trudy Instituta Geologii I Geofyziki. Akad. Nauk SSSR, Sib. Otd. (Novosibirsk: Nauka) Issue 385*, pp 79–86
64. Maschmeyer D, Lehmann G (1983) New hole-centers in natural quartz. *Phys Chem Miner* 10:84–88
65. Azzoni CB, Meinardi F, Paleari A (1994) Trapped-hole centers in neutron-irradiated synthetic quartz. *Phys Rev B* 49:9182–9185
66. Känzig W, Cohen MH (1959) Paramagnetic resonance of oxygen in alkali halides. *Phys Rev Lett* 3:509–510
67. Lunsford JH (1973) ESR of adsorbed oxygen species. *Catal Rev* 8:135–156
68. Bill H (1969) Investigation on colour centres in alkaline earth fluorides. *Helv Phys Acta* 42:771–797
69. Botis SM, Adriaens DA, Pan Y (2009) Ab initio calculations on the O₂³⁻Y³⁺ center in CaF₂ and SrF₂: its electronic structure and hyperfine constants. *Phys Chem Miner* 36:1–7
70. Ogoh K, Yamanaka C, Ikeya M, Ito E (1996) Two center model for radiation induced aluminum hole center in stishovite. *J Phys Chem Solids* 57:85–88
71. Schlick S (1972) ESR spectrum of O₃⁻ trapped in a single crystal of potassium chlorate. *J Chem Phys* 56:654–661
72. Che M, Tench AJ (1983) Characterization and reactivity of molecular-oxygen species on oxide surfaces. *Adv Catal* 32:1–148
73. Nuttall RHD, Weil JA (1981) The magnetic properties of the oxygen-hole aluminum centers in crystalline SiO₂.1. [AlO₄]⁰. *Can J Phys* 59:1696–1708
74. Nuttall RHD, Weil JA (1981) The magnetic properties of the oxygen-hole aluminum centers in crystalline SiO₂.3. [AlO₄]⁺. *Can J Phys* 59:1886–1892
75. Walsby CJ, Lees NS, Claridge RFC, Weil JA (2003) The magnetic properties of oxygen-hole aluminum centres in crystalline SiO₂. VI: a stable AlO₄/Li centre. *Can J Phys* 81:583–598
76. Pacchioni G, Frigoli F, Ricci D, Weil JA (2001) Theoretical description of hole localization in a quartz Al center: the importance of exact electron exchange. *Phys Rev B* 63:054102
77. To J, Sokol AA, French SA, Kaltsoyannis N, Catlow CRA (2005) Hole localization in [AlO₄]⁰ defects in silica materials. *J Chem Phys* 122:144704
78. Botis SM, Pan Y (2011) Modeling of [AlO₄/Li⁺]⁺ paramagnetic defects in alpha-quartz. *Can J Phys* 89:809–816
79. Gillen R, Robertson J (2012) Hybrid functional calculations of the Al impurity in alpha quartz: hole localization and electron paramagnetic resonance parameters. *Phys Rev B* 85:014117
80. Schnadt R, Räuber A (1971) Motional effects in the trapped-hole center in smoky quartz. *Solid State Commun* 9:159–161
81. Griscom DL (2011) Trapped-electron centers in pure and doped glassy silica: a review and synthesis. *J Non-Cryst Solids* 357:1945–1962
82. Nuttall RHD, Weil JA (1980) Two hydrogenic trapped-hole species in alpha-quartz. *Solid State Commun* 33:99–102
83. Lees NS, Walsby CJ, Williams JAS, Weil JA, Claridge RFC (2003) EPR of a hydrogen/double-lithium centre in alpha-quartz. *Phys Chem Miner* 30:131–141
84. Griscom DL, Friebele EJ, Sigel GH (1974) Observation and analysis of the primary ²⁹Si hyperfine structure of the E' center in non-crystalline SiO₂. *Solid State Commun* 15:479–483
85. Griscom DL (1979) E' center in glassy SiO₂: microwave saturation properties and confirmation of the primary ²⁹Si hyperfine structure. *Phys Rev B* 20:1823–1834
86. Griscom DL (1984) Characterization of three E'-center variants in X- and γ-irradiated high purity α-SiO₂. *Nucl Instrum Methods Phys Res Sect B* 1:481–488
87. Griscom DL (1985) Defect structure of glasses: some outstanding questions in regard to vitreous silica. *J Non-Cryst Solids* 73:51–77
88. Griscom DL (1991) Optical properties and structure of defects in silica glass. *J Ceram Soc Jpn* 99:899–916
89. Shendrik AV, Yudin DM (1978) A new concept of the model for the paramagnetic E'-centre in the SiO₂-x system. *Phys Stat Sol (b)* 85:343–349

90. Griscom DL, Friebele EJ (1986) Fundamental radiation-induced defect centers in synthetic fused silicas: atomic chlorine, delocalized E' centers, and a triplet state. *Phys Rev B* 34:7524–7533
91. Stapelbroek M, Griscom DL, Friebele EJ, Sigel GH (1979) Oxygen-associated trapped-hole centers in high-purity fused silicas. *J Non-Cryst Solids* 32:313–326
92. Friebele EJ, Griscom DL, Stapelbroek M, Weeks RA (1979) Fundamental defect centers in glass: the peroxy radical in irradiated, high-purity, fused silica. *Phys Rev Lett* 42:1346–1349
93. Griscom DL, Friebele EJ (1981) Fundamental defect centers in glass: ^{29}Si hyperfine structure of the nonbridging oxygen hole center and the peroxy radical in a-SiO₂. *Phys Rev B* 24:4896–4898
94. Nishikawa H, Nakamura R, Tohmon R, Ohki Y, Sakurai Y, Nagasawa K, Hama Y (1990) Generation mechanism of photoinduced paramagnetic centers from preexisting precursors in high-purity silicas. *Phys Rev B* 41:7828–7834
95. Imai H, Arai K, Isoya J, Hosono H, Abe Y, Imagawa H (1993) Generation of E' centers and oxygen hole centers in synthetic silica glasses by γ irradiation. *Phys Rev B* 48:3116–3123
96. Nuccio L, Agnello S, Boscaino R, Brichard B (2009) Effects of high pressure thermal treatments in oxygen and helium atmospheres on amorphous silicon dioxide and its radiation hardness. *J Non-Cryst Solids* 355:1046–1049
97. Kajihara K, Skuja L, Hirano M, Hosono H (2004) Role of mobile interstitial oxygen atoms in defect processes in oxides: interconversion between oxygen-associated defects in SiO₂ glass. *Phys Rev Lett* 92:015504–015504
98. Nishikawa H (2001) Structure and properties of amorphous silicon dioxide—issues on reliability and novel applications 93–122. In Nalwa HS (ed) *Silicon-based materials and devices*. Academic, USA.
99. Friebele EJ, Griscom DL, Sigel GH Jr (1974) Defect centers in a germanium-doped silica-core optical fiber. *J Appl Phys* 45:3424–3428
100. Agnello S, Alessi A, Gelardi FM, Boscaino R, Parlato A, Grandi S, Magistris A (2008) Effect of oxygen deficiency on the radiation sensitivity of sol-gel Ge-doped amorphous SiO₂. *Eur Phys J B* 61:25–31
101. Tsai TE, Griscom DL (1987) On the structures of hydrogen-associated defect centers in irradiated high-purity a-SiO₂:OH. *J Non-Cryst Solids* 91:170–179
102. Griscom DL (1980) E' center in glassy SiO₂: ^{17}O , ^1H , and “very weak” ^{29}Si superhyperfine structure. *Phys Rev B* 22:4192–4202
103. Conley JF, Lenahan PM (1993) Room temperature reactions involving silicon dangling bond centers and molecular hydrogen in amorphous SiO₂ thin films on silicon. *Appl Phys Lett* 62:40–42
104. Li J, Kannan S, Lahman RL, Sigel GH Jr (1994) Drawing-enhanced defect precursors in low-OH content, oxygen deficient synthetic silica optical fibers. *Appl Phys Lett* 64:2090–2092
105. Li J, Kannan S, Lahman RL, Sigel GH Jr (1995) Electron paramagnetic resonance hyperfine spectrum of the Si E' defect associated with weakly bonded hydrogen molecules in synthetic silica optical fibers. *Appl Phys Lett* 66:2816–2818
106. Agnello S, Boscaino R, Gelardi FM, Boizot B (2001) Weak hyperfine interaction of E' centers in gamma- and beta-irradiated silica. *J Appl Phys* 89:6002–6006
107. Vaccaro G, Agnello S, Buscarino G, Nuccio L, Grandi S, Mustarelli P (2009) ^{29}Si attribution of the 1.3 mT hyperfine structure of the E'_γ centers in amorphous SiO₂. *J Appl Phys* 105:093514–093516
108. Griscom DL, Cook M (1995) ^{29}Si superhyperfine interactions of the E' center: a potential probe of range-II order in silica glass. *J Non-Cryst Solids* 182:119–134
109. Griscom DL (2000) The nature of point defects in amorphous silicon dioxide 117–159; Askins CG (2000) Periodic UV-induced index modulations in doped-silica optical fibers: formation and properties of the fiber Bragg grating 391–426. In: Pacchioni G, Skuja L, Griscom DL (eds) *Defects in SiO₂ and related dielectrics: science and technology*. Kluwer Academic, Dordrecht

110. Mukhopadhyay S, Sushko PV, Stoneham AM, Shluger AL (2004) Modeling of the structure and properties of oxygen vacancies in amorphous silica. *Phys Rev B* 70:195203–195215
111. Sushko PV, Mukhopadhyay S, Mysovsky AS, Sulimov VB, Taga A, Shluger AL (2005) Structure and properties of defects in amorphous silica: new insights from embedded cluster calculations. *J Phys: Condens Matter* 17:S2115–S2140
112. Warren WL, Lenahan PM, Robinson B, Stathis JH (1988) Neutral E' centers in microwave downstream plasma-enhanced chemical-vapor-deposited silicon dioxide. *Appl Phys Lett* 53:482–484
113. Conley JF, Lenahan PM, Evans HL, Lowry RK, Morthorst TJ (1994) Observation and electronic characterization of “new” E' center defects in technologically relevant thermal SiO₂ on Si: an additional complexity in oxide charge trapping. *J Appl Phys* 76:2872–2880
114. Afanas'ev VV, de Nijs JMM, Balk P, Stesmans A (1995) Degradation of the thermal oxide of the Si/SiO₂/Al system due to vacuum ultraviolet irradiation. *J Appl Phys* 78:6481–6490
115. Afanas'ev VV, Stesmans A (2000) Charge state of paramagnetic E' centre in thermal SiO₂ layers on silicon. *J Phys: Condens Matter* 12:2285–2290
116. Kalnitsky A, Ellul JP, Poindexter EH, Caplan PJ, Lux RA, Boothroyd AR (1990) Rechargeable E' centers in silicon-implanted SiO₂ films. *J Appl Phys* 67:7359–7367
117. Uchino T, Takahashi M, Yoko T (2001) E' centers in amorphous SiO₂ revisited: a new look at an old problem. *Phys Rev Lett* 86:5522–5525
118. Uchino T (2001) Ab initio cluster calculations on point defects in amorphous SiO₂. *Curr Opin Sol State Mat Sci* 5:517–523
119. Uchino T (2005) Structure and properties of amorphous silica and its related materials: recent developments and future directions. *J Ceram Soc Jpn* 113:17–25
120. Lu ZY, Nichlaw CJ, Fleetwood DM, Schrimpf RD, Pantelides ST (2002) Structure, properties, and dynamics of oxygen vacancies in amorphous SiO₂. *Phys Rev Lett* 89:285505–285504
121. Agnello S, Boscaino R, Buscarino G, Cannas M, Gelardi FM (2002) Structural relaxation of E'γ centers in amorphous silica. *Phys Rev B* 66:113201–113204
122. Agnello S, Boscaino R, Buscarino G, Gelardi FM (2004) Experimental evidence for two different precursors of E'γ centers in silica. *J Non-Cryst Solids* 345, 346:505–508
123. Buscarino G, Agnello S, Parlato A (2007) Electron paramagnetic resonance line shape investigation of the ²⁹Si hyperfine doublet of the E'γ center in a-SiO₂. *Phys Stat Sol (c)* 4:1301–1304
124. Agnello S, Buscarino G, Gelardi FM, Boscaino R (2008) Optical absorption band at 5.8 eV associated with the E'γ centers in amorphous silicon dioxide: optical absorption and EPR measurements. *Phys Rev B* 77:195206–195207
125. Messina F, Cannas M (2005) In situ observation of the generation and annealing kinetics of E' centres induced in amorphous SiO₂ by 4.7 eV laser irradiation. *J Phys: Condens Matter* 17:3837–3842
126. Messina F, Cannas M (2006) Photochemical generation of E' centres from Si-H in amorphous SiO₂ under pulsed ultraviolet laser radiation. *J Phys: Condens Matter* 18:9967–9973
127. Imai H, Arai K, Hosono H, Abe Y, Arai T, Imagawa H (1991) Dependence of defects induced by excimer laser on intrinsic structural defects in synthetic silica glasses. *Phys Rev B* 44:4812–4818
128. Leclerc N, Pflleiderer C, Hitzler H, Wolfrum J, Greulich KO, Thomas S, Englisch W (1992) Luminescence and transient absorption bands in fused SiO₂ induced by KrF laser radiation at various temperatures. *J Non-Cryst Solids* 149:115–121
129. Nishikawa H, Nakamura R, Ohki Y, Hama Y (1993) Enhanced photogeneration of E' centers from neutral oxygen vacancies in the presence of hydrogen in high-purity silica glass. *Phys Rev B* 48:2968–2973
130. Buscarino G, Agnello S (2007) Experimental evidence of E'γ centers generation from oxygen vacancies in a-SiO₂. *J Non-Cryst Solids* 353:577–580
131. Buscarino G, Agnello S, Gelardi FM (2006) Characterization of E'γ and triplet point defects in oxygen-deficient amorphous silicon dioxide. *Phys Rev B* 73:045208–045208

132. Buscarino G, Boscaino R, Agnello S, Gelardi FM (2008) Optical absorption and electron paramagnetic resonance of the E'_{α} center in amorphous silicon dioxide. *Phys Rev B* 77:155214–155215
133. Buscarino G, Agnello S, Gelardi FM, Boscaino R (2009) Polyamorphic transformation induced by electron irradiation in a-SiO₂ glass. *Phys Rev B* 80:094202–094211
134. Buscarino G, Vaccaro G, Agnello S, Gelardi FM (2009) Variability of the Si–O–Si angle in amorphous-SiO₂ probed by electron paramagnetic resonance and Raman spectroscopy. *J Non-Cryst Solids* 355:1092–1094
135. Devine RAB, Arndt J (1987) Si–O bond-length modification in pressure-densified amorphous SiO₂. *Phys Rev B* 35:9376–9379
136. Dooryhee E, Duraud JP, Devine RAB (2000) Radiation-induced defects and structural modifications. 349–421; KurKjian CR, Krol (2000) DM Science and Technology of silica lightguides for telecommunications 449–474. In: Devine RAB, Duraud JP, Dooryh e E (eds) *Structure and Imperfections in Amorphous and Crystalline Silicon Dioxide*. Wiley, New York
137. Tsai TE, Griscom DL, Friebele EJ (1990) Si E' centers and UV-induced compaction in high purity silica. *Nucl Instrum Methods Phys Res Sect B* 46:265–268
138. Douillard L, Jollet F, Duraud JP, Devine RAB, Dooryhee E (1992) Radiation damage produced in quartz by energetic ions. *Radiat Eff Defects Solids* 124:351–370
139. Douillard L, Dooryhee E, Duraud JP, Jollet F, Devine RAB (1993) Modifications of the atomic and electronic structure of quartz by high-energy ion irradiation. *Radiat Eff Defects Solids* 126:237–241
140. Buscarino G, Agnello S, Gelardi FM (2009) Structural modifications induced by electron irradiation in SiO₂ glass: local densification measurements. *Europhys Lett* 87:26007–26004
141. Buscarino G, Agnello S, Gelardi FM, Boscaino R (2010) The role of impurities in the irradiation induced densification of amorphous SiO₂. *J Phys: Condens Matter* 22:255403–255407
142. Stesmans A, Cl emer K, Afanas'ev VV (2005) Electron spin resonance probing of fundamental point defects in nm-sized silica particles. *J Non-Cryst Solids* 351:1764–1769
143. Cl emer K, Stesmans A, Afanas'ev VV (2007) Paramagnetic intrinsic point defects in nm-sized silica particles: interaction with SiO at elevated temperatures. *Mat Sci Engin C* 27:1475–1478
144. Stesmans A, Cl emer K, Afanas'ev VV (2008) The E' center as a probe of structural properties of nanometer-sized silica particles. *J Non-Cryst Solids* 354:233–238
145. Stesmans A, Cl emer K, Afanas'ev VV (2005) Electron spin resonance probing of fundamental point defects in nanometer-sized silica particles. *Phys Rev B* 72:155335–155312
146. Stesmans A, Cl emer K, Afanas'ev VV (2008) Primary ²⁹Si hyperfine structure of E' centers in nm-sized silica: probing the microscopic network structure. *Phys Rev B* 77:094130–094112
147. Vaccaro G, Buscarino G, Agnello S, Sporea A, Oproiu C, Sporea DG, Gelardi FM (2012) Structure of amorphous SiO₂ nanoparticles probed through the E'_{γ} Centers. *J Phys Chem C* 116:144–149
148. Roder A, Kob W, Binder K (2001) Structure and dynamics of amorphous silica surfaces. *J Chem Phys* 114:7602–7614
149. Alessi A, Iovino G, Buscarino G, Agnello S, Gelardi FM (2013) Entrapping of O₂ molecules in nanostructured silica probed by photoluminescence. *J Phys Chem C* 117:2616–2622
150. Alessi A, Agnello S, Buscarino G, Gelardi FM (2013) Structural properties of core and surface of silica nanoparticles investigated by Raman spectroscopy. *J Raman Spectrosc* 44:810–816
151. Uchino T, Takahashi M, Yoko T (2001) Structure and formation mechanism of the E'_{α} center in amorphous SiO₂. *Appl Phys Lett* 78:2730–2732
152. Buscarino G, Agnello S, Gelardi FM (2006) ²⁹Si Hyperfine Structure of the E'_{α} center in amorphous silicon dioxide. *Phys Rev Lett* 97:135502–135504
153. Buscarino G (2007) PhD thesis. <http://www.fisica.unipa.it/amorphous/downloads.html>

154. Almaz Optics online catalog.
155. Quartz and Silice, Nemours, France, catalogue OPT-91-3.
156. Starna LTD (Romford England)
157. Tohmon R, Shimogaichi Y, Tsuta Y, Munekuni S, Ohki Y, Hama Y, Nagasawa K (1990) Triplet-state defect in high-purity silica glass. *Phys Rev B* 41:7258-7260
158. Zhang L, Leisure RG (1996) The E'₈ and triplet-state centers in x-irradiated high-purity amorphous SiO₂. *J Appl Phys* 80:3744-3749
159. Nishikawa H, Watanabe E, Ito D, Sakurai Y, Nagasawa K, Ohki Y (1996) Visible photoluminescence from Si clusters in γ -irradiated amorphous SiO₂. *J Appl Phys* 80:3513-3517
160. Zvanut ME, Stahlbush RE, Carlos WE (1992) Radiation-induced E' centers in H₂-annealed oxide films. *Appl Phys Lett* 60:2989-2991
161. Devine RAB, Mathiot D, Warren WL, Fleetwood DM, Aspar B (1993) Point defect generation during high temperature annealing of the Si-SiO₂ interface. *Appl Phys Lett* 63:2926-2928
162. Conley JF, Lenahan PM, Evans HL, Lowry RK, Morthorst TJ (1994) Observation and electronic characterization of two E' center charge traps in conventionally processed thermal SiO₂ on Si. *Appl Phys Lett* 65:2281-2283
163. Warren WL, Fleetwood DM, Shaneyfelt MR, Winokur PS, Devine RAB (1994) Defect-defect hole transfer and the identity of border traps in SiO₂ films. *Phys Rev B* 50:14710-14713
164. Zvanut ME, Chen TL, Stahlbush RE, Steigerwalt ES, Brown GA (1995) Generation of thermally induced defects in buried SiO₂ films. *J Appl Phys* 77:4329-4333
165. Stesmans A, Afanas'ev VV (1996) Annealing induced degradation of thermal SiO₂: S center generation. *Appl Phys Lett* 69:2056-2058
166. Stesmans A, Nouwen B, Pierreux D, Afanas'ev VV (2002) Characterization of S centers generated by thermal degradation in SiO₂ on (100)Si. *Appl Phys Lett* 80:4753-4755
167. Stesmans A, Nouwen B, Afanas'ev VV (2002) Structural degradation of thermal SiO₂ on Si by high-temperature annealing: defect generation. *Phys Rev B* 66:045307-045318
168. Warren WL, Shaneyfelt MR, Schwank JR, Fleetwood DM, Winokur PS, Devine RAB, Maszara WP, McKitterick JB (1993) Paramagnetic defect centers in BESOI and SIMOX buried oxides. *IEEE Trans Nucl Sci* 40:1755-1764
169. Warren WL, Fleetwood DM, Shaneyfelt MR, Schwank JR, Winokur PS, Devine RAB (1993) Excess-Si related defect centers in buried SiO₂ thin films. *Appl Phys Lett* 62:3330-3332
170. Vanheusden K, Stesmans (1993) A Characterization and depth profiling of E' defects in buried SiO₂. *J Appl Phys* 74:275-283
171. Conley JF, Lenahan PM (1995) Electron spin resonance analysis of EP center interactions with H₂: evidence for a localized EP center structure. *IEEE Trans Nucl Sci* 42:1740-1743
172. Lopez N, Illas F, Pacchioni G (2000) Mechanisms of Proton Formation from Interaction of H₂ with E' and oxygen vacancy Centers in SiO₂: cluster Model Calculations. *J Phys Chem B* 104:5471-5477
173. Nicklaw CJ, Lu ZY, Fleetwood DM, Schrimpf RD, Pantelides ST (2002) The structure, properties, and dynamics of oxygen vacancies in amorphous SiO₂. *IEEE Trans Nucl Sci* 49:2667-2673
174. Alemany MMG, Chelikowsky JR (2006) Ab initio calculations for the interconversion of optically active defects in amorphous silica. *Phys Rev B* 73:235211-235215
175. Chavez JR, Karna SP, Vanheusden K, Brothers CP, Pugh RD, Singaraju BK, Warren WL, Devine RAB (1997) Microscopic structure of the E'₈ center in amorphous SiO₂: a first principles quantum mechanical investigation. *IEEE Trans Nucl Sci* 44:1799-1803
176. Pineda AC, Karna SP (2000) Effect of hole trapping on the microscopic structure of oxygen vacancy sites in a-SiO₂. *J Phys Chem A* 104:4699-4703
177. Karna SP, Pineda AC, Pugh RD, Shed WM, Oldham TR (2000) Electronic structure theory and mechanisms of the oxide trapped hole annealing process. *IEEE Trans Nucl Sci* 47:2316-2321

178. Mukhopadhyay S, Sushko PV, Mashkov VA, Shluger A (2005) Spectroscopic features of dimer and dangling bond E' centres in amorphous silica. *J Phys: Condens Matter* 17:1311–1318
179. Mukhopadhyay S, Sushko PV, Edwards AH, Shluger AL (2004) Calculation of relative concentrations of E' centres in amorphous silica. *J Non-Cryst Solids* 345, 346:703–709
180. Karna SP, Pineda AC, Shedd WM, Singaraju BK (1999) Electronic structure studies of the $E'\delta$ and the triplet centers in a-SiO₂. The Electrochemical Society, Pennington. NJ 99-3:161–166
181. Buscarino G, Agnello S, Gelardi FM (2006) Investigation on the microscopic structure of E'_δ center in amorphous silicon dioxide by electron paramagnetic resonance spectroscopy. *Mod Phys Lett B* 20:451–474
182. Buscarino G, Agnello S, Gelardi FM (2005) Delocalized Nature of the E'_δ center in amorphous silicon dioxide. *Phys Rev Lett* 94:125501–125504
183. Buscarino G, Agnello S, Gelardi FM (2006) Hyperfine structure of the $E'\delta$ centre in amorphous silicon dioxide. *J Phys: Condens Matter* 18:5213–5219
184. Buscarino G, Agnello S, Gelardi FM, Parlato A (2007) Electron paramagnetic resonance investigation on the hyperfine structure of the E'_δ center in amorphous silicon dioxide. *J Non-Cryst Solids* 353:518–521
185. Stesmans A, Jivanescu M, Afanas'ev VV (2011) Multi-frequency ESR analysis of the E'_δ defect hyperfine structure in SiO₂ glasses. *EPL* 93:16002–16006
186. Jivanescu M, Stesmans A, Afanas'ev VV (2011) Multifrequency ESR analysis of the E'_δ defect in a-SiO₂. *Phys Rev B* 83:094118–094116
187. Chiodini N, Meinardi F, Morazzoni F, Pelari A, Scotto R, Spinolo G (1998) Identification of Sn variants of the E' center in Sn-doped SiO₂. *Phys Rev B* 58:9615–9618
188. Skuja L, Kajihara K, Hirano M, Saitoh A, Hosono H (2006) An increased F₂-laser damage in 'wet' silica glass due to atomic hydrogen: a new hydrogen-related E' -center. *J Non-Cryst Solids* 352:2297–2302
189. Skuja L, Kajihara K, Hirano M, Hosono H (2012) Oxygen-excess-related point defects in glassy/amorphous SiO₂ and related materials. *Nucl Instrum Methods Phys Res Sect B* 286:159–168
190. Cannas M, Gelardi FM (2004) Vacuum ultraviolet excitation of the 1.9-eV emission band related to nonbridging oxygen hole centers in silica. *Phys Rev B* 69:153201–153203
191. Skuja L, Kajihara K, Hirano M, Hosono H (2011) Visible to vacuum-UV range optical absorption of oxygen dangling bonds in amorphous SiO₂. *Phys Rev B* 84:205206–205209
192. Alessi A, Agnello S, Gelardi FM (2012) Properties and generation by irradiation of Germanium point defects in Ge-doped silica 75–150. In Germano RV (ed) Germanium properties, production and applications. Nova Science Publishers, Inc., New York
193. Neustruev VB (1994) Colour centers in germanosilicate and optical fibers. *J Phys: Condens Matter* 6:6901–6936
194. Watanabe Y, Kawazoe H, Shibuya K, Muta K (1986) Structure and mechanism of formation of drawing- or radiation-induced defects in SiO₂:GeO₂ optical fiber. *Jap J Appl Phys* 25:425–431
195. Friebele EJ, Griscom DL (1986) Color center in glass optical fiber waveguides. *Mat Res Soc Symp Proc* 61:319–331
196. Anokin EV, Guryanov AN, Gusovskii DD, Mashinskii VM, Miroshnichenko SI, Neustruev VB, Tikhomirov VA, Zverev YB (1991) Photoinduced defects in silica glass doped with germanium and cerium. *Sov Lightwave Commun* 1:123–131
197. Itoh H, Shimizu M, Horiguchi M (1986) Observation of defect centers in gamma-ray irradiated GeO₂ glass. *J Non-Cryst Solids* 86:261–264
198. Du J, Corrales LR, Tsemekhman K, Bylaska EJ (2007) Electron, hole and exciton self-trapping in germanium doped silica glass from DFT calculations with self-interaction correction. *Nucl Instrum Methods Phys Res Sec B* 255:188–194
199. Carbonaro CM, Fiorentini V, Bernardini F (2002) Stability of Ge-related point defects and complexes in Ge-doped SiO₂. *Phys Rev B* 66:233201–233204

200. Pacchioni G, Mazzeo C (2000) Paramagnetic centers in Ge-doped silica: a first-principles study. *Phys Rev B* 62:5452–5460
201. Dianov EM, Sokolov VO, Sulimov VB (1991) Theory of germanium-related defects in vitreous silicon dioxide [GeO₄]-center. *Phys Stat Sol (b)* 163:177–182
202. Chiodini N, Meinardi F, Morazzoni F, Paleari A, Scotti R (1999) Optical transitions of paramagnetic Ge sites created by x-ray irradiation of oxygen-defect-free Ge-doped SiO₂ by the sol-gel method. *Phys Rev B* 60:2429–2435
203. Tsai TE, Griscom DL, Friebele EJ, Fleming JW (1987) Radiation-induced defect centers in high-purity GeO₂ glass. *J Appl Phys* 62:2264–2268
204. Griscom DL (2011) On the natures of radiation-induced point defects in GeO₂-SiO₂ glasses: reevaluation of a 26-year-old ESR and optical data set. *Opt Mat Express* 1:401–412
205. Fujimaki M, Watanabe T, Katoh T, Kasahara T, Miyazaki N, Ohki Y, Nishikawa H (1998) Structures and generation mechanisms of paramagnetic centers and absorption bands responsible for Ge-doped SiO₂ optical-fiber gratings. *Phys Rev B* 57:3920–3926
206. Awazu K, Kawazoe H, Yamane M (1990) Simultaneous generation of optical absorption bands at 5.14 and 0.452 eV in 9 SiO₂:GeO₂ glasses heated under an H₂ atmosphere. *J Appl Phys* 68:2713–2718
207. Skuja L (1992) Isoelectronic series of twofold coordinated Si, Ge, and Sn atoms in glassy SiO₂: a luminescence study. *J Non Cryst Sol* 149:77–95
208. Fujimaki M, Kasahara T, Shimoto S, Miyazaki N, Tokuhiro S, Seol KS, Ohki Y (1999) Structural changes induced by KrF excimer laser photons in H₂-loaded Ge-doped SiO₂ glass. *Phys Rev B* 60:4682–4687
209. Alessi A, Agnello S, Grandi S, Parlato A, Gelardi FM (2009) Refractive index change dependence on Ge(1) defects in γ -irradiated Ge-doped silica. *Phys Rev B* 80:014103–014106
210. Alessi A, Agnello S, Gelardi FM, Messina G, Carpanese M (2011) Influence of Ge doping level on the EPR signal of Ge(1), Ge(2) and E'Ge defects in Ge-doped silica. *J Non-Cryst Solids* 357:1900–1903
211. Nishii J, Fukumi K, Yamanaka H, Kawamura K, Hosono H, Kawazoe H (1995) Photochemical reactions in GeO₂-SiO₂ glasses induced by ultraviolet irradiation: comparison between Hg lamp and excimer laser. *Phys Rev B* 52:1661–1665
212. Awazu K, Onuki H, Muta K (1997) Mechanisms of photo-bleaching of 5 eV optical absorption band in hydrogen loaded Ge-doped SiO₂. *J Non-Cryst Solids* 211:158–163
213. Yamaguchi M, Saito K, Ikushima AJ (2002) Formation and relaxation processes of photo-induced defects in a Ge-doped SiO₂ glass. *Phys Rev B* 66:132106–132104
214. Fujimaki M, Katoh T, Kasahara T, Miyazaki N, Ohki Y (1999) Paramagnetic centres induced in Ge-doped SiO₂ glass with UV irradiation. *J Phys: Condens Matter* 11: 2589–2594
215. Essid M, Albert J, Brebner JL, Awazu K (1999) Correlation between oxygen-deficient center concentration and KrF excimer laser induced defects in thermally annealed Ge-doped optical fiber preforms. *J Non-Cryst Solids* 246:39–45
216. Alessi A (2010) PhD thesis <http://www.fisica.unipa.it/amorphous/downloads.html>.
217. Alessi A, Agnello S, Sporea DG, Oproiu C, Brichard B, Gelardi FM (2010) Formation of optically active oxygen deficient centers in Ge-doped SiO₂ by γ - and β -ray irradiation. *J Non-Cryst Solids* 356:275–280
218. Alessi A, Girard S, Marcandella C, Agnello S, Cannas M, Boukenter A, Ouerdane Y (2011) X-ray irradiation effects on a multistep Ge-doped silica fiber produced using different drawing conditions. *J Non-Cryst Solids* 357:1966–1970
219. Alessi A, Agnello S, Gelardi FM, Grandi S, Magistris A, Boscaino R (2008) Twofold coordinated Ge defects induced by gamma-ray irradiation in Ge-doped SiO₂. *Opt Exp* 16:4895–4900
220. Alessi A, Agnello S, Gelardi FM, Boscaino R (2008) Ge-doping dependence of gamma-ray induced germanium lone pair centers in Ge-doped silica. *Phys Stat Sol (b)* 245: 2128–2131
221. Alessi A, Girard S, Cannas M, Agnello S, Boukenter A, Ouerdane Y (2011) Evolution of photo-induced defects in Ge-doped fiber/preform: influence of the drawing. *Opt Exp* 19:11680–11690

Part III
Biochemistry, Biophysics, and Biology
Applications

Chapter 8

Electron Spin Resonance of Radicals in Irradiated DNA

Amitava Adhikary, David Becker and Michael D. Sevilla

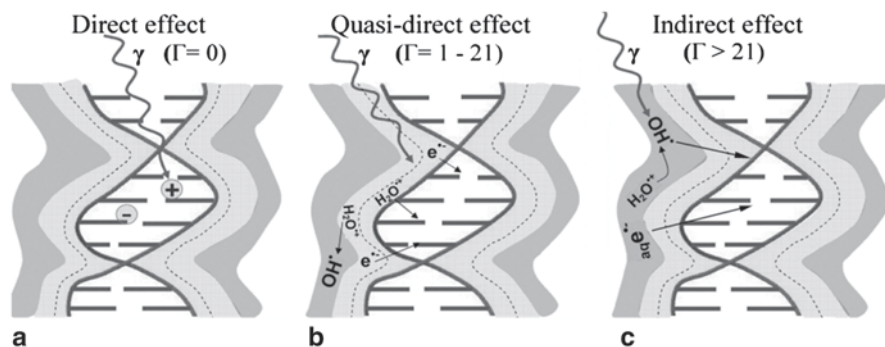
Abstract Ionizing radiation produces DNA-cation radical (hole) and DNA-anion radical formation by random direct ionization of DNA and its microenvironments (e.g., layer of hydration) as well as excitation events. The best overall estimate of the probability of direct ionization at a given site in DNA (e.g., the sugar-phosphate backbone or the DNA bases) is provided by the number of valence electrons at that site. ESR spectroscopic studies at low temperature (e.g., 4 K, 77 K) have provided the direct evidence that via rapid charge (hole and excess electron transfer) processes, the hole is localized on the base of lowest ionization energy, guanine, and the excess electron is localized on the most electron affinic bases—thymine and cytosine. The guanine cation radical may deprotonate, undergo nucleophilic addition reactions such as water addition, or may even cause one-electron oxidation of a proximate sugar radical (double oxidation). The anion radical can undergo reversible as well as irreversible protonations. Also, prior to its thermalization, the prehydrated excess electron leads to frank strand break formation in DNA via dissociative electron attachment. In addition, recent ESR efforts have established that in the excited base cation radical, charge and spin transfer occur to the sugar-phosphate backbone and its subsequent kinetically controlled deprotonation within the lifetime of the excited state leads to the formation of strand break precursor sugar radical. These and other mechanisms of direct-type effect-induced DNA-radical formation that lead to production of stable damage, such as, strand breaks, are discussed in this chapter.

8.1 Introduction

This chapter reviews recent developments in the understanding of free radicals in irradiated DNA as explored by Electron Spin Resonance (ESR) spectroscopy from approximately 2000 to the present. DNA radicals can lead to important biological ramifications. For instance, radicals formed on the DNA sugar-phosphate backbone often result in double-strand breaks (dsb) [1, 2]. Unrepaired radicals on the bases

A. Adhikary (✉) · D. Becker · M. D. Sevilla
Department of Chemistry, Oakland University, Rochester, MI 48309, USA

© Springer International Publishing 2014
A. Lund, M. Shiotani (eds.), *Applications of EPR in Radiation Research*,
DOI 10.1007/978-3-319-09216-4_8



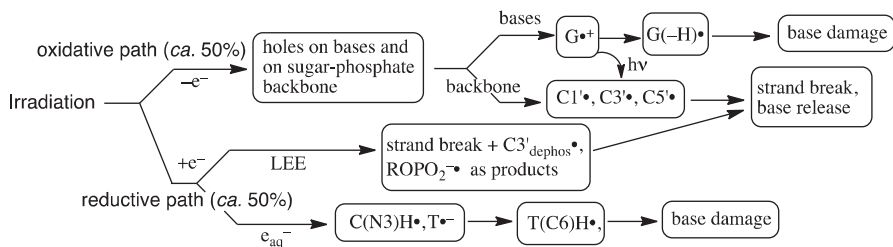
Scheme 8.1 DNA ion-radicals formed by the direct-type effects and indirect effects: **a** Direct effect. Ionization occurs directly on DNA bases or backbone. **b** Quasi-direct effect. Ionization forms holes in water (H_2O^+) which transfer from the first solvation layer of 8–10 waters/nucleotide to the DNA, and electron transfer from the surrounding 21 waters/nucleotide into DNA. **c**. Indirect Effect: Ionization in bulk water ($\Gamma > 21$ H_2O /nucleotide) results in $\cdot OH$, e^-_{aq} , and H^\cdot , which can diffuse to and attack DNA

lead to base damage which may result in mutations on replication [1, 2]. When a dsb and base damage lesions are formed within about 10 base pairs of each other, a damage cluster results [3]. These clustered damage sites are known to have a much greater biological effect than isolated damage sites, as they are the most difficult for the cell to repair and are often lethal [3–5]. Thus, an understanding of the nature of the radical damage in irradiated DNA, and the spatial characteristics of the damage, are highly relevant to an understanding of the biological effects of radiation [1–3].

The principal focus of this review will be on direct-type effect radicals, those that are formed by the direct ionization of the DNA itself (direct effect), or by ionization of water in the first solvation shell of *ca.* 8–10 water molecules (quasi-direct effect) (Scheme 8.1; [1, 2, 6–12]). When the DNA itself is ionized, the initial processes that occur are hole formation and excess electron capture on the DNA bases and backbone. When the first shell waters of solvation are ionized, the holes and electrons formed on the water transfer to the DNA before any chemical reactions occur in these water molecules, resulting in additional hole formation and electron capture on the DNA, very much like the direct effect. This process is called the quasi-direct effect ([1, 6, 7, 11, 12] and Sect. 8.3). Bernhard has described the sum of the direct effect and the quasi-direct effect as direct-type effects [8].

Investigations of the indirect effect (Scheme 8.1c), in which bulk water is ionized and the resulting radicals, principally $\cdot OH$, e^-_{aq} , and H^\cdot (in smaller amounts), diffuse to and attack the DNA have been extensively and comprehensively reviewed [2, 13, 14] and will not be a focus of this review.

With direct-type effects, as with the indirect effect, there are two principal paths of radiation damage (Scheme 8.2), *viz.*, an oxidative path that originates with ionization and hole formation, and a reductive path that originates with electron capture. With low linear energy transfer radiation (X-rays, γ -radiation), ionization at a site in a molecule is roughly proportional to the number of valence electrons at the



Scheme 8.2 Reductive and oxidative paths from irradiation. Only radicals actually observed using ESR are shown. With low LET radiation, the radicals shown are stabilized mostly in spurs at 77 K. However, with high Z ion-beam irradiation, the sugar and backbone radicals are predominantly stabilized in the track core and the base radicals predominantly in the penumbra. T(C6)H• is observed mostly after annealing. As shown, UV-Vis excitation of G^{•+} leads to formation of sugar radicals

site [6, 7, 11]. Thus, as the DNA is irradiated, ionization occurs at all the bases and on the sugar-phosphate backbone. However, fast hole transfer occurs and at 77 K, the majority of holes are stabilized on the base with the lowest ionization energy, guanine. Holes formed on the deoxyribose sugar undergo deprotonation at the sugar in competition with hole transfer to a base. Such fast deprotonation of the sugar results in trapped neutral sugar radicals at 77 K and this occurs for approximately 30% of the original ionizations on the DNA [6, 7, 11, 15, 16]. Recent ESR work has also shown that excited states of DNA cation radicals lead to sugar radical formation and this mechanism may contribute to radiation-induced sugar radical formation (Sect. 8.8.2).

For the reductive path (Scheme 8.2), there are two principal modes of damage. In the first, electrons are captured by the bases with the largest electron affinities, cytosine and thymine. At 77 K, an anionic thymine radical and a reversibly protonated form of the cytosine anion are observed (Sect. 8.5). Irreversible protonations of these anion radicals lead to base damage [1, 2, 6–12]. In the second mode of reductive damage, low energy electrons (LEE) with energies in the range of 0–20 eV add to the sugar-phosphate backbone and cause damage, including strand breaks and base damage through dissociative electron attachment (DEA) and subsequent bond fragmentation ([17–20], and Sect. 8.8.4)

The oxidative and reductive processes are schematically illustrated in Scheme 8.2 in broad stroke. Much of this review will include a delineation of some of the details of these processes that have been uncovered in ESR studies over the last several years.

Irradiation of DNA generally results in the formation of a cohort of radicals from both the reductive and oxidative paths. Computer deconvolution techniques have been employed to identify the individual radicals [1, 6–12, 21–26]. To date, several base and backbone trapped radicals had been identified in irradiated, hydrated DNA at 77 K using ESR techniques (Scheme 8.2). Typically, these radicals are observed by irradiating DNA at low temperatures, usually 77 or 4 K, in order to stop or retard the chemical reactions that they would undergo at higher temperatures. The trapped

radicals can then be observed and characterized, since they remain stable at these low temperatures. Note that even at low temperatures, hole and electron recombination by tunneling does occur on long time scales [1, 2, 6–12]. On annealing, these radicals undergo reactions to form secondary product radicals (Scheme 8.2).

One focus of this chapter will be primarily ESR investigations that characterize the various reaction pathways that lead to secondary radicals. The structural formulae of the trapped DNA-radicals at 77 K and some secondary DNA-radicals are shown below in Scheme 8.3. Note that although both σ and π radicals are found in DNA bases, only π radicals are found in DNA-oligomers and in long polymeric DNA (e.g., salmon testes) [27].

8.2 Trapped Radicals at 77 K in Irradiated DNA

8.2.1 Analyses of 77 K ESR Spectra of γ -Irradiated (77 K) DNA Using Benchmark Spectra

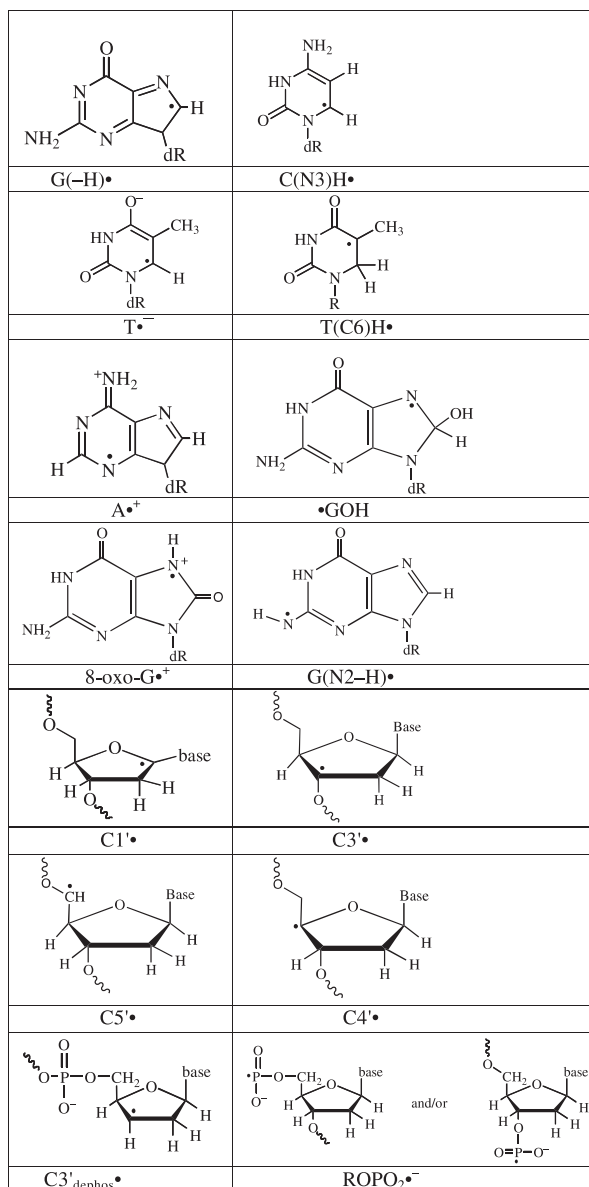
The cohort of stabilized radicals trapped in hydrated DNA at 77 K after irradiation at the same temperature has been extensively studied using ESR spectroscopy [1, 2, 6–12, 25, 26]. A representative ESR spectrum of γ -irradiated DNA hydrated to $\Gamma = 12 \pm 2$ D₂O/nucleotide is shown in Fig. 8.1 spectrum A. The benchmark spectra of the individual radicals required to analyze this spectrum are also shown in spectra B–E.

A number of studies use linear least square fittings of the benchmark spectra shown to determine the fractional composition of individual DNA-radicals in experimental spectra [6–12, 15, 16, 21–36]. The percentage that a particular benchmark spectrum contributes to an overall spectrum is based on the double integrated area of the spectra which is itself directly proportional to the total numbers of each radical. The benchmark spectra used were those from G(N1–H)[•], or more precisely, G(N1–H)[•]:C(+H⁺) from d[GCGCGCGC]₂ [30, 31], thymine anion radical (T^{•-}) from 5'-TMP [32], N3-protonated cytosine anion radical (C(N3)H[•]) from polydG: polydC [28, 29, 32], and of a cohort of backbone radicals (C1'', C3'', C5'', C3''_{dephos}) labeled Σ S[•] [6, 7, 11, 12, 15, 16, 28–35]. When employed to deconvolute the spectrum of γ -irradiated DNA the G-values shown in Table 8.1 are obtained [11, 15]. These are estimated to have an error limit of $\pm 10\%$ [11, 15, 29, 30].

In Table 8.2, the G-values in $\mu\text{mol/J}$ of the total trapped radicals in various irradiated DNA systems are presented. The estimated value of ionizations occurring within 10^{-15} – 10^{-16} s after irradiation is $1.2 \mu\text{mol/J}$ [25], so it is evident that significant recombination occurs before radical trapping at 77 K.

From Tables 8.1 and 8.2, the following important conclusions could be drawn.

1. The identities and compositions of the trapped radicals found at 77 K are due to electron and hole transfer (see Sects. 8.2.3 and 8.4) taking place after the irradiation [1, 2, 6–12, 25, 26].

Scheme 8.3 Structures of DNA-radicals discussed in this chapter

- The G-values of trapped radicals are strongly dependent on the hydration level of the DNA. They increased by a factor of about 2 from $\Gamma=2.5$ to 14 for salmon testes DNA, and from $\Gamma=2.5$ to 22.5 for pUC18 plasmid DNA. This indicates that the DNA hydration layer plays a role in determining the extent of recombination and charge transfer after hydration (Sect. 8.2.2).

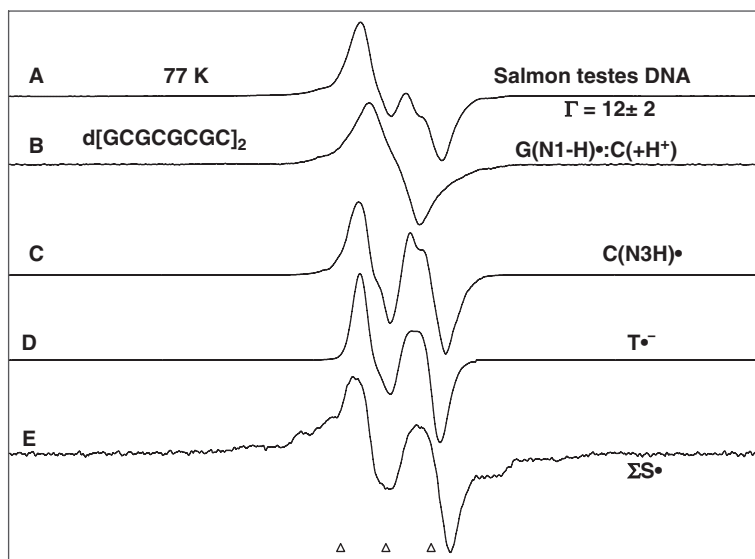


Fig. 8.1 **a** ESR spectrum recorded at 77 K of γ -irradiated (8.8 kGy) hydrated ($\Gamma = 12 \pm 2$ D₂O/nucleotide) DNA after irradiation at 77 K [28]. **b–e** are the benchmark spectra of various DNA-radicals. **b** Intra-base pair proton transferred form of the guanine cation radical G(N1-H) \cdot :C(+H \cdot) [30]. **c** N3-protonated cytosine anion radical (C(N3H) \cdot) (one-electron reduced cytosine) [32]. **d** Thymine anion radical (T \cdot ⁻) (one-electron reduced thymine) [32]. **e** Mixture of neutral sugar-phosphate backbone radicals [16]. The three reference markers in this figure and in subsequent figures are Fremy's salt resonances with $g = 2.0056$ and $A_N = 13.09$ G

3. The G-values also strongly depended on the temperature of trapping with higher G values at 4 K than 77 K, likely as a result of increased trapping efficiency.
4. The G-values of the trapped radicals for plasmid DNA (e.g., pUC18) are found to be higher than those found in polymeric DNA. This was attributed to the packing of supercoiled plasmid DNA [8, 38].
5. Most importantly, in comparison to the estimated value of ionization events occurring within 10^{-15} – 10^{-16} s after irradiation, 1.2 $\mu\text{mol/J}$ [25], the G-values of the trapped radicals are always found to be significantly lower and this has been attributed to the recombination events of the initially formed radicals.

Table 8.1 Percentage composition of trapped radicals in γ -irradiated hydrated DNA at 77 K^a

Radical	Type	G-value ($\mu\text{mol/J}$) ^{b,c}	Percent composition ^{a,b}
G(N1-H) \cdot	Electron-loss	0.11	43 [58]
Sugar radicals ^d		0.034	13
T \cdot ⁻	Electron-gain	0.055	22 [47]
C(N3)H \cdot		0.055	22
C3 \cdot _{dephos}		–	~0.5 ^c
ROPO ₂ \cdot ⁻		–	0.02–0.04

^a $\Gamma = 14 \pm 2$ D₂O/nucleotide; ^b Based on the total sample mass; ^c Ref. [11] and [15]

^d Sum of C1 \cdot , C3 \cdot , C5 \cdot ; ^e Ref. [34]

Table 8.2 G-values of total trapped radicals in irradiated DNA

DNA Type	Γ (D ₂ O or H ₂ O/nucleotide)	G-value ($\mu\text{mol/J}$)	Irradiation	Ref.
Salmon testes	14 \pm 2	0.25	γ (77 K)	[15]
Salmon testes	2.5	0.13	γ (77 K)	[36]
Herring sperm	“Desiccated residual H ₂ O”	0.41	X-ray (4 K)	[37]
Calf thymus	“Desiccated”	0.29	X-ray (4 K)	[37]
pUC18	2.5	0.302	X-ray (4 K)	[38]
pUC18	22.5	0.718	X-ray (4 K)	[38]

8.2.2 Effect of Hydration on the Yield of the Trapped Radicals

Bernhard and coworkers studied the role of hydration in the distribution of free radicals trapped in directly ionized solid-state films of pUC18 (2686 bp) plasmids hydrated in the range of $\Gamma=2.5$ to 22.5 waters per nucleotide [8, 38]. Based on a semi-empirical model of damage, they suggested that two-thirds of the holes formed on the inner solvation shell (first 10 waters of hydration) transfer to the sugar-phosphate backbone [8, 38]. Of the holes directly formed on the sugar-phosphate backbone, about one-third deprotonate to form neutral sugar-phosphate radical species, while the remaining two-thirds transfer to the bases. The authors use these values to predict that the distribution of holes formed in fully hydrated DNA at 4 K will be 78% on the bases and 22% on the sugar-phosphate [8, 38]. Including the reductive pathway (anion radicals on thymine and cytosine), the distribution of all trapped radicals is predicted to be 89% on the bases and 11% on the sugar-phosphate backbone [8, 38]. These results are in good agreement with previous results found at 77 K [15] which reported 12% sugar phosphate backbone radicals, 88% on the bases.

8.2.3 Analyses of 77 K ESR Spectra of γ -Irradiated (77 K) DNA-Hole and -Electron Scavengers

Use of Ferricyanide $[\text{Fe}(\text{CN})_6]^{-3}$ as an electron scavenger in irradiated DNA was pioneered by Weiland and Hüttermann [21, 22]. We note here that the effect of binding of Fe (III) as well as that of Fe(II) were studied in DNA employing circular and linear dichroism [39]. Employing uncomplexed ferric ion it has been found that at levels of one Fe(III) per 60 base pairs (bp), the Fe(III) captured 70% of the radiation-produced electrons at 77 K in a γ -irradiated (77 K) frozen aqueous solution of DNA [39]. Moreover, warming this sample to 200 K did not result in TH[•] formation [39]. This work is complicated by the fact that uncomplexed Fe(III) causes changes in DNA structure, whereas ferricyanide is less likely to do so.

Following these works, Shukla et al. [15] employed the electron scavenger ferricyanide, Fe(III), and hole scavenger ferrocyanide, Fe(II) to scavenge electrons and holes in γ -irradiated hydrated ($\Gamma=14\pm 2$ D₂O/nucleotide) DNA to isolate and to determine the yield of backbone radicals (Fig. 8.2).

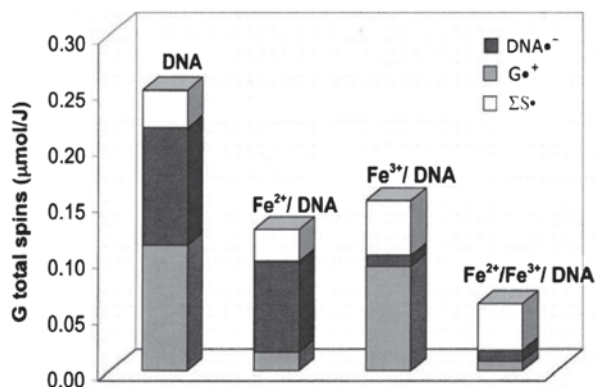


Fig. 8.2 The relative yields of DNA anion radicals ($T^{\cdot-}$ and $(C(N3)H^{\cdot})$) guanine cation radical, $G(N1-H)^{\cdot+}:C(+H^+)$ (or $G^{\cdot+}$) and sugar radicals, ΣS^{\cdot} for DNA and DNA with scavengers for holes, Fe (II), electrons, Fe(III), and both holes and electron, Fe(II)/Fe(III), Fe(II) and Fe(III) represent ferro- and ferricyanide respectively. Adapted with permission from Ref. [15], *Radiation Research*, Copyright (2005), Radiation Research Society

The loading of 1 scavenger/20 bp has been found to nearly completely remove trapped electrons or holes from DNA [15]. Employing both scavengers, a spectrum due to predominantly neutral sugar radicals is obtained (Fig. 8.1e) [15]. The spectrum of the sugar radicals is reported to be an overlap of the spectra of a number of radicals on the sugar-phosphate backbone including the $C1''$, $C3''$, $C5''$ formed by deprotonation of sugar cation radicals as well as radicals resulting from LEE-induced cleavage of the phosphate-sugar link e.g., $C3''_{\text{dephos}}$ (Table 8.1, Scheme 8.3; [15, 16, 33]). Analyses employing benchmark spectra for the sugar radicals, $C1''$, $C3''$, $C5''$, and $C3''_{\text{dephos}}$ have indicated that $C5''$ which gives rise to the central anisotropic doublet (ca. 21 G) accounts for a substantial part (ca. $40 \pm 10\%$) of the intensity of the spectrum [16]. This $C5''$ spectrum does not show observable β H-atom at $C4'$ or β P-atom hyperfine coupling; this result predicts that the phosphate group lies near the nodal plane of the radical site p-orbital in its equilibrium position accounting for the lack of β -P atom coupling [16]. This is supported by theoretical calculations by Close [40] and Colson et al. [41, 42] and the ESR and theoretical work on $CH_3OP(O_2^-)OCH_2^{\cdot}$ produced from dimethyl phosphate [16].

It is evident from Fig. 8.2 that, compared to DNA alone, an increased amount of trapped sugar radical formation was observed in irradiated DNA in the presence of Fe(III). However, a slight decrease in the amount of trapped sugar radical formation was observed in the presence of Fe(II). This suggests that the initial sugar cation radicals are likely to be protected from recombination with excess electrons produced via ionizations by electron scavenging due to ferricyanide; whereas, the ferrocyanide does not significantly reduce the levels of the final neutral sugar radical by electron donation to its precursor sugar cation radical before the cation radical deprotonates to form the neutral sugar radical.

8.3 ESR Studies of the Hydration Layer

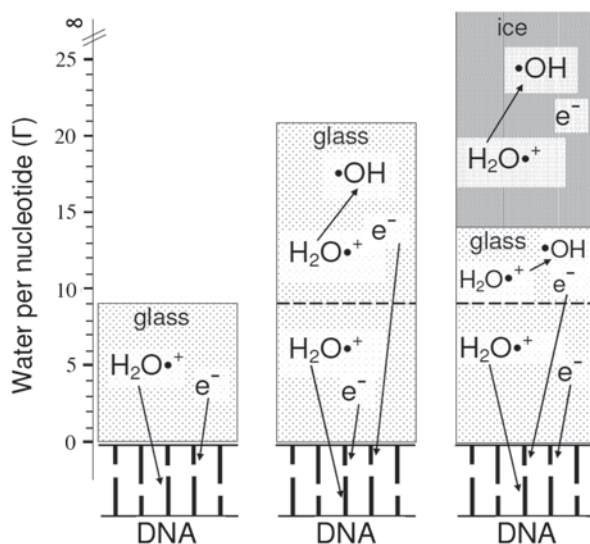
The hydration layer is a critical component of the direct-type effect and its detailed radiation chemical behavior is of fundamental importance to elucidate the processes involved in radiation damage to DNA.

Using ESR spectroscopy, Gregoli and co-workers were the first to point out that hole and electron transfer from the hydration layer can increase the radiation yields of DNA-radicals up to double [43]. Subsequently, measurements of electrical conductivity in solid DNA by van Lith and co-workers had shown that the conductivity of the pre-solvated (or “dry”) electrons depend critically on the water content and temperature [44].

A number of ESR groups have, thereafter, investigated the radiation behavior of the DNA hydration layer in γ -irradiated hydrated highly polymerized DNA (e.g. “salmon testes”) at 77 K [6, 45–52] and in X-ray irradiated defined double stranded (ds) oligomers at 4 K [53] and provided important insights which distinguish the nature of the water molecules with increase in Γ (Γ = number of water molecules per nucleotide). Note that Γ ranging from 0 to 2.5 is not experimentally accessible [54]. These ESR works have established that at low temperatures the hydration layer is critical to DNA damage process. For $\Gamma = 1$ –21, the waters of the primary hydration shell around DNA are in an amorphous non-crystalline state (glassy) [48–50, 52]. Once freezing begins ($\Gamma > 21$), ice is formed in a separate phase including all waters beyond 14 waters/nucleotide (Fig. 8.3). These ice phase waters do not significantly contribute to DNA damage at low temperatures. At elevated temperatures, they contribute to the indirect effect (Scheme 8.1). Thus, waters at $\Gamma = 15$ –21 form a metastable glassy state until waters beyond $\Gamma = 21$ are added and on cooling crystallization occurs to form the stable boundary between glassy phase and ice phase DNA at $\Gamma = 14$ that does not change with additional water addition [7–12]. Thus, waters around DNA can be classified into three regions—glassy ($\Gamma = 1$ –14), metastable glass ($\Gamma = 15$ to 21) and ice phase ($\Gamma > 21$) [7–9]. We note that these ESR studies are corroborated by investigations of the OH-stretching frequencies in hydrated DNA films that have clearly established that there is distinct primary hydration shell of ca. 21 water molecules per nucleotide around DNA of which the first six water molecules are directly bound to the sugar-phosphate backbone—two are bound to the ionic phosphates along with four are bound to phosphodiester bond along with the furanose sugar moiety; another 6 to 8 water molecules are less tightly bound to the bases (e.g. to $>C=O$, N, $-NH$, $-NH_2$) [54].

The trapped $\cdot OH$ formation at 77 K either in γ -irradiated hydrated DNA or in X-ray irradiated hydrated crystals of double stranded oligomers was found to be crucially dependent on Γ [48–50, 53]. Both hole and electron (charge) transfer occur between the inner hydration shell ($\Gamma < 9$) to DNA [48–53]. At $\Gamma \leq 9$, no significant amount of trapped $\cdot OH$ formation at 77 K was detected [48, 49, 53]. Thus, the most tightly bound of waters do not lead to trapped $\cdot OH$ formation at 77 K and this is in agreement with the original proposition of Gregoli and co-workers [43] that

Fig. 8.3 Schematic diagram showing processes involved in radiation behavior of DNA hydration layer with waters per nucleotide (Γ). For Γ ca. 1 to 9 both holes and electrons transfer to DNA. From ca. $9 < \Gamma < 21$, electrons transfer to DNA and holes form $\cdot\text{OH}$ that show ESR amorphous (glassy) phase ESR spectra (Figs. 8.4 and 8.5). For samples with $\Gamma > \text{ca. } 21$ waters form a crystalline ice phase that freezes back to $\Gamma = 14$. $\cdot\text{OH}$ for all waters of hydration $\Gamma > 14$ show ESR spectra indicative of $\cdot\text{OH}$ in a crystalline ice environment (Figs. 8.4 and 8.5)

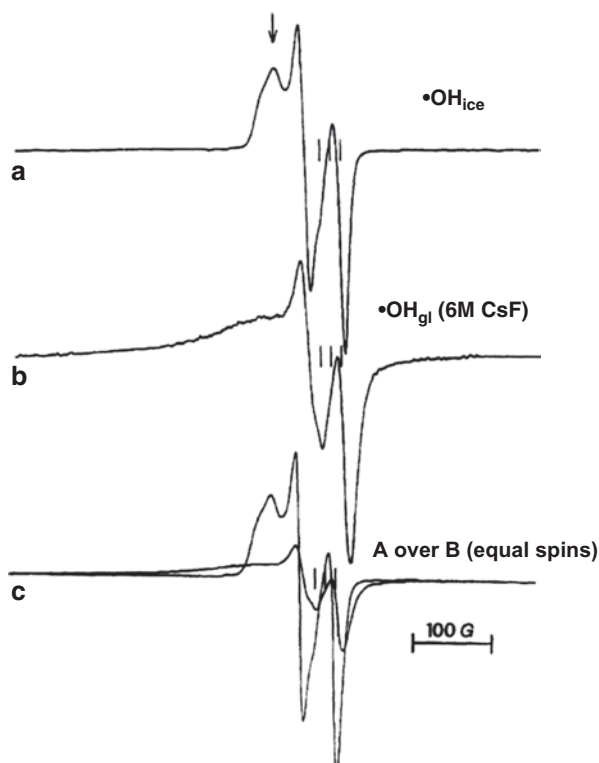


charge transfer processes are the primary mode of damage transfer process between hydration shell and DNA.

From ESR studies in γ -irradiated hydrated DNA ($\Gamma = 2.5\text{--}76$ [48–50]) and in X-ray irradiated hydrated crystals of ds oligomers ($\Gamma = \text{ca. } 4.2\text{--}15.6$ [53]), trapped $\cdot\text{OH}$ formation at 77 K was detected at $\Gamma > 9$. From $\Gamma = 10$ to up to 21 the glassy hydroxyl radical ($\cdot\text{OH}_{\text{gl}}$) is found with a characteristic glassy amorphous ESR spectrum (Figs. 8.4 and 8.5) [48, 49]. On the other hand, for $\Gamma > 21$, the ice phase appearance results in $\cdot\text{OH}_{\text{ice}}$ (Figs. 8.4 and 8.5; [48, 49]). It is evident from Figures 8.4 and 8.5 and from the original work [48, 49] that the ESR spectra of $\cdot\text{OH}_{\text{gl}}$ and $\cdot\text{OH}_{\text{ice}}$ are markedly different and allow for the distinction of the two phases.

As shown in Fig. 8.3, electron transfer occurs from all waters in glassy states up to $\Gamma = 21$ [48–50]. No significant electron or $\cdot\text{OH}$ transfer occurs from ice phase whose crystalline boundaries maintain a radiolytically separate phase [48–50]. However, $\cdot\text{OH}$ formed in the glassy portion of the DNA hydration shell likely reacts with DNA and results mostly in $\cdot\text{OH}$ addition to bases thereby forming base damage products and also in H-atom abstraction from the sugar-phosphate backbone producing DNA strand breaks and abasic sites (Sect. 8.1). It is of interest to note that hole transfer from the inner hydration layer ($10 < \Gamma < 14$) to DNA bases (predominantly guanine) acts to prevent formation of $\cdot\text{OH}$ and its subsequent attack on to DNA [46–53]. Thus, instead of strand break formation, formation of a hole on guanine results in the formation of more easily repaired 8-oxo-G (Sect. 8.6).

Fig. 8.4 ESR spectra of **a** trapped $\cdot\text{OH}_{\text{ice}}$ at 77 K in polycrystalline ice; **b** trapped $\cdot\text{OH}_{\text{gl}}$ at 77 K in 6 M CsF; **c** superimposition of $\cdot\text{OH}_{\text{ice}}$ spectrum in **(a)** on to spectrum of $\cdot\text{OH}_{\text{gl}}$ **(b)** representing higher signal height for **(a)** than for **(b)** provided the number of spins are equal. Reprinted with permission from Ref. [49], *Radiation Research*, Copyright (1996) Radiation Research Society

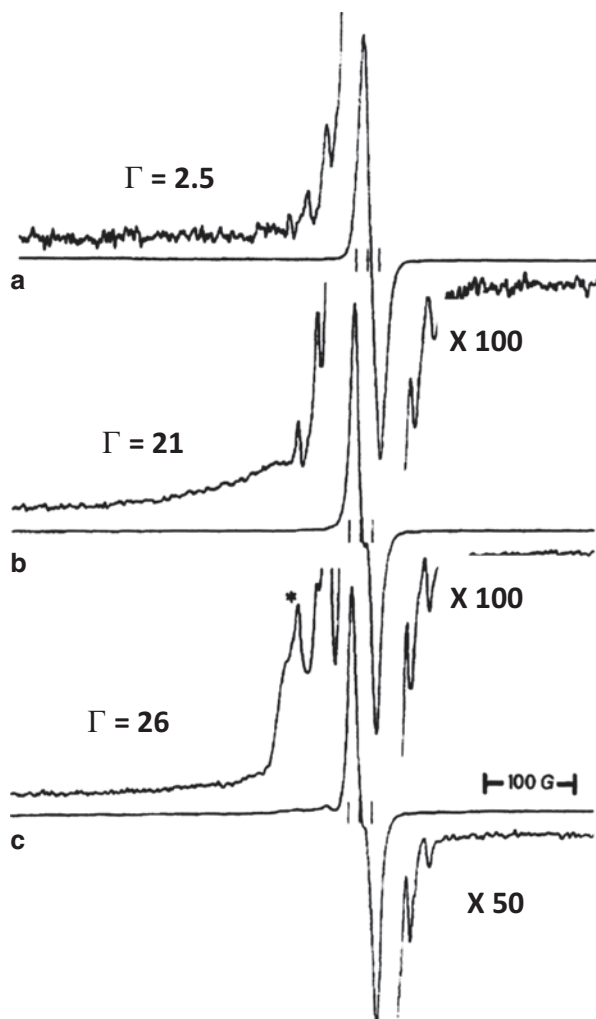


8.4 ESR Studies of Charge and Spin Transfer Through DNA

8.4.1 Is DNA a “Molecular Wire”?

ESR has played a significant role in aiding the understanding of hole and electron transfer after direct ionization of DNA. These studies have shown that radiation produced electrons and holes are trapped at low temperatures in irradiated DNA systems with an efficiency of between 30 and 60% depending on the state of the DNA (hydrated, dry, crystalline or amorphous) [1, 6–12, 25, 26, 52]. Bernhard and coworkers [8, 25, 55], observed that crystalline oligomers at 4 K showed the highest trapping levels and pointed out that hole and electron migration at 4 K must be limited to *ca.* 10 bp [55]. They concluded that DNA cannot be considered a true “molecular wire” under these conditions for, if it were, long range hole and electron transfer would result in highly efficient hole-electron recombination and no trapped radicals would be found.

Fig. 8.5 ESR spectra of DNA samples at various Γ at 77 K. **a** $\Gamma=2.5$, no line component due to $\cdot\text{OH}_{\text{gl}}$ is present. **b** $\Gamma=21$, the low field broad line component due to $\cdot\text{OH}_{\text{gl}}$ is present and sharp line component due to $\cdot\text{OH}_{\text{ice}}$ is absent. **c** $\Gamma=21$, line components (marked by asterisks) due to both $\cdot\text{OH}_{\text{gl}}$ and $\cdot\text{OH}_{\text{ice}}$ are present. Reprinted with permission from Ref. [49], *Radiation Research*, Copyright (1996) Radiation Research Society



8.4.2 Tunneling vs. Activated Hopping

Work by Sevilla and coworkers has suggested that for hydrated DNA at 77 K all ions within 3 nm of each other recombine by tunneling within a minute, and the remainder undergoes only slow recombination on a longer time scale [6, 7, 52, 56–61]. At higher temperatures, activated (hopping) processes account for the longer range transfer found in so many studies [6, 7, 52, 56–65].

8.4.2.1 Electron and Hole Transfer to Mitoxantrone

ESR work by Cai and Sevilla [6, 7, 52, 56–60] employing mitoxantrone (MX) at intercalating trapping sites in DNA further delineated the distance dependent role of

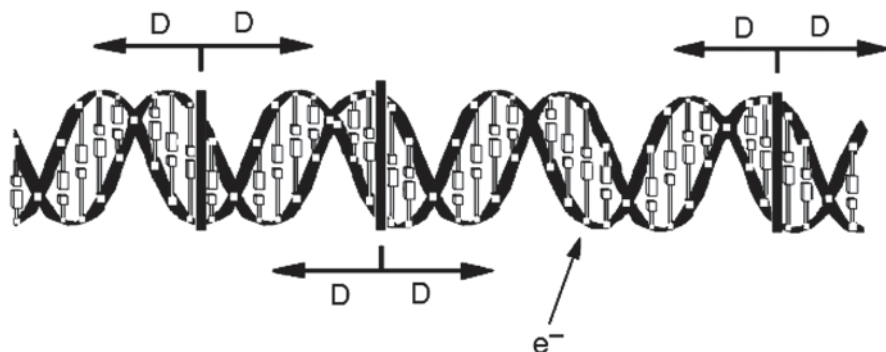


Fig. 8.6 Diagram depicting random MX intercalator and the scavenging range, D . D is time dependent and extends outward in time following a log relationship: $D(t) = (1/\beta) \ln(k_0 t)$. Adapted with permission from Ref. 56, *J. Phys. Chem. B*, Copyright (2000), American Chemical Society

Table 8.3 Distance decay constants for electron tunneling to MX in DNA-MX systems at 77 K

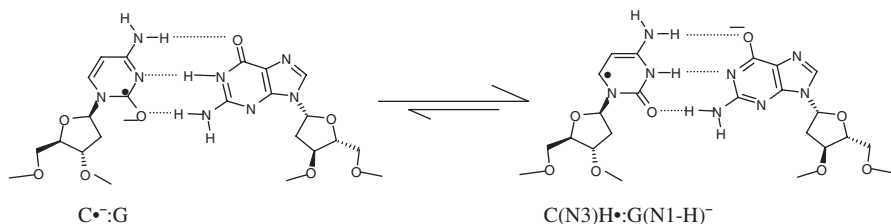
DNA system ^a	Medium	Donor site ^b	β (\AA^{-1})
DNA (ST)	D ₂ O glass	T \rightarrow • + CD•	0.9
DNA (ST)	H ₂ O glass	T \rightarrow • + CD•	0.8
polydAdT	D ₂ O glass	T \rightarrow •	0.75
polyIdC	D ₂ O glass	CD•	1.4
polyG polyC	D ₂ O ice	CD•	0.8
DNA (ST)	D ₂ O ice	T \rightarrow • + CD•	0.7

^a ST=salmon testes

^b C(N3)D• is the N3 protonated cytosine anion radical

tunneling at low temperatures in DNA, and also showed that at $\geq ca.$ 200 K activated processes occurred. They found evidences of intra-duplex and inter-duplex electron transfer, and, quantified the distance dependent transfer between DNA duplexes. At low temperatures, transfer of holes and electrons occurred by tunneling only and the rate was found to be the same at 4 K and 77 K, (as expected for tunneling [52]).

The transfer rates and distances followed the expected tunneling decay constant expression for the rate constant, i.e., $k = k_0 e^{-\beta D}$, where D is the tunneling distance and β is the decay constant (Fig. 8.6). The decay constants for electron transfer and hole transfer were found to be sequence and environment dependent [6, 7, 52, 56–60]. The value of β for excess electron transfer to a trapped MX [6, 7, 52, 56–60] in a variety of DNA systems in glasses (7 M LiCl) and frozen water solutions (ice) is shown in Table 8.3. Note that the electron transfer rates increase as β decreases. The value of β for electron transfer was relatively constant with various oligomers and conditions except for the sequence polyIdC. In this case, the transfer rates were much slower. This was explained by noting that the proton transfer from I to the reversibly deuterated C anion radical [C(N3)D•] was substantially more downhill energetically than in the other systems studied, which provided for a significant barrier to further electron transfer. Thus, this downhill proton transfer acted as a barrier for further electron transfer [6, 7, 52, 56–60]. For GC anion radical (Scheme 8.4),



Scheme 8.4 Prototropic equilibrium of GC anion radical

the rate of electron transfer was less affected because the proton transfer was less downhill and was reversible [6, 7, 52, 56–60].

8.4.2.2 Inter-Duplex Charge Transfer

Studies of electron transfer at different levels of hydration [6, 7, 52, 57] showed that the rates of transfer varied with the distances between duplexes (Fig. 8.7). Thus, the electron transfer rate from a DNA base ion-radical to a MX trapping site decreased with increasing intervening waters of hydration between DNA duplexes [57]. As can be seen, the tunneling transfer rate was strongly (exponentially) dependent on the interduplex distance so that a quantitative treatment allowed for the estimation of interduplex distances. By replacing the sodium counterion of MX-DNA with various aliphatic amine cations, e.g., spermine tetrahydrochloride (SP), dodecyltrimethylammonium bromide (DOD), and octadecyltrimethylammonium bromide (OCT) and polymeric amine cations, e.g., poly-L-lysine hydrobromide (PLL) and polyethylenimine hydrochloride (PEI) Cai et al. [52, 59] varied the separation between DNA duplexes. The radiation-produced electrons from these complexing agents were found to be readily transferred to the more electron affinic DNA. They also found that the addition of a second layer of aliphatic amine cations further suppressed the transfer of DNA radicals to near that found for isolated DNA duplexes [52, 59]. Thus, they quantified the distance dependent electron transfer between DNA double strands [59].

Electron spin resonance studies showed that as the temperature was increased from 77 K to near 200 K, the rate of activated processes (hopping) became clearly dominant over tunneling [1, 2, 6–12, 25, 26, 52, 62]. At room temperature, since tunneling is only competitive over short ranges, long range charge transfer takes place by hopping combined with tunneling [1, 2, 6–12, 25, 26, 52, 62]. Studies of electron and hole transfer rates at ambient conditions using pulse radiolysis, laser flash photolysis and steady state photolysis coupled with strand break measurements have provided strong evidence for long range hole transfer of 100 bp and more [1, 2, 6–12, 25, 26, 52, 66–70].

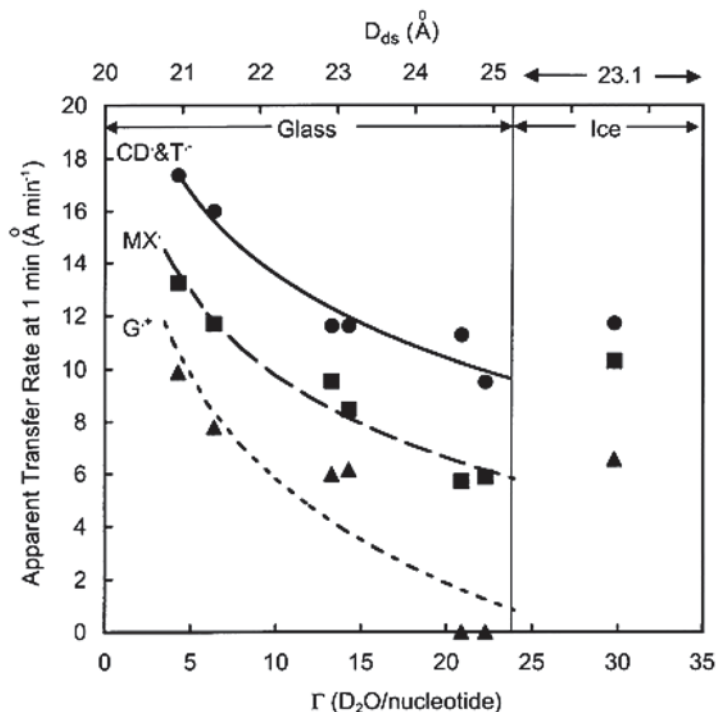


Fig. 8.7 Combined Intra- and Inter-duplex strand transfer rate. The transfer rate of excess electrons, holes to MX in DNA at 77 K as a function of Γ is shown. The distance between DNA duplexes increases with hydration and slows the inter duplex electron and hole transfer rates. Ice formation at 30 waters/nucleotide forces the DNA together with 14 waters/nucleotide between them in the amorphous phase. The accompanying increase in transfer rates provides striking evidence of inter-duplex charge transfer. Reprinted with permission from Ref. [59], *J. Phys. Chem. B*, Copyright (2001), American Chemical Society

8.5 General Reactions of Stabilized (or Trapped) DNA Ion-Radicals (Cation and Anion Radicals)

Direct-type effects produce (Scheme 8.1), both DNA-cation radicals ($\text{DNA}^{\bullet+}$) and DNA-anion radicals ($\text{DNA}^{\bullet-}$). $\text{DNA}^{\bullet+}$, is, in general, much stronger proton donor, i.e., a stronger Brönsted acid and $\text{DNA}^{\bullet-}$ is a stronger proton acceptor, i.e., a stronger Brönsted base, than their parent compounds [2, 71, 72]. The prototropic equilibria of $\text{DNA}^{\bullet+}$ and $\text{DNA}^{\bullet-}$ will be explored in this section. Of special interest will be specific examples in which the prototropic equilibria are between the base pairs.

For $\text{DNA}^{\bullet+}$, deprotonation [70] competes with electrophilic addition by a proximate nucleophile, either an anion such as OH^- or a neutral molecule such as H_2O [72]. As an example, an ESR spectroscopic study of 3-methylthymidine cation radical ($\text{N}^3\text{-Me-Thd}^{\bullet+}$) at pH *ca.* 7 and at *ca.* 160 K shows *ca.* 70% irreversible

deprotonation from the methyl group at C5 in the base moiety and *ca.* 30% OH⁻/H₂O addition also at C5. At pH near 7, reversible deprotonation is the main reaction that DNA^{•+} undergoes [1, 2, 6–12, 25, 26, 73]. However, at pHs *ca.* 9 and 12, the OH⁻/H₂O addition to N3-Me-Thd^{•+} at C5 in the base moiety prevails over the deprotonation [73].

DNA⁻ undergoes both reversible and irreversible protonations [1, 2, 6–12, 25, 26]. For example, C(N3)H[•] is produced via reversible protonation at N3 of C⁻ from N1 of the complementary base guanine (Scheme 8.4), and the driving force for this protonation was shown to be an enthalpy change of -52 kJ/mol [8, 25]. ESR/ENDOR studies employing X-ray irradiated (4 K) single crystals of cytosine monohydrate have shown that even at 4 K, C⁻ is protonated at N3. Thus, it is not surprising that C⁻ has not been observed in DNA [8, 25].

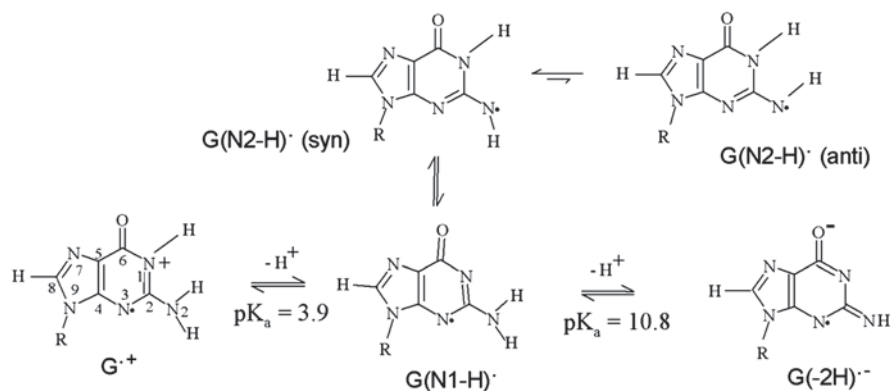
T⁻ in dsDNA, unlike C⁻, does not undergo a similar reversible protonation reaction [74]. We note here that all DNA base anion radicals as free bases have been shown to undergo irreversible protonations at carbon sites [75]. In DNA, owing to electron tunneling (Sect. 8.4), the excess electrons are localized onto the electron affinic pyrimidine bases C⁻ and T⁻, so that G⁻ and A⁻ are not observed even at 4 K [1, 6–12, 25, 26]. However, upon annealing from 77 K to 130 K, the T⁻ population was shown to decrease from *ca.* 50 to 25% with a concomitant increase in C(N3H)[•] indicating that electron transfer occurs from T⁻ to C [76]. Upon further annealing, T⁻ is observed to undergo irreversible protonation from solvent to produce the C6 hydrogen adduct, T(C6)H[•] (Scheme 8.2). T(C6)H[•] was the earliest identified and the most well-investigated radical by ESR studies of irradiated DNA [77].

8.5.1 Prototropic Equilibria of G^{•+} in Various Model Systems

The acid-base characters of the DNA ion-radicals are manifested in their pK_a values. These pK_a values have been extensively studied in aqueous solutions at ambient temperatures using pulse radiolysis [2, 71]. Recently, a combination of systematic ESR and UV-VIS absorption spectroscopic studies have been undertaken to study the prototropic equilibria of DNA cation-radicals in different DNA-model systems, monomers [29, 78–80], ss DNA-oligomers [29, 79], and dsDNA-oligomers [29, 81, 82]. These results have been summarized in recent reviews [11, 12].

8.5.1.1 Prototropic Equilibria of G^{•+} in Monomers

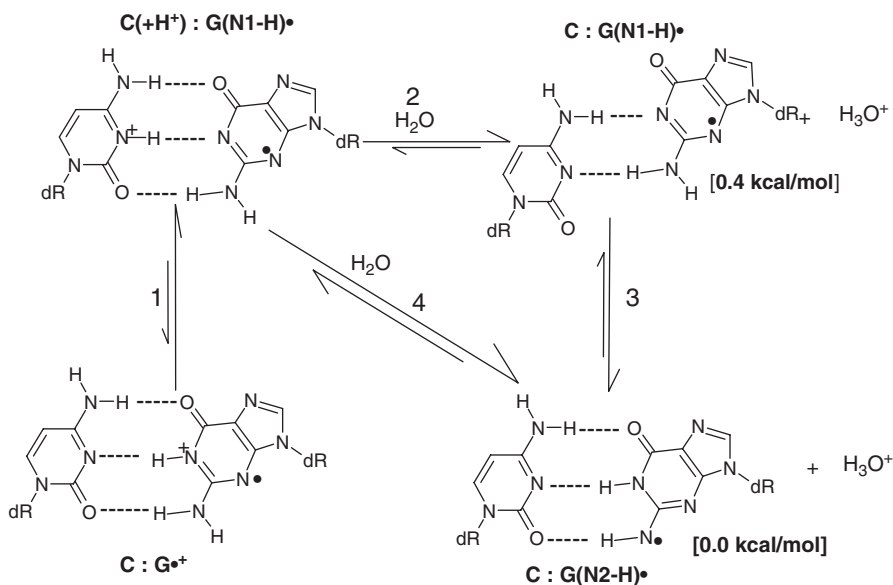
Using pulse radiolysis of various analogs of dGuo, Steenken proposed that G^{•+} in dGuo by deprotonation from N1 at pH 3.9 to give G(N1-H)[•] and then G(-2H)⁻ via a second deprotonation from the exocyclic N-atom (N2) at pH > 10.8 (Scheme 8.5) [2, 71]. Moreover, in nucleotides of dGuo (e.g., 5'-dGMP), the phosphate group at 5' did not significantly affect the prototropic equilibria shown in Scheme 8.5 [2, 71]. Steenken and his co-workers obtained the pK_a value of G^{•+} in dGuo as well as that



Scheme 8.5 The prototropic equilibria of guanine cation radical ($G^{+\bullet}$), its mono-deprotonated species ($G(N1-H)^\bullet$ and $G(N2-H)^\bullet$), in syn and anti-conformers with respect to the N3 atom and the di-deprotonated species ($G(-2H)^{\bullet-}$) along with the numbering scheme of $G^{+\bullet}$ are represented. Adapted with permission from Ref. [78], *J. Phys. Chem. B*, Copyright (2006), American Chemical Society

of the exocyclic amine group in 1-methylguanosine cation radical (1-Me-Guo $^{+\bullet}$) in aqueous solutions at ambient temperature as *ca.* 3.9 and *ca.* 4.7 respectively [2, 71]. The closeness of these two pK_a values implies that, for $G^{+\bullet}$ in dGuo, the deprotonation from N1 should be competitive with the deprotonation from the exocyclic nitrogen (N2) (Scheme 8.5). On the basis of theoretical calculations, von Sonntag did propose that $G(N1-H)^\bullet$ would be favored over $G(N2-H)^\bullet$ in environments with high dielectric constants, such as water [2, 82]. Also, the energies involved in producing $G(N1-H)^\bullet$ and $G(N2-H)^\bullet$ have been theoretically predicted to be similar [2, 82–85].

In X-ray-irradiated single crystals of Guo, dGuo, 5'-dGMP and 3',5'-cyclic guanosine monophosphate, ENDOR studies have shown that deprotonation of $G^{+\bullet}$ results in $G(N2-H)^\bullet$ rather than in $G(N1-H)^\bullet$ in these crystalline environments [8, 10–12, 25]. Moreover, employing pulse radiolysis and theoretical calculations, Chatgililoglu et al. [86–88] have proposed that formation of $G(N1-H)^\bullet$ takes place via a water-assisted tautomerization of the transiently formed $G(N2-H)^\bullet$. Thus, despite a considerable number of experimental and theoretical studies of $G^{+\bullet}$ and its deprotonated species, the initial specific site of deprotonation (at N1 or at N2) in $G^{+\bullet}$ was still an open question [2, 78, 83]. In order to address this issue, Adhikary and coworkers have used specific deuterium isotopic substitution at the guanine C8 and ^{15}N substitution at N1, N2 and N3 atoms in the guanine ring, in an ESR investigation coupled with UV-Visible spectroscopic and theoretical calculations to yield new insights into the problem [78]. This has led to the following conclusions regarding the specific protonation states of one-electron oxidized guanine in dGuo at various pHs: (i) at pHs 3 to 5, $G^{+\bullet}$ exists as a cation radical, (ii) in the pH range 7 to 9, the singly deprotonated species $G(N1-H)^\bullet$, is present, and (iii) at $pH \geq 11$, the doubly deprotonated species $G(-2H)^{\bullet-}$ is present [78].



Scheme 8.6 Schematic representation of various species involved in the prototropic equilibria in $C:G^+$. The intra-base pair proton transfer in $C:G^+$ (process 1) and proton transfer to water either from the N1 atom (process 2) or from the nitrogen atom in the exocyclic amine (N2) of the guanine moiety in the one-electron oxidized G:C (process 4) are shown. Process 3 shows the interconversion between $C:G(N1-H)^\bullet$ and $C:G(N2-H)^\bullet$. The relative stabilities between $C:G(N1-H)^\bullet$ and $C:G(N2-H)^\bullet$ have been calculated using fully optimized geometries of $C:G(N1-H)^\bullet$ and $C:G(N2-H)^\bullet$ in the presence of 11 water molecules employing the B3LYP/6-31+G** method. These near identical values, thus obtained, are provided in parentheses. Ref. [81] should be consulted for details. Adapted with Permission from Ref. [81], *Phys. Chem. Chem. Phys.*, Copyright (2010) Royal Society of Chemistry

In this work, the experimental and theoretical ^{14}N and proton hyperfine coupling constants (HFCC) found for the various radicals involved in one electron oxidized guanine in Guo as a function of pH, i.e., G^+ , $G(N1-H)^\bullet$, and in $G(-2H)^-$ have been compared [78]. *Ab-initio* DFT calculations for various one-electron oxidized guanine radicals with seven to ten waters of hydration, confirmed assignments of experimentally observed hyperfine couplings to nitrogen atoms [78]. These results have unambiguously established that the N1 site is the thermodynamically favored site of deprotonation in G^+ even at 77 K and N1-atom does not have an observable spin density in G^+ , in $G(N1-H)^\bullet$, and in $G(-2H)^-$ [78].

8.5.1.2 Prototropic Equilibria of G^+ in the Base Pair ($G^+:C$)

The various radical species involved in the prototropic equilibria of $G^+:C$ are presented in Scheme 8.6 which shows that the equilibria consists of two distinct deprotonation processes: (a) intra base pair proton transfer from N1 of G to N3 of

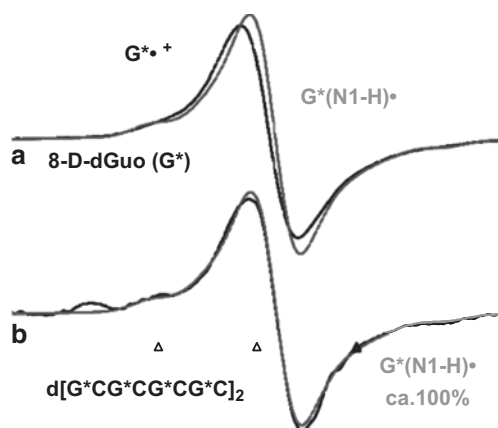


Fig. 8.8 **a** ESR spectra of: **a** $G^{*\bullet+}$ and $G^*(N1-H)\bullet$ obtained from glassy (7.5 M LiCl in D_2O) samples of G^* [$G^*=8\text{-D-dGuo}$, 96% D] (3 mg/mL). **b** Spectrum of the one-electron oxidized dsDNA oligomer $d[G^*CG^*CG^*CG^*C]_2$ (2 mg/mL), again with $G^*(N1-H)\bullet$ from **a** in *grey* superimposed. The match of *black* and *grey* spectra in **(b)** shows that one-electron oxidized guanine in dsDNA oligomer $d[G^*CG^*CG^*CG^*C]_2$ exists as $G^*(N1-H)\bullet$. Ref. [30] should be consulted for details. Reprinted with permission from Ref. [30], *J. Am. Chem. Soc.*, Copyright (2009) American Chemical Society

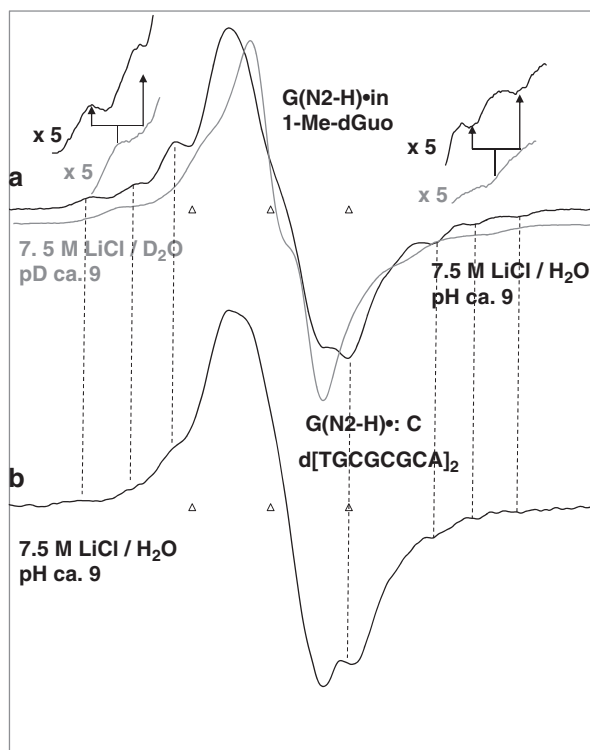
C, and (b) duplex-to-solvent deprotonation, either from N1 of G or from N2 of G or both.

Intra-Base Pair Proton Transfer

Intra-base proton transfer is of great interest with respect to hole transfer (Scheme 8.2) and the reactions of the cation radical [2, 8, 11, 12, 30, 31, 71, 81, 89–91]. As part of a study to investigate the transfer, it has been shown that the ESR spectra of C8-deuterated dGuo cation radical ($G^{*\bullet+}$) is easily distinguishable from that of its N1-deprotonated form ($G^*(N1-H)\bullet$) (Fig. 8.8a) [30, 31, 78]. Using G^* incorporated into double stranded (ds) DNA-oligomers, only the ESR spectrum of $G^*(N1-H)\bullet:C(+H^+)$ has been observed (Fig. 8.8b) [30, 31]. This has provided the direct evidence of intra-base pair proton transfer in $G^{*+}:C$ [30, 31]. Also, this result has confirmed Steeken's prediction [71] that, via this intra-base pair proton transfer, the spin would remain on the guanine and the charge would move to cytosine. Also, ESR studies employing G^* incorporated into a ssDNA model oligomer TG*T has established that the one-electron oxidized guanine exists as an equal mixture of $G^{*\bullet+}$ and $G(N1-H)\bullet$ [30, 31]. Therefore, the cytosine base in dsDNA is a better proton acceptor than the surrounding solvent available to ssDNA.

DFT calculations using 11 explicit waters of hydration around the various GC-radical species as a model of the hydration shell showed that $\Delta G = -0.65$ kcal/mol, so that intra-base pair proton transfer in the $G^{*+}:C$ pair is slightly favorable [89].

Fig. 8.9 a Authentic ESR spectra (77 K) of $G(N2-H)^{\bullet}$ produced via one-electron oxidation of 1-Me-dGuo in glassy (7.5 M LiCl) in H_2O (black) and in D_2O (grey) samples. The A_{zz} component of the N2-H coupling of $G(N2-H)^{\bullet}$ in H_2O is shown with the aid of expansion of the wings by factor of 5; this coupling is lost in D_2O . **b** Spectrum (77 K) of the one-electron oxidized $d[TGCGCGCA]_2$ found in a matched sample of $d[TGCGCGCA]_2$ in H_2O (black). Comparison of spectrum (b) with the black spectrum shown in figure (a) represents that the A_{zz} component of the remaining N2-H proton hyperfine coupling of $G(N2-H)^{\bullet}$ is visible (as indicated by the dotted lines) in the wings. Ref. [81] should be consulted for details

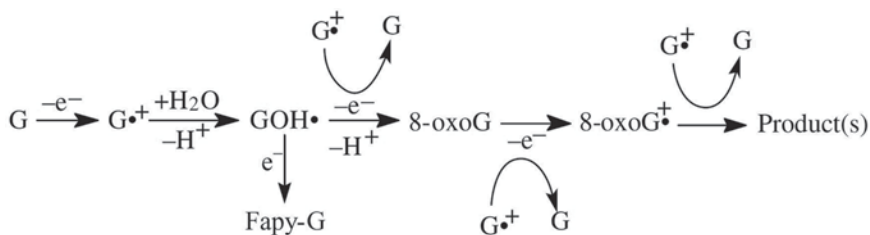


Therefore, these ESR (Fig. 8.8) and theoretical results have confirmed Steenken's [71] and Bernhard's [8] suggestion that intra-base pair proton transfer from the guanine N1 to the cytosine N3 in the $G^{\bullet+}:C$ pair should be favorable.

Duplex-to-Solvent Deprotonation from the Exocyclic N-atom (N2) of Guanine in one-Electron Oxidized G:C

Based on experimental (pulse radiolysis and ESR) [2, 71, 81] as well as theoretical (DFT) [12] evidence, it has been shown that one-electron oxidized 1-Me-dGuo is the best model for dGuo itself that allows for deprotonation of the cation radical only from N2. Thus, the benchmark spectra of the actual cation radical and its corresponding N2 deprotonated form ($G(N2-H)^{\bullet}$) have been obtained employing 1-methyl-2'-deoxyguanosine (1-Me-dGuo) [81] and were employed to establish the duplex-to-solvent deprotonation process from N2 of guanine in one-electron oxidized G:C in DNA systems (Scheme 8.6).

A further elaboration of the nature of duplex-to-solvent deprotonation has been provided by the ESR spectra of $G(N2-H)^{\bullet}$ formed via one-electron oxidation by $Cl_2^{\bullet-}$ in matched samples of 1-Me-dGuo in 7.5 M LiCl (H_2O) (black) and in 7.5 M LiCl (D_2O) (grey) (Fig. 8.9a). In the expanded wings of Fig. 8.9a, the ca. 8 G A_{zz} hyperfine coupling of the N2-H proton of $G(N2-H)^{\bullet}$ in H_2O (black) is evident;



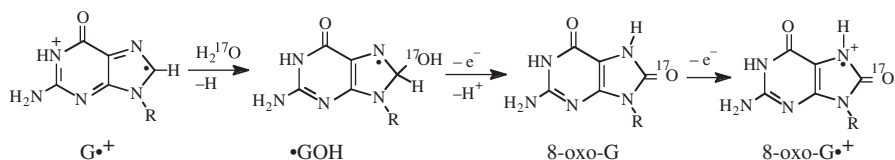
Scheme 8.7 Reprinted with permission from Ref. 28a, *Nucleic Acids Res.*, Copyright (2004), Oxford University Press

this coupling is lost in D_2O glasses (grey). When the spectrum of one-electron oxidized $d[\text{TGCGCGCA}]_2$ (black) obtained from a matched sample in an H_2O glass (Fig. 8.9b) is compared with that from 1-Me-dGuo the A_{zz} hyperfine component of the exchangeable N-H atom of $G(\text{N}2\text{-H})^{\bullet+}$ is observed. This thereby identifies the $G(\text{N}2\text{-H})^{\bullet+}$ spectrum as a contributor to the spectrum of one-electron oxidized $d[\text{TGCGCGCA}]_2$; analyses have suggested that $G(\text{N}2\text{-H})^{\bullet+}$ contributes *ca.* 60% and $G(\text{N}1\text{-H})^{\bullet+}$ accounts for *ca.* 40% [81]. This finding is in accord with DFT calculations which predicts near identical stabilities of these radicals (Scheme 8.6) [81].

8.6 Role of $G^{\bullet+}$ as a Hole Scavenger and Radioprotector

One-electron oxidized DNA constituents, i.e., the oxidized bases ($G^{\bullet+}$, $A^{\bullet+}$, $C^{\bullet+}$, $T^{\bullet+}$) and the sugar-phosphate backbone ($[\text{sugar-phosphate}]^{\bullet+}$), are produced on direct ionization when DNA is irradiated [6–12, 25, 26]. Via base-to-base and backbone-to-base hole transfer processes [16, 92], the hole is localized to the site with the lowest ionization potential, guanine, the dominant oxidized site in DNA forming $G^{\bullet+}$ (Scheme 8.2). The subsequent reactions of $G^{\bullet+}$ that lead to the formation of various diamagnetic stable lesions have been well investigated, and among these lesions, 8-oxo-G is the most studied one [93–96]. 8-Oxo-G is the most often observed guanine modification upon exposure of cells to oxidative stress and has significant biological consequences [93–96]. Therefore, elucidation of the mechanism of formation 8-oxo-G and its subsequent products in irradiated DNA is of interest. Direct ESR spectroscopic evidence of the mechanistic pathway from $G^{\bullet+}$ to 8-oxo-G has been elaborated (Scheme 8.7) [28, 29]. It is well established that for the formation of diamagnetic 8-oxo-G in dsDNA, the one-electron oxidized G must remain in its cation radical state ($G^{\bullet+}:\text{C}$) [30, 31, 81, 82, 97–100].

The ESR investigation has used matched samples of γ -irradiated hydrated ($\Gamma = 12 \pm 2$ $D_2O/\text{nucleotide}$) DNA in the presence and absence of the electron scavenger [thallium(III)] in the absence of oxygen [28, 29]. Additionally, to confirm the nucleophilic addition of water at C-8 of guanine base (Scheme 8.8), the samples were hydrated with either H_2O^{17} or H_2O^{16} [28, 29].



Scheme 8.8 Mechanism of formation of $\bullet\text{GOH}$ by nucleophilic addition of water to $\text{G}^{\bullet+}$ and the subsequent conversion of $\bullet\text{GOH}$ to 8-oxo- $\text{G}^{\bullet+}$ in γ -irradiated DNA- Ti^{3+} -samples hydrated in H_2O enriched with ^{17}O (59.9%) by two one-electron oxidations. Reprinted with permission from Ref. [28, 29], *Nucleic Acids Res.*, Copyright (2004), Oxford University Press

Figure 8.10 shows mainly $\text{G}^{\bullet+}:\text{C}$ formed after γ -irradiation in H_2O^{16} and in H_2O^{17} . No reaction with H_2O occurs at 77 K, so the spectra are identical. Figure 8.10b presents the subtraction of H_2O^{17} samples from otherwise identical H_2O^{16} samples. Figure 8.10b clearly shows the conversion of $\text{G}^{\bullet+}:\text{C}$ to the intermediate doublet of $\bullet\text{GOH}$ from 214 K to 222 K and to the sharp singlet of 8-oxo- $\text{G}^{\bullet+}$ from 214 (starting) to 258K (complete conversion via an overall three one-electron oxidation steps) (Schemes 8.7 and 8.8). This doublet ESR spectrum of $\bullet\text{GOH}$ formed via the nucleophilic addition of water at C-8 of guanine is shown in Fig. 8.10c. The sharp singlet that is observed at 258 K in Fig. 8.10b is due to 8-oxo- $\text{G}^{\bullet+}$, and as expected, in H_2O^{17} , the ESR spectrum broadened due to unresolved hyperfine coupling from O^{17} (Fig. 8.10d).

The spectra of radicals labeled with ^{17}O are broadened by unresolved ^{17}O hyperfine couplings, and thus only the spectra of radicals formed due to ^{16}O water addition and the subsequent reactions are directly isolated by the simple subtraction technique used and described in the figure legend. Note that all non-water addition radicals formed in each set are subtracted out as they are unaffected by ^{17}O couplings and the associated line broadening. These ESR studies provide an unambiguous detection of the intermediate $\bullet\text{GOH}$ involved in the formation of 8-oxo- $\text{G}^{\bullet+}$ (Scheme 8.8) in DNA.

Recent studies on prototropic equilibria of one-electron oxidized guanine in DNA and DNA-model systems (Sect. 8.5) when combined with the results above have led to the following pertinent findings:

(a) *The Guanine Cation Radical Form ($\text{G}^{\bullet+}:\text{C}$) is Necessary for 8-oxo- $\text{G}^{\bullet+}$ Formation* The results shown in γ -irradiated DNA- Ti^{3+} -samples hydrated in H_2O enriched with ^{17}O (59.9%) in Fig. 8.10 in conjunction with the mass spectrometric studies in H_2O^{18} , Shafirovich et al. [97, 98], Cullis et al. [99], and Cadet et al. [100] clearly establish that the cation radical form ($\text{G}^{\bullet+}:\text{C}$, Scheme 8.6) is necessary for the formation of $\bullet\text{GOH}$ by water addition and subsequent formation of 8-oxo- $\text{G}^{\bullet+}$ (Schemes 8.7 and 8.8).

(b) *The Activation Barriers of Formation of $\bullet\text{GOH}$ and Its Conversion to 8-oxo- $\text{G}^{\bullet+}$ Are Low* The low temperature range 200 to 258 K at which formation of $\bullet\text{GOH}$ and its conversion to 8-oxo- $\text{G}^{\bullet+}$ take place [28, 29] suggests that these reactions both have small activation barriers (<5 kcal/mol). Therefore, at ambient temperatures

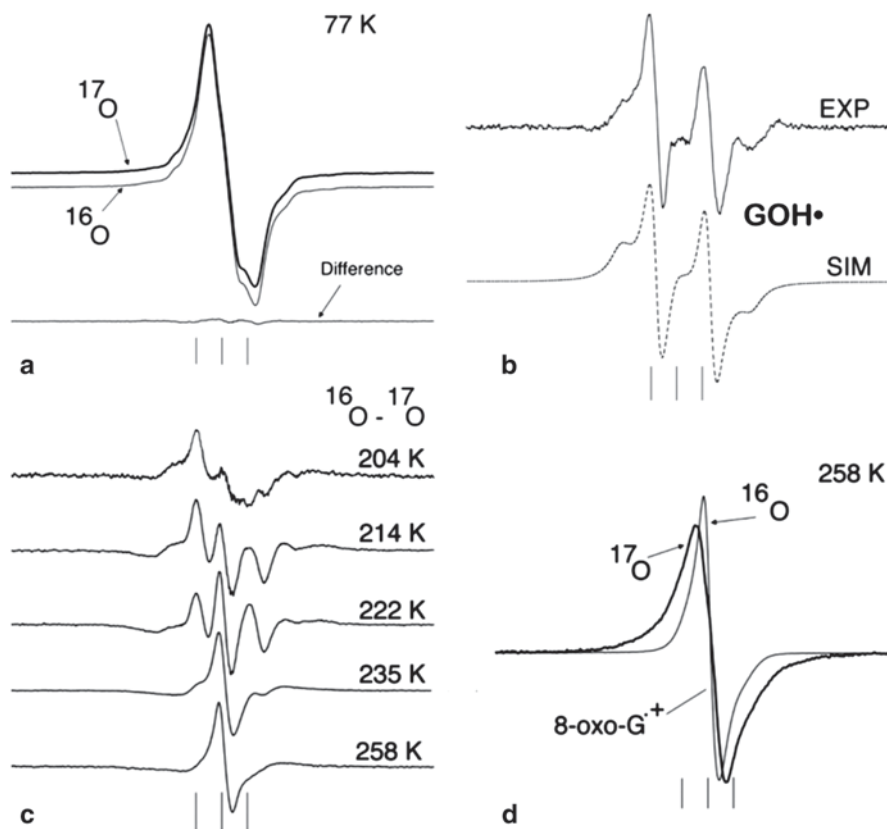


Fig. 8.10 ESR spectra observed in γ -irradiated (22 kGy) DNA-Tl³⁺ (Tl³⁺, 1/10 bp) samples with and without water enriched with ¹⁷O (59.9%) **a** At 77 K, with only G^{•+}:C present no difference in the spectra in H₂¹⁶O or H₂¹⁷O is observed, as expected. **b** Subtraction of the H₂O¹⁷ spectra from the H₂O¹⁶ spectra at each temperature from 204 K to 258 K shows the initial formation of the doublet in **(c)** due to [•]GOH and its conversion to the singlet in **(d)** due to 8-oxo-G^{•+} at 258 K. This technique isolates only the water addition radicals. **c** The *upper* spectrum is the isolated spectrum of [•]GOH from subtractions of spectra shown in panel **(b)**. The *lower* spectrum is the computer simulated spectrum of [•]GOH employing the hyperfine parameters A(1H)=28 G, A(1N)=(20, 0, 0) G, with $g=2.0026, 2.0037, 2.0037$, and linewidth=(8, 6, 6) G. **d** After 15 min of annealing at 258 K, the spectra of 8-oxo-G-radical (8-oxo-G^{•+}) with ¹⁷O and ¹⁶O labeling at C8 are presented. The ¹⁷O spectrum has the appropriate amount of ¹⁶O 8-oxo-G^{•+} spectrum subtracted. The increased breadth of the ¹⁷O spectrum in **B** is attributed to unresolved ¹⁷O hyperfine couplings and is clear evidence for the hydration reaction. Adapted with permission from Ref. [28, 29], *Nucleic Acids Res.*, Copyrights (2004 and 2007) Oxford University Press

which are more biologically relevant, the rates of these one-electron oxidations shown in Schemes 8.7 and 8.8 should be quite fast.

(c) Formation of 8-oxo-G and Its Subsequent One-Electron Oxidation Products Is a Radioprotective Process It is evident from Scheme 8.7 that the multiple one-electron oxidation processes lead to formation of 8-oxo-G^{•+} and subsequent dia-

magnetic products. Such funneling of holes to a single guanine moiety can occur via long range hole hopping and this has been suggested to be a radioprotective mechanism even at therapeutically relevant low doses [7, 28, 29].

(d) Mechanisms of 8-oxo-G Formation in Direct-Type and in Indirect Effects In case of the indirect effect, the electrophilic addition of $\cdot\text{OH}$ at C-8 of the guanine base in neutral G:C pair leads to $\cdot\text{GOH}$ [2, 101] whereas in case of direct-type effect, the nucleophilic addition of water at the guanine base in $\text{G}^{+\cdot}\text{:C}$ leads to $\cdot\text{GOH}$ [28, 29]. $\cdot\text{GOH}$ is a highly reducing radical [2, 28, 29, 101] and hence Fig. 8.10 shows that $\cdot\text{GOH}$ is very easily and rapidly oxidized to 8-oxo-G by various oxidants (e.g., singlet oxygen, $\text{G}^{+\cdot}\text{:C}$ etc.). Thus, once $\cdot\text{GOH}$ is formed, further one-electron oxidations (Scheme 8.7) are possible even by oxidants that are milder than singlet oxygen (for example, O_2 , $\text{HO}_2\cdot$ [102])

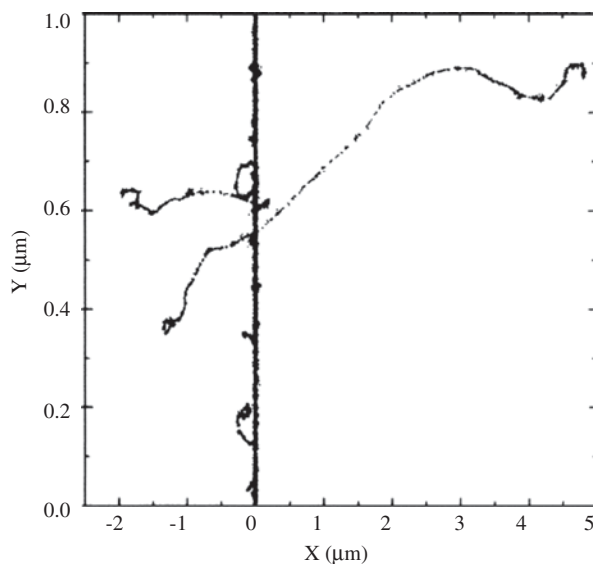
8.7 Ion-Beam Irradiated DNA

In this section, we present an overview of radical formation in ion-beam irradiated hydrated DNA and, because ion-beam studies of DNA are sparse [7, 11, 33–35], a review of some early studies on DNA components. The yields of radicals found trapped at 77 K are significantly affected by the track structure and relatively high LET inherent in ion-beam irradiation [11]. By comparing the yields of specific radicals in ion-beam irradiated samples with the yields of the same radicals in γ -irradiated samples, the spatial organization of the stabilized radicals can be inferred [11]. The higher absolute yields of some specific backbone radicals in ion-beam irradiated samples, relative to γ -irradiated samples suggests, that there are mechanisms of radical formation that are specific to the ion-beam track core [11].

8.7.1 Ion-Beam Track Structure

The population mix, spatial organization, and yields of irradiation formed radicals in ion-beam irradiated DNA is heavily dependent on the track structure of the ion-beam used. Although there are many different experimental and theoretical models that attempt to characterize track structures [103–110], all share the common feature of postulating the existence of a small volume, along the beam path, of very high energy deposition. In this volume there is a high density of ionizations of the target material caused by direct interaction of the ion with electrons in the target, as well as ionizations caused by scattered electrons that stay within the volume, and the LET is extremely high. In the model used by Chatterjee [107, 110], this volume is called the track core. Electrons that escape the core, called delta rays, cause sparse ionization in a very large volume surrounding the core. In this volume, the so-called penumbra, the LET is low and the energy deposition much like that which would be expected from low LET radiation such as γ - and X-irradiation. Figure 8.11

Fig. 8.11 Track structure of a 97.5 MeV/nucleon $^{20}\text{Ne}^{10+}$ ion in water with LET=ca. 70 keV/ μm . Ions are generated at the bottom. Each dot represents a point where energy is deposited. Reprinted with permission from Ref. [111], *Radiation Research*, Copyright (2006), Radiation Research Society



illustrates this picture for a 97.5 MeV/nucleon $^{20}\text{Ne}^{10+}$ ion in H_2O with LET=ca. 70 keV/ μm .

In order to understand the radiation chemistry and spatial organization of the radicals formed after ion beam irradiation, the processes that occur in the core must be experimentally distinguished from those that occur in the penumbra.

8.7.2 $^{16}\text{O}^{8+}$ studies

In what appears to be the first published report on heavy ion irradiation of hydrated DNA, fully stripped oxygen-16 ions (60 MeV/nucleon) were used to irradiate salmon testes DNA hydrated to $\Gamma = 18 \text{ D}_2\text{O}/\text{nucleotide}$ [33]. D_2O was used for hydration because it resulted in narrower ESR line components than H_2O , and allowed for more accurate computer analyses of the composite ESR spectra that result. Two samples were stacked along the beam path such that the average beam LET was 100 keV/ μm in the front sample and 300 keV/ μm in the rear, with the Bragg peak occurring in the rear sample [33].

Comparison of the ESR spectra from $^{16}\text{O}^{8+}$ irradiated samples with those from γ -irradiated samples revealed a much higher spectral intensity in the wings of the spectra of the ion-beam irradiated samples. In all these spectra, the central portion of the spectra is dominated by a signal from the three base radicals trapped at 77 K, $\text{G}(-\text{H})\cdot$, $\text{C}(\text{N}3)\text{H}\cdot$ and T^- (Sect. 8.2). On the other hand, the wings are dominated by line components now believed to originate with the sugar radicals, $\text{C}1''$, $\text{C}3''$, $\text{C}5''$, and $\text{C}3''_{\text{dephos}}$ (Scheme 8.2). Thus, it has been concluded that $^{16}\text{O}^{8+}$ irradiation results in the formation of a higher percentage of sugar radicals than did γ -irradiation. The

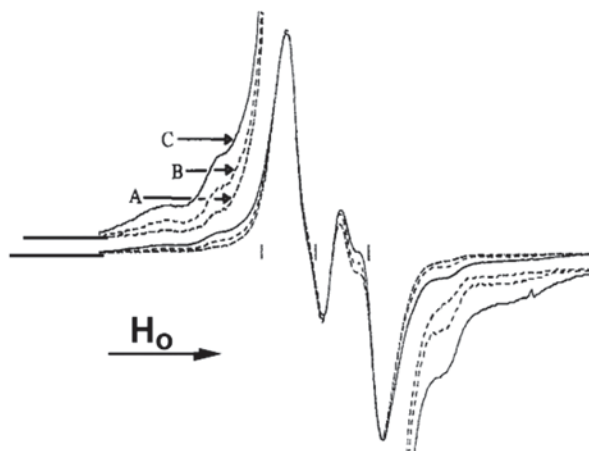


Fig. 8.12 ESR spectra of γ - and ion-beam irradiated hydrated ($\Gamma=18$ D_2O /nucleotide) DNA at 77 K. **a** γ -irradiated to 100 kGy, LET *ca.* 0.3 keV/ μ m. **b** Ion-beam irradiated to *ca.* 240 kGy with LET *ca.* 100 keV/ μ m. **c** Ion-beam irradiated to *ca.* 625 kGy with LET *ca.* 300 keV/ μ m, includes Bragg peak. Note the increase in intensity in the wings in B and C, indicating higher concentrations of sugar radicals. This is likely due to both the higher doses in B and C, as well as the higher LETs. Reprinted with permission from Ref. [33], *Radiation Research*, Copyright (1996), Radiation Research Society

central portions of the two different spectra, i.e. that from γ -irradiation and that from ion irradiation, when normalized to equal intensity, overlapped well, indicating the relative amounts of the base radicals produced in each irradiations were similar (Fig. 8.12).

Dose-response curves constructed from five different samples irradiated for different times in the ion-beam using the relationship (8.1), gave the G-values shown in Table 8.4.

$$Y = \frac{G}{k}(1 - e^{-kD}) \quad (8.1)$$

In Eq. (8.1), Y is the yield of radicals (μ mol/kg) at dose D (Gy). G is the yield in μ mol/J and k (Gy^{-1}) is a constant that characterizes the sensitivity of pre-existing radicals to destruction by radiation. A larger k for a specific previously trapped radical indicates that it is more easily destroyed by radiation than if it had a smaller k. The G-value for total radical formation, that is the sum of the yields for base radicals and sugar radicals, is much smaller for ion irradiated samples than for γ -irradiated samples. This is attributed to the track structure of the ion, specifically to rapid ion radical recombination in the track core (*vide infra*.)

A hitherto unreported phosphoryl radical ($ROPO_2^{\cdot-}$) was also found in $^{16}O^{8+}$ irradiated DNA, as about 0.1% of the total trapped radical population at 77 K

Table 8.4 G-values for total radical yield in ion-beam irradiated hydrated DNA

Radiation type	LET (keV/ μm)	G ($\mu\text{mol}/\text{J}$)		
		$\Gamma=2.5$	$\Gamma=12$	$\Gamma=18$
γ	ca. 0.3	0.133 ^a	0.22 ^b	0.304 ^a
X ^c	ca. 0.3	0.122		
¹⁸ O ^d	100			0.1
	300			0.04
⁴⁰ Ar ^e	350		0.148	
³⁶ Ar	600		0.136	
⁴⁰ Ar	800		0.063	
⁸⁶ Kr ^f	1080		0.083	
	1175		0.097	
	1460		0.078	
	2000		0.063	
	4000		0.020	
⁵⁰ Ti ^e	1521	0.064		
⁶⁸ Zn ^e	3861	0.035		
¹⁹⁷ Au ^e	11650	0.101		
²⁰⁹ Bi ^e	12440	0.042		

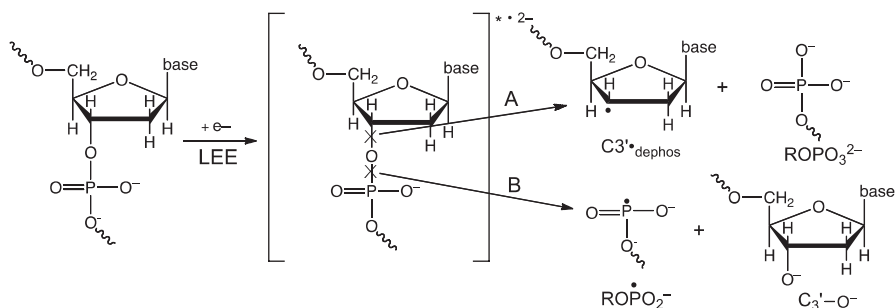
^a Ref. [36]; ^b Ref. [35]; ^c Ref. [22]; ^d Ref. [33]; ^e Ref. [34]; ^f Ref. [35]

in a sample that contained the Bragg peak [33]. This radical was attributed to a LEE-initiated dissociative electron attachment process that causes a strand break, and the radical is a direct product of the strand break, caused by rupture of a P–O bond proximate to C3' and/or to C5' (Scheme 8.9). In this process, there are two separate paths for bond cleavage, as shown in Scheme 8.9, for reaction at C3', both of which cause a strand break.

The C3''_{dephos} was observed in later experiments using argon [34] and krypton [35] ion-beams, as described below.

8.7.3 Dry DNA

An investigation that used four different heavy ion-beams (Table 8.4) to irradiate “dry DNA” reported G-values for total radical formation at 77 K after annealing to 140 K, and the radical mix as a function of temperature for ²⁰⁹Bi irradiated samples [22]. So called “dry DNA” is prepared by storing polymeric DNA in a desiccation chamber over Drierite for 10 days, or by pumping on the DNA using a vacuum line. In actuality, “dry” DNA retains 2.5 H₂O per nucleotide at the phosphate groups [54]. With low LET irradiation, the total yield of DNA-radicals in dry DNA is lower than that found for higher hydrations levels [36], and the radical population mix is slightly altered [76]. An electron scavenger, [Fe(CN)₆]³⁻, was incorporated into some DNA samples so that the oxidative path could be investigated; there was little difference found with electron scavenger present. In this work the samples were only ca. 0.05 mm thick. Even so, the LET increased as the beam penetrated the sample,



Scheme 8.9 Formation of $C3'_{\text{dephos}}\cdot$ and $ROPO_2\cdot^-$ in DNA from LEE. LEE attack results in formation of an excited state transient anion radical. Two alternate reactions may then occur. With path A and cleavage of a C–O bond, $C3'_{\text{dephos}}\cdot$ and a diamagnetic anion are formed. On the other hand, path B, with cleavage of a P–O bond, results in formation of $ROPO_2\cdot^-$ and, also, a diamagnetic anion. Both paths cleave a bond in the sugar-phosphate backbone and, thereby, cause an immediate strand break. Reprinted with permission from Ref. [35], *Radiation Research*, Copyright (2012), Radiation Research Society

so the LETs reported are initial LETs. However, none of the samples contained the Bragg peak. The ion-beams used are given in Table 8.4.

As observed with ^{16}O irradiation and with other ion-beams (*vide infra*), overall G-values for total radical formation at low temperatures are lower than that found with low LET irradiation (Table 8.4). An analysis of the ^{209}Bi irradiated sample spectra at 140 K shows the presence of a form of G^{++} radical (23% of radicals), the pyrimidine anions (40%), a possible $\text{UCH}_2\cdot$ (23%), and the $\text{T(C6)H}\cdot$ (3%) on the bases [22]. A possible $\text{C1}'\cdot$ is also proposed [22]. In this sample, the authors could not distinguish the $\text{UCH}_2\cdot$ spectrum from the $\text{C1}'\cdot$ spectrum so the 23% figure quoted for $\text{UCH}_2\cdot$ includes any $\text{C1}'\cdot$ present [22]. An ESR triplet spectrum thought to originate with cytosine protonated at the exocyclic nitrogen is assigned to another 11% of the total spectrum intensity at 140 K [22]. As the sample is annealed above 200 K, two low intensity spectra appear [22]. These are a doublet, now known to originate with $\cdot\text{GOH}$ (appears at *ca.* 200 K) and a sharp singlet, now known to originate with 8-oxo- G^{++} (appears at *ca.* 240 K) (Sect. 8.6 and Ref. 28).

When compared to X-irradiated DNA investigated in the same lab, ^{209}Bi irradiated DNA has a higher percentage of sugar radicals present [22]. Even though the total yield of radicals for ^{209}Bi irradiated samples is about 34% that of X-irradiated radicals, the percentage each of the radicals found, except for sugar radicals, is very similar in X-irradiated and ^{209}Bi irradiated samples [22].

8.7.4 Ar and Kr Ion-Beam Irradiation

An investigation of hydrated DNA ($\Gamma = 12 \text{ D}_2\text{O}/\text{nucleotide}$) irradiated with a variety of Ar ion-beams provided a model for a radiation chemistry track structure model

Table 8.5 Yields of radicals in irradiated hydrated ($\Gamma = 12$ D₂O/nucleotide) DNA

Irradiation Type	LET (keV/ μ m)	G(base radicals) ^a	G(sugar radicals) ^a	G(Ar _{base})/G(γ _{base})
γ	Ca. 0.3	0.19 ^b	0.030	–
Ar	350	0.116	0.032	0.61
Ar	600	0.104	0.032	0.55
Ar	800	0.045	0.018	0.24

^a μ mol/J; ^b Ref. [34]

^c With DNA hydrations different from $\Gamma = 12$, G(Ar_{base})/G(γ _{base}) ranges from 0.49 to 0.56

for this type of irradiation [34], as opposed to a physical track structure model. Various physical track structure models strive to understand the nature of the energy deposition in the heavy ion track [103–111], whereas the radiation chemistry track structure model describes the different radical chemical reactions that occur in different parts of the track. Clustered damage has been shown as a particularly dangerous DNA lesion in plasmid DNA [3]. If we assume that clustered damage originates with specific chemical processes, elucidation of the spatial location of the reactions that occur after irradiation can help explicate the formation of clustered damage.

The specifics of the Ar ion-beams used, the LETs that resulted and the total yields of radicals found are given in Table 8.5. As found in previous and later work, the total yield of trapped radicals at 77 K is less than that found for γ -irradiation (Table 8.4). The difference in total yields is inextricably bound up in the details of the ion-beam track structure.

The bulk of the population of radicals trapped at 77 K are base radicals [G(N1–H)[•], C(N3)H[•], and T[•]] and sugar radicals (C1[•], C3[•], C5[•], and C3[•]_{dephos}). Analyses of the yields of these radicals (Fig. 8.13) indicated that the base radical yield was highly depressed in the ion-beam irradiated samples, relative to γ -irradiated samples.

Table 8.5 presents these results for samples with $\Gamma = 12$ D₂O/nucleotide. In the radiation chemistry track structure model proposed in this work, this discrepancy was accounted for by assuming that few of the base radicals stabilized at 77 K originate with the track core. Because of the high energy density in the core, ionizations occur very close to each other and a rapid recombination of positive ion radicals with nearby electrons, driven by Coulomb attractions, destroys most base ion-radicals. The base radicals are assumed to form predominantly in the track penumbra, in a low LET type environment consisting of spurs, blobs and short tracks.

With this model, it was possible to calculate the partition of energy between the core and the penumbra. It was assumed, for the sake of simplicity, that all the base radicals are formed in the penumbra and that the penumbra is a γ -irradiation like region, thus, the ratio G(Ar_{base})/G(γ _{base}) gives the percentage of the beam energy deposited in the penumbra. The remainder of the energy is, of course, deposited in the core. For Ar ion-beam irradiated samples at various hydrations and LETs from 350–650 keV/ μ m, the energy partition found is about 50% in the core and about 50% in the penumbra. For a sample at LET=800 keV/ μ m, 24% of the energy is deposited in the penumbra and 76% in the core (Table 8.5).

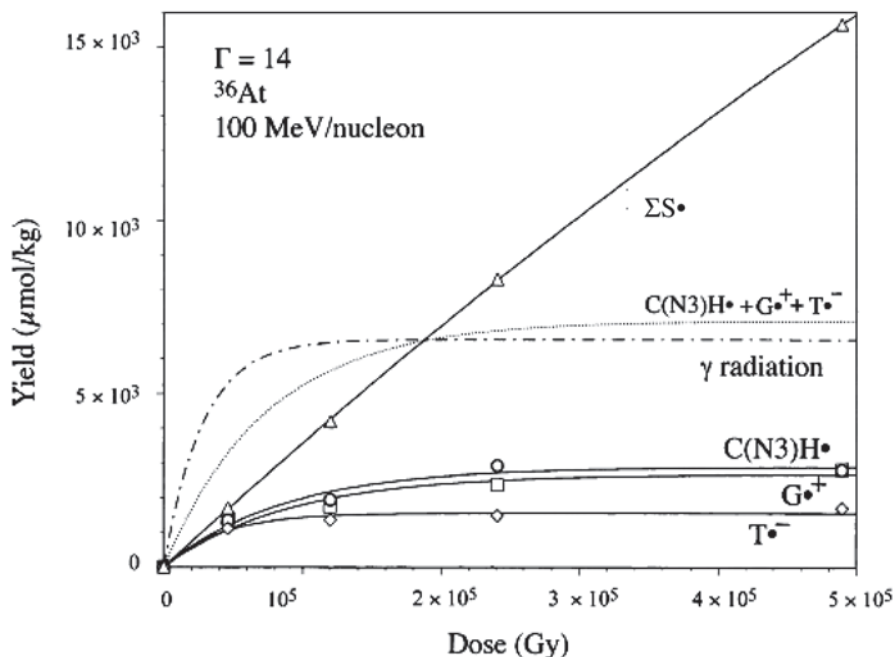


Fig. 8.13 Dose-response of radicals found in an Ar ion-beam irradiated sample. The G values of C(N3)H•, G(-H)• and T•⁻ were lower than in γ -irradiated DNA. Because pre-existing neutral radicals are not very susceptible to destruction by further radiation, the sum of sugar radicals, symbolized by ΣS^\bullet , gives a linear dose-response up to the highest dose used. The profile of the sum of the three base radicals was very similar to that from γ -irradiation, consistent with the model that posits that the base radicals are produced in the γ -irradiation like penumbra. Adapted with permission from Ref. [34], *Radiation Research*, Copyright (2003), Radiation Research Society

Even though the yields of sugar radicals for Ar irradiated samples at 350 keV/ μm and 600 keV/ μm seemed to be the same as that for γ -irradiated samples, the yields are calculated based on the total energy deposited in the sample even though only about half the energy is actually deposited in the core [34]. This indicates that there are processes that result in sugar radicals that occur in the core that do not occur in γ -irradiated samples [34]. The most likely candidates are excited state reactions (Sect. 8.8.2). Approximately 90% of the relatively high yield of sugar radicals is formed in the low volume core [34]. These radicals are known to lead to strand breaks, and, because of their proximity, may result in damage clusters [34].

A hitherto unknown sugar radical, C3''_{dephos}• (Scheme 8.2) was found in irradiated, hydrated DNA in all argon ion-beam irradiated samples. This is an immediate strand break radical, in the sense that it is formed as a direct product of a strand break, and is almost certainly formed from LEE (Scheme 8.9). ROPO₂•⁻ and C3''_{dephos}• are found in a roughly 20/1 ratio, indicating that path B in Scheme 8.9 is more favorable than path A.

Table 8.6 Radical Yields and Energy Partition in ^{86}Kr ion-beam irradiated hydrated ($G = 12 \text{ D}_2\text{O}/\text{nucleotide}$) DNA^a

LET (keV/ μm)	G_{Base} ($\mu\text{mol}/\text{J}$)	G_{sugar} ($\mu\text{mol}/\text{J}$)	Fraction energy in penumbra ^b	Fraction energy in core
1080	0.056	0.027	0.29	0.71
1175	0.070	0.027	0.37	0.63
1460	0.051	0.027	0.27	0.73
2000	0.038	0.025	0.20	0.80
4000	0.013	0.0075	0.068	0.93

^a Adapted from Ref. [35]^b Fraction energy in penumbra = $G_{\text{base}}(\text{Kr})/G_{\text{base}}(\gamma)$, with $G_{\text{base}}(\gamma) = 0.19 \mu\text{mol}/\text{J}$

Further development of a radiation chemical track structure model suggested by the oxygen and argon ion-beam irradiation studies has recently been provided by an investigation using $^{86}\text{Kr}^{36+}$ as the irradiating ion [35]. In this work, LETs from 1080 keV/ μm to 4000 keV/ μm were achieved. The DNA has been hydrated to $\Gamma = 12 \text{ D}_2\text{O}/\text{nucleotide}$. As previously observed, the overall yields of trapped radicals at 77 K were lower than that found using γ -irradiation (Table 8.6). Computer analyses of the composite ESR spectra that resulted have allowed the absolute yields of base radicals and of sugar radicals to be determined. From these the partition of energy between the core and penumbra could also be determined (Table 8.6; [35]).

Using the G - and k -values obtained employing Eq. (8.1), it has been possible to calculate, Y_{∞} , the theoretical (not actual) yield of base radicals at infinite dose for both Kr- and γ -irradiated DNA. For Kr ion-beam irradiated samples, $Y_{\infty} = 4970 \pm 324 \mu\text{mol}/\text{J}$ and for γ -irradiated samples, $Y_{\infty} = 5278 \mu\text{mol}/\text{J}$. This latter number likely has a $\pm 20\%$ error. Both Kr and γ -irradiated samples have shown similar distributions of DNA base radicals. This is considered further evidence that the base radicals are formed predominantly in a low LET γ -like environment in the track penumbra.

From Tables 8.5 and 8.6, it can be seen that the yields of sugar radicals in Kr ion-beam irradiated samples were somewhat lower than that found in most Ar ion-beam irradiated samples. This suggests that the higher LETs for the Kr ion-beam irradiated samples and concomitant higher density of ionizations in the core resulted in higher recombination rates of the core-early sugar cation radicals that are precursors of neutral sugar radicals [35].

The familiar $\text{ROPO}_2^{\cdot-}$ and a second new unidentified phosphorus radical have also been found in Kr ion-beam irradiated samples [35]. An ESR spectrum of these radicals is shown in Fig. 8.14.

The G -values for formation of $\text{ROPO}_2^{\cdot-}$ in Kr ion-beam irradiated DNA samples have also been determined [35]. Table 8.7 shows these for the five different LETs used. The increase in G -values as LET increases from 1080 to 2000 keV/ μm are expected from a core process as more energy is diverted to the core. As mentioned previously, $\text{ROPO}_2^{\cdot-}$ was thought to be formed largely in the core because of its very low yield in γ -irradiated samples. The drop in yield at the highest LET of

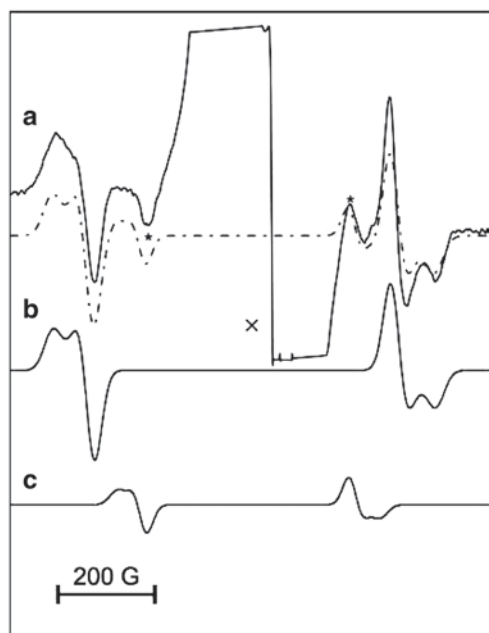


Fig. 8.14 ESR spectra of Kr ion beam (LET=2180 keV/ μm) irradiated hydrated ($\Gamma=12$ D₂O/nucleotide), DNA with dose=479 kGy. **a** *Solid line*, experimental spectrum. Off scale components in *center* originate with base and sugar radicals. *Dotted line*, sum of **b** plus **c**. **b**. Simulated spectrum of ROPO₂⁻. **c** Simulated spectrum of unidentified phosphorus centered radical. **c** has 20% the intensity of **b**. Consult Ref. [35] for ESR parameters used to simulate spectra **b** and **c**. The centrally located “x” is at $g=2.00$. All spectra have been recorded at 77 K. Reprinted with permission from Ref. [35], *Radiation Research*, Copyright (2012), Radiation Research Society

4000 keV/ μm has been suggested to originate with fast recombination in the core, driven by Coulomb forces, at the highest core energy density [35].

In this work using Kr ion-beam irradiation, the yield of unaltered base release has also been investigated [35]. The total yields of unaltered bases have been observed to be virtually identical to the sugar radical yields for the four lowest LETs used, and similar at the highest LET (Table 8.7) [35], at which the authors note that experimental error may be large. This is consistent with a model that presumes that all base release occurs from the reactions of sugar radicals. It is believed that base release is a surrogate for strand breaks ([35], also Sect. 8.8.3.2). This suggests that strand breaks originate with sugar radicals in case of the direct effect as found for the indirect effect [2, 13, 14].

A radiation chemistry track structure model, using Kr ion-beam results, is schematically represented in Scheme 8.10. The model includes an energy partition as well as major chemical events in each ion track region. In the high LET core, there is a competition between fast recombination of early sugar cation radicals (part of the hole (h^+) population) and their deprotonation to form the neutral sugar radicals

Table 8.7 G-values for sugar radical formation and base release

LET (keV/ μ mol)	G (dR') ^a	G (base release) ^a
1080	0.027	0.028
1175	0.027	0.026
1460	0.027	0.024
2000	0.025	0.025
4000	0.0075	0.011

^a (μ mol/J), Reprinted with permission from Ref. [35], *Radiation Research*, Copyright (2012), Radiation Research Society

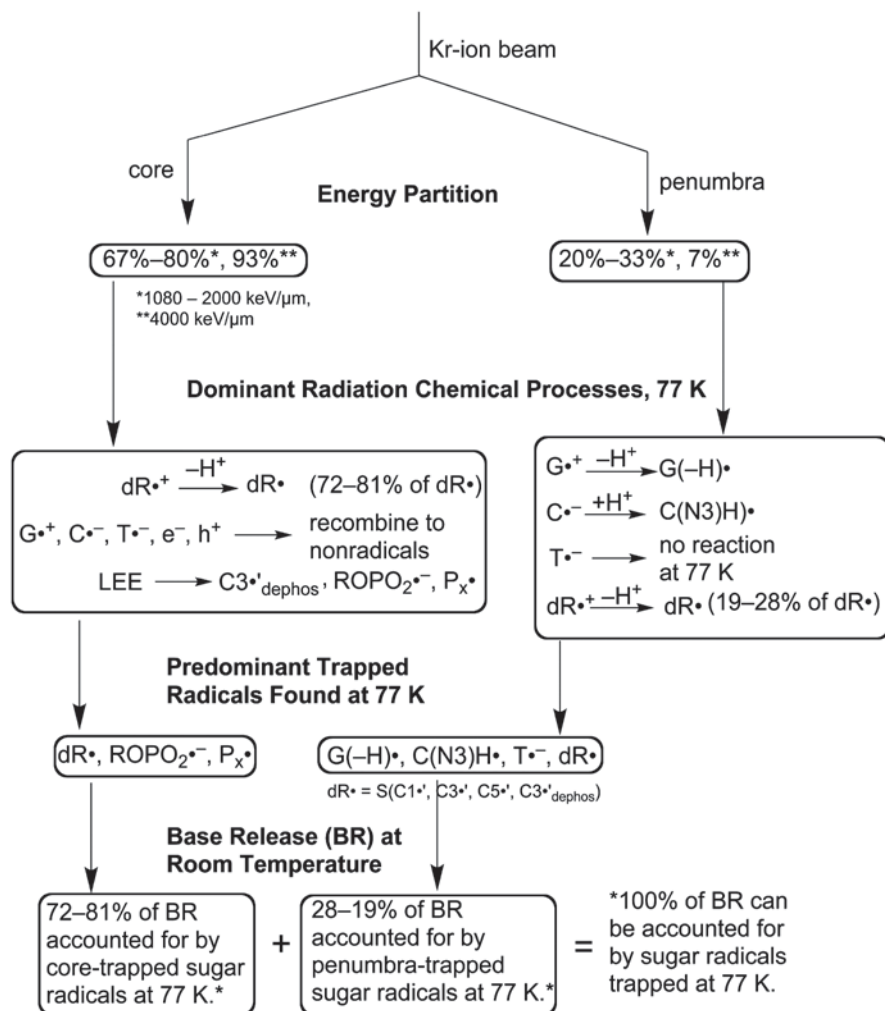
which eventually evolve to strand breaks [35]. Fast recombination of base radicals precludes their being a major core product. LEE reactions to form immediate strand breaks and the product radicals $\text{ROPO}_2^{\cdot-}$ and $\text{C3}^{\cdot-}_{\text{dephos}}$ also occur predominantly in the core. In the low LET penumbra, processes similar to that found with γ -irradiation are observed [35]. Relatively high yields of base radicals are formed, as are a small population of sugar radicals.

8.7.5 Spatial Arrangement of Radicals in Argon Ion-Beam Irradiated DNA

Clustered DNA damage, which is difficult or impossible to repair, is considered to be the most dangerous form of irradiation damage [3–5]. Therefore, understanding the spatial organization of radicals is important to assessing the potential biological effect they may cause. A PELDOR investigation of argon irradiated hydrated DNA was undertaken in order to gain insight into just this concern [112]. The PELDOR experiment uses the dipolar interaction between radicals to determine the average number of nearby radical neighbors for the radicals being probed [112]. For this work, the observing magnetic field was set at a point of the ESR spectrum that is dominated by sugar radicals (Fig. 8.15).

In these experiments, there was a fairly consistent picture of radical disposition for three samples with doses of 1.7, 15 and 50 kGy [112]. Using pooled data from all three samples for a global analysis, there was an average of 17.7 ± 0.7 radicals per spherical cluster with a cluster radius of 6.79 nm [112]. Chatterjee estimated the core radius for high energy ions of 100 MeV/n to be about 4.4 nm, in reasonable agreement with the experimental value found [11, 107, 110, 112].

Because the sugar radicals were being probed, it is reasonable to imagine that the spherical clusters exist as a segment of the core and that the radius measured is also the core radius. The spherical shape was used to keep the mathematical analysis tractable. The authors note that, because of the sharp drop-off of a $1/r^3$ interaction, the PELDOR spectrum may detect radicals out to only about 7.5 nm. Thus, the penumbra which extends up to 4 mm from the track core is not significantly probed in this experiment [11, 112]. Sugar radicals formed in the penumbra may have some effect on the overall results [112].

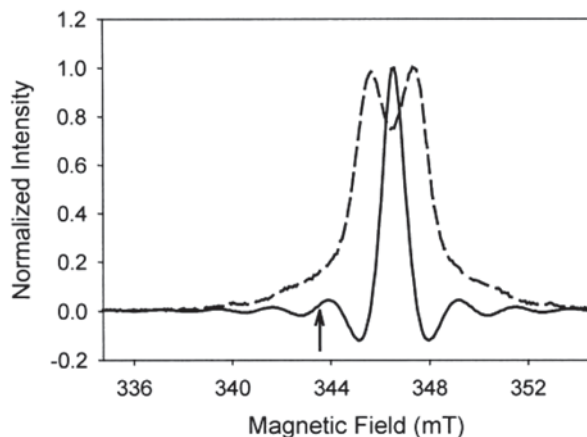


Scheme 8.10 Radiation chemistry track structure model

8.8 Mechanisms of Formation of DNA Backbone-Radicals by Direct-Type Effects

As it has been well-established that the backbone-radicals, particularly, the sugar radicals are the precursors of DNA strand breaks, various mechanisms that have so far been proposed in the literature for the formation of DNA backbone-radicals by direct-type effect in irradiated DNA, are summarized here: (a) Direct ionization, (b) Excited states of base cation radicals, (c) Double oxidation, and (d) LEE-induced dissociative electron attachment.

Fig. 8.15 The *dashed curve* is the ESR absorption spectrum of argon irradiated hydrated DNA, measured using the intensity of the electron spin echo. The *solid line* is the impulse response function using a 16 ns pulse. The *arrow* indicates the position of the observing field. Reprinted with permission from Ref. [112], *Radiation Research*, Copyright (2005), Radiation Research Society



8.8.1 Direct Ionization

These processes have been discussed in Sects 8.2–8.4 and in 8.7.

8.8.2 Role of Excited States Towards Formation of Radiation-Induced DNA Damage

During irradiation of DNA and its model structures, excited states are formed abundantly via either direct excitation (Coulomb interaction) or via geminate ion-pair recombination [113]. In case of low LET radiations, excited states along with ionization events are formed in discrete widely dispersed spurs and as a result, they rapidly deactivate and are not effective towards causing damage to DNA. However, in the track core of high LET radiations, excited states are in very close proximity with ionization events and hence should be more effective towards production of DNA damage. Though the ground states of various DNA-radicals have been well-investigated both experimentally and theoretically (see Sects 8.2–8.7), there is not an extensive literature regarding the excited states of various DNA-radicals [6, 7, 11, 12, 19]. Between 1994 and 2003 only two ESR spectroscopic studies of irradiated DNA [34, 76] suggested that excited DNA-radicals played a role in formation of the DNA-strand break precursor sugar radicals. The first study [76] suggested evidence of sugar radical formation from G^{++} at very high doses in γ -irradiated (77 K) hydrated ($\Gamma = 12 \pm 2$ D_2O /nucleotide) DNA. The second study showed formation of the neutral sugar radicals in high yields along the Argon ion-beam track in Ar^{18+} ion-beam irradiated (77 K) hydrated ($\Gamma = 12 \pm 2$) DNA relative to the γ -irradiated (77 K) hydrated ($\Gamma = 12 \pm 2$) DNA ([34], also Sect. 8.7) postulated formation of neutral sugar radicals in relatively high yields along the Argon ion-beam track core, relative to γ -irradiated DNA. This work proposed that formation of neutral sugar

radicals could occur via deprotonation of an excited state sugar cation radical and that the deprotonation must occur within the lifetime of its excited state.

This hypothesis has been validated with the aid of the both ESR and theoretical evidence. ESR spectroscopic studies have directly shown the formation of the neutral sugar radicals via photoexcited one electron oxidized DNA model systems including: 1. photoexcited base (purine (guanine and adenine) and pyrimidine (5-methylcytosine, and N3-deprotonated-thymine)) cation radicals in nucleosides, and nucleotides [114–117], 2. photoexcited guanine cation radical in ss and ds DNA-oligomers [81, 82, 118, 119], 3. photoexcited cation radicals in oligomers with a 5-methylcytosine/adenine mismatch [117]), 4. photoexcited guanine and adenine cation radicals in RNA-model systems (nucleosides and nucleotides [120, 121], 5. photoexcited guanine cation radical in ss RNA oligomer [120]), and 6. photoexcited guanine cation radical in highly polymerized salmon testes dsDNA [115, 119]. Theoretical calculations using time dependent density functional theory (TD-DFT) have been carried out which aid the understanding of these experimental results [19, 115–118, 121–125]. Both these experimental and theoretical results have been described in several recent reviews [6, 8, 11, 12, 19, 122, 125].

8.8.2.1 Sugar Radical Formation via Excitation of G^{++} in Highly Polymerized DNA

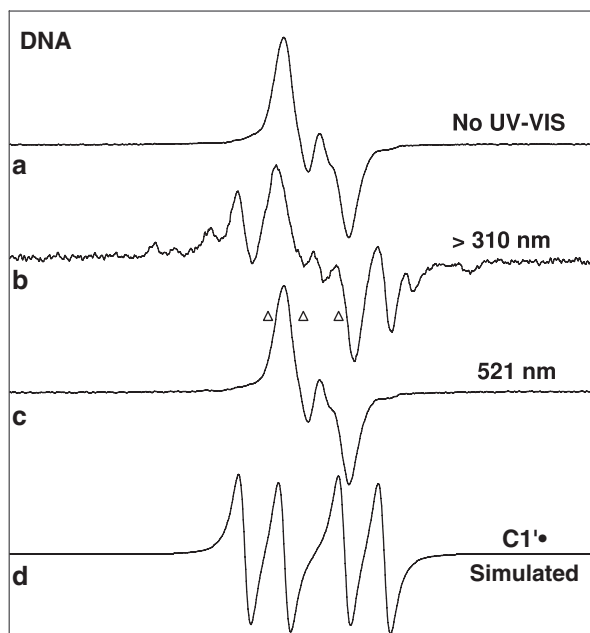
Formation of $C1^{\bullet}$ via photoexcitation of G^{++} in highly polymerized salmon testes dsDNA was found to occur in the wavelength range of 310–480 nm (Fig. 8.16). However, no sugar radical formation was observed at wavelengths ≥ 520 nm (Fig. 8.16).

8.8.2.2 Sugar Radical Formation via Excitation of Base Cation Radicals in Model Compounds

Employing DNA and RNA purine nucleosides, formation of $C5^{\bullet}$ (ca. 55 to 80%) and $C3^{\bullet}$ (ca. 15 to 35%) were reported [82, 115, 116, 119–121] to form via photoexcitation of purine base cation radical at 143 K. Photoexcitation of 5-methyl-2'-deoxycytidine cation radical (5-Me-2'-dC⁺) and of N3-deprotonated thymidine (Thd) cation radical (T(-H)⁺) resulted in only $C3^{\bullet}$ formation [117]. However, in dinucleosides, e.g., TpdG [118] and dGpdG [119], photoexcitation of G^{++} resulted predominantly in formation of $C1^{\bullet}$ and $C5^{\bullet}$ along with a small amount of $C3^{\bullet}$ (ca. 10%) (Fig. 8.17).

Experiments using photoexcitation of G^{++} in DNA oligomers of various length showed that as the length increased from TTGTT to TTGGTT to TTGGTTGGTT the extent of $C1^{\bullet}$ formation increased and $C5^{\bullet}$ formation decreased [119]. Photoexcitation of G^{++} in various dsDNA-oligomers, resulted in predominantly $C1^{\bullet}$ formation along with very small amount of $C5^{\bullet}$ [81, 82, 117]. However, in dsDNA-oligomers with a 5-methylcytosine/adenine mismatch, predominantly $C5^{\bullet}$ production was observed [117]. The type and amount of each sugar radical formed was

Fig. 8.16 **a** ESR spectrum at 77 K of DNA ice samples (50 mg/mL D₂O) γ -irradiated to 15.4 kGy dose, annealed to 130 K to eliminate $\cdot\text{OH}$. **b** After illumination at 77 K for 1 h with light >310 nm. **c** After illumination of an identically prepared sample as in **a**, at 521 nm for 30 min. **d** Simulated spectrum of C1^{\bullet} obtained using the isotropic HFCC values of two βH -atom HFCC values— $1\beta\text{H}$ (15 G) and another $1\beta\text{H}$ (37 G), along with 5 G line-width, and g (2.0029, 2.0029)). This spectrum matches line components due to C1^{\bullet} in spectrum B. Reprinted with permission from Ref. [115], *Nucleic Acids Res.*, Copyright (2005), Oxford University Press



found to be wavelength independent for nucleosides and nucleotides, and in ssDNA oligomers in which the oligomer length was less than 4 (e.g., TGT) [82, 119].

The formation of the type of sugar radical formed was found to be wavelength dependent for longer ssDNA oligomers (e.g., 10 bases or more) [119] as well as for dsDNA oligomers [82, 117]. For example, in dsDNA-oligomers, sugar radical formation via photoexcitation of G^{++} has been observed to be substantial at 405 nm but negligible at 640 nm [82]. Excitation of G^{++} in dsDNA with 405 nm light in addition to forming sugar radicals was shown to result in oxidation of Cl^- in the surrounding solution (7.5 M LiCl) producing $\text{Cl}_2^{\bullet-}$ via an excited state hole transfer process [82, 117]. These results imply that highly reactive guanine excited states, G^{++} , are formed [82, 117] and suggest that dsDNA is able to protect itself from damage from such reactive cation radical excited states by the transfer of holes and their associated damage to the surrounding environment [82].

8.8.2.3 Sugar Radical Formation via Excitation of Base Cation Radicals is Kinetically Controlled

Recent ESR studies have shown that UV/Vis excitation of the 5-methyl-2',3'-dideoxycytidine cation radical ($(5\text{-Me-2}', 3'\text{-ddC}^{++})^{\bullet}$), the 2',3'-dideoxyadenosine cation radical ($(2',3'\text{-ddAdo}^{++})^{\bullet}$), and also the N3-deprotonated 2',3'-dideoxythymidine cation radical ($(2',3'\text{-dd T(-H)})^{\bullet}$) resulted in the formation of $\text{C3}^{\bullet}_{\text{dephos}}$ (Sect. 8.7). Since the site of formation has one of the stronger C-H bonds, the

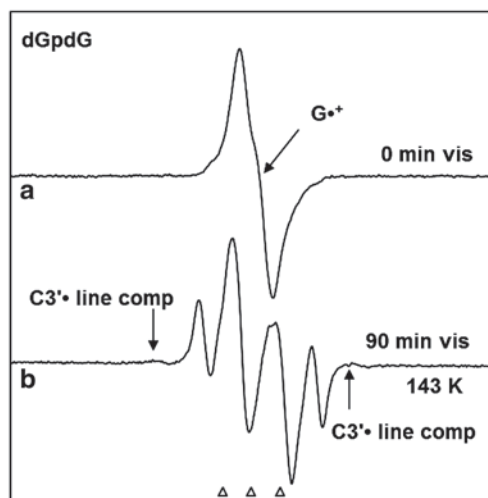


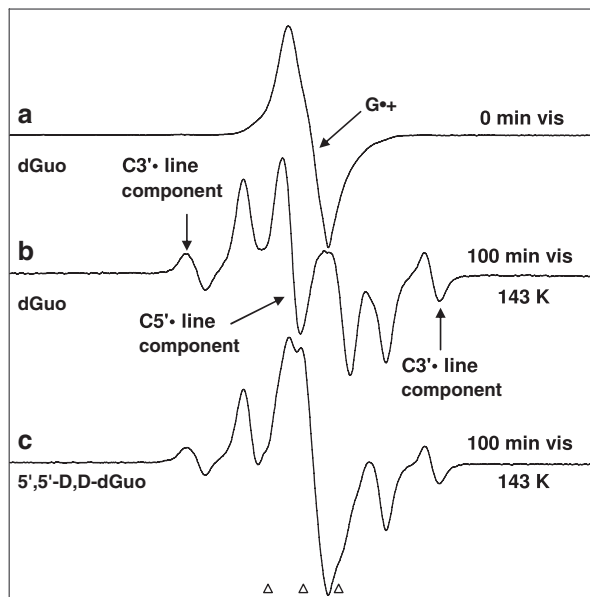
Fig. 8.17 **a** ESR spectrum of one-electron oxidized dGpdG (1 mg/ml) after $\text{Cl}_2^{\cdot-}$ attack in the presence of $\text{K}_2\text{S}_2\text{O}_8$ (5 mg/ml) as an electron scavenger in 7.5 M LiCl glass/ D_2O . **b** Spectrum found after visible photoexcitation of the sample in **a** for 90 min at 143 K. Nearly complete conversion of $\text{G}^{\cdot+}$ to sugar radicals is found. Analyses show three radicals: C5^{\cdot} (prominent doublet at the centre), C1^{\cdot} (prominent quartet) and a very small amount of C3^{\cdot} visible in the wings. All spectra were recorded at 77 K. Reprinted with permission from Ref. [119], *J. Phys. Chem. B*, Copyright (2007) American Chemical Society

formation of $\text{C3}'_{\text{dephos}}$ from these excited radicals is attributed to the transfer of the hole to the sugar moiety in the excited cation radical followed by deprotonation from $\text{C3}'$ [117].

Identification of Sugar Radicals in Nucleosides Having Isotopic Substitution at Specific Sites in the Sugar Moiety

ESR studies of sugar radical formation via photoexcitation of base cation radicals in nucleosides with isotopic substitution at specific sites in the sugar moiety resulted in the unambiguous identification of specific sugar radicals (e.g. C5^{\cdot}) and characterization of their hyperfine coupling constants. Specifically, deuterium substitution at $\text{C3}'$ -, $\text{C5}'$ -sites in dGuo [115], at $\text{C1}'$ -, $\text{C2}'$ -, $\text{C3}'$ -, $\text{C5}'$ - sites in Guo [120], at $\text{C1}'$ -, $\text{C2}'$ -, $\text{C5}'$ - sites in Ado and at $\text{C5}'$ -site in 5'-AMP [121], as well as ^{13}C substitution at the $\text{C5}'$ -atom in dAdo [116] resulted in the unambiguous identification of specific sugar radicals (e.g. C5^{\cdot}) and their hyperfine coupling(s). The spectra presented in Fig. 8.18, confirmed that C5^{\cdot} is formed on photoexcitation of $\text{G}^{\cdot+}$. In this case, matched samples of dGuo and in 5',5'-D,D-dGuo were used [115]. The central anisotropic doublet (ca. 19 G) from C5^{\cdot} (spectrum B, Fig. 8.18) in dGuo has collapsed to a singlet (spectrum C, Fig. 8.18) in 5',5'-D,D-dGuo owing to the much smaller hyperfine coupling of deuterium to that of hydrogen.

Fig. 8.18 **a** Spectrum of G^{++} in dGuo before illumination; **b** After visible illumination at 143 K of G^{++} in dGuo, showing a nearly complete conversion to sugar radicals. Analyses show three radicals are present: $C5^{\bullet}$ (prominent doublet at the centre), $C1^{\bullet}$ (prominent quartet) and $C3^{\bullet}$ visible in the wings. **c** After visible illumination at 143 K of G^{++} in 5',5'-D,D-dGuo. The central doublet from $C5^{\bullet}$ has collapsed to a singlet. All spectra were recorded at 77 K. Adapted with permission from Ref. [115], *Nucleic Acids Res.*, Copyright (2005), Oxford University Press



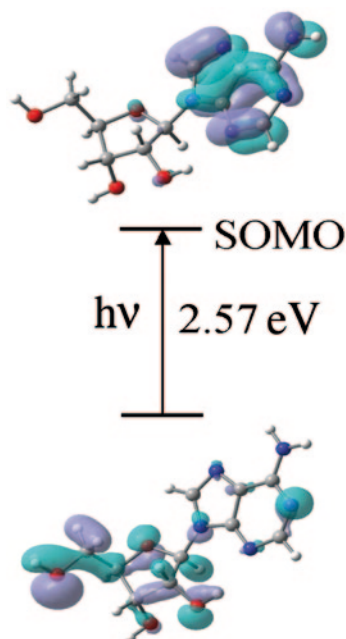
No Evidence of $C4^{\bullet}$ Formation via Excitation of Base Cation Radicals in DNA-Model Compounds

Theoretical calculations show that $C4^{\bullet}$ is energetically as stable as $C1^{\bullet}$ and $C3^{\bullet}$ [115, 116, 126]. Thus, we would expect that $C4^{\bullet}$ should be formed in irradiated DNA based on C-H bond energies. However, analyses employing ESR benchmark spectra of sugar radicals have found no ESR evidence for $C4^{\bullet}$ formation as yet via photoexcitation of purine cation radical in DNA and RNA model systems (monomers to oligomers) or in highly polymerized dsDNA [6–12, 81, 82, 115–121]. In X-ray irradiated, crystalline, dsDNA oligonucleotide samples, where direct ionization and hole formation at the sugar moiety is expected, the products identified also showed no evidence for $C4^{\bullet}$ as an intermediate [127]. These results are in keeping with our understanding that sugar radical formation both from holes on sugar from direct ionization and excitation of base cation radicals is controlled not by bond energies but by hole distribution. (Sect. 8.8.2.3 and Ref. [117]).

8.8.2.4 Factors Dictating the Extent and Type of Sugar Radical Formation via Excitation of Base Cation Radicals

ESR studies of sugar radical formation by photoexcitation of base cation radicals in various DNA-model structures, e.g. nucleosides, nucleotides and their derivatives, in DNA-oligomers, and in DNA have shown that a number of factors crucially influence the yields of each sugar radical (i.e., $C1^{\bullet}$, $C3^{\bullet}$, and $C5^{\bullet}$) formed. The

Fig. 8.19 A representative TD-B3LYP/6–31G(d) calculated electronic transition (10th) in adenosine occurring from inner core doubly occupied molecular orbital (62β) to 70β the singly occupied molecular orbital (SOMO). Significant hole localization at C5' is apparent in the excited state. The lower figure represents the SOMO after the transition showing the hole moves from base to sugar. Reprinted with permission from Ref. [121], *J. Phys. Chem. B*, Copyright (2008) American Chemical Society

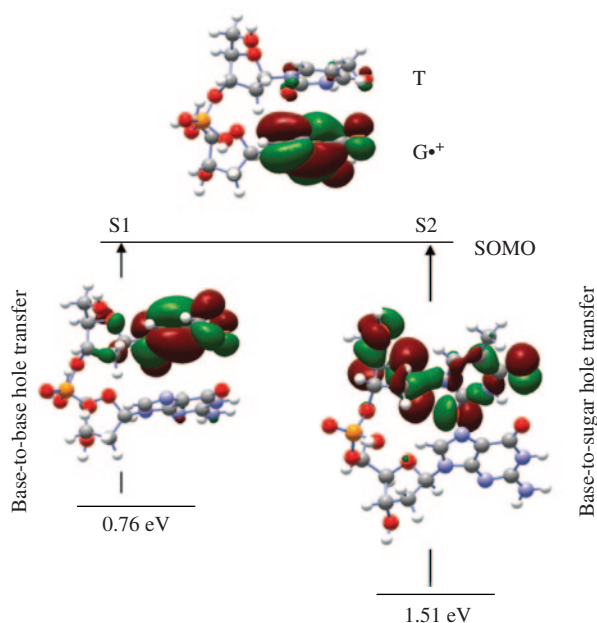


factors cited were: (i) the site of phosphate substitution (at 3'- or 5, (ii) the pH (i.e., the protonation state of the cation radical), (iii) the wavelength or the excitation energy, (iv) the temperature during photoexcitation, (v) the length and sequence of the oligomer, and (vi) whether the oligomer was single or double stranded. [6–12, 81, 82, 115–121]. The effects of these factors upon the sugar radical formation via excited base cation radical have recently been reviewed [11].

8.8.2.5 TD-DFT Studies of the Mechanism Involved in Sugar Radical Formation by Excitation of Base Cation Radicals

The TD-DFT calculations for excited states of DNA base cation radicals (Fig. 8.19) have been successfully employed to explain the wavelength dependence of sugar radical formation in DNA [115], in dsDNA-oligomers [81, 82], and in ssDNA-oligomers [82, 118, 119]. These calculations have also elucidated the mechanism of sugar radical formation by photoexcitation of purine cation radicals in a number of model systems [6–12, 19, 118, 122–125]. The ground state geometries of $G^{+\bullet}$ in dGuo [113], $A(-H)^{\bullet}$ in dAdo [114], $A^{+\bullet}$ in Ado [121], and several dinucleosides phosphates (TpdG, dGpdG, dApdA, dApT, TpdA, and dGpT) in their cation radical states were optimized employing B3LYP/6–31G* and B3LYP/6–31G(d) methods and subsequently, their vertical excited states were examined [19, 118, 122–125]. For example, for $A^{+\bullet}$ in Ado, TD-DFT (B3LYP) calculations were carried out employing the 6–31G(d) basis set and the 13 lowest transition energies were calculated [121].

Fig. 8.20 Schematic representation of the MOs and their energies from TD-DFT/6-31G(d) calculations. The transition energies of inner-shell (core) MOs to SOMO suggest sugar radical formation at lower (UVA-vis) wavelengths via *base-to-sugar* hole transfer, and *base-to-base* transitions at longer wavelengths. Adapted with permission from Ref. [118], *Radiation Research*, Copyright (2006), Radiation Research Society

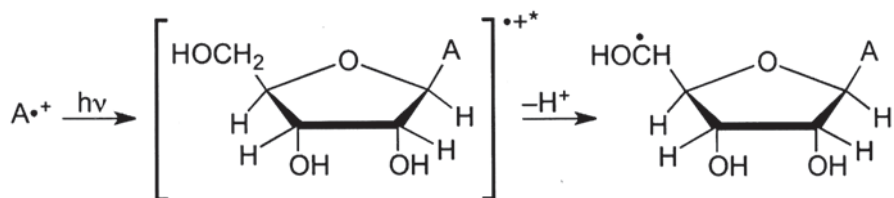


It is evident from molecular orbital plots shown in Fig. 8.19 that, the SOMO is localized on the adenine base in $A^{+\bullet}$ of Ado in the ground state in agreement with experiment [121]. During electronic excitations, the hole transfers from the adenine base to the sugar moiety in which the hole is significantly localized on C5'. Deprotonation this site results in the formation of C5' $^{\bullet}$ as found by experiment [121].

TD-DFT/6-31G(d) calculations of base cation radicals in dinucleoside phosphates have also shown evidence of *base-to-base* hole transfer as the lowest energy transition in all the dinucleosides phosphates studied, whereas, higher energy transitions involved *base-to-sugar* hole transfer. This is illustrated in TpdG in Fig. 8.20. Thus, ESR combined with TD-DFT studies show that the spin and charge localization changes from the base cation radical to the sugar in the excited state. Deprotonation is found to occur at sites of high spin and charge (hole localization) which results in formation of a neutral sugar radical. Of course, this deprotonation must occur within the lifetime of the excited state (Scheme 8.11).

8.8.3 Frank Strand Breaks Via a Double Oxidation Mechanism

The correlation between the yield of free radicals and the yield of strand breaks was investigated by Bernhard and his group [8, 38, 128–133]. X-ray irradiated (4 K) crystalline, dsDNA-oligomers, and pUC18 plasmid films were used. These studies led to the proposal of a “double oxidation” mechanism of frank strand break formation via the direct-type effects of ionizing radiation [8, 38, 128–133], and are



Scheme 8.11 Formation of a sugar radical e.g., C5[•] via photo-excited A^{•+}. Adapted with permission from Ref. [80], *J. Phys. Chem. B*, Copyright (2008) American Chemical Society

described below in sections 8.8.3.1 and 8.8.3.2. We note here that the probability of a double oxidation process was mentioned as a possibility in the literature earlier in γ -irradiated (high dose, 77 K) hydrated DNA ($\Gamma = 12 \pm 2$ D₂O per nucleotide) [76].

8.8.3.1 Distinguishing Sugar Radicals from Base Radicals

Employing well-defined crystalline samples of dsDNA-oligomers [8, 129], the authors showed that sugar radicals in X-irradiated crystalline DNA oligomers at 4 K can be distinguished from the DNA-base anion and cation radicals by their different dose saturation behavior. The G values for radical production and the k values for destruction was obtained by fitting dose-yield data to Eq. 8.1 in Sect. 8.7.2. This was done assuming that the sugar and base radicals acted independently so that separate G-value and k-value were obtained for each [129]. From these values, it was found that 80 to 90% of the initial radicals were on the bases and the remainder (10 to 20%) were on the sugar-phosphate backbone. These values were in excellent agreement with the results obtained earlier in γ -irradiated (77 K) highly polymeric DNA hydrated to $\Gamma = 14 \pm 2$ D₂O per nucleotide (Table 8.1 and Fig. 8.2) [15]. Further differentiation of the base and sugar radicals was achieved using the k values in Eq. 8.1. The k values for radiation-induced destruction of pre-existing sugar radicals has been observed to be 28–81 times lower than those for base radicals [129]. From these studies, and with the assumption that base-centered radicals do not lead to frank strand breaks [129], the authors concluded that radiation-induced frank strand breaks produced via direct-type effects resulted from sugar radicals [129].

8.8.3.2 Correlation of Trapped Radical Yields with Strand Break and Unaltered Base Release Yields (4 K)

On warming irradiated DNA samples to room temperature, the stable DNA damage products, e.g., single and double strand breaks [8, 38, 128–131] and base release yields [132, 133] were measured and compared with the yields of sugar radicals at 4 K.

Single strand break (SSB) measurements in X-ray-irradiated pUC18 plasmid DNA films as a function of hydration showed that at Γ ca. ≤ 10 H₂O/nucleotide, the

yield of strand breaks observed at room temperature exceeded the yield of trapped sugar radicals at 4 K in the same samples. In crystalline $d[\text{CGCGCG}]_2$ or in films of $d[\text{CGCGCG}]_2$ at $\Gamma=2.5$ to 7.5 waters/nucleotide, the yields of sugar radicals and free base release were compared [132, 133]. A “shortfall” of trapped sugar radicals as compared to the base release [8, 132, 133] was reported. Since it has been well-accepted in the literature that free unaltered base release is a good estimate of single strand breaks [2, 35, 132, 133], this indicates a shortfall of sugar radicals relative to strand breaks [8, 38, 128–131].

From the G and k-values of base-centered radicals, it is possible that the low trapping efficiency of ion-radicals at low hydrations may account for the shortfall. Thus, the base cation radicals that escape being trapped might lead to increased double oxidations on sugars with subsequent strand break formation, and, consequently, free radicals yields would not correlate with strand break yields. On this basis, the authors proposed a double oxidation event in which oxidation of a sugar radical by a nearby base cation radical leads to a diamagnetic (ESR-mute) sugar carbocation which forms a strand break [8, 133].

8.8.3.3 Further Investigation of Strand Break Yields in pUC18

The radiation-induced frank strand breaks produced in X-ray irradiated pUC18 DNA at hydrations $\Gamma=4$ to 34.5 $\text{H}_2\text{O}/\text{nucleotide}$ were measured by O’Neill [11, 134] and Yokoya et al. [11, 134, 135]. The G-values for strand breaks [134] reported by these authors at $\Gamma=4\pm 1.5$ were *ca.* 1.5 to 2 times lower than those reported by Bernhard and co-workers [131]. They explained their lower G-values by proposing that the number of radiation-induced clustered lesions such as strand breaks, base damage, or abasic sites in each strand may be greater than one. Bernhard and co-workers attributed this underestimation of strand breaks to the fact that the plasmid will register a single strand break even if there are other single strand breaks in the plasmid. [38, 131]. Thus, multiple damages especially in clustered DNA lesions would not be properly accounted for.

8.8.3.4 Free Radical Yields vs. Base Release Yields in Kr Ion-Beam Irradiated Samples

It is evident from Table 8.7 that the G-values for sugar radical formation (77 K) in Kr ion-beam irradiated hydrated ($\Gamma=12\pm 2$ $\text{D}_2\text{O}/\text{nucleotide}$) highly polymerized salmon testes DNA samples are the same as the G-values of release of unaltered base [35]. These data do not provide evidence for “double oxidations” even though they would likely be more probable with high LET radiation, in which the high energy density may cause multiple oxidations at a single site, than with low LET irradiation. However, this lack of a shortfall of free radicals may be a result of compensating processes and is not necessarily proof that double oxidations do not occur. For γ -irradiated hydrated salmon testes DNA ($\Gamma=12\pm 2$), this work [35] and the

earlier work by Swarts et al. [46] have shown that the G-value of the free unaltered base release is *ca.* 1.5 times higher than the G-values for sugar radical formation (77 K). Since, recent theoretical work suggests that a double oxidation process in which a base cation radical oxidizes a pre-existing sugar radical is energetically quite favorable [136], this mechanism must be considered likely.

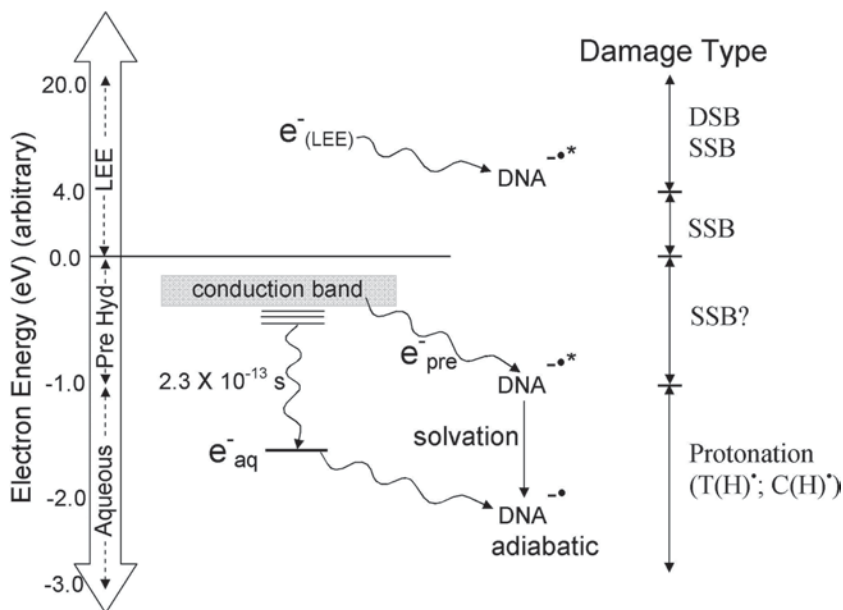
8.8.4 DNA-Radicals from Electron Addition Reactions: Thermal Electrons vs. Low Energy Electron (LEE) Effects

With each ionization event, high energy radiation such as γ -rays, produces electrons of various energies, from very high (keV) to near zero [113, 137]. The number of electrons produced increases as the energy decreases since the high energy electrons result in cascades of lower energy electrons [113, 137, 138]. Although the average electron energy due to an ionization event by a γ -ray photon is ~ 30 to 40 eV, the largest grouping by energy is so-called low energy electrons (LEE) with energies from 0 to 20 eV [17–20, 138]. Upon thermalization, most electrons are trapped on the DNA bases [1, 2, 6–12, 25, 26]. Although initial electron capture likely occurs at all four bases, rapid electron transfer via tunneling to the most electron affinic bases, T and C, resulting in formation of the anion radicals T $^{\cdot-}$ and C $^{\cdot-}$ (Scheme 8.2). C $^{\cdot-}$ rapidly reversibly protonates at N3 forming C(N3)H $^{\cdot}$; the proton that transfers is the N1 hydrogen on the base paired guanine (Scheme 8.4).

Before thermalization of electrons, LEE may add to DNA and result in processes that induce bond cleavage [17–20]. LEEs have been shown to induce reactions through dissociative electron attachment (DEA) to the bases or to the sugar-phosphate backbone. Attachment to the backbone can result in immediate single strand break (ssb) and double strand break (dsb) formation [11, 17–20, 122, 139–142]. It is well known, in the gas phase, that LEE-induced DEA and a concomitant bond cleavage occurs in mass spectroscopic experiments [17–20]. The works of Sanche and coworkers have convincingly established that LEE are also potent radiation damage agents in condensed media, as well [17–20].

In Scheme 8.12, a summary of the effects of LEE on DNA is presented. For gas phase electrons impinging on DNA in the condensed phase, Sanche and coworkers have shown that both DSBs and SSBs are formed due to $LEE \geq 5$ eV and only SSBs are formed due to LEE in the energy range 0 to 4 eV [11, 17–20, 122]. The fact that a near zero eV electron can induce bond cleavage in DNA is non-intuitive; but, the fact that the DNA base electron affinity and the solvation processes result in several eV of excess energy in the condensed media is apparently sufficient to drive these bond cleavage processes leading to a strand break. The fact that the excess electron induced strand breaks have only a small activation barrier of *ca.* 0.5 eV facilitates the process [11, 17–20, 122, 139–142].

The experimental [11, 17, 20, 139–142] and theoretical [11, 17–20, 122] evidence is strong for LEE (0 to 20 eV) resulting in DNA strand cleavage. However, for DNA in aqueous solution, LEE would quickly thermalize to presolvated electrons (e_{pre}^-) of *ca.* -0.5 to 1 eV and shortly thereafter to aqueous electrons (e_{aq}^-) of *ca.*

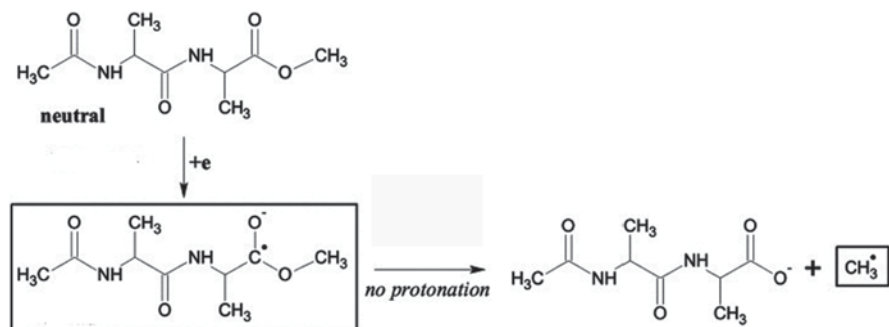


Scheme 8.12 Effects of LEE on DNA. Bond cleavage and DNA strand breaks occur for LEE but, upon thermalization, electrons are trapped by the bases and are converted to neutral radicals via protonation. These do not lead to strand breaks but, instead, to base damage

–1.6 eV (adiabatic) [17–20, 142, 143, 152] which do not cause DNA strand breaks [2, 144, 145]. Instead they add to T and C forming TH^\bullet and C(N3)H^\bullet (Schemes 8.2 and 8.4). However, the energy available after e_{pre}^- addition to DNA of several eV is clearly sufficient to result in a SSB via DEA (Scheme 8.12). DNA-strand break formation due to the attack of e_{pre}^- via DEA has also been proposed [142, 143]. But these results are suspect [19] and need confirmation.

Electrons in irradiated LiCl aqueous glasses exist in shallow traps of ca. –0.5 eV and can be considered to be prehydrated [146]. Recently, several ESR studies have been carried out in these glasses that provide evidence of bond cleavage induced by e_{pre}^- [146, 147]. In this work with peptide methyl esters such as N-acetylalanylalanine methyl ester [146] the e_{pre}^- resulted in methyl radical (CH_3^\bullet) formation at 77 K via addition to the ester groups followed by C–O bond cleavage (DEA) at 77 K (Scheme 8.13).

We note here that the thermal energy at 77 K is not sufficient to overcome the activation barrier of C–O bond cleavage in the adduct anion radical; yet, CH_3^\bullet is found abundantly [147] owing to the electron energy and electron affinity of the ester group. Similar results have been found for ESR experiments of irradiated single crystals of dimethyl phosphate [16] and diethyl phosphate [148]. Here, alkyl radicals are produced which were attributed to DEA [16, 148]. These works establish the potential for both sub-zero eV presolvated electrons, e_{pre}^- or LEE to induce bond cleavage via DEA in condensed systems.



Scheme 8.13 Reaction scheme showing e_{pre}^- -induced CH_3^{\bullet} formation in N-acetylalanylalanine methyl ester by C–O bond cleavage. Adapted with permission from Ref. [147], *J. Phys. Chem. B*, Copyright (2013), American Chemical Society

For DNA systems, ESR work with both γ -ray (see Sect. 8.2) and ion-beam (see Sect. 8.7) irradiated DNA shows evidence of radicals such as $\text{C3}'_{\text{dephos}}^{\bullet}$. This radical was proposed to result from DEA cleavage of the $\text{C3}'\text{--O}$ bond of the phosphoryl ester link by addition of LEE to the sugar-phosphate backbone (Scheme 8.9). LEE attachment to the base followed by transfer to the sugar phosphate or direct LEE addition to the sugar phosphate have been both proposed as mechanisms [17–20, 122]. Recently, the resonant attachment profiles of LEE to 5'-dCMP have been studied in the gas phase and it was suggested that the sugar-phosphate moiety was the predominant site of initial LEE localization [149]. Furthermore, $\text{C3}'_{\text{dephos}}^{\bullet}$ formation by LEE due to DEA has been supported by product analyses in ambient temperature X-irradiated TpTpT [150, 151] and in TpTpT films hydrated to $\Gamma=2.5 \text{ H}_2\text{O}/\text{nucleotide}$ [151].

The theoretical aspects of LEE-induced formation of DNA damage products, e.g., strand break formation have been recently reviewed [17–19, 122].

Acknowledgements We thank the National Cancer Institute of the National Institutes of Health (Grant RO1CA045424) for support. We thank Dr. Anil Kumar for his help in preparing this manuscript.

References

1. Sevilla MD, Becker D (2004) ESR studies of radiation damage to DNA and related biomolecules. In: Gilbert BC, Davies MJ, Murphy DM (eds) Specialist periodical reports: electron paramagnetic resonance, vol 19. Royal Society of Chemistry, Cambridge, pp 243–317
2. von Sonntag C (2006) Free-radical-induced DNA damage and its repair: a chemical perspective. Springer-Verlag, Berlin
3. Kouass SS, Girouard S, Cloutier P, Sanche L, Hunting D (2014) The relative contributions of DNA strand breaks, base damage and clustered lesions to the loss of DNA functionality induced by ionizing radiation. *Radiat Res* 181:99–110

4. Georgakilas AG, O'Neill P, Stewart RD (2013) Induction and repair of clustered DNA lesions: what do we know so far? *Radiat Res* 180:100–109
5. Swindall AF, Stanley JA, Yang ES (2013) PARP-1: friend or foe of DNA damage and repair in tumorigenesis? *Cancers (Basel)* 5:943–958
6. Becker D, Adhikary A, Sevilla MD (2007) The role of charge and spin migration in DNA radiation damage. In: Chakraborty T (ed) *Charge migration in DNA physics, chemistry and biology perspectives*. Springer-Verlag, Berlin, pp 139–175
7. Becker D, Adhikary A, Sevilla MD (2010) Mechanism of radiation induced DNA damage: direct effects. In: Rao BSM, Wishart J (eds) *Recent trends in radiation chemistry*. World Scientific Publishing Co, Singapore pp 509–542
8. Bernhard WA (2009) Radical reaction pathways initiated by direct energy deposition in DNA by ionizing radiation. In: Greenberg MM (ed) *Radical and radical ion reactivity in nucleic acid chemistry*. Wiley, New Jersey, pp 41–68
9. Sagstuen E, Hole EO (2009) Radiation produced radicals. In: Brustolon M, Giamello E (eds) *Electron paramagnetic resonance*. Wiley, New Jersey, pp 325–381
10. Close DM (2008) From the primary radiation induced radicals in DNA constituents to strand breaks: low temperature EPR/ENDOR studies. In: Shukla MK, Leszczynski J (eds) *Radiation-induced molecular phenomena in nucleic acids: a comprehensive theoretical and experimental analysis*. Springer-Verlag, Berlin, pp 493–529
11. Becker D, Adhikary A, Sevilla MD (2010) Physicochemical Mechanisms of Radiation Induced DNA Damage. In: Hatano Y, Katsumura Y, Mozumder A (eds) *Charged particle and photon interactions with matter—recent advances, applications, and interfaces*. CRC Press, Taylor & Francis Group, Boca Raton, pp 503–541
12. Adhikary A, Kumar A, Becker D, Sevilla MD (2012) Theory and ESR spectral studies of DNA-radicals. In: Chatgililoglu C, Struder A (eds) *Encyclopedia of radicals in chemistry, biology and materials*. Wiley, Chichester, pp 1371–1396
13. von Sonntag C (2010) Radiation-induced DNA damage: indirect effects. In: Rao BSM, Wishart J (eds) *Recent trends in radiation chemistry*. World Scientific Publishing Co, Singapore, pp 543–562
14. O'Neill P (2001) Radiation-induced damage in DNA. In: Rao BSM, Jonah CD (eds) *Radiation chemistry: present status and future trends*. Elsevier, Amsterdam, pp 585–622
15. Shukla LI, Pazdro R, Becker D, Sevilla MD (2005) Sugar radicals in DNA: isolation of neutral radicals in gamma-irradiated DNA by hole and electron scavenging. *Radiat Res* 163:591–602
16. Adhikary A, Becker D, Palmer BJ, Heizer AN, Sevilla MD (2012) Direct formation of the C5'-radical in the sugar-phosphate backbone of DNA by high energy radiation. *J Phys Chem B* 116:5900–5906
17. Caron LC, Sanche L (2012) Theoretical studies of electron interactions with DNA and its subunits from tetrahydrofuran to plasmid DNA. In: Čársky P, Čurík R (eds) *Low-energy electron scattering from molecules, biomolecules and surfaces*. CRC Press, Taylor & Francis Group, Boca Raton, pp 161–230
18. Gu J, Leszczynski J, Schaefer HF III (2012) Interactions of electrons with bare and hydrated biomolecules: from nucleic acid bases to DNA segments. *Chem Rev* 112:5603–5640
19. Kumar A, Sevilla MD (2012) Low-Energy-Electron (LEE)-Induced DNA damage: theoretical approaches to modeling experiment. In: Shukla MK, Leszczynski J (eds) *Handbook of computational chemistry volume III: applications—biomolecules*. Springer-Verlag, Berlin, pp 1215–1256
20. Arumainayagam CR, Lee HL, Nelson RB, Haines DR, Guanwardane RP (2010) Low-energy electron-induced reactions in condensed matter. *Surface Sci Rep* 65:1–44
21. Weiland B, Hüttermann J (1998) Free radicals from X-irradiated 'dry' and hydrated lyophilized DNA as studied by electron spin resonance spectroscopy: analysis of spectral components between 77K and room temperature. *Int J Radiat Biol* 74:341–358

22. Weiland B, Hüttermann J (1999) Free radicals from lyophilized 'dry' DNA bombarded with heavy-ions as studied by electron spin resonance spectroscopy. *Int J Radiat Biol* 75:1169–1175
23. Debije MG, Bernhard WA (2000) Electron and hole transfer induced by thermal annealing of crystalline DNA X-irradiated at 4 K. *J Phys Chem B* 104:7845–7851
24. Adhikary A, Khanduri D, Pottiboyina V, Rice CT, Sevilla MD (2010) formation of aminyl radicals on electron attachment to AZT: abstraction from the sugar phosphate backbone vs. one-electron oxidation of guanine. *J Phys Chem B* 114:9289–9299
25. Bernhard WA, Close DM (2004) DNA damage dictates the biological consequences of ionizing radiation: the chemical pathways. In: Mozumdar A, Hatano Y (eds) *Charged particle and photon interactions with matter chemical, physicochemical and biological consequences with applications*. Marcel Dekkar, New York, pp 431–470
26. Becker D, Sevilla MD (2008) EPR studies of radiation damage to DNA and related molecules. In: Gilbert BC, Davies MJ, Murphy DM (eds) *Specialist periodical reports: electron paramagnetic resonance*, vol 21. Royal Society of Chemistry, Cambridge, pp 33–58
27. Kumar A, Sevilla MD (2013) π - vs. σ -radical states of one-electron-oxidized DNA/RNA bases: a density functional theory study. *J Phys Chem B* 117:11623–11632
28. Shukla LI, Adhikary A, Pazdro R, Becker D, Sevilla MD (2004) Formation of 8-oxo-7,8-dihydroguanine-radicals in γ -irradiated DNA by multiple one-electron oxidations. *Nucleic Acids Res* 32:6565–6574
29. Shukla LI, Adhikary A, Pazdro R, Becker D, Sevilla MD (2007) Formation of 8-oxo-7,8-dihydroguanine-Radicals in γ -irradiated DNA by multiple one-electron oxidations. *Nucleic Acids Res* 35:2460–2461
30. Adhikary A, Khanduri D, Sevilla MD (2009) Direct Observation of the Protonation State and Hole Localization Site in DNA-Oligomers. *J Am Chem Soc* 131:8614–8619
31. Adhikary A, Sevilla MD (2011) Comment on “Theoretical study of polaron formation in poly(G)-poly(C) cations”. *J Phys Chem B* 115:8947–8948
32. Sevilla MD, Becker D, Yan M, Summerfield SR (1991) Relative abundances of primary ion radicals in γ -irradiated DNA: cytosine vs. Thymine anions and guanine vs. adenine cations. *J Phys Chem* 95:3409–3415
33. Becker D, Razzkazovskii Y, Callaghan MU, Sevilla MD (1996) Electron spin resonance of DNA irradiated with a heavy-ion beam ($^{16}\text{O}^{8+}$): evidence for damage to the deoxyribose phosphate backbone. *Radiat Res* 146:361–368
34. Becker D, Bryant-Friedrich A, Trzasko C, Sevilla MD (2003) Electron spin resonance study of DNA irradiated with an argon-ion beam: evidence for formation of sugar phosphate backbone radicals. *Radiat Res* 160:174–185
35. Becker D, Adhikary A, Tetteh ST, Bull AW, Sevilla MD (2012) Kr-86 ion-beam irradiation of hydrated DNA: free radical and unaltered base yields. *Radiat Res* 178:524–537
36. Wang W, Becker D, Sevilla MD (1993) The influence of hydration on the absolute yields of primary ionic free-radicals in γ -irradiated DNA at 77-K. Total radical yields. *Radiat Res* 135:146–154
37. Spalletta RA, Bernhard WA (1992) Free radical yields in A:T polydeoxynucleotides, oligodeoxynucleotides, and monodeoxynucleotides at 4 K. *Radiat Res* 130:7–14
38. Purkayastha S, Milligan JR, Bernhard WA (2007) On the chemical yield of base lesions, strand breaks, and clustered damage generated in plasmid DNA by the direct effect of X-rays. *Radiat Res* 168:357–366
39. Ambroz HB, Kemp TJ, Rodger A, Przybytniak G (2004) Ferric and ferrous ions: binding to DNA and influence on radiation-induced processes. *Radiat Phys Chem* 71:1023–1030
40. Close DM (1997) Where are the sugar radicals in irradiated DNA? *Radiat Res* 147:663–673
41. Colson AO, Sevilla MD (1995) Structure and relative stability of deoxyribose radicals in a model DNA backbone: *ab initio* molecular orbital calculations. *J Phys Chem* 99:3867–3874
42. Colson AO, Sevilla MD (1995) Elucidation of primary radiation damage in DNA through application of *ab initio* molecular orbital theory. *Int J Radiat Biol* 67:627–645

43. Gregoli S, Olast M, Bertinchamps A (1979) Charge-migration phenomena in gamma-irradiated costacking complexes of DNA nucleotides 2. ESR study of various complexes in frozen solution. *Radiat Res* 77:417–431
44. van Lith D, Dehaas MP, Warman JM, Hummel A (1986) Electron migration in hydrated DNA and collagen at low-temperatures. I. Effect of water concentration. *J Chem Soc Faraday Trans 1*(82):2933–2943
45. Symons MCR (1991) The role of radiation induced charge migration with DNA: ESR studies. In: Martin FE, O'Neill P (eds) *The early effects of radiation on DNA*, vol 54. Springer-Verlag, Berlin, pp 111–124 (NATO ASI Series, Series H: Cell Biology)
46. Swarts SG, Sevilla MD, Becker D, Tokar CJ, Wheeler KT (1992) Radiation-induced DNA damage as a function of hydration. I. Release of unaltered bases. *Radiat Res* 129:333–344
47. Hüttermann J, Röhrig M, Köhnlein W (1992) Free radicals from irradiated lyophilized DNA: influence of water of hydration. *Int J Radiat Biol* 61:299–313
48. Becker D, La Vere T, Sevilla MD (1994) ESR Detection at 77 K of the Hydroxyl Radical in the Hydration Layer of Gamma-Irradiated DNA. *Radiat Res* 140:123–129
49. La Vere T, Becker D, Sevilla MD (1996) Yields of $\cdot\text{OH}$ in gamma-irradiated DNA as a function of DNA hydration: hole transfer in competition with $\cdot\text{OH}$ formation. *Radiat Res* 145:673–680
50. Sevilla MD, Becker D, Razskazovskii Y (1997) Electron and hole transfer within DNA and its hydration layer. *Nukleonika* 42:283–292
51. Becker D, Sevilla MD (1998) Radiation damage to DNA and related biomolecules. In: Gilbert BC, Davies MJ, Murphy DM (eds) *Specialist periodical reports: electron paramagnetic resonance*, vol 16. Royal Society of Chemistry, Cambridge, pp 79–114
52. Cai Z, Sevilla MD (2004) Studies of excess electron and hole transfers. In: Schuster GB (ed) *Long range charge transfer in DNA II*. *Topics In Current Chemistry* 237:103–127
53. Debije MG, Strickler MD, Bernhard WA (2000) On the efficiency of hole and electron transfer from the hydration layer to DNA: An EPR study of crystalline DNA X-irradiated at 4 K. *Radiat Res* 154:163–170
54. Falk M, Hartman KA Jr, Lord RC (1963) Hydration of deoxyribonucleic acid. II. An infrared study. *J Am Chem Soc* 85:387–391
55. Debije MG, Milano MT, Bernhard WA (1999) DNA responds to ionizing radiation as an insulator, not as a “molecular wire”. *Angew Chem Int Ed* 38:2752–2756
56. Messer A, Carpenter K, Forzley K, Buchanan J, Yang S, Razskazovskii Y, Cai Z, Sevilla MD (2000) Electron spin resonance study of electron transfer rates in DNA: determination of the tunneling constant beta for single-step excess electron transfer. *J Phys Chem B* 104:1128–1136
57. Cai Z, Sevilla MD (2000) Electron spin resonance study of electron transfer in DNA: inter-double-strand tunneling processes. *J Phys Chem B* 104:6942–6949
58. Cai Z, Gu Z, Sevilla MD (2000) Electron spin resonance study of the temperature dependence of electron transfer in DNA: competitive processes of tunneling, protonation at carbon, and hopping. *J Phys Chem B* 104:10406–10411
59. Cai Z, Gu Z, Sevilla MD (2001) Electron spin resonance study of electron and hole transfer in DNA: effects of hydration, aliphatic amine cations, and histone proteins. *J Phys Chem B* 105:6031–6041
60. Cai Z, Li X, Sevilla MD (2002) Excess electron transfer in DNA: effect of base sequence and proton transfer. *J Phys Chem B* 106:2755–2762
61. Sevilla MD (2006) Comment on electron transfer vs. differential decay in irradiated DNA. *J Phys Chem B* 110:25122–25123
62. Wagenknecht HA (2003) Reductive electron transfer and transport of excess electrons in DNA. *Angew Chem Int Ed* 42:2454–2460
63. Debije MG, Bernhard WA (1999) Free radical yields in crystalline DNA X-irradiated at 4 K. *Radiat Res* 152:583–589
64. Debije MG, Bernhard WA (2000) Electron and hole transfer induced by thermal annealing of crystalline DNA X-irradiated at 4 K. *J Phys Chem B* 104:7845–7851

65. Razskazovskii Y, Swarts SG, Falcone JM, Taylor C, Sevilla MD (1997) Competitive electron scavenging by chemically modified pyrimidine bases in bromine-doped DNA: relative efficiencies and relevance to intrastrand electron migration distances. *J Phys Chem B* 101:1460–1467
66. Fujitsuka M, Majima T (2012) Hole and excess electron transfer dynamics in DNA. *Phys Chem Chem Phys* 14:11234–11244
67. Genereux JC, Barton JK (2010) Mechanisms for DNA charge transport. *Chem Rev* 110:1642–1662
68. Giese B (2002) Long-distance electron transfer through DNA. *Ann Rev Biochem* 71:51–70
69. Wagenknecht HA (ed) (2005) Charge transfer in DNA: from mechanism to application. Wiley-VCH Verlag GmbH & Co. KGaA, Weinheim
70. Schuster GB (ed) (2004) Long range charge transfer in DNA. I and II in topics in: current chemistry. Springer, Berlin
71. Steenken S (1997) Electron transfer in DNA? Competition by ultra-fast proton transfer? *Biol Chem* 378:1293–1297
72. Todres ZV (2009) Ion-radical organic chemistry principles and applications. CRC Press, Taylor & Francis Group, Boca Raton, pp 1–74
73. Adhikary A, Kumar A, Heizer AN, Palmer BJ, Pottiboyina V, Liang Y, Wnuk SF, Sevilla MD (2013) Hydroxyl ion addition to one-electron oxidized thymine: unimolecular interconversion of C5 to C6 OH-adducts. *J Am Chem Soc* 135:3121–3135
74. Black PJ, Bernhard WA (2012) Excess electron trapping in duplex DNA: long range transfer via stacked adenines. *J Phys Chem B* 116:13211–13218
75. Wang W, Sevilla MD (1994) Protonation of nucleobase anions in gamma-irradiated DNA and model systems. Which DNA base is the ultimate sink for the electron? *Radiat Res* 138:9–17
76. Wang W, Yan M, Becker D, Sevilla MD (1994) The influence of hydration on the absolute yields of primary free radicals in gamma-irradiated DNA at 77 K. II. individual radical yields. *Radiat Res* 137:2–10
77. Ormerod MG (1965) Free-radical formation in irradiated deoxyribonucleic acid. *Int J Radiat Biol* 9:291–300
78. Adhikary A, Kumar A, Becker D, Sevilla MD (2006) The guanine cation radical: investigation of deprotonation states by ESR and DFT. *J Phys Chem B* 110:24171–24180
79. Adhikary A, Kumar A, Khanduri D, Sevilla MD (2008) The effect of base stacking on the acid-base properties of the adenine cation radical [A⁺] in solution: ESR and DFT studies. *J Am Chem Soc* 130:10282–10292
80. Adhikary A, Khanduri D, Kumar A, Sevilla MD (2008) Photo-excitation of adenine cation radical [A⁺] in the near UV-Vis region produces sugar radicals in adenosine and in its nucleotides. *J Phys Chem B* 112:15844–15855
81. Adhikary A, Kumar A, Munafa SA, Khanduri D, Sevilla MD (2010) Prototropic equilibria in DNA containing one-electron oxidized GC: intra-duplex vs. Duplex to solvent deprotonation. *Phys Chem Chem Phys* 12:5353–5368
82. Khanduri D, Adhikary A, Sevilla MD (2011) Highly oxidizing excited states of one-electron oxidized guanine in DNA: wavelength and pH dependence. *J Am Chem Soc* 133:4527–4537
83. Naumov S, von Sonntag C (2008) Guanine-derived radicals: dielectric constant-dependent stability and UV/Vis spectral properties: a DFT study. *Radiat Res* 169:364–372
84. Luo Q, Li QS, Xie Y, Schaefer HF III (2005) Radicals derived from guanine: structures and energetics. *Collect Czech Chem Commun* 70:826–836
85. Mundy CJ, Colvin ME, Quong AA (2002) Irradiated guanine: a car-parrinello molecular dynamics study of dehydrogenation in the presence of an OH Radical. *J Phys Chem A* 106:10063–10071
86. Chatgililoglu C, Caminal C, Altieri A, Vougioukalakis GC, Mulazzani QG, Gimisis T, Guerra M (2006) Tautomerism in the guanyl radical. *J Am Chem Soc* 128:13796–13805
87. Chatgililoglu C, Caminal C, Guerra M, Mulazzani QG (2005) Tautomers of one-electron-oxidized guanosine. *Angew Chem Int Ed* 44:6030–6032

88. Chatgililoglu C, D'Angelantonio M, Kciuk G, Bobrowski K (2011) New insights into the reaction paths of hydroxyl radicals with 2'-deoxyguanosine. *Chem Res Toxicol* 24:2200–2206
89. Kumar A, Sevilla MD (2009) Influence of hydration on proton transfer in the guanine-cytosine radical cation (G^{•+})-C base pair: a density functional theory study. *J Phys Chem B* 113:11359–11361
90. Cerón-Carrasco JP, Requena A, Perpete EA, Michaux C, Jacquemin D (2010) Theoretical study of the tautomerism in the one-electron oxidized guanine-cytosine base pair. *J Phys Chem B* 114:13439–13445
91. Kobayashi K, Yamagami R, Tagawa S (2008) Effect of base sequence and deprotonation of guanine cation radical in DNA. *J Phys Chem B* 112:10752–10757
92. Adhikary A, Kumar A, Palmer BJ, Todd AD, Sevilla MD (2013) Formation of S-Cl phosphorothioate adduct radicals in dsDNA S-oligomers: hole transfer to guanine vs. disulfide anion radical formation. *J Am Chem Soc* 135:12827–12838
93. Greenberg MM (2004) In vitro and In vivo effects of oxidative damage to deoxyguanosine. *Biochem Soc Trans* 32:46–50
94. Cadet J, Douki T, Ravanat JL (2011) Measurement of oxidatively generated base damage in cellular DNA. *Mutat Res* 711:3–12
95. Fleming AM, Muller JG, Dlouhy AC, Burrows CJ (2012) Structural context effects in the oxidation of 8-oxo-7,8-dihydro-2'-deoxyguanosine to hydantoin products: electrostatics, base stacking, and base pairing. *J Am Chem Soc* 134:15091–15102
96. van Loon B, Markkanen E, Hübscher U (2010) Oxygen as a friend and enemy: how to combat the mutational potential of 8-oxo-guanine. *DNA Repair (Amst)* 9:604–616
97. Joffe A, Geacintov NE, Shafirovich V (2003) DNA lesions derived from the site selective oxidation of guanine by carbonate radical anions. *Chem Res Toxicol* 16:1528–1538
98. Misiaszek R, Crean C, Joffe A, Geacintov NE, Shafirovich V (2004) Oxidative DNA damage associated with combination of guanine and superoxide radicals and repair mechanisms via radical trapping. *J Biol Chem* 31:32106–32115
99. Cullis PM, Malone ME, Merson-Davies LA (1996) Guanine radical cations are precursor of 7,8-dihydro-8-oxo-2'-deoxyguanosine but are not precursor of immediate strand breaks in DNA. *J Am Chem Soc* 118:2775–2781
100. Kasai H, Yamaizumi Z, Berger M, Cadet J (1992) Photosensitized formation of 7,8-dihydro-8-oxo-2'-deoxyguanosine (8-hydroxy-2'-deoxyguanosine) in DNA by riboflavin: a non singlet oxygen mediated reaction. *J Am Chem Soc* 114:9692–9694
101. Psciuk BT, Schlegel HB (2013) Computational prediction of one-electron reduction potentials and acid dissociation constants for guanine oxidation intermediates and products. *J Phys Chem B* 117:9518–9531
102. Buettner GR (1993) the pecking order of free radicals and antioxidants: lipid peroxidation, alpha-tocopherol, and ascorbate. *Arch Biochem Biophys* 300:535–543
103. Schuhmacher H, Dangendorf V (2002) Experimental tools for track structure investigations: new approaches for dosimetry and microdosimetry. *Radiat Prot Dosimetry* 99:317–323
104. Friedland W, Jacob P, Bernhardt P, Paretzke HG, Dingfelder M (2003) Simulation of DNA damage after proton irradiation. *Radiat Res* 159:401–410
105. Baldacchino G, Katsumura Y (2010) Chemical processes in heavy ion tracks. In: Rao BSM, Wishart J (eds) *Recent trends in radiation chemistry*. World Scientific Publishing Co, Singapore, pp 231–253
106. Nikjoo H, Uehara S (2004) Track structure studies of biological systems. In: Mozumdar A, Hatano Y (eds) *Charged particle and photon interactions with matter chemical, physico-chemical and biological consequences with applications*. Marcel Dekkar, Inc., New York, pp 491–531
107. Chatterjee A, Holley WR (1993) Computer-simulation of Initial events in the biochemical-mechanisms of DNA-damage. *Adv Radiat Biol* 17:181–226

108. Kraft G, Kramer M (1993) Linear-energy-transfer and track structure. *Adv Radiat Biol* 17:1–52
109. Goodhead DT, Leenhouts HP, Paretzke HG, Terrisol M, Nikjoo H, Blaauboer R (1994) Track structure approaches to the interpretation of radiation effects on DNA. *Radiat Prot Dosimetry* 52:217–223
110. Magee JL, Chatterjee A (1987) Track reactions of radiation chemistry. In: Freeman GR (ed) *Kinetics of nonhomogeneous processes*. Wiley, New York, pp 171–214
111. Muroya Y, Plante I, Azzam EI, Meesungnoen J, Katsumura Y, Jay-Gerin JP (2006) High-LET ion radiolysis of water: visualization of the formation and evolution of ion tracks and relevance to the radiation-induced bystander effect. *Radiat Res* 165:485–491
112. Bowman MK, Becker D, Sevilla MD, Zimbrick JD (2005) Track structure in DNA irradiated with heavy ions. *Radiat Res* 163:447–454
113. Hatano Y, Mozumder A (2004) Interaction of fast charged particle with matter. In: Hatano Y, Mozumder A (eds) *Charged particle and photon interactions with matter: chemical, physicochemical, and biological consequences with applications*. Macel Dekkar, New York, pp 1–29
114. Shukla LI, Pazdro R, Huang J, DeVreugd C, Becker D, Sevilla MD (2004) The formation of DNA sugar radicals from photoexcitation of guanine cation radicals. *Radiat Res* 161:582–590
115. Adhikary A, Malkhasian AYS, Collins S, Koppen J, Becker D, Sevilla MD (2005) UVA-visible photo-excitation of guanine radical cations produces sugar radicals in DNA and model structures. *Nucleic Acids Res* 33:5553–5564
116. Adhikary A, Becker D, Collins S, Koppen J, Sevilla MD (2006) C5'- and C3'- sugar radicals produced via photo-excitation of one-electron oxidized adenine in 2'-deoxyadenosine and its derivatives. *Nucleic Acids Res* 34:1501–1511
117. Adhikary A, Kumar A, Palmer BJ, Todd AD, Heizer AN, Sevilla MD (2014) Reactions of 5-methylcytosine cation radicals in DNA and model systems: thermal deprotonation from the 5-methyl group vs. excited state deprotonation from sugar. Clemens von Sonntag memorial issue *Int J Radiat Biol* (Adhikary A, Cadet J, O'Neill P (eds)), <http://informahealthcare.com/doi/pdfplus/10.3109/09553002.2014.884293>
118. Adhikary A, Kumar A, Sevilla MD (2006) Photo-induced hole transfer from base to sugar in DNA: relationship to primary radiation damage. *Radiat Res* 165:479–484
119. Adhikary A, Collins S, Khanduri D, Sevilla MD (2007) Sugar radicals formed by photo-excitation of guanine cation radical in oligonucleotides. *J Phys Chem B* 111:7415–7421
120. Khanduri D, Collins S, Kumar A, Adhikary A, Sevilla MD (2008) Formation of sugar radicals in RNA model systems and oligomers via excitation of guanine cation radical. *J Phys Chem B* 112:2168–2178
121. Becker D, Adhikary A, Khanduri D, Sevilla MD (2009) Radical formation and chemical track structure in ion-beam irradiated DNA. *AIP Conf Proc* 1197:201–208
122. Kumar A, Sevilla MD (2009) Theoretical modeling of radiation-induced DNA damage. In: Greenberg MM (ed) *Radical and radical ion reactivity in nucleic acid chemistry*. Wiley, New Jersey, pp 1–40
123. Kumar A, Sevilla MD (2006) Photoexcitation of dinucleoside radical cations: A time-dependent density functional study. *J Phys Chem B* 110:24181–24188
124. Kumar A, Sevilla MD (2009) Sugar Radical formation by a proton coupled hole transfer in 2'-deoxyguanosine radical cation (2'-dG⁺): a theoretical treatment. *J Phys Chem B* 113:13374–13380
125. Kumar A, Sevilla MD (2010) Proton-coupled electron transfer in DNA on formation of radiation-produced ion radicals. *Chem Rev* 110:7002–7023
126. Li MJ, Liu L, Fu Y, Guo QX (2006) Significant effects of phosphorylation on relative stabilities of DNA and RNA sugar radicals: remarkably high susceptibility of H-2' abstraction in. *RNA J Phys Chem B* 110:13582–13589
127. Razskazovskiy Y, Debije MG, Bernhard WA (2003) Strand breaks produced in X-irradiated crystalline DNA: influence of base sequence. *Radiat Res* 159:663–669

128. Purkayastha S, Milligan JR, Bernhard WA (2006) The role of hydration in the distribution of free radical trapping in directly ionized DNA. *Radiat Res* 166:1–8
129. Purkayastha S, Bernhard WA (2004) What is the initial chemical precursor of DNA strand breaks generated by direct-type effects? *J Phys Chem B* 108:18377–18382
130. Purkayastha S, Milligan JR, Bernhard WA (2005) Correlation of free radical yields with strand break yields produced in plasmid DNA by the direct effect of ionizing radiation. *J Phys Chem B* 109:16967–16973
131. Purkayastha S, Milligan JR, Bernhard WA (2006) An investigation into the mechanisms of DNA strand breakage by direct ionization of variably hydrated plasmid DNA. *J Phys Chem B* 110:26286–26291
132. Sharma KKK, Purakayastha S, Bernhard WA (2007) Unaltered free base release from d(CGCGCG), produced by the direct effect of ionizing radiation at 4 K and room temperature. *Radiat Res* 167:501–507
133. Sharma KKK, Razskazovskiy Y, Purkayastha S, Bernhard WA (2009) Mechanisms of strand break formation in DNA due to the direct effect of ionizing radiation: the dependency of free base release on the length of alternating CG oligodeoxynucleotides. *J Phys Chem B* 113:8183–8191
134. Yokoya A, Cunniffe SMT, O'Neill P (2002) Effect of hydration on the induction of strand breaks and base lesions in plasmid DNA films by gamma-radiation. *J Am Chem Soc* 124:8859–8866
135. Yokoya A, Fujii K, Shikazono N, Ukai M (2010) Spectroscopic study of radiation-induced DNA lesions and their susceptibility to enzymatic repair. In: Hatano Y, Katsumura Y, Mozumder A (eds) *Charged particle and photon interactions with matter—recent advances, applications, and interfaces*. CRC Press, Taylor & Francis Group, Boca Raton, pp 543–574
136. Kumar A, Pottiboyina V, Sevilla MD (2012) One-Electron oxidation of neutral sugar radicals of 2'-deoxyguanosine and 2'-deoxythymidine: a density functional theory (DFT) study. *J Phys Chem B* 116:9409–9416
137. Pimblott SM, LaVerne JA, Mozumber A (1996) Monte Carlo simulation of range and energy deposition by electrons in gaseous and liquid water. *J Phys Chem* 100:8595–8606
138. Pimblott SM, LaVerne JA (2007) Production of low-energy electrons by ionizing radiation. *Radiat Phys Chem* 76:1244–1247
139. Baccarelli I, Bald I, Gianturco FA, Illenberger E, Kopyra J (2011) Electron-induced damage of dna and its components: experiments and theoretical models. *Phys Rep* 508:1–44
140. Konig C, Kopyra J, Bald I, Illenberger E (2006) Dissociative electron attachment to phosphoric acid esters: the direct mechanism for single strand breaks in DNA. *Phys Rev Lett* 97:018105
141. Ptasinska S, Denifl S, Gohlke S, Scheier P, Illenberger E, Märk TD (2006) Decomposition of thymidine by low-energy electrons: implications for the molecular mechanisms of single-strand breaks in DNA. *Angew Chem Int Ed Engl* 45:1893–1896
142. Alizadeh E, Sanche L (2012) Precursors of solvated electrons in radiobiological physics and chemistry. *Chem Rev* 112:5578–5602
143. Nguyen J, Ma Y, Luo T, Bristow RG, Jaffray DA, Lu QB (2011) Direct observation of ultrafast-electron-transfer reactions unravels high effectiveness of reductive DNA damage. *Proc Natl Acad Sci U S A* 108:11778–11783
144. Kuipers GK, Lafleur MVM (1998) Characterization of DNA damage induced by gamma-radiation-derived water radicals, using DNA repair enzymes. *Int J Radiat Biol* 74:511–519
145. Rezaee M, Sanche L, Hunting D (2013) Cisplatin enhances the formation of DNA single- and double-strand breaks by hydrated electrons and hydroxyl radicals. *Radiat Res* 179:323–331
146. Kheir JF, Chomicz L, Rak J, Bowen KH, Sevilla MD (2011) radicals formed in N-acetylproline by electron attachment: electron spin resonance spectroscopy and computational studies. *J Phys Chem B* 115:14846–14851

147. Kheir JF, Chomicz L, Engle A, Rak J, Sevilla MD (2013) Presolvated low energy electron attachment to peptide methyl esters in aqueous solution: C-O bond cleavage at 77 K. *J Phys Chem B* 117:2872–2877
148. Bernhard WA, Ezra FS (1974) Electron spin resonance of γ -irradiated alkyl phosphates: the C_2H_5 radical in magnesium diethyl phosphate (MgDEP). *J Chem Phys* 60:1707–1710
149. Kopyra J (2012) Low energy electron attachment to the nucleotide deoxycytidine monophosphate: direct evidence for the molecular mechanisms of electron-induced DNA strand breaks. *Phys Chem Chem Phys* 14:8287–8289
150. Li Z, Zheng Y, Cloutier P, Sanche L, Wagner JR (2008) Low energy electron induced DNA damage: effects of terminal phosphate and base moieties on the distribution of damage. *J Am Chem Soc* 130:5612–5613
151. Park Y, Peoples AR, Madugundu GS, Sanche L, Wagner JR (2013) Side-by-side comparison of DNA damage induced by low-energy electrons and high-energy photons with solid TpTpT trinucleotide. *J Phys Chem B* 117:10122–10131
152. Jortner J, Noyes RM (1966) Some Thermodynamic Properties of the Hydrated Electron. *J Phys Chem* 70:770–774

Chapter 9

Applications of the Spin-Trapping Method in Radiation Biology

Mikinori Kuwabara, Wakako Hiraoka and Osamu Inanami

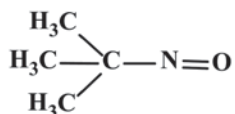
Abstract Ionizing radiation produces many kinds of free radicals in biologically important molecules through direct or indirect actions. In this chapter we have shown that a method that combined ESR, spin trapping and chromatographic separation made it possible to identify free radicals induced by direct ionization as well as OH-radical reactions in nucleic-acid related and protein-related compounds. In addition, combination with enzymatic digestion expanded the potential of this method to detect free radical production in molecules with high molecular weight such as polynucleotides, RNA and DNA, and polypeptides and proteins. The effects of ionizing radiation on biological molecules underlie the primary processes involved in radiation biology. ESR combined with spin trapping remains a useful method for clarifying these processes in a living organism.

9.1 Introduction

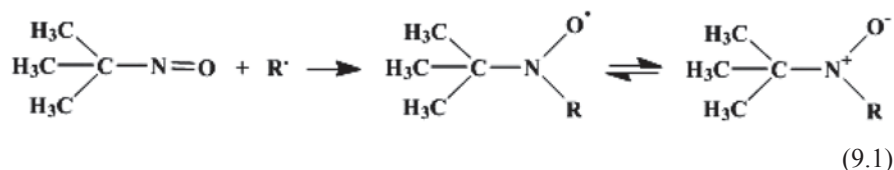
Since the spin trapping method was originally reviewed by Janzen in 1971 [1], it has been widely applied to chemistry, biology and medicine regarding the productions and reactions of free radicals. In particular, free radicals induced in biologically important molecules such as DNA and proteins by ionizing radiation have been studied by this method to elucidate the radiation-induced primary processes when living cells are exposed to ionizing radiation. Generally, the lifetime of these radicals is too short to be recorded by conventional electron spin resonance (ESR) technique. In the spin-trapping method, these short-lived free radicals are converted using a diamagnetic scavenger (the spin trap) to longer-lived radicals (the spin adducts), which can be conveniently investigated by means of ESR. 2-Methyl-2-nitrosopropane (MNP) was mainly employed as the spin trap.

M. Kuwabara (✉) · O. Inanami
Laboratory of Radiation Biology, Graduate School of Veterinary Medicine,
Hokkaido University, Sapporo 060-0818, Japan
e-mail: kuwabara@vetmed.hokudai.ac.jp

W. Hiraoka
Laboratory of Biophysics, School of Science and Technology, Meiji University,
Kawasaki 214-8571, Japan

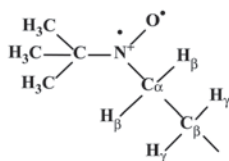


The spin trap reacts with the transient free radicals R^\cdot produced in molecules by ionizing radiation and converts them to spin-adduct nitroxide (Eq. 9.1). Spin trapping of γ -irradiated organic compounds including a few amino acids was early reported by Lagercrantz and Forshult using MNP in 1968 [2]. The application of the spin-trapping method using MNP for DNA bases, nucleoside, nucleotides, amino acids and peptides were then reviewed by Riesz and Rustgi in 1979 [3]; studies involving amino acids and peptides using a method combining spin-trapping and high-performance liquid chromatography (HPLC) were reviewed by Makino et al. in 1985 [4]. These two review papers described the usefulness of the spin-trapping method in identifying radiation-induced free radicals in biologically important molecules with low molecular weight such as bases, nucleosides, nucleotides, amino acids, dipeptides and tripeptides; however, the application of this method regarding macromolecules such as polynucleotides, DNA, polypeptides and proteins was not been fully described. In this chapter, we discuss the usefulness of the ESR-spin trapping method combining enzymatic digestion and HPLC with regard to the precise identification of radical structures produced in biological macromolecules.



9.2 Identification of Radical Structures from the ESR Spectra of the Spin Adducts

The ESR spectrum of the spin adduct nitroxide shows a primary triplet splitting of approximately 1.5 mT due to the ^{14}N nucleus, and secondary splitting that arises from the magnetic nuclei of the trapped R^\cdot radical. The secondary lines generally arise from the interaction of the free electron on the ^{14}N of the nitroxide group with magnetic nuclei of the trapped R^\cdot radical. From the secondary splittings, the structure of R^\cdot can be identified. Hyperfine couplings (hfc) observed for the spin adducts of MNP are characterized by the magnetic nuclei at the α , β and γ positions which are defined with respect to the unpaired electron on the nitrogen of the nitroxide group, as illustrated below.



This structure represents the spin adduct of the carbon-centered radical and MNP. The typical experimentally observed ranges of α , β and γ hfc's have been summarized by Riesz and Rustgi (1979) [3] and are helpful for the assignment of radical structures. The hfc's of the hydrogens at the β -position provide information concerning the stereochemistry of the spin adduct. The following equation is obtained for the isotropic hfc of the β -hydrogen in aqueous solutions where a_{H}^{β} is the observed hfc, θ is the average dihedral angle that the β -hydrogens make with the p_{π} -orbital of the nitrogen of the nitroxide group;

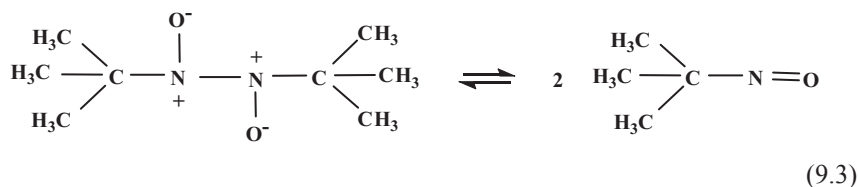
$$a_{\text{H}}^{\beta} = 2.8 \cos^2 \theta (\text{mT}) \quad (9.2)$$

The β -hydrogen splittings are, therefore, in the range of 0–2.8 mT corresponding to $\theta=0$ – 90° . The hfc's of γ -hydrogens usually fall in the range of 0–0.06 mT. For α - and β -nitrogens, the secondary triplet hfc's fall in the range of 0.09–0.35 mT and hence α - and β -nitrogens cannot be distinguished from their observed splittings. For γ -nitrogens, the observed hfc's are in the range of 0.02–0.06 mT.

Although it is usually possible to assign a radical structure consistent with the observed ESR spectrum of a spin-trapped radical, in some cases other structures might also be consistent. The fact that the couplings due to exchangeable hydrogens decrease in D_2O solution to 0.15 times their original level is helpful for the assignment of the radical structures. The use of a compound that is deuterated on some of the non-exchangeable sites also verifies the assignment of the radical structures. The plural spin adducts are usually produced in spin-trapping experiments including the self-trapping product of MNP, namely di-*t*-butyl nitroxide. Spin-trapping experiments in the presence or absence of oxygen are also useful because some radicals have high reactivity with oxygen, resulting in the formation of less spin adducts. Spin-trapping experiments in D_2O instead of H_2O enhance resolution by removing unresolved exchangeable splittings. The most elegant method involving spin-trapping experiments is to chromatographically separate each spin adduct. A SEP-PAK C_{18} cartridge is useful not only in removing undegraded molecules but also in separating the spin adducts formed in the molecules with relatively high-molecular weights. Furthermore, reverse-phase HPLC in the ion-suppression mode combined with enzymatic digestion, or column chromatography using a Sephadex G-25 combined with enzymatic digestion, are useful for precisely separating the spin adducts produced in nucleic-acid related macromolecules and the protein related macromolecules.

9.3 Fundamental Aspects of MNP as a Spin-Trapping Agent

In the solid state MNP exists in the dimer form. When solid MNP is dissolved in an aqueous solution, the dimer gradually decomposes to the monomer to reach a dimer-monomer equilibrium with low solubility as follows.



While only the monomer form can serve as a spin-trapping reagent, an aqueous solution consisting of the monomer alone cannot be prepared. The monomer is volatile and is easily lost from the solution. Furthermore, this compound traps the radicals produced by its decomposition to form byproducts that complicate the radical assignments [5, 6]. Given the problems associated with this compound, precise measurement of the molar concentration of the dimer and monomer in the solution is required. It is also necessary to determine the reaction rate constants regarding OH radicals as well as hydrated electrons for the application of the spin-trapping method to quantitative measurements of free radicals produced by ionizing radiation.

It has been reported that the relative amounts of the dimer and monomer can be measured using NMR spectrometry [3]. ^1H -NMR measurements at $\delta = 1.59$ (dimer) and 1.28 ppm (monomer) have proven that the dimer-monomer equilibrium was reached at 20 h. Similar time dependence in the changes of optical absorbance at 320 nm (dimer) and 662 nm (monomer) has also been observed. From the NMR and optical absorbance spectrometries, the molar absorbance coefficients of the dimer ($\epsilon_{320}^{\text{dimer}}$) and monomer ($\epsilon_{662}^{\text{monomer}}$) were obtained. The reaction rate constants of the dimer and monomer with hydrated electrons (e_{aq}^-) as well as OH radicals have also been determined using the nanosecond pulse radiolysis method; these constants are listed in Table 9.1 [7, 8]. In the case of e_{aq}^- , the dominant form of MNP reacting with them is the dimer, whereas OH radicals have higher reactivity with the monomer than with the dimer. Since the amounts of dissolved MNP powder do not reflect the theoretically calculated concentrations, the molar absorbance coefficients will provide a method to simply and quickly estimate the concentrations of the dimer and monomer when a given amount of MNP powder is dissolved in an aqueous solution. In addition, the reaction-rate constants regarding the reaction of MNP with e_{aq}^- and OH radicals are important in quantitative spin-trapping experiments using MNP.

Table 9.1 Molar absorbance coefficients of the dimer and monomer of MNP and their reaction rate constants with OH radicals as well as hydrated electrons (e_{aq}^-)

	Dimer	Monomer
$\epsilon(M^{-1} cm^{-1})$	410 \pm 40 at 320 nm	10 \pm 5 at 662 nm
$k_{OH}(M^{-1}s^{-1})$	(3.0 \pm 0.3) \times 10 ⁹	(1.3 \pm 0.9) \times 10 ¹⁰
$k_{e_{aq}^-}(M^{-1}s^{-1})$	(2.4 \pm 0.1) \times 10 ¹⁰	

9.4 Spin-Trapping Studies Regarding Radiation-Induced Free Radicals in the Nucleic Acid Constituents and Related Compounds As Well As Proteins in the Solid State

It is well-known that ionizing radiation produces ion pairs in matter with a G-value of 3.3 [9]. For example, when 1 kg of solid glucose with a molecular weight of 180 g/mol is exposed to γ -rays at a dose of 100 kGy (100 kJ/kg), approximately 2×10^{22} ion pairs/kg are produced. This means that an ion pair is born in the ratio of 1 to 160 molecules. Therefore, the use of compounds with high solubility in water is required for spin trapping of free radicals in the solid state. Minegishi et al. first tried the spin-trapping method in 1980 to study radicals produced in γ -irradiated polycrystalline protein constituents at room temperature [10]. We further developed this method to study, pyrimidine bases, nucleosides and nucleotides [11, 12], which are all highly soluble in water. Only one experiment using 3'-UMP has been performed using a method combining spin-trapping and HPLC [13]. For spin-trapping in the presence of oxygen, aqueous solutions of MNP were prepared in D₂O or H₂O at a concentration of 1.5 mg/mL by stirring overnight in the dark at room temperature. Polycrystalline samples were irradiated in a ⁶⁰Co γ source at a dose of 100 kGy and immediately dissolved in 1 mL of D₂O (or H₂O) solution containing MNP. The solutions were transferred to a quartz flat cell (6 \times 1 \times 0.025 cm) designed for the analysis of aqueous samples using ESR spectroscopy. For spin-trapping in the absence of oxygen, a polycrystalline sample (30–100 mg) was placed in one side of a specially designed U-tube [14]. The air inside the tube was replaced by Ar gas. On the other side arm, 5 mg of MNP powder was added to 1 mL D₂O (or H₂O) which was then bubbled with Ar gas using long fine needles inserted into the solution through the rubber septum to remove oxygen. The MNP powder was then dissolved by stirring the solution overnight in the dark. The sample powder in one side arm was irradiated in a ⁶⁰Co γ source at a dose of 100 kGy while the MNP solution in the other side arm was sealed with lead blocks. After irradiation, the MNP solution was transferred to the irradiated powder which was then dissolved by rapid stirring. The U-tube was inverted to fill the ESR flat cell which had already been connected to it by means of a tapered joint. ESR measurements were undertaken using an X-band spectrometer. ESR spectra from spin-trapped radicals were recorded

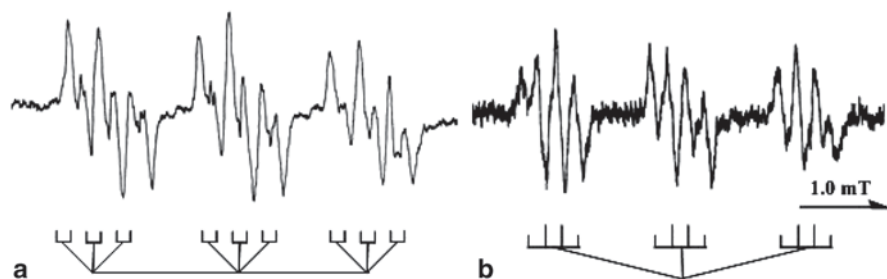
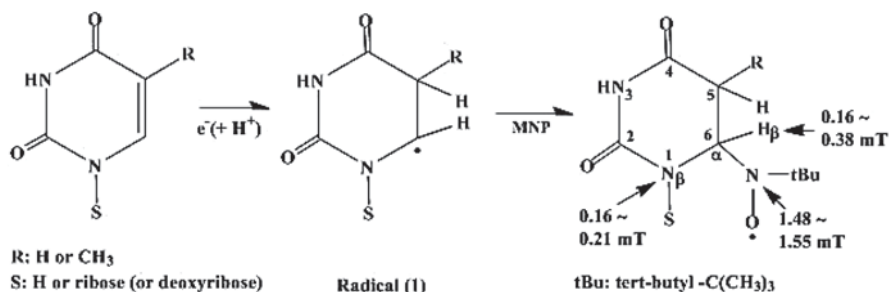


Fig. 9.1 ESR spectra of spin-trapped radicals from polycrystalline **a** uracil and **b** 1-ethyluracil γ -irradiated at room temperature and subsequently dissolved in air-saturated MNP solutions. The figure is adapted from [11] by permission of Informa Healthcare (1981)

at room temperature as first derivatives. ESR scans were mainly traced with a 100-kHz field modulation with 0.02 mT, and to avoid saturation of the ESR signals the microwave power level was usually below 10 mW.

9.4.1 γ -Ray-Induced Free Radicals in Solid Pyrimidine Bases and Nucleosides

The following solid pyrimidine bases and nucleotides were studied by ESR and spin trapping: the pyrimidine bases uracil, 1-methyluracil, 1-ethyluracil, cytosine, thymine and their 5-halogenated derivatives 5-FU, 5-CU and 5-BrU; the pyrimidine nucleosides dC, Cyd, dT, dU and Urd and their 5-halogenated derivatives 5-FdU, 5-FUrd, 5-CdU, 5-CUrd, 5-BrdU and 5-BrUrd as nucleic acid constituents [11]. Figure 9.1 shows the typical ESR spectra obtained from uracil and 1-ethyluracil. The spectral pattern of uracil splits into a primary triplet with a splitting of 1.5 mT and the secondary triplet hyperfine splitting with 0.36 mT due to a β -nitrogen which further splits into a doublet with 0.16 mT owing to the presence of a β -hydrogen. In 1-ethyluracil, the ESR spectrum shows almost equal β -nitrogen and β -hydrogen couplings, which generate a 1:2:2:1 quartet spectrum. Both spectra can be assigned to the same type of radicals generated at the C6 positions, $-\text{C}(5)\text{H}_2-\dot{\text{C}}(6)\text{H}-$ (Radical 1), formed by H-addition to the C5 position of the double bond. The mechanism of the formation of spin adducts is shown in Eq. (9.4).



(9.4)

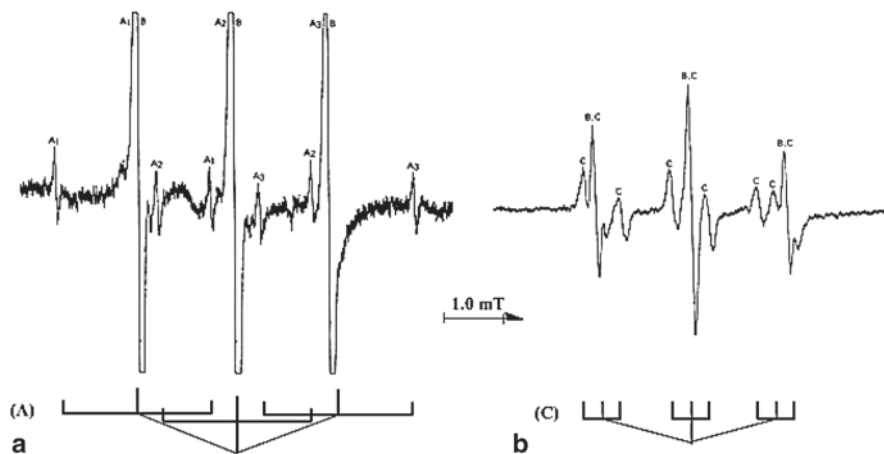
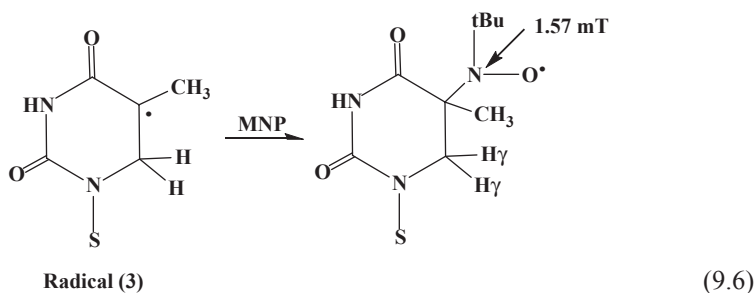
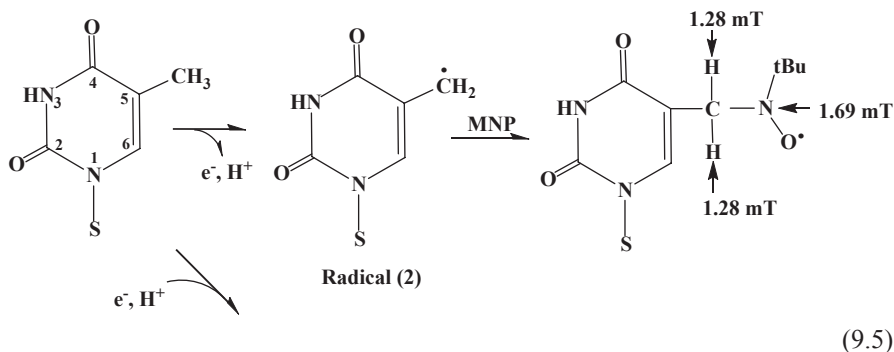


Fig. 9.2 ESR spectra of spin-trapped radicals from polycrystalline thymidine γ -irradiated at room temperature and subsequently dissolved in an H_2O solution of MNP **a** in the absence of oxygen and **b** in the presence of oxygen. The figure is adapted from [11] by permission of Informa Healthcare (1981).

Similar kinds of radicals were trapped not only in other uracil-related compounds (1-methyluracil, 2'-dU, Urd) but also in 2'-dC. The spin adducts obtained from these compounds gave the ESR spectra consisting of a primary triplet ranging from 1.48 to 1.55 mT and the secondary triplet ranging from 0.16 to 0.21 mT owing to a β -nitrogen which further splits into a doublet ranging from 0.16 to 0.38 mT owing to a β -hydrogen (Eq. 9.4). A 1:2:2:1 quartet spectrum due to almost equal β -nitrogen and β -hydrogen couplings was observed in 1-methyluracil, 1-ethyluracil and 2'-dC. These radical identifications are consistent with those in single crystal studies [15].

When γ -irradiated solid dT was dissolved in H_2O solution containing MNP in the absence or presence of oxygen, the ESR spectra displayed in Fig. 9.2 were observed. Similar results were obtained from thymine. The presence of oxygen in the solution changed the pattern of the spectra. In the absence of oxygen the lines marked A consists of a primary triplet with a splitting of 1.69 mT that further splits into the 1:2:1 intensity triplet with a splitting of 1.28 mT, as a result of the presence of two equivalent β -hydrogens (Fig. 9.2a). This pattern can be explained by a radical formed by ionization followed by proton loss at the methyl group at the 5 position on the thymine base (Radical 2 in Eq. 9.5).



The major spectrum labeled B consists of only a primary triplet with a splitting of 1.57 mT without further splitting and can be assigned to the H-addition radical at the C6 position of the thymine base moiety (Radical 3 in Eq. 9.6). The C5-centered radical, the 5,6-dihydrothymidine-5-yl radical (Radical 3), is the most well-known radical among the radicals that have been identified by many researchers in γ - or X-irradiated solid thymine, dT and DNA [16]. When γ -irradiated dT was dissolved in a MNP solution containing oxygen, the new spectrum labeled C appeared instead of spectrum A (Fig. 9.2b). This consisted of a primary triplet with a splitting of 1.43 mT and a secondary triplet with a splitting of 0.29 mT in the ratio 1:1:1 without further splittings. A similar spectrum was observed in thymine. The results from dT and thymine indicate that the spin adducts have a nitrogen at the α -position or β -position. One possible explanation for the spin adducts is that the N-centered radicals at the N1 position in the case of thymine and the N3 position in the case of dT might be trapped by MNP. This radical assignment seems to be consistent with previous reports regarding X-irradiated single crystal ESR studies in thymine and dT [16, 17]. However, application of another spin trap, 4-PyOBN, which can discriminate if a C-centered or an N-centered radical is trapped [18], showed no spin adducts arising from the N-centered radicals (data not shown). Therefore, the assignment of this spectrum to the C6-radical by H-addition to the C5 position (Radical 1 in Eq. 9.4) is more plausible if the dihedral angle θ is assumed to be close to 90° in Eq. 9.2. However, complete evidence for the radical assignment was not provided exclusively by the ESR spectrum. When γ -irradiated polycrystalline

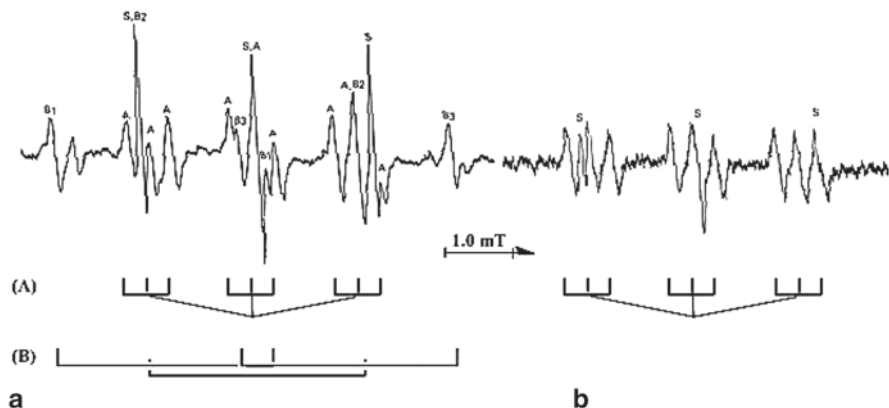


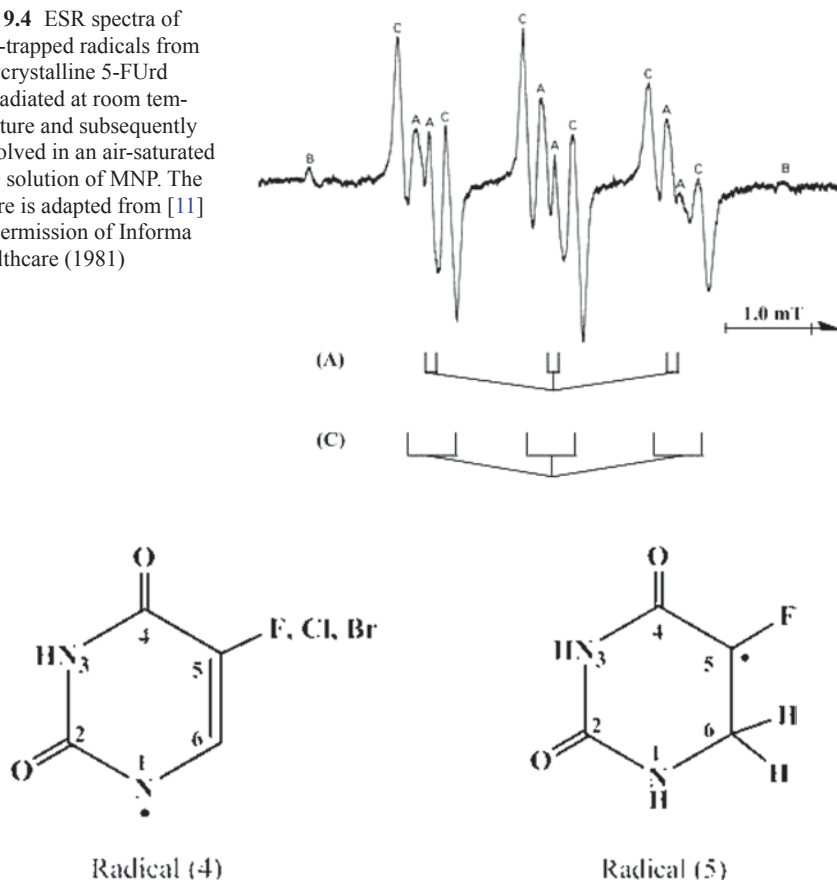
Fig. 9.3 ESR spectra of spin-trapped radicals from polycrystalline solids γ -irradiated at room temperature and subsequently dissolved in an H_2O solution of MNP. **a** 5-FU, air-free solution and **b** 5-BrU, air-saturated solution. The figure is adapted from [11] by permission of Informa Healthcare (1981)

cytosine was dissolved in an H_2O solution of MNP in the absence of oxygen, the ESR spectrum consisting of a quartett with a splitting of 1.44 mT was preferentially observed (data not shown) and assigned to the MNP-H adducts [11]. A weak ESR spectrum consisting of a secondary triplet with a splitting of 0.35 mT which further splits to the doublet with a splitting of 0.07 mT was observed after decay of the dominant signals. This spectrum was assigned to the radical formed by H-abstraction from the N(1) position which was consistent with the results obtained using irradiated single crystals of cytosine [19].

It has been shown that cells in which dT residues of DNA are replaced by 5-halodeoxyuridine become several times more sensitive to the lethal effects of ionizing radiation. For 5-FU, 5-CU and 5-BrU, the secondary 1:1:1 triplet spectrum was observed as common signals. Figures 9.3a and 9.3b show the ESR spectra obtained from 5-FU and 5-BrU, respectively. The triplet lines are assigned to the H-abstraction radical from the N(1) position (Radical 4). Signal labeled S in Fig. 9.3b corresponds to di-*t*-butyl nitroxide which is formed by self-trapping of MNP as by-products [3]. Spectrum labeled B consisting of a secondary doublet with a splitting of 3.12 mT was observed for 5-FU. This large doublet splitting is produced by the interaction of the unpaired spin with the β -fluorine nucleus. The possible structure consistent with this coupling is the H-addition radical located at the C6 position (Radical 5).

In γ -irradiated single crystals of 5-halo bases, three main radicals namely Radicals 4, 5 and the radical at the C6 position due to the H-addition to the O4 position, have been identified [20, 21]. Radical 4 was observed in all 5-halo compounds examined. The α -halo radical at the C5 position (Radical 5) was only spin-trapped in 5-FU. No spin adducts of the C6-centered radicals were observed in any of the samples.

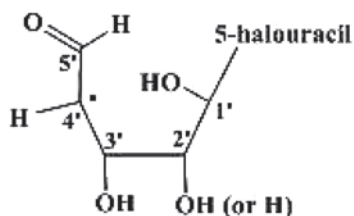
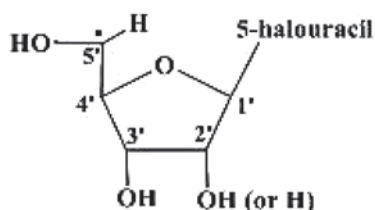
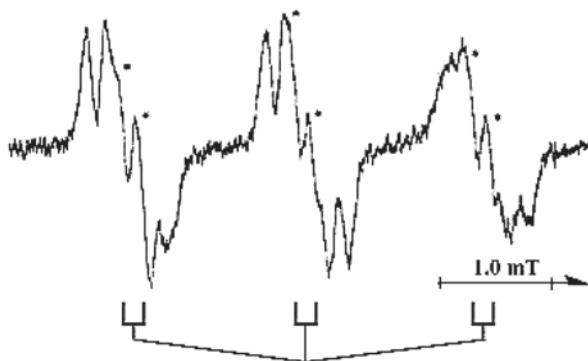
Fig. 9.4 ESR spectra of spin-trapped radicals from polycrystalline 5-FUrd γ -irradiated at room temperature and subsequently dissolved in an air-saturated D_2O solution of MNP. The figure is adapted from [11] by permission of Informa Healthcare (1981)



5-Halo nucleoside derivatives give different results to those of 5-halo bases. Figure 9.4 shows the ESR spectrum of γ -irradiated polycrystalline 5-FUrd after the dissolution of MNP in air-saturated D_2O . Similar spectra were also obtained from other 5-halo nucleosides, with the exception of the lines labeled B; these lines consist of a secondary doublet with a splitting of 2.15 mT due to a β -fluorine hyperfine coupling and, therefore, are assigned to Radical 5. The lines labeled A that are observed in all 5-halo derivatives consist of a secondary doublet with a splitting of 0.17 mT.

The lines labeled C consist of a secondary doublet with a splitting of 0.56 mT. Since these doublet lines are explained by the interaction of unpaired spin with a β -hydrogen, they are assigned to radicals located at the sugar moiety. The spectrum labeled C was assigned to the radical formed by H-abstraction at the C5' position of the sugar moiety (Radical 6 in Eq. 9.7). In the spin-trapping study involving γ -irradiated solid sugars, this large doublet with a splitting of 0.48–0.57 mT could be observed in D-glucose, D-mannose and lactose having the $HOC_5'H_2-$ group at the C5' position [22].

Fig. 9.5 ESR spectra of spin-trapped radicals from polycrystalline 5'-UMP γ -irradiated and subsequently dissolved in an aqueous solution of MNP. The component of the signal marked by the asterisk disappeared after HPLC. The figure is adapted from [13] by permission of Informa Healthcare (1991)



(9.7)

The spectrum labeled A was assigned to Radical 7 in Eq. 9.7, because the radiation chemical studies involving γ -irradiated sugars have provided evidence that the radical at the C5' position may be converted to the radical at the C4' position (Eq. 9.7) [23]. The ESR studies of single crystals have shown that the α -halo radical formed by H-addition to the 5, 6-double bond and the C6 radical formed by protonation of the base anion at the O4 position were prominent [24–26]. On the other hand, the predominant radicals in the spin-trapping studies were all free radicals at the sugar moiety. The results obtained from the spin-trapping studies are not consistent with those from ESR single crystal studies. The exact radiosensitizing mechanisms of 5-halo uracils have not been fully elucidated.

9.4.2 γ -Ray-Induced Free Radicals in Solid Pyrimidine Nucleotides

The spin-trapping method combining HPLC was only used to evaluate γ -irradiated polycrystalline 5'-UMP [13]. After polycrystalline 5'-UMP (50 mg) was γ -irradiated at a dose of 70 kGy under an Ar atmosphere, it was dissolved in 1 mL of aqueous solution of MNP (5 mg/mL). Figure 9.5 shows an ESR spectrum of spin-trapped radicals from γ -irradiated polycrystalline 5'-UMP.

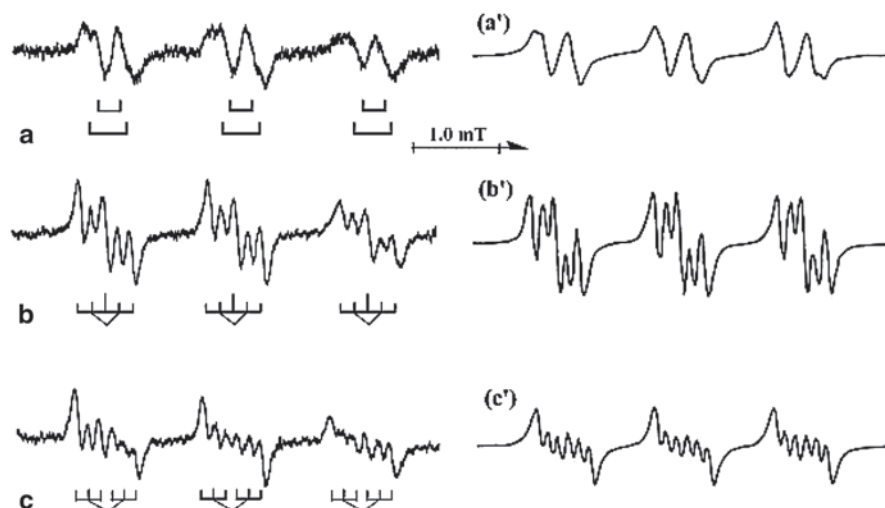
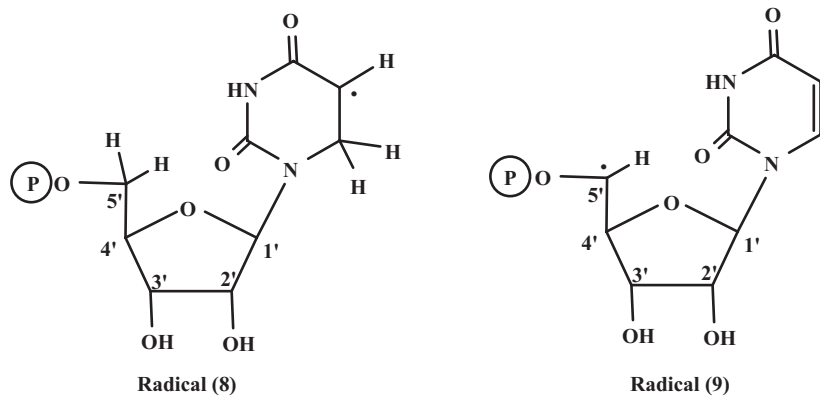


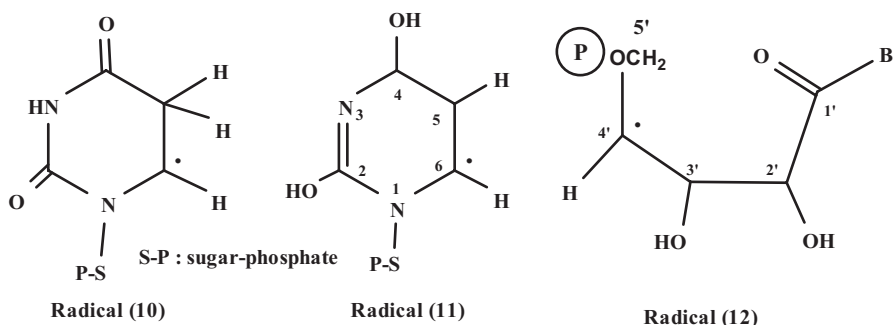
Fig. 9.6 (Left) Experimentally separated ESR spectra of irradiated 5'-UMP (a-c). (Right) Computer simulation spectra calculated by employing a Lorentz function. a' Simulation spectrum of (a), b' simulation spectrum of (b), and c' simulation spectrum of (c). The figure is adapted from [13] by permission of Informa Healthcare (1991)

After the significant amounts of undegraded 5'-UMP were removed using a SEP-PAK C₁₈ cartridge, the spin adducts were separated into each spin adduct using a reverse-phase HPLC in the ion suppression mode. Although the ESR spectrum consisting of 3×2 lines that was originally present (as marked by the asterisk in Fig. 9.5), disappeared during HPLC, it could be distinguished from other components; this was because it became dominant when the irradiated 5'-UMP was dissolved in the presence of oxygen at alkaline pH [12]. The three ESR signals were separated using HPLC. The ESR signal in Fig. 9.6a indicates the overlap of two spectra. Each spectrum consists of a secondary doublet. Since the exact measurements of the hyperfine couplings were impossible from the superimposed spectrum, we simulated this spectrum by analyzing the ESR parameters using a Lorentz function. When two spectra consisting of a primary triplet with a splitting of 1.53 mT and a secondary doublet with a splitting of 0.34 mT with $\Delta H_{\text{msl}} = 0.15$ mT, and a primary triplet with a splitting of 1.56 mT and a secondary doublet with a splitting of 0.55 mT with $\Delta H_{\text{msl}} = 0.08$ mT were superimposed at a ratio of 12:1, a spectrum similar to that in Fig. 9.6a was obtained (Fig. 9.6a').

Since the addition of hydrogen at either position of the 5, 6-double bond in the unsaturated base is a major reaction process in the solid state [16], the former spectrum is assigned to the spin adduct derived from the C5-centered radical at the base moiety (Radical 8).



The latter spectrum with a secondary doublet with a splitting of 0.55 mT can be assigned to Radical 9 by analogy to the spectrum labeled C in Fig. 9.4. The solid state radiation chemistry of 5'-UMP has been studied by means of ESR combined with ENDOR and Radicals 8 and 9 were identified at near room temperature [27–29].



The ESR spectrum shown in Fig. 9.6b and its simulation spectrum shown in Fig. 9.6b' consist of a primary triplet and a secondary doublet, as a result of the presence of a β -hydrogen that further splits into a triplet owing to the presence of a β -nitrogen ($a_N = 1.58$ mT, $a_H^\beta = 0.28$ mT and $a_N^\beta = 0.16$ mT). The ESR spectrum shown in Fig. 9.6c and its simulation spectrum shown in Fig. 9.6c' also consists of a primary triplet and the secondary doublet and triplet ($a_N = 1.52$ mT, $a_H^\beta = 0.4$ mT and $a_N^\beta = 0.13$ mT). Because of the presence of a β -hydrogen and a β -nitrogen, both ESR spectra are attributable to the spin adducts of the C6-centered radicals. A C6-centered radical formed by H-addition to the C5 position of the 5, 6-double bond is proposed in solid-state irradiation (Radical 10) [16]. In addition to this radical, another C6-centered radical (Radical 11) has been reported [28, 29]. It seems difficult at this point to determine which spectrum, the one in Fig. 9.6b or in Fig. 9.6c is appropriate for the assignment of the C6-centered radicals, Radicals 10 or 11. In ESR

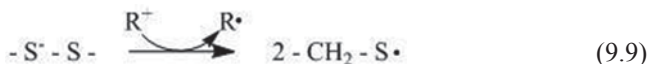
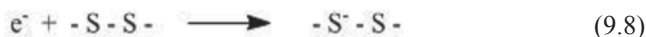
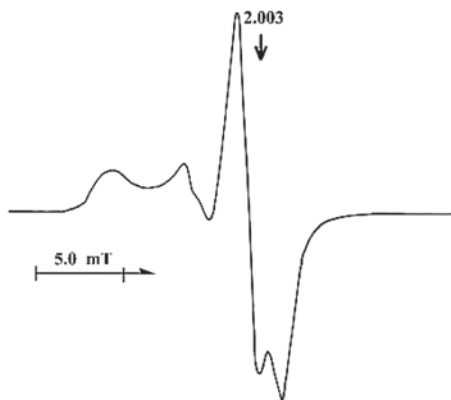
studies involving free radicals in solid 5'-UMP, Radons et al. [29] and Sagstuen [30] assigned the same ESR spectrum to different radical species, Radical 10 and the C4'-centered radical (Radical 12), respectively. The ESR spectrum marked by the asterisk in Fig. 9.5 consists of a primary triplet and a secondary doublet; the roughly estimated hfcs were 1.47 and 0.18 mT, respectively. It may be possible to use this spectrum for the identification of Radical 12.

The results obtained from spin-trapping combined with HPLC in γ -irradiated solid 5'-UMP have clearly shown that two types of radicals at the C6 position of the base moiety are induced; this supports the hypothesis of several authors who proposed two or more types of C6-centered radicals in ESR studies of X-irradiated single crystals of 5'-UMP [27–30]. A spin-trapping study of radicals at room temperature in γ -irradiated polycrystalline pyrimidine nucleotides, 5'-dCMP, 3'-CMP, 5'-CMP, 5'-dUMP and 3'-UMP, has been performed without HPLC [12]. It is worthy to note that the methyl type radical, $-C_4'-\dot{C}_5'H_2$, formed at the C5' position of the sugar moiety was observed in all samples examined. This result is consistent with single crystal studies performed in γ -irradiated Cyd and 3'-CMP [31, 32] and 5'-dCMP [33–35].

9.4.3 γ -Ray-Induced Free Radicals in Solid Protein

The spin-trapping method has been applied to analyze the radical structures produced in γ -irradiated polycrystalline amino acids and dipeptides as model compounds of protein [10, 36]. Decarboxylated and deaminated radicals, as well as deprotonated radicals at α -carbon sites of the peptide (α -carbon radicals) have been identified. It is of significance to extend this method to study radiation-induced free radicals in solid protein. For this purpose we improved this method by combining enzymatic digestion and applied it to solid lysozyme as a model of proteins [37]. Lysozyme is made up of a single polypeptide chain consisting of 129 amino acids that are cross-linked by four disulfide bridges and contains no free SH groups. A few hundred mg of lysozyme was first exposed to γ -rays at a dose of 80 kGy in the solid state at room temperature and subsequently analyzed using ESR spectroscopy. The ESR scan of solid samples was traced using a cylindrical quartz tube at 100 kHz of field modulation with an amplitude of 0.4 mT; the microwave power level was maintained at 1 mW. The ESR spectra obtained from γ -irradiated solid lysozyme is shown in Fig. 9.7. The spectrum is markedly unsymmetrical, and has a doublet signal centered at a g-value of 2.003 and a broad signal that appears at low-field with a g-value between 2.020 and 2.080. Numerous investigations of model proteins have shown that the doublet centered at g-value of 2.003 was due to α -carbon radicals in the peptide ($-\text{NH}-\dot{\text{C}}(\text{R})-\text{CO}-$, R; amino acid side chains) and that the broad signal in the low field was due to the secondary thiyl radicals ($-\text{CH}_2-\text{S}^\cdot$) that were produced on the side chains (Eqs. 9.8 and 9.9).

Fig. 9.7 ESR spectrum obtained after solid lysozyme was exposed to 80 kGy of γ rays at room temperature. The *arrow* indicates the absorption at $g=2.003$. The stick diagram indicates the positions of hyperfine splittings due to carbon-centered radicals. The figure is adapted from [37] by permission of Informa Healthcare (1988)



The spin trapping method combined with enzymatic digestion was employed to clarify the production of these radicals in the solid lysozyme. After irradiated solid lysozyme was dissolved into aqueous MNP solution and subsequently digested with protease (0.1 mg/mL), ESR scans were traced. Figure 9.8a shows the ESR spectrum of spin-trapped radicals before digestion. A broad spectrum consisting of only a primary triplet hyperfine structure was observed. After digestion of lysozyme by protease to form oligopeptides, an ESR spectrum with a more resolved hyperfine structure was obtained (Fig. 9.8b). This spectrum has a primary splitting of 1.59 mT which, further splits into a 0.2 mT doublet and, is assigned to H-abstraction radicals on the side chains of these amino acids in the lysozyme. The α -carbon radicals and the thiyl radicals were not identified in MNP spin-trapping experiments, although it has been reported that these radicals are produced in the solid state [38, 39]. This discrepancy may be explained by the instability of the spin adducts or inefficiency of spin trapping of these radicals. Indeed, even in simple model experiments the α -carbon radicals could not be identified, with the exception of glycine and alanine [40] and it has also been reported that the MNP-thiyl radical adduct is unstable [39]. Another spin trap DMPO agent was used to clarify the thiyl and carbon-centered radical production in the γ -irradiated solid lysozyme. The resulting ESR spectrum was composed of two signals. One was assigned to the carbon-centered radicals produced at the α -carbons of the peptide or at the side-chains of amino acids [41, 42] and another was assigned to the DMPO-thiyl radical adduct [43].

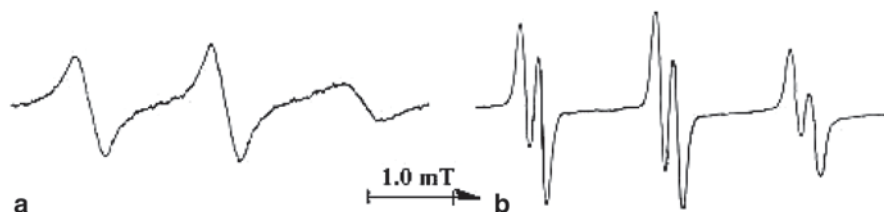
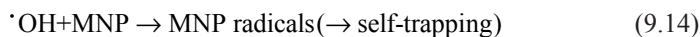
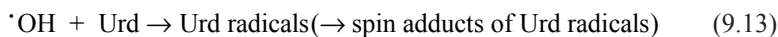
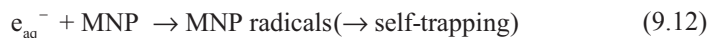


Fig. 9.8 **a** ESR spectrum of spin-trapped radicals from solid lysozyme γ -irradiated at room temperature and subsequently dissolved in aqueous solution containing MNP. **b** ESR spectrum after being digested by protease at 37°C for 3 h. The figure is adapted from [37] by permission of Informa Healthcare (1988)

9.5 Spin-Trapping Studies Regarding Radiation-Induced Free Radicals in the Aqueous Solutions of Nucleic Acid Constituents, Their Related Compounds and DNA As Well As Proteins

9.5.1 Free Radicals Induced by the Reactions of Pyrimidine Nucleosides and Nucleotides with Hydroxyl (OH) Radicals

Identification of OH-induced free radicals in pyrimidine nucleosides and nucleotides have mostly been carried out using a method that combined ESR, spin trapping and liquid chromatography [44–48]. OH radicals were generated by X irradiation of an N_2O -saturated aqueous solution. When an H_2O solution is exposed to 1 Gy (1 J/kg) of X rays, 0.27 μM of OH radicals, 0.265 μM of e_{aq}^- and 0.035 μM of atomic hydrogens are generated.



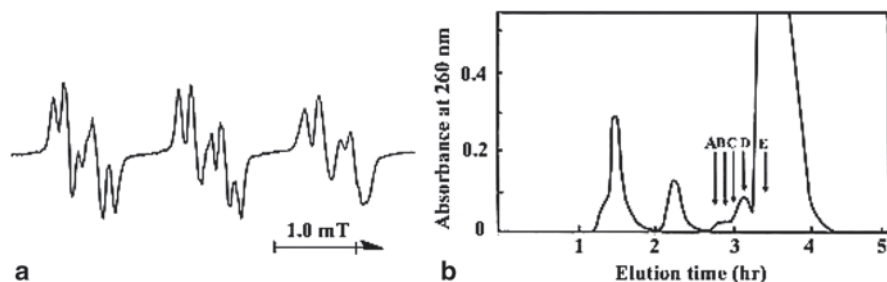
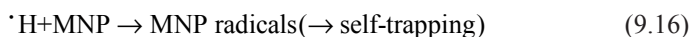


Fig. 9.9 **a** ESR spectrum of spin-trapped radicals from an aqueous solution containing Urd (50 mM) and MNP (1 mg/mL) after X irradiation under N_2O . **b** Chromatogram separated on a Bio-Gel P-2 column (1×80 cm). The figure is adapted from [44] by permission of Radiation Research Society (1986)

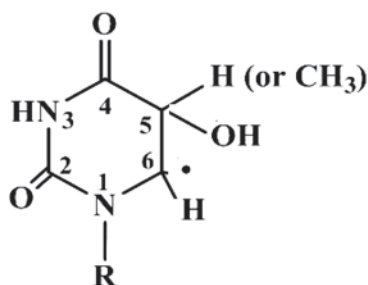


e_{aq}^- are converted to OH radicals by reaction with N_2O (Eq. 9.10). Urd was chosen as a model of the nucleic acid component, and 50 mM of Urd and 5.7 mM of MNP were dissolved in an H_2O solution, respectively. In this reaction system, e_{aq}^- react not only with N_2O but also with Urd and MNP (Eqs. 9.11 and 9.12). Using $[N_2O]=27$ mM, $[Urd]=50$ mM and $[MNP]=5.7$ mM, and their reaction rate constants, $k_{10}=9.1 \times 10^9 \text{ M}^{-1}\text{s}^{-1}$ [49], $k_{11}=1.4 \times 10^{10} \text{ M}^{-1}\text{s}^{-1}$ [49] and $k_{12}=2.4 \times 10^{10} \text{ M}^{-1}\text{s}^{-1}$ (MNP dimer, see Table 9.1) [7], the reaction rates using Eqs. 9.10, 9.11 and 9.12 were calculated to be $2.5 \times 10^8 \text{ s}^{-1}$, $0.7 \times 10^8 \text{ s}^{-1}$ and $1.4 \times 10^8 \text{ s}^{-1}$, respectively. As a result, 54% of the e_{aq}^- was converted to OH radicals as a result of reaction with N_2O ; therefore, irradiation of the solution with X rays at a dose of 5.4 kGy produced 2.9 mM of OH radicals in total. The remaining 15% of the e_{aq}^- reacted with Urd and 31% of the e_{aq}^- reacted with MNP. The reactions of e_{aq}^- with Urd produced 0.2 mM of Urd radicals when exposed to a dose of 5.4 kGy. This value corresponded to 7% of OH-induced Urd radicals. The reactions of e_{aq}^- with MNP resulted in undesirable byproducts. OH radicals react competitively with Urd and MNP with reaction-rate constants of $k_{13}=4.1 \times 10^9 \text{ M}^{-1}\text{s}^{-1}$ [49] and $k_{14}=1.3 \times 10^{10} \text{ M}^{-1}\text{s}^{-1}$ (MNP monomer, see Table 9.1) [8], respectively. Using the molar concentrations of Urd and MNP and their reaction constants, the reaction rates using Eqs. (9.13 and 9.14) were calculated to be $2.0 \times 10^8 \text{ s}^{-1}$ and $0.74 \times 10^8 \text{ s}^{-1}$, respectively. About 73% of OH radicals (2.1 mM) were estimated to react with Urd to induce Urd radicals and 27% of OH radicals reacted with MNP to produce undesirable byproducts. H radicals also reacted competitively with Urd and MNP with the reaction-rate constants of $k_{15}=3.8 \times 10^8 \text{ M}^{-1}\text{s}^{-1}$ [49] and $k_{16}=1.9 \times 10^9 \text{ M}^{-1}\text{s}^{-1}$ (Greenstock et al. 1978, Abst 61st Can Chem Cong, OR-5, 65). The reaction rates calculated using Eqs. 9.15 and 9.16 were $1.9 \times 10^7 \text{ s}^{-1}$ and $1.1 \times 10^7 \text{ s}^{-1}$, respectively. Sixty-five percent of H radicals reacted with Urd resulting

in 0.12 mM of Urd radicals which corresponded to 4% of OH-induced Urd radicals. The remaining 37% of H radicals reacted with MNP to cause the undesirable byproducts. These results suggested that the large amounts of MNP byproducts and about 10% of Urd radicals were produced by the reaction with e_{aq}^- and H radicals. Therefore, for the precise identification of free radicals it is necessary to separate not only each spin adduct, but also the byproducts of MNP in the spin-trapping studies of OH-induced free radicals. For Urd, the spin adducts were separated by a Bio-Gel P-2 column [44]. One milliliter portions of eluent were collected and freeze-dried. The freeze-dried samples were again dissolved in 200 μ L distilled water and then measured by ESR. UV-absorbance measurements were also carried out by dissolving the freeze-dried samples in 2.5 mL of distilled water.

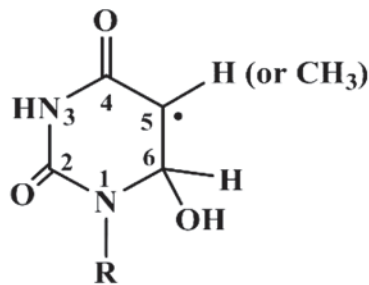
Figure 9.9a shows a typical ESR spectrum obtained from irradiated Urd solution. Figure 9.9b shows the chromatographic profile of an X-irradiated aqueous solution containing Urd and MNP monitored using UV absorbance at 260 nm. ESR signals were observed from five fractions, denoted A-F (Fig. 9.10). The ESR spectrum and the UV-absorbance spectrum obtained from fraction A are presented in Fig. 9.10a. The ESR spectrum consists of a primary triplet with a splitting of 1.52 mT that further splits into a quintet.

The UV-absorbance spectrum of this spin adduct shows that the chromophore at 260 nm, which confirmed the presence of the 5,6-double bond of the base moiety, has disappeared. This proved that this spin adduct was due to the 6-yl radical produced by OH addition to the C5 position of the base moiety (Radical 13). These coupling constants of Urd vary greatly from those of uracil and 1-methyluracil reported by Makino et al. [50] and Rustgi and Riesz [51]. For instance, the coupling constant 0.31 mT of β -hydrogen of Urd was considerably larger than that (0.08 mT) of uracil, whereas the coupling constant (0.14 mT) of β -nitrogen of Urd was smaller than that (0.35 mT) of uracil. The difference indicates that the magnitude of the coupling constants of the β -hydrogen and β -nitrogen of the 6-yl radical is dependent on the substitution pattern at the N1 position.



R: ribose or deoxyribose

Radical (13)



R: ribose or deoxyribose

Radical (14)

The ESR and UV-absorbance spectra obtained from fractions B, C and D are shown in Fig. 9.10b, c and d, respectively. These spectra showed a secondary doublet due to a β -hydrogen which in each case exhibited different hyperfine splittings

Table 9.2 Hyperfine splittings of the spin adducts from uridine

Chromatographic Fraction ^a	Primary ¹⁴ N splittings (mT)	Secondary splittings a _β (mT)
A	1.52	0.31 (H) 0.14 (N)
B	1.48	0.22 (H)
C	1.46	0.60 (H)
D	1.51	0.37 (H)
E	1.52	

^a A–E refer fractions A–E denoted by the arrows in Fig. 9.9b

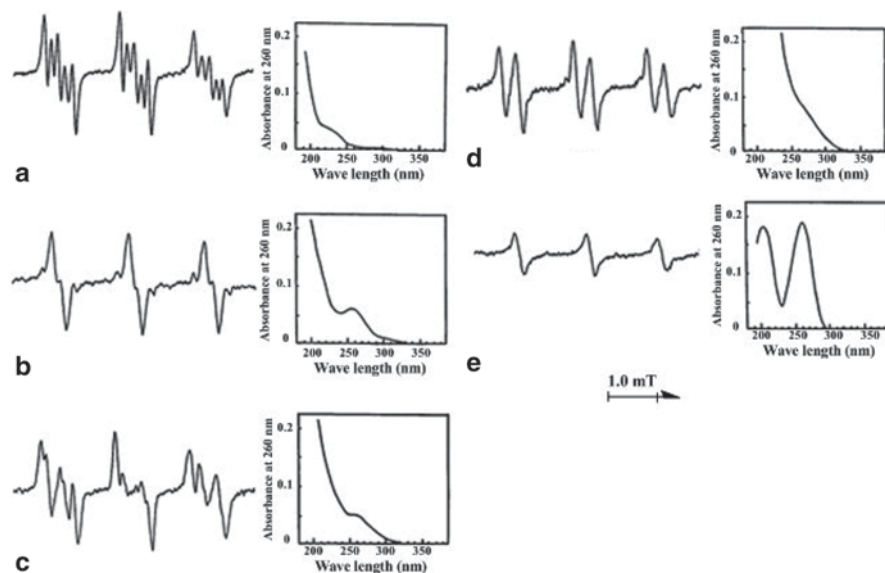
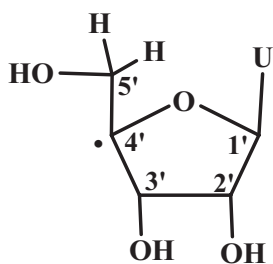


Fig. 9.10 ESR spectra (*left* panel) and UV-absorbance spectra (*right* panel) (a–e) obtained from fractions A–E in Fig. 9.9b. The figure is adapted from [44] by permission of Radiation Research Society (1986)

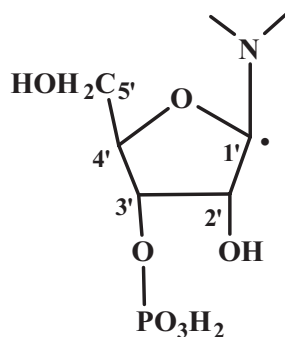
(Table 9.2). Although the separation of the spin adduct in fraction C was incomplete, a secondary doublet with a splitting of 0.60 mT was clearly recognized. The UV-absorbance spectra showed a peak at 260 nm for fractions B and C, but not for fraction D. The signal consisting of a secondary doublet with a splitting of 0.22 mT (Fig. 9.10b) may be assigned to the C4'-centered radical (Radical 12), which was produced by the transformation of the C1' radical, because the secondary doublet with a splitting of 0.14–0.22 mT was commonly observed in γ radiolysis of pyrimidine nucleotides in the solid state as described in Sect. 9.4.2. However, according to a product analysis study, it has been reported that the pathway for the formation of this radical might not be present in aqueous solution [52]. Therefore, the radical structure for the spectrum in Fig. 9.10b could not be conclusively determined, although the UV-absorbance spectrum clearly revealed that this spin-adduct arose from the sugar moiety. The ESR spectrum consisting of a secondary doublet with

a splitting of 0.60 mT shown in Fig. 9.10c was assigned to the radical formed by H abstraction from the C5' position of the sugar moiety (Radical 9). The secondary large doublet (0.50–0.60 mT) was observed in γ -radiolysis of pyrimidine nucleosides, nucleotides and their 5-halo derivatives in the solid state [11, 12], and UV photolysis of pyrimidine nucleoside and nucleotide solutions containing hydrogen peroxide [53, 54], and assigned to the C5' radical of the sugar moiety. This assignment is not in conflict with the results of UV-absorbance measurements. The ESR spectrum shown in Fig. 9.10d consists of a primary triplet with a splitting of 1.51 mT that further splits into a doublet with a splitting of 0.37 mT owing to the presence of β -hydrogen. The ESR spectra consisting of the secondary doublet with a splitting of 0.37–0.44 mT have been observed when pyrimidine nucleosides are exposed not only to OH radicals [45, 47, 54], but also to e_{aq}^- [55]. It is well known that e_{aq}^- react with the base moiety and barely react with the sugar moiety in nucleosides [56]. This strongly suggests that the 0.37–0.44 mT doublet arises from the base moiety. The UV-absorbance spectrum of fraction D showed the decomposition of the 5,6-double bond of the base moiety. It can be concluded that the ESR spectrum in Fig. 9.10d is due to the 5-yl radical produced by OH addition to the C6 position of the base moiety (Radical 14). Both the ESR and UV-absorbance spectra obtained from fraction E are presented in Fig. 9.10e. This spectrum consists of a simple triplet with a splitting of 1.52 mT without further splittings. These types of signals have been observed not only for 2'-dU but also for purine nucleosides including 3'-deoxyadenosine (cordycepin) and nucleotide homopolymers. It has also been shown that the spin adduct obtained from 2'-dA preserves the undegraded base [48]. From these results, one is forced to accept that the spin-trapped radical does not originate from the free radicals produced by H abstraction from the 1'-, 2'- or 3'-positions on the sugar moiety. The H-abstraction radical from the C4' position of the sugar moiety can be taken as a probable site for spin trapping (Radical 15). When the spin adduct in the fraction E was again purified by reverse-phase HPLC, it was revealed that the spin adduct possessed the undegraded base moiety. It is noted at this point that some spin adducts decayed during the HPLC separation. Therefore, in some cases, the gel permeation chromatography is better than HPLC. In any case, it was significant to prove that the sugar radicals (Radicals 9 and 15) were induced by OH-radical reactions as the precursor radicals of DNA strand breaks.



U: uracil base

Radical (15)



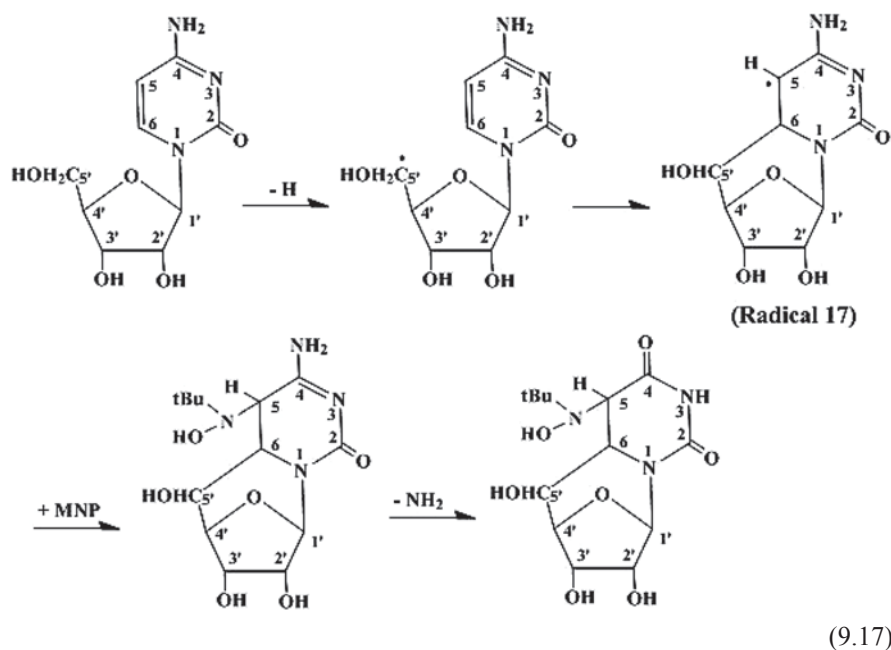
Radical (16)

When OH-induced free radicals in 3'-UMP were examined using a method that combined spin trapping and HPLC, six spin adducts were separated [45]. Four of them that were separated in the second to the fifth fractions of the HPLC profile had similar spectra; these were assigned to the spin adducts at the C5 position (Radical 14) and C6 position (Radical 13) of the base moiety, and at the C4' position (Radical 15) and the C5' position (Radical 9) on the sugar moiety. The spin adduct recovered in the sixth fraction showed that the ESR spectrum consisted of a primary triplet with a splitting of 1.50 mT that further split into a secondary triplet with a splitting of 0.34 mT and possessed the intact base (data not shown). This spectrum was assigned to the spin adduct of the C1'-yl radical formed by the H-abstraction at the C1' position on the sugar moiety (Radical 16). This radical (16) is thought to be the precursor of the C4'-radical (Radical 12). The spin adduct recovered in the first fraction of HPLC profile gave an ESR spectrum consisting of $3 \times 2 \times 2$ lines and its UV-absorbance spectrum showed the loss of a chromophore at 260 nm, but the exact radical structure could not be assigned.

When the OH-radical-induced free radicals in TMP were examined, six spin adducts were separated by HPLC [46]. Among them, three were assigned to the radicals at the C5' (Radical 9), C4' (Radical 15) and C1' (Radical 16) formed by H-abstraction at the sugar moiety, because a gradual increase in the release of unaltered thymine base from these spin adducts was observed during the period of 0–22 h when the solutions were stood at room temperature. The remaining three ESR spectra were assigned to free radicals at the C6 position (Radical 13) and C5 position (Radical 14) of the base moiety. One spin adduct at the C5 position (Radical 14) was used to identify two ESR spectra. This may be explained by assuming that this adduct has two structures. Several stereoisomers of the ring-saturated forms of thymine base in γ -irradiated DNA have been reported [57, 58]. The ESR spectrum assigned to the C4'-radical (Radical 15) consisted of a primary triplet with a splitting of 1.60 mT without further splittings, indicating that this spin adduct had no hydrogen or nitrogen atoms at the β position. In this case, the assignment of the spin adduct between the C3'-yl and MNP was ruled out because a similar ESR spectrum was observed in 2',3'- ddTMP having two hydrogens at the C3' position of the sugar moiety.

OH-radical-induced free radical reactions in the cytosine-related compounds, Cyd, 2'-dC, 3'-CMP, 5'-CMP and 5'-dCMP, have been studied using a method that combined spin trapping and HPLC [47]. To confirm the radical assignment at the base moiety, 5,6-deuterated Cyd (of which 5,6-hydrogens at the 5,6 double bond of the base moiety were replaced by deuterons) was synthesized and used for spin-trapping experiments. Four spin adducts were separated using HPLC when an N_2O -saturated aqueous solution containing Cyd and MNP was exposed to X rays at a dose of 2.7 kGy. Two of them were assigned to the spin adducts at the C5 and C6 positions of the cytosine base (similar to Radicals 14 and 13, respectively) because the hfcs of β -hydrogens was decreased 0.15 times by exchanging them with deuterons. The ESR spectrum consisting of only a primary triplet structure was assigned to the spin trapping at the C4' position of the sugar moiety (similar to Radical 15) because this spin adduct possessed the unaltered cytosine base. An

interesting result was the finding that radical formation at the C5' position of the sugar moiety (Radical 9) was not verified, but the free radical at the C5 position on the base moiety was observed instead of this radical. The radical was formed by intermolecular attack of the Radical 9 on the 5,6-double bond of the base moiety (Eq. 9.17).



The complete loss of UV absorbance of the spin adduct indicated that the deamination reactions occurred in the spin adduct of the 5',6-cyclo-6-hydrocytidine C5 radical (Radical 17). Therefore, Radical 17 was regarded as the precursor of 5',6-cyclo-5,6-dihydrouridine. It was obvious that the effects of proton-deuteron exchange at the 5,6-positions on the ESR spectrum were observed. This spin adduct was seen in all cytosine-related compounds. Shaw and Cadet reported the formation of 5',6-cyclo-5,6-dihydro-2'-deoxyuridine when 2'-dC was irradiated with γ rays in the frozen state [59].

9.5.2 Free Radicals Induced by the Reactions of Purine Nucleosides and Nucleotides with OH Radicals

OH-induced degradation of de-aerated aqueous solutions of purine nucleosides leads to several reactions namely; rupture of the *N*-glycosidic bond followed by the liberation of the bases; opening of the imidazole ring via the addition of OH radicals to the N7-C8 double bond to produce the 4-amino-5-formamidepyrimidine

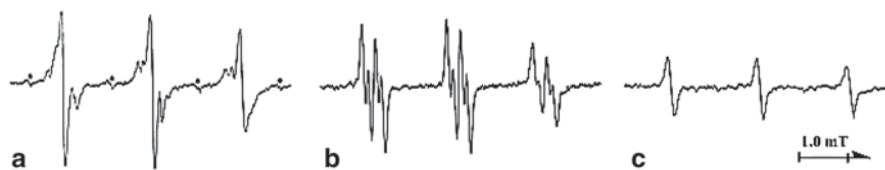


Fig. 9.11 **a** ESR spectrum of spin-trapped radicals from an aqueous solution containing 2'-dA and MNP after X irradiation under N_2O . The ESR spectrum is marked with asterisks (*) owing to the H-addition radical to MNP. **b** and **c** ESR spectra of the separated spin adducts using Gio-Gel P-2 column chromatography. The figure is adapted from [48] by permission of Informa Healthcare (1986)

deoxyribose or ribose; C5'-C8 cyclization formed by hydrogen abstraction from the C5' position followed by the intermolecular attack of C5'-yl radical on 7,8-double bond; and the isomerization reaction involving H-abstraction from the C4' position of the sugar moiety, as reviewed by Cadet and Berger [60] and Breen and Murphy [61]. Therefore, it is important to obtain information concerning the radical intermediates that can explain these reaction mechanisms. 2'-dA, Ado, 2'-dG, Guo, 3'-dA (cordycepin) and inosine as purine nucleosides, and 5'-dAMP, 5'-AMP, 3'-AMP, 5'-dGMP, 5'-GMP and 3'-GMP as purine nucleotides were subjected to spin-trapping experiments. The deuterated forms at the C2 and C8 positions for adenine-related nucleotides and at the C8 position for guanine-related nucleotides were prepared and used for some experiments. After N_2O -saturated aqueous solutions containing 10–80 mM of purine nucleosides, 1 mg/mL of MNP, 50 mM of purine nucleotides and 2 mg/mL of MNP were exposed to X rays at a dose of 5.8 kGy, the resulting samples were applied a Bio-Gel P-2 column for the purpose of separating the spin adducts. HPLC was employed when a more precise separation of the spin adducts from the undegraded original molecules was required.

Figure 9.11a shows the ESR spectrum obtained from X-irradiated aqueous solution of 2'-dA [48]. The ESR signal labeled with asterisks in this figure was assigned to the *t*-butylhydronitroxide radical (MNP-H \cdot). Only two spin adducts were separated with gel chromatography as shown in Figs. 9.11b and c. The ESR spectrum in Fig. 9.11b shows a secondary doublet with a splitting of 0.24 mT owing to the presence of a β -hydrogen which further splits into a doublet with a splitting of 0.11 mT owing to the γ -hydrogen. Figure 9.11c shows the ESR spectrum consisting of only a primary triplet with a splitting of 1.53 mT. The spin adducts giving these spectra possessed unaltered purine bases, suggesting that free radicals induced in the sugar moiety were spin-trapped by MNP. These spectra were observed in all nucleosides except for Guo. Essentially the same results were also obtained from purine nucleotides. In the case of nucleotides, the ESR spectrum consisting of a secondary doublet with a splitting of 0.20–0.28 mT was regarded as the same as that in Fig. 9.11b. This was because the ESR spectrum consisting of 3×2 lines in 3'-GMP was changed to $3 \times 2 \times 2$ lines owing to the presence of a β -hydrogen and a γ -hydrogen when 3'-GMP was treated with the alkaline phosphatase [62]. Furthermore, no effects of proton-deuteron exchange at the C2 and C8 positions on the ad-

enine base moiety and at the C2 position on the guanine base moiety were observed on ESR spectra. Therefore, the ESR spectrum in Fig. 9.11c was assigned to the C4' radical similar to Radical 15 without ambiguity. Figure 9.11b could be assigned to the spin adducts on the sugar moiety, but no exact radical structure was elucidated. No ESR spectra due to the spin adducts at the base moiety were observed. However, this does not necessarily mean that free radicals are not produced at the purine base moiety by OH radicals. Interesting results have been obtained from spin-trapping experiments using a nitron spin trap PBN [63].

9.5.3 Free Radicals Induced by the Reactions of Pyrimidine and Purine Nucleotide Homopolymers or Oligonucleotides with OH Radicals

Using nucleosides and nucleotides, the ESR method combining spin trapping and HPLC or gel permeation chromatography provided evidence that OH radicals produced free radicals at the C4' and C5' positions on the sugar moiety which can be regarded as the precursors of DNA strand breaks (Radicals 15 and 9). Another radical at the C1' position (Radical 16) is regarded as a precursor of apyrimidinic/apurinic-site formation. Therefore, it is important to prove that OH radicals actually produce these radicals in the high-molecular weight compounds closer to DNA. As the model compounds, poly(U), poly(C), poly(A) and poly(I), and oligo(dC)₁₀ and oligo(dT), were employed [45, 47, 48, 64]. In the case of poly(U) (MW ca. 5×10^5) [45], a spectrum with a broad line shape due to the slow tumbling of nitroxide was observed. The broad spectrum was changed to a well-resolved one by digestion with bovine pancreas RNase A for 3 h. When the digested spin adducts were separated by the same system used for 3'-UMP and examined by means of ESR spectroscopy, six ESR spectra were observed. Comparison of the six spectra with those of 3'-UMP demonstrated that the spin adducts were almost identical to those of 3'-UMP. In other words, the formation of C1'-yl, C4'-yl and C5'-yl radicals on the sugar moiety as well as C5-yl and C6-yl radicals on the base moiety was confirmed. In the case of poly(C), results similar to those for cytosine nucleosides and nucleotides were obtained [47]; namely, in addition to the C5-yl, C6-yl and C4'-yl radicals, Radical 17 formed as a result of the cyclization reaction (Eq. 9.17) was found to be produced. Only C4'-yl radicals are identified in poly(A) and poly(I) [48].

To more closely approach actual DNA, the oligomers consisting of deoxyribose such as oligo(dC)₁₀ and oligo(dT)₁₀ were used [64]. These oligomers were chosen as samples because basic information concerning the monomers, dCMP and TMP, had already been obtained as described in Sect. 9.5.1; they had the property of high solubility in aqueous solution, which was advantageous for spin-trapping experiments. Oligo(dC)₁₀ and oligo(dT)₁₀ were prepared with DNA synthesizer. After each oligomer containing MNP was exposed to X rays under anoxic condition, it was digested to smaller size with phosphodiesterase and the spin adducts were separated using HPLC. In the separated spin adducts, the ESR spectrum attributable to

the spin adduct of C4'-deoxyribose radicals (Radical 15) was observed as the sole sugar radical in each oligomer. To obtain evidence that the assigned C4'-yl radical is, in fact, the precursor radical of strand breaks, 5'-³²P-end-labeled oligomers were prepared and exposed to X rays in the presence or absence of MNP. These oligomers were then analyzed using polyacrylamide gel electrophoresis (PAGE). As a result, fragments corresponding to the monomer to the 9mer sequence appeared on the PAGE patterns. When the luminescence intensity of each fragment was plotted against the concentrations of OH radicals (i.e. the radiation dose), a straight line was obtained. The suppression of oligonucleotide fragmentation was observed in the presence of MNP in both samples. MNP suppressed the fragmentation by both scavenging OH radicals and trapping the precursor radicals of strand breaks. The slope of the line in the presence of MNP was found to be gentler than that obtained in the absence of MNP even after it was corrected on the basis of the competitive reaction model between OH radicals and MNP. These results suggested that MNP protected against OH-induced fragmentation of oligomers by trapping the strand-break precursor radicals (the C4'-yl radical).

Only one base radical and one sugar radical were identified in oligo(dC)₁₀, and two base radicals and one sugar radical were identified in oligo(dT)₁₀. These results were in contrast to those obtained from their constituents in which free radicals at the C5, C6 and the C5-methyl positions on the base moiety and free radicals at the C1', C4' and C5' positions on the sugar moiety were identified [46, 47, 65]. Difference between them may be interpreted as suggesting that the polymerized forms of mononucleotides minimize the sites at which OH radicals can attack or restrict the sites at which MNP can trap radicals. It has been reported that the susceptibility of bases in DNA to OH radicals is lower than is the case for free bases [66]. Each fragment consisted of a band with a pair of spots. It is interesting that the PAGE patterns of oligomers which were exposed to X rays and subsequently subjected to piperidine treatments showed that the reactivities of OH radicals with base and deoxyribose moieties differed in oligo(dC)₁₀ and oligo(dT)₁₀ (data not shown) [64]. Half of the OH radicals reacted with the deoxyribose moiety to induce the C4'-yl radical in oligo(dC)₁₀ and less than one-third of OH radicals react with deoxyribose moiety to induce the C4'-yl radical in oligo(dT)₁₀. These results indicate that the thymine base may play a role in protecting DNA strand breaks due to OH radicals. If the thymine-rich and cytosine-rich regions are present in actual DNA, it is possible that OH radicals do not react uniformly with DNA to induce strand breaks. In fact, when OH-induced free radicals in calf thymus DNA were trapped by MNP, the majority of the components of the observed ESR spectrum consisted of the signals due to the spin adducts between thymine base radicals and MNP (see Sect. 9.5.4). This might be a reflection of OH-radical reactivity in the thymine-rich region in DNA. The results obtained from nucleotide homopolymers and oligonucleotides suggest that the spin-trapping technique combining enzymatic digestion and HPLC separation is effective for the identification of OH-induced free radicals in molecules with high MW; although, in some cases, the identification of OH-induced radicals in nucleic acid constituents has been performed in the composite spectra without the separation of spin adducts [65].

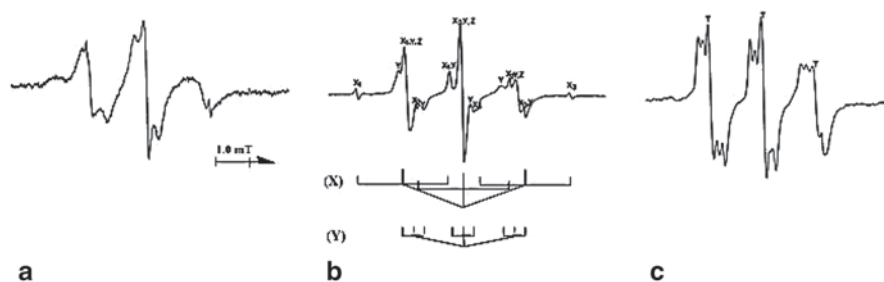


Fig. 9.12 **a** ESR spectrum obtained immediately after an N_2O -saturated aqueous solution containing DNA and MNP was exposed to X rays at a dose of 2.7 kGy of, **b** ESR spectrum recorded at 40°C after digestion with bovine pancreas DNase I. **c** ESR spectrum obtained from yeast RNA. The figure is adapted from [69] with permission of American Chemical Society (1987)

9.5.4 Free Radicals Induced by the Reactions of DNA with OH Radicals

The final purpose of this chapter is to examine whether the spin-trapping method combined with ESR spectroscopy is applicable to actual DNA [67]. Two technical improvements were introduced to the conventional spin-trapping method to make possible its application to DNA: (1) prior to X irradiation, sonolysis of aqueous DNA (calf thymus) solution using 19.5-kHz ultrasound was carried out to obtain a highly concentrated DNA solution and to lower the viscosity of the solution; (2) after precursor radicals in X-irradiated DNA were trapped by a spin-trapping reagent, the DNA was digested to form oligonucleotides by DNase I to obtain an ESR spectrum with a well-resolved hyperfine structure.

Figure 9.12a shows an ESR spectrum immediately after irradiation. This was broad and was insufficient for analyzing the spin-trapping sites. Figure 9.12b shows an ESR spectrum recorded at 40°C after the DNA was digested by DNase I; enzymatic digestion was required to sharpen the ESR spectrum. It can clearly be seen that the spectrum is well-resolved and analyzable. This spectrum consisted of several sets of signals from different spin adducts, but we could not separate them by gel permeation chromatography or HPLC because DNase I digested the DNA to form oligonucleotides of different sizes. From the results obtained from nucleosides and nucleotides, the ESR spectra obtained from thymidine, TMP and oligo(dT)₁₀ are most similar to those of DNA. Signal labeled X in Fig. 9.12b consists of a primary triplet with a splitting of 1.7 mT and a secondary 1:2:1 triplet with a splitting of 1.34 mT. Quite similar spectra were observed in the ESR spectrum of spin-trapped radicals from γ -irradiated solid thymidine as shown in Fig. 9.2. A radical structure consistent with this signal is the 5-methyleneuracil radical (Radical 2) which is the precursor of 5-hydroxymethyluracil. The signal labeled Y is an ESR spectrum consisting of a primary triplet with a splitting of 1.46 mT with a secondary 1:1:1 triplet with a splitting of 0.29 mT which is attributed to the Radical 13 (precursor of thymine glycol, and others), because similar spectra were obtained from thymidine

[54], TMP [46] and oligo(dT)₁₀ [64]. The signal labeled Z is an ESR spectrum consisting of a triplet with a splitting of 1.59 mT without further splittings. In accordance with the conclusions stated for thymidine [54] and TMP [46], this spectrum was regarded as arising from spin trapping of Radical 14 (a precursor of thymine glycol, and others) rather than at the C4' position of the deoxyribose moiety of DNA. As a result, all of the signals were identified as the spin adducts of radicals produced on the thymine base moiety, although OH radicals reacted not only with the thymine base but also with the other bases and the sugar-phosphate back bone. The results regarding DNA radicals may be explained by the higher stability of spin adducts at the thymine base moiety than at the other sites of DNA. The high reactivity of OH radicals to the thymine base may also be another factor responsible for the localization of the spin adducts as discussed in Sect. 9.5.3. In fact, studies regarding the reactions of OH radicals with DNA have shown that the thymine base is particularly susceptible to OH radical attack [68]. In the case of yeast RNA, the signal labeled T that can be assigned to the C4'-yl radical (Radical 15) was clearly observed as shown in Fig. 9.12c.

9.5.5 Free Radicals Induced by the Reactions of Proteins (Histone H1 and Protamine) with e_{aq}^-

In radiation-induced reactions in peptides, polypeptides and proteins, it has been reported that e_{aq}^- (which are produced by radiolysis of water) cause main chain scission through dissociative deamination [69]. We have studied the reactions of e_{aq}^- with proteins by employing protamine (salmon roe; MW=4400) and histone H1 (calf thymus; MW=22,000) [70]. Since protamine and histone H1 are closely associated with DNA in the spermatozoid nucleus and cell nucleus, respectively, radiation damage studies not only involving DNA but also these proteins are important in the elucidation of the mechanisms regarding radiation-induced chromosomal aberrations. Furthermore, an advantageous aspect of these polypeptides is that they contain few amino acid groups with which e_{aq}^- have high reactivity. After an N₂-saturated aqueous solution containing protamine, sodium formate (NaHCO₂) and MNP was irradiated with X rays at a dose of 4.5 kGy, a fraction containing the protamine was once purified using Sephadex G-25 column chromatography and treated with trypsin digestion (Fig. 9.13).

The ESR spectrum consists of a primary triplet with a splitting of 1.55 mT with a secondary doublet with a splitting of 0.36 mT that further splits into a 1:3:4:3:1 intensity quintet arising from equal γ -nitrogen and two γ -hydrogens (0.07 mT). This radical was assigned to the deaminated radical produced by Eq. 9.18. The spin adduct has two hydrogens at the γ -position of the side chain of the amino acid. Similar results were also obtained from proteins and histone H1. From these results, it was confirmed that e_{aq}^- induce the deamination reaction leading to the main-chain scission.

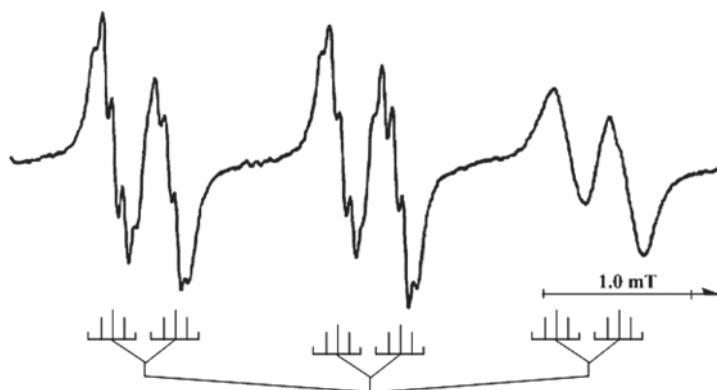
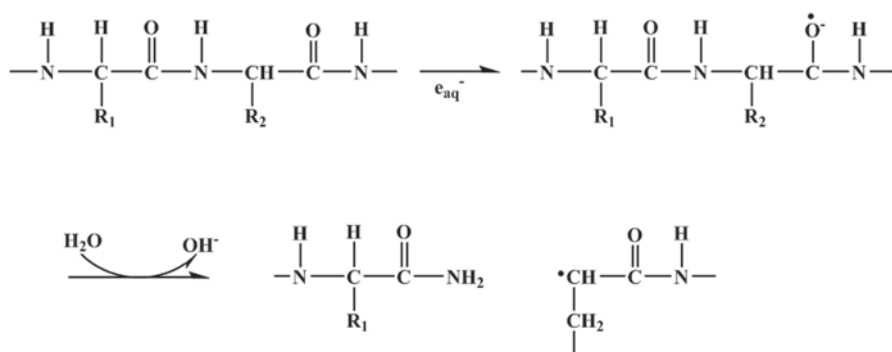


Fig. 9.13 ESR spectrum obtained after an N_2 -saturated aqueous solution containing protamine (3 mg/mL), MNP (1.5 mg/mL) and $NaHCO_2$ (0.5 M) was exposed to X rays at a dose of 4.5 kGy, purified by chromatography followed by trypsin digestion. The figure is adapted from [70] by permission of Informa Healthcare (1986)



(9.18)

9.6 Conclusion

Applications of a technique combining ESR and the spin tapping to identify free radicals induced in DNA, proteins and their related compounds by means of the direct and indirect actions of ionizing radiation are described. MNP was mainly employed as the spin trap because this was suitable for the precise identification of radical structures.

The first section concerning the spin-trapping experiments describes the application of this method with regard to the trapping and identification of the transient free radicals in DNA and protein constituents directly produced by ionizing radiation, the so-called direct actions of ionizing radiation. In some compounds, the ESR and

spin-trapping method was further combined with HPLC to separate spin adducts. The stable, long-lived free radicals produced in the polycrystalline samples by irradiation were trapped by rapidly dissolving them in the aqueous solutions containing MNP in the presence or absence of oxygen and were changed to stable nitroxide spin adducts. After the majority of undamaged molecules was removed by filtration using a SEP-PAK cartridge, each spin adduct was accurately separated by means of HPLC. The assignment of radical structures was undertaken by analyzing the secondary hyperfine splittings in the ESR spectra of the nitroxide spin adducts. Comparison of radical structures deduced from spin-trapping studies with those from ESR studies of single-crystals by other researchers was helpful for the conclusive assignment of radical structures.

The second section of this chapter describes the application of a method combining ESR, spin trapping and HPLC to trap and identify the free radicals produced by the reactions of OH radicals with DNA and protein constituents, the so-called indirect action of ionizing radiation. MNP was again used as the spin trap. N₂O-saturated aqueous solutions containing MNP and each compound were exposed to ionizing radiation. OH-induced short-lived radicals were converted into relatively long-lived nitroxide radicals as the spin adducts. The resulting nitroxide spin adducts were then individually separated using HPLC and analyzed by means of ESR. Examination of the separated spin adducts using UV-absorbance spectrometry was helpful in discriminating if the base or sugar was the radical-trapping site. The assignment of radical structures was further evidenced by referring to the radical reaction processes deduced from the product analysis studies of irradiated compounds reported by other researchers.

In the third section of this chapter, further application of the spin-trapping method regarding high molecular weight compounds, such as polynucleotides, polypeptides DNA and proteins, is described. With the exception of lysozyme, the spin-trapping method concerning these compounds was applied to the free radicals induced by OH radicals as well as e_{aq}^- because of their slow dissolution rate in water. In the case of e_{aq}^- , aqueous solutions containing MNP, each molecule and sodium formate (used as the OH scavenger) were exposed to ionizing radiation. After irradiation, these compounds were converted to fragments with smaller sizes by enzymatic digestion, and the corresponding fragments containing the spin adducts were separated by gel-permeation chromatography or HPLC; each one was analyzable using ESR spectrometry. In particular, observation of free radicals on the sugar moiety in DNA model compounds was significant for outlining the chemical processes regarding the radiation-induced strand breaks of DNA. A spin trap data base with references is available at NIH: <http://tools.niehs.nih.gov/stdb/>.

References

1. Janzen EG (1971) Spin-trapping. *Acc Chem Res* 4:31–40
2. Lagercrantz C, Forshult S (1968) Trapping of free radicals formed by γ -irradiation of organic compounds. *Nature* 218:1247–1248

3. Riesz P, Rustgi S (1979) Aqueous radiation chemistry of protein and nucleic acid constituents: ESR and spin-trapping studies. *Radiat Phys Chem* 13:21–40
4. Makino K, Moriya F, Hatano H (1985) Separation of free radicals by high-performance liquid chromatography with electron spin resonance detection. *J Chromato* 332:71–106
5. Joshi A, Rustgi S, Riesz P (1976) E.s.r of spin-trapped radicals in gamma-irradiated aqueous solutions of nucleic acids and their constituents. *Int J Radiat Biol* 30:151–170
6. Makino K (1980) Studies on spin-trapped radicals in gamma-irradiated aqueous-solutions of 2-methyl-2-nitrosopropane by high-performance liquid-chromatography and electron-spin-resonance spectroscopy. *J Phys Chem* 84:1012–1015
7. Kuwabara M, Hiraoka W, Sawamura S, Katayama M (1991) Reactions and rate constants between hydrated electrons and the monomer and dimer of 2-methyl-2-nitrosopropane determined by the pulse radiolysis method. *J Am Chem Soc* 113:3995–3997
8. Kuwabara M, Miyake S, Jin T, Sawamura S (1995) Reactions and rate constants between hydroxyl radicals and the dimer and monomer of spin trap 2-methyl-2-nitrosopropane determined by the pulse radiolysis method. *J Phys Chem* 99:14078–14082
9. Henglein A, Schnabel W, Wedenburg J (1969) *Einführung in die Strahlenchemie*, Verlag Chemie, Weinheim
10. Minegishi A, Bergene R, Riesz P (1980) E.S.R. of spin-trapped radicals in gamma-irradiated polycrystalline amino acids, N-acetyl amino acids and dipeptides. *Int J Radiat Biol* 38:627–650
11. Kuwabara M, Lion Y, Riesz P (1981) E.S.R. of spin-trapped radicals in gamma-irradiated polycrystalline nucleic acid constituents and their halogenated derivatives. *Int J Radiat Biol* 39:465–490
12. Zhang Z-Y, Kuwabara M, Yoshii G (1983) ESR and spin-trapping study of room-temperature radicals in γ -irradiated polycrystalline nucleotides. *Radiat Res* 93:213–231
13. Hiraoka W, Kuwabara M, Sato F (1991) Characterization of free radicals in γ -irradiated polycrystalline uridine 5'-monophosphate: a study combining ESR, spin-trapping and HPLC. *Int J Radiat Biol* 59:875–883
14. Evans CA (1979) Spin trapping. *Aldrichim Acta* 12:23–29
15. Zehner H, Flossmann W, Westhof E, Müller A (1976) Electron spin resonance of irradiated single-crystals of uracil. *Molec Phys* 32:869–878
16. Hüttermann J, Herak JN, Westhof E (1978) Structure of radicals from nucleic acid constituents. In: Hüttermann J, Köhnlein W, Téoule R, Bertinchamps AJ (eds) *Effects of Ionizing Radiation on DNA*. Springer, Berlin, pp 31–58
17. Hüttermann J, Bernhard WA, Haindle E (1977) Reactions of radiation-induced free-radicals in solid halodeoxyuridines—single-crystals of 5-chlorodeoxyuridine and 5-bromodeoxyuridine. *J Phys Chem* 81:228–232
18. Spalletta RA, Bernhard WA (1982) Spin-trapping free-radicals by solvating X-irradiated crystalline pyrimidines. *Radiat Res* 89:11–24
19. Cook JB, Elliott JP, Wyard SJ (1967) Electron spin resonance of an irradiated single crystal of cytosine. *Molec Phys* 13:49–64
20. Oloff H, Hüttermann J, Symons MCR (1978) Radiation damage in solid 5-halouracils. Electron spin resonance of single crystals of 5-bromouracil. *J Phys Chem* 82:621–622
21. Neumüller W, Hüttermann J (1980) Radiation Damage in Solid 5-halouracils: free radicals in single crystals of 5-fluorouracil. *Int J Radiat Biol* 37:49–60
22. Kuwabara M, Lion Y, Riesz P (1981) E.S.R. of spin-trapped radicals from sugars. Reactions of hydroxyl radicals in aqueous solutions and γ -radiolysis in the polycrystalline state. *Int J Radiat Biol* 39:451–455
23. von Sonntag C (1980) Free radical reactions of carbohydrates as studied by radiation techniques. *Adv Carbohydr Chem Biochem* 37:7–77
24. Hüttermann J, Bernhard WA, Haindle E, Schmidt G (1977) Reactions of radiation-induced free radicals in solid halodeoxyuridines. Single crystals of 5-chloro- and 5-bromodeoxyuridine. *J Phys Chem* 81:228–232

25. Oloff H, Hüttermann J (1977) Radiation damage in solid 5-halouracils. Free radicals in single crystals of 5-chlorouracil and 5-chlorouridine. *J Magn Res* 27:197–213
26. Oloff H, Haindl E, Hüttermann J (1979) Radiation damage in solid 5-halouracils: deoxyribose ring opening in single crystals of 5-chloro- and 5-bromodeoxyuridine. *Radiat Res* 80:447–463
27. Sagstuen E (1980) Radiation damage to nucleosides and nucleotides I. An ESR study of uridine-5'-monophosphate 2Na^+ single crystals. *Radiat Res* 81:188–199
28. Rakvin B, Herak JN (1980) An E.S.R. study of stable radicals in gamma-irradiated single crystal of uridine 5'-phosphate (Na salt). *Int J Radiat Biol* 28:129–138
29. Radons G, Oloff H, Hüttermann J (1981) Free radicals from X-irradiated single crystals of uridine-5'-monophosphate disodium salt. *Int J Radiat Biol* 40:245–263
30. Sagstuen E (1980) Radiation damage to nucleosides and nucleotides III. A C4'-centered radical in the ribose moiety of uridine-5'-monophosphate single crystals. *Radiat Res* 84:164–170
31. Hampton DA, Alexander C Jr (1973) ENDOR and ESR studies of irradiated cytidine. *J Chem Phys* 58:4891–4898
32. Bernhard WA, Hüttermann J, Müller A, Close DM, Fouse GW (1976) A stable radical in the ribose moiety of X-irradiated 3'-cytidilic acid and its relation to a similar radical in cytidine. An ESR-ENDOR study. *Radiat Res* 68:390–413
33. Krilov D, Herak JN (1974) ESR evidence for the radiation-induced breakage of the sugar-phosphate bonds in nucleotides: single crystal of deoxycytidine 5'-monophosphate. *Biochim Biophys Acta* 366:396–401
34. Herak JN, Krilov D, McDowell CA (1976) ENDOR study of the stable radicals in γ - or X-ray-irradiated single crystal of deoxycytidine-5'-monophosphate. *J Magn Reson* 23:1–7
35. Close DM, Fouse GW, Bernhard WA (1977) ENDOR study of the $3\alpha\text{H}$ radical in deoxycytidine 5'-phosphate H_2O . *J Chem Phys* 66:4689–4693
36. Makino K, Riesz P (1982) Electron-spin-resonance of spin-trapped radicals in gamma-irradiated polycrystalline amino-acids—chromatographic-separation of radicals. *Int J Radiat Biol* 41:615–624
37. Inanami O, Kuwabara M, Sato F (1988) ESR and spin-trapping study of free radicals in γ -irradiated solid lysozyme. *Free Rad Res Comms* 5:43–49
38. Garrison WM (1985) Reaction mechanisms in the radiolysis of peptides, polypeptides and proteins. Lawrence Berkeley Laboratory-18613, University of California-48
39. Riesz P, White FH (1970) Radical distributions in gamma-irradiated dry proteins at 195 degrees K. *Radiat Res* 44:24–34
40. Rustgi S, Joshi A, Moss H, Riesz P (1977) ESR of spin-trapped radicals in aqueous-solutions of amino-acids—reactions of hydroxyl radical. *Int J Radiat Biol* 31:415–440
41. Felix CC, Reska K, Sealy TF (1983) Free-radicals from photo-reduction of hematoporphyrin in aqueous-solution. *Photochem Photobiol* 37:141–147
42. Davies MJ, Slater TF (1986) Studies on the photolytic breakdown of hydroperoxides and peroxidized fatty acids by using electron spin resonance spectroscopy. Spin trapping of alkoxy and peroxy radicals in organic solvents. *Biochem J* 240:789–795
43. Eling TE, Cutris JF, Hartmann LS, Mason RP (1986) Oxidation of glutathione to its thyl free radical metabolite by prostaglandin H synthase. A potential endogenous substrate for the hydroperoxidase. *J Biol Chem* 261:5023–5208
44. Inanami O, Kuwabara M, Endoh D, Sato F (1986) OH-induced free radicals in uridine studies by a method combining ESR, spin-trapping and liquid chromatography. *Radiat Res* 108:1–11
45. Inanami O, Kuwabara M, Sato F (1987) OH-induced free radicals in 3'-UMP and poly(U): spin-trapping and radical chromatography. *Radiat Res* 112:36–44
46. Kuwabara M, Hiraoka W, Sato F (1989) Evidence for the formation of strand-break precursors in hydroxyl-attacked thymidine 5'-monophosphate by the spin trapping method. *Biochemistry* 28:9625–9632
47. Hiraoka W, Kuwabara M, Sato F, Matsuda A, Ueda T (1990) Free-radical reactions induced by OH-radical attack on cytosine-related compounds: a study by a method combining ESR, spin trapping and HPLC. *Nucleic Acids Res* 18:1217–1223

48. Kuwabara M, Inanami O, Sato F (1986) OH-induced free radicals in purine nucleosides and their homopolymers: E.S.R. and spin-trapping with 2-methyl-2-mitosopropane. *Int J Radiat Biol* 49:829–844
49. Buxton GV, Greenstock CL, Helman WP, Ross AB (1988) Critical review of rate constants for reactions of hydrated electrons, hydrogen atoms and hydroxyl radicals (OH/O^-) in aqueous solution. *J Phys Chem Ref Data* 17:513–886
50. Makino K, Mossoba MM, Riesz P (1983) Electron spin resonance of spin-trapped radicals in γ -irradiated aqueous uracil solutions: chromatographic separation of radicals. *J Phys Chem* 87:1074–1080
51. Rustgi S, Riesz P (1978) E.S.R. of free radicals in aqueous solutions of substituted pyrimidines. *Int J Radiat Biol* 33:21–39
52. von Sonntag C (1984) Carbohydrate radicals: from ethylene glycol to DNA stand breakage. *Int J Radiat Biol* 46:507–519
53. Kuwabara M, Lion Y, Riez P (1981) E.S.R. of spin-trapped radicals in gamma-irradiated aqueous solutions of nucleic acids and their constituents. *Int J Radiat Biol* 39:491–514
54. Kuwabara M, Zhang ZY, Yoshii G (1982) E.S.R. of spin-trapped radicals in aqueous solutions of pyrimidine nucleosides and nucleotides: reactions of the hydroxyl radical. *Int J Radiat Biol* 41:241–259
55. Kuwabara M, Yoshii G, Itoh T (1983) Reactions of the hydrated electron with pyrimidine nucleosides halogenated at the sugar moiety: E.S.R. and spin-trapping with 2-methyl-2-nitropropane. *Int J Radiat Biol* 44:219–224
56. Scholes G (1978) Primary events in the radiolysis of aqueous solutions of the nucleic acids and related substances. In: Hüttermann J, Köhnlein W, Téoule R, Bertinchamps AJ (eds) *Effects of ionizing radiation on DNA*. Springer, Berlin, pp 153–170
57. Breimer LH, Lindahl T (1985) Thymine lesions produced by ionizing-radiation in double-stranded DNA. *Biochemistry* 24:4018–4022
58. Furlong EA, Jorgensen TJ, Henner WD (1986) Production of dihydrothymidine stereoisomers in DNA by gamma-irradiation. *BioChemistry* 25:4344–4349
59. Shaw AA, Cadet J (1988) Formation of cyclopyrimidines via the direct effects of gamma irradiation on pyrimidine nucleosides. *Int J Radiat Biol* 54:987–997
60. Cadet J, Berger M (1985) Radiation-induced decomposition of the purine bases within DNA and related model compounds. *Int J Radiat Biol* 47:127–143
61. Breen AP, Murphy JA (1995) Reactions of oxyl radicals with DNA. *Free Rad Biol Med* 18:1033–1077
62. Hiraoka W, Kuwabara M, Sato F (1998) OH-induced free radicals in purine nucleoside monophosphates: E.S.R. and spin-trapping. *Int J Radiat Biol* 55:51–58
63. Ohshima H, Ono A, Matsuda A, Sawamura S, Kuwabara M (1997) Reactions between hydroxyl-radical-induced 7,8-dihydro-8-oxo-2'-deoxyguanosine precursor and the spin trap α -phenyl-*N-tert*-butylnitron. *J Radiat Res* 38:15–25
64. Kuwabara M, Ohshima H, Sato F, Ono A, Matsuda A (1993) Spin-trapping detection of precursors of hydroxyl-radical-induced DNA damage: identification of precursor radicals of DNA strand breaks in oligo(dC)₁₀ and oligo(dT)₁₀. *Biochemistry* 32:10599–10606
65. Davis MJ, Gilbert BC, Hazelwood C et al (1995) EPR spin-trapping studies of radical damage to DNA. *J Chem Soc Perkin Trans* 2:13–21
66. von Sonntag C (1987) *Chemical Basis of Radiation Biology*. Taylor & Francis, London
67. Kuwabara M, Inanami O, Endoh D, Sato F (1987) Spin trapping of precursors of thymine damage in X-irradiated DNA. *Biochemistry* 26:2458–2465
68. Téoule R, Cadet J (1978) Radiation-induced degradation of the base component in DNA and related substances—final products. In: Hüttermann J, Köhnlein W, Téoule R, Bertinchamps AJ (eds) *Effects of ionizing radiation on DNA*. Springer, Berlin, pp 171–203
69. Garrison WM (1987) Reaction mechanisms in the radiolysis of peptides, polypeptides, and proteins. *Chem Rev* 87:381–398
70. Inanami O, Kuwabara M, Hayashi M, Yoshii G, Syuto B, Sato F (1986) Reaction of the hydrated electron with histone H1 and related compounds studied by E.S.R. and spin-trapping. *Int J Radiat Biol* 49:47–56

Part IV
Materials Science

Chapter 10

EPR Application to Polymers: Radiation Induced Crosslinking and Graft Polymerization

Tadao Seguchi

Abstract EPR application to polymers has been closely related to the research and development of polymer modification by radiation processing. The free radicals induced in polymer chains by irradiation can initiate chemical reactions at rather low temperature ranges, therefore, the radical reactions can be followed by EPR measurement. EPR studies of polymers were applied mainly for the analysis of graft polymerization by the pre-irradiation method and the analysis of radiation crosslinking, which contributed to the development of polymer materials by radiation processing. For graft polymerization, the radicals trapped in the crystalline regions of polymers migrate to the surface and initiate the graft reaction. The concentration of the trapped radicals and their rate of decay are closely related to the graft yield and rate of the grafting reaction. As the radical migration rate in the crystalline part, namely the decay rate of the trapped radicals, is determined by the temperature, the graft polymerization is much affected by the temperature. And also the trapped radicals in any polymers can be conserved for a long time by cooling the irradiated polymers even in air. Therefore, the irradiation and the graft-polymerization can be separated in place and in time. For the crosslinking of polymers, polytetrafluoroethylene (PTFE), polyacrylonitrile (PAN) fiber and polycarbosilane (PCS) fiber were selected for a specific application. The PAN fiber is a precursor of carbon fiber formation and PCS fiber is the precursor of SiC ceramic fiber. Especially the EPR studies for PCS fiber and the pyrolysis were useful for the development of radiation processing. The process of pyrolysis of PCS fiber at a high temperature involves radical reactions and could be followed by EPR measurements. A knowledge of the radical reaction mechanism contributed much to the development of a new method for SiC fiber synthesis.

T. Seguchi (✉)
Takasaki Advanced Radiation Research Institute,
Japan Atomic Energy Agency, Takasaki, Japan
e-mail: seguchi@aj.wakwak.com

© Springer International Publishing 2014
A. Lund, M. Shiotani (eds.), *Applications of EPR in Radiation Research*,
DOI 10.1007/978-3-319-09216-4_10

387

10.1 Reaction Mechanism for Radiation Crosslinking and Graft Polymerization

10.1.1 Introduction

The radiation treatment of polymers leads to polymer modification which can cause crosslinking between polymers chains and also to graft-polymerization. Both modifications are induced via free radicals produced by the radiation, so the EPR technique is suitable for the analysis of radical reactions in polymer materials. Research on the effects of radiation on polymers has been reported by many authors, and several books have been published [1–3]. The first stage of EPR research in the period 1958–1970 involved the determination of radical species trapped in the polymers, and a lot of fundamental studies were carried out. The polymers were irradiated at low temperature in liquid nitrogen and the behavior of the radicals was followed by annealing at higher temperatures, and the observations discussed with respect to molecular motions of the polymer chains and also to the reactions for crosslinking, degradation with chain scission, oxidation, and graft polymerization. For the analysis of the reaction mechanisms in polymer modification, the target polymers were mainly the crystalline polymers such as polyethylene (PE), polypropylene (PP), polytetrafluoroethylene (PTFE), polyamide (PA), etc., because the radicals were generally too unstable in amorphous polymers above their glass transition temperatures under the conditions for radiation modification. The second stage of EPR researches after 1970 was stepped up to follow the radical behavior in chemical reactions for the crosslinking, oxidative degradation, and graft polymerization. Of course the fundamental studies of polymer materials by irradiation have continued for the analysis of irradiation effects at the experienced laboratories such as at the University of Queensland [4, 5].

This section is a review on polymers for the analysis of reaction mechanism for radiation induced crosslinking and graft polymerization from the view point of their applications. The applications of crosslinking for polymers has progressed since 1960, for example, for the processing of heat-shrinkable tubes, polymer foams, heat resistant wire and cables, hydrogels, etc. [6]. The crosslinking of PTFE by radiation was a new aspect in 1990s, because PTFE had been classified to be a typical chain scissioning polymer for a long time. The crosslinking of PTFE was found as early as 1970 by Tutiya, when PTFE was irradiated by γ -rays under vacuum above the melting temperature [7], but his finding was ignored for more than 20 years. The same phenomenon was rediscovered by Sun et al [8] at the end of the 1980s, and was confirmed by Oshima et al. [9, 10], and later by Lappan et al. [11].

The application of radiation graft polymerization started at the beginning of 1980 for the development of ion exchange membranes for butane type batteries [12]. The applications have since then been expanded to filters and membranes with high performance for the absorption of specific chemicals [13, 14]. In particular, fibers or nonwoven fabrics have been the major base polymer materials for modification by radiation graft polymerization. In the middle of the 1990s, the study of

graft polymerization was much promoted with expectations for the ion exchange membrane of a fuel battery and the absorbent fibers for the collection of rare metals from sea water [15]. The EPR studies on polymer radicals contributed much to the fundamental knowledge and technique for the development of the radiation induced graft polymerization and related reactions.

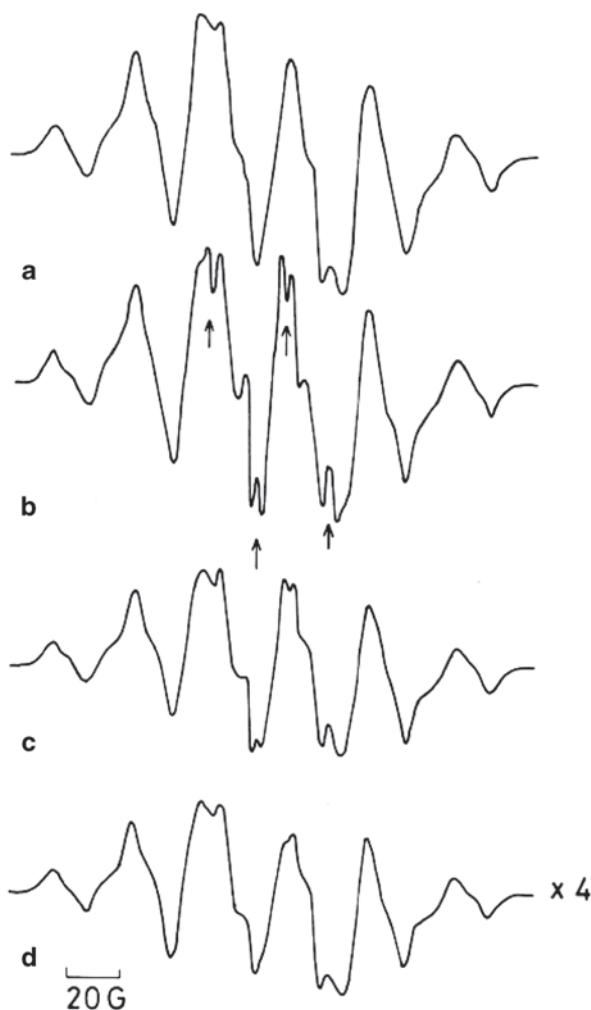
10.1.2 Mechanism of Graft Polymerization onto Polyethylene

In the applications of radiation induced graft polymerization, the pre-irradiation method has been selected [12–15], that is, at first the base polymer was irradiated, after which the graft polymerization was carried out at 40–60 °C by contacting the grafting monomer with the irradiated polymer. For this application of graft polymerization, the base polymers are always crystalline polymers such as PE, PP. By irradiation, free radicals are produced in both the crystalline and amorphous parts of base polymers. As the radicals formed in the amorphous parts decay rapidly above the glass transition temperature during irradiation or after irradiation, the radicals in the crystalline region are the ones that induce the grafting reaction at ambient temperature. In the presence of oxygen, it has been considered that the radicals trapped in both the crystalline and amorphous parts react preferentially with oxygen and finally form the oxidation products. Therefore, in the case of pre-irradiation in air, the graft reaction had been assumed to be initiated by the thermal decomposition of hydro-peroxide at a relatively high temperature. However, in many experiments the graft polymerization of various monomers progressed well at relatively low temperature, from room temperature (RT) to 50 °C on crystalline polymers pre-irradiated in air. On the other hand, there are EPR studies indicating that the radicals in crystalline regions of PE migrate by hydrogen abstraction across or along the polymer chains to amorphous regions from the crystalline regions [16, 17].

The radical migration model was applied for graft polymerization by pre-irradiation in air [18–20]. As the monomers could not penetrate into the crystalline phase, the graft reaction must be initiated at the surface of the crystallites and the polymerization should proceed in the amorphous phase. In the case of PE, the percentage crystallinity is 40–80%, and the crystallites have a lamella structure with chain folding and a size of 5–20 nm. The crystallinity and the crystallite size are defined by the PE molecular structures and the processing conditions for film, sheet, or fiber.

When the pre-irradiated PE was stored in butadiene (BD) gas as a monomer for graft polymerization, the EPR spectrum changed with storage time, as seen in Fig. 10.1 [18]. The PE specimen was in a powder form prepared by cooling down from a solution in xylene solvent above the melting temperature, and the apparent powder size was 20–30 μm. For the film specimen, the rate of monomer penetration into PE film was changed with the progress of the graft reaction and also the radical decay rate during reaction tended to decrease, so the powder specimen was used to minimize the penetration effect.

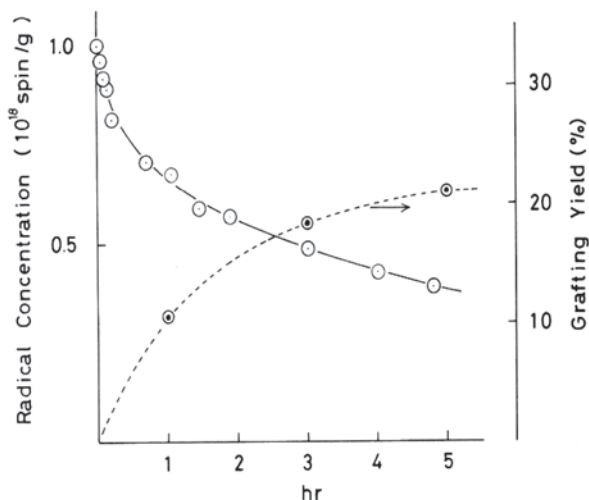
Fig. 10.1 EPR spectra for polyethylene (PE: powder in the high density form) under graft polymerization of butadiene (BD) at RT. **a** PE after irradiation 30 kGy in air at RT by 2 MeV electron beam with 1 kGy/s, **b** Immediately after BD (2.4 bar) contacted with PE of (a) at RT, **c** After 0.5 h storage in DB, **d** After 9 h in BD (four times magnified). The figure is adapted from [18] by permission of John Wiley & Sons (1974)



The alkyl type radical ($-\text{CH}_2-\dot{\text{C}}\text{H}-\text{CH}_2-$) trapped in PE crystalline regions decayed gradually with the reaction time, but the EPR spectrum remained almost same during the reaction. A small amount of the spectrum with fine structure due to the BD propagating radical was superposed on the spectrum of an alkyl radical.

With the decay of the alkyl radical concentration, the yield of graft polymerization increased as seen in Fig. 10.2. The alkyl radical decay during graft reaction shown in Figs. 10.1 and 10.2 supports well the above assumption, that is, the alkyl radical migrates to the crystal surface and initiates the grafting reaction. When a monomer of methyl-methacrylate (MMA) was reacted instead of BD, the decay of alkyl radical was similar to that in BD grafting, and the spectrum of the propagating radical of MMA polymerization overlapped that for the alkyl radical.

Fig. 10.2 Decay of PE alkyl radicals in BD monomer and yield of grafting during graft polymerization at 20°C. PE and BD are the same as in Fig. 10.1, PE irradiated 20 kGy. The figure is adapted from [18] by permission of John Wiley & Sons (1974)



On the other hand, it is well known that the alkyl radical in crystalline regions converts to the allyl radical ($-\text{CH}=\text{CH}-\bullet\text{CH}-$) on storage under vacuum. However, the allyl radicals are stable under vacuum, but reacted rapidly with BD and form BD propagating radicals with high intensity as shown in Fig. 10.3 [19]. As the BD propagating radical decays within a short time, the yield of graft polymerization is at a low level even after a prolonged reaction time. The propagating radicals would terminate within a short time by radical recombination. As tetra-chloromethane (CCl_4) reacts with radicals, the PE specimen containing allyl radicals was brought into contact with CCl_4 . The broad components of the EPR spectrum in Fig. 10.3a decayed rapidly and the sharp components remained the same as in the case of the BD graft reaction. Therefore, most of the allyl radicals would be trapped at the surface of crystallites, while a small amount of allyl radicals with sharp components, about 10%, would be trapped in the interior of the crystallites.

Even in the case where the base polymer is in powder form, the monomer supply to the crystal surface becomes insufficient to increase of the yield of graft polymerization. So, the decay of alkyl radicals in the crystalline region is affected by the progress of the graft reaction. Therefore, the decay behavior of alkyl radicals was investigated in an oxygen atmosphere (in air), because the oxygen molecule could not penetrate into the crystalline parts of PE, and may react with radicals only when the radicals come to the surface. The alkyl radicals were produced within a short irradiation time (30 s) by electron beam (EB) irradiation (30 kGy with 1 kGy/s), and the decay of the radicals was measured immediately after irradiation.

Figure 10.4 shows the decay of alkyl radicals trapped in three different PE crystallites during storage in air at 20°C [20]. When the radical migrates along or across PE chains in a crystallite, and decays at the surface, the decay rate could be analyzed by the diffusion equation. The diffusion equation can be derived to be (10.1) for a plate like crystallite for the migration along PE chain and (10.2) for a spherical

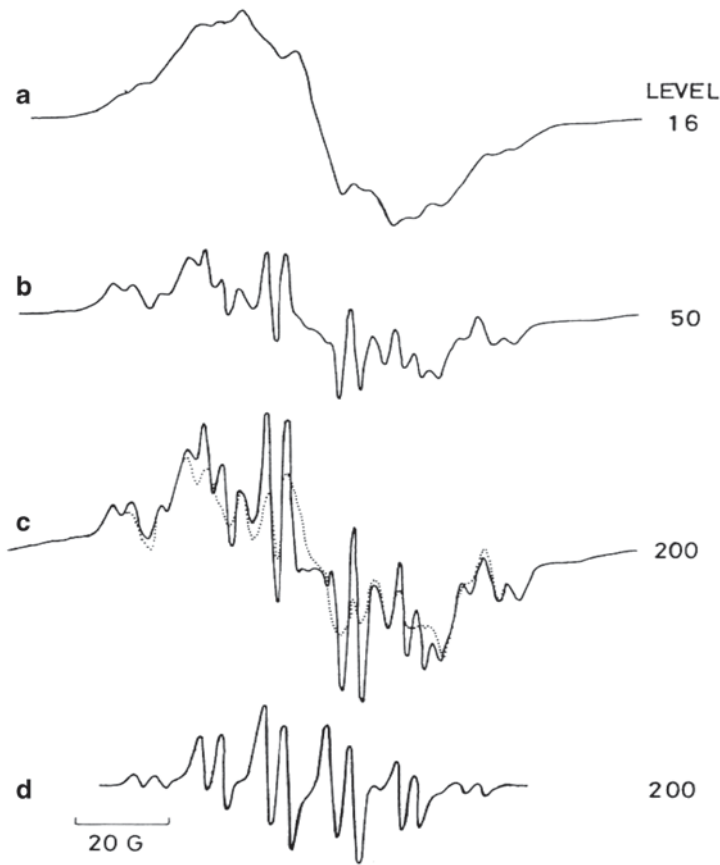


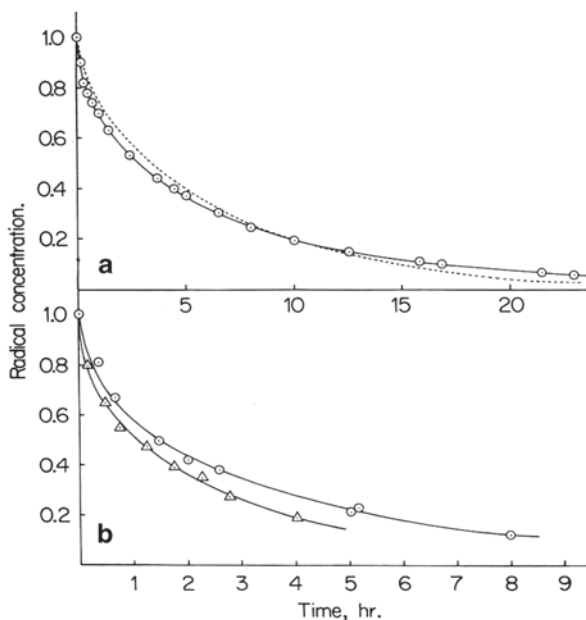
Fig. 10.3 EPR spectral changes after reaction of BD with PE allyl radicals at 20°C. **a** Allyl radicals observed for PE after 2 weeks storage under vacuum at RT after irradiation up to 60 kGy in air. **b** After 3 min reaction with BD, **c** After 6 min reaction with BD, the dotted line is estimated to be allyl radical component, **d** Propagating radicals of BD polymerization by subtraction of dotted line from solid line in (c). The figure is adapted from [19] by permission of John Wiley & Sons (1974)

crystallite for the migration across PE chains. Here, D is diffusion constant corresponding to the migration rate, L is the thickness of plate and R is radius of sphere, $u(x, t)$ or $u(r, t)$ is radical concentration in a crystallite at position x or at r and t is the storage time, and $U(t)$ is the radical concentration in the crystallite at time t (details in reference [20]).

$$\frac{\partial u(x, t)}{\partial t} = D(\frac{\partial^2 u(x, t)}{\partial x^2}), \quad U(t) = \int^L u(x, t) dx \quad (10.1)$$

$$\frac{\partial u(r, t)}{\partial t} = D(\frac{\partial^2 u(r, t)}{\partial r^2} + 2\frac{\partial u(r, t)}{\partial r}), \quad U(t) = \int^R 4\pi r^2 u(r, t) dr \quad (10.2)$$

Fig. 10.4 Decay of PE alkyl radicals on storage in air at 20°C. **a** Powder form PE of high density, *solid line* is calculated from Eq. (10.2) for $D/R^2=9.6 \times 10^{-6}$ ($D=3 \times 10^{-18}$ cm²/s, $R=5.3 \times 10^{-7}$ cm), *dotted line* is calculated from Eq. (10.1) for $D/L^2=4.6 \times 10^{-6}$ ($D=3 \times 10^{-18}$ cm²/s, $L=8 \times 10^{-7}$ cm), **b** Powder form PE with smaller sized crystallites, *white circle* PE crystallite size $R=4.6 \times 10^{-7}$ cm, *solid line* is calculated from Eq. (10.2) for $D/R^2=1.4 \times 10^{-5}$, *white triangle* PE crystal size $R=3.2 \times 10^{-7}$ cm, *solid line* for $D/R^2=2.5 \times 10^{-5}$, D is the same as for (a). The figure is adapted from [20] by permission of American Chemical Society (1973)



Applying the diffusion constant (D) and L or R as the parameters in Eqs. (10.1) or (10.2), the radical decay curve can be calculated. The kinetics of alkyl radical decay showed a better agreement with the diffusion Eq. (10.2) in a model of spherical crystallites than for the Eq. (10.1) for a model of plate-like crystallites. Namely, the radical decay rate was proportional to $(1/R)^2$. If the radical migrates along PE chains, the decay rate fits to $(1/L)^2$. The results indicated that the model for migration of radicals in the crystals via across the molecular chains was more plausible than that for migration along the molecular chains. Of course, a small amount of the spectrum is due to the presence of peroxy radicals which are superposed on the spectrum of the alkyl radical, but the peroxy radicals decayed rather quickly at the crystal surface. The decay of the alkyl radicals at elevated temperatures (30°C, 40°C) showed a similar behavior to that at 20°C, and the activation energy of alkyl radical decay was 75 kJ/mol (18 kcal/mol) obtained using the Arrhenius equation for the decay rate over a range of elevated temperatures.

The first successful application of radiation graft polymerization into polyethylene film was the synthesis of ion exchange membranes. The experiment for pre-irradiation graft polymerization was conducted according to the mechanisms of trapped radical migration in PE crystallites. PE film (25–100 μm thick) was pre-irradiated by EB at ambient temperature in air or in a N_2 gas flow. The irradiated film was immersed in aqueous acrylic acid (AAc) deaerated by bubbling N_2 gas at temperatures (25–40°C) [21–23]. The rate and yield of graft polymerization depended on the crystallinity of PE, that is, the rate was higher for low density PE (small crystallite size) and the yield was higher at long reaction time for high density PE

(large crystallite size). The effects of the pre-irradiation dose, reaction temperature, storage time in air after irradiation until graft reaction, and PE film thickness were examined. The results for the rate and yield in the graft polymerization could be well explained by the model of alkyl radical migration in the crystallites deduced from the EPR studies [20]. The effect of atmosphere in air and in N_2 gas flow was slight for the short time irradiation at a high dose rate by EB.

As the decay rate of alkyl radicals trapped in the crystallites decreased at lower temperature, according to the Arrhenius equation, the radical content trapped in the PE film could be kept for a long time by storage at low temperature after irradiation, for example, the activity of the graft reaction was 80% after 20 days storage at -24°C (249 K) in a freezer. The method to keep the radical activity by cooling has been applied widely for graft polymerization, that is, irradiation and graft polymerization can be separated in time and place. For the polyethylene film, the yield of acrylic acid (AAc) graft polymerization was not homogeneous across the film due to the penetration of AAc monomer into PE amorphous part, and the distribution along the film thickness was changed by the graft reaction conditions [22]. For the application of membranes for ion exchange, the graft polymerization had to proceed throughout the film. The inhomogeneous distribution was clearly observed for the radiation oxidation of polymer film by irradiation at a high dose rate, and the mechanism was analyzed by the diffusion of oxygen throughout the amorphous area and the oxygen uptake by oxidation during irradiation [3].

For styrene graft polymerization on poly(vinylidene fluoride) (PVDF) by pre-irradiation, a similar radical reaction was observed [24]. PVDF film was irradiated with γ -rays in air at room temperature, and contacted with styrene monomer at 60°C . The radicals trapped in the crystallites of PVDF were alkyl type radicals ($-\text{CH}_2-\bullet\text{CF}-\text{CH}_2-$) as the major component and peroxy radical as the minor component. The site of the alkyl radical was supposed to be at the interface of the crystallites and the peroxy radical to be in the inter-crystalline amorphous zone. The styrene graft polymerization was initiated by the alkyl radicals but the hydro-peroxides formed from the peroxy radicals did not contribute to graft polymerization.

The graft polymerization proceeded scarcely after the disappearance of radicals at low temperature, below around 60°C for many polymers. The model suggested in the 1960s that the decomposition of hydroperoxides formed by radiation oxidation induced the graft reaction was applied to the graft polymerization of acrylamide (AAm) at 80°C and acrylic acid (AAc) at 70°C onto polypropylene (PP) film [25]. The peroxy radicals in the PP films, and their decay by graft reactions were detected, and the authors concluded that hydroperoxide initiated both of these grafting reactions.

Ultra-high molecular weight polyethylene (UHMWPE) has been utilized for medical implants, such as replacement prostheses for human joints, and UHMWPE fiber for use as high tensile materials. These applications were first reported at the end of the 1990s. EPR studies have been expanded to investigate the radiation effects on UHMWPE from the view point of life-time estimation in these applications [26–28].

The specific property of the trapped radicals that was of note was their long life at ambient temperature. The long-lived radicals (more than 10 years in an ambient environment) were suggested to be polyenyl and peroxy radical types [26].

Fig. 10.5 EPR spectral changes observed by annealing of UHMWPE film irradiated to 100 kGy by EB under vacuum at RT. **a** After irradiation, **b** After subsequent annealing at 100°C for 2 h, **c** Subsequent 1 h photo-irradiation by a xenon lamp, **d** After subsequent annealing at 100°C for 2 h. The figure is adapted from [27] by permission of American Chemical Society (2010)

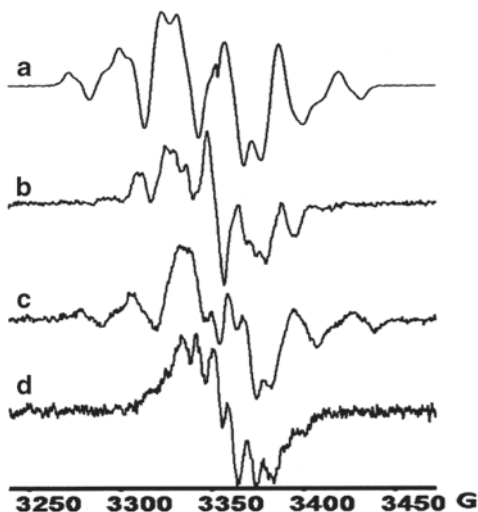


Figure 10.5 shows the EPR spectra of UHMWPE irradiated under vacuum by EB at room temperature and the annealing at 100°C or during photo-irradiation under vacuum [27]. The radicals trapped after the irradiation were of alkyl type (Fig. 10.5a), which converted to an allyl radical on annealing under vacuum (Fig. 10.5b), like for HDPE. The spectrum observed after subsequent annealing, with six poorly resolved peaks with a nine gauss hyperfine splitting, was attributed to the dienyl radical ($-\text{CH}=\text{CH}-\text{CH}=\text{CH}-\bullet\text{CH}-$). At longer annealing times, the hyperfine structure disappeared and the singlet that remained was assigned to the polyenyl radical ($(-\text{CH}=\text{CH}-)_n-\bullet\text{CH}-$). The above assignments were supported by the UV absorption spectrum [26]. The dienyl and polyenyl radicals were stable under vacuum, but were oxidized by exposure to an oxygen atmosphere to form peroxy radicals, and the peroxy radicals decayed with storage time.

The radicals trapped in a UHMWPE fiber showed a longer life under vacuum or in air [28]. Figure 10.6 shows the EPR spectra after irradiation under vacuum (sample-A) and in air (sample-B) and the change of the two with their storage at ambient temperature.

The radical found after irradiation was mainly the alkyl radical and the spectrum showed ten lines (2×5 lines) when the fiber sample (yarn of 500 filaments of 10 μm diameter) was set up perpendicular to the EPR magnetic field. The ten line spectrum is that of four H protons at the β -position of the alkyl radical that have the same hyperfine splitting (hfs) and one H at the α -position which has half of the hfs of H at the β -position. By annealing under vacuum the alkyl radical converted to the allyl radical, which was much more stable like that for HDPE shown in Fig. 10.2. In the presence of oxygen the alkyl radical decayed gradually and a single peak remained after longer storage time. The peroxy radical might be expected to be formed, but the relative amount of this radical was scarce, as seen in Fig. 10.6 (sample-B). The single peak might be that of the polyenyl radical as assigned in the report [28]. The

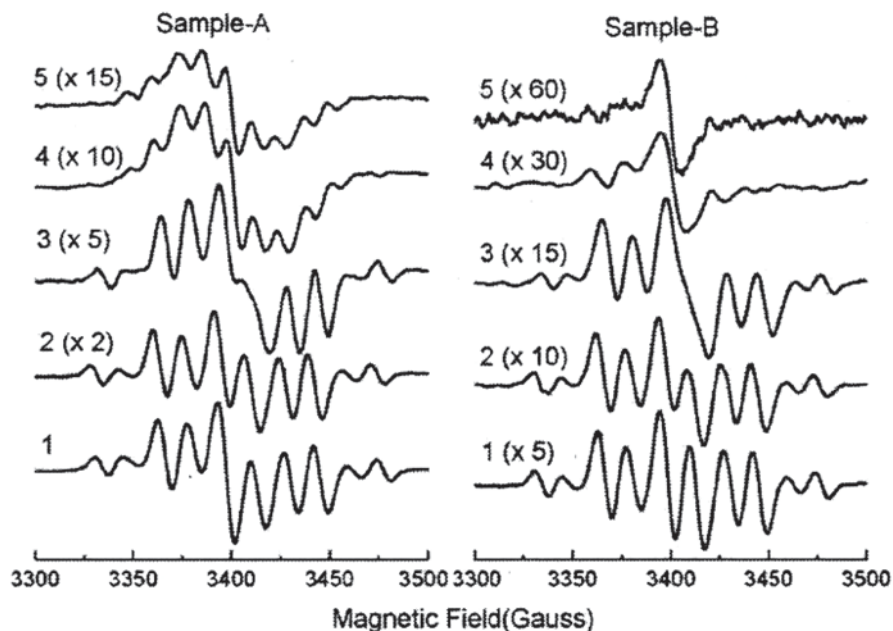


Fig. 10.6 EPR spectra of UHMWPE fiber irradiated to 90 kGy by γ -rays and stored in vacuum (*Sample-A*) and in air (*Sample-B*) at RT. *Magnetic field* is perpendicular to the fiber axis. 1: 0.5 day, 2: 13 day, 3: 77 day, 4: 107 day, 5: 137 day. The figure is adapted from [28] by permission of Elsevier (2010)

decay of the alkyl radical for both sample-A and sample-B was very slow, and the rate was about 1/100 of the rate for HDPE. Therefore, by applying the mechanism of radical migration in the crystallite, the size of the crystallite for UHMWPE fiber would be ten times larger than that of HDPE. The fiber was recrystallized after melting at 180°C, and then irradiated under vacuum and in air, respectively at RT. The decay rate of the radicals increased by about ten times for both environments, as seen in Fig. 10.7. The reason could be a decrease in the crystallite size as a result of the recrystallization. The UHMWPE fiber is processed by highly extending it at high temperature with chemical crosslinking, so the effective crystallite size would be increased by several times. The order of crystallites sizes is UHMWPE fiber > UHMWPE > HDPE. Considering the small decay rate of the radicals in UHMWPE, the processing temperature might be increased in order to accelerate the reaction for the radiation modification, such as is done in graft polymerization.

10.1.3 Crosslinking of Polytetrafluoroethylene and Graft Polymerization

The crosslinked PTFE, which is prepared by irradiation of PTFE above the melting temperature in inert gas atmosphere, was found to produce acceptable mechanical

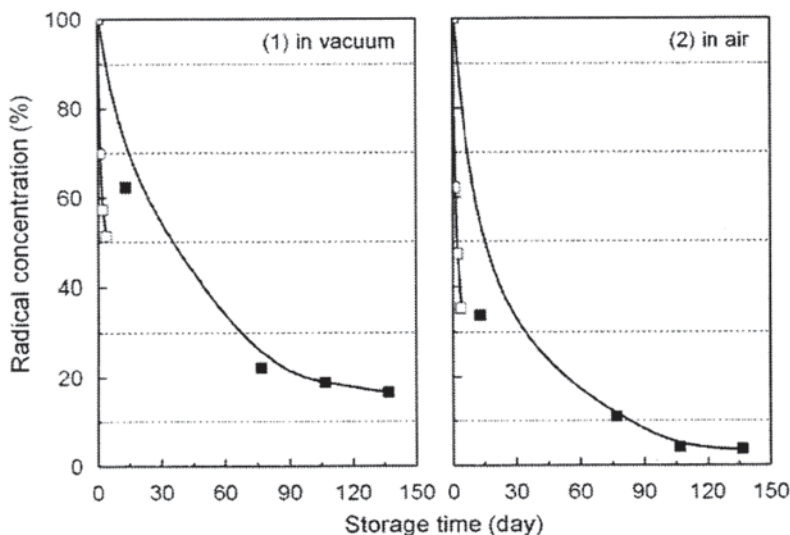


Fig. 10.7 Total radical concentration versus storage time under vacuum and in air at RT for UHMWPE fibers and for the samples recrystallized by melting at 180 °C, Dose 90 kGy by γ -rays at RT, *black squares* UHMWPE fiber, *white squares* recrystallized UHMWPE. The figure is adapted from [28] by permission of Elsevier (2010)

properties, to improve the radiation resistance and wear resistance [29–31]. Also the yield of radical induced by irradiation increased significantly with the crosslinking density [32, 33]. Therefore, radiation graft polymerization onto crosslinked PTFE has been of very great interest for the processing of specific functional materials, such as for the ion exchange membranes of fuel cell batteries.

Figure 10.8 shows the ESR spectra of crosslinked and virgin PTFE after irradiation under vacuum. The spectrum of virgin PTFE was assigned to alkyl radicals trapped in the crystalline regions in many previous studies [34, 35]. For crosslinked PTFE a broad singlet is superposed on the virgin PTFE spectrum (alkyl radical), and the intensity of the overall spectrum increased with the crosslinking density, especially the singlet component increased significantly in intensity for the cross-linked PTFE. As the crystalline parts decreases with the crosslinking density, the broad singlet would arise from the radicals trapped in the intermediate regions between crystalline and amorphous regions produced by the crosslinking, and might be mainly alkyl radicals. The stability of the singlet was almost the same as for the alkyl radicals trapped in the crystalline regions (sharp spectrum) at RT, but the singlet decayed significantly at the higher temperature. The radical yield in cross-linked PTFE (100 kGy for crosslinking) is ten times of that in virgin PTFE, as seen in Fig. 10.9. Also, the yield by irradiation at RT is higher by 2–3 times than that observed at RT after irradiation at 77 K. Of course, the radical concentration decreased by warming up to RT from 77 K after irradiation at 77 K for any of the PTFE specimens, because the radicals trapped in the amorphous area decayed by the warming. The radical yield dependency on irradiation temperature in Fig. 10.9

Fig. 10.8 EPR spectra of PTFE radicals observed at RT by γ -ray irradiation under vacuum for *virgin* PTFE and crosslinked PTFE (*RX-500* is 500 kGy for radiation cross-linking). Spectral magnification is 1/10 for *RX-500*. The figure is adapted from [32] by permission of Elsevier (1997)

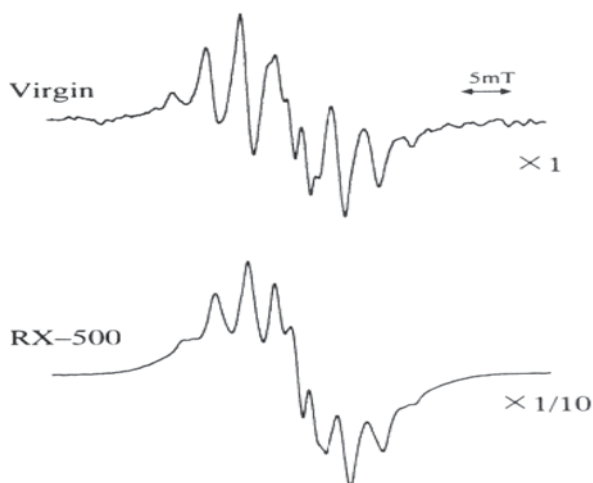
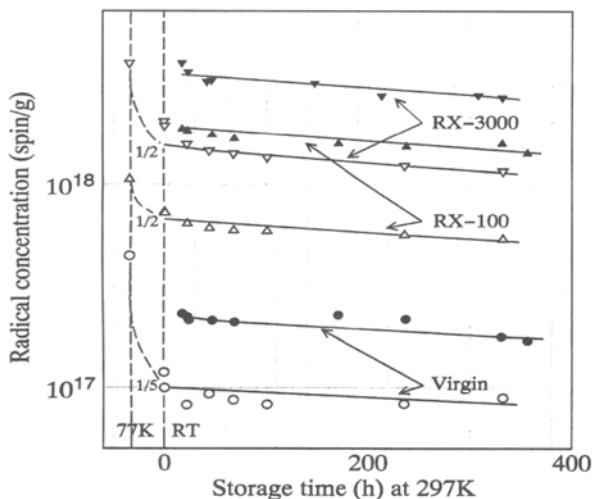


Fig. 10.9 Yield of PTFE radicals and the decay under vacuum at 297K (24°C) for *virgin* and crosslinked PTFE (*RX-100* and *RX-300*). *White circles and triangles*, irradiated at 77 K (−196°C); *black circles* irradiated at 77 K (−196°C). The figure is adapted from [32] by permission of Elsevier (1997)



suggests that the overall chemical reactions should be considerably dependent on the irradiation temperature.

The radicals trapped in PTFE converted completely to peroxy radicals on exposure to air at RT [32, 33]. Because the PTFE crystal has a specific molecular motion, that is, PTFE molecules in crystals start to undergo rotational motion at 19°C, and then the oxygen can penetrate into PTFE crystallites with the molecular motion and react with the radicals. The peroxy radical is therefore stable in air, just like the alkyl radical under vacuum [34, 35]. The oxidation in PTFE crystallites is different from that for other polymer crystallites such as PE, PP, and other polymers.

The trapped radicals in PTFE can induce graft polymerization, as is well known. For the crosslinked PTFE, the radical yield was high and the radical site is in amorphous area where the monomer of grafting can penetrate easily. These facts are of advantage for the graft polymerization. In the 2000s studies of styrene graft polymerization onto crosslinked PTFE progressed in many laboratories, with expectations to obtain a high quality ion exchange membrane for fuel cell batteries [36–38]. The graft polymerization onto the crosslinked PTFE film was successful by pre-irradiation excluding oxidation, and the yield of graft polymerization increased with increasing radical concentration trapped in the crosslinked PTFE, as expected by the EPR results seen in Fig. 10.9. After graft polymerization, the sulfone unit ($-\text{SO}_3\text{H}$) was bonded at the grafted polystyrene by the reaction with sulfuric acid for ion exchange. The ion exchange capacity (IEC) showed an excellent value. The merits of crosslinked PTFE were the high yield of graft polymerization and the scarce mechanical degradation of the PTFE base polymer. But the pre-irradiation of PTFE and the storage until graft polymerization must be kept in an oxygen free condition, because the alkyl radical in PTFE will convert to the peroxy radical with oxidation and the peroxy radical could not initiate a graft reaction. In a special case where the crosslinked PTFE with peroxy radicals was heat treated under vacuum, the alkyl radical was recovered gradually at higher temperatures, above 100°C [33]. But the recovered radical concentration was too low for graft polymerization. Research for the synthesis of ion exchange membranes using crosslinked PTFE has thus been progressed, even though the application is still scarce. The ion exchange capacity (IEC) decays within a rather short period in applications, so modification for a longer life is required. For a long life IEC, the aromatic polymers such as poly(ether-ether ketone) are being studied instead of crosslinked PTFE [39].

10.1.4 Crosslinking of Polyacrylonitrile Fiber for Carbon Fiber

In another application to polymers, the radiation crosslinking of polyacrylonitrile (PAN) fiber was studied by EPR for the precursor of carbon fiber formation [40, 41]. The curing (crosslinking) of PAN fiber for carbon fiber processing is carried out by thermal oxidation. Of course, the radiation crosslinking was tried in the 1970s, but it had not been successful. The observed radical at RT was of the alkyl type trapped in the crystallites and it decayed gradually in an oxygen atmosphere with the formation of a peroxy radical. By gel fraction measurement, it was concluded that the crosslinking proceeded with dose under vacuum irradiation, but not under oxidizing conditions. However, the curing of PAN fiber for carbon fiber formation was not attained by the crosslinking under vacuum. On the other hand, the oxidized fiber by radiation was crosslinked by heat treatment under vacuum and the curing was attained. By understanding the curing mechanism of PAN fiber, the radiation oxidation for the curing might be a useful technique for a new application of carbon fiber processing.

10.2 Ceramic (SiC) Fiber Synthesis by Radiation Crosslinking

10.2.1 Introduction

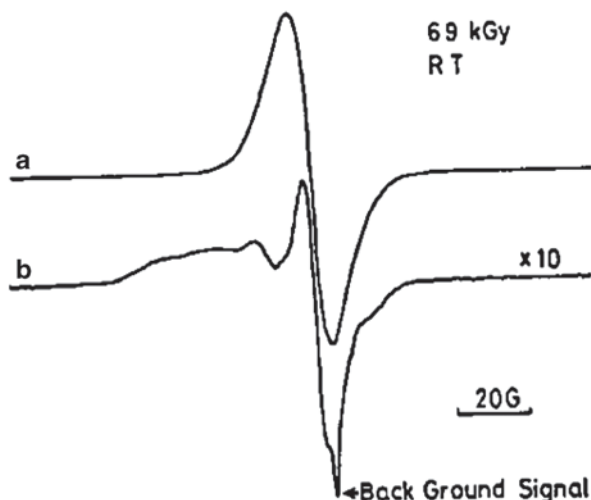
A ceramic fiber of silicon carbide (SiC) is one of the excellent materials for high temperature technology, such as for gas turbines. The SiC fiber was invented by Yajima in 1975 [42–46]. The processing was by the pyrolysis of a polymer fiber of polycarbosilane (PCS) as the precursor of ceramic fiber. Prior to the pyrolysis, the PCS fiber was cured by thermal oxidation to retain the fiber shape. The SiC fiber (Nicalon®: Trade mark of SiC fiber of Nippon Carbon Co. Ltd.) has a diameter of 14 microns (μm) and is flexible with a tensile strength of 3 GPa. However, the heat resistance is limited to around 1200 °C. As Nicalon® contains oxygen in the SiC matrix, the amorphous phase of the Si–O–C part is decomposed with emission of SiO and CO gases above 1200 °C [47]. The oxygen in the SiC fiber is introduced in the process of PCS fiber curing by thermal oxidation. As the silicon atom has a high affinity to oxygen, the oxygen supplied to the PCS fiber at the time of curing remained in the SiC fiber formed by the pyrolysis, and the oxygen content in the SiC fiber was 10–12% by weight. The method to improve the heat resistance of the SiC fiber was therefore to decrease the oxygen content.

To decrease the oxygen content, radiation curing (crosslinking) of PCS fibers was attempted to replace the thermal oxidation process. The application of EPR was very useful for the analysis of the curing mechanism and also for the analysis of pyrolysis followed by the PCS fiber curing. The mechanisms derived from the EPR studies provided important knowledge for the development of SiC fibers with low oxygen content, and finally the heat resistance of the SiC fiber was much improved.

10.2.2 Radiation Curing of Polycarbosilane as Precursor of SiC Fiber

The radiation induced crosslinking of polymers such as polyolefins has been well recognized. Therefore, radiation crosslinking was tried for PCS fiber by many researchers by γ -ray irradiation. However, the trials were not successful for the reduction of oxygen content in SiC fiber in the first stage of research in 1980–1985 [48]. The reason for the failure was a lack of knowledge of the irradiation effects on PCS fiber. In 1986–1990, the fundamental reactions for the radiation crosslinking of PCS fiber were investigated for free radical formation and gas evolution by γ -rays, and also by high energy electron beam (EB) irradiation [49–52]. In principle, the irradiation effects were the same between γ -rays and EB for polymers, although the dose rate is much different, that is, the dose rate for EB is higher than that for γ -rays by three orders or more. However, the high dose rate irradiation by EB induces a heating of the material by the radiation energy, so the stability or yield of radicals was affected by the heating. The reaction mechanism of PCS fiber was studied using γ -rays and the development of the curing process was by EB [53–61].

Fig. 10.10 EPR a spectrum of PCS fibers γ -irradiated under vacuum at RT and b spectrum after exposure to air (ten times magnification) at RT. The figure is adapted from [49] by permission of Japan Soc. Powder & Powder Metallurgy (1988)



The chemical structure of PCS is $(-\text{Si}(\text{CH}_3)_2-\text{CH}_2-\text{Si}(\text{CH}_3)\text{H}-\text{CH}_2-)_n$, and the molecular weight is about $2 \times 10^3 \text{ g mol}^{-1}$. PCS is an amorphous polymer with a density of 1.1 g/cm^3 and the melt flow temperature is $230\text{--}245^\circ\text{C}$. The PCS fiber (monofilament) is processed by melt spinning at around 300°C in an inert gas atmosphere. The monofilament of the PCS fiber was $20 \mu\text{m}$ in diameter and a few kilometers long, and the strand was composed of 500 filaments. The details of the PCS fiber were described in the review by Okamura et al. [47]. The fiber is brittle due to its low molecular weight and is transparent. The PCS fiber (strand) was cut to $5\text{--}10 \text{ cm}$ length and used for the fundamental studies. The sample container used was a quart tube for the lower temperature experiments, and a specific ceramic tube for the higher temperature experiments.

Figure 10.10a shows the EPR spectrum of PCS fiber γ -ray irradiated at room temperature under vacuum [49, 50]. The spectrum was a singlet and the radical was rather stable at room temperature, with a half-life of ca. $5 \times 10^2 \text{ h}$. The yield of radical (spectral intensity) increased linearly with dose at a lower dose and the G-value (number of radicals per 100 eV absorbed) was about 0.25. With increasing dose, the yield tended to saturate. The radicals, which were stable under vacuum, reacted rapidly with oxygen at room temperature and most of the radicals decayed. An unsymmetrical spectrum due to peroxy radicals and rather narrow singlet spectrum remained after the decay, as seen in Fig. 10.10b. The peroxy radicals decayed gradually with storage time in an oxygen atmosphere at room temperature. When the PCS fiber was irradiated in an oxygen atmosphere, the EPR spectrum was similar to Fig. 10.10b and the intensity was very low. For irradiation at the temperature of liquid nitrogen (77 K), the radical yield was $G=2.5$.

The gaseous products from PCS fiber by irradiation under vacuum at room temperature were hydrogen gas (H_2) and methane (CH_4) [49]. The yields increased linearly with dose up to higher doses, and the G-values are listed in Table 10.1. The

Table 10.1 G-value of gas evolution and free radical formation for PCS fiber by γ -ray irradiation (1.7 Gy/s) under vacuum and in oxygen (0.8 atm) at room temperature. The table is adapted from [49] by permission of Japan Soc. Powder & Powder Metallurgy (1988)

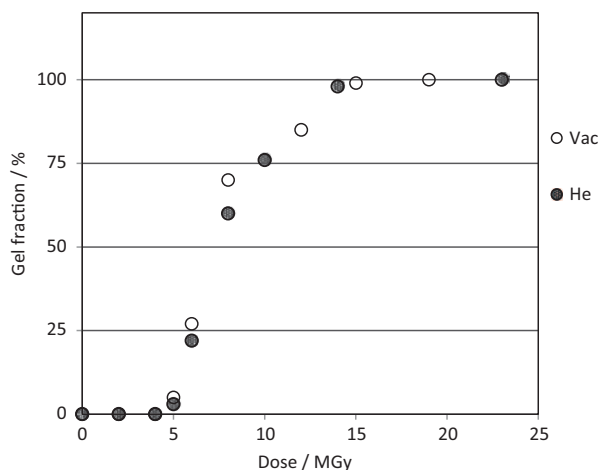
Product	G-value	
	Vacuum	In oxygen ^a
Hydrogen (H ₂)	1.4	4.1
Methane (CH ₄)	0.07	<0.01
Carbon oxide (CO)	0	5.2
Carbon di-oxide (CO ₂)	0	6.4
Oxygen consumption (-O ₂)	0	78
Free radical	0.25 (at RT) ^b 2.5 (at 77 K)	<0.01

^a G-values depend on dose rate

^b Low dose less than 10 kGy

crosslinking of PCS fiber by irradiation was confirmed by gel fraction measurements (solvent: tetrahydrofuran, THF) [52]. The relationship between the gel fraction and dose are shown in Fig. 10.11 for EB irradiation (EB: 2 MeV) under vacuum and in a helium (He) gas atmosphere. The change in gel fraction by γ -ray irradiation was the same as that for EB irradiation. The dose at the gel point was around 5 MGy, and the gel fraction of 100% was reached at 13–15 MGy. As He gas was used to cool down the PCS fiber during EB irradiation, the EB irradiation could be done at a relatively high dose rate in the He gas flow in the case where a large amount of PCS fiber was used. The radiation curing of PCS fiber was attained when the gel fraction reached above 50% in Fig. 10.12, that is, the PCS fiber retained the fiber shape without melting during the pyrolysis, so yielding a SiC fiber.

Fig. 10.11 Gel fraction of PCS fibers versus dose by EB irradiation under vacuum (*Vac*) and in He gas at RT. The figure is adapted from [50] by permission of Japan Soc. Powder & Powder Metallurgy (1988)



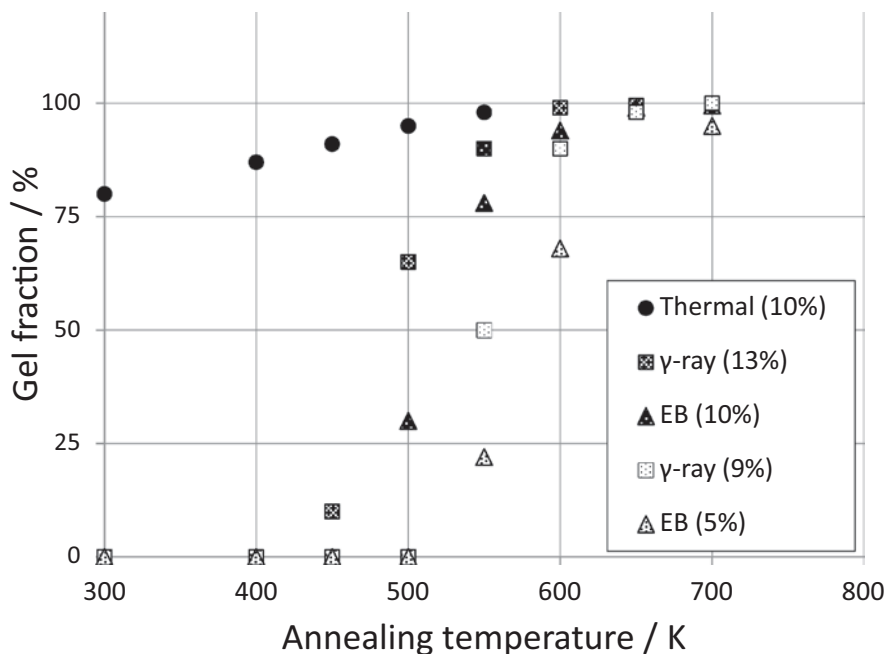


Fig. 10.12 Gel fraction of PCS fibers versus annealing temperature for PCS fibers containing different oxygen content by thermal and radiation oxidation. The annealing time was 30 min, and the oxidation conditions are as in Table 10.2

On the other hand, by γ -ray irradiation in an oxygen atmosphere at room temperature, oxygen was consumed and gaseous oxidation products (CO , CO_2) were evolved [49]. The G-values of oxygen consumption and for production of gaseous products are listed in Table 10.1. However, a gel was not formed even at a high dose of irradiation at room temperature. This was because the oxidation of the PCS fiber proceeded within a limited depth where oxygen could penetrate during the irradiation.

The yield of oxidation products depended on the dose rate and the oxygen partial pressure in the atmosphere during irradiation [52], like for other polymer materials [62]. Also, the G-value of oxygen consumption was much higher than that of the evolved gases of the oxidation products (CO , CO_2 , and H_2O); therefore, most of the oxygen would remain in the PCS fiber as oxidation products. The oxygen content and the oxidation depth in PCS fiber could be controlled by the dose, dose rate, and oxygen pressure during irradiation for both γ -ray and EB irradiation, as shown in Table 10.2. The PCS fiber after radiation oxidation was heated in an inert gas atmosphere, then, the crosslinking occurred as in thermal oxidation curing. The changes in the gel fraction vs. heat treatment temperature for PCS fibers irradiated in the presence of oxygen under various conditions are shown in Fig. 10.12. For the crosslinked PCS fibers with oxidation, the SiC fiber was obtained by pyrolysis as for the PCS fiber cured by thermal oxidation.

Table 10.2 PCS fiber curing and oxygen content in SiC fiber after pyrolysis. The table is adapted from [60] by permission of John Wiley & Sons (2005)

Curing method	Curing condition ^a	Oxygen content (wt%)
Radiation crosslinking	12 MGy in He with 1.3 kGy/s (2 MeV, EB)	1.1 ^b
Radiation oxidation (surface)	2.5 MGy in air with 1.9 kGy/s (2 MeV, EB)	12
Radiation oxidation (surface)	3.5 MGy in air with 1.9 kGy/s (2 MeV, EB)	17
Radiation oxidation	0.7 MGy in oxygen with 3.3 Gy/s (γ -ray)	9
Radiation oxidation	1.2 MGy in oxygen with 3.3 Gy/s (γ -ray)	13
Thermal oxidation	460 K (187 °C) in O ₂ gas flow	13

^a PCS fiber was heated up to 573 K in N₂ gas after radiation curing for decay of trapped radicals (EB in He), and for crosslinking (radiation in air or oxygen)

^b Amount of PCS fiber was 0.5 g in this case. For a large amount of PCS fiber (more than 100 g) the oxygen content was less than 0.5 wt% in SiC fiber after pyrolysis

A reaction mechanism of the radiation curing for the PCS fiber was proposed as shown in Fig. 10.13 on the basis of radical behavior, gas analysis and gel fraction [50]. The observed free radical was assigned to the $-\bullet\text{Si}(\text{CH}_3)-$ radical on the main chain formed by scission of the Si-CH₃ bond at a branch site. The radicals $-\text{Si}-\text{CH}_2\bullet$ or $-\text{Si}-\bullet\text{CH}-$ would be formed by scission of the -CH bond at a branch $-\text{Si}-\text{CH}_3$ or by scission of a -CH bond in the main chain $-\text{CH}_2-$, and these radicals would react with the other radicals to form the crosslinks during irradiation. If H₂ and CH₄ gases were formed via the radicals, the yield of radicals (G-value of total radical formation) might be about 3 for irradiation at room temperature. Thus the G-value of crosslinking could be estimated to be 1.5 for irradiation without oxidation. The G-value of radical formation by irradiation at 77 K was 2.5, which is lower than that at room temperature due to the temperature effect on the radiation chemistry.

In the presence of oxygen, the radicals reacted quickly with oxygen and many oxygen molecules were consumed with the emission of oxidative gases like CO and CO₂, as seen in Table 10.1. Therefore, one radical on PCS would induce the oxidation of many PCS molecules nearby the radical, and most of the oxygen was trapped in the PCS as products such as Si-OH and Si-O₂H. These oxidation products would induce crosslinking by heat treatment above around 150 °C, causing the decomposition. The chemical structure of the crosslink was supposed to be a Si-O-Si bond between PCS molecules.

By radiation curing of PCS fibers, that is, by crosslinking via irradiation under vacuum, the oxygen content in the SiC fiber was expected to be sufficiently low. However, the oxygen content was found to be 3–7% (by weight) in the SiC fiber, and the reason for this was that the free radicals that remained in the PCS fiber induced further oxidation when exposed to air after the irradiation [57]. The radical concentration tended to saturate with increasing dose above several 10 kGy at room

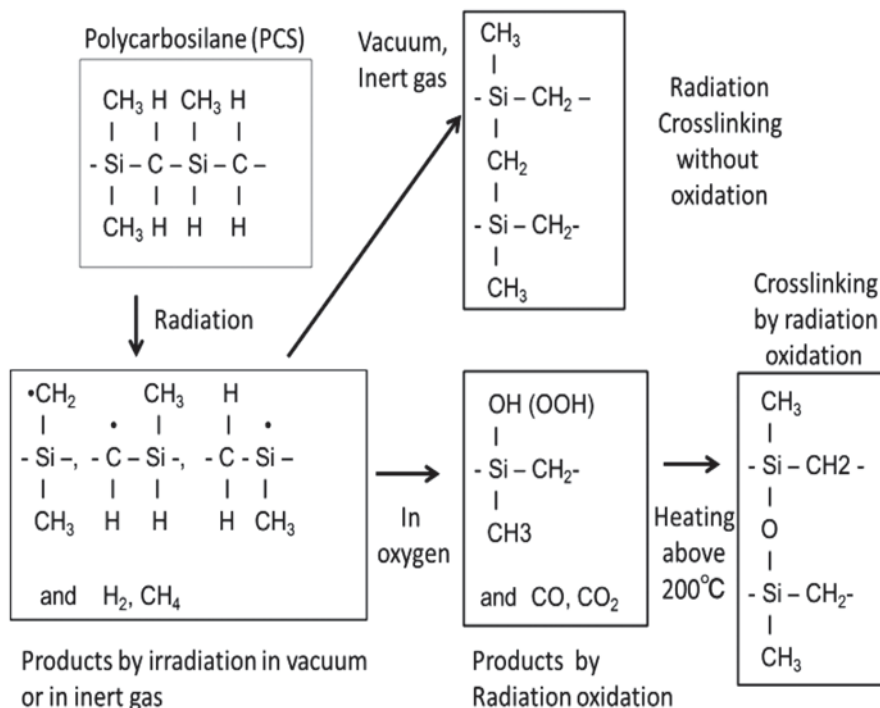


Fig. 10.13 Reaction mechanisms of PCS fiber curing (*crosslinking*) by *irradiation*. The figure is adapted from [59] by permission of John Wiley & Sons (2005)

temperature under vacuum, so the concentration at a dose of the order MGy was estimated to be less than 10^{18} spin/g. But the concentration observed by EPR at 5–10 MGy under vacuum was $(1-2) \times 10^{19}$ spin/g, which was higher by 20 times than the estimated value. By increasing the crosslinking density, the decay of the radicals during irradiation would be lowered, so a greater concentration of radicals remained with increasing dose.

In order to remove the trapped radicals in PCS fiber, the irradiated PCS fiber was heated up to 300 °C [49, 52]. The radicals decayed step by step with increasing temperature, as shown in Fig. 10.14. The radical concentration that survived above a temperature of around 240 °C was less than 1 % of the initial value, and this could stop the oxidation of the irradiated fiber on exposure to air at room temperature. The SiC fiber obtained from the PCS fiber by the removal of radicals after radiation crosslinking was of low oxygen content, less than 0.5 wt%. As the PCS fiber contained a residual oxygen of 0.2 wt%, the additional 0.3 wt% was formed during the processes of radiation curing and pyrolysis. Finally, it was confirmed that the obtained SiC fiber was much improved with respect to heat resistance, which increased by about 500 °C (1300 → 1800 °C) as a result of decreasing the oxygen content from 12 wt% to 0.5 wt% [47].

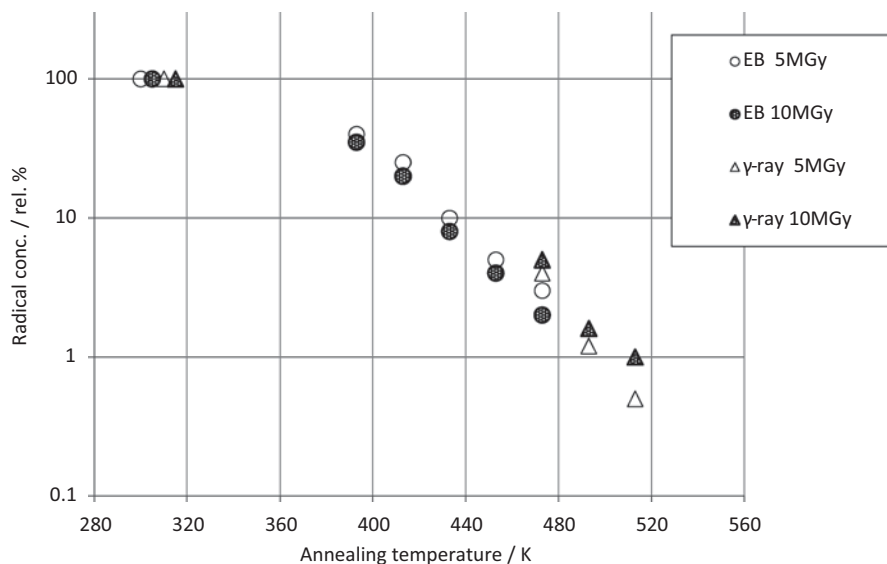


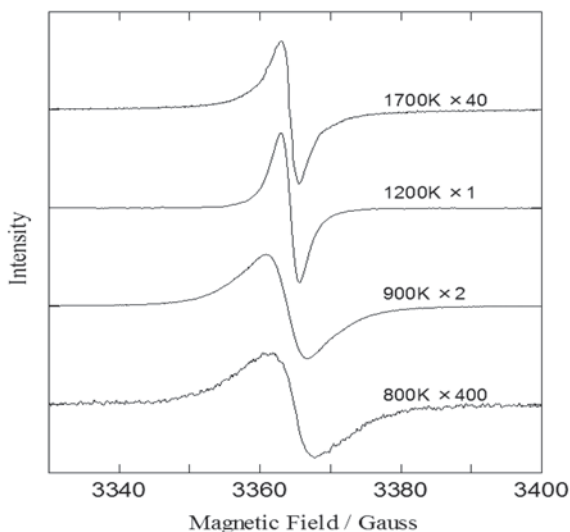
Fig. 10.14 Decay of radical concentration versus annealing temperature for PCS fiber irradiated under vacuum at RT by γ -rays and EB. Annealing time was 10 min at elevated temperature, and cooled down to RT for EPR measurement. The figure is adapted from [49] by permission of Japan Soc. Powder & Powder Metallurgy (1988)

At the beginning, many trials of radiation curing of the fibers were not successful. The reasons were that an insufficient dose was used for curing and a lack of knowledge about the subsequent radiation induced oxidation. For most polymers, such as polyethylene, the dose for radiation crosslinking was in the range of 50–500 kGy, so the use of doses higher than 1 MGy was not tried for the PCS fiber. In the case of the PCS fiber which is of a low molecular weight of $2 \times 10^3 \text{ g mol}^{-1}$, the density of crosslinking must be increased much more than in other polymers in order to induce gel formation. For the oxidation of the PCS fiber by radiation, the oxygen uptake was very large and the oxidation level was sufficient at a dose of 0.5 MGy by γ -rays for a dose rate of 3 Gy/s (10 kGy/h), and 5 MGy by EB at a dose rate of 1 kGy/s. The difference between γ -rays and EB is the effect of dose rate on the oxidation depth from the surface of the PCS fiber.

10.2.3 Radical Reaction Mechanism in Pyrolysis

A SiC (ceramic) fiber can be obtained from a PCS (organic polymer) fiber by pyrolysis. For the PCS fiber cured by thermal oxidation, the pyrolysis is carried out at 500–1200 °C in an inert gas (N_2) atmosphere by increasing the temperature step by step using the several furnaces at different temperatures. For the radiation cured PCS fiber, the reactions occurring during pyrolysis showed a different behavior for gas evolution from that for the thermal oxidation. As the free radicals were easily

Fig. 10.15 EPR spectra observed at RT after cooling from different pyrolysis temperatures for PCS fibers cured by EB irradiation in He gas. The figure is adapted from [60] by permission of John Wiley & Sons (2005)



observed by EPR at RT after the pyrolysis of cured PCS fiber, EPR measurements could be applied for the analysis of the reaction mechanism during pyrolysis [58, 60, 61].

The EPR spectra observed at room temperature for PCS fibers after pyrolysis at different temperatures are shown in Fig. 10.15 [60]. The PCS fiber was cured (crosslinked) by EB irradiation in He and the radicals trapped in the PCS fibers were then sufficiently quenched by heat treatment. The PCS fiber was heated in an argon (Ar) gas flow up to a certain temperature and was held for 30 min at that temperature. The sample was then cooled down to room temperature and the EPR spectrum was observed. The radical concentration was very high, and was very stable at room temperature and not affected by exposure to air. As seen in Fig. 10.15, the spectrum was a singlet and the line width decreased with increasing temperature for the pyrolysis. The radical concentration was determined from the EPR spectral intensity and plotted against the pyrolysis temperatures in Fig. 10.16 for the PCS fibers cured under various conditions which are listed in Table 10.2. The radical production started at around 400 °C (673 K) for any PCS fiber, and the concentration increased sharply by increasing the temperature. The radical concentration showed a peak at a specific temperature, after which it decayed with increasing temperature up to about 1550 °C (1823 K) for all PCS fibers. The profile of radical concentration as a function of pyrolysis temperature was very different for PCS fibers cured under different conditions. The radical concentration at the peak along the pyrolysis temperature axis was $(3-5) \times 10^{19}$ spins/g. The EPR spectrum was a singlet for any PCS fiber and the peak to peak line width decreased with the pyrolysis temperature, as shown in Fig. 10.15. The peak to peak width for the pyrolysis temperature was plotted in Fig. 10.17 for PCS fibers cured under the various conditions.

Fig. 10.16 Concentration of radicals observed after fiber cooled down to RT from the pyrolysis temperature for the cured PCS fibers containing different oxygen contents. The figure is adapted from [60] by permission of John Wiley & Sons (2005)

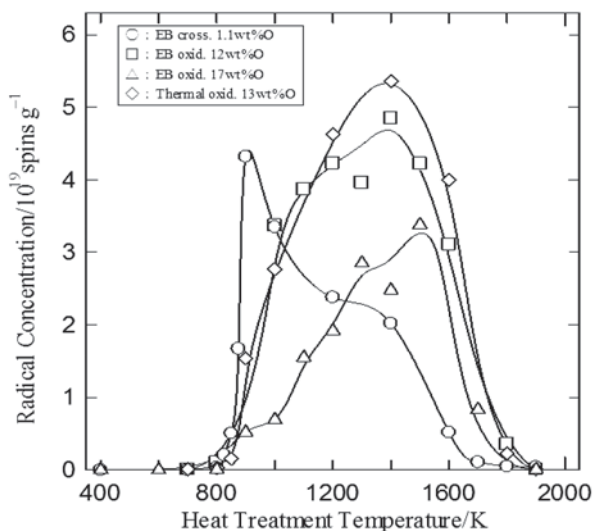
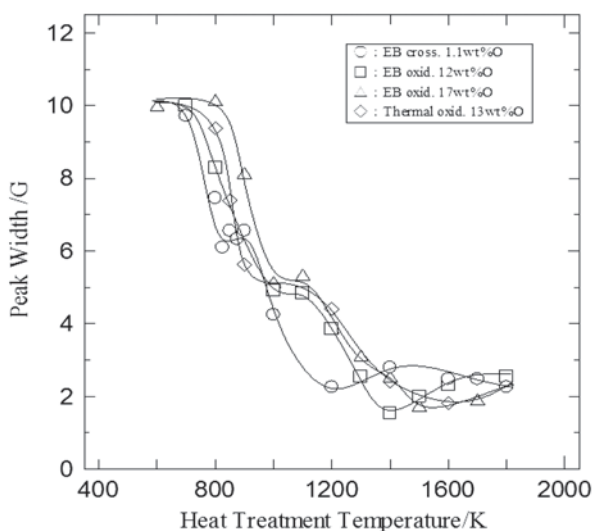
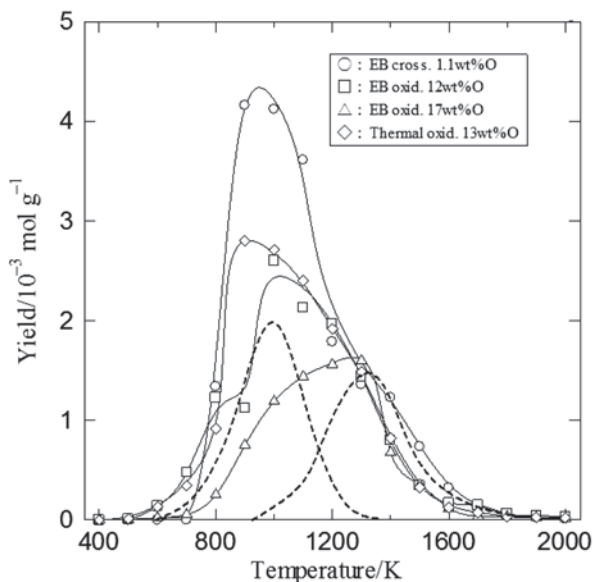


Fig. 10.17 Peak width (peak to peak) of EPR spectrum observed at RT after pyrolysis at different temperature for the cured PCS fibers containing different oxygen contents. The figure is adapted from [60] by permission of John Wiley & Sons (2005)



The change in the radical yield during the pyrolysis was compared with the yield of gas evolution for the same specimens [60]. The gaseous products were hydrogen (H_2), methane (CH_4), and carbon mono-oxide (CO). The methane evolution occurred in the 800–1200 K temperature range for all PCS fibers, and the yield of evolution was almost the same for the PCS fibers cured under different conditions. The CO evolution occurred in the temperature range above 1750 K for the PCS fibers containing oxygen, and the yield was nearly proportional to the oxygen content of the fibers. However, for H_2 evolution as shown in Fig. 10.18, the range

Fig. 10.18 Hydrogen gas evolution versus pyrolysis temperatures for the cured PCS fibers containing different oxygen contents. The figure is adapted from [59] by permission of John Wiley & Sons (2005)



of temperature was very broad from 673 to 1800 K, and the profile for the pyrolysis temperature was dependent on the different conditions under which the PCS fibers were cured. The profile of H_2 evolution was analyzed to be composed of two different temperature ranges—one at the peak at 900–1000 K and the other at around 1300 K, as seen in dotted lines.

The profile of the free radical concentration in Fig. 10.16 was similar to that of H_2 evolution in Fig. 10.18 for the PCS fibers cured under the respective conditions. The radical formation had two different temperature ranges which corresponded to those for H_2 evolution. It was proposed that the decomposition chemical reaction for the components of Si–H and Si–CH₃ occurs at 900–1000 K, and that for the C–H of –CH₂– in the main chain occurs at 1300 K. Therefore, the radicals at 900–1000 K are –Si• type and those at 1300 K are –C• type. The reaction mechanisms are illustrated in Fig. 10.19. The reaction at the lower temperature range was greatly affected by the curing conditions for the PCS fiber, but the reaction at higher temperature was scarcely affected by the conditions. For the PCS fiber cured with oxidation, a Si–O bond was formed, so the concentration for –Si• radical formation would decrease proportionally. In the case of thermal oxidation, the oxidation would take place throughout the PCS fiber, whereas the area of oxidation in radiation oxidation is at the surface of the PCS fiber. Therefore, the difference between thermal oxidation and radiation oxidation in respect to the radical yield for the lower temperature range might reflect the different oxidation areas in a cross section of the PCS fiber.

The radical concentration and the profile in Fig. 10.16 were observed at room temperature after cooling from the pyrolysis temperature, so the concentration measured at room temperature might be different from that at the pyrolysis temperature. However, the observed profile would reflect the behavior of the radical yield during

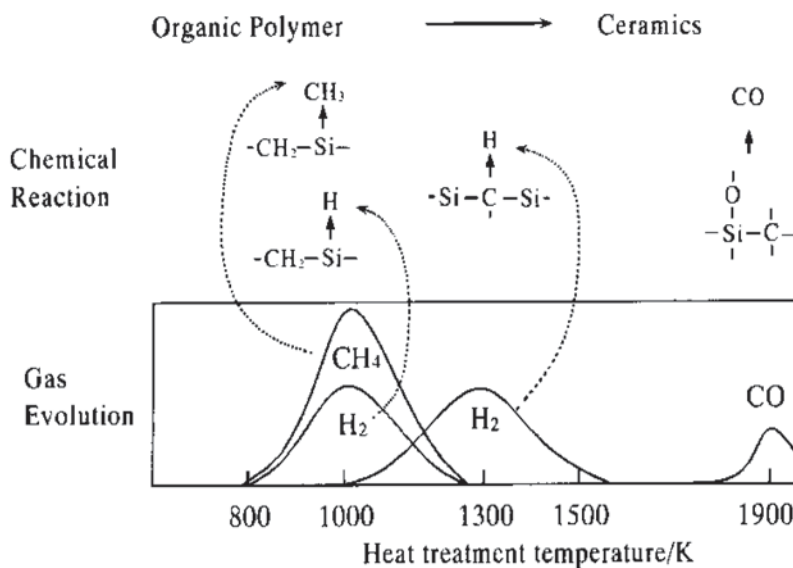


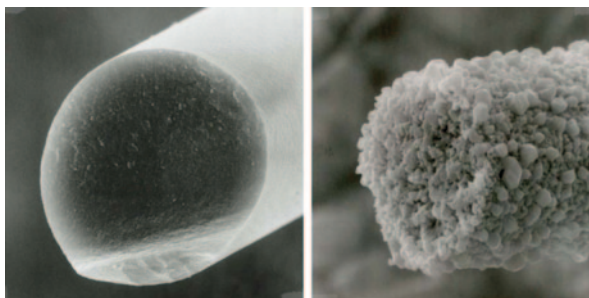
Fig. 10.19 Model of *chemical reaction* mechanisms for SiC fiber synthesis from PCS fiber. The figure is adapted from [59] by permission of John Wiley & Sons (2005)

the reactions occurring under pyrolysis at the high temperature. The information obtained from the radical profile observed at room temperature after pyrolysis was very useful for the control of temperature in the practical pyrolysis for the SiC fiber processing. For the radiation cured PCS fiber with low oxygen content, the heat treatment in the pyrolysis could be increased up to 2000 °C with only a minor decomposition of fiber. For the PCS fiber cured by thermal oxidation, the temperature of pyrolysis was limited at 1300 °C due to the destruction caused by the oxygen included in the structure of the fiber [55, 56]. Electron microphotographs of SiC fiber (filament) after the heat treatment at 1827 K are shown in Fig. 10.20 for the PCS fiber cured by EB irradiation under He and by thermal oxidation [57]. The tensile strength of the SiC fiber after heat treatment at high temperature is plotted in Fig. 10.21 for the PCS fibers cured by the respective methods [58]. It was confirmed that the heat resistance of SiC fiber was greatly improved by decreasing the oxygen content, namely by the curing of PCS fiber by radiation crosslinking in the absence of oxygen. The new processing of SiC fiber (Hi-Nicalon[®]) has been applied for use in a high temperature environment.

10.2.4 Application for New Ceramic Materials Development

The curing of PCS fibers by radiation oxidation was applied for the development of SiC micro tube as seen in Fig. 10.22 [63]. When a PCS fiber of 20 μm diameter was irradiated in oxygen to 300 kGy by EB, oxidation took place at the surface area

Fig. 10.20 Photographs of SiC fiber by scanning electron microscopy (SEM) after pyrolysis at 1500°C for PCS fiber cured by radiation crosslinking (*left* 0.4 wt% oxygen) and by thermal oxidation (*right* 12 wt% oxygen)



of the PCS fiber because of the high dose rate irradiation. The crosslinking of PCS fiber in the oxidation area was achieved by progressing, preferentially by heating up to 300°C, and the area was converted to almost 100% gel. The inner area of the PCS fiber without oxidation had a low degree of crosslinking (no gel formation), where curing was not attained in the low dose regions exposed to less than 3 MGy. The inner part of the PCS fiber was extracted by a solvent, and a PCS tube was formed. The PCS tube was converted to a SiC tube by pyrolysis in an inert gas atmosphere. The diameter of the tube was about 14 μm as for the SiC fibers. The thickness of

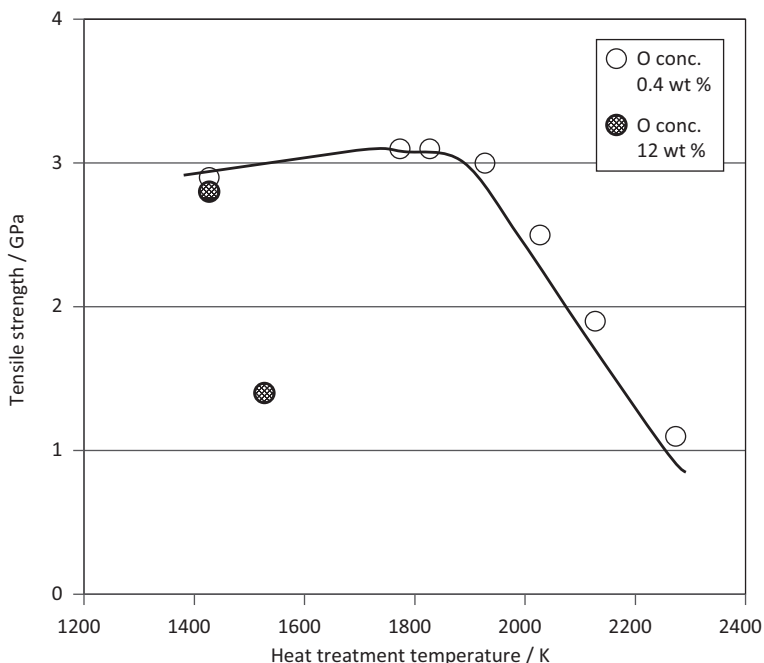
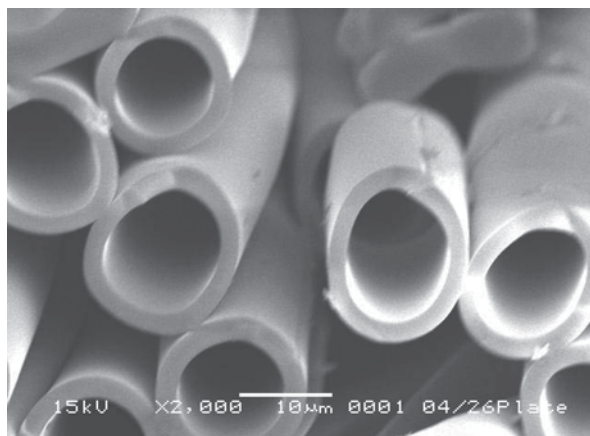


Fig. 10.21 Heat resistance of SiC fiber obtained for PCS fiber cured by radiation crosslinking excluded oxidation (0.4 wt% oxygen) and by thermal oxidation (12 wt% oxygen). Tensile testing was at RT

Fig. 10.22 SiC *micro-tube* synthesized from PCS fiber cured by radiation oxidation. Diameter of the tube is 14 μm , and thickness of wall is 3 μm . The figure is adapted from [63] by permission of Trans Tech Publications (2003)



the wall of tube, which was related to the oxidation depth from the surface, could be controlled by the dose rate and the oxygen pressure during irradiation. The SiC tube was flexible and the heat resistance was around 1400 K. The applications for SiC micro-tubes are under research.

Silicon nitride fibers (Si_3N_4) were synthesized from PCS fiber by radiation curing without oxidation [50, 64, 65]. The PCS fiber cured by radiation crosslinking was heat treated in an ammonia gas atmosphere at the temperature range of 500–1300 °C. The carbon atoms in the PCS were replaced by nitrogen atoms in the reactions of pyrolysis. For PCS fibers cured by thermal oxidation or radiation oxidation, the silicon nitride fiber could not be obtained. Free radicals were not observed by EPR under the pyrolysis in a NH_3 gas atmosphere. By analysis of the elements present (Si, C, N, H) and by FT-IR measurements, the reaction mechanism in the pyrolysis for the PCS fiber at different temperatures was obtained as follows. The CH_3 at $-\text{Si}-\text{CH}_3$ was replaced by NH_3 to form $-\text{Si}-\text{NH}$ at 500–700 °C, CH_2 in $-\text{Si}-\text{CH}_2-\text{Si}-$ was replaced to form $-\text{Si}-\text{NH}-\text{Si}-$ at 700–1000 °C, and the H atom was removed at 1000–1300 °C. The Si_3N_4 fiber was white in color with a diameter of 15 μm . The tensile strength was 2 GPa and the heat resistance was at around 1200 °C. The important specific property of the silicon nitride fiber was its high electric resistance at high temperature. Industrial production of these fibers has been suspended until practical applications can be realized.

10.3 Summary

Free radicals are the key intermediate species in radiation induced chemical reactions of polymer materials, and have a long enough life time for EPR measurements to be made after irradiation or during chemical reactions, especially for crystalline polymers. Therefore, the EPR can be used to follow the radical reactions induced

by the radiation processing and the modifications of various polymers. Of course, although the determination of radical species in polymers is the useful information, the concentration of radicals is also an important factor for the analysis of chemical reaction mechanisms. Both the radical species and the concentration change significantly with the transition temperature where the radical reactions are progressing. The finding of a transition temperature is an important point for the applications of EPR to polymers. In the case of graft-polymerization on polyethylene by the pre-irradiation, the decay rate of the radicals in the crystalline regions is equivalent to the rate of graft initiation, and both rates depend on the size of the PE crystallites and the temperature during the reactions. Therefore, the graft-polymerization could be controlled in principle by the radical content trapped in the PE, the reaction temperature, and the period of graft-polymerization for a selected PE. In a practical graft-polymerization, the monomer supply to the radicals in the polymer matrix is affected by the shape and thickness of the matrix and the properties of monomer, so these factors must be considered. The graft-polymerization onto crosslinked PTFE for proposed ion exchange membranes was started from the results of an EPR study which showed the high yield of radicals. For the practical application, more studies of the trapped radicals in crosslinked PTFE may be necessary in order to find out the mechanism or reason of the increase. For the crosslinking of polycarbosilane (PCS) fiber, the radical species formed and the relationship between the radical yield and the dose indicated the possibility of radiation crosslinking, and finally the optimum curing condition for SiC fiber processing was found. The mechanism for PCS crosslinking is an assumption, because the process could not be followed by EPR measurement. The crosslinking proceeded quickly during irradiation and may proceed even at lower temperatures. While the trapped radicals in the PCS fiber induced significant oxidation on exposure to air, the oxidation could be reduced by the removal of radicals by heating. By extending the annealing of the radicals to higher temperatures, it was found that new radicals were produced during the pyrolysis of the PCS fiber. The production of radicals by pyrolysis and the decay were a useful indicator for the analysis of SiC fiber processing. The EPR information contributed to the development of high quality SiC fibers.

For EPR application to polymer processing, the radical concentration and their behavior during chemical reaction should be checked by the other measurements such as gas evolution, IR absorption, etc. As EPR has a high sensitivity for detecting radicals, it is important not to follow a minor radical and ignore the main chemical reaction. For example, peroxy radicals or polyenyl radicals can be trapped in the crystalline regions of polymers at low concentrations and may not contribute to the major chemical reactions taking place. Generally the radical concentration is at a rather high level if the radicals are involved in the major reaction in the radiation processing of polymers.

References

1. Dole M (1973) The radiation chemistry of macromolecules, I and II. Academic, Boston
2. Ranby B, Rabek J-F (1977) ESR spectroscopy in polymer research (Polymers/properties and application). Springer, Berlin
3. Lund A, Shiotani M, Shimsda T (2010) Principles and applications of ESR spectroscopy. Springer, Berlin
4. Hill DJT, Thurecht KJ, Whittaker AK (2003) A study of the radiation chemistry of poly(chlorotrifluoro-ethylene) by ESR spectroscopy. *Radiat Phys Chem* 68:857–864
5. Gamage NJW, Hill DJT, Lukey CA, Pomery PJ (2004) The use of high energy radiation as a probe for the characterization of polyester melamine coating matrices. *Radiat Phys Chem* 69:487–493
6. Singh A, Silverman J (1991) Radiation processing of polymers. Hanser Publishers, New York
7. Tutiya M (1972) Nuclear magnetic resonance absorption of polytetrafluoroethylene γ -irradiated at high temperature. *Jpn J Appl Phys* 11:1542–1546
8. Sun J, Zhan Y, Zhong X (1994) Radiation crosslinking of polytetrafluoroethylene. *Polymer* 35:2881–2883
9. Oshima A, Seguchi T, Tabata Y (1994) Radiation induced crosslinking of polytetrafluoroethylene and its properties. Proceedings of 14th international symposium on fluorine chemistry, 31 July–5 Aug (Yokohama, Japan)
10. Oshima A, Tabata Y, Kudoh H, Seguchi T (1995) Radiation induced crosslinking of polytetrafluoroethylene. *Radiat Phys Chem* 45:269–273
11. Lappan U, Geissler U, Uhlmann S (2000) Changes in the chemical structure of polytetrafluoroethylene induced by electron beam irradiation in the molten state. *Radiat Phys Chem* 59:317–322
12. Tanso S, Okamoto J, Ishigaki I, Sugo T, Murata K, Takayama T (1983) A new alkaline battery separator made by pre-irradiation graft polymerization. *Yuasa-Jiho* (GS-Yuasa Co. Ltd.) 54:57–67
13. Takeda T, Tamada M, Seko N, Ueki Y (2010) Ion exchange fabric synthesized by graft polymerization and its application to ultra-pure water production. *Radiat Phys Chem* 79:223–226
14. Sugo T (1998) Development of separation membrane by radiation induced graft polymerization. *Chemical Industry* (in Japanese) 7:53–60
15. Seko N, Tamada M, Yoshii F (2005) Current status of adsorbent for metal ions with radiation grafting and crosslinking techniques. *Nucl Instrum Methods B* 236:21–29
16. Waterman DC, Dole M (1970) Radiation chemistry of polyethylene. X. Kinetics of the conversion of alkyl to allyl free radicals. *J Phys Chem* 74:1913–1918
17. Shimada S, Kashiwabara H, Sohma J (1970) ESR studies of the photodegradation of polyethylene containing trapped allylic free radicals. *J Polym Sci (Part A-2)* 8:1291–1298
18. Seguchi T, Tamura N (1974) Electron spin resonance studies on radiation graft copolymerization in polyethylene. I. Grafting by alkyl radicals trapped in irradiated polyethylene. *J Polym Sci Poly Chem Ed* 12:167–1682
19. Seguchi T, Tamura N (1974) Electron spin resonance studies on radiation graft copolymerization in polyethylene. II. Grafting by allyl radicals trapped in irradiated polyethylene. *J Polym Sci Poly Chem Ed* 12:1953–1964
20. Seguchi T, Tamura N (1973) Mechanism of decay of alkyl radicals in irradiated polyethylene on exposure to air as studied by electron spin resonance. *J Phys Chem* 77:40–44
21. Ishigaki I, Sugo T, Senoo K, Takayama T, Machi S, Okamoto J, Okada T (1981) Synthesis of ion exchange membrane by radiation grafting. *Radiat Phys Chem* 18:899–905
22. Ishigaki I, Sugo T, Senoo K, Okada T, Okamoto J, Machi S (1982) Graft polymerization of acrylic acid onto polyethylene film by preirradiation method. I. Effects of preirradiation dose, monomer concentration, reaction temperature, and film thickness. *J Appl Polym Sci* 27:1033–1041

23. Ishigaki I, Sugo T, Senoo K, Takayama T, Okada T, Okamoto J, Machi S (1982) Graft polymerization of acrylic acid onto polyethylene film by preirradiation method. II. Effects of oxygen at irradiation, storage time after irradiation, Mohr's salt, and ethylene dichloride. *J Appl Polym Sci* 27:1043–1051
24. Aymes-Chodur C, Esnouf S, LeMoel A (2001) ESR studies in γ -irradiated and PS-radiation-grafted poly(vinylidene fluoride). *J Polym Sci Part B: Polym Phys* 39:1437–1448
25. Chen J, Yang L, Wu M, Xi Q, He S, Li Y, Nho Y (2000) Preparation of interpenetrating polymer networks by two times grafting of monomers onto pre-irradiated polypropylene film. *Radiat Phys Chem* 59:313–316
26. Shah J M, Fuzail M (2007) Examination of the long-lived, oxygen-induced radicals in irradiated ultra-high molecular weight polyethylene. *Nucl Instrum Methods Phys (Part B)* 265:67–71
27. Kasser M J, Silverman J, Al-Sheikhly M (2010) EPR simulation of polyenyl radicals in ultra-high molecular weight polyethylene. *Macromolecules* 43:8262–8867
28. Zhao Y, Wang M, Tang Z, Wu G (2010) ESR study of free radicals in UHMW-PE fiber irradiated by gamma rays. *Radiat Phys Chem* 79:429–433
29. Kusano H, Asai T, Setogawa A, Nishi H, Yamamoto Y (2001) Development of crosslinked PTFE and the applied products. *Hitachi Cable Rev* 20:153–158
30. Tang Z, Wang M, Zhao Y, Wu G (2010) Tribological properties of radiation crosslinked polytetrafluoroethylene sheets. *Wear* 269:485–490
31. Oshima A, Ikeda S, Seguchi T, Tabata Y (1997) Improvement of radiation resistance for polytetrafluoroethylene (PTFE) by radiation crosslinking. *Radiat Phys Chem* 49:279–284
32. Oshima A, Seguchi T, Tabata Y (1997) ESR study on free radicals trapped in crosslinked polytetrafluoroethylene (PTFE). *Radiat Phys Chem* 50:601–606
33. Oshima A, Seguchi T, Tabata Y (1999) ESR study on free radicals trapped in crosslinked polytetrafluoroethylene (PTFE)—II radical formation and reactivity. *Radiat Phys Chem* 55:61–71
34. Tamura N (1962) Temperature dependence of ESR spectra of irradiated polytetrafluoroethylene. *J Phys Chem* 37:479–484
35. Iwasaki M (1971) Electron spin resonance of irradiated fluorine compounds. *Fluorine Chem Rev* 5:1–10
36. Yamaki T, Asano M, Maekawa Y, Morita Y, Suwa T, et al (2003) Radiation grafting of styrene into crosslinked PTFE films and subsequent sulfonation for fuel cell applications. *Radiat Phys Chem* 67:403–407
37. Sato K, Ikeda M, Oshima A, Tabata Y, Washio M (2003) Study on polyelectrolyte membrane of crosslinked PTFE by radiation-grafting. *Nucl Instrum Methods B* 208:424–428
38. Lapan U, Geissler U, Uhlmann S (2005) Radiation-induced grafting of styrene into radiation-modified fluoropolymer films. *Nucl Instrum Methods B* 236:413–419
39. Hasegawa S, Takahashi S, Maekawa Y, et al (2011) Radiation-induced graft polymerization of functional monomer into poly(ether-ether ketone) film and structure-property analysis of the grafted membrane. *Polymer* 52:98–106
40. Liu W, Wang M, Xing Z, Wu G (2012) The free radical species in polyacrylonitrile fibers induced by γ -irradiation and their decay behaviors. *Radiat Phys Chem* 81:835–839
41. Liu W, Wang M, Xing Z, Wu G (2014) Radiation oxidation and subsequent thermal curing of polyacrylonitrile. *Radiat Phys Chem* 94:9–13
42. Yajima S, Hayashi J, Omori M (1975) Continuous silicon carbide fiber of high tensile strength. *Chem Lett* 9:931–934
43. Yajima S, Okamura K, Hayashi J, Omori M (1976) Synthesis of continuous SiC fibers with high tensile strength. *J Am Ceram Soc* 59:324–327
44. Yajima S, Okamura K, Matsuzawa T, Hasegawa Y, Shishido T (1979) Anomalous characteristics of the microcrystalline state of SiC fibers. *Nature* 279:706–707
45. Yajima S et al (1978) United States Patent, 4,100,233, July 11
46. Yajima S, (1985) Handbook of composites, vol 1, Strong fibers. North Holland, Amsterdam, pp 201–237

47. Okamura K, Shimoo T, Suzuya K, Suzuki K (2006) SiC-based ceramic fibers prepared via organic-to-inorganic conversion process—a review. *J Ceram Soc Jpn* 114:445–454
48. Okamura K, Matsuzawa T, Hasegawa Y (1985) γ -ray irradiation curing on polycarbosilane fibers as the precursor of SiC fibers. *J Mater Sci Lett* 4:55–57
49. Sato M, Okamura K, Kawanishi S, Seguchi T (1988) Radiation effects of polycarbosilane as precursor of ceramic fiber. *J Jpn Soc Powder Powder Metal* 35:679–682
50. Okamura K, Sato M, Seguchi T, Kawanishi S (1988) SiC fiber and Si₃N₄ fiber obtained from electron irradiated polycarbosilane. *J Jpn Soc Powder Powder Metal* 35:170–173
51. Taki T, Okamura K, Sato M, Seguchi T, Kawanishi S (1988) A study on the electron irradiation curing mechanism of polycarbosilane fibers by solid-state ²⁹Si high-resolution nuclear magnetic resonance spectroscopy. *J Mater Sci Lett* 7:209–211
52. Sato M, Yamamura T, Seguchi T, Okamura K (1995) Behavior of radicals on radiation cross-linking of polycarbosilane as SiC fiber precursor. *Chem Soc Jpn* 5:554–556
53. Okamura K, Seguchi T (1992) Application of radiation curing in the preparation of polycarbosilane-derived SiC fibers. *J Inorg Organomet Polym* 2:171–179
54. Seguchi T, Sugimoto M, Okamura K (1996) Radiation application for silicon carbide fiber synthesis from polycarbosilane fiber with controlled Oxygen content. *Adv Mater Mech ICAM* 96:221–225
55. Takeda M, Imai Y, Ichikawa H, Ishikawa T, Seguchi T, Okamura K (1991) Properties of the low oxygen content SiC fiber on high temperature heat treatment. *Ceram Eng Sci Proc* 12(7–8):1007–1018
56. Takeda M, Imai Y, Ichikawa H, Ishikawa T, Kasai N, Seguchi T, Okamura K (1992) Thermal stability of the low oxygen silicon carbide fibers derived from polycarbosilane. *Ceram Eng Sci Proc* 13(7–8):209–217
57. Seguchi T, Okamura K (1993) Radiation application for ceramic fiber synthesis from the precursor fiber. *Kobunshi Kakou (Japanese)* 42(4):163–168
58. Seguchi T, Sugimoto M, Okamura K (1993) Heat resistant SiC fiber synthesis and reaction mechanisms from radiation cured polycarbosilane fiber. *HT-CMC (I)*:51–57 (Woodhead Publishing) ed. by Naslain R, Lamon J, Doumeingts D (Bordeaux)
59. Sugimoto M, Shimoo T, Okamura K, Seguchi T (1995) Reaction mechanisms of silicon carbide fiber synthesis by heat treatment of polycarbosilane fibers cured by radiation: I, Evolved gas analysis. *J Am Ceram Soc* 78(4):1013–1017
60. Sugimoto M, Shimoo T, Okamura K, Seguchi T (1995) Reaction mechanisms of silicon carbide fiber synthesis by heat treatment of polycarbosilane fibers cured by radiation: II, Free radical reaction. *J Am Ceram Soc* 78(7):1849–1852
61. Narisawa M, Shimoda M, Okamura K, Seguchi T (1995) Reaction mechanism of the pyrolysis of polycarbosilane and polycarbosilazane as ceramic precursors. *Bull Chem Soc Jpn* 68:1098–1104
62. Kashiwabara H, Seguchi T (1992) Radiation-induced oxidation of plastics. In: Singh A, Silverman J (eds) *Radiation processing of polymers*. Hanser, New York
63. Sugimoto M, Idesaki A, Tanaka S, Okamura K (2003) Development of silicon carbide micro-tube from precursor polymer by radiation oxidation. *Key Eng Mater* 247:133–136
64. Taki T, Inui M, Okamura K, Sato M, Seguchi T (1991) A study of nitridation process of polycarbosilane fibers by solid state high resolution NMR. *Appl Mag Res* 2:61–68
65. Kamimura S, Seguchi T, Okamura K (1999) Development of silicon nitride fiber from Si-containing polymer by radiation curing and its application. *Radiat Phys Chem* 54:575–581

Chapter 11

Electronic Defects in Electron-Irradiated Silicon Carbide and III-Nitrides

Nguyen Tien Son and Erik Janzén

Abstract Recent advances in electron paramagnetic resonance (EPR) studies of radiation-induced defects in SiC and III-nitrides are reviewed. The identification and electronic structure investigation of vacancies, interstitials, antisites and their associated complexes in these wide-bandgap semiconductors using EPR in combination with theoretical modeling and other optical and electrical characterizations are presented. The use of intrinsic defects in controlling properties of materials for power electronics is discussed.

11.1 Introduction

Intrinsic defects in a compound semiconductor, such as vacancies, interstitials or antisites, often introduce deep energy levels in the bandgap which may work as recombination or carrier compensation centers, having strong influence on the electrical and optical properties of the material. Depending on the formation energy, some intrinsic defects may be introduced into the material during the crystal growth while others can only be created by irradiation of high-energy particles. For electron paramagnetic resonance (EPR) studies, it is desirable to have a large defect concentration so that weak ligand hyperfine (hf) structures due to the interaction between the electron spin and nuclear spins of neighboring atoms can be observed. Irradiation of high-energy particles, such as electrons with energies of several MeV, can replace the host atoms, creating lattice vacancies, interstitials and antisites at desired concentrations. At temperatures when the interstitials or vacancies become mobile, the interaction between these primary defects or between intrinsic defects with impurities initially present in the material leads to the formation of different secondary defects such as divacancies, di-interstitial, vacancy-interstitial pairs, and vacancy-impurity complexes. Among different types of radiations, electron irradiation is most commonly used for intentionally introducing intrinsic defects into semiconductors for characterization.

N. T. Son (✉) · E. Janzén
Semiconductor Materials, IFM, Linköping University, Linköping, Sweden
e-mail: son.tien.nguyen@liu.se

© Springer International Publishing 2014
A. Lund, M. Shiotani (eds.), *Applications of EPR in Radiation Research*,
DOI 10.1007/978-3-319-09216-4_11

Radiation-induced defects in semiconductors have been studied by EPR since the 1950s. It has been shown that interstitial-related defects in some semiconductors become mobile at temperatures well below room temperature [1–3] and irradiation at low temperatures is the way to create these defects at a well-controlled concentration for the study. Being the most important semiconductor, silicon (Si) was also the most studied material. Radiation-induced defects in Si have been studied by EPR since the 1960s [2]. Several radiation-induced defects in Si were found to be efficient recombination centers and have been used for controlling the minority carrier lifetime in the material [4, 5]. Nowadays, electron irradiation is a standard technique for carrier lifetime control in Si material and devices. The transmutation of ^{30}Si into ^{31}P by neutron irradiation is known to be an effective way for achieving very homogeneous *n*-type doping in Si [6] and has widely been used in the modern Si technology.

Defects were also intensively studied in other semiconductors, such as II-VI and III-V compounds. However, due to material problems, such as the lack of *p*-type material for ZnO, and/or the difficulties in competing with the successful Si technology, the interest in many semiconductors is focused on applications using their nanostructures which are not easy to be studied by EPR. Since the last two decades, the interest in wide-bandgap semiconductors, such as SiC and III-nitrides, for replacing Si in high-voltage, high-frequency power device applications has been renewed when high-quality materials have become available. During the last decade, thanks to the successful applications of EPR and theoretical calculations based on the density functional theory in the local density approximation (DFT-LDA) [7], a rapid progress in characterization of intrinsic defects in SiC has been made. Having nuclear-spin $I = 1/2$ isotopes with the natural abundance detectable in EPR spectra ($\sim 4.7\%$ for ^{29}Si and $\sim 1.1\%$ for ^{13}C) but still small enough to provide narrow EPR linewidths (typically ~ 1 G or slightly less), SiC is a good material for EPR studies. High-quality bulk materials of the most important SiC polytypes, 4H- and 6H-SiC, of both *n*- and *p*-type conductivity have been commercially available since many years. III-nitride semiconductors, such as GaN and AlN, are more difficult for magnetic resonance studies. With 100% naturally abundant isotopes having nuclear spins $I \neq 0$ (^{69}Ga : $I = 3/2$, $\sim 60.1\%$ and ^{71}Ga : $I = 3/2$, $\sim 39.9\%$, ^{14}N : $I = 1$, $\sim 99.63\%$, and ^{15}N : $I = 1/2$, $\sim 0.37\%$), the typical EPR linewidth in GaN is ~ 20 G or larger, resulting in unresolved hf structures. This together with limited access to high-quality bulk GaN single crystals make EPR studies of radiation-induced defect in GaN difficult. As a result, intrinsic defects in GaN are still much less known compared to the standard of SiC.

In this chapter, recent advances in magnetic resonance studies of radiation-induced defects in SiC and in the two most common nitride compounds, GaN and AlN, are reviewed. Results from EPR studies of intrinsic defects in SiC and their use in manipulation of the material properties are presented in Sect. 11.2, whereas the progresses in EPR and optical detection of magnetic resonance (ODMR) studies of radiation-induced defects in GaN and AlN during the last two decades are briefly described in Sect. 11.3.

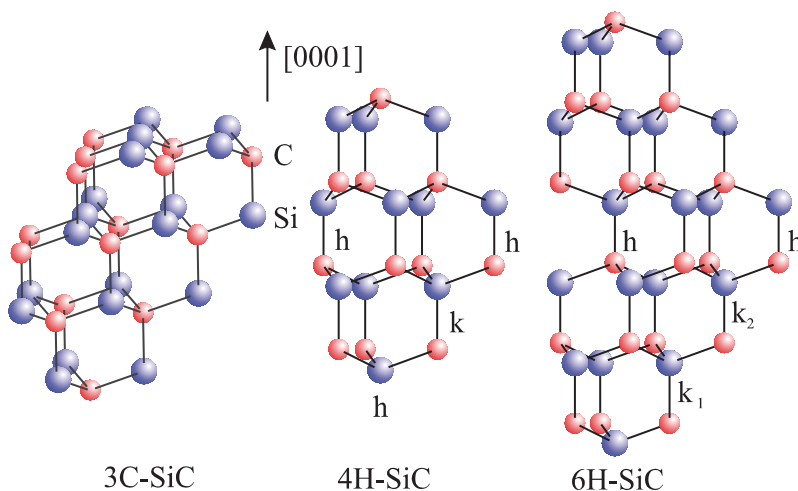
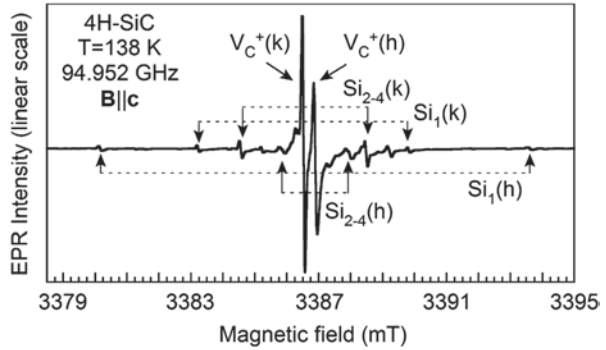


Fig. 11.1 The cubic lattice of 3C-SiC and hexagonal lattice of 4H- and 6H-SiC. There are two inequivalent sites, one hexagonal (h) and one quasicubic (k) sites, in 4H-SiC. The closest surroundings follow the wurtzite structure at the h -site and the zinc blende structure at the k -site. There are one h -site and two quasicubic (k_1 and k_2) sites in 6H-SiC. The k_1 and k_2 sites have different arrangement from the third neighbor shell

11.2 Radiation-Induced Defects in SiC

SiC exists in many polytypes which are different in the stacking sequence of the tetrahedrally bonded Si-C bilayers [8]. The three most common polytypes are 3C-, 4H- and 6H-SiC. Their lattices are shown in Fig. 11.1. 3C-SiC has zinc blende lattice with cubic symmetry while the lattice of the other two is hexagonal. In 4H-SiC, there are two inequivalent lattice sites, one called hexagonal (h) site with the second neighbor arrangement following the wurtzite structure and the other is the quasicubic (k) site with the closest surroundings resembling the zinc blende structure (Fig. 11.1). There are one h -site and two quasicubic (k_1 and k_2) sites in the 6H polytype. As can be seen in the figure, the k_1 and k_2 sites have different arrangement from the third neighbor shell. It is known that a single defect or an impurity occupying different inequivalent sites can introduce different energy levels in the bandgap, giving rise to different EPR spectra. Identification of spectra related to a defect occupying different inequivalent sites is difficult and often requires combination of EPR and supercell calculations, such as calculations of the ligand hf interaction and ionization energies of different configurations of the defect model. For a paired defect in 4H-SiC, there can be four different configurations corresponding to four possible combinations of lattice sites of two components which may not be distinguishable based only on EPR data. The existence of inequivalent lattice sites makes defect characterization in SiC more complicated but also provides a unique possibility to study a defect at different environments. Comparing EPR spectra of a defect in different polytypes can also help in the assignment of EPR signals to the defect at different inequivalent lattice sites.

Fig. 11.2 High-frequency (94.952 GHz) EPR spectra of $V_C^+(k)$ and $V_C^+(h)$ in *p*-type 4H-SiC irradiated with 2.5 MeV electrons at room temperature measured at 138 K for $B\parallel c$ showing the hf structures due to the hf interactions between the unpaired spin and the nuclear spin of a ^{29}Si atom occupying one of the four nearest Si neighbors



11.2.1 Carbon Vacancy

Positive Charge State The carbon vacancy (V_C) in SiC is predicted to have low formation energies and, hence, expected to be abundant in as-grown material [9–12]. The single positive charge state of V_C (V_C^+) was identified in 4H- and 6H-SiC by EPR [13–18]. It was shown from EPR and supercell calculations that V_C^+ conserves its C_{3v} symmetry at the h-site but reconstructs to C_{1h} symmetry at the k-site, resulting in a significant difference in spin distribution [16]. Figure 11.2 shows W-band EPR spectra of V_C^+ at the k- and h-site in *p*-type 4H-SiC irradiated by 2.5 MeV electrons measured for $B\parallel c$ at 138 K. At such high microwave (MW) frequency, the main lines of $V_C^+(h)$ and $V_C^+(k)$ are well separated from each other, showing different hf structures due to the interaction between the unpaired electron spin at the vacancy and the nuclear spin of a ^{29}Si atom occupying one of the four nearest Si neighbor sites. In $V_C^+(h)$, the spin density is mainly on the Si_1 atom along the *c* axis ($\sim 47.3\%$ compared to $\sim 6.8\%$ on each of the three Si_{2-4} atoms in the basal plane, see Table 11.1) and the defect keeps its C_{3v} symmetry even at low temperatures. $V_C^+(k)$ has C_{1h} symmetry with the spin density being more evenly distributed among the four nearest neighbors with two dangling bonds, one on the Si_1 along the *c* axis and the other on one of three $\text{Si}_{2,3,4}$ in the basal plane. The formation of dangling-bond pairs, such as $\text{Si}_1\text{--Si}_2$ and $\text{Si}_3\text{--Si}_4$, induced by Jahn-Teller distortion results in C_{1h} distorted structure. The transition from C_{1h} to C_{3v} symmetry occurs for $V_C^+(k)$ at ~ 40 K as the result of thermally activated reorientation of three equivalent C_{1h} configurations with atomic pairs $\text{Si}_1\text{--Si}_2$, $\text{Si}_1\text{--Si}_3$ and $\text{Si}_1\text{--Si}_4$. The energy barrier for this reorientation was determined to be ~ 14 meV [16].

In 6H-SiC, three EPR spectra, labeled Ky_1 , Ky_2 and Ky_3 , were observed at low temperatures [17]. The Ky_3 center keeps its C_{3v} symmetry at all temperature ranges and is identified to be $V_C^+(h)$, while the other two, Ky_1 and Ky_2 , show similar Jahn-Teller distortion as $V_C^+(k)$ in 4H-SiC and were assigned to V_C^+ at the two quasicubic sites in 6H-SiC. The spin distribution of V_C^+ in 6H-SiC is similar to that in the 4H polytype (Table 11.1). In 3C-SiC, the T5 EPR center observed in *p*-type irradiated materials was assigned to V_C^+ [18]. However, the annealing temperature of this center is only $\sim 200^\circ\text{C}$ [18], while the V_C^+ signal in irradiated 4H- and 6H-SiC is still

Table 11.1 Spin-Hamiltonian parameters of V_C^+ in 4H- and 6H-SiC at different temperatures. X, Y and Z are the directions of the principal axes of \mathbf{g} and \mathbf{A} tensors. θ is the angle between the principal Z axis and the c axis. The principal A values are given in mT. η^2 is the fraction of the total spin density localized at one of the neighboring Si atoms. The assignment of spectra to V_C^+ at k_1 - and k_2 sites was not made in [17]

Center	Parameters	X(\perp)	Y(\perp)	Z(\parallel)	θ	$\eta^2(\%)$	Reference
4H-SiC	\mathbf{g} (5 K)	2.0056	2.0048	2.0030	22.7°		[16]
V_C^+ (k)	\mathbf{g} (138 K)	2.00484	2.00484	2.00322	0°		[13]
	$\mathbf{A}(\text{Si}_1)$ (5 K)	4.44	4.36	6.46	7.7°	19.9	[16]
	$\mathbf{A}(\text{Si}_2)$ (5 K)	3.25	3.19	4.74	121.5°	14.7	[16]
	$\mathbf{A}(\text{Si}_{3,4})$ (5 K)	3.85	3.81	5.52	103.2°	16.5	[16]
	$\Sigma\eta^2(\text{Si}_{1-4})$					67.6	
V_C^+ (h)	\mathbf{g} (10 K)	2.0052	2.0052	2.0026	0°		[16]
	\mathbf{g} (293 K)	2.0046	2.0046	2.0032	0°		[16]
	$\mathbf{A}(\text{Si}_1)$ (5 K)	10.61	10.61	15.48	0°	47.3	[16]
	$\mathbf{A}(\text{Si}_{2-4})$ (5 K)	1.40	1.40	2.11	98°	6.8	[16]
	$\Sigma\eta^2(\text{Si}_{1-4})$					67.6	
6H-SiC	$\mathbf{g}(\text{E15})$ (102 K)	2.00461	2.00461	2.00316	0°		[13]
V_C^+ (k_1, k_2)	$\mathbf{g}(\text{Ky1})$ (4.2 K)	2.0060	2.0026	2.0025	34°		[17]
	$\mathbf{A}(\text{Si}_1)$ (4.2 K)	3.94	3.94	5.74	8°	17.5	[17]
	$\mathbf{A}(\text{Si}_2)$ (4.2 K)	3.79	3.79	5.49	119°	16.5	[17]
	$\mathbf{A}(\text{Si}_{3-4})$ (4.2 K)	3.82	3.82	5.55	104°	16.8	[17]
	$\Sigma\eta^2(\text{Si}_{1-4})$				27°	67.7	
	$\mathbf{g}(\text{Ky2})$ (4.2 K)	2.0050	2.0040	2.0023	8°		[17]
	$\mathbf{A}(\text{Si}_1)$ (4.2 K)	4.33	4.33	6.44	121°	20.3	[17]
	$\mathbf{A}(\text{Si}_2)$ (4.2)	3.09	3.09	4.60	104°	14.5	[17]
	$\mathbf{A}(\text{Si}_{3,4})$ (4.2 K)	3.85	3.85	5.52	0°	16.3	[17]
	$\Sigma\eta^2(\text{Si}_{1,2,3,4})$				0°	67.5	
V_C^+ (h)	$\mathbf{g}(\text{Ky3})$ (15 K)	2.0046	2.0046	2.0020	0°		[17]
	$\mathbf{g}(\text{Ky3})$ (77 K)	2.0045	2.0045	2.0025	101		[17]
	$\mathbf{A}(\text{Si}_1)$ (77 K)	10.09	10.09	14.65		44.3	[17]
	$\mathbf{A}(\text{Si}_{2-4})$ (77 K)	1.45	1.45	2.23		7.4	[17]
	$\Sigma\eta^2(\text{Si}_{1-4})$					66.6°	

detectable after annealing at $\sim 1600^\circ\text{C}$ [19]. Therefore, it is unlikely that the T5 center is related to the C vacancy.

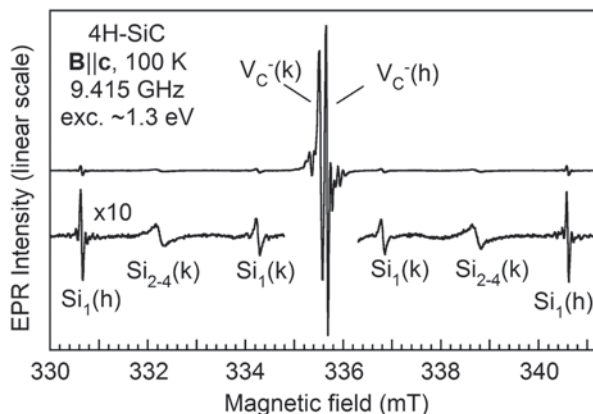
In 4H-SiC, calculations by Zywietz and co-workers [9] predicted the $(0|+)$ state to be located at ~ 1.37 – 1.44 eV above the valence band E_V and below the $(+|2+)$ state (at $\sim E_V + 1.68$ eV). Hence, V_C is a negative-U center which, in equilibrium, would be in either the neutral or double positive charge state and, thus, EPR inactive. A later calculation using Madelung correction [10] found the $(0|+)$ level at ~ 1.22 – 1.34 eV without negative-U behavior. EPR observations of V_C^+ in darkness at low temperatures in irradiated [13, 14, 16] and as-grown [20–22] materials indicate that

the single positive charge state is stable. Photoexcitation EPR (photo-EPR) experiments in *p*-type irradiated 4H-SiC found energy thresholds to quench the V_C^+ signal at $\sim E_V + 1.47$ eV [23] (or $\sim E_V + 1.6$ eV in high-purity semi-insulating 4H-SiC [24]) and to recover the signal at $\sim E_C - 1.81$ eV [23] and $\sim E_C - 1.9$ eV [24]. The (0|+) level of V_C was assigned at ~ 1.5 – 1.6 eV above E_V . A later calculation by Bockstedte *et al.* [25] reinterpreted the energy threshold of ~ 1.5 – 1.6 eV as the optical transition from the (0|+) level to the conduction band minimum E_C and the threshold of ~ 1.8 – 1.9 eV to the transition from the valence band to the (2+|+) state, reactivating the single positive (+) charge state of V_C . However, in the photo-EPR study by Carlsson *et al.* [26] in *n*-type 4H-SiC layers irradiated with low-energy (200 keV) electrons, the same threshold of ~ 1.8 eV for activating the V_C^+ signal, which was not detected in darkness, was observed. This observation supports the assignment of optical transitions in previous photo-EPR studies [23, 24]. Comparison between photo-EPR and deep level transient spectroscopy (DLTS) [26], the (0|+) level of V_C was suggested to be related to the deep level EH7 at $\sim E_C - 1.6$ eV in 4H-SiC [27, 28].

Negative Charge State In calculations by Zywiets and co-workers [9], the single (–|0) and double (2–|1–) acceptor levels of V_C were predicted to be close to each other in the conduction band. Nevertheless, the single negative charge state of V_C , V_C^- , was observed and identified by EPR for the h-site [29]. In *n*-type 4H-SiC substrates irradiated with 2 MeV electrons at 850 °C, the $V_C^-(h)$ signal is one of several dominating EPR spectra. The $V_C^-(h)$ center shows C_{1h} symmetry at low temperatures. The thermal average of different C_{1h} configurations occurs at temperatures above ~ 60 K, resulting in C_{3v} symmetry. At low temperatures (< 60 K), the spin density is mainly distributed on two Si neighbors, one along the *c* axis (Si_1) and the other is one of three Si atoms in the basal plane. At higher temperatures when the thermal average occurs, the hf lines due to the hf interaction with the Si atom in the basal plane are not detectable due to line broadening and only the Si_1 hf lines could be detected [29]. Recently, using high-doped *n*-type freestanding 4H-SiC layers irradiated with low-energy (250 keV) electrons, which can mainly replace C atoms, creating the C vacancy, C interstitials and their associated defects, the missing signal of V_C^- at the k-site was observed [30] and identified [31].

Figure 11.3 shows EPR spectra of $V_C^-(h)$ and $V_C^-(k)$ in such irradiated layer measured for B||*c* at 100 K under illumination of light with photon energies ~ 1.3 eV. In samples irradiated with a fluence of $\sim 7.5 \times 10^{18}$ cm $^{-2}$ in darkness, these two lines are not seen at low temperatures but can be very weakly detected when warming up the sample to ~ 100 K or higher. Under illumination with light of photon energies above ~ 1.3 eV, these lines dramatically increase in intensity and, in addition to the known hf structure of Si_1 of $V_C^-(h)$, hf structures due to the hf interaction between the unpaired electron spin and the nuclear spin of a ^{29}Si atom occupying one of four nearest Si neighbors were observed. Such temperature dependence and light sensitive behavior of $V_C^-(h)$ and $V_C^-(k)$ signals are typical for a negative-U center [32]. It has been suggested by Anderson [32] that the energy gain associated with electron pairing in the dangling bonds of a defect and coupled with a large lattice relaxation might overcome the Coulomb repulsion of the two electrons, resulting in a net effective attractive interaction between the electrons at the site (a negative

Fig. 11.3 EPR spectra of $V_C^-(h)$ and $V_C^-(k)$ in *n*-type 4H-SiC layer irradiated by 250 keV electrons at room temperature to a fluence of $7.5 \times 10^{18} \text{ cm}^{-2}$ measured for $B \parallel c$ at 100 K under illumination showing their Si hf structures



correlation energy U or negative U). This happened to V_C with the $(-|0)$ level lying shallower than the $(2-|0)$ state. It has been shown that in irradiated region, the Fermi level locates at $\sim E_C - 0.53$ eV and all the N shallow donors were compensated by deep radiation-induced defects [33]. In the neutral charge state, V_C prefers capturing two electrons and relaxes to the lower energy $(2-|0)$ state which is EPR inactive. At elevated temperatures when the thermal energy can induce a measurable population on the higher-lying $(-|0)$ state, the EPR signal of V_C^- can be detected. The intensity of the $V_C^-(k)$ signal measured in darkness is smaller than that of $V_C^-(h)$, suggesting that the energy distance between the $(-|0)$ and $(2-|0)$ levels is larger for $V_C^-(k)$ than for $V_C^-(h)$.

Although the total spin density is similar for $V_C^-(h)$ and $V_C^-(k)$, the spin distribution is different between the two centers. In $V_C^-(h)$, the spin density is mainly found on the Si_1 atom along the c axis and on one of three Si atoms in the basal plane (e.g., two dangling bonds of Si_1 and Si_2 atoms in the $\{11\bar{2}0\}$ plane) [29]. For $V_C^-(k)$, calculations found two configurations with one being more stable than the other by 0.03 eV [31]. In the stable configuration, the spin density is mainly on two nearest Si neighbors ($Si_{3,4}$) and spreads to two $C_{1,2}$ atoms in the second neighbor next to $Si_{3,4}$ and further to two $Si_{5,6}$ atoms in the third neighbor in the basal plane. The calculated hf constants of these ligand hf interactions for the stable configuration of $V_C^-(k)$ agree well to the corresponding values determined by EPR for the center at low temperatures, supporting the identification of V_C at the k-site in 4H-SiC [31]. The spin-Hamiltonian parameters of $V_C^-(h)$ and $V_C^-(k)$ in 4H-SiC at different temperatures are summarized in Table 11.2.

Photo-EPR experiments in *n*-type 4H-SiC irradiated at $\sim 850^\circ\text{C}$ observed a weak increase of the EPR signal of $V_C^-(h)$ at photon energies of $h\nu \sim 0.8$ eV and a clear energy threshold at ~ 1.1 eV [29]. This energy is close to the $(2-|1-)$ level of V_C calculated by Torpo and co-workers [10] and was therefore assigned to the double acceptor level of V_C [29]. Similar energy thresholds were also observed in a later EPR study of low-doped *n*-type freestanding 4H-SiC layers irradiated with 200 keV electrons [26].

Table 11.2 Spin-Hamiltonian parameters of V_C^- in 4H-SiC at different temperatures. X, Y and Z are the directions of the principal axes of \mathbf{g} and \mathbf{A} tensors. θ is the angle between the principal Z axis and the c axis. The principal A values are given in mT. η^2 is the fraction of the total spin density localized at one of the neighboring Si and C atoms

Center	Parameters	X(\perp)	Y(\perp)	Z(\parallel)	θ	η^2 (%)
$V_C^-(k), C_{3v}$ 140 K [30]	\mathbf{g}	2.0035	2.0035	2.0046	0°	
	$\mathbf{A}(\text{Si}_1)$	2.96	22.96	3.69	0°	8
	$\mathbf{A}(\text{Si}_{2-4})$	6.05	5.94	7.49	67.1°	16.2
	$\Sigma\eta^2(\text{Si}_{1-4})$					56.6
$V_C^-(h), C_{3v}$ 140 K [30]	\mathbf{g}	2.0038	2.0038	2.0040	0°	
	$\mathbf{A}(\text{Si}_1)$	7.72	7.72	9.92	0°	23.2
	$\mathbf{A}(\text{Si}_{2-4})$	4.11	4.05	5.21	75.9°	12.1
	$\Sigma\eta^2(\text{Si}_{1-4})$					59.8
$V_C^-(k), C_{1h}$ 30 K [31]	\mathbf{g}	2.0027	2.0038	2.0054	9.9°	
	$\mathbf{A}(\text{Si}_{3,4})$	10.04	10.15	12.99	68.9°	30.4
	$\Sigma\eta^2(\text{Si}_{3,4})$					60.8
	$\mathbf{A}(\text{C}_{1,2})$	1.33	1.31	1.85	82.3°	5.7
	$\Sigma\eta^2(\text{C}_{1,2})$					11.4
	$\mathbf{A}(\text{Si}_{5,6})$	0.87	0.85	1.12	62.6°	2.7
	$\Sigma\eta^2(\text{Si}_{5,6})$					5.4
$V_C^-(h), C_{1h}$ 60 K [16]	\mathbf{g}	2.00407	2.00208	2.00459	38°	
	$\mathbf{A}(\text{Si}_1)$	7.76	7.76	10.07	7°	24.1
	$\mathbf{A}(\text{Si}_2)$	11.67	11.78	15.19	101°	36.6
	$\Sigma\eta^2(\text{Si}_{1,2})$					60.7

In DLTS studies of n -type 4H-SiC epitaxial layers irradiated with low-energy (110–250 keV) electrons, which can create mainly defects in the C sublattice, such as V_C and C interstitials, Storasta *et al.* [28] and Danno *et al.* [34] suggested the Z_1/Z_2 deep level at $\sim E_C - (0.60 \div 0.65)$ eV in 4H-SiC [35] to be related to either V_C or a V_C -related defect. The Z_1/Z_2 center is a negative-U center having two higher-lying excited states at $\sim E_C - 0.52$ eV (for Z_1) and at $\sim E_C - 0.45$ eV (for Z_2) [36, 37]. In equilibrium, the excited states prefer to capture another electron to relax to the lower energy Z_1/Z_2 level. The Z_1/Z_2 defect is always present in pure SiC epitaxial layers grown by chemical vapor deposition (CVD) [38] and is known to be the lifetime limiting defect in bulk SiC [39–42]. From the correlation in defect formation, concentration, and annealing behavior observed in as-grown and irradiated materials, the Z_1/Z_2 and EH7 centers were suggested to belong to the same V_C -related defect [34]. This has been further supported by the fact that both centers can be effectively annealed out by C implantation and subsequent annealing [43, 44] or by thermal oxidation [45, 46].

In recent hybrid functional calculations, Hornos and co-workers [47] found the (2–|–) levels of $V_C(h)$ and $V_C(k)$ to be very close to the Z_1/Z_2 level. However, the charge correction was overcorrected and the negative-U behavior was found only for $V_C(k)$. The problem with charge correction was solved in later calculations us-

ing supercells up to 3200 atoms [30], which found the $(-|0)$ and $(2-|0)$ levels at $\sim E_C - 0.53$ eV and $\sim E_C - 0.56$ eV for $V_C(h)$ and at $\sim E_C - 0.43$ eV and $\sim E_C - 0.53$ eV for $V_C(k)$, respectively. These levels are in good agreement with the levels of the Z_1/Z_2 negative-U center and the photo-EPR results [30], where the optical transition to the conduction band from the $(-|0)$ and $(2-|0)$ levels were found to be ~ 0.74 eV and ~ 0.78 eV, respectively, for $V_C(h)$. For $V_C(k)$, the corresponding transition from the $(2-|0)$ level to the conduction band was determined to be ~ 0.74 eV. Thus, photo-EPR, DLTS and supercell calculations provide a clear correlation in energy levels between the Z_1/Z_2 center and V_C . In a recent study [33], a one-to-one correlation between the concentrations of Z_1/Z_2 determined by DLTS and of V_C^- estimated by EPR was observed, providing further support for identification of the Z_1/Z_2 level at $\sim E_C - 0.6$ eV and its higher-lying excited state at $\sim E_C - 0.52$ eV (for Z_1) and $\sim E_C - 0.45$ eV (for Z_2) as the double and single acceptor levels, respectively, of V_C . It was shown from calculations and EPR [31] that Z_1 and Z_2 are related to the acceptor levels of V_C at the h- and k-site, respectively.

With two deep acceptor levels at ~ 0.4 – 0.6 eV below the conduction band, V_C (or Z_1/Z_2) is an efficient electron trap and a lifetime limiting defect in bulk *n*-type SiC [39–42]. In pure SiC layers grown by CVD, typical carrier lifetime is less than 2 μ s. After C implantation and subsequent annealing or thermal oxidation, the reduction of the Z_1/Z_2 concentration leads to the enhancement of the carrier lifetime several times and can reach to more than 10 μ s [43–46, 48]. Changing the concentration of V_C during CVD by varying the C/Si ratio in precursor gases in the range ~ 0.9 – 1.2 can lead to the variation of carrier lifetime in the range of a few μ s [49]. For a more precise lifetime control in a wider range, the lifetime was first enhanced by thermal oxidation or C implantation and subsequent Ar annealing, then irradiation with low-energy electrons was performed to create the C vacancy to a concentration that can reduce carrier lifetime as desired [50].

Photo-EPR studies of high-purity semi-insulating (HPSI) and electron-irradiated *p*-type 6H-SiC suggested the $(0|+)$ state of V_C to be at $\sim E_V + 1.47$ eV or $\sim E_C - 1.55$ eV [51]. The optical transition of ~ 1.55 eV is likely to be related to the E_7 level at $\sim E_C - 1.25$ eV observed by DLTS in 6H-SiC p^+n diodes [52]. The acceptor levels of V_C in 6H-SiC have not been determined by photo-EPR. However, the negative-U centers E_1 at $\sim E_C - 0.38$ eV and E_2 at $\sim E_C - 0.44$ eV [53, 54], which correspond to the Z_1/Z_2 center in the 4H polytype, should be related to the double acceptor level of V_C in 6H-SiC.

11.2.2 Silicon Vacancy

The vacancy at the Si site (V_{Si}) was first identified by EPR in irradiated *n*-type 3C-SiC [55, 56]. In the single negative charge state, V_{Si}^- , the C dangling bonds do not form long bonds and the defect keeps the T_d symmetry with two electrons on the a_1 state in the valence band and other three electrons on the degenerated t_2 state in the bandgap, giving rise to the high-spin state with $S=3/2$. In 4H-SiC, calculations predicted that the C_{3v} symmetry is kept for all charge states of V_{Si} and at different

inequivalent lattice sites [9, 10, 57, 58]. The same V_{Si}^- spectrum was observed in 4H-SiC and its spin $S=3/2$ was confirmed by electron nuclear double resonance (ENDOR) experiments [59]. The EPR spectrum consists of only a single isotropic line with $g=2.0029$. The missing of other lines expected for $S=3/2$ center was explained by too small zero-field splitting. In ODMR studies of the near-infrared photoluminescence (PL) band with the no-phonon lines (NPLs) V1 (1.438 eV) and V2 (1.352 eV) in 4H-SiC and V1 (1.433 eV), V2 (1.398 eV) and V3 (1.366 eV) in 6H-SiC, ODMR spectra, T_{V1} , T_{V2} and T_{V3} , related to these NPLs were observed [60–62]. The observation of the C hf structures due to the hf interaction between the electron spin and the nuclear spin on one ^{13}C atom occupying one of four nearest C sites indicates that these centers are related to the isolated Si vacancy [60, 61]. For resonance excitation at the energies of NPLs, these spectra showed only two lines and no middle line expected for $S=3/2$ center was detected. Therefore, the centers were assigned to the neutral Si vacancy, V_{Si}^0 . EPR studies also suggested the T_V centers to V_{Si}^0 [63–65]. However, EPR and ENDOR studies by Mizuochi and co-workers [66, 67] confirmed that the T_{V2a} center has spin $S=3/2$ and should be related to V_{Si}^- . EPR spectra measured in darkness usually show a strong middle line and very weak low- and high-field lines of the $S=3/2$ centers. In EPR experiments using low modulation fields and low MW powers, the T_{V1a} spectra in 4H- and in 6H-SiC could be resolved from the hf structure due to the interaction with 12 Si in the second neighbor shell [68]. Figure 11.4a shows the T_{V1a} spectrum in 4H-SiC. The T_{V1a} center has the same g value as T_{V2a} and a zero-field splitting at $\mathbf{B}||\mathbf{c}$ of only 0.367 mT. Figure 11.4b shows the EPR spectrum in electron-irradiated HPSI 6H-SiC measured at 293 K in darkness for $\mathbf{B}||\mathbf{c}$. T_{V1a} and T_{V3a} have slight different zero-field splitting and can be separated at this direction (Fig. 11.4b). These centers have the same g value which is slightly larger than the g value of T_{V2a} , causing a small splitting of the main lines as can be seen in the inset of Fig. 11.4b.

In both the 4H and 6H polytypes, the fine-structure splitting is largest for T_{V2a} , while T_{V1a} and T_{V3a} in 6H-SiC have almost the same parameters. This suggests that T_{V2a} may be related to V_{Si}^- at the h-site and T_{V1a} and T_{V3a} may be related to V_{Si}^- at two quasicubic sites. Spin-Hamiltonian parameters of the Si vacancies in different polytypes are summarized in Table 11.3.

11.2.3 Other Primary Radiation-Induced Defects

Frenkel Pairs It has been shown in ZnSe irradiated by electrons at temperatures below 20 K that initial products of radiation damage are close pairs of Zn vacancy and Zn interstitials, $V_{\text{Zn}}^- \text{Zn}_i^{2+}$, in different configurations, whereas the single vacancy production is at least a two-step process [69, 70]. In SiC, EPR studies of n -type 3C-SiC [71] and n - and p -type 4H- and 6H-SiC [72] irradiated with 2 MeV electrons at 80–100 K found a large number of EPR centers which were annealed out at room temperature. In irradiated 3C-SiC, several EPR centers were observed together with the strong signals of V_{Si}^- (Fig. 11.5a). Figs. 11.5b and 11.5c show EPR

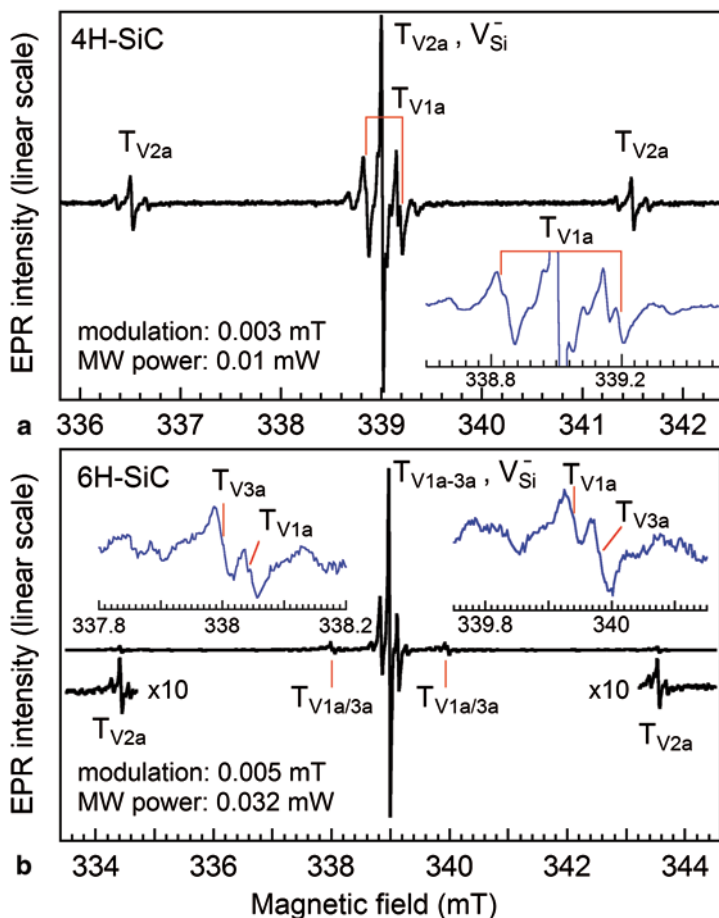


Fig. 11.4 EPR spectra of T_{V1a} and T_{V2a} and T_{V3a} centers measured in darkness at 293 K for $\mathbf{B}||c$ in electron-irradiated semi-insulating (a) 4H-SiC and (b) 6H-SiC. The inset in (a) shows the T_{V1a} lines in 4H-SiC that can be separated from the hf structure due to hf interaction with Si atoms in the second neighbor shell. Due to a slight difference in fine-structure splitting, the T_{V1a} and T_{V3a} lines in 6H-SiC can be seen separately at directions close to the c axis. The MW frequency is 9.503 GHz

signals of LE1 and LE1' centers which were assigned to Frenkel pairs between the negative Si vacancy and Si interstitial in different charge states [71, 72].

The LE1 center shows a hyperfine interaction with four nearest C neighbors which is very similar to that of the negative Si vacancy [71, 72]. However, it has lower symmetry C_{2v} . For usual C_{2v} centers, the distortion occurs randomly along the [100] or equivalent directions and two separated resonances are expected at [100] [73]. In the case of LE1, only one EPR lines was observed for $\mathbf{B}||[100]$ as shown in Figs. 11.5b,c, suggesting that the distortion is preferentially occurred along this direction. This is expected since samples were irradiated with the electron beam

Table 11.3 Spin-Hamiltonian parameters of the negative Si vacancy in 3C-, 4H- and 6H-SiC. X, Y and Z are the directions of the principal axes of \mathbf{g} and \mathbf{A} tensors. θ is the angle between the principal Z axis and the c axis. The A values are given in mT. η^2 is the fraction of the total spin density localized at one of the neighboring C atoms

Center	Parameters	X(\perp)	Y(\perp)	Z(\parallel)	θ	$\eta^2(\%)$	Reference
3C-SiC	\mathbf{g}	2.0029	2.0029	2.0029	0°		[55]
V_{Si}^- , T_{d}	$\mathbf{A}(C_{1-4})$	1.18	1.18	2.86	0°	15.9	[55]
	$\Sigma\eta^2(C_{1-4})$					63.6	[55]
4H-SiC	\mathbf{g}	2.0032	2.0032	2.0032	0°		[64]
V_{Si}^-	\mathbf{g}	2.0028	2.0028	2.0028	0°		[66]
	D			<0.05	0°		[64]
T_{V1a}	$\mathbf{A}(C_1)$	1.21	1.21	2.86	0°	15.7	[59]
	\mathbf{g}	2.004	2.004	2.004	0°		[60]
T_{V2a}	$D(S=1)$			0.16	0°		[60]
	\mathbf{g}	2.0029	2.0029	2.0029	0°		[66]
	$D(S=3/2)$			1.252	0°		[66]
	$\mathbf{A}(C_1)$	1.24	1.24	2.87	0°	15.5	[66]
6H-SiC	$\mathbf{A}(C2-4)$	0.97	1.12	2.7	107.5°	15.6	[66]
	$\Sigma\eta^2(C_{1-4})$					62.2	[66]
	V_{Si}^-	\mathbf{g}	2.0032	2.0032	2.0032	0°	
$T_{\text{V1a}}/T_{\text{V3a}}$	$\mathbf{A}(C_1)$	1.15	1.15	2.87	0°	16.2	[59]
	\mathbf{g}	2.0037	2.0037	2.0035	0°		[60]
	\mathbf{g}	2.0030	2.0030	2.0030	0°		[63]
T_{V2a}	$D(S=1)$			0.98	0°		[60]
	$D(S=1)$			0.855	0°		[63]
	\mathbf{g}	2.0038	2.0038	2.0035	0°		[60]
	\mathbf{g}	2.0030	2.0030	2.0030	0°		[63]
	$D(S=1)$			4.57	0°		[60]
	$D(S=1)$			4.56	0°		[63]
	$\mathbf{A}(C_1)$	1.34	1.34	2.279	0°	14.6	[61]
	$\mathbf{A}(C2-4)$	1.1	1.1	2.86	0°	16.7	[61]
	$\Sigma\eta^2(C_{1-4})$				0°	62.2	[61]

along the [100] direction. With the energy of 2 MeV, electrons can kick out Si atoms which receive enough energies to continue their way. Such a Si atom then kicks the next Si atom along the line at 4.36 \AA (the lattice constant a_0 of 3C-SiC) away from the vacancy and replaces the position. The process leads to the formation of a Frenkel pair between a Si vacancy and a next-nearest Si interstitial along the [100] direction at a distance of $1.5a_0 = 6.54 \text{ \AA}$ from the vacancy. Similar to the case of Frenkel pairs in ZnSe [69, 70], the vacancy will keep its negative charge state, V_{Si}^- , while the interstitial is fully ionized, Si_i^{4+} . The $V_{\text{Si}}^- \text{Si}_i^{4+}$ or $(V_{\text{Si}}^- \text{Si}_i)^{3+}$ Frenkel pair then has the same electron spin $S=3/2$ as V_{Si}^- . After warming up the sample to room

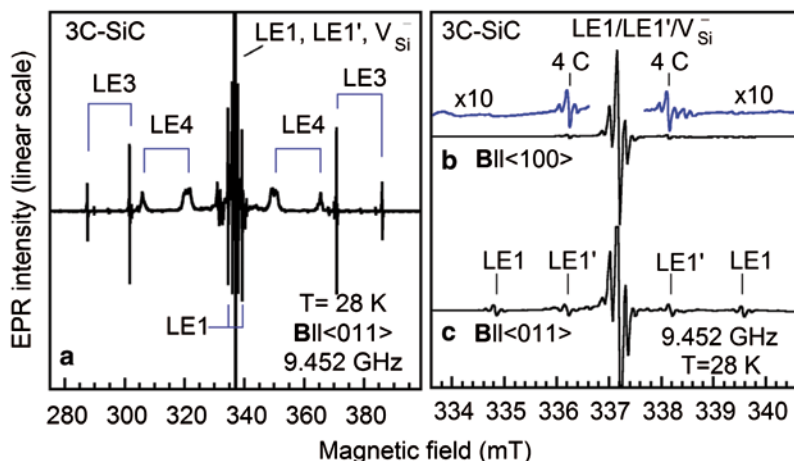


Fig. 11.5 a EPR spectra of the LE1-LE4 centers in *n*-type 3C-SiC irradiated at 80–100 K measured at 28 K for $\mathbf{B}||<011>$. The spectra of LE1 and LE1' centers measured for $\mathbf{B}||<100>$ and $\mathbf{B}||<011>$ are shown in extended magnetic field scale in (b) and (c), respectively. (Source: Reproduced with permission from Son et al. [72]. Copyright 2009, Trans Tech Publications)

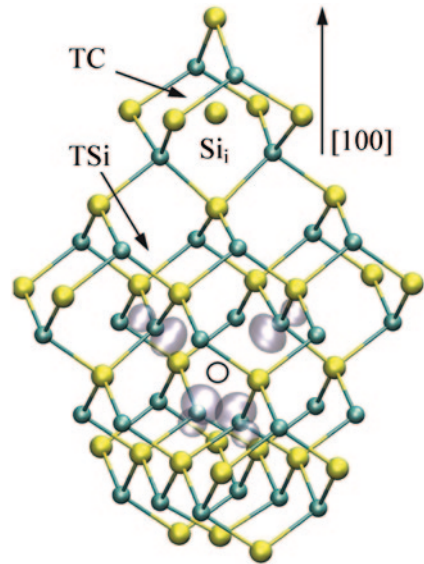
temperature, both the LE1 and LE1' centers were annealed out. The temperature dependence study in the range of 6–295 K suggests that before annealing the central line in Figs. 11.5b–c is mainly from LE1 and no or negligible contribution from the negative Si vacancy.

Supercell calculations of Frenkel pairs $V_{Si}-Si_i$ found that along the $<100>$ direction, Si_i has a stable configuration at the two tetrahedral sites of the cubic lattice, caged by four C atoms (TC) or by four Si atoms (TSi), of which only the TC site has a common rotation axis with the Si vacancy along $<100>$ direction (Fig. 11.6) [71]. The distances between the TC sites along the common $<100>$ direction are: $0.5a_0$, $1.5a_0$ and $2.5a_0$. It is found that the pair with the nearest TC site ($\sim 2.2 \text{ \AA}$ way from the Si vacant site) is unstable and Si_i will recombine with the vacancy without barrier, while pairs with Si_i at the next-nearest-neighbor TC site are stable. The hf constants calculated for the $V_{Si}Si_i^{4+}$ pair are in good agreement with that obtained from EPR for the LE1 center [71], suggesting that LE1 is the Frenkel pair between the negative Si vacancy and Si_i at the next-nearest TC site along the $<100>$ direction.

The LE1' signal is weak and its hf structure could not be detected. Having the same *g*-values and a similar annealing behavior as LE1, the LE1' center may be also related to a $V_{Si}Si_i$ Frenkel pair, but with $S=1$, i.e. with the charge state of either $2+$ or $4+$. Spin-Hamiltonian parameters of LE1 and LE1' are given in Table 11.4.

Similar Si vacancy-Si interstitial pairs were reported earlier in *p*-type 6H-SiC irradiated with low-energy (300 keV) electrons at 77 K [74]. Two EPR spectra with $S=3/2$, one with C_{3v} and the other with C_{1h} symmetry, were assigned to $V_{Si}Si_i$ Frenkel pairs with the Si vacancy in the single negative charge state, carrying the electron spins as in the case of the isolate V_{Si}^- center. In that study, the irradiation was along the *c* axis and only distant Frenkel pairs ($\sim 6.5 \text{ \AA}$ for the axial pair and $\sim 4.5 \text{ \AA}$

Fig. 11.6 The defect model for the LE1 center: the Si vacancy-interstitial Frenkel pair with the second neighbor Si_i at a TC site along the $[100]$ direction. *Open circle* denotes the vacant site. The selected isosurface of the calculated spin density is shown to be localized mainly on four nearest C neighbors of V_{Si} . (Source: Reproduced with permission from Son et al. [71]. Copyright 2009 by the American Physical Society)



for the one that inclined an angle of $\sim 24^\circ$ to the c axis) were observed [74]. No annealing behavior was reported for these defects, but they seem to be stable at room temperature since EPR measurements were performed at 300 K.

Other Primary Radiation-Induced Defects The other two dominant EPR centers, LE3 and LE4, in irradiated 3C-SiC (Fig. 11.5a) have the same isotropic g -value of 2.004 and an effective electron spin $S = 1$. Both centers are characterized by large fine-structure parameters but have different symmetries (C_{2v} for LE3 and D_{2d} for LE4), indicating a distortion along the $\langle 100 \rangle$ direction as LE1. Comparing to the predicted symmetry for C split-interstitials in 3C-SiC [12], the LE3 and LE4 centers may be related to the $\langle 100 \rangle$ C split-interstitials at the Si and C site, respectively.

In 4H- and 6H-SiC irradiated at 80–100 K, several $S = 1$ EPR centers, LE6-LE10, with C_{1h} symmetry and zero-field splitting in the range of ~ 554 – 670 G were observed. Most of them were annealed out after warming up the sample to room temperature. In p -type materials irradiated at low temperatures, the C vacancy was not observed (neither in darkness nor under illumination) while the dominating EPR signals are EI1 and EI3 [75]. The EI1 and EI3 centers were previously suggested to be related to complexes between H and the C vacancy [14]. A later calculation [58] suggested the C split-interstitial in different charge states as defect models for these centers, but available data are still not sufficient for identification. For LE6-LE10 centers, the studies of ligand hf interaction were hindered by severe overlapping between the spectra. Identification of these defects may require help from theoretical modeling of the spin-spin interaction to determine the fine-structure parameters for comparison with EPR data.

The LE5a-LE5c spectra are also the products of electron irradiation at low temperatures [72]. They are also known as spectra I, II in 4H-SiC and I, II, and III in

Table 11.4 Spin-Hamiltonian parameters of EPR centers in SiC irradiated at ~80–100 K. Fine-structure parameters D and E are given in mT. θ is the angle between the principal z axis of the g tensor and the c axis. Here $D=3D_{zz}/2$ and $E=(D_{xx}-D_{yy})/2$. The LE5a-c centers are also known as the I, II, and III centers in 4H- and 6H-SiC [76]. Data for LE1-LE10 are from Refs. [71, 72] and for EI1 and EI3 are from Ref. [75]

Center	Spin	g_{xx}	g_{yy}	g_{zz}	θ	D	E
3C-SiC							
LE1, C_{2v}	3/2	2.0029	2.0029	2.0029		1.19	-0.40
LE1', C_{2v}	1	2.0029	2.0029	2.0029		1.00	-0.33
LE2, C_{3v}	1/2	2.0023	2.0023	2.0035			
LE3, C_{2v}	1	2.0040	2.0040	2.0040		49.49	-6.63
LE4, D_{2d}	1	2.0040	2.0040	2.0040		59.00	
4H-SiC							
EI1, C_{1h}	1/2	1.9962	2.0019	2.0015	41°		
EI1', C_{1h}	1/2	1.9960	2.0019	2.0016	30°		
LE5a, C_{1h}	1/2	2.0162	2.0035	2.0412	63.5°		
LE5b, C_{1h}	1/2	2.0144	2.0029	2.0337	51.3°		
LE6, C_{1h}	1	2.0060	2.0060	2.0060	45.3°	55.42	
LE7, C_{1h}	1	2.0060	2.0060	2.0060	59.5°	67.06	-0.75
LE8, C_{1h}	1	2.0060	2.0060	2.0060	44.5°	63.75	1.14
LE9, C_{1h}	1	2.0060	2.0060	2.0060	45.9°	66.74	0.75
LE10, C_{1h}	1	2.0060	2.0060	2.0060	47.5°	57.66	
6H-SiC							
LE5a, C_{1h}	1/2	2.0164	2.0037	2.0407	63.3°		
LE5b, C_{1h}	1/2	2.0139	2.0041	2.0327	48.3°		
LE5c, C_{1h}	1/2	2.0079	2.0021	2.0452	65.2°		
LE6, C_{1h}	1	2.0060	2.0060	2.0060	44.5°	55.42	
LE7, C_{1h}	1	2.0060	2.0060	2.0060	58.5°	67.06	-0.75

the 6H polytype, forming in p -type materials after electron irradiation at room temperature [76]. These centers are characterized by a large anisotropy in the g -values. Based on calculations of g -values, these centers were assigned to the antisite $Si_C C_{Si}$ pairs [77, 78].

11.2.4 Secondary Radiation-Induced Defects

Carbon Antisite-Vacancy Pairs In compound semiconductors, the antisite-vacancy (AV) pairs are the counterpart of the isolated vacancies and can be energetically stable or metastable defects with respect to the vacancies. Theory predicted that in III-V semiconductors, such as GaAs, the cation Ga vacancy can transform into more stable anion (As) AV pairs [79, 80]. In SiC, being more electronegative than silicon, carbon is an anion. The formation energy of the carbon AV pair ($C_{Si} V_C$)

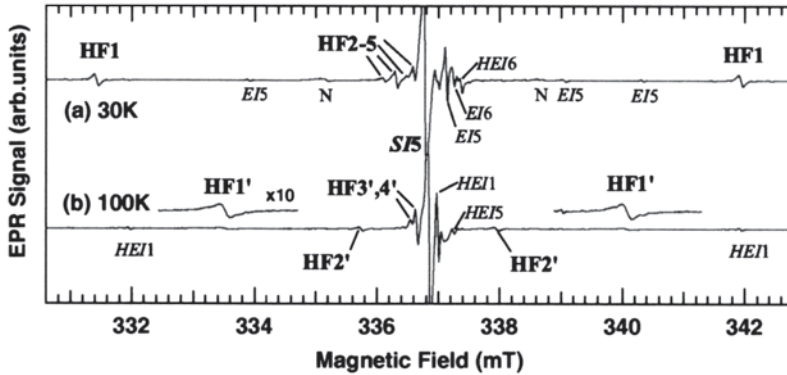


Fig. 11.7 EPR spectra of $C_{Si}V_C^-$ (or the SI5 center [21, 22]) in *n*-type 4H-SiC irradiated with 2 MeV electrons at 850 °C measured under illumination at (a) 30 K and (b) 100 K for $B||c$ at 9.452 GHz. The signals of EI5/6 (or V_C^+), HEI1 (or V_C^-), and HEI5/6 centers and the shallow N donors are indicated. (Source: Reproduced with permission from Umeda et al. [84]. Copyright 2006 by the American Physical Society)

is predicted to be relative low and the complex is stable [12, 81, 82]. In the hexagonal SiC polytypes, the AV pair can have on- and off-axis configurations corresponding to the position of the C_{Si} antisite being along or off the *c* axis, respectively. In the on-axis configuration, both C_{Si} and V_C being on the same *h*- or *k*-site and the $C_{Si}V_C(hh)$ and $C_{Si}V_C(kk)$ pairs have C_{3v} symmetry. If C_{Si} is off-axis, the corresponding $C_{Si}V_C(hk)$ and $C_{Si}V_C(kh)$ centers have C_{1h} symmetry.

The negative charge state of the carbon AV pair, $C_{Si}V_C^-$, was identified by Umeda and co-workers [83, 84] in *n*-type 4H-SiC irradiated with 2 MeV electrons at 850 °C. In the single negative charge state, the pair has an electron spin $S=1/2$ and is EPR active. Figs. 11.7a and 11.7b show the $C_{Si}V_C^-$ spectrum measured under illumination at 30 K and 100 K, respectively. The spectrum can also be weakly detected in samples irradiated at room temperature and the signal becomes much stronger after annealing at 800–850 °C. At low temperatures ($T < 50$ K) the center has C_{1h} symmetry and the spectrum shows a large-splitting Si hf structure due to the hf interaction with two nearest Si neighbors, and two small-splitting hf structures of Si and C (labeled as HF1–HF3 in Fig. 11.7b). The assignment of these hf structures to Si and C was confirmed by ENDOR measurements [84]. In the temperature range of 50–60 K, the center transforms from C_{1h} to C_{3v} symmetry which induces a large change in the hf interaction (Fig. 11.7). The spin-Hamiltonian parameters of the center are in good agreement with those obtained from supercell calculations for the negative carbon AV pair and the center has therefore been assigned to $C_{Si}V_C^-$. The spin-Hamiltonian parameters for the center are summarized in Table 11.5. It is noticed that $C_{Si}V_C^-$ has the same spin-Hamiltonian parameters as the SI5 defect which is often found in HPSI SiC substrates [21, 22] and was previously assigned to the negative divacancy [85].

The observation of the $C_{Si}V_C^-$ signal often requires illumination with light of photon energies larger than ~ 1.1 eV. In the calculations, the $(-|0)$ and $(2-|1-)$ levels

Table 11.5 Spin-Hamiltonian parameters of $C_{Si}V_C^-$ and $C_{Si}V_C^+$ in 4H-SiC at different temperatures. X, Y and Z are the directions of the principal axes of \mathbf{g} and \mathbf{A} tensors. θ is the polar angle of the principal Z axis, measured in degrees. The principal A values are given in mT

Center	Parameters	X(\perp)	Y(\perp)	Z(\parallel)	θ
$C_{Si}V_C^-, C_{3v}$ 100 K [84]	\mathbf{g}	2.00339	22.00339	2.00484	0°
	$\mathbf{A}(\text{Si} \times 1)$	6.38	6.38	8.02	109°
	$\mathbf{A}(\text{C} \times 1)$	1.77	1.77	2.22	0°
$C_{Si}V_C^-, C_{1h}$ 30 K [84]	\mathbf{g}	2.00372	2.00259	2.00534	10°
	$\mathbf{A}(\text{Si} \times 2)$	10.16	10.04	12.99	111°
	$\mathbf{A}(\text{C} \times 2)$	1.3	1.3	1.8	
	$\mathbf{A}(\text{Si} \times 2)$	0.9	0.9	1.1	
$C_{Si}V_C^+(\text{hh}), C_{3v}$ HEI9a, 295 K [88]	\mathbf{g}	2.00408	2.00408	2.00227	0°
	$\mathbf{A}(\text{C})$	2.27	2.27	8.25	0°
	$\mathbf{A}(\text{Si})$	1.7–2.9	1.7–2.9	1.7–2.9	
$C_{Si}V_C^+(\text{kk}), C_{3v}$ HEI9b, 295 K [88]	\mathbf{g}	2.00379	2.00379	2.00195	0°
	$\mathbf{A}(\text{C})$	3.71	3.71	9.95	0°
	$\mathbf{A}(\text{Si})$	1.7–2.9	1.7–2.9	1.7–2.9	
$C_{Si}V_C^+(\text{kh}), C_{1h}$ HEI10a, 295 K [88]	\mathbf{g}	2.00348	2.00258	2.00226	145°
	$\mathbf{A}(\text{C})$	2.60	2.65	8.75	109°
	$\mathbf{A}(\text{Si})$	1.7–2.9	1.7–2.9	1.7–2.9	
$C_{Si}V_C^+(\text{hk}), C_{1h}$ HEI10b, 295 K [88]	\mathbf{g}	2.00399	2.00345	2.00263	116°
	$\mathbf{A}(\text{C})$	2.31	2.45	8.44	109°
	$\mathbf{A}(\text{Si})$	1.7–2.9	1.7–2.9	1.7–2.9	

of the center were found to be at ~ 1.0 eV and 0.9 eV below the conduction band minimum E_C [84]. Photo-EPR studies [86] suggested that the $(2-|1-)$ level of $C_{Si}V_C^-$ is in the range ~ 0.8 – 1.1 eV below E_C .

In the single positive charge state, the carbon AV pair has also spin $S=1/2$. In p -type 4H-SiC irradiated with 3 MeV electrons at ~ 800 – 850 °C, the EPR signal of the positive C vacancy is dominating. However, when using very low MW powers, only the HEI9a/9b and HEI10a/10b signals are observed as shown in the EPR spectrum measured at 295 K in darkness for $\mathbf{B} \parallel \mathbf{c}$ (Fig. 11.8) [87, 88]. Several ^{29}Si hf lines of these centers can be seen in the figure. Four different ^{13}C hf structures related to these four main lines can be seen in the $\times 10$ and $\times 20$ scale parts of the spectrum. The angular dependence studies showed that HEI9a and HEI9b have C_{3v} symmetry, while the HEI10a/10b centers have C_{1h} symmetry. Their principal values of the \mathbf{g} tensor and the ^{29}Si and ^{13}C hf A-tensors are given in Table 11.5. The hf parameters obtained from calculations for four different configurations of the $C_{Si}V_C^+$ center are shown to be in very good agreement with those determined from EPR, allowing the identification of HEI9a and HEI9b to the on-axis configurations of the AV pair, $C_{Si}V_C^+(\text{hh})$ and $C_{Si}V_C^+(\text{kk})$, and the HEI10a and HEI10b to its off-axis configurations, $C_{Si}V_C^+(\text{kh})$ and $C_{Si}V_C^+(\text{hk})$, respectively [88].

Divacancy Divacancies are common defects in semiconductors, comprising two vacant nearest-neighbor lattice sites. In silicon, with the isolated vacancy being mobile already at low temperatures (~ 70 K in n -type and ~ 200 K in p -type materials [89]), divacancies can be formed directly during irradiation by high-energy

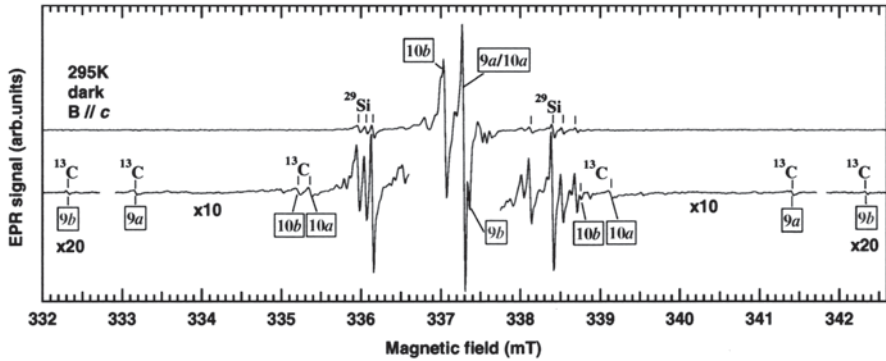


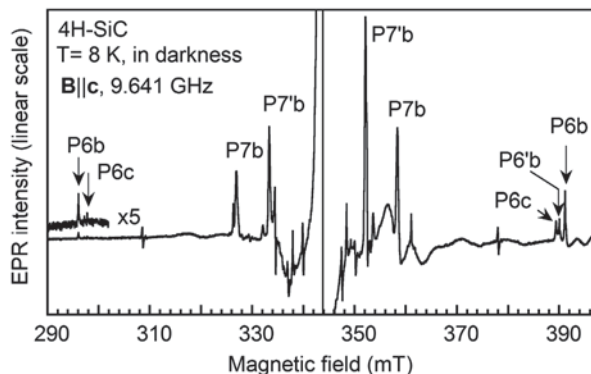
Fig. 11.8 EPR spectra in *p*-type 4H-SiC irradiated with 3 MeV electrons at ~ 800 – 850°C showing the HEI9a/9b and HEI10a/10b lines (depicted as 9a, 9b, 10a and 10b, respectively) from four different configurations of $\text{C}_{\text{Si}}\text{V}_{\text{C}}^+$ measured at 295 K using MW power of $0.2 \mu\text{W}$. The MW frequency is 9.452 GHz. (Source: Reproduced with permission from Umeda et al. [88]. Copyright 2007 by the American Physical Society)

electrons at room temperature [90]. In SiC, single vacancies are highly thermally stable and post annealing after irradiation is required to form divacancies, $\text{V}_{\text{Si}}\text{V}_{\text{C}}$, in a measurable concentration. The divacancy is predicted to be a very stable defect in SiC [85, 91, 92]. The neutral divacancy, $\text{V}_{\text{Si}}\text{V}_{\text{C}}^0$, was identified in 4H- and 6H-SiC by EPR and ab initio calculations [93–97]. The $\text{V}_{\text{Si}}\text{V}_{\text{C}}^0$ centers is known as the P6/P7 EPR centers which were first reported in heat-treated *n*-type 6H-SiC [98] and were later found to be common in as-grown *n*-type [99] and HPSI SiC substrates [21, 22, 51, 100].

In *n*-type 6H-SiC heated to 2000°C and quenched, the P6/P7 EPR spectra with $S=1$ were observed under illumination [98]. Based on their symmetry (C_{3v} for P6 and C_{1h} for P7), the centers were suggested to be related to excited states of divacancies [98]. Later EPR and ab initio calculations [101] suggested the P6/P7 centers to be the C vacancy-antisite pairs. Their magnetic circular dichroism of the absorption (MSDA) and MCDA-detected EPR experiments showed that in 6H-SiC, the EPR spectra of the P6/P7 centers at the three inequivalent lattice sites are related to NPLs in the near-infrared spectral region: 1.075 eV (P6a), 1.048 eV (P6b), 1.011 eV (P6c), 1.049 eV (P7a), 1.030 eV (P7b) and 0.999 eV (P7c) [101]. In 4H-SiC samples having strong EPR signal of P6/P7 centers, several NPLs with similar energies at 0.9975, 1.0136, 1.0507, and 1.0539 eV were observed in absorption spectra [102]. The relation between these NPLs and the EPR P6/P7 centers has not been confirmed.

Figure 11.9 shows an EPR spectrum in electron-irradiated and annealed (at $\sim 800^\circ\text{C}$) *n*-type 4H-SiC measured in darkness at 8 K for $B||c$, confirming that the EPR signals of P6/P7 centers are related to a triplet ground state. As can be seen in the figure, for the large zero-field splitting lines P6b/P6c, the high-field lines corresponding to the transitions $M_S = -1 \leftrightarrow M_S = 0$ are much stronger than the low-field components, indicating a positive zero-field splitting ($D > 0$). The principal values

Fig. 11.9 EPR spectrum in electron-irradiated and annealed (at 850 °C) *n*-type 4H-SiC measured in darkness at 8 K for **B**||**c** showing the signals of the P6/P7 centers. (Source: Reproduced with permission from Son et al. [93]. Copyright 2006 by the American Physical Society)



and the direction of the symmetry axis of the hf tensors of nearest C neighbors obtained from EPR are in good agreement with the calculated values for the neutral divacancy. Even small differences in the hf tensors of P6b and P6'b are also observed by EPR and calculations, allowing the assignment of P6b and P6'b to the axial configurations of the neutral divacancy at the h- and k-site, respectively [93]. The spin-Hamiltonian parameters of $V_{Si}V_C^0$ in 4H-SiC are given in Table 11.6.

Supercell calculations predicted the $(+|0)$ and $(0|-)$ levels of $V_{Si}V_C$ to be at ~ 0.5 and ~ 1.4 eV above the valence band maximum, respectively [93]. EPR studies in irradiated HPSI 4H-SiC showed that in darkness and at 77 K, only the signal of V_C^+ could be detected. However, when increasing temperature to 293 K, the signal of $V_{Si}V_C^0$ could be weakly observed [100]. This suggests that the $(0|-)$ level of the divacancy may lie slightly below the $(+|0)$ level of V_C at $\sim E_V + (1.5-1.6)$ eV, so that at room temperature it could be partly thermally ionized and changed to the neutral charge state. A possible candidate for the $(0|-)$ level of the divacancy is the EH6 center at $\sim E_C - 1.65$ eV, which often appears together with EH7 in materials irradiated with high-energy electrons [27].

Neutral ($V_C-C_{Si}V_C$)⁰ Complex The formation of the complex between a C_{Si} anti-site and two nearest neighbor C vacancies, $V_C C_{Si} V_C$, as products of annealing of the carbon AV pair, $C_{Si} V_C$, in V_C -rich materials has theoretically been predicted [85]. Those calculations also suggested that further annealing transforms this complex defect to the divacancy. Such a defect has not so far been observed by EPR. However, a complex between $C_{Si} V_C$ and another V_C in the third neighbor of the C_{Si} anti-site has been identified by EPR and *ab initio* supercell calculations [102]. This $S=1$ defect was reported before as the P4 center in heat-treated 6H-SiC [98, 104] and as the EI4 center in *p*-type 4H- and 6H-SiC irradiated by electrons at 400 °C [105]. In those studies, only an isotropic and small-splitting Si hf structure was observed and the model of a coupled V_C pair was suggested based on the symmetry of the center and the direction of the principal axis of the **D** tensor.

Figure 11.10 shows the EPR spectrum of the EI4 center in HPSI 4H-SiC after electron-irradiation and annealing at ~ 750 °C. After irradiation, the signal of V_C^+ is dominating while the EI4 signal can be weakly detected. After annealing at

Table 11.6 Spin-Hamiltonian parameters of the neutral divacancy in 4H-SiC. All the centers have the same isotropic $g=2.003$. The polar angle θ of the principal Z axis with respect to the c axis is given in degrees. The principal values of the \mathbf{A} tensor and the fine-structure parameters D and E are given in mT. Here $D=(3/2)D_{zz}$ and $E=(D_{xx}-D_{yy})/2$. η^2 is the fraction of the total spin density localized at one of the neighboring C atoms

Center	Parameters	X(\perp)	Y(\perp)	Z(\parallel)	θ	$\eta^2(\%)$
$V_{Si}V_C^0(hh)$	D			47.80	0°	
P6b, C_{3v}	$\mathbf{A}(C_{1-3})$	1.89	1.78	3.93	73°	20.1
	$\mathbf{A}(Si_{2-4})$	~ 0.1	~ 0.1	~ 0.1		0.06
	$\Sigma\eta^2(C_{1-3}+Si_{2-4})$					60.5
	D			46.62	0°	
$V_{Si}V_C^0(kk)$	$\mathbf{A}(C_{1-3})$	1.68	1.61	3.71	73°	19.7
P6'b, C_{3v}	$\mathbf{A}(Si_{2-4})$	~ 0.1	~ 0.1	~ 0.1		0.06
	$\Sigma\eta^2(C_{1-3}+Si_{2-4})$					59.3
	D			47.80	70.5°	
	E			9.62		
$V_{Si}V_C^0(hk)$	$\mathbf{A}(C_1)$	Not observed				
P7b, C_{1h}	$\mathbf{A}(C_{3,4})$					
	D			43.63	71°	
	E			1.07		
$V_{Si}V_C^0(kh)$	$\mathbf{A}(C_{1-3})$	1.86	1.86	3.93	2°	19.9
P7'b, C_{1h}	$\mathbf{A}(Si_{2-4})$	1.71	1.61	3.89	70°	21.2
	$\Sigma\eta^2(C_{1-3})$					62.3

$\sim 750^\circ\text{C}$, the EI4 signal becomes comparable to the V_C^+ signal and its large-splitting Si hf structures could be seen (Fig. 11.10). Several other Si and C hf structures with smaller splittings were also observed.

Supercell calculations of the distant $V_C V_C$ showed inconsistent hf interactions compared to the experiment, ruling out the previous suggestion of the V_C pair model for EI4. Annealing studies [103] showed that the EI4 center is indeed transformed to the divacancy, suggesting the possible combination between a $C_{Si}V_C$ pair and an isolated V_C . Calculations of $C_{Si}V_C-V_C$ complexes with the $C_{Si}V_C$ pair approaching V_C from its V_C part showed that the complex will have the singlet and not triplet ground state as EI4. Other configurations of the complex with $C_{Si}V_C$ approaching V_C by its C_{Si} part, where C_{Si} and V_C are not immediate neighbors, can have either C_1 or C_{1h} symmetry. Calculations found equally stable $S=1$ and $S=0$ state for C_1 configuration a more stable (by 0.04 eV) triplet $S=1$ state for the C_{1h} configuration. The model for the $C_{Si}V_C-V_C$ defect in the neutral charge state and C_{1h} symmetry with V_C in the third neighbor of C_{Si} is shown in Fig. 11.11. The hf interactions with Si and C neighbors of this complex were calculated and the obtained Si and C hf constants showed a good agreement with corresponding values determined by EPR, allowing a conclusive identification of the EI4 center as the neutral $(C_{Si}V_C-V_C)^0$ defect [103]. The Spin-Hamiltonian parameters of the center are given in Table 11.7.

Fig. 11.10 EPR spectrum in HPSI 4H-SiC after irradiation with 2 MeV electrons and subsequent annealing at $\sim 750^\circ\text{C}$ measured at 77 K in darkness for $\mathbf{B}\parallel\mathbf{c}$, showing the EI4 signal appearing together with the V_C^+ signal. Two large-splitting hf lines of EI4 due to the interaction with ^{29}Si atoms are indicated

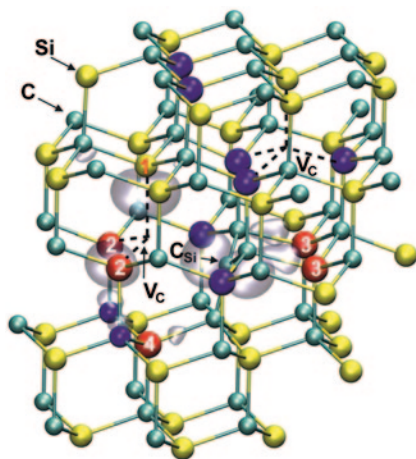
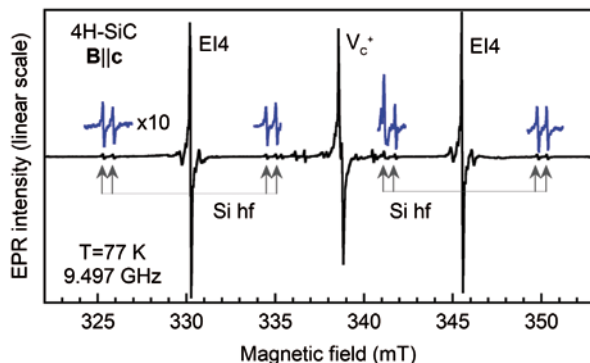


Fig. 11.11 Suggested defect model for the EI4 center in the 4H-SiC crystal structure. The grey lobes are the isosurfaces of the calculated spin density. The atoms most important for the detected hf structure are indicated by 1–4 which should read as Si_{1-4} atoms. The C_{Si} atom binds to three other C atoms in the middle of the figure, having the Si_3 and Si_4 atoms as its second neighbors. The Si_{2-4} atoms have hyperfine splitting larger than 1 mT while the other dark (blue) balls show those Si and C atoms that have hf splitting of about 0.5 mT. (Reproduced with permission from Carlsson et al. [103]. Copyright 2006 by the American Physical Society)

11.2.5 Intrinsic Defects in High-Purity Semi-Insulating SiC

For minimizing the parasitic capacitance, which limits the performance of high-frequency wide bandwidth devices at high frequencies, semi-insulating (SI) substrates are often used. In such substrates, deep levels of either impurities or intrinsic defects are introduced at a concentration high enough to compensate all shallow dopants to pin the Fermi level near the middle of the bandgap. High resistivity can then be obtained, but at a price of the presence of deep levels in the material. These

Table 11.7 Spin-Hamiltonian parameters of the $(C_{Si}V_C-V_C)^0$ complex (or E14 center) in 4H-SiC. Parameters and units are defined as in Table 11.6. The center has an isotropic g value of 2.004

Parameters	X(\perp)	Y(\perp)	Z(\parallel)	θ	$\eta^2(\%)$
4H-SiC					
D			36.77	54°	
E			6.95		
$A(Si_1)$	6.73	6.20	9.20	5°	27
$A(C_{Si})$	1.50	1.50	4.49	71°	9
$A(Si_2)$	~ 1.07	~ 1.07	$\sim 0.86-1.60$		
$A(Si_3)$	~ 1.07	~ 1.39	$\sim 0.86-1.60$		
$A(Si_4)$	~ 1.39	~ 1.60	$\sim 0.86-1.60$		
6H-SiC					
D			35.06	54°	
E			6.84		
$A(Si_1)$	6.41	6.41	8.87	1°	25

deep levels may act as electron traps, leading to the drop of the drain current of the device. HPSI SiC substrates are desirable and have been developed since more than a decade [106–109]. In such materials, the concentrations of common impurities, such as the N donor and B acceptor, are reduced to typically less than mid 10^{15} cm^{-3} which then can be compensated by deep levels of intrinsic defects introduced during the growth.

In the first generation of HPSI SiC materials grown by physical vapor transport (PVT) or high-temperature CVD (HTCVD), V_C , V_{Si} , $V_{Si}V_C$ and $C_{Si}V_C$ are common defects [21, 22, 100, 110, 111]. These defects were introduced during the growth but their concentrations were not well controlled, ranging from high $\sim 6-7 \times 10^{14} \text{ cm}^{-3}$ to $\sim 5-6 \times 10^{15} \text{ cm}^{-3}$ [100]. Depending on the relative concentration of intrinsic defects, HPSI SiC substrates can be classified into different types having different activation energies $E_a \sim 0.8-0.9$, $\sim 1.1-1.3$ and $\sim 1.5-1.6$ eV. In substrates with lowest activation energies, V_{Si} and $C_{Si}V_C$ are dominating, while in substrates with $E_a \sim 1.1-1.3$ eV, V_C is also present with a comparable concentration. In substrates with $E_a \sim 1.5-1.6$ eV, the concentration of V_C and $V_{Si}V_C$ is in the mid 10^{15} cm^{-3} range, while the EPR signals of V_{Si}^- and $C_{Si}V_C^-$ are absent. High-temperature annealing studies (up to $\sim 1600^\circ\text{C}$) [100] showed that in V_{Si}^- and $C_{Si}V_C^-$ -rich substrates the activation energies reduces to $E_a \sim 0.6-0.7$ eV and the resistivity also decreases from more than $\sim 10^9$ to $\sim 10^5 \Omega \text{ cm}$, whereas substrates with $E_a \sim 1.5-1.6$ eV show stable SI properties. Annealing behaviors of these defects are shown in Fig. 11.12.

The studies suggested V_C and $V_{Si}V_C$ as suitable defects for controlling the SI properties in SiC. With a single donor level EH7 at $E_C - (1.5-1.6)$ eV and the double acceptor level at $\sim E_C - (0.6-0.65)$ eV, V_C can compensate both p -type and n -type materials. Controlling the concentration of V_C during growth is also easier compared to the divacancy. Therefore, V_C appears as the most suitable defect for controlling the SI properties in SiC. We have noticed that after a decade of development, current commercial HPSI 4H-SiC substrates are pure and show only the EPR signal of V_C^+ . It seems that in current HPSI 4H-SiC material, the N shallow donor has lower concentrations than residual B acceptor and is compensated by B, which

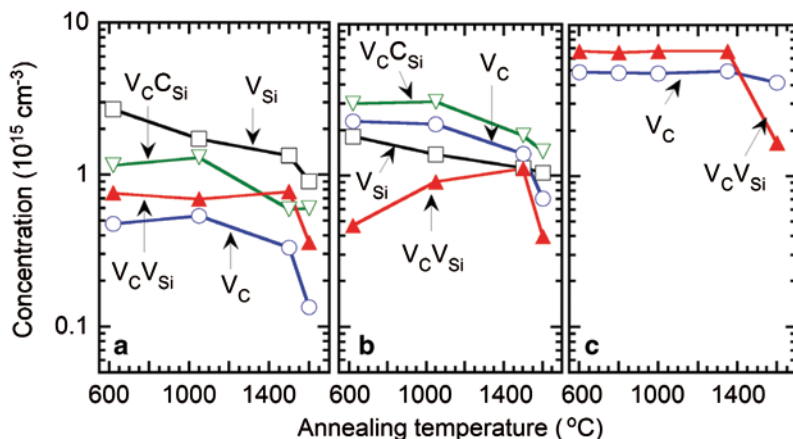


Fig. 11.12 Annealing behavior of intrinsic defects in different types of HPSI 4H-SiC substrates with different activation energies E_a : **a** ~ 0.8 – 0.9 eV, **b** ~ 1.1 – 1.3 eV and **c** ~ 1.5 – 1.6 eV. (Source: Reproduced with permission from Son et al. [100]. Copyright 2006 by the American Physical Society)

is in turn compensated by the C vacancy, pinning the Fermi level at the (+|0) level of V_C .

11.3 Radiation-Induced Defects in III-Nitrides

11.3.1 Defects in Irradiated GaN

ODMR Studies Magnetic resonance has been used to study defects in GaN during the last 20 years. In the 1990s and 2000s, GaN was mainly available in thin films grown on foreign substrates such as sapphire and EPR studies were mainly related to impurities and dopants which can be doped at high concentrations. For radiation-induced defects in thin films, ODMR is more suitable. Several defects were observed by ODMR in GaN films irradiated with high-energy electrons at room temperature but their origin was not clear [112–114].

In an ODMR study of n -type GaN irradiated at 4.2 K, a defect labelled as L5 with $S=1/2$ was observed by monitoring the broad PL band at ~ 0.95 eV [115–117]. Figure 11.13 shows the L5 spectra measured at two different directions of the magnetic field, 90° ($B \perp c$) and 45° from the c axis. The L5 center has C_{3v} symmetry and anisotropic g values: $g_{\parallel} = 2.000(1)$ and $g_{\perp} = 2.000(3)$ [117]. A slightly anisotropic hf structure due to the interaction between the electron spin and the nuclear spin of a single Ga nucleus having two $I=3/2$ isotopes ^{69}Ga ($\sim 60.1\%$) and ^{71}Ga ($\sim 39.9\%$) with the ratio of the magnetic moment $\mu^{69}/\mu^{71} \sim 0.78703$ was observed. The principal values of the A tensor for ^{69}Ga were determined as $A_{\parallel} = 4.01(3)$ GHz (~ 143.2 mT) and $A_{\perp} = 3.77(1)$ GHz (~ 134.6 mT) [117]. Isochronal annealing shows

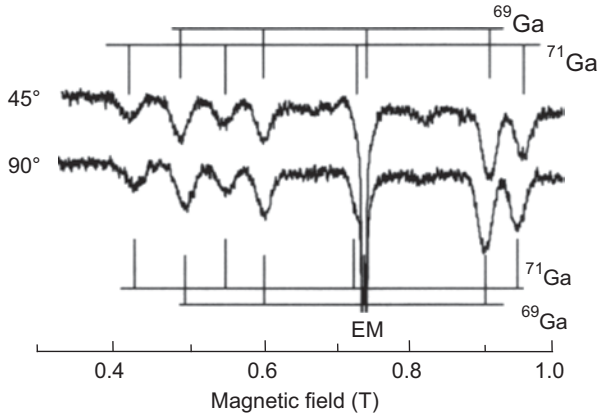


Fig. 11.13 ODMR signals observed in the PL band at ~ 0.95 eV in *n*-type GaN after 2.5 MeV electron irradiation *in situ* at 4.2 K to a fluence of $\sim 5 \times 10^{17}$ cm $^{-2}$, showing the ^{69}Ga and ^{71}Ga hf structures of the L5 spectrum at $\mathbf{B} \perp c$ (90°) and at \mathbf{B} 45° off the *c* axis. The signals of the L5 and the effective mass (EM) donor are negative, indicating spin-dependent recombination between the two which competes with the luminescence process. (Source: Reproduced with permission from Chow et al. [115]. Copyright 2000 by the American Physical Society)

that the L5 defect becomes mobile at room temperature, while other ODMR signals, L1 and L2 [112, 113], previously seen after irradiation at room temperature appear. Based on its large hf splitting of a single Ga atom and low-temperature migration, the L5 center was identified as the Ga interstitial in the 2+ charge state, Ga_i^{2+} [115]. In more heavily irradiated GaN samples, a positive ODMR signal, labelled L6, emerges at various stages throughout the low-temperature annealing [117, 118]. The L6 center has *g* values: $g_{\parallel} = 1.999(2)$, $g_{\perp} = 1.999(4)$ and a similar hf interaction with a single Ga atom as L5 with slightly larger hf constants (for ^{69}Ga): $A_{\parallel} = 4.05(4)$ GHz (~ 144.7 mT) and $A_{\perp} = 3.85(2)$ GHz (~ 137.5 mT). Both L5 and L6 disappear upon prolonged annealing at room temperature and so does the 0.95 eV PL band. The L5 and L6 defects were assigned to Ga_i^{2+} at two different interstitial sites in the hexagonal lattice. L6 is less stable than L5; it anneals faster at 295 K. It is not clear which defect is related to the tetrahedral (T) and octahedral (O) interstitial sites. Calculations by Boguslawski et al. [119] predicted the T site to be ~ 0.2 eV more stable than the O site. However, other calculations [120–122] suggested that the O site is the more stable for Ga_i in all charge states.

Irradiation of Mg-doped *p*-type GaN *in situ* at 4.2 K by 2.5 MeV electrons also creates the broad PL band at ~ 0.95 eV but ODMR signals related to this near infrared emission are much weaker [123]. In addition, after annealing at 180 K, an ODMR center with $S=1$, labeled L8, was observed by monitoring the visible PL band at ~ 2.8 eV. The L8 has an isotropic *g* value of 2.007(4) and an axial fine-structure tensor with the principal values $D_{zz} = \pm 8.35(14)$ GHz (~ 298.0 mT) and $D_{xx} = D_{yy} = \mp 4.18(7)$ GHz (~ 149.4 mT), where the *z* axis is $\sim 54.7^\circ$ off the *c* axis. This defect is stable at room temperature and can also be produced by irradiation at room temperature but at a greatly reduced rate. The L8 center was tentatively as-

signed to a Frenkel excitonic state with the two $S=1/2$ spins separated by a distance of $\sim 1.84 \text{ \AA}$ which is roughly equal to a Ga-N bond (1.94 \AA) along the direction of a basal bond [123]. The validity of this defect model for L8 should be checked by calculations to verify if a Frenkel pair with such a short distance between the components can be stable at room temperature.

The L1 center [$g_{\parallel}=2.008(1)$ and $g_{\perp}=2.004(1)$] in irradiated n -type shows a partly resolved hf structure at some directions of the magnetic field. The hf structure was assigned to be due to the interaction between the electron spin and the nuclear spins of three nearest Ga neighbors [for ^{69}Ga : $A_{\parallel}=A_{\perp}\sim 0.10(1)$ GHz (~ 3.6 mT)]. Based on this Ga hf structure, three defect models were suggested for L1 [117]: (i) Trapped N vacancy where one of the Ga neighbor is replaced by an impurity of group II such as Mg or Zn, (ii) Trapped Ga vacancy with one of the N neighbor is replaced by a group-V donor such as O, and (iii) The isolated Ga vacancy in the double negative charge state, V_{Ga}^{2-} . In the third model, the Ga hf structure would be due to the interaction with three Ga atoms in the second neighbor shell. The electronic structure of L1 still remains unclear.

Interestingly, Hai et al. [124] observed an ODMR center, labeled Ga-1, in as-grown GaN doped with Zn. The Ga-1 center is related to the blue PL band at 2.8 eV. It has $S=1/2$ with axial symmetry [$g_{\parallel}=2.008(2)$ and $g_{\perp}=2.001(2)$] and shows a clear hf structure due to the interaction with a single Ga atom. Its hf parameters [for ^{69}Ga : $A_{\parallel}=0.760(5)$ GHz (~ 27.1 mT), $A_{\perp}\sim 0.560(5)$ GHz (~ 20 mT), and for ^{71}Ga : $A_{\parallel}=0.965(5)$ GHz (~ 34.5 mT), $A_{\perp}\sim 0.713(5)$ GHz (~ 24.5 mT)] indicate that the defect involves a single Ga atom. The axial symmetry, the hf interaction and the defect formation suggest a Ga-related complex nature of the Ga-1 center.

To our best knowledge, since the study by Johannesen *et al.* in 2004 [118], no ODMR investigation of radiation-induced defects in GaN has been reported. Thus, except for the L5 and L6 centers, which are related to isolated Ga_i^{2+} , other ODMR centers have not been identified.

EPR Studies The availability of bulk GaN since the last ten years makes it possible for EPR studies of radiation-induced defects in GaN. However, it appears that GaN irradiated by high-energy electrons with fluences up to $\sim 10^{18} \text{ cm}^{-2}$ gives rise to no EPR signals or just a weak signal of the shallow donor. It was predicted by theoretical calculations that in equilibrium both cation and anion vacancies in GaN will be in the charge states that are not EPR active. According to calculations [119–122, 125–127] the neutral and negative charge states of the N vacancy, V_{N} , lie in the conduction band and the defect will be in the positive charge state ($S=0$), while the Ga vacancy, V_{Ga} , will capture three more electrons to become triply negatively charged V_{Ga}^{3-} with $S=0$. The cation vacancy-donor pair is also predicted to be in the EPR inactive 2^{-} charge state, $V_{\text{Ga}}\text{O}_{\text{N}}^{2-}$. Using illumination alone for activating other charge states of vacancy-related defects seems to be rather inefficient in n -type GaN irradiated to fluences up to $\sim 1 \times 10^{18} \text{ cm}^{-2}$. However, increasing the electron fluence to $\sim 4 \times 10^{18} \text{ cm}^{-2}$ or higher, several EPR spectra can be detected even in darkness [128, 129]. Figs. 11.14a-c show EPR spectra D1-D4 observed at 77 K in n -type GaN irradiated with 2 MeV electrons to a fluence of $1 \times 10^{19} \text{ cm}^{-2}$. If the starting

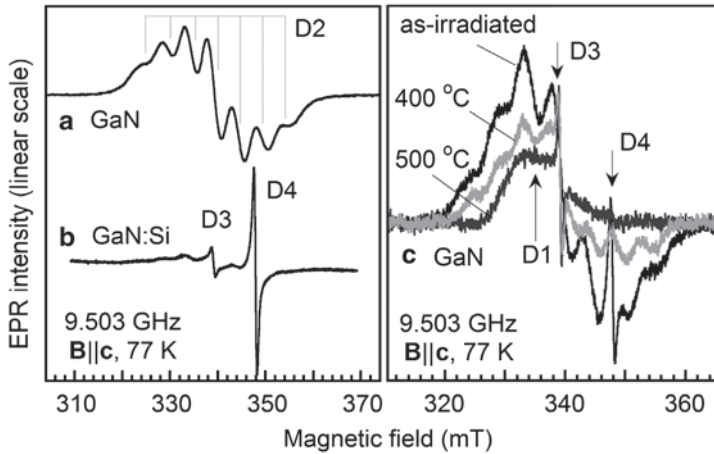


Fig. 11.14 Radiation-induced EPR spectra measured at 77 K for $\mathbf{B}||\mathbf{c}$ **a** in undoped GaN with the concentration of shallow donors (O and Si) in the low 10^{16} –mid 10^{17} cm^{-3} range, **b** in Si-doped ($[\text{Si}] \sim 1 \times 10^{18}$ cm^{-3}) GaN and **c** in undoped GaN before and after annealing at different temperatures. The electron energy is 2 MeV and the fluence is 1×10^{19} cm^{-2} . (Reproduced with permission from Son et al. [128]. Copyright 2009 by the American Physical Society)

material is undoped GaN with the concentration of the residual O and Si shallow donors in the low 10^{16} to mid 10^{17} cm^{-3} range, a strong signal of the D2 spectrum with a resolved hf structure consisting of seven equidistant lines is always observed even in darkness (Fig. 11.14a). In some undoped samples, the D3 and D4 signals are also detected together with D2. In heavily Si-doped ($[\text{Si}] \sim 1 \times 10^{18}$ cm^{-3}) GaN, the D3 and D4 signals are strong while the D2 signal is very weak (Fig. 11.14b).

The D2 center has an effective electron spin $S = 1/2$. Its main line has the g values $g_{||} = 2.001$ and $g_{\perp} = 1.999$, but since the line width is broad (~ 2.5 mT), the symmetry of the center is not evident from the experiment. The hf splitting is ~ 4.7 mT in the c direction and increases to ~ 5 mT for $\sim 70^\circ$ off the c axis. The D1 signal can be detected at room temperature. This broad signal has the g value of ~ 2.03 . Its intensity is rather weak compared to other signals. In undoped GaN irradiated with a fluence of $\sim 6 \times 10^{18}$ cm^{-2} , the isotropic D3 signal ($g \sim 2.0036$) is dominating, but in heavier irradiated samples, it is not clear how much this signal contributes to the central line of the D2 spectrum. The D4 signal appears in some samples. Its g values ($g_{||} = 1.9529$ and $g_{\perp} = 1.9505$) are close to those of the shallow donors in GaN [130], but the D4 center is a different defect and can be detected at temperatures above 77 K (EPR signal of the shallow donor disappears at temperatures above 40 K).

The annealing behavior of these centers is shown in Fig. 11.14c. The D2 and D4 signals decrease after annealing at 300 °C (by half for D2). The D4 signal is almost disappeared after annealing at ~ 400 °C. At this annealing temperature, the signal of the shallow donor is recovered. In darkness and at low temperatures, only the signal of the shallow donor could be detected, indicating that the Fermi level is pinned at the shallow donor level. The D2 signal can still be detected but its detec-

tion required illumination. After annealing at 500 °C, only the signal of D3 could be observed. The annealing behavior of D2 is close to that of the $V_{\text{Ga}}O_{\text{N}}$ pair studied by positron annihilation spectroscopy, i.e. reducing by half after annealing at ~600 K [131]. Based on the observed hf structure and the annealing behavior, the D2 center was assigned to the negative Ga vacancy-O pair, $V_{\text{Ga}}O_{\text{N}}^-$ [128, 129]. The origins of the D1, D3 and D4 defects are still not clear.

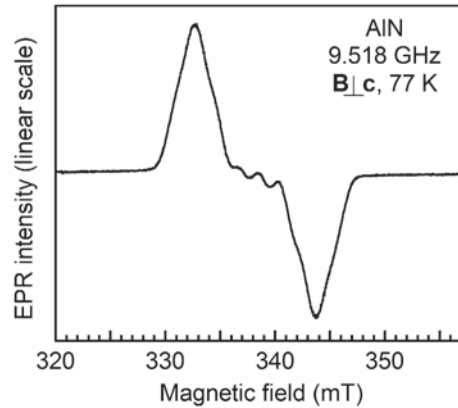
In a more recent EPR and theoretical study of irradiated GaN, the D2 center was reassigned to the N-split interstitial in the neutral charge state, $(\text{N-N})_{\text{N}}^0$ [132]. Based on the hf calculations for different defect models, Von Bardeleben et al. [133] found that the hf structure of D2 at the *c* direction can be better described by the hf interaction with two N interstitials and four nearest Ga neighbors. The calculations predicted low symmetry C_1 for the defect and its change in the hf interaction at low temperatures (below 50 K).

11.3.2 Defects in Irradiated AlN

AlN has the bandgap of ~6.2 eV [133] and there is no light source suitable for over bandgap excitation in ODMR experiments. Nevertheless, ODMR studies of radiation-induced defects in AlN using below-bandgap excitation have been reported [134]. In AlN single crystals grown in the 1960s and 1970s containing very high concentrations of different impurities, several ODMR centers were detected. It was not clear if these defects are related to impurities or native defects. However, one ODMR center, D5, observed only after electron irradiation was believed to be related to a native defect. The broad signal with the linewidth ranging from ~20 to 30 mT at different directions of the magnetic field was assumed to be an unresolved hf structure of a single Al atom with the nuclear spin $I=5/2$ and 100% natural abundance [134]. Although the involvement of other impurities with high nuclear spins and large natural abundance present in the samples could not be excluded, it is highly possible that the defect is related to a native defect. (It is known that common transition metal impurities in GaN, such as Mn and V, have high electron spin and well-resolved hf structures.)

In an EPR and ENDOR study of as-grown AlN, Evans and co-workers [135] observed an EPR center with $S=1/2$ and axial symmetry ($g_{\parallel}=2.002$ and $g_{\perp}=2.006$). ENDOR studies show that the center has a strong hf interaction with an Al atom along the *c* axis ($A_{\parallel}=111.30$ MHz ~3.97 mT, $A_{\perp}=54.19$ MHz ~1.93 mT) and much weaker hf interactions with three other Al neighbors (principal values are in the range of 8–20 MHz) [135]. The center was assigned to either the neutral N vacancy, V_{N}^0 , or the neutral O_{N} shallow donor. In a later EPR and ENDOR study of as-grown AlN, Soltamov and co-workers [136] observed also Al hf splittings in the range of ~4–9 MHz for this center and attributed it to V_{N}^0 . Using thermal luminescence, they estimated the energy level of the V_{N}^0 donor to be at ~0.5 eV below the conduction band minimum.

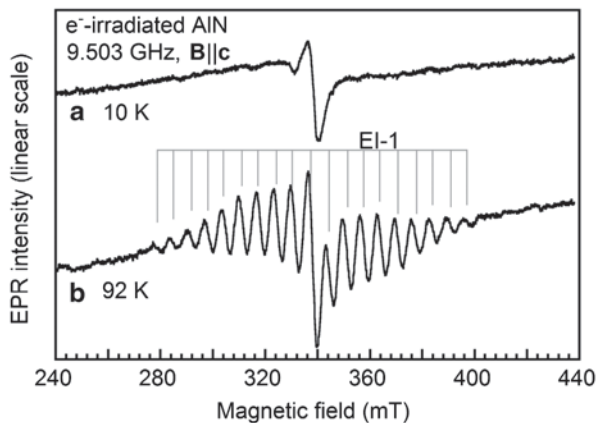
Fig. 11.15 EPR spectrum in as-grown AlN measured in darkness at 77 K for $\mathbf{B} \perp \mathbf{c}$. The spectrum was previously assigned to either V_N^0 or the O_N donor [135, 136]



The above defect is rather common in as-grown AlN bulk material. Figure 11.15 shows the EPR spectrum of this center measured at 77 K for $\mathbf{B} \perp \mathbf{c}$ in bulk AlN with high resistivity. Our recent studies showed that after electron irradiation, this EPR signal disappeared. Figure 11.16 shows EPR spectra in AlN after irradiation by 2 MeV electrons at room temperature to a fluence of $1 \times 10^{19} \text{ cm}^{-2}$ for $\mathbf{B} \parallel \mathbf{c}$ at different temperatures. At 10 K, the spectrum consists of only a broad and isotropic line with the g value of ~ 2.009 (Fig. 11.16a) [137]. This signal is already seen before irradiation. At elevated temperatures, another spectrum with $S=1/2$ emerges. This spectrum, labeled EI-1, shows a hf structure consisting of 21 equidistant lines (Fig. 11.16b). The stronger central line is due to the overlap with the broad signal shown in Fig. 11.16a. The hf structure can be described by the interaction between the electron spin with nuclear spins of four equivalent ^{27}Al atoms in the nearest neighbor. The principal values of the hf tensor for EI-1 were estimated as $A_{xx} \sim A_{yy} \sim 6.0 \text{ mT}$ and $A_{zz} \sim 7.2 \text{ mT}$ with the angle between the principal z axis and the c axis of $\sim 40\text{--}45^\circ$. The total spin density on four Al neighbors is found to be $\sim 72\%$ with $\sim 18\%$ and $\sim 54\%$ on the s and p orbitals, respectively.

Calculations of the N vacancy using a 432-atom hexagonal AlN supercell showed that V_N introduces levels in the fundamental bandgap [137]. In the unrelaxed case under C_{3v} point group, V_N has an s -like a_1 state and the second a_1 and e levels which are p -like contribution from the Al dangling bonds split in the hexagonal crystal field. In the neutral charge state, the first a_1 level is close to the valence band and fully occupied, while the second a_1 and e levels are close to the conduction band edge with a_1 singly occupied. It is found that in the case if the C_{3v} point group is preserved during geometry optimization, the Al neighbor along the c axis is found to move farther from the vacancy site and the spin density will mainly be localized on the dangling bond of this single Al atom. In this C_{3v} configuration, the second a_1 level is found to be at $\sim 0.7 \text{ eV}$ from the conduction band minimum. In the case if two Al neighbors in the basal plane move closer to each other and the symmetry is lowered to C_{1h} then the spin density is found to be more equally distributed among four nearest Al neighbors. The singly occupied a' level is $\sim 0.14 \text{ eV}$ lower than the corresponding a_1 level in C_{3v} configuration, suggesting that the C_{1h} is more stable.

Fig. 11.16 EPR spectra in AlN irradiated by 2 MeV electrons to a fluence of $1 \times 10^{19} \text{ cm}^{-2}$ at room temperature measure for $\mathbf{B} \parallel \mathbf{c}$ at (a) 10 K and (b) 92 K. The *broad line* in (a) is from an unidentified defect. The EI-1 signal in (b) shows a hf structure consisting of 21 equidistant lines. The strong *central line* is due to overlapping between EI-1 and the broad the signal in (a). (Source: Reproduced with permission from Son et al. [137]. Copyright 2011 AIP Publishing LLC)



The hf calculations for the C_{1h} configuration showed that the hf interactions with two pairs of Al neighbors are similar with the principal values $A_{xx} \sim A_{yy} \sim 6.0$ and ~ 6.7 mT and $A_{zz} \sim 8.0$ and 8.2 mT [137]. Based on the agreement between EPR and calculations in determination of the hf parameters, EI-1 was assigned to the C_{1h} configuration of the neutral N vacancy.

Acknowledgments Support from the Swedish Energy Agency, the Swedish Foundation for Strategic Research, the Swedish Research Council (VR) and the VR Linköping Linnaeus Initiative for Novel Functional Materials (LiLi-NFM) is gratefully acknowledged.

References

1. MacKay JW, Klontz EE (1964) Low temperature irradiation of semiconductors and ionization effects. In: Radiation Damage in Semiconductors, Paris-Royaumont, 1964. Dunod, Paris, pp 11–25
2. Watkins GD (1964) A review of EPR studies in irradiated silicon. In: Radiation Damage in Semiconductors, Paris-Royaumont, 1964. Dunod, Paris, pp 97–113
3. Hasiguti RR, Ishino S (1964) Defects mobility and annealing in irradiated germanium and silicon. In: Radiation Damage in Semiconductors, Paris-Royaumont, 1964. Dunod, Paris, pp 261–273
4. Rai-Choudhury P, Bartko J, Johnson JE (1976) Electron irradiation induced recombination centers in silicon-minority carrier lifetime control. IEEE T Electron Dev 23:814–818
5. Carlson RO, Sun YS, Assalit HB (1977) Lifetime control in silicon power devices by electron or gamma irradiation. IEEE T Electron Dev 24:1103–1108
6. Herrmann HA, Herzer H (1975) Doping of Si by neutron irradiation. J Electrochem Soc 122:1568–1569
7. Kohn W, Sham LJ (1965) Self-consistent equations including exchange and correlation effects. Phys Rev 140:A1133–A1138
8. Morkoç H, Strite S, Gao GB, Lin M, Sverdlov B, Burns M (1994) Large-band-gap SiC, III-V nitride, and II-VI ZnSe-based semiconductors device technologies. J App Phys 76:1363–1398
9. Zywiec A, Furthmüller J, Bechstedt F (1999) Vacancies in SiC: Influence of Jahn-Teller distortions, spin effects, and crystal structure. Phys Rev B 59:15166–15180

10. Torpo L, Marlo M, Staab TEM, Nieminen RM (2001) Comprehensive ab initio study of properties of monovacancies and antisites in 4H-SiC. *J Phys: Condens Matter* 13:6203–6231
11. Aradi B, Gali A, Deák P, Lowther JE, Son NT, Janzén E, Choyke WJ (2001) Ab initio density-functional supercell calculations of hydrogen defects in cubic SiC. *Phys Rev B* 63:245202
12. Bockstedte M, Mattausch A, Pankratov O (2003) Ab initio study of the migration of intrinsic defects in 3C-SiC. *Phys Rev B* 68:205201
13. Son NT, Hai PN, Janzén E (2001) Carbon vacancy-related defect in 4H and 6H SiC, *Phys Rev B* 63:R201201
14. Son NT, Hai PN, Janzén E (2001) Intrinsic defects in silicon carbide polytypes. *Mater Sci Forum* 353–356:499–504
15. Bratus V Ya, Makeeva IN, Okulov SM, Petrenko TL, Petrenko TT, von Bardeleben HJ (2001) Positively charged carbon vacancy in 6H-SiC: EPR study. *Physica B* 308–310:621–624
16. Umeda T, Isoya J, Morishita N, Ohshima T, Kamiya T, Gali A, Deák P, Son NT, Janzén E (2004) EPR and theoretical studies of positively charged carbon vacancy in 4H-SiC. *Phys Rev B* 70:235212
17. Bratus V Ya, Petrenko TT, Okulov SM, Petrenko TL (2005) Positively charged carbon vacancy in three inequivalent lattice sites of 6H-SiC: combined EPR and density functional theory study. *Phys Rev B* 71:125202
18. Itoh H, Kawasuso A, Ohshima T, Yoshikawa M, Nashiyama I, Tanigawa S, Misawa S, Okumura H, Yoshida S (1997) Intrinsic defects in cubic silicon carbide. *Phys Status Solidi A*, 162:173–198
19. Zolnai Z, Son NT, Hallin C, Janzén E (2004) Annealing behavior of the carbon vacancy in electron-irradiated 4H-SiC. *J Appl Phys* 96:2406–2408
20. Zvanut ME, Kononov VV (2002) The level position of a deep intrinsic defect in 4H-SiC studied by photoinduced electron paramagnetic resonance. *Appl Phys Lett* 80:410–412
21. Son NT, Magnusson B, Zolnai Z, Ellison A, Janzén E (2003) Defects in semi-insulating SiC substrates. *Mater Sci Forum* 433–436:45–50
22. Son NT, Magnusson B, Zolnai Z, Ellison A, Janzén E (2004) Defects in high-purity semi-insulating SiC. *Mater Sci Forum* 457–460:437–442
23. Son NT, Magnusson B, Janzén E (2002) Photoexcitation-electron-paramagnetic resonance studies of the carbon vacancy in 4H-SiC. *Appl Phys Lett* 81:3945–3947
24. Dashdorj J, Zvanut ME, Harrison JG (2008) Measurements of optical cross sections of the carbon vacancy in 4H-SiC by time-dependent photoelectron paramagnetic resonance. *J Appl Phys* 104:113707
25. Bockstedte M, Marini A, Pankratov O, Rubio A (2010) Many-body effects in the excitation spectrum of a defect in SiC. *Phys Rev Lett* 105:026401
26. Carlsson P, Son NT, Beyer FC, Pedersen H, Isoya J, Morishita N, Ohshima T, Janzén E (2009) Deep levels in low-energy electron-irradiated 4H-SiC. *Phys Status Solidi RRL* 3:121–123
27. Hemmingsson C, Son NT, Kordina O, Bergman JP, Janzén E, Savage S, Nordell N (1997) Deep-level defects in electron-irradiated 4H SiC epitaxial layers. *J Appl Phys* 81:6155–6159
28. Storasta L, Bergman JP, Janzén E, Henry A, Lu J (2004) Deep levels created by low energy electron irradiation in 4H-SiC. *J Appl Phys* 96:4909–4915
29. Umeda T, Ishitsuka Y, Isoya I, Son NT, Janzén E, Morishita N, Ohshima T, Itoh H, Gali A (2005) EPR and theoretical studies of negatively charged carbon vacancy in 4H-SiC. *Phys Rev B* 71:193202
30. Son NT, Trinh XT, Løvlie LS, Svensson BG, Kawahara K, Suda J, Kimoto T, Umeda T, Isoya J, Makino T, Ohshima T, Janzén E (2012) Negative-U system of carbon vacancy in 4H-SiC. *Phys Rev Lett* 109:187603
31. Trinh XT, Szasz K, Hornos T, Kawahara K, Suda J, Kimoto T, Gali A, Janzén E, Son NT (2014) Negative-U carbon vacancy in 4H-SiC: assessment of the charge correction schemes and identification of the negative carbon vacancy at quasicubic site. *Phys Rev B* 88:235209
32. Anderson PW (1975) Model for the Electronic Structure of Amorphous Semiconductors. *Phys Rev Lett* 34:953–955

33. Kawahara K, Trinh XT, Son NT, Janzén E, Suda J, Kimoto T (2013) Investigation on origin of $Z_{1/2}$ center in SiC by deep level transient spectroscopy and electron paramagnetic resonance. *Appl Phys Lett* 102:112106
34. Danno K, Kimoto T (2006) Investigation of carrier lifetime in 4H-SiC epilayers and lifetime control by electron irradiation. *J Appl Phys* 100:113728
35. Dalibor T, Pensl G, Matsunami H, Kimoto T, Choyke WJ, Schöner A, Nordell N (1997) Deep Defect Centers in Silicon Carbide Monitored with Deep Level Transient Spectroscopy. *Phys Status Solidi A* 162:199–225
36. Hemmingsson CG, Son NT, Ellison A, Zhang J, Janzén E (1998) Negative-U centers in 4H silicon carbide. *Phys Rev B* 58:R10119–R10122
37. Hemmingsson CG, Son NT, Ellison A, Zhang J, Janzén E (1999) Erratum: negative-U centers in 4H silicon carbide. *Phys Rev B* 59:7768–7768
38. Kimoto T, Itoh H, Matsunami H, Sridhara S, Clemen LL, Devaty RP, Choyke WJ, Dalibor T, Peppermüller C, Pensl G (1995) Nitrogen donors and deep levels in high-quality 4H-SiC epilayers grown by chemical vapor deposition. *Appl Phys Lett* 67:2833–2835
39. Zhang J, Storasta L, Bergman P, Son NT, Janzén E (2003) Electrically active defects in n-type 4H-silicon carbide grown in a vertical hot-wall reactor. *J Appl Phys* 93:4708–4714
40. Tawara T, Tsuchida H, Izumi S, Kamata I, Izumi K (2004) Evaluation of free carrier lifetime and deep levels of the thick 4H-SiC epilayers. *Mater Sci Forum* 457–460:565–568
41. Klein PB, Shanabrook BV, Huh SW, Polyakov AY, Skowronski M, Sumakeris JJ, O’Loughlin MJ (2006) Lifetime-limiting defects in n-4H-SiC epilayers. *Appl Phys Lett* 88:052110
42. Danno K, Nakamura D, Kimoto T (2007) Investigation of carrier lifetime in 4H-SiC epilayers and lifetime control by electron irradiation. *Appl Phys Lett* 90:202109
43. Storasta L, Tsuchida H (2007) Reduction of traps and improvement of carrier lifetime in 4H-SiC epilayers by ion implantation. *Appl Phys Lett* 90:062116
44. Storasta L, Tsuchida H, Miyazawa T, Ohshima T (2008) Enhanced annealing of the $Z_{1/2}$ defect in 4H-SiC epilayers. *J Appl Phys* 103:013705
45. Hiyoshi T, Kimoto T (2009) Reduction of Deep Levels and Improvement of Carrier Lifetime in n-Type 4H-SiC by Thermal Oxidation. *Appl Phys Express* 2:041101
46. Hiyoshi T, Kimoto T (2009) Elimination of the Major Deep Levels in n- and p-Type 4H-SiC by Two-Step Thermal Treatment. *Appl Phys Express* 2:091101
47. Hornos T, Gali A, Svensson BG (2011) Large-scale electronic structure calculations of vacancies in 4H-SiC using the Heyd-Scuseria-Ernzerhof screened hybrid density functional. *Mater Sci Forum* 679–680:261–264
48. Miyazawa T, Tsuchida H (2013) Point defect reduction and carrier lifetime improvement of Si- and C-face 4H-SiC epilayers. *J Appl Phys* 113:083714
49. Kimoto T, Danno K, Suda J (2008) Lifetime-killing defects in 4H-SiC epilayers and lifetime control by low-energy electron irradiation. *Phys Status Solidi* 245:1327–1336
50. Hayashi T, Asano K, Suda J, Kimoto T (2012) Enhancement and control of carrier lifetimes in p-type 4H-SiC epilayers. *J Appl Phys* 112:064503
51. Son NT, Carlsson P, Gällström A, Magnusson B, Janzén E (2007) Prominent defects in semi-insulating SiC substrates. *Physica B* 401–402:67–72
52. Carlsson P, Son NT, Magnusson B, Henry A, Janzén E (2009) Intrinsic Defects in HPSI 6H-SiC: an EPR Study. *Mater Sci Forum* 600–603:381–384
53. Hemmingsson C, Son NT, Kordina O, Janzén E (1998) Capture cross sections of electron irradiation induced defects in 6H-SiC. *J Appl Phys* 84:704–708
54. Hemmingsson CG, Son NT, Janzén E (1999) Observation of negative-U centers in 6H silicon carbide. *Appl Phys Lett* 74:839–841
55. Itoh H, Yoshikawa M, Nashiyama I, Misawa S, Okumura H, Yoshida S (1990) Radiation induced defects in CVD-grown 3C-SiC. *IEEE Trans Nucl Sci* 37:1732–1738.
56. Itoh H, Kawasuso A, Ohshima T, Yoshikawa M, Nashiyama I, Tanigawa S, Misawa S, Okumura H, Yoshida S (1997) Intrinsic defects in cubic silicon carbide. *Phys Status Solidi A* 162:173–198.

57. Torpo L, Nieminen RM, Laasonen KE, Pölykko S (1999) Silicon vacancy in SiC: A high-spin state defect. *Appl Phys Lett* 74:221–223.
58. Bockstedte M, Heid M, Mattausch A, Pankratov O (2003) Identification and annealing of common intrinsic defect centers. *Mater Sci Forum* 433–436:471–476
59. Wimbauer T, Meyer B, Hofstaetter A, Scharmann A, Overhof H (1997) Negatively charged Si vacancy in 4H SiC: A comparison between theory and experiment. *Phys Rev B* 56:7384–7388
60. Sörman E, Son NT, Chen WM, Kordina O, Hallin C, Janzén E (2000) Silicon vacancy related defect in 4H and 6H SiC. *Phys Rev B* 61:2613–2619
61. Wagner Mt, Thinh NQ, Son NT, Chen WM, Janzén E, Baranov PG, Mokhov EN, Hallin C, Lindström JL (2002) *Phys. Rev. B* 66:155214
62. Janzén E, Gali A, Henry A, Ivanov IG, Magnusson B, Son NT (2008) Defects in SiC. In: Fleetwood DM, Pantelides ST, Schrimpf RD (eds) *Defects in microelectronic materials and devices*. CRC Press, Boca Raton, pp 615–669
63. Von Bardeleben HJ, Cantin JL, Vickridge I, Battistig G (2000) Proton-implantation-induced defects in n-type 6H- and 4H-SiC: an electron paramagnetic resonance study. *Phys Rev B* 62:10126–10134
64. Orlinski SB, Schmidt J, Mokhov EN, Baranov PG (2003) Silicon and carbon vacancies in neutron-irradiated SiC: a high-field electron paramagnetic resonance study. *Phys Rev B* 67:125207
65. Son NT, Zolnai Z, Janzén E (2003) Silicon vacancy related $T_{V_{2a}}$ center in 4H-SiC. *Phys Rev B* 68:205221
66. Mizuochi N, Yamasaki S, Takizawa H, Morishita N, Ohshima T, Itoh H, Isoya J (2002) Continuous-wave and pulsed EPR study of the negatively charged silicon vacancy with S=32 and C3v symmetry in n-type 4H-SiC. *Phys Rev B* 66:235202
67. Mizuochi N, Yamasaki S, Takizawa H, Morishita N, Ohshima T, Itoh H, Umeda T, Isoya J (2005) Spin multiplicity and charge state of a silicon vacancy ($T_{V_{2a}}$) in 4H-SiC determined by pulsed ENDOR. *Phys Rev B* 72:235208
68. Janzén E, Gali A, Carlsson P, Gällström A, Magnusson B, Son NT (2009) The silicon vacancy in SiC. *Physica B* 404:4354–4358
69. Watkins GD (1974) EPR Observation of Close Frenkel Pairs in Irradiated ZnSe. *Phys Rev Lett* 33:223–225
70. Rong F, Watkins GD (1986) Observation by optically detected magnetic resonance of frenkel pairs in irradiated ZnSe. *Phys Rev Lett* 56:2310–2313
71. Son NT, Janzén E, Isoya J, Morishita N, Hanaya H, Takizawa H, Ohshima T, Gali A (2009) Identification of a Frenkel-pair defect in electron-irradiated 3C SiC. *Phys Rev B* 80:125201
72. Son NT, Isoya J, Morishita N, Ohshima T, Itoh H, Gali A, Janzén E (2009) Defects introduced by electron-irradiation at low temperatures in SiC. *Mater Sci Forum* 615–617:377–380
73. Ammerlaan CAJ (1989) Paramagnetic centers in silicon. In Madelung O, Schulz M (eds) *Landolt-Börnstein New Series III/22b*. Springer-Verlag, Berlin, Heidelberg, pp. 365–381
74. Von Bardeleben HJ, Cantin JL, Henry L, Barthe MF (2000) Vacancy defects in p-type 6H-SiC created by low-energy electron irradiation. *Phys Rev B* 62:10841–10846
75. Son NT, Chen WM, Lindström JL, Monemar B, Janzén E (1999) Carbon-vacancy related defects in 4H- and 6H-SiC. *Mater Sci Engineering B* 61–62:202–206
76. Son NT, Hai PN, Huy PT, Gregorkiewicz T, Ammerlaan CAJ, Lindström JL, Chen WM, Monemar B, Janzén E (1999) Electron paramagnetic resonance studies of defects in electron-irradiated p-type 4H and 6H SiC. *Physica B* 273–274:655–658
77. Gerstmann U, Seitsonen AP, Mauri F, von Baderleben HJ (2009) $Si_C C_{Si}$ antisite pairs as dominant irradiation induced defects in p-Type 4H-SiC. *Mater Sci Forum* 615–617:357–360
78. Gerstmann U, Seitsonen AP, Ceresoli D, Mauri F, von Bardeleben HJ, Cantin JL, Lopez JG (2010) $Si_C C_{Si}$ antisite pairs in SiC identified as paramagnetic defects with strongly anisotropic orbital quenching. *Phys Rev B* 81:195208
79. Baraff GA, Schuluter M (1985) Bistability and metastability of the gallium vacancy in GaAs: The Actuator of EL? *Phys Rev Lett* 55:2340–2343

80. Bar-Yam Y, Joannopoulos JD (1986) Gallium vacancy and EL 2 in GaAs. *Phys Rev Lett* 56:1123–1123
81. Cubiotti G, Kucherenko Yu, Yaresko A, Perlov A, Antonov V (2000) Local electronic structure around vacancies and vacancy–antisite complexes in β -SiC. *J Phys Condens Matter* 12:3369–3381
82. Rauls E, Frauenheim Th, Gali A, Deák P (2003) Theoretical study of vacancy diffusion and vacancy-assisted clustering of antisites in SiC. *Phys Rev B* 68:155208
83. Umeda T, Son NT, Isoya J, Ohshima T, Morishita N, Itoh H, Janzén E (2006) Electron paramagnetic resonance study of the SI5 center in 4H-SiC. *Mater Sci Forum* 527–529:543–546
84. Umeda T, Son NT, Isoya J, Janzén E, Ohshima T, Morishita N, Itoh H, Gali A, Bockstedte M (2006) Identification of the carbon antisite-vacancy pair in 4H-SiC. *Phys Rev Lett* 96:145501
85. Gerstmann U, Rauls E, Overhof H (2004) Annealing of vacancy-related defects in semi-insulating SiC. *Phys. Rev. B* 70:201204
86. Carlsson P, Son NT, Umeda T, Isoya J, Janzén E (2007) Deep acceptor levels of the carbon vacancy-carbon antisite pairs in 4H-SiC. *Mater Sci Forum* 556–557:449–452
87. Umeda T, Morishita N, Ohshima T, Itoh J, Isoya J (2007) Electron paramagnetic resonance study of carbon antisite-vacancy pair in p-Type 4H-SiC. *Mater Sci Forum* 556–557:453–456
88. Umeda T, Isoya J, Ohshima T, Morishita N, Itoh J, Gali A (2007) Identification of positively charged carbon antisite-vacancy pairs in 4H-SiC. *Phys Rev B* 75:245202
89. Watkins GD (2000) Intrinsic defects in silicon. *Mater Sci Semicond Processing* 3:227–235
90. Corbett JW, Watkins GD (1961) Silicon divacancy and its direct production by electron irradiation. *Phys Rev Lett* 7:314–316
91. Torpo L, Staab TEM, Nieminen RM (2002) Divacancy in 3C- and 4H-SiC: an extremely stable defect. *Phys Rev B* 65:085202
92. Bockstedte M, Mattausch A, Pankratov O (2004) Ab initio study of the annealing of vacancies and interstitials in cubic SiC: vacancy-interstitial recombination and aggregation of carbon interstitials. *Phys Rev B* 69:235202
93. Son NT, Carlsson P, Ul Hassan, Janzén E, Umeda T, Isoya J, Gali A, Bockstedte M, Morishita N, Ohshima T, Itoh H (2006) Divacancy in 4H-SiC. *Phys Rev Lett* 96:055501
94. Gali A, Bockstedte M, Son NT, Umeda T, Isoya J, Janzén E (2006) Divacancy and its identification: theory. *Mater Sci Forum* 527–529:523–526
95. Son NT, Umeda T, Isoya J, Gali A, Bockstedte M, Magnusson B, Ellison A, Morishita N, Ohshima T, Itoh H, Janzén E (2006) Identification of divacancies in 4H-SiC. *Physica B* 376–377:334–337
96. Ilyin IV, Muzafarova MV, Mokhov EN, Sankin VI, Baranov PG, Orlinski SB, Schmidt J (2006) Evidence of the ground triplet state of silicon-carbon divacancies, P6, P7 centers in 6H-SiC: an EPR study. *Mater Sci Forum* 527–529:535–538
97. Son NT, Umeda T, Isoya J, Gali A, Bockstedte M, Magnusson B, Ellison A, Morishita N, Ohshima T, Itoh H, Janzén E (2006) Divacancy model for P6/P7 centers in 4H- and 6H-SiC. *Mater Sci Forum* 527–529:527–530
98. Vainer VS, Il'in VA (1981) Electron spin resonance of exchange-couple vacancy pairs in hexagonal silicon carbide. *Fiz Tverd Tela* 23:3659; (1981) *Sov Phys Solid State* 23:2126–2133
99. Son NT, Hai PN, Wagner Mt, Chen WM, Ellison A, Hallin C, Monemar B, Janzén E (1999) Optically detected magnetic resonance studies of intrinsic defects in 6H SiC. *Semicond Sci Technol* 14:1141–1146
100. Son NT, Carlsson P, ul Hassan J, Magnusson B, Janzén E (2007) Defects and carrier compensation in semi-insulating 4H-SiC substrates. *Phys Rev B* 75:155204
101. Lingner Th, Greulich-Weber S, Spaeth JM, Gerstmann U, Rauls E, Hajnal Z, Frauenheim Th, Overhof H (2001) Structure of the silicon vacancy in 6H-SiC after annealing identified as the carbon vacancy–carbon antisite pair. *Phys Rev B* 64:245212
102. Magnusson B, Janzén E (2005) Optical characterization of deep level defects in SiC. *Mater Sci Forum* 483–485:341–346

103. Carlsson P, Son NT, Gali A, Morishita N, Ohshima T, Magnusson B, Janzén E (2010) EPR and ab initio calculation study on the E14 center in 4H- and 6H-SiC. *Phys Rev B* 82:235203
104. Vainer VS, Veinger VI, Il'in VA, Tvestkov VF (1980) Electron spin resonance associated with the triplet state of secondary thermal defects in 6H-SiC. *Sov Phys Solid State* 22:2011–2013. (1980) *Fiz Tverd Tela* 22:3436
105. Son NT, Hai PN, Shuja A, Chen WM, Lindström JL, Monemar B, Janzén E (2000) The carbon vacancy pairs in 4H- and 6H-SiC. *Mater Sci Forum* 338–342:821–824
106. Ellison A, Magnusson B, Hemmingsson C, Magnusson W, Iakimov T, Storasta L, Henry A, Henelius N, Janzén E (2001) HTCVD growth of semi-insulating 4H-SiC crystals with low defect density. *Mat Res Soc Symp* 640:H1.2.1–H1.2.10
107. Ellison A, Magnusson B, Son NT, Storasta L, Janzén E (2003) HTCVD grown semi-insulating SiC substrates. *Mater Sci Forum* 433–436:33–38
108. Müller St G, Brady MF, Brixius WH, Glass RC, Hobgood H McD, Jenny JR, Leonard RT, Malta DP, Powell AR, Tsvetkov VF, Allen T, Palmour JW, Carter CH Jr (2003) Sublimation-Grown semi-insulating SiC for high frequency devices. *Mater Sci Forum* 433–436:39–44
109. Jenny JR, Malta DP, Calus MR, Müller St G, Powell AR, Tsvetkov VF, Hobgood H McD, Glass RC, Carter CH Jr (2004) Development of large diameter high-purity semi-insulating 4H-SiC wafers for microwave devices. *Mater Sci Forum* 457–460:35–40
110. Zvanut ME, Konovalov VV (2002) The level position of a deep intrinsic defect in 4H-SiC studied by photoinduced electron paramagnetic resonance. *Appl Phys Lett* 80:410–412
111. Carlos WE, Glaser ER, Shanabrook BV (2003) Optical and magnetic resonance signature of deep levels in semi-insulating 4H-SiC. *Physica B* 340–342:151–155
112. Linde M, Uftring SJ, Watkins GD, Härle V, Scholz F (1997) Optical detection of magnetic resonance in electron-irradiated GaN. *Phys Rev B* 55:R10177–R10180
113. Bozdog C, Przyblinska H, Watkins GD, Härle V, Scholz F, Mayer M, Kamp M, Molnar RJ, Wickenden AE, Koleske DD, Henry RL (1999) Optical detection of electron paramagnetic resonance in electron-irradiated GaN. *Phys Rev B* 59:12479–12486
114. Wagner Mt, Buyanova IA, Thinh NQ, Chen WM, Monemar B, Lindström JL, Amano H, Akasaki I (2000) 62:16572–16577
115. Chow KH, Watkins GD, Usui A, Mizuta M (2000) Detection of interstitial Ga in GaN. *Phys Rev Lett* 85:2761–2764.
116. Watkins GD, Chow KH, Johannesen P, Vlasenko LS, Bozdog C, Mizuta M, Sunakawa H, Kuroda N, Usui A (2003) Intrinsic defects in GaN: what we are learning from magnetic resonance studies. *Physica B* 340–342:25–31
117. Chow KH, Vlasenko LS, Johannesen P, Bozdog C, Watkins GD, Usui A, Sunakawa H, Sasaoka C, Mizuta M (2004) Intrinsic defects in GaN. I. Ga sublattice defects observed by optical detection of electron paramagnetic resonance. *Phys Rev B* 69:045207
118. Johannesen P, Zakrzewski A, Vlasenko LS, Watkins GD, Usui A, Sunakawa H, Mizuta M (2004) Intrinsic defects in GaN. II. Electronically enhanced migration of interstitial Ga observed by optical detection of electron paramagnetic resonance. *Phys Rev B* 69:045208
119. Boguslawski P, Briggs EL, Bernholc J (1995) Native defects in Gallium nitride. *Phys Rev B* 51:17255–17258
120. Stampfl C, Van de Walle CG (2002) Theoretical investigation of native defects, impurities, and complexes in aluminum nitride. *Phys Rev B* 65:155202
121. Limpijumnong S, Van de Walle CG (2004) Diffusivity of native defects in GaN. *Phys Rev B* 69:035207
122. Van de Walle CG, Neugebauer J (2004) First-principles calculations for defects and impurities: Applications to III-nitrides. *J Appl Phys* 95:3851–3879
123. Vlasenko LS, Bozdog C, Watkins GD, Shahedipour F, Wessels BW (2002) Defects observed by optical detection of electron paramagnetic resonance in electron-irradiated p-type GaN. *Phys Rev B* 65:205202
124. Hai PN, Chen WM, Buyanova IA, Monemar B (2000) Ga-related defect in as-grown Zn-doped GaN: An optically detected magnetic resonance study. *Phys Rev B* 62:R10607–R10609

125. Gorczyca I, Svane A, Christensen NE (1999) Theory of point defects in GaN, AlN, and BN: Relaxation and pressure effects. *Phys Rev B* 60:8147–8157
126. Mattila T, Nieminen RM (1997) Point-defect complexes and broadband luminescence in GaN and AlN. *Phys Rev B* 55:9571–9576
127. Ganchenkova MG, Nieminen RM (2006) Nitrogen Vacancies as Major Point Defects in Gallium Nitride. *Phys Rev Lett* 96:196402
128. Son NT, Hemmingsson CG, Paskova T, Evans KR, Usui A, Morishita N, Ohshima T, Isoya J, Monemar B, Janzén E (2009) Identification of the gallium vacancy–oxygen pair defect in GaN. *Phys Rev B* 80:153202
129. Son NT, Hemmingsson CG, Paskova T, Evans KR, Usui A, Morishita N, Ohshima T, Isoya J, Monemar B, Janzén E (2010) Radiation-induced defects in GaN. *Phys Scr T* 141:014015
130. Carlos WE, Freitas JA Jr, Khan MA, Olson DT, Kuznia JN (1993) Electron-spin-resonance studies of donors in wurtzite GaN. *Phys Rev B* 48:17878–17884
131. Tuomisto F, Ranki V, Look DC, Farlow GC (2007) Introduction and recovery of Ga and N sublattice defects in electron-irradiated GaN. *Phys Rev B* 76:165207
132. Von Bardeleben HJ, Cantin JL, Gerstmann U, Scholle A, Greulich-Weber S, Rauls E, Landmann M, Schmidt WG, Dentils A, Botsos J, Barth MF (2012) Identification of the nitrogen split interstitial (N-N)_N in GaN. *Phys Rev Lett* 109:206402
133. Yamashita H, Fukui K, Misawa S, Yoshida S (1979) Optical properties of AlN epitaxial thin films in the vacuum ultraviolet region. *J Appl Phys* 50:896–898
134. Mason PM, Przybylinska, Watkins GD, Choyke WJ, Slack GA (1999) Optical detected electron paramagnetic resonance of AlN single crystals. *Phys Rev B* 59:1937–1947
135. Evans SM, Giles NC, Halliburton LE, Slack GA, Schujman SB, Schowalter LJ (2006) Electron paramagnetic resonance of a donor in aluminum nitride crystals. *Appl Phys Lett* 88:062112
136. Soltamov VA, Ilyn IV, Soltamova AA, Mokhov EN, Baranov PG (2010) Identification of the deep level defects in AlN single crystals by electron paramagnetic resonance. *J Appl Phys* 107:113515
137. Son NT, Gali A, Szabó Á, Bickermann M, Ohshima T, Isoya J, Janzén E (2011) Defects at nitrogen site in electron-irradiated AlN. *Appl Phys Lett* 98:242116

Chapter 12

Radiation Induced Reactions and Fragmentation in Room Temperature Ionic Liquids

Ilya A. Shkrob, Timothy W. Marin and James F. Wishart

Abstract Recent progress in understanding the structural and mechanistic aspects of radiolysis in room temperature ionic liquids (ILs) using electron paramagnetic resonance (EPR) spectroscopy is reviewed, with particular emphasis on ILs serving as replacements for molecular diluents used in nuclear fuel cycle separations.

12.1 Introduction

Room temperature ionic liquids (IL) are salts that remain molten under ambient conditions [1–4]. To avoid crystallization, these compounds consist of oddly shaped, conformationally active organic and/or inorganic ions, often having flexible arms that pack poorly, thereby depressing the melting points to such an extent that crystallization occurs either at low temperature or not at all. Typical examples of organic and inorganic ions that are used to compose room-temperature ILs are shown in Fig. 12.1. Ionic liquids are electrically conductive, have low volatility and high viscosity, and exist in a netherworld between two classes of familiar materials: molecular solvents and ionic salts. Such liquids can be hydrophilic or hydrophobic, chemically inert or reactive, solubilizing molecules and ions or strongly repelling them. It is as difficult to find general trends between these liquids as between organic solvents, except that all of these ILs contain inherently polar domains.

What is remarkable about these ILs is their versatility. While there are less than 500 molecular liquids—out of several millions of the known synthetic chemicals (not counting their mixtures and oligomers)—the estimated number of unique compositions of *pure* room-temperature ILs exceeds 10^{10-12} [5]. Due to this sheer variety, one can be reasonably certain that whatever combination of physical or chemical properties is being sought, there is a pure IL matching these properties. In

I. A. Shkrob (✉) · T. W. Marin
Chemical Sciences and Engineering Division,
Argonne National Laboratory, Argonne, Illinois, USA
e-mail: Shkrob@anl.gov

J. F. Wishart
Department of Chemistry, Brookhaven National Laboratory, Upton, New York, USA

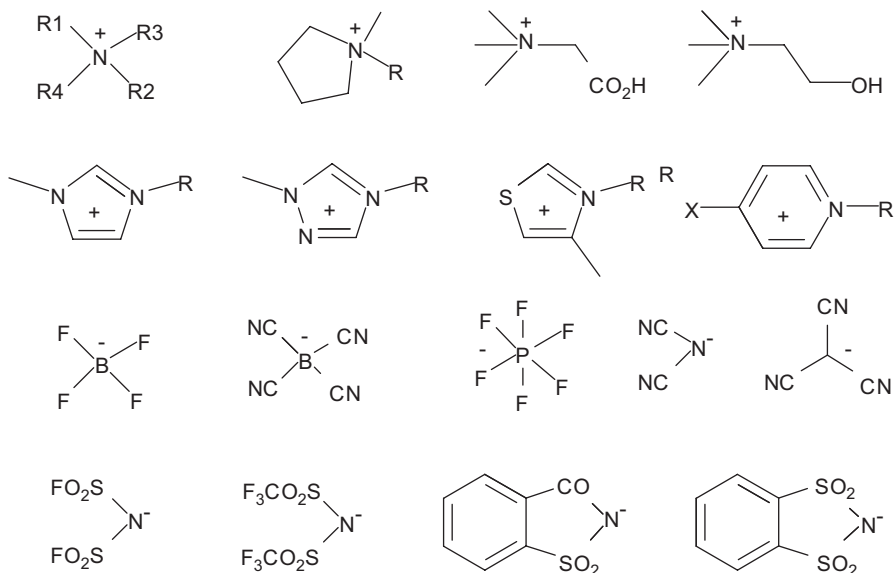


Fig. 12.1 Examples of ions that are used to compose ILs. Cations: tetraalkylammonium, 1-methyl-1-alkylpyrrolidinium, betainium, choline, 1-alkyl-3-methylimidazolium, 1-alkyl-3-methyl-1,3,4-triazolium, 1-alkyl-5-methylthiazolium, and 4-substituted 1-alkylpyridinium. Anions: tetrafluoroborate, tetracyanoborate, hexafluorophosphate, dicyanamide, tricyanomethanide, bis(fluorosulfonyl)imide, bistriflimide, saccharinate, and 1,2-benzenedisulfonimide

the imaginary “chemical universe” of all possible chemical compounds, the typical liquid would be an *ionic* liquid, whereas fluids that surround us in everyday life would occupy an infinitely small space.

We do not live in this “chemical universe.” The chemical evolution of our own Universe was more likely to yield simple fluids, such as hydrocarbon oceans on Titan and water oceans on Earth and Europa. Before the invention of distillation and organic synthesis, the human experience of room temperature liquids was limited to aqueous solutions and a few mineral oils. If intermolecular interactions are too strong, a solid is formed instead of a liquid; and if it is too weak, evaporation occurs; the energy scale of such interactions (25 meV) is set so low by the conditions at the surface of our planet that fluidity is a rare property indeed. Our intuition instructs us that “water, water is everywhere.” That is not quite true from the cosmic perspective. Water mainly exists as amorphous ice and low-pressure vapor; liquid water and hexagonal ice are exceedingly uncommon. ILs are even more wondrous. While there are no physical laws prohibiting Mother Nature from making such liquids in the course of geochemical evolution, so far she has seemingly failed to produce even one member of this most diverse class of fluids. This task has been delegated to human chemists.

Room temperature ILs are entirely artificial. The discovery of the first classes of ILs in the 1990s opened the door from our own Universe to this “chemical

universe,” and the limits of what these liquids can be are circumscribed only by our imagination. If one wants to understand the general properties of liquids, ILs make the best choice for study, because probability dictates that *most pure liquids are ILs*. There is currently a massive, interdisciplinary effort to understand all aspects of liquid behavior in these ionic compounds, and we refer the reader to a few seminal reviews for a general introduction [1–3, 6–12]. The scope of this review is modest: we seek only to understand a particular aspect of these properties, viz. radiation stability of ionic liquids. This motivation is goal oriented. ILs are considered as replacements for molecular diluents in a wide variety of industrial applications: electrolytes in electric storage devices and photoelectrochemical cells, solvents for organic synthesis and drug delivery, lubricants and hypergolic propellants, carbon and sulfur dioxide sequestration, and many other uses.

Among these new emerging applications is using of ILs as solvents for liquid-liquid extraction and ion exchange, in particular, as diluents for separations involved in “wet” processing of spent nuclear fuel. Uranium that burns in nuclear reactors is converted by <5% before the fuel needs to be replaced, as accumulation of neutron “poisons” (radioisotopes that have high cross section for thermal neutron capture) inhibit the chain reaction. The current fuel cycle is once-through: there is no economic incentive for reusing and reprocessing spent nuclear fuel, as mineable uranium ore is still abundant in the crust, and more uranyl carbonate is contained (albeit in a very dilute form) in sea water. In the past, this spent fuel has been processed only for obtaining plutonium. Given this Cold War history, reprocessing is viewed with caution, in equal parts due to nonproliferation concerns and the inherent safety hazards. Nevertheless, such reprocessing will become necessary in the future, as the room for long-term storage of high-level nuclear waste in the geological repositories is limited. Furthermore, as the world runs out of fossil fuels while facing the threat of climate change, using but a small fraction of the energy available in this precious natural resource looks increasingly wasteful and irresponsible. The advanced nuclear technology of the future will depend on industrial scale reprocessing of spent fuel on a global scale. This consideration provides the motivation for our studies.

The current scenarios for a nuclear fuel cycle overhaul posit that the (relatively) short lived isotopes (such as ^{90}Sr and ^{137}Cs) will be stored in deep geological repositories, whereas longer lived isotopes will be transmuted to short lived isotopes in specially designed reactors. This approach puts great demands on chemical separations, as the streams destined for reuse need to be free of neutron “poisons” interfering with transmutation. Among these problematic isotopes are minor actinides (such as Am and Cm) that have similar chemical properties to lanthanides (U fission products that are also neutron “poisons”). Over the period of $>10^5$ years, the residual radioactivity of spent nuclear fuel is dominated by radioactive decay of these minor actinides; only on the geological time scale is this radioactivity taken over by α decay of Pu. Other elements of concern include Kr, Tc, Ru and platinumoid metals. Closing of the nuclear cycle will require technologies that separate elements into those destined for reuse and/or those destined for containment in metallic, ceramic, or vitreous waste forms. As each one of these waste forms is compatible with some

elements but not the others, these waste streams need to be subdivided. This is a challenging, complicated, and hazardous task, and the critics of the nuclear option do not exaggerate their claims as such, but without this recycling long-term use of nuclear energy and safeguarding of nuclear waste will not become sustainable. We may not have the luxury of better options.

ILs have obvious advantages as diluents in nuclear separations (specifically, liquid-liquid extraction of *f*-block ions) as they exhibit low volatility and combustibility (some of these ILs are, actually, fire retardants). By nature, ILs strongly solvate metal ions and they are natural ion exchangers and electrolytes, which offer new ways of waste processing. The extractants and ionophores can be integrated into the constituent IL ions; such ILs are called task-specific ILs (TSIL) or functional ILs [13, 14]. This approach eliminates concerns with interphase transfer and third phase formation during the separations (that provide criticality hazards). Electric conduction potentially allows these ILs to serve as one-pot extraction solvents and electrolytes for metal deposition [15, 16]. Some functionalized ILs can dissolve metal oxides, simplifying waste processing [17–19]. Their high thermal stability (300–400 °C) permits increasing the processing temperature, accelerating separations, and there are ILs that are immiscible with aqueous solutions, organic solvents [20, 21], and supercritical CO₂ [22], suggesting novel methods for IL based phase separations. However, all of these suggested applications depend on radiation stability of the IL diluents, as the solvent is continuously exposed to ionizing radiation emitted by decaying radionuclides. In the current processes, the solvent is exposed to 50 Mrad (100 rad = 1 J/kg) of ionizing radiation over the life cycle [23]; ideally, this tolerable lifetime dose should be higher. Even in well-established separations schemes, gradual accumulation of radiation damage causes much concern. For example, tri(*n*-butyl)phosphate (Sect. 12.5) serves as an extracting agent and solvent modifier in many of separations processes; this compound readily undergoes radiolytically induced dealkylation with the release of di(*n*-butyl)phosphoric acid that forms complexes with trivalent metal ions in the aqueous phase. This interference results in contamination of the organic phase with undesirable fission products. Consequently, the solvent needs a continuous carbonate wash for removal of these interfering products, which greatly complicates operations and increases the treatment plant footprint.

The dream of separations chemists is that within the haystack of all possible ILs in the “chemical universe,” there is a needle—a class of radiation-resistant ILs that are also suitable for high performance nuclear separations. This task requires understanding of the mechanisms for radiation-induced reactions in various classes of ILs. Electron Paramagnetic Resonance (EPR) spectroscopy proved a very useful tool for extricating these reaction mechanisms and assessing the extent of radiation damage.

Since the ensuing radicals are reactive, low-temperature matrix isolation is required for structural studies and identification, so the results discussed below pertain to amorphous solids (frozen ILs) rather than ionic *liquids*. The same reactions, however, also occur in these liquids at higher temperature, so no generality is lost. Before embarking on a survey of radicals and radical reactions studied by

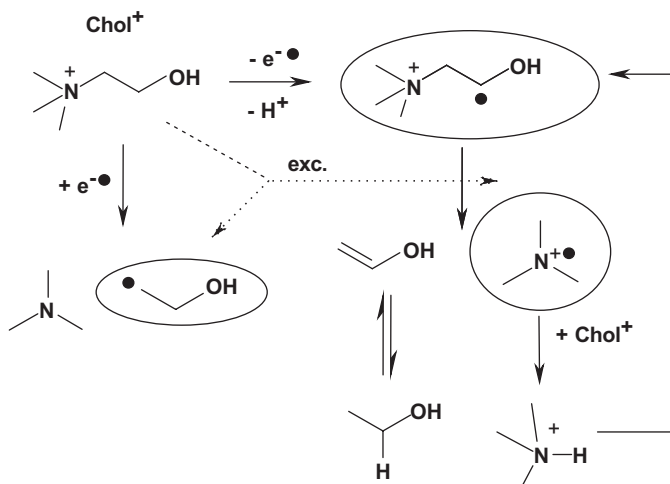


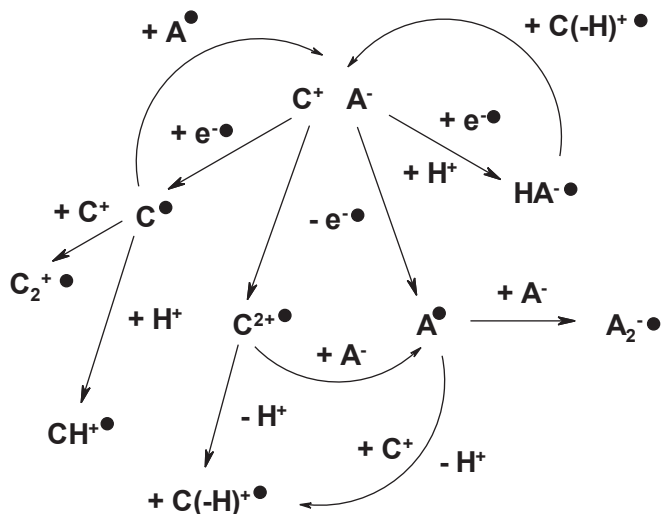
Fig. 12.2 Radiation-induced decomposition of choline cations in room-temperature crystalline choline chloride, according to ref. [28]. Reduction of choline causes deamination, whereas oxidation yields an unstable radical that initiates a chain reaction decomposition of the material

EPR, a preliminary introduction to the peculiar radiation chemistry of ILs is due (Sect. 12.2), as this chemistry is not fully analogous to radiolysis in molecular systems, which is discussed in other chapters of this book.

Historically, these peculiarities were first noticed in the 1950s by Melvin Calvin and his co-workers at the University of California at Berkeley [24]. Calvin studied CO_2 fixation and examined metabolites in plants using radioactive ^{14}C labeling (work for which he later received the Nobel prize). Most of the isolated metabolites were stable, but one of them—the α -polymorph of choline chloride (Fig. 12.2) decomposed almost as soon as it crystallized from an aqueous solution, with G values of decomposition approaching 5×10^4 species per 100 eV (vs. the typical 1–5 species per 100 eV for other organic compounds). Calvin challenged his colleagues to explain these observations. This task took 20 years [24–28], and it was partially completed by Martyn Symons, the EPR wizard [28]. He suggested that radiolytic oxidation of choline yields the unstable $\text{Me}_3\text{N}^+\text{CH}_2\text{C}^{\bullet}\text{HOH}$ radical that fragments to $\text{Me}_3\text{N}^{\bullet}$ and the enol of acetaldehyde (Fig. 12.2).

The $\text{Me}_3\text{N}^{\bullet}$ radical cation abstracts hydrogen from the parent cation, yielding protonated trimethylamine (Me_3NH^+) and another $\text{Me}_3\text{N}^+\text{CH}_2\text{C}^{\bullet}\text{HOH}$ radical. This chain reaction propagates rapidly through the room-temperature crystal, causing destruction of the material with efficiency that still holds a record in radiation chemistry. This example illustrates why extreme caution is required in replacement of organic diluents with ILs, as radiation-induced fragmentation of the constituent ions can yield reactive radicals capable of sustaining chain reactions and causing rapid deterioration of the solvent and the formation of byproducts that interfere with metal ion separations.

Fig. 12.3 Summary of the major redox reactions in radiolysis of ionic liquids (C^+A^-)



12.2 An Overview of Radiation Chemistry of ILs

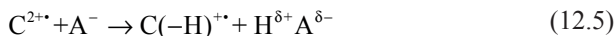
Ionic liquids can be represented as C^+A^- , where C^+ is a cation and A^- is an anion. Both species typically involve heteroatoms ($X=S, N, P$) that provide the locus for the electric charge. The $C-X$ bonds are often weak compared to other bonds, and the fragmentation of these bonds can occur in radiolytically-generated electronic excited states. In addition to this excitation, the ions also undergo radiation-induced redox reactions (Fig. 12.3) that are analogous to ionization of solvent molecules in common organic liquids [29–43],



that is complemented by associative or dissociative electron attachment (DEA)



In reactions (12.1–12.4), following the general convention of radiation chemistry, we visualize these redox reactions as the release of an electron or a hole (electron deficiency), but these reactions can also be thought of as radiation-induced charge separation, although the release of presolvated and solvated electrons has been observed in some ILs [10–12, 44–50]. Radical diions undergo prompt fragmentation and/or (de)protonation,



Reaction (12.5) accounts for radiation-induced acidification of ILs, which is yet another practical concern. As hydrophobic IL diluents are often in contact with strong inorganic acids in aqueous solutions, the constituent anions are chosen among the bases of strong acids, in order to avoid protonation of these anions. The latter would cause re-constitution of the IL with the anions of inorganic acids (which is generally undesirable). Strong acids generated via reaction (12.5) catalyze various detrimental organic reactions involving both the IL diluent and the extracting agents.

However, the main problem with the ILs is the occurrence of reaction (12.2). Indeed, the majority of organic anions can be represented as RB^- , where R is an organic moiety and B^- is a heteroatom containing negatively charged group (such as $-\text{CO}_2^-$, $-\text{SO}_3^-$, $-\text{OSO}_3^-$, etc.) Their oxidized, neutral forms undergo irreversible expulsion of such groups (“oxidative fragmentation”) [35], that is



The resulting residual radicals R^\cdot can be readily observed in EPR spectra of irradiated ILs. Such reactions (e.g., Kolbe reaction for carboxylates) are well-known in organic chemistry, and their occurrence excludes many of popular IL designs from the pool of suitable candidates for radiation-resistant IL diluents. Our realization of ubiquity of this oxidative fragmentation (that transpired from EPR observations of irradiated ILs) [35] is perhaps the single most important general insight concerning radiolysis of ILs.

Unfortunately, the trouble does not stop there. IL diluents that are used in liquid-liquid extraction from aqueous feeds must be hydrophobic in order to provide immiscibility with the aqueous phase and suppress ion exchange with inorganic ions in this aqueous phase (when that is desirable). High chemical resistance is also desired, and fluorination of organic ions is common, as it helps to achieve these properties. Such fluorinated anions (X-U^- , where $\text{X}=\text{F}$) are particularly problematic due to the occurrence of DEA and fragmentation of excited states involving weak C–F bonds [29, 35, 43]:



Two common anions that undergo this dehalogenation are triflate TfO^- ($\text{Tf}=\text{CF}_3\text{SO}_2$) and bistriflimide, NTf_2^- (Fig. 12.1) The latter is extremely popular with the IL community due to its high hydrophobicity, the superacidity of HNTf_2 , outstanding chemical stability, and the ease of obtaining room-temperature ILs with a large variety of organic cations due to poor packing of these anions. Not only does the bistriflimide yield fluoride (that eventually combines with radiolytically-generated

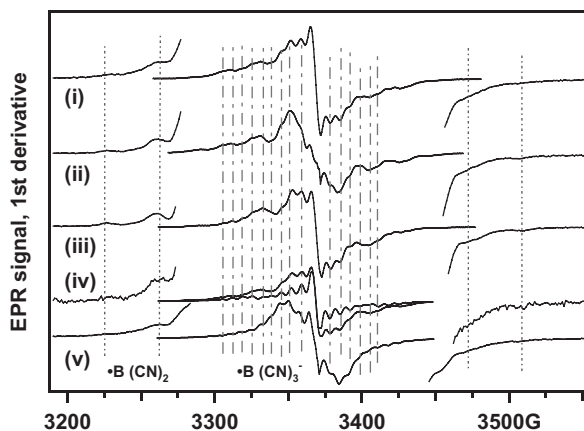
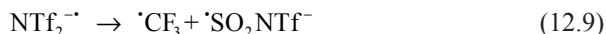
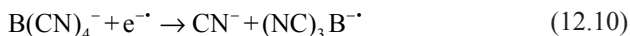


Fig. 12.4 X band EPR spectra (solid lines) obtained from irradiated tetracyanoborate ILs (3 MeV electron, 77 K irradiation, observed at 50 K). The cations are (i) 1-octyl-1-methylpiperidinium, (ii) 1-octylpyridinium, (iii) 1-octyl-1-methylmorpholinium, (iv) trihexyltetradecyl phosphonium (130 K spectrum is also shown), and (v) 1-ethyl-3-methylimidazolium [35]. The vertical lines indicate the resonance lines of the trapped hole center ($(\text{NC})_2\text{B}^\bullet$ radical) and trapped electron center ($(\text{NC})_3\text{B}^{\bullet-}$ radical anion), as indicated in the plot. The resonance lines of the latter radical overlap with the resonance lines of the C^\bullet and $\text{C}(\text{-H})^{\bullet+}$ radicals. The magnetic field is indicated in Gauss ($1 \text{ G} = 10^{-4} \text{ T}$)

protons to yield corrosive and reactive HF) and the residual $\cdot\text{CF}_2\text{SO}_2\text{NTf}^-$ radical; the corresponding excited state also dissociates to yield $\cdot\text{CF}_3$ radicals:



The latter radical anion readily protonates to $\cdot\text{SO}_2\text{NHTf}$. Both the trifluoromethyl and this protonated $\cdot\text{SO}_2\text{NHTf}$ radical can be observed in EPR spectra of irradiated bistriflimide compounds [29, 35]. Reaction (12.8) is not limited to fluorine; it also occurs with other halide and pseudohalide groups, e.g.



with the resulting radical anion yielding an EPR spectrum (shown in Fig. 12.4) with characteristic ^{11}B and ^{14}N coupling [35]. In addition, the ionized tetracyanoborate anion (Fig. 12.1) dissociates to cyanogen (C_2N_2) and the $\cdot\text{B}(\text{CN})_2$ radical, whose $M(^{11}\text{B}) = \pm 3/2$ lines can be seen in the magnified wings (see Fig. 12.4).

This radiation-induced dehalogenation is especially vexing from a synthetic standpoint. The superacidity of $\text{H}^{\delta+}\text{A}^{\delta-}$ is typically achieved through modifying the organic anion with electronegative groups (like triflate) that involve halide or pseudohalide atoms; that is, chemical resistance considerations favor those anions that have the least radiation resistance. These considerations suggest that radiation-resistant hydrophobic ILs need to be composed of rather uncommon anions that avoid such detrimental reactions. In Sect. 12.3 we present examples of such anions.

Inorganic ionic crystals, such as alkali halides, Alk^+X^- (where Alk^+ is the alkali cation and X^- is a halide anion), are as natural reference systems for ILs composed of organic ions as there are organic solvents. Irradiation of Alk^+X^- solids yields F-centers (electrons that are trapped in anion vacancies) and V_K centers (trapped $\text{X}_2^{\cdot-}$ radicals) that are formed when oxidized interstitial X^- ions (halogen atoms) form two-center three-electron $\sigma^2\sigma^{1*}$ bonds with the parent X^- anion in the lattice. In the $\text{X}_2^{\cdot-}$ radical anion, two paired electrons occupy the bonding σ_g orbital, while the unpaired electron occupies an antibonding σ_u^* orbital. While the $\text{X}-\text{X}$ bond is weak (<0.5 eV), the energy gain through sharing of the unpaired electron between two centers outweighs the repulsion between the cores. In the F-centers, electrostatic interactions of the s -like electron filling the vacancy with the positively charged Alk^+ cations localize and stabilize this electron, which to a first approximation can be viewed as a particle in the box [51]. Can such species form in ILs?

Pulse radiolysis studies of Wishart and co-workers [10–12] and the subsequent laser photolysis studies [50, 52, 53] demonstrated the occurrence of “solvated electrons” in ILs consisting of onium ions (cyclic or acyclic tetrasubstituted ammonium cations shown in Fig. 12.1) that lack electron-accepting groups. The light absorption properties of such trapped electrons are similar to those in hydrocarbons and weakly polar solvents; it is likely that structurally these species are analogous to previously known solvated electrons and F-centers, though the electrostatic interactions are weakened by screening of the positive charge in the cations by their arms. Very recently [44], such trapped electrons were observed in frozen ILs using EPR, and that pioneering study also established the occurrence of photobleaching due to the promotion of the electrons from the shallow traps to a mobile state. By pulse radiolysis, the lifetime of the solvated and pre-solvated electrons is limited by their secondary reactions that may involve proton transfer, deamination, and reactions with protic products and impurities, such as acids generated via reaction (12.5).



The latter reactions become very prominent when protic constituent anions (like HOSO_3^-) are present in the solution [34]. Reactions of radiolytically generated hydrogen atoms typically involve H^{\cdot} atom abstraction from the aliphatic arms of cations and addition to the π -rings of aromatic cations.

Turning to the V_K center analogs, both the “Br $^{\cdot}$ atoms” (in which the unpaired electron is coupled to the single $^{79}\text{Br}/^{81}\text{Br}$ nucleus) and $\text{Br}_2^{\cdot-}$ radicals can be observed (Fig. 12.5) in the EPR spectra of irradiated bromide-doped ILs [33, 38]. As the sample temperature increases, these “Br $^{\cdot}$ atoms” become mobile and react with Br^- anions in the matrix, converting to $\text{Br}_2^{\cdot-}$ radical anions. Closer examination of the EPR spectra of these “Br $^{\cdot}$ atoms” reveals superhyperfine structure from ^{19}F nuclei in the ILs composed of TfO^- and NTf_2^- anions and ^{14}N nuclei in the ILs composed of $\text{N}(\text{CN})_2^-$ anions. These observations indicate that the tentative “Br $^{\cdot}$ atoms” are, in fact, $\text{BrA}^{\cdot-}$ radicals, in which the bromine forms $\sigma^2\sigma^{1*}$ bonds with the heteroatoms of IL anions:

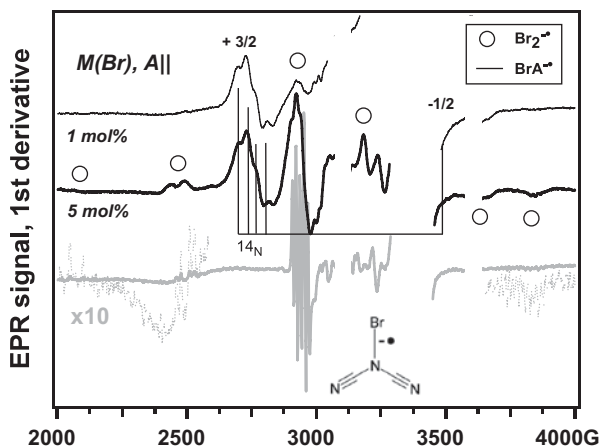


Fig. 12.5 X band EPR spectrum of irradiated frozen IL 1-ethyl-3-methylimidazolium dicyanamide (Fig. 12.1) doped with 1 mol% and 5 mol% 1-ethyl-3-methylimidazolium bromide observed at 50 K (3 MeV electron, 77 K irradiation) compared to the EPR spectrum of irradiated crystalline 1-ethyl-3-methylimidazolium bromide (bottom trace). The open circles indicate the resonance lines of the $\text{Br}_2^{\bullet-}$ radical, the vertical lines indicate the resonance lines of the $\text{BrN}(\text{CN})_2^{\bullet-}$ radical anion with resolved hyperfine structure in the $M(\text{Br}) = +3/2$ resonance from the unique ^{14}N nucleus [38]. Resonance lines from trapped H^{\bullet} atoms and organic radicals are removed from the plot



The hyperfine coupling constants (hfcc's) for these $\text{BrA}^{\bullet-}$ species agree with density functional theory (DFT) estimates, thereby corroborating the Br-heteroatom bond formation [38]. Such $\text{BrA}^{\bullet-}$ species can also be observed through electron trapping reactions of BrA molecules (such as *N*-bromosuccinimide):



The formation of $\text{Cl}_2^{\bullet-}$ radicals was observed in some chloride ILs (such as 1-benzylpyridinium chloride and 1-benzyl-3-methylimidazolium chloride) [39, 40]; however, in most of these ILs, the released Cl^{\bullet} atom promptly abstracts hydrogen from the arms of the cation in preference to $\text{ClA}^{\bullet-}$ and/or $\text{Cl}_2^{\bullet-}$ formation [35, 39, 40]. Photolytic generation of Br^{\bullet} atoms via two-photon excitation also results in a short-lived species that promptly abstracts hydrogen from the cation; reactions (12.12) and (12.13) were not observed [38].

The formation of dihalide radical anions in ILs indicates that the same tendency for delocalization of the unpaired electron that is observed in inorganic solids also operates in neat ionic liquids: there is sufficient driving force for the neutral radicals generated through reactions (12.2) and (12.3) to bind to the like ions and yield dimer radical ions:



Reaction (12.12) in bromide ILs is a specific example of reaction (12.16). One might have expected that “ionization” of IL ions would produce pairs of *neutral radicals* in the same fashion that ionization of molecular solvents generates pairs of *radical ions*. However, the energetic cost for the formation of neutral radical pairs in a material that consists of ions can be so prohibitively high that the system “tries” to restore the initial ion pair through spreading of the excess charge and spin density over one (or several) constituent ions.

From the standpoint of the EPR spectroscopy, the unpaired electron delocalization in dimer radical ions generated via reactions (12.15) and (12.16) reveals itself through increasing of the number of hyperfine couplings to magnetic nuclei in the ions (e.g., ^{14}N and $^{1,2}\text{H}$) and reducing the magnitude of the corresponding hfcc's. Species that are structurally and electronically analogous to the $C_2^{+\bullet}$ radical cations in the ILs are known in molecular systems as $M_2^{+\bullet}$ dimer radical cations obtained through the reactions of $M^{+} + M$, where M is a (neutral) solvent molecule [54–61]. In this $M_2^{+\bullet}$ species, two molecules share the hole. In the $C_2^{+\bullet}$ radical cation, two positive ions share the electron.

The formation of arene $M_n^{+\bullet}$ radical cations ($n=2-4$) is an example of charge delocalization in molecular systems, and the resulting species have been studied using magnetic resonance [56, 57, 59] and absorption spectroscopy [59–62], and there have been several recent theoretical advances in better understanding of their structure and energetics [60, 61]. The suggested formation of polarons in the (photo)ionization of DNA (that involves stacked aromatic nucleobases) is another example of this tendency [63–65]. Even in simple ionic solids, such as alkali glasses, the excess electrons are present as $\text{Alk}_n^{(n-1)+\bullet}$ clusters (the so-called alkali-associated trapped-electron centers) [66] analogous to the F-centers in ionic crystals. Formation of dimer and multimer radical anions in supercritical CO_2 , CS_2 , acetonitrile, hexafluorobenzene, and compressed benzene are familiar examples for *negatively* charged centers of this kind [51]. In the same vein, the formation of solvated electrons in molecular liquids with no electron affinity (such as ammonia, amines, water, acetonitrile, and alcohols) can be considered as the extreme case of this tendency that causes sharing of the excess (cavity) electron by antibonding orbitals of several solvent molecules. Reactions (12.15) and (12.16) exemplify this general trend in a novel way, but the trend itself is familiar.

Our EPR studies indicate that the occurrence of reaction (12.15) has a considerable effect on secondary radical chemistry, as only monomer radicals C^{\bullet} can be subsequently protonated by radiolytically-generated acids via reaction (12.17) [33, 39, 40]



where the CH^{++} can be viewed either as a protonated form of C^* or an H atom adduct of the parent cation (Sect. 12.4). No protonation was observed for C_2^{++} [30, 33].

While the IL anions are more problematic from the standpoint of radiation stability, the cations are also prone to fragmentation (Sect. 12.1). Many organic cations can be represented as RB^+ , where B is the base (amine, pyridine, imidazole, etc.) and R- is the arm attached to the heteroatom of this base (typically, nitrogen, sulfur, or phosphorus atom). Examples of such cations include tetraalkyl onium (ammonium, phosphonium), 1-methyl-3-alkylimidazolium (the most popular cation for formulation of the room-temperature ILs), 1-alkylpyridinium, 1,1-dialkylpyrrolidinium, and many other such cations (Fig. 12.1). In addition to the C-H dissociation and deprotonation from the side arms (reaction (12.5)), three other reactions can occur in which the *entire* side arm is released [37, 39, 40, 42]:



Reactions (12.18) and (12.19) involve the excited states of the parent cation and yield spin-silent products, whereas reaction (12.20) is the DEA reaction that yields terminal radicals derived from the outgoing arms. Our attempt to establish the occurrence of reaction (12.19) for cations with aliphatic arms (through exclusive formation of terminal alkyl radicals) yielded a negative result. It seems that the DEA reaction is always a minor reaction for such cations, whereas reaction (12.19) is prominent, and it can be observed using mass spectrometry and product analyses [37, 39–42]. Reaction (12.18) becomes prevalent when the outgoing carbocation is stabilized, as was observed for benzyl derivatives [39, 40]. As the same stabilization occurs in the outgoing radical R^* , the same cations are prone to reductive fragmentation via reaction (12.20). Such DEA reactions are known from studies of the radiation chemistry of aqueous surfactants [67]. Thus, observation of radical R^* by EPR is a useful diagnostic for the suitability of a given organic cation to withstand reductive fragmentation. Note that reactions (12.19) and (12.20) are irreversible, whereas the reverse of reaction (12.18) is the quarternization of the base through which the organic cations are usually synthesized. Steering the chemical pathway from reaction (12.19) to reaction (12.18) would increase the overall radiation stability (by introducing reversible reactions) had not it promoted detrimental reaction (12.20).

In fact, there is a deep connection between the ILs and chemically-amplified photoacid generating resists, which are also ionic compounds involving the bases of superacids (such as SbF_6^- , AsF_6^- , BF_4^- and PF_6^-) [68–72]. The typical light-absorbing cation in such photoresists is dialkylarylsulfonium, ArS^+R_2 , whose photoexcitation causes homo- or hetero-lytic dissociation of the S–C bond:



Photogenerated Ar^+ and $\text{}^{*}\text{SR}_2$ subsequently react with the proton-donating polymer matrix releasing $\text{H}^{\delta+}\text{A}^{\delta-}$. Similar reactions occur in ILs (reaction (12.5) through reactions of R^+ carbocations (generated in reaction (12.18)). Thus, what makes an organic cation unsuitable for radiation-resistant ILs automatically makes it a candidate for acting as a photoacid generator in extreme ultraviolet photolithography (that is used in the manufacture of electronic microcircuits), and vice versa.

Among the approaches developed for the improvement of photoresists is deliberate introduction of deprotonation sites into the cation structure, e.g. by hydroxylation of the aryl groups

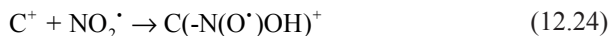


Photoexcitation of HOArS^+R_2 yields zwitterion and proton instead of inducing C–S bond dissociation. Similar principles can be used to improve the radiation stability of cations in ILs [42]. (Sect. 12.4)

Finally, as IL diluents remain in contact with other phase(s) during the separations, radiation stability of neat IL is only one aspect of the problem. The typical aqueous raffinate is acidic (to inhibit hydrolysis of polyvalent metal ions), usually containing 0.01–5 M nitric acid [34]. Even nominally hydrophobic ILs extract a significant amount of nitric acid from this aqueous raffinate. The NO_3^- and undissociated HNO_3 are efficient quenchers of electronic excited states and rank among the strongest electron acceptors. EPR studies of equilibrated IL solutions indicate that the electrons are accepted in the matrix yielding short-lived $\text{NO}_3^{2-\cdot}$ radicals that either decompose to stable NO_2^{\cdot} radicals or attach to aromatic cations forming nitrosubstituted radicals,

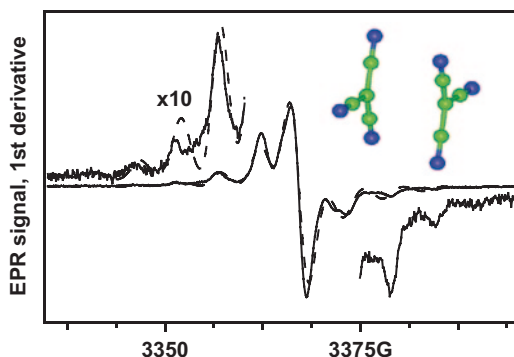


No EPR evidence was obtained for radiolytic oxidation of NO_3^- to NO_3^{\cdot} radical (this reaction commonly occurs in aqueous solutions), as the oxidation of the organic cation is energetically favored. Direct excitation of NO_3^- in IL proceeds mainly through the N–O bond dissociation with the formation of NO_2^{\cdot} and O^{\cdot} radicals, and the latter radical promptly adds to the aromatic rings of the cations yielding the corresponding $\text{C}(-\text{OH})^{\cdot}$ radical. As the temperature increases, the NO_2^{\cdot} radicals become mobile and react with the C^+ cations to yield nitroso adducts



The same adducts are formed through the protonation of the $\text{C}(-\text{NO}_2)^{\cdot}$ radicals generated in reaction (12.23). All in all, the extracted nitric acid present in the IL diluent has a surprisingly mild effect on the radiation stability of the ILs, and in the rest of the review we focus on neat ILs and solutions of extracting agents in these ILs.

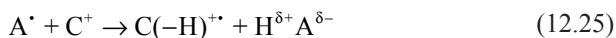
Fig. 12.6 *Solid lines:* X- band EPR spectrum of irradiated potassium tricyanomethanide observed at 50 K (irradiated at 300 K). *Dashed lines:* simulated EPR spectrum for $C_2(CN)_6^-$ dimer radical anion shown in the inset. The hyperfine structure results from six magnetically equivalent ^{14}N nuclei with isotropic constant of 1.8 G [43]



12.3 Anions

As observed in Sect. 12.2, radiation stability of IL anions is the main concern in mitigation of radiation damage, and most ILs exhibit an unacceptably high degree of anion fragmentation. This poor stability also translates to a high yield of cation modification due to decoration of the cations with small reactive fragments of the anions [39, 40, 73–75]. We found only a few exceptions to this general rule, and in this section we examine such “exceptional” systems.

The first example of a radiation resistant anion, dicyanamide $(N(CN)_2)^-$, see Fig. 12.1), was inadvertently found in ref. [30]. Following our general scheme discussed in Sect. 12.2, oxidation of this anion via reaction (12.2) should have yielded the imidyl radical, $\cdot N(CN)_2$. EPR observations of imidyl radical $\cdot Nf_2$ in irradiated ionic crystals and frozen ILs composed of the bistriflimide anion (Fig. 12.1) were among our first results in the studies of ILs [29]. At room temperature, the imidyl radicals are known to be reactive, oxidizing radicals, abstracting hydrogen from organic compounds, including the aliphatic arms of the cations (Fig. 12.3),



In the EPR spectra of irradiated dicyanamide solids, the imidyl radical was not observed. Instead, a different radical with a more complicated hyperfine coupling pattern was observed that was indicative of spin sharing between two $N(CN)_2^-$ anions, suggesting the occurrence of reaction (12.16). The latter is a stabilized C_2 symmetrical dimer radical anion with an elongated N–N $\sigma^2\sigma^{1*}$ bond (that can also be viewed as a radical anion of tetracyanohydrazine) [30].

A similar reaction was later observed in the radiolysis of tricyanomethanide compounds (Fig. 12.1). No $\cdot C(CN)_3$ radical was observed despite the fact that it is a stable planar radical with an easily recognized spectroscopic signature [43]. Instead, the EPR spectrum shown in Fig. 12.6 was observed that corresponds to a D_{3d} symmetrical $C_2(CN)_6^-$ dimer radical anion with the elongated C–C $\sigma^2\sigma^{1*}$ bond. Unlike dicyanamide, the reduced tricyanomethanide anion is unstable, as it undergoes

DEA reaction (12.8) causing the loss of cyanide (we remind that cyanide is a pseudohalide), but these two examples suggested to us that the problems identified in Sect. 12.2 can be addressed using anions that are (i) inherently incapable of reaction (12.7) and (ii) yield neutral radicals which can be stabilized via reaction (12.16).

A particular approach to synthesizing such anions is to retain the imide structure without introduction of the halide and pseudohalide groups, by replacing them with 1,2-benzene group (Fig. 12.1). The resulting anions have weaker conjugate acids than the bistriflimide and dicyanamide anions, but these acids are still sufficiently strong for many applications. For example, the saccharinate and 1,2-benzenedisulfonimide anions (Fig. 12.1) have pK_a 's of 1.48 and -4.1 in the aqueous solution, respectively. Our EPR experiments indicate that radiolysis of these anions yields imidyl (A^*) radicals via reaction (12.2) and HA^* radicals through reactions (12.4) and (12.6), respectively, i.e., these anions are efficient electron *and* hole traps. The HA^* radicals occur in two varieties: H^* atom adducts at the phenyl ring and N-atom protonated dianions. Due to steric hindrance, no A_2^* radical anions are formed, which is also the case for NTf_2^- , but not for $N(CN)_2^-$ and $N(SO_2F)_2^-$. Thermal activation facilitates reactions (12.25) and (12.26)



The latter reaction closes the redox cycle in Fig. 12.3, making it possible to achieve near-perfect chemical reversibility. No concomitant ring-opening and ring-contraction reactions were observed for these aromatic imide anions, whereas another cyclical imide, acesulfamate, underwent several such transformations [36]. Even prolonged radiolysis of these aromatic imide anions causes little (less than 0.01 per 100 eV) fragmentation, mainly through SO_2 elimination in their excited state; the residual path for their degradation during long-term radiolysis becomes gradual C–C bond formation between their aromatic moieties [36, 43].

More recently [43], we found another class of radiation resistant anions, which are polynitrile anions with the general formula of $C_xN_y^-$ (Fig. 12.7). The dicyanamide and tricyanomethanide anions are part of this family, in which high acidity of the conjugate acids is achieved by strategic placement of multiple $C\equiv N$ groups [76]. Some of these anions are organic analogs of inorganic anions, such as NO_2^- (for $TCAP^-$) and CO_3^{2-} (for $TCPD^{2-}$), as the $C(CN)_2$ group is isoelectronic with the oxygen. It is easy to see that oxidation of these anions yields stable N- or C-centered radicals, so the only problematic redox reaction is reduction of the anion followed by the elimination of the cyanide (reaction (12.8)) that competes with reactions (12.4) and (12.6) that yield hydrogen atom adduct instead (Fig. 12.8).

Representing the parent anion as UCN^- four radical species can form via one-electron reduction, depending which tendency (protonation or cyanide loss) prevails: UCN^{2*} , U^* , $HUCN^*$, and HU^* .

EPR spectroscopy was indispensable in permitting us to establish the prevalent fragmentation pathway for a given anion (Fig. 12.8). For example, for tricyanomethanide, the loss of cyanide prevails, and the main product of radiolytic reduction is HU^* . For the $TCAP^-$ and $HCAP^-$ anions (Figs. 12.7 and 12.8), only the

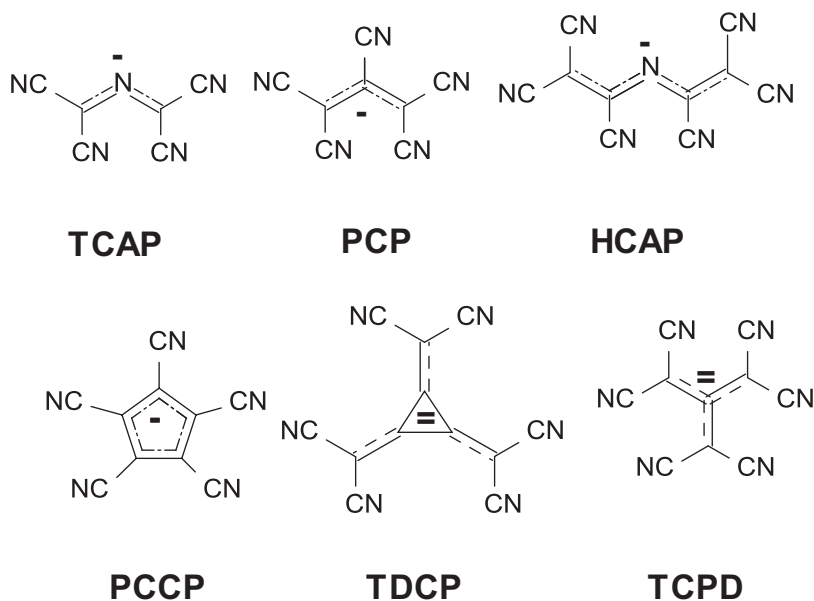


Fig. 12.7 Polynitrile mono- and di-anions: tetracyano-2-azapropenide (TCAP⁻), 1,1,2,3,3-pentacyanopropenide (PCP⁻), 1,1,2,4,5,5-hexacyano-3-azapentadienide (HCAP⁻), 1,2,3,4,5-pentacyanocyclopentadienide (PCCP⁻), 1,2,3-tris(dicyanomethylene)cyclopropanediide (TDCP²⁻), and 2-dicyanomethylene-1,1,3,3-tetracyanopropanediide (TCPD²⁻)

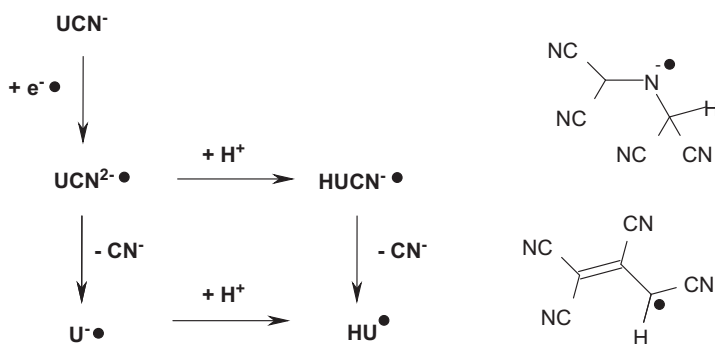


Fig. 12.8 On the *left*: the general scheme for secondary reactions of reduced polynitrile anions (UCN). On the *right*: examples of HUCN⁻• radical anions for TCAP⁻ and HU• radicals for PCP⁻ observed by EPR of irradiated ILs composed of these two anions (see Fig. 12.7) [43]

HUCN⁻• radical is observed, suggesting that protonation of the radical dianion occurs faster than cyanide elimination. For the PCP⁻ anion (Figs. 12.7 and 12.8), UCN²⁻•, HUCN⁻•, and HU• were observed, suggesting competing pathways due to the increasing stability of the radical anion. For the PCCP⁻ anion (Fig. 12.7), no protonated or fragment radicals were observed, suggesting that the radical dianion

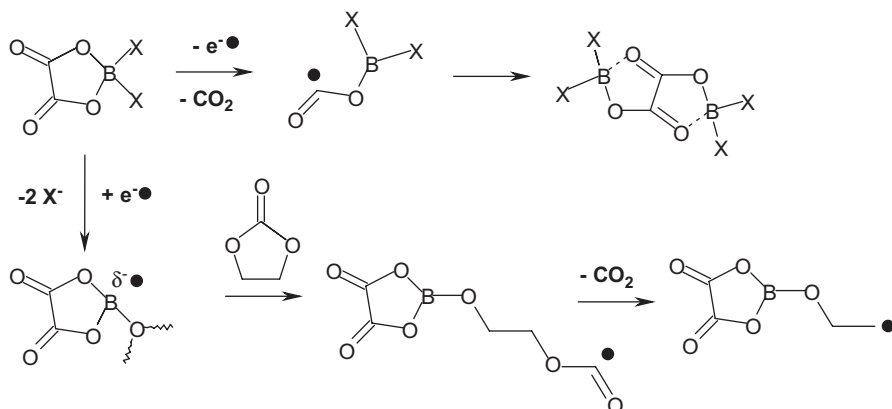
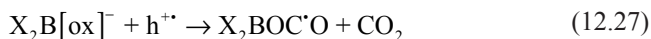


Fig. 12.9 Redox reactions of BOB⁻ (X₂=oxalate) and DFOB⁻ (X=F) anions [29, 77]

is stable. No evidence for one-electron reduction was observed for dicyanamide and TDCP²⁻ (Fig. 12.7). As the rate of protonation increases with temperature, even IL anions that eliminate cyanide at low temperature can become stable, as they are protonated more rapidly than this elimination occurs, which accounts for the stability of the PCCP⁻ based ILs in room temperature radiolysis and as also suggested by mass spectrometry and nuclear magnetic resonance measurements [43].

As seen from these examples, radiation stability of anions is largely determined by the facility of redox reactions involving these anions. Such redox reactions occur not only in radiolysis but also in electrochemistry, and these two fields are closely connected, as the same organic and inorganic anions occur in battery electrolytes, including the IL electrolytes in the next generation Li-metal, Li-air, and Li-ion batteries [6].

In carbonate based electrolytes, lithium cations in Li-ion batteries are typically introduced as LiPF₆. It has been found empirically that certain additives, such as lithium bis(oxalato)borate (BOB⁻, B[ox]₂⁻) and difluorooxalato borate (DFOB⁻, F₂B[ox]⁻) significantly improve battery performance. The electrochemical and radiolytic oxidation of these anions releases CO₂ molecules yielding carbonyl radicals (X₂=ox, F₂) [29, 77]:



(See Fig. 12.9) The same reaction occurs in ILs consisting of the BOB⁻ and DFOB⁻ anions [77]. The resulting radical does not easily add to carbonate solvents and decays by dimerization. In the (F₂BOCO)₂ dimer, the F₂B- group serves as a strong Lewis acid, so it readily forms B–O bonds with the carbonyl oxygens in the solvent and bridging oxygens at the transition metal lithium oxide surfaces (that serve as positive electrodes in the Li-ion batteries). As the oxidation of these dimers (as opposed to the parent anions) is energetically prohibitive, they form a protective layer retarding further oxidation of the carbonate electrolyte thereby improving battery

performance. The reduction of these anions yields a B-centered radical that is analogous to the so-called boron electron centers discovered using EPR spectroscopy by Griscom [78, 79] in irradiated alkali borate glasses. These centers can be thought of as $[\text{ox}]\text{B}^{\bullet}$ σ -radicals so strongly interacting with the oxygens in the neighboring matrix that the boron becomes pyramidal (Fig. 12.9), and the unpaired electron acquires significant B $2p$ character [80]. Such radicals are very reactive, readily adding to the electrolyte molecules (such as the ethylene carbonate shown in Fig. 12.9), in this way initiating radical polymerization at the graphite electrode (Fig. 12.9) and eventually catalyzing the formation of the protective solid electrolyte interphase. EPR identification of the B-centered and carbonyl radicals has excluded many other scenarios for the chemical mode of the protective action of these increasingly common electrolyte additives [77].

As the carbonate electrolytes are oxidized during operation of Li-ion batteries at the high voltages that are desired for automotive applications (and also totally unsuitable for Li-air batteries), there is much effort to replace these electrolytes with less oxidizable solvents, including aliphatic ILs [6]. As the latter typically have prohibitively high viscosity, only the most fluid of these ILs are considered. Many of the currently examined compositions are based on bis(fluorosulfonyl)imide ($\text{N}(\text{SO}_2\text{F})_2^-$) that is closely related to bistriflimide. Unfortunately, the more common IL anions cannot be used in the IL electrolytes, as they form soluble complexes with Al(III) ions generated during oxidation of aluminum collector on which the positive oxide electrode is dispersed; $\text{N}(\text{SO}_2\text{F})_2^-$ and PF_6^- are unique in this respect, whereas NTf_2^- is particularly problematic [81–86]. For bistriflimide, the culprit is the elimination of F^- via reaction (12.8). No such reaction was observed for bis(fluorosulfonyl)imide [82]. Oxidation of this NX_2^- anion ($\text{X}=\text{SO}_2\text{F}$) yields imidyl $\cdot\text{NX}_2$ radicals and $(\text{X}_2\text{N}\cdot\text{NX}_2)^{\bullet-}$ radical anions, whereas the oxidation of NTf_2^- yields only imidyl radicals, as the trifluoromethyl groups introduce repulsion between the two subunits. The N–N $\sigma^2\sigma^{1*}$ bond formation decreases reactivity of oxidized anions, causing reduced deterioration of electrochemical performance during battery cycling.

12.4 Cations

We turn to organic cations, whose chemistry is even richer than that of the anions. As oxidation of A^- to A^{\bullet} is “natural” for anions, so the reduction of C^+ to C^{\bullet} is “natural” for many of cations, as both of these reactions turn charged species into neutral radicals. However, the latter mode is not the only option for stabilization of the excess charge in the IL medium.

Two classes of organic cations that are most commonly used for IL synthesis are onium cations (cyclic and acyclic quaternary ammonium and phosphonium cations) and 1-alkyl derivatives of imidazolium. These onium cations represent a broader class of aliphatic cations, while the imidazolium cations represent a broader class of aromatic cations with electron-accepting π -systems. In the aliphatic onium salts, electron trapping occurs through the formation of metastable trapped electrons (F-centers) or

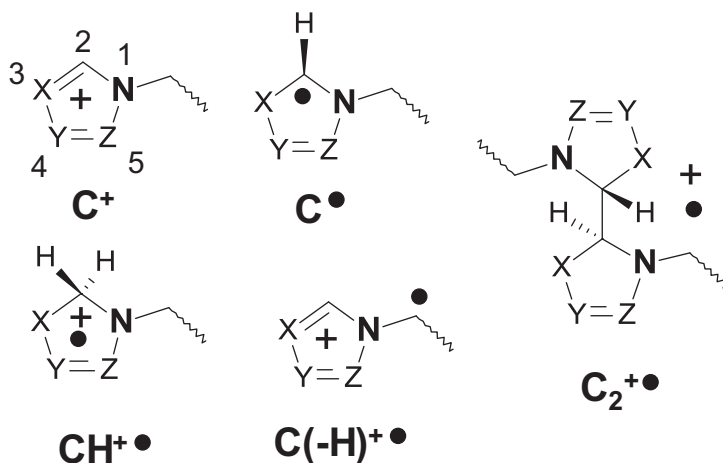


Fig. 12.10 Structural formulas for radicals and radical cations derived from 5-carbon aromatic cations (C^+). All of these radicals can be observed using EPR spectroscopy of irradiated frozen ILs [39]

reactions with electron-accepting anions (reaction (12.2)), whereas hole trapping by the cation (reaction (12.1)) causes prompt deprotonation or charge transfer to a nearby anion, reaction (12.5). The deprotonation reaction (12.5) preferentially involves terminal and penultimate hydrogens in the extended long aliphatic arms [29]. In this tendency, ILs are similar to normal paraffins that also exhibit such a preference (see, for example, [87]). For branched derivatives, complete loss of aliphatic arms is also observed via reaction (12.20) due to the greater stabilization of the outgoing radical [33].

The formation of $C(-H)^\bullet$ radicals in the long aliphatic arms of the cations is common to both aliphatic and aromatic cations, whereas only the latter accept electrons. In most of imidazolium ILs, the electron is accepted by the monomer cation (reaction (12.3)), yielding the corresponding 2-imidazolyl radical. The same reaction is observed in two other 5-carbon aromatic cations: the derivatives of 1,2,4-triazole and 5-methylthiazole (Figs. 12.1 and 12.10). In these carbon-2 centered radicals, the carbon is pyramidal, with the nonplanarity increasing from thiazole to 1,2,4-triazole to imidazole, which is in agreement with DFT calculations [39]. In this sequence, the C 2p character of the singly occupied orbital decreases, and the σ -character increases, resulting in the systematic increase in the hyperfine coupling constant for $^1H(2)$. In ref. [30] and elsewhere [33, 39], we demonstrated that in some of imidazolium ILs, reaction (12.15) takes place with the formation of C(2)–C(2) two-center three-electron $\sigma^2\sigma^{1*}$ bonds (Fig. 12.10).

In this C_2 symmetrical species, the unpaired electron density is equally shared by two subunits. Such species can be generated using other means [88, 89] and presently there is consensus that electron trapping in such ILs can occur either through the formation of the monomer radical or dimer radical cation.

It is worth observing that reaction (12.15) is reversible. Given the relatively weak C(2)–C(2) bond energy of 0.4–0.8 eV in the gas phase (depending on the

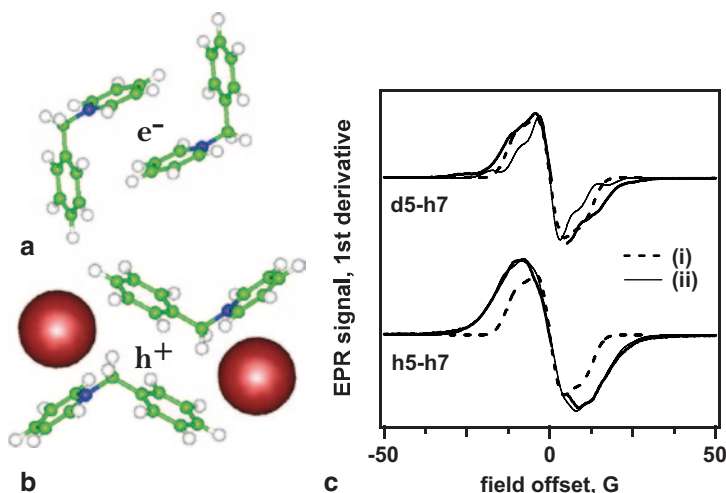


Fig. 12.11 To the *left*: DFT optimized structures for **a** $(\text{BzPy})_2^{\bullet-}$ and **b** $(\text{BzPy})_2^{\bullet3+}$ (A^-)₂ radical ions (trapped electron and trapped hole centers). The balls represent the counter anion. In structure **(a)** the excess electron is shared by the two face-to-face pyridinium moieties, and in structure **(b)**, the electron deficiency is shared by the two phenyl rings. To the *right*: *Solid bold lines* in panel **c** are the experimental X-band EPR spectra of irradiated 1-benzylpyridinium bistriflimide (3 MeV electrons, 77 K) observed at 50 K for two isotopomers having protonated benzyl arm and either perdeutero or perprotio pyridinium head groups, as indicated in the plot. Traces (i) and (ii) are simulated EPR spectra for radicals **(a)** and **(b)** using the magnetic parameters obtained in our DFT calculations [40]

derivatization of the cation), the overall enthalpy of the forward reaction depends on the solvation energy, as the dimer radical cation is larger than the parent cation, so the corresponding Born energy is lower. The dimer cation is observed only in irradiated ILs consisting of bulky anions, whereas ILs consisting of small anions yield the monomer radical. Based on the similarity with other ionic solids, it is likely that the excess electron is trapped at the site of anion vacancy, and the formation of the dimer radical cation is facilitated by fortuitous orientation of cations at such sites.

More recently, we demonstrated that similar chemistry occurs for other 5-carbon aromatic cations, in particular, for thiazolium cations [39], with the formation of a radical cation species that is intermediate between the C–C $\sigma^2\sigma^{1*}$ bound radical cation observed for imidazolium [30] and the stacked π -sandwich dimer radical cation that is observed for 6-carbon aromatic cations, such as 1-alkyl and 1-benzylpyridinium cations [40]. Observation of this dimer radical cation in radiolysis of pyridinium ILs was surprising, as the corresponding pyridinyl radicals are well-known intermediates that have been thoroughly studied in polar solvents using EPR spectroscopy and spectroelectrochemistry. However, no pyridinyl radical was observed in radiolysis of pyridinium salts, which can be demonstrated using H/D isotope substitution in the pyridine moiety and the side arms. The latter experiments suggest charge delocalization involving at least two cations, with the unpaired electron density shared by their pyridine moieties (Fig. 12.11, panel (a)).

This collective mode of electron localization is unprecedented in other IL systems, whereas even more extensive charge sharing was suggested in theoretical studies, where the resulting excess electron species can be viewed either as an extreme case of a cavity electron (with large transfer of electron density into the antibonding π -orbitals of several cations) or a solvent-supported multimer radical ion [48, 90–93]. The same uncertainty exists for many of the excess electron and hole centers in molecular fluids [51], and understanding of the structural aspects of such species remains an open problem.

1-Benzylpyridinium (BzPy⁺) presents the only known example of the cation that supports collective modes for localization of positive *and* negative charge. In pulse radiolysis of ILs consisting of this cation, there is a strong absorption band in the near infrared that corresponds to the so-called charge resonance (CR) observed in pulse radiolysis of aromatic hydrocarbons in *molecular* liquids. The highest occupied wavefunctions ϕ_1 and ϕ_2 of the two units in a π -sandwich dimer of two planar aromatic molecules combine into a symmetrical ($\phi_1 + \phi_2$) and antisymmetrical ($\phi_1 - \phi_2$) wavefunctions that form the highest occupied bonding and the lowest unoccupied antibonding molecular orbitals with an allowed optical transition between them; this electronic transition is responsible for the CR band.

For trapped electron centers, this CR optical transition is weak (although still observable), but for trapped hole centers (Fig. 12.11, panel (b)), it is quite strong. In the EPR spectra of irradiated BzPy⁺ compounds (e.g., Fig. 12.11, panel (c)) there is a narrow line component (that overlaps with the resonance line of (BzPy)₂^{•+}) that changes upon H/D substitution in such a way that it can only be from a radical species in which the unpaired electron is shared by the benzyl moieties, and the spectral envelope of this species is consistent with the one predicted by DFT calculations for (BzPy)₂^{3•+} radical trications, in which two phenyl groups face each other in a stacked π -sandwich (Fig. 12.11, panel (b)) [40]. The formation of this species seems counter-intuitive due to the expected strong electrostatic repulsion, but this repulsion is much reduced due to the interaction with several anions. We conclude that the PyBz⁺ cations form face-to-face dimer ions whether they trap electrons or holes. The resulting trapped hole centers do not deprotonate, which accounts for the remarkable radiation stability of this cation demonstrated through product analysis [40].

Given the connection with the photoacid generators emphasized in Sect. (12.2) (reaction (12.21)), one can ask whether the design principles developed for the latter can be used for improving *radiation* stability of ILs. To this end, we designed “antioxidant” cations whose fragmentation and/or radiolytically induced deprotonation yield stable, unreactive radicals [42]. In these cations, we deliberately introduced deprotonation sites: the 4-hydroxy-3,5-dialkylbenzyl and diphenylmethyl groups attached to imidazolium, pyridinium, and sulfonium cations (Fig. 12.12). The formation of the corresponding aryloxy and trityl radicals was observed in the EPR spectra of irradiated ionic compounds. Overall, this strategy for reduction of cation fragmentation results in improved radiation stability, at least in some cases [42].

The perils of integrating task-specific functional groups into structural cations in TSILs (which is one of the recent trends in separations sciences) has already been

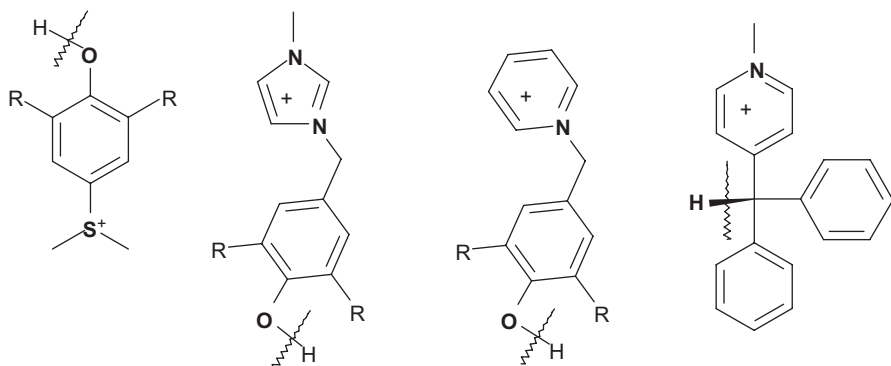


Fig. 12.12 “Antioxidant” cations with designated deprotonation sites ($R = \textit{tert}$ -butyl). The corresponding stable aryloxy and trityl radicals are observed in EPR spectra of irradiated ILs consisting of such cations [42]

discussed in the Introduction through the example of choline (Chol^+) in crystalline choline chloride that is believed to undergo deamination ($\text{Me}_3\text{N}^+\text{CH}_2\text{CH}_2\text{OH}$) in its reduced state and N-C bond scission in the deprotonated state after hydrogen atom loss at β -carbon (Fig. 12.2). Previous research indicates that the decomposition is much lower in solutions of Chol Cl in aqueous and polar solvents [26]; suggesting that mobile Cl^- atoms released in oxidation of choline chloride play important role in the initiation of the chain reaction [28]. (Such reactive atoms are not formed in solution).

Low temperature radiolysis of Chol Cl and Chol NTf_2 yields the radical that was previously attributed to $\cdot\text{CH}_2\text{CH}_2\text{OH}$ (a product of cation *reduction*), providing that the latter assumes a frozen conformation in which the dihedral angle $\text{H}_\alpha\text{CCO}$ is fixed at 90° [28]. However, our scrutiny indicates that in both cases the radical observed is, actually, $\text{Me}_3\text{N}^+\text{CH}_2\text{C}^*\text{HOH}$ radical action, which is a product of cation *oxidation*, which is contrary to the reaction scheme shown in Fig. 12.2. There seems to be *no reductive deamination* in this system, as is also the case in all other onium compounds that we studied by EPR. Furthermore, no N-C bond scission in the oxidation of Chol^+ was observed in Chol NTf_2 , suggesting that radiolytic *oxidation* occurs mainly in NTf_2^- anions (reaction (12.2)), and the resulting imidyl radicals are relatively unreactive towards the parent cation, abstracting only α -hydrogen, whereas the more reactive Cl^- atoms also abstract β -hydrogen, starting the chain reaction (Fig. 12.2).

Different results were observed for a closely related betainium ($\text{Me}_3\text{N}^+\text{CH}_2\text{CO}_2\text{H}$) cation (Fig. 12.1), where radiolytic oxidation to $\text{Me}_3\text{N}^+\text{C}^*\text{HCO}_2\text{H}$ radical (via deprotonation and/or H^\cdot atom abstraction) and $\text{Me}_3\text{N}^+\text{CH}_2^\cdot$ radical (via CO_2 elimination) is equally facile, and the latter radical readily abstracts hydrogen from the parent cation.

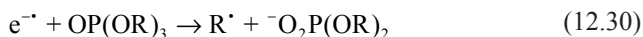
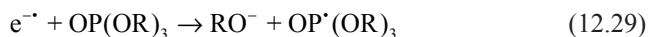
It is seen from these two examples that functionalization can considerably weaken bonds in the cation and facilitate multiple fragmentation pathways, which casts doubt on the appropriateness of the strategy of incorporating metal-ion binding groups into the structural ions.

12.5 Solutes: Extraction Agents and Ionophores

Radiation stability of neat ILs is important, but in the target application, these ILs are used as *diluents* for extraction agents and ionophores. Radiation stability of these solutes takes precedence over the radiation stability of the diluent itself. Such solutes typically have several heteroatoms and, therefore, possess weaker bonds than IL ions. One particular concern with radiolysis of extraction solvents is that the radiation damage can be channeled from the solvent to the solute, either by electronic energy transfer or charge transfer. While being detrimental, fragmentation of the structural ions in the IL does not necessarily translate into the loss of functionality, provided that the fragments and radiolytic products do not interfere with metal ion separations. In fact, *it is preferable that the radiation damage is limited to the solvent, i.e. the direction of the flow of excitation and charge is reversed*. This situation is referred to as the radioprotection property of the diluent. This radioprotection can be understood more broadly, as any mitigating effect on the damage to the component of interest. We emphasize that some effects of ionizing radiation are inherently irreversible due to deposition of vast amounts of energy (2–10 eV) per ionization event, which is sufficient to cause multiple bond breakages. This deterioration cannot be retarded, but it is possible to strive for greater reversibility of reactions or use less important components of the system as sacrificial agents to protect the other, more important components.

In this respect, ILs have an edge over many molecular solvents: as some of the constituent ions serve as deep traps for electrons and holes thereby preventing or inhibiting charge transfer to the solute.

A telling category of reactions that demonstrate this protective action includes the DEA reactions of organophosphates, such as tri(*n*-butylphosphate), TBP (briefly mentioned in the Introduction). This ligand readily forms metal ion complexes with *f*-ions (including uranyl, UO_2^{2+} and Pu^{4+}) through the P=O group; it is also used to increase the polarity of hydrocarbon solvents (such as *n*-dodecane) serving as a phase transfer catalyst (see below). In a hydrocarbon solution, the organophosphates can react with the excess electrons either by forming phosphoranyl radicals (reaction (12.28)) or via DEA yielding phosphoryl or alkyl radicals (reactions (12.29) and (12.30), respectively)



Reaction (12.30) is the main reaction of concern, as the dealkylation product (the dialkylphosphate) strongly binds to trivalent ions of lanthanides and minor actinides, and these ions become co-extracted into the organic phase. Analogous reactions

occur with mono- and di- phosphates. In the radiolysis of $(\text{MeO})_2\text{PO}_2\text{Na}$, all three types of radicals are observed [34]. When the corresponding acid $((\text{MeO})_2\text{PO}_2\text{H})$ is irradiated, the yield of dealkylation is greatly decreased as the electron reacts mainly through reaction (12.31)



The same reaction occurs in solutions of $(\text{MeO})_2\text{PO}_2\text{H}$ in imidazolium ILs, where the released H^\bullet atoms promptly add to the cation ring; reactions (12.28–29) are suppressed. It appears that electron scavenging by imidazolium rings and protons in the dialkylphosphoric acid out-competes the detrimental DEA reactions. Direct excitation of the phosphate derivatives also causes the dealkylation via reaction

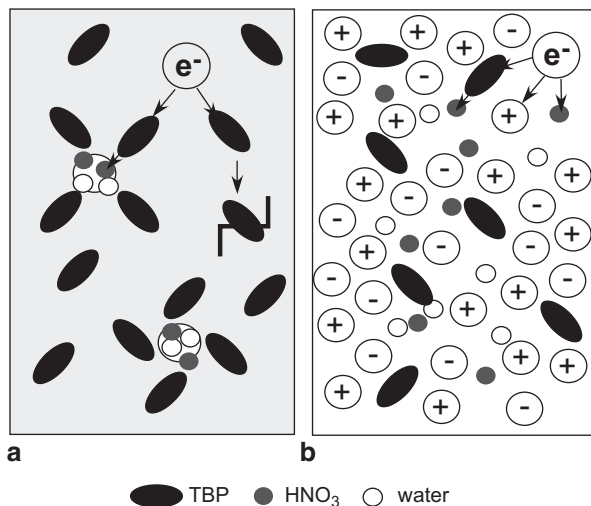


which yields hydroxylated C-centered radicals following the internal H^\bullet atom transfer. The very low yield of all these radicals suggests that imidazolium cations not only scavenge the excess electrons but also serve as quenchers of electronic excitations causing the P–O bond scission in reaction (12.32). Using EPR, we quantified the efficiency of electron scavenging in reactions (12.31) and (12.32) by measuring the relative yield of $\text{CH}^{+\bullet}$ radicals (H atom adducts of imidazolium ions) to the yield of C-centered radicals that are derived from the aliphatic arms of the IL cations and the aliphatic arms in bis(ethylhexyl)phosphoric acid, which is an important and widely used extracting agent for trivalent f -ions. It follows that at 10 mol% loading, the solute traps 50% of the electrons via reaction (12.31), i.e. the imidazolium cations can compete even with the relatively strong phosphororganic acid. For TBP solutions in these imidazolium ILs, there is almost no dealkylation occurring even when the mole fraction of the TBP is 40 mol%. These systems exemplify the philosophy of radioprotection stipulated above.

An interesting question is, how can the dealkylation of TBP occur in an organic diluent contacting 2–10 M HNO_3 , as up to 1 M of this nitric acid is extracted into the organic phase? Nitric acid and nitrate are extremely efficient electron scavengers and excited state quenchers (Sect. 12.2), so it appears that dealkylation should not occur in such solutions at all.

The solution of this puzzle lies in recent studies [94–96] indicating that water and HNO_3 are extracted into the TBP modified organic phase as nanoscale aggregates (reverse micelles), containing 2–4 molecules that form strong H bonds to each other and the P=O groups of the TBP (Fig. 12.13). Only a fraction of TBP molecules are bound to HNO_3 in this fashion, whereas the rest are dispersed in the solvent (aliphatic hydrocarbon) bulk. The TBP molecules that are involved in these nanoaggregates avoid fragmentation, whereas those dispersed in the solvent bulk accept charge or energy from the solvent and dissociate before reacting with spatially segregated HNO_3 molecules contained in the reverse micelles: *radiation damage occurs because the modified organic phase is microheterogeneous*. Such molecular diluents are quite unlike the ILs, because these IL solvents fully disperse polar

Fig. 12.13 Radiolysis in **a** microheterogeneous water-HNO₃-TBP-*n*-dodecane system, where water and nitric acid form aggregates stabilized by H-bond TBP acting like surfactant, and **b** microhomogeneous water-HNO₃-TBP-IL system. Since nitric acid serves as a sacrificial electronic excitation quencher and charge scavenger in these systems, microheterogeneity causes decomposition of TBP molecules dispersed in the solvent bulk



solutes throughout their polar domains, which permeate the fluid on the nanoscale. This permits effective diversion of reactivity towards HNO₃ and away from TBP, affording “radioprotection” of such extractants. That is, the radioprotective properties of the ILs are not limited exclusively to their own chemistry, but also occur through the non-trivial effects of solvent morphology.

While the organophosphates illustrate the possibility of radioprotection in IL diluents, similar studies for other classes of extracting agents and ionophores revealed difficulty in reversing the damage that results from the *oxidation* (as opposed to the *reduction*) of the solutes. The problem is that even when the oxidation occurs in the IL component of the solution, the resulting oxidizing radicals are still sufficiently reactive to migrate and oxidize the solute. We have not observed the situation when the oxidation is efficiently channeled to the solute (as these oxidizing species also react with the organic cations, so there is competition disfavoring the solute), but no such system behaves quite like the organophosphate solutions, in which the reductive dealkylation can be almost fully suppressed. It is yet to be seen whether this kind of damage can be mitigated by the use of sacrificial “antioxidant” constituent ions introduced at the end of Sect. 12.5. Even if that is possible, this mitigation action would last only as long as the antioxidant survives.

Even in molecular solvents, the mechanisms for degradation of the solutes of this type are poorly understood, although empirically it is known that radiolytic damage is impeded in aromatic solvents, most likely due to the formation of the solvent dimer radical cations that have lower oxidation capacity than the radical cations (trapped holes) in other types of the solvents. So far we have explored three classes of such solutes: (i) crown ethers and their model compounds [97], (ii) monoamides [98], and (iii) diglycolamides [99]. In all of these cases, the damage to the solute in the IL solutions scales sublinearly with the concentration of the solute.

Crown ethers (CE) are macrocyclic ionophores used for alkali and alkaline earth metal extractions, including radioactive isotopes of cesium and strontium that contribute significantly to thermal generation in nuclear waste forms. Radiation damage in the CE macrocycles is triggered through oxidation of the bridging methylene groups, causing the C–O bond scission and the formation of several classes of radicals through rearrangements of the resulting species through CO elimination and 1,2-shifts. Replacement of bridging oxygens with >S and >NH bridges improves the radiation stability, as does the use of 1,2-dioxoaryl bridges, but too often such modifications are useless due to the adverse effect on metal ion binding specificity. The effect of the 1,2-dioxoaryl substitution can be traced to the formation of stable aryloxy radicals and phenolic products that inhibit radical reactions.

A particularly interesting reaction occurring in CE solutions is the formation of H[•] atoms through reduction of protons and hydronium ions associated with the macrocycle [97]. In the presence of the CE, radiolytically generated H^{δ+}A^{δ-} acids form (CE•H^{δ+})A^{δ-} complexes. One-electron reduction of such complexes releases the H[•] atoms at the solute site, causing the formation of H loss radicals through rapid hydrogen abstraction. This initiates secondary transformation of such radicals causing ring-opening and the loss of function. As (CE•H^{δ+})A^{δ-} complexes are deep electron traps, this reaction occurs even in aromatic ILs; therefore efficient electron scavengers are required to prevent this reaction. Thus, even in the ILs there are situations where the chemical damage is efficiently *channeled towards the solute*, and mitigation is required to prevent performance deterioration.

Diglycolamides serve as neutral extracting agents for *f*-ions [99] and find increasing use in nuclear separations due to the relative ease of their disposal by combustion and also due to their increased radiation stability [9, 100]. *N, N, N', N'*-Tetraalkyl diglycolamides ((R₂NCOCH₂)₂O), such as TODGA (tetra(*n*-octyl) substitution), and the closely related dimalonamides are particularly popular. The corresponding monoamides are used as solvent modifiers to improve metal ion solubility in organic solvents.

Diglycolamides are polyfunctional molecules, and product analyses indicate the existence of multiple fragmentation pathways during radiolysis [23]. The most damaging of these is deamination (that yields dialkylamines, which cause retention of molybdate in the organic phase) and the formation of the complementary 2-(2-(diocetylamino)2-oxoethoxy)acetate that competitively binds metal ions at high pH. Irradiation causes H[•] atom loss from the methylene groups of the glycolate groups, which remains high even when the aliphatic arms increase in length, suggesting the involvement of a dissociative excited state as opposed to deprotonation of the radical cation [99]. There is also significant yield of carbonyl (O[•]CCH₂OCH₂CONR₂) radicals due to deamination, while the yields of H[•] loss radicals in the aliphatic arms and dialkylamidogen (R₂N[•]) radicals are low, and these radicals are observed only at high mole fraction of the solute. The large disparity in the yields of the carbonyl and R₂N[•] radicals excludes their simultaneous generation via C–N bond dissociation, suggesting that these radicals are formed through the dissociation of the electronically excited radical cation. As these reactions are very rapid, little can be done to mitigate this kind of damage whether in molecular or

ionic liquids. As any medium, the ILs have limitations in their ability to protect the solute from radiation-induced fragmentation that involves highly exothermic reactions occurring on a short time scale.

12.6 Conclusion

In order to avoid crystallization, ILs are composed of structurally complex ions, and studying their radiation chemistry is challenging. Most of the traditional tools of the trade do not provide direct structural information; many of these methods have been developed for dilute (mainly, aqueous or hydrocarbon) solutions of (e.g., optically absorbing) intermediates in non-interfering solvent. In this regard, EPR methods proved to be very useful, as they allowed us to obtain direct structural insight even in systems where multiple radicals coexisted in the reaction mixture after radiolysis. This advantage comes along with the disadvantage of using low-temperature matrix isolation, which complicates studies of chemical reactions and largely ignores the dynamic aspects of this radical chemistry. It is likely that time-resolved EPR methods can provide a means to extend the range of the observations and make studies of their dynamics possible.

Several cross cutting themes appeared time and again in this review. The most important of these is a description of the sheer variety of radiation-induced redox reactions in ILs, with ILs themselves comprising the largest class of room-temperature liquids.

At the inception of our studies on the radiation chemistry of ILs, it was expected that molecular liquids and ionic solids would provide useful reference points for understanding ILs. Instead, this chemistry proved to be unique in more than one respect and, furthermore, it re-emphasized many of the familiar problems already encountered in the studies of molecular liquids. The chief problem is the mode of excess charge localization in condensed matter systems. Molecular liquids exhibit multiple modes for this localization; ionic liquids exhibit all of these modes and then some more. It was expected that ion neutralization (electron attachment to cations and electron detachment from anions) would be the prevalent process in the ILs, informing the subsequent chemistry. While this is the case in some IL systems, in many of them the excess charge is localized through collective modes. Dimer radical ions are formed [30, 33, 39, 40], and even more extended modes of charge delocalization can be expected, in agreement with recent theoretical predictions [90–92]. As the extent of delocalization positively correlates with radiation resistance, the way to achieve the latter is through better understanding of the former.

Another cross cutting theme is the connection between ion functionalization and radiation stability. This connection is quite convoluted. It appears that radiation damage of the ILs chiefly originates through fragmentation of *anions* and the subsequent reactions of their fragments with the cations, although there is non-negligible cation fragmentation, too. As the radiolytic products can interfere with radionuclide separations, off-the-shelf IL diluents are generally inappropriate for applications

in nuclear waste processing, i.e., the IL diluents need to be engineered for this demanding application. New degrees of complexity are added when (i) radiolytically-induced deterioration of extracting agents and (ii) chemical modifications due to the contact with other phases are taken into account.

These multiple considerations caused branching of our research into several thrusts, and this review followed the most important directions, such as (i) the discovery of radiation-hard anions (that do not undergo oxidative fragmentation), (ii) understanding of factors controlling the cation stability and mitigation of these factors, and (iii) our scrutiny of the charge and energy flow between the IL solvent and the extracting agent solutes. EPR spectroscopy was important in all of these tasks, as it provided a convenient means for screening many classes of ILs and allowing us to identify the general trends concerning the potential of a given class of the ILs to serve for a given application. EPR spectroscopy also provided direct mechanistic insight that guided our synthetic effort in addressing these challenges.

Our studies indicate that radiation resistant ILs are indeed possible, but such systems tend to be under-explored compared to the systems that are currently pursued by the majority of IL chemists. We identified rational principles for selection of such systems and illustrated how EPR can be used to assess the potential of these designs for mitigation and reversal of radiation damage. We also formulated principles for redirecting the damage from the solute to the IL solvent, which is yet another important concern, as the protection of the extracting agents and the ionophores is more important than the protection of the diluent.

Still, we only scratched the surface. The “chemical universe” of the ionic liquid is very vast indeed, and the exploration of the ILs has only begun. It is unrealistic to expect that we can catch up at this point with studies of molecular solvents, given their multi-millennial head start. Even for these molecular solvents understanding of their radiation chemistry decreases precipitously as one moves away from water and a handful of organic solvents. This lack of fundamental knowledge, in turn, slows down the IL research. For example, the mode of electron localization in amide [98] and carbonate [101–103] solvents remains poorly known. It proved difficult to progress to a new level of complexity while there remains so much uncertainty regarding these much simpler systems. This backlog of unsolved radiation chemistry problems is haunting us today, whereas technological applications cannot wait until a better understanding is reached. Inadequacies of our current understanding of the ILs reflect our general ignorance of molecular liquids, and vice versa, and any significant advance in either area would foster an advance in the other area.

As a final note, in at least one respect there is no great difference between ILs and molecular liquids from the standpoint of radiation chemistry. Both of these fluid states remain poorly understood.

Acknowledgments This material is based upon work supported by the U. S. Department of Energy Office of Science, Office of Basic Energy Sciences Division of Chemical Sciences, Geosciences and Biosciences under Award Numbers DE-AC02-06CH11357 (Argonne) and DE-AC02-98CH10886 (Brookhaven). Programmatic support via a DOE SISGR grant “An Integrated Basic Research Program for Advanced Nuclear Energy Separations Systems Based on Ionic Liquids” is gratefully acknowledged.

References

1. Welton T (1999) Room-temperature ionic liquids. Solvents for synthesis and catalysis. *Chem Rev* 99:2071–2083
2. Hallett JP, Welton T (2011) Room-temperature ionic liquids: solvents for synthesis and catalysis. 2. *Chem Rev* 111:3508–3576
3. Plechkova NV, Seddon KR (2008) Applications of ionic liquids in the chemical industry. *Chem Soc Rev* 37:123–150
4. Earle MJ, Seddon KJ (2000) Ionic liquids. Green solvents for the future. *Pure Appl Chem* 72:1391–1398
5. Katritzky AR, Jain R, Lomaka A, Petrukhin R, Karelson M, Visser AE, Rogers RD (2002) Correlation of the melting points of potential ionic liquids (Imidazolium Bromides and Benzimidazolium Bromides) using the CODESSA program. *J Chem Inf Comput Sci* 42:225–231
6. Navarra MA (2013) Ionic liquids as safe electrolyte components for Li-metal and Li-ion batteries. *MRS Bull* 38:548–553
7. Kolarik Z (2013) Ionic liquids: how far do they extend the potential of solvent extraction of f-elements? *Solv Extr Ion Exch* 31:24–60
8. Scammells PJ, Scott JL, Singer RD (2005) Ionic liquids: the neglected issues. *Austr J Chem* 58:155–169
9. Sun XQ, Luo HM, Dai S (2012) Ionic liquids-based extraction: a promising strategy for the advanced nuclear fuel cycle. *Chem Rev* 112:2100–2128
10. Wishart JF (2014) Ionic liquid radiation chemistry. In: Plechkova N, Seddon KR (eds) *Ionic liquids further uncoiled: critical expert overviews*. Wiley, Chichester, pp 259–274
11. Wishart JF (2011) Radiation-induced reactivity in ionic liquids. *Houshasen Kagaku* 91:39–43
12. Wishart JF (2010) Ionic liquids and ionizing radiation: reactivity of highly energetic species. *J Phys Chem Lett* 1:3225–3231
13. Davis JH (2004) Task-specific ionic liquids. *Chem Lett* 33:1072–1077
14. Visser AE, Swatloski RP, Reichert WM, Mayton R, Sheff S, Wierzbicki A, Davis JH, Rogers RD (2001) Task-specific ionic liquids for the extraction of metal ions from aqueous solutions. *Chem Comm* 2001:135–136
15. Tsuda T, Hussey CL, Luo H, Dai S (2006) Recovery of cesium extracted from simulated tank waste with an ionic liquid: water and oxygen effects. *J Electrochem Soc* 153:D171–D176
16. Giridhar P, Venkatesan KA, Subramaniam S, Srinivasan TG, Vasudeva Rao PR (2008) Extraction of uranium (VI) by 1.1 M tri-*n*-butylphosphate/ionic liquid and the feasibility of recovery by direct electrodeposition from organic phase. *J Alloys Comp* 448:104–108
17. Nockemann P, Thijs B, Pittois S, Thoen J, Glorieux C, Van Hecke K, Van Meervelt L, Kirchner B, Binnemans K (2006) Task-specific ionic liquid for solubilizing metal oxides. *J Phys Chem B* 110:20978–20992
18. Nockemann P, Thijs B, Parac-Vogt TN, Hecke KV, Meervelt LV, Tinant B, Hartenbach I, Schleid T, Ngan VT, Nguyen MT, Binnemans K (2008) Carboxyl-functionalized task-specific ionic liquids for solubilizing metal oxides. *Inorg Chem* 47:9987–9999
19. Nockemann P, Thijs B, Van Hecke K, Van Meervelt L, Binnemans K (2008) Polynuclear metal complexes obtained from the task-specific ionic liquid betainium bistriflimide. *Cryst Growth Design* 8:1353–1363
20. Hoogerstraete TV, Onghena B, Binnemans K (2013) Homogeneous liquid–liquid extraction of metal ions with a functionalized ionic liquid. *J Phys Chem Lett* 4:1659–1663
21. Hoogerstraete TV, Onghena B, Binnemans K (2013) Homogeneous liquid–liquid extraction of rare earths with the betaine-betainium bis(trifluoromethylsulfonyl)imide ionic liquid system. *Int J Mol Sci* 14:21353–21377
22. Mekki S, Wai CM, Billard I, Moutiers G, Burt J, Yoon B, Wang JS, Gaillard C, Ouadi A, Hessemann P (2006) Extraction of lanthanides from aqueous solution by using room-temperature ionic liquid and supercritical carbon dioxide in conjunction. *Chem Eur J* 12:1760–1766

23. Berthon L, Chabronnel M-C (2010) Radiolysis of solvents used in nuclear fuel reprocessing. In: Moyer BA (ed) Ion exchange and solvent extraction, a series of advances, vol 19. CRC Press, Boca Raton, pp 429–513
24. Lindblom RO, Lemmon RM, Calvin M (1961) Kinetic and electron spin resonance studies of the radiation decomposition of crystalline choline chloride. *J Am Chem Soc* 83:2484–2489
25. Lemmon RM, Parsons MA, Chin DM (1955) Effects of ionizing radiation on choline chloride and its analogs. *J Am Chem Soc* 77:4139–4142
26. Lemmon RM, Gordon PK, Parsons MA, Mazzetti F (1958) Effects of ionizing radiation on choline chloride and its analogs. II. *J Am Chem Soc* 80:2730–2733
27. Smith MA, Lemmon RM (1965) A study of the radical termination mechanisms in the radiolysis of crystalline choline chloride. *J Phys Chem* 69:3370–3373
28. Symons MCS (1972) Unstable intermediates. Part 107. Radiation damage products in choline chloride. *J Chem Soc Faraday Trans II*:216–220
29. Shkrob IA, Chemerisov SD, Wishart JF (2007) The initial stages of radiation damage in ionic liquids and ionic liquid-based extraction systems. *J Phys Chem B* 111:11786–11793
30. Shkrob IA, Wishart JF (2009) Charge trapping in imidazolium ionic liquids. *J Phys Chem B* 113:5582–5592
31. Wishart JF, Shkrob IA (2009) The radiation chemistry of ionic liquids and its implications for their use in nuclear fuel processing. In: Plechkova NV, Rogers RD, Seddon KR (eds) *Ionic liquids: from knowledge to application*, vol 1030. American Chemical Society, Washington, pp 119–134
32. Shkrob IA (2010) Deprotonation and oligomerization in photo-, radiolytically, and electrochemically induced redox reactions in hydrophobic alkylalkylimidazolium ionic liquids. *J Phys Chem B* 114:368–375
33. Shkrob IA, Marin TW, Chemerisov SD, Hatcher JL, Wishart JF (2011) Radiation induced redox reactions and fragmentation of constituent ions in ionic liquids. 2. Imidazolium cations. *J Phys Chem B* 115:3889–3902
34. Shkrob IA, Marin TW, Chemerisov SD, Wishart JF (2011) Radiation and radical chemistry of NO_3^- , HNO_3 , and dialkylphosphoric acids in room-temperature ionic liquids. *J Phys Chem B* 115:10927–10942
35. Shkrob IA, Marin TW, Chemerisov SD, Wishart JF (2011) Radiation induced redox reactions and fragmentation of constituent ions in ionic liquids. 1. Anions. *J Phys Chem B* 115:3872–3888
36. Shkrob IA, Marin TW, Chemerisov SD, Hatcher JL, Wishart JF (2012) Toward radiation-resistant ionic liquids. Radiation stability of sulfonyl imide anions. *J Phys Chem B* 116:9043–9055
37. Shkrob IA, Wishart JF (2012) Free radical chemistry in room-temperature ionic liquids. In: Chatgililoglu C, Studer A (eds) *Encyclopedia of radicals in chemistry, biology and materials*. Wiley, Chichester, pp 433–448
38. Shkrob IA, Marin TW, Crowell RA, Wishart JF (2013) Photo- and radiation- chemistry of halide anions in ionic liquids. *J Phys Chem A* 117:5742–5756
39. Shkrob IA, Marin TW, Luo H, Dai S (2013) Radiation stability of cations in ionic liquids. 1. Alkyl and benzyl derivatives of 5-membered ring heterocycles. *J Phys Chem B* 117:14372–14384
40. Shkrob IA, Marin TW, Hatcher JL, Cook AR, Szreder T, Wishart JF (2013) Radiation stability of cations in ionic liquids. 2. Improved radiation resistance through charge delocalization in 1-benzylpyridinium. *J Phys Chem B* 117:14385–14399
41. Shkrob IA, Marin TW, Luo H, Dai S (2013) Radiation stability of cations in ionic liquids. 3. Cyclical guanidinium cations. *J Phys Chem B* 117:14400–14407
42. Shkrob IA, Marin TW (2013) Radiation stability of cations in ionic liquids. 4. Task-specific antioxidant cations for nuclear separations and photolithography. *J Phys Chem B* 117:14797–14807
43. Shkrob IA, Marin TW, Wishart JF (2013) Ionic liquids based on polynitrile anions: hydrophobicity, low proton affinity, and high radiolytic resistance combined. *J Phys Chem B* 117:7084–7094
44. Saenko EV, Takahashi K, Feldman VI (2013) EPR evidence for a physically trapped excess electron in a glassy ionic liquid. *J Phys Chem Lett* 4:2896–2899

45. Wishart JF, Neta P (2003) Spectrum and reactivity of the solvated electron in the ionic liquid methyltributylammonium bis(trifluoromethylsulfonyl)imide. *J Phys Chem B* 107:7261–7267
46. Wishart JF, Lall-Ramnarine SI, Raju R, Scumpia A, Bellevue S, Ragbir R, Engel R (2005) Effects of functional group substitution on electron spectra and solvation dynamics in a family of ionic liquids. *Radiat Phys Chem* 72:99–104
47. Wishart JF, Funston AM, Szreder T, Cook AR, Gohdo M (2012) Electron solvation dynamics and reactivity in ionic liquids observed by picosecond radiolysis techniques. *Farad Disc* 154:353–363
48. Xu C, Durumeric A, Kashyap HK, Kohanoff J, Margulis CJ (2013) Dynamics of excess electronic charge in aliphatic ionic liquids containing the bis(trifluoromethylsulfonyl)amide anion. *J Am Chem Soc* 135:17528–17536
49. Molins iDF, FitzPatrick B, Healy AT, Blank DA (2013) Photodetachment and electron reactivity in 1-methyl-1-butyl-pyrrolidinium bis(trifluoromethylsulfonyl)amide. *J Chem Phys* 137:034512
50. Nese C, Unterreiner A-N (2010) Photochemical processes in ionic liquids on ultrafast timescales. *Phys Chem Chem Phys* 12:1698–1708
51. Shkrob IA, Sauer MC (2004) Radical ions in liquids. In: Hatano Y, Mozumder A (eds) Charged particle and photon interactions with matter. Chemical, physicochemical, and biological consequences with applications. Marcel Dekker, New York, pp 301–331
52. Takahashi K, Sato T, Katsumura Y, Yang J, Kondoh T, Yoshida Y, Katoh R (2008) Reactions of solvated electrons with imidazolium cations in ionic liquids. *Radiat Phys Chem* 77:1239–1243
53. Asano A, Yang J, Kondoh T, Norizawa K, Nagaishi R, Takahashi K, Yoshida Y (2008) Molar absorption coefficient and radiolytic yield of solvated electrons in diethylmethyl(2-methoxy) ammonium bis(trifluoromethanesulfonyl)imide ionic liquid. *Radiat Phys Chem* 77:1244–1247
54. Badger B, Brocklehurst B (1969) Absorption spectra of dimer cations. Part 2.-Benzene derivatives. *Trans Farad Soc* 65:2582–2587
55. Badger B, Brocklehurst B (1970) Absorption spectra of dimer cations. Part 4.-Theoretical considerations and dimer structure. *Trans Farad Soc* 66:2939–2947
56. Itagaki Y, Benetis NP, Kadam RK, Lund A (2000) Structure of dimeric radical cations of benzene and toluene in halocarbon matrices: an EPR, ENDOR and MO study. *Phys Chem Chem Phys* 2:2683–2689
57. Kadam RK, Erickson R, Komaguchi K, Shiotani M, Lund A (1998) ENDOR and EPR studies of benzene radical cations in halocarbon matrices: the static Jahn-Teller distortion of the monomer and geometry of the dimer cation. *Chem Phys Lett* 290:371–378
58. Inokuchi Y, Naitoh Y, Ohashi K, Saitow K, Yoshihara K, Nishi N (1997) Formation of benzene dimer cations in neat liquid benzene studied by femtosecond transient absorption spectroscopy. *Chem Phys Lett* 269:298–304
59. Todo M, Okamoto K, Seki S, Tagawa S (2004) Formation of benzene trimer radical cation in gamma-irradiated low temperature 2-methylpentane matrices. *Chem Phys Lett* 399:378–383
60. Pieniasek PA, Krylov AI, Bradforth SE (2007) Electronic structure of the benzene dimer cation. *J Chem Phys* 127:044317
61. Pieniasek PA, Bradforth SE, Krylov AI (2008) Charge localization and Jahn-Teller distortions in the benzene dimer cation. *J Chem Phys* 129:074104
62. Okamoto K, Seki S, Tagawa S (2006) Formation of trimer and dimer radical cations of methyl-substituted benzenes in γ -irradiated low-temperature matrices. *J Phys Chem A* 110:8073–8080
63. Conwell EM, Rakhmanova SV (2000) Polarons in DNA. *Proc Natl Acad Sci U S A* 97:4556–4560
64. Conwell EM (2005) Charge transport in DNA in solution: the role of polarons. *Proc Natl Acad Sci U S A* 102:8795–8799
65. Berlin YA, Burin AL, Ratner F (2001) Charge hopping in DNA. *J Am Chem Soc* 123:260–268
66. Griscom DL (1971) ESR and optical studies of alkali-associated trapped-electron centers in alkali borate glasses irradiated at 77°K. *J Non-Cryst Solids* 6:275–282
67. Bobrowski K (1981) Pulse radiolysis of aqueous solutions of benzyltrialkylammonium cations: reactions with the primary transients from water radiolysis. *J Phys Chem* 85:381–388

68. Crivello JV (1984) Cationic polymerization-iodonium and sulfonium salt photoinitiators. *Adv Polym Sci* 62:2–48
69. Crivello JV (1999) The discovery and development of onium salt cationic photoinitiators. *J Polymer Sci A* 37:4241–4254
70. Crivello JV, Lam JHW (1980) Photoinitiated cationic polymerization by dialkyl-4-hydroxyphenolsulfonium salts. *J Polymer Sci/Polymer Chem Ed* 18:1021–1034
71. Crivello JV, Lee JL (1981) Photosensitized cationic polymerizations using dialkylphenacysulfonium and dialkyl(4-hydroxyphenyl)sulfonium salt photoinitiators. *Macromolecules* 14:3780–3813
72. Crivello JV, Ahn J (2003) Synthesis and characterization of second-generation S, S-dialkyl-S-(dimethylhydroxyphenyl)sulfonium salt photoinitiators. *J Polymer Sci A* 41:2556–2569
73. Berthon L, Nikitenko SI, Bisel I, Berthon C, Faucon M, Saucerotte B, Zorz N, Moisy P (2006) Influence of gamma irradiation on hydrophobic room-temperature ionic liquids [BuMeIm] PF_6 and [BuMeIm](CF₃SO₂)₂N. *Dalton Trans* 2006: 2526–2534
74. Le Rouzo G, Lamouroux C, Dauvois V, Dannoux A, Legand S, Durand D, Moisy P, Moutiers G (2009) Anion effect on radiochemical stability of room-temperature ionic liquids under gamma irradiation. *Dalton Trans* 2009:6175–6184
75. Bosse E, Berthon L, Zorz N, Monget J, Berthon C, Bisel I, Legand S, Moisy P (2008) Stability of [MeBu₃N][Tf₂N] under gamma irradiation. *Dalton Trans* 2008: 924–931
76. Kutt A, Rodima T, Saame J, Raamat E, Maemets V, Kaljurand I, Koppel IA, Garlyauskayte RY, Yagupolskii YL, Yagupolskii LM, Bernhardt E, Willner H, Leito I (2011) Equilibrium acidities of superacids. *J Org Chem* 76:391–395
77. Shkrob IA, Zhu Y, Marin TW, Abraham DP (2013) Mechanistic insight into the protective action of bis(oxalato)borate and difluoro(oxalato)borate anions in li-ion batteries. *J Phys Chem C* 117:23750–23756
78. Griscom DL (1971) ESR studies of an intrinsic trapped-electron center in X-irradiated alkali borate glasses. *J Chem Phys* 55:1113–1123
79. Griscom DL (2011) Trapped-electron centers in pure and doped glassy silica: a review and synthesis. *J Non-Cryst Solids* 357:1945–1962
80. Shkrob IA, Tadjikov BM, Trifunac AD (2000) Magnetic resonance studies on radiation-induced point defects in mixed oxide glasses. I. Spin centers in B₂O₃ and alkali borate glasses. *J Non-Cryst Solids* 262:6–34
81. Cho E, Mun J, Chae OB, Kwon OM, Kim H-T, Ryu JH, Kim YG, Oh SM (2012) Corrosion/passivation of aluminum current collector in bis(fluorosulfonyl) imide-based ionic liquid for lithium-ion batteries. *Electrochem Comm* 22:1–3
82. Kramer E, Schedlbauer T, Hoffmann B, Terborg L, Nowak S, Gores HJ, Passerini S, Winter M (2013) Mechanism of anodic dissolution of the aluminum current collector in 1 M LiTFSI EC:DEC 3:7 in rechargeable lithium batteries. *J Electrochem Soc* 160:A356–A360
83. Kühnel R-S, Lübke M, Winter M, Passerini S, Balducci A (2012) Suppression of aluminum current collector corrosion in ionic liquid containing electrolytes. *J Power Sources* 214:178–184
84. Yang H, Kwon K, Devine TM, Evans JW (2000) Aluminum corrosion in lithium batteries. An investigation using the electrochemical quartz crystal microbalance. *J Electrochem Soc* 147:4399–4407
85. Choen Hyams T, Go J, Devine TM (2007) Corrosion of aluminum current collectors in high-power lithium-ion batteries for use in hybrid electric vehicles. *J Electrochem Soc* 154:C390–C396
86. Zhang SS, Jow TR (2002) Aluminum corrosion in electrolyte of Li-ion battery. *J Power Sources* 109:458–464
87. Toriyama K, Nunome K, Iwasaki M (1986) Structures and reactions of radical cations of linear alkanes: ESR evidence for selective deprotonation. *J Phys Chem* 90:6836–6842
88. Gierz V, Melomedov J, Forster C, Deissler C, Rominger F, Kunz D, Heinze K (2012) Consequences of the one-electron reduction and photoexcitation of unsymmetric bis-imidazolium salt. *Chem Eur J* 18:10677–10688

89. Sherren CN, Mu C, Webb MI, McKenzie I, McCollum BM, Brodovitch J-C, Percival PW, Storr T, Seddon KR, Clyburne JAC, Walsby CJ (2011) Merging the chemistry of electron-rich olefins with imidazolium ionic liquids: radicals and hydrogen-atom adducts. *Chem Sci* 2:2173–2177
90. Wang ZP, Zhang L, Chen XH, Cukier RI, Bu YX (2009) Excess electron solvation in an imidazolium-based room-temperature ionic liquid revealed by ab initio molecular dynamics simulations. *J Phys Chem B* 113:8222–8226
91. Wang Z, Zhang L, Cukier RI, Bu Y (2010) States and migration of an excess electron in a pyridinium-based, room-temperature ionic liquid: an ab initio molecular dynamics simulation exploration. *Phys Chem Chem Phys* 12:1854–1861
92. Liu J, Wang Z, Zhang M, Cukier RI, Bu Y (2013) Excess dielectron in an ionic liquid as a dynamic bipolaron. *Phys Rev Lett* 110:107602
93. Margulis CJ, Annappureddy HV, De Biase PM, Coker D, Kohanoff J, Del PMG (2011) Dry excess electrons in room-temperature ionic liquids. *J Am Chem Soc* 133:20186–20193
94. Chiarizia R, Jensen MP, Borkowski M, Ferraro JR, Thiyagarajan P CLK (2003) Third phase formation revisited: the U(VI), HNO₃-TBP, *n*-dodecane system. *Solv Extr Ion Exch* 21:1–27
95. Chiarizia R, Urban V, Thiyagarajan P HBA, Dietz ML (2000) A small angle neutron scattering investigation of the species formed in the extraction of Sr(II) by mixtures of di-*n*-octylphosphoric acid and dicyclohexano-18-crown-6. *Solv Extr Ion Exch* 18:471–478
96. Antonio MR, Chiarizia R, Gannaz B, Berthon L, Zorz N, Hill C, Cote G (2008) Aggregation in solvent extraction systems containing a malonamide, a dialkylphosphoric acid, and their mixtures. *Sep Sci Technol* 43:2572–2605
97. Shkrob IA, Marin TW, Dietz ML (2011) On the radiation stability of crown ethers in ionic liquids. *J Phys Chem B* 115:3903–3911
98. Shkrob IA, Marin TW (2012) Electron localization and radiation chemistry of amides. *J Phys Chem A* 116:1746–1757
99. Shkrob IA, Marin TW, Bell JR, Luo H, Dai S, Hatcher JL, Rimmer RD, Wishart JF (2012) Radiation induced fragmentation of diamide extraction agents in ionic liquid diluents. *J Phys Chem B* 116:2234–2243
100. Ansari SA, Pathak P, Mohapatra PK, Manchanda VK (2012) Chemistry of diglycolamides: promising extractants for actinide partitioning. *Chem Rev* 112:1751–1772
101. Torche F, El Omar AK, Babilotte P, Sorgues S, Schmidhammer U, Marignol JL, Mostafavi M, Belloni J (2013) Picosecond pulse radiolysis of the liquid diethyl carbonate. *J Chem Phys* A 117:10801–20810
102. Shkrob IA, Zhu Y, Abraham DP (2013) Reduction of carbonate electrolytes and the formation of solid-electrolyte interface (SEI) in lithium batteries. 2. Radiolytically induced polymerization of ethylene carbonate. *J Phys Chem C* 117:19270–19279
103. Shkrob IA, Zhu Y, Abraham DP (2013) Reduction of carbonate electrolytes and the formation of solid-electrolyte interface (SEI) in lithium ion batteries. 1. Spectroscopic observations of radical intermediates generated in one-electron reduction of carbonates. *J Phys Chem C* 117:19255–19269

Part V
Radiation Metrology

Chapter 13

Alanine-EPR High-Dose Radiation Metrology

Marc F. Desrosiers

Abstract A comprehensive guide to the calibration, use, and maintenance of the alanine-EPR metrology system for high-dose radiation dosimetry is presented. Alanine dosimetry is the system of choice for calibration services for all major primary and secondary calibration laboratories worldwide. Over the past 50 years alanine dosimetry has been transformed from an art to a state-of-the-art technology that serves the metrology specialist as well as the industrial technician. This guide outlines the critical elements that must be addressed to operate an EPR measurement service at the highest levels of accuracy and precision. The nuances of EPR, the harsh environment of high-dose high energy radiation processing, and the complexities of free radical chemistry combine to present many challenges. The success of alanine-EPR metrology has led many to search for new EPR dosimeters, it is hoped that the information presented here may serve as a template for the development of new systems that will improve or expand current metrology services.

13.1 Introduction

High-dose dosimetry services support a broad range of applications and industries including the treatment of blood products, food preservation, medical device sterilization, and aerospace device testing [1]. The measurement of alanine-derived radicals by Electron Paramagnetic Resonance (EPR) for the purpose of quantifying the absorption of energy from ionizing radiation revolutionized modern high-dose dosimetry. In the early years, the use of EPR in the dosimetry laboratory was slow to integrate because a magnetic resonance spectrometer was not common to dosimetry. Before the introduction of alanine dosimetry, the analytical technique of choice was based on optical measurements [2]. Optical techniques have the benefit of being a visual indicator that is readily adaptable to variations in detector designs, all at a relatively low cost. However, the overall superiority of the alanine dosimetry system outweighed the technological and financial barriers to implementation. The

M. F. Desrosiers (✉)

Radiation Physics Division, National Institute of Standards and Technology, Gaithersburg, USA
e-mail: marc.desrosiers@nist.gov

© Springer International Publishing 2014

A. Lund, M. Shiotani (eds.), *Applications of EPR in Radiation Research*,
DOI 10.1007/978-3-319-09216-4_13

early foundation of the modern system was built with government investment through several National Metrology Institutes (NMIs), primarily those of Italy [3], Germany [4], United Kingdom [5], and the United States [6], with significant contributions from Denmark [7], France [8] and Japan [9]. Through technology transfer, the alanine dosimetry system is now an important tool for the private sector that has improved production efficiency and quality.

A significant early driver towards adapting the alanine dosimeter over dye-based optical dosimeters was the complex sensitivities of optical systems to the harsh environmental factors present in an irradiator facility. Aside from the optical dosimeter's sensitivity to common influences (e.g., irradiation temperature), its sensitivity to ambient light and relative humidity made handling practices a critical factor in measurement accuracy and precision [2]. In contrast, the robust alanine dosimeter required no extraordinary handling and is well-suited to the rugged and varied environment of industrial irradiation processing. Also contributing to its wide-reaching appeal was that its response spanned several decades of dose, allowing very diverse applications to share a common interest in its successful implementation. As the system advanced and commercial ventures provided a stable measurement platform, it became evident that the alanine system would also offer lower measurement uncertainties relative to the conventional dosimeters in use. A lower system uncertainty offers the end-user increased throughput, efficiency, and profitability.

Alanine dosimetry is the system of choice for NMIs worldwide. International comparisons of NMI standards are conducted every 10 years through the Bureau International des Poids et Mesures (BIPM) to ensure their mutual equivalence [10]. Measurement traceability to national standards is essential to national and international commerce. Alanine dosimetry provides this traceability, the measurement link between commercial products and national standards, with a high degree of confidence in large part due to its aforementioned qualities and the nature of magnetic resonance as an analytical technique. As such, alanine dosimetry plays an enormous role in facilitating trade of consumer products, ensuring the safety of food, medical devices and the national blood supply, as well as the performance of satellite components that are the life blood of countless technologies that support the daily functions of people from remote mountain villages to Wall Street.

This chapter intends to capture the requirements of establishing a high-dose dosimetry service with a focus on the unique aspects of magnetic resonance techniques. Included with the elements of the system calibration is an emphasis on system maintenance and best practices that contribute to its quality. Recognizing that the quest for new EPR dosimetry systems based on non-alanine detectors is ongoing, this overview serves as a resource and guide for their characterization and implementation.

13.1.1 History

Early EPR studies of irradiated biomaterials led to the serendipitous discovery of a long-lived radical in gamma-irradiated crystalline alanine [11]. Subsequent studies elucidated much of the alanine solid state radiation chemistry [12]. This longevity

encouraged the development of a new class of radiation detector. Though early efforts were promising, the hindrance to implementing this technology was the size of the EPR spectrometer and the special skills needed to operate it with high precision [13]. The advent of the computer age and the subsequent modernization of the EPR spectrometer encouraged a succession of researchers to lay the foundation for modern EPR dosimetry. Rapid advancements in dosimeter formulation, mass production, measurement configuration, and attribute characterization laid the foundation for the modern dosimetry system [14]. This seminal work advanced alanine dosimetry into the metrology laboratory by standardizing the dosimeter formulation, its measurement geometry and radiation response, its environmental influence quantities, and EPR spectrometer stability [14]. With the groundwork laid, demand for mass quantities of detectors and dedicated EPR spectrometers, once available, would fuel the interest of the dosimetry community. In turn, the availability of uniform batches of dosimeters led to a series of works aimed at providing the guidelines for their use in industrial irradiation processing [15–17].

13.1.2 Dosimeter

There are several isomeric forms of alanine: L-alanine; D- alanine; DL- alanine; and β -alanine. Modern commercial dosimeters use L-alanine exclusively as the favorable attributes of L-alanine were recognized early [14].

A key element of the alanine dosimeter formulation is the selection of crystal size [18]. Control of the crystal size is critical to the accuracy and precision of the system. The alanine is ground and sieved, and a narrow range of crystal size is used for the dosimeter [19]. The selection range is a balance between a size small enough to minimize the anisotropy effect on the measurement but not adversely affect the bulk flow characteristics necessary to manufacture it in mass quantities with a high degree of uniformity. To fabricate a dosimeter of a specific shape the alanine crystals are blended with an EPR-silent polymer binder and pressed into shape [14]. Presently, the most common shape is a pellet that is a cylinder approximately 5 mm in diameter and 3 mm in height. Thin film alanine dosimeters have also been mass produced [20]. The film dosimeters are well suited to the industrial applications. The dosimeter is an alanine-binder layer (4.5 cm long) deposited on a 14.5 cm polymer support that serves as a handle. A barcode is located on the handle of each dosimeter that identifies the dosimeter and its associated lot. To match the barcode tracking feature of films, alanine dosimeter pellets have been blister packed with a barcode.

13.1.3 The Spectrum

The alanine dosimeter measurement response is derived from an EPR spectrum that is a sum of two or more spectra from alanine-derived paramagnetic species. The

long-lived radical that contributes the majority of the measured response is formed by deamination of the primary radical anion [12]. The formation of a secondary radical is initiated by a hydrogen abstraction reaction of the deamination species with a neighboring neutral alanine molecule [21]. Mechanisms for the formation of secondary and tertiary radicals have been studied extensively [21]. Though the secondary radicals have not been physically isolated, they have been detected after thermal annealing [21], photobleaching [22], and spin trapping techniques [23]. The relative abundance of the alanine-derived radicals with increasing absorbed dose is presumed constant (within the stated uncertainty) [21]. The high uncertainty associated with the assessment of the radical's relative abundance is impractical for dosimetry. The EPR spectral features of all alanine-derived radicals combine to yield an observed spectrum from which the central, most prominent feature is used as a measure of the radiation-induced radical yield.

13.2 System Operation and Use

Dosimeters are used for several aspects of radiation processing [24]. In the initial phase of radiation source installation, they are used to calibrate the radiation field. Before products are processed, dosimetry is used to map the dose distribution for specific product geometries. During product processing, routine monitoring is conducted by dosimetry for quality assurance. For most products, these measurements must be demonstrated to be equivalent to national standards through metrological traceability, a documented unbroken chain of calibrations accompanied by a statement of uncertainty. For large industrial radiation sources, traceability to national standards is achieved (at least in part) by transfer dosimetry. Transfer dosimetry is a system that is sufficiently robust to be mailed from the national laboratory and returned for certification.

There are several dosimeter classes [1, 24]. A primary standard dosimeter is of the highest metrological quality and its value is accepted without reference to other standards. Examples include calorimeters and ionization chambers. A reference standard dosimeter is used to calibrate other dosimetry systems and is of high metrological quality with well characterized parameters. Alanine is the reference class dosimeter of choice by all major NMI's. Transfer dosimeters, mentioned above, comprise a dosimeter class that possesses qualities enabling it to withstand the variable conditions of postal transit both in the irradiated and unirradiated state. Alanine is currently the best transfer dosimeter for reasons that will be made evident later in this chapter. The final dosimeter class is routine dosimeters; these are used in large numbers for in-plant dose measurements and process control. Its selection for routine use is a balance of system cost, desired system uncertainty, and the practicalities of its operation within a specific industrial environment. Some processes may find an inexpensive radiochromic dosimetry system with high uncertainty perfectly acceptable to their product line and protocols, whereas others may benefit from a premium system such as alanine because its low uncertainty and robust qualities reduce long-term costs by increasing product throughput and decreasing calibration frequency.

Despite alanine's excellent qualifications for the majority of dosimeter classes, it does not qualify as a primary standard dosimeter. A path to its use as a primary standard could be envisioned. The radiation response of alanine is proportional to the number of unpaired spins [25] and this can be quantified by double integration of the EPR spectrum [14]. This double integral must be related to an EPR standard of known concentration that is determined by other methods. Herein lies the issue: the multitude of steps required, each with their associated uncertainty, for the route to an absolute measure of spins presents an unacceptable or at least unattractive resultant combined uncertainty [14]. Whereas if one forgoes the use of absolute spin concentration and instead relates the spectral radiation response, measured as the height of the central resonance, to a calibrated gamma source of relatively low uncertainty, significant gains are recognized in measurement processing time and uncertainty. The calibration of alanine dosimeters in a highly-reproducible irradiation geometry is a critical step in achieving exceptional measurement uncertainty.

Another improvement in system uncertainty can be gained from normalization of the measurement response to dosimeter mass. A 3 by 5 mm alanine pellet centered in the EPR resonator is of sufficient size that small changes in its mass can be correlated linearly with the measured response. As such, a small but significant uncertainty gain can be had from either presorting the dosimeters by mass into sublots or normalizing the response to individual pellet mass. An alanine film dosimeter response cannot be normalized to mass (*vide infra*). The EPR spectral response is proportional to the number of spins over much of this length; however, a significant portion of this response is from non-linear regions of the resonator [14]. Any non-uniformity in the detector formulation or the dose distribution would yield a mass normalization of an alanine film imprecise if not inconsistent.

13.2.1 EPR Measurement

The sensitivity of the EPR measurement to sample position and/or sample holder positioning is a critical factor in the system optimization. Immobilization of the holder is the key to achieving the lowest measurement uncertainty. A holder that is highly concentric and free of structural flaws is desirable. The holder should enable the alanine pellet placement to be highly reproducible; ideally, that position should be a mapped region of the resonator that has maximum sensitivity and minimal position dependence. A mechanism to load and unload the pellet from the sample holder without any movement of the holder is a requirement. For alanine films that span the vertical length of the resonator, it is only necessary that their resting position is fixed and the holder immobilized.

Once the EPR measurement geometry is set, the next largest contributor to the measurement uncertainty is the signal anisotropy [26, 27]. As mentioned previously, alanine crystal size selection greatly reduces this effect. The uncertainty due to anisotropy in modern commercial dosimeters is effectively indistinguishable from the dosimeter-to-dosimeter variation at a fixed dose. It is possible to get a measurement

improvement by averaging the response of a dosimeter measured at different angles; however, the dosimeter rotation would have to be made in a manner that only the pellet would rotate and not the sample holder. If a holder with minor, seemingly imperceptible flaws were rotated in the resonator's microwave field the uncertainty of the measurement would increase. Most commonly, the uncertainty arising from response anisotropy is included in the dosimeter interspecimen response variation.

As discussed previously, the best measurement uncertainty is achieved by measuring the peak-to-peak (P2P) height of the central resonance of the spectrum. This approach greatly simplifies the measurement process; for example, baseline corrections are not required. Eliminating a baseline measurement reduces the spectrum scan time. The scan time can be shortened by reducing the magnetic field sweep width to only that of the central resonance line; a near factor of ten reduction in time over a full spectrum sweep.

The P2P measurement is subject to the EPR spectrometer stability that includes influence on the signal output from electronic components, sensitivity drift over long measurement session periods, as well as influences on sensitivity derived from subtle differences between dosimeters. The use of an EPR intensity reference material placed adjacent to the dosimeter in the resonator can significantly reduce these effects [17, 28]. At NIST a synthetic ruby crystal is used as an in situ EPR intensity reference [17]. The EPR reference measured in tandem with the alanine dosimeter yields a measure of the dosimeter radiation response and the in situ spectrometer sensitivity. The ruby reference measurement captures response variations from the spectrometer as well as sample-derived influences. For example, two pellets irradiated to the same dose should give an equivalent response, however, if the moisture content of these pellets differ significantly, the resonator sensitivity (Q-factor) is reduced, resulting in a lower dosimeter response. If not for the reference material, system sensitivity changes attributable to an individual pellet would go uncorrected. Routine use of the alanine and reference signal ratio to represent the system response will correct for these influences on each dosimeter measurement over the course of a measurement session. For example, a depression in the alanine signal output due to a dosimeter of higher moisture content would be mirrored by the reference material signal since it is recorded in the same measurement environment as the dosimeter. The dosimeter/reference tandem measurement can be achieved by either a rapid succession of spectral scans at their respective resonance conditions or by a single inclusive field sweep of both signals. The optimum number of sweeps is determined by the measurement geometry and the positioning of the reference material resonance in the magnetic field sweep. The use of an internal reference material permits one to monitor the spectrometer stability and other effects in real time, thereby increasing the confidence and measurement quality [17].

13.2.2 System Calibration

The calibration procedure includes irradiating the dosimeters, EPR measurement of the dosimeters, and determining a mathematical best fit to the dosimeter dose response. The irradiation protocol for the dosimetry aspects is described in documents

from international standards organizations [29]. These expert consensus documents provide the current guidelines and best practices.

For alanine dosimetry, the calibration event includes more than the dosimeter. The calibration includes the EPR spectrometer in addition to the specific manufactured batch of dosimeters. The dosimeters and their performance in a specific EPR measurement geometry constitutes the system, and once established any alteration of that system would require a check to verify the system is operating within the calibration guidelines. Modifications to the spectrometer are an obvious red flag for a system check, but consider that seemingly minor changes like the movement/rotation of the sample holder, however slight, could influence the system performance.

Modern commercial dosimeters are of high quality, and the expectation of interspecimen uniformity is high. However, to use the system for calibration services there are a number of tests that should be performed on the batch before applying the system to industrial applications. The primary lot acceptance criteria are dosimeter response, post-irradiation time dependence, and a determination of the temperature coefficient. A sampling of the dosimeters across the batch should also be undertaken. Another test would be for dose fractionation. Interruptions to the irradiation process are not uncommon and the possibility that the total dose had been supplied in one or more fractions is a possibility; moreover, it is an event that may not be conveyed to the calibration lab. Lastly, if the potential exists to irradiate the dosimeter unpackaged in an industrial environment, the effects of relative humidity should also be examined.

For calibration services to industrial applications the minimum dose of the calibration range is 20 Gy. The alanine dose response from 20 Gy to at least 1000 Gy is strictly linear. Deviation from linearity begins at about 3 to 4 Gy and above that the response becomes sublinear and continues to saturate through 100 kGy. The response does not fully saturate until several hundred kGy, however, the increase in the uncertainty of the interpolated dose in this region restricts the practical working range to less than 200 kGy. Because the working range of alanine is broad, 20 Gy to 200 kGy, it is practical to segment the calibration into four or five calibration ranges. Doing so allows the establishment of range-specific EPR spectrometer settings that contribute to optimization of the uncertainty, as well as practical factors including system maintenance.

13.3 Influence Quantities

The primary factor responsible for the dosimeter response is absorbed dose. Several other factors influence the dosimeter response to a lesser extent though they significantly affect the measurement uncertainty. These factors are called influence quantities. Influence quantities can be grouped into three categories: pre-irradiation, irradiation, and post-irradiation.

13.3.1 *Pre-irradiation Influences*

Storage There is an expectation of stability since the alanine is in the crystalline form, however, the dosimeter is comprised of alanine with polymeric materials and as such should be monitored. There are no reports that indicate an influence of time since manufacture on alanine dosimeters.

Temperature The pre-irradiation storage temperature has no influence on alanine dosimeters. Dosimeter suppliers/manufacturers should provide a recommended range; exposure to extreme temperatures should be avoided or minimized to the extent possible.

Relative Humidity The relative humidity during pre-irradiation storage may influence the EPR signal response of irradiated alanine dosimeters [5, 15, 20]. However, there are several ways to compensate for or minimize any potential effect. The best option is to use in situ EPR reference materials. As such, short-term effects due to dosimeter equalization with the relative humidity of the environment that can potentially influence the uncertainty are minimized significantly. Large differences between storage and measurement relative humidity may require up to an hour of equilibration time before measurement [15]. Despite these measures, it is prudent to minimize its potential influence to the extent possible by conditioning the dosimeters at a relative humidity that approximates the relative humidity of the measurement laboratory environment. In the absence of an in situ EPR reference material to compensate for relative humidity effects, the potential influence of relative humidity as it relates to pre-irradiation storage, alanine system calibration, and dosimeter response should be investigated. Moderate to low relative humidity storage/measurement conditions are recommended.

Light Ambient light has no known influence on alanine dosimeters during storage.

Packaging Dosimeter packaging may be required for certain industrial applications. The packaging for calibration purposes should be a material suitable for achieving electronic equilibrium of a thickness appropriate for the ionizing energy. Moisture barrier packaging should be used for irradiations in a water phantom or environments with high moisture content [20]. The packaging should be inspected to ensure it achieves the desired result.

Mass The influence of mass on the alanine pellet dosimeter response is linear for dosimeters that are sufficiently small, fixed in the center of the EPR resonator, and whose mass range is relatively narrow and well defined. The accuracy and precision of the dosimetry system are directly influenced by mass. The system uncertainty can be reduced by normalizing the measured response to the dosimeter mass. If measurement throughput is a higher priority than achieving a lower uncertainty through dosimeter mass normalization, the option to weigh each dosimeter can be replaced by a method that instead presorts the dosimeter batch into mass-specific sub-lots prior to calibration/irradiation. The mean mass of the subplot and the calibration curve dosimeters should be equivalent. As currently formulated, commercial alanine film dosimeters cannot be normalized to mass (*vide infra*).

13.3.2 Irradiation Influences

Temperature The effect of irradiation temperature on the alanine dosimeter response is relatively small (approximately one-tenth percent per degree) [30]. However, due to the extreme environment of irradiation processing it often represents a significant contribution to measurement corrections. Irradiation temperatures can vary on the order of tens of degrees C over the course of a processing cycle that moves product and their dosimeters about the gamma radiation source. During this cycle products experience large gradients in dose rate that in turn give rise to complex temperature profiles. Fortunately, complete knowledge of these complexities is not required for accurate dosimetry. An estimate of the average irradiation temperature is sufficient for gamma-ray processing measurements. The peak irradiation temperature is more accurate for electron beam processing dosimetry; the temperature rise for electron beam irradiations is effectively instantaneous.

The relationship between the dosimeter's radiation response to the absorbed dose and its temperature during irradiation is the irradiation temperature coefficient. This temperature coefficient is typically expressed in percentage change per absolute temperature (K). The temperature coefficient, R_t (K^{-1}) is described by the relationship, $(\Delta s/s)/\Delta T$, where s is the dosimeter response (in arbitrary units) and T is the irradiation temperature (in K). The temperature effect on dosimeter response is linear from -10 to $+70$ °C [30]. This temperature range represents the vast majority of irradiation processing applications from low temperature treatment of foods to high-energy electron-beam polymer crosslinking applications. For irradiation temperatures above $+70$ °C the dosimeter response is unpredictable and use of the alanine system is not advised. The alanine system response is sublinear in the range from -10 to -77 °C [31]. A relationship between relative response and temperature in this range was determined for accurately adjusting the low-temperature dosimeter response to the calibration temperature [31]. The dosimeter response with temperature below -77 °C is complex and less defined; use of the alanine system below -77 °C is not routine or straightforward [32].

Typical values for the L-alanine temperature coefficient in the linear range (-10 to $+70$ °C) register between 0.12 and 0.14 %/K [30]. The temperature coefficient is slightly dependent on absorbed dose but this effect is very small over a broad range (1 to 70 kGy) and nonlinear (effectively equivalent at high and low doses with an asymmetric depression in the coefficient for doses in between) [16, 30]. Since the differences are small, in practice a single value is generally assigned to a dosimeter lot for use at all dose levels. Comparisons of L-alanine dosimeters of different formulations from different manufacturers reveal very small variation (hundredths of a percent) in the temperature coefficient at a specific dose [16, 30]. The depression in the temperature coefficient trend over the dose range from 1 kGy up to 100 kGy has been measured for several alanine systems and is apparently independent of the dosimeter formulation, and likely intrinsic to alanine [16, 30].

Alanine dosimeters manufactured with DL-alanine have a temperature coefficient that is 50% greater than that of L-alanine [33]. Alanine dosimeters manufactured with DL-alanine would not be the optimum choice for use in applications with large temperature variations.

Absorbed Dose Rate Since the initial characterization of the alanine dosimetry system in the early 1980s and for decades thereafter, alanine dosimetry was considered dose rate independent [14]. More recently, check-standard measurement deviations revealed an obscure rate effect for the alanine dosimetry system [34, 35]. This rate-effect study characterized a complex relation between the radiation chemistry of crystalline alanine and the applied dose rate that was also dependent on the absorbed dose. That the rate effect only becomes significant above 5 kGy likely contributed to its discovery being recent despite decades of research in alanine dosimetry. It was learned that the effect is intrinsic to alanine and is not dependent on the chemical form or manufacturing formulation of the alanine dosimeter [34]. The study postulated that the production of one (or more) of the radiation-induced alanine radicals is dependent on the dose rate [34].

Since the dose rate effect is restricted to very low rates, it would not apply to industrial radiation processing conditions. The effect of absorbed dose rate has been characterized for alanine dosimeters irradiated to high doses at low dose rates. The dose-rate effect is absorbed-dose dependent but shows no effect below 5 kGy. Alanine dosimeters irradiated with gamma-rays to absorbed doses >5 kGy at low dose rates (<2 Gy/s) exhibit a progressive decrease in response relative to that found at dose rates greater than 2 Gy/s [34]. The combined effect of dose and dose rate may reach several percent. In a follow-up study the effect is irradiation temperature dependent; though relatively constant above 0°C , no rate effect was measured at -10 and -40°C [35]. This effect is relatively inconsequential to the typical end user, however, it has manifested itself in international dosimetry comparisons at the NMI level [10, 36]. There is no detectable dose rate effect at very high dose rates [37].

Dose Fractionation There is no known influence of dose fractionation; however, in some instances the fractionation of dose to alanine dosimeters may not be straightforward. Influence quantities that contribute to the dosimeter response may not be equivalent for the fractionated and non-fractionated irradiations. For example, the fractionation of dose changes the irradiation temperature profile relative to that experienced by a dosimeter irradiated to a single dose (equal to the sum of the fractionated doses). An accurate comparison of fractionated and non-fractionated doses is dependent on an accurate knowledge of the irradiation temperature for the irradiations.

Relative Humidity There are no data that indicate the relative humidity during irradiation influences the EPR response of alanine dosimeters. A study of irradiated alanine film dosimeters pre-equilibrated over a range of relative humidity demonstrated measurement equivalence [20]. As discussed previously, the primary concern regarding relative humidity is a change in the relative humidity; as such, the control of relative humidity is more important than the specific relative humidity level. For irradiation conditions that have the potential to directly expose dosimeters to water, precautions should be taken to seal the dosimeters in a material impervious to water [29].

Exposure to Light There is no known influence of ambient light on alanine dosimeters during irradiation.

Radiation Energy For most radiation processing applications there is no known influence of radiation energy for photons and electrons. Differences have been reported between the absorbed dose to water response of alanine dosimeters irradiated by photons and electrons over a range of energies in clinical applications [38–40]. For low-energy electron-beam processing the response to 100 keV electrons was found to be equivalent to the response to high-energy electrons [41, 42].

13.3.3 *Post-irradiation Conditions*

Conditioning Treatment Post-irradiation treatment of the alanine dosimeter prior to measurement is not applicable.

Time Measurement of the alanine dosimeter post-irradiation is not time critical [43]. Given this luxury, end users may adapt protocols that best suit their workflow needs. Good practice dictates that the time interval between irradiation and dosimeter reading be standardized and be consistent with the manufacturer's recommendations. A recent temporal study of commercial alanine dosimeters determined that irradiated alanine dosimeters may be stored in a protected environment without the need for extraordinary environmental controls if the EPR spectrometer employs an internal reference material [44]. Irradiated alanine pellet dosimeters are expected to be stable for up to 3 months under controlled ambient conditions. However, for alanine film dosimeters the possibility exists for individual dosimeters to exhibit unusual sensitivity to environmental influences and the use of multiple film dosimeters at each dose level accompanied by consistent monitoring are recommended for accurate dosimetry past 1 day post irradiation [44].

The stability of the alanine-derived radical has strongly suggested that it is possible to archive alanine dosimeter for post-irradiation measurements months or years after irradiation. A recent study measured the time dependence of a commercial dosimeter at several dose levels for up to 7 years [44]. This long-term study found that the multi-year decay profile was complex and non-uniform. The decay profiles were marked by periods of stability with decay steps over specific time periods. The multi-featured temporal response may be related to the multi-radical nature of irradiated crystalline alanine.

Temperature There is no known influence of storage temperature on alanine dosimeters. However, temperature extremes should be avoided to the extent possible and manufacturer's recommendations should be used as guidance.

Storage Relative Humidity The humidity during post-irradiation storage can influence the EPR response of alanine dosimeters. Before measurement, sufficient time should be allowed for dosimeters to equilibrate with the conditions of the system calibration. An EPR spectrometer that employs an internal reference material is advised to assure the most accurate measurement.

Exposure to Light A recent study that demonstrated an insensitivity of alanine dosimeters to ambient light [44] is consistent with earlier findings [14].

13.4 System Maintenance

13.4.1 *Source Calibration and Traceability*

For most irradiated products involved in national and international commerce the measurements that control the process have metrological traceability. Metrological traceability requires the establishment of an unbroken chain of calibrations connecting the end-user measurement to specified standards. An unbroken chain of calibrations requires a complete, explicitly described, and documented series of measurements that successively link the value and uncertainty of the result of a measurement with the values and uncertainties of the standard to which traceability is claimed. For irradiation processing facilities that lack an in-house radiation source suitable for calibrations, alanine dosimeters for a specific lot can be sent to a recognized standards laboratory for irradiation to a range of absorbed doses sufficient to produce a calibration curve on the end-user measurement system. An end-user dosimetry facility with a suitable radiation source can calibrate the dose rate for a defined irradiation geometry through transfer reference standards from a national laboratory or accredited service. Alanine dosimeters irradiated in this calibrated geometry can be used to construct a calibration curve. An established protocol that sets a frequency for ongoing system calibration checks against national standards is advised.

Checks against national standards at the highest level of metrology occur in the form of measurement comparisons. When possible, dosimetry comparisons are performed between NIST and the National Physical Laboratory of the United Kingdom. Dosimeters from each facility are exchanged, measured, and the results compared. Large-scale multi-NMI international comparisons are organized by the BIPM every 10 years and the results are published. The dosimetry system of choice for these high-level comparisons is alanine dosimetry [10, 36].

13.4.2 *Internal System Checks*

Internal dose-rate comparisons are useful for assuring quality in a multi-source facility. For example, at NIST, approximately annually, alanine dosimeter measurement comparisons are conducted between several gamma-ray sources that are used for service work. Ratios of source dose-rates are determined and ongoing control charts are maintained [34].

As stated previously, measurement reproducibility for the alanine dosimetry system is best achieved by maintaining a fixed EPR measurement geometry. A calibration may be used for more than 1 year as long as the EPR measurement configuration and dosimeter lot remain unchanged. The validity of the dosimetry system calibration is assessed through the use of check standards [34]. The check standards are alanine dosimeters that have been irradiated in a calibrated source geometry to absorbed doses representative of the calibration curve range. These check standards

are routinely measured within 48 h after irradiation, as well as prior to a dosimetry measurement session, and as needed either during a session or for system checks between session dates. The decision to proceed with a calibration measurement session is based on the response of the check standard. The measurement tolerances that require action are set based on the system uncertainty; at NIST this is 1% at one sigma. Check standard measurements that fall outside set limits must be resolved through re-measurement or the creation of replacement check standards. Continued check standard failure would require a complete recalibration of the system and possibly a reconfiguration of the sample geometry and/or EPR parameters. Data from these check standards may be compiled into a control chart for long-term tracking and comparison.

13.4.3 Uncertainty

A measurement result is complete when accompanied by a quantitative statement of uncertainty. The uncertainty characterizes the dispersion of values attributed to the measurand that is, in this case, absorbed dose. Rules for the expression of uncertainties have been established [45].

The purpose of this section is to explain the derivation of the various components of uncertainty for absorbed-dose measurements. The intent is to recognize all possible sources of uncertainty such that they may be considered in assembling an uncertainty budget. Some entries may not be applicable to a specific alanine system in use, or may be determined to be negligible. One approach to expressing the system uncertainty is to address all uncertainties that can be reasonably attributed to the system even if a component is estimated to be negligible. This approach acknowledges that the component was considered and does not risk the question of omission. A comprehensive list of the uncertainty components associated with the measurement of absorbed dose for alanine-EPR dosimetry is given below.

Dose Rate Uncertainty in the dose rate used to calibrate the alanine. For NIST this includes several sub-components that include the primary standard, that is the realization of the Gy with a water calorimeter, as well as several source dose-rate ratio comparisons that transfer the dose rate from the water calorimeter to the NIST calibration sources, and any associated irradiation geometry correction factors.

Field Uniformity Radiation field uniformity within a dosimeter volume.

Timer Uncertainty of timer readout relative to shortest irradiation time interval (defined by the user).

Decay Correction Source half-life correction factor uncertainty.

Repeatability Standard deviation of replicate pellet measurements.

Mass Uncertainty of microbalance relative to pellet mass.

Internal EPR Reference Correction For systems with a significant time between the recording of the alanine pellet measurement and the reference measurement an

Table 13.1 An example of the sources of uncertainty and their magnitude for the NIST alanine dosimetry service

Uncertainty source	Type A (%)	Type B (%)
<i>Irradiation dose rate</i>		
Realization of the Gy by water calorimetry	0.16	0.51
Calibration source rate	0.20	
Irradiation geometry	0.11	
Field uniformity		0.01
Source timer		0.20
⁶⁰ Co decay correction		0.02
<i>Alanine response measurement</i>		
Repeatability	0.30	
Mass determination	0.20	
EPR reference correction		0.05
System drift		0.10
<i>Dose measurement</i>		
Temperature correction		0.10
Calibration curve	0.50	0.10
Square root of sum of squares	0.68	0.58
Combined in quadrature		0.89
Coverage factor		2.0
Expanded uncertainty at 95 % confidence		1.8

uncertainty can be assigned to account for an EPR spectrometer sensitivity change during this interval.

System Drift Uncertainty arising from temporal EPR spectrometer sensitivity changes.

Temperature Correction Uncertainty associated with the response correction for the difference in the irradiation temperature relative to the calibration temperature.

Calibration Curve Uncertainty from alanine dosimeter calibration curve.

Miscellaneous Additional uncertainties are applied to irradiations in electron beams and ¹³⁷Cs, or for absorbed dose to silicon conversions.

Table 13.1 is an example of a NIST uncertainty budget.

13.5 Summary and Prospective

13.5.1 Key System Elements

Control of the measurement process and characterization of the potential influences are the keys to optimizing an EPR metrology system. Consistency of the process

and materials leads to good repeatability and reproducibility. Influences from environmental and irradiation process sources are less controllable and for these a characterization of the influences reduces the uncertainty. Control can be summarized into four critical elements:

EPR Measurement Geometry Best measurements are achieved with a sample holder that is immobile in the EPR resonator. There should be no translational movement of the holder in any direction, and the holder should not be allowed to rotate. The holder should have a fixed means of positioning the dosimeter that remains unchanged over the course of a measurement session as well as from day-to-day. A mechanism to insert and extract the dosimeter that does not perturb in any manner the position of the holder within the resonator or the positioning of the dosimeter within the holder is critical. A gravity feed with either vacuum or forced air expelling of the dosimeter is common.

Dosimeter Quality The manufacturing quality of the dosimeter is critical to large-scale commercial use. The consistency of the composition and control of the dosimeter dimensions are keys to the repeatability and reproducibility of the system. Dosimeters of the same dimensions present an unchanged EPR measurement geometry from dosimeter to dosimeter despite the fact that they are different artifacts. The homogeneity of detector material (e.g., alanine crystals) for a 3 by 5 mm pellet dosimeter placed in the absolute center of the EPR resonator is not significant. This dosimeter volume is small relative to the uniform region of the resonator [14]. However, a dosimeter cylinder or film that is longer than 10 mm is not uniformly measured over the length of the EPR resonator. As such, the homogeneity of the detector material is important to measurement quality. Another consideration is the dose distribution; if the dose over the length of the dosimeter is not uniform, the dosimeter position in the resonator could affect the measurement accuracy.

EPR Reference Standard As detailed previously, a number of factors that contribute to measurement uncertainty can be mitigated by using the relative response of the alanine to an in situ stable paramagnetic reference material. The largest effect is due to changes in relative humidity and accordingly the greatest need for employing a reference material is for dosimeters that are hygroscopic.

Measurement Influences Influence quantities from the irradiation process and environmental sources must be carefully characterized through well-designed experiments. System users should be vigilant to monitor the system's performance even after implementation. Subtle effects or performance observations should be documented. An excellent example of the importance of system control and documentation is the discovery of the dose rate effect in alanine [34]. For approximately two decades the alanine system was considered dose rate independent. A check standard program at NIST captured the effect during routine system monitoring. This obscure effect was important in explaining NMI comparison data in the most recent international comparison [36].

13.5.2 *The Future*

The success of alanine spurred a search for new systems based on other materials. Much of this search was to find a system that could extend the application of EPR dosimetry into lower dose applications such as medical physics. Alanine dosimetry measurements in this range have been demonstrated but its use is non-routine. One focus was to search for new materials that, when irradiated, produced a single EPR resonance. The hyperfine structure of the alanine-derived radical splits the intensity into several resonances of reduced intensity. Presumably a system where the EPR response is concentrated rather than split would extend the range of use [46]. Examples of other systems include but are not limited to: ascorbic acid [47], dithionates [46, 48], formic acid [46], lithium lactate [49], methyloalanine [46], quartz [50], sucrose [51, 52], tartrate [46].

The extension of alanine to low-dose medical therapy applications is needed to address the difficult problems of small-field dosimetry in radiation therapy. Dosimeter size and the reduced sensitivity that accompanies a lower mass dosimeter are issues along with establishing traceability to national standards based on large reference fields. One promising path to small-field dosimetry is through the use of alanine/EPR dosimetry. A smaller alanine pellet, 3 x 3 mm or less, would need to be mass produced to address the issues of small field dosimetry as well as new measurement protocols and techniques to meet the challenges of low-dose measurements in a reduced mass dosimeter.

There are opportunities for change in the design of the conventional alanine dosimeter. The use of alanine films is driven by their handling convenience and company information system integration via a printed bar code on the handle. Alanine pellets perform better than films in terms of sensitivity and uncertainty but are less convenient to handle and cannot be barcoded directly. While it is possible to barcode pellets on packaging of individual pellets, the identification issue remains once the dosimeter is removed from the package. Recently, a hybrid of these two designs was conceived: a blister-packed alanine pellet at the end of a long barcoded handle. This concept combines the best attributes of each dosimeter.

Regarding the delivery of services, the concept of building an Internet-based service based on alanine dosimetry was born from information technology (IT) advances that enabled remote control of instrumentation [53]. That freedom questioned the need to have the controlling computer in the same location as the measurement instrument. A first-generation system was devised based on the concept of NIST control over customer instrumentation for instantaneous certification [53]. However, soon thereafter a second generation service evolved from the realization that the system control was software-based and thus not bound to any physical device [54]. The system would require extensive testing and independent verification to provide traceability to national standards. Continuing advances in information technology offer exciting possibilities for metrology and the delivery of services, be it alanine or a new system based on a yet-to-be-discovered EPR dosimeter.

References

1. McLaughlin WL, Boyd AW, Chadwick KH, McDonald JC, Miller A (1989) Dosimetry for radiation processing. Taylor and Francis, London
2. Barrett JH (1982) Dosimetry with dyed and undyed acrylic plastic. *Int J Appl Radiat Isot* 33:1177–1187
3. Bartolotta A, Indovina PL, Onori S, Rosati A (1984) Dosimetry for cobalt-60 gamma rays with alanine. *Radiat Prot Dosimetry* 9:277–281
4. Deffner U, Regulla DF (1980) Influences of physical parameters on high-level amino acid dosimetry. *Nucl Instrum Methods* 175:134–135
5. Arber JM, Sharpe PHG (1993) Fading characteristics of irradiated alanine pellets; the importance of pre-irradiation conditioning. *Appl Radiat Isot* 44:19–22
6. McLaughlin WL, Desrosiers MF (1995) Dosimetry systems for radiation processing. *Radiat Phys Chem* 46:1163–1174
7. Hansen JW, Olsen KJ, Wille M (1987) The alanine radiation detector for high and low LET dosimetry. *Appl Radiat Isot* 19:43–47
8. Mosse DC (1988) ESR/alanine dosimetry applied to radiation processing. *Int J Radiat Appl Instrum Part C* 31:413–417
9. Kojima T, Tanaka R, Morita Y, Seguchi T (1986) Alanine dosimeters using polymers as binders. *Appl Radiat Isot* 37:517–520
10. Burns DT, Allisy-Roberts PJ, Desrosiers MF et al (2006) CCRI supplementary comparison of standards for absorbed dose to water in ^{60}Co gamma radiation at radiation processing dose levels. *Radiat Phys Chem* 75:1087–1092
11. Miyagawa I, Gordy W (1960) Electron spin resonance of an irradiated single crystal of alanine: second-order effects in free radical resonances. *J Chem Phys* 32:255–263
12. Sinclair JW, Hanna MW (1967) Electron paramagnetic resonance study of L-alanine irradiated at low temperatures. *J Phys Chem* 71:84–88
13. Bradshaw WW, Cadena DG, Crawford GW, Spetzler HAW (1962) The use of alanine as a solid dosimeter. *Radiat Res* 17:11–21
14. Regulla DF, Deffner U (1982) Dosimetry by ESR spectroscopy of alanine. *Int J Appl Radiat Isot* 33:1101–1114
15. Sleptchonok OF, Nagy VY, Desrosiers MF (2000) Advancements in accuracy of the alanine dosimetry system. Part 1. The effects of environmental humidity. *Radiat Phys Chem* 57:115–133
16. Nagy VY, Puhl JM, Desrosiers MF (2000) Advancements in accuracy of the alanine dosimetry system. Part 2. The influence of the irradiation temperature. *Radiat Phys Chem* 57:1–9
17. Nagy VY, Sleptchonok OF, Desrosiers MF et al (2000) Advancements in accuracy of the alanine dosimetry system. Part 3: usefulness of an adjacent reference sample. *Radiat Phys Chem* 59:429–441
18. Garcia T, Dolo JM (2007) Study of the influence of grain size on the ESR angular response in alanine radicals. *Radiat Meas* 42:1207–1212
19. Nichiporov D, Kostjuchenko V, Puhl J et al (1995) Investigation of applicability of alanine and radiochromic detectors to the dosimetry of proton clinical beams. *Appl Radiat Isot* 46:1355–1362
20. Garcia RMD, Desrosiers MF, Attwood JG et al (2004) Characterization of a new alanine film dosimeter: relative humidity and post-irradiation stability. *Radiat Phys Chem* 71:375–380
21. Malinen E, Heydari MZ, Sagstuen E, Hole EO (2003) Alanine radicals, Part 3: properties of the components contributing to the EPR spectrum of x-irradiated alanine dosimeters. *Radiat Res* 159:23–32
22. Wieser A, Lettau C, Fill A, Regulla DF (1993) The influence of non-radiation induced ESR background signal from paraffin-alanine probes for dosimetry in the radiotherapy dose range. *Appl Radiat Isot* 44:59–65

23. Desrosiers MF, Burlinska G, Kuppasamy P et al (1995) Research and development activities in electron paramagnetic resonance dosimetry. *Radiat Phys Chem* 46:1181–1184
24. McLaughlin WL (1989) Reference dosimetry and measurement quality assurance. *Appl Radiat Isot* 40:945–951
25. Nakagawa K, Eaton SS, Eaton GR (1993) Electron spin relaxation times of irradiated alanine. *Appl Radiat Isot* 44:73–76
26. Kojima T, Kashiwazaki S, Tachibana H (1995) Orientation effects on ESR analysis of alanine-polymer dosimeters. *Appl Radiat Isot* 46:1407–1411
27. Dolo JM, Garcia T (2007) Angular response of alanine samples: from powder to pellets. *Radiat Meas* 42:1201–1206
28. Yordanov ND, Gancheva V (1999) Selfcalibrated alanine/EPR dosimeters: a new generation of solid state/EPR dosimeters. *J Radioanal Nucl Chem* 240:215–217
29. American Society for Testing and Materials (ASTM) (2004) Standard practice for use of the alanine-EPR dosimetry system. International Standards Organization & American Society for Testing and Materials, Designation ISO/ASTM 51607:(E)
30. Desrosiers MF, Forney AM, Puhl JM (2012) A comparison of Harwell & FWT alanine temperature coefficients from 25 °C to 80 °C. *NIST J Res* 117:143–153
31. Desrosiers MF, Cooper SL, Puhl JM et al (2004) A study of the alanine dosimeter irradiation temperature coefficient in the -77°C to $+50^{\circ}\text{C}$ range. *Radiat Phys Chem* 71:365–370
32. Sharpe PHG, Sephton JP, Gouldstone CA (2009) The behavior of alanine dosimeters at temperatures between 100 and 300 K. *Radiat Phys Chem* 78:477–480
33. Desrosiers MF, Lin M, Cooper SL et al (2006) Study of the irradiation temperature coefficient for L-alanine and DL-alanine dosimeters. *Radiat Prot Dosim* 120:235–237
34. Desrosiers MF, Puhl JM, Cooper SL (2008) Discovery of an absorbed-dose/dose-rate dependence for the alanine-EPR dosimetry systems and its implications in high-dose ionizing radiation metrology. *NIST J Res* 113:79–95
35. Desrosiers MF, Puhl J (2009) Absorbed-dose/dose-rate dependence studies for the alanine-EPR dosimetry system. *Radiat Phys Chem* 78:461–464
36. Burns DT, Allisy-Roberts PJ, Desrosiers MF et al (2011) Supplementary comparison CCRI(I)-S2 of standards for absorbed dose to water in Co-60 gamma radiation at radiation processing dose levels. *Metrologia* 48(Tech Suppl 06009):1–18
37. Kudoh H, Celina M, Kaye RJ et al (1997) Response of alanine dosimeters at very high dose rate. *Appl Radiat Isot* 48:497–499
38. Bergstrand ES, Shortt KR, Ross CK, Hole EO (2003) An investigation of the photon energy dependence of the EPR alanine dosimetry system. *Phys Med Biol* 48:1753–1771
39. Zeng GG, McCaffrey JP (2005) The response of alanine to a 150 keV x-ray beam. *Radiat Phys Chem* 72:537–540
40. Zeng GG, McEwen MR, Rogers DWO, Klassen NV (2005) An experimental and Monte Carlo investigation of the energy dependence of alanine/EPR dosimetry: II. Clinical electron beams. *Phys Med Biol* 50:1119–1129
41. Waldeland E, Hole E, Sagstuen E, Malinen E (2010) The energy dependence of lithium formate and alanine EPR dosimeters for medium energy x rays. *Med Phys* 37:3569–3575
42. Helt-Hansen J, Miller A, Sharpe P (2005) Dose response of thin-film dosimeters irradiated with 80–120 keV electrons. *Radiat Phys Chem* 74:341–353
43. Nagy VY, Desrosiers MF (1996) Complex time dependence of the EPR Signal of irradiated L- α -alanine. *Appl Radiat Isot* 47:789–793
44. Desrosiers MF (2014) Post-irradiation study of the alanine dosimeter. *NIST J Res* 119:277–295
45. Taylor BN, Kuyatt CE (1994) Guidelines for evaluating and expressing the uncertainty of NIST measurement results. *NIST Technical Note* 1297
46. Lund A, Olsson S, Bonora M et al (2002) New materials for ESR dosimetry. *Spectrochim Acta Part A* 58:1301–1311
47. Basly JP, Basly I, Bernard M (1998) Electron spin resonance identification of irradiated ascorbic acid: dosimetry and influence of powder fineness. *Anal Chim Acta* 372:373–378

48. Baran MP, Bugay OA, Kolesnik SP et al (2006) Barium dithionate as an EPR dosimetric material for radiation accidents. *Radiat Prot Dosimetry* 120:202–204
49. Hassan GM, Ikeya M, Toyoda S (1998) Lithium lactate as an ESR dosimeter. *Appl Radiat Isot* 49:823–828
50. Wieser A, Regulla DF (1989) ESR dosimetry in the gigarad range. *Appl Radiat Isot* 40:911–914
51. Fattibene P, Duckworth T, Desrosiers MF (1996) Critical evaluation of the sugar-EPR dosimetry system. *Appl Radiat Isot* 47:1375–1379
52. Peimel-Stuglik Z, Fabisiak S (2009) Sucrose as a double-signal high-dose dosimeter for ionizing radiation. *Radiat Phys Chem* 78:449–452
53. Desrosiers M, Nagy V, Puhl J et al (2002) e-Calibrations: using the internet to deliver calibration services in real time at lower cost. *Radiat Phys Chem* 63:759–763
54. Desrosiers MF, Klemick M, Puhl JM (2004) Next-generation services for e-traceability to ionizing radiation national standards. *Radiat Phys Chem* 71:371–374

Chapter 14

EPR Dosimetry in Clinical Applications

Eirik Malinen

Abstract This chapter presents a literature review on the use of EPR dosimetry in clinical applications. Due to the rather low sensitivity of the method, applications are predominantly within radiotherapy. In this field, accuracy requirements are high, requiring emphasis on careful dose measurements in clinically relevant settings. EPR dosimetry has been used to measure output from linear accelerators and other radiotherapy sources, proving to be a reliable method for these purposes. Furthermore, EPR dosimetry in anthropomorphic phantoms is feasible, but has not been demonstrated to a great extent. This is also evident for patient (*in vivo*) dosimetry. Interesting applications of proton/ion beam dosimetry are presented. Most clinical applications of EPR dosimetry have employed polycrystalline alanine as detector material, but the use of other materials is also discussed. It is concluded that EPR dosimetry is a vital research field and very useful for some applications, but that the method is not in widespread clinical use.

14.1 Introduction

Dosimetry is the science of measuring and estimating absorbed dose in matter from ionizing radiation. Dosimetry using electron paramagnetic resonance (EPR), *EPR dosimetry*, utilizes that the number of radiation-induced free radicals is proportional to the absorbed dose in a given material [1, 2]. As free radicals most often are short lived, also in the solid phase, a key issue in EPR dosimetry is to identify materials where substantial amounts of free radicals are stabilized following irradiation. Such solid materials utilized for dosimetry are commonly denoted *EPR dosimeters*. Furthermore, the EPR acquisition procedure and the resulting EPR spectrum (i.e. the dosimeter signal) should be as simple as possible, facilitating fast and easy dosimeter readout. In this chapter, a short introduction to EPR dosimetry will be

E. Malinen (✉)

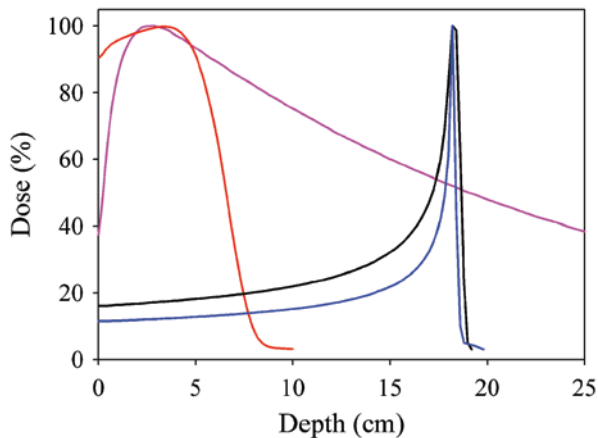
Department of Physics, University of Oslo, P. O. Box 1048 Blindern, 0316 Oslo, Norway
e-mail: eirik.malinen@fys.uio.no

Department of Medical Physics, Oslo University Hospital,
P. O. Box 4953 Nydalen, 0424 Oslo, Norway

© Springer International Publishing 2014

A. Lund, M. Shiotani (eds.), *Applications of EPR in Radiation Research*,
DOI 10.1007/978-3-319-09216-4_14

Fig. 14.1 Percentage depth dose curves for different types of radiation used in radiation therapy. Examples given are 15 MV X-rays (pink), 16 MeV electrons (red), 165 MeV protons (black) and 310 MeV/u carbon ions (blue)



given before we embark on clinical applications. Of relevance here are dose estimates in diagnostic X-ray examinations and in radiotherapy. However, as very few applications of EPR dosimetry in diagnostic radiology have been identified, this chapter will mostly focus on EPR dosimetry in radiotherapy. Also, biodosimetric applications such as EPR dosimetry of tooth enamel [3] will not be covered. It is referred to Chap. 13 for a more detailed description of the principles of EPR metrology.

Radiotherapy is the utilization of ionizing radiation in the treatment of cancer, where the ultimate aim is to eradicate all cancer cells while inflicting as little damage as possible on the healthy normal tissue. There is a quite narrow dose region where the clinical effect in both the tumor and normal tissue becomes pronounced [4]. It has been argued that the accuracy in the dose delivery to the patient should be better than 3–4% [5–7]. This estimate includes all factors leading to inaccuracies in the patient dose, such as radiotherapy beam characteristics, patient data, treatment planning dose calculations and last but not least, absorbed dose determination. In radiotherapy, we have seen a rapid progress in new principles of dose delivery such as intensity modulated radiotherapy (IMRT) and volumetric modulated arc therapy (VMAT) [8–10]. Furthermore, older techniques such as stereotactic radiotherapy [11] and proton/particle therapy [12] are continuously being refined. For these new and refined techniques, new dosimetric issues may arise. Prior to clinical implementation, it is thus pivotal to investigate the dose distributions that are delivered by these delivery techniques.

Different types of Ionizing radiation deposits energy in distinctly different patterns (Fig. 14.1). A perfect dosimetry system should be able to measure and reproduce these features with a high degree of accuracy. High-energy X-rays produced from linear accelerators used for radiotherapy show a high penetration capacity, but the X-ray attenuation is not ideal for shaping the dose distribution inside a patient. Clinical electron beams are good for superficial lesions, due to their short range. However, for high electron energies (>20 MeV), the penetration characteristics becomes less favorable due to increased energy straggling and multiple scattering. Protons and other heavy ions, on the other hand, have well-defined range in tis-

sue. This means that if an appropriate kinetic energy is selected, the ions travel more or less to the same depth in the patient. Just before the ions stop, they have greatly elevated energy deposition called the ‘Bragg peak’. This is highly advantageous in radiotherapy, as the ions produced from a cyclotron or synchrotron can be programmed to certain energies to cover a particular depth range in the patient. However, as the ionization density is much greater in the Bragg peak, this causes a higher biological effect per absorbed dose in tissue. Also, this may cause unwarranted effects in detector materials used in dosimetry, to be discussed later (Sect. 14.6).

The use of EPR for dosimetry was suggested as early as 1962 by Bradshaw et al. [13]. They suggested using polycrystalline samples of the amino acid L- α -alanine (alanine hereafter) as detector material (*dosimeter*) due to its “high sensitivity to radiation damage (1), stability (2), and similarity to biological systems in absorbing radiation (3)”. (1) refers to that large amounts of free radicals are stabilized in alanine after irradiation. (2) refers to that the radical population formed at room temperature is stable in time, making the dosimeter signal virtually independent of the time of irradiation. (3) refers to that the atomic composition of alanine is similar to that of human tissue. Although it is commonly stated that alanine is tissue- or water equivalent, this is in fact not the case for some radiation beams. This is to be discussed in Sect. 14.2. Furthermore, the paper by Bradshaw and co-workers addressed issues that since have become major research topics. First, it was noted that polycrystalline alanine can be molded into different shapes and sizes, and also wrapped in various materials. For instance, a 50 mg pellet could easily be fit into the EPR cavity and gave a detectable signal after some Gy’s of irradiation. It was also noted that the lower dose detection limit was roughly 0.5 Gy. It was found that the number of free radicals was linearly related to the absorbed dose from ^{60}Co γ rays, 260 kV X-rays, ^{90}Sr electrons, and 14 MeV protons. These radiation qualities are all of relevance for clinical applications.

Since the paper by Bradshaw et al. [13], we have seen progress, refinements and new applications of EPR dosimetry. Other dosimeter materials than alanine have been proposed [14–17], and new methods for EPR dose estimation have greatly reduced the uncertainty associated with the method at clinical dose levels [18, 19]. For the applications to be discussed in the following sections, the results from EPR dosimetry have most often been compared to reference measurements or calculations. Typically, ionometry (dosimetry by ionization chambers), treatment planning dose calculations or Monte Carlo simulations have been included for comparison. As will become evident in the following sections, EPR dosimetry is a method that most often show a high show high correspondence with these methods. In some cases, EPR dosimetry may even be the method of choice.

14.2 Quality Dependence

In clinical dosimetry it is normally chosen to calibrate dosimeters at a selected (‘reference’) radiation quality, as calibration at all the different radiation qualities at a clinical department is too time consuming. Furthermore, water is the recommended medium for specifying clinical doses. In order to apply dosimeters previously cali-

brated at the reference radiation quality Q_0 at a different radiation quality Q , a correction factor is necessary when deriving the dose estimate from the measurement. This correction factor takes the impact of radiation quality on dosimeter signal into account. The subsequent section follows our review on the topic [20]. Consider the dosimeter reading r , resulting from a dose to water D_w given with a specific radiation quality Q . The reading per dose is thus $(r/D_w)_Q$. Relative to a reference beam quality, the quality dependence may be defined as $F_{Q,Q_0} = (r/D_w)_Q / (r/D_w)_{Q_0}$ [20, 21]. In EPR dosimetry, in a dose range where the dosimeter is linear with dose, F may deviate from unity due to two distinctly different causes: (1) that the dosimeter signal (per absorbed dose in the dosimeter) is sensitive to changes in radiation quality and (2) that the dosimeter absorbs radiation differently from water. The quality factor may be separated into two components, G and H . The factor H simply reflects that the dosimeter material (e.g. alanine) absorbs radiation with a different probability compared to water. Typically, H may be predicted from analytical approaches such as Bragg-Gray cavity theory or from numerical methods such as Monte Carlo simulations of radiation transport [22, 23]. If the atomic composition of the dosimeter material is close to that of water (effective atomic number Z_w of about 7.7), H should be close to unity for all types of radiation. Large deviations from unity only occurs if low to intermediate energy X-rays are used and the atomic number is significantly lower or higher than Z_w . In radiotherapy, employing high-energy X-rays or electrons, H should typically not vary with more than $\pm 5\%$, as long as solid state dosimeter materials are being used. On the other hand, the factor G reflects differences in the yield of the radiation-induced signal in the dosimeter, and is often referred to as the relative effectiveness. Variations in relative effectiveness may occur if e.g. the ionization density differs between the radiation quality in question and the reference quality. The linear energy transfer is typically used as a measure of ionization density, giving the energy loss per unit path length of the ionizing particles. Low-LET radiation such as photons or electrons roughly have a LET of 0.3 keV/ μm . To put this in perspective, as one ionization in organic materials typically requires 30 eV of radiant energy, an LET of 0.3 keV/ μm will result in on average 10 ionizations per μm . For intermediate to high-LET radiation such as carbon ions the LET may vary from 10 to 300 keV/ μm . If the LET is high, the likelihood of radical destruction and pristine ionization product recombination inside the particle tracks becomes higher. In EPR dosimetry, neutral (non-paramagnetic) products do not result in a dosimeter signal. Thus, the factor G is expected to be lower than unity if the LET of the radiation quality in question is higher than the LET of the reference beam. Furthermore, as has been noted [24] the G -value is not a simple function of LET, but rather reflects both the particle type and LET. Thus, if a dosimeter series is calibrated with ^{60}Co γ rays (low LET) and then used for dosimetry of particle beam, a correction factor specific for the particle type and LET must be applied.

The quality dependence of alanine following electron and photon irradiation has been presented in numerous reports [20, 21, 25–31]. Only recent papers with up-to-date terminology and clearly stated dosimetry protocols used should be conferred for quality factors. In our review on clinical photon and electron irradiation [20], we concluded that the factors G and H are very close to unity for alanine at high energy photon and electron irradiation with ^{60}Co as reference quality. However, for

low- to intermediate energy X-rays, H varied between 0.72 and 0.94, and G between 0.92 and 0.97 [21]. It was rather surprising that the relative effectiveness G deviated from unity, as low- to intermediate energy X-rays also are classified as ‘low-LET’. Yet, low-energy X-rays release secondary electrons with a higher LET compared to those released from high-energy X-rays, which could explain this deviation. However, the experimental uncertainty in our study [21] prohibited us from making firm conclusions, although our findings corresponded well with results from an independent experimental study [30] and from mathematical modelling [32].

With respect to quality dependence, alanine has also been subjected to irradiation with protons and heavier charged particles (see [33] for a review). These studies were mostly performed between the 1970s and 1990s, where the key interest was to investigate, understand and model the physical-chemical response pattern following ion irradiation. As opposed to photon and electron irradiation, G factors as low as 10% was reported, meaning that 90% of the radiant energy causing radicals at low LET resulted in neutral (non-radical) products at high LET for a given particle type. Several analytical models were developed to estimate the relative effectiveness theoretically [32–34], and the models typically employed a ‘saturation dose’ estimated from γ irradiation of alanine. Furthermore, the dose distribution around the ionizing particle track was modelled. Still, the experimental uncertainties and lack of uniformity in reporting in the early studies prevented the use of the theoretical G in estimating the quality factor. Thus, accurate alanine dosimetry for high-LET beams could generally not be accomplished. However, this modelling work has been revitalized in the last years, and very high correspondence has been found between experimental and theoretical G ’s for carbon ions and antiprotons [35, 36]. This has opened for new applications of alanine/EPR dosimetry in ion beam therapy, as will be discussed in Sect. 14.6.

The quality dependence of other types of EPR dosimeters has also been investigated. The most well-characterized dosimeter is lithium formate monohydrate, which we have described for photon, electron, proton and nitrogen irradiation [20, 21, 37–41]. It has been shown that the quality factor of lithium formate is similar to alanine for high-energy X-rays and electrons [20]. However, the quality dependence is significantly closer to unity compared to alanine at low- to intermediate energy X-rays [21], mainly due to that the effective atomic water of lithium formate is closer to that of water. For protons and nitrogen ions [41], compared with literature data, it seems that lithium formate behaves similarly to alanine, maybe with a slightly higher LET dependence due to that the saturation dose is lower for lithium formate [42].

14.3 Dosimetry of Therapy Devices Under Standardized Conditions

In radiotherapy, measurements of absolute dose output and beam profiles from clinical linear accelerators are essential, both with respect to acceptance testing, quality assurance and for providing input to treatment planning systems. The beam output and profile depends typically on, among others, the energy spectrum of the photons or electrons generated by the linear accelerator and the collimation of beam. Small,

energy-independent dosimeters are ideal for measurements of such dosimetric features. In this section, we review the applications of EPR dosimetry of therapy devices under standardized conditions, including brachytherapy systems.

Tomotherapy is a tomographic treatment unit utilizing a rotating linear accelerator, delivering a 6 MV fan-beam as the patient couch is moving through the tomograph. Also, the unit has a binary collimation system basically providing temporal slits for the fan beam as it rotates around the patient. Thus, highly complex, intensity-modulated radiotherapy beams may be delivered to the patient. Still, the clinical implementation of this technique requires extensive quality assurance and dosimetry tests, since such radiation delivery systems challenge current dosimetry systems and procedures. The special design of the Tomotherapy unit restricts the use of dosimetry codes of practice usually employed for clinical linear accelerators. For instance, a field size of $10 \times 10 \text{ cm}^2$ is recommended for photon dose determination under reference conditions in the TRS398 code of practice [45], which cannot be achieved by the Tomotherapy system. Perichon et al. [43] used alanine/EPR dosimetry to measure the absorbed dose rate in static irradiation mode and to evaluate the dose calculation accuracy of the Tomotherapy planning system. The EPR dosimetry was traceable to a primary standards laboratory employing ^{60}Co γ rays. A cylindrical PMMA phantom dedicated to Tomotherapy dosimetry was employed, where alanine dosimeters could be located centrally. A rather complicated methodology was undertaken, where, among others, Monte Carlo simulations were used to calculate conversion factors between different irradiation conditions. A 1σ uncertainty level of 1.5% was obtained (dose level not explicitly given), and a good agreement between the nominal and measured dose rate was found (within 2%). For the testing the performance of the Tomotherapy dose calculation engine, the cylindrical phantom was CT-scanned at imported into the planning system. A hypothetical planning target volume and organ at risk was set up, and the treatment was optimized. For this situation, a 4% difference was found between expected and measured doses, attributed to errors in the CT Hounsfield numbers employed by the dose calculation engine to assign tissue densities. Alanine/EPR dosimetry has also been used as a reference dosimetry system for Tomotherapy in a multicenter setting [44]. In this work, a more straightforward methodology was used, following published recommendations for Tomotherapy quality assurance [46]. The reported uncertainty in the alanine/EPR dose assessment was as low as 0.9% at a dose of about 6 Gy. A common set-up for phantom irradiation, including ion chamber measurements, was used at all four participating centers. Measurements were done both in a quadratic water tank (fixed beam delivery) and a cylindrical PMMA phantom (rotational beam delivery). The correspondence between ionometry and alanine/EPR dosimetry was typically within 1% for different non-modulated beam deliveries. In conclusion, alanine/EPR dosimetry was shown to be a good concept for reference dosimetry of Tomotherapy units.

The Cyberknife is another radiotherapy system capable of delivering highly complex dose distributions. In this case, a robotic arm carrying a linear accelerator can deliver a narrow 6 MV beam to the patient from a multitude of directions. As

for Tomotherapy, implementation of conventional dosimetry codes of practice is difficult for this delivery system. Alanine/EPR dosimetry was used for dose calibration and verification of the Cyberknife system in the study by Garcia et al. [47]. The authors used the same dosimetric methodology as described above for Tomotherapy [44], irradiating alanine dosimeters in water phantom at a primary standards laboratory. The 1σ uncertainty in the dose estimate was about 1.6%. A cylindrical PMMA phantom and an anthropomorphic head phantom was also used. A 6 cm diameter field size was first employed at the Tomotherapy unit. Here, the maximum deviation between expected and measured dose was about 2.5% for both the water and PMMA phantoms. Then, the head phantom, containing alanine dosimeters, was treated using different collimators. Unfortunately, little information was provided regarding these experiments. In any case, a maximum deviation between expected and measured dose was in this case 3.6%, and a trend of higher deviation with smaller collimators was observed. This could point to inaccuracies in the radiation transport modelling of the treatment planning system.

Cronholm et al. [48] studied, among others, the perturbation effect of alanine dosimeters in a water phantom using Monte Carlo simulations of 6 MV photons. Although they did not explicitly calculate perturbation *factors* as such, it was found that alanine did not perturb the radiation field to a high degree. Here, for large dosimeters (5 mm diameter and 2.5 mm thickness; typical clinical dosimeter), an overall change in the perturbation effect by about 5% was observed from relatively large (40 mm Ø) to small (2 mm Ø) field sizes. The effect was less pronounced for miniature dosimeters (1 mm diameter, 2.5 mm thickness), as could be expected. Small alanine dosimeters ('miniALA'; 80% alanine, 20% paraffin) of 1 mm diameter and 3 mm thickness were indeed used by Baffa et al. for measurements in radiotherapy [49, 50]. K-band EPR was employed, as this frequency band gives a higher sensitivity. In their initial study [50], it was found that doses down to about 1 Gy could be detected with these small dosimeters, although explicit reporting of uncertainties at this dose level was lacking. In a more elaborate follow-up [49] the small alanine dosimeters were used to measure radiotherapy output factors and beam profiles. A reproducibility of 3% at 20 Gy was reported, with a total dose uncertainty of 5–6%. Thus, the uncertainty was substantially higher than the studies using conventionally sized dosimeters discussed in this chapter. The EPR measurements were compared with ionometry, TLD and film dosimetry. The output factor may be defined as the dose at a nominal point in a phantom for a given field size relative to the dose in the same point for a reference field size (10×10 cm² squared field). The factor was measured for squared field sizes ranging from 0.5×0.5 to 5×5 cm², and a good agreement (within 7%) was found between the minidosimeters, TLD and film dosimetry. Strangely, it was for the largest field sizes that the greatest discrepancies were found. For the beam profile measurements, the minidosimeters gave penumbral widths crudely comparable to those resulting from TLD and film dosimetry. However, larger data scatter was found for the minidosimeters in the flat dose region, most likely pointing to the relative high uncertainty associated with these dosimeters. The group also developed miniature EPR dosimeters of methylalanine for small field dosimetry with similar applications as for 'miniALA'

dosimeters [51], but this dosimetry system appears to have been abandoned due to the lack of other published applications. In conclusion, although the minidosimeters are attractive for measurements in radiotherapy, the inherent uncertainties associated with the methodology limits the range of applications.

In brachytherapy, radioactive sources are brought as close as possible to the tumor either by inserting applicators into body cavities such as the trachea or vagina/cervical canal, or using needles. As the dose drops with the square of the distance from the source, accurate positioning of dosimeters is important. Furthermore, the radiation emitted from these sources does not have the same radiation quality as high energy radiotherapy photon beams, so different quality correction factors are necessary. EPR dosimetry has been widely studied for applications in brachytherapy. In a well-planned and carefully conducted study, De Angelis et al. [52] used alanine/EPR dosimetry for measuring the absorbed dose rate in water from a ^{137}Cs brachytherapy source. A cross-shaped PMMA holder was developed, intended for irradiating alanine dosimeters in water. Sealed dosimeters were positioned along four arms of the holder, with the ^{137}Cs source applicator located centrally in the holder. The source was positioned so that the perpendicular bisector axis of the source intersected the center of the dosimeters. Doses of about 10–20 Gy were given dosimeters located 1–7 cm from the source. The coefficient of variation of the mean readout (four dosimeters at each distance from the source) was 2.4%, reflecting both the dosimeter batch homogeneity/reproducibility and the irradiation reproducibility. Interestingly, dose-to-water correction factors for alanine at varying distances from the source, based on Monte Carlo calculated photon spectra [53], were employed. The resulting estimated dose rate in water could be determined with a 1σ accuracy of 3%. Moreover, the so-called radial dose function along the transverse axis, a quantity of primary interest in brachytherapy, could be determined at 3.4% accuracy. This study demonstrated the usability of alanine/EPR dosimetry for determining doses from brachytherapy. Additional studies on brachytherapy applications have since then been undertaken by other groups. Calcina et al. [54] used alanine/EPR dosimetry to determine doses from high dose rate brachytherapy with ^{192}Ir . First, as the ^{192}Ir source is moved stepwise to discrete dwell positions for irradiation, there is a significant dose contribution as the source moves from one position to the other. This is called the “transit dose”, and depends among others on the speed of the wire moving the source through the catheter-needle. The transit dose was determined by a rather simple experimental setup, and it was found that this contributed to roughly 5% of the total dose 5 mm from the needle. Furthermore, the radial dose function (see also De Angelis et al. [52]) was determined. The results were found to be in line with earlier studies using TLD and Monte Carlo simulations.

Antonovic et al. [55] did EPR dosimetry with lithium formate as detector material to measure doses from ^{192}Ir sources. Custom-made cylindrical dosimeters (diameter of 4.5 mm, thickness 4.8 mm, density 1.26 g/cm³) were produced for the study. A PMMA phantom, with a centrally drilled hole for the source (from two different brachytherapy models), was used. The phantom had an insert for dosimeters, positioned at 1, 3, and 5 cm from the source. The EPR dosimetry was compared with treatment planning calculations, with delivered doses ranging from 2.5 to 25 Gy.

The agreement was excellent, with deviations ranging from 1.4 to 2.9% only. The authors displayed a high degree of proficiency in dosimetric theory in this paper, deriving the necessary correction factors in order to estimate absorbed doses to water from the EPR dosimetry. For instance, the volume averaging effect of the dosimeters was assessed and an elaborate uncertainty budget was presented. The authors continued their work on lithium formate EPR dosimetry in the study by Adolffson et al. [37]. Here, the main aim was to present a methodology to derive energy correction factors of relevance for brachytherapy. A combination of theoretical and experimental work was undertaken, again being highly proficient, and it was shown that the energy response at energies below about 100 keV varied by no more than 5–6%. Although this was statistically significant, the work still shows that lithium formate may be preferable over alanine for low-energy photon dosimetry.

An alanine/agarose gel system and alanine films were used by Olsson et al. to measure the dose around an ^{192}Ir source in a vaginal cylinder applicator [56]. The alanine/agarose system was developed based on previous studies [57, 58]. Briefly, an agarose gel supersaturated with polycrystalline alanine was placed in a cylindrical phantom of 11 cm diameter and 10 cm height. The vaginal cylinder applicator, with diameter of 30 mm, was placed in the center of the phantom. Alanine films in dedicated cassettes could also be placed in the gel. A treatment planning system was used to optimize the phantom dose distribution, giving a constant dose in the axial direction at a given radial distance from the source train. After irradiation, the gel was cut in slices (1 or 2 mm thick) and pressed into pellets (2.5 mm thickness, 4.5 mm diameter) to remove water and to have a reproducible shape in the EPR cavity. The combined uncertainty of the alanine/agarose was up 4.5%, where uncertainty increased with distance from the source. The uncertainty in the film readings was similar. The alanine/EPR measurements were compared with Monte Carlo simulations, and an agreement typically within 5% was found for both the gel phantom and film system. However, larger discrepancies were found closest to the applicator wall, which could not be explained. Although this study was interesting and relevant, the alanine/agarose gel system seems rather complicated and cumbersome to handle, and no applications with this system have since been published.

Kolbun et al. [59] used electron paramagnetic resonance imaging (EPRI) and small cylindrical phantoms of lithium formate monohydrate and ammonium formate to determine the radial dose distribution around ^{192}Ir wires. The phantoms were made by pressing polycrystalline powder into pellets with diameter of 22 mm and a height of 10 mm. A ^{192}Ir wire was placed centrally in the pellet through a 0.4 mm centrally drilled hole (Fig. 14.2). After 2 weeks of irradiation, the wire was removed and the radial dose distribution was mapped with EPRI (Fig. 14.2). Due to that the EPR resonance line of ammonium formate is much narrower than that of lithium formate, the spatial resolution was twice as high for EPRI using ammonium formate. This was demonstrated by exposing a cubic phantom by a homogeneous X-ray beam, resulting in a much broader EPRI edge spread function for phantoms made by lithium formate. Ammonium formate was thus chosen for the subsequent measurement series on ^{192}Ir wires. The results were compared with Gafchromic EBT film dosimetry and Monte Carlo simulations. Using a Gaussian filter in the

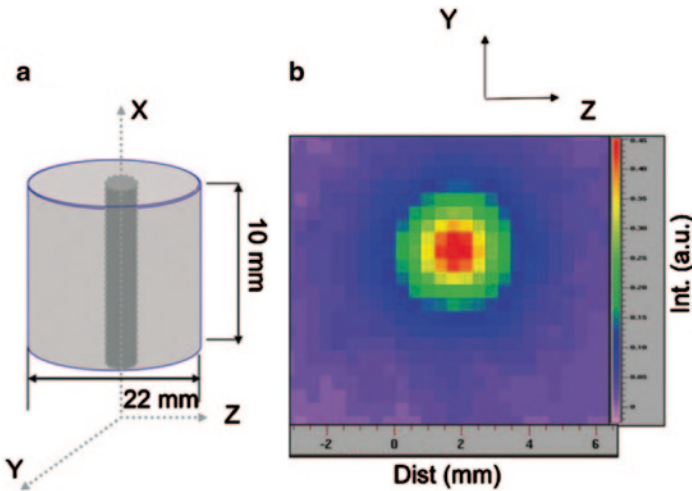


Fig. 14.2 Electron paramagnetic resonance imaging of the radial dose distribution around ^{192}Ir wires used for brachytherapy. The EPR dosimeter phantom, with a centrally placed wire, is shown (a) together the resulting measured dose distribution (b). (The figure is adapted from [59] by permission of American Association of Physicists in Medicine (2014))

EPR image reconstruction procedure gave a good correspondence (within 1 %) between EPRI and the other methods close (typically 1–2 mm) to the ^{192}Ir wires. Further away from the source, greater differences were found. However, the discrepancies were much greater if a Fermi-Dirac filter was used, showing that EPRI is highly sensitive to the image reconstruction settings. Still, from an experimental point of view, this is one of the most interesting applications of EPR dosimetry to date.

14.4 Dosimetry in Anthropomorphic Phantoms

In Sect. 14.3, we discussed dose measurements under standardized conditions in homogeneous phantoms, usually made of water. However, for clinically more realistic dosimetry (apart from *in vivo* dosimetry; Sect. 14.4), anthropomorphic phantoms are preferred. There are some anthropomorphic models commercially available that allow for the study of three-dimensional dose distributions. In radiotherapy, the dose calculations algorithms employed in treatment planning studies all work well under standardized conditions [60]. As such standardized measurements are used to benchmark e.g. the source size and photon energy spectrum in the dose calculation algorithm a high agreement between measurements and treatment planning calculations is expected. For inhomogeneous media, which both changes the path-length and the scattering of the radiation field, larger discrepancies may be expected depending on the level of approximation in the dose calculation algorithms [60].

We constructed an inhomogeneous cylindrical phantom for studying the effect of low-density tissues on measured and calculated dose distributions of therapeutic photon beams [61]. PMMA, Poly(methyl methacrylate), was used to mimic soft tissue while Styrofoam, extruded polystyrene foam, acted as ‘light’ lung tissue. The phantom was CT-scanned and dose calculations were performed using a commercial treatment planning system. Also, the phantom was reconstructed in the EGSnrc simulation package, allowing for Monte Carlo simulations of the radiation transport throughout the phantom. Alanine film dosimeters (134 μm thick) were used to assess the depth dose characteristics in the cylindrical phantom. Incidentally, there were few studies in the literature on the use of alanine films. Thus, as a first step, we performed a detailed dose-response evaluation of these dosimeters. It was shown that the film dosimeters gave a linear response for doses above 5 Gy, with a precision of better than 2% in this dose range. Regarding the phantom measurements, the presence of Styrofoam radically altered the measured depth dose characteristics. This was also confirmed by the Monte Carlo calculations and, with slightly less agreement, by one of the dose calculation algorithms (‘collapsed cone’) provided by the treatment planning system. However, the other dose calculation algorithm (‘pencil beam’) failed to reproduce the measured dose distributions in the low-density region, which is due to the oversimplifications done by this algorithm with respect to lateral electron transport. In conclusion, the alanine films were quite sensitive and the EPR measurements corresponded well with Monte Carlo simulations.

A study similar to the one discussed above was done by Ramirez et al. [62]. They used a cylindrical phantom, but employed bone-equivalent material as the perturbing heterogeneity. Furthermore, the group used in-house developed mini-ALA dosimeters of 3 mm height and 1 mm diameter, which consisted of 95% alanine and 5% PVA (polyvinyl acetate) (see also Sect. 14.3). The dosimeter readout was done with K-band EPR spectroscopy, giving a higher sensitivity than the conventional X-band methods. Still, the precision in the dosimeter reading was rather low; roughly 6% as evaluated by the error bars presented in that study. The dosimetric effects caused by the bone insert were quite small, as shown by both Monte Carlo simulations and miniALA measurements. Still, a good correspondence was found between simulations and measurements. However, the lack of precision in the mini-ALA dosimeter reading is of concern and warrants further improvements of this dosimetry system.

Stereotactic intracranial radiosurgery is the treatment of small lesions in the head. This requires a highly focal tumor dose with little dose to surrounding tissues. The treatment can for instance be delivered as an arc rotation technique, where the linear accelerator is rotated around the patient during irradiation. Small collimators are usually used, resulting in very narrow photon beams. In this case, it is vital to correctly model photon and electron scatter inside the patient. We investigated the dose distribution in the head of an anthropomorphic phantom using lithium formate EPR dosimetry (Fig. 14.3) [63]. Using a grid of small custom-made dosimeters (diameter 3 mm, thickness 2 mm) in a single measurement plane, a good correspondence was found between measurements and treatment planning calculations: the mean measured and calculated dose in the central region was 17.0 and 17.3 Gy,

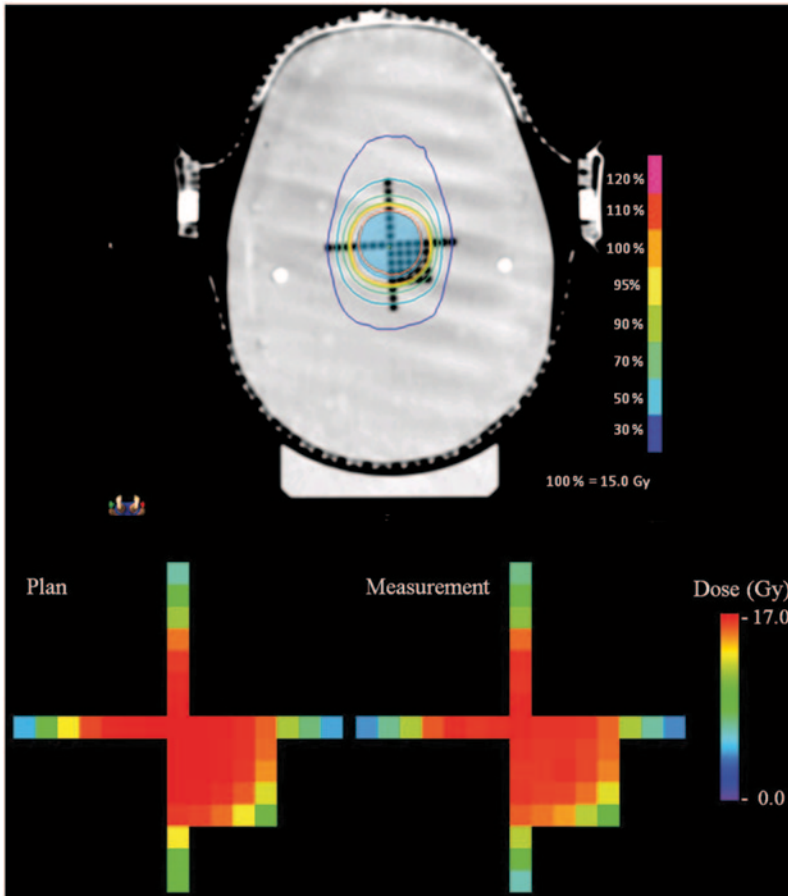


Fig. 14.3 CT-scan of an anthropomorphic head phantom holding an insert for lithium formate dosimeters (*top*). The expected isodose levels from stereotactic radiotherapy are indicated. Measured and calculated dose distributions in the dosimeter grid (*bottom*). (The figure is adapted from [63] by permission of IOP Publishing Ltd. (2010))

respectively. Furthermore, the geometric accuracy in the dose delivery was around or better than 1.0 mm. Although some small discrepancies were found outside the target volume, the study both showed that lithium formate is useful for dosimetry of stereotactic radiosurgery and that the planning and treatment procedures are safe and accurate for the relevant patients.

Total body irradiation is the application of radiation to primarily suppress the entire immune system in leukemia patients prior to bone marrow transplantation. The lungs are organs at risk that should be partially shielded during treatment. As the technique is non-standardized and varies from center to center, it is important to verify doses delivered to different parts of the patient. Schaecken et al. [64] placed alanine dosimeters inside a commercially available anthropomorphic ‘Aldersson’

phantom, and carried out an irradiation procedure according to the local guidelines. Following procedures outlined by Anton [19], the uncertainty in the estimated alanine doses was very low; 0.6%. The dose to the soft tissue and the lung was measured to be 2 and 3%, respectively, lower than that predicted by the treatment planning system. Although the difference between measurement and planning calculations was statistically significant, the treatment planning calculation accuracy may still be considered clinically acceptable.

Alanine has been used for measuring the dose distribution following electron arc treatment [65]. In such a treatment, the linear accelerator is revolving over a certain arc length while continuously irradiating the patient. The chest wall of breast cancer patients is a difficult region to treat with homogeneous doses, and this technique can be used to overcome this problem. Still, accurate electron transport calculation for arc treatments could not be achieved, at least with older planning algorithms, which limited the clinical use of this method. Alanine pellets (4.9 mm diameter, 2 mm thickness, 5% polyethylene) were used together with a cylindrical ionization chamber. First, the electron energy dependence of the dosimeters was evaluated in a cubic phantom. 10, 20 and 30 Gy doses were employed for each electron energy. For this type of dosimeters (containing polyethylene), absolutely no energy dependence could be seen. Then, the arc delivery of electrons (covering an angular segment of 100°) was investigated at various measurement points in a cylindrical PMMA phantom. It was found that the ionometry underestimated the dose relative to alanine, although the underestimation was not properly quantified. It was speculated whether this was due to a higher fluence of low energy electrons for arc delivery compared to irradiation at reference conditions. This is in fact in line with that the chamber response (relative to water) decreases with decreasing electron energy due to that the density effect becomes less significant. So for these measurements, the alanine dosimeters were better suited due to the insignificant energy dependence. Finally, alanine dosimeters were inserted into an anthropomorphic chest wall phantom and irradiated by the arc therapy. Major differences could be seen between some of the measurements and doses estimated from a dose calculation formula. The causes of these differences were not adequately discussed.

As noted in Sect. 14.3, intracavitary and interstitial brachytherapy employs radioactive sources which are brought as close as possible to the target region of the patient. Thus, the dose fall-off in the patient is very high and it is quite challenging to accurately position dosimeters relative to the brachytherapy applicators. In the very thorough work by Anton and coworkers [66], alanine was used to estimate urethral doses following interstitial brachytherapy with ^{192}Ir . Interestingly, a new dosimeter system using alanine powder contained inside PVC rods was developed. The rods with alanine, ‘alanine strands’, were planned to be positioned inside the urethra via Foley tubes. After irradiation, the alanine powder could be pressed to pellets of 1.5 mm height. In the first experiments, the alanine strands were placed in a water-equivalent phantom and irradiated either with ^{60}Co γ rays or by the ^{192}Ir source. The authors saw a noteworthy significant signal fading over 5 days in the home-made samples based on alanine powder. After establishing the corrections necessary to estimate the dose from the EPR signal after irradiation, the dose to the urethra inside a prostate phantom

(holding an interstitial needle for the ^{192}Ir source) was determined and compared to that from a treatment planning system. The range of deviations between measurements and treatment planning calculations was -4.4 to 1.0% (median -1.4%), which is very good considering the challenges in establishing a new dosimetry system and the complex measurement setup in the prostate phantom. However, it does not seem that the dosimetry system developed in this work has been applied for *in vivo* dosimetry (see Sect. 14.5).

In intensity modulated radiotherapy, the multi-leaf collimator of the linear accelerator changes configuration during irradiation [8, 9, 67]. The changes can be continuous or stepwise. For the latter, ‘step-and-shoot’, the radiation is delivered to the patient in beam segments. Adding the segments in space effectively results in an intensity modulated beam. Together with inverse planning, which is an optimization procedure, complex radiation deliveries can be created which better conform to the radiotherapy target volume. However, this complexity makes IMRT more prone to dosimetric errors, which are both due to technical aspects of the linear accelerator and to limitations in the treatment planning physics models describing small radiation fields (see Sect. 14.3). Gustafsson et al. used lithium formate EPR dosimetry to measure IMRT dose distributions in a cylindrical phantom [38]. The IMRT beams were generated by inverse treatment planning of a patient with cancer in the head and neck region. Doses from the IMRT beams in the cylindrical phantom were calculated by a commercial treatment planning system. The home-made lithium formate dosimeters could be placed in the phantom for irradiation. The performance of the dosimetry system was first investigated. It was found that the 95 % confidence in the dose estimate was about 2.5 % for doses over 3 Gy. A measurement time of 15 min per dosimeter was employed, which is rather long. Comparing measurements with ionization chamber and EPR dosimetry, agreement within -4.3 and 3.2% was found. Comparison with the doses calculated by the treatment planning system was not reported. In conclusion, a good agreement between ionometry and lithium formate dosimetry was found, making lithium formate a promising method for IMRT dosimetry.

14.5 *In vivo* Dosimetry

In radiotherapy, the dose to the patient must be delivered with as high accuracy as possible, ensuring a high probability of tumor cure and minimizing the risk of normal tissue toxicity. *In vivo* is Latin for “in the living”, and *in vivo* dosimetry refers to procedures involving dose measurements with the patient in treatment position at the therapy unit. The ultimate goal is to estimate doses that are actually delivered to the patient at a given treatment.

There are many potential sources of error that can lead to reduced radiotherapy efficacy. Among these are the absolute dose determination and the dose calculation

algorithm [60]. In addition, there are uncertainties associated with the treatment delivery. First, the treatment unit itself is a potential source of error: the beam intensity and collimator system may both show random and systematic deviations from the intended treatment delivery [68]. Second, the positioning of the patient may vary and the patient can experience anatomical changes over the fractionated treatment course. Regarding the latter, both loss of body weight and radiation induced alterations in the high-dose region of the patient are of relevance [69]. It has been argued that *in vivo* dosimetry may enable the detection of treatment-related errors that cannot be identified by other quality assurance procedures [70]. Thus, there is a need for accurate dosimetric procedures providing estimates of doses actually delivered to the patient, and EPR dosimetry is a relevant method. As there are rather few relevant studies reported, each study is presented in detail below.

One of the first reports on *in vivo* EPR dosimetry, with alanine as dosimeter material, was the feasibility study by Kuntz et al. [71]. Home-made dosimeters, 5 mm diameter and 3 mm height, showed a precision of 2% after a dose of 20 Gy. Surprisingly, a non-linear dose response was found. Their alanine/EPR system was used for beam characterization in addition to the *in vivo* applications. Regarding the latter, doses were first measured at high dose rate brachytherapy (^{192}Ir source) of the vagina. Slightly lower doses than expected (16%) were found 5 mm from the brachytherapy applicator, but these discrepancies were still not of great concern, considering the potential sources of errors in brachytherapy. Finally, doses to a patient receiving intra-operative radiotherapy (X-ray based, photon energy not reported) were estimated. Very few details concerning the treatment were given, but dosimeters in a vacuum-packed polyethylene sachet were placed on the open operation wound and given a prescribed dose of 14.8 Gy. The mean measured EPR dose was 14.0 Gy. The reason for this discrepancy was not discussed, but as the authors did not report on the use of bolus material to ensure appropriate buildup of secondary radiation, this could be a possible explanation.

Schaeken and Scalliet reported on the experience with alanine/EPR dosimetry in radiotherapy [72]. Different types of alanine dosimeters were purchased from three different vendors. The background signal and the radiation sensitivity of the different dosimeter types were shown to vary considerably, pointing to differences in the dosimeter composition and production. Still, the intra-batch dosimeter homogeneity was rather good (around 1% at 10 Gy). One of the dosimeter types was used to estimate the dose for two cervical cancer patients treated with brachytherapy. Patient 1 was treated with high dose rate using a stepped ^{192}Ir source, while patient 2 was treated with low dose rate (LDR) using ^{192}Ir wires. Alanine dosimeters, sealed in plastic sachets, were positioned in the vaginal mould applicator. However, although the dosimeters were provisionally sealed, some were still damaged from vaginal secretion, in particular at the longer-lasting LDR treatment. The effect of temperature in the human body (37°C) during irradiation was corrected for. Differences between calculated and measured doses ranged from—14 to 8% (HDR) and—4 to 13% (LDR), and only one dose measurement deviated significantly from the dose

calculation. Difficulty in positioning of the dosimeter in a high dose gradient was suggested being the cause of the discrepancy. Schultka et al. [73] also used alanine/EPR dosimetry to determine vaginal doses in 13 patients from LDR brachytherapy with ^{137}Cs or ^{192}Ir sources of gynecological cancer. The dosimeters were cellulose capsules (diameter 5 mm, length 15 mm) filled with 0.5 g of polycrystalline alanine sealed in waterproof Parafilm pockets. The capsules were enclosed in a cupronickel frame in order to be visualized in the X-ray radiographs used for treatment planning. The measurements were compared with treatment planning calculations. The authors addressed the problem of determining the effective point of measurement in the dosimeter, and the subsequent uncertainty in the determining the dose. However, by extracting the mean computed dose over 4 points at opposite edges of the dosimeter, a better correspondence was found between measurements and planning calculations compared to when a single computed dose was extracted from the center of the dosimeter. This study nicely illustrated the impact of large dosimeters in high dose gradients.

The feasibility of using alanine/EPR dosimetry in external beam radiotherapy with ^{60}Co γ rays and high energy electrons was investigated by Ciesielski et al. [74]. With respect to the number of patients and measurements, this is the most comprehensive *in vitro* EPR dosimetry study to date. The dosimeters used were polyethylene sachets tightly packed with pure polycrystalline L- α alanine. The height and width of these homemade square sachets was 1.5 (± 0.3) mm and 1.6 cm, respectively. After irradiation, the alanine powder was transferred to a quartz tube. Then, the tube was tapped to ensure a homogeneous filling. The dosimeter readout had to be corrected for variations in packing density from sample to sample. This procedure could potentially have been improved by pressing the irradiated alanine powder into solid pellets, which would not require density corrections. Also, several pellets could have been obtained from one dosimeter sachet. The scan time per measurement was 16 min, which is very long for routine single point dose measurements. First, a calibration series in a phantom was performed to estimate the 1σ precision in the determined dose. The measured precision was 6.7, 3.0 and 2.8% for 0.5, 1.1 and 2.0 Gy, respectively. Doses from ^{60}Co γ treatment of 19 patients with cancer in the head and neck region and 8 patients receiving electron and photon treatment of the chest wall were then reported. The dosimeters were taped onto the radiotherapy fixation mask or directly on the skin of the patients. Both irradiations with and without buildup material was used. In brief, it was found that the deviations between doses calculated by the treatment planning and measured doses were larger than expected from the precision in dosimeter readings from the calibration series. Skin doses deviated on average by about 1.5%, but with a standard deviation of 7–9%. Setups including buildup gave about the same mean difference, but smaller standard deviations (2–4%). As delivered skin doses typically were lower, the authors argued that error contributions to the estimated doses from e.g. the EPR background signal had a substantial impact. Also, measurements on the skin are in general less robust compared to measurements at depths beyond the range of secondary radiation.

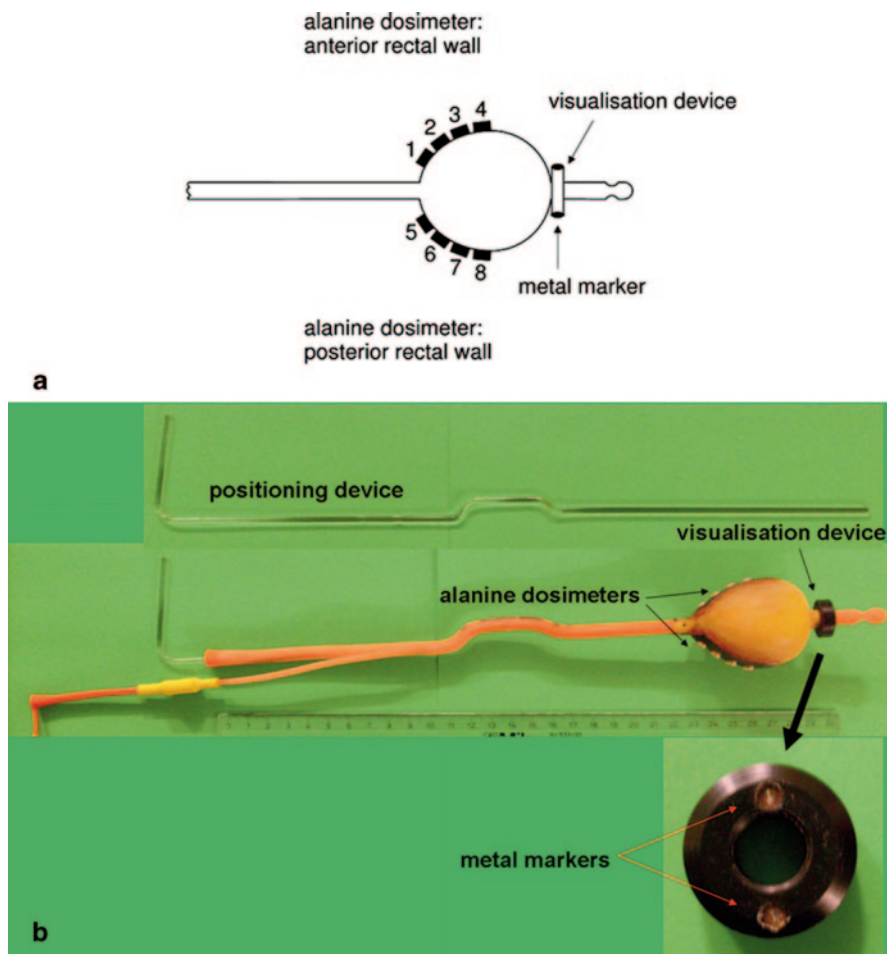


Fig. 14.4 **a** Illustration of the rectal balloon used for *in vivo* dosimetry of prostate cancer patients receiving external radiotherapy. Four *alanine dosimeters* were placed at the anterior rectal wall (1–4) and four *alanine dosimeters* at the posterior rectal wall (5–8). A *visualization device* with radiopaque *metal markers* can be seen on top of the balloon. **b** One rectal balloon holding *alanine dosimeters*. (The figure is taken from [75] by permission of Elsevier (2014))

Wagner et al. [75] did a study on using alanine/EPR dosimetry for estimating doses to the rectal wall following radiotherapy of prostate cancer. Due to its close proximity to the prostate, the rectum is the most important organ at risk during external beam radiotherapy. Therefore, measures to reduce the dose to the rectum are highly relevant, and inflated rectal balloons may help to increase the distance between the prostate and the major part of the rectum. However, the insertion of such an air cavity gives dosimetric challenges in the air-tissue interface. In this study, alanine dosimeters contained in polyethylene foil where positioned on the rectal balloon, with four dosimeters facing the anterior and posterior rectal wall, respectively (Fig. 14.4).

A radiopaque device was placed on the top of the balloon in order to locate it with the dosimeters inside the patient with the radiotherapy verification beam at the time of treatment. For three patients, the alanine dosimeters were exposed over ten consecutive treatment fractions to accumulated doses ranging from 11 to 20 Gy delivered with 20 MV photons. A comprehensive uncertainty budget was presented both for the applied dose and the measured dose, where the relative standard uncertainty was about 3.5 and 1%, respectively. For two of the patients, an excellent correspondence was found between the dose calculations by the planning system and the alanine/EPR measurements (mean relative difference typically 1.5%). However, for the third patient, having a metal hip prosthesis, the planning system seemed to underestimate the dose to the posterior rectal wall and overestimate the dose to anterior wall. It could well be that the accuracy of the treatment planning system's radiation transport model was seriously challenged by metal artifacts from the prosthesis in the planning CT images together with the problematic air/tissue interface at the rectal wall. Still, the mean difference between calculated and measured doses was 11% anteriorly and -7% posteriorly for this patient, most likely not of high clinical relevance.

The latest reported study on *in vivo* alanine/EPR dosimetry is that by Wagner et al. on patients with cancer in the head and neck [76], which follows much of the same methodology in the work on prostate cancer [75] outlined above. In brief, a low-density mouthpiece, usually used to reduce mucosal doses, was equipped with alanine/EPR dosimeters during IMRT. The mouthpiece was equipped with radiopaque markers. In five patients, doses were accumulated over 7 to 24 treatment fractions and ranged from about 7 to 48 Gy. Again, an ample uncertainty budget was presented, resulting in a total standard uncertainty in the dose ratio (measured against planned) of about 4.6%. For two out of eight dosimeter positions, the measured and applied dose did not agree within this uncertainty. This corresponded to the tip of the mouthpiece, i.e. the part of mouthpiece located at the back of the mouth. The authors argued that the main cause of these discrepancies was the reconstruction of the alanine measurement point in the planning CT images, as the mouthpiece may move during treatment. As the tip of the mouthpiece was located farthest away from the bite groove (fixation point), a higher positional variability and greater dosimetric uncertainty may be experienced there. However, it was rather puzzling that the authors concluded that the use of a mouthpiece should be abandoned due to these *dosimetric* uncertainties. If the mouthpiece was shown to give significantly higher doses than the standard situation (no mouthpiece), such a conclusion could have been supported, but this did not seem to be the case.

14.6 Proton and Heavy Ion Irradiation

As discussed in Sects. 14.1 and 14.2, accelerated heavy charged particles differ from therapeutic photons and electrons in that their energy transfer spectrum and density may result in altered radical yields. This may have negative consequences for EPR dosimetry, in particular with respect to absolute dose determination. Still,

some applications of EPR dosimetry for therapeutic particle beams have been undertaken, and will be discussed in this chapter.

First, applications with respect to beam characterization will be presented. The depth dose characteristics of therapeutic proton beams have been most widely studied. Ionization chambers, either of cylindrical or parallel plate type, have most often been used for comparison. One of the first reports on therapeutically relevant proton beams was that by Gall et al. [77]. Although being rather limited with respect to information on irradiation and analysis, 3 mm thick pellets were irradiated with 160 MeV protons at different depths in a water phantom of variable length. Quite high doses were applied (25–75 Gy). A good consistency between alanine/EPR measurements and ionometry was found (within 3%), hinting towards the potential usefulness of alanine/EPR dosimetry for this purpose. In the more comprehensive work by the group of Onori et al. [78–80], alanine pellets (diameter 4.9 mm, thickness 1, 2 mm and 10 mm, density 1.26 g/cm³) and alanine films (thickness 0.25 mm, density 0.99 g/cm³) were employed to estimate doses in a solid water phantom from 62 MeV protons. The proton beam was used for treating ocular cancers, mainly melanomas. The range in water of such protons is about 3 cm. Both unmodulated (monoenergetic) and modulated (polyenergetic) proton beams were used. Doses ranging from 5 to 250 Gy were applied. First, no differences in the EPR spectra between γ - and proton irradiated samples were found, regardless of the proton irradiation depth. Thus, it appears that protons do not alter the underlying composition of radical species following irradiation. The detector reading per dose following proton irradiation was slightly lower (3%) than that for γ -irradiation, although this difference was not significant. For a highly modulated proton beam at three different positions in the Bragg plateau, ionization chamber measurements and alanine/EPR dosimeters (2 mm height) differed by only 2%, well within the combined uncertainty of the two dosimetry systems (6%). For unmodulated proton beams, again a good correspondence between ion chamber measurements and alanine/EPR dosimetry was found for both 1 and 2 mm thick dosimeters and film dosimeters. As the highest deviation was seen at the end of the Bragg peak, this could both be due to (a) averaging effect of the finite-sized dosimeters (the deviation was smallest for film dosimeters) and (b) a lower relative effectiveness (see Sect. 14.2) for low-energy protons. Regarding (a), a 1 or 2 mm box-car smoothing of the longitudinal ion chamber dose profile could have indicated whether this was the main factor, but this was not done. Regarding (b), in a later study on 1.6–6.1 MeV protons, the authors showed that the relative effectiveness for 2 mm alanine pellets was about 0.6 [81]. However, this appears to be somewhat contradictory to the excellent agreement found by the same group between ionometry and alanine film measurements at the distal part of the Bragg peak. This could potentially point to difficulties when estimating the dose to a partially irradiated 2 mm thick dosimeter by low energy protons with a very short range. In conclusion, the studies discussed above show that alanine/EPR is a good and reliable solid state dosimetry system for proton therapy, at least at depths not too close to the distal edge of the Bragg peak.

For ions heavier than protons, very few studies have been published that have a direct clinical relevance. As discussed in Sect. 14.2, recombination effects in the

EPR dosimeters are expected to give a relative effectiveness considerably smaller than unity. Thus, rather large deviations between measured and expected doses may result if appropriate corrections are not applied. Also, the relative effectiveness is expected to decrease with increased ion penetration, as the mean beam energy decreases and the LET thus increases. These effects were elegantly handled by Hermann et al. [36], who used alanine/EPR dosimetry to estimate doses in a PMMA phantom irradiated with therapeutic carbon ion beams. First, the authors used a previously established detector efficiency model [35] to estimate the relative effectiveness in alanine for carbon ions at different energies. The model was validated against measurements. Furthermore, it was shown that Monte Carlo simulations using the FLUKA code [22] reproduced measured depth dose characteristics (from ionometry) with a high accuracy. The Monte Carlo simulations were employed to estimate ion spectra at given depths following energy modulation, and the spectra were then used in the detector efficiency modelling. The measured depth dose by alanine/EPR dosimetry was then compared with the theoretical detector response. Thin dosimeters (thickness 0.44 mm) were used to measure doses primarily around the peak region while more conventional dosimeters (thickness 5.05 mm), were used at the entrance region. Doses of typically 20 Gy were delivered to the entrance region, resulting in doses of up to 80 Gy in the peak region. The best correspondence was found between measurements and calculations in the entrance region, although deviations up to around 5% were observed in the case of spread out Bragg peak (Fig. 14.5). In the peak region for monoenergetic and slightly energy modulated protons, larger deviations (up about 9%) were found. Causes for these discrepancies were discussed, and the authors emphasized difficulties in modelling the geometry of the slanted alanine pellets used. Still, this work represents a significant step forward with respect to solid state alanine/EPR dosimetry of ions heavier than protons.

The concept outlined in the paper by Hermann et al. [36] was taken further in the recent study by Ableitinger et al. [82], where alanine/EPR dosimetry was used to estimate doses in a water-equivalent phantom from proton and carbon therapy beams. Also, cylindrical ionization chambers and Gafchromic films [83] were used. 10 Gy in the spread out Bragg peak was delivered to the dosimeters (diameter 5 mm diameter, thickness 2.3 mm, density 1.23 g/cm³) positioned at four different depths in the phantom. Depth-specific theoretical estimates of the relative effectiveness were used to correct the alanine dose reading. The relative effectiveness at the different measurement points varied from 0.97 to 0.99 for protons, and from 0.74 to 0.90 for carbon ions. The mean deviation between treatment planning calculations and alanine/EPR measurements (corrected for relative effectiveness, among others) was very low; 2.4% for protons and 2.2% for carbon ions. For comparison, the difference between treatment planning calculations and ionometry was 1.7% and 1.0% for protons and carbon ions, respectively. However, it is important to stress that the large cylindrical ionization chamber gave a dose reading at one point only in the phantom. Also, ionization chambers are not suitable for mailed dosimetry audits. This comprehensive and skillful work showed that the alanine/EPR dosimetry system is suitable for auditing in ion beam therapy.

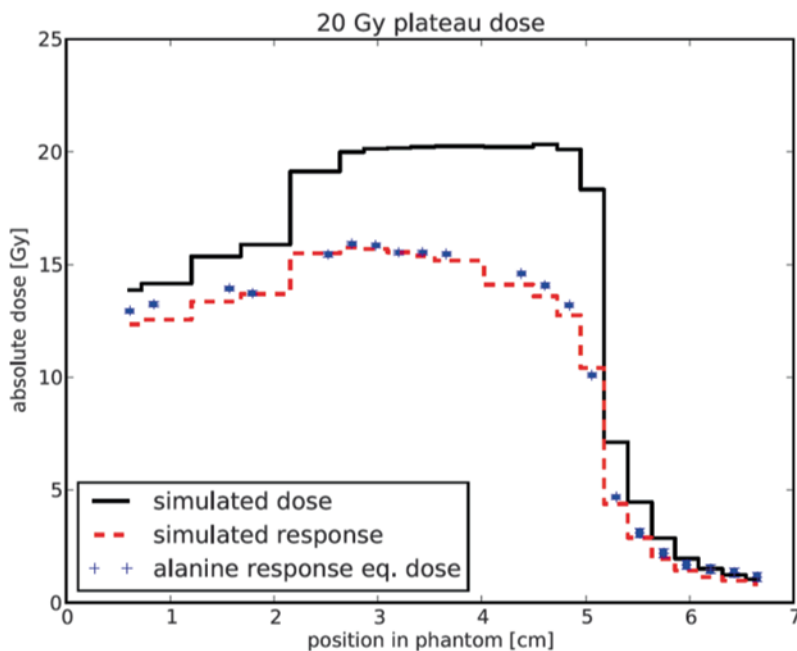


Fig. 14.5 Spread-out Bragg peak for a therapeutic, scanned carbon ion beam, as measured with alanine dosimeter (*blue crosses*). The Monte Carlo simulated dose distribution (*black line*) and the theoretical alanine response (*stippled red line*) are also given. (The figure is taken from [36] by permission of American Association of Physicists in Medicine (2014))

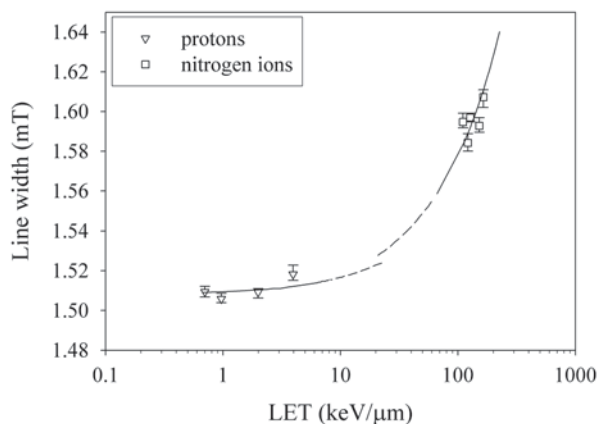
In addition to the rather few applications outlined above, there are some studies of indirect relevance to proton and ion beam therapy. Of particular interest are studies which have found that ion-irradiated EPR dosimeter materials may exhibit EPR signal characteristics different from that following photon irradiation. If the radicals stabilized along the ion tracks give a distinct fingerprint, this could potentially be employed to identify the type of radiation causing radical formation. Microwave power saturation analysis is an EPR experiment where the sample is measured under different microwave power levels, and may provide qualitative and quantitative information on the spin population(s) constituting the EPR signal. Using appropriate theoretical models and fitting to experimental microwave saturation curves, estimates of T_1 (spin-lattice) and T_2 (spin-spin) relaxation times may be obtained [84]. Krushev et al. [85] irradiated alanine with γ -rays and low-energy (3 MeV) protons and He ions, and showed that the microwave power saturation behavior for ions and γ -rays was different. More precisely, they showed that radicals generated by (high-LET) ions saturated more slowly compared to radicals generated by (low-LET) γ -rays. They interpreted these findings as reflecting the increased radical concentration following ion beam irradiation, causing more effective relaxation compared to photon irradiation. In fact, they saw that He-irradiated samples saturated even more slowly than those irradiated with protons, as expected due to differences in track structure. The microwave power saturation principle was further explored by

Ciesielski et al. [86, 87] using alanine irradiated with many different types of radiation. Following earlier work by Arber et al. [88], the intensity of the main EPR resonance line (denoted x) and the intensity of the closest satellite lines (denoted y) were extracted at different microwave powers. The x/y ratio was shown to reflect the type of ion beam used; high-LET radiation such as neutrons and iron ions gave a significantly lower x/y ratio compared to low-LET photons. Thus, the x/y ratio could thus potentially be used to identify the type of radiation causing the dose deposition. However, both Krushev et al. [85] and Ciesielski et al. [86, 87] employed very high doses in their studies, typically kGy, which is far beyond the clinical regime. The question is whether such a microwave power analysis is feasible for dosimeters exposed to clinical dose levels. In a study emphasizing the neutron response of lithium formate dosimeters, we did a small substudy on the microwave power saturation of alanine [89]. For a dose of 20 Gy and EPR acquisition times in the order of 1 min per spectrum, an x/y ratio of 0.92 ± 0.03 for dosimeters irradiated with fast neutrons relative to the ratio for γ -irradiated samples was found. Ciesielski et al. [87] found a corresponding value of 0.83 ± 0.01 for thermal neutrons, which have a higher LET than the fast neutrons employed in our study. This indicates that estimates of the radiation quality may be obtained even at clinical dose levels using this method.

Other dosimeter materials have also been employed for evaluating the EPR signal in terms of identifying the radiation causing the radicals. We have studied the properties of dosimeters made from polycrystalline lithium formate monohydrate with respect to microwave power saturation characteristics and other features [41, 84, 89]. Clinically relevant doses (2–20 Gy) were always applied. We noted a small but significant broadening of the central EPR resonance line for dosimeters irradiated with fast neutrons compared to γ -rays [89]. By fitting a theoretical model describing the microwave power dependence to experimental power saturation curves, it was found that neutron irradiation primarily increased the T2 relaxation time. This is plausible, as the secondary ions generated from neutron irradiation cause more dense ionizations and thus a higher local concentration of radicals, leading to a greater spin-spin relaxation rate and broader resonance lines. This analysis was later extended to samples irradiated with protons and nitrogen ions, where again the T2 time was reduced compared to γ -irradiation [84]. Also, we saw a line broadening which increased with the linear energy transfer of the impinging ions [41] (Fig. 14.6). The increase in line width could be explained by a model describing the LET dependence of the Lorentzian component of a general line shape function. As seen in Fig. 14.6, the LET-dependence of the line width is rather small, and the line width may not provide the required accuracy for estimating the radiation quality in ion beam therapy applications. The change in T2 time was a more sensitive metric, although not studied to the same level of detail, but microwave power saturation analysis is more cumbersome than assessing the width of the EPR resonance line at a given microwave power.

Marralle et al. [90] performed a microwave power analysis of irradiated ammonium tartrate dosimeters similar to our studies described above. The dosimeters were irradiated with ^{60}Co γ -rays, 7 and 14 MeV electrons and 19.3 MeV protons to dose

Fig. 14.6 The peak-to-peak line width of lithium formate EPR dosimeters plotted against the LET value for *protons* and *nitrogen ions*. The *solid lines* correspond to a theoretical model incorporating detector effectiveness and line broadening. The *error bars* represent the range of line widths. © Radiation Research Society, with permission. (The figure is taken from [41] by permission of Radiation Research Society (2014))



ranging from 0.1–5 kGy. Smaller differences in the microwave saturation behavior between samples irradiated with γ -rays/electrons and protons were found compared to our studies, reflecting most likely that the differences in LET were not that great. Still, a reduction in the T2 time was found following proton irradiation, in line with our findings for lithium formate monohydrate.

Gustafsson et al. [91, 92] used dosimeters of potassium dithionate to study radiation effects from ion beam irradiation. The dosimeters were irradiated with X-rays, carbon ions and nitrogen ions. However, the absorbed dose levels were not given. First, by 2D EPRI, the longitudinal dose deposition pattern (including the Bragg peak) in a dosimeter could be visualized [91]. Slight differences in these patterns were observed for samples irradiated with different ions, as could be expected. Also, the EPR spectrum shape changed qualitatively with irradiation depth (reflecting the LET) and microwave power. This was explained by that the EPR spectrum of potassium dithionate is constituted by two slightly different SO_3^- radical species, R1 and R2. The likelihood of radical formation for the two species appears to change with ionization density (LET), as we have seen in other model systems [93], and the microwave power saturation features are different for the two species. Selecting an appropriate microwave, the R1/R2 ratio was studied in more detail for samples irradiated with nitrogen ions [92]. The ratio was shown to drop from 1.24 for 6 MV photons (LET of 0.3 keV/mm) to 0.86 for nitrogen ions at a depth of about 2 mm in the dosimeters (LET of about 250 keV/ μm). It was later shown that the EPR spectrum of irradiated potassium dithionate was constituted by three different radical species [94], although the findings from the earlier studies (focusing on two distinctly different spectral components) still holds. However, the largest concern with dithionates in general is that the compounds are far from water equivalent [16]. Still, the ion beam studies on potassium dithionate are promising, and clinically relevant studies should be encouraged to investigate the applicability of such dosimeters in more detail.

14.7 Neutron Dosimetry

There are currently two approaches where neutrons are employed clinically: fast neutron radiotherapy and boron neutron capture therapy (BNCT). Fast neutron therapy [95] is an external radiotherapy principle where neutrons are generated from a target bombarded with e.g. protons or deuterons. The delivery and planning of such treatment was similar to that of photon based radiotherapy. Many cancer patients were treated with fast neutrons up to the early 1980s, but the technique was largely abandoned as many patients developed severe side effects. Conferring the clinical trials website [96], there seems to be no ongoing clinical trials using fast neutron therapy. Thus, the clinical impact of fast neutron dosimetry appears limited. On the other hand, BNCT [97] is a technique of continuing interest exploiting that the boron isotope ^{10}B has a very high cross section for thermal neutrons. Pharmaceutical boron delivery agents that are differentially taken up in malignant tumors may be injected into the body. Thus, exposure to thermal neutrons will create very high doses in regions of the body where ^{10}B is present. However, the spectrum of charged and uncharged particles released during BNCT is rather complex, and accurate dose assessment is therefore challenging.

The sensitivity of alanine to thermal neutrons is low due to the low cross section of its atomic constituents (H, C, N, O). Thus, methods to enhance the sensitivity are of interest in thermal neutron dosimetry, of relevance to BCNT. Marralle et al. have extensively studied the neutron response of alanine dosimeters (also ammonium tartrate dosimeters, not discussed here) enriched with compounds sensitive to thermal neutrons [98–100]. Alanine was blended with for instance boric acid or gadolinium oxide. Gadolinium has two natural isotopes showing an extremely high cross section for thermal neutrons. The blended alanine dosimeters were irradiated with thermal neutrons at a nuclear reactor. As expected, the gadolinium-based dosimeter was more sensitive by roughly a factor 3, where the effect of changing the amount of gadolinium was nicely reproduced by Monte Carlo simulations. However, the dose response was not linear for this type of dosimeter, clearly being a disadvantage. Also, the addition of gadolinium reduces the water equivalence of the dosimeters. A different approach could be to exchange one of the isotopes of the parent molecule in a given EPR dosimeter with a neutron-sensitive isotope. Lund et al. [101, 102] studied the properties of ^6Li exchanged lithium formate monohydrate and lithium dithionate. The purpose of the isotope exchange was in fact twofold: (1) to increase the general radiation sensitivity of the dosimeters and (2) to enhance neutron absorption. With respect to (1), ^6Li has a lower nuclear spin and magnetic moment compared to ^7Li . Thus, electron hyperfine coupling of the CO_2^- radical to ^6Li results in a narrower EPR resonance, increasing the intensity of the spectrum compared to dosimeters with a natural abundance of Li isotopes. After irradiation with 4 MV photons, it was indeed shown that ^6Li enriched dosimeters were more sensitive compared to standard dosimeters; a factor two for ^6Li enriched lithium formate. Regarding (2), ^6Li has a much higher cross section for thermal neutron capture compared to ^7Li . After exposure to thermal neutrons at a BNCT facility, a signal enhancement of about 5 and 2.5 was found for ^6Li enriched lithium formate

and lithium dithionate, respectively. Although these results were promising, there seems currently to be little development around these ^6Li enriched dosimeters in the community. Reasons may possibly be that chemicals enriched with ^6Li are expensive, and that few groups consider manufacturing their own dosimeters.

Schmitz et al. have discussed the use of alanine/EPR dosimetry for estimating doses from BNCT of liver tumors [103, 104]. The group has developed an experimental and theoretical basis for calculating and measuring the dose from neutrons and γ -rays at arbitrary points in a given geometry. Neutron entrance flux at the irradiator was measured by a gold activation foil, and this flux level was used as input for calculating doses inside the irradiator using Monte Carlo simulations. Following procedures outlined above for carbon ion therapy [36], the dose to alanine was calculated by combing the Monte Carlo simulations with modeling of detector effectiveness. These theoretical results were in turn compared with alanine/EPR measurements in both a PMMA phantom and in a resected lobe of a human liver. Applied doses ranged from about 9 to 23 Gy. The expected and measured doses showed a good correspondence, well within the uncertainties associated with the alanine dosimetry and the estimates of relative detector effectiveness.

14.8 Conclusions and Outlook

There is a great variety of clinical applications of EPR dosimetry, as shown in the current review. As the lowest detectable dose in practical EPR dosimetry is roughly 0.5–1 Gy, mostly radiotherapy applications have been reported. The uncertainty in the EPR dose estimates range from roughly 0.5 to 5%, where older studies typically show less accurate results. In line with this, better correspondence between EPR dosimetry and other estimates (ion chamber measurements, Monte Carlo simulations, treatment planning calculations) is seen in more recent studies. Also, exciting applications such as EPR imaging and carbon ion beam EPR dosimetry have shown great potential.

In this review, we have covered the majority of relevant papers. Apart from some comparable applications on quality response and on brachytherapy, single feasibility studies are common. Of course, routine clinical use of EPR dosimetry is not expected to be reported in the literature, but it is not our impression that EPR dosimetry is in widespread routine clinical use. For *in vivo* studies, doses must be accumulated in the detectors for a number of treatment fractions, and no immediate dose estimate may be obtained. Therefore, it seems that pursuing *in vivo* applications is not highly relevant. Although new dosimeter materials have been proposed, they do not show an extreme improvement in low-dose sensitivity compared to alanine. Thus, it makes more sense to utilize EPR dosimetry for dose measurements under non-standardized conditions. The reported results in phantoms, either homogeneous or anthropomorphic, are most often solid and show the usefulness of this dosimetry system. Also, EPR dosimetry may play a future role in auditing and mailed dosimetry.

References

1. Regulla D (2000) From dating to biophysics—20 years of progress in applied ESR spectroscopy. *Appl Radiat Isot* 52:1023–1030
2. Regulla DF, Deffner U (1982) Dosimetry by electron-spin-resonance spectroscopy of alanine. *Int J Appl Radiat Isot* 33:1101–1114
3. Fattibene P, Callens F (2010) EPR dosimetry with tooth enamel: a review. *Appl Radiat Isot* 68:2033–2116
4. Kogel A van der, Joiner M (eds) (2009) *Basic clinical radiobiology*, 4th edn. Hodder Arnold, London
5. Brahme A (1984) Dosimetric precision requirements in radiation-therapy. *Acta Radiol On* 23:379–391
6. Mijnheer BJ, Battermann JJ, Wambersie A (1987) What degree of accuracy is required and can be achieved in photon and neutron therapy. *Radiother Oncol* 8:237–252
7. Dische S, Saunders MI, Williams C, Hopkins A, Aird E (1993) Precision in reporting the dose given in a course of radiotherapy. *Radiother Oncol* 29:287–293
8. Guerrero Urbano MT, Nutting CM (2004) Clinical use of intensity-modulated radiotherapy: part II. *Br J Radiol* 77:177–182
9. Guerrero Urbano MT, Nutting CM (2004) Clinical use of intensity-modulated radiotherapy: part I. *Br J Radiol* 77:88–96
10. Otto K (2008) Volumetric modulated arc therapy: IMRT in a single gantry arc. *Med Phys* 35:310–317
11. Kirkpatrick JP, Kelsey CR, Palta M, Cabrera AR, Salama JK et al (2014) Stereotactic body radiotherapy: a critical review for nonradiation oncologists. *Cancer* 120:942–954
12. Loeffler JS, Durante M (2013) Charged particle therapy-optimization, challenges and future directions. *Nat Rev Clin Oncol* 10:411–424
13. Bradshaw WW, Spetzler HA, Cadena DG, Crawford GW (1962) Use of alanine as a solid dosimeter. *Radiat Res* 17:11–21
14. Daniczuk M, Gustafsson H, Sastry MD, Lund E, Lund A (2008) Ammonium dithionate—a new material for highly sensitive EPR dosimetry. *Spectrochim Acta A Mol Biomol Spectrosc* 69:18–21
15. Lund A, Olsson S, Bonora M, Lund E, Gustafsson H (2002) New materials for ESR dosimetry. *Spectrochim Acta A Mol Biomol Spectrosc* 58:1301–1311
16. Lund E, Gustafsson H, Danilczuk M, Sastry MD, Lund A et al (2005) Formates and dithionates: sensitive EPR-dosimeter materials for radiation therapy. *Appl Radiat Isot* 62:317–324
17. Olsson SK, Bagherian S, Lund E, Carlsson GA, Lund A (1999) Ammonium tartrate as an ESR dosimeter material. *Appl Radiat Isot* 50:955–965
18. Anton M (2005) Development of a secondary standard for the absorbed dose to water based on the alanine EPR dosimetry system. *Appl Radiat Isot* 62:779–795
19. Anton M (2006) Uncertainties in alanine/ESR dosimetry at the Physikalisch-Technische Bundesanstalt. *Phys Med Biol* 51:5419–5440
20. Waldeland E, Malinen E (2011) Review of the dose-to-water energy dependence of alanine and lithium formate EPR dosimeters and LiF TL-dosimeters—comparison with Monte Carlo simulations. *Radiat Meas* 46:945–951
21. Waldeland E, Hole EO, Sagstuen E, Malinen E (2010) The energy dependence of lithium formate and alanine EPR dosimeters for medium energy x rays. *Med Phys* 37:3569–3575
22. Battistoni G, Broggi F, Brugger M, Campanella M, Carboni M et al (2008) The FLUKA code and its use in hadron therapy. *Nuovo Cimento Della Societa Italiana Di Fisica C-Colloquia on Physics* 31:69–75
23. Kawrakow I (2000) Accurate condensed history Monte Carlo simulation of electron transport. I. EGSnrc, the new EGS4 version. *Med Phys* 27:485–498
24. Koizumi H, Ichikawa T, Yoshida H, Namba H, Taguchi M et al (1996) Radical formation in the radiolysis of solid alanine by heavy ions. *Nucl Instrum Methods Phys Res Sect B Beam Interact Mater Atoms* 117:431–435.

25. Anton M, Kapsch RP, Krauss A, von Voigts-Rhetz P, Zink K et al (2013) Difference in the relative response of the alanine dosimeter to megavoltage x-ray and electron beams. *Phys Med Biol* 58:3259–3282
26. Zeng GG, McEwen MR, Rogers DWO, Klassen NV (2004) An experimental and Monte Carlo investigation of the energy dependence of alanine/EPR dosimetry: I. Clinical x-ray beams. *Phys Med Biol* 49:257–270
27. Zeng GG, McEwen MR, Rogers DWO, Klassen NV (2005) An experimental and Monte Carlo investigation of the energy dependence of alanine/EPR dosimetry: II. Clinical electron beams. *Phys Med Biol* 50:1119–1129
28. Bergstrand ES, Bjerke H, Hole EO (2005) An experimental investigation of the electron energy dependence of the EPR alanine dosimetry system. *Radiat Meas* 39:21–28
29. Voros S, Anton M, Boillat B (2012) Relative response of alanine dosimeters for high-energy electrons determined using a Fricke primary standard. *Phys Med Biol* 57:1413–1432
30. Zeng GG, McCaffrey JP (2005) The response of alanine to a 150 keV X-ray beam. *Radiat Phys Chem* 72:537–540
31. Anton M, Kapsch RP, Krystek M, Renner F (2008) Response of the alanine/ESR dosimetry system to MV x-rays relative to Co-60 radiation. *Phys Med Biol* 53:2753–2770
32. Olko P (1999) Calculation of the relative effectiveness of alanine detectors to X-rays and heavy charged particles using microdosimetric one-hit detector model. *Radiat Prot Dosimetry* 84:63–66
33. Waligorski MPR, Danialy G, Loh KS, Katz R (1989) The response of the alanine detector after charged-particle and neutron irradiations. *Appl Radiat Isot* 40:923–933
34. Hansen JW, Olsen KJ (1985) Theoretical and experimental radiation effectiveness of the free-radical dosimeter alanine to irradiation with heavy charged-particles. *Radiat Res* 104:15–27
35. Bassler N, Hansen JW, Palmans H, Holzscheiter MH, Kovacevic S et al (2008) The antiproton depth-dose curve measured with alanine detectors. *Nucl Instrum Methods Phys Res Sect B Beam Interact Mater Atoms* 266:929–936
36. Herrmann R, Jakel O, Palmans H, Sharpe P, Bassler N (2011) Dose response of alanine detectors irradiated with carbon ion beams. *Med Phys* 38:1859–1866
37. Adolfsson E, Carlsson GA, Grindborg JE, Gustafsson H, Lund E et al (2010) Response of lithium formate EPR dosimeters at photon energies relevant to the dosimetry of brachytherapy. *Med Phys* 37:4946–4959
38. Gustafsson H, Lund E, Olsson S (2008) Lithium formate EPR dosimetry for verifications of planned dose distributions prior to intensity-modulated radiation therapy. *Phys Med Biol* 53:4667–4682
39. Malinen E, Waldeland E, Hole EO, Sagstuen E (2007) The energy dependence of lithium formate EPR dosimeters for clinical electron beams. *Phys Med Biol* 52:4361–4369
40. Vestad TA, Malinen E, Olsen DR, Hole EO, Sagstuen E (2004) Electron paramagnetic resonance (EPR) dosimetry using lithium formate in radiotherapy: comparison with thermoluminescence (TL) dosimetry using lithium fluoride rods. *Phys Med Biol* 49:4701–4715
41. Waldeland E, Hole EO, Stenerlow B, Grusell E, Sagstuen E et al (2010) Radical formation in lithium formate EPR dosimeters after irradiation with protons and nitrogen ions. *Radiat Res* 174:251–257
42. Waldeland E, Helt-Hansen J, Malinen E (2011) Characterization of lithium formate EPR dosimeters for high dose applications—comparison with alanine. *Radiat Meas* 46:213–218
43. Perichon N, Garcia T, Francois P, Lourenco V, Lesven C et al (2011) Calibration of helical tomotherapy machine using EPR/alanine dosimetry. *Med Phys* 38:1168–1177
44. De Ost B, Schaeken B, Vynckier S, Sterpin E, Van den Weyngaert D (2011) Reference dosimetry for helical tomotherapy: practical implementation and a multicenter validation. *Med Phys* 38:6020–6026
45. IAEA (2000) Absorbed dose determination in external beam radiotherapy: an international code of practice for dosimetry based on standards of absorbed dose to water. International Atomic Energy Agency, Vienna, Austria

46. Langen KM, Papanikolaou N, Balog J, Crilly R, Followill D et al (2010) QA for helical tomotherapy: report of the AAPM Task Group 148. *Med Phys* 37:4817–4853
47. Garcia T, Lacomberie T, Popoff R, Lourenco V, Bordy JM (2011) Dose verification and calibration of the Cyberknife (R) by EPR/alanine dosimetry. *Radiat Meas* 46:952–957
48. Cronholm RO, Andersen CE, Behrens CF, Helt-Hansen J (2012) Volume dose ratios relevant for alanine dosimetry in small, 6 MV photon beams. *Radiat Meas* 47:1014–1017
49. Abrego FC, Calcina CSG, de Almeida A, de Almeida CE, Baffa O (2007) Relative output factor and beam profile measurements of small radiation fields with an L-alanine/K-band EPR minidosimeter. *Med Phys* 34:1573–1582
50. Chen F, Graeff CFO, Baffa O (2005) K-band EPR dosimetry: small-field beam profile determination with miniature alanine dosimeter. *Appl Radiat Isot* 62:267–271
51. Chen F, Calcina CSG, de Almeida A, de Almeida CE, Baffa O (2007) Small radiation field dosimetry with 2-methylalanine miniature dosimeters at K-band electron paramagnetic resonance. *Radiat Meas* 42:1213–1216
52. De Angelis C, Onori S, Petetti E, Piermattei A, Azario L (1999) Alanine EPR dosimetry in brachytherapy. *Phys Med Biol* 44:1181–1191
53. Meigooni AS, Meli JA, Nath R (1988) Influence of the Variation of Energy-Spectra with Depth in the Dosimetry of Ir-192 Using Lif Tld. *Phys Med Biol* 33:1159–1170
54. Calcina CSG, de Almeida A, Rocha JRO, Abrego FC, Baffa O (2005) Ir-192HDR transit dose and radial dose function determination using alanine/EPR dosimetry. *Phys Med Biol* 50:1109–1117
55. Antonovic L, Gustafsson H, Carlsson GA, Tedgren AC (2009) Evaluation of a lithium formate EPR dosimetry system for dose measurements around (192)Ir brachytherapy sources. *Med Phys* 36:2236–2247
56. Olsson S, Bergstrand ES, Carlsson AK, Hole EO, Lund E (2002) Radiation dose measurements with alanine/agarose gel and thin alanine films around a Ir-192 brachytherapy source, using ESR spectroscopy. *Phys Med Biol* 47:1333–1356
57. Ciesielski B, Wielopolski L, Reinstein LE (1988) The energy response of agar-alanine phantom dosimeter to gamma-radiation. *Med Phys* 15:380–383
58. Olsson S, Lund E, Erickson R (1996) Dose response and fading characteristics of an alanine-agarose gel. *Appl Radiat Isot* 47:1211–1217
59. Kolbun N, Leveque P, Abboud F, Bol A, Vynckier S et al (2010) Experimental determination of the radial dose distribution in high gradient regions around Ir-192 wires: comparison of electron paramagnetic resonance imaging, films, and Monte Carlo simulations. *Med Phys* 37:5448–5455
60. Ahnesjo A, Aspradakis MM (1999) Dose calculations for external photon beams in radiotherapy. *Phys Med Biol* 44:R99–R155
61. Osteras BH, Hole EO, Olsen DR, Malinen E (2006) EPR dosimetry of radiotherapy photon beams in inhomogeneous media using alanine films. *Phys Med Biol* 51:6315–6328
62. Ramirez JLV, Chen F, Nicolucci P, Baffa O (2011) Dosimetry of small radiation field in inhomogeneous medium using alanine/EPR minidosimeters and PENELOPE Monte Carlo simulation. *Radiat Meas* 46:941–944
63. Waldeland E, Horling M, Hole EO, Sagstuen E, Malinen E (2010) Dosimetry of stereotactic radiosurgery using lithium formate EPR dosimeters. *Phys Med Biol* 55:2307–2316
64. Schaecken B, Lelie S, Meijnders P, Van den Weyngaert D, Janssens H et al (2010) Alanine/EPR dosimetry applied to the verification of a total body irradiation protocol and treatment planning dose calculation using a humanoid phantom. *Med Phys* 37:6292–6299
65. De Angelis C, Mattacchioni A, Onori S, Aragno D, de Paula U et al (2000) Electron arc therapy treatment planning verification with alanine/EPR dosimetry. *Appl Radiat Isot* 52:1203–1207
66. Anton M, Wagner D, Selbach HJ, Hackel T, Hermann RM et al (2009) In vivo dosimetry in the urethra using alanine/ESR during Ir-192 HDR brachytherapy of prostate cancer—a phantom study. *Phys Med Biol* 54:2915–2931

67. Intensity Modulated Radiation Therapy Collaborative Working Group (2001) Intensity-modulated radiotherapy: current status and issues of interest. *Int J Radiat Oncol Biol Phys* 51:880–914
68. Essers M, Mijneer BJ (1999) In vivo dosimetry during external photon beam radiotherapy. *Int J Radiat Oncol Biol Phys* 43:245–259
69. Barker JL, Garden AS, Ang KK, O'Daniel JC, Wang H et al (2004) Quantification of volumetric and geometric changes occurring during fractionated radiotherapy for head-and-neck cancer using an integrated CT/linear accelerator system. *Int J Radiat Oncol Biol Phys* 59:960–970
70. Mijneer B, Beddar S, Izewska J, Reft C (2013) In vivo dosimetry in external beam radiotherapy. *Med Phys* 40:070903
71. Kuntz F, Pabst JY, Delpuch JP, Wagner JP, Marchioni E (1996) Alanine-ESR in vivo dosimetry: a feasibility study and possible applications. *Appl Radiat Isot* 47:1183–1188
72. Schaecken B, Scalliet P (1996) One year of experience with alanine dosimetry in radiotherapy. *Appl Radiat Isot* 47:1177–1182
73. Schultka K, Ciesielski B, Serkies K, Sawicki T, Tarnawska Z et al (2006) EPR/alanine dosimetry in LDR brachytherapy—a feasibility study. *Radiat Prot Dosimetry* 120:171–175
74. Ciesielski B, Schultka K, Kobierska A, Nowak R, Peimel-Stuglik Z (2003) In vivo alanine/EPR dosimetry in daily clinical practice: a feasibility study. *Int J Radiat Oncol Biol Phys* 56:899–905
75. Wagner D, Anton M, Vorwerk H, Gsanger T, Christiansen H et al (2008) In vivo alanine/electron spin resonance (ESR) dosimetry in radiotherapy of prostate cancer: a feasibility study. *Radiother Oncol* 88:140–147
76. Wagner D, Anton M, Vorwerk H (2011) Dose uncertainty in radiotherapy of patients with head and neck cancer measured by in vivo ESR/alanine dosimetry using a mouthpiece. *Phys Med Biol* 56:1373–1383
77. Gall K, Desrosiers M, Bensen D, Serago C (1996) Alanine EPR dosimeter response in proton therapy beams. *Appl Radiat Isot* 47:1197–1199
78. Onori S, d'Errico F, DeAngelis C, Egger E, Fattibene P et al (1997) Alanine dosimetry of proton therapy beams. *Med Phys* 24:447–453
79. Onori S, d'Errico F, DeAngelis C, Egger E, Fattibene P et al (1996) Proton response of alanine based pellets and films. *Appl Radiat Isot* 47:1201–1204
80. Fattibene P, Calicchia A, d'Errico F, DeAngelis C, Egger E et al (1996) Preliminary assessment of LiF and alanine detectors for the dosimetry of proton therapy beams. *Radiat Prot Dosimetry* 66:305–309
81. Fattibene P, De Angelis C, Onori S, Cherubini R (2002) Alanine response to proton beams in the 1.6–6.1 MeV energy range. *Radiat Prot Dosimetry* 101:465–468
82. Ableitinger A, Vatnitsky S, Herrmann R, Bassler N, Palmans H et al (2013) Dosimetry auditing procedure with alanine dosimeters for light ion beam therapy. *Radiother Oncol* 108:99–106
83. Martisikova M, Jakel O (2010) Gafchromic (R) EBT films for ion dosimetry. *Radiat Meas* 45:1268–1270
84. Lund A, Sagstuen E, Sanderud A, Maruani J (2009) Relaxation-time determination from continuous-microwave saturation of EPR spectra. *Radiat Res* 172:753–760
85. Krushev VV, Koizumi H, Ichikawa T, Yoshida H, Shibata H et al (1994) Relation between track structure and LET Effect on free-radical formation for ion beam-irradiated alanine dosimeter. *Radiat Phys Chem* 44:521–526
86. Ciesielski B, Stuglik Z, Wielopolski L, Zvara I (1998) The effect of high-linear energy transfer ions on the electron paramagnetic resonance signal induced in alanine. *Radiat Res* 150:469–474
87. Ciesielski B, Wielopolski L (1994) The effects of dose and radiation quality on the shape and power saturation of the EPR signal in alanine. *Radiat Res* 140:105–111
88. Arber JM, Sharpe PHG, Joly HA, Morton JR, Preston KF (1991) The ESR/alanine dosimeter—power dependence of the X-band spectrum. *Appl Radiat Isot* 42:665–668

89. Malinen E, Waldeland E, Hole EO, Sagstuen E (2006) LET effects following neutron irradiation of lithium formate EPR dosimeters. *Spectrochim Acta A Mol Biomol Spectrosc* 63:861–869
90. Marrale M, Brai M, Triolo A, Bartolotta A, D'Oca MC (2006) Power saturation of ESR signal in ammonium tartrate exposed to Co-60 gamma-ray photons, electrons and protons. *Radiat Res* 166:802–809
91. Gustafsson H, Kruczala K, Lund E, Schlick S (2008) Visualizing the dose distribution and linear energy transfer by 1D and 2D ESR imaging: a potassium dithionate dosimeter irradiated with C6+ and N7+ ions. *J Phys Chem B* 112:8437–8442
92. Gustafsson H, Lund A, Lund E (2011) Potassium dithionate EPR dosimetry for determination of absorbed dose and LET distributions in different radiation qualities. *Radiat Meas* 46:936–940
93. Malinen E, Sagstuen E (2003) Radical formation in pyrimidine bases after X, proton and alpha-particle irradiation. *Radiat Res* 160:186–197
94. Gustafsson H, Lund A, Hole EO, Sagstuen E (2013) SO3-radicals for EPR dosimetry: X- and Q band EPR study and LET dependency of crystalline potassium dithionate. *Radiat Meas* 59:123–128
95. Jones DTL, Wambersie A (2007) Radiation therapy with fast neutrons: a review. *Nucl Instrum Methods Phys Res Sect a-Accel Spectrom Detect Assoc Equip* 580:522–525
96. U.S. National Institutes of Health (2014) *ClinicalTrials.gov*. <http://www.clinicaltrials.gov/>.
97. Coderre JA, Turcotte JC, Riley KJ, Binns PJ, Harling OK et al (2003) Boron neutron capture therapy: cellular targeting of high linear energy transfer radiation. *Technol Cancer Res Treat* 2:355–375
98. Marrale M, Brai M, Gennaro G, Bartolotta A, D'Oca MC (2008) The effect of gadolinium on the ESR response of alanine and ammonium tartrate exposed to thermal neutrons. *Radiat Res* 169:232–239
99. Marrale M, Brai M, Gennaro G, Triolo A, Bartolotta A et al (2007) Alanine blends for ESR measurements of thermal neutron fluence in a mixed radiation field. *Radiat Prot Dosimetry* 126:631–635
100. Marrale M, Gennaro G, Brai M, Basile S, Bartolotta A et al (2008) Exposure of Gd2O3-alanine and Gd2O3-ammonium tartrate ESR dosimeters to thermal neutrons: experiments and Monte Carlo simulations. *Radiat Meas* 43:471–475
101. Lund E, Gustafsson H, Danilczuk M, Sastry MD, Lund A (2004) Compounds of Li-6 and natural Li for EPR dosimetry in photon/neutron mixed radiation fields. *Spectrochim Acta A Mol Biomol Spectrosc* 60:1319–1326
102. Komaguchi K, Matsubara Y, Shiotani M, Gustafsson H, Lund E et al. (2007) An ESR and ENDOR study of irradiated Li-6-formate. *Spectrochim Acta A Mol Biomol Spectrosc* 66:754–760
103. Schmitz T, Blaickner M, Schutz C, Wiehl N, Kratz JV et al (2010) Dose calculation in biological samples in a mixed neutron-gamma field at the TRIGA reactor of the University of Mainz. *Acta Oncol* 49:1165–1169
104. Schmitz T, Blaickner M, Ziegner M, Bassler N, Grunewald C et al (2011) Dose determination using alanine detectors in a mixed neutron and gamma field for boron neutron capture therapy of liver malignancies. *Acta Oncol* 50:817–822

Part VI
Geological Applications

Chapter 15

EPR of Primitive Organic Matter: A Tool for Astrobiology

Didier Gourier, Laurent Binet and Hervé Vezin

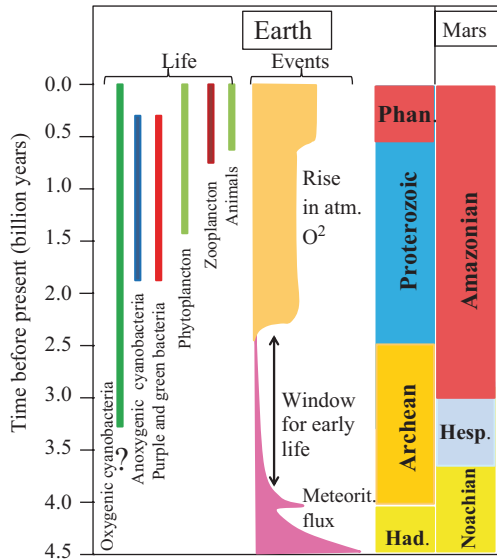
Abstract Insoluble organic matter (IOM) conserved in ancient sedimentary rocks and in carbonaceous meteorites can reveal valuable information about the origin of Life on Earth and on the birth of the Solar System, respectively. These IOMs are also reference materials for the search for possible organic traces of extinct life on Mars. The combination of continuous-wave and pulsed EPR of the radicals in IOM provided several markers distinguishing these materials and related to their histories. For terrestrial IOM, the EPR linewidth of the radicals is mostly determined by unresolved ^1H hyperfine interactions for IOM younger than 2500 million years (H-rich), and by dipolar interactions for older (H-depleted) IOM. The age of very primitive IOM could be estimated through the lineshape, which continuously evolves from Lorentzian to stretched Lorentzian upon ageing due to a change in the dimensionality of the radical spatial distribution. Nuclear spins within or near the radicals and the hyperfine interactions probed by pulsed EPR (through ESEEM and HYSCORE sequences) clearly distinguish meteoritic from terrestrial IOM. Radicals in meteorites are massively enriched in deuterium compared to terrestrial radicals, as a result of specific deuterium enrichment processes in the outer early Solar System. Meteoritic and terrestrial IOMs are also distinguished by the isotropic vs dipolar relative contributions in the ^1H hyperfine interactions and by the $^{13}\text{C}/^1\text{H}$ HYSCORE signal ratio. Strong ^{31}P and ^{14}N HYSCORE signals were detected in terrestrial IOM, which point to possible P and N rich biological precursors. The spin states of the radicals could also be determined either indirectly from the temperature dependence of the EPR intensity or directly by transient nutation spectroscopy. Meteoritic IOM, in addition to $S=1/2$ radicals, specifically contains species with either triplet ground state or thermally excited triplet states, which are lacking in terrestrial IOM.

D. Gourier (✉) · L. Binet
Institut de Recherche de Chimie-Paris, CNRS, PSL Research University,
Chimie-Paristech-CNRS, 11 rue Pierre et Marie Curie, 75005 Paris, France
e-mail: didier.gourier@chimie-paristech.fr

H. Vezin
Laboratoire Spectrochimie Infrarouge et Raman, CNRS, University of Lille 1,
Villeneuve d'Ascq, France

© Springer International Publishing 2014
A. Lund, M. Shiotani (eds.), *Applications of EPR in Radiation Research*,
DOI 10.1007/978-3-319-09216-4_15

Fig. 15.1 Schematic diagram showing the different eons in Earth and Mars history, with the main geological and biological events on Earth. Had=Hadean; Phan=Phanerozoic; Hesp=Hesperian. Conditions of Mars during Noachian were compatible with life (atmosphere and water)



15.1 Introduction

Astrobiology makes use of all scientific disciplines to study life in the universe, including the origin of life on Earth, and the origin of the organic matter in the Solar System. All the planets and the Sun appeared 4560 million years (Myr) ago. It is generally agreed that life appeared rapidly on Earth, when ocean temperature decreased to about 80 °C [1, 2]. The main steps in history of Earth and its biosphere are schematized in Fig. 15.1. Although life emerged probably around 4000–3800 Myr ago, the most ancient putative traces of life on Earth are recorded in the form of carbonaceous microstructures fossilized in silicified sediments (cherts) deposited in ~3500 Myr-old seas. Although there is no doubt that the most primitive life was microbial in nature, the interpretation of these remains are complicated by the fact that very ancient rocks have often been subjected to high temperatures and (or) pressure (metamorphism). Also, even when sedimentary rocks are well preserved and have been subjected only to a moderate metamorphism, which is the case with several geological formations from Pilbara in Australia and Barberton in South Africa, the interpretation of these remains is further complicated by the possibility of more recent contaminations by endolithic microorganisms, weathering, hydrothermalism etc... [3–5]. In addition to this “syngeneity” problem, another important question is that of “biogenicity”. As very ancient rocks are concerned, a part of the organic matter may be of chemical origin, such as decomposition of carbonates for example [6], or also of extraterrestrial origin (carbonaceous meteorites, interplanetary dust particles, comets). These extraterrestrial objects, which are among the most primitive of the solar system (4560 Myr), contain a significant amount of carbonaceous matter similar to that of terrestrial kerogens

[7]. Earth and Mars were intensively bombarded during the early history of the solar system (Fig. 15.1), so that considerable amounts of organic carbon have been deposited on these planets [8], with a fraction of it possibly fossilized in marine sediments. Although the meteoritic bombardments at the epoch of the most ancient preserved carbonaceous fossils on Earth (~3500 Myr) were much weaker than during the “Late Heavy Bombardment” event that occurred approximately 4100 to 3800 Myr ago, the possibility for extraterrestrial organic matter to be preserved in sediments is highly relevant for the search of fossilized organic carbon on Mars [9]. This is because the major part of this organic matter is exceptionally stable and for this reason is called *Insoluble Organic Matter* (IOM) in the geological literature. It would thus resist over geological timescales even under the harsh Martian surface conditions [9]. In the case of any possible discovery of organic matter preserved in the oldest Mars sediments, it would be crucial to assess its origin. Indeed, Early Mars was warmer and wetter during Noachian (Fig. 15.1), and it had sufficient water to fill impact craters and to give a small sea covering its northern hemisphere [10], in which both extraterrestrial IOM and IOM from fossilized microorganism could be preserved. The problematic is the same for the IOM of primitive Earth sediment, and the biologic origin of the most primitive fossilized carbonaceous microstructures has been vehemently debated in recent years [6, 11–13]. For all these reasons, it becomes of primary interest to develop non invasive techniques that will allow to detect biomarkers of primitive life in the fossil carbonaceous matter, and to assess its syngeneity with the host rock.

Also, in addition to their possible role as a source of organic matter on Early Earth, carbonaceous meteorites can be considered as fossils of the Solar System birth, 4560 Myr-ago. They come from parent bodies with size of the order of tens of kilometers, which were too small to undergo differentiation by partial melting. For this reason their elemental composition is the same as Sun except the most volatile elements. These parent bodies were heated by radioactive decay of short live radionuclides, giving variable degrees of aqueous alteration and thermal metamorphism [14, 15]. Despite these modifications which occurred after the accretion of the parent body, the IOM retained molecular and isotopic signatures of the pre-accretionary history in the protosolar nebula, or before the formation of this protosolar nebula (*ie* before 4560 Myr) [16–18].

Among all the possible spectroscopic methods to study the primitive IOM in the context of the origin of life, Raman spectroscopy is one of the most emblematic one, since its first use in paleobiology in the seventies [19, 20]. This technique is now sufficiently mature so that ESA/NASA ExoMars planetary mission (proposed for launch in 2018) will contain a miniaturized Raman spectrometer [21]. However, in addition to some pitfalls such as autofluorescence and laser heating of IOM by the incident laser beam, the latter is highly absorbed by the brown or dark rocks containing carbon (usually cherts), so that Raman spectroscopy is limited to the surface, and 3D Raman hyperspectral imaging is limited to depth smaller than 20 μm in samples [20]. In the perspective of combining complementary techniques for the analysis of fossilized IOM, EPR spectroscopy presents interesting characteristics that are not shared with other techniques. In particular

the radiation-matter interaction involved in magnetic resonance being of magnetic-dipolar nature (compared with electric-dipolar interaction for other spectroscopic techniques), the microwave radiation-interaction is so weak that the bulk rather than the surface of the sample is probed with EPR spectroscopy. In this chapter, we focus on the primitive Earth's oldest rocks containing IOM, and on IOM from carbonaceous meteorites. The rather good combination of sensitivity, spectral resolution and selectivity of EPR is well adapted to the identification of markers for the origin and the age of biogenic and extraterrestrial IOM. It is important to note that EPR in such Astrobiological context is only emerging, so that considerable work remains to be done before reaching an EPR's maturity equivalent to that of Raman spectroscopy. It is worth noticing that EPR of transition metal ions can also be used to search for biosignatures of the origin of life [22, 23], however this aspect of EPR is not treated in the present chapter.

15.2 EPR of IOM in the Context of Origin of Life

The insoluble organic matter (IOM), which corresponds to the definition of kerogens in contrast with extractable organic matter, is the form of mature carbonaceous matter that is preserved in ancient sedimentary rocks, such as coals for example [24]. Also, the IOM present in carbonaceous meteorites is often described as “kerogen-like” [7]. Only kerogens originating from the evolution of biological materials are relevant in the context of the origin of life on Earth and the search for traces of extinct life on Mars. Moreover these materials must be clearly distinguished from kerogens originating from chemical origin, such as Fischer-Tropsch reactions or decarbonation of carbonate minerals, and also from interplanetary delivery. During evolution at geological timescales, the organic matter is subjected to cracking and aromatization-condensation reactions, with the progressive elimination of functional groups (H_2O , CO_2 , ...) and linkage between aromatic molecules, leading to an increasing stacking of aromatic sheets [24]. This evolution manifests itself by a decrease of O/C ratio (diagenesis) followed by a decrease of H/C ratio (catagenesis), giving a disordered carbonaceous network made of more or less branched, stacked and disoriented aromatic domains with sizes corresponding to less than ten fused rings. The next stage (metagenesis) corresponds to an increase of the size of aromatic stacks, with a further release of CO_2 , CH_4 , N_2 etc. Paramagnetic radicals are formed during this geological evolution, giving a single EPR line growing up during catagenesis (radical formation) and then decreasing during metagenesis (radical condensation). This transition occurs at $\text{H/C} \approx 0.5$ in the case of coals [25]. At the molecular scale, this evolution corresponds to a progressive loss of memory of the biological origin of this material. In the case of Archean cherts, identification of the biological precursors syngenetic with the sediment formation is complicated due to possible organic contaminations during the formation of sediments (interplanetary

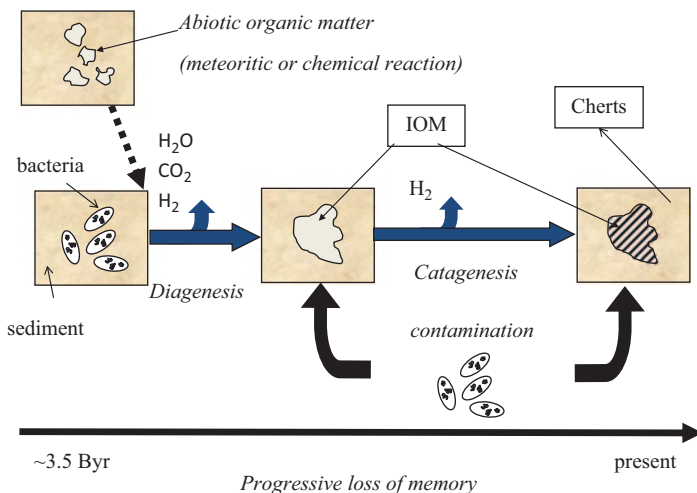


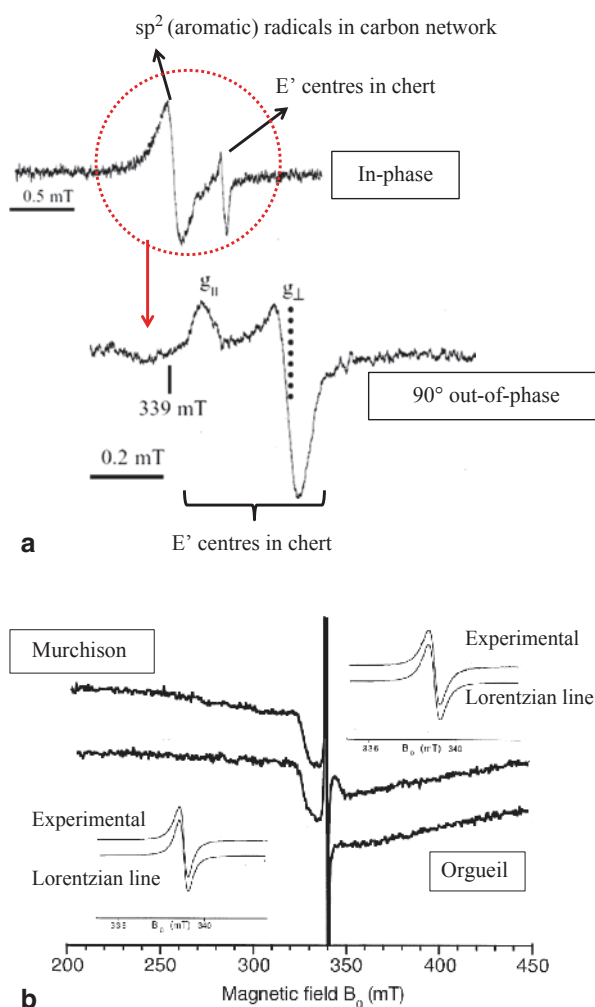
Fig. 15.2 Evolution of biological matter in sediments deposited in an Archean sea, including bacterial and abiotic contamination

material, abiotic IOM) or long after, by endolithic bacteria for example. All this evolution is schematized in Fig. 15.2.

In the case of Precambrian cherts, with ages ranging between ~ 3800 Myr and 540 Myr (Fig. 15.1), the IOM is generally very well preserved in microcrystalline siliceous rocks (cherts). In all cases, the EPR signal is a more or less symmetrical line at nearly free electron spin g -value. In this field range the signal is often superimposed to signals of defects and impurities of the mineral matrix, such as Fe^{III} , VO^{II} , E' centres and $\text{Al}_{\text{Si}}^{\circ}$ centres in SiO_2 (in Kröger-Vink notation) [22, 26]. At room temperature and at X-band, the EPR signal of radicals in IOM is superimposed with the g_{\parallel} component of E' centre of the chert. This centre can be detected selectively by recording the signal 90° -out-of-phase with the modulation (Fig. 15.3a). The E' centre spectrum can then be subtracted from the *in-phase* spectrum to give the pure IOM spectrum. In the case of carbonaceous meteorites, which contain a large fraction of magnetic minerals, the EPR spectrum is dominated by a broad (~ 130 mT) ferromagnetic resonance (FMR) signal, which masks the weak IOM signal [27]. The latter can be observed by isolating the IOM from the mineral matrix by a demineralizing treatment with concentrated HCl [28]. An example of EPR signal of IOM extracted by HF-HCl treatment of Orgueil and Murchison meteorites is given in Fig. 15.3b, where the narrow IOM line is superimposed to a broad and distorted FMR signal due to residual magnetic minerals [29].

Despite the single line character of the EPR spectrum of primitive IOM, a lot of information can be obtained (a) from the cw-EPR spectrum, such as g -factor, line-width, lineshape, magnetism, (b) from analysis of the unresolved hyperfine interaction by using ENDOR or pulsed EPR methods, and (c) from direct measurement of

Fig. 15.3 Room temperature X-band EPR spectra of **a** 3500 Myr-old chert from Dresser Formation, Warra-woona Group, Pilbara Craton, Australia, recorded in-phase and 90° out-of-phase with the modulation, and **b** IOM from Orgueil and Murchison carbonaceous meteorites (~4500 Myr). Experimental condition: **a** Microwave power 0.02 mw (in-phase spectrum) and 2 mW (out-of-phase spectrum), **b** Microwave power 30 mW (main spectra) and 0.2 mW (inserts). Figure 15.3b is adapted from [29] with permission from Elsevier (2002)



electron spin states by nutation spectroscopy. All these data give information on the evolution stage of the IOM, its age and its origin as developed in next sections of this chapter (Table 15.1).

15.3 g-Factor and EPR Linewidth

15.3.1 IOM of Meteorites

Curiously, it has been often argued that the abiotic IOM of carbonaceous meteorites is chemically similar to terrestrial type III kerogens [7], which are of biological

Table 15.1 Relation between EPR parameters and astrobiological information

Parameter	Method	Structural information	Astrobiological information
Linewidth	cw-EPR	H/C, radical concentration, disorder	Evolution of IOM, metamorphism
g-factor	cw-EPR	O/C and H/C of IOM	Evolution and alteration of IOM
Lineshape	cw-EPR	Spatial distribution of radicals	Evolution and dating of IOM
Intensity $I=f(T)$	cw-EPR	Magnetism	Origin of IOM (Earth versus interplanetary)
Electron spin value (S)	Nutation spectroscopy	Structure of aromatic radicals	Origin of IOM (Earth versus interplanetary)
^1H and ^{13}C hf interaction	HYSCORE (ESEEM)	Aliphatic branching of IOM radicals	Origin of IOM (Earth versus interplanetary)
^{31}P , ^{14}N , ... hf interaction	HYSCORE (ESEEM)	Presence of heteroelements	Biosignatures
^2H hf interaction	HYSCORE (ESEEM)	D/H ratio	Origin of protosolar organic matter

origin! Based on their O/C and H/C ratio, terrestrial kerogens are classified in three types I, II and III. Kerogen type II originates from planktonic precursors deposited in open marine and fresh-water lacustrine environment, while type III originates from higher terrestrial plants deposited into lacustrine or marine settings [24]. Kerogen type I is due to different types of precursors in different sediment environments. As g-factor reflects the presence of heteroelements (mainly O) in the vicinity of radicals, it is closely related to the maturation degree of the IOM, reflected by its O/C and H/C ratios. Figure 15.4 shows variation of the g-factor versus O/C and H/C in kerogens of different origins [30], compared with data (in red) from Orgueil, Murchison and Tagish Lake meteorites [29, 31]. It appears that the similarity based on average chemical composition is also true for the environment of organic radicals. However it must be stressed that this similarity does not mean that protosolar IOM preserved in meteorites is of biological origin! It only indicates that radicals in abiotic IOM that preceded Earth and its life are of the same nature as radicals formed during maturation of IOM of biologic origin. The similarity of EPR lines and their g-factor for abiotic IOM (protosolar, 4500 Myr-old) and biogenic IOM clearly emphasizes the difficulty to find biosignatures of primitive life from the single EPR line of organic radicals.

15.3.2 IOM in Primitive Sedimentary Rocks

The complex evolution during geological timescale of the IOM fossilized in sedimentary rock can be studied by considering kinetics that controls the maturation

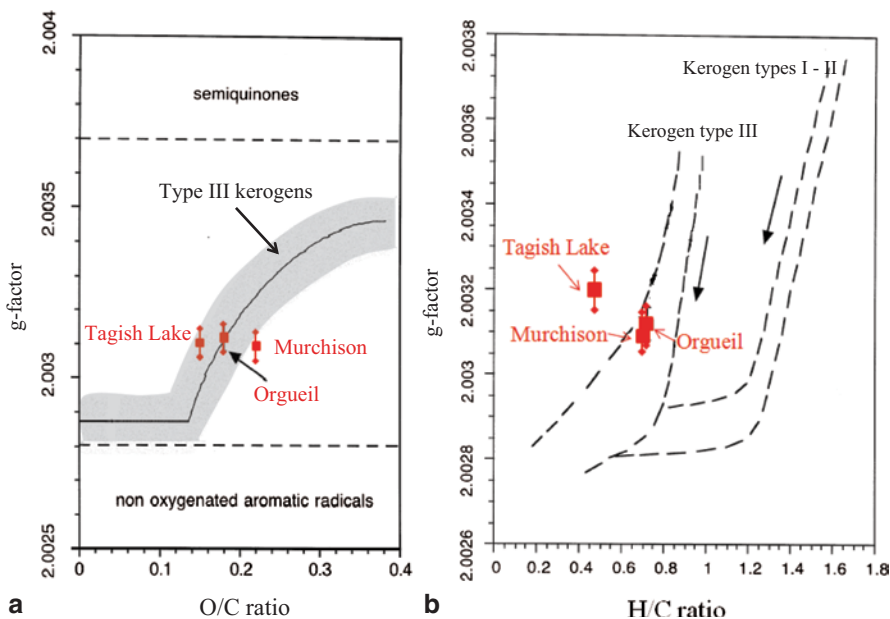


Fig. 15.4 g-factor versus O/C (a) and H/C (b) for radicals of IOM from Orgueil, Murchison and Tagish Lake meteorites (from refs [29] and [31]) compared with data from 31 type III kerogen samples of different origins (a, grey area, after ref [30]), and data for types I, II and III kerogens (b, dashed lines, from ref [25])

of kerogens, which is thought to be a first order kinetics [32, 33]. The amount of radicals N_{rad} created at time t is proportional to $N_{rad} \propto A \exp(-kt)$, with the kinetic constant given by:

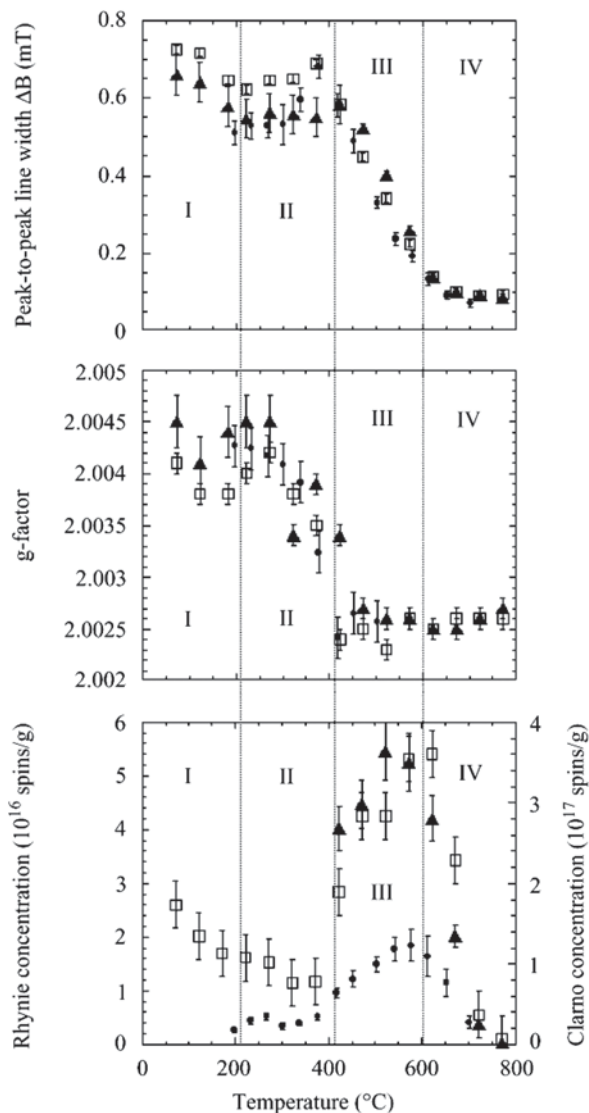
$$k = A \exp\left(-\frac{E_a}{kT}\right) \tag{15.1}$$

where A is the collision constant (s^{-1}) and E_a the activation energy of maturation reactions. The intensity of the EPR line produced in IOM depends on both time and temperature $N_{rad}(t, T)$. This implies that the same amount of radicals, ie the same maturation stage, can be formed by using two different time-temperature couples (t_1, T_1) and (t_2, T_2) [34]:

$$t_1 \exp\left(-\frac{E_a}{kT_1}\right) = t_2 \exp\left(-\frac{E_a}{kT_2}\right) \tag{15.2}$$

This points out that ~1000 Myr at room temperature creates as many spins as 5 min at 670 °C. According to Eq. 15.2, an accelerated evolution of the IOM along geological timescale can be experimentally observed by step annealing treatment of cherts considered as very recent compared to the birth of Earth (4500 Myr). Figure 15.5 shows the evolution of EPR parameters of two cherts (396 and 45 Myr-old, respec-

Fig. 15.5 Variation of room temperature EPR parameters of IOM radicals upon cumulative step heating treatment (15 min at each temperature) of cherts from the Rhynie formation, Aberdeenshire, Scotland (396 Myr-old) and the Clarno formation, Oregon, USA (45 Myr-old). *Top*: peak-to-peak linewidth ΔB ; *middle*: g -factor; *bottom*: spin concentration. *Full triangles*: Rhynie chert; *Open squares*: Clarno chert under vacuum; *Full circles*: Clarno chert in ambient air. Adapted from [26] with permission from Springer (2008)



tively) upon cumulative step annealing treatments (15 min at each step) from room temperature to about 800 °C [26]. Four domains can be distinguished. In domain I, temperature is too low to produce significant variations of EPR parameters. Domain II corresponds to a decrease of the g -factor, reflecting a loss of oxygen in the form of H_2O and CO_2 . This evolution is thus characteristic of *diagenesis* reactions observed on coals [25]. In domain III, the sharp decrease of the linewidth indicates a hydrogen loss and a significant increase of the amount of radicals. Indeed, as shown by spin echo experiments (see Sect. 15.5), the EPR linewidth is due to unresolved

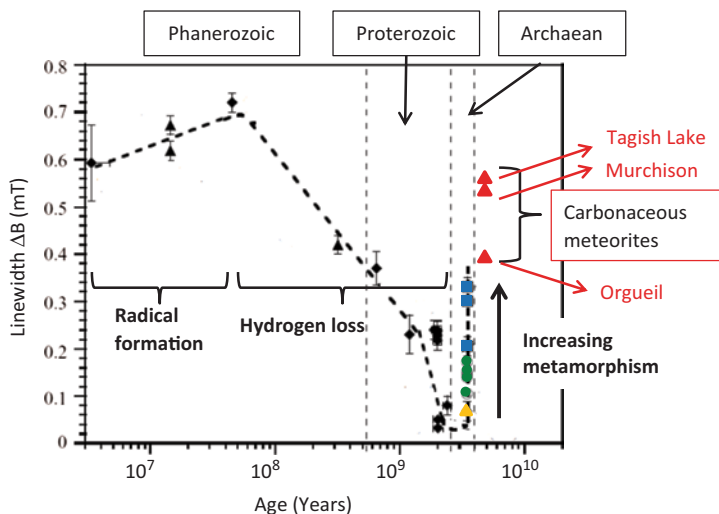


Fig. 15.6 Variation of the peak-to-peak EPR linewidth of IOM radicals in cherts of Phanerozoic, Proterozoic and Archean ages. Archean cherts are distinguished by their increasing metamorphic grade. These data are compared with those measured for the IOM of 4500 Myr-old carbonaceous meteorites. The *dashed line* is a guide for the eyes. Adapted from [26] with permission from Springer (2008)

hyperfine structure with ^1H nuclei of the IOM. Consequently, domain III can be related to *catagenesis* [24]. Finally, the high temperature domain IV is characterized by a constant linewidth and a decrease of the number of radicals, due to the condensation of aromatic groups observed in *metagenesis* [24].

Accordingly, EPR of IOM radicals in cherts of different geological ages will reflect the degree of evolution of this IOM. This is illustrated on Fig. 15.6, which shows the variation of the peak-to-peak linewidth ΔB of the IOM line in cherts with ages ranging from 2.9 Myr to ~ 3500 Myr [26]. According to Fig. 15.5, the decrease of ΔB with increasing age for Phanerozoic and Proterozoic cherts is due to the progressive hydrogen loss observed in domain III. However, for Archean cherts, which should correspond to domain IV, ΔB exhibits a broad distribution which cannot be due to a distribution of H/C ratio, as shown below by the lack of ^1H signal in HYSORE spectra. It was found that in Archean IOM, the linewidth increases with the metamorphism of the rocks (yellow, green and blue symbols in Fig. 15.6). This indicates that the origin of line broadening of Archean IOM lines is different from the hyperfine broadening which characterizes Proterozoic and Phanerozoic cherts. However the observation of spin echoes (see Sect. 15.5 below) shows that the EPR lines are still inhomogeneously broadened, so that a broadening due to dipolar interactions between neighboring radicals appears the most likely for Archean IOM.

With this mechanism, the EPR linewidth in domain IV of Archean cherts is driven by the R^{-3} dependence of dipolar interactions between unpaired electron spins of radicals. Statistical theory predicts that the peak-to-peak linewidth of a Lorentzian line in a magnetically diluted spin system is related to the spin concentration N by [35]:

$$\Delta B = \frac{4\pi^2}{9} g\beta N \approx 8.12 \times 10^{-21} N \quad (15.3)$$

with N in cm^{-3} and ΔB in mT. As domain IV of the IOM evolution corresponds to a condensation of aromatic groups with a decrease of N , the fact that ΔB increases by a factor 5–7 shows that the surviving radicals concentrate in the form of shallow aggregates with local concentrations $N_{loc} > N$. These aggregates of radicals are probably localized in the boundary between ordered aromatic domains [36].

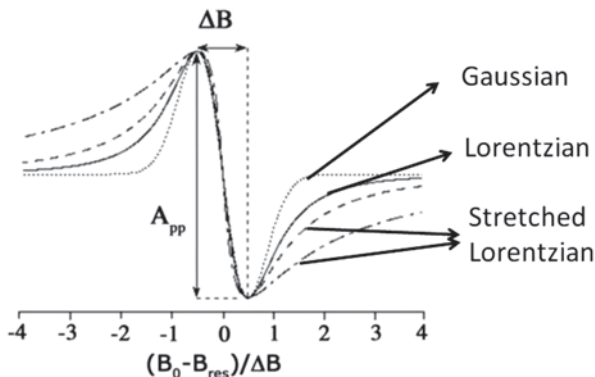
The EPR linewidth of IOM radicals in carbonaceous meteorites are shown in red in Fig. 15.6. Although these meteorites are among the most ancient objects of the solar system (4560 Myr), ΔB in the range 0.4–0.6 mT is the signature of a significant hydrogen content, in agreement with chemical analyses and with HYSCORE results shown in Sect. 15.5. These important hydrogen contents indicate that the parent bodies of these meteorites (which were destroyed by impacts shortly after their formation, giving meteorites) did not suffer from pronounced thermal episodes.

In principle, Fig. 15.6 shows that the EPR linewidth could give information on the evolution stage, and thus the age, of the fossil IOM. However this diagram must be used with caution because a linewidth $\Delta B \leq 0.3$ mT can correspond to two different periods (Proterozoic and Archean). For example, a 3500 Myr-old Archean chert containing fossil IOM with $\Delta B = 0.3$ mT corresponds either to bacteria fossilized 3500 Myr ago (syngenetic IOM) or to endolithic bacteria that lived in the rock ~500–700 Myr later (contamination). To assess syngeneity of the IOM (*i.e.* dating IOM with respect to the host rock), we need a parameter which varies monotonically with the age of IOM.

15.4 Dating Primitive IOM by the EPR Lineshape

EPR spectra of IOM trapped in ancient sedimentary rocks and in carbonaceous meteorites are always characterized by a single symmetrical line with nearly free electron spin g -value. After considering the evolution of the linewidth in Sect. 15.3, we consider in this section the evolution of the lineshape, which exhibits three different types: Lorentzian, Lorentzian with Gaussian character, and stretched Lorentzian characterized by tails falling-off more slowly than pure Lorentzian. Four limit cases of lineshapes are shown in Fig. 15.7, where the magnetic field axis is normalized with respect to g -factor and linewidth. We observed that the lineshape varies continuously from Lorentzian-Gaussian to Lorentzian and to stretched Lorentzian with increasing stretching upon increasing age of the IOM of cherts [26]. Despite the fact that narrow Lorentzian-type EPR lines are generally associated to motional narrowing (in liquid) or to exchange narrowing (in solids) and are thus homogeneous [37], EPR lines of primitive IOM (cherts and meteorites) always give spin-echoes modulated by hyperfine interactions (ESEEM effect). This shows that EPR lines of IOM are inhomogeneously broadened by dipolar interactions [38, 39].

Fig. 15.7 Theoretical EPR lineshapes corresponding to limit cases of dipolar broadening. Gaussian lineshape corresponds to high spin concentration regime (electron spins or electron + nuclear spins). Lorentzian and the two stretched Lorentzian correspond to 3D, 2D and 1D electron spin distributions in diluted spin regime (see text). Adapted from [41] by permission from Mary Ann Liebert (2013)



The most detailed analysis of magnetic resonance lineshape of a diluted spin system randomly distributed in solid state has been given by Fel’dman and Lacelle [40]. They showed that the relaxation function $G_d(t)$ of the diluted spin system has the general form:

$$G_d(t) = B \exp(-at^{D/3}) \tag{15.4}$$

For electron spins, this function describes the decay with time t of the spin magnetization perpendicular to the magnetic field, after an infinitely short microwave pulse. Constant a depends linearly on the spin concentration, and D is the dimensionality of the spatial spin distribution, with $D=1$ for a linear distribution, $D=2$ for a distribution in a plane, and $D=3$ for a distribution in a volume. The EPR line is the first derivative of the Fourier transform of $G_d(t)$. The classical Lorentzian lineshape corresponds to the case $D=3$. The lower-dimensional distributions ($D<3$) give stretched Lorentzian. However there is no analytical expression for these lineshapes, which can only be calculated numerically. The two stretched Lorentzian shapes shown in Fig. 15.7 correspond to the limiting cases $D=2$ and $D=1$ (the most stretched line). In order to quantify the stretching character of EPR lines, it is more convenient to use a system of coordinates (X, Y) given by:

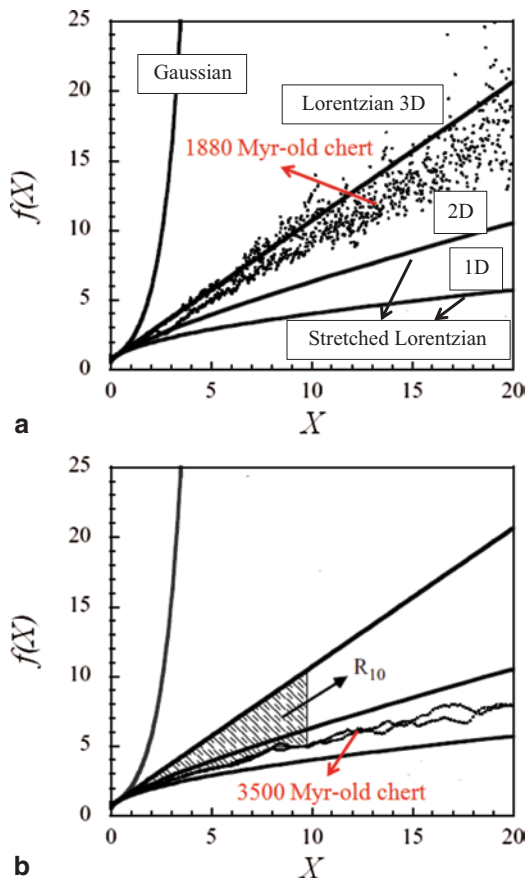
$$X = \left(\frac{B_0 - B_{res}}{\Delta B} \right)^2 \tag{15.5}$$

and:

$$Y = f(X) = \left(\frac{A_{pp}}{F(B_0 - B_{res})} \times \frac{B_0 - B_{res}}{\Delta B} \right)^{1/2} \tag{15.6}$$

where B_0 , B_{res} and A_{pp} are the applied magnetic field, the field at the center of the line and the peak-to-peak amplitude, respectively. The function $F(B_0 - B_{res})$ represents the field derivative of a Lorentzian or a Gaussian absorption line. In this representation, the Lorentzian lineshape is represented by a straight line of equation:

Fig. 15.8 EPR lineshape in a representation where a Lorentzian is linear with **a** experimental point for a 1880 Myr-old chert (Gunflint formation, Ontario, Canada) and **b** a 3500 Myr-old chert (Dresser Formation, Warrawoona group, Australia). 3D, 2D and 1D represent the extreme case $D=3$, $D=2$ and $D=1$ for dimensionality of the spin distribution. The hatched area (R_{10}) between Lorentzian line and experimental points measures the deviation from the Lorentz shape function. Adapted from [26] with permission from Springer (2008)



$$Y = X + \frac{3}{4} \tag{15.7}$$

and the Gaussian lineshape is represented by an increasing exponential:

$$Y = \exp\left(X - \frac{1}{4}\right) \tag{15.8}$$

Stretched Lorentzian lineshapes are given by the (Y, X) representation of the first derivative of the Fourier transform of expression 15.4 with $D=2$ and $D=1$. The four limit cases of EPR lineshapes in this representation are shown in Fig. 15.8a.

Experimental spectra can be represented in this scheme by using Eq. 15.6 where $F(B_0 - B_{res})$ is measured from experimental points. The case of a 1880 Myr-old chert (Gunflint, Ontario, Canada) and a ~3500 Myr-old chert (Dresser Formation, Warrawoona Group, Australia) are given in Fig. 15.8a and b, respectively. We

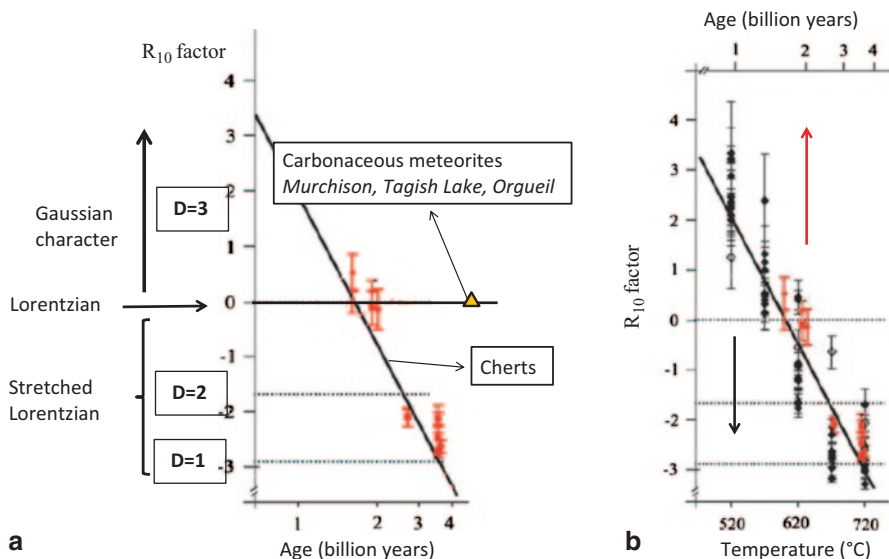


Fig. 15.9 **a** Variation of the lineshape factor R_{10} with the age of Precambrian chert samples (red symbols). Data for the IOM of three meteorites are given for comparison. **b** Black symbols and bottom abscissa represent the variation of R_{10} versus step annealing temperature for the 45 Myr-old Clarno chert (open diamonds) and for cyanobacteria (full diamonds). Red symbols and top abscissa represent the data of **a** for comparison. Adapted from [41] by permission from Mary Ann Liebert (2013)

quantified the experimental lineshape by defining a lineshape factor R_{10} given by (adapted from ref [26]):

$$R_{10} = \frac{1}{10} \int_0^{10} [f(X) - f_L(X)] dX \quad (15.9)$$

where $f_L(X)$ represents the Lorentzian line (Eq. 15.7). This lineshape factor corresponds to the algebraic surface between the experimental spectrum $f(X)$ and the Lorentzian line $f_L(X)$ (Fig. 15.8b). Integration is limited to $X=10$ in Eq. 15.9 because in most case, the signal-to-noise ratio becomes too low for $X \geq 10$, so that the integral may not converge for $X \rightarrow \infty$. The R_{10} factor is equal to 0 for a Lorentzian line, and any Gaussian or stretched Lorentzian character of the EPR line gives $R_{10} > 0$ or $R_{10} < 0$, respectively. For the limit case of diluted electron spin system without hyperfine broadening by ^1H nuclei, the limit values of R_{10} are $R_{10} = 0, -1.78$ and -2.95 for dimensionality of the spin distribution $D=3, 2$ and 1 , respectively. Details of data processing are given in [41].

R_{10} factors measured for a collection of Precambrian cherts coming from China, Canada, Australia and South Africa are shown in Fig. 15.9a [41]. It appears that the EPR line is nearly Lorentzian around 2000 Myr (Proterozoic), with a clear stretched character for Archean cherts. This indicates that the electron spins are homogeneously distributed ($D=3$) in the IOM around 2000 Myr, and acquire a low

dimensional distribution ($2 \geq D \geq 1$) for Archean IOM (2500–3500 Myr). In order to get further insight into this effect, accelerated ageing experiment were performed by cumulative step annealing treatment as described above (Fig. 15.5) on a 45 Myr-old chert (Clarno Formation, Oregon, USA) containing a variety of fossil remains, and on cyanobacteria *microcoleus chthonoplastes* collected in the lake “La Salada de Chiprana” (Spain) [36]. The evolution of R_{10} factor with temperature for these two samples is shown as black symbols in Fig. 15.9b. Data below $\sim 500^\circ\text{C}$ are not reported because the poor signal-to-noise ratio at lower temperature introduced too much error in R_{10} data processing. It appears that upon increasing step annealing temperature, R_{10} decreases linearly from $R_{10} \sim 3$ (Lorentzian with Gaussian character) to 0 (Lorentzian, $D=3$) and next to negative values corresponding to $D=2$ and $D=1$ for stretched Lorentzian [41]. The variation of R_{10} with age of Fig. 15.9a is also reported in Fig. 15.9b (red symbols, upper abscissa in Log scale). The temperature (T)-age (A) correlation (black line) corresponds to the following equation [26]:

$$T(^{\circ}\text{C}) = 353 \log A - 2650 \quad (15.10)$$

with A in years. This evolution shows that R_{10} varies continuously and not by steps as could be suggested by data of Fig. 15.9a. The positive R_{10} values of IOM younger than ~ 1500 Myr (step temperature $T < \sim 600^\circ\text{C}$ in the T - A correlation) corresponds to domain III in Fig. 15.5, where the line narrowing is due to hydrogen loss. This shows that the decreasing Gaussian character in the R_{10} variation is due to a decreasing unresolved hyperfine interaction with hydrogen nuclei. The Lorentzian shape observed around 2000 Myr indicates that radicals (small aromatic groups) are magnetically diluted and homogeneously distributed in the IOM. For Archean IOM (2500–3500 Myr), corresponding to step annealing temperatures $T > \sim 620^\circ\text{C}$, the decreasing dimensionality of the spin distribution from $D=3$ to $D=1$ corresponds likely to the increasing size and increasing linkage of aromatic groups. This pushes the unpaired electron spins on the edges of these disordered aromatic networks, giving a bidimensional character to the spin distribution. Upon increasing ordering of these aromatic networks, leading to large aromatic sheets, defects become distributed along more or less linear edges, giving an apparent pseudo $D=1$ spin distribution. All this evolution of R_{10} from 0 to negative values corresponds to domain IV in Fig. 15.5. With the help of the age-temperature correlation, we obtain the following expression for the variation of R_{10} factor with the age of the IOM [41]:

$$R_{10} = \alpha \log A + \beta \quad (15.11)$$

with A in years and $\alpha = -9.0 \pm 0.3$ and $\beta = 83.0 \pm 2.9$. Expression 15.11 may be useful to assess the syngeneity of the IOM with respect to the host rock. For example if bacteria were fossilized in sediment of a 3500 Myr-old sea, we expect an EPR line of IOM with $R_{10} \approx -2.9$. Let us now consider a chert dated 3500 Myr by isotopic methods on minerals and giving an EPR line of IOM with $R_{10} \approx +1$, this strongly suggests that this IOM originates from endolithic bacteria that contaminated the rocks ~ 1200 Myr later, *ie* during Lower Proterozoic 2300 Myr ago.

It is interesting to note that IOM from carbonaceous meteorites, formed during the condensation of the protosolar nebula 4560 Myr ago, have an EPR lineshape factor R_{10} strictly equal to 0 (purely Lorentzian line), as shown in Figs. 15.3b and 15.9a. This is clearly related to the different history of the IOM in terrestrial and extraterrestrial conditions. In the first case, the evolution is governed by thermally activated processes, which can be even accelerated during metamorphic events. Extraterrestrial IOM has been submitted to very low temperature during the major part of its existence, to aqueous alteration when the radioactivity was sufficiently high to allow liquid water to circulate in the parent body, and to high flux of cosmic radiations from the Sun and the galaxy. The g -factor (Fig. 15.4) and the linewidth (Fig. 15.6) for meteoritic IOM are the signatures of high O/C and H/C ratios, indicating a low maturity, while the $R_{10}=0$ (Fig. 15.9a) is the signature of small aromatic radicals distributed in the volume of the IOM. These results for IOM radicals agree with ^{13}C NMR, FTIR, XANES, HRTEM and pyrolysis methods of meteoritic IOM, which give the image of a disordered IOM made of a network of small polyaromatic groups linked by highly branched and short aliphatic groups [42]. Despite these differences between meteoritic IOM and biogenic IOM fossilized in Archean cherts, it appears likely that any meteoritic input into the organic materials preserved in Archean sediments would be submitted to the same conditions of temperature as biological remains, so that the structure of the final IOM and the corresponding EPR spectra should be undistinguishable. In the perspective of searching for the origin of life on Earth and traces of extinct life on Mars, it is important to identify EPR markers which could discriminate biogenic IOM and IOM originating from an interplanetary input. As shown in the next section, such markers can be obtained from the hyperfine (hf) interaction between the unpaired spins and magnetic nuclei of radicals and their surroundings.

15.5 Searching for Nuclear Spin Signatures

Elements with spin $I=1/2$, such as Hydrogen ^1H (99.985%), ^{13}C (1.11%), ^{15}N (0.366%) and ^{31}P (100%), or with spin $I=1$, such as deuterium ^2H (0.0148%, also noted D) and ^{14}N (99.63%), can be present in IOM radicals or in their neighboring. Numbers in parenthesis are the natural abundances on Earth. However these abundances are generally different in extraterrestrial IOM. Hyperfine interaction (and quadrupolar interaction for nuclei with $\text{spin} \geq 1$) is sensitive to the nature of chemical bond, the structure of electron ground state and to electron-nuclei distances, and thus gives direct information on the structure of IOM radicals. Also, the presence of particular heteroelements, of specific C–H bonds and isotopic compositions reflect the history of the IOM. This memory of the origin and evolution of IOM is recorded in the unresolved hf interactions, which can be measured by ENDOR and by pulsed EPR methods. Methods based on Electron spin echo envelope modulation (ESEEM) effect are well adapted to the very disordered and complex structure of IOM, because ESEEM allows the detection of all types of isotopes, and is particularly sensitive to those with small magnetic moment [43]. We used the two-dimensional version of

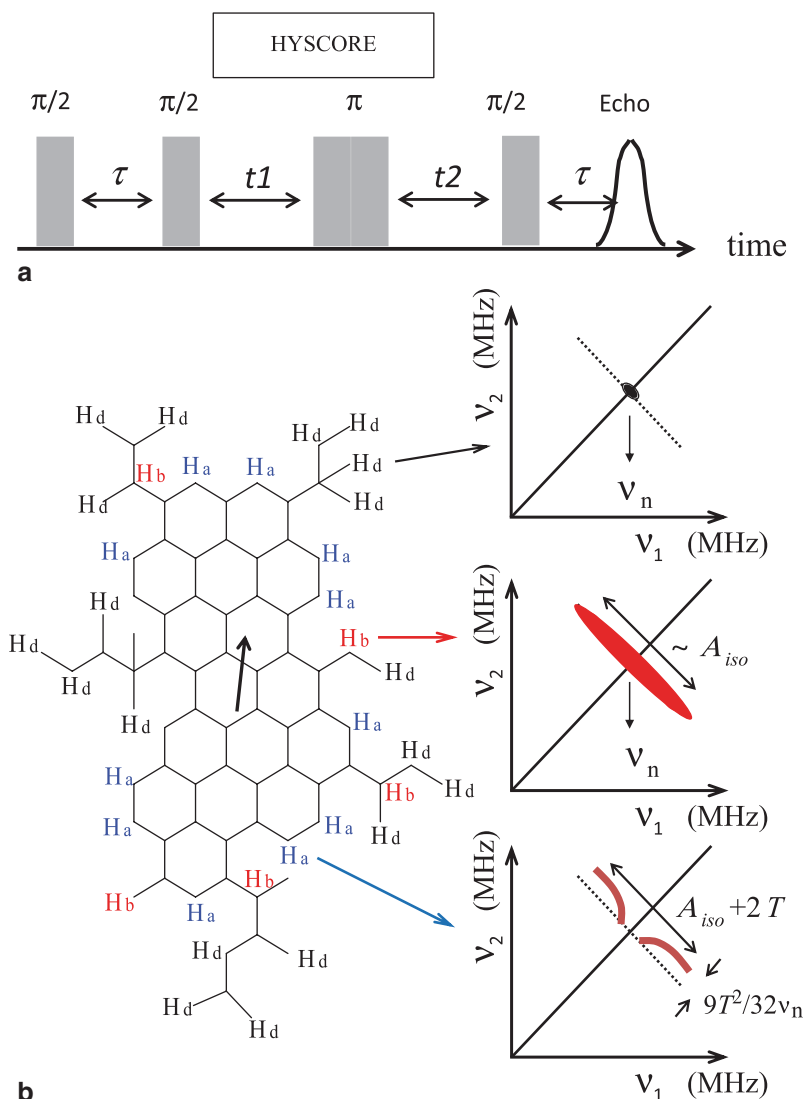


Fig. 15.10 **a** Pulse scheme for the HYSOCORE experiment, **b** Schematic representation of a hypothetical branched polyaromatic fragment in IOM. The unpaired electron delocalized over the aromatic network is represented by an *arrow*. Three types of hydrogen atoms are distinguished: distant hydrogen (H_d), “benzylic” hydrogen (H_b) and aromatic hydrogen (H_a). The corresponding HYSOCORE spectra are schematized on the *right*

4-pulse ESEEM, referred to as Hyperfine Sublevel Correlation (HYSOCORE) method, corresponding to the pulse sequence shown in Fig. 15.10a [43, 44]. A first $\pi/2$ pulse that creates electron spin coherences, is followed by a second $\pi/2$ pulse after waiting time τ which transfers the coherence to neighboring nuclear spins. A third π pulse after time t_1 introduces correlations between m_I states of the two m_S states,

and these nuclear correlations are transferred back to electron spins by a $\pi/2$ pulse after time t_2 , generating a spin echo after time τ . Waiting times t_1 and t_2 are varied stepwise at constant τ . The resulting two-dimensional set of echo modulations gives, after Fourier transform, a two-dimensional HYSORE spectrum.

To illustrate the kind of information that can be obtained from hf interaction, let us consider in Fig. 15.10 a hypothetical polyaromatic radical, with the unpaired electron spin delocalized on a π -type molecular orbital made of carbon $2p_z$ orbitals (z perpendicular to the aromatic plane). The $2p_z$ orbital on i^{th} carbon on the edge of polyaromatic radical bears an electron spin density ρ_i . Owing to the extremely disordered character of IOM, where polyaromatic groups may exhibit various sizes and shapes, and a variety of aliphatic branching, a rigorous interpretation of HYSORE spectra is a difficult task. Whatever the size and shape of the polyaromatic group, the radicals always contain three main types of hydrogen atoms depending on their distance from the edge carbon atom C_i : (i) aromatic hydrogen (noted H_a) which are directly bonded to this carbon, (ii) hydrogen atoms in benzylic position (noted H_b) in an aliphatic group linked to this carbon, and (iii) more distant hydrogen atoms (noted H_d). From the point of view of ^1H hyperfine interaction, the polyaromatic radical can thus be considered as an association of $C_i\text{-H}_a$ fragments and $C_i\text{-R}$ fragments, with aliphatic groups $R = C(\text{H}_b)_2\text{-R}'$ or $\text{CH}_b(\text{R}')_2$ or $\text{C}(\text{R}')_3$, with carbon C_i bearing an electron spin density ρ_i . Distant hydrogen atoms H_d are localized in R' fragments or in neighboring polyaromatic units. For a given H atom, nuclear modulation of the spin echo gives peaks located on (or close to) the ridge perpendicular to the diagonal of the HYSORE spectrum and crossing it at the proton nuclear frequency ν_n . These peaks are characterized by frequency coordinates ν_- and ν_+ which depend on ν_n and two hyperfine parameters A and B [45, 46]:

$$\begin{aligned}\nu_+ &= \left[(\nu_n - A/2)^2 + (B/2)^2 \right]^{1/2} \\ \nu_- &= \left[(\nu_n + A/2)^2 + (B/2)^2 \right]^{1/2}\end{aligned}\quad (15.12)$$

with the hf interaction A given by $A = (\nu_-^2 - \nu_+^2) / 2\nu_n$. It is the sum of the isotropic Fermi contact term A_{iso} and the dipolar term A_{dip} . In principle Eq. 15.12 is valid when A_{dip} is described by a point dipole approximation, which may not be rigorously true for a $C_i\text{-H}_a$ fragment. For a spin density $\rho_i = 1$ on C_i atom, the Fermi contact term of a $C_i\text{-H}_a$ fragment is characterized by the McConnell parameter Q_α which takes values in the range -67.3 to -84.1 MHz for a neutral radical [47]. The negative value is due to the negative spin density at the hydrogen nucleus originating from the spin polarization of the C-H bond by the electron in p_z orbital. The corresponding dipolar interaction contains three components $A_{dip,z} = 38$ MHz, $A_{dip,y} = -36$ MHz and $A_{dip,x} = -2.8$ MHz [48], with z axis along the C-H bond. The three hyperfine components of the $C_i\text{-H}_a$ fragment are thus given by:

$$\begin{aligned}A_{i,x} &= \rho_i (Q_\alpha + A_{dip,x}) \\ A_{i,y} &= \rho_i (Q_\alpha + A_{dip,y}) \\ A_{i,z} &= \rho_i (Q_\alpha + A_{dip,z})\end{aligned}\quad (15.13)$$

Thus even with a small spin density ρ_p , the hyperfine interaction with an aromatic hydrogen H_a is anisotropic. For a given ρ_p , the HYSORE spectrum in an amorphous system gives peaks and ridges that are positively shifted from the anti-diagonal and exhibit a “horn shape” (Fig. 15.10). The splitting between the extrema of the ridge is equal to $A_{iso} + 2T$, and the shift from the anti-diagonal is $9T^2/32\nu_n$, with $2T = A_{dip,z}$ [43, 49]. In disordered systems the distribution of ρ_i can lead to relatively complex HYSORE lineshapes.

For branched C_1 -R fragments, with aliphatic groups $R = C(H_b)_2-R'$ or $CH_b(R')_2$, the spin density at the hydrogen nucleus in benzylic position H_b is due to a direct spin transfer from the carbon p_z orbital, so that A_{iso} is large and positive:

$$A_{iso} = B_2 \cos^2 \theta \quad (15.14)$$

with $B_2 = +140$ to $+160$ MHz for a neutral π radical [47]. The angular dependence takes into account the efficiency of the spin transfer with the angle θ between the axis of the p_z carbon orbital and the orientation of the C-H bond. The dipolar interaction is smaller than 10 MHz [48], so that it can be neglected. Consequently, we expect for a H_b hydrogen $A_{i,x,y,z} \approx A_i \approx \rho_i A_{iso}$. For a given value of ρ_i , the spectrum is a pair of peaks along the anti-diagonal, with a splitting A_{iso} . In disordered IOM, we expect a distribution of ρ_i values so that all the peaks distributed along the anti-diagonal will overlap, giving a straight ridge. Finally, distant hydrogen atoms H_d are characterized by weak dipolar interactions, and they appear as a single peak at the proton frequency $\nu_n = 14.5$ MHz. These three limit cases of HYSORE lineshapes are illustrated in Fig. 15.10.

Figure 15.11 shows representative HYSORE spectra at 9 K of three cherts dating 45 Myr (Clarno), 1880 Myr (Gunflint) and 3500 Myr (Dresser), and the IOM from Orgueil meteorite (4500 Myr). Tagish Lake meteorite gives the same type of spectrum as Orgueil [39], not shown here. These spectra show peaks and ridges of 1H , ^{13}C , ^{31}P , ^{14}N and ^{29}Si nuclei, with the following characteristics.

15.5.1 1H and ^{13}C : Signatures of the Extraterrestrial/Terrestrial Origin?

We can first observe in Fig. 15.11 that the intensity of the 1H -HYSORE signal decreases with the age of the chert, which agrees with the EPR line narrowing with increasing age, resulting from the hydrogen loss during evolution of the IOM (Fig. 15.6). The fact that the 1H signal vanishes in Archean cherts may be used to check the antiquity of the IOM and its syngeneity with the host rock. Indeed a late contamination would give IOM with a detectable proton signal. The lack of 1H signal in the 3500 Myr-old Dresser chert clearly confirms that the dipolar broadening of its EPR line (Fig. 15.6) is a consequence of metamorphism and not the effect of an unresolved proton hyperfine interaction. The second important point is that the shape of 1H -HYSORE spectra of biogenic IOM (cherts) and abiotic IOM

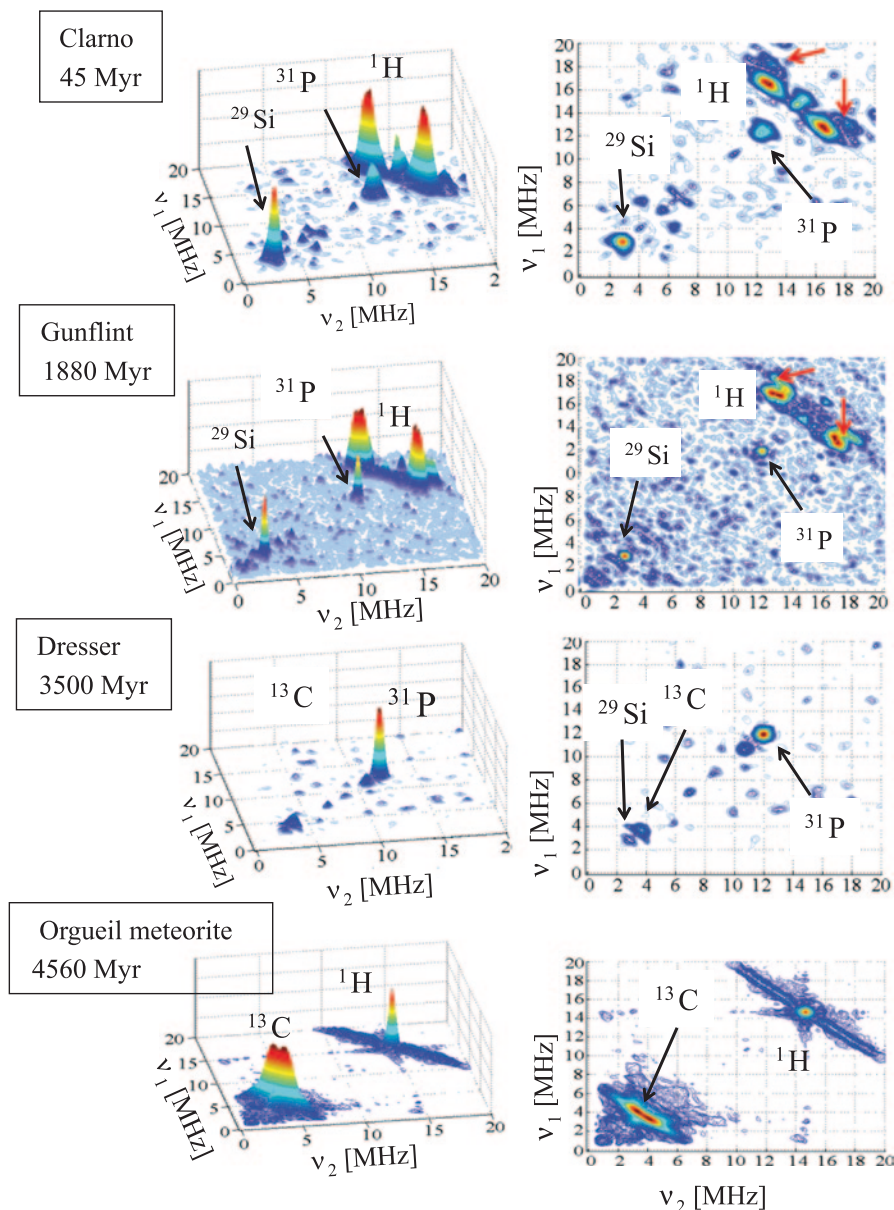


Fig. 15.11 HYSORE spectra at 9 K and $\tau=136$ ns for Clarno chert (45-Myr), Gunflint chert (1880 Myr) and Dresser chert (3500 Myr), and the IOM extracted from the Orgueil meteorite. Adapted from [39] with permission from Mary Ann Liebert (2013)

(meteorites) are different. The proton ridge is linear with a central peak at the proton frequency in meteoritic IOM, which indicates that the major part of hydrogen atoms of organic radicals is of “benzylic” type H_b and distant type H_d . This implies that most aromatic hydrogen atoms H_a in aromatic radicals have been exchanged by

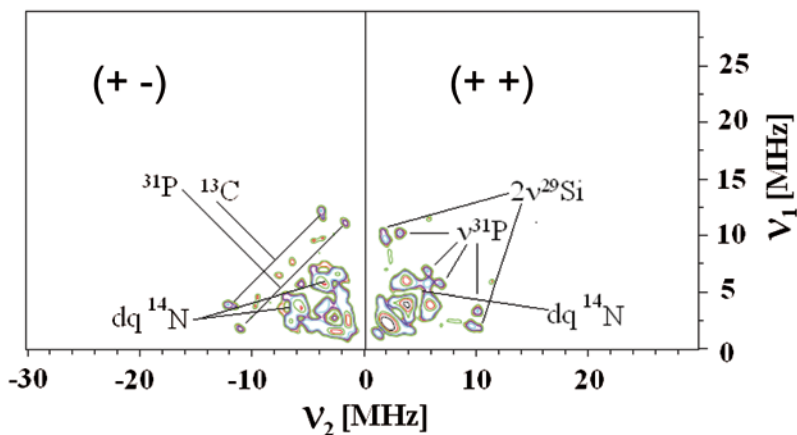
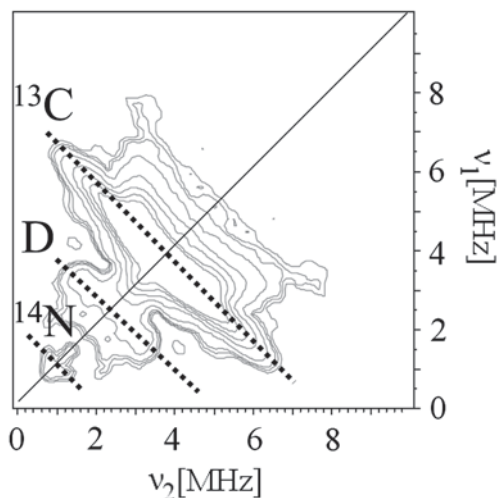


Fig. 15.12 HYSCORE spectrum at 4 K and $\tau = 130$ ns of the IOM extracted from the 3500 Myr-old chert of the Dresser Formation, Warrawoona Group, Australia. The $(++)$ quadrant corresponds to $\nu_1 > 0$ and $\nu_2 > 0$, and the $(+-)$ quadrant corresponds to $\nu_1 > 0$ and $\nu_2 < 0$. Double quantum transitions are noted dq. Adapted from [39] with permission from Mary Ann Liebert (2013)

aliphatic chains (the sources of H_b and H_d atoms). This result agrees with previous ^{13}C -NMR studies showing that meteoritic IOM is made of highly branched aromatic groups linked by short and branched aliphatic chains [50, 51]. Alternatively, proton ridges of biogenic IOM (cherts) exhibit a “horn shape” characteristic of anisotropic hyperfine interaction. In the case of the 1880 Myr-old Gunflint chert, analysis of ^1H -HYSCORE spectrum reveals the presence of several types of hydrogen atoms, the dominant one being characterized by hf parameters $A_{\text{iso}} \approx -3$ MHz and $T \approx +7$ MHz. The significant dipolar contribution and the negative value of A_{iso} show that these dominant hydrogen atoms are aromatic (H_a). In conclusion, aromatic radicals of biogenic IOM in cherts are poorly branched contrary to those of meteoritic IOM.

The same type of information can be obtained from the ^{13}C signal (frequency $\nu_n = 3.7$ MHz, natural Earth abundance 1.11%) (Fig. 15.11). Surprisingly, this signal is very weak and narrow in IOM of cherts, and should not be confused with the ^{29}Si signal of the SiO_2 matrix ($\nu_n = 2.9$ MHz, natural Earth abundance 4%). On the contrary, ^{13}C gives an intense ridge in meteoritic IOM. Ikoma et al. [52, 53] showed that $^{13}\text{C}/^1\text{H}$ intensity ratio increases with the number of equivalent carbon nuclei interacting with the electron spin. This ratio is clearly larger in meteorites than in cherts, which can be related to the highly (poorly) branched character of aromatic groups in the IOM of meteorites (of chert). The large number of carbon atoms at short distance of the polyaromatic group increases the probability for the electron spin to interact with a ^{13}C nucleus [39]. In order to detect ^{13}C signals in fossil IOM, it was necessary to increase the amount of IOM in the EPR cavity by removing the mineral part of the chert with the standard HF/HCl demineralization procedure [54]. The resulting HYSCORE spectrum for the IOM of the 3500 Myr-old Dresser chert is shown in Fig. 15.12 [39]. In the $(+, -)$ quadrant corresponding to $|A| > 2\nu_n$, a doublet of ^{13}C peaks is centered at $|A/2| = 7.8$ MHz. The fact that two narrow peaks are observed instead of a broad frequency distribution indicates that the electron spin density is

Fig. 15.13 Low frequency part of the HYSORE spectrum at 10 K and $\tau=136$ ns of the IOM extracted from the Orgueil meteorite. Adapted from [38] with permission from Elsevier (2008)



mainly localized on a single type of carbon atom in the edge of aromatic groups. This is clearly different from Meteoritic IOM, where the ^{13}C signal is localized in the (+, +) quadrant characterized by $|A| < 2\nu_n = 7.4$ MHz (Figs. 15.11 and 15.13).

15.5.2 ^{31}P and ^{14}N : Signatures of Extinct Life?

Another prominent difference of hf signatures of the two types of IOM concerns heteroelements such as phosphorous and nitrogen. All cherts exhibit a peak at 12.2 MHz which is absent in meteorites (Fig. 15.11) [39]. It corresponds to a double frequency transition of ^{31}P ($\nu_n = 6.1$ MHz) occurring at $2\nu_n = 12.2$ MHz. Compared with ^1H signal, ^{31}P signal increases with the age of the IOM and dominates the HYSORE spectrum for the oldest (Archean) IOM (Fig. 15.11). This double frequency ^{31}P peak, with no measurable hyperfine interaction, probably originates from phosphorous-rich nanophases in contact with the IOM [39]. Their systematic presence in cherts is an indication of their biologic origin, for example the degradation of nucleic acids (DNA, RNA). The attribution of this signal to ^{31}P is demonstrated by the study of IOM extracted for the 3500 Myr-old Dresser chert (Fig. 15.12). ^{31}P signals are clearly seen in both (+, +) and (+, -) quadrants. In the (+, +) quadrant, single frequency transitions of ^{31}P ($A_{\text{iso}} = 8$ MHz, $T = 1$ MHz) are seen in the vicinity of double frequency transitions of ^{29}Si . Two single frequency transitions of ^{31}P are also observed in the (+, -) quadrant, with $A \approx 13.8$ MHz. Such strong hf interactions are the indication of covalent C-P bonds at the periphery of IOM network [39]. On the opposite, ^{31}P signal is lacking in IOM from meteorites [38].

Differences between cherts and meteorites exist also in the ^{14}N -HYSORE of extracted IOM. For meteorites, only a weak signal is observed at ^{14}N nuclear frequency ($\nu_n = 1.06$ MHz) with no measurable hyperfine interaction (Fig. 15.13),

while IOM from the 3500 Myr-old Dresser chert exhibits double quantum (dq) transitions in (+, +) and (+, -) quadrants, revealing at least two types of nitrogen atoms (Fig. 15.12). The fact that they have resisted to carbonization indicates that they are strongly bonded to the aromatic network. The presence of various types of nitrogen atoms in fossil IOM is also a strong indication of their biologic origin, which may result from the decomposition of proteins and nucleic acids, the latter being also responsible for the phosphorous signal.

15.5.3 *Deuterium: A Marker of the Protoplanetary Disk Chemistry*

In the following deuterium ^2H is noted D. Organic molecules of the interstellar medium are considerably enriched in deuterium ($\text{D}/\text{H} \approx 20,000 \times 10^{-6}$) relative to the solar hydrogen ($\text{D}/\text{H} = 25 \pm 5 \times 10^{-6}$) [55–57]. It was shown that this deuterium enrichment was produced by ion-molecule reactions at low temperature (down to 10 K) and at density $< 10^3 \text{ H m}^{-3}$ [58]. An important characteristic of meteoritic IOM is a systematic enrichment of the meteoritic IOM relative to terrestrial IOM [16], with reported values in the range $300\text{--}500 \times 10^{-6}$ [16, 59, 60]. However the origin of this enrichment is not clear as it is intermediate between the solar system abundance and interstellar abundance. To complicate the situation, it was recently shown that meteoritic IOM is highly heterogeneous in composition. Using Sims analyses, deuterium-rich hot-spots of micrometer sizes were found in the IOM, with D/H ratios up to 3200×10^{-6} [61, 62]. Two interpretations were proposed to account for the origin of these D-enriched regions [61, 62]: (1) Preserved interstellar D-rich molecules, (2) local concentrations of molecular species having the most exchangeable C–H bonds. In interpretation (2), the exchange would have taken place at the low temperature periphery of the protosolar disk, which exhibited a high degree of ionization caused by a massive irradiation from the young Sun [63].

With HYSCORE measurements on deuterium and hydrogen hyperfine interactions, it was possible to gain a deeper insight into the deuterium enrichment problem. Figure 15.13 shows the low frequency part of the HYSCORE spectrum of IOM extracted from the Orgueil meteorite. Deuterium signal is clearly observed between the broad ^{13}C ridge and the weak ^{14}N signal. By normalizing the intensity ratio D/H of IOM with a reference organic sample with known D/H, a high value $\text{D}/\text{H} = 15,000 \pm 5000 \times 10^{-6}$ was measured for Orgueil meteorite [38], which is close to interstellar values. It was shown quantitatively that organic radicals account for the entire excess of deuterium associated to the D-rich IOM hot spots [62]. Despite the extremely disordered character of meteoritic IOM, it was possible to localize the D-rich C–H bonds of the radicals. As shown in Sect. 15.5.1, the highly branched character of aromatic radicals implies that distant hydrogen atoms H_d and “benzylic”-type hydrogen atoms H_b dominate the ^1H -HYSCORE spectrum, as revealed by its linear shape (Fig. 15.12). Assuming that deuterium atoms partially exchange H_b hydrogen atoms, the ratio of hyperfine couplings should be equal to the ratio of nuclear g -factors:

$$\frac{A_H}{A_D} = \frac{g_{n,H}}{g_{n,D}} = 6.5 \quad (15.15)$$

From the values $|A_{H,\max}| = 12.3 \pm 0.2$ MHz and $|A_{D,\max}| = 2.0 \pm 0.3$ MHz measured from the lengths of hydrogen and deuterium ridges, a ratio $A_{H,\max} / A_{D,\max} = 6.2$ is obtained, very close to the expected value 6.5. Thus, assuming a “benzylic” position for deuterium atoms, their hyperfine coupling is calculated from Eqs. 15.14 and 15.15:

$$A_D \approx \rho_i \frac{g_{n,D}}{g_{n,H}} B_2 \cos^2 \theta \quad (15.16)$$

This corresponds to the hyperfine coupling of a methylene deuterium adjacent to an aromatic carbon atom C_i bearing a spin density ρ_i in its p_z orbital. Hydrogen interaction shows that $\rho_i \leq 0.12$. As aromatic radicals are more or less stacked, angle θ should be closed to 30° for an aliphatic chain fixed on C_i carbon. With B_2 in the range 140–168 MHz [47], a deuterium coupling $1.9 \text{ MHz} < |A_{D,\max}| < 2.3 \text{ MHz}$ is predicted, in good agreement with the experimental value 2.0 ± 0.3 MHz.

This analysis shows that the considerable deuterium excess of meteoritic IOM is mostly localized in “benzylic” positions of branched aliphatic chains fixed to the aromatic radicals [38]. The energy of the C-H_b bond (≈ 40 kcal/mol) is much smaller than that of the C-H_a bond (≈ 110 kcal/mol) [64]. This indicates that the deuterium atoms occupy the most exchangeable C-H bonds [38]. The temperature corresponding to the experimental D/H ratio of 15000×10^{-6} for the radicals is estimated to about 35 K, which is obtained in the outer regions of the protosolar disk at distances from the young Sun corresponding to the present day orbits of Kuiper Belt objects of the solar system [62]. It has been proposed that the heterogeneous composition of meteoritic IOM is the consequence of the accretion, on the parent body of meteorites, of two families of IOM particles [65]. The more abundant family is deuterium and radical poor, while the less abundant one contains a high quantity of D-rich particles (hot-spots) carried by radicals. In this model, proto-IOM grains localized in the inner and warm part of the disk are characterized by low D/H values. A small fraction of them could be brought by turbulences in the cold outer regions of the disk submitted to intense UV irradiation. Radicals could have formed and enriched in deuterium in this external proto-IOM, and next mixed by turbulences with internal proto-IOM to give the heterogeneous IOM found in carbonaceous meteorites. Particles with high quantity of D-rich radicals are less abundant than the other type of particles because of the large distance between the irradiated area and the inner accretion area.

15.6 Triplet State Radicals: Markers of Extraterrestrial IOM

In the preceding section, all the information on the IOM has been obtained from the hf interaction with ^1H , ^2H , ^{13}C , ^{31}P and ^{14}N nuclei in (or around) polyaromatic radicals. However this interaction gives no information on the size, the shape (and their distributions) of these radicals. As both fossil IOM and meteoritic IOM always give a single symmetric cw-EPR line with lineshape ranging from Lorentzian (with more or less Gaussian character) to stretched Lorentzian, it is natural to assume an electron spin $S = 1/2$ for all these aromatic radicals. This has been previously demonstrated for radicals in coals [52, 66–68] and in synthetic hydrogenated amorphous carbon [69, 70]. As shown below, this is also the case for the radicals of IOM in cherts. However the spin state of radicals has to be checked for meteorites owing to their complex history and the organic synthesis in conditions (temperature, pressure, irradiation) that do not exist on Earth. In the following we show that the major part of the radicals in meteoritic IOM possess a spin $S = 1$.

Radicals with $S = 1/2$ of terrestrial IOM are characterized by the spin Hamiltonian:

$$H(1/2) = \beta_e B_0 g S_z / \hbar + \sum_{k=1}^m \mathcal{S} A_k I_k - \beta_n \sum_{k=1}^m g_{n,k} B_0 I_{k,z} / \hbar \quad (15.17)$$

where the three terms, from left to right, are the electron Zeeman, the hf and the nuclear Zeeman interactions, respectively. We neglect the quadrupolar interaction term, which occurs for nuclei with spin $I \geq 1$. Two additional terms are added for $S = 1$ diradicals:

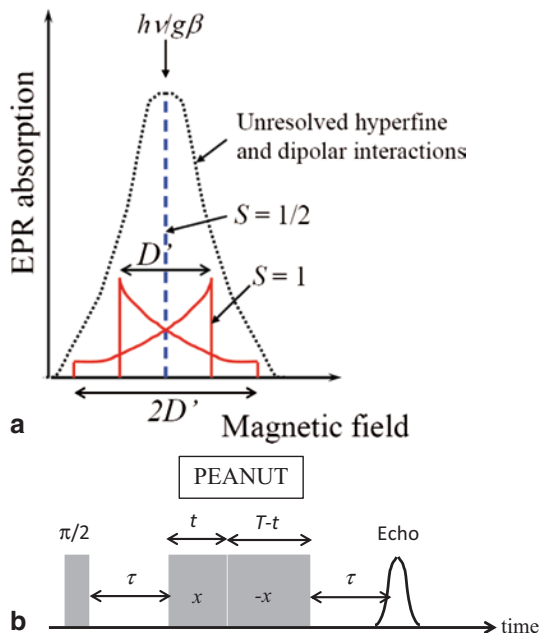
$$H(1) = \beta_e B_0 g S_z / \hbar + \mathbf{S}_1 \mathbf{J} \mathbf{S}_2 + \mathbf{S}_1 \mathbf{D} \mathbf{S}_2 + \sum_{k=1}^m \mathcal{S} A_k I_k - \beta_n \sum_{k=1}^m g_{n,k} B_0 I_{k,z} / \hbar \quad (15.18)$$

with $S_1 = S_2 = 1/2$. The additional interactions J and D are the exchange and the zero field splitting (ZFS) interactions, respectively. As the EPR spectrum of a radical is characterized by $2S$ lines, we should expect two lines for $S = 1$. Figure 15.14 shows a stick diagram representation of an $S = 1/2$ radical (blue interrupted line) and an $S = 1$ radical (red line), both with a nearly isotropic free spin g -factor. As the spin-orbit contribution to the ZFS is negligible (isotropic g -value close to 2.002), D can be written in the simple dipole-dipole approximation:

$$\begin{aligned} D_{dd} &= \frac{\mu_0}{4\pi\hbar} \frac{g^2 \beta_e^2}{r^3} (3 \cos^2 \theta - 1) \\ &= D' (3 \cos^2 \theta - 1) \end{aligned} \quad (15.19)$$

where μ_0 stands for the permeability of vacuum, r for the electron-electron distance and θ for the angle between the magnetic field and the interconnection line between the two electron spins. The diradical gives a pair of EPR line at magnetic field

Fig. 15.14 **a** Schematic representation of an EPR absorption line (dotted curve) formed by the sum of $S=1/2$ radicals (discontinuous line) and $S=1$ diradicals (full lines) with unresolved structure due to broadening by proton hyperfine interactions and dipolar interactions between neighbouring defects. **b** Pulse sequence for the spin nutation (PEANUT) experiment. The time domain data are obtained by monitoring the echo intensity versus $t/T/2$. Nutation pulse length $T=2\ \mu\text{s}$; $\tau=256\ \text{ns}$



$B_0 \pm (3 \cos^2 \theta - 1)D' / 2$ (with D' in magnetic field units). As the IOM is amorphous, θ spans all the possible values between 0 and π , so that the theoretical spectrum exhibits a typical “Pake pattern” with two prominent peaks at $B_0 \pm |D'|/2$ and two weak extrema at $B_0 \pm |D'|$ (Fig. 15.14). However these unrealistic stick spectra are broadened by hf interactions with ^1H nuclei, by dipolar interactions between neighbouring radicals, and by a distribution of interspin distances r , leading to a distribution of D' value. If $\langle D' \rangle$ is smaller than these two sources of broadening (i. e. $\langle D' \rangle < 11\ \text{MHz}$), the composite spectrum may finally result in a simple unresolved and symmetrical line (dotted curve in Fig. 15.14).

15.6.1 Measurement of Spin States

In the absence of resolved ZFS structure, the spin states present in a solid can be measured by transient nutation spectroscopy, which is the rotational motion of the magnetization by the interaction of spins with the microwave (mw) field. The nutation frequency ω_{TN} is related to S by [71]:

$$\omega_{TN} = [S(S+1) - m_s(m_s + 1)]^{1/2} g\beta B_1 / \hbar \quad (15.20)$$

An $S=1/2$ radical is thus characterized by $\omega_{TN} = g\beta B_1 / \hbar$, and a $S=1$ radical by $\omega_{TN} = \sqrt{2}g\beta B_1 / \hbar$, i.e. they differ by a factor $\sqrt{2}$. However this nutation frequency is often difficult to measure because of the rapid defocusing under B_1 field

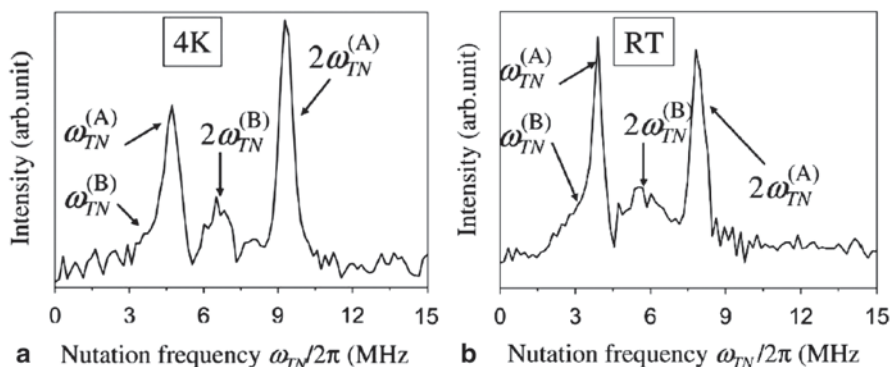


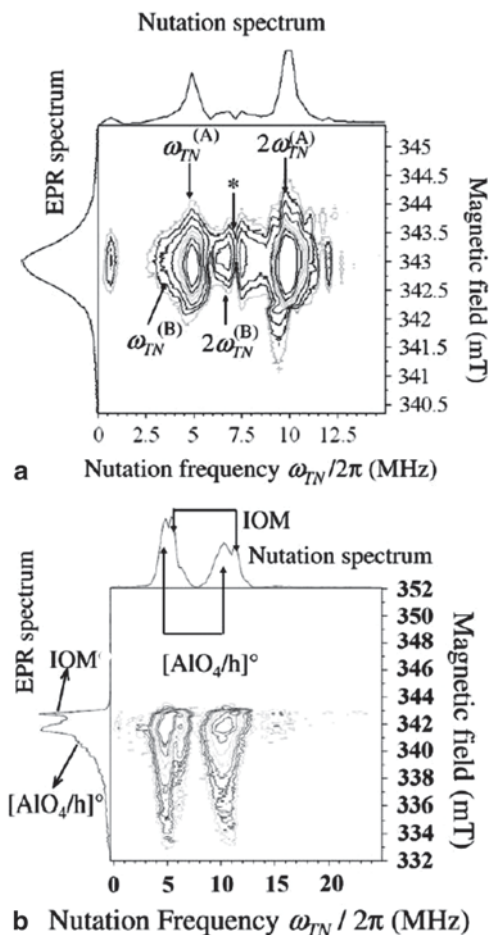
Fig. 15.15 Transient nutation (PEANUT) spectra at 4 K and room temperature of the IOM of the Orgueil meteorite. Adapted from [74] with permission from Elsevier (2011)

inhomogeneity. It can be refocused by detecting the so-called rotary echo [43, 72], whereby the nutation pulse of length T is divided into two parts of variable length t and $T-t$ with opposite microwave phase. To minimize nuclear modulations at nuclear frequencies (ESEEM effect), the rotary echo can be detected via a spin-locked echo by the *Phase-inverted Echo-Amplitude detected NUTation* (PEANUT) method developed by Stoll et al. [73]. The corresponding pulse sequence is shown in Fig. 15.14b.

Nutation spectra at room temperature and at 4 K of the IOM of Orgueil meteorite are shown in Fig. 15.15 [74]. They show peaks at ω_{TN} and $2\omega_{TN}$ for two species labeled A and B. The nutation frequencies are characterized by the ratio $2\omega_{TN}^{(A)} / 2\omega_{TN}^{(B)} = 9.9 / 6.9 = 1.435 \approx \sqrt{2}$, which corresponds to $S=1$ and $S=1/2$ for A and B, respectively. This interpretation was verified by monitoring the variation of $\omega_{TN}^{(A)}$ and $\omega_{TN}^{(B)}$ with the microwave field amplitude B_1 . As expected, the two slopes differed by $\sqrt{2}$ [74]. The participation of these two types of radicals to the EPR line was confirmed by recording the two-dimensional PEANUT spectrum, *i.e.* the nutation spectrum as a function of the magnetic field (Fig. 15.16a). The skyline projections along the nutation axis and along the magnetic field axis represent the nutation spectrum and the absorption EPR spectrum, respectively. This 2D-representation clearly demonstrates that both $S=1$ and $S=1/2$ radicals contribute to the EPR line in meteoritic IOM.

The presence of only $S=1/2$ radicals in the IOM in cherts is more difficult to demonstrate because different types of paramagnetic centers overlap with IOM radicals. However, the nutation frequency corresponding to $S=1/2$ for these well-known defects can be used as reference for the determination of S in organic radicals. Figure 15.16b shows the 2D-PEANUT spectrum at 4 K of the 1880 Myr-old Gunflint chert. At low temperature, the E' centre of SiO_2 is undetectable (completely saturated), and the cw-EPR spectrum is the superposition of the IOM radical and a defect of the SiO_2 matrix consisting of a hole trapped in a 2p oxygen orbital adjacent to an Al^{3+} ion in an Si^{4+} site, denoted $[\text{AlO}_4/\text{h}]^0$ centre or $\text{Al}_{\text{Si}}^\circ$ [26]. The projection of the nutation spectrum along the magnetic field axis shows two distinct EPR spectra. The projection along the nutation axis also shows peaks at ω_{TN} and $2\omega_{TN}$ for

Fig. 15.16 Contour plots of 2D-PEANUT spectra at 4 K of the IOM of the Orgueil meteorite a) and the 1880 Myr-old Gunflint chert b) The narrow feature marked by * in a) is an artifact introduced by the data handling. Adapted from [74] with permission from Elsevier (2011)



the two species. The ratio of their nutation frequencies is equal to $\omega_{TN}^{(1)} / \omega_{TN}^{(2)} = 1.1$, where (1) and (2) represent the IOM radical and the [AlO₄/h]^o centre, respectively. This ratio should be equal to 1 and to $\sqrt{2}$ for IOM radicals with spin 1/2 and 1, respectively. As $2\omega_{TN}^{(2)} = 10$ MHz for the [AlO₄/h]^o centre with $S = 1/2$, we should expect $2\omega_{TN}^{(1)} = 14.1$ MHz (for $S = 1$) and 10 MHz (for $S = 1/2$) for the IOM radicals. The experimental value $2\omega_{TN}^{(1)} = 11$ MHz clearly points to a spin value $S = 1/2$ for the fossil IOM. Consequently the presence of $S = 1$ organic radicals is a specificity of extraterrestrial IOM.

15.6.2 The Different Types of Radicals in Meteoritic IOM

More quantitative information on the different types of radicals in meteoritic IOM can be obtained from the temperature dependence of the magnetic susceptibility.

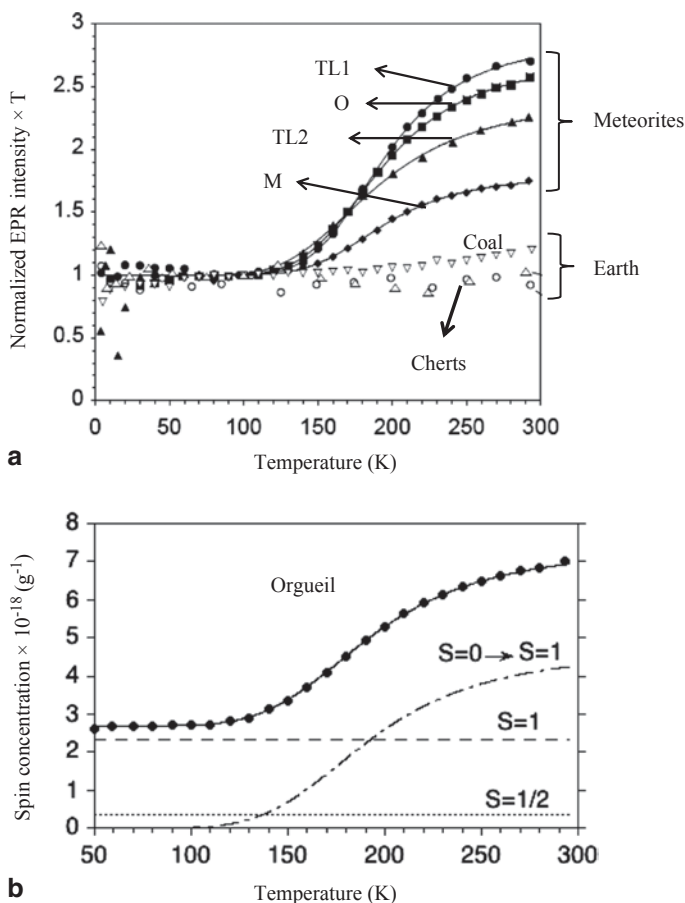


Fig. 15.17 **a** Normalized temperature dependence of the EPR intensity of organic radicals in meteoritic IOM and in fossil IOM. Meteorite samples: Tagish Lake (TL1 and TL2), Orgueil (O) and Murchison (M); Earth samples: a 320 Myr-old coal from Solway Basin, UK, a 1880-Myr-old chert from the Gunflint formation, Canada (*open circles*) and a 3500 Myr-old chert from the Dresser formation, Australia (*open triangles*). Full lines for meteoritic IOM are calculated with Eq. 15.21. Adapted from [39] with permission from Mary Ann Liebert (2013) and from [75] with permission from Elsevier (2004). **b** Simulation (*full line*) of the temperature dependent spin concentration in the Orgueil meteorite by the sum of three components: $S=1/2$ radicals, ferromagnetically coupled $S=1$ diradicals, and antiferromagnetically coupled $S=0$ diradicals with thermally accessible $S=1$ state. Adapted from [74] with permission from Elsevier (2011)

The temperature dependence of the EPR intensity of IOM radicals for different types of materials are shown in Fig. 15.17a). The EPR intensity is multiplied by T to take into account the Curie paramagnetism, and normalized to the intensity at 100K to compare samples with very different radical contents. As expected this normalized intensity is nearly constant for $S=1/2$ radicals of Earth IOM. However, IOM from different meteorites exhibit a significant increase of the normalized EPR intensity, revealing the thermal population of magnetic states from non magnetic ($S=0$)

Table 15.2 Concentrations of the different types of radicals in the IOM of Orgueil meteorite. ΔE and $\Delta\sigma$ are the singlet-triplet splitting and the entropy variation between the two spin states of the antiferromagnetically coupled diradicals, respectively. (From [74, 75])

ΔE (cm ⁻¹)	$\Delta\sigma$ (cm ⁻¹ K ⁻¹)	N_1^a (g ⁻¹)	N_1^f (g ⁻¹)	$N_{1/2}$ (g ⁻¹)
816	4.2	1.80±0.005	0.92±0.05	0.24±0.05

states. This has been accounted for by assuming the presence of diradicals with $S=0$ ground state and a thermally accessible triplet state $S=1$ (antiferromagnetic coupling) [75]. This is confirmed by nutation experiments showing the presence of intense $S=1$ nutation frequency peaks at room temperature (Fig. 15.15). However, the presence of a less intense $S=1$ nutation at 4 K indicates also the presence of diradicals with $S=1$ ground state (ferromagnetic coupling). The temperature dependence of the spin concentration N per gram of IOM is given by [74, 75]:

$$N = N_{1/2} + \frac{8}{3}N_1^f + \frac{8}{3}N_1^a \frac{1}{1 + \exp(-\Delta\sigma / kT)\exp(\Delta E / kT)} \quad (15.21)$$

where $N_{1/2}$, N_1^f and N_1^a are the spin concentrations for monoradicals, ferromagnetically coupled diradicals and antiferromagnetically coupled diradicals, respectively. $\Delta E = -J$ and $\Delta\sigma$ are the energy splitting and entropy difference, respectively, between $S=1$ and $S=0$ spin states of antiferromagnetically coupled diradicals. The details of the measurements are given in [74, 75]. To compare the behavior of the seven samples, the EPR intensity at each temperature T were normalized with respect to the intensity at 100 K. The results are shown in Fig. 15.17a. For terrestrial IOM, the nearly constant normalized EPR intensity indicates that Equation 15.21 reduces to $N \approx N_{1/2}$. For meteoritic IOM, the solid curves were calculated with very similar values $\Delta E \approx 816$ cm⁻¹ (0.10 eV) and $\Delta\sigma \approx 4.2$ cm⁻¹K⁻¹ [31, 75]. This indicates that the three meteorites possess the same type of radicals. Absolute spin concentrations in the IOM were calculated for Orgueil meteorite, by assuming that $J \gg kT$ for ferromagnetically coupled diradicals. The results are shown in Fig. 15.17b and in Table 15.2. This shows that monoradicals ($S=1/2$) contribute only to ~8% to the radicals in the IOM, while ferromagnetic ($S=1$) and antiferromagnetic ($S=0$) diradicals contribute to ~31% and ~61%, respectively [74].

15.6.3 Nature of Diradicals

Diradicals detected in meteoritic IOM are not fundamentally different from monoradicals of terrestrial IOM, as shown in Sect. 15.3. They are made of polycyclic aromatic units (sp² carbons) linked by aliphatic chains (sp³ carbons). Moreover, ¹H- and ¹³C HYSCORE spectra of meteoritic IOM are very similar to those of partially carbonized organic molecules [39]. From DFT and extended Hückel (EH) calculations, a model was first proposed for these diradicals, based on diradicaloid species hosted by aromatic structures of 10–15 rings and having a quinoidal structure [75].

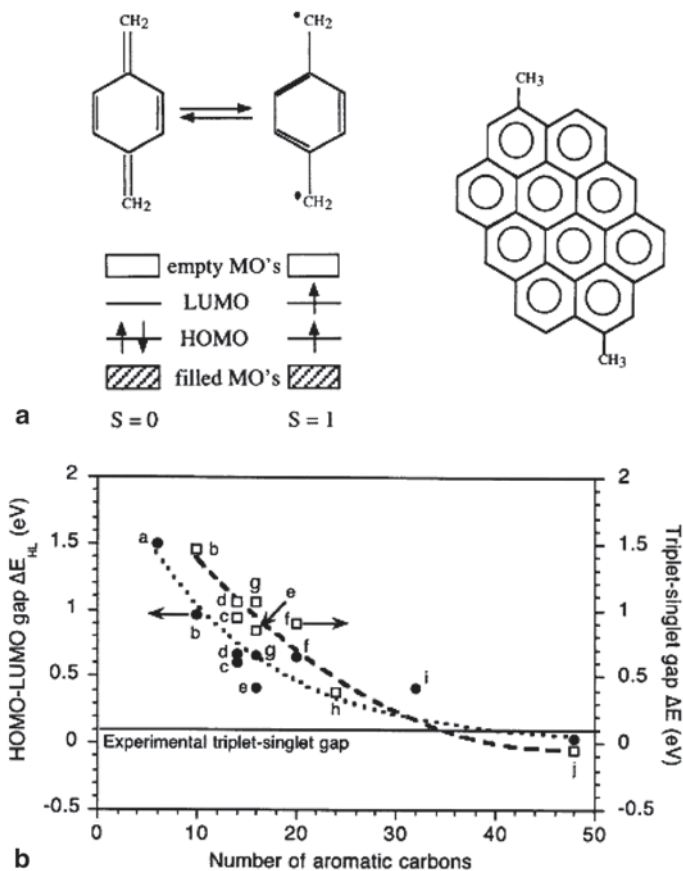


Fig. 15.18 **a** Left: description of a diradical with quinoidal structure (diradicaloid), showing the HOMO-LUMO gap and the two spin states $S=0$ and $S=1$; Right: example of model structure (molecule (i) used for the calculation of the singlet-triplet splitting ΔE and the HOMO-LUMO gap ΔE_{HL} . **b** Variation of ΔE (open squares) and ΔE_{HL} (full circles) with the number of aromatic carbons in polycyclic aromatic units. ΔE was calculated by DFT method, and ΔE_{HL} by extended Hückel method. Letters represent the molecules. Adapted from [75] with permission from Elsevier (2004)

The two spin states of a diradical with quinoidal structure (diradicaloid) are represented on Fig. 15.18a, with the example of a simple benzene ring [75]. Calculations were performed on model polycyclic aromatic units with variable number of rings and variable shapes, where aliphatic branching is simulated by two $-CH_3$ groups (Fig. 15.18a). The variations with the number of aromatic carbon atoms of the singlet-triplet (ST) splitting ΔE (calculated by DFT method), and of the HOMO-LUMO (HL) gap (calculated by the EH method) are shown in Fig. 15.18b. A positive (negative) ST gap means that the $S=0$ ($S=1$) state is the ground state, which corresponds to an antiferromagnetically (ferromagnetically) coupled diradicaloid. These calculations show that the experimental value of the ST gap $\Delta E \approx 0.1$ eV (ground

state $S=0$) is obtained for molecules containing about 30–40 aromatic carbon atoms (10–15 fused benzene rings), while molecules with more than about 40 aromatic carbon atoms have an $S=1$ ground state. These calculations indicate also that the two types of diradicals found in meteoritic IOM may be of the same type, differing only by the sizes of the polyaromatic group. The fact that the same values of ΔE and $\Delta\sigma$ are measured for three meteorites of different origin in the solar system (Orgueil, Murchison, Tagish Lake), strongly suggests that the antiferromagnetically coupled diradicals have a well defined size. As diradicals represent more than 98% of the radicals in the Orgueil meteorite, and the fact that it was quantitatively demonstrated that radicals (of all types) are the carriers of the deuterium excess [62], we may conclude that diradicals are responsible for the major deuterium excess in IOM. We may also expect that diradicaloids with much less than ~ 10 fused rings would exhibit an ST gap much larger than 0.10 eV, and thus would be EPR silent. Such small diradicaloids are not present in the IOM because this would imply that non magnetic organic molecules are also the carriers of deuterium excess, which is not the case.

Although the diradicaloid model accurately explains most of the experimental features, it suffers from a major drawback which is the very high instability of these species, except in some exceptional cases [76]. It was argued that the very high chemical stability of the IOM could protect these reactive diradicaloids against destructive reactions [75]. However this was only a working hypothesis.

An alternative model may appear more likely, which possesses the same characteristics as the diradicaloid model, *ie* a ST gap with size and sign which depends on the number of fused rings in the polyaromatic radical, without the instability problem of diradicaloids. The recent achievements in chemistry, physics and technology of graphene have revealed the unconventional electronic properties of this family of materials [77]. The so-called nanographene of physicists is nothing else than a hydrogenated polyaromatic carbon molecule for chemists. Decreasing the size of graphene to the nanometer range results in an increasing contribution of edge states (zigzag edges and armchair edges, see Fig. 15.19) for the electronic structure ([78–83] and references therein). Although the details are model dependent, it has been found that upon increasing the size of polyaromatic groups, the electronic structure evolves from a close shell singlet ($S=0$) ground state to an open shell singlet diradical ground state and next to a triplet diradical ($S=1$) ground state. The spin density is localized on zigzag edges, with one spin on one edge and the other spin on the other edge (Fig. 15.19). Elongation of the zigzag edge increases the diradical character whereas elongation of the armchair edge decreases the diradical character [81]. As expected, the HOMO-LUMO gap decreases upon increasing the zigzag edge length N (number of benzene rings) and the singlet-triplet transition in diradicals occurs for $N \approx 5-8$, depending on the length of the armchair edge and the shape of the nanographene sheet [81, 83]. This nanographene model appears more likely than the diradicaloid model, as the singlet and triplet diradical states are a direct consequence of the polyaromatic character of the molecule in the nanographene model, whereas homolytic breaking of the C-H bond in benzylic position in branching aliphatic chains are necessary to give a diradicaloid [75]. The common feature of these two models is that singlet to triplet transition in diradicals is induced

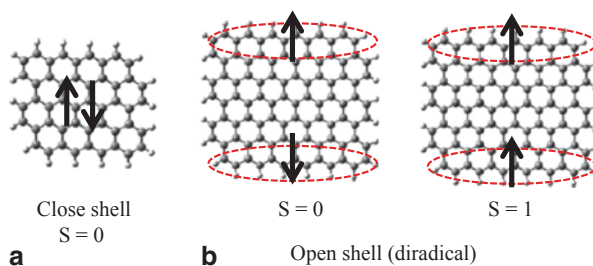


Fig. 15.19 Schematic representation of the spin distribution upon increasing the size of a nanographene sheet; **a** close shell $S=0$ character for small size; **b** transition to open shell diradical state above a critical size (model dependent); The spin density becomes localized on *zigzag edges*. For moderate size, $S=0$ state is lowest (antiferromagnetic coupling). Upon further increasing size, the singlet-triplet gap decreases and $S=1$ state is lowest above a second critical size (ferromagnetic coupling)

upon increasing the size of the polyaromatic core. The fact that diradicals with the two types of ground state (singlet and triplet) represent the major part of deuterium carriers in meteoritic IOM, points out that deuterium is localized mostly on large polyaromatic molecules with two different sizes. As deuterium is an important marker in Astrochemistry, further work must focus on these diradicals to get deeper insight into the history of organic matter in the Early solar system.

15.7 Conclusion

Carbonaceous matter with an age in the range ~ 1 –4.5 billion years contains paramagnetic radicals that record the history of the primitive organic matter, stored in the various interactions of the electron spins with surrounding atoms. This history started with the formation of the solar system (origin of the organic matter) and includes the apparition of life. Various information can be recovered by combining EPR methodologies, among which the origin (biologic versus abiotic) of the fossil organic matter, the age of the organic matter with respect to that of the host rock (syngeneity versus contamination), and the origin of the deuterium enrichment of extraterrestrial organic matter. EPR thus appears an emerging tool for tracking the first traces of life on Earth or on returned rocks from future Mars missions.

References

1. Westall W (2008) Morphological biosignatures in early terrestrial and extraterrestrial materials. *Space Sci Res* 135:95–114
2. Ehrenfreund P, Rasmussen S, Cleaves J, Chen L (2006) Experimentally tracing the key steps in the origin of life: the aromatic world. *Astrobiology* 6:490–520

3. Roeder E (1981) Are the 3800-Myr-old Isua objects microfossils, limonite-stained fluid inclusions, or neither? *Nature* 293:159–162
4. Knoll AH, Golubic S, Green J, Swett K (1986) Organically preserved microbial endoliths from the late Proterozoic of East Greenland. *Nature* 321:856–857
5. Westall W, Folk RL (2003) Exogenous carbonaceous microstructures in Early Archean cherts and BIFs from the Isua Greenstone Belt: implications for the search for life in ancient rocks. *Precambrian Res* 126:313–330
6. Garcia-Ruiz JM, Hyde ST, Carnerup AM, Christy AG, van Kranendonk MJ, Welham NJ (2003) Self-assembled silica-carbonate structures and detection of ancient microfossils. *Science* 302:1194–1197
7. Hayatsu R, Matsuoka S, Scott RG, Studier MH, Anders E (1977) Origin of the organic matter in the early solar system, VII: the organic polymers in carbonaceous chondrites. *Geochim Cosmochim Acta* 41:1325–1339
8. Chyba C, Sagan K (1992) Endogenous production, exogenous delivery and impact-shock synthesis of organic molecules: an inventory for the origin of life. *Nature* 355:125–132
9. Summons RF, Amend JP, Bish D, Buick R, Cody GD, Des Marais DJ, Dromart G, Eigenbrode JL, Knoll AH, Sumner DY (2011) Preservation of Martian organic and environmental records: final report of the Mars Biosignature Working Group. *Astrobiology* 11:157–181
10. Bibring J-P, Langevin Y, Gendrin A, Gondet B, Poulet F, Berthe M, Soufflot A, Arvidson R, Mangold N, Mustard J, Drossart P, and the Omega team (2005) Mars surface diversity as revealed by the OMEGA/Mars Express observations. *Science* 307:1576–1581
11. Mojzsis ST, Arrhenius G, McKeegan KD, Harrison TM, Nutman AP, Friend CRI (1996) Evidence for life on Earth before 3,800 million years ago. *Nature* 384:55–59
12. Brasier MD, Green OR, Jephcoat AP, Kleppe AT, van Kranendonk MJ, Lindsay JF, Steele A, Grassineau NV (2002) Questioning the evidence for earth's oldest fossils. *Nature* 416:76–81
13. Schopf JW, Kudryavtsev AB (2012) Biogenicity of earth's earliest fossils: a resolution of the controversy. *Gondwana Res* 22:761–771
14. Krot AN, Hutcheon ID, Brearley AJ, Pravdivtseva OV, Petaev MI, Hohenberg CM (2006) In Meteorites and the early solar system II (eds Lauretta D and McSween HYJJ). University of Arizona Press, Tucson, p 525
15. Huss GR, Rubin AE, Grossman JN (2006) In Meteorites and the early solar system II (eds Lauretta D and McSween HYJJ). University of Arizona Press, Tucson, p 567
16. Robert F, Epstein S (1982) The concentration of isotopic compositions of hydrogen carbon and nitrogen in carbonaceous chondrites. *Geochim Cosmochim Acta* 16:81–95
17. Alexander CMO'D, Fogel M, Yabuta H, Cody GD (2007) The origin and evolution of chondrites recorded in the elemental and isotopic compositions of their macromolecular organic matter. *Geochim Cosmochim Acta* 71:4380–4403
18. Remusat L, Palhol F, Robert F, Derenne S (2006) Enrichment of deuterium in insoluble organic matter from primitive meteorites: a solar system origin? *Earth Planet Sci Lett* 243:15–25
19. Pflug HD, Jaeschke-Boyer H (1979) Combined structural and chemical analysis of 3,800-Myr-old microfossils. *Nature* 280:483–486
20. Marschall CP, Marschall AO (2013) Raman hyperspectral imaging of microfossils: potential pitfalls. *Astrobiology* 13:920–993
21. Vago J, Gardini B, Kminek G, Baglioni P, Gianfiglio G, Santovicenzo A, Bayon S, van Winendael M (2006) ExoMars-searching for life on the red planet. *ESA Bull* 126:16–23
22. Gourier D, Delpoux O, Skrzypczak-Bonduelle A, Binet L, Ciofini I, Vezin H (2010) EPR, ENDOR and HYSCORE study of the structure and the stability of vanadyl-porphyrin complexes encapsulated in silica : potential paramagnetic biomarkers for the origin of life. *J Phys Chem B* 114:3714–3725
23. Kim SS, Bargar J, Nealson KH, Flood B, Kirschvink J, Raub T, Tebo B, Villalobos M (2011) Searching for biosignatures using electron paramagnetic resonance (EPR) analysis of manganese oxides. *Astrobiology* 11:775–786

24. Vandenbroucke M, Largeau C (2007) Kerogen origin, evolution and structure. *Organic Geochem* 38:719–833
25. Marchand A, Conard J (1980), Electron paramagnetic resonance in kerogen studies. In: Durand B (ed) *Kerogen: Insoluble organic matter from sedimentary rocks*. Technip, Paris, pp 243–270
26. Skrzypczak-Bonduelle A, Binet L, Delpoux O, Vezin H, Derenne S, Robert F, Gourier D (2008) EPR of radicals in primitive organic matter: a tool for the search of biosignatures of the most ancient traces of life. *Appl Magn Reson* 133:371–397
27. Villée F, Duchesne J, Depireux J (1964) Radicaux libres dans les météorites carbonées. *CR Acad Sci Paris* 258:2376–2379
28. Schulz KF, Eloffson RM (1965) Electron spin resonance studies of organic matter in the Orgueil meteorite. *Geochim Cosmochim Acta* 29:157–160
29. Binet L, Gourier D, Derenne S, Robert F (2002) Heterogeneous distribution of paramagnetic radicals in insoluble organic matter from the Orgueil and Murchison meteorites. *Geochim Cosmochim Acta* 66:4177–4186
30. Silbernagel BG, Gebhard LA, Dyrkacz GR (1984) ESR of carbon radicals in isolated coal macerals. In: Petrakis L and Fraissard J-P (eds) *Magnetic resonance, introduction, advanced topics and applications to fossil energy*. Reidel, Dordrecht, pp 645–653
31. Binet L, Gourier D, Derenne S, Pizarello S, Becker L (2004) Diradicaloids in the insoluble organic matter from the Tagish lake meteorite: comparison with the Orgueil and Murchison meteorites. *Meteoritic Planetary Science* 39:1649–1616
32. Singer LS, Lewis IC (1978) ESR study of the kinetics of carbonization. *Carbon* 16:417–423
33. Carniti P, Beltrame PL, Gervasini A, Castelli A, Bergamasco L (1997) Formation of radicals in thermal degradation of kerogen. A kinetic study. *J Anal Appl Pyrolysis* 40–41:553–568
34. Mrozowski S (1988) ESR studies of carbonization and coalification processes part II: biological materials. *Carbon* 26:531–541
35. Abragam A (1961) *Principle of nuclear magnetism*. Clarendon, Oxford
36. Bourbin M, Derenne S, Gourier D, Rouzaud J-N, Gautret P, Westall F (2012) Electron paramagnetic resonance study of a photosynthetic microbial mat and comparison with Archean cherts. *Orig Life Evol Biosph* 42:569–485
37. Wertz JE, Bolton JR (1986) *Electron spin resonance: elementary theory and applications*. Chapman & Hall, London
38. Gourier D, Robert F, Delpoux O, Binet L, Vezin H, Moissette A, Derenne S (2008) Extreme deuterium enrichment of organic radicals in the Orgueil meteorite: revisiting the interstellar interpretation? *Geochim Cosmochim Acta* 72:1914–1923
39. Gourier D, Delpoux O, Binet L, Vezin H (2013) Nuclear magnetic biosignatures in the carbonaceous matter of ancient cherts: comparison with carbonaceous meteorites. *Astrobiology* 13:932–947
40. Fel'dman EB, Lacelle S (1996) Configurational averaging of dipolar interactions in magnetically diluted spin networks. *J Chem Phys* 104:2000–2009
41. Bourbin M, Gourier D, Derenne S, Binet L, Le Du Y, Westall F, Kremer B, Gautret P (2013) Dating carbonaceous matter in Archean cherts by electron paramagnetic resonance. *Astrobiology* 13:151–162
42. Derenne S, Robert F (2010) Model of molecular structure of the insoluble organic matter isolated from Murchison meteorite. *Meteorit Planet Sci* 45:1461–1475
43. Schweiger A, Jeschke G (2001) *Principle of pulsed electron paramagnetic resonance*. Oxford University Press, Oxford
44. Höfer P, Grupp A, Nebenführ H, Mehring M (1986) Hyperfine sublevel correlation (HYSCORE) spectroscopy: a 2D ESR investigation of squaric acid radical. *Chem Phys Lett* 132:279–282
45. Rowen LG, Hahn EL, Mims WB (1965) Electron spin echo modulation. *Phys Rev* 137:A61–A71
46. Anderson MW, Kevan LJ (1986) Electron spin resonance and electron spin echo study of Cu^{2+} in zeolites H-RHO and CSH-RHO. *J Phys Chem* 90:6452–66459

47. Gerson F, Huber W (2003) *Electron spin resonance spectroscopy of organic radicals*. Wiley, Weinheim
48. Gordy W (1980) *Theory and application of electron spin resonance*. Wiley, New York
49. Pöppl A, Kevan L (1996) A practical strategy for determination of proton hyperfine interaction parameters in paramagnetic transition metal ion complexes by two-dimensional HYSCORE electron spin resonance spectroscopy in disordered systems. *J Phys Chem* 100:3387–3394
50. Gardinier A, Derenne S, Robert F, Behar F, Largeau C, Maquet J (2000) Solid state CP/MAS ^{13}C NMR of the insoluble organic matter of the Orgueil and Murchison meteorites: quantitative study. *Earth Planet Sci Lett* 184:9–21
51. Cody GD, Alexander CMO'D (2005) NMR studies of chemical structural variation of insoluble organic matter from different carbonaceous chondrite groups. *Geochim Cosmochim Acta* 69:1085–1097
52. Ikoma T, Ito O, Tero-Kubota S, Akiyama K (1998) HYSCORE study on coal radicals. *Energy Fuels* 12:1363–1368
53. Ikoma T, Ito O, Tero-Kubota S (2002) Exploring radicals in carbonaceous solids by means of pulsed EPR spectroscopy. *Energy Fuels* 16:40–47
54. Durand B, Nicaise G (1980) Procedures for kerogen isolation, in *Kerogen* (edited by Durand B). Technip, Paris, pp 35–53
55. Jefferts KB, Penzias AA, Wilson RW (1973) Deuterium in the Orion Nebula. *Astrophys J* 179:L57–L61
56. Geiss J, Reeves H (1972) Cosmic and solar system abundances of deuterium and helium-3. *Astron Astrophys* 18:126–132
57. Mahaffy PR, Donahue TM, Atreya SK, Owen TC, Niemann HB (1998) Galileo probe measurements of D/H and $^3\text{He}/^4\text{He}$ in Jupiter's atmosphere. *Space Sci Res* 84:251–263
58. Brown PD, Millar TJ (1989) Models of the gaz-grain interaction-D chemistry. *Monthly Notices R Astron Soc* 237:661–671
59. Halbout J, Robert F, Javoy M (1990) Hydrogen and oxygen isotope compositions in kerogens from the Orgueil meteorite: clues to the solar origin. *Geochim Cosmochim Acta* 54:1453–1462
60. Kerridge JF (1985) Carbon, hydrogen and nitrogen in carbonaceous meteorites: abundances and isotopic compositions in bulk samples. *Geochim Cosmochim Acta* 49:1707–1714
61. Busemann H, Young AF, Alexander CM, Hoppe P, Mukhopadhyay S, Nittler LR (2006) Interstellar chemistry recorded in organic matter from primitive meteorites. *Science* 312:727–730
62. Remusat L, Robert F, Meibom A, Mostefaoui S, Delpoux O, Binet L, Gourier D, Derenne S (2009) Proto-planetary disk chemistry recorded by D-rich organic radicals in carbonaceous chondrites. *Astrophys J* 698:2087–2092
63. Glassgold A, Feigelson ED, Montmerle T (2000) Effects on energetic radiation in young stellar objects. In: Mannings V, Boss AP and Russel SS (eds) *Protostars and planets IV*. University Arizona Press, Arizona, pp 429–455
64. Zhang XM (1998) Homolytic bond dissociation of the C–H bonds adjacent to radical centers. *J Org Chem* 63:1872–1877
65. Remusat L, Ghan Y, Wang Y, Eiler JM (2010) Accretion and preservation of D-rich organic particles in carbonaceous chondrites: evidence for important transport in the early solar system nebula. *Astrophys J* 713:1048–1058
66. Retcovsky HL, Hough MR, Maguire MM, Clarkson RB (1981) Nature of the free radicals in coals, pyrolyses coals, solvent-refined coals and coal liquefaction products. In *Coal Structure*. Am Chem Soc Advances in Chem Series, 192, n°4, pp 37–58
67. Conard J (1984) EPR in fossil carbonaceous materials. In: Petrakis L, Fraissard JP (eds) *Magnetic resonance, introduction, advanced topics and application to fossil energy*. Reidel, Dordrecht, pp 441–459
68. Rothenberger KS, Sprecher RF, Castellano SM, Retcovsky HL (1993) Temperature dependence of the electron paramagnetic resonance intensity of whole coals. In: Botto RE, Sanada

- Y (eds) Magnetic resonance of carbonaceous solids, vol 299 (Advances in Chemistry Series). American Chemical Society, Washington, DC
69. Barklie RC, Collins M, Silva SRP (2000) EPR linewidth variation, spin relaxation times, and exchange in amorphous hydrogenated carbon. *Phys Rev B* 61:3546–3554
 70. Robertson J (2002) Diamond-like amorphous carbon. *Mater Sci Eng R37*:129–281
 71. Astashkin AV, Schweiger A (1990) Electron-spin transient nutation: a new approach to simplify the interpretation of ESR spectra. *Chem Phys Lett* 174:595–602
 72. Solomon I (1959) Rotary spin echoes. *Phys Rev Lett* 2:301–302
 73. Stoll S, Jeschke G, Willer M, Schweiger A (1998) Nutation frequency correlated EPR spectroscopy: the PEANUT experiment. *J Magn Reson* 130:86–96
 74. Delpoux O, Gourier D, Vezin H, Binet L, Derenne S, Robert F (2011) Biradical character of D-rich carriers in the insoluble organic matter of carbonaceous meteorites: a relic of the protoplanetary disk chemistry. *Geochim Cosmochim Acta* 75:326–336
 75. Binet L, Gourier D, Derenne S, Robert F, Ciofini I (2004) Occurrence of abundant diradicaloid moieties in the insoluble organic matter from the Orgueil and Murchison meteorites: a fingerprint of its extraterrestrial origin? *Geochim Cosmochim Acta* 68:881–891
 76. Jung Y, Head-Gordon M (2003) How diradicaloid is a stable diradical? *Chem Phys Chem* 4:522–525
 77. Geim AK, Novoselov KS (2007) The rise of grapheme. *Nat Mater* 6:183–191
 78. Fernandez-Rossier J, Palacios JJ (2007) Magnetism in grapheme nanoislands. *Phys Rev Lett* 99(177204):1–4
 79. Philpott MR, Kawazoe Y (2009) Bonding and magnetism in nanosized grapheme molecules: Singletstates of zigzag edged hexangulenes $C_{6m}H_{6m}$ ($m=2,3, \dots,10$). *J Chem Phys* 131(214706):1–12
 80. Enoki T, Takai K (2009) The edge state of nanographene and the magnetism of the edge-state spins. *Solid State Comm* 149:1144–1150
 81. Wang J, Zubarev DY, Philpott MR, Vukovic S, Lester WA, Cui T, Kawazoe Y (2010) Onset of diradical character in small nanosized grapheme patches. *Phys Chem Chem Phys* 12:9839–9844
 82. Philpott MR, Kawazoe Y (2011) Triplet states of zigzag edged hexagonal grapheme molecules $C_{6m}2H_{6m}$ ($m=1,2,3, \dots,10$) and carbon based magnetism. *J Chem Phys* 134(124706):1–9
 83. Pham BQ, Truong TN (2012) Electronic spin transitions in finite-size graphene. *Chem Phys Lett* 535:75–79

Part VII
Advanced EPR Techniques

Chapter 16

EPR Measurement of the Spatial Distribution of Radiation Damage

Michael K. Bowman, Alexander G. Maryasov and Yuri D. Tsvetkov

Abstract EPR methods to determine the nanometer-scale distribution of radiation damage products in solids are reviewed. The emphasis is on pulsed EPR methods that measure weak dipolar interactions between radiation-induced paramagnetic centers. The dipolar interactions provide a convenient ruler for distance measurement that is well-matched to the sizes of spurs and tracks created by photons and particles. The properties of dipolar interactions between paramagnetic centers are discussed with their effect on various EPR measurements. Electron spin echo measurements have determined the pair correlation function between geminate products produced by UV photolysis. Measurements on tracks of ionizing particles show that the paramagnetic centers resulting from the initial holes and electrons have quite different spatial distributions resulting from their different mobilities. Newer methods of EPR dipolar spectroscopy, particularly DEER, have considerable promise for obtaining detailed profiles of the structure of damage distributions in irradiated solids. The radius of the damage region and the number or density of paramagnetic centers created in it can be determined. Both quantities depend on LET of the radiation and can help characterize radiation for dosimetric applications and can aid in understanding the differential effects of irradiation from different sources.

16.1 Introduction

One distinctive characteristic of ionizing radiation in the condensed phase is the inhomogeneous production of initial damage products in pairs as geminate ions such as an electron and a hole. Those ions may produce additional ions as they become thermalized; the ions may recombine with their geminate partners or other radiation damage products; or they may separate and react with other molecules to form more

M. K. Bowman (✉)

Department of Chemistry, The University of Alabama, Tuscaloosa, USA
e-mail: mkbowman@as.ua.edu

A. G. Maryasov · Y. D. Tsvetkov

V. V. Voevodsky Institute of Chemical Kinetics and Combustion, Siberian Branch,
Russian Academy of Science, Novosibirsk, Russia

© Springer International Publishing 2014

A. Lund, M. Shiotani (eds.), *Applications of EPR in Radiation Research*,
DOI 10.1007/978-3-319-09216-4_16

stable products trapped in the matrix. Generally, each geminate ion is paramagnetic, having an unpaired electron spin, and unless it reacts with another paramagnetic center (PC) such as a free radical, its trapped product will also be a PC. Because the PCs are usually produced in pairs and destroyed in pairs, the spatial distribution of surviving PCs contains some information about the distribution of initial damage products as modified by transport and further reactions.

The spatial distribution of radiation-induced damage is a major factor in determining the consequences of irradiation in a number of situations: such as, mutagenesis and carcinogenesis from background radiation; radiation sterilization of pharmaceuticals and medical supplies; food irradiation; cancer radiation therapy; and even radiation dosimetry. In fact, the spatial distribution of damage is a major reason that many different types of radiation (photons, electron beams, ion beams, etc.) and energies are used for irradiation. The different initial distributions of damage products result in different biological, chemical and physical effects. The deposition of energy in condensed phases is well-characterized and can be calculated in detail. However, the transport and fate of the resulting excited states, ions and other damage products depend critically on the chemical, physical and structural properties of the material and is not readily calculable.

Electron Paramagnetic Resonance (EPR) spectroscopy has been used to study radiation-induced products with lifetimes ranging from fractions of a second to many years. EPR has most often been used in radiation chemistry to identify PC products, determine the amount of products and to measure kinetics. Yet PCs in irradiated solids have been noted as having noticeable broadening and shortened spin relaxation times attributed to dipolar interactions with the unpaired electron spins of nearby PCs. These dipolar interactions are pair-wise interactions that depend on the distance between the two interacting PCs as $1/r^3$ and are largely independent of the matter separating them. EPR methods have long been used to investigate dipolar interactions between PCs in irradiated solids and yield information ranging from 'average' dipolar field from all PCs in the sample, to dipolar spectra showing the entire range of dipolar interactions and the intensity for each. Dipolar EPR data has been interpreted in terms of average distance to the closest PC; local concentration of PCs; size and shape of spurs or tracks; and even pair distribution functions.

This chapter focuses on the measurement and characterization of dipolar interactions by EPR methods in the context of irradiated materials. We mention recent advances in pulsed dipolar spectroscopy (PDS) from the field of structural biology; techniques known variously as double electron-electron resonance (DEER), pulsed electron double resonance (PELDOR), or double quantum coherence (DQC) spectroscopies where pairs of spin labels are introduced into biomacromolecules synthetically or using site-directed spin labeling. We consider the nature and limitations of the information obtained from the various EPR methods for investigating dipolar interactions. Irradiation can produce PCs in very unusual oxidation and spin states having large anisotropy of the magnetogyric ratio (g -factor). We consider how a large g -factor anisotropy affects dipolar interactions and their measurement by EPR.

The use of EPR methods to investigate the spatial distribution of PCs in irradiated materials has a long history dating from the 1960–1970s and is well reviewed

in a number of publications [1–3]. However, experimental EPR capabilities have expanded and new approaches to the spatial distribution of radiation damage products are feasible. This chapter therefore emphasizes experimental EPR methods that appear to hold additional capabilities, tempered by consideration of possible limitations and pitfalls. We hope this prospective focus attracts researchers to ask new questions about spatial distributions and to implement and perfect the approaches outlined here.

We consider in Sect. 16.2 the dipolar interaction between PCs and how it is manifested in EPR spectra and relaxation properties, both for isotropic spins and for PCs with very anisotropic g -factors. That section may be skipped on first reading and can be supplemented by standard EPR texts. Where possible, assumptions appropriate for irradiated materials will be made. We then consider continuous-wave (CW) EPR methods for measuring dipolar interactions in Sect. 16.3; electron spin echo (ESE) based methods in Sect. 16.4; and finally recent PDS methods in Sect. 16.5. There are a number of recent sources for more information on EPR spectroscopy [4–7].

16.2 Background

The dipolar interaction is a through-space coupling between the magnetic dipoles of two PCs that is largely unaffected by the material between the PCs. The coupling perturbs the electron spin states of each PC resulting in broadening of the EPR spectrum and increased spin relaxation.

16.2.1 The Dipolar Interaction

We consider the general case of a pair of PCs with anisotropic g -tensors following Bedilo and Maryasov [8]. The spin Hamiltonian for PC₁ and PC₂ coupled by a dipole-dipole interaction is

$$\hat{H} = \hat{H}_{Z1} + \hat{H}_{Z2} + \hat{H}_{dd}^{1,2} \quad (16.1)$$

$H_{Z,i}$ describes the Zeeman interaction of PC_{*i*}'s magnetic moment with the external magnetic field B_0 directed along the laboratory Z axis [9].

$$\hat{H}_{Zi} = \beta \vec{B}_0^+ \vec{g}_i \hat{S}_i \quad (16.2)$$

The Bohr magneton is β , taken to be positive; g_i is the g -tensor of PC_{*i*}; and S_i is its vector spin operator. The cross superscript denotes the Hermitian conjugate (in this case, it reduces to transposition). Single-headed arrows indicate vectors, taken to be columns, while a double-headed arrow indicates a tensor and '^' indicates an

operator. The properties of the g “tensor” are considered in detail by Abragam and Bleaney [9]. Equation (16.2) can readily be rewritten as

$$\hat{H}_{Zi} = \beta B_0 g_{i\text{eff}} \hat{S}_{iz'} \quad (16.3)$$

where g_{eff} is the effective value of the g -tensor of the PC,

$$g_{i\text{eff}} = \sqrt{\vec{b}^+ \cdot \vec{g}_i^+ \cdot \vec{g}_i^+ \cdot \vec{b}} \quad (16.4)$$

The unit vector along the Z axis is b and the z' axis is the direction of spin quantization by the Zeeman interaction and is parallel to

$$\vec{g}_i^+ \vec{b} \quad (16.5)$$

The Zeeman Hamiltonian, Eq. (16.2), is ‘solved’ (diagonalized) along the quantization axis for the PC in Eq. (16.5). Using that quantization axis, the eigenvalues $\varepsilon_{i,m}$ of the Zeeman Hamiltonian are

$$\varepsilon_{i,m} = g_{i\text{eff}} \beta B_0 m \quad (16.6)$$

where m is the projection of the PC spin onto its quantization axis, with $m = \pm 1/2$ for a PC with $S = 1/2$. The Zeeman frequency of the PC is

$$\omega_{Zi} = g_{i\text{eff}} \beta B_0 / \hbar \quad (16.7)$$

In general, the dipole-dipole interaction is between magnetic moments of two PCs with a spin Hamiltonian (see, e.g. [9])

$$\hat{H}_{dd}^{i,j} = \frac{1}{r_{ij}^3} \left[(\hat{\mu}_i \cdot \hat{\mu}_j) - 3 (\vec{n} \cdot \hat{\mu}_i) (\vec{n} \cdot \hat{\mu}_j) \right] \quad (16.8)$$

where n is the unit vector in the direction connecting the interacting PCs; r_{ij} is the intra-pair distance; and the magnetic moment operator is

$$\hat{\mu}_i = -\beta \vec{g}_i^+ \hat{S}_i \quad (16.9)$$

The negative charge of electron is accounted explicitly in the above relation.

The spin Hamiltonian parameters of the coupled PCs may differ and the principal axes of the g -tensors need not coincide. In this chapter, we consider the most common case in EPR when both PCs have $S = 1/2$. Dipole coupling of high-spin PCs having significant zero-field splitting was considered in [10].

The standard approach for a weak dipole-dipole interaction [9] is to use first-order perturbation theory with a zero-order Hamiltonian consisting of the Zeeman interactions. When the two PCs have quite different EPR frequencies such cor-

rections are simple. Differences in EPR resonance frequencies may be caused by different values of g_{eff} , or by a local field from interactions with surrounding nuclei. Such local fields may be treated as a distribution of B_0 values or by a redefinition of g_{eff} . The dipolar interaction is small if

$$B_0 |g_{1\,eff} - g_{2\,eff}| \gg \frac{g_{1\,eff} g_{2\,eff} \beta}{r_{12}^3} \quad (16.10)$$

When this inequality is fulfilled, the eigenfunctions of the zero-order Hamiltonian may be written as products of the eigenfunctions of the individual PCs. To calculate the first-order correction to energy levels it is possible to replace vector spin operators in Eq. (16.9) by projections onto their quantization axes,

$$\hat{S}_i \Rightarrow \frac{\vec{g}_i^+ \cdot \vec{b}}{g_{i\,eff}} \hat{S}_{iz'} \quad (16.11)$$

and then substitute that result into Eq. (16.8) to obtain the dipolar interaction D_{12}

$$\hat{H}_{dd}^{1,2} \approx D_{12} \hat{S}_{1z'} \hat{S}_{2z'} \quad (16.12)$$

$$D_{12} = \beta^2 \frac{\left\{ \left(\vec{G}_1 \vec{b} \cdot \vec{G}_2 \vec{b} \right) - 3 \left(\vec{n} \cdot \vec{G}_1 \vec{b} \right) \left(\vec{n} \cdot \vec{G}_2 \vec{b} \right) \right\}}{r_{ij}^3 g_{1\,eff} g_{2\,eff}} \quad (16.13)$$

with the symmetric tensor G introduced by Abragam and Bleaney [9],

$$\vec{G}_i = \vec{g}_i \vec{g}_i^+ \quad (16.14)$$

The eigenvalues of the spin Hamiltonian for the pair Eq. (16.1) to first-order are functions of projections of the PC electron spins on their quantization axes,

$$\varepsilon(m_1, m_2) = \beta B_0 g_{1\,eff} m_1 + \beta B_0 g_{2\,eff} m_2 + D_{12} m_1 m_2 \quad (16.15)$$

The dipolar interaction produces a shift in each energy level proportional to D_{12} and splits each line in the EPR spectrum. Equation (16.15) is the basis for analysis of spectral changes produced in EPR spectra by weak dipolar couplings. The spectral changes appear somewhat differently in CW and pulsed EPR measurements.

16.2.2 Dipolar Features in CW EPR

The selection rules for EPR transitions caused by a weak, oscillating, CW microwave field B_1 along the laboratory X axis (perpendicular to B_0 and Z) are $\Delta m_1 + \Delta m_2 = \pm 1$ for $S = \frac{1}{2}$ PCs. This means that the spectrum of two coupled PCs consists of the sum of their individual spectra, each of which is split into a doublet with a splitting of D_{12} . A ‘weak’ mw field is weaker than D_{12} and is unable to affect both components of either doublet simultaneously. Positions of the spectral lines of the PC_i depend on the spin state of PC_j and are

$$\begin{aligned}\omega_{12}(m_j) &= \frac{g_{i,eff}\beta B_0 + m_j D_{12}}{\hbar} \\ B_i(m_j) &= \frac{\hbar\omega_0 - m_j D_{12}}{\beta g_{i,eff}}\end{aligned}\quad (16.16)$$

for frequency-domain and for magnetic-field-domain spectra, respectively. B_i is the resonant magnetic field of PC_i , ω_0 is EPR spectrometer frequency.

If the relation in Eq. (16.10) is not fulfilled, then we have the case of ‘like’ spins with two energy levels that are nearly degenerate and may be coupled by additional pseudosecular terms of the dipole-dipole Hamiltonian containing the spin flip-flop terms, $S_{1+}S_{2-}$ and $S_{1-}S_{2+}$. This leads to larger splitting of EPR lines; in the limit of $g_{1,eff} = g_{2,eff}$ the splitting is a factor of 3/2 larger when the g -tensor anisotropy is relatively small [11] and is discussed further in Sect. 16.2.3. The behavior of ‘like’ spins is a bit more complex when g -tensor anisotropy is great ($\delta g \sim g$), but ‘like’ spins are important only in single crystals for PCs having the same orientation. In orientationally disordered systems with reasonable separations typical of irradiated materials, anisotropic PCs are always ‘unlike’.

In the high-temperature limit, when

$$\frac{\beta B_0 g_{i,eff}}{2k_B T} \ll 1 \quad (16.17)$$

the doublet of dipole-split components of PC_i have equal intensities. The high-temperature limit is valid above 4 K for nearly all EPR measurements at X- or Q-band (9.5 or 35 GHz, respectively) in irradiated materials.

It is possible to obtain the spectrum of PC_1 with isotropic g_1 -tensor split by a dipole-dipole interaction with an anisotropic PC_2 . Consider a pair with a rigid structure. The vector r_{12} connecting the two PCs has a fixed orientation and length in the principal axes of the g_2 -tensor. The transition probability of PC_1 does not depend on the pair’s orientation in the laboratory frame, so that over the narrow spectrum of PC_1 in the high-temperature limit is

$$f(B) = \sum_{m_2} \iint \delta\left(B - B_{01} + \frac{m_2 D_{12}}{\beta g_1}\right) d(\cos\theta) d\phi \quad (16.18)$$

The sum consists of just two terms corresponding to the doublet components. Here g_1 is the g -factor of the isotropic PC_1 , the angles θ and ϕ define the orientation of B_0 in the molecular frame of the anisotropic PC_2 , integration is performed over a hemisphere of possible orientations with δ the Dirac delta function, and B_{01} is the PC_1 line position in the absence of dipole coupling,

$$B_{01} = \hbar\omega_0 / \beta g_1 \quad (16.19)$$

The dipolar splitting D_{12} in Eq. (16.13) simplifies in this case where g_1 is isotropic, to

$$D_{12} = g_1 g_{2,eff} \frac{\beta^2}{r_{ij}^3} \left[1 - 3(\vec{n} \cdot \vec{b}) \frac{(\vec{n} \cdot \vec{G}_2 \vec{b})}{g_{2,eff}^2} \right] \quad (16.20)$$

The Dirac delta function in Eq. (16.18), in principle, allows integration but the result is too bulky and too complex to be useful. In practice, the requirement that g_2 and r_{12} be fixed relative to each other is rarely encountered in irradiated materials.

An even simpler equation for D_{12} occurs when the PC_2 is also isotropic with g -factor of g_2 that fulfills Eq. (16.10), so that doublets of each PC do not overlap. Equation (16.20) simplifies to the well-known relation with D_{perp} the perpendicular component of the dipolar interaction tensor

$$D_{12} = g_1 g_2 \frac{\beta^2}{r_{ij}^3} (1 - 3 \cos^2(\theta)) = D_{perp} (1 - 3 \cos^2(\theta)) \quad (16.21)$$

Omitting the normalization factor, the EPR spectrum, Eq. (16.18), for PC_1 in a pair of isotropic PCs has the shape

$$f(\Delta\tilde{B}) \propto \sum_m \int_0^1 dx \delta[\Delta\tilde{B} + m(1 - 3x^2)] \quad (16.22)$$

where $x = \cos(\theta)$, and a dimensionless lineshift is introduced,

$$\Delta\tilde{B} = r_{ij}^3 \frac{(B - B_{01})}{\beta g_2} \quad (16.23)$$

The integral in Eq. (16.22) may be calculated analytically, giving

$$f(\Delta\tilde{B}) \propto \frac{1}{\sqrt{1 + 2\Delta\tilde{B}}} \times \begin{cases} 1 & -1/2 \leq \Delta\tilde{B} \leq 1 \\ 0 & \text{otherwise} \end{cases} + \frac{1}{\sqrt{1 - 2\Delta\tilde{B}}} \times \begin{cases} 1 & -1 \leq \Delta\tilde{B} \leq 1/2 \\ 0 & \text{otherwise} \end{cases} \quad (16.24)$$

This high-temperature lineshape is known as the Pake, or Pake-like, doublet. The dipolar interaction D_{12} is a tensor with three principal values. For two isotropic PCs, the trace, or sum of the three principal values relative to the unsplit EPR line, is zero. The components have equal intensities and the average fields of both components coincide. When one or both g -tensors are anisotropic, the centers of each Pake component may differ.

Figure 16.1 shows Pake patterns for several different situations of an anisotropic PC₂. The centers of the Pake doublet components for the isotropic PC₁ do not coincide due to the anisotropy of the g_2 -tensor. The structure of each doublet component may also vary from the standard Pake lineshape with two turning points to a lineshape with three turning points. However, it is rare to see a resolved dipolar pattern because a distribution of distances and interactions with multiple PCs will obliterate the characteristic sharp edges.

16.2.3 Dipolar Features in Pulsed EPR

Observation of Pake patterns via CW EPR are extremely rare because the Pake pattern is obscured by much larger inhomogeneous broadening. Spin echo measurements, Sect. 16.4, drastically reduce the influence of inhomogeneous broadening so that dipolar couplings can have a clear impact on the signal measured. When all the EPR transitions of a weakly-coupled pair of isotropic PCs are excited, the dipolar interaction causes a periodic modulation of the electron spin echo amplitude

$$V(\tau) \propto \cos(D_{12}\tau/\hbar) \quad (16.25)$$

Here τ is time interval between the echo-generating pulses, and D_{12} is the dipolar coupling given in Eqs. (16.13, 16.20 or 16.21). Fourier transformation of such signal produces the same Pake pattern as would CW EPR.

Analytical equations for the primary echo signal were obtained in [12] for arbitrary dipolar coupling of isotropic PCs. The equations for the echo signal are quite bulky but show that relatively weak inhomogeneous broadening decouples ‘like’ PCs. Figure 16.2 shows the frequency-domain spectrum of the oscillating echo amplitude for like PCs having a Gaussian lineshape whose dispersion σ is comparable to D_{perp} in Eq. (16.21). D_{perp} is used as the normalized frequency unit in the figure. The spectrum looks like a mixture of a standard Pake pattern with edges at D_{perp} and $2D_{\text{perp}}$ (with frequencies of 1 and 2) and a rather distorted Pake pattern with splittings $3/2$ larger at $3/2 D_{\text{perp}}$ and $3D_{\text{perp}}$. Strong coupling should be rarely encountered in irradiated materials even with rather narrow lines. The broader pattern becomes more prominent as σ decreases.

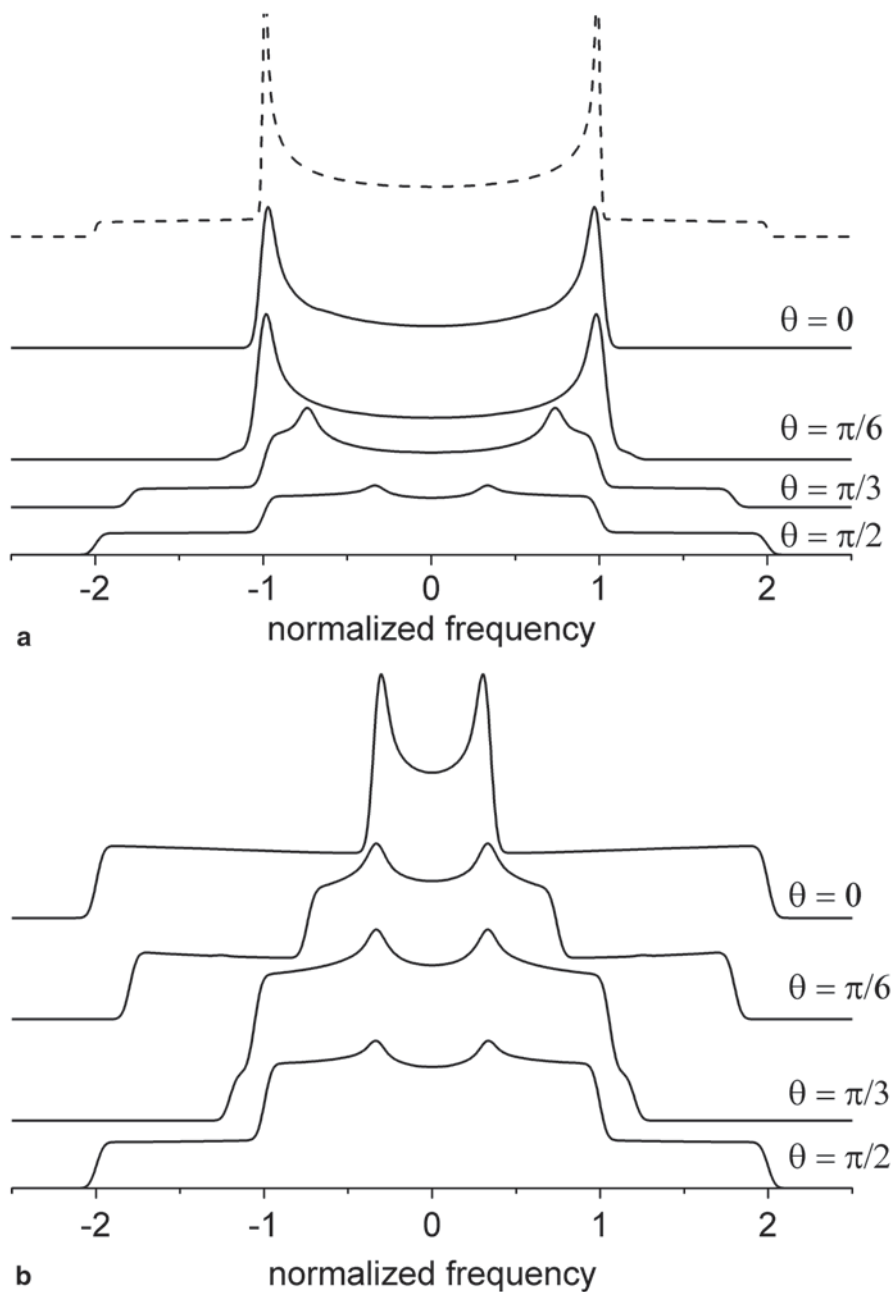
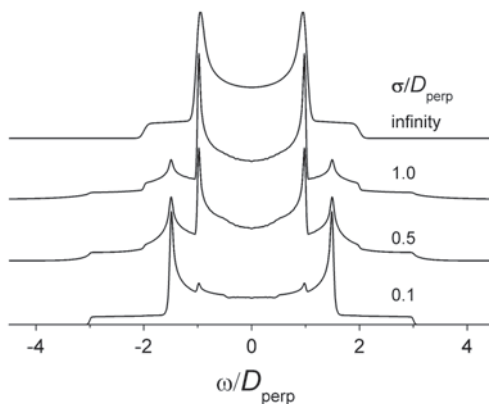


Fig. 16.1 The Pake-like patterns caused by interaction of isotropic PC with a partner having anisotropic axially symmetric g -tensor are shown in integral form. The patterns strongly depend on the pair geometry. The labels show the angle between the vector r connecting the two PCs and direction of the unique dipolar axis. **a** $g_{\text{parallel}} = 1.0$, $g_{\text{perp}} = 3.0$, standard Pake pattern is shown as dashed line for comparison; **b** $g_{\text{parallel}} = 3$, $g_{\text{perp}} = 1$

Fig. 16.2 The Pake-like pattern for a dipolar interaction D_{perp} comparable to the difference in frequencies of the $S=1/2$ PCs. The spectrum is symmetric about 0. The PCs have the same g -factors and have a Gaussian inhomogeneous broadening with a standard deviation σ . For large broadening, the pattern approaches the lineshape of Eq. 16.21



16.2.4 The Exchange Interaction

The exchange interaction J between PCs also couples spins in a similar fashion to the dipole-dipole interaction. When J is small, it can simply be added as an isotropic constant to D_{12} [13]. Fortunately, J depends very strongly on the distance between the PCs because it is proportional to the overlap between the wavefunctions containing the unpaired electrons on the two PCs. In molecular solids, J falls typically by a factor of ten for every 0.1–0.2 nm increase in separation. Beyond 1.5 nm J is considered to be negligible in comparison to the dipolar interaction [14, 15]. Strong J completely alters the EPR spectrum and will not be considered because it is unexplored territory in the measurement of distances between PCs. For isotropic PCs, the exchange interaction is isotropic and a small J appears as a non-zero trace for the measured ‘dipolar’ interaction. Yet, the trace can be non-zero for anisotropic PCs even if $J=0$ and is not a valid criterion for the presence of exchange.

16.2.5 More than one PC

When there are several PCs interacting with each other in a group, the pairwise dipolar interactions provide the PC being observed with dipolar splittings that act independently in magnetically-diluted systems. Independence of the dipolar splittings means that the spectrum of the observed PC consists of 2^{N-1} lines, when there are N PCs in the group. This means that instead of a single $\cos(D\tau)$ in Eq. (16.25) there will be a product of such cosines for the set of D_{ij} . The product can be expressed as a series of sums and differences of the D_{ij} or as a convolution of Pake doublets that quickly loses all distinctive structure. It should be noted that in EPR, broadening caused by dipole interactions in diluted systems never approaches a Gaussian lineshape as might be expected. Averaging products of cosine functions from interactions with different PCs will provide with a number of oscillating terms whose

amplitudes decay as $\ln(\tau)/\tau$, in some degenerate situations there may be also terms decaying as $\tau^{-1/2}$. These slowly decaying oscillations produce spectra with sharp or even diverging features that are definitely non-Gaussian.

16.2.6 Spatial Distributions

A number of descriptive terms such as ‘track’, ‘spur’ and ‘blob’ are used to refer to the inhomogeneous distributions of radiation damage products in solids. These terms are useful for evoking mental pictures of distributions of radiation damage, but EPR measurements of dipolar interactions are more readily discussed in terms of the radial distribution function, $f_{pc}(r)$ [3]. This is a second-order, pair-correlation function of the distances between PCs. In other fields, $f_{pc}(r)$ is known variously as the pair distribution function or pair correlation function and written as $g(r)$, $g^{(2)}(r_{12})$ or $g^{(2)}(r_1, r_2)$ which could cause some confusion with the g -factor in EPR.

The $f_{pc}(r)$ is the probability of finding one PC a distance r from another PC and can be built up by making a histogram of all inter-PC distances in a sample. If we consider having one PC at the center of a volume V , then the number $n(r)$ of PCs at a distance r is $dn(r) = f_{pc}(r)r^2 dr$. The total number, N , of PCs in the volume V (including the one at the center) and their concentration, C , are easily calculated from $f_{pc}(r)$.

$$N = \int f_{pc}(r) r^2 dr + 1$$

$$C = \frac{1 + \int f_{pc}(r) r^2 dr}{\int r^2 dr} = \frac{N}{V} \quad (16.26)$$

For a uniform or random distribution of PCs, $f_{pc}(r) = C$ for large r . On the other hand, a single radiation event, such as a single γ -ray or a single ion, can only generate a finite number of PCs, so f_{pc} must approach zero for large r . At very high doses many spatially overlapping events can approach a uniform distribution of PCs. However, f_{pc} always reaches zero at some small distance r_0 . One reason that f_{pc} must vanish is the finite size of each PC and its excluded volume—two PCs cannot occupy the same space and one is already at $r=0$. A more practical reason is that the dipolar interaction is infinite at $r=0$ and this singularity needs to be avoided in many calculations.

Near a PC it is possible to treat $dn(r)/dV(r)$ as the local concentration of PCs, representative of the typical environment of a PC, e.g., within a spur or track. EPR properties that depend on dipolar interactions are particularly well-suited for determining the local concentration because the dipolar interaction falls off very rapidly with distance, depending primarily on PCs in the immediate vicinity. We can take the uniform concentration that produces the same average dipolar broadening or spin relaxation seen in a sample and call it the local concentration [1, 16]. This definition gives a simple relation between f_{pc} and C_{loc} .

$$\begin{aligned}
 C_{loc} &= \frac{\int_{r_0}^{\infty} f_{pc}(r) D_{perp}(r)^2 r^2 dr}{\int_{r_0}^{\infty} D_{perp}(r)^2 r^2 dr} = \frac{\int_{r_0}^{\infty} f_{pc}(r) r^{-6} r^2 dr}{\int_{r_0}^{\infty} r^{-6} r^2 dr} \\
 &= 3r_0^3 \int_{r_0}^{\infty} \frac{f_{pc}(r)}{r^6} r^2 dr \quad (16.27)
 \end{aligned}$$

More than 99% total of the dipolar interaction for a uniform distribution arises from PCs in a spherical shell between r_0 and $5 r_0$ from each PC.

C_{loc} is a single parameter that depends on the distance to nearby PCs and the number of nearby PCs, but determines neither quantity without additional knowledge. Yet C_{loc} is a very useful parameter. At low radiation doses, it is dominated by the characteristics of single, isolated radiation events and reflects the size and distribution of a spur, track, etc. When damage starts to overlap at high doses, C_{loc} approaches the average concentration of the sample.

C_{loc} and other related parameters, such as the second moment of the spectrum or spin relaxation rate, have long been used to estimate the dimensions of spurs and tracks in irradiated materials. When C_{loc} is plotted versus the average concentration $C_{ave} = N/V$, C_{loc} is often constant at low C_{ave} but eventually they become equal. The intersection point between these two regions is taken as the point at which the total volume of tracks, spurs, etc. equals the sample volume. With some knowledge of LET or PCs per spur, rough estimates of their dimensions can be made.

The f_{pc} has enough information to define the dimensions and number of PCs, e.g., in a spur or track. But third-order (and higher) correlations functions are needed to determine the distribution of spur sizes or the mix of spurs and tracks in a sample. It is not yet clear how to measure these higher-order correlation functions by EPR, so f_{pc} needs to be interpreted in the context of a model for the spatial distribution of PCs.

The distribution of PCs within the path of a single particle or photon is not the only factor producing the f_{pc} . Most irradiated materials contain multiple paths that are uncorrelated with each other. As the dose increases, the number of paths and their overlap increases until the dipolar contribution of PCs within a single ionization path is swamped by contributions between PCs in different paths. Yet even at low radiation doses, one can usually expect penetrating radiation to produce a background f_{pc} with a uniform distribution proportional to $r^2 dr$.

16.2.7 Scope of the Chapter

The aim of this chapter is to illustrate EPR methods that can investigate the spatial distribution of radiation-damage products in solids, the various approaches that have been used and major results that were obtained. It is intended to interest the reader in the possibilities offered by EPR rather than to be a detailed guide for making and interpreting EPR measurements. Consequently we focus on typical PC properties and measurement conditions intended to represent the vast majority of

cases. This simplifies the discussion by eliminating details restricted to rarely-encountered special cases, such as EPR measurements below 1 K.

Unless the contrary is explicitly stated, we tacitly make a number of assumptions. The PCs are assumed to have a single unpaired electron with total spin $S = \frac{1}{2}$ and interact with each other only by the dipolar interaction with $J = 0$. The irradiated material is assumed to have no diffusion or slow motions during the measurements. The f_{pc} is taken as being isotropic and smooth, with no abrupt changes with distance so that turning points in the dipolar lineshape and characteristic dipolar modulation are smeared out and unobservable. D_{perp} is less than the difference in the unsplit EPR frequencies of the PCs involved.

Any long-range order in the material is assumed not to produce a corresponding long-range structure in f_{pc} . Higher-order correlations of PCs are taken to be insignificant. In particular, that the orientations of the g -tensors of the PCs are not correlated with each other or with the vector between the PCs, or with the magnetic field B_0 . That spin-lattice relaxation is isotropic and flip-flop transitions among the PCs are negligible. Finally, that the high-temperature limit holds so that thermal energy $k_B T$ is much greater than the energy of a microwave photon.

16.3 CW EPR Methods

The dipolar interaction between two PCs affects the CW EPR spectrum in two ways. The normal $\Delta m_s = \pm 1$ EPR transitions of each individual PC are additionally split by the dipolar interaction. The resulting spectrum is generally the convolution of the EPR spectrum of the isolated PC with a Pake-like pattern provided the orientations of the PCs are uncorrelated. New EPR absorptions also appear from transitions of the pair in which both unpaired electrons flip, the $\Delta m_s = \pm 2$ transitions which occur at approximately half the usual B_0 and are often called half-field transitions. The $\Delta m_s = \pm 2$ transitions are formally forbidden and their intensity provides an indirect measure of the dipolar interaction while their spectrum, to first order, is independent of the dipolar interaction. The intensity of the half-field transitions scales with PC separation as r^{-6} , and is generally detected only for r in the range of 0.3–1.0 nm.

When there are dipolar interactions with n other PCs, the $\Delta m_s = \pm 1$ transitions are a convolution of splittings from each of the other n PCs, giving $n + 1$ (for identical dipolar splittings with the other PCs) up to 2^n transitions (for completely different dipolar splittings), but preserving the total integrated EPR intensity. The half-field transition intensity scales roughly as the sum of the intensity from each pairwise interaction.

16.3.1 Measurement of the Dipolar Spectrum

Resolved dipolar splittings from radical pairs in irradiated solids were observed by Kurita [17] and by Gordy and Morehouse [18] using radiolysis and by Lebedev [19] using UV photolysis to generate the pairs. The well-resolved dipolar splittings gave

separations of 0.3–1.0 nm between PCs. Resolved splittings from radical pairs are generally observed only under a rather restrictive set of conditions. (1) The solid has very high local order—single crystal or polycrystalline solids. The PCs are highly constrained by the structure of the solid to specific locations in the same or adjacent unit cells. (2) Irradiation and measurement is performed at low temperature, often below 77 K, to rapidly thermalize the products, and to prevent their recombination or escape. (3) Products are produced by bond cleavage or atom transfer reactions (rather than hole or electron transfer) which favor small initial separations but suppresses recombination of the thermalized products by back transfer or tunneling.

The dipolar splittings relevant to PC distributions on the multi-nanometer scale are small, less than 10 MHz and are not resolved in typical CW EPR measurements. EPR spectra are inhomogeneously broadened by *g*-factor and hyperfine anisotropy and by unresolved hyperfine interactions from hydrogen nuclei in nearby molecules so that the minimum linewidth is typically > 10 MHz. The dipolar splittings are lost in the wings of the inhomogeneous lineshape and produce no distinct features. In addition, dipolar interactions from more than one PC produce a convoluted dipolar lineshape that further smears out any distinctive structure.

Although resolved features rarely result from dipolar interactions characterizing the spatial distribution of PCs in irradiated materials, the dipolar interaction still has an impact on the EPR spectrum. There is some broadening because the resulting spectrum is a convolution of the dipolar broadening function and the EPR spectrum of an isolated, non-interacting PC. The convolution relation provides an opportunity to recover dipolar information if the EPR spectrum of isolated-non-interacting PCs can be obtained. Several different approaches have been used with some success. They generally seek to produce the same PCs at low concentration and more random distribution to minimize dipolar interactions but with the same structure, conformation and environment. One approach is to generate the same PC by another means. If the structure of heavy ion tracks is studied, production of PCs by low-dose UV-photolysis or low LET irradiation may be adequate. Irradiation at a higher temperature can increase transport before reaction or trapping and result in a more uniform distribution. The other approach starts with a non-uniform sample and mobilizes the PCs and uses diffusion to randomize the distribution and/or decrease the number of PCs through recombination or other reactions. Thermal annealing, optical bleaching/photolysis, and long-term storage have been used successfully. This second approach can be repeatedly applied to a sample until a limiting spectral shape is reached, presumably corresponding to a random distribution with minimal dipolar interactions.

The dipolar broadening spectrum can be recovered from the two EPR spectra using a Fourier deconvolution method developed for site-directed spin-labeling EPR studies. A similar problem is faced there for CW EPR spectra of biomacromolecules with one or two nitroxide spin labels attached at specific locations [20]. Rabenstein and Shin [21] divided the Fourier transforms of the EPR spectrum of the singly- and doubly-labeled biomacromolecules (with and without the dipolar interaction) to produce the Fourier transform of the dipolar broadening function. An inverse-Fourier transform then produced the dipolar broadening spectrum and this method

is used routinely in the structural biology community to analyze site-directed spin-labeling data. Occasionally the deconvolution produces a recognizable Pake-like pattern which gives the distance between labels. More often conformational flexibility results in a distribution of inter-label distances, not unlike the distribution of PC separations in irradiated solids, smoothing the features of the Pake-like pattern. Nevertheless a weighted average distance can be obtained.

The second approach is based on standard second moment theory for EPR spectra [22–24]. The second moment M_2 of a spectrum is basically its variance and has the property that the second moment of the convolution of two spectra is just the sum of their individual second moments. Subtracting the second moments of the spectra without and with dipolar interactions yields the second moment of the dipolar broadening function or $2\langle D_{perp}^2 \rangle$ for a pair with a distribution of distances.

Unfortunately, both of these procedures have a major limitation when applied to irradiated solids. The second moment or the dipolar broadening function corresponds to a distance only for a single pair of PCs. This is generally an excellent approximation for site-directed spin-labeling and some UV-photolysis experiments, but not for investigating spatial distributions of radiation-generated PCs. This limitation arises because as additional PCs interact, the total EPR spectrum is convoluted with more and more pair-wise dipolar interactions. The dipolar broadening function becomes broader and its second moment increases. Unless a Pake-like structure is resolved in the Fourier-deconvoluted dipolar broadening function, there is only a single parameter, the width or second moment, and no means to distinguish between a cluster with a few strongly-interacting PCs and a large mob of many weakly-interacting PCs. This is the same limitation that C_{loc} has and can be seen clearly for the second moment by expressing it in terms of f_{pc} or C_{loc} .

$$\begin{aligned}
 M_2 &= \int_{r_0}^{\infty} f_{pc}(r) D_{perp}(r)^2 r^2 dr = \int_{r_0}^{\infty} \frac{f_{pc}(r)}{2} \left(\frac{\mu_0}{4\pi} \frac{g^2 \beta^2}{h r^3} \right)^2 r^2 dr \\
 &= \frac{1}{2} \left(\frac{\mu_0}{4\pi} \frac{g^2 \beta^2}{h} \right)^2 \int_{r_0}^{\infty} \frac{f_{pc}(r)}{r^6} r^2 dr \\
 C_{loc} &= \frac{3}{r_0^3 D_{perp}(r_0)^2} M_2
 \end{aligned} \tag{16.28}$$

16.3.2 Non-linear Methods

There are quite a few standard and not-so-standard non-linear CW EPR methods that are sensitive to dipolar interactions. They range from progressive power saturation of the EPR signal [25, 26]; through ELDOR [27], passage effects [28] and saturation transfer [29]; to multiple quantum EPR [30]. In each approach, the intensity, and sometimes shape, of the signal depends on magnetic relaxation parameters influenced, in part, by dipolar interactions. However, these approaches are all limited by the same fundamental problem. The dipolar interaction is but one factor influencing the signal and cannot be cleanly disentangled from the other determinants

of relaxation. The evolution and relaxation of magnetization in solids is usually not accurately described by the Bloch equations that provide the starting point for quantitative analysis of non-linear CW-EPR spectroscopy. One is forced to use trends in the behavior of the EPR signal as an indication of qualitative changes in the PC f_{pc} , such as the onset of spur overlap.

16.3.3 CW EPR Results

The most extensive study of PC distribution in radiation chemistry by non-linear CW-EPR was by the Kevan group [31–41]. Power saturation of the EPR signal was used to investigate the distribution of trapped electrons, hydrogen atoms, and silver atoms, among others, in γ -irradiated frozen organic and aqueous glasses and the effect of irradiation temperature and photoexcitation. EPR saturation curves were measured for different doses and a phenomenological spin relaxation rate was extracted using simple models of the EPR response [25, 26]. The measured rate was recognized as being a complex mixture of relaxation routes, including spin-lattice relaxation, caused by interactions of a PC with the lattice, along with spin-spin interactions among the PCs. However, only spin-spin interactions should be dose dependent and only after damage from different γ -ray tracks began to overlap, providing a way to detect the onset of overlap.

The relaxation rate was constant at low radiation doses but eventually started to increase at higher doses, which was taken as the point where the spurs could completely fill the sample volume had there been no overlap. Then, assuming uniform spurs with 100 eV of energy deposited per spur, it was possible to determine the spur radius. In different aqueous and organic glasses irradiated at 77 K, the spur radius varied from 4 to > 13 nm for trapped electrons and hydrogen atoms which are fairly mobile before they are thermalized and trapped. Less mobile PCs were found to have spur radii as small as 2 nm. These studies achieved an important characterization of the size scale for spurs in these materials. Yet they rest on a very idealized spur model that misses the complex energy distribution by γ -rays.

16.4 ESE Methods

The CW EPR signal from PCs in solids depends on many parameters that are poorly understood or difficult to measure, making the study of spatial distributions inexact. Pulsed EPR has an important feature that makes measurements more convenient and more exact. Pulsed EPR provides greater control over signal generation, enabling a strategy known as refocusing. When applied properly, refocusing makes a signal independent of most interactions and allows quantitative measurement of the desired parameter, such as the distribution of dipolar fields. The principle of refocusing is demonstrated in the electron spin echo and is employed extensively in PDS.

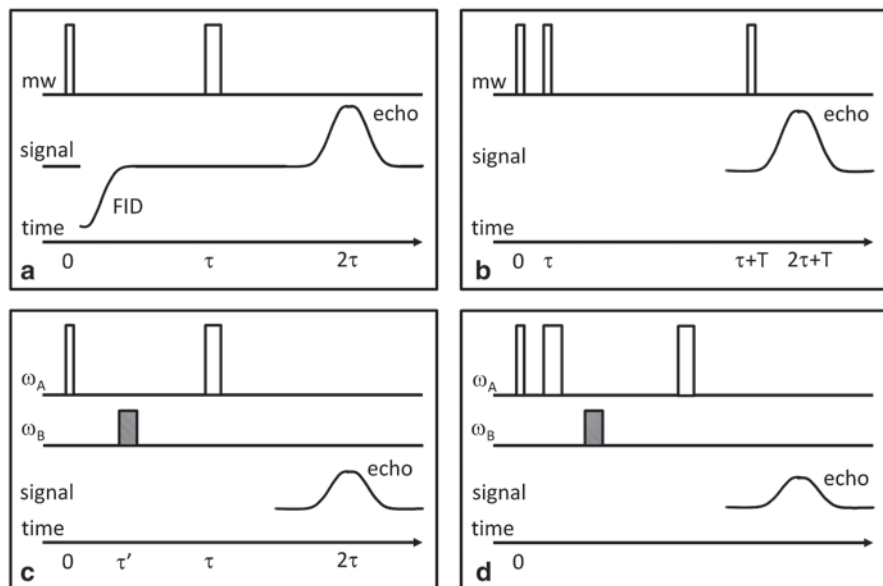


Fig. 16.3 Pulse sequences for different pulsed EPR measurements. The microwave pulse channel is labelled as mw, the signal channel shows the position of the detected echo, and a common timing convention. Typical relative widths of the microwave pulses are indicated. **a** the two-pulse or primary electron spin echo sequence with the position of the FID signal indicated, **b** three-pulse or stimulated echo, **c** three-pulse DEER experiment with the two microwave channels labelled with their frequencies, **d** four-pulse DEER sequence

Erwin Hahn produced the first spin echo [42] with nuclear spins and quickly followed with PCs. The basic experiment starts with magnetization arising from the interaction of a static, applied magnetic field and the PCs in a sample. Microwave pulses at a frequency corresponding to energy differences between spin states of the PCs are applied. The spin echo is produced by a pair of pulses separated by a short time known as τ , Fig. 16.3a. Each pulse tilts a portion of the sample magnetization, with which it is nearly in resonance, away from the applied magnetic field.

Following the first pulse, the magnetization precesses freely around the applied magnetic field, emitting a signal known as the free-induction decay or FID. The FID is a time-domain signal that is intimately related, via the Fourier Transform, to the frequency-domain CW-EPR spectrum. The FID contains much the same information about dipolar interactions and the spatial distribution as does the CW-EPR spectrum, but intertwined with all the anisotropies, inhomogeneous broadening, etc. that make quantitative dipolar studies using the CW-EPR spectrum so problematic. A sub-ensemble of PCs that have the same EPR frequency, ω , is often called a ‘spin packet’ or ‘isochromat’. Each spin packet precesses relative to the microwave frequency, ω_0 , at a rate $\Delta\omega = (\omega - \omega_0)$ so that its phase relative to the microwaves at the time of the second pulse is $\Delta\omega\tau$. The magnetization from each spin packet is rotated by the second pulse leaving it with a phase $\pi - \Delta\omega\tau$. Most things that determine the

EPR frequency of a spin packet, e.g., g -factor, hyperfine couplings, are unchanged by the microwave pulses so that $\Delta\omega$ remains unchanged. At time t after the second pulse, the spin packet has a phase $\pi - \Delta\omega\tau + \Delta\omega t$ which equals π at $t = \tau$ after the second pulse. Every spin packet has the same phase independent of $\Delta\omega$, just like all spin packets have a phase of 0 at the start of the FID. The magnetization from all the spin packets excited by the microwave pulses interfere constructively and produce a spin echo—a FID-like signal with opposite phase, τ after the second pulse and 2τ after the first.

At the center of an echo, the magnetization of each spin packet is independent of $\Delta\omega$ and the inhomogeneous broadening and anisotropies that contribute to $\Delta\omega$. The precessing magnetization is said to be refocused into an image of the FID where $\Delta\omega$ has no influence on the echo intensity at different values of τ . The echo intensity does decay at large τ , e.g., by the T_2 of the Bloch equations or the more general phase memory time T_{M^*} , but not by interactions that remain invariant during generation and formation of the spin echo. There is one notable interaction that does change—the dipolar interaction of an observed PC with other PCs in the sample, allowing the study of the spatial distribution of PCs. The dipolar interaction can change because the second microwave pulse excites the other PC, or because the other interacting PC relaxes. The change in dipolar interaction changes its contribution to $\Delta\omega$ and ω , resulting in a variation of the EPR frequency of each PC, known as spectral diffusion, and in a failure of the magnetization to completely refocus in the echo.

It is largely a matter of personal taste whether to speak of spectral diffusion as a part of T_2 or T_{M^*} decay of the spin echo or as a separate process, but for convenience, we will consider them as separate. The primary reason for doing so is to split the decay of the spin echo $V(\tau)$ into the product of two terms: the ‘intrinsic’ relaxation of the PC in isolation, V_{int} ; and the decay resulting from spectral diffusion and dipolar interactions, V_{SD} . Usually, the intensity of the spin echo appearing at the time 2τ can be expressed as a product.

$$V(\tau) = V_{\text{int}}(T_{M^*}, \tau) V_{\text{SD}}(\tau) \quad (16.29)$$

It is much easier to separate these two quantities in experimental spin echo decays than it is to extract quantitative dipolar information from CW EPR spectra or saturation studies. The spin echo experiment refocuses most interactions that have no bearing on dipolar interactions, makes the echo signal decay independent of those extraneous interactions, and allows a clean determination of the pertinent dipolar interactions.

This two-pulse, or primary, echo experiment has been expanded into a large family of experiments to measure different PC properties, with more pulses and/or microwave frequencies, and refocusing as many extraneous influences as possible. Some of these experiments are discussed later in this chapter. When discussing pulsed measurements, it is common to distinguish the PCs that produce the measured EPR signal (known as A spins) from the PCs that have dipolar couplings to and affect the A spins (B spins). This is not always a unique distinction because

some PCs act as both A and B spins while others are neither A spins nor affect the A spins.

16.4.1 Spectral Diffusion

Spectral diffusion is a general term for the variation of the EPR frequency of a PC with time. It can arise from a variety of causes unrelated to the spatial distribution of PCs, e.g., molecular motion of the PC or the surrounding matrix, or nuclear spin diffusion of matrix nuclei which are typically considered parts of the intrinsic V_{int} relaxation of the PC. Although spectral diffusion enters into many pulsed experiments, it is most often studied using the primary echo.

Nuclear spin diffusion makes an important contribution in nearly all samples because PCs have weak, but non-zero hyperfine interactions (primarily dipolar) with nuclear spins even a few nanometers away [1, 43]. Flip-flops (T_2 -like events) between nuclear spins modulate the net hyperfine interaction and EPR frequency of the PC. Although the hyperfine interaction with any distant nuclear spin is weak and the rate of flip-flops is slow, there are large numbers of nuclei that potentially participate. Decay of the spin echo is often dominated by nuclear spin diffusion for PCs in samples with significant aqueous or organic components. Depending on its rate and the strength of the hyperfine interaction with the PC, the spin echo decay from nuclear spin diffusion often has the form $\text{Exp}[-(2\tau/T_M)^n]$ where n lies between 1.75 and 3 [2]. Deuteration of the sample, replacing ^1H with ^2H , slows V_{int} relaxation in most cases by decreasing $1/T_M$ and n , but may perturb the spatial distribution, e.g., by affecting thermalization of holes and electrons or the rate of hydrogen abstraction.

Spectral diffusion arising from dipolar interactions between PCs is more relevant to the study of spatial distributions. Spectral diffusion can occur if the second microwave pulse generating the spin echo also affects B spins with a dipolar coupling to the A spins. This can happen when the B spin's EPR frequency is close to that of the microwave pulse. In that case, the spectral diffusion occurs at the instant of the second microwave pulse and is known as 'instantaneous' diffusion. Spectral diffusion can also take place as a result of flip-flops between B spins or from the spin-lattice (T_1) relaxation of nearby B spins which can occur one or more times during the entire 2τ of the echo-generating sequence.

16.4.1.1 Instantaneous Diffusion

Instantaneous diffusion was treated by Klauder and Anderson [44] for a homogeneous distribution of PCs and was later generalized for a uniform distribution in a lower dimensional object such as a plane or a line by Milov et al. [13]. Instantaneous diffusion can be expanded from the response of an A spin with a dipolar coupling to a B spin [45–47]. The contribution to the primary echo response is

$$\begin{aligned}
V_{pair,B}(\tau) &= Tr\left(\hat{\rho}_{A,B} \hat{S}_{Ay}\right) \\
&= \left[\cosh(R_B \tau) + \frac{W_B}{R_B} \sinh(R_B \tau)\right]^2 \\
&\quad + \frac{D_B^2}{4R_B^2} \sinh(R_B \tau)^2 (1 - 2p_B) e^{-2W_B \tau}
\end{aligned} \tag{16.30}$$

The density matrix for the pair composed of the A and B spin is $\rho_{A,B}$, the dipolar coupling between the pair of PCs is D_B , W_B is the rate at which S_z of the B spin changes, $R_B^2 = W_B^2 - D_B^2/4$ and p_B is the probability that the second microwave pulse flips the B spin. The instantaneous diffusion is distinguished from all other types of relaxation of the spin echo by its dependence on p_B . If the B spin relaxes very rapidly so that $W_B \tau \gg 1$, then $V_{pair,B}(\tau)$ becomes independent of p_B and that A spin no longer contributes to instantaneous diffusion. On the other hand, if $W_B \tau \ll 1$ for the measured range of τ , it is possible to set $W_B = 0$ and obtain the instantaneous diffusion signal

$$\begin{aligned}
V_{ID}(\tau) &= V_{pair,B}(\tau) = 1 - 2p_B \sin\left(\frac{D_B \tau}{2}\right)^2 \\
&= 1 - p_B (1 - \cos(D_B \tau))
\end{aligned} \tag{16.31}$$

If an intermediate value of W_B results from flip-flops transitions and interactions with other B spins, then higher-order correlation functions and not just the simple radial distribution function are involved; this case will not be considered here. However, if W_B is determined by spin-lattice relaxation of the isolated B spin, it can be slowed by decreasing the measurement temperature until $W_B \tau \ll 1$, to allow use of Eq. (16.31) rather than (16.30).

Each A spin typically interacts with more than one B spin. The instantaneous diffusion decay of the A spin from its interactions with all the B spins in the sample (or more generally the spectral diffusion decay when $W_B > 0$) is

$$V_{SD}(\tau) = Tr\left(\hat{\rho} \hat{S}_{Ay}\right) \tag{16.32}$$

A major simplification is possible as long as interactions among the B spins can be ignored, i.e., neglect of all dipolar and exchange interactions that do not involve the A spin. Such a situation can occur in magnetically dilute solids. The density matrix of the system is just the tensor product of density matrices for the pairwise interaction of the A spin with each of the B spins in the sample. And V_{SD} or V_{ID} is simply the product of the individual $V_{pair,B}$ terms [48].

$$\begin{aligned}
\hat{\rho} &= \hat{\rho}_{A,B_1} \times \hat{\rho}_{A,B_2} \times \cdots \times \hat{\rho}_{A,B_i} \times \cdots \\
Tr\left(\hat{\rho} \hat{S}_{Ay}\right) &= \prod_i Tr\left(\hat{\rho}_{A,B_i} \hat{S}_{Ay}\right) \\
V_{SD}(\tau) &= \prod_i V_{pair,B_i}(\tau)
\end{aligned} \tag{16.33}$$

This is an important result that allows expression of spectral diffusion as a product of terms, for example, from PCs within the same spur or track and from PCs of different tracks, or for different radiation damage products. However, this result is possible only if all pairwise interactions that do not involve the A spin can be ignored. In particular, it does not allow dipolar and exchange interactions responsible for spin diffusion, spin flip-flops and cross relaxation among the B spins. When their rate, W_B , is not negligible, as in samples known as ‘ T_2 ’-type, Eq. (16.33) does not apply. Therefore we focus on ‘ T_1 ’-type samples at temperatures where W_B is negligible. Instantaneous diffusion can also be observed through the stimulated echo. The theory has been developed [1, 2, 43, 44] but will not be discussed here because it is rarely used to determine spatial distributions.

16.4.1.2 Uniform Distribution

Equation (16.33) enables calculation of $V_{ID}(\tau)$ for $W_B=0$, from a uniform distribution of PCs by averaging Eq. (16.31) over all possible distributions of B spins. If the second term in Eq. (16.31) is small, which can always be achieved at $p_B \ll 1$,

$$\begin{aligned} V_{pair,B}(\tau) &= 1 - p_B (1 - \cos(D_B \tau)) \\ &\approx e^{-p_B(1 - \cos(D_B \tau))} \\ V_{ID}(\tau) &= V_{SD}(\tau, (W_B = 0)) \\ &= \prod_i V_{pair,B_i}(\tau) \approx \prod_i e^{-p_{B_i}(1 - \cos(D_{B_i} \tau))} \\ &= e^{-\sum_i p_{B_i}(1 - \cos(D_{B_i} \tau))} \end{aligned} \quad (16.34)$$

If the probability, p_B , of flipping the spin of a B spin by the second microwave pulse is the same for all B spins, then for a uniform distribution of PCs, the spin echo decay due to instantaneous diffusion is

$$\begin{aligned} \langle V_{ID}(\tau) \rangle &= \left\langle e^{-\sum_i p_{B_i}(1 - \cos(D_{B_i} \tau))} \right\rangle = e^{-p_B \sum_i \langle 1 - \cos(D_{B_i} \tau) \rangle} \\ &= e^{-p_B \int_0^{\pi/2} (1 - \cos(D_B(r, \theta) \tau)) r^2 \sin(\theta) d\theta dr} \\ &= e^{-2\tau p_B \left(\frac{4\pi^2 g^2 \beta^2}{9\sqrt{3} h} C \right)} = e^{-2\tau p_B k_{ID}} = e^{-2\tau p_B \alpha C} \end{aligned} \quad (16.35)$$

C is the concentration of B spins having this uniform distribution and the angular brackets indicate an average over the appropriate distribution. For A and B spins having a g -factor of about 2.0 and $S = 1/2$, α in Eq. (16.35) approaches $8.2 \times 10^{-13} \text{ cm}^3 \text{ s}^{-1}$. This exponential decay is proportional to the Fourier Transform of the nearly Lorentzian dipolar spectrum [9]. We note that the second moment of this Lorentzian spectrum is infinite if the excluded volume is ignored when integrating

over r in Eq. (16.35). This is a feature common to magnetically-diluted systems; estimates of the second moment do not converge smoothly. The rate of decay in Eq. (16.35) is proportional to the dipolar interaction between spins at the distance given by $\langle 1/r^3 \rangle = C$.

Other sources of echo decay, such as instantaneous diffusion from other B spins, spectral diffusion, spin relaxation and even ESEEM, contribute multiplicatively to the decay of the echo during the time period 2τ . However, only instantaneous diffusion depends on p_B and this dependence is used to extract the instantaneous diffusion from all other sources of echo decay. The p_B can be calculated if the EPR spectrum, $g(\omega_0)$, of the B spins is known and the microwave field, ω_1 , is uniform.

$$p_B = \left\langle \sin\left(\frac{\omega_1 t_p}{2}\right)^2 \right\rangle = \int_0^\infty \frac{\omega_1^2 I(\omega_0)}{\omega_1^2 + (\omega - \omega_0)^2} \sin\left(\frac{t_p}{2} \sqrt{\omega_1^2 + (\omega - \omega_0)^2}\right)^2 d\omega_0 \quad (16.36)$$

It is best if small samples are used so that ω_1 is uniform over the sample. A distribution of ω_1 affects both excitation of the signal and the efficiency of detection of the echo signal from that region of the sample. In addition, A spins with different ω_1 decay at different rates in Eq. (16.35) so that the overall decay can be non-exponential.

Equation (16.35) yields a simple result from a simple integration, but includes the very unrealistic assumption that a uniform distribution of B spins extends beyond the sample to infinite distances. For macroscopic samples, the extension of the averaging to infinity is justifiable. Distant B spins have tiny dipolar interactions so that $D_i\tau$ is insignificant during the $\tau = 0.1\text{--}10 \mu\text{s}$ range of typical spin echo measurements and the very distant B spins have no effect on echo decay. Therefore, sample size and shape are irrelevant for instantaneous diffusion with uniform distributions. At the other integration limit, very close B spins have an immediate effect on the spin echo of the A spin. A pair of PCs with random orientation, θ , relative to the applied magnetic field produces an average decay [49] expressed in terms of C and S , the Fresnel sine and cosine integrals respectively [50]

$$\begin{aligned} \langle V_{pair,B}(\tau) \rangle_\theta &= 1 - p_B \langle 1 - \cos(D_B \tau) \rangle_\theta \\ &= 1 - p_B \left(1 - \frac{\cos\left(\frac{\pi y}{6}\right) C(\sqrt{y}) + \sin\left(\frac{\pi y}{6}\right) S(\sqrt{y})}{\sqrt{y}} \right) \\ y &= \frac{6D_{perp}\tau}{\pi} \end{aligned} \quad (16.37)$$

The factor following p_B approaches unity at large τ and exceeds 0.8 after about $0.15 \mu\text{s}$ for a pair of PCs with $g \sim 2.0$ separated by 3 nm. That suggests the exponential

decay limit in Eq. (16.35) requires $p_B < 0.1$. Fortunately the major deviation is at even shorter times, within the deadtime of the measurement. Provided that the distribution of B spins is not highly correlated, the principal consequence of exciting an extremely close B spin with the second microwave pulse is to cause the A spin to disappear; leaving the measured echo to decay according to Eq. (16.35) during the experimentally accessible time window.

The distribution of B spins cannot be uniform at short distances for a number of reasons mentioned in Sect. 16.2.4. Any distribution must go to zero for distances smaller than some r_0 but affects the spin echo decay only at short times that typically are lost in the deadtime of a spin echo measurement. Klauder and Anderson [44] calculated that the echo decay from instantaneous diffusion by a uniform distribution of B spins with an r_0 is initially Gaussian but smoothly becomes the exponential decay in Eq. (16.35), which explained earlier experimental observations by Mims et al. [51].

16.4.1.3 Within the Track or Spur

The contribution of uniformly-distributed PCs to instantaneous diffusion is multiplied by a similar decay for PCs within the same track or spur. It then becomes necessary to average $V_{ID}(\tau)$ over the $f_{pc}(r)$ for the track or spur in the limit of $p_B < 0.1$ as

$$\begin{aligned} \langle V_{ID}(\tau) \rangle &= e^{-p_B \int_0^\infty f_{pc}(r) \int_0^{\pi/2} (1 - \cos(D_B(r, \theta)\tau)) r^2 \sin(\theta) d\theta dr} \\ &= e^{-p_B \int_0^\infty f_{pc}(r) \langle 1 - \cos(D_B(r, \theta)\tau) \rangle_\theta r^2 dr} \end{aligned} \quad (16.38)$$

This contains the same average in angular brackets encountered in Eq. (16.37). If the functional form of f_{pc} is known, Eq. (16.38) can be evaluated and parameters of the distribution determined, but if f_{pc} is not known, there seems to be limited information available. For small values of τ , the cosine function can be expanded, while for long τ , the term in brackets approaches unity, giving two asymptotic limits. The decay is initially Gaussian, yielding the average dipolar interaction, and at long times becomes constant, giving the number ($N+1$) of PCs ‘in’ the spur or track. For PCs with $g \sim 2.0$, D in MHz and r in nm, the limiting forms are

$$\langle V_{ID}(\tau) \rangle \approx \begin{cases} e^{-p_B 13.3 \tau^2 \int_0^\infty f_{pc}(r) D_{perp}^2 r^2 dr} \rightarrow e^{-p_B 13.3 N \langle D_{perp}^2 \rangle \tau^2}, & \tau \rightarrow 0 \\ e^{-p_B \int_0^\infty f_{pc}(r) r^2 dr} \rightarrow e^{-p_B N}, & \tau \rightarrow \infty \end{cases} \quad (16.39)$$

Salikhov et al. [52] place the break between the short- and long-time behavior at the time $t^* = 2.5/D_{perp}$. To observe part of the early, Gaussian decay of Eq. (16.39) in the spin echo with a spectrometer deadtime of 0.1 μ s requires $D_{perp} < 4$ MHz ($r > 2.5$ nm for $g \sim 2.0$ PCs). To reach the constant, long-time limit by $\tau = 10$ μ s requires $D_{perp} \gg 0.04$ MHz ($r < 10$ nm). Instantaneous diffusion actually probes a narrow distance range of roughly 2.5–10 nm which is similar to the diameter of spurs and tracks.

16.4.1.4 Other Spectral Diffusion

Instantaneous diffusion represents the limit in which dipolar interactions change only as a result of the second microwave pulse. The opposite limit occurs when p_B approaches zero and spectral diffusion occurs by spin relaxation of the B spins.

‘ T_1 ’ Samples

The S_z component of a B spin is part of the dipolar interaction and can change through spin-lattice relaxation. The rate W_B is assumed to be the same for all B spins of the same type. The echo response for an A spin coupled to a relaxing B spin can be calculated using Eq. (16.30) with $p_B = 0$. The response reaches limiting cases for W_B much smaller or much larger than the dipolar interaction. The echo decays at W_B for large dipolar interactions while there is ‘motional averaging’ or decoupling of the dipolar interaction for $W_B \gg D_B$.

$$V_{pair,B}(\tau) = \left[\cosh(R_B \tau) + \frac{W_B}{R_B} \sinh(R_B \tau) \right]^2 + \frac{D_B^2}{4R_B^2} \sinh^2(R_B \tau) \right] e^{-2W_B \tau}$$

$$= \begin{cases} e^{-2W_B \tau}, & W_B \ll D_B \\ e^{-2\frac{D_B^2}{8W_B} \tau}, & W_B \gg D_B \end{cases} \quad (16.40)$$

The echo decay for a sample can be derived as in Eqs. (16.34 and 16.35) for a uniform distribution to give

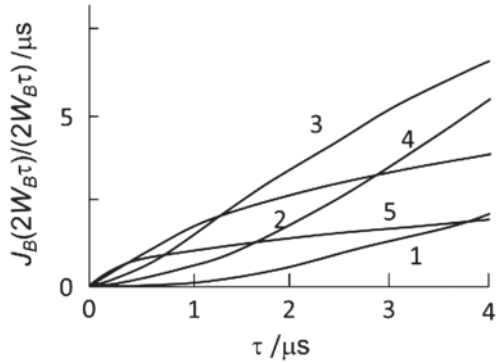
$$\langle V_{SD}(\tau) \rangle = e^{-\frac{9\sqrt{3}}{4\pi^2} \alpha C \frac{J_B(2W_B \tau)}{2W_B}} \quad (16.41)$$

The J_B function has been derived and experimentally verified a number of times [1, 43, 45, 53–55]. For τ in the range of 0.4–4.0 μs , $J_B(2W_B \tau)/(2W_B)$ is largely linear, giving a nearly exponential decay for $\langle V_{SD} \rangle$ although the slope does vary, Fig. 16.4. The asymptotic forms are known along with the limiting decay functions.

$$J_B(2W_B \tau) = \begin{cases} \frac{16\pi^2}{9\sqrt{3}} W_B^2 \tau^2, & W_B \tau \ll 1 \\ \frac{16\pi^2}{9\sqrt{3}} W_B \sqrt{\frac{\tau}{\pi W_B}}, & W_B \tau \gg 1 \end{cases}$$

$$\langle V_{SD}(\tau) \rangle = \begin{cases} e^{-2\alpha C W_B \tau^2}, & W_B \tau \ll 1 \\ e^{-2\alpha C \sqrt{\frac{\tau}{\pi W_B}}}, & W_B \tau \gg 1 \end{cases} \quad (16.42)$$

Fig. 16.4 Plot of $J_B(2W_B\tau)/(2W_B)$ versus τ for various values of W_B : 1) $0.3 \times 10^5 \text{ s}^{-1}$, 2) $1.25 \times 10^5 \text{ s}^{-1}$, 3) $5.0 \times 10^5 \text{ s}^{-1}$, 4) $2.0 \times 10^6 \text{ s}^{-1}$, 5) $8.0 \times 10^6 \text{ s}^{-1}$



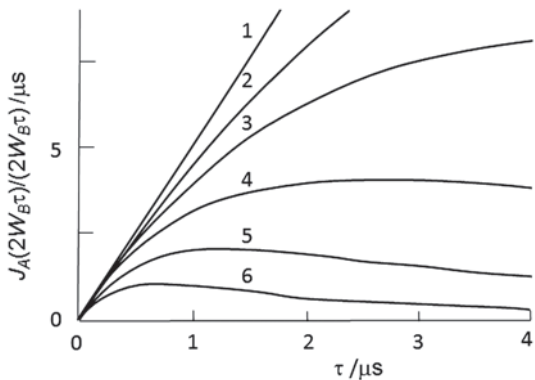
Determining a non-uniform distribution is a challenge. The two limits in Eq. (16.40) show that distant B spins do not contribute to the echo decay while all close B spins make precisely the same contribution. Fortunately, the transition between these two regions occurs rather abruptly. Calculations by Raitsimring and Salikhov [3] suggest that the transition occurs over a change in distance of only a factor of two. They suggest that the echo intensity at large $W_B\tau$ measures the fraction of A spins which lacks a nearby B spin with $D_B > W_B$. This effect enables estimation of f_{pc} for PCs in pairs or small clusters by systematic variation of $W_B\tau$.

The echo decay caused by spectral diffusion was calculated for a uniform distribution with finite p_B [3, 45]. An additional term appears in Eq. (16.41) (Fig. 16.5).

$$\langle V_{SD}(\tau) \rangle = e^{-\frac{9\sqrt{3}}{4\pi^2} \alpha C \frac{J_B(2W_B\tau) + p_B J_A(2W_B\tau)}{2W_B}}$$

$$J_A(2W_B\tau) = \begin{cases} \frac{16\tau^2}{9\sqrt{3}} W_B\tau, & W_B\tau \ll 1 \\ 0, & W_B\tau \gg 1 \end{cases} \quad (16.43)$$

Fig. 16.5 Plot of $J_A(2W_B\tau)/(2W_B)$ versus τ for various values of W_B : 1) 0 s^{-1} , 2) $0.625 \times 10^5 \text{ s}^{-1}$, 3) $1.25 \times 10^5 \text{ s}^{-1}$, 4) $2.5 \times 10^5 \text{ s}^{-1}$, 5) $5.0 \times 10^5 \text{ s}^{-1}$, 6) $1.0 \times 10^6 \text{ s}^{-1}$



For irradiated samples with more than one type of B spin, there are different $\langle V_{SD} \rangle$ for each type which are all multiplied together, each with its appropriate values of C , W and p .

‘ T_2 ’ Samples

Spin relaxation is considerably more complicated in solid samples of dilute PCs than in the simple Bloch equation model [56]. S_z can change by a mutual flip-flop with another nearby PC having the opposite value of S_z . This is often called spin diffusion since it involves the migration of a spin but not the PC, however in the context of spectral diffusion measurements, it is often referred to as a T_2 event. The flip-flops are made possible by dipolar and exchange interactions so their rate is strongly dependent on the distance between the two PCs involved. Typically there will be a broad distribution of flip-flop rates in a sample, because each PC does not have the same distribution of PCs around it. In these ‘ T_2 ’ samples the decay of the A spins depends on the distribution of B spins around it AND the distribution of PCs around the B spins, in other words, third-order correlation functions. Because each flip-flop involves two B spins, their dipolar interactions with the observed A spin are not uncorrelated which further complicates the calculation of $\langle V_{SD} \rangle$.

Calculations have been made for these ‘ T_2 ’ samples for a uniform distribution of B spins, resulting in an equation for $\langle V_{SD} \rangle$ analogous to Eq. (16.43) with J_A and J_B replaced by Q_A and Q_B [3, 45]. The derivations of Q_A and Q_B use a phenomenological distribution for W_B that is uncorrelated with D values and the distribution of PCs, and also does not account for correlations between terms appearing in both Q_A and Q_B .

16.4.1.5 Spectral Diffusion Kernel

The stimulated echo is produced by three microwave pulses with a separation of τ between the first pair and T between the second and third pulses, Fig. 16.3b. The stimulated echo appears τ following the final pulse and its normalized intensity is represented as $V(\tau, T)$. Mims [43, 57] noted that for ‘ T_1 ’ samples for $W_B \tau$ and $W_B T \ll 1$, the Fourier transform of $V(\tau, T)/V(\tau)$ is the spectral diffusion kernel, $K_{SD}(\Delta\omega, T)$.

The spectral diffusion kernel indicates how much the EPR frequency of a PC has changed in the time T [58]. A slice from K_{SD} taken at $T \ll 1/W_B$ gives the spectrum of dipolar interactions which could be deconvoluted to give f_{pc} . Such an approach would be expected to work best for relatively small clusters of PCs. This experimental approach was used by Kulik et al. [59] as the basis for the RIDME method which has been applied to PC pairs in biological systems [60–68].

16.4.2 Cross Relaxation

Dipolar interactions between PCs can produce a change in S_z in one or both PCs. When this results in flip-flops among PCs of the same type it is called spin diffusion. But if it is between distinctly different PCs, particularly if one has a fast spin-lattice relaxation rate, it is often called cross relaxation. Both phenomena can be extremely complex, depending on the EPR spectra of both PCs, T_1 , T_2 and the interaction D_B .

A common situation is where B spins are a different type of PC with rapid T_1 and act as a relaxation sink. The A spins are excited or inverted by a microwave pulse and their relaxation is monitored in time. There are two important limiting cases. One occurs when spin diffusion among the A spins is much faster than cross relaxation to the B spin relaxation sink. The A spin relaxation is exponential. On the other hand, when spin diffusion is negligible, the rate of cross relaxation for each A spin is proportional to its strongest D_B^2 . If the f_{pc} between A and B spins is uniform, relaxation of the A spins has the well-known kinetics for any dipolar-mediated quenching: $\exp[-(k t)^{1/2}]$. If the sample is composed of dilute pairs of PCs, there is some possibility of extracting f_{pc} [69, 70] although uncertainty as to the angular dependence of cross relaxation can complicate matters [71].

16.4.3 Experimental Studies

An early focus of the electron spin echo spectrometer at the Institute of Chemical Kinetics and Combustion in Novosibirsk, Russia was the study of relaxation and spatial distribution of PCs in irradiated frozen solids. That effort helped develop and validate many of the spin echo methods described here in Sect. 16.4. The experimental work has been reviewed a number of times [1–3]. It is amazing what was accomplished without the sensitivity of modern instruments, without modern computer applications and with analog data taken by hand from chart paper. Considerable information was derived by varying radiation dose and the type of radiation from UV, which could produce only one PC pair per photon, to ^{60}Co γ -rays, which produce a trail of spurs, as well as neutrons and β -, α - and fission particles spanning almost three orders of magnitude in LET.

16.4.3.1 Validation

Detailed investigations of spin-lattice relaxation of hydrogen atoms trapped in amorphous quartz at 77 K have been made [72, 73]. At sufficiently low hydrogen atom concentrations, the main echo decay is due to T_1 . The spin-lattice relaxation kinetics of the hydrogen atoms is $\exp(-a t^{1/2})$. There is a distribution of spin-lattice relaxation times caused by cross relaxation to a fast relaxing PC in the quartz. The most probable value of T_1 for hydrogen atoms is 2×10^{-2} s at 77 K and about 100 s at

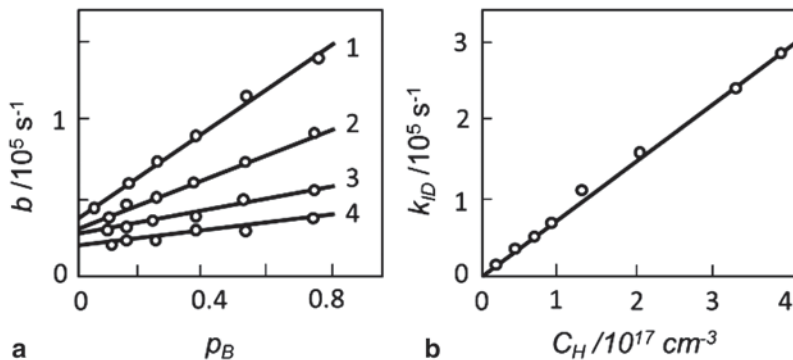


Fig. 16.6 **a** The p_B dependence of the echo decay rate b of hydrogen atoms for various concentrations of hydrogen atoms in γ -irradiated fused quartz at 77 K: (1) $3.8 \times 10^{17} \text{ cm}^{-3}$, (2) $2.0 \times 10^{17} \text{ cm}^{-3}$, (3) $0.9 \times 10^{17} \text{ cm}^{-3}$, (4) $0.5 \times 10^{17} \text{ cm}^{-3}$, **b** Instantaneous diffusion rate k_{ID} versus the hydrogen atom concentration. The slope is α

4.2 K. Because of weak interaction between hydrogen atoms and the lattice, instantaneous diffusion should be the main mechanism of two pulse ESE signal decay.

The two-pulse echo decay of hydrogen atoms trapped in glassy quartz at 77 K was studied at various hydrogen atom concentrations and p_B . The EPR spectrum consists of two lines separated by the hyperfine coupling of 50.5 mT, each line having a linewidth at 77 K of 0.03 mT. Either hydrogen line could be uniformly excited. The spin echo decay kinetics for hydrogen atoms are described by the simple exponential function

$$\begin{aligned} V(\tau) &= e^{-2\tau b(C_H)} = e^{-2\tau \left(b_0 + \frac{p_B}{2} k_{ID} \right)} \\ &= e^{-2\tau b_0} e^{-2\tau \frac{p_B}{2} \alpha C_H} \end{aligned} \quad (16.44)$$

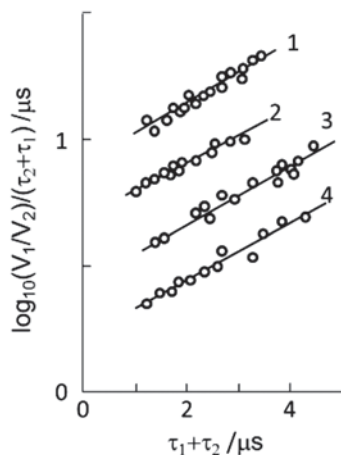
C_H is the hydrogen atom concentration in the sample and α was found to be $8 \times 10^{-13} \text{ C}_H \text{ cm}^3 \text{ s}^{-1}$, where p_B is calculated for one and not both of the hydrogen atom lines, introducing the factor of 1/2. The decay rates are plotted in Fig. 16.6 and show that the echo decay is caused by instantaneous diffusion from a uniform distribution of hydrogen atoms.

Two types of PCs, H atoms and SO_4^- ion radicals, are stabilized at 77 K in irradiated solutions of 8 M sulfuric acid. The two-pulse spin echo decay of the hydrogen atoms [74] is

$$V(\tau) = e^{-2\tau b - m\tau^2} \quad (16.45)$$

The experimental data falls on a straight line when it is plotted in special coordinates, providing good evidence for the validity of Eq. (16.45). The values of m were determined from the slopes of the straight lines, and the values for b were obtained from the intercepts (Fig. 16.7).

Fig. 16.7 Kinetics (linear plot) of hydrogen atom spin echo decay in irradiated sulfuric acid at 77 K for various hydrogen atom concentrations (cm^{-3}): (1) $2.4 \times 10^{18} \text{ cm}^{-3}$, (2) $2 \times 10^{17} \text{ cm}^{-3}$, (3) $2.2 \times 10^{17} \text{ cm}^{-3}$, (4) $2 \times 10^{17} \text{ cm}^{-3}$. V_1 and V_2 are the amplitudes of the ESE signal corresponding to the times τ_1 and τ_2



The $\exp(-m \tau^2)$ term in the decay is indicative that nuclear spin diffusion among the matrix protons contributes significantly. The parameter m is independent of the PC concentrations and equals $2.6 \times 10^{11} \text{ s}^{-2}$. This is in good agreement with the theoretical values and m depends on the matrix proton concentration as $m = 7 \times 10^{-35} \text{ cm}^6 \text{ s}^{-2} C_{\text{proton}}^2$ in the 8 M H_2SO_4 .

The SO_4^- ion radicals in the frozen γ -irradiated sulfuric acid solutions were investigated [45] over a wide range of concentrations and temperature. The main contribution to their echo decay at low concentrations ($\sim 10^{17} \text{ cm}^{-3}$) is from nuclear spin diffusion and from their own spin-lattice relaxation. This system can be regarded a ' T_1 '-sample. At high concentrations of $\text{SO}_4^- (> 5 \times 10^{18} \text{ cm}^{-3})$ an additional decay component appeared, corresponding quantitatively to the spectral diffusion of Eq. (16.43).

These studies were conducted at high doses where the overlap of spurs and hydrogen atom diffusion before trapping was expected to produce a uniform distribution. In fact, the shapes of the decays are those expected for a uniform distribution. The echo decay could be measured over the limited range of $\tau \sim 0.3\text{--}5 \mu\text{s}$. At shorter τ , the echo was obscured by the ringing of the cavity and switching transients and at longer τ , the echo had decayed into the noise. The expected drop in f_{pc} at short distances would be apparent only during the $0.3 \mu\text{s}$ deadtime. These measurements confirmed the theory for echo decay caused by instantaneous diffusion and by spectral diffusion in ' T_1 ' and to a lesser extent ' T_2 ' samples.

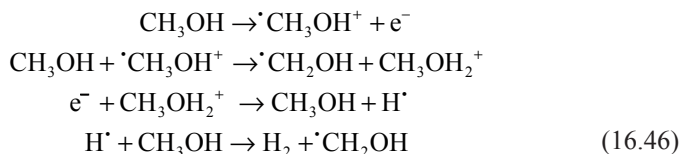
16.4.3.2 Track Structure in Methanol

Several systems were then studied at low dose to determine the point at which spurs and tracks failed to overlap and the spatial distributions were no longer uniform. These were easiest using particles to irradiate the samples rather than X- or γ -rays because the higher concentrations of PCs within particle tracks provided better

Table 16.1 Experimental data on radiation-chemical yields, track radii, and local concentrations in irradiated methanol at 77 K

Radiation source	LET (keV/ μm)	G_R (1/100 eV)	$C_{loc} \times 10^{-18}$ (cm^{-3})	R_{tr} (nm)
β (T)	11	5.5	2.5	9
${}^6\text{Li}(n, \alpha)\text{T}$	160	2.6	7	13
${}^{210}\text{Po}(\alpha)\text{Pb}$	200	3.3	8	15.5
${}^{10}\text{B}(n, \alpha){}^7\text{Li}$	430	1.0	7.5	13
${}^{235}\text{U}(n, f)\text{Pr}$	5400	0.2	7.5	18
β (${}^{35}\text{S}$)	10	6	1.7	9

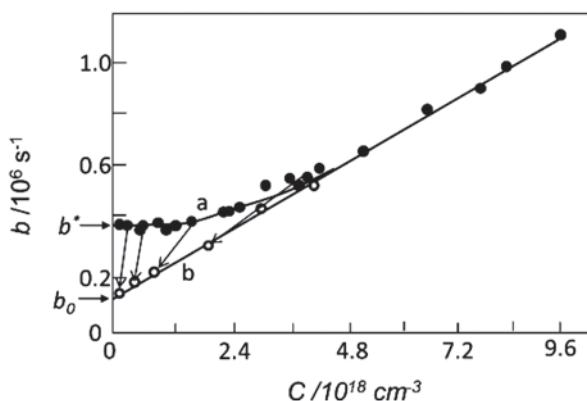
sensitivity. The most detailed studies were carried out for methanol [75–78]. The mechanism of radical formation is well understood in frozen methanol irradiated at 77 K. It is a convenient system for investigation of track effects because it is possible to move radicals from localized tracks to a uniform distribution throughout the volume. The radical formation mechanism in glassy methanol at 77 K is as follows:



Radiation with different linear energy transfer, LET, was used, Table 16.1. Thermal neutron irradiation was carried out in a nuclear reactor. The mean LET for the various sources are included. Small amounts of the corresponding isotopes were dissolved in methanol before freezing as transparent glasses at 77 K, and the echo decay for the CH_2OH radical was investigated. The average radical concentration C_{ave} was determined by CW EPR.

Plots of the echo decay rate b versus the CH_2OH radical C_{ave} during β -irradiation are given in Fig. 16.8 (curve a). At low C_{ave} , b is independent of radical concentration

Fig. 16.8 Concentration dependence of phase relaxation rate of CH_2OH radicals **a** under β -irradiation and **b** after UV photolysis of the irradiated samples. The limiting values of b at $C=0$ are b^* and b_0 for curves **a** and **b** respectively



with a limiting value $b^* = 0.4 \times 10^6 \text{ s}^{-1}$. Above a C_{ave} of about $4 \times 10^{18} \text{ cm}^{-3}$, the decay rate becomes a linear function of concentration for β -irradiation

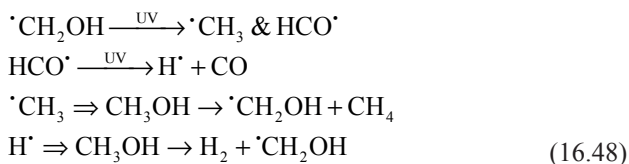
$$b = 0.12 \times 10^6 \text{ s}^{-1} + 1.1 \times 10^{-13} \text{ cm}^3 \text{ s}^{-1} C_{ave} \quad (16.47)$$

The C_{ave} of CH_2OH radicals is linear over the range of absorbed dose and was used to determine the radiation chemical yield G_R in Table 16.1.

Similar experiments were performed with the other types of radiation. The dependence of the echo decay rate on C_{ave} always has the same form characteristic of track spatial inhomogeneity. At small C_{ave} , up to the point of overlapping tracks, the decay rate is constant. With further dose increases, the dependence becomes linear, with the slope expected for a uniform spatial distribution of PCs at the concentration C_{ave} . Only in the case of neutron irradiation was the linear region not observed. The value of $b^* = 0.88 \times 10^6 \text{ s}^{-1}$ was large and the small absorbed dose would not have reached the linear region.

The results of these experiments indicate a non-uniform spatial distribution of radicals. Independent experimental corroboration of such a distribution was obtained by studying the echo decay of the CH_2OH radicals after UV photolysis of the irradiated samples.

It is well known that UV light decomposes CH_2OH radicals into CH_3 , H, and CO [79]. The methyl radicals and hydrogen atoms are unstable in an alcohol matrix at 77 K because they diffuse and react with each other and with the alcohol molecules. This results in the formation of new CH_2OH radicals but with some decrease in their numbers relative to the initial CH_2OH radicals:



The diffusion indicated by the thick arrow must decrease the initial inhomogeneity of their spatial distribution. If irradiated samples are illuminated by UV light and then kept in darkness, the spatial distribution of CH_2OH radicals will be more uniform.

Experiments with UV light exposure were performed as part of the echo decay measurements. Typical results are shown, Fig. 16.8b, for β -irradiation. The arrows show changes in C_{ave} and echo decay rate for CH_2OH radicals in particular samples following UV photolysis and extended storage in darkness. As expected, the echo decay rate became linear with C_{ave} over the entire concentration range and corresponds to a uniform distribution of PCs.

The results allowed one to determine C_{loc} in methanol irradiated by various types of ionizing particles. For a random radical distribution, the dipolar interactions contribute $1.1 \times 10^{-13} \text{ cm}^3/\text{s} C_{ave}$ to the spin echo decay rate, Eq. (16.47). Therefore, for a uniform spatial distribution of radicals inside the tracks, the C_{loc} is given by

$$C_{loc} = \frac{b^* - b_0}{1.1 \times 10^{-13}} \text{ cm}^3 \text{ s} \quad (16.49)$$

Here b^* is the decay rate for C_{ave} (doses) in the initial flat region, Fig. 16.8, where track effects are observed, and b_0 is the y-axis intercept from the linear region. The C_{loc} calculated in this way are listed in Table 16.1.

The geometrical dimensions of the tracks are estimated from C_{loc} . Suppose that the tracks are cylindrical with a radius R_{tr} and a length L equal to the path of the ionizing particle, then

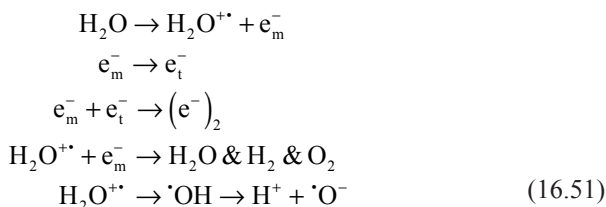
$$R_{tr} = \sqrt{\frac{G_R \cdot LET}{100\pi C_{loc}}} \text{ cm}^3 \text{ s} \quad (16.50)$$

C_{loc} and R_{tr} in methanol irradiated by various types of particles are summarized in Table 16.1. The track structure has been studied by similar methods in other polar compounds irradiated by high-LET particles at low temperatures [75].

16.4.3.3 Detailed Track Structure

The mechanism of CH_2OH radical formation, Eq. (16.46), shows that there are two types of initial damage species produced. One arises from the primary electron. The other from the positive charge or hole, in the case of methanol, the CH_3OH^+ radical cation. But in methanol the electrons and holes produced a single trapped radical product CH_2OH , making it impossible to know the precise origin of the radical being measured. The experiments measure a single mean value for the track radius. Yet, one can argue that radical tracks may have different radii for electron versus hole products if the mobility of their precursors differ, i.e. R_{tr}^- and R_{tr}^+ . This issue was hotly debated in the development of radiation chemistry starting from the early 1950s, for example [80–82]. Detailed track structure from spin echo studies helped resolve the issue.

Two PCs are stabilized in irradiated alkaline glasses at 77 K: trapped electrons (e_t^-) and oxygen radical ions (O^-), produced by a simple sequence of reactions.



Here the t and m subscripts indicate trapped and mobile electrons and $(e^-)_2$ is the di-electron [83, 84]. The spatial distribution of e_t^- is a result of the path length of mobile

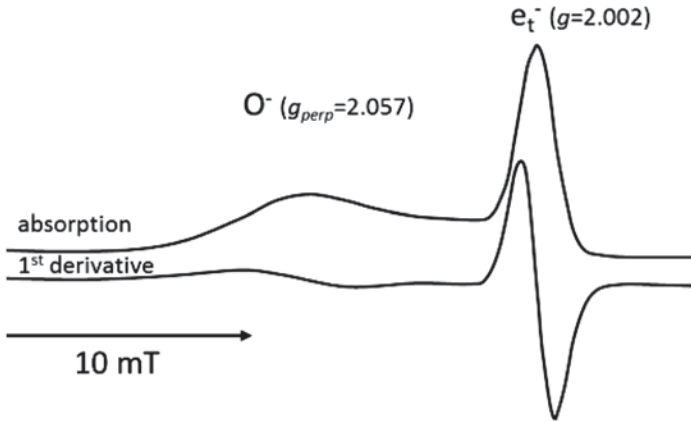


Fig. 16.9 EPR absorption and first-derivative EPR spectra of trapped electrons, e_t^- , and O^- radical ions in γ -irradiated 9M NaOH at 77 K

e_m^- formed in the initial ionization process before they are thermalized and trapped. The O^- radical ions are formed by the last sequence of reactions in Eq. (16.51) which may be preceded by hole transfers from H_2O^+ to H_2O . These reactions allow hole migration through the medium and ultimately determine the spatial distribution of the trapped O^- radical ions. The EPR spectra of O^- and e_t^- overlap negligibly because of the difference in their g -factors, Fig. 16.9. The echo decay of these PCs can be measured separately. Thus there was the possibility to separately study O^- and e_t^- spatial distributions. Frozen solutions of 9 M NaOH were γ -irradiated or doped with small amounts of tritiated water, T_2O , for β -irradiation [85]. The echo decay rate was determined for e_t^- at 77 K and for O^- ion radicals at 77 and 4.2 K.

Instantaneous diffusion is the principal route of echo decay for these PCs. The temperature dependence on the rate for O^- radical ions indicates that it is a ' T_1 '-type sample with $W \leq 10^3 \text{ s}^{-1}$ at 4.2 K. The e_t^- echo decay rate is described by Eq. (16.45) but for O^- by

$$V(\tau) = e^{-2\tau b - a\tau^3} \quad (16.52)$$

The nuclear spin diffusion terms m and a are independent of C_{ave} of the PCs, and the difference in the echo decay kinetics might be caused by different local nuclear environments around e_t^- and O^- . In both cases b depends on p_B and the concentration of PCs. The effect of spatial inhomogeneity was observed only for O^- in β -irradiated samples, Fig. 16.10. The echo decay rates coincide for e_t^- in β - and γ -irradiated samples. The slope of the straight line, Fig. 16.10, gives the value of $\alpha = (6 \pm 2) \times 10^{-13} \text{ cm}^3/\text{s}$, Eq. (16.35), for e_t^- and $7.2 \times 10^{-13} \text{ cm}^3/\text{s}$ for O^- which are close to the theoretical value of $8.2 \times 10^{-13} \text{ cm}^3/\text{s}$ for a uniform distribution of PCs.

The departure from linearity for O^- in β -irradiated samples makes it possible to determine C_{loc} for O^- in a β -track from $b^*/\alpha = 2 \times 10^{18} \text{ cm}^{-3}$, where b^* is the echo decay rate in the region where b is independent of C_{ave} for O^- . Such a C_{loc} corresponds

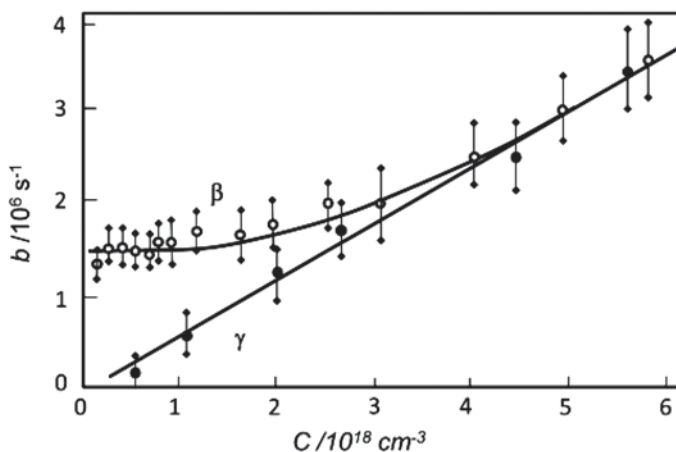


Fig. 16.10 Plots of echo decay rate b vs C_{ave} of O^- radical ions in γ - and β -irradiated samples

to $R_{tr} = 7.5$ nm. The e_t^- are uniformly distributed at least for $C_{ave} > 2 \times 10^{17} \text{ cm}^{-3}$. This value indicates $R_{tr} > 20$ nm for the e_t^- . Thus it is clear that the e_t^- and the O^- radical ions are distributed non-uniformly with respect to each other [85] and have different spatial distributions. Since the mean distance between O^- radical ions in a track is about 7.5 nm, the formation of O^- from H_2O^+ would occur after at least 15 hole transfers.

Frozen glassy solutions of sulfuric and phosphoric acids are also systems in which the detailed structure of radical tracks can be obtained by electron spin echo studies. The e_m^- become trapped as hydrogen atoms after they react with H^+ , and the positively-charged holes react with the acid anions, e.g., SO_4^{2-} , after charge migration, producing the corresponding radical ions (SO_4^-). Behavior of the echo decay for γ -irradiated samples of these acids could be described by a uniform spatial distribution of hydrogen atoms and the radical ions even at the lowest doses that could be studied. Therefore the echo decay rate was studied in α - and β -irradiated solutions of 8 M H_2SO_4 and 12 M H_3PO_4 [86], but we will not describe these studies in detail because the results are similar to those obtained for alkaline glasses. The main results for these systems are summarized in Table 16.2.

The anion PCs resulting from the positively charged H_2O^+ holes are localized in a region with a radius of about 7 nm, while the trapped electrons or hydrogen atoms, with mobile electrons as precursors, are localized in much larger volumes with radii exceeding 20 nm.

It is much more difficult to distinguish electron and hole products in organic matrices because the products are PCs with very similar, overlapping spectra or, as in the case of methanol, Eq. (16.46), the products are identical. The use of electron scavengers can allow determination of the spatial distribution of electron and hole products. The β -radiolysis of 1 M solutions of cadmium perchlorate $Cd(ClO_4)_2$ in methanol results in two types of PCs: Cd^+ ions with mobile or trapped electrons as precursors

Table 16.2 Radiation-chemical yields, local concentrations, and track radii in methanol and in aqueous acid and alkaline solutions irradiated at 77 K

Solution	PC	Radiation	G_R (1/100 eV)	$C_{loc} \times 10^{-17}$ (cm ⁻³)	R_{tr} (nm)
8 M H ₂ SO ₄	H	$\beta(^3\text{H})$	2.0	<2	>20
	H	$\alpha(^{110}\text{Po})$	0.85	~10	~25
	SO ₄ ⁻	$\beta(^3\text{H})$	2.0	15	6.5
	SO ₄ ⁻	$\alpha(^{110}\text{Po})$	1.7	120	10
12 M H ₃ PO ₄	H	$\alpha(^{110}\text{Po})$	0.46	~4	~30
	PO ₄ ⁻	$\alpha(^{110}\text{Po})$	1.1	110	8.5
8 M NaOH	e _t ⁻	$\beta(^3\text{H})$	2.7±0.3	<2	>20
	O ⁻	$\beta(^3\text{H})$	3.7±1	20	7.5
Methanol	Cd ⁺	$\beta(^3\text{H})$		25	>13
	holes	$\beta(^3\text{H})$		25	2.5

and CH₂OH radicals with CH₃OH⁺ as precursors. Their EPR spectra overlap only partially. Cd⁺ has an asymmetric doublet that overlaps the CH₂OH radical spectrum but is approximately six times more intense. The low-field portion of the CH₂OH spectrum is free of overlap. It is possible to make echo decay measurements for each PC due to the large differences in their EPR signal intensities at different fields.

Within experimental error of 30–40%, in β - or γ -irradiated samples, equal amounts of Cd⁺ and CH₂OH are formed with radiation-chemical yields of 2.5×10^{-2} eV⁻¹ in β -irradiated and 3×10^{-2} eV⁻¹ in γ -irradiated samples [87]. The dipolar interactions, the local concentrations and the track radii were determined for each PC from the echo decay rates. Measurements in the β -irradiated samples were made at 4.2 K at concentrations of 10^{17} – 10^{19} cm⁻³. The echo decay kinetics for both PCs is described by Eq. (16.45) for uniform distributions of paramagnetic centers. But in contrast to systems that really have a uniform distribution, the decay rate for CH₂OH in β -irradiated samples is constant up to $C_{ave} \sim 2.5 \times 10^{18}$ cm⁻³. For larger C_{ave} , the decay becomes linear with C_{ave} ; with the same slope obtained for uniform CH₂OH distribution. The hole products are trapped in spatially restricted regions—the tracks of ionizing particles with $R_{tr} = 2.5$ nm in β -irradiated methanol. The local concentration of Cd⁺ ions is apparently so low that the dipolar interaction for their track cannot be measured. Estimations of the minimum radius gives $R_{tr} > 13$ nm for the electron products in methanol. These results may be considered a direct verification of models for the structure of ionizing particle tracks in condensed phases that were put forward as far back as 1951 by Lea, Gray, and Platzman [80, 81].

16.4.3.4 Ammonium Tartrate

Instantaneous diffusion of X-irradiated single crystals and powders of ammonium tartrate was studied at room temperature by Brustolon et al. [88]. Irradiated ammonium tartrate has a single long-lived free radical with rather slow relaxation rates at room temperature and has been proposed as a convenient chemical dosimeter. The

rate of echo decay by instantaneous diffusion was exponential and k_{ID} of Eq. (16.35) for different radiation doses was measured by varying p_B . A straight line was fit to a plot of k_{ID} versus radical concentration in single crystals and the distribution of radicals was concluded to be uniform. An extension of this work discussed later in Sect. 16.5.3 found that at lower doses, k_{ID} is constant and corresponds to the C_{loc} of isolated ionization events. If a line going through the origin, consistent with Eq. (16.35) is drawn through the data, then a break appears at low dose similar to those discussed for non-uniform distributions.

Measurements were also made on ammonium tartrate powder at doses above the apparent break in the single crystal response. Again, the k_{ID} could be fit by a straight line that did not pass through the origin. The scatter in the points is much less than for single crystal samples and it is clear that the data is incompatible with a uniform distribution in Eq. (16.35). The empirical data does support the suggestion by Brustolon et al. [88] to measure radical concentration and hence dose from the rate of instantaneous diffusion in powders rather than by quantitative EPR.

16.4.3.5 Other Approaches

Ichikawa et al. [89–91] examined several γ -irradiated solids. Cross relaxation between PCs was extrapolated to zero dose to estimate the cross relaxation between PCs within the same spur. Average local concentrations and spur sizes were consistent with those found by the Kevan group using CW EPR and discussed in Sect. 16.3.3.

The determination of the tail of f_{pc} for PC pairs produced by photolysis [92, 93] or γ -radiation [94] was reviewed by Raitsimring and Salikhov [3]. Metal ions were photolyzed or sulfuric acid solutions were irradiated to produce a free radical trapped near a fast-relaxing PC, creating ‘ T_1 ’ spectral diffusion. The tail of f_{pc} extending beyond 1.7 nm was determined and diffusion of hydrogen atoms during thermal annealing was observed. W_B of the metal ions was too small to enable observation of pairs with distances any smaller than 1.7 nm.

16.4.3.6 Summary

In several studies mentioned here, the kinetics of the echo decay had the form expected for a uniform spatial distribution of PCs, while variation of the dose and C_{ave} indicated an inhomogeneous distribution at low doses. This apparent contradiction arises because of the small window of distances that contribute to the observed decay. One can expect that within the spur or track radius, the f_{pc} is fairly constant and corresponds to the C_{loc} derived from the instantaneous diffusion. There is good consistency among the number of PCs in the sample, C_{loc} and the size of the tracks. PCs formed by low-mobility holes lie in a track with radii of 2.5 nm (frozen methanol) to 8.5 nm (frozen acid glasses) around the path of β -particles. Electrons or mobile hydrogen atoms in the same samples have track radii at least 13–30 nm.

Much of the uncertainty in the size of the track of electron products results from the low doses necessary for their measurement and the limited sensitivity of pulsed EPR spectrometers when the measurements were made.

16.5 Pulsed Dipolar Spectroscopy

The spin echo based measurements of distance distributions discussed in Sect. 16.4 are a major advance over CW measurements because refocusing of inhomogeneous broadening allows more precise measurement of dipolar interactions. Yet, a number of other effects still are present in the intrinsic echo decay $V_{int}(T_M, \tau)$ of Eq. (16.29). V_{int} is often a non-exponential or even non-monotonic decay that must be separated from V_{SD} based on variation of the decay with dose, temperature or p_B . Errors in separating these two contributions to the total echo decay propagate into f_{pc} .

Just as the spin echo is able to ‘refocus’ inhomogeneous broadening, pulse sequences for pulsed dipolar spectroscopy, PDS, ‘refocus’ the intrinsic decay that is unrelated to dipolar interactions. Most PDS methods belong to a class of constant time measurements in which an echo is measured, but delay times, such as τ and T , are kept constant so that V_{int} remains constant. One family of techniques has its roots in double resonance spectroscopy [13] while the other is known as double quantum coherence or DQC spectroscopy [95].

16.5.1 DEER

The most common electron double resonance experiment, known as DEER or PELDOR [13, 49, 96–98], uses two different microwave frequencies while a variant known as the ‘2+1’ sequence uses only one frequency [47]. They are, in fact, two limiting cases of the same technique. The ‘2+1’ sequence is suited for measurements on a single type of PC with a narrow EPR spectrum while DEER is ideal for two kinds of PCs with very different EPR spectra.

The three-pulse DEER experiment generates a spin echo from A spins using a pair of pulses at one microwave frequency, ω_A , with a fairly large τ . A pulse at a second microwave frequency, ω_B , is applied at a time τ' between the two detection pulses, Fig. 16.3c. In the simple model of DEER with $W_B=0$, the detection pulses only excite A spins while the pump pulse only excites B spins. The intrinsic decay V_{int} of the A spins does attenuate the echo, but does not change during a DEER measurement with constant τ . For $\tau'=0$, the dipolar interaction between A and B spins is refocused, but as τ' increases from 0 to τ , the dipolar interaction suddenly shifts the EPR frequency of the A spins, causing abrupt ‘instantaneous’ spectral diffusion.

$$V(\tau) = V_{int}(T_M, \tau) V_{Dip}(\tau')$$

$$\langle V(\tau) \rangle \approx \langle V_{int}(T_M, \tau) \rangle \langle V_{Dip}(\tau') \rangle \quad (16.53)$$

Virtually every analysis of DEER data is based on the ability to factor the dipolar response, and its averages, from all other effects, Eq. (16.53). The dipolar interaction impacts the signal only during τ' , as V_{Dip} , while the intrinsic decay V_{int} is totally independent of dipolar interactions and occurs only during τ . The echo intensity for an A spin interacting with several B spins is related to $V_{\text{pair,B}}$ of Eq. (16.31).

$$V_{\text{Dip}}(\tau') = \prod_i V_{\text{pair,B}_i}(\tau') \quad (16.54)$$

The same averaging in Eqs. (16.33–16.39) for instantaneous diffusion applies as long as V_{int} does not depend on dipolar interactions and Eq. (16.53) holds. There is a four-pulse variant of DEER, Fig. 16.3d, that overcomes practical problems when two microwave pulses overlap at $\tau'=0$ [99].

This simple model provides an easily-understood picture of how DEER works and why distance distributions can be derived from it. Unfortunately this simple model often does not correspond to the actual experiment. The detection pulses typically excite B spins and the pump pulse excites A spins. These possibilities have long been recognized in ‘2+1’ measurements [46, 47] where the pump and detection pulses have the same frequency, but have just been considered in detail for three-pulse DEER [52] and remain to be dealt with in four-pulse DEER.

When the second detection pulse at ω_A excites B spins, the DEER response depends not just on $\cos(D\tau')$, but also on $\cos(D\tau)$ and $\cos(D(\tau-\tau'))$ [52]. This last term is significant only when the B spin is excited by pulses at both frequencies. This term may be neglected under normal conditions when the difference of the two mw frequencies is large compared to the mw field strength. Then the $\cos(D\tau')$ term may be recovered as $\cos(D\tau') = [V(\tau') - V(\infty)]/[V(0) - V(\infty)]$. In general, even if τ is constant during a measurement, the DEER signal cannot be separated, as implied in Eq. (16.53), into a V_{int} term independent of dipolar couplings and a V_{Dip} term depending only on dipolar-driven spectral diffusion during τ' . A partial solution to this problem lies in the careful selection of pump and detection parameters [100] or having p_A and $p_B \ll 1$ for A and B spins for both ω_A and ω_B . However, unless $W\tau \ll 1$, B spin relaxation and flip-flops still prevent the clean separation of terms in Eq. (16.53) [52].

16.5.1.1 Uniform Distribution

Equation (16.53) applies in the limit of $W \sim 0$ and with selective pump and detection pulses that only excite the desired PCs, and the DEER signal in Eq. (16.54) has the same form as Eq. (16.34) for instantaneous diffusion if τ is replaced by τ' . Equation (16.54) allows the DEER decay to be broken into products of decays from conveniently chosen sets of PCs. The distinction often made for instantaneous diffusion studies is quite appropriate: a background decay from a uniform distribution of B spins belonging to different spurs or tracks and a decay from B spins within the same spur or track. The uniform distribution of B spins produces an exponential

decay in Eq. (16.35). The decay rate is proportional to p_B and can be made arbitrarily slow, but the DEER signal decays smoothly to zero.

The DEER decay is derived from averages of $\cos(D\tau')$ which is symmetrical around $\tau'=0$. The decay in a four-pulse DEER from a uniform distribution is also symmetric and should have a peak with a sharp corner at $\tau'=0$. Any departure from a uniform distribution at short distances caused by excluded volume [101], recombination or tunneling will round off this peak and make it smoother, but still symmetric. This part of the decay can be experimentally measured with DEER but it is lost in the deadtime in spin echo measurements. DEER has much smaller deadtime because the pump pulse can be placed adjacent to the detection pulses in three-pulse DEER for a deadtime of approximately the pulsewidth, while four-pulse DEER lacks even this restriction. The smallest values of τ' provide data on the largest dipolar interactions and the shortest PC separation distances. A number of reviews consider the DEER decay from free radicals distributed uniformly in various dimensions [13, 49, 98] which may be relevant to damage at surfaces or to extended polymers.

16.5.1.2 Within the Track or Spur

The decay from PCs within the same spur or track is given by the same averages as for $\langle V_{ID} \rangle$, Eqs. (16.38 and 16.39), which require p_A and $p_B \ll 1$. An important advantage of DEER relative to instantaneous diffusion measurements is the lack of deadtime which can reveal the initial decay in Eq. (16.39) that is important for determining the number of PCs in the spur and the dipolar second moment. This is the same distance range where the uniform distribution assumption fails. Fortunately it is possible to disentangle them because the intra-spur or track contributions to the DEER decay are independent of dose while the contribution from PCs in different spurs or tracks depends linearly with dose, at least initially.

DEER has been applied to the determination of PC cluster sizes and spatial distributions in several areas including radiation chemistry, structural biology and polymers. A critical examination of both abilities was made using a series of bi-, tri-, and tetra-radicals by Bode et al. [101]. Counting the number of PCs in a cluster rests on the difference in DEER decay for a finite cluster versus a uniform distribution. The cluster has a decay rate that is not linear with p_B and the DEER intensity for small p_B reaches a non-zero limiting value at long τ' [13, 102]. Bode et al. [101] successfully counted the number of radicals when only a single compound was present. In mixtures of mono- through tetra-radicals, average numbers of spins per radical were obtained for DEER data with high signal to noise ratios.

In multi-radicals, each pair of spins produces DEER modulation and the distance between spins can be determined at low p_B . The relative amplitudes for different inter-spin distances did not match the structure of the multi-radicals [101] and was ascribed, in part, to the use of analysis software designed only for pairs of PCs. This study has some relevance to measurement of f_{pc} for systems with more than pairs of PCs and it does support an earlier measurement of multiple inter-spin distances by Bowman et al. [103] in end-to-end stacks of spin-labelled RNA duplexes.

16.5.2 DQC

Double Quantum Coherence spectroscopy or DQC [104, 105] uses a double quantum filter to ensure that only the dipolar evolution of PCs is measured. In its usual implementation, DQC uses a single microwave frequency and requires the PCs to have relatively narrow EPR spectra. One advantage relative to DEER is that there is no signal background from isolated PCs, which have no double quantum coherence. DQC works well with pairs of PCs, but larger clusters would appear to produce responses with sums and differences of dipolar interactions. These combinations of dipolar interactions are suppressed in instantaneous diffusion and DEER measurements in the $p_B \ll 1$ limit, but this remedy does not seem to be practical in DQC. However, development of rigorous filtering and rejection of higher-order coherences may make such techniques applicable beyond the realm of pairs of PCs.

16.5.3 Experimental Studies

One of the first applications of DEER was the study of semiquinone radical—deuterium atom pairs formed by photolysis of hydroquinone in frozen solutions of deuterated sulfuric acid [106]. The deuterium atom was rapidly thermalized and trapped in close proximity to the semiquinone radical. Strong DEER signals indicated pairs of PCs relatively isolated from each other. The f_{pc} was extracted from this data in the original paper [106] and later by a more exact procedure [107]. The f_{pc} in both analyses has a peak near 4 nm with a shoulder between 6 and 9 nm before tailing to zero at long distances. The f_{pc} falls sharply to zero at distances less than about 1.5 nm.

Kurshev et al. [46] used the ‘2+1’ sequence (DEER with only one microwave frequency) to determine the distribution of pairs of hydroxyalkyl radicals produced by photolysis of frozen acidic solutions of deuterated alcohols. They obtained good fits to the data for a f_{pc} proportional to $\exp[-(r/r_c)^6]$ for a set of alcohols with 1–4 carbons. The value of r_c ranged from 6.5 to 7.2 nm across these alcohols. This f_{pc} is roughly a uniform distribution to r_c where it drops to zero. The r_c determined by the ‘2+1’ sequence are 0.6–1.3 nm larger than those measured in γ -irradiated protiated alcohols by Ichikawa et al. [90] using a cross relaxation method. It is significant that both sets of data were fit with the same functional form of f_{pc} . This relatively flat f_{pc} seems consistent with the uniform distributions found in instantaneous diffusion measurements where the decays were primarily caused by PCs at distances shorter than r_c .

DEER was used by Bowman et al. [108] to probe the spatial distribution of PCs in DNA irradiated at 77 K to doses of 1.7–50 kGy by heavy-ion beams of 100 MeV per nucleon ^{40}Ar ions having an LET of 300–400 keV/ μm . These ions produce dense tracks of damage in their wake with extensive recombination of PCs. At these doses, the tracks are well separated from each other and the samples had superimposable DEER spectra. Smoothly-decaying DEER spectra were measured over

a range of p_B that varied by a factor of 12. At the smaller values of p_B , the signal intensity reached an asymptotic value that allowed determination of the number N of PCs contributing to the DEER decay. The rate at which it approached the asymptote gave the local concentration of those PCs. Unfortunately, p_B was incorrectly calculated and is underestimated, leading to an overestimation of N and local concentration. This error is partly offset when the track radius is calculated. A global fit of all samples and data reported $N \sim 18$, $C_{loc} \sim 13.5 \times 10^{19}$ PC cm⁻³ and a track radius of 6.8 nm. These numbers were consistent with the known LET and radiation chemical yield.

Marrale et al. [109] extended the instantaneous diffusion study of irradiated polycrystalline ammonium tartrate with a study that includes DEER and γ -, neutron- and 19.3 MeV proton-irradiation. A careful examination of k_{ID} following up [88] for each radiation type ensured that the DEER reflected spatial distribution of a single ionization event. This appears to be the first case reported of DEER decays in irradiated materials showing pronounced modulation that was not traced to nuclear modulation (ESEEM) artifacts [98]. The resolved modulation was assigned to radicals being trapped at the sites of molecules within the crystal structure. Unfortunately, these remarkable DEER spectra were not shown. The f_{pc} extracted from the DEER data lies almost entirely between 2.0 and 5.5 nm with ripples corresponding to translations of the unit cell. This distribution was reproduced very closely by detailed simulations incorporating the crystal structure and anisotropic recombination. The observed and simulated differences in PC distribution with different types of radiation were suggested as providing a way to determine LET of unknown radiation by using the ammonium tartrate dosimeter.

16.6 Future Prospects

The main advantage of pulsed EPR is the removal of the inhomogeneous broadening of EPR lines and the removal of decay not caused by dipolar interactions. This reveals the dipolar width and, therefore, opens new possibilities to detect non-uniform spatial distribution of PCs in radical tracks and spurs. The two-pulse ESE is the simplest and most direct experimental approach to these problems but DEER holds greater potential.

The two-pulse spin echo spectroscopy has its limitations. In analyzing ESE data in order to get dipolar broadening, it is necessary to subtract the other relaxations and spin dynamics effects that appear in the two-pulse echo decay, such as spectral diffusion, nuclear-spin diffusion and ESEEM. This is not a simple task as one pushes sensitivity to probe large structures. DEER provides a much cleaner signal free from many of the competing decays, but at the price of a significant loss of sensitivity. Fortunately sensitivity continually increases as a result of advances in microwave and magnet technology coupled with digital control and data acquisition. Many of these advances are now being driven by the use of DEER in structural biology where spectacular sensitivity has been achieved with high-field pulsed EPR.

Currently, the theoretical basis to extract spatial distributions from DEER has significant gaps, particularly for treating the higher-order correlations needed in spectral diffusion of ' T_2 '-samples and for extracting f_{pc} when there is more than a single pair of PCs involved. But both issues affect the application of DEER in fields beyond radiation chemistry. Likewise, the spatial distribution of PCs is often correlated with the spatial inhomogeneity of the sample and may be a major opportunity for new applications of pulsed EPR studies. The interaction of plasmas with surfaces and nanomaterials; radiation chemistry at interfaces; and the distribution of electrons and holes in nanoparticles used for energy conversion provide new challenges and opportunities that can be addressed by well-designed EPR studies.

References

1. Salikhov KM, Semenov AG, Tsvetkov YD (1976) Electron spin echoes and their applications. Nauka, Novosibirsk
2. Salikhov KM, Tsvetkov YD (1979) Electron spin echo studies of spin-spin interactions in solids. In: Kevan L, Schwartz RN (eds) Time domain electron spin resonance. Wiley, New York, pp 231–278
3. Raitsimring AM, Salikhov KM (1985) Electron spin echo method as used to analyze the spatial distribution of paramagnetic centers. Bull Magn Reson 7(4):184–217
4. Weil JA, Bolton JR, Wertz JE (2007) Electron paramagnetic resonance elementary theory and practical applications, 2nd edn. Wiley-Interscience, New York
5. Schweiger A, Jeschke G (2001) Principles of pulse electron paramagnetic resonance. Oxford University Press, Oxford
6. Bowman MK (2011) Pulsed methods in electron spin resonance. In: Meyers RA (ed) Encyclopedia of analytical chemistry, vol S1–S3. Wiley, Chichester, pp 1548–1572
7. Brustolon M, Giannello E (2009) Electron paramagnetic resonance—a practitioner's toolkit. Wiley, Hoboken
8. Bedilo AF, Maryasov AG (1995) Electron spin resonance of dipole-coupled anisotropic pairs in disordered systems. Secular approximation for point dipoles. J Magn Reson Ser A 116:87–96
9. Abragam A, Bleaney B (1986) Electron paramagnetic resonance of transition ions. Dover, New York
10. Maryasov AG, Bowman MK, Tsvetkov YD (2006) Dipole-dipole interactions of high-spin paramagnetic centers in disordered systems. Appl Magn Reson 30(3–4):683–702
11. Abragam A (1961) The principles of nuclear magnetism. The international series of monographs on physics. Clarendon, Oxford
12. Yudanov VF, Salikhov KM, Zhidomirov GM, Tsvetkov YD (1969) Modulation effects in the electron spin echo of biradical systems. Teor Eksp Khim 5:663–668
13. Milov AD, Maryasov AG, Tsvetkov YD (1998) Pulsed electron double resonance (PELDOR) and its applications in free-radicals research. Appl Magn Reson 15(1):107–143
14. Jeschke G (2002) Determination of the nanostructure of polymer materials by electron paramagnetic resonance spectroscopy. Macromol Rapid Comm 23(4):227–246. doi:10.1002/1521-3927(20020301)23:4<227::Aid-Marc227>3.0.Co;2-D
15. Weber A, Schiemann O, Bode B, Prisner TF (2002) PELDOR at S- and X-band frequencies and the separation of exchange coupling from dipolar coupling. J Magn Reson 157(2):277–285. doi:10.1006/jmre.2002.2596
16. Pshchetskii SY, Kotov AG, Milinchuk VK, Roginskii VA, Tupikov VI (1974) EPR of free radicals in radiation chemistry. Halsted Press, New York

17. Kurita Y (1964) Electron spin resonance study of radical pairs trapped in irradiated single crystals of dimethylglyoxime at liquid-nitrogen temperature. *J Chem Phys* 41(12):3926–3927. doi:10.1063/1.1725837
18. Gordy W, Morehouse R (1966) Triplet-state electron spin resonance of an H-atom-methyl-radical complex in a solid matrix. *Phys Rev* 151(1):207–210. doi:10.1103/PhysRev.151.207
19. Lebedev YS (1966) Radical pairs in photolytic decomposition of azobisisobutyronitril as investigated by ESR method. *Dokl Akad Nauk SSSR* 171(2):378–381
20. Steinhoff HJ (2004) Inter- and intra-molecular distances determined by EPR spectroscopy and site-directed spin labeling reveal protein-protein and protein-oligonucleotide interaction. *Biol Chem* 385(10):913–920. doi:10.1515/Bc.2004.119
21. Rabenstein MD, Shin YK (1995) Determination of the distance between 2 spin labels attached to a macromolecule. *Proc Natl Acad Sci U S A* 92(18):8239–8243. doi:10.1073/pnas.92.18.8239
22. Vincow G, Johnson PM (1963) Second moments of electron spin resonance proton hyperfine spectra. *J Chem Phys* 39(5):1143–1153. doi:10.1063/1.1734404
23. Bales BL, Helbert J, Kevan L (1974) Electron-paramagnetic resonance and electron-nuclear double resonance line shape studies of trapped electrons in gamma-irradiated deuterium-substituted 10 M sodium-hydroxide alkaline ice glass. *J Phys Chem* 78(3):221–231. doi:10.1021/J100596a006
24. Mikhailov AI, Lebedev YS (1967) Evaluation of local concentrations of free radicals in irradiated solids from the change in the EPR line widths. *Khimiya Vysokikh Energii* 1(4):397–399
25. Castner TG (1959) Saturation of the paramagnetic resonance of a V-center. *Phys Rev* 115(6):1506–1515. doi:10.1103/PhysRev.115.1506
26. Portis AM (1953) Electronic structure of *F* centers: saturation of the electron spin resonance. *Phys Rev* 91(5):1071–1078
27. Kevan L, Kispert LD (1976) *Electron spin double resonance spectroscopy*. Wiley, New York
28. Weger M (1960) Passage effects in paramagnetic resonance experiments. *Bell Labs Tech J* 39(4):1013–1112
29. Thomas DD, Dalton LR, Hyde JS (1976) Rotational diffusion studied by passage saturation transfer electron-paramagnetic resonance. *J Chem Phys* 65(8):3006–3024. doi:10.1063/1.433512
30. Sczaniecki PB, Hyde JS, Froncisz W (1990) Continuous wave multi-quantum electron-paramagnetic resonance spectroscopy. *J Chem Phys* 93(6):3891–3898. doi:10.1063/1.458775
31. Zimbrick J, Kevan L (1966) Paramagnetic relaxation of trapped electrons in irradiated alkaline ices. *J Am Chem Soc* 88(15):3678–3679. doi:10.1021/Ja00967a059
32. Zimbrick J, Kevan L (1967) Paramagnetic relaxation of trapped electrons in irradiated alkaline ices. *J Chem Phys* 47(7):2364–2371. doi:10.1063/1.1703319
33. Zimbrick J, Kevan L (1967) Paramagnetic relaxation of trapped hydrogen atoms in irradiated frozen aqueous solutions. *J Chem Phys* 47(12):5000–5008. doi:10.1063/1.1701751
34. Zimbrick J, Kevan L (1967) Paramagnetic relaxation of trapped hydrogen atoms in irradiated frozen solutions. *Nature* 214(5089):693. doi:10.1038/214693a0
35. Hase H, Kevan L (1969) Paramagnetic relaxation of radiation-produced electrons in annealed glassy and polycrystalline alkaline ices. *J Phys Chem* 73(10):3290–3293. doi:10.1021/J100844a024
36. Chen DH, Kevan L (1969) Paramagnetic relaxation of trapped electrons in gamma-irradiated organic glasses. *Mol Cryst Liq Cryst* 9:183–196. doi:10.1080/15421406908082738
37. Bales BL, Kevan L (1970) Paramagnetic relaxation of silver species in gamma-irradiated frozen aqueous solutions. *J Chem Phys* 52(9):4644–4653. doi:10.1063/1.1673697
38. Lin DP, Kevan L (1971) Paramagnetic relaxation study of spatial distribution of trapped electrons in gamma-irradiated organic glasses. *J Chem Phys* 55(6):2629–2635. doi:10.1063/1.1676470

39. Lin DP, Kevan L, Hamlet P (1972) Paramagnetic relaxation study of spatial-distribution of trapped radicals in gamma irradiated alkaline ice and organic glasses at 4.2 degrees K. *J Phys Chem* 76(8):1226–1227. doi:10.1021/J100652a024
40. Lin DP, Kevan L (1972) Optical bleaching effects on paramagnetic relaxation of trapped electrons in methyltetrahydrofuran at 77 degrees K. *J Phys Chem* 76(5):636–639. doi:10.1021/J100649a004
41. Hase H, Feng DF, Bowman MK, Kevan L (1975) On the applicability of slow passage EPR relaxation theories to saturation curves for trapped electrons in organic glasses. *Chem Phys Lett* 30(2):204–207
42. Hahn EL (1950) Spin echoes. *Phys Rev* 80(4):580–594
43. Mims WB (1972) Electron spin echoes. In: Geschwind S (ed) *Electron paramagnetic resonance*. Plenum, New York, pp 263–352
44. Klauder JR, Anderson PW (1962) Spectral diffusion decay in spin resonance experiments. *Phys Rev* 125(3):912–932. doi:10.1103/PhysRev.125.912
45. Salikhov KM, Dzuba SA, Raitsimring AM (1981) The theory of electron spin-echo signal decay resulting from dipole-dipole interactions between paramagnetic centers in solids. *J Magn Reson* 42(2):255–276
46. Kurshev VV, Raitsimring AM, Ichikawa T (1991) Spatial-distribution of free-radicals in gamma-irradiated alcohol matrices determined by the 2 + 1 electron-spin echo method. *J Phys Chem* 95(9):3564–3568. doi:10.1021/J100162a025
47. Kurshev VV, Raitsimring AM, Tsvetkov YD (1989) Selection of dipolar interaction by the 2 + 1 pulse train ESE. *J Magn Reson* 81(3):441–454
48. Mims WB (1972) Envelope modulation in spin-echo experiments. *Phys Rev B-Solid St* 5(7):2409–2419. doi:10.1103/PhysRevB.5.2409
49. Tsvetkov YD, Milov AD, Maryasov AG (2008) Pulse electron-electron double resonance (PELDOR) as nanometre range EPR spectroscopy. *Usp Khim* 77(6):515–550
50. Abramowitz M, Stegun IA (1964) *Handbook of mathematical functions with formulas, graphs, and mathematical tables*. U.S. Govt. Print. Off., Washington, DC
51. Mims WB, Nassau K, Mcgee JD (1961) Spectral diffusion in electron resonance lines. *Phys Rev* 123(6):2059–2069. doi:10.1103/PhysRev.123.2059
52. Salikhov KM, Khairuzhdinov IT, Zaripov RB (2014) Three-pulse ELDOR theory revisited. *Appl Magn Reson* 45(6):573–619. doi:10.1007/s00723-014-0541-7
53. Raitsimring AM, Salikhov KM, Umanskii BA, Tsvetkov YD (1974) Instantaneous diffusion in electron-spin echo of paramagnetic centers stabilized in solid matrices. *Fiz Tverd Tela* 16(3):756–766
54. Hartmann SR, Hu P (1974) Theory and support for an uncorrelated-sudden-jump model of spectral diffusion decay. *J Magn Reson* 15(2):226–233. doi:10.1016/0022-2364(74)90074-2
55. Hu P, Hartmann SR (1974) Theory of spectral diffusion decay using an uncorrelated-sudden-jump model. *Phys Rev B* 9(1):1–13. doi:10.1103/Physrevb.9.1
56. Bloch F (1946) Nuclear induction. *Phys Rev* 70(7-8):460–474
57. Mims WB (1968) Phase memory in electron spin echoes lattice relaxation effects in CaWO_4 -Er, Ce, Mn. *Phys Rev* 168(2):370–389. doi:10.1103/PhysRev.168.370
58. Brown IM (1979) Electron spin echo studies of relaxation processes in molecular solids. In: Kevan L, Schwartz RN (eds) *Time domain electron spin resonance*. Wiley, New York, pp 195–229
59. Kulik LV, Dzuba SA, Grigoryev IA, Tsvetkov YD (2001) Electron dipole-dipole interaction in ESEEM of nitroxide biradicals. *Chem Phys Lett* 343(3-4):315–324. doi:10.1016/S0009-2614(01)00721-7
60. Savitsky A, Dubinskii AA, Flores M, Lubitz W, Mobius K (2007) Orientation-resolving pulsed electron dipolar high-field EPR spectroscopy on disordered solids: I. Structure of spin-correlated radical pairs in bacterial photosynthetic reaction centers. *J Phys Chem B* 111(22):6245–6262. doi:10.1021/Jp070016c
61. Milikisyants S, Scarpelli F, Finiguerra MG, Ubbink M, Huber M (2009) A pulsed EPR method to determine distances between paramagnetic centers with strong spectral anisotropy and

- radicals: the dead-time free RIDME sequence. *J Magn Reson* 201(1):48–56. doi:10.1016/j.jmr.2009.08.008
62. Astashkin AV, Elmore BO, Fan WH, Guillemette JG, Feng CJ (2010) Pulsed EPR determination of the distance between Heme iron and FMN centers in a human inducible nitric oxide synthase. *J Am Chem Soc* 132(34):12059–12067. doi:10.1021/ja104461p
 63. Savitsky A, Dubinskii AA, Zimmermann H, Lubitz W, Mobius K (2011) High-field dipolar electron paramagnetic resonance (EPR) spectroscopy of nitroxide biradicals for determining three-dimensional structures of biomacromolecules in disordered solids. *J Phys Chem B* 115(41):11950–11963. doi:10.1021/Jp206841v
 64. Milikisyants S, Scarpelli F, Finiguerra M, Ubbink M, Huber M (2011) Distances between paramagnetic metal centers and spin labels in proteins by pulsed EPR: the RIDME method as a new tool. *Biophys J* 100(3):143–143
 65. Zaripov RB, Dzhabarov VI, Knyazev AA, Galyametdinov YG, Kulik LV (2011) Use of additional fast-relaxing paramagnetic species for improvement of RIDME performance. *Appl Magn Reson* 40(1):11–19. doi:10.1007/s00723-010-0170-8
 66. Astashkin AV, Rajapakshe A, Cornelison MJ, Johnson-Winters K, Enemark JH (2012) Determination of the distance between the Mo(V) and Fe(III) Heme centers of wild type human sulfite oxidase by pulsed EPR spectroscopy. *J Phys Chem B* 116(6):1942–1950. doi:10.1021/Jp210578f
 67. Savitsky A, Niklas J, Golbeck JH, Mobius K, Lubitz W (2013) Orientation resolving dipolar high-field EPR spectroscopy on disordered solids: II. Structure of spin-correlated radical pairs in photosystem I. *J Phys Chem B* 117(38):11184–11199. doi:10.1021/Jp401573z
 68. Konov KB, Knyazev AA, Galyametdinov YG, Isaev NP, Kulik LV (2013) Selective hole-burning in RIDME experiment: dead-time free measurement of dipolar modulation. *Appl Magn Reson* 44(8):949–966. doi:10.1007/s00723-013-0464-8
 69. Kulikov AV, Likhtenstein GI (1977) The use of spin relaxation phenomena in the investigation of the structure of model and biological systems by the method of spin labels. *Adv Mol Relax Interact Process* 10(1):47–79
 70. Likhtenshtein GI (2000) Depth of immersion of paramagnetic centers in biological systems. In: Berliner LJ, Eaton GR, Eaton SS (eds) *Distance measurement in biological systems by EPR. Biological magnetic resonance*, vol 19. Kluwer, New York, pp 309–345
 71. Bowman MK, Norris JR (1982) Cross relaxation of free radicals in partially ordered solids. *J Phys Chem* 86(17):3385–3390
 72. Milov AD, Salikhov KM, Tsvetkov YD (1972) Spin-lattice relaxation of hydrogen-atoms and paramagnetic ions in glassy aqueous-solutions of sulfuric-acid at 77 degrees K. *Fiz Tverd Tela* 14(8):2211–2215
 73. Milov AD, Salikhov KM, Tsvetkov YD (1972) Spin diffusion and kinetics of spin-lattice relaxation of hydrogen-atoms in glassy matrices at 77 degrees K. *Fiz Tverd Tela* 14(8):2259–2264
 74. Milov AD, Salikhov KM, Tsvetkov YD (1973) Spin diffusion and kinetics of spin-lattice relaxation of hydrogen-atoms in glassy matrices at 77 degrees K. *Fiz Tverd Tela* 14(8):1956–1960
 75. Raitsimring AM, Moralev VM, Tsvetkov YD (1973) Spatial distribution and yields of radicals formed under the action of radiations with LET of 1–600 eV/A in certain polar compounds. *Khimiya Vysokikh Energii* 7(2):125–128
 76. Raitsimring AM, Pomytkin AP, Tsvetkov YD (1970) Space distribution of radicals during g-irradiation of methanol at 77 K. *Khi Vys Energ* 4(4):369–370
 77. Tsvetkov YD, Raitsimring AM (1970) Electron spin echo technique for spatial radical distribution investigation in irradiated solid substances: influence of let and spur effects. *Radiat Eff* 3(1):61–64. doi:10.1080/00337577008235617
 78. Raitsimring AM, Tsvetkov YD, Moralev VM (1973) LET-effects on free-radical yields and spatial-distribution in irradiated methanol—investigation by means of ESR and ESE methods. *Int J Radiat Phys Chem* 5(3):249–269

79. Shelimov BN, Fok NB, Voevodsky VV (1963) The photochemical decomposition of alcohols at low temperatures: the kinetics of the decomposition of methyl alcohol. *Kinet Katal* 4(4):539–548
80. Gray LH (1952) The energy transfer from ionizing particles to an aqueous medium and its bearing on the interpretation of radiochemical and radiobiological change. *J Cell Physiol Suppl* 39(Suppl 1):57–74
81. Fröhlich H, Platzman RL (1953) Energy loss of moving electrons to dipolar relaxation. *Phys Rev* 92(5):1152–1154. doi:10.1103/PhysRev.92.1152
82. Magee JL, Burton M (1951) Elementary processes in radiation chemistry. II. Negative ion formation by electron capture in neutral molecules 1,2,3. *J Am Chem Soc* 73(2):523–532. doi:10.1021/ja01146a006
83. Zimbrick J, Kevan L (1967) Evidence for trapped dielectrons in ice. *J Am Chem Soc* 89(10):2483–2484. doi:10.1021/Ja00986a043
84. Kevan L, Renneke DR, Friauf RJ (1968) Optical absorption spectrum of trapped dielectrons in alkaline ice. *Solid State Commun* 6(7):469–471 doi:10.1016/0038-1098(68)90057-4
85. Raitsimring AM, SamoiloVA RI, Moralev VM, Tsvetkov YD (1976) Spatial distribution of trapped electrons and O⁻ in b- and g-irradiated NaOH glasses at 77 K. In: Hedvig P, Schiller R (eds) Proceedings of the fourth Tihany symposium on radiation chemistry. Akadémiai Kiadó, Budapest, pp 691–700
86. Raitsimring AM, Moralev VM, Tsvetkov YD (1975) Electron-spin echo study of detailed track structure in irradiated frozen aqueous-solutions of sulfuric and phosphoric acids. *High Energy Chem* 9(6):449–454
87. SamoiloVA RI, Raitsimring AM, Tsvetkov YD (1980) The structure of radical tracks in methanol irradiated by tritium beta-particles. *Radiat Phys Chem* 15(4):553–559. doi:10.1016/0146-5724(80)90070-9
88. Brustolon M, Zoleo A, Lund A (1999) Spin concentration in a possible ESR dosimeter: an electron spin echo study on X-irradiated ammonium tartrate. *J Magn Reson* 137(2):389–396. doi:10.1006/jmre.1998.1671
89. Ichikawa T, Yoshida H (1984) Spatial-distribution of paramagnetic entities in gamma-irradiated 2-methyltetrahydrofuran glass as studies by the electron-spin echo method. *J Phys Chem* 88(15):3199–3203. doi:10.1021/J150659a013
90. Ichikawa T, Wakasugi S, Yoshida H (1985) Structure of spurs in gamma-irradiated alcohol matrices determined by electron spin-echo method. *J Phys Chem* 89(16):3583–3586. doi:10.1021/J100262a032
91. Ichikawa T, Kawahara S, Yoshida H (1985) Local-distribution of alkyl radicals in gamma-irradiated polyethylene studied by electron-spin echo method. *Radiat Phys Chem* 26(6):731–737. doi:10.1016/0146-5724(85)90115-3
92. Dzuba SA, Raitsimring AM, Tsvetkov YD (1979) Distance distribution of radical-paramagnetic ion-pairs studied by the electron-spin echo method-spatial regularities of radical diffusion in glassy alcohols. *Chem Phys* 44(3):357–365. doi:10.1016/0301-0104(79)85219-2
93. Kononov VV, Dzyuba SA, Raitsimring AM, Salikhov KM, Tsvetkov YD (1980) Spatial-distribution of hydrogen in ion-atom pairs formed by the photolysis of frozen acidic solutions of chromium and iron ions. *High Energy Chem* 14(6):406–411
94. Dzyuba SA, Raitsimring AM, Tsvetkov YD (1981) Range distribution of cation-electron pairs formed in the gamma-radiolysis of a vitrified solution of sulfuric-acid. *High Energy Chem* 15(1):30–34
95. Borbat P, Freed JH (1999) Multiple-quantum ESR and distance measurements. *Chem Phys Lett* 313:145–154
96. Maryasov AG, Tsvetkov YD, Raap J (1998) Weakly coupled radical pairs in solids: ELDOR in ESE structure studies. *Appl Magn Reson* 14(1):101–113
97. Jeschke G, Polyhach Y (2007) Distance measurements on spin-labelled biomacromolecules by pulsed electron paramagnetic resonance. *Phys Chem Chem Phys* 9(16):1895–1910. doi:10.1039/B614920k

98. Jeschke G (2012) DEER distance measurements on proteins. *Annu Rev Phys Chem* 63(1):419–446. doi:10.1146/annurev-physchem-032511-143716
99. Pannier M, Veit S, Godt A, Jeschke G, Spiess HW (2000) Dead-time free measurement of dipole-dipole interactions between electron spins. *J Magn Reson* 142(2):331–340
100. Raitsimring A, Peisach J, Lee HC, Chen X (1992) Measurement of distance distribution between spin labels in spin-labeled hemoglobin using an electron-spin echo method. *J Phys Chem* 96(8):3526–3531
101. Bode BE, Margraf D, Plackmeyer J, Durner G, Prisner TF, Schiemann O (2007) Counting the monomers in nanometer-sized oligomers by pulsed electron-electron double resonance. *J Am Chem Soc* 129(21):6736–6745. doi:10.1021/Ja065787t
102. Milov AD, Ponomarev AB, Tsvetkov YD (1984) Modulation beats of signal of double electron-electron resonance in spin-echo for biradical systems. *Zhurnal Strukturnoi Khimii* 25(5):710–713
103. Bowman MK, Maryasov AG, Kim N, DeRose VJ (2004) Visualization of distance distribution from pulsed double electron-electron resonance data. *Appl Magn Reson* 26(1–2):23–39
104. Saxena S, Freed JH (1997) Theory of double quantum two-dimensional electron spin resonance with application to distance measurements. *J Chem Phys* 107(5):1317–1340
105. Borbat PP, Mchaourab HS, Freed JH (2002) Protein structure determination using long-distance constraints from double-quantum coherence ESR: study of T4 lysozyme. *J Am Chem Soc* 124(19):5304–5314. doi:10.1021/Ja020040y
106. Milov AD, Salikhov KM, Shirov MD (1981) Application of ELDOR in electron-spin echo for paramagnetic center spatial distribution in solids. *Fiz Tverd Tela* 23(4):975–982
107. Pusep AY, Shokhirev NV (1984) Application of a singular expansion in the analysis of spectroscopic inverse problems. *Opt Spektrosk* 57(5):792–798
108. Bowman MK, Becker D, Sevilla MD, Zimbrick JD (2005) Track structure in DNA irradiated with heavy ions. *Radiat Res* 163(4):447–454. doi:10.1667/rr3338
109. Marrale M, Brai M, Barbon A, Brustolon M (2009) Analysis of the spatial distribution of free radicals in ammonium tartrate by pulse EPR techniques. *Radiat Res* 171(3):349–359. doi:10.1667/Rr1358.1

Chapter 17

Study of Spin-Correlated Radical Ion Pairs in Irradiated Solutions by Optically Detected EPR and Related Techniques

Vsevolod Borovkov, Dmitri Stass, Victor Bagryansky and Yuriy Molin

Abstract The strong Coulomb attraction and recombination dramatically shorten the lifetime of radical ion pairs generated by ionizing irradiation in organic solutions, which complicates the use of conventional EPR spectroscopy to study these short-lived radical ions. However, the recombination of the oppositely charged ions gives birth to a fluorescence response of the irradiated media. This response appears to depend on the same properties of the radical ions that are studied by EPR spectroscopy. The dependence can be revealed with an external magnetic field, thus allowing a quantitative study of hyperfine couplings, spin-orbit interaction, paramagnetic relaxation times of radical ions, whose lifetime can amount to only a few nanoseconds. In this chapter we consider experimental approaches, both steady-state and time-resolved, which are based on the registration of the fluorescence response influenced by an external magnetic field. These are Optically Detected EPR, MARY (Magnetically Affected Reaction Yield) spectroscopy, and the technique of Time-Resolved Magnetic Field Effect (TR MFE) in recombination fluorescence. A brief history, a theoretical background, methodological details, as well as some unique experimental results obtained with these techniques are discussed.

17.1 Introduction

It is difficult to tell when the chemical effect of radiation on a molecular medium ends, but it begins at the moment when the radiation makes electrons leave the closed electron shells of the molecules forming (super)excited and ionized molecular states. Within several picoseconds a lot of species with open electronic shells appear in the region where an ionizing particle has passed. Some of them have electric charge, some are neutral. Although conventional EPR is generally sensitive to any paramagnetic species, in practice it is only applicable to study neutral radicals that

V. Borovkov (✉) · D. Stass · V. Bagryansky · Y. Molin
V. V. Voevodsky Institute of Chemical Kinetics and Combustion, SB RAS, 3, Institutskaya Str.,
Novosibirsk, Russia
e-mail: borovkov@kinetics.nsc.ru

V. Borovkov · D. Stass · V. Bagryansky
Novosibirsk State University, 2, Pirogova Str., Novosibirsk, Russia

© Springer International Publishing 2014

A. Lund, M. Shiotani (eds.), *Applications of EPR in Radiation Research*,
DOI 10.1007/978-3-319-09216-4_17

escape from the track into the bulk with high probability. Radical ions arising as the pairs of oppositely charged species recombine quite quickly with their partners, with only few of them (several per cent in non-polar solutions) becoming separated by a very large distance. Thus, the Coulomb interaction and recombination dramatically limit the applicability of conventional EPR to study the radiation-generated radical ions in organic solutions.

In this chapter we discuss a somewhat different approach to study such radical ions. It is based on the spin correlation between the partners in a substantial fraction of the recombining radical ion pairs. Experimentally it can be implemented by detecting the luminescence response of the irradiated medium and investigating the effect of an external magnetic field on this response. In this chapter we discuss several ways to develop this approach, including Optically Detected EPR (OD EPR), MARY (Magnetically Affected Reaction Yield) spectroscopy, and the technique of Time-Resolved Magnetic Field Effect (TR MFE) in recombination fluorescence. All these methods share their basic principles with EPR and thus provide information similar to information obtained by magnetic resonance techniques: *g*-values, hyperfine coupling (HFC) constants, paramagnetic relaxation times of the recombining radical ions. For practical use it is important to realize that they have their own, often adjacent, but not fully overlapping, areas of optimal use.

The discussion is arranged as follows: first, we give a very brief historical overview, outline the basic principles of the approach, and provide an overview of the processes in the track of an ionizing particle where radical ion pairs arise and decay. Then, we discuss several key theoretical notions that the techniques rely upon, the experimental implementation of the techniques, and results obtained from the study of various radical ions, including many that were not studied by other techniques. This chapter mostly focuses on results obtained in this century.

17.2 Historical Sketch

The history of the controlled effect of radiation on the matter starts from the discovery of cathode rays [1], X-rays [2], and radioactivity [3]. These very discoveries and the active exploration of the properties of radiation became possible, to a large extent, due to the fact that the radiation-induced luminescence of matter is a widespread phenomenon that can be easily observed by eye.

In the beginning of the XX century it was realized that at least some part of the luminescence comes from the recombination of oppositely charged ions [4, 5]. A little later it was found that the recombination of ions in an irradiated matter can only be described if their pairwise generation is taken into account, which means that their initial spatial correlation is important [6]. Those days, the luminescence itself was interesting to the explorers of radiation primarily as an indicator of the presence of ionizing radiation or as a measure of certain atomic parameters. Only in the 1960-s it was understood that it was ion recombination that produced a considerable fraction of the luminescence response from irradiated organic solutions,

and that the ratio of singlet (S) and triplet (T) states of the excited recombination products was not statistical, i.e., it differed from $S:T=1:3$ [7, 8].

In the milestone work [9] it was proposed that, due to the initial spin correlation in the primary pairs, the relation between the singlet and the triplet-excited states in radiolysis could change with time in a static external magnetic field or a resonance microwave field driving EPR transitions. An applied magnetic field modifies the proportion of singlet and triplet pairs, which was detected experimentally by Brocklehurst et al. [10] as an increasing yield of singlet excited states with a simultaneous decrease of the yield of triplet states. The variations of predicted magnetic field effects in time were found to depend on the hyperfine interactions in the radical ions [11, 12]. This opened the possibility to use the method of Time-Resolved Magnetic Field Effect (TR MFE) in recombination fluorescence to study the properties of the radical ions themselves, more specifically, those of them, whose recombination leads to the excited states of luminescent molecules. Quantum beats driven by the hyperfine interactions in the spin-correlated radical ion pair, the precursor of the excited molecule, were detected in the recombination fluorescence [13]. Very prominent quantum beats driven by the difference in the g -values of the geminate radical ions, the so-called Δg -beats, were also observed [14–16].

The dependence of the integrated yield of singlet excited states on the static external magnetic field strength—the so-called magnetic field effect curve—often has the form of a monotonously rising curve as the magnetic field strength is increased from zero to values much higher than the EPR spectrum width of the radicals [10]. However, it was found [17, 18] that features providing detailed information about both HFC in the radicals and their lifetimes appear in stationary MFE curve.

In 1979, the idea of the effect of the microwave field on the yield of singlet excited states was implemented in the optical detection of the EPR spectra of organic radical ions in a solution irradiated by continuous ionizing radiation [19, 20]. A year later, a time-resolved version of the EPR registration technique named Fluorescence Detected Magnetic Resonance (FDMR) was developed in Argonne National Laboratory (USA) based on a pulsed electron accelerator [21].

The OD EPR technique was used to study the primary charge carriers and the secondary radical ions in irradiated organic solutions [22–25]. Both the experimental method and the theoretical approaches were further developed. This considerably extended the range of objects studied by techniques, which focus on spin-correlated radical ion pairs generated in organic solutions by ionizing irradiation.

17.3 Track Structure and Spin-Correlated Radical Ion Pairs

After an ionizing particle passes through an organic medium, within several picoseconds primary ion pairs are formed consisting of a radical cation (hole) of the matrix/solvent and an excess electron. The ejected electron reaches thermodynamic equilibrium with the medium at a distance of about several nanometers [26].

Typically, radical ion pairs (RIPs) do not arise as isolated objects, and there is a non-zero probability of recombination of the charged species produced by ionization of different molecules. Such RIPs are called non-geminate. It is usually assumed that their recombination produces excited singlet and triplet states in the proportion S:T=1:3. On the contrary, geminate RIPs, originating from the same molecule, can exhibit a non-trivial evolution of the S:T proportion in time, since these RIPs are spin-correlated.

For the approaches discussed in this chapter it is essential that this evolution also depends on the external magnetic field. Thus, the magnitude of the TR MFEs related to spin-correlated RIPs depends on the ionization density. For solutions of aromatic luminophores, the typical TR MFE magnitude decreases from 40% for irradiation with fast electrons to several per cent for irradiation with helium ions [27] in accord with the expected decrease in the fraction of singlet RIPs. In refs [28, 29] similar effect was observed on going from soft X-rays to fast electrons. The maximum amplitude of the TR MFE curves in recombination fluorescence—up to 80%—was observed under synchrotron radiation with quantum energy 15 eV [30]. For 40 eV quanta the effects were comparable to β -electron irradiation, decreasing to about 40%.

A quantitative comparison of the local structure of the radiation track and the degree of the manifestation of spin correlation between the recombining ions can only be performed using computer simulation of the intra-track processes [31–33]. In particular, such simulations show that the ratio of the recombination rates for geminate and non-geminate RIPs in low viscosity liquids only weakly depends on time already after several nanoseconds.

17.4 Theoretical Background

Although the theoretical basis of the method of optically detected EPR is similar to conventional EPR, the application of the other two techniques, TR MFE and MARY, required an essential development to study the spin-correlated RIPs. The principles of spin effects in the reactions of species with open electronic shells were discussed in many works, including several reviews and monographs (e.g., see [34–38] and references therein). The experiments discussed in this chapter are focused on radical ions in non-polar solutions, and the measured value is the fluorescence intensity from the singlet-excited recombination products of RIPs. Such products are believed to arise from the recombination of RIPs in singlet spin state. Any phosphorescence generated upon the recombination of triplet pairs in solutions is either strongly quenched or can be rejected with an optical filter.

Thus, the intensity of the recombination fluorescence $I(t)$ is generally determined by the recombination kinetics $F(t)$ and the singlet state population $\rho_{SS}(t)$ of the radical ion pairs. Importantly, in non-polar solutions the Coulomb interaction is likely to result in equally effective recombination from both singlet and triplet states, independently on the magnetic field. Therefore, for RIP recombination in non-polar

solvents $F(t)$ and $\rho_{SS}(t)$ are believed to be independent, and the experimentally observed kinetics $I(t)$ is given by a convolution involving their product. At any rate, there is no known experimental evidence that contradicts this statement. For a short fluorescence time of the luminophore the convolution turns into a simple product, and $I(t)$ can be represented as follows:

$$I(t) \propto F(t) \cdot \rho_{SS}(t). \quad (17.1)$$

This relationship in turn lets us separate the problem of describing the RIP spin dynamics from the very sophisticated task of calculating the time dependent yield of singlet excited molecules. In this chapter, the Time-Resolved Magnetic Field Effect (TR MFE) is defined as the ratio:

$$\frac{I_B(t)}{I_0(t)} \approx \frac{\rho_{SS}^B(t)}{\rho_{SS}^0(t)}. \quad (17.2)$$

The subscript and superscript B or 0 correspond to the measurements in high or zero magnetic field, respectively.

17.4.1 Evolution of Spin State of Spin-Correlated Radical Ion Pairs

In terms of spin chemistry, the evolution of an ensemble of RIPs proceeds as transitions between S and T states of the pair of unpaired electron spins of the radicals. The quantum beats between these states are driven by various interactions the two electron spins experience. These are, first of all, the interactions with external magnetic fields, either static or oscillating, and HFC with the magnetic nuclei of the radical ions. The interactions between the electron spins of the two organic radicals in a RIP are quite weak and can be neglected. Indeed, the exchange interaction has no effect for a RIP in non-polar solution, as the pairs mostly recombine from a distance of at least 10 Å [39] where these interactions are negligible. Also, due to the fast rotation of radicals in solution, only the isotropic components of both the hyperfine and g-tensors in each radical need to be considered. The fluctuating anisotropic components of the couplings can be accounted for as a contribution to paramagnetic relaxation.

Dynamics of Spin State of a Singlet Born RIP The results of the calculations can be most concisely presented using the density matrix $\hat{\rho}(t)$ of the spin system of the radical pair, as suggested by Schulten and Wolynes [40]. The population $\rho_{SS}(t)$ of the singlet electronic spin state can be obtained using the projection operator $\hat{P}_S = |S\rangle \langle S|$ applied to the density matrix

$$\rho_{SS}(t) = Tr \left\{ \hat{P}_S \hat{\rho}(t) \right\}, \quad (17.3)$$

where Tr is the trace over the electron and nuclear indices. If there is no interaction between the electron spins of the radicals in the RIP, expression (17.3) can be written as

$$\rho_{ss}(t) = \frac{1}{4} + \sum_{i,k} T_{ik}^{(1)}(t)T_{ik}^{(2)}(t), \quad (17.4)$$

in terms of the components of the correlation tensor $T_{ik}^{(1,2)}(t)$

$$T_{ik}^{(1)}(t) = \left\langle Tr_e \left\{ \hat{S}_{1i}(t) \hat{S}_{1k}(0) \right\} \right\rangle, T_{ik}^{(2)}(t) = \left\langle Tr_e \left\{ \hat{S}_{2i}(t) \hat{S}_{2k}(0) \right\} \right\rangle. \quad (17.5)$$

Here, $i, k = \{x, y, z\}$, $\hat{S}_{1,2}(t) = \exp(i\hat{H}_{1,2}t)\hat{S}_{1,2}\exp(-i\hat{H}_{1,2}t)$ are the operators of the electron spins of the RIP partners in the Heisenberg representation, Tr_e is the trace over the electron spin variables, and the brackets mean averaging over the projections of the magnetic nuclei, H_1 and H_2 are the Hamiltonian terms (frequency units) for the interactions in each radical. This approach simplifies the solution of the quantum problem for two nearly isolated sub-systems whose initial state is entangled, and makes it possible to account for different types of interactions in the radicals.

An analytical expression for the components of the correlation tensor (17.5) only exists for several special cases. For an arbitrary magnitude of the magnetic field along the z axis, an exact solution of this problem has only been found for the simplest case of one magnetic nucleus with spin I and HFC constant a [41, 42]. In this case, the components of the tensor are:

$$T_{xx} = T_{yy} = \frac{1}{2} \operatorname{Re} h(t), T_{xy} = -T_{yx} = \frac{1}{2} \operatorname{Im} h(t), T_{zz} = \frac{1}{2} g(t), \quad (17.6)$$

where

$$g(t) = 1 - \frac{a^2}{2I+1} \sum_{m=-I}^I \frac{I(I+1) - m(m+1)}{(2R_m)^2} [1 - \cos(2R_m t)],$$

$$h(t) = \frac{1}{4(2I+1)} \sum_{m=-I}^I [(1+D_m)e^{iR_m t} + (1-D_m)e^{-iR_m t}] [(1+D_{m-1})e^{iR_{m-1} t} + (1-D_{m-1})e^{-iR_{m-1} t}].$$

Here the following notation was used:

$$2R_m = \sqrt{\omega_0^2 + a\omega_0(2m+1) + a^2(I+0.5)^2}, D_m = \frac{\omega_0 + a(m+0.5)}{2R_m}, \text{ and } \omega_0 = \frac{g\beta B}{\hbar}$$

is the Larmor precession frequency of the electron spin in external magnetic field of strength B , β is the Bohr magneton, and \hbar is the Planck constant.

In zero field, the tensor (17.6) becomes diagonal with the non-zero components equal to

$$T_{xx}(t) = T_{yy}(t) = T_{zz}(t) = \frac{4I(I+1) + 3 + 8I(I+1)\cos(a(I+0.5)\cdot t)}{6(2I+1)^2}. \quad (17.7)$$

Expressions (17.6) and (17.7) can be generalized for the case of several magnetic nuclei with equal HFC constants. To this end, these expressions should be averaged over I , the total nuclear spin [42]. In zero field an analytical solution can be obtained, for example, for n spin $\frac{1}{2}$ nuclei with equal HFC constants a [43]:

$$T_{xx}(t) = T_{yy}(t) = T_{zz}(t) = \frac{1}{6} \left[\frac{n+3}{n+1} + \frac{2n(n+2)}{n+1} \left(\cos \frac{at}{2} \right)^{n+1} - 2n \left(\cos \frac{at}{2} \right)^{n-1} \right]. \quad (17.8)$$

In the limit of strong field $B \gg a_n$ an analytical solution exists for an arbitrary set of magnetic nuclei with spins I_n and HFC constants a_n , with the nonzero components of the tensor equal to

$$T_{zz} = \frac{1}{2}, T_{xx} = T_{yy} = \frac{1}{2} \cos(\omega_0 t) G(t), T_{xy} = -T_{yx} = \frac{1}{2} \sin(\omega_0 t) G(t),$$

$$G(t) = \prod_n \left[\frac{1}{(2I_n + 1)} \times \sin \frac{a_n (2I_n + 1) \cdot t}{2} / \sin \frac{a_n t}{2} \right]. \quad (17.9)$$

There is also an analytical solution at $B=0$ [44], although a quite cumbersome one, for two magnetic nuclei with different HFC constants, which can be generalized for two groups of equivalent nuclei.

For many magnetically non-equivalent nuclei with different HFC constants the semiclassical approximation can be used [40]. In this approximation, in the limit of strong field $B \gg \sigma$, where $\sigma^2 = 1/3 \times \sum_n a_n^2 I_n (I_n + 1)$ is the second moment of the EPR spectrum of the radical, the function $G(t)$ in (17.9) takes the form

$$G(t) = \exp(-\sigma^2 t^2 / 2). \quad (17.10)$$

For zero field the semiclassical approximation gives:

$$T_{xx} = T_{yy} = T_{zz} = \frac{1}{6} (1 + 2C(\sigma t)), \text{ where } C(x) = (1 - x^2) \exp(-0.5x^2). \quad (17.11)$$

For an arbitrary magnetic field the expressions for the correlation tensor in the semiclassical approximation are quite cumbersome. These expressions were first provided by Bagryansky et al. [45].

Paramagnetic Relaxation In practice, it is also necessary to take into account paramagnetic relaxation. The simplest phenomenological way to take the relaxation into account is to multiply spin operators $\hat{S}_z(t)$ and $\hat{S}_{x,y}(t)$ by factors $\exp(-t/T_1)$ and $\exp(-t/T_2)$, respectively, where T_1 and T_2 are the longitudinal and the transverse paramagnetic relaxation times [46]. For zero field, assuming $T_1 = T_2 = T_0$, this gives

$$\rho_{ss}(0, t) = \frac{1}{4} + 3e^{-t/T_0} T_{zz}^{(1)}(t) T_{zz}^{(2)}(t). \quad (17.12)$$

For a strong field the expression for $\rho_{ss}(t)$ can be written in compact form using the functions $G(t)$ determined by the relevant expressions (17.9) or (17.10):

$$\rho_{ss}(B, t) = \frac{1}{4} + \frac{1}{4} e^{-t/T_1} + \frac{1}{2} e^{-t/T_2} \cos(\omega_0^{(1)} - \omega_0^{(2)})t \cdot G^{(1)}(t) G^{(2)}(t). \quad (17.13)$$

Here $1/T_{0,1,2}$ is the sum of the corresponding relaxation rates of the two radicals.

Expressions (17.6–17.13) were derived for an isolated singlet-born RIP. In order to apply them for fitting the experimental TR MFE curves, it is usually assumed that the ensemble of RIPs in the track can be divided into two parts. One part consists of those RIPs that are singlet-born spin-correlated pairs, whose spin evolution obeys the above equations, while another part includes uncorrelated RIPs related to cross recombination. This picture is of course only approximate. It is generally not as easy as it might appear to distinguish between spin-correlated and non-correlated recombining ion pairs in an ensemble. Finer effects connected with the transfer of spin polarization between pairs can also be expected [47], although they have not so far been detected experimentally.

In this approximation, the total singlet spin state population of the RIPs is written as $\theta \cdot \rho_{ss}(t) + (1-\theta)/4$ [37], where θ is the fraction of spin-correlated pairs among all of the RIPs, which recombine at a given moment. Although this fraction should generally depend on time, it was demonstrated that for a radiation spur of moderate size it is almost independent on time after the first nanoseconds [32]. In this chapter θ is assumed to be constant.

Examples of TR MFE Curves Figure 17.1 shows several TR MFE curves, i.e., the ratios of singlet state populations (17.2), calculated using Eqs. (17.3–17.13), and several curves for two groups of spin $1/2$ nuclei. Unresolved EPR spectra of the RIP partners with very different widths appear in the TR MFE curve as two different peaks (Fig. 17.1a) at $t(\text{ns})$ of about $9/\sigma(\text{mT})$. The peaks disappear if paramagnetic relaxation is fast enough. If the EPR spectra of both partners are narrow, the rate of the singlet-triplet transitions caused by HFC and the rate of the increase in the TR MFE curve are low, letting observe the Δg -beats in a high enough field.

A HFC with magnetically equivalent nuclei manifests itself as periodic peculiarities with positions in time determined by the HFC constant (Fig. 17.1b).

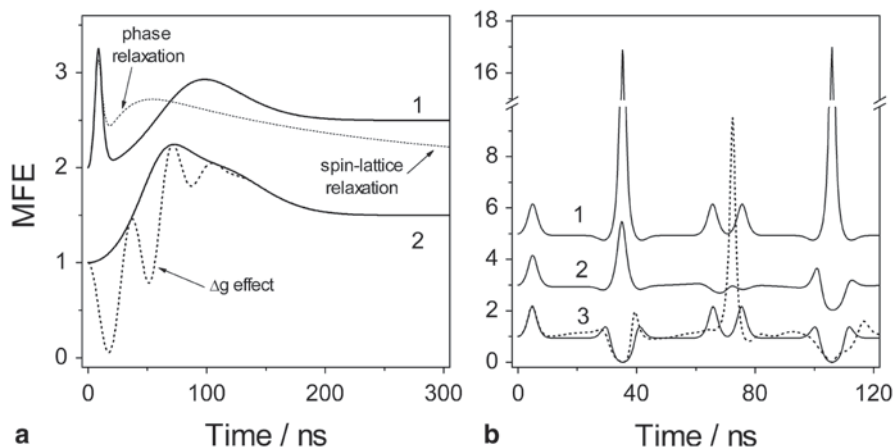


Fig. 17.1 Calculated TR MFE curves for a singlet-born ($\theta=1$) RIP composed of partners with equal g -values in the absence of paramagnetic relaxation (except as otherwise noted). The RIP partners are assumed to either both have unresolved EPR spectrum (**a**) or only one of them has non-zero HFC (**b**). Panel (**a**): $\sigma^{(1)}=1$ mT, $\sigma^{(2)}=0.1$ mT (solid curve 1); the same but $T_1=200$ ns, $T_2=T_0=20$ ns (dashed curve 1); $\sigma^{(1)}=\sigma^{(2)}=0.1$ mT (solid curve 2); the same assuming the difference of g -values $\Delta g=0.002$ for the RIP partners at magnetic field $B=1$ T (dashed curve 2). Panel (**b**): HFC constants with spin $\frac{1}{2}$ nuclei $a(12H)=1$ mT (curve 1); $a(12H)=1$ mT, and $a(1H)=0.5$ mT (curve 2); $a(13H)=1$ mT (solid curve 3); $a(12H)=1$ mT and $a(1H)=-1$ mT (dashed curve 3) calculated using the results reported in ref [44]

The presence of nonequivalent magnetic nuclei changes the relative amplitudes of the peculiarities, peaks or dips. The change also depends on the relative sign of the HFC constants, since the spin state evolution at $B=0$ depends on this sign. A finite paramagnetic relaxation would result in the damping of the peculiarities with time.

The model presented above in Eqs. (17.3–17.13) can be applied with success to describe the experimental TR MFE curves. As an example, Fig. 17.2a shows TR MFE curves for RIPs that have magnetically equivalent nuclei only in one partner, either the radical anion or the radical cation, while the contribution of the other partner to HFC is negligible [42, 48]. Figure 17.2b shows a TR MFE curve for the RIP that is composed of these two radical ions, now both having HFC. A simulation shows that the maxima of the peaks correspond to the moments of time when the population of the singlet state in zero field is low. Since $\rho_{SS}(t)$ is determined by the product of contributions from each partner, the positions of the maxima in case (b) remain approximately the same. We also note that the amplitude of the experimental curve is lower as compared to the theoretical curves shown in Fig. 17.1, because in experiment $\theta < 1$ [29, 31, 33].

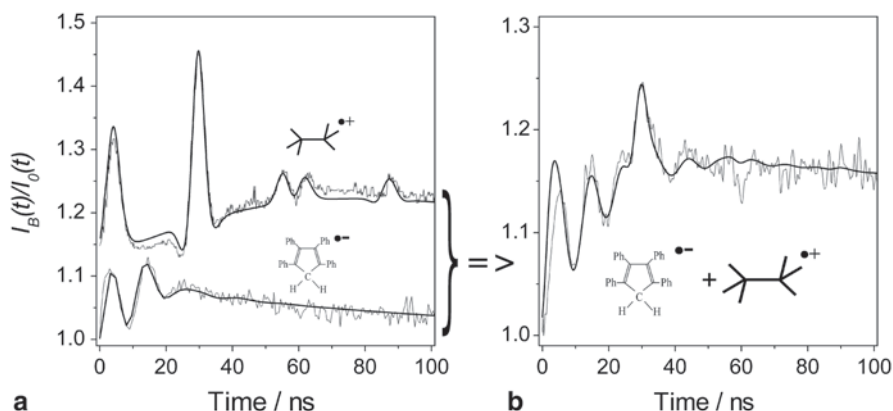


Fig. 17.2 **a** Experimental (noisy) and calculated TR MFE curves for solutions of 0.1 M hexamethylethane (+30 μ M *para*-terphenyl- d_{14}) in *n*-hexane (upper curve, shifted by 0.15) ([42], adapted by permission of the PCCP Owner Societies) and 1 mM tetraphenylcyclopentadiene (TPCP) in *n*-decane (Adapted with permission from [48]. Copyright 1997, Mendeleev Communications). The smooth lines show the results of modeling for $a(18H)=1.22$ mT (the radical cation of hexamethylethane) and $a(2H)=2.5$ mT (the radical anion of TPCP). **b** Experimental (noisy) and calculated TR MFE curves for solutions of 0.1 M hexamethylethane +0.3 mM TPCP in *n*-octane (Adapted from Quantum beats in radical pairs. [38], Copyright 2007, Pleiades Publishing, Ltd). For both panels the temperature is 293 K, $B=0.1$ T

17.4.2 MARY Spectroscopy

The expressions given above can be used to calculate the dependence of the recombination fluorescence intensity on the magnetic field strength in the conditions of continuous generation of radical ion pairs. Such dependences were named Magnetic Field Effect (MFE), or Magnetically Affected Reaction Yield (MARY) spectra (e.g., see [49–51]). For their theoretical description one has to calculate the integral yield of singlet states, $S(B)$, upon the recombination of RIPs:

$$S(B) = \int \rho_{ss}(t, B) \cdot F(t) dt \quad (17.14)$$

Even if $F(t)$ is approximated by an exponential function, an analytical expression to describe the MARY spectra can only be obtained for the case of equivalent nuclei, Eq. (17.6). Using a more experimentally adequate non-exponential kinetics requires, in practice, a numerical simulation [52].

The left-hand part of Fig. 17.3 qualitatively shows a typical view of the signal in MARY spectroscopy, exemplified by the calculated function $S(B)$, for a pair with equivalent magnetic nuclei. When RIPs are generated in singlet spin state, one can always see a gradual increase of the luminescence intensity with the magnetic field, i.e., the so-called magnetic field effect. In zero field and in weak fields relatively sharp lines can also be observed where the energy levels of the radical ion pair cross

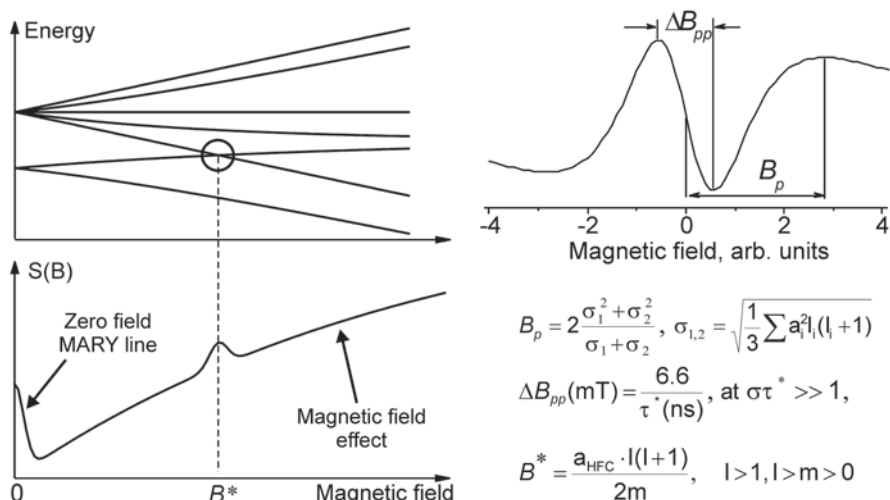


Fig. 17.3 A schematic diagram of the energy levels of a RIP and the field dependence of the singlet yield $S(B)$ (left); a typical shape of the first derivative MARY spectrum (right) in the region of low magnetic field with indicated major features and their relation to the second moments of the EPR spectra σ^2 , the lifetime of the spin correlated RIP τ^* , and to HFC constant, a_{HFC} , for the RIP with only equivalent nuclei in one of the partners. See text for more details

[41]. The lines appear due to the fact that for a part of the ensemble of RIPs the rate of singlet-triplet transitions drops as a result of destructive interference of several available transition channels. The zero-field line, also known as the MARY line or the Low Field Effect [53], is universal and appears in a wide range of systems [54–57]. This peculiarity appears due to a higher symmetry of the system in the absence of the preferred direction of the external magnetic field.

The right-hand part of Fig. 17.3 shows a characteristic view of the first derivative of the field dependence, $S(B)$, as obtained in the modulation experiment. The shape of this curve provides a quick estimate of the EPR spectrum width and the characteristic lifetime τ^* of the spin-correlated RIP. The former parameter is connected with the so-called magnetic field effect half-saturation width $B_{1/2}$ first suggested by Weller [58], which was later adapted to the more convenient in this setting position of the maximum in the modulation spectrum B_p [59, 75]. The time τ^* characterizing the overall rate of all processes shortening the lifetime of the spin-correlated state of the pair is connected with the width of the zero-field MARY line [41, 54, 60]. The connection between the width of the zero field line and the rate of decay of a spin-correlated RIP allows using the stationary MFE for estimating the rates of reactions involving short-lived radical ions (see below).

Additional lines can appear for radical ion pairs that have only equivalent nuclei in one of the partners (see also Fig. 17.5). They are observed in the fields that are the multiples of the HFC constant [49, 61]. Such lines in non-zero fields have also been observed for RIPs with a more complex HFC pattern [55]. Due to the presence of the additional lines in the MFE curve with positions determined by the

structure of the radical ions and with shape and width determined by the processes they are involved in, the observation of such effects evolved into a spectroscopy, and the curves are now referred to as MARY spectra [50]. The term MARY has been in use since the 1970s to refer to the studies of the static applied magnetic field in photogenerated radical pairs [62–64], however, it was radiation-generated RIPs that turned it into spectroscopy in the mid-1990s. The physical principles, typical experimental approaches, and a review of some results it has provided for radiation-generated pairs are discussed in detail elsewhere [49, 57].

17.4.3 *Optically Detected EPR*

In the technique of OD EPR the measured value is the intensity of recombination fluorescence vs. the external magnetic field in the conditions of continuous generation of RIPs and with applied microwave field. When the microwave quantum is in resonance with the energy difference between the Zeeman sublevels of the triplet state of a RIP, an additional depletion of the RIP singlet state occurs. The resonances thus observed via the decrease in the intensity of recombination fluorescence reproduce the EPR spectra of the radical ions composing the RIP. The theory of OD EPR [65–68] is similar to the theory outlined in Sect. 17.4.1, with a conversion to the frame of reference rotating with the microwave field frequency and using the strong field approximation valid for the region where the EPR resonances are actually located. Like in the case of MARY, the major difficulty in the quantitative simulation is the lack of information on the geminate recombination kinetics that needs to be convolved with the time dependent singlet state population. However, this uncertainty only affects the shapes of the lines in the described spectrum but not their positions.

At a low MW power OD EPR signals are very similar to the spectra observed in conventional EPR, but there are also some essential differences. One important peculiarity should be mentioned: a very short spin-lattice relaxation time, of the order of $T_1 \sim 10$ ns, makes the OD EPR line amplitude very small since the typical MW power (~ 1 W) cannot induce S-T transitions faster than the relaxation equilibrates the spin states. Increasing the MW power increases the signal but also results in a non-trivial saturation effect and a distortion of the OD EPR lines due to the so-called spin locking [69].

17.5 Experiment

17.5.1 *Techniques*

The Method of Time Resolved Magnetic Field Effects Figure 17.4 shows the experimental setup that was developed in the Institute of Chemical Kinetics and Combustion SB RAS (ICKC) [70] and provided most of the TR MFE data discussed

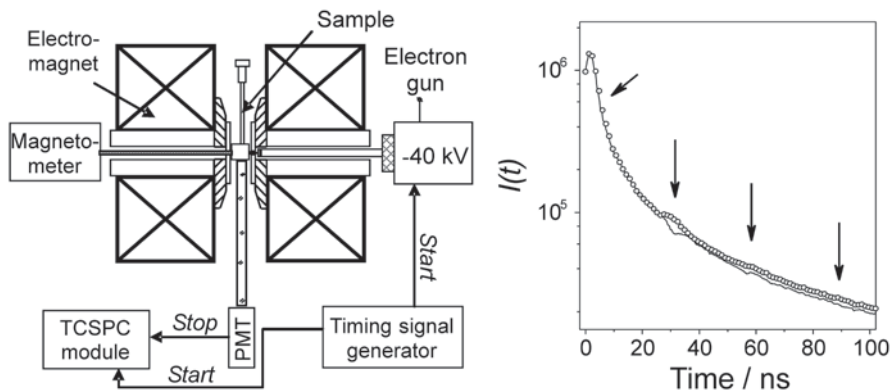


Fig. 17.4 A flow chart of the fluorimeter (*left*) and an example of the fluorescence decay kinetics (*right*) from an irradiated solution of 0.1 M hexamethylethane + 30 μM $p\text{TP-}d_{14}$ in n -hexane in magnetic field $B=0$ (*line*) and $B=0.1$ T (*circles*), $T=293$ K. The *arrows* show the positions of the features arising in the TR MFE curve (see Fig. 17.2)

in this Chapter. The fluorescence is generated by short—about 1.5–3 ns—X-ray pulses with a characteristic energy of about 20 keV. This is mostly the characteristic radiation of a molybdenum target hit by a bunch of electrons with the energy of 30 to 40 keV. The bunch is guided through a hole in the electromagnet pole to the target located 20 mm away from the irradiated sample, which is positioned between the poles of the electromagnet. The fluorescence is registered by the Time-Correlated Single Photon Counting (TCSPC) technique. The magnetic field at the sample can be controlled in the range of 0–1.9 T.

As an example of the kinetics registered using this setup, Fig. 17.4 shows a raw kinetic curve of the fluorescence intensity decay for a solution of 0.1 M hexamethylethane + 30 μM *para*-terphenyl- d_{14} ($p\text{TP-}d_{14}$) in n -hexane. The radical cation of hexamethylethane has HFC with 18 equivalent protons, which results in the pronounced quantum beats. Although the shape of the kinetic curve itself only allows this kind of conclusion to be made for the features at 30 ns, Fig. 17.2 justifies that for a high enough operation stability the coherent features can also be observed at 90 ns. The damping of the beats is due to the contribution from the HFC in the $p\text{TP-}d_{14}$ radical anion ($\sigma \approx 0.068$ mT) and to phase relaxation.

MARY Spectroscopy To record a MARY spectrum, the static magnetic field at the irradiated sample has to be swept within several tens of mT through the zero of the field. To increase sensitivity, as in conventional EPR, lock-in detection with modulation of the swept magnetic field is used. In contrast with the standard magnetic resonance techniques, no microwave power is applied to the sample. Figure 17.5 shows a flow chart of the setup built in ICKC based on a commercial Bruker ER-200D EPR spectrometer [49]. A sample placed in the cavity of the EPR spectrometer is irradiated by an CW X-ray tube. The external magnetic field is generated by the magnet of the spectrometer, and its modulation coils are used to modulate the applied field at 12.5 kHz. To sweep through the zero of the field, a constant “nega-

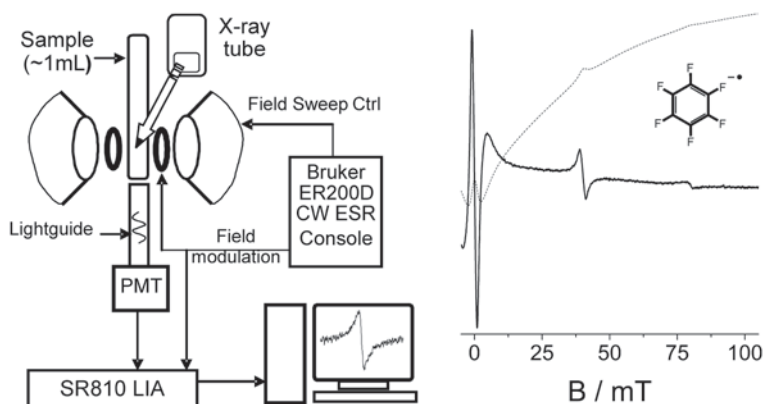


Fig. 17.5 A flow chart of the MARY spectrometer (*left*) and an example of a MARY spectrum registered as the first derivative for a solution of 10 mM C_6F_6 and 1 mM $pTP-d_{1,4}$ in *n*-decane (*noisy line*) and the corresponding $S(B)$ dependence shown by the dashed line (*right*)

tive field shift” is applied by an additional coil. The PMT signal at the modulation frequency is recovered by an SR810 lock-in amplifier.

The right panel of Fig. 17.5 shows an example of a first derivative MARY spectrum with all the possible features: the MFE signal appearing as a curve with a maximum around 5 mT, a strong zero-field line in the phase opposite to the MFE in the first derivative, and the extra lines in the fields ≈ 40 and ≈ 80 mT due to the presence of six equivalent nuclei with a HFC constant of 13.7 mT in the C_6F_6 radical anion.

MARY spectroscopy proved to be a helpful indicatory express technique to study the extremely short-lived radical ions with lifetimes down to 1 ns and their fast reactions. Its ease of use and short-time sensitivity balances the loss of the structural information, and thus this method complements the more powerful TR MFE and OD EPR techniques that are more demanding to the conditions of observation of the radical ions.

Optically Detected EPR The OD EPR spectra presented in this work were registered on the same setup described in the previous Section. The differences were that the sample was additionally exposed to a microwave field with a frequency about 10 GHz, and that the magnetic field was swept near the resonances located around 0.35 T [22, 71]. As can be seen in the examples below, the shape of the OD EPR spectra is similar to the shape of conventional EPR spectra.

A time-resolved version of the OD EPR technique was also developed using a pulsed electron accelerator [21, 72]. Here a pulse of the microwave field is applied to the sample with a controlled time lag after the irradiating pulse. Examples of the time-resolved OD EPR spectra can be found elsewhere [72–74].

Applications to Non-Alkane Solvents In most cases, the techniques discussed in this chapter have been applied to study radical ions in liquid alkanes. The advantages of alkanes, due to their low polarity, are the highest probability of the geminate ion recombination and the energy gain upon the ion pair recombination. The latter is due to the relatively low polarization energy of the recombining ions.

In other solvents certain obstacles could arise for applying a particular technique. Thus, the use of TR MFE is rather problematic in aromatic liquids, since aromatic molecules typically have a long fluorescence time, which distorts the pattern of the quantum beats. However, MARY and OD EPR can be readily used with these solvents [73, 75].

In ethers and alcohols a very fast deprotonation of the primary radical cations occurring within picoseconds is possible, leading to independent neutral radicals and cations and thus separating the spin and charge [76]. As a result, the newly formed ion pairs do not contain spin correlated electrons, and their recombination fluorescence is not magnetosensitive. However, magnetic resonance spectra of the radical ions of some aromatic solutes in liquid ethers and even alcohols can be detected using the recombination fluorescence [73]. Therefore, a portion of the delayed fluorescence from the irradiated solutions of aromatic compounds in these solvents comes from the recombination of spin-correlated radical ions of the solute molecules. Very recently [77] the precursors of aromatic radical cations were found in a series of ethereal solvents. So, the use of non-alkane solvents for the studies of magnetosensitive luminescence response of irradiated solutions is a subject of further work.

17.5.2 Experiment: Radical Anions

The mobility of electrons in alkanes is two to five orders of magnitude higher than the mobility of molecular ions. For concentrations of acceptors ~ 1 mM in liquid alkanes the radical anions (RAs) of the solute will quickly arise, while the solvent radical cations are not scavenged up to the times of the order of 100 ns (for viscosity ~ 1 cP). In these conditions, it is easy to study the contribution of RAs to TR MFE curves. Another way to study the radical anions is the use of a positive charge acceptor that does not scavenge the excess electrons in alkanes, like tetramethyl-*p*-phenylenediamine [78].

Radical Anions of Metaloles OD EPR and TR MFE were used to study RAs of tetraphenyl-substituted 1-heterocyclopenta-2,4-dienes (metaloles), siloles and germoles, including their chloro derivatives [79, 80]. Figure 17.6 shows the OD EPR spectra obtained for solutions of two of the studied compounds in a liquid alkane. The HFC constants were found to be about 1.5 mT for the two protons in the RA of compound (a) and 1.12 mT for ^{35}Cl in compound (b).

The TR MFE curves obtained in alkane solutions of the same compounds clearly demonstrate quantum beats induced by HFC in the RAs, which is dictated by the experimental conditions, as mentioned above. The dominant HFC constants in the RAs were determined from the simulation of the TR MFE curves. A very good agreement between the two techniques was achieved, thus indicating that in the OD EPR spectrum the same species are observed that are formed as early as few nanoseconds after the irradiation due to electron scavenging by the solute.

Radical Anions of Fluorobenzenes The RAs of fluorobenzenes were investigated in many studies (e.g., [81, 82] and references therein). They are interesting due to

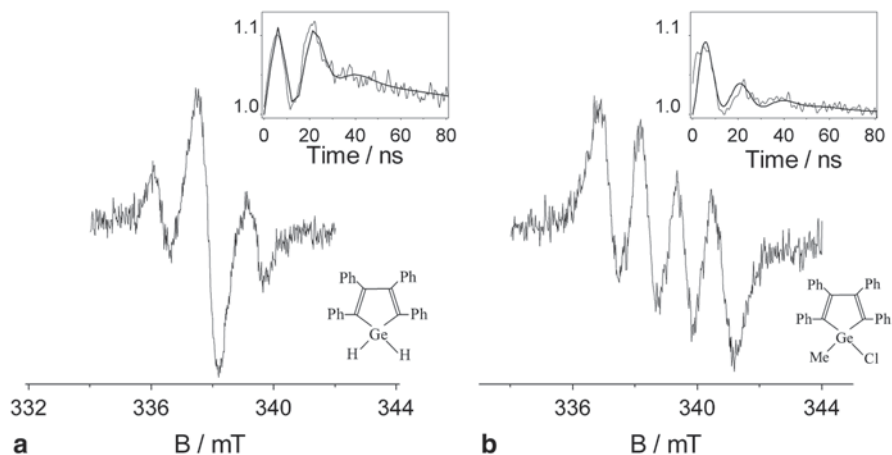


Fig. 17.6 OD EPR spectra (adapted with permission from [80]. Copyright 1998, Mendeleev Communications) and TR MFE curves (in the inserts, [79]. Copyright 1998, with permission from Elsevier BV) for solutions of compounds shown in the plots in liquid alkanes

their special electron and spatial structure. The HFC constants in these RAs are abnormally high because the flat molecular structure is disturbed by pseudo Jahn-Teller distortions in RAs [83]. The adiabatic potential energy surface (PES) for these RAs is a surface of pseudorotation with several minima. The motion along the pseudorotation trough modulates the HFC constants for the fluorines.

Because of their short lifetimes in solutions, these RAs cannot be studied using conventional EPR, but can be detected by OD EPR [84]. In particular, a nontrivial case of intra-molecular dynamics in a fluorobenzene RA was investigated in ref [85], where the OD EPR spectrum of the 1,2,3-trifluorobenzene (1,2,3-TFB) radical anion in a liquid squalane solution was registered (Fig. 17.7a).

The relatively high accuracy of measuring the HFC constants allowed detecting and analyzing the temperature dependence of the observed HFC. In Fig. 17.7b the experimental results are compared with the quantum chemical predictions. The predicted HFC constants were calculated by averaging in the model of fast exchange between the conformations along the pseudorotation trough. The relative weights of the conformations were estimated by the classical Boltzmann distribution, which gave a good agreement between the experiment and theory. Similar results were also obtained for the RAs of several other fluorobenzenes [86].

Symmetric 1,3,5-Trifluorobenzene Among the partially fluorinated benzenes, 1,3,5-TFB is remarkable for its highly symmetric structure. Its RA remained unobserved for a long time. All attempts to register its EPR spectrum using matrix isolation [87] or OD EPR in low-temperature squalane solution [84] failed. The difficulties preventing the registration of the EPR spectra of 1,3,5-TFB RA were usually attributed to the fast spin relaxation due to Jahn-Teller effect in the RAs of aromatic molecules having at least a third order symmetry axis (e.g., see [88]).

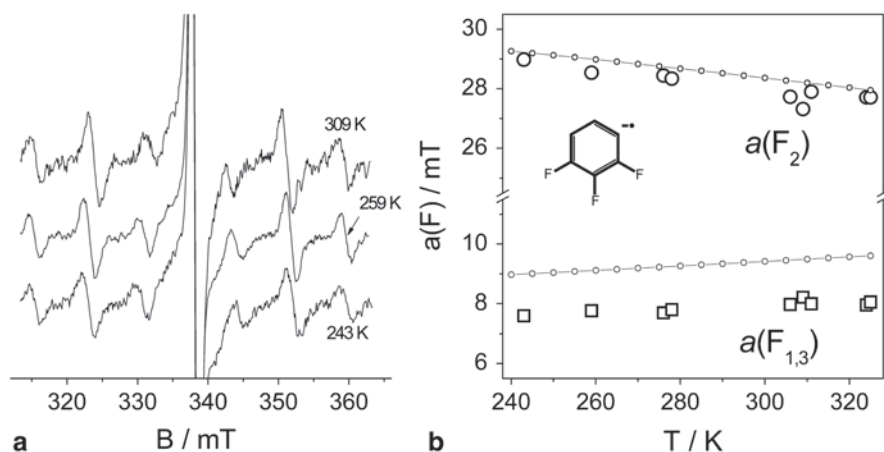


Fig. 17.7 **a** OD EPR spectra for a squalane solution of 10 mM 1,2,3-TFB (+1.5 mM $pTP-d_{14}$). Temperatures are given in the plot, **b** The temperature dependence of the experimentally measured averaged HFC constants (*open circles* for the fluorine atom in the second position (F_2) and *squares* for $F_{1,3}$) and the calculated results for this dependence in the quasi-classical model (-o-). Adapted with permission from [85]. Copyright 2005 American Chemical Society

The RA of 1,3,5-TFB was successfully registered in MARY experiments [89] in an alkane solution at room temperature. In theory the MARY spectrum of this radical anion should have a characteristic line in the field $15a_F/4$, where a_F is the HFC constant with the three equivalent fluorine nuclei. Indeed, a spectrum of this type was registered in a solution of 1,3,5-TFB in *n*-dodecane (Fig. 17.8a, the feature is shown with arrow), and its fitting provided the first estimate of the HFC constant of the ^{19}F nuclei in this RA.

OD EPR was also successful in registering the RA of 1,3,5-TFB [90]. The HFC constants with three equivalent ^{19}F nuclei in this RA estimated from MARY and OD EPR spectra are consistent and equal to $a(3\text{F}) \approx 7.4$ mT. Quantum chemical calculations predict a fast intramolecular exchange between the non-planar structures of this RA, thus confirming the observed equivalence of the fluorine nuclei. The lifetime of the spin-correlated state of the radical ion pair involving the 1,3,5-TFB RA was estimated from the width of the MARY line as ~ 20 ns.

Radical Anions of Al, Ga and In *tris*-8-Oxyquinolines Radical ionic states not only play an important role in chemistry, they are also critical for modern molecular electronic devices including organic light-emitting diodes (OLEDs). OLEDs are multi-layer heterogeneous films capable of emitting light when an electric current passes through them. Here, the layers of coordination compounds such as aluminum *tris*-8-oxyquinolate (Alq_3) functioning as electron transport and electroluminescent layers are important. The charge transport proceeds via the formation of radical ionic states of the coordination compounds, while their recombination is the source of the optical emission of the device. Studying the properties of their isolated radical ions in model systems can help understand the potential ways to improve these

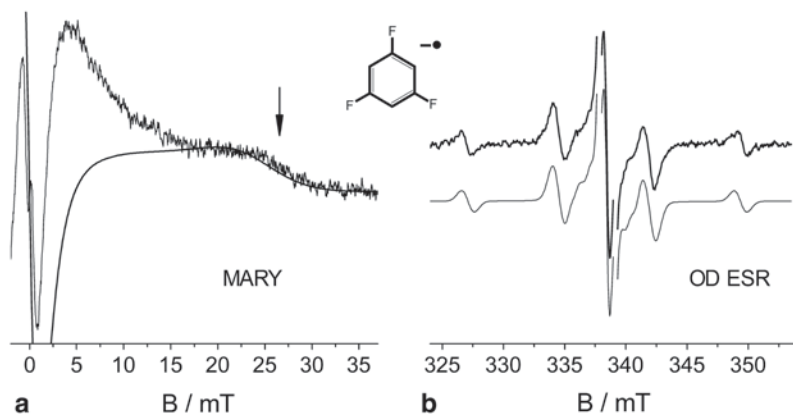


Fig. 17.8 **a** A MARY spectrum of a solution of 10 mM 1,3,5-TFB (+1 mM $pTP-d_{14}$) in *n*-dodecane and the results of fitting for a radical ion pair with a dominant HFC at three equivalent spin $\frac{1}{2}$ nuclei with $a=7.3$ mT. The difference between the predicted and the experimental spectra is due to the additional signal from pairs “solvent RC/ $pTP-d_{14}^{\bullet-}$ ” [89], **b** An OD EPR spectrum of a solution of 10 mM 1,3,5-TFB (+1.5 mM $pTP-d_{14}$) in squalane at 309 K. The smooth line shows the fitting with $a(3F)=7.4$ mT, $g=2.0039$ in the radical anion. Reprinted from [90]. Copyright 2013, with permission from Russian Chemical Bulletin

electro-optical systems. As a system of this type, an X-irradiated solution of Alq_3 (as well as Inq_3 and Gaq_3) in benzene was used [75]. MARY spectra of radical ion pairs involving the RAs of the corresponding oxyquinolate were successfully registered in these conditions, and their simulation provided the estimates of the HFC constants at the metal center (Fig. 17.9).

Experiments in liquid benzene demonstrated that the observed signal is produced by a pair consisting of the Mq_3 radical anion and the solvent radical cation narrowed by degenerate charge exchange. The registered MARY spectra are typical of a series of systems with a similar structure and demonstrate an increase in the second moment of the EPR spectrum of the pair partner with the dominant HFC, which in this case is the RA of the corresponding oxyquinolate. Since all these three coordination compounds have the same number of identical ligands, the different behavior of the MFE is due to the different nature of the central ion. The shown spectra were simulated in the approximation of exponential distribution over the coherent lifetime of the pair, considering only one nucleus with the spin of the central metal ion in the radical anion ($I(^{27}Al)=5/2$, $I(^{70}Ga)=3/2$, $I(^{115}In)=9/2$), the EPR spectrum width of the geminate pair partner, the benzene radical cation, could be neglected.

17.5.3 Experiment: Radical Cations

As mentioned above, in alkane solutions the secondary radical cations (RCs) are usually formed later than the RAs due to the very high electron mobility in these solvents. This significant time delay makes the techniques of TR MFE and MARY

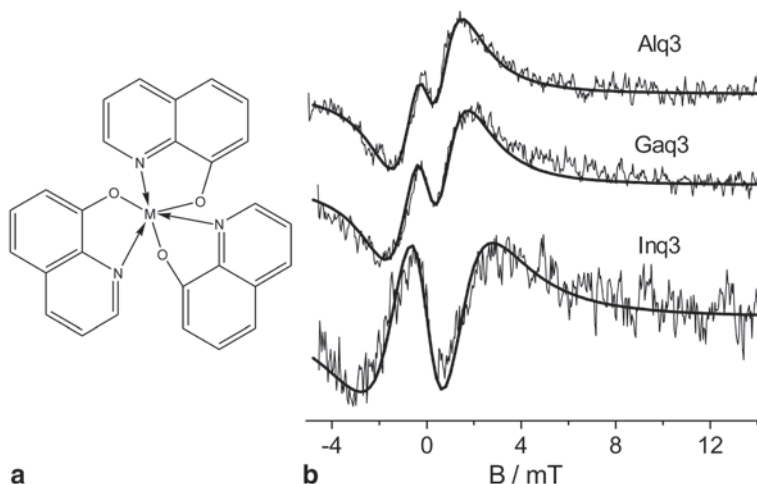


Fig. 17.9 **a** The structure of *tris*-8-oxyquinolate M(III), where M=Al, Ga, In, (Mq_3). **b** Peak-to-peak normalized MARY spectra of benzene solutions of 1 mM Al, Ga, In *tris*-oxyquinolates with superimposed simulated spectra with the following parameters: (Alq_3) $a(I=5/2)=0.45$ mT; (Gaq_3) $a(I=3/2)=0.8$ mT, (Inq_3) $a(I=9/2)=0.6$ mT. Reprinted from [75]. Registration of radical anions of Al, Ga, In *tris*-8-oxyquinolates by magnetosensitive and spectrally resolved recombination luminescence in benzene solutions. Copyright 2012, with permission from Elsevier BV

virtually inapplicable to study RCs in diluted solutions, although still allows observing the secondary RCs using OD EPR. To observe the secondary RCs by TR MFE or MARY, either a higher concentration of the solute is required, or a solvent with a high mobility of the primary radical cations, like some cycloalkanes [91–93] or squalane [93], can be used. Molecules that cannot scavenge electrons are more convenient for the study of their radical cationic states. A luminophore giving a radical anion with a suitable HFC pattern can then be used as an electron acceptor.

The discussed techniques were used to study the RCs of a series of olefins [95, 96], aliphatic amines [97, 98], and aromatic compounds with negative electron affinity, like methyl substituted benzenes [99, 100]. This chapter focuses on the RCs of aliphatic hydrocarbons and their metalorganic analogues. For these compounds, the discussed techniques allowed obtaining EPR parameters of a series of their RCs in solution for the first time.

Data on Alkane Radical Cations from Other Techniques The RCs of alkanes, along with the excess electrons, are the primary species arising upon irradiation of alkanes in liquid or solid phase, and the history of their studies counts decades. The structural information on the RCs of alkanes was mostly obtained for low molecular weight (up to 8–10 carbon atoms) alkanes stabilized in low temperature matrices (e.g., see review [101] and references therein).

The RCs of normal, branched, and cyclic alkanes exhibit very different electron and spin density distributions. The ground states of both the neutral molecules of *n*-alkanes and their radical cations were found to be the elongated *all-trans* confor-

mation. In this conformation of the RCs the molecular orbital occupied by the unpaired electron embraces the entire carbon skeleton. The major HFC of the unpaired electron are observed for the two protons of the methyl groups located in the plane of the carbon skeleton. The value of the HFC constants decreases with increasing the skeleton length from ~ 10 mT (propane) to ~ 2 mT (*n*-decane).

In the RCs of branched alkanes the unpaired electron is mostly localized at one C-C bond, and thus more β -protons are involved in the hyperconjugation [101]. A typical value of the dominant HFC constants with the protons in the non-rotating methyl groups is 4–5 mT. The results from the studies of the RCs of cyclic and bicyclic alkanes in matrices (see, e.g., [102–104]) showed that many of them typically have several energetically close or identical structures with considerable HFC constants and substantially different distribution of spin density due to vibronic interaction [83].

Experiments on pulsed radiolysis of liquid alkanes demonstrated that the chemical lifetimes of the RCs of *n*-alkanes at ambient conditions should be in the range of several nanoseconds to several tens of nanoseconds [105]. For cyclohexane RC, numerous studies suggest that its lifetime in solution should be at least about a microsecond [92]. As for the RCs of branched alkanes, the usual techniques gave contradictory information on the lifetimes of the species in solution. In particular, in a study of neopentane and 2,2,4-trimethylpentane a hypothesis was put forward that these RCs transform into products in the sub-nanosecond time domain [106].

A study of the magnetic resonance parameters of alkane RCs in liquid phase became possible after the Optically Detected EPR and its time-resolved counterpart were developed. OD EPR was used to register the RCs of hexamethylethane, some cyclic alkanes with rigid structure like *cis*-decalin, norbornane etc. in solution [25, 71, 107]. As the solvent, alkanes with a higher ionization potential (cyclopentane, *n*-pentane, *n*-hexane) were usually used. OD EPR lines about 0.3 mT wide attributed to the solvent RCs were successfully observed in irradiated pentadecane and squalane [107]. The small EPR spectrum width was explained by the degenerate electron exchange involving the primary radical cation.

A considerable progress in the investigation of alkane RCs in solutions was made using the TR MFE technique. These results are discussed below.

Normal Alkanes In most cases the same approach was used to study alkane RCs in solutions: addition of the studied alkane (RH) in a concentration of $0.01 \div 1$ M to an alkane with a higher ionization potential, usually *n*-hexane [108]. As the electron acceptor and luminophore, *p*TTP- d_{14} at a low, 10–100 μ M, concentration was used. Under these conditions the observed TR MFE is determined by spin evolution in the spin-correlated pairs (RH $^{\bullet+}$ /*p*TTP- d_{14} $^{\bullet-}$). The radical anion has small HFC constants, and its effect on the evolution of the RIP spin state becomes noticeable only at times longer than 50 ns.

Figure 17.10a shows TR MFE curves for solutions of *n*-alkanes at a relatively low concentration. A further increase in the *n*-alkane concentration modifies the curves as a result of slowing down the S-T transitions in the RIP due to the degenerate electron exchange, as discussed below. The shape of the curves clearly shows

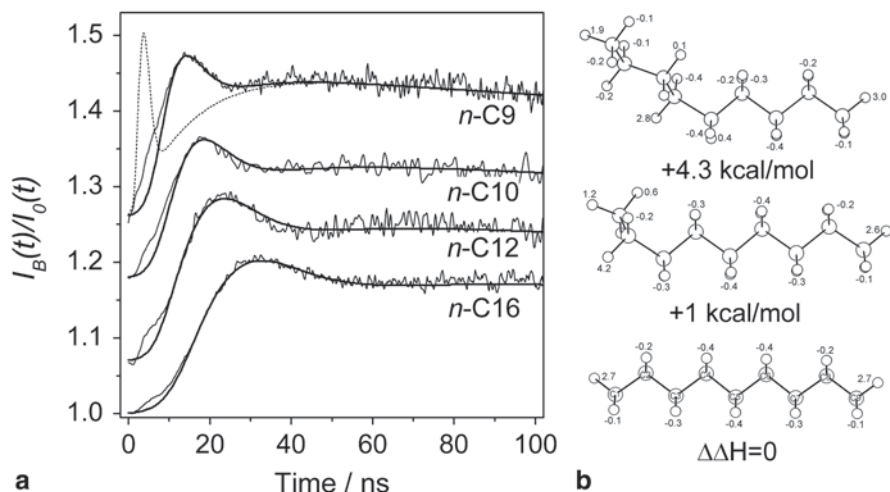


Fig. 17.10 **a** Experimental (noisy) and calculated TR MFE curves for solutions of 0.1 M *n*-alkanes (indicated in the plot) in *n*-hexane (+30 μ M *p*TP- d_{14}) at 293 K. The smooth lines show the results of modeling with the second moment of the EPR spectrum of *n*-alkane RC corresponding to σ equal to 0.68, 0.5, 0.38, and 0.25 mT (C9–C16) in good accordance with data reported in Ref. [108]. For *n*-C9 the dashed curve demonstrates the change of the calculated TR MFE curve when σ is increased to 2.5 mT, which is typical for low temperature matrices [109]. **b** The all-trans structure of *n*-C9 RC and the conformations formed by rotation about either C₂–C₃ bond or C₄–C₅ bond by about 120°. The HFC constants with protons in mT and the relative values of the formation enthalpy as calculated by the UB3LYP/6–31G(d) method are also shown. Adapted with permission from [119]. Copyright 2006, American Chemical Society

that the RCs of *n*-alkanes with a sufficiently long carbon skeleton in solution have an unresolved EPR spectrum. A simulation of the TR MFE curves gives the σ values [108] for the EPR spectra from 0.81 mT (*n*-C8) to 0.25 mT (*n*-C16), which is much lower than the characteristic values for the spectra of the corresponding RCs in freon matrices. This is illustrated in Fig. 17.10a, where the experimental curves are fitted with Eqs. (17.10–17.13) taking the spectral exchange into account. For *n*-nonane solutions, a curve calculated for the value of σ typical for low temperature matrices is also shown with the dashed line. A small peculiarity at the time range <10 ns is likely due to the effect of the RCs of either the solvent or isomeric hexanes, for which σ values of about 2 mT were observed (see below).

The significant decrease in the EPR spectrum width of *n*-alkane RCs on going to liquid solution was explained in ref [119] using quantum chemical calculations. It was shown that in solution, similar to solid matrices, the most probable conformations of an *n*-alkane RC were the all-trans structure and the structure differing from it by rotation of the ethyl fragment, as demonstrated in Fig. 17.10b by the example of the nonane RC. The transition barriers between these conformations are only 23 kcal/mol [110]. The HFC constants are averaged not only by the fast rotation of the end methyl groups, but also by the rotation of ethyl fragments. Other conforma-

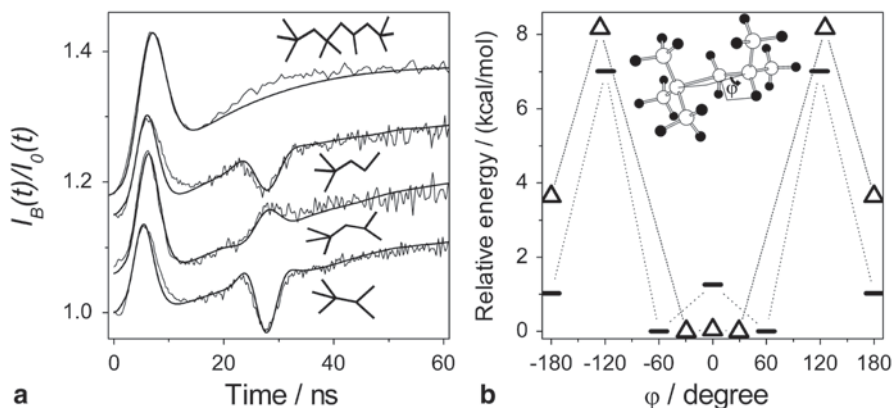


Fig. 17.11 **a** Experimental (noisy) and calculated TR MFE curves for solutions of 0.1 M branched alkanes (structures are indicated in the plot) in *n*-hexane (+ 30 μ M *p*TP-*d*₁₄) at 293 K. Adapted with permission from [112]. Copyright 2012, American Chemical Society. The *smooth lines* show the results of modeling for the dominant HFC constants with β -protons of about 1.3 mT. **b** The relative energies of the stationary points at the energy profile for 2,2,4-trimethylpentane (triangles) and its RC (–) for the rotation about the C₃-C₄ bond. Adapted with permission from [111]. Copyright 2007, American Chemical Society

tions, even with a higher statistic weight, are unlikely to exist in solution due to high formation enthalpy.

Branched Alkanes The radical cations of branched alkanes were studied using the same approach as described above for normal alkanes. In this case, additional features (Fig. 17.11a) in the TR MFE curves appear indicating the presence of a significant number of magnetically equivalent protons with HFC constants of about 1.3 mT [111, 112]. This value is nearly equal to the HFC value expected for β -protons with the hyperfine couplings averaged by the fast rotation of the methyl groups. The change of the second feature from peak to dip for some compounds is due to the different parity of the number of protons with the dominant HFC in the corresponding RCs (see also Fig. 17.1b). Spin density in the RCs of isomeric butanes and pentanes is localized near the *tert*-butyl moiety. For higher substituted alkanes, such as 2,2,4,4,6,8,8-heptamethylnonane (Fig. 17.11a), the TR MFE curve becomes closer to the curve expected for a RC with a large number of magnetically non-equivalent nuclei (see Fig. 17.1).

In the RC of 2,2,4-trimethylpentane (Fig. 17.11b) for angle $\varphi \approx 180^\circ$ the predicted HFC constant at the methine proton is about 7 mT. However, this large constant has no noticeable effect because in thermal equilibrium the parent neutral molecules mostly have conformations with $|\varphi| < 120^\circ$. Since ionization is a vertical process, the RC appears in a similar geometry. A transition to the conformation with $\varphi \approx 180^\circ$ required passing over a barrier of about 7 kcal/mol (Fig. 17.11b), which is unlikely at room temperature at times up to 50 ns where the quantum beats are observed. As one can see in Fig. 17.11a, a calculation neglecting the above conformation at $\varphi \approx 180^\circ$ adequately describes the experiment.

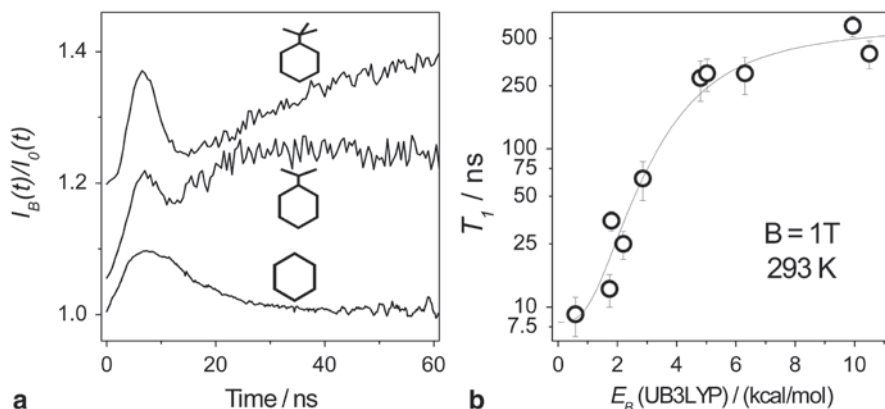


Fig. 17.12 **a** Experimental TR MFE curves for solutions of 0.1 M cyclic alkanes (structures are indicated in the plot) in *n*-hexane (+30 μM *p*TP-*d*₁₄) at 293 K. **b** The correlation between the pseudorotation barrier height E_B according to B3LYP calculations and the spin-lattice relaxation time T_1 of cycloalkane RCs (in the order of increasing E_B : cyclohexane, *trans*-decalin, ethylcyclohexane, 1,4-dimethylcyclohexane, methylcyclohexane, propylcyclohexane, *iso*-propylcyclohexane, 1,1-dimethylcyclohexane, 1,2-dimethylcyclohexane, *tert*-butylcyclohexane, *cis*-decalin). The *smooth line* is given as an eyeguide. Reprinted with permission from [115]. Copyright 2012, American Institute of Physics

The studied RCs were identified by the values of the HFC with protons and the *g*-values (~ 2.0035). Additionally, to check that the observed RCs are not the products of the possible decomposition of the parent alkane RC due to elimination of dihydrogen, TR MFE experiments for solutions of the corresponding alkenes were also performed. All these experiments confirmed that TR MFE allows registration of RCs of branched alkanes in solution and established that the lifetime of these RCs in solution at room temperature is at least tens of nanoseconds.

Cyclic Alkanes The RC of cyclohexane was probably one of the most elusive species that was sought by OD EPR in liquid solution. In pure cyclohexane the RC undergoes a fast degenerate electron exchange with the surrounding molecules, and it surely could be a precursor of the secondary RCs of solutes [15, 92, 113]. However, no signals were detected in the solutions where the cyclohexane RC was expected as an isolated species. A progress in studying this RC, as well as the RCs of alkylsubstituted cyclohexanes, was made using TR MFE, which allowed measurement of spin-lattice relaxation rates in these RCs.

As Fig. 17.12a shows, the features in the TR MFE curves reflecting the second moment of the EPR spectrum can only be observed if a bulky substituent like *tert*-butyl is present in the cyclohexane ring. In *iso*-propylcyclohexane, the effect of paramagnetic relaxation becomes more apparent as a faster decay of the TR MFE curve at longer times (see also Fig. 17.1a). In the RC of unsubstituted cyclohexane the time of spin-lattice relaxation in solution becomes so short ($T_1 \sim 10$ ns [114]) that this RC cannot be detected by OD EPR.

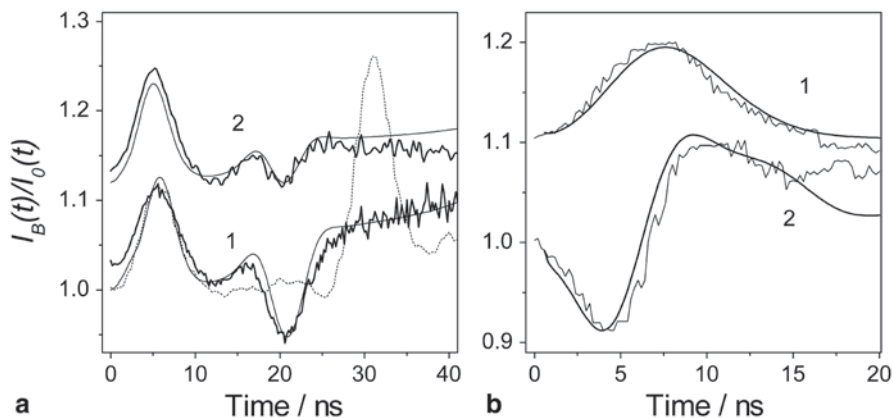


Fig. 17.13 Experimental (*noisy*) and calculated TR MFE curves obtained at 293 K for solutions of: **a** 0.1 M *tert*-butyltrimethylsilane (1) and *tert*-butyltrimethylgermane (2, shifted vertically by 0.12) in *n*-hexane (+30 μ M *p*TP- d_{14}) at $B=0.1$ T. The model curves correspond to two sets of HFC constants: $a(9H)=1.87$ mT and $a(9H)\approx 0.3$ mT. The dashed line shows the experimental curve for a hexamethylethane solution in the same conditions. Reprinted from [117]. The study of radical cations of $\text{Me}_3\text{C-SiMe}_3$ and $\text{Me}_3\text{C-GeMe}_3$ in alkane solutions using the method of time-resolved magnetic field effect and DFT calculations. Copyright 2008, with permission from Elsevier; **b** 0.06 M solutions of Me_6Ge_2 (+30 μ M *p*TP- d_{14}) in *n*-hexane at $B=0.03$ T (1, shifted vertically by 0.1) and 0.3 T (2). The simulation parameters correspond to the data for RC of Me_6Ge_2 ($g\approx 2.03$, $a(18H)=0.52$ mT [116, 118]. Adapted by permission of the PCCP Owner Societies)

Paramagnetic spin-lattice relaxation in the RCs of a series of cycloalkanes was analyzed from the viewpoint of the correlation between the relaxation rate and the structure of the adiabatic PES of the RCs [115]. The PES structure was obtained with DFT quantum chemical calculations. It was found that for RCs of all considered cycloalkanes, including alkyl-substituted ones, the corresponding adiabatic PES was a surface of pseudorotation due to avoided crossing composed of several minima on the PES separated by moderate potential barriers. A group of such minima forms a pseudorotation trough, along which the system moves without the rotation of the molecule. A correlation was revealed between the spin-lattice relaxation time and the calculated barrier height (Fig. 17.12b).

To explain the abnormally high paramagnetic relaxation rate in some cycloalkane RCs, it was proposed [115] that relaxation in radicals with nearly degenerate low-lying vibronic states originated from stochastic crossings of the vibronic levels caused by fluctuations of the radical interaction with the solvent. In the case of cyclohexane RC, an estimate for the relaxation rate derived using the Landau-Zener model of nonadiabatic transitions at the level crossing agrees well with the experimental data.

Radical Cations of Metalorganic Compounds Radical cations of aliphatic compounds with Group IV elements other than carbon were studied in alkane solutions using TR MFE [116, 117]. As an example, Fig. 17.13 shows TR MFE curves for solutions of *tert*-butyltrimethylsilane, *tert*-butyltrimethylgermane, and hexameth-

ylethane (a), and hexamethyldigermane (b), together with the results of fitting using the theory described in Section 17.4.1.

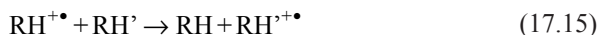
According to experimental data (Fig. 17.13a), when a metalorganic compound of the type $(\text{CH}_3)_3\text{C}-\text{E}(\text{CH}_3)_3$ ($\text{E}=\text{Si}, \text{Ge}$) is added to *n*-hexane, a positive charge carrier appears that has a considerably shifted *g*-value and a resolved EPR spectrum. In these RCs, the HFC constants are larger than in the RC of hexamethylethane (the dashed line in Fig. 17.13a). Using quantum chemical calculations this was explained by the shift of spin density at the C–E bond towards the carbon atom almost to equal extent in both compounds. As a result, the features in the TR MFE curves appear earlier than for hexamethylethane and change their sign because the number of nuclei with the dominant HFC constants becomes odd instead of even. The value of the HFC constants agrees very well with the calculations.

For compounds $(\text{CH}_3)_3\text{E}-\text{E}(\text{CH}_3)_3$ ($\text{E}=\text{Ge}, \text{Sn}$) the RCs are less stable in solution, although at sufficiently short times a positive charge carrier was observed with the second moment of the EPR spectrum and the *g*-value similar to those of $(\text{CH}_3)_3\text{E}-\text{E}(\text{CH}_3)_3^{\bullet+}$ observed in low temperature matrix, provided that the HFC constants are averaged by rotation of the methyl groups [116]. As Fig. 17.13b shows, the experimental curves are adequately fitted using the literature data.

The major qualitative result of the studies described in this Section is the estimation of the lifetime of the radical cations of aliphatic heteroorganic compounds in solution, which amounts to at least tens of nanoseconds.

17.5.4 Reactions of Radical Ions

Degenerate Electron Transfer An electron transfer between a radical ion and a molecule modifies the magnetic environment of the unpaired electron. This is also valid for the degenerate electron transfer, which we shall discuss in this Section using the example of an alkane RC reaction



involving the molecules of an alkane added as a solute. In this reaction, the magnetic environment changes many times. The uncorrelated spectral exchange decreases the steepness of the TR MFE curve rise. This becomes readily detectable when the condition of the fast spectral exchange $(\sigma\tau_c)^2 \ll 1$ is met, as illustrated in Fig. 17.14a showing TR MFE obtained at various concentrations of *n*-nonane in *n*-hexane [119]. A simulation showed that the rate constant of reaction (17.15) for nonane is two orders of magnitude lower than the encounter rate for a radical cation and a molecule. The difference can be explained by assuming a noticeable probability of electron transfer in reaction (17.15) only if the *n*-alkane RC and its parent molecule are in the same conformation. As mentioned above, *n*-nonane RC can be found mainly in *all-trans* conformation, while the fraction of the appropriate conformations among the neutral nonane molecules in solution is quite low (~20%). Another factor is the activation energy of the transfer (4–6 kcal/mol).

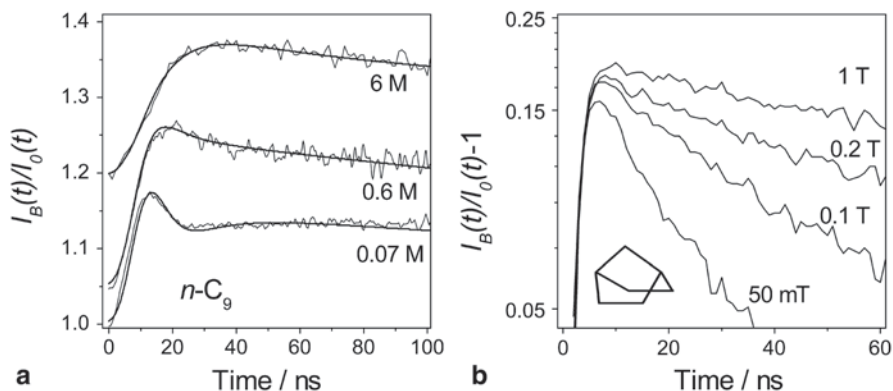


Fig. 17.14 TR MFE curves in solutions of *n*-nonane **a** in the field $B=0.1$ T for various alkane concentrations (shown in the figure, adapted with permission from [119]. Copyright 2006, American Chemical Society) and 0.2 M norbornane **b** at varying magnetic field, $T=293$ K, adapted with permission from [120]. Copyright 2006, American Chemical Society. The structure of the norbornane molecule is shown in the plot

If the RC has a considerable EPR spectrum width, the condition of the fast spectral exchange $(\sigma\tau)^2 \ll 1$ cannot be met for a realistic solution viscosity. In this case, the increasing rate of the exchange does not significantly affect the TR MFE curve. However, the spectral exchange contributes to spin-lattice relaxation. Figure 17.14b shows in semi-log coordinates TR MFE curves registered in *n*-hexane solution of norbornane at different magnetic fields [120]. The curve decay pattern is close to exponential in accordance with Eq. (17.13), so the dependence of the spin-lattice relaxation rate in the norbornane RC on the magnetic field and norbornane concentration can be determined. This, in turn, allows estimating the rate of reaction (17.15). Since the HFC in norbornane RC is determined by four equivalent protons ($a(4H) \approx 6.4$ mT), the spin evolution can be calculated exactly [42] taking into account the reaction of charge transfer for any exchange rate. A comparison with the exact solution demonstrated that the Redfield theory of paramagnetic relaxation can be used even in weak magnetic fields at a low spectral exchange rate.

Irreversible Reactions Involving Geminate Radical Ions In OD EPR the effect of a reaction involving geminate radical ions can be successfully observed if the initial radical ion and the final reaction product have resolved and sufficiently different spectra. For example, the reaction of RC dimerization was thus observed [100, 121]. The estimation of the rate constant of a reaction in OD EPR or FDMR experiment is not very accurate. Other techniques can estimate it with a relatively high accuracy, including through indirect information from the MARY spectrum.

A reaction resulting in the formation of a new radical ion with a different EPR spectrum affects the dynamics of the spin state of the ensemble of spin-correlated RIPs. An appropriate TR MFE experiment then allows the real-time observation of the entire process. Figure 17.15a shows the transformation of TR MFE curves due to electron transfer from a molecule of 1,3-dimethyladamantane (DMAD) to the

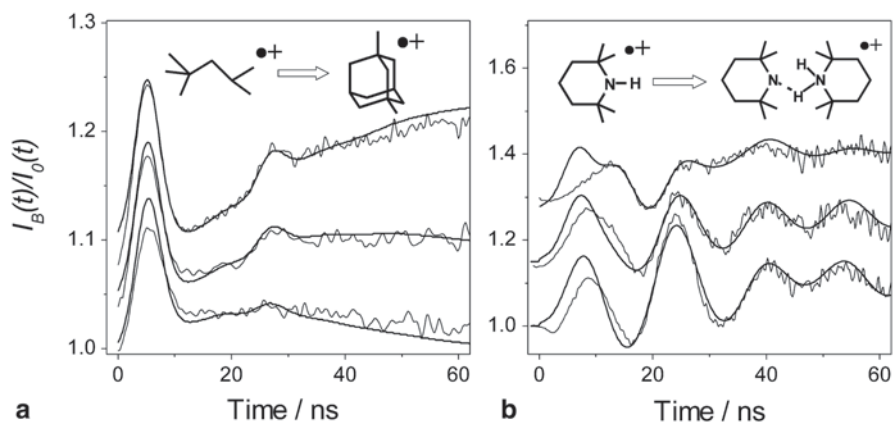
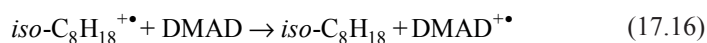


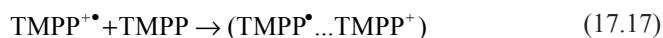
Fig. 17.15 Experimental (*noisy*) and calculated TR MFE curves recorded for: **a** *n*-hexane solutions of 0.1 M 2,2,4-trimethylpentane without (*curve 1*) and with 1 mM (*curve 2*) and 3 mM (*curve 3*) of 1,3-dimethyladamantane. The smooth lines show the results of calculation for reaction (17.16) at the rate constant of $1.5 \times 10^{10} \text{ M}^{-1}\text{s}^{-1}$. Adapted with permission from [112]. Copyright 2012 American Chemical Society. **b** cyclohexane solutions (+ 30 μM *pTP-d*₁₄) of 3 mM (*curve 1*), 20 mM (*curve 2*), and 30 mM (*curve 3*) tetramethylpiperidine. The smooth lines show the results of calculation for reaction (17.17) at the rate constant of $6 \times 10^9 \text{ M}^{-1}\text{s}^{-1}$. The curves are shifted vertically for convenience. Adapted from [123], Copyright 2008, Pleiades Publishing, Ltd

RC of 2,2,4-trimethylpentane (*iso*-C₈H₁₈) in hexane solution. The DMAD RC has a short spin-lattice relaxation time [122], so its formation in reaction



leads to a rapid loss of spin correlation in the radical ion pair DMAD^{•+}/*p*-TP[•] that produces fluorescence upon recombination. In this case, the extra decay rate of the TR MFE due to the reaction (17.16) is approximately equal to the rate of the formation of the rapidly relaxing species.

More complicated for analysis is the transformation of the TR MFE curves in the case shown in Fig. 17.15b, when the reaction modifies the hyperfine structure of the radical ion. This was demonstrated using the example of the formation of a distonic complex of a RC with a molecule in irradiated solution of tetramethylpiperidine (TMPP) [123]:



The spin density distribution in this complex is similar to N-centered radicals.

The experimental TR MFE curves can be successfully described if the complex is considered to be formed from the RC with the rate constant of $6 \times 10^9 \text{ M}^{-1}\text{s}^{-1}$, i.e., in a diffusion-controlled process involving molecular species. The process of the distonic complex formation was also detected in the OD EPR spectrum, although the rate constant of the reaction cannot be readily estimated from the spectrum.

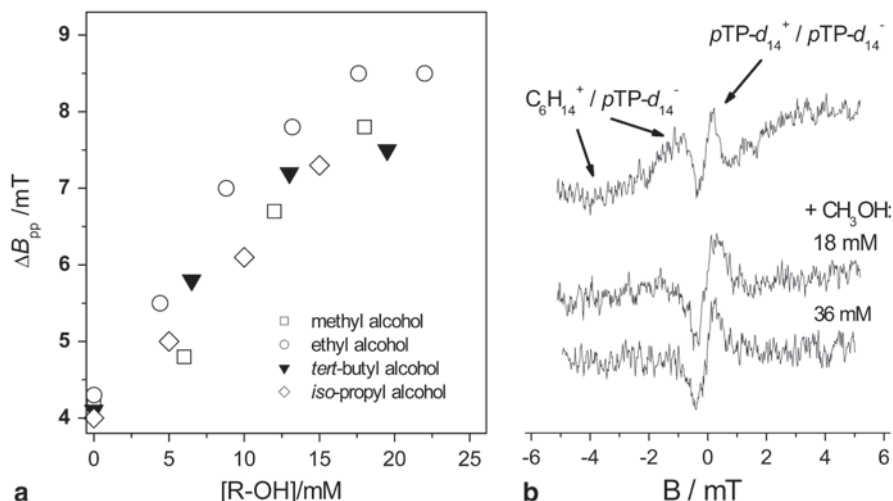


Fig. 17.16 **a** The dependence of the width of the zero-field MARY line in a solution of 10 mM hexafluorobenzene in *n*-hexane vs. the concentration of four different alcohols. The slope of the dependences corresponds to the rate constant of the deprotonation reaction $2 \div 3 \times 10^{10} \text{ M}^{-1} \text{ s}^{-1}$. **b** A MARY spectrum for a solution of 2.5 mM $pTP-d_{14}$ in *n*-hexane (the upper curve) and its change after adding methyl alcohol (the lower two curves) Adapted from [124]. Copyright 2003, with permission from Elsevier Science Ltd

Deprotonation of Alkane Radical Cations in MARY Information about the decay rate of the geminate radical ions can be obtained from the measurement of steady-state MFE as well. As mentioned above, the shortening of the lifetime (τ) of the pair increases the width (ΔB_{pp}) of the zero-field MARY line according to the relation for the Lorentz line contour $\Delta B_{pp}(\text{mT}) \approx 6.6/\tau$ (ns) known in the theory of EPR [60].

Such a shortening of the lifetime occurs, for example, during a reaction that separates the spin and the charge in one of the partners in a RIP. In irradiated alkanes such a reaction can be the proton transfer from an alkane RC ($RH^+\bullet$) to an aliphatic alcohol molecule, as Fig. 17.16a shows.

In refs [124, 125] it was shown that addition of an alcohol to a solution of hexafluorobenzene (C_6F_6) in *n*-alkane (*n*-C₆ to *n*-C₁₀) broadened the zero field MARY line proportionally to alcohol concentration in the range of up to ~20 mM, which is the threshold of alcohol association in alkane. From the analysis of the obtained MARY spectra it was determined, which of the decay channels of the spin-correlated radical ion pair $RH^+\bullet/C_6F_6^-\bullet$ was responsible for this broadening. As an example, Fig. 17.16b shows how the addition of an alcohol to a solution of $pTP-d_{14}$ in alkane (RH) suppresses the characteristic signal from the pair $RH^+\bullet/pTP-d_{14}^-\bullet$ leaving the signal from the other pair $pTP-d_{14}^+\bullet/pTP-d_{14}^-\bullet$ unaffected. In this experiment it was established that there is no interaction between the radical anion in the pair and the alcohol molecule. As a result, in ref [124] it was concluded that a proton is transferred from the RC of a linear alkane to a monomeric molecule of an aliphatic alcohol with a diffusion-controlled rate.

17.6 Concluding Remarks

The methods of Optically Detected EPR, Time-Resolved Magnetic Field Effect, and MARY spectroscopy discussed in this chapter open new possibilities for registration and systematic investigation of radical ions in irradiated liquid solutions. Although invoking fluorescence for the detection, they can provide information on the radical ions of compounds exhibiting no luminescence. The methods are based on exploiting the spin correlation in the radical ion pairs generated in solution. This lends them sensitivity to the local track structure on the hitherto unexplored scale between a single pair and the entire path of high energy particles.

The methods have a very high sensitivity to the radical ions and open access to radical ions at the nanosecond time scale at their extremely low steady state concentrations in the irradiated sample. The method of OD EPR directly yields the CW EPR spectra of the radical ions of the pair partners. The method of TR MFE provides the time-resolved picture of the evolution of the spin state of the radical ion pairs, with simulations yielding the EPR spectral parameters. MARY spectroscopy proved to be a helpful indicative express technique to estimate the width of the EPR spectra and the lifetimes of short-lived radical ions.

An advantage of the method of OD EPR is the conventional presentation of the spectrum and the simplicity of its interpretation. Furthermore, as opposed to time-resolved methods, both CW OD EPR and MARY spectroscopy do not require luminophores with short luminescence lifetime. On the other hand, the major advantage of TR MFE is its ability to directly determine relaxation times in a wide range of magnetic fields in addition to HFC and g -values, as well as the possibility to follow the transformations of a radical ion at the nanosecond time scale.

Regarding the most interesting results provided as examples in this chapter, we first of all mention the registration of radical ions in solutions, which either could not be detected by other techniques, or the very formation of which under irradiation was under question. Other interesting application fields for these methods include the study of intramolecular conformational transitions and the formation of intermolecular complexes of short-lived radical ions, the study of the processes of degenerate electron exchange, the study of the peculiarities of spin relaxation of these elusive species. It is clear that the potential of these methods by now has been anything but exhausted.

Acknowledgments The work was supported by the Council for Grants of the President of the Russian Federation for State Support of Leading Scientific Schools (Grant NSh-5744.2014.3).

References

1. Crookes W (1879) On the illumination of lines of molecular pressure, and the trajectory of molecules. *Phil Trans Royal Soc Lond* 170:135–164
2. Röntgen WC (1895) Über eine neue Art von Strahlen. Vorläufige Mitteilung. In: *Aus den Sitzungsberichten der Würzburger Physik-Medic Ges Würzburg*, pp 132–141

3. Becquerel H (1896) Sur les radiations invisibles émises par les corps phosphorescents, vol 22. Comptes rendus de l'Académie des sciences, Paris, pp 501–503
4. Child CD (1913) LXXVIII. Line spectrum from uncharged molecules. *Phil Mag (Ser 6)* 26:906–911
5. Merritt E (1915) Luminescence. *Phys Rev* 5:319–334
6. Marshall LC (1929) The recombination of ions and electrons in gases. *Phys Rev* 34:618–634
7. Morrow T, Salmon GA, Frankevich EL (1968) Effect of an electric field on the radiation induced fluorescence from solutions of aromatic hydrocarbons in cyclohexane. *Nature* 219:481–482
8. Dainton FS, Salmon GA, Morrow T, Thompson GF (1968) The formation of excited states on pulse radiolysis of organic solutions. *Chem Commun* 6:326–328
9. Brocklehurst B (1969) Formation of excited states by recombining organic ions. *Nature* 221:921–923
10. Brocklehurst B, Dixon RS, Gardy EM et al (1974) The effect of a magnetic field on the singlet/triplet ratio in geminate ion recombination. *Chem Phys Lett* 28:361–363
11. Brocklehurst B (1976) Magnetic field effect on the pulse shape of scintillations due to geminate recombination of ion pairs. *Chem Phys Lett* 44:245–248
12. Klein J, Voltz R (1976) Time-resolved optical detection of coherent spin motion for organic-radical-ion pairs in solution. *Phys Rev Lett* 36:1214–1217
13. Anisimov OA, Bizyaev VL, Lukzen et al (1983) The induction of quantum beats by hyperfine interactions in radical-ion pair recombination. *Chem Phys Lett* 101:131–135
14. Veselov AV, Melekhov VI, Anisimov OA, Molin YN (1987) The induction of quantum beats by the Δg mechanism in radical ion pair recombination. *Chem Phys Lett* 136:263–266
15. Grigoryants VM, Tadjikov BM, Usov OM, Molin YN (1995) Phase shift of quantum oscillations in the recombination luminescence of spin-correlated radical ion pairs. *Chem Phys Lett* 246:392–398
16. Veselov AV, Anisimov OA, Molin YN (1991) Time-resolved single-photon counting technique in radiolysis of hydrocarbons. In: Tabata Y (ed) *Pulse radiolysis*. CRC, Boston, pp 27–51
17. Anisimov OA, Grigoryants VM, Kiyarov SV et al (1982) Influence of magnetic field on recombination fluorescence in nonpolar solutions of hexafluorobenzene. *Theor Exp Chem* 18:256–261
18. Sukhenko SA, Purtov PA, Salikhov KM (1983) Proyavlenie peresecheniya urovney radikal'nyh par v magnitnyh effektah I effektah himicheskoy polarizatsii yader (The manifestation of energy level intersection for radical-pair spins in magnetic effects and in the effects of magnetic nuclear polarization. In Russian). *Khim Fiz* 1:21–27
19. Anisimov OA, Grigoryants VM, Molchanov VK, Molin YN (1979) Optical detection of ESR absorption of short-lived ion-radical pairs produced in solution by ionizing radiation. *Chem Phys Lett* 66:265–268
20. Anisimov OA, Grigoryants VM, Molin YN (1979) Observation of hyperfine structure in the optical detection of the EPR spectrum of short-lived ion-radical pairs in a liquid. *JETP Lett* 30:555–557
21. Trifunac AD, Smith JP (1980) Optically detected time resolved EPR of radical ion pairs in pulse radiolysis of liquids. *Chem Phys Lett* 73:94–97
22. Molin YN, Anisimov OA (1983) Optical detection OD ESR spectra of short-lived ion-radical pairs in spurs under radiolysis. *Radiat Phys Chem* 21:77–82
23. Veselov AV, Bizyaev VL, Melekhov VI et al (1989) Detection of solvent holes by the method of quantum beats in recombination luminescence. *Radiat Phys Chem* 34:567–573
24. Trifunac AD, Werst DW (1991) Study of radical cations by time-resolved magnetic resonance. In: Lund A, Shiotani M (eds) *Radical ionic systems*. Kluwer, Dordrecht, pp 195–229
25. Werst DW, Bakker MG, Trifunac AD (1990) The fate of alkane radical cations in liquid and solid hydrocarbons. Time-resolved fluorescence detected magnetic resonance. *J Am Chem Soc* 112:40–50

26. Freeman GR (1987) Ionization and charge separation in irradiated materials. In: Freeman GR (ed) Kinetics of nonhomogeneous processes. Wiley, New York, pp 19–87
27. LaVerne JA, Brocklehurst B (1996) Magnetic field effects on the solute luminescence of alkane solutions irradiated with heavy ions. *J Phys Chem* 100:1682–1688
28. Holroyd RA, Preses JM, Hanson JC (1997) Excited singlet-state yields in hydrocarbon liquids exposed to X-rays. *J Phys Chem A* 101:6931–6935
29. Anishchik SV, Usov OM, Anisimov OA, Molin YN (1998) Study of a fraction of spin-correlated pairs in radiation spurs by the methods of time-resolved magnetic field effects and quantum beats. *Radiat Phys Chem* 51:31–36
30. Baker GJ, Brocklehurst B, Hayes M et al (1989) Ion-recombination luminescence in alkanes excited by synchrotron radiation in the range 10–40 eV. *Chem Phys Lett* 161:327–331
31. Brocklehurst B (1992) Model calculation on hydrocarbon radiolysis. Part 1—spin correlation effects in pure alkanes. *J Chem Soc Faraday Trans* 88:167–175
32. Lozovoy VV, Anishchik SV, Medvedev NN et al (1990) Monte Carlo modelling of radical ion recombination in multiparticle tracks. *Chem Phys Lett* 167:122–128
33. Borovkov VI, Velizhanin KA (2007) Experimental and computer simulation study of delayed fluorescence decay from irradiated *n*-dodecane solutions of TMPD. *Radiat Phys Chem* 76:998–1010
34. Salikhov KM, Molin YN, Sagdeev RZ, Buchachenko AL (1984) Spin polarization and magnetic effects in chemical reactions. Elsevier, Amsterdam
35. Steiner UE, Ulrich T (1989) Magnetic field effects in chemical kinetics and related phenomena. *Chem Rev* 89:51–147
36. Brocklehurst B (2002) Magnetic fields and radical reactions: Recent developments and their role in nature. *Chem Soc Rev* 31:301–311
37. Hayashi H (2004) Introduction to dynamic spin chemistry: magnetic field effects on chemical and biochemical reactions. World Scientific, Singapore
38. Bagryansky VA, Borovkov VI, Molin YN (2007) Quantum beats in radical pairs. *Russ Chem Rev* 76:493–506
39. Brocklehurst B (1973) An electron-tunnelling model for recombination of aromatic hydrocarbon radical ions in non-polar solvents. *Chem Phys* 2:6–18
40. Schulten K, Wolynes PG (1978) Semiclassical description of electron spin motion in radical including the effect of electron hopping. *J Chem Phys* 68:3292–3297
41. Stass DV, Lukzen NN, Tadjikov BM et al (1995) Ion-molecular charge-transfer reactions of hexafluorobenzene and *cis*-decalin in nonpolar solutions studied by linewidth broadening in MARY spectra. *Chem Phys Lett* 243:533–539
42. Bagryansky VA, Borovkov VI, Molin YN (2004) Spectroscopic capabilities of the time-resolved magnetic field effect technique as illustrated in the study of hexamethylethane radical cation in liquid hexane. *Phys Chem Chem Phys* 6:924–928
43. Bagryansky VA, Usov OM, Borovkov VI et al (2000) Quantum beats in recombination of spin-correlated radical ion pairs with equivalent protons. *Chem Phys* 255:237–245
44. Bagryansky VA, Ivanov KL, Borovkov VI et al (2005) Spin evolution of radical pairs with radicals containing two groups of equivalent magnetic nuclei. *J Chem Phys* 122(22):224503
45. Bagryansky VA, Borovkov VI, Molin YN (2002) Singlet-triplet oscillations of spin-correlated radical pairs due to the Larmor precession in low magnetic field. *Mol Phys* 100:1071–1078
46. Bagryansky VA, Usov OM, Lukzen NN et al (1997) Spin relaxation parameters in recombining radical ion pair (diphenylsulfide- d_{10}^+)/(*p*-terphenyl- d_{14}^-) obtained by OD ESR and quantum beats techniques. *Appl Magn Reson* 12:505–512
47. Brocklehurst B (1985) Spin correlation effects in radiolysis. *Int Rev Phys Chem* 4:279–306
48. Bagryansky VA, Borovkov VI, Molin YN et al (1997) Quantum beats in the recombination of radical ion pairs caused by hyperfine interaction in radical anions. *Mendeleev Commun* 4:132–133

49. Stass DV, Lukzen NN, Tadjikov BM, Molin YN (1995) Manifestation of quantum coherence upon recombination of radical ion pairs in weak magnetic fields. Systems with non-equivalent nuclei. *Chem Phys Lett* 233:444–450
50. Rodgers CT (2009) Magnetic field effects in chemical systems. *Pure Appl Chem* 81:19–43
51. Timmel CR, Henbest KB (2004) A study of spin chemistry in weak magnetic fields. *Phil Trans R Soc Lond A* 362:2573–2589
52. Toropov YV, Sviridenko FB, Stass DV et al (2000) Influence of geminate recombination kinetics on the shape of low field MARY line. *Chem Phys* 253:231–240
53. Timmel CR, Till U, Brocklehurst B et al (1998) Effects of weak magnetic fields on free radical recombination reactions. *Mol Phys* 95:71–89
54. Tadjikov BM, Stass DV, Molin YN (1996) MARY-detected ESR spectra of radical ions in liquid solutions for systems with crossing Zeeman levels. *Chem Phys Lett* 260:529–532
55. Kalneus EV, Kipriyanov AA Jr, Purtov PA et al (2006) Specific MARY spectrum from radical anion of pentafluorobenzene. *Appl Magn Reson* 30:549–554
56. Kalneus EV, Stass DV, Molin YN (2005) Typical applications of MARY spectroscopy: radical ions of substituted benzenes. *Appl Magn Reson* 28:213–229
57. Stass DV, Anishchik SV, Verkhovlyuk VN (2011) Coherent spin control of radiation-generated radical ion pairs in liquid alkanes. In: Stass DV, Feldman VI (eds) *Selectivity, control, and fine tuning in high-energy chemistry*. Research Signpost, Kerala, pp 143–189
58. Weller A, Nolting F, Staerk H (1983) A quantitative interpretation of the magnetic field effect on hyperfine-coupling-induced triplet formation from radical ion pairs. *Chem Phys Lett* 96:24–27
59. Justinek M, Grampp G, Landgraf S et al (2004) Electron self-exchange kinetics determined by MARY spectroscopy: theory and experiment. *J Am Chem Soc* 126:5635–5646
60. Slichter CP (1990) *Principles of magnetic resonance*. Springer, Berlin
61. Saik VO, Ostafin AE, Lipsky S (1995) Magnetic field effects on recombination fluorescence in liquid *iso*-octane. *J Chem Phys* 103:7347–7358
62. Lersch W, Michel-Beyerle ME (1983) Magnetic field effects on the recombination of radical ions in reaction centers of photosynthetic bacteria. *Chem Phys* 78:115–126
63. Hoff AJ, Gast P, van der Vos R et al (1993) Magnetic field effects: MARY, MIMS and MODS. *Z Phys Chem* 180(1-2):175–192
64. Batchelor SN, McLauchlan KA, Shkrob IA (1992) Reaction yield detected magnetic resonance in exciplex systems: I. B_0 and B_1 spectra. *Mol Phys* 75:501–529
65. Doktorov AB, Anisimov OA, Burshtein AI, Molin YN (1982) Theory of optically detected magnetic resonance spectra of radical pairs. *Chem Phys* 71:1–8
66. Saik VO, Lukzen NN, Grigoryants VM et al (1984) Ion-molecular charge transfer as studied by the method of optically detected ESR of radical pairs. *Chem Phys* 84:421–430
67. Morozov VA, Doktorov AB (1991) Theory of multiquantum optically detected ESR spectra of radical pairs. I. General theory. Resonances in parallel radio-frequency field. *Chem Phys* 153:313–331
68. Lukzen NN, Saik VO, Anisimov OA et al (1985) Saturation of optically detected ESR spectra: Its relationship with kinetic and relaxation parameters of recombining radical-ion pairs. *Chem Phys Lett* 118:125–129
69. Koptyug AV, Saik VO, Anisimov OA et al (1989) Spin-locking in concentration-narrowed OD ESR spectra. *Chem Phys* 138:173–178
70. Anishchik SV, Grigoryants VM, Shebolaev IV et al (1989) Impulsny rentgenovskiy fluorimetr s nanosekundnym rasresheniem (Pulse X-ray fluorimeter with the nanosecond resolution. In Russian). *Prib Tech Exper* 4:74–76
71. Anisimov OA (1991) Ion pairs in liquids. In: Lund A, Shiotani M (eds) *Radical ionic systems*. Kluwer, Dordrecht, pp 285–309
72. Trifunac AD, Bartels DM, Werst DW (1991) Time-resolved magnetic resonance study. In: Tabata Y (ed) *Pulse radiolysis*, CRC, Boca Raton, pp 53–75
73. Trifunac AD, Werst DW (1991) Study of radical cations by time-resolved magnetic resonance. In: Lund A, Shiotani M (eds) *Radical ionic systems*. Kluwer, Dordrecht, pp 195–229

74. Shkrob IA, Trifunac AD (1997) Spin and time-resolved magnetic resonance in radiation chemistry. Recent development and perspectives. *Radiat Phys Chem* 50:227–243
75. Sergey NV, Verkhovlyuk VN, Kalneus EV et al (2012) Registration of radical anions of Al, Ga, In *tris*-8-oxyquinolinates by magnetosensitive and spectrally resolved recombination luminescence in benzene solutions. *Chem Phys Lett* 552:32–37
76. Martini IB, Barthel ER, Schwartz BJ (2000) Mechanisms of the ultrafast production and recombination of solvated electrons in weakly polar fluids: comparison of multiphoton ionization and detachment via the charge-transfer-to-solvent transition of Na⁻ in THF. *J Chem Phys* 113:11245–11257
77. Borovkov VI, Ivanishko IS (2013) Measurement of the relative mobility of geminate ions in ethereal solutions of aromatic compounds using the fluorescence response of the solutions to pulsed irradiation. *J Phys Chem B* 117:15122–15130
78. Werst DW (1996) Self-exchange reactions of radical anions in *n*-hexane. *Chem Phys Lett* 251:315–322
79. Bagryansky VA, Borovkov VI, Molin YN (1998) Quantum beats in the recombination of radical ion pairs caused by hyperfine interaction in radical anions. *Chem Phys Lett* 295:230–236
80. Bagryansky VA, Molin YN, Egorov MP, Nefedov OM (1998) The first experimental detection, by OD ESR spectroscopy, of radical anions of siloles and germales bearing hydrogen and chlorine substituents attached to heteroatom. *Mendeleev Comm* 6:236–237
81. Steingarts VD, Kobrina LS, Bilkis II, Starichenko VF (1991) Himiya polyftorarenov: Mehanizm reakciy, intermediaty (Chemistry of polyfluoroarenes: reaction mechanisms, intermediates. In Russian). Nauka, Novosibirsk
82. Hasegawa A, Itagaki Y, Shiotani M (1997) EPR spectra and structure of the radical cations of fluorinated benzenes. *J Chem Soc Perkin Trans 2*(9):1625–1632
83. Shastnev PV, Shchegoleva LN (1995) Molecular distortions in ionic and excited states. CRS, Boca Raton
84. Lozovoy VV, Grigoryants VM, Anisimov OA et al (1987) The HFI parameters and structure of radical-anions of substituted tetra- and pentafluorobenzenes. Theory and experiment (OD ESR). *Chem Phys* 112:463–471
85. Barlukova MM, Beregovaya IV, Vysotsky VP et al (2005) Intramolecular dynamics of 1,2,3-trifluorobenzene radical anions as studied by OD ESR and quantum-chemical methods. *J Phys Chem A* 109:4404–4409
86. Blinkova SV, Shchegoleva LN, Beregovaya IV et al (2011) Intramolecular dynamics of the 1,2,4-trifluorobenzene radical anion: an optically detected EPR and quantum chemistry study. *Appl Magn Reson* 41:229–238
87. Yim MB, Wood DE (1976) Free radicals in an adamantane matrix. XII. EPR and INDO study of $\sigma^*-\pi^*$ crossover in fluorinated benzene anions. *J Am Chem Soc* 98:2053–2059
88. Das MR, Wagner SB, Freed JH (1970) ESR relaxation studies on orbitally degenerate free radicals. II. *J Chem Phys* 52:5404–5417
89. Kalneus EV, Stass DV, Ivanov KL, Molin YN (2006) A MARY study of radical anions of fluorinated benzenes. *Mol Phys* 104:1751–1763
90. Blinkova SV, Vyushkova MM, Shchegoleva LN et al (2013) Isuchenie strukturnykh osobennostey anion-radicala 1,3,5-triflorbenzola metodami OD EPR i kvantovoy himii (Study of 1,3,5-trifluorebenzene radical anion structure by means of OD EPR and quantum chemistry). *Russ Chem Bull* 11:2311–2316
91. de Haas MP, Warman JM, Infelta PP et al (1975) The direct observation of a highly mobile positive ion in nanosecond pulse irradiated liquid cyclohexane. *Chem Phys Lett* 31:382–386
92. Shkrob IA, Sauer MC Jr, Trifunac AD (2001) Radiation chemistry of organic liquids: saturated hydrocarbons. In: Jonah CD, Rao BSM (eds) *Radiation chemistry. Present studies and future trends*. Elsevier, Amsterdam, pp 175–221
93. Borovkov VI, Usov OM, Kobzeva TV et al (2002) Highly mobile primary radical cations (holes) in irradiated cyclooctane. *Dokl Phys Chem* 384:97–100

94. Usov OM, Stass DV, Tadjikov BM et al (1997) Highly mobile solvent holes in viscous squalane solutions as detected by quantum beats and MARY spectroscopy techniques. *J Phys Chem A* 111:7711–7717
95. Desrosiers MF, Trifunac AD (1985) Observation of transient cyclohexene and 1,4-cyclohexadiene radical cations. Time-resolved fluorescence detected magnetic resonance. *Chem Phys Lett* 118:441–443
96. Werst DW, Desrosiers MF, Trifunac AD (1987) Olefin radical cations in pulse radiolysis of hydrocarbons. Time-resolved fluorescence-detected magnetic resonance. *Chem Phys Lett* 133:201–206
97. Lefkowitz SM, Trifunac AD (1984) Time-resolved fluorescence-detected magnetic resonance and fluorescence studies of trialkylamines irradiated by pulse radiolysis in alkane solvents. *J Phys Chem* 88:77–81
98. Vyushkova MM, Bagryansky VA, Molin YN (2010) Application of optically detected EPR to study the stability of sterically hindered amine radical cations to proton transfer reaction. *Appl Magn Reson* 38:39–49
99. Grigoryants VM, Anisimov OA, Molin YN (1982) Study of the radical-cations of triethylamine and benzene derivatives by the optical detection of the EPR spectra of radical-ion pairs. *J Struct Chem* 23:327–333
100. Saik VO, Anisimov OA, Lozovoy VV, Molin YN (1985) Fast reaction involving radical cations during their geminate recombination as studied by the OD ESR method. *Z Naturforsch* 40a:239–245
101. Toriyama K (1991) ESR studies on cation radicals of saturated hydrocarbons. In: Lund A, Shiotani M (eds) *Radical ionic systems*. Kluwer, Dordrecht, pp 99–124
102. Shiotani M, Lindgren M, Ohta N et al (1991) Radical cations of cyclohexanes alkyl-substituted on one carbon: An ESR study of the Jahn-Teller distorted HOMO of cyclohexane. *J Chem Soc Perkin Trans 2*(5):711–719
103. Lindgren M, Shiotani M (1991) ESR studies of radical cations of cycloalkanes and saturated heterocycles. In: Lund A, Shiotani M (eds) *Radical ionic systems*. Kluwer, Dordrecht, pp 125–150
104. Melekhov VI, Anisimov OA, Sjoqvist L, Lund A (1990) The electronic structure of *cis*- and *trans*-decalin radical cations in halocarbon matrices: An ESR and MNDO study. *Chem Phys Lett* 174:95–102
105. Mehnert R (1991) Radical cations in pulse radiolysis. In: Lund A, Shiotani M (eds) *Radical ionic systems*. Kluwer, Dordrecht, pp 231–284
106. Tagawa S, Hayashi N, Yoshida Y et al (1989) Pulse radiolysis studies on liquid alkanes and related polymers. *Radiat Phys Chem* 34:503–511
107. Veselov AV, Bizyaev VL, Melekhov VI et al (1989) Detection of solvent holes by the method of quantum beats in recombination luminescence. *Radiat Phys Chem* 34:567–573
108. Borovkov VI, Bagryansky VA, Yeletskikh IV, Molin YN (2002) Radical cations of *n*-alkanes in irradiated solutions as studied by time resolved magnetic field effects. *Mol Phys* 100:1379–1384
109. Ichikawa T, Shiotani M, Ohta N, Katsumata S (1989) ESR and optical studies of solute *n*-alkane cations formed in γ -irradiated *n*-pentane and *n*-hexane matrixes. *J Phys Chem* 93:3826–3831
110. Kowalewski J, Liljefors T (1979) On the relationship between the potential barrier and the activation energy for the internal rotation of a methyl group. *Chem Phys Lett* 64:170–174
111. Borovkov VI, Potashov PA, Shchegoleva LN et al (2007) Radical cations of branched alkanes as observed in irradiated solutions by the method of time-resolved magnetic field effect. *J Phys Chem A* 111:5839–5844
112. Potashov PA, Borovkov VI, Shchegoleva LN et al (2012) Radical cations of branched alkanes in solutions: Time-resolved magnetic field effect and quantum chemical studies. *J Phys Chem A* 116:3110–3117
113. Shkrob IA, Liu AD, Sauer MC et al (1998) Reversible hole trapping in liquid cyclohexane. *J Phys Chem B* 102:3371–3378

114. Borovkov VI, Molin YN (2004) Paramagnetic relaxation of cyclohexane radical cation in solution as measured by the method of time-resolved magnetic field effect. *Phys Chem Chem Phys* 6:2119–2124
115. Borovkov VI, Beregovaya IV, Shchegoleva LN et al (2012) Radical ions with nearly degenerate ground state: Correlation between the rate of spin-lattice relaxation and the structure of adiabatic potential energy surface. *J Chem Phys* 137:104305
116. Borovkov VI, Bagryansky VA, Molin YN et al (2003) Detection of radical cations of Group 14 element organometallics in alkane solutions using the method of time-resolved magnetic field effect. *Phys Chem Chem Phys* 5:2027–2033
117. Borovkov VI, Potashov PA, V. A. Bagryansky et al (2008) The study of radical cations of $\text{Me}_3\text{C-SiMe}_3$ and $\text{Me}_3\text{C-GeMe}_3$ in alkane solutions using the method of time-resolved magnetic field effect and DFT calculations. *Chem Phys Lett* 465:307–310
118. Iley J (1995) ESR of organogermanium, organotin and organolead radicals. In: Patai S (ed) *The chemistry of organic germanium, tin and lead compounds*. Wiley, pp 267–289
119. Borovkov VI, Gritsan NP, Yeletskikh IV et al (2006) Degenerate electron exchange reaction of *n*-alkane radical cations in solution. *J Phys Chem A* 110:12752–12759
120. Borovkov VI, Ivanov KL, Bagryansky VA, Molin YN (2006) Longitudinal electron spin relaxation induced by degenerate electron exchange as studied by time-resolved magnetic field effects. *J Phys Chem A* 110:4622–4628
121. Werst DW (1992) Radical cation complexes formed by π -lone pair interactions. *J Phys Chem* 96:3640–3646
122. Borovkov VI, Molin YN (2004) Paramagnetic relaxation of adamantane radical cation in solution. *Chem Phys Lett* 398:422–426
123. Vyushkova MM, Borovkov VI, Shchegoleva LN et al (2008) Unusual proton-transfer complex between the 2,2,6,6-tetramethylpiperidine radical cation and neutral molecule. *Dokl Phys Chem* 420(2):125–127
124. Stass DV, Sviridenko FB, Molin YN (2003) Magnetic field effect study of solvent hole deprotonation in X-irradiated liquid *n*-alkanes. *Radiat Phys Chem* 67:207–210
125. Sviridenko FB, Stass DV, Molin YN (2003) Study of interaction of aliphatic alcohols with primary radical cations of *n*-alkanes using MARY spectroscopy. *Mol Phys* 101:1839–1850

Part VIII
Theoretical Tools

Chapter 18

Uncovering Radiation Chemistry in the Solid State Through Periodic Density-Functional Calculations: Confrontation with Experimental Results and Beyond

Ewald Pauwels

Abstract Three questions are crucial to unravel the radiation chemistry of any solid-state molecular system: what is the structure of the radicals formed, how are they formed and why? Molecular modeling methods based on Density Functional Theory—in confrontation with experimental Electron Paramagnetic Resonance (EPR) results—can help in finding an answer to all three questions. In this contribution, one view on how to perform such computational research is presented, with emphasis on the application of a periodic approach to biomolecules such as amino acids and carbohydrates. General strategies are outlined and common pitfalls are indicated. Topics include: effect of level of theory, model space and temperature on calculated EPR properties, formation mechanisms of radiation-induced radicals, and reaction path simulations for radiochemical transformations. In three case studies, these principles are applied to several radiation-induced radicals of sucrose.

18.1 Introduction

The chemical processes and conformational changes to the radicals that are generated in condensed-phase systems as a consequence of radiation damage have been of interest for many years [1]. The advent of EPR spectroscopy and derived techniques has sparked a way to elucidate these processes and analyze which radicals are generated *in situ* by radiation, owing greatly to their longevity in this phase.

Ever since the emergence of EPR as the leading technique to obtain insight into the radiation-induced processes, first-principles calculations—in some form or other—have been used to facilitate the analysis and interpretation of the spectroscopic properties. Ranging from the “simple” Heller-McConnell relations

E. Pauwels (✉)

UGent HPC, Ghent University, Krijgslaan 281 S9, B-9000 Gent, Belgium
e-mail: ewald.pauwels@ugent.be

Center for Molecular Modeling, Ghent University,
Technologiepark 903, B-9052 Zwijnaarde, Belgium

© Springer International Publishing 2014

A. Lund, M. Shiotani (eds.), *Applications of EPR in Radiation Research*,
DOI 10.1007/978-3-319-09216-4_18

[2, 3], over semi-empirical INDO calculations (e.g. [4]) to current-day density functional theory (DFT) calculations, an interesting historical perspective on the use of calculations has been presented by Neese and Munzarova in the seminal book by Kaupp, Bühl and Malkin [5].

Disregarding the hardships in performing EPR measurements for a moment, deriving structural and mechanistic information from the resulting spectroscopic properties is usually hard and open to ambiguity, certainly for condensed-phase molecular systems. First-principles calculations, and DFT in particular, have provided the experimentalist with a formidable tool to reach new insight into the radiation chemistry. Not surprisingly, ever since 1995, joint computational-experimental research in this respect has steadily grown in popularity.

In this contribution, I present my point of view on how molecular modeling methods can be applied to elucidate radiation chemistry in condensed-phase systems. I will draw heavily on experiences throughout 13-odd years of computational research, often in collaboration with several experimental EPR groups, focusing on two types of solid-state biomolecules: amino acids and carbohydrates. Both systems are abundantly present in the natural world and are vital to the existence of life in all its forms. They can therefore be considered as model systems to examine radiation chemistry and the principles that govern it on a molecular level.

Three questions are key to unravel the radiation chemistry for condensed-phase molecular systems:

1. *WHAT?*—What is the structural identity of the radiation-induced radicals that are generated in the (solid-state) matrix?
2. *HOW?*—Through which processes are these radicals formed and which conformational changes take place to transform one radical structure into another?
3. *WHY?*—Why do we see the radicals that we see? Radiation clearly favors the production of specific radicals. What is the origin of this specificity? Or rather, why are only specific radicals formed by radiation?

It goes without saying that solution of question 2 or 3 requires a solution of all preceding questions. Below, I will outline how molecular modeling methods, in confrontation with experimental data, can contribute to solving these questions. For reasons that will become clear, I will rely solely on periodic DFT calculations (using the CP2K software package [6, 7]) since this methodology is most apt to treat the solid state.

Several radiation-induced radicals in (crystalline) sucrose will serve to illustrate the discussion via three case studies. The motivations for studying these radicals have already been elaborately discussed in Chap. 6 of this book. Recent developments on the radiation chemistry of sucrose were brought about by De Cooman et al., often relying on a combined experimental-computational approach [8–11]. In this work, new computational research will add to that body of work, although these new calculations mainly serve a didactic purpose.

Whenever possible, proper reference to key studies was made, but literature was not scanned exhaustively. I apologize if, in this process, an important study was overlooked.

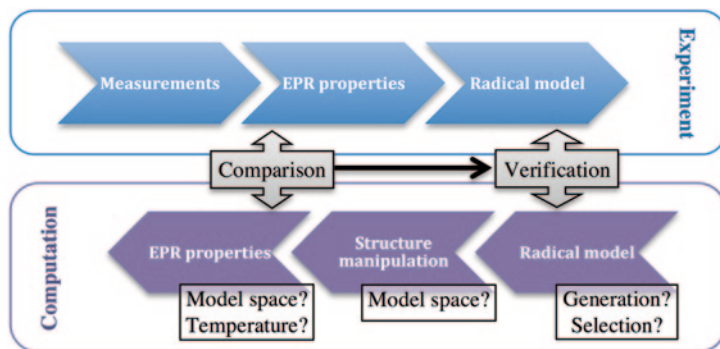


Fig. 18.1 General strategy to identify the structure of radiation-induced radicals by confronting *experiment* and *computation*

18.2 Identifying Radiation-Induced Radicals—*WHAT?*

18.2.1 General Strategy

An essential prerequisite to solving the *WHAT?* question is that the radiation-induced radicals in the molecular system under question have already been examined with the aid of EPR spectroscopy. Without it, confrontation between computation and experiment is obviously not possible, and, despite 50-odd years of research, still not enough is known about radiation chemistry to start making educated guesses. When hyperfine coupling tensors and/or g-tensor (and possibly even zero-field splitting tensor) for a specific radical are available, confrontation with molecular modeling computations is possible. The general strategy to identify the structure of radiation-induced radicals in this way is illustrated in Fig. 18.1.

In the experimental setup, structural information regarding a radiation-induced radical species is deduced by thorough analysis of spectroscopic properties, obtained through EPR, ENDOR and/or EIE studies. For instance, the principal directions of the hyperfine coupling tensors can be compared to interatomic directions observed in the pristine crystal structure, or conformational information can be obtained from the Heller-McConnell relations [2, 3]. Both have been applied frequently to examine the radiation-induced radicals in carbohydrates, amino acids or other biomolecules (e.g. [12–15]).

In molecular modeling, this procedure is instead reversed and one starts out by proposing one or more radical models. Subsequently, the initial structures for these selected radical models are subject to some form of structure manipulation. Usually, a stable radical conformation—a global (or local) energetic minimum in terms of all possible degrees of freedom—is sought via an energy minimization algorithm. Alternatively, molecular dynamics simulations can be used here to explore the conformational space of the radical model. Next, the EPR properties are calculated for the optimal radical conformation. DFT is quite successful in determining such properties, owing largely to advances in the theoretical framework. See the reference

work by Kaupp, Bühl and Malkin [5] for an in-depth treatment on this subject. For the periodic implementations in the CP2K code, consult references [16, 17].

By now comparing measured and calculated EPR properties with each other, the validity of the radical model can be verified: if the spectroscopic properties match within reasonable extent, the proposed radical model in the DFT calculations is likely correct. If not, the experimentally observed radical species probably has a different structure.

A perfect agreement between theory and experiment with respect to the EPR properties is almost never obtained. To assess the agreement, one has to look at the characters of the hyperfine coupling tensors involved (α -type, β -type), the size of the isotropic and anisotropic couplings (or g -tensor components), the agreement between corresponding eigenvectors. Especially the eigenvector directions (for both g - and hyperfine tensors) turn out to be good gauges for the validity of a radical model [18], in contrast with the size of the isotropic coupling, which can vary considerably with the density functional and the extent of the basis set chosen [19].

18.2.2 Case Study 1: Sucrose Radical R2

In the body of work produced by De Cooman et al. on the radiation chemistry of sucrose, several radicals have been unequivocally identified using a combination of EPR experiments and a computational approach (see Chap. 6 and Refs. [8–11]). One of these is R2, a radical likely produced via the oxidative branch in the radiation chemistry of sucrose. This species was observed after in situ X irradiation at 10 K and EPR measurements at the same temperature [9]. R2 is one of four dominant species present in the crystalline matrix at this low temperature, indicating that it is a primary radiation-induced radical. It is characterized by only one hyperfine coupling tensor (see Table 18.1) for a non-exchangeable proton, as determined from EPR measurements on deuterated crystals. Below, the procedure leading up to a positive structural identification for this radical is reprised, consistent with the methodology in Fig. 18.1.

Given that R2 is a primary radiation-induced radical, no major changes to the carbohydrate structure can be expected as a result of the radiative action: simple hydrogen abstractions may be considered as a first possibility. The measured hyperfine coupling tensor is indicative of a non-exchangeable β -type proton, which is therefore directly bound to a carbon adjacent the site of the unpaired electron. However, not all carbons C1 to C6 and C1' to C6' (see Fig. 18.2 for the atom numbering scheme in sucrose) are possible locations for net hydrogen abstraction and the site of the unpaired electron: one and only one hyperfine coupling tensor was recorded, excluding the possibility that α -type or other β -type protons would interact with the unpaired electron. In principle, this excludes sites C2, C3, C4, C5, C6 in the glucopyranose unit of sucrose, and C1', C4', C5', C6' in the fructofuranose unit, leaving as only remaining possibilities hydrogen abstraction from C1 or from C3'. The molecular structures of these models—referred to as M(C1) and M(C3')—are shown in Fig. 18.2. In a very simplistic approach, only these radical models would be considered in the computational cycle.

Table 18.1 Overview of EPR properties for radical species R2 (taken over from Ref. [9]) and for models M(C1) and M(C3'), as obtained from periodic DFT calculations. Isotropic (A_{iso}) and anisotropic hyperfine couplings (A_{aniso}) are in MHz. Principal directions are given with respect to the orthogonal $\langle a^*bc \rangle$ reference frame. The last column indicates the angle (in degrees) between corresponding experimental and calculated eigenvector directions. Note that calculated tensors slightly differ from those reported in [9] since a larger periodic cell was considered in that study: the unit cell duplicated along the crystallographic c axis

Atom/ Coupling	A_{iso}	A_{aniso}	Principal directions			Angle
<i>Experiment: R2</i>						
HF1	29.88	-5.93	0.759	-0.001	-0.651	
		-4.80	0.272	0.909	0.316	
		10.73	0.591	-0.417	0.690	
<i>Computation: M(C1)</i>						
H(C2)	30.43	-5.86	0.791	0.058	-0.609	4.5
		-4.54	0.230	0.894	0.384	4.6
		10.40	0.567	-0.444	0.694	2.1
<i>Computation: M(C3')</i>						
H(C1')	13.13	-2.17	0.441	0.898	-0.009	70.2
		-0.79	-0.766	0.381	0.517	72.4
		2.96	0.468	-0.221	0.856	16.4
H(C4')	96.45	-6.16	0.893	0.348	-0.284	30.3
		-0.95	-0.266	0.920	0.289	31.3
		7.12	0.362	-0.182	0.914	22.9
H(O2')	120.63	-8.40	0.032	-0.040	-0.999	47.6
		-5.97	0.998	0.061	0.030	70.3
		14.37	0.060	-0.997	0.042	61.3

However, the hyperfine coupling of a β -type proton is very sensitive to its orientation with respect to the site of the unpaired electron (which is immediately clear from the Heller-McConnell relation—see Chap. 6 or Ref. [2]). It is not inconceivable that its orientation in the radical is such that the corresponding hyperfine coupling is weak in strength and that it remained undetectable in the EPR measurements. Hence, the absence of a β -type coupling in the experiment does not necessarily mean that there are no protons in the radical in a β -position with respect to the unpaired electron. Hydrogen abstractions from C2, C3, C4, C5, C4' or C5' should therefore not be rejected *a priori*. Only models M(C6), M(C1') and M(C6') can be safely disregarded as they would yield a clear α -type hyperfine coupling (which hardly goes undetected in EPR or ENDOR spectra). This brings the total of radical models to be investigated with DFT to eight: M(C1), M(C2), M(C3), M(C4), M(C5), M(C3'), M(C4'), M(C5').

In the original paper by De Cooman et al. [9] a further reduction of tentative radical models was made. A point-dipole approximation was used and the direction of the eigenvector associated with the most positive principal hyperfine coupling value was compared with various interatomic directions in the pristine crystal lattice of sucrose. In this way, the list of potential candidates was reduced from eight to three.

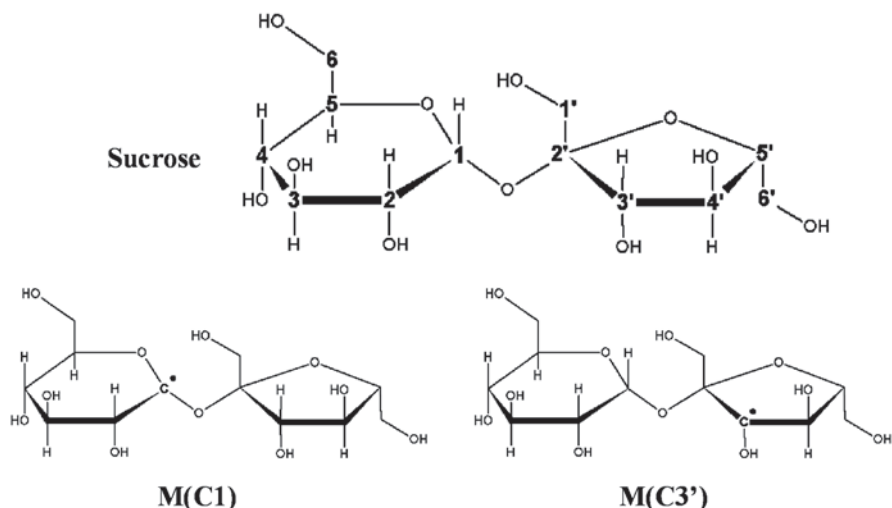


Fig. 18.2 *Top*: molecular structure of sucrose and atom numbering scheme. *Bottom*: molecular structure of radical models $M(C1)$ and $M(C3')$

The validity of the point-dipole approximation, however, hinges on the structural and conformational similarity of the radical and the crystal structure. If the radical assumes a dramatically different conformation, the correct radical model might be falsely disregarded. In this work, all eight potential candidates are considered, albeit with more emphasis on models $M(C1)$ and $M(C3')$ for illustrative purposes.

For all selected models, initial geometries are created, illustrated in Fig. 18.3 for $M(C1)$ and $M(C3')$. One of the molecules in the crystallographic unit cell of sucrose is adapted in accordance with the chemical structure of the radical model. In this case, the hydrogen bound to C1 or C3' is simply removed from the periodic cell altogether, yielding the initial geometries. Subsequently, these are subject to energy minimization using a limited memory version of the Broyden–Fletcher–Goldfarb–Shanno (BFGS) algorithm [21]. The BLYP density functional [22, 23] is used in conjunction with the Gaussian and plane waves (GPW) dual basis set method [24] using a TZVP triple- ζ Gaussian basis set [25] and plane waves (400 Ry density cut-off) with GTH pseudopotentials [26, 27]. The optimized geometries are shown on the right hand side of Fig. 18.3. For both radical models, the final optimized conformation is very similar to that of the initial geometry. Similar energy minimizations are also performed for the other radical models.

The EPR properties can now be calculated for the optimized geometries of all eight radical models, relying on recent implementations [16, 17] in CP2K [6, 7] and the all-electron Gaussian and augmented plane wave (GAPW) method [28]. The density cut-off of the auxiliary plane wave basis is set to 200 Ry and the all-electron TZVP basis [29] is used. Note that not necessarily the same basis set, density

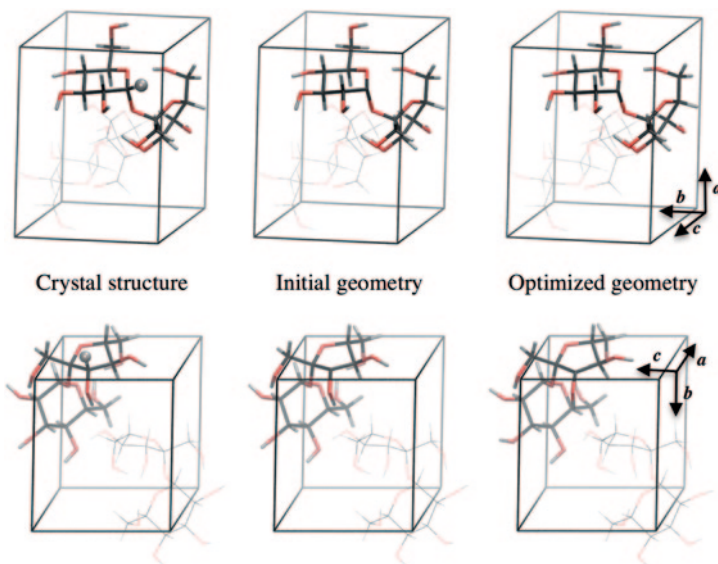


Fig. 18.3 From *crystal structure* to *optimized geometry* for radical models M(C1) (*top*) and M(C3') (*bottom*). In one molecule in the unit cell (shown as *licorice*), a single proton is removed (shown as *sphere*) to generate the initial geometry. Energy minimization of that structure yields the *optimized geometry*. 3D-renders produced with the aid of VMD [20]

functional or plane wave approach need to be followed in the EPR calculation and the structure manipulation steps. In fact, the dual methodology outlined above has proven quite successful in various other studies [30–33].

The calculated EPR properties are listed in Table 18.1 for models M(C1) and M(C3'), and in Table 18.2 for the other six radical models. From a qualitative point of view, only one radical model meets the one-hyperfine-tensor-only criterion: M(C1). All the others have at least one other significant proton hyperfine coupling interaction. Also, not many of the calculated tensors display the almost prototypical β -type character of the measured HF1 interaction in radical R2 (see Table 18.1): H(C2) in M(C1), H(C1) in M(C2), H(C6)a/b in M(C5) and H(C6')a/b in model M(C5'). Of these, only H(C2) matches quantitatively with the experimental HF1 coupling, both for the isotropic and anisotropic parts. Furthermore, the principal directions for this calculated hyperfine tensor are very similar to those of the experiment. The deviation (expressed in degrees) between corresponding directions is below 5° at all times, which is an extremely good agreement. None of the principal directions in the other calculated hyperfine tensors come even close.

Reviewing the agreement between calculated and measured hyperfine tensors, there is very little doubt that the structure of radical R2 observed experimentally corresponds to that of radical model M(C1). Our new simulations therefore concur with the results of De Cooman et al. [9].

Table 18.2 Overview of calculated EPR properties for various hydrogen abstraction radical models of sucrose. Isotropic (A_{iso}) and anisotropic hyperfine couplings (A_{aniso}) are in MHz. The angle (in degrees) indicates the agreement in direction between the calculated eigenvectors and those of the experimental HF1 tensor (see Table 18.1)

Atom	A_{iso}	A_{aniso}	Angle	Atom	A_{iso}	A_{aniso}	Angle
<i>M(C2)</i>				<i>M(C3)</i>			
H(C1)	26.61	-5.72	32.7	H(C2)	96.60	-4.61	52.6
		-3.86	66.7			-2.35	56.5
		9.58	56.8			6.95	27.6
H(C3)	98.33	-5.15	23.8	H(C4)	84.43	-4.85	75.2
		-0.97	28.6			-1.68	43.7
		6.12	24.3			6.53	76.2
H(O2)	3.48	-10.60		H(O3)	-7.44	-11.55	
		-9.10				-8.30	
		19.70				19.85	
<i>M(C4)</i>				<i>M(C5)</i>			
H(C3)	88.79	-5.57	81.8	H(C4)	94.55	-5.29	43.3
		-0.77	63.4			-1.24	46.4
		6.34	79.0			6.54	18.0
H(C5)	88.67	-4.33	29.2	H(C6)a	2.84	-6.00	63.8
		-2.65	28.9			-3.54	75.0
		6.98	17.8			9.54	63.6
H(O4)	-5.11	-11.27		H(C6)b	15.61	-6.01	75.1
		-8.35				-3.49	59.0
		19.62				9.50	60.1
<i>M(C5')</i>				H(O6)	-4.31	-7.59	
H(C4')	69.20	-4.92	37.0			0.45	
		-2.31	39.6			7.14	
		7.24	30.0	<i>M(C4')</i>			
H(C6'a)	5.40	-5.75	64.8	H(C3')	81.90	-5.14	71.5
		-3.45	22.1			-1.58	7.9
		9.20	60.2			6.72	71.6
H(C6'b)	9.31	-6.39	72.8	H(C5')	80.11	-4.52	26.3
		-3.43	46.0			-2.62	39.9
		9.83	64.7			7.14	45.8
H(O6')	-5.36	-8.80		H(O4')	-4.00	-12.21	
		0.70				-9.16	
		8.10				21.38	

18.2.3 Radical Model Generation and Selection

As case study 1 points out, selecting a radical model to initiate the DFT calculation cycle is not trivial. Nor is generating an initial structure for the selected model. Usually, an initial structure for the radical is generated by introducing alterations to the crystallographic structure of the molecule under study, e.g. by removing a hydrogen atom. These alterations should reflect the action of the radiation damage, but proposing and executing these alterations is very hands-on. One can usually draw on prevailing radiation chemistry theories [34] for inspiration, but human

interaction is always required. Also, often a large amount of candidate structures must be examined before a radical model is found with calculated EPR properties that successfully match with experiment. The case of R2 is ‘lucky’ in that respect, since only eight models were required. But in some cases, even a cornucopia of candidate models is not enough to home in on the true identity of a radiation-induced radical: the structure of the room-temperature radical in β -D-fructose is still a mystery [35] even though over 60 different models have been examined.

The level of ‘realism’ that is introduced by the structural alterations in the computational approach is also important. Removing a hydrogen atom altogether from the crystal structure corresponds to the situation where radiation has knocked off the hydrogen, which has then—somehow—diffused throughout the crystal, away from the radical site. This simple approach has worked wonderfully well in various carbohydrates, amino acids and other biomolecules (e.g. [8–11, 13, 18, 35–43]). Alternatively, the abstracted hydrogen might stick around in the vicinity of the radical, influencing its molecular environment and also its EPR properties. This latter situation is even more likely to apply when larger molecular fragments are involved, such as abstracted hydroxyl or even larger groups. In these cases, it might be necessary to include those abstracted fragments in the molecular model in order to get a good agreement between measured and calculated EPR properties. Knowing exactly in what way the radiation damage proceeds, which processes and conformational changes are involved (i.e. solving the *HOW?* question) then becomes a prerequisite for identification. In alanine, such an examination was required to identify the structure of the main room temperature stable radical [30].

As problematic cases (such as the elusive room-temperature radical in β -D-fructose [35]) point out, coming up with new radical models to input at the computational side of the identification process can be a limiting factor. This is due to, what I often call, the *human Monte Carlo algorithm* that is used to furnish new radical models: a human needs to come up with a bright new idea of what structure a particular radical could have. Inspiration from established radiation chemistry [34] or human imagination only go so far, and so this poses a big challenge to joint computational-experimental EPR studies into radiation chemistry.

One way to surpass this bottleneck is by automating the way in which possible radical models are generated: implementing a *non-human Monte Carlo algorithm*. To the best of my knowledge, no substantial research has been conducted in this field. Perhaps the approach by Tachikawa et al. [44, 45] comes close: direct ab-initio molecular dynamics is used to examine the structural and conformational events immediately following a drastic change in the potential energy surface (e.g. going from a neutral to an ionized and paramagnetic state). Whether a similar approach could be useful as a semi-automated *generator* for potential radical models in carbohydrates or other biomolecules requires further computational research [46].

18.2.4 Model Space

For condensed phase systems, the most important computational parameter throughout the computational cycle is the *model space*: the extent with which the molecular

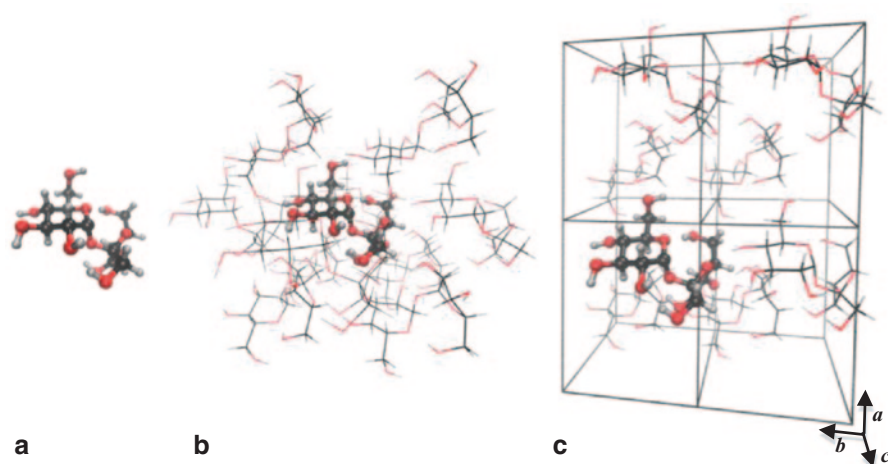


Fig. 18.4 Illustration of the three model space approaches applied to the R2 radical structure of sucrose: single molecule (a), cluster (b) and periodic approach (c). The radical is represented by “ball-and-stick”, its molecular environment in the model space approach by lines. Note that, in the cluster approach, considerably more surrounding molecules must be taken up in the model as compared to the periodic approach. 3D-renders produced with the aid of VMD [20]

environment of a radiation-induced radical is taken up in the DFT calculation. This aspect is of importance in the ‘structure manipulation’ as well as the ‘EPR calculation’ steps. Three types of model space approaches can be distinguished. Illustrative examples for sucrose are shown in Fig. 18.4.

Single Molecule Approach The simplest approximation is to completely neglect the molecular environment. In this approach, the optimal conformation of the radical is determined in a vacuum. The obvious benefit is the simplicity of the model and concomitant speed of the calculation. The downside is that all-important intermolecular interactions in the solid state are not at all incorporated in the computational model. Nevertheless, this approximation can be used with success and remains quite popular.

Cluster Model Approach One rung up is to include the medium in a so-called cluster model: a small part of the crystal lattice is explicitly modeled, by placing discrete molecules around the target radical. Though this offers an immediate, easy way of including some intermolecular interactions (e.g. all hydrogen bonds in the crystal), this model space can be totally unreliable [40]. For the main radiation-induced radical in solid-state α -glycine, for example, the selection of the number and position of the pristine molecules surrounding the radical proved to determine the results heavily, but in a seemingly unphysical way: larger clusters offered a *worse* description of the solid state than smaller ones. In addition to their unreliability related to the biased or arbitrary selection of molecules to include, cluster models tend to impose a considerable computational burden, especially in comparison with a periodic approach. Furthermore, constraints have to be imposed to the molecules at the outskirts of the cluster. These molecules are in contact with the

vacuum and need to be held in place in one way or another to prevent the entire cluster from distorting, possibly altering the bulk-like interactions at the center of the cluster. This can give rise to boundary problems [18].

Periodic Approach This approach offers the most natural and cost-effective way of describing the solid-state environment. The model space consists of the actual crystallographic unit cell, which is subject to periodic boundary conditions, in which a certain amount of radical defects has been introduced. In the sucrose example outlined below, this is achieved by altering one of the two molecules in the unit cell. Depending on how densely the molecules are packed together in the crystal, it might be necessary to double the original unit cell in one or more crystal directions, to ensure that the radical defects are sufficiently separated from each other under periodic boundary conditions.

The model space treatment in any computational approach has a severe impact on the results that are obtained. In an energy minimization ('structure manipulation' step), neglect of the medium can lead to erroneous conformations. Sometimes this is blatantly apparent: zwitterionic amino acids *cannot* be properly described in a single molecule approach and undergo intramolecular proton transfer [36]. But in other cases the effect can be more subtle, leading to erroneous identification of radical structures (e.g. in fructose [47]) or unjustified rejection of a candidate radical structure. An extensive analysis of the effect of the model space on radical conformation (and concomitantly the EPR properties) has been conducted on the main glycine radical [18].

The model space is also important in the calculation of the EPR properties, irrespective of its effect on the conformation of the radical. As shown by Declerck et al. on glucose and fructose radicals [37], the model space alone can have a direct influence on the hyperfine coupling tensors: calculated principal directions can easily deviate by 30°, and the isotropic coupling size can vary by as much as 20 MHz. But even more fundamentally, an appropriate model space approximation needs to be in place to properly compare the calculated principal directions of g- and hyperfine tensors with their experimental counterparts.

In experiment, principal directions are specified as direction cosines with respect to the crystal axes (or an orthogonal projection of them). Calculated principal directions must therefore also be specified with respect to the same reference frame for proper comparison. In a periodic or cluster approach, some part of the undamaged crystal is comprised in the model space and consequently the orientation of the crystal axes is always known. Thus, whatever conformational changes the radical undergoes during the 'structure manipulation' step, the absolute orientation of the resulting structure(s) with respect to the crystal axes can at all times be traced. In a single molecule approach, on the other hand, no such information is retained during the calculation, and analysis of calculated principal directions becomes more cumbersome. One way to get by this problem is to assume that the global orientation of the radical does not change dramatically with respect to the pristine crystal structure (in the Gaussian software [48], this is most easily achieved via the NOSYM keyword), or alternatively, to perform a least-squares fit on the radical prior to the EPR calculation. This is illustrated in Fig. 18.5a. This method is by far not always valid:

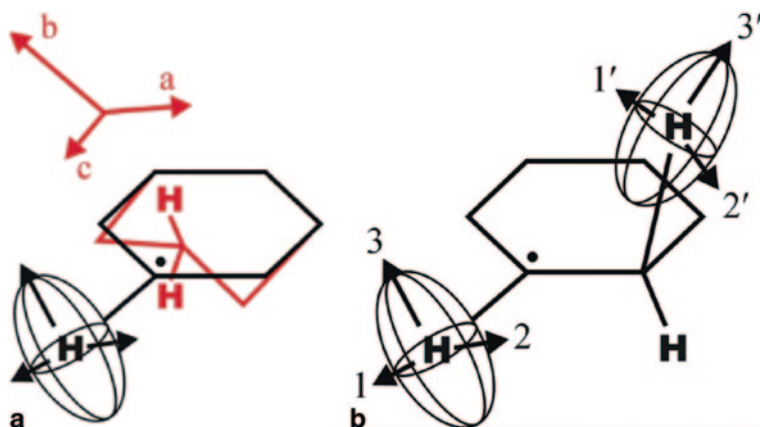


Fig. 18.5 **a** In a single molecule approach, the calculated principal directions of, e.g. a hyperfine tensor in a radical (represented by an *ellipsoid—black*) can be referred to the crystallographic axes $\langle abc \rangle$ by first performing a least-squares fit between the radical structure and the pristine crystal structure (*red*). **b** Alternatively, the relative orientations of the principal directions from two different hyperfine tensors can be used as a measure to compare with experiment: for instance the angles between principal directions 1 and $1'$, 1 and $2'$, and so on

the structure of a radical often differs substantially from the undamaged crystal structure. In several radiation-induced carbohydrate radicals, for example, the ring structure is dramatically broken up (see Chap. 6).

Another way to cope with the unavailability of the crystal axes' orientation in the single molecule approach is to consider the relative orientations of two or more EPR spectroscopic properties (see Fig. 18.5b). The angles can be determined between the principal directions ($1, 2, 3$) of one hyperfine coupling tensor and those ($1', 2', 3'$) of another hyperfine tensor, or the g -tensor. The resulting data matrix can then be compared to that determined in a similar fashion for the experimental data. Yet, application of this complex procedure to identify radiation-induced radicals in fructose has worked out rather disappointingly. The structure predicted in this way [47] for the most abundant room-temperature stable radical was later shown to be not correct [35]. An absolute analysis of the principal directions of hyperfine and g -tensors remains preferential, unless of course there is no direct link to the crystallographic axes in the experiment itself. This is frequently the case in EPR studies of biomolecules (e.g. proteins) where crystals are hard to grow and measurements are much easier to perform in powders or frozen solution. In that case, a relative analysis of the principal directions does make sense [38, 41].

As stated, the model space is the single most important computational parameter. Its impact should never be underestimated, especially not in favor of other, more technical parameters such as the density functional or extent of the basis set. Although the latter parameters are obviously of importance and of interest, I do not believe that any novelty density functional or extended basis set can make up for the neglect of the molecular environment in, e.g. a single molecule approximation

of what would be a condensed-phase molecular system. In a nutshell: efforts should first go to providing a sufficient computational description of the model space; only then should other parameters be contemplated. In line with that view, a periodic approach is always followed throughout this chapter, usually with triple- ζ basis sets [25, 29] and the BLYP functional [22, 23].

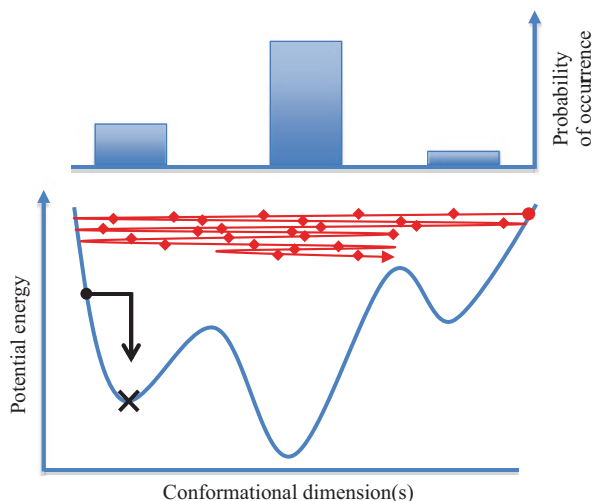
18.2.5 Temperature

Usually, the calculations in the ‘structure manipulation’ and ‘EPR calculation’ steps (see Fig. 18.1) are static. That is, only one radical conformation is considered, typically one obtained from an energy minimization. These algorithms (e.g. LBFGS [21]) do not guarantee that the resulting conformation is effectively the global energetic minimum on the potential energy surface in terms of all possible degrees of freedom. They are only able to locate a minimum, possibly a local one. This is illustrated in Fig. 18.6 where, starting from an initial structure (black circle) the algorithm drops into the nearest local minimum (black cross), instead of the central global energetic minimum. Hence, static structure manipulation calculations could result in a ‘wrong’ conformation, and the ensuing radical model identification might be equally erroneous.

But even when the ‘correct’ radical conformation is obtained, a static EPR calculation on this one conformation only does not exactly correspond to reality either. From a methodological point of view, this amounts to simulating the radical at 0 K, whereas experimental measurements on the radical occur at a finite temperature. And in reality, the radical and its environment undergo rapid conformational changes that do affect the spectroscopic properties: an average property is measured over a considerable time epoch (of the order of *ms*) during typical EPR experiments, be they continuous wave or pulsed. Therefore, for the hypothetical potential energy surface of Fig. 18.6, the observed EPR properties will be the Boltzmann-weighted average of the spectroscopic properties for all three minima. Those of the central, global minimum will certainly dominate, but the properties of the local minima will contribute as well.

Going beyond the static approximation in a computational approach is possible by using, e.g. molecular dynamics (MD) in which Newton’s equations of motion are solved iteratively. In a series of consecutive discrete timesteps (typically 1 fs), the atomic coordinates of a radical model evolve in time. For each step, the force due to the potential energy (calculated at the DFT level of theory) and a kinetic energy contribution (finite temperature) is evaluated and integrated. This yields a trajectory, an ensemble of snapshots (one for each timestep) that represent the atomic motion of the molecular system during the total simulated time. On current-day High Performance Computing facilities, it usually takes several seconds to evaluate the ab-initio forces for a molecular system at one timestep (1 fs). Hence, MD simulations relying on DFT usually span just several *ps* or *ns* only. The effective calculation time for such a simulation often takes several weeks or even months!

Fig. 18.6 Illustration of a (fictitious) *potential energy* surface and the effect of an energy minimization algorithm (in *black*) and molecular dynamics (in *red*)



Relying on MD as the main algorithm in the ‘structure manipulation’ step offers the possibility to locate new, more stable minima. Even when a poor initial conformation is chosen (e.g. the red sphere in Fig. 18.6), a large part of the multidimensional potential energy can still be reached: the introduction of kinetic energy enables that barriers in the potential energy surface can be crossed. Sufficiently long MD simulations, then, allow complete sampling of the potential energy surface. More optimal conformations will occur more during the trajectory, with their probability of occurrence directly (but inversely) related to their potential energy (illustrated at the top of Fig. 18.6).

An MD trajectory can also be used to account for temperature effects on the calculated EPR properties. Instead of determining these for just one conformation (e.g. the black cross in Fig. 18.6), a whole bunch of conformations attained during the MD can be considered. Usually, a subsampling of the trajectory is used—100–1000 snapshots (e.g. the red diamonds in Fig. 18.6)—for which the EPR properties are each time calculated. Subsequently, the resulting data is averaged. This is straightforward for scalar data, such as the isotropic hyperfine coupling tensor, but for other tensorial data care should be taken that diagonalization is only performed after the averaging.

If EPR properties are calculated for N snapshots from an MD trajectory, the average hyperfine coupling tensor (for example) is:

$$\langle \mathbf{A} \rangle = \frac{1}{N} \sum_{i=1}^N \mathbf{A}_i \quad (18.1)$$

Subsequently, this average tensor is diagonalized:

$$(\mathbf{V}_1 \ \mathbf{V}_2 \ \mathbf{V}_3)^T \langle \mathbf{A} \rangle (\mathbf{V}_1 \ \mathbf{V}_2 \ \mathbf{V}_3) = \begin{bmatrix} A_1 & & \\ & A_2 & \\ & & A_3 \end{bmatrix} \quad (18.2)$$

This yields three average eigenvalues $A_1 - A_3$ (expectation values) and their corresponding principal directions $V_1 - V_3$. The same procedure can obviously be used for the g tensor.

Although temperature does affect the calculated EPR properties, the effect is usually quite subtle for solid-state radicals. Solvated radicals are much more flexible (e.g. [49]) than those trapped inside a crystalline matrix, with concomitant effect on their spectroscopic properties. In fact, static EPR calculations usually suffice for structural identification purposes. The added value of dynamic calculations is that insight is obtained in the structural dependence of the spectroscopic properties involved. For instance, in the main α -type glycine radical, out-of-plane motion of the paramagnetic center has a marked effect on the hyperfine coupling tensor of the associated α -carbon and α -proton (e.g. [40, 42]).

18.2.6 Case Study 2: Sucrose Radicals T2/T3

The radicals that are stable at room temperature in irradiated sucrose have been elaborately characterized by De Cooman et al. in joint experimental-computational studies [8, 10, 11]. Three different radicals are present in the irradiated crystalline matrix, labeled T1, T2 and T3. The latter two radicals are very similar, as can be seen from their spectroscopic properties (Table 18.3), and both were identified as having the same chemical structure. The origin of the minor differences in spectroscopic properties for both radicals is still unclear, although it is suspected that changes in the molecular environment might be the cause [8, 10, 11].

The structure of the T2/T3 radicals is shown in Fig. 18.7. Considerably more than simple hydrogen abstraction has occurred: the glycosidic linkage between the glucose and fructose unit is broken, a carbonyl group is present at C2 and the unpaired electron is localized at C1. In the original publication [8], this structure was identified from a limited set of plausible radical models that was first obtained by adopting the point-dipole approximation. Subsequent DFT calculations, relying on the CPMD software [50] for periodic structure calculations and ensuing cluster calculations with Gaussian [48], yielded the conclusive identification.

Repeating the identification in a uniform periodic approach with the aid of CP2K [6] and the same computational parameters mentioned in paragraph 18.2.2, at first an initial geometry is generated starting from the crystallographic unit cell. The H2 and HO2 hydrogens are removed, and an additional proton is placed at the O1 position. The C1–O1 bond is broken during the energy minimization, by applying a restraint force keeping both atoms apart, followed by an unrestrained minimization. The structure resulting from this rather straightforward approach, in line with that in the previous showcase, is shown in Fig. 18.8a and will be referred to as radical model M(T2/T3-a).

Calculated EPR properties for this radical model are given in Table 18.4 and the nice agreement with the experimental properties of Table 18.3 is immediately clear. The proton at C1 gives rise to an α -type hyperfine coupling, the other couplings are due to γ -protons H(C3) and H(C5). Even though the size of the isotropic coupling

Table 18.3 Overview of EPR properties for radical species T2/T3 (taken over from Ref. [8]). Principal directions are given with respect to the orthogonal $\langle a^*bc \rangle$ reference frame. Although g -tensor information is also available [10], the focus in this chapter will be on the hyperfine coupling tensors

Coupling	A_{iso}	A_{aniso}	Principal directions		
<i>T2</i>					
H α	-38.69	-19.66	0.424	-0.163	-0.891
		-2.11	0.886	0.280	0.371
		21.77	0.189	-0.946	0.263
H β 1	16.37	-2.32	0.869	-0.355	-0.344
		-1.72	-0.209	0.368	-0.906
		4.04	0.448	0.86	0.246
H β 2	13.68	-3.09	0.718	-0.65	0.248
		-2.17	0.638	0.473	-0.608
		5.26	0.278	0.595	0.754
<i>T3</i>					
H α	-35.81	-18.98	0.584	-0.184	-0.79
		-2.11	0.755	0.481	0.446
		21.09	0.298	-0.857	0.420
H β 1	16.42	-2.1	0.84	-0.541	-0.034
		-1.77	0.178	0.334	-0.926
		3.87	0.512	0.772	0.377
H β 2	12.24	-3.62	0.528	-0.822	0.214
		-2.12	0.804	0.402	-0.439
		5.74	0.275	0.403	0.873

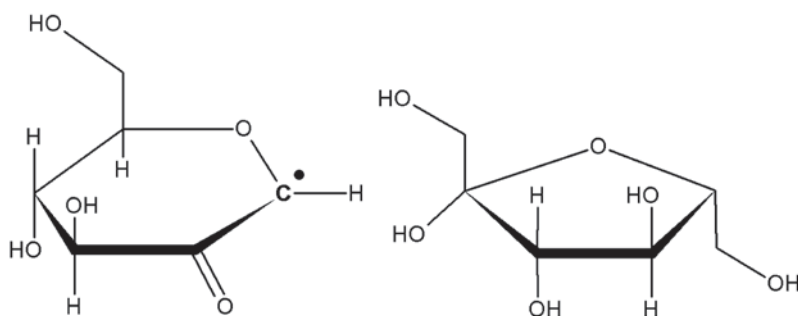


Fig. 18.7 Molecular structure for radicals T2/T3, identified by De Cooman et al. in [8]

for H(C1) is slightly underestimated in the calculations, this agreement can still be considered as very good, especially considering the agreement between the corresponding principal directions: calculated and measured eigenvectors align to within $\sim 10^\circ$ for radical T3 and even less than 5° for radical T2. These calculations yield similar results as those of the cluster calculations by De Cooman et al. [8], although there slightly better isotropic values were obtained (possibly owing to the use of the B3LYP functional [51] in the EPR calculation step).

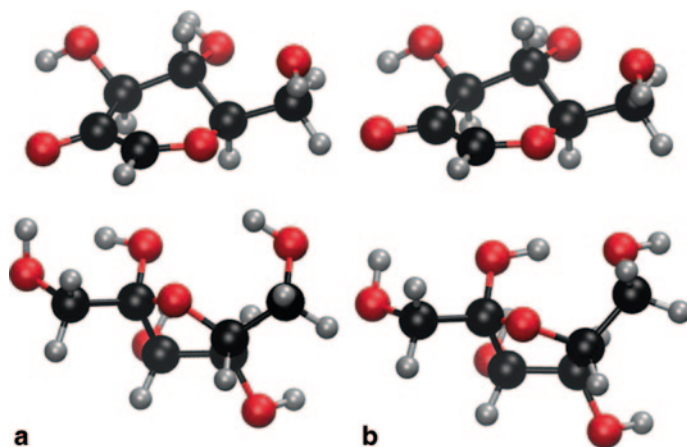


Fig. 18.8 Conformation of the radical models corresponding to measured radicals T2/T3: **a** M(T2/T3-a) after ‘simple’ energy minimization starting from the adapted crystallographic unit cell structure. **b** M(T2/T3-b) after energy minimization ensuing an 11 ps MD run. 3D-renders produced with the aid of VMD [20]

To go beyond this static approach, *ab initio* MD simulations are initiated on the optimized structure of radical model M(T2/T3-a). Simulations are performed in the NVT ensemble, employing a time step of 1 fs for a total of 11,000 steps (11 ps). A fast velocity-rescaling thermostat algorithm [52] is used in the first 1000 steps, after which the Nosé-Hoover thermostat [53, 54] is selected for the final 10 ps (which are considered of *production* quality). An illustration of the conformational changes to the radical model is given in Fig. 18.9, where several snapshots throughout the production part of the MD trajectory are shown.

In the glucose unit, mostly the planarity of the radical center (C1) changes as it undergoes an umbrella-like motion. In the fructose unit, the position changes of the hydroxyl proton on oxygen O1 (which constituted the former glycosidic linkage). The former molecular motion can be quantified to some extent by the *improper* dihedral angle H(C1)–C2–O5–C1, the latter molecular motion by the dihedral angle H(O1)–O1–C2’–C3’. The variation of these two angles throughout the MD trajectory is shown in Fig. 18.10.

The conformation of the radical center (blue) remains planar on average, but out-of-plane digressions of about $-20^\circ/+20^\circ$ occur due to the umbrella-like motion. The orientation of the hydroxyl proton on oxygen O1 (red) changes by 60° after about 2 ps in the MD: clearly a new, stable conformation is obtained. This is confirmed when the last snapshot from the MD trajectory is subject to full energy minimization. The resulting conformation M(T2/T3-b), shown in Fig. 18.8, has an absolute energy of -513.57366 a.u. which is lower by about 35 kJ/mol than that of conformation M(T2/T3-a) at -513.56042 a.u.

The EPR properties of this new energetic minimum M(T2/T3-b) are quite similar to those of the other conformation (see Table 18.4). The isotropic hyperfine coupling values for protons H(C3) and H(C5) are slightly raised, but the anisotropic parts have hardly changed and the principal directions are roughly in the same direction as for

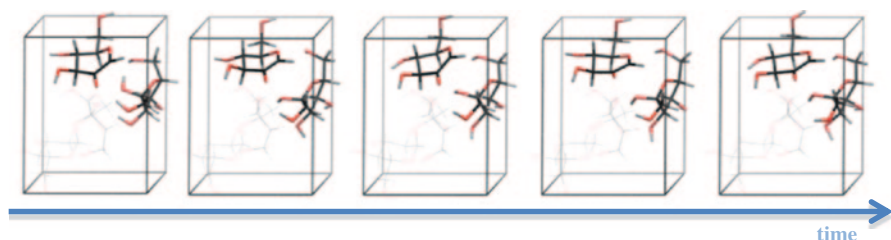


Fig. 18.9 Conformations of radical M(T2/T3) representatively sampled throughout the last 10 ps of the MD simulation. 3D-renders produced with the aid of VMD [20]

Table 18.4 Calculated EPR properties for radical models M(T2/T3-a) and M(T2/T3-b). Isotropic (A_{iso}) and anisotropic hyperfine couplings (A_{aniso}) are in MHz. The angle (in degrees) indicates the agreement in direction between the calculated eigenvectors and those of the experimental tensors of radicals T2 and T3, respectively (see Table 18.3)

Atom	A_{iso}	A_{aniso}	Angle (T2)	Angle (T3)	Coupling
<i>M(T2/T3-a)</i>					
H(C1)	-23.20	-16.91	1.1	9.9	$H\alpha$
		-4.99	4.6	10.5	
		21.90	4.5	8.3	
H(C3)	21.04	-2.19	7.7	14.3	$H\beta_1$
		-1.85	7.8	14.7	
		4.04	2.3	8.7	
H(C5)	13.44	-3.26	14.7	24.5	$H\beta_2$
		-1.72	16.3	24.5	
		4.99	12.0	1.0	
<i>M(T2/T3-b)</i>					
H(C1)	-24.65	-15.88	2.5	9.3	$H\alpha$
		-4.76	5.9	9.9	
		20.64	6.3	6.0	
H(C3)	24.00	-2.38	1.7	21.4	$H\beta_1$
		-1.63	8.9	21.4	
		4.01	9.0	1.0	
H(C5)	15.80	-3.49	13.0	21.5	$H\beta_2$
		-1.81	14.4	21.5	
		5.30	13.1	0.3	

conformation M(T2/T3-a). This can be expected, since the main changes between both conformations have not happened to the radical center itself but merely in its vicinity. Accordingly, one cannot easily state that one conformation or the other agrees better with experimental data. But given that it has a lower potential energy, conformation M(T2/T3-b) is much more likely to correspond with reality.

So far still, the EPR properties were calculated in a *static* fashion: for one conformation only (even though its structure might have sprung from a dynamic simulation). To go beyond that, EPR properties are calculated for 1000 snapshots, regularly sampled (every 10 fs) during the last 10 ps of the MD simulation. The variation of the spectroscopic properties is illustrated in Fig. 18.11, where the isotropic hyper-

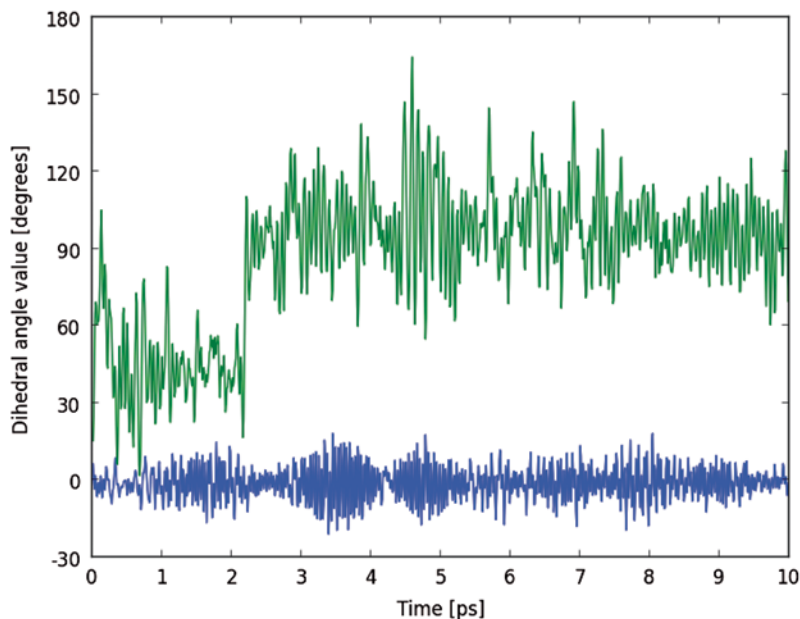


Fig. 18.10 Variation of *dihedral angles* H(C1)–C2–O5–C1 (*blue*) and H(O1)–O1–C2'–C3' (*green*) in sucrose radical model M(T2/T3) during the last 10 ps of an MD simulation at 300 K

fine coupling values of H(C1), H(C3) and H(C5) are plotted as a function of simulation time.

The isotropic couplings vary considerable as (even minor) conformational changes occur during the MD run. Yet, on average, the values fluctuate about -23.47 MHz for H(C1), 21.11 MHz for H(C3), and 16.51 MHz for H(C5), close to what is found in the static approaches for conformations M(T2/T3-a/b). The variation of the proton coupling values during the dynamics is perhaps best seen in a histogram (Fig. 18.12). This type of plot reverberates the typical experimental EPR spectra, but more importantly gives insight in the “variability” that can be attained in a prototypical computational approach. For the H(C1) α -type coupling, the isotropic value easily covers the interval -30 to -20 MHz. The variability for the γ -type couplings H(C3) and H(C5) is even bigger. Here, the dispersion in values can be of the 20 MHz order. Note that this is not an “error” nor standard deviation for the computational setup; this analysis merely indicates how susceptible the calculated EPR properties are to (minor) conformational changes during the molecular dynamics.

To fully analyze the calculated hyperfine tensor data for the snapshots from the MD simulation, an average tensor is calculated according to Eqs. (18.1)–(18.2). To distinguish the possible effect of the H(O1) hydroxy proton rearrangement (see Fig. 18.10) on the calculated EPR properties, average hyperfine tensors are calculated for three time epochs: one for the snapshots in the time range 0.00–2.25 ps, another for the range 2.35–10.00 ps, and another for *all* snapshots from the MD simulation. These results are presented in Table 18.5.

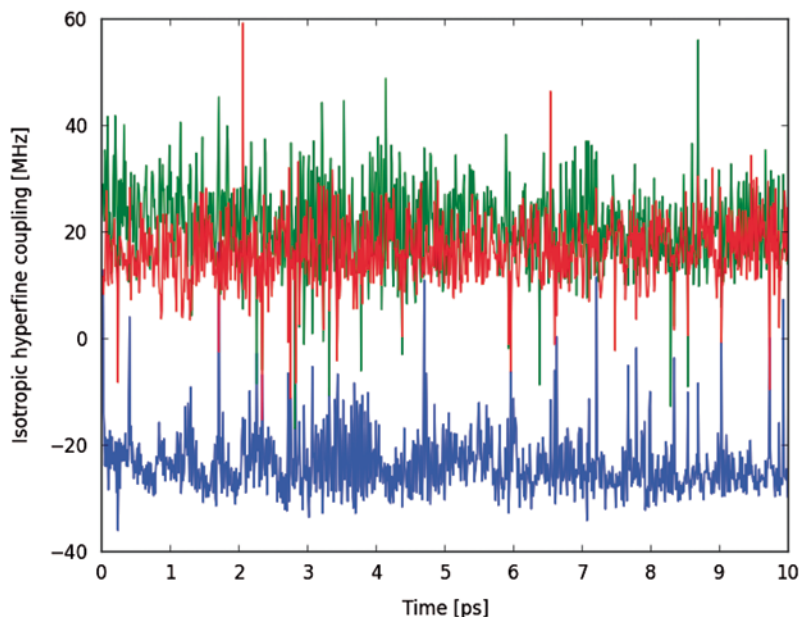


Fig. 18.11 Variation of the *isotropic hyperfine coupling* values (in MHz) of protons H(C1) (in *blue*), H(C3) (in *green*), H(C5) (in *red*) for sucrose radical model M(T2/T3) during a 10 ps MD simulation at 300 K

There are no major differences between the average hyperfine tensors for the three time epochs. Isotropic and anisotropic values differ by 1 MHz at most, eigenvector directions change by merely a couple of degrees. Clearly, the hydroxy proton rearrangement in the vicinity of the radical has no significant influence on the EPR properties, in line with the observations on the static calculations for conformations M(T2/T3-a and b). Furthermore—and unfortunately—the hydroxy proton conformational change cannot explain the difference in spectroscopic properties between T2 and T3.

From a comparison between the results in Tables 18.4 and 18.5 (e.g. those for all snapshots in the MD), it can be concluded that the dynamic treatment does not yield a better agreement with experiment than the static approach. It can give insight, however, into which molecular motions modulate the hyperfine coupling tensor. α -type tensors (such as that for H(C1)) are known to depend near-quadratically on the planarity of the radical center [42]. Although this effect is less pronounced and less clear than in glycine, it is still apparent (with some imagination) from a scatter-plot of the isotropic hyperfine coupling versus the radical planarity, as measured by the H(C1)–C2–O5–C1 *improper* dihedral angle (Fig. 18.13).

This showcase illustrates that going beyond a *static* approach to simulate the EPR properties in a *dynamic* fashion is not always necessary, especially if the intention is only to identify a radical structure. But an MD approach may lead to the identification of new conformational minima that are more optimal in energetic terms.

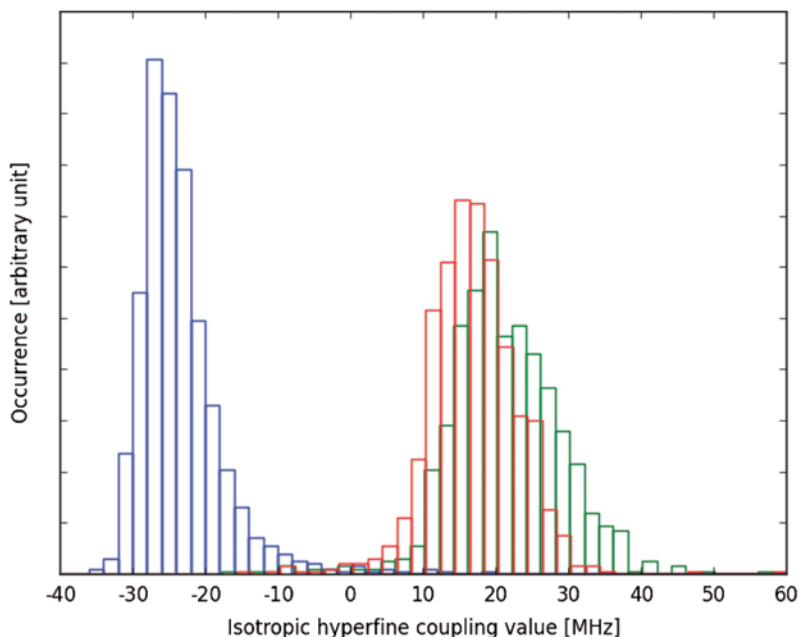


Fig. 18.12 Histograms of isotropic hyperfine coupling values encountered during a 10 ps MD simulation of sucrose radical model M(T2/T3) at 300 K. *Blue, green, and red boxes*, respectively, indicate the *occurrence* for proton couplings H(C1), H(C3) and H(C5)

18.3 Uncovering Radical Formation—*HOW?* and *WHY?*

18.3.1 General Strategy

Once the structure of a radical has been identified, the obvious question springs to mind: which radiation-induced molecular processes lead up to the formation of this particular radical? Sometimes, as for “simple” hydrogen abstraction products, the underlying radiochemical reactions may seem trivial. For other radicals, that have undergone more elaborate changes with respect to the pristine crystal structure, these processes might be entirely unclear. Yet, caution should always be in place when considering the formation mechanisms of radicals, even when it concerns the “simplest” radiation-induced species. A fine example of this is solid-state alanine. This model system for radiation damage in proteins has attracted numerous studies and its radiation chemistry is commonly considered to be well established [55]. Yet, a recent study [30] has shown that several of the radiation-induced reactions and rearrangements involved were poorly understood, highlighting the value of a computational approach supporting available (experimental) data.

An even more fundamental question that is raised when the identity and formation of a specific radical have been established is: why is this particular radical formed as a result of irradiation? Consider the example of a model decamer DNA

Table 18.5 Time-averaged hyperfine coupling tensors for sucrose radical model M(T2/T3) for various parts of the MD simulation. Isotropic (A_{iso}) and anisotropic hyperfine couplings (A_{aniso}) are in MHz. ψ (T2) and ψ (T3) indicate the angles (in degrees) between the calculated eigenvectors and those of the experimental tensors of radicals T2 and T3, respectively (see Table 18.3)

Atom	Average (0.00–2.25 ps)			Average (2.35–10.00 ps)			Average (0.00–10.00 ps)			Coupling		
	A_{iso}	A_{aniso}	ψ (T2)	A_{iso}	A_{aniso}	ψ (T2)	A_{iso}	A_{aniso}	ψ (T2)			
H(C1)	-22.77	-15.27	2.3	8.6	8.6	1.9	10.9	-15.44	1.6	10.2	H α	
		-4.37	7.1	8.3	11.3	4.3	10.5	-4.20	4.3	10.5		
		19.64	6.9	6.1	10.5	3.6	10.5	19.64	4.1	9.5		
H(C3)	23.27	-2.33	9.0	13.0	20.47	-2.25	2.8	18.1	-2.26	5.0	H β 1	
		-1.49	10.1	12.4	19.9	-1.61	2.7	19.9	-1.59	5.1		17.3
		3.82	5.0	6.3	9.6	3.86	0.6	9.6	3.85	1.1		8.6
H(C5)	15.61	-3.11	10.6	16.7	16.87	-3.12	11.5	19.5	-3.10	11.2	H β 2	
		-1.87	11.4	16.7	20.1	-1.69	10.0	20.1	-1.74	9.8		18.8
		4.98	13.6	0.8	4.8	4.80	9.5	4.8	4.84	10.6		3.6

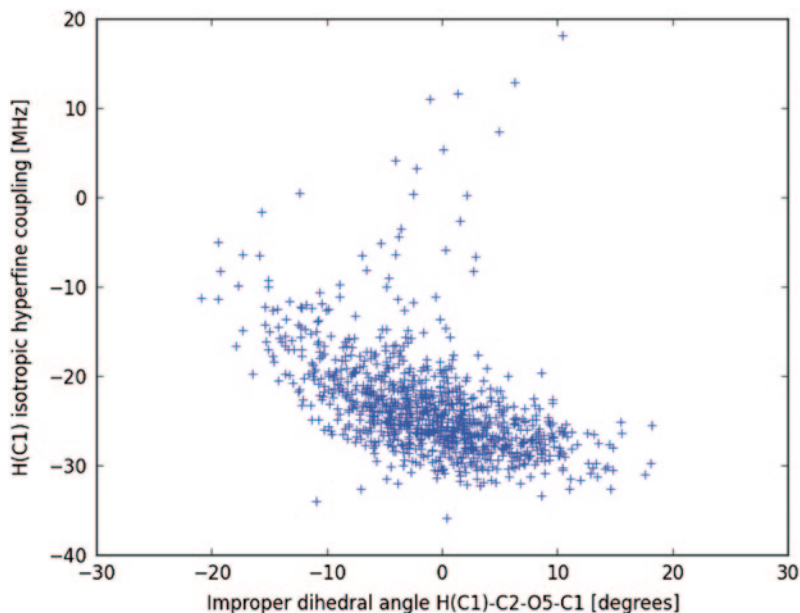


Fig. 18.13 Variation of the $H(C1)$ isotropic hyperfine coupling value as a function of the radical planarity, measured by the improper dihedral angle $H(C1)-C2-O5-C1$, for 1000 snapshots sampled from a 10 ps MD simulation at 300 K of sucrose radical model M(T2/T3)

system [56] in which a main radiation-induced radical was identified as being deprotonated at one specific carbon in the deoxyribose sugar subunit of a guanine base. The regioselectivity involved is very intriguing: four other similar carbon centers are present in the sugar at which site deprotonation could occur. To date, no satisfying explanation for this regioselective action of radiation has been presented, for the model DNA system, or for various other biomolecular systems. Here, as well, a computational approach can be of assistance.

Molecular modeling, and DFT methods in particular, can be applied to gain insight in (radio)chemical reactions [57]. Once stationary points have been found and characterized for the reactant and product states, the structural rearrangements that transform one into the other can be determined by mapping all elementary steps along the reaction coordinate(s). Hence, by shedding light on the conformational changes, these methods can help to solve the *HOW?* question. The variation of the (potential) energy along this reaction path, or the energy difference between key points along that path, can assist in solving the *WHY?* question.

This is illustrated in Fig. 18.14 for a hypothetical (potential) energy surface. Once stationary points **A** and **B** have been identified, molecular modeling algorithms allow the characterization of the pathway connecting both states. From that, the changes in the conformational dimensions can be deduced, indicating *how* conformation **A** transforms into conformation **B** and what the nature is of the transition state connecting both minima. At the same time, the changes in energy along the

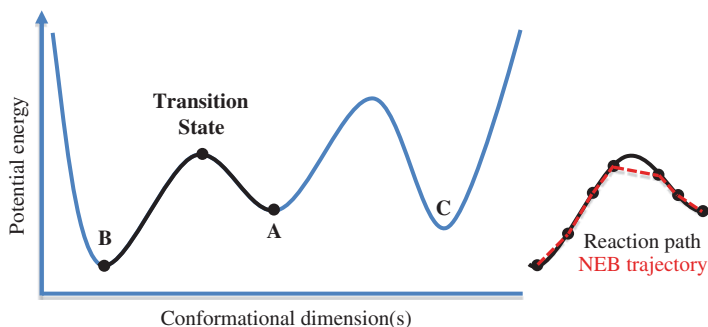


Fig. 18.14 Hypothetical (potential) energy surface illustrating reaction pathway concepts

path enable an estimation of the barrier height (or activation energy), giving insight in the rate of the transformation. This, together with the absolute (potential) energy differences between conformational states can be applied to rationalize preferential formation. In the hypothetical example of Fig. 18.14, reaction from state **A** towards **B** is preferred over **C**, both thermodynamically as well as kinetically.

Several molecular modeling algorithms exist to characterize reaction pathways, but their usefulness for solid-state systems depends on the implementation and on the desired model space approach. Transition state searches in terms of internal coordinates [58] (e.g. in Gaussian [48]) have been used for single-molecule treatments in amino acids and DNA/RNA sugars [39, 43, 59, 60], but are difficult from a computational point of view in condensed states, due to the multitude in degrees of freedom. Reaction pathway modeling in solid-state systems that are described with a periodic approach can be achieved with the aid of the Nudged Elastic Band (NEB) method [61–63]. In this approach, the minimal energy path between two stable molecular conformations is sought by optimizing the energy of a set of intermediate replicas that represent the gradual transition between both end points and that are successively connected by harmonic springs. This is illustrated in Fig. 18.14 for the path from **A** to **B**, where seven replicas discretize the “true” energy path. Though this method likely yields an underestimate of the actual reaction path, it has been used successfully to get insight in the radiation chemistry of amino acids [64] and sugars [31]. This method will also be applied in this chapter.

When comparing different radiation-induced reaction pathways—in an attempt to solve the *WHY?* question—the stoichiometry involved in those reactions needs to be consistent. This implies that all “waste”-products generated in a radiolysis reaction (e.g. net hydrogen abstraction) are sustained inside the simulation cell. This is certainly a hard requirement in NEB simulations and effectively mimics reality. In a real organic crystal, such abstracted products would diffuse throughout the lattice and either reconnect with another neighboring molecule or remain trapped close to the radical site. Depending on the distance between this reattached or trapped residue and the radiation-induced radical, certain interaction effects can be expected. In a more simplified approach, these radiolysis products are eliminated altogether from the simulation and its energetic contribution assumed to be the same

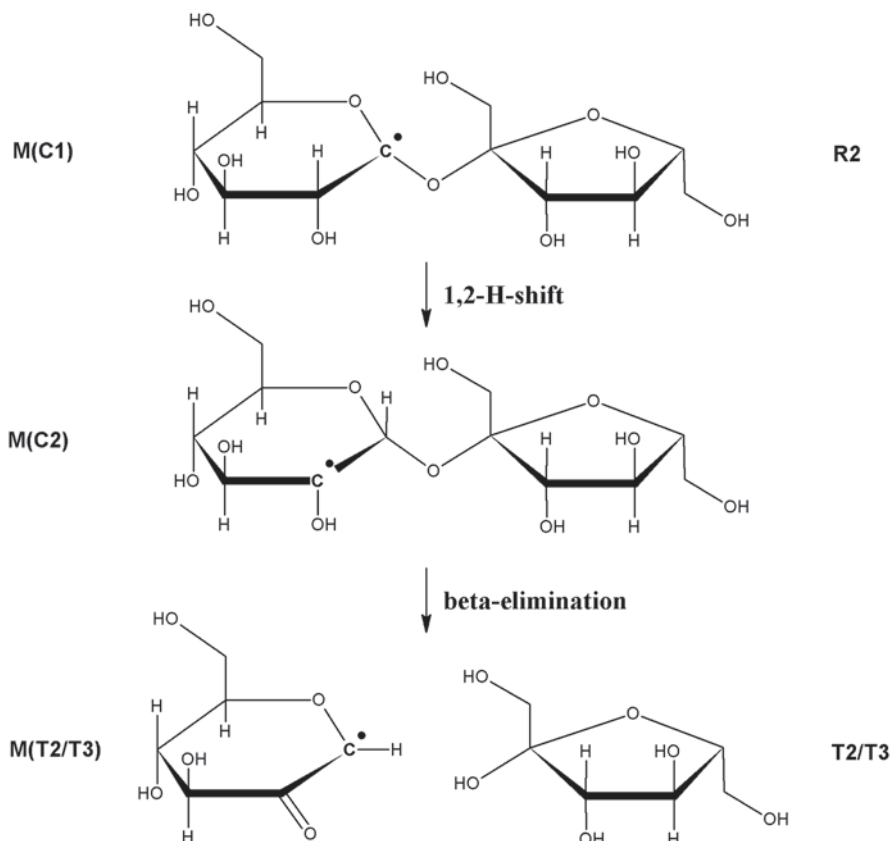


Fig. 18.15 Sucrose radical *R2* (which has only been detected at temperatures below ~ 100 K) transform into radicals *T2/T3* at room temperature via a *1,2-H-shift* followed by a *beta-elimination* reaction

for a variety of similar radiochemical reactions. Such a methodology is adopted in the determination of, e.g. bond dissociation energies [65], ionization potentials [39, 66] or electron attachment energies [65, 66]. These correspond to very rudimentary reaction pathways, since only the formation energy of a particular radical fragment is considered without looking at barriers encountered. It might nevertheless yield useful information on the selective action of radiation.

18.3.2 Case Study 3: Conversion of Sucrose Radical *R2* into *T2/T3*

A hypothesis put forward by De Cooman et al. [67] is that sucrose radical *R2* is a precursor for radical *T2/T3*. The proposed transformation process (illustrated in Fig. 18.15) involves first a *1,2-H-shift* [68, 69], where a hydrogen atom is transferred

from carbon C2 to the adjacent C1. Then, this intermediate species undergoes beta-elimination [68, 69]: the hydroxy proton at O2 is transferred to the oxygen (O1) of the glycosidic linkage, the C1–O1 bond is ruptured and a C2=O2 carbonyl group is introduced in the glucose subunit of sucrose. The entire process would rationalize the fact that R2 can only be observed at low temperatures. When enough thermal energy is available, energy barriers can be surpassed and the transformation process is initiated, up until T2/T3 species is formed. The driving force is likely the greater stability of the latter radical species, which is consistent with the fact that T2/T3 have only been observed at room temperature.

A computational approach in line with the previous general strategy serves to shed light on this tentative transformation process. Although the full radiation chemistry of sucrose is not explored exhaustively, the new results presented below provide a sufficient treatment of the formation of radical R2 up to the transformation into T2/T3.

Selective Formation of R2-Radical Model M(C1) As reviewed in Sect. 18.2.2, the structure of radical R2 has been positively identified as corresponding to that of radical model M(C1), where a net hydrogen abstraction from carbon C1 in the pristine sucrose structure has occurred. Yet, several other, similar hydrogen abstractions from carbon are possible in the sucrose structure: from C2, C3, C4, C5, C6, C1', C3', C4', C5' and C6'. Why is abstraction from C1 seemingly favored?

Although the primary effects of radiation damage on a molecular level remain debated, current understanding is that radiation leads to the formation of primary oxidative (one-electron loss) and reductive (one-electron gain) free radicals [69]. Subsequently, these primary species decay and transform into more stable (radical) fragments. In carbohydrates, this is likely achieved by the ejection of a proton or even a hydride anion, which then can diffuse through the crystal lattice or be trapped near the original radical site. To a first approximation, the fate of this ejected proton/hydride can simply be disregarded. This simplifies tremendously a comparison of the formation energies for the various possible radical models. All models share a common reference (the pristine sucrose structure) and preferential formation can be deduced from the relative energy differences between the possible radical models.

Energy minimizations are performed for radical models M(C1) to M(C6') using the same computational parameters as mentioned in Sect. 18.2.2. The final (potential) energies for these species are compared in Table 18.6. Formation of M(C1) and M(C2) is energetically favored, with slight preference (6 kJ/mol) for the latter. This does not correspond entirely to the findings of low-temperature EPR experiments [9]. In that study, six radical species were found to be generated at low temperature, three of which were structurally identified: radical models M(C1) and M(C6), and an alkoxy radical formed by abstracting a hydrogen from oxygen O3'.

Though the simple energy computations in the present work confirm that M(C1) is among the preferentially formed radical species, they do not explain the observation of M(C6) in the experiment: the energy of M(C6) is 149 kJ/mol higher than that of M(C1), based on which one would expect this radical not to be formed. The computations also don't explain why radical M(C2) is not observed in experiment. It has the lowest potential energy and would clearly be the most favorably formed species.

Table 18.6 Energy comparison for all radical models where one hydrogen has been abstracted from a carbon in sucrose. The absolute energy of M(C2) is used as reference: -513.5641 a.u.

H-abstraction model	Relative energy (kJ/mol)
M(C1)	6.0
M(C2)	0.0
M(C3)	150.6
M(C4)	152.5
M(C5)	153.7
M(C6)	155.1
M(C1')	141.7
M(C3')	163.7
M(C4')	153.8
M(C5')	147.1
M(C6')	142.3

Obviously, the assumptions made in the computations above are flawed and the potential energy only is not a very good approximation of the formation energy. For instance, an abstracted proton or hydride will likely be trapped in a different site when it is ejected from either C1 or C3, or will at least disturb the immediate surrounding of the radical in a different fashion when it diffuses through the lattice. This will have a concomitant effect on the relative (formation) energies (as was already demonstrated in case study 2). The fate of these abstracted atomic or molecular fragments should therefore not be disregarded. Also, it should not necessarily be assumed that a radiochemical formation reaction is thermodynamically controlled. Kinetic control could also be in place, requiring knowledge on the barriers associated with radical formation. Unfortunately, this considerably complicates relative comparison of formation energies since the *HOW?* question should be solved in detail for every radical model contemplated. This approach was used successfully to explain selective alkoxy radical formation in rhamnose crystals [31], but at a substantial computational cost.

So, for now, the question why hydrogen abstraction from C1 is seemingly favored by radiation remains unanswered. In all further calculations, the abstracted hydrogen from C1 is not considered in the simulation cell.

Conversion of M(C1) to M(C2) via 1,2-H-Shift Nevertheless, using M(C1) as a starting point, it is possible to determine the energetic landscape for the reaction pathway subsequent to the initial radiation damage. For that, Nudged Elastic Band simulations are used to determine the minimal energy path between consecutive minima and obtain an estimate of the associated energy profile. Each time, ten replicas are used together with a combined steepest descent—DIIS optimizer [71]. The initial guess for the band is generated by linear interpolation between optimized radical structures. The IT-NEB algorithm [62] is then applied for several cycles, followed by CI-NEB [63] until sufficient convergence is reached. The replica with maximal energy along the NEB path is taken as an approximation to the transition state. The resulting energy path, compounded for all reactions discussed below, is shown in Fig. 18.16.

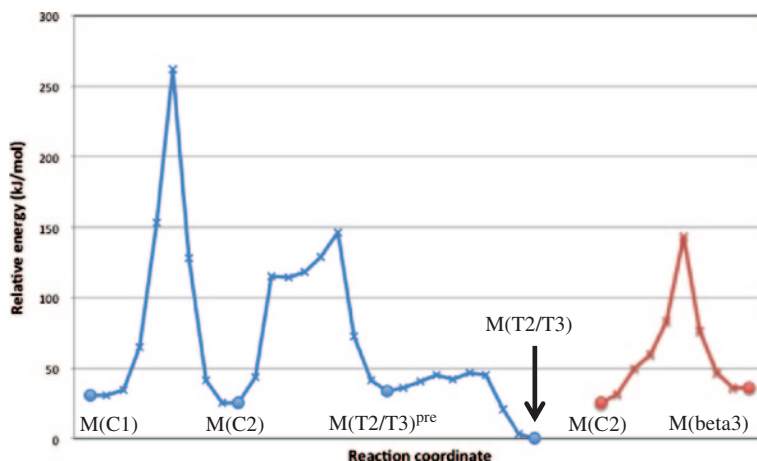


Fig. 18.16 Compound minimal energy path for the radiation-induced transformation pathway of sucrose radical model $M(C1)$ into $M(T2/T3)$ as obtained from NEB simulations. A competitive transformation path from $M(C2)$ to $M(\beta 3)$ is shown on the *right*. Stationary points are represented by *circles*, intermediate replica along the NEB path by *crosses*. The absolute energy of the $M(T2/T3)$ species is used as a reference: -513.5737 a.u.

According to the NEB runs, the 1,2-H-shift from $M(C1)$ to $M(C2)$ is associated with a huge energy barrier, 230 kJ/mol, although this is not unsurpassable considering the energy amount deposited by irradiation. $M(C2)$ has a lower potential energy than $M(C1)$ and so this process is thermodynamically favored. Representative points along the reaction path are shown in Fig. 18.17. Near the transition state, the transferred hydrogen is virtually shared by both carbons C1 and C2. It is not unlikely that this transfer would be assisted by another molecular fragment in the vicinity of that hydrogen, lowering the energy barrier. However, exploratory computational runs in this respect have not yielded any candidates: certainly hydroxyl groups in the vicinity are not prone for such an interaction.

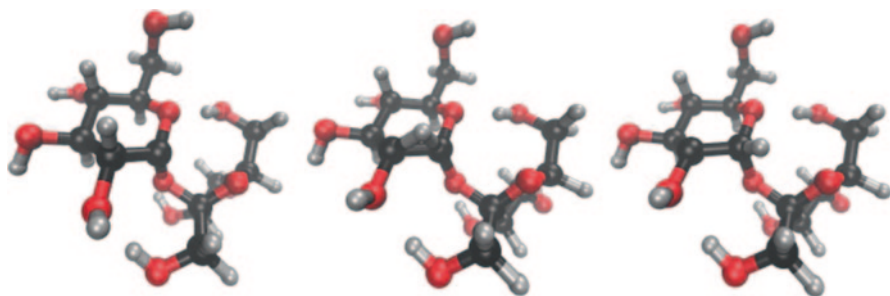


Fig. 18.17 Molecular structure of representative points along the energy path from sucrose radical model $M(C1)$ to $M(C2)$ via a 1,2-H-shift reaction. *Left* $M(C1)$. *Center* near the transition state. *Right* $M(C2)$. 3D-renders produced with the aid of VMD [20]

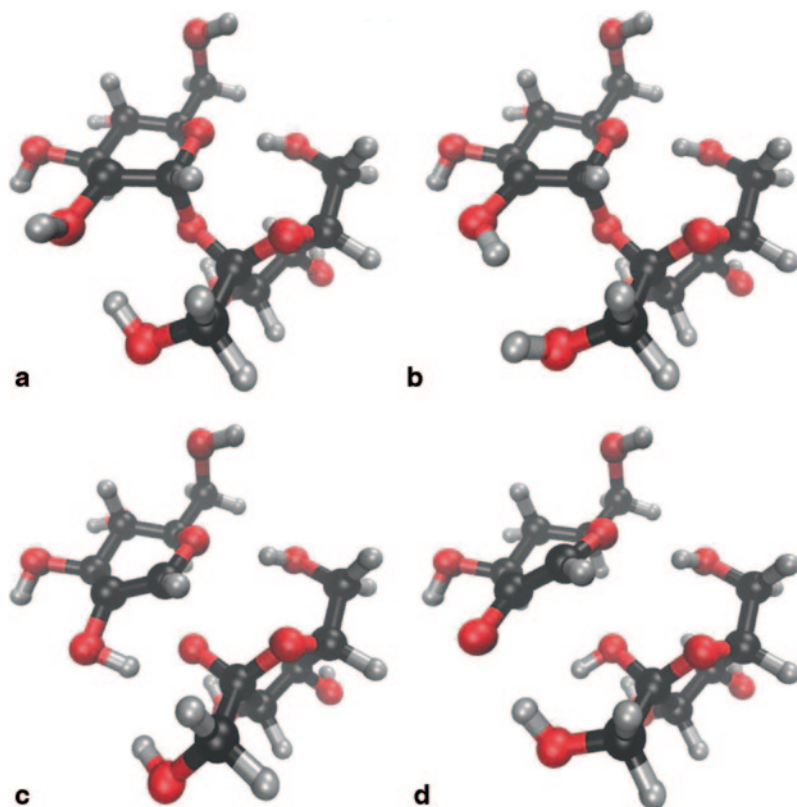


Fig. 18.18 Molecular structure of representative points along the energy path from sucrose radical model M(C2) to M(T2/T3)^{pre} via a beta-elimination reaction. **a** M(C2), **b** O2 hydroxyl group reorientation, **c** proton transfer to O1 and C1–O1 bond rupture, **d** local energetic minimum M(T2/T3)^{pre}. 3D-renders produced with the aid of VMD [20]

Conversion of M(C2) to M(T2/T3) via Beta-Elimination Once M(C2) is generated, it can convert into M(T2/T3) but several molecular rearrangements need to occur, illustrated in Figs. 18.18 and 18.19.

Before the hydroxy proton on O2 can come near the O1 oxygen of the glycosidic linkage, it needs to reorient. In model M(C2) (and in the pristine crystal structure), the proton of O2 is involved in a hydrogen bond to oxygen O6' of an adjoining sucrose molecule in the lattice. This hydrogen bond is broken when the O2 hydroxyl group reorients, but a new hydrogen bond is almost immediately made with O1' of the radical (compare structures (a) and (b) in Fig. 18.18). These concomitant reorientations give rise to a considerable barrier: the first cusp in Fig. 18.16 corresponds to structure (b) and is almost 90 kJ/mol higher in energy than M(C2).

Subsequent to the reorientation, hydroxy proton H(O2) attaches to the glycosidic oxygen and triggers rupture of the C1–O1 bond, effectively separating the glucose- and fructose subunits in sucrose. The structure near the transition state for this ensuing process is shown in Fig. 18.18c. Although the energy rise is not as much as for the

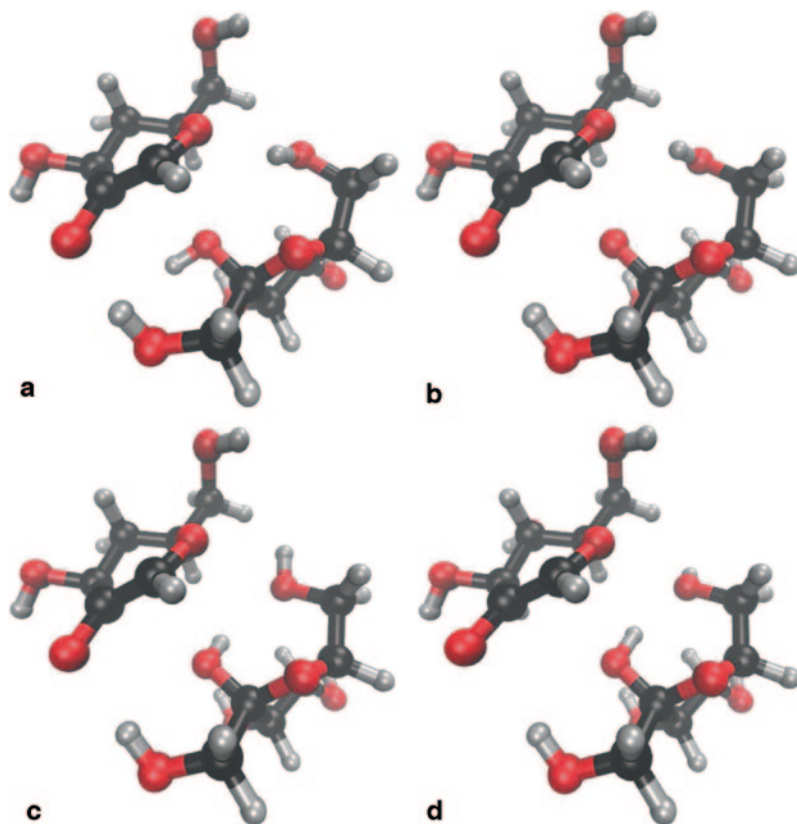


Fig. 18.19 Molecular structure of representative points along the energy path from sucrose radical model $M(T2/T3)^{pre}$ to $M(T2/T3)$. **a** $M(T2/T3)^{pre}$, **b** O1 hydroxyl group reorientation, **c** O6' hydroxyl group reorientation, **d** $M(T2/T3)$. 3D-renders produced with the aid of VMD [20]

hydroxyl rearrangement, the total energy barrier for rearrangement and bond rupture is at ~ 125 kJ/mol with respect to the potential energy of $M(C2)$. This barrier should be easily surpassed, since sufficient (thermal) energy is available in the irradiated sucrose crystal after the $M(C1) \rightarrow M(C2)$ transformation has occurred.

After the C1–O1 bond has been ruptured, a local energetic minimum is obtained: radical model $M(T2/T3)^{pre}$, corresponding to structure (d) in Fig. 18.18. Its potential energy is actually higher by 9 kJ/mol than that of $M(C2)$. The entire process would therefore not be thermodynamically favored were it not that subsequent hydroxyl reorientations in model $M(T2/T3)^{pre}$, give rise to a considerable drop in energy to arrive at the final structure $M(T2/T3)$. These conformational rearrangements are illustrated in Fig. 18.19. First, the newly formed hydroxyl group involving oxygen O1 (the former glycosidic oxygen) reorients by almost 180° : its hydroxy proton no longer points towards O1' but now makes a hydrogen bond with O6'. Concomitantly, the hydroxy proton on O6' reorients as well, to arrive at the final $M(T2/T3)$ structure. Note that all these conformational changes do not take place in the radical

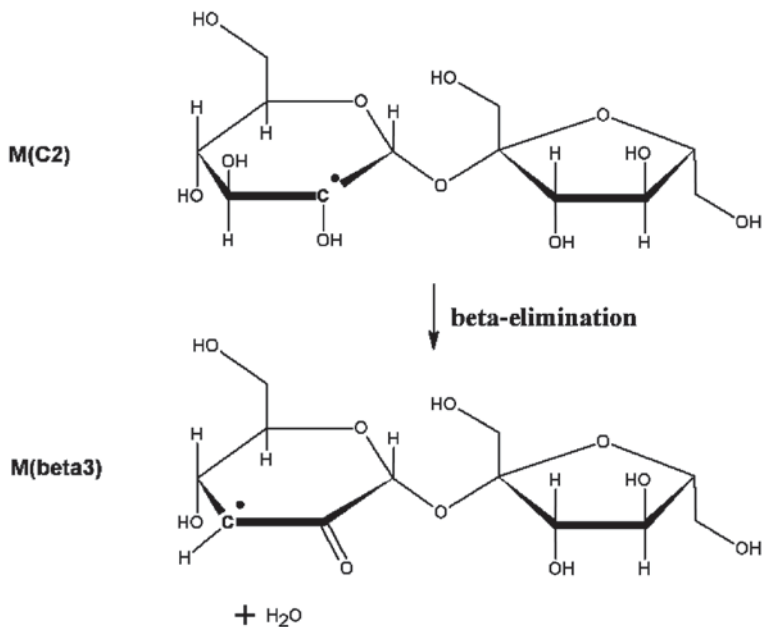


Fig. 18.20 Could a competitive *beta-elimination* reaction from sucrose radical model $M(C2)$ lead to the formation of another product $M(beta3)$?

fragment itself (which is in the glucose subunit) but in the fructose subunit, which is in the near vicinity of the radical center. The changes in energy are, however, considerable. After a small barrier (13 kJ/mol) has been passed, the energy quickly drops by 34 kJ/mol between structures $M(T2/T3)^{pre}$ and $M(T2/T3)$.

Total Transformation Process of M(C1) into M(T2/T3) The NEB simulations give unique insight into the conformational changes that occur throughout the overall transformation process of $M(C1)$ into $M(T2/T3)$, and therefore solve the *HOW?* question for this particular process. They also shed light on *WHY?* radicals T2/T3 (corresponding to model $M(T2/T3)$) can only be observed at room temperature. The entire transformation process is thermodynamically favored: $M(T2/T3)$ is 30.6 kJ/mol lower in potential energy than $M(C1)$. However, the 1,2-H-shift associated with the $M(C1)$ to $M(C2)$ conversion constitutes the rate determining step, with a significant energy barrier of 230 kJ/mol. Enough thermal energy needs to become available in the sucrose crystal, before this process can proceed. But, once this particular barrier has been surpassed, all subsequent transformation steps can proceed without further debilitation, and the intermediate radical species encountered throughout this process would not be observed in experiment.

Competitive Beta-Elimination Products from M(C2)? In the above, $M(T2/T3)$ was obtained from radical model $M(C2)$ via beta-elimination. Yet, this same mechanism applied to model $M(C2)$ could also lead to another radical $M(beta3)$, as outlined in Fig. 18.20. However, this species has not been detected in experiment,

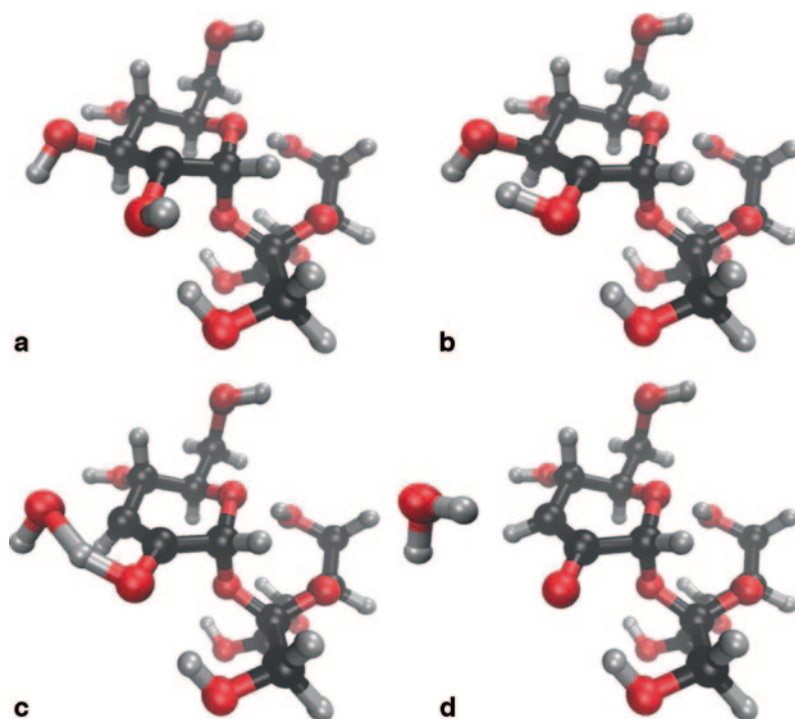


Fig. 18.21 Molecular structure of representative points along the energy path from sucrose radical model M(C2) to M(beta3) via a beta-elimination reaction. (a) corresponds to M(C2), (d) to radical model M(beta3). (b) and (c) are intermediate points 3D-renders produced with the aid of VMD [20]

at low temperature nor at room temperature. Could NEB simulations give insight into why this species is not formed, or rather, why formation of radical M(T2/T3) is favored over M(beta3)?

Representative snapshots along the NEB reaction path are shown in Fig. 18.21. In this beta-elimination reaction, the hydroxy proton on O2 approaches oxygen O3 and connects to it. This causes rupture of the C3–O3 bond and a water molecule is formed. In radical model M(beta3), this molecule remains in the vicinity of the radical (see Fig. 18.21d). The variation of the energy throughout the NEB path is also included in Fig. 18.16 (in red). The barrier is similar in height to that between M(C2) and M(T2/T3), but it is clear that formation of M(beta3) is not advantageous from a thermodynamical point of view: the potential energy of M(beta3) is 11 kJ/mol higher than that of M(C2).

Although in this particular example, all possible transformation processes have not been exhaustively explored, it is clear by far that the energy landscape really dictates the transformation process. By exploring these pathways via NEB simulations, it is possible to gain insight into preferential formation pathways ensuing

radiation damage to biomolecules, and so, solve the *WHY?* question along with the *HOW?* question.

Acknowledgments This work is supported by the Fund for Scientific Research—Flanders (FWO) and the Research Board of the Ghent University. All computational resources (Stevin Supercomputer Infrastructure) and services used in this work were provided by Ghent University, the Hercules Foundation and the Flemish Government—department EWI. This chapter is dedicated to children lost.

References

1. Lund A, Shiotani M (2010) EPR of free radicals in solids: trends in methods and applications. Springer, Dordrecht
2. Heller C, McConnell HM (1960) Radiation damage in organic crystals. ii. electron spin resonance of (CO₂H)CH₂CH(CO₂H) in β -succinic acid. J Chem Phys 32:1535–1540. doi:10.1063/1.1730955
3. McConnell HM (1956) Indirect hyperfine interactions in the paramagnetic resonance spectra of aromatic free radicals. J Chem Phys 24:764–766. doi:10.1063/1.1742605
4. Close DM, Bernhard WA (1977) INDO Calculations of spin-density distribution in pyrimidine electron adducts. J Chem Phys 66:5244–5245. doi:10.1063/1.433754
5. Kaupp M, Bühl M, Malkin VG (2004) Calculation of NMR and EPR parameters: theory and applications. WILEY-VCH: Weinheim doi:10.1002/3527601678
6. CP2K. <http://www.cp2k.org>
7. VandeVondele J, Krack M, Mohamed F et al (2005) QUICKSTEP: fast and accurate density functional calculations using a mixed Gaussian and plane waves approach. Comput Phys Commun 167:103–128. doi:10.1016/j.cpc.2004.12.014
8. De Cooman HP, Vrielinck H et al (2008) Identification and conformational study of stable radiation-induced defects in sucrose single crystals using density functional theory calculations of electron magnetic resonance parameters. J Phys Chem B 112:7298–7307. doi:10.1021/jp712004g
9. De Cooman HP, Vrielinck H et al (2010) Oxidation and reduction products of X irradiation at 10 K in sucrose single crystals: radical identification by EPR, ENDOR, and DFT. J Phys Chem B 114:666–674. doi:10.1021/jp909247z
10. De Cooman HK, Kusakovskij J et al (2013) Dominant stable radicals in irradiated sucrose: g tensors and contribution to the powder electron paramagnetic resonance spectrum. J Phys Chem B 117:7169–7178. doi:10.1021/jp400053h
11. De Cooman HP, Vrielinck H et al (2009) ENDOR and HYSCORE analysis and DFT-assisted identification of the third major stable radical in sucrose single crystals X-irradiated at room temperature. Phys Chem Chem Phys 11:1105–1114. doi:10.1039/b816641b
12. Vanhaelewyn G, Pauwels E, Callens FJ et al (2006) Q-band EPR and ENDOR of low temperature X-irradiated beta-D-fructose single crystals. J Phys Chem A 110:2147–2156. doi:10.1021/jp056632v
13. De Cooman HV, Pauwels E et al (2008) Radiation-induced radicals in glucose-1-phosphate. I. Electron paramagnetic resonance and electron nuclear double resonance analysis of in situ X-irradiated single crystals at 77 K. J Phys Chem B 112:15045–15053. doi:10.1021/jp804290e
14. Krivokapić A, Øhman KT, Nelson WH et al (2009) Primary oxidation products of 5-methylcytosine: methyl dynamics and environmental influences. J Phys Chem A 113:9633–9640. doi:10.1021/jp904747j

15. Øhman KT, Sanderud A, Hole EO, Sagstuen E (2006) Single crystals of L-O-serine phosphate X-irradiated at low temperatures: EPR, ENDOR, EIE, and DFT studies. *J Phys Chem A* 110:9585–9596. doi:10.1021/jp061265o
16. Declerck R, Pauwels E, Van Speybroeck V, Waroquier M (2006) First-principles calculations of hyperfine parameters with the Gaussian and augmented-plane-wave method: application to radicals embedded in a crystalline environment. *Phys Rev B* 74:8. doi:245103 10.1103/PhysRevB.74.245103
17. Weber V, Iannuzzi M, Giani S et al (2009) Magnetic linear response properties calculations with the Gaussian and augmented-plane-wave method. *J Chem Phys* 131:11. doi:014106 10.1063/1.3156803
18. Pauwels E, Van Speybroeck V, Waroquier M (2004) Evaluation of different model space approaches based on DFT to examine the EPR parameters of a radiation-induced radical in solid-state alpha-glycine. *J Phys Chem A* 108:11321–11332. doi:10.1021/jp049251a
19. Hermosilla L, Calle P, de la VJMG, Sieiro C (2006) Density functional theory study of N-14 isotropic hyperfine coupling constants of organic radicals. *J Phys Chem A* 110:13600–13608. doi:10.1021/jp064900z
20. Humphrey W, Dalke A, Schulten K (1996) VMD: visual molecular dynamics. *J Mol Graph* 14:33–38, 27–28. doi:10.1016/0263-7855(96)00018-5
21. Byrd RH, Lu PH, Nocedal J, Zhu CY (1995) A limited memory algorithm for bound constrained optimization. *SIAM J Sci Comput* 16:1190–1208. doi:10.1137/0916069
22. Becke AD (1988) Density-functional exchange-energy approximation with correct asymptotic-behavior. *Phys Rev A* 38:3098–3100
23. Lee CT, Yang WT, Parr RG (1988) Development of the Colle-Salvetti correlation-energy formula into a functional of the electron-density. *Phys Rev B* 37:785–789
24. Lippert G, Hutter J, Parrinello M (1997) A hybrid Gaussian and plane wave density functional scheme. *Mol Phys* 92:477–487
25. VandeVondele J, Hutter J (2007) Gaussian basis sets for accurate calculations on molecular systems in gas and condensed phases. *J Chem Phys* 127:9. doi:114105 10.1063/1.2770708
26. Goedecker S, Teter M, Hutter J (1996) Separable dual-space Gaussian pseudopotentials. *Phys Rev B* 54:1703–1710
27. Hartwigsen C, Goedecker S, Hutter J (1998) Relativistic separable dual-space Gaussian pseudopotentials from H to Rn. *Phys Rev B* 58:3641–3662
28. Krack M, Parrinello M (2000) All-electron ab-initio molecular dynamics. *Phys Chem Chem Phys* 2:2105–2112
29. Godbout N, Salahub DR, Andzelm J, Wimmer E (1992) Optimization of gaussian-type basis-sets for local spin-density functional calculations. 1. Boron through neon, optimization technique and validation. *Can J Chem Can Chim* 70:560–571
30. Pauwels E, De Cooman H, Waroquier M et al (2010) On the identity of the radiation-induced stable alanine radical. *Phys Chem Chem Phys* 12:8733–8736. doi:10.1039/c004380j
31. Aalbergsjo SG, Pauwels E, De Cooman H et al (2013) Structural specificity of alkoxy radical formation in crystalline carbohydrates. *Phys Chem Chem Phys* 15:9615–9619. doi:10.1039/c3cp50789k
32. Pauwels E, Declerck R, Van Speybroeck V, Waroquier M (2008) Evidence for a Grothuss-like mechanism in the formation of the rhamnose alkoxy radical based on periodic DFT calculations. *Radiat Res* 169:8–18
33. Tarpan MA, De Cooman H, Sagstuen E et al (2011) Identification of primary free radicals in trehalose dihydrate single crystals X-irradiated at 10 K. *Phys Chem Chem Phys* 13:11294–11302. doi:10.1039/c0cp02616f
34. Box HC (1977) Radiation effects: ESR and ENDOR analysis. Academic Press, New York
35. Tarpan MA, Pauwels E, Vrielinck H et al (2010) Electron magnetic resonance and density functional theory study of room temperature X-irradiated β -D-fructose single crystals. *J Phys Chem A* 114:12417–12426. doi:10.1021/jp107777v
36. Barone V, Adamo C, Grand A et al (1995) Structure and ESR features of glycine radical. *J Am Chem Soc* 117:12618–12624. doi:10.1021/ja00155a026

37. Declerck R, Pauwels E, Speybroeck V Van, Waroquier M (2008) Molecular environment and temperature dependence of hyperfine interactions in sugar crystal radicals from first principles. *J Phys Chem B* 112:1508–1514. doi:10.1021/jp076571w
38. Kay CWM, Schleicher E, Hitomi K et al (2005) Determination of the g-matrix orientation in flavin radicals by high-yield/high-frequency electronuclear double resonance. *Magn Reson Chem* 43:S96–S102. doi:10.1002/mrc.1667
39. Kumar A, Pottiboyina V, Sevilla MD (2012) One-electron oxidation of neutral sugar radicals of 2'-deoxyguanosine and 2'-deoxythymidine: a density functional theory (DFT) Study. *J Phys Chem B* 116:9409–9416. doi:10.1021/jp3059068
40. Pauwels E, Asher J, Kaupp M, Waroquier M (2011) Cluster or periodic, static or dynamic—the challenge of calculating the g tensor of the solid-state glycine radical. *Phys Chem Chem Phys* 13:18638. doi:10.1039/c1cp21452g
41. Pauwels E, Declerck R, Verstraelen T et al (2010) Influence of protein environment on the electron paramagnetic resonance properties of flavoprotein radicals: a QM/MM study. *J Phys Chem B* 114:16655–16665. doi:10.1021/jp109763t
42. Pauwels E, Verstraelen T, De Cooman H et al (2008) Temperature study of a glycine radical in the solid state adopting a DFT periodic approach: vibrational analysis and comparison with EPR experiments. *J Phys Chem B* 112:7618–7630. doi:10.1021/jp711997y
43. Petrenko TL (2002) Transformation and structure of cation radicals in L-alpha-alanine. *J Phys Chem A* 106:149–156. doi:10.1021/jp0106395
44. Tachikawa H, Takada T (2013) Ionization dynamics of the water trimer: a direct ab initio MD study. *Chem Phys* 415:76–83. doi:10.1016/j.chemphys.2012.12.027
45. Tachikawa H, Fukuzumi T (2011) Ionization dynamics of aminopyridine dimer: a direct ab initio molecular dynamics (MD) study. *Phys Chem Chem Phys* 13:5881–5887. doi:10.1039/c0cp01542c
46. Aalbergsjø SG, Pauwels E, Van Yperen-De Deyne A, Van Speybroeck V, Sagstuen E (2014) Automated generation of radical species in crystalline carbohydrates using ab initio MD simulations. *Phys Chem Chem Phys* 16: 17196–17205. doi: 10.1039/c4cp02179g
47. Pauwels E, Lahorte P, Vanhaelewyn G et al (2002) Tentative structures for the radiation-induced radicals in crystalline beta-D-fructose using density functional theory. *J Phys Chem A* 106:12340–12348. doi:10.1021/jp0264174
48. Frisch MJ, Trucks GW, Schlegel HB et al (2009) Gaussian 09, Revision A.02. Gaussian Inc Wallingford CT 34:Wallingford CT. doi:10.1159/000348293
49. Asher JR, Kaupp M (2008) Car-Parrinello molecular dynamics simulations and EPR property calculations on aqueous ubisemiquinone radical anion. *Theor Chem Acc* 119:477–487. doi:10.1007/s00214-007-0408-1
50. CPMD. <http://www.cpmc.org>, 1990–2008, Copyright IBM Corp 1997-2001, Copyright MPI für Festkörperforschung Stuttgart
51. Becke AD (1996) Density-functional thermochemistry.4. A new dynamical correlation functional and implications for exact-exchange mixing. *J Chem Phys* 104:1040–1046. doi:10.1063/1.470829
52. Bussi G, Donadio D, Parrinello M (2007) Canonical sampling through velocity rescaling. *J Chem Phys* 126:014101. doi:10.1063/1.2408420
53. Hoover WG (1985) Canonical dynamics: equilibrium phase-space distributions. *Phys Rev A* 31:1695–1697. doi:10.1103/PhysRevA.31.1695
54. Nosé S (1984) A unified formulation of the constant temperature molecular dynamics methods. *J Chem Phys* 81:511. doi:10.1063/1.447334
55. Sagstuen E, Sanderud A, Hole EO (2004) The solid-state radiation chemistry of simple amino acids, revisited. *Radiat Res* 162:112–119. doi:10.1667/r3215
56. Debije MG, Bernhard WA (2001) Electron paramagnetic resonance evidence for a C3' sugar radical in crystalline d(CTCTCGAGAG) X-irradiated at 4 K. *Radiat Res* 155:687–692. doi:10.1667/0033-7587(2001)155[0687:EPREFA]2.0.CO;2
57. Koch W, Holthausen MC (2001) A chemist's guide to density functional theory. 3:294. doi:10.1002/3527600043

58. Peng CY, Ayala PY, Schlegel HB, Frisch MJ (1996) Using redundant internal coordinates to optimize equilibrium geometries and transition states. *J Comput Chem* 17:49–56. doi:10.1002/(SICI)1096-987X(19960115)17:1%3C49::AID-JCC5%3E3.0.CO;2-0
59. Adhikary A, Kumar A, Heizer AN et al (2013) Hydroxyl ion addition to one-electron oxidized thymine: unimolecular interconversion of C5 to C6 OH-adducts. *J Am Chem Soc* 135:3121–3135. doi:10.1021/ja310650n
60. Adhikary A, Kumar A, Palmer BJ et al (2013) Formation of S-Cl phosphorothioate adduct radicals in dsDNA S-oligomers: hole transfer to guanine vs disulfide anion radical formation. *J Am Chem Soc* 135:12827–12838
61. Elber R, Karplus M (1987) A method for determining reaction paths in large molecules: application to myoglobin. *Chem Phys Lett* 139:375–380. doi:10.1016/0009-2614(87)80576-6
62. Henkelman G, Jonsson H (2000) Improved tangent estimate in the nudged elastic band method for finding minimum energy paths and saddle points. *J Chem Phys* 113:9978–9985. doi:10.1063/1.1323224
63. Henkelman G, Uberuaga BP, Jonsson H (2000) A climbing image nudged elastic band method for finding saddle points and minimum energy paths. *J Chem Phys* 113:9901–9904. doi:10.1063/1.1329672
64. Pauwels E, De Cooman H, Waroquier M et al (2014) Solved? The reductive radiation chemistry of alanine. *Phys Chem Chem Phys* 16:2475–2482. doi:10.1039/c3cp54441a
65. Li X, Sanche L, Sevilla MD (2006) Base release in nucleosides induced by low-energy electrons: a DFT study. *Radiat Res* 165:721–729. doi:10.1667/RR3568.1
66. Sagstuen E, Close DM, Vågane R et al (2006) Electron transfer in amino acid-nucleic acid base complexes: EPR, ENDOR, and DFT study of X-irradiated N-formylglycine-cytosine complex crystals. *J Phys Chem A* 110:8653–8662. doi:10.1021/jp0610822
67. De Cooman H (2009) A combined EMR and DFT study of radiation-induced defects in sucrose and glucose 1-phosphate. PhD Thesis, Ghent University.
68. Von Sonntag C, Schuchmann H-P (2001) Carbohydrates. In: Jonah CD, Rao BSM (eds) *Radiation chemistry present status future trends*. Elsevier, Amsterdam, pp 481–512
69. Von Sonntag C (1987) *The chemical basis of radiation biology*. 515
70. Sagstuen E, Hole EO (2009) Radiation produced radicals. In: Brustolon M, Giamello E (eds) *Electron paramagnetic resonance a practitioner's toolkit*. Hoboken New Jersey: John Wiley & Sons, pp 325–382
71. Pulay P (1980) Convergence acceleration of iterative sequences—the case of SCF iteration. *Chem Phys Lett* 73:393–398. doi:10.1016/0009-2614(80)80396-4

Chapter 19

Applications of EPR and ENDOR Spectrum Simulations in Radiation Research

Roland Erickson and Anders Lund

Abstract Applications of EPR and ENDOR simulations of relevance in radiation research involving free radicals, radical pairs, triplet states and to less extent metal complexes are treated. Early fundamental work involving in situ radiolysis of liquids and stickplot analysis of spectra is reviewed, while single crystal analysis is only briefly discussed. The analysis of data obtained with continuous wave methods of species trapped in disordered solids, “powders” is emphasized. Simulations based on first and second order and exact theory are described and exemplified. Methods to obtain parameters for the dynamics of radicals in irradiated solids and for the simulation of spectra at microwave saturation are discussed. Procedures for the simulation of powder ENDOR spectra of radicals are described in detail, with special emphasis on the influence of nuclear quadrupole couplings due to nuclei with $I \geq 1$. EPR and ENDOR simulation programs known to us are presented in an Appendix, including addresses for downloading when available.

19.1 Introduction

The assignment of the EPR spectral features to specific paramagnetic species is of fundamental importance to clarify the radiation induced reactions in a sample. A majority of the studies has involved free radicals. For those systems the assignment is mainly based on the hyperfine structure, and to some extent on the g-factors obtained by an analysis of the EPR spectra. The assignment of the radicals formed in X-irradiated amino acids and other solid bio-materials was first considered in work

R. Erickson (✉) · A. Lund
Department of Physics, Chemistry and Biology, Linköping University,
581 83 Linköping, Sweden
e-mail: roland.erickson@comhem.se

A. Lund
e-mail: alund@ifm.liu.se

R. Erickson
Systems Development, SAAB Aeronautics, SAAB AB, 581 88 Linköping, Sweden
e-mail: roland.erickson@saabgroup.com

© Springer International Publishing 2014

A. Lund, M. Shiotani (eds.), *Applications of EPR in Radiation Research*,
DOI 10.1007/978-3-319-09216-4_19

initiated almost 60 years ago [1]. The well resolved EPR spectra obtained by in situ radiolysis of liquids, reported some years later, were in most cases interpreted by stick plot analyses of the hyperfine structure. The features due to ^1H or ^2H nuclei of the radicals formed in liquid hydrocarbons during irradiation with 2.8-MeV electrons were thus analysed by this method in studies initiated more than 50 years ago [2].

The applications of EPR in radiation research have since then been reviewed in several treatises both on the general technique [3–13] and on special subjects [14–19]. Simulation methods are frequently applied for the refinement of the parameters in recent work. In solids the parameters are usually anisotropic, *i.e.* their values depend on the orientation of a crystal sample in the magnetic field. The structure is then deduced from the g -, hyperfine coupling (hfc) and for nuclei with $I \geq 1$ also nuclear quadrupole coupling (nqc) tensors. For systems with $S > \frac{1}{2}$ one may also need to take into account the zero-field splitting (zfs) or fine structure as well. The treatise [16] dealing with studies of primary radiation effects and damage mechanisms in molecules of biological interest is also valuable as a source of information of ENDOR spectroscopy of primary paramagnetic components formed after irradiation at liquid helium temperature. Other specialised treatises of free radicals in irradiated solids involve studies of inorganic systems [14], disordered systems [17], radical ionic systems [18] and radicals on surfaces [19]. The Landolt-Börnstein database [20, 21] provides useful structural information. The book by Rånby and Rabek [22] about EPR spectroscopy in polymer research contains more than 2500 references. The development of advanced methods in this field has been treated in a recent work [23]. The developments, including multiple frequency EPR and pulsed methods in addition to the established continuous wave EPR and ENDOR techniques, have been further treated in a series of books from the Royal Chemical Society [24] and in a recent review [25]. In many instances the experimental studies were complemented by simulations as well as quantum chemistry calculations to support the assignments. In the present treatment the methods employed for the simulation of CW-EPR and ENDOR spectra are reviewed with emphasis on applications to disordered solid systems of interest in radiation research.

19.2 Liquids

The well resolved EPR spectra obtained in early studies of radicals formed by in situ radiolysis of liquids were in most cases interpreted by stick plot analyses of the hyperfine structure. The EPR lines were narrow permitting assignment of the radical species by the accurate hfc constants for a large number of organic radicals [2]. We refer to the literature for similar early studies in aqueous solution by radiolysis, see e.g. [26], and to [27–29] for studies of the kinetics and spin dynamics of radicals by pulse radiolysis with EPR detection.

19.2.1 Stick Plot Analysis

The analysis of EPR spectra of free radicals in liquid solution by means of stick plots to obtain the *hfc* constants due to ^1H is described e.g. in [5, 8].

Equivalent Protons A special case occurs when several nuclei are chemically equivalent as in the methyl radical; one proton gives rise to a doublet splitting of the energy levels, two protons a triplet since two levels coincide, three protons a quartet. The relative intensities depend on the degeneracies of the levels. Four lines split by $a_{\text{CH}_3} = 2.304$ mT with intensities 1:3:3:1 were thus observed in the liquid [2] in accordance with the binomial distribution (19.1) and the selection rule $\Delta m_l = 0$.

$$R_i = \frac{N!}{(i-1)!(N-i+1)!} \quad (19.1)$$

N is the number of equivalent protons or other $I = \frac{1}{2}$ nuclei, giving rise to totally $N+1$ lines, with intensity R_i of line i . The values can also be obtained from the so-called Pascal triangle [5, 8] which is practical to apply when the number of equivalent nuclei with $I = \frac{1}{2}$ is not too high.

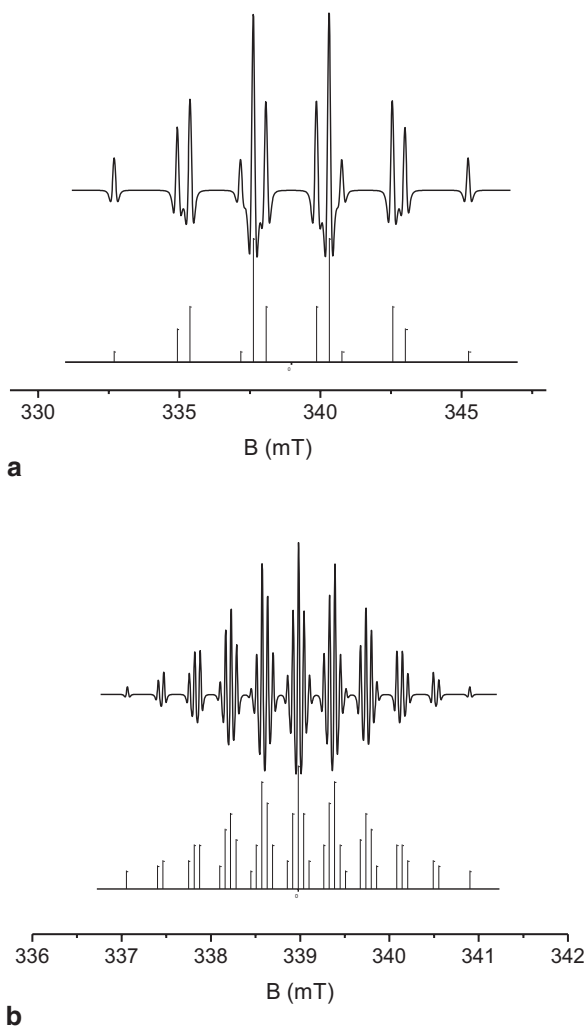
Isotropic couplings have also been observed in solids, for instance in the spectrum at 210 K of the methyl radical in γ -irradiated NaA zeolite/ CH_4 [30]. Extremely well resolved EPR spectra of matrix-isolated methyl radicals were also observed after X-irradiation at 4 K of methane in argon. We refer to [31] for an analysis of the quantum effects observed in this system.

Inequivalent Nuclei The hyperfine structure of the alkyl radicals formed during irradiation of liquid hydrocarbons with 2.8-MeV electrons was frequently attributed to two or more sets of chemically inequivalent ^1H or ^2H nuclei. The *hfc* constants were typically in the range 2.1–2.3 mT for H_α and usually slightly larger for the methyl protons in alkyl radicals of the type $\text{H}_3\text{C}-\dot{\text{C}}\text{H}_\alpha-\text{R}-$, while larger variations occurred for the methylene protons ($\text{R}=\text{CH}_2$) [2]. The ethyl radical for example gave a spectrum with twelve lines that could be attributed to the *hfc* constants of two groups of equivalent protons, one from the methylene, $a_{\text{CH}_2} = 2.238$ mT, the other from the methyl group, $a_{\text{CH}_3} = 2.687$ mT. This gives rise to a spectrum with 3×4 lines, yielding the stickplot in Fig. 19.1a.

Nuclei With $I > \frac{1}{2}$ Isotopic substitution, particularly with ^2H ($I = 1$) has frequently been employed in radiation chemistry studies. The Pascal triangle method does not apply to nuclei with spins $I > \frac{1}{2}$; two equivalent ^2H nuclei yield for example a quintet hyperfine pattern in the 1:2:3:2:1 ratio, three ^2H gives a septet pattern with intensities 1:3:6:7:6:3:1. A stick plot analysis of the deuterated ethyl radical thus predicts a total of 5×7 lines due to the deuterons of the CD_2 and CD_3 groups. The coupling constants, $a_{\text{CD}_2} = 0.347$ mT and $a_{\text{CD}_3} = 0.408$ mT are smaller, approximately by the factor $a_{\text{D}}/a_{\text{H}} = g_{\text{D}}/g_{\text{H}} = 0.153$ compared to C_2H_5 , yielding the stickplot for the deuterated ethyl radical schematically shown in Fig. 19.1b.

An algorithm reproduced in [32] can be used for the calculation of more complex diagrams to first order.

Fig. 19.1 Stick diagrams of **a** the ethyl radical, $\text{H}_2\dot{\text{C}}-\text{CH}_3$, with $a_{\text{CH}_2}=2.238$ mT and $a_{\text{CH}_3}=2.687$ mT. **b** the deuterated ethyl radical, $\text{D}_2\dot{\text{C}}-\text{CD}_3$, with $a_{\text{CD}_2}=0.347$ mT and $a_{\text{CD}_3}=0.408$ mT. The line-widths of the second derivative simulated spectra were adjusted for best fit to the experimental ones in liquid solution [2]

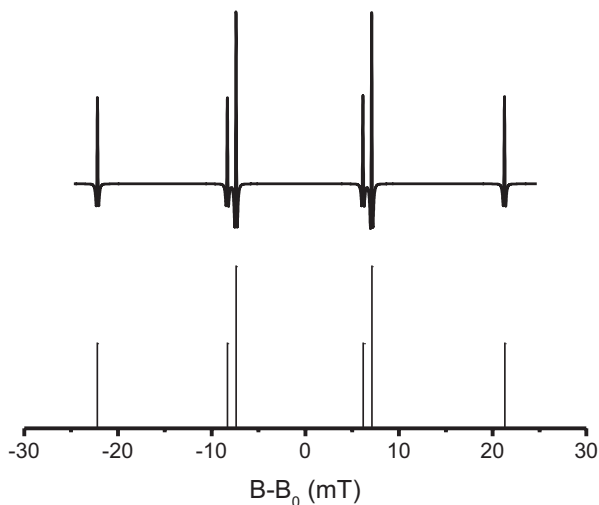


Large hfc Constants The analysis of *hfc* constants in the EPR spectra of liquids differs from the first order treatment when the high field approximation, $a \ll g\mu_B B$, does not strictly apply. In comparison with the “first order” spectrum the hyperfine lines are shifted towards lower field by second order effects according to (19.2) where the *hfc* constant a is in magnetic field, e.g. mT units [5].

$$B = B_0 - a \left(m_l + \frac{a}{B_0} \times \frac{I(I+1) - m_l^2}{2} \right) \quad (19.2)$$

The displacement is proportional to a^2/B and therefore needs to be taken into account when the *hfc* is relatively large compared to the electron Zeeman energy. Due

Fig. 19.2 Stickplot of the perfluoro methyl radical, $\dot{C}F_3$, obtained by second order perturbation theory with $a_F = 14.475$ mT. The line-width of the second derivative spectrum, calculated with the Breit-Rabi equation [36], was adjusted for best fit to the experimental spectrum obtained in liquid solution [33]



to this displacement the g -factor is not obtained at the centre of the spectrum, but at a higher field, $B_0 = h\nu / g\mu_B$. For nuclei with $I > 1/2$ the separation of the hyperfine lines is not constant but increases towards high field. The Pascal triangle method for equivalent $I = 1/2$ nuclei does not apply when the high-field approximation does not hold.

One of the first EPR studies where second and even higher order perturbation theory had to be used was in the analysis of the fluorinated methyl radicals formed during radiolysis of liquid fluorocarbons [33]. The ^{19}F nuclei ($I = 1/2$) are chemically equivalent. Effective nuclear spin values, $I_{eff}(N_I)$, were calculated by vector addition of the angular momenta of the individual spins. The multiplicity N_I is the number of times a specific value of I_{eff} appears. The resulting values of $I_{eff}(N_I)$, 1.5 (1), and 0.5 (2) were then used to obtain the line positions and intensities by second and third order formulas, as schematically shown in Fig. 19.2.

Radical anions formed by radiation induced electron attachment to perfluoro-cycloalkanes in frozen matrices have been investigated experimentally and theoretically [34, 35]. Nearly isotropic EPR spectra were observed in hexamethylethane (HME) and tetramethylsilane (TMS) matrices. Effective nuclear spin values, $I_{eff} = 0, 1, 2$ and 3 , with multiplicities $N_I = 5, 9, 5$ and 1 , were employed in a stick plot analysis of the $c-C_3F_6^-$ radical anion with an isotropic hfc constant, $a_F = 19.9$ mT, for the six equivalent ^{19}F nuclei, see Chapter 3 for additional details. The corresponding stickplot for the $c-C_4F_8^-$ radical anion is reproduced in Fig. 19.4. A Matlab script was employed to obtain this and other stickplots to second order in this chapter.

One reason to use high microwave frequencies and corresponding high fields is that the analysis becomes simpler—the first order analysis can be applied to measure larger hfc constants than is possible at X-band. Not all EPR laboratories can afford the price and running costs of a high field EPR spectrometer equipped with a superconducting magnet, however. The larger samples used at X-band may also be more conveniently prepared. Thus the need for analysis beyond first order remains.

19.2.2 Simulation of Isotropic EPR Spectra

A stick plot analysis can often provide a satisfactory analysis for isotropic EPR spectra of free radicals with well resolved hyperfine structure due to a few magnetic nuclei. In more complex systems the values of the coupling constants may, however, need refinement by simulation, after a preliminary assignment by stickplots has been made.

19.2.2.1 Approximate Treatments

A majority of the paramagnetic species that so far have been observed in irradiated liquid systems are free radicals with relatively small hfc constants. The spectrum can then be simulated by the superposition of Lorentz, Gauss or Voigt line-shapes [5, 8] on the stick plot obtained to first or second order as exemplified in Figs. 19.1 and 19.2. Some free-ware and commercial simulation programs are presented in the Appendix.

Multi-Component Spectra It is usually quite difficult to control the experimental conditions so that only one paramagnetic species is present in an irradiated material. The field-swept ENDOR method [37] is capable of discriminating between different species but has lower sensitivity than EPR and is not always available. A simple procedure for the analysis of an EPR-spectrum containing two components is illustrated in Fig. 19.3 for a sample containing methylmetacrylate, MMA, adsorbed on silica gel γ -irradiated and recorded at 77 K. The seven equidistant lines split by 2.2 mT, labeled MMA-h in the figure, were assigned to the radical $(\text{CH}_3)_2\dot{\text{C}}\text{COOCH}_3$ formed by a hydrogen atom addition to the vinyl group. The hydrogen atoms originated partly from the hydroxyl groups on the surface of the silica gel as verified by an experiment in which a sample of MMA adsorbed on deuterated silica gel was irradiated. The spectrum obtained from this system, Fig. 19.3 (Exp.), was assumed to be composed of the ordinary 7-line spectrum (MMA-h) due to $(\text{CH}_3)_2\dot{\text{C}}\text{COOCH}_3$ and a 6-line structure (MMA-d) with a splitting constant of 2.2 mT assigned to the radical $(\text{CDH}_2)\dot{\text{C}}(\text{CH}_3)\text{COOCH}_3$. In the latter species the five equivalent methyl protons gave rise to the sextet, while the hyperfine structure of the added deuterium atom was too small to be resolved. Standard programs like Excel, software for graphic manipulations like Origin, or Matlab scripts for least squares fits as in Fig. 19.3 have been used to superimpose the component spectra in an appropriate ratio.

A more advanced procedure for the fitting of multi-component isotropic spectra [38] was employed for the analysis of irradiated fluorinated polymers to obtain hfc constants, g-factors, linewidths, and concentrations of up to seven different radicals in polyvinylidene fluoride based polymers [39, 40]. A Simplex algorithm in the WinSim program [41] was used to refine the parameters.

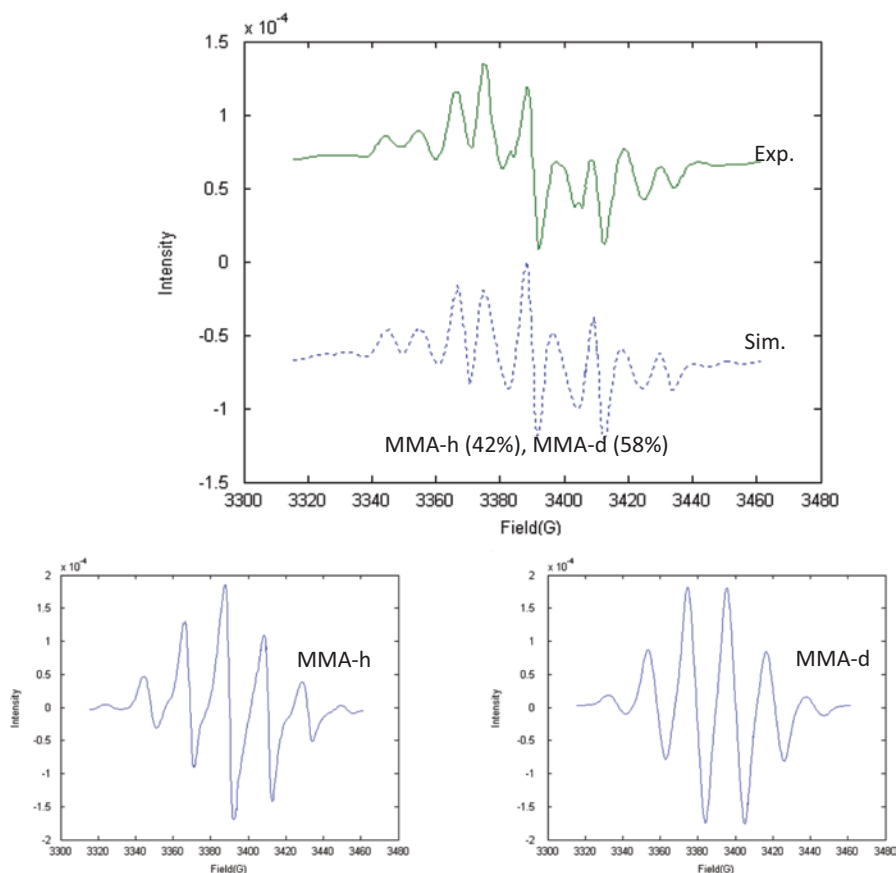


Fig. 19.3 Top: Experimental and simulated EPR spectra of MMA/SiO₂-d γ -irradiated and recorded at 77 K. Bottom: Component spectra MMA-h and MMA-d used in the the least squares fit (Sim.) to the experimental spectrum (Exp.)

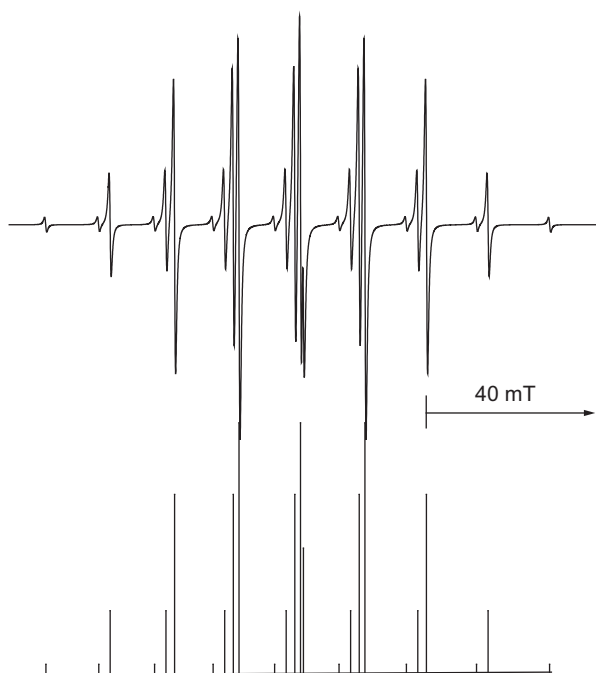
19.2.2.2 Exact Treatments

Exact methods have recently been employed for the simulation of radiation induced radicals in liquid solution, see e.g [42] for a reanalysis of the EPR spectra of radicals of the type $\dot{C}X_3$, $X=^1H, ^2H, ^{19}F$. The spectrum was then calculated by employing a spin-Hamiltonian of the type (19.3).

$$H = g\mu_B \mathbf{B} \cdot \mathbf{S} + \sum_{k=1}^K a_k \mathbf{I}_k \cdot \mathbf{S} - g_k \mu_N \mathbf{B} \cdot \mathbf{I}_k \quad (19.3)$$

Here K is the number of nuclei, while the other symbols have their usual meaning. The line positions and intensities were obtained by diagonalizing the Hamiltonian matrix to obtain the transition energies and intensities. In recent applications the

Fig. 19.4 Isotropic X-band EPR spectrum calculated with the Breit-Rabi equation and the corresponding stickplot for the $c\text{-C}_4\text{F}_8^-$ anion radical with 8 equivalent ^{19}F ($I=1/2$) nuclei with $a_F=14.8$ mT, see [34, 35] for comparison with the experimental spectra in the γ -irradiated HME and TMS matrices



spectra were usually calculated in frequency space [43]. We refer to the Appendix for software known to us.

For radicals with equivalent spin nuclides a method based on the Breit-Rabi equation (19.4) can provide a simpler alternative when accurate values of the intensities are not required.

$$E(F, M_F) = -\frac{\Delta W}{2(2I+1)} - g'_l \mu_B B M_F \pm \frac{\Delta W}{2} \sqrt{1 + \frac{4M_F x}{2I+1} + x^2} \quad (19.4)$$

Here the symbols $g'_l = g_l \frac{\mu_N}{\mu_B}$, $x = (g_e - g'_l) \frac{\mu_B B}{\Delta W}$, and $\Delta W = (I+1/2)a$, have been introduced. The plus and minus signs correspond to the two possible values of $F=I \pm 1/2$ having $2F+1$ components of M_F in the range $-F$ to $+F$. The equation [36], originally derived for a single nucleus with hfc a , also applies for a group of equivalent nuclei, provided that effective nuclear spin values, $I_{eff}(N_l)$, are used while the intensities of the lines are set equal to the number of times (N_l) each I_{eff} value appears. The isotropic spectra obtained by γ -irradiation of the perfluorocyclalkanes $c\text{-C}_3\text{F}_6$, $c\text{-C}_4\text{F}_8$, and $c\text{-C}_5\text{F}_{10}$ in plastically crystalline HME or TMS matrices showed for example second-order hyperfine structures with six, eight and ten equivalent ^{19}F nuclei ($I=1/2$), attributed to the corresponding radical anions. The experimental spectra of the C_4F_8^- radical anion at increased temperature were in fact similar to the simulated one in Fig. 19.4 [34, 35].

19.3 Solids

EPR spectra obtained from irradiated solids are usually much less resolved than those observed in liquid solution. This applies particularly in studies of disordered systems, “powders”, where the anisotropic features of the g -factor and the hfc constants have frequently been difficult to extract by inspection. Simulation programs to facilitate the interpretation of powder spectra were therefore developed at an early stage [44, 45].

19.3.1 Simulation of $S=1/2$ EPR Powder Spectra

A program for the simulation of free radical spectra in amorphous samples [45] was the first general treatment taking into account the anisotropy of the g - and hfc -tensors and the occurrence of satellite lines for nuclei of any spin with $I \leq 3/2$ by perturbation theory. The program has frequently been employed by experimentalists for the interpretation of spectra of irradiated samples in the past. Perturbation theory was also employed in a commercially available program [46]. The latter program was apparently not intended for the simulation of the spectra where satellite lines occur, however. Such lines, commonly but somewhat misleadingly attributed to $\Delta m_I = 1$ transitions, have often been observed in spectra of organic radicals having an anisotropic proton hfc of the same magnitude as the ^1H nuclear Zeeman splitting at X-band [47, 48]. This “direct field effect” can also affect the line shape of the powder spectra, see e.g. [49] for an illustration concerning the malonyl radical $(\text{HOOC})_2\dot{\text{C}}\text{H}$.

19.3.1.1 First Order Simulation Methods

The methods used in [45] were adequate for the simulation of a majority of the EPR spectra observed in the past of irradiated solids, even though the nqc in radicals containing nuclei with $I \geq 1$ were neglected. The ^{14}N nqc interaction is for example usually weaker than the hfc term and affects the EPR spectrum only to a minor extent. Simulations of this type can be performed with several of the presently available software packages described in the Appendix.

A procedure for the simulation of the EPR spectra of radicals containing nuclear spins with appreciable nqc due e.g. to ^{23}Na , ^{27}Al , ^{33}S , ^{35}Cl , ^{37}Cl , ^{79}Br , ^{81}Br was presented in [50–52]. An anisotropic radical system containing several nuclei was considered, assuming that the electronic Zeeman term is dominant while the relative magnitudes of the hyperfine and nuclear terms are arbitrary. The perturbation operator consisting of the hfc , nqc and nuclear Zeeman interactions for each nucleus (i) with $I_i > 1/2$ is then given by (19.5).

$$H'_i = \mathbf{I}_i \mathbf{A}_i \mathbf{u} S_u + \mathbf{I}_i \mathbf{Q}_i \mathbf{I}_i - \mu_N g_i \mathbf{B} \mathbf{I}_i \quad (19.5)$$

The unit vector $\mathbf{u} = \mathbf{gB}/|\mathbf{gB}|$ is along the effective field direction, the other symbols have their usual meaning. The first order energies cannot be obtained by traditional perturbation theory, but have to be computed by diagonalization of the corresponding perturbation matrices [50–53]. The transition energies for each nucleus were obtained from the energy differences between the eigenvalues for the $m_s = +\frac{1}{2}$ and $-\frac{1}{2}$ electronic manifolds, while the intensities were calculated using the corresponding eigenfunctions of (19.5). The spectrum at each orientation of the magnetic field was obtained by superimposing a lineshape on the stickplot, as for isotropic spectra. The first derivative powder EPR line shape $S(B, P)$ at the static magnetic field B was approximated by the formula (19.6) where f is a Gauss, Voigt or Lorentz derivative function, with a width, w , that may be orientation dependent. The symbols φ and θ denote the polar angles describing the orientation of the magnetic field.

$$S(B, P) = C \int_{\theta=0}^{\pi} \int_{\varphi=0}^{2\pi} \sum_{p < q} I_{pq} f\left(\frac{B - B_{pq}}{w}\right) \sin\theta d\theta d\varphi \quad (19.6)$$

The summation is over the transitions between the states p and q . I_{pq} is the transition probability and B_{pq} is the resonance field. The microwave frequency is constant and the spectrum is calculated as a function of the applied magnetic field B . The shape of the spectrum is determined by a set of parameters, P , representing the components of the g and hfc tensors, the nuclear terms, the line width, and the total intensity C . The spectrum in Fig. 19.5c, calculated with this method, is seen to agree well with that obtained in (b) by an exact calculation, indicating that the procedure is applicable even when the hfc and nqc interactions are of comparable magnitudes. The second order perturbation methods employed in [54, 55] are not suitable to simulate spectra under those conditions, as seen in Fig. 19.5a, however.

A factor, $|G|^2 = \frac{\mu_B^2 B_1^2}{8g} (\text{Tr}(\mathbf{g}^2) - \mathbf{ug}^2\mathbf{u})$, was proposed to account for the anisotropy of the g -tensor on the EPR intensity [53] under the normal experimental condition with the static field perpendicular to the microwave magnetic field B_1 . The factor might improve the accuracy in the simulations of spectra with significant g -anisotropy, but is of less importance for most organic radicals.

19.3.1.2 Second Order Simulation Methods

Several second order perturbation treatments of general spin Hamiltonians have been presented in a suitable form for the development of simulation programs, see e.g. [54, 55]. The second order corrections were computed for arbitrary orientations of the g -, hfc - and nqc - tensors under the assumption that the nqc ($I > \frac{1}{2}$) is small, i.e. $nqc < hfc$. Energy cross terms involving the hfc of two nuclei, were taken into account in [56]. These treatments are of interest when the simulation by first order in presence of large hfc is inaccurate, and exact treatment is slow, like when many nuclei contribute to the hfc . The methods are not suitable when the interactions

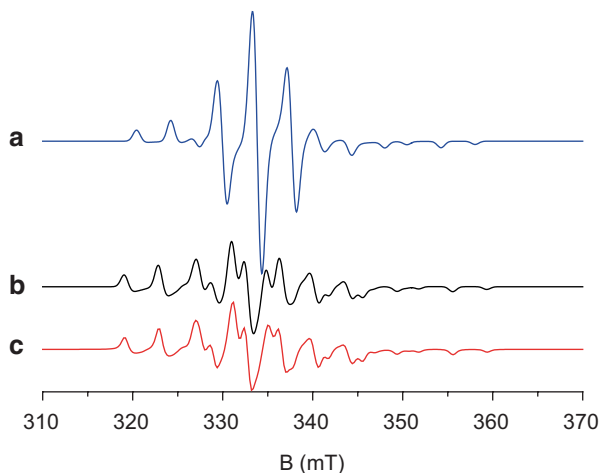


Fig. 19.5 Simulated EPR powder spectra for the $>\dot{\text{C}}\text{-}^{81}\text{Br}$ radical [57] with $g_x=2.0003$, $g_y=2.0240$, $g_z=2.0215$, $A_x=10.0$ mT, $A_y=-2.0$ mT, $A_z=-3.2$ mT, and $e^2qQ=330$ MHz simulated with Easyspin [60], **a** by the second order perturbation theory in [55], **b** exactly, **c** by the perturbation method in [50–52]. Two β protons with $A_x=3.8$ mT, $A_y=3.9$ mT, $A_z=3.7$ mT and $A_x=3.8$ mT, $A_y=4.7$ mT, $A_z=3.7$ mT and a weak ^{14}N hyperfine interaction with $A_x=0.095$ mT, $A_y=-0.385$ mT, $A_z=-0.289$ mT were also included in the simulations

are of the same magnitude, $nqc \approx hfc$, however, as was illustrated in Fig. 19.5a. An extension of the method in [50, 51] to treat this case to second order was discussed in [52], but was not fully implemented in the simulations. Powder simulations taking all interactions into account by exact theory [58–62] can nevertheless be performed quite rapidly for calculations like that in Fig. 19.5b.

In the absence of nqc , the second-order hfc due to equivalent nuclei can be obtained as in isotropic systems by the effective nuclear spin values, I_{eff} and the number of times they appear, N_p , for any number and value of the nuclear spin. The total spectrum can thereby be obtained by adding the separate spectra of each I_{eff} weighted by N_p . This procedure was applied to simulate the spectrum in Fig. 19.6 of Ag_3^{2+} trapped in an irradiated zeolite matrix. The experimental spectrum contains in addition signals from other species, but the simulation in Fig. 19.6b, is in agreement with the parts attributed to $^{109}\text{Ag}_3^{2+}$ as indicated by the stick diagrams. The agreement with a simulation based on exact theory [59] was also satisfactory, indicating that a second order treatment of the hyperfine structure due to equivalent nuclei might be employed, unless high accuracy is required. As seen by comparison with Fig. 19.6c it is necessary to use the effective nuclear spin values, I_{eff} . The procedure was, however, not successful for systems containing several nuclei with large, differently oriented hfc -tensors as discussed in the following section.

19.3.1.3 Exact Simulation Methods

Simulations of powder spectra based on perturbation methods may deviate significantly from those obtained by an exact treatment in the presence of large hfc

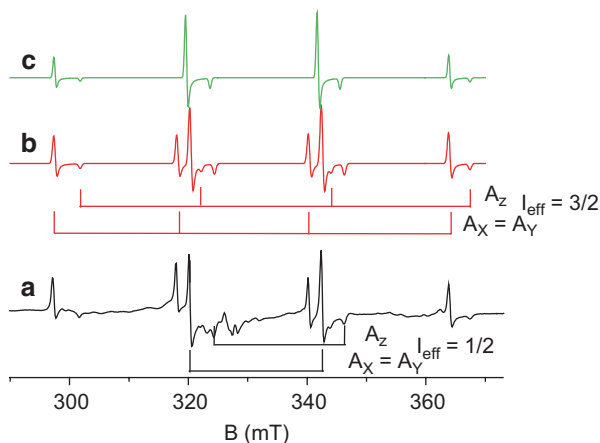


Fig. 19.6 **a** Experimental first derivative EPR spectrum of Ag_3^{2+} , trapped in a γ -irradiated zeolite matrix, showing second order *hfc* splittings due to three equivalent ^{109}Ag nuclei, **b** simulated by second order theory, with $g_{\parallel}=1.958$, $g_{\perp}=1.981$, $A_{\parallel}=21.88$ mT, $A_{\perp}=22.16$ mT, Gaussian peak-peak line-width=0.5 mT, using effective nuclear spins $I_{\text{eff}}=3/2$ and $1/2$, **c** simulated by second order theory using Simfonia [46] with $I=1/2$ for the three nuclei. Adapted from [52] with kind permission from Acta Chemica Scandinavica using experimental spectrum provided by Prof. J. Michalik

constants, see e.g. [59]. Powder spectra were therefore calculated by exact theory rather than by perturbation methods even in early work. This applied particularly for systems containing ions of transition metals [43], but also for free radicals and triplet state molecules. Exact theory was for instance employed in early work for the analysis of strong *nqc* interactions in the radiation induced chlorodisulfanyl (CISS \cdot) radical [63]. Several software packages employing exact theory have since then been developed [58–62]. Some applications involving EPR simulations of radiation induced radicals in low and high molecular fluorinated compounds, including the trifluoromethyl radical, are presented below. Quite large anisotropic splittings due to ^{19}F hyperfine structure were often observed [64–69], both for the neutral radicals formed in the pure systems and in matrices in which ionic radical species were frequently trapped.

The trifluoromethyl radical, $\dot{\text{C}}\text{F}_3$ The EPR spectra of UV-irradiated CF_3I in rare gas matrices at 4.2 K were interpreted in terms of randomly oriented, non-inverting $\dot{\text{C}}\text{F}_3$ radicals with nearly axial *hfc* tensors in early work [64, 65]. The complex shape of the EPR spectrum was attributed to the different orientations of the principal directions of the three ^{19}F *hfc* tensors with equal, strongly anisotropic principal values. The anisotropic *hfc* constants calculated by INDO and *ab initio* theory obtained for an assumed pyramidal structure of the radical were close to the experimental values, $A_x=26.2$ mT, $A_y=8.7$ mT, $A_z=8.0$ mT [66]. The largest splitting did not occur perpendicular to the C-F bond as previously assumed, but at an angle α with the C_{3v} symmetry axis as indicated in Fig. 19.7. The result was explained by the contribution to the dipolar couplings from spin density on fluorine as well as carbon

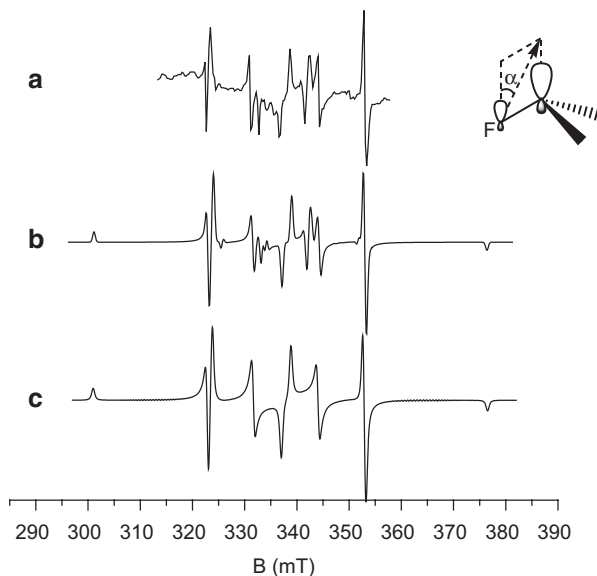


Fig. 19.7 Experimental and simulated X-band EPR spectra of $\dot{\text{C}}\text{F}_3$ in rigid state with $g_{\parallel}=2.0024$, $g_{\perp}=2.0042$ (\parallel -direction along the 3-fold symmetry axis), $A_x=26.2$ mT, $A_y=8.7$ mT, $A_z=8.0$ mT, with symmetry-related principal axes of the three ^{19}F [64–66] (x -direction ($\alpha=17.8^\circ$) for one nucleus indicated by an *arrow*). The line widths in the simulations were adjusted to fit the experimental spectrum provided by Prof. J. Maruani. **a** experimental spectrum in rare gas matrix at 4.2 K, **b** exact simulation using EasySpin, **c** second order perturbation simulation using EasySpin. Adapted from [8] with kind permission from Springer Science+Business Media (2011)

2p orbitals. Values of α in the range $20\text{--}27^\circ$, were estimated. It was concluded that in this instance bond directions cannot be obtained from EPR data without detailed analysis of the electronic structure. As can be seen in Fig. 19.7 the experimental spectrum is well accounted for by the exact simulation with $\alpha=17.8^\circ$, while the extra lines in the centre part could not be reproduced with second order perturbation theory in Fig. 19.7c. It is nevertheless remarkable that the ^{19}F hfc tensor of the $\dot{\text{C}}\text{F}_3$ radical could be accurately determined by an analysis of the X-band spectrum in rigid rare gas matrix at an early stage [64, 65], in spite of the difficulties to obtain satisfactory simulations based on perturbation theory.

Fluorinated Polymers The anisotropic ^{19}F hfc constants of the chain, $-\text{CF}_2\dot{\text{C}}\text{FCF}_2-$, and propagating, $-\text{CF}_2\dot{\text{C}}\text{F}_2$, radicals in γ -irradiated polytetrafluoroethylene and linear perfluoroalkanes were reported in early EPR studies at low temperatures [67]. The values agreed well with those obtained in DFT calculations and were also consistent with data from EPR studies of fluorinated radicals in single crystals [68, 69]. Simulations were not employed, however. Considerably smaller isotropic couplings were obtained for the long-lived radicals observed in the radiolysis of liquid perfluorocarbons [70].

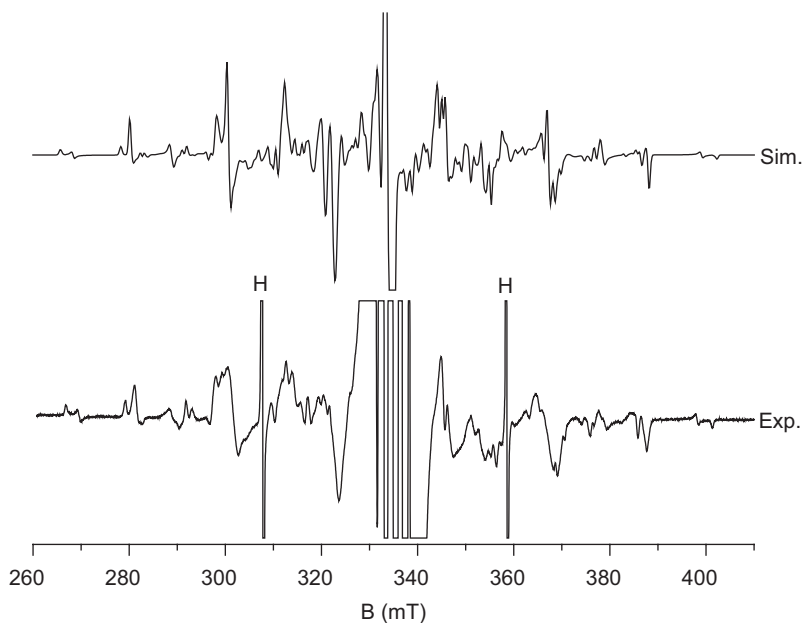


Fig. 19.8 X-band EPR spectrum of a solid solution of 1 mol% $c\text{-C}_4\text{F}_8$ in MTHF, γ -irradiated and recorded at 77 K, and simulated spectrum of $c\text{-C}_4\text{F}_8^-$ computed exactly with Easyspin, using the isotropic and anisotropic ^{19}F hfc tensors obtained by DFT calculations [35]. Adapted from [35] by permission of the American Chemical Society (2007)

Fluorobenzenes The EPR spectra of γ -irradiated fluorobenzenes in halocarbon solid matrices were analysed by simulation to have axially symmetric hfc constants due to fluorine nuclei and were attributed to cation radicals by comparison with calculated values from *ab initio* calculations [71], see further Chapter 3.

Perfluorocycloalkanes The identification of the radical anions of perfluorocycloalkanes produced by γ -irradiation in frozen matrices was confirmed by generating identical EPR spectra in photoionization experiments as described in Chapter 3. Density functional theory (DFT) predicted geometrical structures that were significantly altered by the electron attachment. Electron attachment to $c\text{-C}_4\text{F}_8$ resulted for example in a geometrical change from the puckered D_{2d} to the planar D_{4h} symmetrical structure. The isotropic ^{19}F hfc constants computed by the B3LYP method were in almost perfect agreement with the experimental values. The corresponding calculated anisotropic couplings were also quite close to the experimental values as indicated by simulations [35], further elaborated below.

Simulation of $c\text{-C}_4\text{F}_8^-$ EPR Spectra in Frozen Matrices Simulations were applied to further analyse the anisotropic spectra of the radical anions at 77 K of perfluorocycloalkanes reported in [35]. The principal hfc values and the direction cosines of the tensor axes obtained from DFT calculations were employed for the simulation. The spectrum in Fig. 19.8 (Sim.), calculated with an exact method [60], shows a similar structure of the outer features as observed in Fig. 19.8 (Exp.). Those features

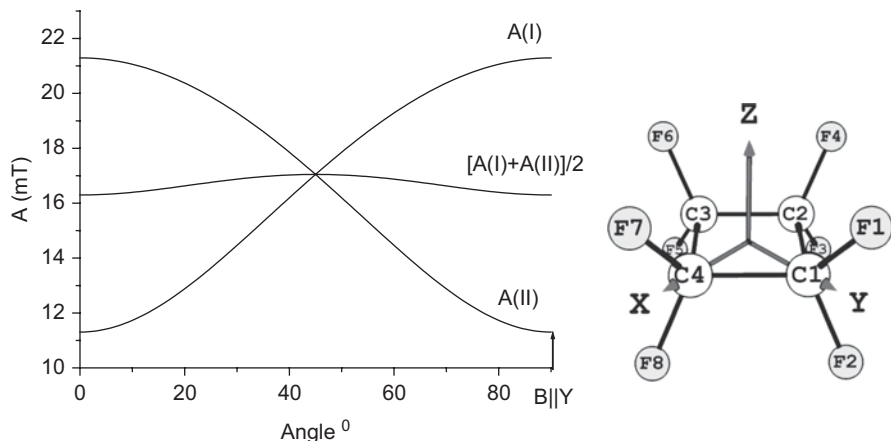


Fig. 19.9 Schematic variation with the magnetic field orientation in the XY plane of the two different ^{19}F hf splittings, A(I) and A(II) due to the two diagonally placed sets of four nuclei of $c\text{-C}_4\text{F}_8^-$ with symmetry D_{4h} . The line marked “[A(I)+A(II)]/2” corresponds to the average ^{19}F hf splitting due to I and II nuclei. Adapted from [35] by permission of the American Chemical Society (2007)

could also be reproduced by simulation (not shown) using the second order option in Easyspin [60]. Similar results were obtained in earlier work [35] with software described in [72, 73]. The inner features differed significantly between the exact and approximate treatments, however, like for the spectra of CF_3 (Fig. 19.7).

Because of the high symmetry the same ^{19}F hf splitting is expected for all eight ^{19}F nuclei of $c\text{-C}_4\text{F}_8^-$ along the C_4 symmetry axis (Z in Fig. 19.9). In the XY plane two different splittings are expected, due to the two diagonally placed sets of four nuclei in the structure formula shown. As seen in the figure the individual ^{19}F splittings evaluated from the hf tensors obtained by DFT vary quite much with the direction of the magnetic field in the XY-plane. The effective splitting should, however, vary as the average of the two ^{19}F splittings, yielding the observed outer features in the experimental and simulated spectra in Fig. 19.8. The small apparent anisotropy of the outer hyperfine features of $c\text{-C}_4\text{F}_8^-$ observed experimentally was thus accounted for by considering the effective ^{19}F hf splittings.

Simulation of $c\text{-C}_3\text{F}_6^-$ EPR Spectra in Frozen Matrices The six ^{19}F nuclei would all have the same splitting constant along the C_3 symmetry axis. In the plane perpendicular to the axis three different hf splittings are expected from groups of two ^{19}F nuclei. According to DFT theory the individual splittings are quite anisotropic, but the average of the three ^{19}F hf splittings varied much less than for $c\text{-C}_4\text{F}_8^-$. The asymmetric sharp outermost features observed in Fig. 9 of [35] may therefore result from the angular variation of the effective splittings in the XY plane, consistent with the line shape simulations, predicting a quite small apparent axial anisotropy of the outermost features. A small apparent anisotropy was also predicted for the $c\text{-C}_5\text{F}_{10}^-$ anion. The experimental spectrum was not sufficiently resolved to make an analysis, however, see further Chapter 3.

c-Perfluoroalkenes The experimental anisotropic spectra of $c\text{-C}_4\text{F}_6^-$, $c\text{-C}_5\text{F}_8^-$ and $\text{CF}_2=\text{CF}_2^-$ were also satisfactorily reproduced by the EPR spectral simulation method using the computed *hfc* principal values and orientations of ^{19}F nuclei [74], see further Chapter 3.

19.3.2 Simulation of Radical Pair and Triplet State EPR Spectra

EPR signals assigned to radical pairs and triplet state molecules were observed in early studies of solids exposed to ionizing or UV radiation at low temperature [3, 75]. A sharp $\Delta m_s=2$ line was frequently present at approximately half the centre field of the two $\Delta m_s=1$ transitions. The latter became broadened in the powder spectra, due to the anisotropy of the *zfs*.

19.3.2.1 Radical Pair EPR Spectra

The dipolar interaction between the two unpaired electrons gives rise to a doublet of $\Delta m_s=1$ transitions with an anisotropic splitting. The average distances, R , between the radicals, typically in the range 0.5–1 nm, are usually estimated by the point dipole formula, $D = \frac{3}{2} \frac{\mu_0}{4\pi} \frac{g\mu_B}{R^3}$, with the *zfs* D in field units. In an initial study [75] a distance $R=0.56$ nm was for example obtained for the radical pairs trapped in X-irradiated dimethylglyoxime. The *hfc* splittings, if present, are one half of those in the separated radicals. Numerous studies have since then been performed to obtain information about the trapping sites of radical pairs in irradiated solids [76–97], as well as the structure of the radical constituents in certain organic systems of fundamental importance, like methane. An EPR spectrum attributed to a $\text{H}\dots\text{CH}_3$ radical pair separated by one methane molecule was thus observed in an early EPR study of irradiated solid methane at 4.2 K [82]. A spatial distribution of the $\text{H}\dots\text{CH}_3$ and $\text{D}\dots\text{CD}_3$ distances was proposed in a later study [78]. Highly resolved EPR spectra of selectively D-labelled radical pairs of a series of D-labeled methyl radicals were recently observed for X-irradiated solid Ar containing CH_4 , CH_2D_2 and CD_4 molecules at 4.2 K [98]. The EPR spectra due to the triplet radical-pairs $\text{H}\dots\text{CH}_3$, $\text{H}\dots\text{CHD}_2$, $\text{D}\dots\text{CH}_2\text{D}$ and $\text{D}\dots\text{CD}_3$ were identified by the $\Delta m_s=1$ and $\Delta m_s=2$ transitions. Three different sets of *zfs* parameters corresponding to separation distances of $R=0.87$, 0.83, and 0.82 nm were resolved and supported by simulation. The most probable location of the counter H-atom was at an interstitial site of the Ar lattice.

Singlet-Triplet Splitting Effects Provided that the exchange interaction between the two unpaired electrons is stronger than the Zeeman term the spectrum can be analysed as for the triplet state systems discussed in Sect. 19.3.2.2. In the opposite case a theoretical analysis that took the effect of singlet-triplet splitting into account was required for the interpretation of the EPR spectra of radical pairs in irradiated solids. A theory for the EPR spectra of weakly interacting radical pairs developed by Itoh et al. [99] was applied to the radical pair in dimethylglyoxime. An observed

unequal spacing between the ^{14}N *hfc* lines was attributed to the influence of a small singlet-triplet interaction, $J = -3000 \pm 300$ MHz. For the radical pair produced by X-irradiation of pentaerythritol crystals at 26 K [100] the trace of the *zfs* deviated significantly from zero, and the *zfs* depended on the different strengths of the magnetic fields at X- and Q-bands. A procedure derived from a second order perturbation calculation was employed to obtain the g-tensors of the monoradicals, the *zfs* tensor, and the exchange term, $J = 8200$ MHz. The radical pair was ascribed to an alkoxy...alkyl radical pair, $(\text{CH}_2\text{OH})_3\text{CH}_2\text{O}\cdots\text{CH}_2(\text{CH}_2\text{OH})_3$. The assignment was supported by simulations. Attempts to analyze the EPR results using pure triplet states for H...H, H...D and D...D, spin-pair radicals in rare gas matrices at 4 K [101, 102] yielded significantly different *D* values for each different isotopomer, while a theoretical model that treated these spin-pairs as weakly interacting atoms gave a consistent set of magnetic parameters. Spectra were simulated by exact diagonalization using a phenomenological Hamiltonian of the individual hydrogen atoms denoted *a* and *b*, the zero field, $\mathbf{S}_a \cdot \mathbf{D}_{ab} \cdot \mathbf{S}_b$, and Heisenberg spin exchange, $J \cdot \mathbf{S}_a \cdot \mathbf{S}_b$, terms. The latter term accounted for the effects of singlet-triplet mixing in the simulation of the observed EPR spectra. A similar study of the $^{14}\text{N}\dots^{14}\text{N}$ and $^{15}\text{N}\dots^{15}\text{N}$ spin-pair radicals reported in [103] was interpreted on the basis of weakly interacting atoms developed for the H...H spin-pair. The $^{15}\text{N}\dots^{15}\text{N}$ radical pair in the dominant trapping site in neon matrix had magnetic parameters $g = 2.0016$, $A(^{15}\text{N}) = 15.9$ MHz, $D = -178$ MHz and $J = 468$ MHz, corresponding to a N...N separation distance of 6.41 Å using the point dipole approximation.

19.3.2.2 Triplet State EPR Spectra

The work by Kottis and Lefebvre [104] might be the first where $S=1$ EPR powder spectra were calculated exactly. No assumption was made about the relative strengths of the electronic Zeeman and *zfs* terms. The eigenfunctions of the spin Hamiltonian matrix, expressed in the T basis of the zero-field Hamiltonian [3], were employed to obtain the intensities of the electronic transitions. The powder spectra were computed by numerical integration over the orientation of the magnetic field like in Eq. (19.6). A cubic equation was derived for the calculation of the field strengths at which the electronic transitions occur at a constant value of the microwave energy in a later study [105]. The procedure was adopted in [106] for the simulation of single crystal EPR spectra of ground state triplet trimethylenemethane (TMM), $(\text{H}_2\text{C})_3\text{C}$. The influence of the *zfs* was thus treated exactly while the energy contributions due to the hyperfine and nuclear interactions of the methylene groups were obtained as for the free radical case by diagonalization of the perturbation matrix (19.5). A similar “hybrid” method is an option in modern simulation programs like EasySpin and SOPHE [60, 62].

Anomalous hfc and the Sign of the zfs As first pointed out by Minakata and Iwasaki [107] the *hfc* splitting of the $m_s = -1 \leftrightarrow 0$ and $m_s = 0 \leftrightarrow +1$ electronic transitions can be entirely different. This anomaly was attributed to the combined effects of the hyperfine and the nuclear Zeeman interactions which had previously often been neglected. In addition, the anomalous features of the spectra made it possible to

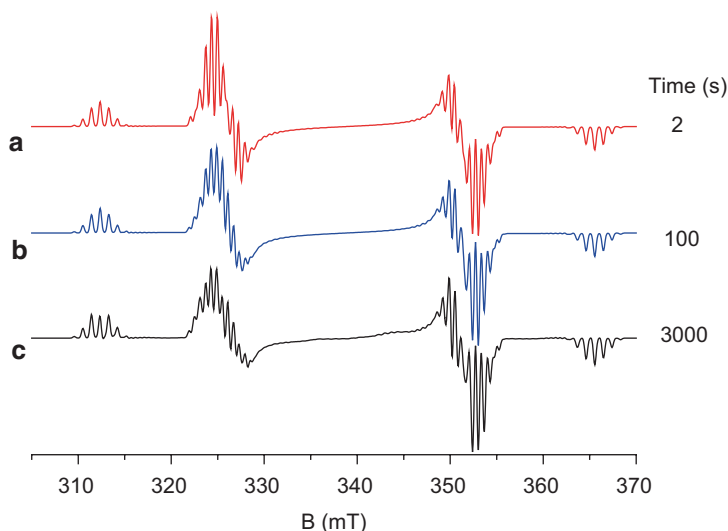


Fig. 19.10 Powder EPR spectra of $S=1$ trimethylenemethane, $(\text{H}_2\text{C})_3\text{C}$, simulated with $D=0.0248\text{ cm}^{-1}$, $|E|\leq 0.0003\text{ cm}^{-1}$ and $\mathbf{A}=(-14, -38, -26)$ MHz of the six methylene protons with principal axes related by the threefold symmetry axis of the molecule with **a** second order theory, **b** the “hybrid” option (see text), **c** matrix diagonalization in Easyspin. The computer times are indicated

determine the relative signs of the *hfc* and the *zfs*. The method was applied in a study of triplet state TMM, formed by the radiolysis of methylenecyclopropane. The sign of the *zfs* could accordingly be determined relative to the signs of the *hfc* tensor components of the methylene protons by simulations of single crystal spectra, supporting the assignment $D>0$ [108]. The difference in the *hfc* of the two electronic transitions is apparent in the powder spectra calculated by the hybrid and exact methods in Fig. 19.10b and c, and also with simulations [52] using the method in [106], but not with second order theory, Fig. 19.10a. The observed powder spectrum [109] was not sufficiently resolved for an experimental determination of the sign.

Triplet state spectra featuring large *hfc* and/or *nqc* splittings are best simulated with the exact methods in the Appendix. We refer to the literature [110] for experimental studies by the highly sensitive ODMR (optically detected magnetic resonance) method.

19.3.3 Simulation of Transition Metal Complexes

Irradiated samples of complexes containing metal ions have been investigated both in fundamental studies e.g. of metal ions in unusual valence states [111] and from technological points of view [112], for instance in treatment of nuclear waste. EPR spectra of transition metal complexes have frequently been simulated exactly in recent treatments [43, 58–62, 113–117]. The second order equations for the transi-

tion energies and intensities obtained for a general spin Hamiltonian in an arbitrary coordinate system [55] have also been employed for the analysis of zfs and hfc patterns and were in fact implemented in publically available software packages [49, 60]. This method might be of advantage in high field EPR where the high field approximation applies for larger values of the hfc or zfs than at X-band.

19.4 EPR Analysis of Motional Effects

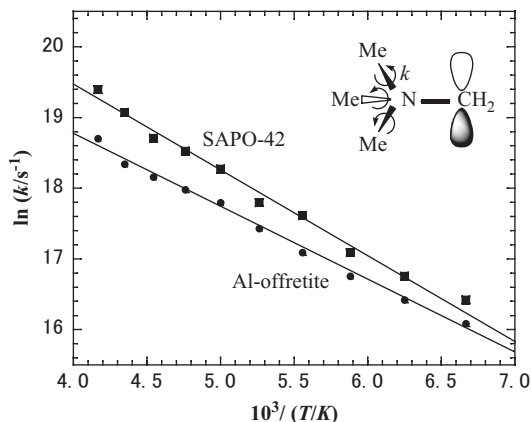
Studies of reversible changes of the EPR spectra with temperature can provide information about internal (or intramolecular) motions within a paramagnetic species and of the motions of diamagnetic molecules probed by spin labels. The terms “chemical exchange” and “slow-motion EPR” are frequently used in those contexts.

Motional Studies with Nitroxide Spin Probes The analysis of the temperature dependence in the EPR spectra of nitroxide radicals, commonly used as spin labels and probes in studies of polymeric and biological samples, is well established using methods based on the stochastic Liouville equation (SLE) [118]. Chain and local molecular motions of spin-trapped radicals were experimentally studied in thermally treated or irradiated polymers, see for example [121, 122].

Motional Studies with Peroxy Spin Probes Motional effects have been investigated, particularly in irradiated polymers and on surfaces. Peroxy radicals $-\text{CF}_2\text{CFOOCF}_2-$ and $-\text{CF}_2\text{CF}_2\text{OO}$ were stabilized when PTFE was irradiated in air. Temperature dependent effects were probed [123] using simulations based on the modified Bloch equations to obtain information about the dynamics of motions like chain axis rotation, bond rotations, and motions of the polymer chain ends from the observed averaging of the g anisotropy. We refer to the literature for a related study of the motional dynamics of O_2^- adsorbed on titanium supported surfaces [124].

Chemical Exchange The analysis of intramolecular motion of radicals in irradiated systems [125–141] has in general been made by comparison of experimental spectra recorded at different temperatures with simulations of spectra at different interchange rates between two or more geometric configurations. Procedures based on the Liouville formalism for the analysis of intramolecular motions in *anisotropic systems* have been developed [125–131]. Non-perturbative simulations of the temperature-dependent EPR line-shapes were employed in studies of ring puckering in heterocyclic radical systems [132–134]. Powder spectra were also analysed by this method. A complementary use of simulations of the temperature dependent EPR spectra by the density matrix formalism and potential energy surface calculations has been proposed as a means to obtain a picture of the motions of larger radicals [129–131]. Software designed for the simulation of chemical exchange in liquids has been used even for solid systems when the hfc constants of the nuclei involved in the dynamics were isotropic. This condition was found to approximately apply for the treatment of the dynamics in a number of irradiated frozen matrices. The temperature dependent spectra of cationic and neutral radicals [138–141] were for

Fig. 19.11 Arrhenius plots of the exchange rates, $\ln k$ (s^{-1}) vs. T^{-1} (K^{-1}) for $[(\text{CH}_3)_3\text{NCH}_2]^+$ in SAPO-42 (■) and Al-offretite (●). Adapted from [146] with permission from the PCCP Owner Societies (2001)



instance analyzed by the Heinzer method [142, 143] for exchange-broadened isotropic EPR spectra. This method was also employed for the study of the intramolecular motion of radiation induced radicals trapped in zeolites [144–146]. Strongly temperature dependent EPR spectra observed for the $[(\text{CH}_3)_3\text{NCH}_2]^+$ species in Al-offretite and SAPO-42 were attributed to methyl-group rotation about the C-N bond, with activation energies of $E_a = 9$ kJ/mol in Al-offretite and $E_a = 11$ kJ/mol in SAPO-42, Fig. 19.11.

The dynamics involved a three-site jump model for each methyl group in the temperature range 110–300 K. It was concluded that the size of the channels or cages affected the dynamics.

19.5 Simulation of Microwave Saturated EPR Spectra

CW-microwave saturation studies were performed at an early stage in EPR studies of irradiated solids and frozen glasses [147–152]. The interest in this old method has been revived in part due to recent developments in EPR dosimetry, see e.g. [153]. To increase the sensitivity such studies have often involved measurements at high microwave power. Attempts were therefore made to simulate the EPR line shape at saturation conditions, taking into account the different saturation properties of allowed ($\Delta m_1 = 0$) and forbidden ($\Delta m_1 = 1$) hyperfine lines in the standard L-alanine EPR dosimeter and other organic materials. Two approaches have been attempted [48, 154, 155] by adaption of locally used software [50–52].

In [155] the influence of microwave power P was taken into account by a saturation factor $(1 + \beta_l P / P_0)^{-\alpha}$ for each transition (l) with transition probability β_l in a spectrum of L lines in Eq. (19.7):

$$S(B, P) = \sum_{l=1}^L \frac{\beta_l}{(1 + \beta_l P / P_0)^\alpha} f\left(\frac{B - B_l}{\Delta B_G}\right) \quad (19.7)$$

A Gaussian derivative line-shape f of line-width ΔB_G that is unaffected by saturation was employed, i.e. inhomogeneous broadening was assumed. In theory a value of $\alpha = 1/2$ should then apply [156], while a larger value might indicate that the assumption of a Lorentzian line-width much smaller than the Gaussian width is not valid. In practice the parameter α was adjusted empirically to be in the range $1/2 \leq \alpha \leq 3/2$, the upper limit corresponding to a homogeneous line when the first derivative is recorded. The saturating power, P_0 , was estimated from microwave saturation measurements at room temperature [155]. The EPR spectrum was dominated by the so-called “stable alanine radical” (SAR), $\text{CH}_3\dot{\text{C}}\text{HCOO}^-$. The g - and hfc -tensor data of this radical, including the interaction with three distant protons were used for the simulation of the EPR spectra obtained at different microwave powers. At high power the intensity of satellite lines, attributed to $\Delta m_l = 1$ transitions due to the distant protons, became prominent. Good agreement was obtained in the fits of single crystal spectra over a wide microwave power range. The simulated powder spectra at saturation conditions deviated more from those obtained experimentally, possibly due to the influence of two other radicals known to be present in irradiated L-alanine. The unsaturated powder spectrum could in fact be accurately simulated as a superposition of three components [157]. The saturation properties of the two minor components are not known, however.

A theory utilising the saturated Voigt line shape function was employed as a physically more satisfactory method for the simulation of EPR spectra at saturation [48] when the assumption of a Lorentzian line-width much smaller than the Gaussian width is not valid. The method was based on the assumption that the EPR line shape is a convolution of a Gauss and a saturated Lorentz function [150], i.e. the Voigt function $V(x)$ in (19.8). The function was evaluated by a standard procedure [158–160], while its derivative employed in the simulation was obtained numerically.

$$V(x) \propto \int_{-\infty}^{\infty} \frac{e^{-a^2 t^2}}{1 + \beta P / P_0 + (x - t)^2} dt \quad (19.8)$$

The differences in the transition probability β accounted for the different saturation properties of the main and satellite lines. The parameter P_0 was adjusted empirically to obtain a semiquantitative description of the dependency of the microwave power P [48].

19.6 Simulation of ENDOR Powder Spectra

Spectra from CW ENDOR (termed ‘ENDOR’ in the following) of species observed in radiation research are commonly fairly simple in solutions and single crystals, and may be interpreted without simulation. However, in disordered solids (termed ‘powders’ in the following) the ENDOR spectrum may not be trivial to interpret. The spectral lines are often broad and anisotropy of hfc and nqc tensors can produce

complex lineshapes. Intensities are also affected by a number of factors, e.g., hyperfine enhancement, magnetic relaxation, instrumental factors, and angular selection, some of which are orientationally dependent, contributing to the complexity of the lineshape. It may be difficult to determine accurately the magnitude and anisotropy of the couplings from the observed spectral features without performing simulations. Concerning the angular selectivity, the ENDOR spectrum originates from a single position in the EPR spectrum, since the magnetic field is kept constant in the experiment, and in a powder sample the EPR resonance condition is met only for a certain range of orientations¹. This is in contrast to the EPR spectrum which is a superposition of spectral intensities from all possible orientations. Anisotropy of the magnetic couplings results in different resonance conditions for each orientation. In cases when the EPR spectrum is dominated by a single anisotropic coupling it is sometimes possible to resolve portions that correspond to a single orientation. Rist and Hyde were the first to use the dominating *g*-anisotropy of Cu and Ag complexes to obtain single crystal-like ENDOR spectra at *g*-value extrema in the powder EPR spectrum [161]. In free radicals, especially carbon-centered species, there is usually no single dominating coupling and it is impossible to obtain such 'single crystal' spectra. Instead, ENDOR spectra are made up of a large number of orientations. Computer simulation can take into account the angular selectivity and predict the ENDOR spectrum at a specific position in the EPR spectrum. Paired with other electron magnetic resonance (EMR) methods and the chemical and physical knowledge of the species, ENDOR simulations can facilitate the determination of *hfc* and *nqc* tensors.

It should be emphasized that the lack of a dominant *g*-anisotropy in many free radicals can actually be an advantage in some cases. An example is when the single crystal EPR spectrum consists of an odd number of lines and the *g*-anisotropy is small. In the centre of the corresponding powder spectrum, contributions from all orientations will more or less overlap. An ENDOR spectrum obtained at this position will contain contributions from practically all directions. In this case it may be possible to observe all the principal components of, e.g., a *hfc* tensor in the same spectrum. This is demonstrated by simulations of experimental spectra made of both the biphenyl [162] and the naphthalene radical cations [163].

Several powder ENDOR simulation methods, including appropriate theory, have been described in the literature [61, 117, 162–186]. ENDOR transition frequencies are calculated by taking the difference between appropriate eigenvalues of the spin Hamiltonian involved, using perturbation theory methods or exact diagonalisation of the spin Hamiltonian [52, 58, 59, 61, 117, 164, 169, 172–175, 183, 184]. But whereas transition intensities in EPR can often be predicted with good agreement with experiment, simulation of ENDOR intensities often show poorer agreement. As mentioned above, ENDOR intensities are affected by a number of factors. Theo-

¹ This is valid when the electron spin-spin cross relaxation rate is much slower than the electron spin-lattice relaxation rate, so that only the EPR transitions located at the field setting are brought into resonance by the microwaves, see further Sect. 19.6.1.

ries to account for hyperfine enhancement, angular selection, and the distribution of orientations of the resonant paramagnetic species relative to the radio frequency (RF) field, have been developed, and are commonly incorporated in simulation software for solid state ENDOR spectra. However the majority of simulation software packages for solid state ENDOR currently known to us, ignore spin relaxation, and possible instrumental factors. A model of relaxation in solution ENDOR has been worked out by Freed and co-workers [165]. Clarkson et al [166–168] have applied a theory, developed by Dalton and Kwiram [169], to the powder ^1H ENDOR spectra of perylene $^{•+}$ generated on silica-alumina catalysts. Transition probabilities were calculated to first order and relaxation effects were taken into account. Orientational selectivity was neglected, as the method assumed that all possible orientations are observed simultaneously in the ENDOR spectrum, independent of the EPR field position. However, none of the other simulation software packages for solid state ENDOR known to us [58–61, 117, 172–175] seem to have included relaxation effects. The detailed knowledge of all relaxation rates needed in a theoretical model makes the calculations complex and only a few experimental investigations [170, 171] have been made of relaxation in ENDOR of solid samples at low temperatures. The neglect of relaxation in simulations may contribute to the discrepancies between simulated and experimental ENDOR intensities observed. However the use of exact or first order transition probabilities and angular selection to predict intensities, while neglecting relaxation, can still in many cases give a sufficiently good fit to facilitate a spectral interpretation, as demonstrated e.g. in Refs. [162, 163, 172] and the examples in Sect. 19.6.2.5.

Methods to compute ENDOR signals from transition metal complexes obtained at arbitrary field positions have been developed by Hoffman [173–176], Henderson [178–179], Gochev [180] and their coworkers. In general it is impossible to resolve the g -value extrema of all three principal values in EPR spectra, in order to obtain single crystal-like ENDOR spectra from all three principal directions. Instead signals acquired at general positions in the EPR spectrum must be analysed. Orientational selectivity was taken into account in their theories but ENDOR probabilities were not computed. Kreiter and Hüttermann [117] have described a general theory to calculate powder ENDOR spectra due to arbitrary zfs , hfc and nqc constants. Magnetic energies and wave functions were calculated by exact diagonalization of the spin Hamiltonian. ENDOR transition probabilities were calculated to zeroth order, neglecting hyperfine enhancement effects. A similar theory, but incorporating first order transition probabilities, has been described by Keijzers et al. [61]. A general treatment of simulating both CW and pulsed ENDOR spectra in solids has been developed by Stoll and Schweiger [60, 183, 184]. The theory for transition frequencies was based on exact diagonalization of the spin Hamiltonian, and transition intensities were calculated in a similar way as by Keijzers [61]. The theory is implemented in the Matlab software EasySpin, see the Appendix. EasySpin also includes the option to calculate frequencies using perturbation theory according to Iwasaki [55], but transition intensities are then not computed and instead set equal to one [60, 164].

19.6.1 The ENDOR Powder Lineshape

Ignoring spin relaxation and instrumental effects the first derivative line shape at the ENDOR frequency f and static magnetic field B can be modelled by the formula [172]:

$$\frac{d}{d\nu} \chi(B, \nu) = \int_{\theta} \sin\theta \int_{\phi} \sum_j \left[s(B - B_j) I_j^2 \left(\frac{d}{d\nu} \sum_k t(\nu - \nu_{jk}) \int_{\psi} W_{jk}^2 d\psi \right) \right] d\phi d\theta \quad (19.9)$$

Equation (19.9) is similar to the ENDOR lineshape function derived by Kreiter and Hüttermann [117], following the principles of powder ENDOR lineshapes given by Hoffman and coworkers [173–175]. The summations run over the EPR transition fields $B_j(\theta, \phi)$ and the ENDOR transition frequencies, $\nu_{jk}(\theta, \phi)$, connected to EPR transition j , with the corresponding transition probabilities $I_j^2(\theta, \phi)$ and $W_{jk}^2(\theta, \phi, \psi)$. The signal is integrated over all angles (θ, ϕ) of the static field \mathbf{B} in the molecular frame and the ENDOR transition probability $W_{jk}^2(\theta, \phi, \psi)$ is in addition integrated over angle ψ , the angle relating the molecular frame to the RF-field \mathbf{B}_2 , for each direction of the static field \mathbf{B} : This is further explained in Sect. 19.6.2.4.

The function t is a convolution function describing the line shape of the ENDOR transition. The component EPR line shape function s , defined in the magnetic field domain, acts as a weighting function and selects the transitions that contribute to the ENDOR signal at a particular field setting. Similar principles taking into account angular selectivity have been adopted in other ENDOR simulation theories such as [92, 183]. In the program Easyspin, see the Appendix, based on the theory in [183] the angular selectivity is set in the frequency domain, by the square root of the squared sum of an excitation window around the microwave frequency, and a residual line width due to broadening from unresolved hyperfine couplings [164]. The angular selectivity depends on the ratio between the electron spin-spin relaxation rate (T_{xe}^{-1}) and the electron spin-lattice relaxation rate (T_{le}^{-1}) [169]. Angular selectivity is efficient if $T_{\text{xe}}^{-1} \ll T_{\text{le}}^{-1}$, which is the common situation for transition metal complexes and radicals in frozen solution above 77 K [181]. The ENDOR spectrum is then the sum of all transitions that are connected to the EPR transitions in resonance. In the other limit, when $T_{\text{xe}}^{-1} \gg T_{\text{le}}^{-1}$, the ENDOR spectrum is the sum of all possible orientations irrespective of which part of the EPR spectrum that is monitored. This situation has been encountered for organic radicals at very low temperatures, < 4 K [169, 181]. This case is not dealt with in Eq. (19.9) but has been treated for $I = 1/2$ nuclei by Dalton and Kwiram [169].

19.6.2 First Order $S = 1/2$ ENDOR Spectra

To simulate ENDOR spectra of $S = 1/2$ radicals with multiple interacting nuclei a first order method was developed [52, 172], based on the perturbation treatment

for EPR spectra described in Sect. 19.3.1.1 [50–52]. The treatment formed the basis for calculation of corresponding ENDOR transition frequencies and intensities. ENDOR frequencies were calculated neglecting second-order hyperfine contributions. ENDOR transition probabilities were computed to first order, including nqc and hyperfine enhancement effects. The theory differed from the usual perturbation schemes for multiple nuclei in that nqc of the same order as the hfc could be treated. First-order formulas given previously [182, 185] neglected nqc splittings. Orientational selection was taken into account in a similar way as in Ref. [117]. The method has been implemented in the simulation program ENDORF2, see further the Appendix.

19.6.2.1 Calculation of ENDOR Transition Frequencies

The ENDOR transition frequency between two nuclear eigenstates $|h_j\rangle$ and $|k_i\rangle$, $\Delta m_s = 0$, is obtained using the eigen-energies of the perturbation (19.5) as

$$n_{h_j k_i} = \left| E'(h_j) - E'(k_i) \right| \quad (19.10)$$

where $|h_j\rangle$ and $|k_i\rangle$ belong to the same m_s -manifold. Note that in general the eigenstates are mixtures of nuclear spin states. $E'(h_j)$ and $E'(k_i)$ are the first-order nuclear energies of the two states, calculated by diagonalisation of the spin Hamiltonian (19.5). The neglect of higher-order terms is justified for hfc splittings smaller than 40–60 MHz, measured at high magnetic fields, unless they are also interacting with nuclei with very large hfc , as described in [52]. Simulated ENDOR frequencies of nuclei in the tyrosyl free radical in ribonucleotide reductase from *Escherichia coli*, incorporating hfc up to 60.8 MHz, were shown in [52] to agree within 0.1 MHz with experimental observations from [187], using proton hfc parameters from the same reference. For cases incorporating larger couplings the second order corrections proposed in [52] can be applied. However, they were not implemented in our ENDOR program, since the major application was to measure small hfc splittings that are unresolved in the EPR spectra. Another second-order effect occurs for magnetically equivalent nuclei where cross terms may split the basic, first order ENDOR frequency into several transitions, but these are generally too small to be resolved in broad powder ENDOR lines. For the four equivalent protons of naphthalene^{•+}, described in [163], the largest second-order splitting is ca. 0.023 MHz occurring for a hfc tensor component of -7.9 MHz [186]. Since the linewidth is 0.6 MHz the splitting is not resolved. The second-order splitting might be noticeable for larger hfc measured in single crystals. Splittings/shifts of up to 0.2 MHz have been observed by Toriyama and coworkers [182] for methyl protons with a hfc of ca 60 MHz in a single crystal of $\text{CH}_3\text{COOLi} \cdot 2\text{H}_2\text{O}$. These are not taken into account in Eq. (19.10), but as mentioned above, the second order correction formulas proposed in [52] can be applied, if necessary.

19.6.2.2 Calculation of ENDOR Transition Probabilities

The probability for a radiation induced transition in ENDOR between nuclear spin states $|h_j\rangle$ and $|k_i\rangle$, $\Delta m_s = 0$, for a nucleus with spin I , is given by Fermi's golden rule [6, 7, 182]:

$$P = 2\pi W^2 \rho(\omega) \quad (19.11)$$

where $\rho(\omega)$ is the frequency distribution function of the radiation, and

$$W^2 = \langle \Phi(m_s, h_1, \dots, h_{j-1}, h_j, h_{j+1}, \dots, h_n) | \mathbf{B}_2 \cdot (\mu_B \mathbf{gS} - \sum_j g_j \mu_N \mathbf{I}_j) | \Phi(m_s, h_1, \dots, h_{j-1}, k_i, h_{j+1}, \dots, h_n) \rangle^2. \quad (19.12)$$

The Hamiltonian operator used in Eq. (19.12) represents the coupling between the RF-field, \mathbf{B}_2 , and the electron and nuclear magnetic moments. The transition probability, W^2 , selects the allowed transitions and predicts the relative intensities, neglecting relaxation effects. The theory developed uses first-order eigenfunctions, see Ref. [172] for details. The use of first-order wavefunctions is important to predict ENDOR transition probabilities properly. Thus, as described by Schweiger and Günthard [185] first-order probabilities show good performance, whereas zeroth-order formulas may differ from exact values by orders of magnitude. An example of the resulting difference in simulated intensities using zeroth and first order transition probabilities is discussed in Sect. 19.6.2.5, for ^{14}NO -ligated ferrocycochrome *c*-heme a_3 . The transition probability in a single crystal is, in general, anisotropic and depends on the orientation of the molecule relative to both the static and the RF field [182, 185]. In powders transition probabilities require integration over the directions of both the static and the RF field, as discussed further below. Zeroth-order transition probabilities only show orientational dependence when the static field is oriented away from the principal axes of the *hfc* tensor [6, 7]. Further, zeroth-order calculations are insufficient to predict hyperfine enhancement effects.

19.6.2.3 Formulae of ENDOR Transition Probabilities in Single Crystals

The transition probability, Eq. (19.12), calculated with first order wavefunctions derived in [52, 172] is given by

$$W^2 = (\mathbf{B}_2/\mathbf{B})^2 |\langle h | \mathbf{ICr} | k \rangle|^2 \quad (19.13)$$

for a transition between nuclear states $|h_j\rangle$ and $|k_i\rangle$, $\Delta m_s = 0$, of a nucleus with spin \mathbf{I} in a single crystal. The nuclear index j has been dropped to simplify the formula. The term \mathbf{C} is defined as:

$$\mathbf{C} = m_s \mathbf{Ag}/g - \nu_N \mathbf{1} \quad (19.14)$$

Table 19.1 First order ENDOR transition probabilities, W^2 , in multiples of $(B_2/B)^2$ in a single crystal for a transition between nuclear states $|a\rangle \leftrightarrow |b\rangle$, $\Delta m_s = 0$ of a nucleus with spin I

Case	W^2 (in multiples of $(B_2/B)^2$)	Ref.
(19.16a) Arbitrary \mathbf{A} , \mathbf{Q} Modest g -anisotropy ^a	$ \langle a \mathbf{I}\mathbf{C}\mathbf{r} b\rangle ^2$	[172]
(19.16b) $\mathbf{Q}=0$ Arbitrary \mathbf{A} Modest g -anisotropy ^a	$f_{\pm}^2[\mathbf{r}\mathbf{C}\mathbf{C}\mathbf{r} - (\mathbf{r}\mathbf{C}\mathbf{C}\mathbf{I})^2/(\mathbf{I}\mathbf{C}\mathbf{C}\mathbf{I})]$	[52, 182 ^b , 185 ^b , 186]
(19.16c) $\mathbf{Q}=0$ \mathbf{B} // principal axis \mathbf{i} of \mathbf{A} \mathbf{B}_2 // principal axis \mathbf{j} of \mathbf{A} Isotropic g	$f_{\pm}^2 v_N^2 [1 - m_s A_j / v_N]^2$	[52, 182 ^b , 185 ^b , 186, 189 ^b]
(19.16d) $\mathbf{Q}=0$ Arbitrary \mathbf{A} , \mathbf{g}	$f_{\pm}^2 [\mathbf{r}\mathbf{C}\mathbf{C}\mathbf{r} - (\mathbf{r}\mathbf{C}\mathbf{I})^2 + (\mathbf{r}\mathbf{C}\mathbf{I} - \mathbf{r}\mathbf{g}\mathbf{g}\mathbf{I} \cdot v_N / g^2) - (\mathbf{r}\mathbf{C}\mathbf{C}\mathbf{I} - \mathbf{r}\mathbf{g}\mathbf{g}\mathbf{I} \cdot \mathbf{I}\mathbf{C}\mathbf{I} \cdot v_N / g^2) / (\mathbf{I}\mathbf{C}\mathbf{C}\mathbf{I})]$	[185 ^c]
<i>Notation:</i> $\mathbf{C} = m_s \mathbf{A}\mathbf{g}/g - v_N \mathbf{1}$ $f_{\pm}^2 = [I(I+1) - m_I(m_I \pm 1)]/4$	Formulas for W^2 when $\mathbf{Q}=0$, cases (19.16b)–(d), apply to $ a\rangle = m_I, \pm 1\rangle$, $ b\rangle = m_I\rangle$. Wave functions $ m_I\rangle$ are eigenfunctions of $I_k = \mathbf{I} \cdot \mathbf{k}$ where $\mathbf{k} = \mathbf{C}\mathbf{I}/ \mathbf{C}\mathbf{I} $	

^a The g -anisotropy is here defined as modest if \mathbf{g} fulfills: $(1/g^2)\mathbf{r}\mathbf{g}\mathbf{g}\mathbf{I} \ll 1$ when $\mathbf{r} \cdot \mathbf{I} = 0$

^b Corresponding expressions have been published in Refs. [182, 185] (case b) and [182, 185, 189] (case c)

^c Adapted to the notation of this chapter

where symbol \mathbf{A} is the hfc matrix, $\mathbf{1}$ is the identity matrix, v_N is the nuclear Larmor frequency. Symbols B_2 and \mathbf{r} are the strength and direction of the RF field \mathbf{B}_2 , oriented perpendicular to the microwave field, and the static field direction \mathbf{I} , as found in conventional ENDOR spectrometers. The static field \mathbf{B} has the strength B .

Equation (19.13) covers the case of strong nqc , compared to the hfc , in which case the usual $\Delta m_I = \pm 1$ selection rule breaks down. In Table 19.1 the equation is collected as Eq. (19.16a) together with formulae neglecting nqc . With zero nqc Eq. (19.13) can be simplified to an analytical formula, Eq. (19.16b) of Table 19.1, first reported by Toriyama et al. [182]. The reported formulae in the previously mentioned work [169] were derived under similar assumptions. Without nqc the nuclear spins are quantised along the direction:

$$\mathbf{k} = \mathbf{C}\mathbf{I}/|\mathbf{C}\mathbf{I}|. \quad (19.15)$$

The nuclear wavefunctions are then eigenstates $|m_I\rangle$ to the operator $I_k = \mathbf{I} \cdot \mathbf{k}$. In Eq. (19.16a), and hence also (19.16b), it is assumed that the g -anisotropy is small enough that the relation $(1/g^2)\mathbf{r}\mathbf{g}\mathbf{g}\mathbf{I} \ll 1$ is valid. Here \mathbf{r} is assumed to be perpendicular to the static field. The relation is fulfilled for most free radicals since their g -anisotropy amounts only to a few percent of the isotropic value.

For large g -anisotropy, but neglecting nqc splittings, Schweiger and Günthard [185] have derived a very accurate formula, given in our notation as Eq. (19.16d) in Table 19.1. The equation shows perfect agreement with exact numerical calculations even for g -anisotropies exceeding 30% of the isotropic value [185]. Inspection of the equation gives that it agrees with Eq. (19.16b) if $\mathbf{r}\mathbf{g}\mathbf{g}\mathbf{I}/g^2$ -terms are neglected. For g -anisotropies up to a few percent these terms have negligible effect. For a

larger anisotropy of 10% Eq. (19.16b) is, as a rule of thumb, accurate to within 1–2% of the more exact value of Eq. (19.16d). For a methylene proton in Cu(II)-doped α -glycine, with g and proton hfc tensors $\mathbf{g}=(2.0434, 2.0715, 2.2644)$ and $\mathbf{A}=(6.35, 1.99, 1.14)$ MHz [188], the relative difference between the two equations varies from 0.4% up to 1.5% of the ‘exact’ value, for twelve transitions calculated for different combinations of \mathbf{B} and \mathbf{B}_2 parallel to either of the crystal axes \mathbf{a} , \mathbf{b} and \mathbf{c}' [52]. The largest discrepancy of 1.5% occurs for the $m_s=+1/2$ transition with \mathbf{B} along crystal axis \mathbf{b} and \mathbf{B}_2 along \mathbf{a} [52].

19.6.2.4 Formulae of ENDOR Transition Probabilities in Powders

Calculating the transition probability W^2 in a powder sample requires integration of W_{jk}^2 over angle ψ , for each set of the polar coordinates θ and φ of \mathbf{B} , in the molecular frame. The angle ψ relates the orientation of the molecule to the direction of the RF field \mathbf{B}_2 for each direction of \mathbf{B} . In a powder all molecules with the same orientation with respect to \mathbf{B} will have the same resonance frequency, but they will be randomly oriented relative to \mathbf{B}_2 . The variation in W with the orientation of \mathbf{B}_2 can be significant, as pointed out by several authors [172, 185, 189]. Although the effect of the RF field orientation had been known it was for many years never fully taken into account when calculating ENDOR transition probabilities in powders. Analytical integration of W^2 over the distribution of \mathbf{B}_2 directions in the plane perpendicular to \mathbf{B} gives the expression [172]:

$$\overline{W^2} = \int W(\theta, \varphi, \psi)^2 d\psi = \frac{1}{2} \left(\frac{B_2}{B} \right)^2 (\boldsymbol{\alpha}^* \mathbf{C}^2 \boldsymbol{\alpha} - \boldsymbol{\alpha}^* \mathbf{C} \mathbf{I} \cdot \boldsymbol{\alpha} \mathbf{C} \mathbf{I}) \quad (19.17)$$

Here $\boldsymbol{\alpha}$ is a vector with the components $\langle h | I_x | k \rangle$, $\langle h | I_y | k \rangle$ and $\langle h | I_z | k \rangle$, and $\boldsymbol{\alpha}^*$ is obtained by complex conjugation of the components. The nuclear index i has been dropped for simplicity. The integration is done in a similar fashion as by Kottis and Lefebvre [104] for triplet state EPR spectra. Analytical integration avoids the need for a time consuming numerical integration of W^2 over ψ .

19.6.2.5 Applications of first Order ENDOR Theory

The accuracy of the theory was tested against data of ^{14}NO -ligated ferrocycytochrome c -heme a_3 . Powder ENDOR spectra obtained by LoBrutto et al [190] have been simulated [117] employing an exact diagonalization of the spin Hamiltonian, but with transition probabilities to zeroth order. Nitrogen ENDOR signals were detected from the histidine and NO ligands of the central ferrous ion. The calculated spectrum (absorbtion lineshape) in Fig. 19.12² was made with the parameters from Refs. [117, 190], see also the figure legend. The nqc constants are small compared

² Note that there is a misprint in Table 1 of Ref. [172] in the order of the principal components of $Q(^{14}\text{N-His})$.

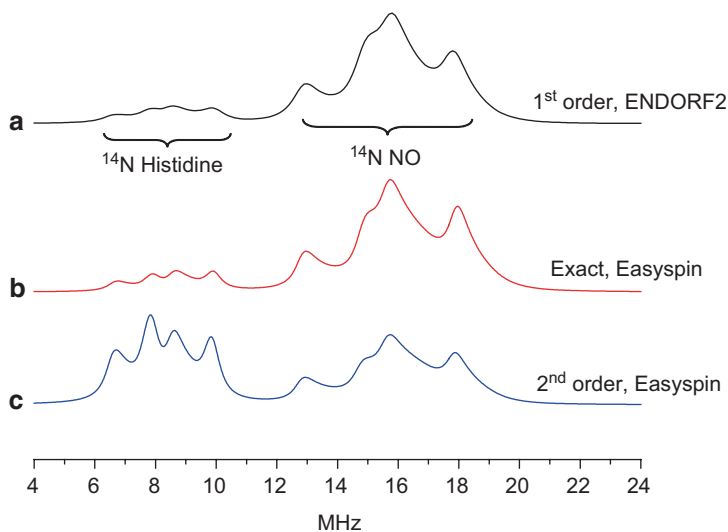


Fig. 19.12 Simulated powder ENDOR spectra (in absorption) of ^{14}NO -ligated ferrocycytochrome c heme a3, at the field setting ($g=2.079$) in the X-band ESR spectrum ($\nu=9.32$ GHz), using: **a** ENDORF2 (first order theory), **b** Easyspin (exact calculation) and **c** Easyspin (second order theory). Transition probabilities are calculated to first order in **(a)**, exactly in **(b)**, while Easyspin in **(c)** sets them equal to one for all allowed transitions [164]. For experimental spectra see [190], for simulation with an exact method, but to zeroth order in transition probabilities, see [117]. All simulations employed $g=(2.082, 1.979, 2.008)$, $A(^{14}\text{N-His})=(16.5, 16.1, 19.3)$ MHz, $Q(^{14}\text{N-His})=(+0.45, +0.67, -1.12)$ MHz, $A(^{14}\text{N-NO})=(30.56, 30.56, 59.90)$ MHz, $Q(^{14}\text{N-NO})=(+1.03, -0.51, -0.52)$ MHz. The simulation in **a**) employed a line width of 0.6 mT in weight function s (Gaussian shape) and a line width of 0.5 MHz in the ENDOR convolution function t (Lorentzian shape) of Eq. (19.9). The simulation in **(c)** employed an equivalent excitation width of 16.8 MHz, and an ENDOR line width of 0.6 MHz (Lorentzian shape). The spectrum in **(a)** is adapted from [172] with permission from Elsevier (1996)

to the hfc . All tensors have parallel principal directions except the A-tensor of the NO-nitrogen which is rotated 17.5° around the x-direction.

The spectra were obtained at $g=2.079$, near the principal value $g=2.082$. The peak positions obtained with the first order perturbation theory in Fig. 19.12a agree well with those obtained with Easyspin using exact diagonalisation, Fig. 19.12b and second order perturbation theory, Fig. 19.12c, except for the peak with highest intensity, near 15.8 MHz, which is shifted to higher frequency by around 0.15 MHz in **(a)**. Line positions of Fig. 19.12a agreed within less than 0.07 MHz with results obtained with a previous simulation employing exact diagonalisation [117], and agreement with experimental peak positions was as good as in [117]. The transition probabilities in Fig. 19.12a are calculated by Eq. (19.17). This is valid to first order since the g -anisotropy fulfils the condition $(1/g^2)\mathbf{r}g\mathbf{g}I \ll 1$. To account for angular selectivity the simulation in **(a)** employed a line width of 0.6 mT in the weight function s (Gaussian shape) of Eq. (19.9). The simulations in **(b)** and **(c)** employed an equivalent excitation width of 16.8 MHz, zero strain, and an ENDOR line width of 0.6 MHz (Lorentzian shape). Excitation widths up to 150 MHz have

been successfully tested for this case. For biphenyl¹⁺, described later in this section, even the default value (infinite excitation width) was acceptable. However, as shown in Fig. 19.13 there are cases where the dependency of the lineshape on the excitation width is more substantial, and needs to be investigated for a more accurate interpretation of the spectrum. The relative intensities of the histidine and NO-nitrogen lines are similar in Fig. 19.12a, b, but are quite different from (c), as well as the simulation in Ref. [117], where transition probabilities are calculated to zeroth order. Zeroth order probabilities do not take into account hyperfine enhancement effects [6, 7, 185, 189] which can be important for nuclei with low magnetic moments such as ¹⁴N. The intensity distribution in Fig 19.12a and b does not perfectly reproduce the experiment in Ref. [190], but the agreement with experiment is substantially better than simulations obtained in either (c) or using the zeroth order intensities in [117] exhibit.

To further test the capability of the theory developed we have investigated the ENDOR spectrum of the $\dot{\text{C}}\text{H}_2\text{NHCOC}_6\text{H}_5$ radical formed in X-irradiated polycrystalline hippuric acid, Fig. 19.13. Only the region containing ¹⁴N-signals is shown. The lowest ENDOR lines cannot be experimentally observed as the region below 2 MHz is affected by a sharp decline in baseline and other instrumental effects. The experimental spectrum was obtained at 110 K in the centre of the EPR spectrum. The system has been investigated with ENDOR in single crystal at 77 K [191], and powder ENDOR [172]. The nitrogen nucleus is characterized by a substantial *nqc* term compared to the *hfc* and nuclear Zeeman splittings. The microwave frequency, field setting, and α -¹H and ¹⁴N-parameters in [172] were used in the simulations in Fig. 19.13; (b), (d), and (e) including, but (c) excluding *nqc* terms. The nitrogen parameters $A(^{14}\text{N})=(-7.58 -8.47 -9.44)$ and $Q(^{14}\text{N})=(-0.843 0.582 0.261)$ MHz, are those of Ref. [191] apart from the two smaller principal *hfc* values, which were slightly altered from -7.38 and -8.77 MHz of Ref. [191] to improve the fit.³ The *hfc* tensors of the two α -protons included in the calculation were as in Ref. [191]. The *g*-anisotropy is small and was neglected [191]. Simulations (b) and (c) employed a Gaussian weight function *s* (see Eq. (19.9)) with line width 0.1 mT and Lorentzian convolution function *t* with line width 0.5 MHz. Simulations (d) and (e) employed a line width of 0.35 MHz, and (d) 2.8 MHz and (e) infinite excitation width respectively. A finite excitation width (b) and (d) gave a significantly better fit to the experimental curve, (a), than the infinite excitation width in (e).

A comparison of the simulations Fig. 19.13b and d, using similar finite weight/excitation widths, shows that the first order simulation in (b) agrees very well with the exact simulation in (d), apart from slightly more pronounced resonances in the region of 3.5 MHz in (d) than in (b), which also agrees slightly better with the experiment in (a). This can partly be attributed to a smaller ENDOR line width in (d). The simulations obtained with finite weight/excitation widths, (b) and (d), agree considerably better with experiment in the region below 5.5 MHz, than using

³ Note that in [191] the vectors of the $Q(^{14}\text{N})$ -tensor are not orthogonal, apparently due to a misprint in the sign of one of the direction cosines of the smallest *nqc* principal component 0.261 MHz; $(+0.050+0.909+0.415)$. The vectors become orthogonal with a sign change to $(-0.050+0.909+0.415)$, which has been used in the simulations.

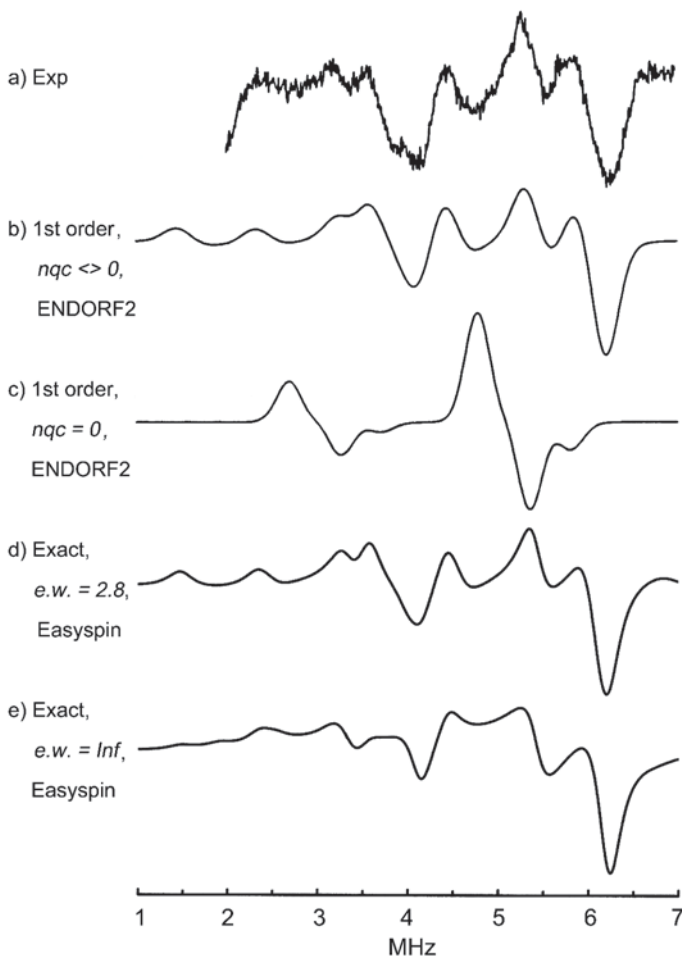


Fig. 19.13 Experimental **a** and simulated **b–e** ENDOR spectra at 110 K of the $\dot{\text{C}}\text{H}_2\text{NHCOC}_6\text{H}_5$ radical formed in X-irradiated polycrystalline hippuric acid. Only the region containing ^{14}N -signals is shown. The ^{14}N parameters in [172] were used in simulations; **(b)**, **(d)**, and **(e)** including, but **(c)** excluding nuclear quadrupole terms. The hfc tensors of the two α - ^1H were as in Ref. [191]. Simulations in **(b)** and **(c)** employed a Gaussian line width of 0.1 mT in weight function s of Eq. (19.9), and an equivalent excitation width (e.w) in **(d)** of 2.8 MHz. The simulation in **(e)** employed an infinite excitation width (e.w). Simulations in **(b)** and **(c)** employed a Lorentzian convolution function t with line width 0.5 MHz, and in **(d)** and **(e)** an ENDOR line width of 0.35 MHz. (Figures **(a)–(c)** adopted from [172] with kind permission from Elsevier 1996)

infinite excitation width, **(e)**. Further comparison of the ENDORF2 simulations in Fig. 19.13**b** and **c** shows that the nqc terms must be included to fit the observed line positions. The hfc tensor is fairly isotropic in character. Neglect of the nqc therefore produces essentially two broad ENDOR lines not observed experimentally [172]. Inclusion of the nqc in Fig. 19.13**b** gives a better fit of the line positions and accounts well for the intensity distribution observed experimentally.

An interesting comparison can be made between the powder ENDOR simulation, Fig. 19.14b, and the single crystal simulations presented in Ref. [172], Figs. 4b–d. These were obtained along the principal directions of the *hfc* tensor, at the same field position. The *hfc* and *nqc* tensors have nearly parallel principal axes and the *g*-anisotropy is very small in this system. The strongest intensity found at 6.3 MHz is near the high frequency transition of the three principal directions. The three lowest peak positions are near the low frequency transitions of the three directions respectively. Experimental intensities are also reproduced quite well.

As described in the theoretical section the transition probability formula (19.17), represents the averaged probability of all radicals in the powder with the same set of θ and φ values. These are randomly ordered with respect to the RF-field. The significance of taking this average was demonstrated in Ref. [172]. The transition probabilities for the ^{14}N -transitions in a single crystal case with $\text{B} // \text{X}$, located at 2.42, 4.04, 4.51 and 6.11 MHz respectively, were calculated as function of the B_2 -orientation in the YZ-plane, described by the angle ψ . The orientational variations of the transition probabilities were significant enough to require that an average is taken in a powder. The relative differences, $(W^2_{\text{max}} - W^2_{\text{min}})/W^2_{\text{min}} \times 100\%$, amounted to 29, 150, 16 and 73 %, respectively. Here W^2_{min} and W^2_{max} refer to the minimum and maximum values of W^2 of each transition over the ψ -range.

Simulations have also been applied to the ENDOR spectra from ring protons of the α -proton type in radical cations of biphenyl ($\text{Ph}_2^{+\bullet}$) in frozen CFCl_3 [162] and naphthalene on H-ZSM-5 zeolite [163]. In these cases the *hfc* anisotropy is of the same order as the isotropic contribution. ENDOR was beneficial since the EPR spectra of the irradiated samples had low resolution in both matrices. Well resolved signals were observed despite the pronounced anisotropy since the principal components are fairly small, 5–30 MHz. The transitions are hence spread over a relatively small region compared to radicals with localized spin density where α -couplings are of the order 30–90 MHz. The matrices were polycrystalline, and single crystals of sufficient size were not available. Experimental [162] and simulated ENDOR spectra of $\text{Ph}_2^{+\bullet}$ in CFCl_3 are shown in Fig. 19.14. The spectra were obtained at the centre of the EPR spectrum. The simulations were made employing the parameters in [162], using; (b) the perturbation theory of this chapter; (c) Easyspin with exact theory and including hyperfine enhancement; and (d) Easyspin with second order perturbation theory for the transition frequencies. Note that in this option all transition probabilities are set equal [164]. The assigned lines are caused by intensity build-up at positions corresponding to principal values of the anisotropic *para* and *ortho* proton *hfc* tensors. The lines are placed symmetrically around the proton Larmor frequency ν_{H} , near $\nu_{\text{H}} \pm A/2$ MHz, where $\nu_{\text{H}} = 14.54$ MHz. Fluorine matrix nuclei and *meta* protons with small *hfc* constants were excluded in the simulations. They produce lines in the region 10.5 to 16.5 MHz in the experimental spectrum [162]. As can be seen from Fig. 19.14 the lines below ν_{H} are of lower intensity than the matching lines above, which we attribute to the hyperfine enhancement effect. In the simulation Fig. 19.14b, intensities are calculated to first order using Eq. (19.17), but relaxation and instrumental effects are neglected. The relative intensity distribution is predicted, but slightly overestimated in the calculated spectrum. The simulations (c) and (d) were both made using Easyspin [184],

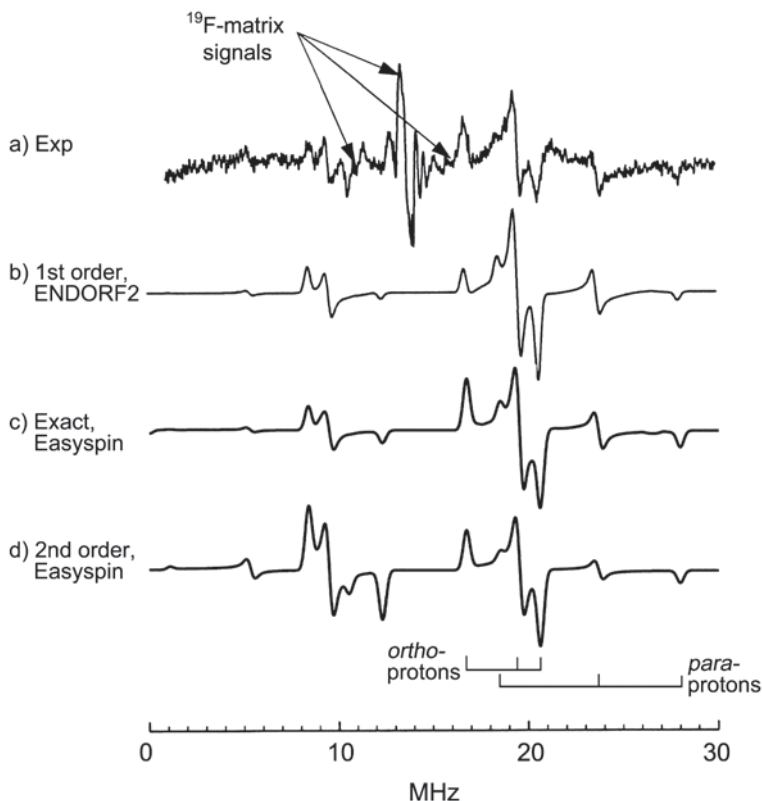


Fig. 19.14 Experimental (a), and simulated first order (b), exact (c) and second order (d) powder ENDOR spectra of the biphenyl radical cation in CFCl_3 matrix at 120 K. The simulated spectra were calculated using the spin Hamiltonian parameters from Ref. [162], at magnetic field $B=341.40$ mT and microwave frequency $\nu=9.5670$ GHz. The simulations included *para*- and *ortho*-protons (spectral lines above ^1H -Larmor frequency indicated), but matrix fluorine and *meta* protons were excluded in the simulations. The weight function s and convolution function t (see Eq. (19.9)) had line widths of 0.1 mT, and 0.3 MHz (both Gaussian shaped) in (b). Simulations in (c) and (d) employed an equivalent excitation width of 2.8 MHz, and an ENDOR line width of 0.35 MHz. Figures (a)–(b) adapted from [172] with kind permission from Elsevier (1996)

case (c) with exact calculation including hyperfine enhancement, and case (d) using second order perturbation theory of Iwasaki [55].

19.7 Summary

Approximative or exact simulation methods may be employed depending on the system, the experimental conditions, the required accuracy, and the computer resources. The following considerations, in part based on our own experience, apply particularly for disordered, “powder”, samples frequently investigated in radiation

research. One should note, however, that not all simulation software packages presented in the literature [46, 49, 58–62, 113–117] were available to us.

EPR Spectra of Radicals with Small hfc Simulation of hfc structure by first order theory is an adequate method when the high field approximation, $hfc \ll g\mu_B B$, applies as usually observed for organic radicals. Simulation of anisotropic proton hfc should include the effect of the nuclear Zeeman term, because of the unusually large g_H factor. The effect, introduced in earlier programs [45, 50–52] is taken into account in [49], but not with the perturbation option in [60] or with Simfonia [46], according to our test runs (not shown) for the malonyl radical, $\dot{H}C(COOH)_2$.

EPR Spectra of Radicals with Moderately Large hfc Simulation by second order theory may be employed for hfc , up to ca. 10% of the Zeeman energy, using the theory in [55], unless high accuracy is required. Small nqc terms, $nqc < hfc$, can be taken into account for nuclei with $I > 1/2$. Effective nuclear spins should be employed for the hfc of equivalent nuclei. It is not clear that this feature has been implemented in publically available software, however. Exact calculations may therefore be necessary in this case, unless the codes can be modified.

EPR Spectra of Radicals with Large hfc and/or nqc Simulation by exact theory can be computed quite rapidly (within minutes) for small systems (≤ 6 nuclei) using a modern PC with the software [60] we have been able to test. For large systems many hours may be required as for the radical $C_4F_8^-$ discussed in Sect. 19.3.1.3.

Radical Pair EPR Spectra Software for the simulation of $S=1$ EPR spectra is adequate, provided that the exchange rate (J) is rapid, $J \gg g\mu_B h$. In the opposite case simulations are best made with the exact methods exemplified in the Appendix. Such simulations might be an alternative to the special methods discussed in Sect. 19.3.2.1 to obtain the values of the zfs and exchange terms. Test runs with Easyspin [60] have indicated that the calculation times are relatively short.

Triplet State EPR Spectra Test runs have indicated that exact calculations can become tedious in the presence of hfc even with modern software, see Fig. 19.10 for a comparison with the second order and hybrid options in [60]. A similar hybrid option, with exact treatment of the electronic terms and perturbation theory for the nuclear and hyperfine parts, has been proposed as a reasonable balance between efficiency and accuracy for the simulation of relatively small hfc of several nuclei [52, 106, 108].

EPR Spectra of Transition Metal Ions Simulation based on full matrix diagonalization is a standard method in the software packages of the general type given in the Appendix. Efficient procedures for the integration of powder spectra have been described [115].

Special Perturbation Methods Diagonalization of the matrix containing the hfc , nqc , and nuclear Zeeman terms for an $I > 1/2$ nucleus can occasionally be employed for the simulation of radical and triplet state EPR spectra when the three interactions are small but of comparable magnitudes, see Sect. 19.3.1.1. The method is particularly suited for the ENDOR simulations presented in Sect. 19.6.

ENDOR Spectra with hfc due to $I = \frac{1}{2}$ Nuclei Calculations by matrix diagonalization are quite fast for free radical systems with hfc due to a few nuclei (≤ 6), as indicated by simulations for the biphenyl cation radical, Fig. 19.14. Hyperfine enhancement effects had to be taken into account for best agreement with experiment. Simulation based on the perturbation treatment in [55] differed slightly (Fig. 19.14d), while the spectrum obtained by the method described in Sect. 19.6 agreed well with experiment and exact calculation. Perturbation methods may be employed for systems with hfc due to several nuclei.

ENDOR Spectra with $hfc > nqc$ due to $I \geq 1$ Nuclei The similarity of the spectra in Fig. 19.12, calculated by matrix diagonalization [60] and by the method in Sect. 19.6 indicates that also the latter method is applicable for $S = \frac{1}{2}$ systems, provided that the high field approximation applies. The intensity distribution obtained with the second order perturbation option in Easyspin deviated considerably from those in an exact calculation and experimentally, however.

ENDOR Spectra with $hfc \approx nqc$ due to $I \geq 1$ Nuclei The condition may occur in biological samples with weakly coupled ^{14}N nuclei, but also in irradiated substances [191]. As shown in Fig. 19.13 the spectrum shape may strongly depend on the excitation width in Easyspin [164] and the corresponding weight function, s , in ENDORF2 [172]. The method employed in Sect. 19.6 yields intensity distributions of very similar quality as those obtained by matrix diagonalization. This may be attributed to the use of formula (19.17) for the intensity in a powder sample.

Appendix

EPR and ENDOR Simulation Software

A large number of simulation methods has been presented during the last 50 years, the earlier ones, e.g. in [45, 46] being based on perturbation theory. Methods based on exact diagonalization of the spin Hamiltonian have been developed more recently and in many instances replaced the perturbation methods [43, 58–63]. The simulated CW-EPR spectra have traditionally been assumed to have the form (19.6), but a more recent method of calculation in frequency space [43] has been employed in several of the programs listed in Table 19.2. The programs of the general type are usually applicable both for EPR and ENDOR simulations of general spin systems. The fitting by visual inspection is not an objective method, and efforts were therefore made even at an early stage to make the final refinement by automatically optimising the coupling constants and the line width of the computed spectrum to the experimental one, see e.g. [38]. Optimised values of hfc constants can also be obtained with several of the recently developed programs. The references in Table 19.2 may be consulted for details. Hyperfine enhancement and angular selection effects are taken into account in the programs dedicated to the simulation of powder ENDOR spectra. Several commercial and free-ware program packages can

be downloaded electronically, where updates are also reported. Some previously commonly used programs, e.g. in [45, 104] were excluded as it was not clear that they were still available or had been maintained. We refer to a literature survey [52] for programs dedicated to the powder spectrum simulation of free radicals and triplet state molecules.

Isotropic Spectra

Public electron spin resonance software tools from National Institute of Environmental Health Sciences are available electronically [41]. Software may also be available at the International EPR (ESR) Society, which also provides contact details with a number of EPR-groups [113, 114]. Codes primarily intended for calculations of powder spectra can as a rule also be employed, e.g. the following software.

EasySpin The tools for isotropic CW-EPR in EasySpin apply to $S=1/2$ species with arbitrary number of nuclei [60]. Resonance fields are calculated exactly. The magnetic field range is automatically determined. A least-squares fitting to an experimental spectrum can be made. Matlab must be installed on the computer and is not provided with EasySpin.

HRESOL High resolution spectra are calculated of radicals in fluid isotropic media with *hfc* of several nuclei of any spin, taking into account the second order shift of resonance lines and the dependence of the line widths on the magnetic quantum number m_l of the nucleus [49]. The program is written in APL, which must be obtained separately.

SimFonia Spectra of radicals in fluid solution are calculated using up to third order perturbation theory for isotropic *hfc* constants [46]. Parameters for the simulation are given in an easy-to-use graphical interface. The software is a commercial product but one version might still be available free of charge.

Anisotropic Spectra

Definite simulation procedures were published already in 1965 for the analysis of the *hfc* structure of free radicals in amorphous solid samples [45]. Improved second order as well as exact methods have been implemented in the more recently developed free-ware and commercial software packages, presented in Table 19.2. The programs of the general type are usually applicable both for EPR and ENDOR simulations, and can handle complex spin systems. The references in the table may be consulted for details.

EasySpin Tools are included for CW and pulse EPR and ENDOR spectra of solid samples [60, 183, 184]. An arbitrary number of electron and nuclear spins can be treated taking all interactions, including high-order operators and nuclear quadrupole couplings into account by exact and second order treatments. Line broadening

Table 19.2 Programs for the simulation of EPR and ENDOR spectra

Program	Order	Supplier
EasySpin ^a (general)	Exact	http://www.easyspin.org/
EPR-NMR ^b (general)	Exact	http://www.chem.queensu.ca/eprnmr/
HRESOL ^c	2	http://www.esr-spectsim-softw.fr
RIGMAT ^c	2	
MULTIP ^c	2	
HMLT ^c	Exact	
Simfonia	1–3	http://www.bruker.com/products/mr/epr/epr-software/simulation-suites/overview.html
XEMR ^d (general)	Exact	http://xemr.sourceforge.net/
SOPHE ^e (general)	Exact	http://www.bruker.com/products/mr/epr/epr-software/simulation-suites/overview.html
Sim ^f (general)	Exact	
MAGRES ^g (general)	Exact	
MSPEN ^h (EPR/ENDOR)	Exact	
GENDOR ⁱ ($S = \frac{1}{2}$)	1	http://chemgroups.northwestern.edu/hoffman/endor_files/simulationprograms.htm
ENDOR F2 ^k ($S = \frac{1}{2}$)	1	http://www.liu.se/simarc/downloads/?l=en

^a Matlab toolbox for simulating EPR and ENDOR spectra. Matlab version 7.5 or later must be installed on the computer and is not provided with EasySpin

^b EPR-NMR simulation of single crystal and powder spectra for any computer capable of running 32-bit Fortran77 [116]

^c EPR simulation programs for the simulation of radicals or metal ions in rigid glassy or polycrystalline matrices. APL must be installed on the computer

^d Spectrum manipulation and EPR and ENDOR simulation package written for Linux systems

^e The SOPHE simulation software suite is described in [115]

^f Programs developed by Dr H. Weihe, Department of Chemistry, University of Copenhagen for treatment of general spin Hamiltonians

^g General program for EPR, ENDOR and ESEEM [61]

^h Simultaneous EPR and ENDOR powder spectra synthesis by direct Hamiltonian diagonalization [117]

ⁱ Simulation of powder ENDOR spectra featuring angular selection due to *g*-factor anisotropy

^k Simulation of powder ENDOR spectra treating *hfc*-, *nqc*- and nuclear Zeeman interactions as a joint perturbation [172]

by *g*, *A* and *D* strain and unresolved *hfc* splittings are considered as well as non-equilibrium populations. Spectra with perpendicular and parallel detection modes can be analysed. *EasySpin* is available free of charge. Matlab version 7.5 or later must, however, be installed on the computer and is not provided with EasySpin.

EPR-NMR This program was written primarily for the handling of magnetic resonance spectra of single crystals and powders, but spectra of liquids can also be dealt with [116]. The number of spins included is arbitrary, as is their assignment as either electronic or nuclear. The program sets up spin-Hamiltonian matrices, and determines their eigenvalues using “exact” diagonalization. A variety of applications

can be treated as energy-level calculation, spectrum simulation, comparison with observed data, and parameter optimization. EPR-NMR contains capabilities for NMR as well as EPR calculations and for handling of several unpaired electronic spins. Boltzmann factors are also available. The program, including the source code and utilities, runs on any computer capable of running 32-bit FORTRAN 77.

Sim Software for simulation and fitting of EPR spectra has been developed during long time at the University of Copenhagen. Simulations are performed by diagonalization of the spin Hamiltonian used to model the complex under study. General Hamiltonians can be treated like exchange-coupled complexes of transition metal ions. Single crystal and powder spectra can be analysed. Fits to experimental spectra are obtained by the least squares method. The software was developed by Dr Høgni Weihe, Department of Chemistry, University of Copenhagen.

HRESOL, RIGMAT, MULTIP, HMLT A suite of EPR simulation programs prepared by Dr C. Chachaty are available free of charge [49]. Simulation can be made for radicals or metal ions of electron spin $S=1/2$, and of triplet states, of biradicals, radical or ion pairs in rigid matrices for $\Delta m_s=1$ and $\Delta m_s=2$ transitions. The second order treatment in [55] was utilized. Diagonalization of the spin Hamiltonian matrix can also be applied to free radicals in liquid phase and to triplet states, biradicals or ion pairs in rigid matrices.

SOPHE The XSophe-Sophe-XeprView computer simulation software suite is applicable for the analysis of isotropic, randomly oriented, and single crystal CW and pulse EPR spectra from isolated and clusters of paramagnetic centres [62]. XSophe provides a graphical user interface to the Sophe computer simulation software programme. The simulations available include CW-EPR spectra, orientation dependent CW-EPR spectra, energy level diagrams and transition surfaces diagrams. Spectra are simulated based on full matrix diagonalization. Superhyperfine interactions may be treated with up to third order perturbation theory. Isolated systems, magnetically coupled systems for unlimited electron and nuclear spins including multiple nuclear isotopes can be treated. Details are given in [115].

Xemr Xemr is an EPR, ENDOR, and TRIPLE (electron-nuclear-nuclear triple resonance) spectrum manipulation and simulation package written for Linux systems [59]. First order simulation is restricted to $S=1/2$ and to electron Zeeman and hyperfine interaction whereas a numerical method can handle electron and nuclear Zeeman, hyperfine, electron-electron, and nuclear quadrupole interactions exactly in simulations of both EPR and ENDOR spectra. Absorption, first derivative and second derivative spectra can be generated. The powder spectrum integrator can be added on top of these methods. The parameters for the simulations are provided interactively. The program is distributed free of charge under the GNU general public license.

ENDORF2 ENDOF2 is an ENDOR simulation program for $S=1/2$, treating *hfc*-, *nqc*-, and nuclear Zeeman interactions as a joint perturbation. Numerical diagonalisation of the perturbation matrix is used for nuclei with $I=2$ and higher, but for $I=1$

and 3/2 species the eigen-energies and -waveforms can be obtained by the analytical formulas in [192]. These are implemented in ENDORF2, together with the simple case of species with $I=1/2$. The program is written in FORTRAN77 and is distributed free of charge. Details are given in [52, 172, 186], see also <http://www.liu.se/simarc/downloads/?l=en?l=en>.

Motional Effects

Procedures for the analysis in the slow motional region are well documented, while computer programs for the simulation of intramolecular motion are not always publicly available or are in obsolete code.

Slow Motion Several programs for the CW spectrum simulation of reorienting nitroxide radicals used as spin labels described in [118–120] are freely available. The software packages include the original PC version of the CW spectrum simulation programs, and the least squares version of the program described in [119]. CW- EPR spectra of a slow tumbling nitroxide radical can also be simulated in the EasySpin package, see [120] for details of the algorithm. The EasySpin program runs with Matlab 7.5 or later.

Chemical Exchange The program ESREXN [142, 143] simulates multiline exchange- broadened EPR spectra from the coupling constants, the line widths, and the populations of the different chemical configurations. The original program might not be available. Heinzer's intramolecular exchange model is, however, implemented in the XEMR spectrum manipulation and simulation package written for Linux systems. A slightly modified stand-alone version was used in the works [144–146]. We are not aware of publicly available software for the treatment of chemical exchange in anisotropic systems.

References

1. Gordy W, Ard WB, Shields H (1955) Microwave spectroscopy of biological substances. I. Paramagnetic resonance in X-irradiated amino acids and proteins. PNAS 41:983–996
2. Fessenden RW, Schuler RH (1963) Electron spin resonance studies of transient alkyl radicals. J Chem Phys 39:2147–2195
3. Carrington A, McLachlan AD (1967) Introduction to magnetic resonance with applications to chemistry and chemical physics. Harper & Row, New York
4. Wertz JE, Bolton JR (1972) Electron spin resonance: elementary theory and practical applications. McGraw-Hill, New York
5. Weil JA, Bolton JR (2007) Electron paramagnetic resonance: elementary theory and practical applications, 2nd edn. Wiley, New York
6. Atherton NM (1973) Electron spin resonance: principles and applications. Ellis Horwood, Chichester
7. Atherton NM (1993) Principles of electron spin resonance. Ellis Horwood, New York
8. Lund A, Shiotani M, Shimada S (2011) Principles and applications of ESR spectroscopy. Springer, Dordrecht

9. Ayscough PB (1967) *Electron spin resonance in chemistry*. Methuen & Co Ltd, London
10. Bljumenfeld LA, Wojewodski WW, Semjonov AG (1966) *Anwendung der paramagnetischen Elektronenresonanz in der Chemie*, Akademische Verlagsgesellschaft. Guest & Portig K-G, Leipzig
11. Gordy W (1980) *Theory and applications of ESR*. Wiley, New York
12. Rieger PH (2007) *Electron spin resonance—analysis and interpretation*. RSC Publishing, Cambridge
13. Brustolon MR, Giamello E (eds) (2009) *Electron paramagnetic resonance: a practitioner's toolkit*. Wiley, Hoboken
14. Atkins PW, Symons MCR (1967) *The structure of inorganic radicals. An application of ESR to the study of molecular structure*. Elsevier, Amsterdam
15. Pshchetskii SYa, Kotov AG, Milinchuk VK, Roginski VA, Tupilov VI (1974) *EPR of free radicals in radiation chemistry*. Wiley, New York
16. Box HC (1977) *Radiation effects, ESR and ENDOR analysis*. Academic Press, New York
17. Yordanov ND (ed) (1992) *Electron magnetic resonance in disordered systems*. World Scientific, Singapore
18. Lund A, Shiotani M (eds) (1991) *Radical ionic systems*. Kluwer, Dordrecht
19. Lund A, Rhodes C (eds) (1995) *Radicals on surfaces*. Kluwer, Dordrecht
20. <http://www.springermaterials.com/docs/index.html>. Accessed 02 Jan 2014
21. Fischer H (ed) (1965–1989) *Magnetic properties of free radicals*. In: Landolt-Börnstein, Numerical data and functional relationships in science and technology. Springer, Berlin
22. Rånby B, Rabek JF (1977) *ESR spectroscopy in polymer research*. Springer, Berlin
23. Schlick S (ed) (2006) *Advanced ESR methods in polymer research*. Wiley, Hoboken
24. Royal Society of Chemistry (1973–2013) *Electron paramagnetic resonance*. Thomas Graham House, Cambridge
25. Lund A, Shiotani M (eds) (2013) *EPR of free radicals in solids I-II, trends in methods and applications*, 2nd ed. Springer, Dordrecht
26. Greenstock C, Ruddock GW, Neta P (1976) Pulse-radiolysis and ESR studies of electron-affinic properties of nitroheterocyclic radiosensitizers. *Radiat Res* 66:472–484
27. Smaller B, Avery EC, Remko JR (1971) EPR pulse radiolysis studies of the hydrogen atom in aqueous solution. I. Reactivity of the hydrogen atom. *J Chem Phys* 55:2414–2418
28. Trifunac AD, Avery EC (1974) Chemically induced dynamic electron polarization. The isotropic g-factor differences and the CIDEP of radicals produced by pulse radiolysis. *Chem Phys Lett* 27:141–143
29. Shkrob IA, Trifunac AD (1995) Pulse radiolysis of alkanes: a time-resolved epr study part I. Alkyl radical. *Radiat Phys Chem* 46:83–96
30. Danilczuk M, Pogoćki D, Lund A, Michalik J (2006) EPR and DFT study on the stabilization of radiation-generated methyl radicals in dehydrated Na-A zeolite. *J Phys Chem B* 110:24492–24497
31. Yamada T, Komaguchi K, Shiotani M, Benetis NP, Sørnes AR (1999) High-resolution EPR and quantum effects on CH₃, CH₂D, CHD₂, and CD₃ radicals under argon matrix isolation conditions. *J Phys Chem A* 103:4823–4829
32. <http://mission.igic.bas.bg/downloads/Lecture4.pdf>, Accessed 30 Dec 2013
33. Fessenden RW, Schuler RH (1965) ESR spectra and structure of the fluorinated methyl radicals. *J Chem Phys* 43:2704–2712
34. El-Sohly AM, Tschumper GS, Crocombe RA, Wang JT, Williams F (2005) Computational and ESR studies of electron attachment to decafluorocyclopentane, octafluorocyclobutane, and hexafluorocyclopropane: electron affinities of the molecules and the structures of their stable negative ions as determined from ¹³C and ¹⁹F hyperfine coupling constants. *J Am Chem Soc* 127:10573–10583
35. Shiotani M, Lund A, Lunell S, Williams F (2007) Structures of the hexafluorocyclopropane, octafluorocyclobutane, and decafluorocyclopentane radical anions probed by experimental and computational studies of anisotropic electron spin resonance (EPR) spectra. *J Phys Chem A* 111:321–338

36. Breit G, Rabi I (1931) Measurement of nuclear spin. *Phys Rev* 38:2082–2083
37. Hyde JS (1965) ENDOR of free radicals in solution. *J Chem Phys* 43:1806–1818
38. Duling DR (1994) Simulation of multiple isotropic spin-trap EPR spectra. *J Magn Reson Ser B* 104:105–110
39. Dumas L, Albela B, Bonneviot L, Portinha D, Fleury E (2013) Electron spin resonance quantitative monitoring of five different radicals in γ -irradiated polyvinylidene fluoride. *Radiat Phys Chem* 86:102–109
40. Dumas L, Albela B, Bonneviot L, Portinha D, Fleury E (2013) ESR investigation of radicals formed in γ -irradiated vinylidene fluoride based copolymer: P(VDF-co-HFP). *Radiat Phys Chem* 86:118–128
41. <https://www.niehs.nih.gov/research/resources/software/tox-pharm/tools/index.cfm>. Accessed 30 Dec 2013
42. Weil JA, Howarth DF (2009) Magnetic resonance in systems with equivalent spin-1/2 nuclides. Part 3: ket analysis and spectral intensities. *J Magn Reson* 197:28–35
43. Pilbrow JR (1990) Transition ion electron paramagnetic resonance. Clarendon, Oxford
44. Lefebvre R (1961) Calculation of the electron spin resonance line shape for a polycrystalline radical with anisotropic g tensor and proton hyperfine interactions. *J Chem Phys* 35:762–763
45. Lefebvre R, Maruani J (1965) Use of computer programs in the interpretation of electron paramagnetic resonance spectra of dilute radicals in amorphous solid samples. 1. High field treatment. X-band spectra of π -electron unconjugated hydrocarbon radicals. *J Chem Phys* 42:1480–1496
46. Simfonia EPR simulation programme. <http://www.bruker.com>. Accessed 30 Dec 2013
47. McConnell HM, Heller C, Cole T, Fessenden RW (1960) Radiation damage in organic crystals. I. $\text{CH}(\text{COOH})_2$ in malonic acid. *J Am Chem Soc* 82:766–775
48. Sagstuen E, Lund A, Itagaki Y, Maruani J (2000) Weakly coupled proton interactions in the malonic acid radical: single crystal ENDOR analysis and EPR simulation at microwave saturation. *J Phys Chem A* 104:6362–6371
49. <http://www.esr-speclsim-softw.fr>. Accessed 30 Dec 2013
50. Thuomas KA, Lund A (1976) Analysis of EPR with large quadrupole interaction. *J Magn Reson* 22:315–325
51. Lund A, Thuomas K, Maruani J (1978) Calculation of powder ESR spectra with hyperfine and quadrupole interactions. Application to mono- and dichloroalkyl radicals. *J Magn Reson* 30:505–514
52. Lund A, Erickson R (1998) EPR and ENDOR simulations for disordered systems: the balance between efficiency and accuracy. *Acta Chem Scand* 52:261–274
53. Lund A, Andersson P, Eriksson J, Hallin J, Johansson T, Jonsson R, Löfgren H, Paulin C, Tell A (2008) Automatic fitting procedures for EPR spectra of disordered systems: matrix diagonalization and perturbation methods applied to fluorocarbon radicals. *Spectrochim Acta* 69A:1294–1300
54. Rockenbauer A, Simon P (1973) Second-order perturbation treatment of spin Hamiltonian for low symmetry. *J Magn Reson* 11:217–218
55. Iwasaki M (1974) Second-order perturbation treatment of the general spin Hamiltonian in an arbitrary coordinate system. *J Magn Reson* 16:417–423
56. Skinner R, Weil JA (1978) Spin-Hamiltonian energies and state vectors. II. *J Magn Reson* 29:223–241
57. Haindl E, Hüttermann J (1978) An α -bromo radical in X-irradiated single crystals of 5-bromo-deoxyuridine. *J Magn Reson* 30:13–25
58. EPR-NMR. <http://www.chem.queensu.ca/eprnmr/>. Accessed 12 Dec 2013
59. XEMR software package version 0.8. <http://xemr.sourceforge.net/>. Accessed 30 Dec 2013
60. EasySpin version: 4.5.0 (2012) <http://www.easyspin.org/>. Accessed 12 Dec 2013
61. Keijzers CP, Reijerse EJ, Stam P, Dumont MF, Gribnau MCM (1987) MAGRES: a general program for electron spin resonance, ENDOR and ESEEM. *J Chem Soc Faraday Trans* 183:3493–3503

62. <http://www.bruker.com/products/mr/epr/epr-software/epr-software.html>. Accessed 13 Jan 2014
63. Herring FG, McDowell CA, Tait JC (1972) Electron spin resonance spectrum of the chlorodisulfanyl (S_2Cl) radical in inert matrices at 4.2 K. *J Chem Phys* 57:4564–4570
64. Maruani J, McDowell CA, Nakajima H, Raghunathan P (1968) The electron spin resonance spectra of randomly oriented trifluoromethyl radicals in rare-gas matrixes at low temperatures. *Mol Phys* 14:349–366
65. Maruani J, Coope JAR, McDowell CA (1970) Detailed analysis of the singularities and origin of the 'extra' lines in the ESR spectrum of the $\bullet CF_3$ radical in a polycrystalline matrix. *Mol Phys* 18:165–176
66. Edlund O, Lund A, Shiotani M, Sohma J, Thuomas K-Å (1976) Theory for the anisotropic hyperfine coupling with fluorine: the $\bullet CF_3$ radical. *Mol Phys* 32:49–69
67. Siegel S, Hedgpeth H (1967) Chemistry of irradiation induced polytetrafluoroethylene radicals: I. Reexamination of the EPR spectra. *J Chem Phys* 46:3904–3912
68. Allayarov SR, Konovalikhin SV, Olkhov YuA, Jackson VE, Kispert LD, Dixon DA, Ila D, Lappan U (2007) Degradation of γ -irradiated linear perfluoroalkanes at high dosage. *J Fluorine Chem* 128:575–586
69. Kispert LD (1978) Electron spin resonance studies of fluorine-containing radicals in single organic crystals. In: Roat JW (ed) Fluorine-containing free radicals, kinetics and dynamics of reactions 66:349–385. ACS Symposium Series
70. Goldanskii VI, Barkalov IM (1986) Formation of stable radicals in the radiolysis of fluoroorganic compounds. *Int J Radiat Appl Instrum, Part C, Radiat Phys Chem* 28:189–193
71. Hasegawa A, Itagaki Y, Shiotani M (1997) EPR spectra and structure of the radical cations of fluorinated benzenes. *J Chem Soc Perkin Trans 2*:1625–1630
72. Yahiro H, Lund A, Aasa R, Benetis NP, Shiotani M (2000) Association forms of NO in sodium ion-exchanged A-type zeolite. *J Phys Chem A* 104:7950–7956
73. Lund A (2004) Applications of automatic fittings to powder EPR spectra of free radicals, $S > 1/2$, and coupled systems. *Applied Magn Reson* 26:365–385
74. Shiotani M, Persson P, Lunell S, Lund A, Williams F (2006) Structures of tetrafluorocyclopropane, hexafluorocyclobutene, octafluorocyclopentene and related perfluoroalkene radical anions revealed by epr spectroscopic and computational studies. *J Phys Chem A* 110:6307–6323
75. Kurita Y (1964) Radical pairs trapped in irradiated single crystals of dimethylglyoxime at liquid nitrogen temperature. *J Chem Phys* 41:3926–3927
76. Iwasaki M, Toriyama K (1967) Pairwise trapping of dissimilar radical species and radical conversion in a single crystal of monofluoroacetamide γ irradiated at 77°K as studied by electron spin resonance. *J Chem Phys* 46:4693–4697
77. Iwasaki M, Toriyama K, Muto H, Nunome K (1976) Pairwise trapping of radicals in single crystals of n-decane irradiated at 1.5 and 4.2°K. *J Chem Phys* 65:596–606
78. Toriyama K, Iwasaki M, Nunome K (1979) ESR studies of irradiated methane and ethane at 4.2 K and mechanism of pairwise trapping of radicals in irradiated alkanes. *J Chem Phys* 71:1698–1705
79. Iwasaki M, Ichikawa T, Ohmori T (1969) Pairwise trapping of radicals in irradiated n-hydrocarbons and related compounds as studied by electron spin resonance. *J Chem Phys* 50:1991–1997
80. Iwasaki M, Toriyama K, Muto H, Nunome K (1976) Initial mode of radical pair formation in n-hydrocarbons irradiated at 1.5 and 4 K. *Chem Phys Lett* 39:90–94
81. Lebedev YS (1969) The radical pairs in irradiated organic solids as studied by EPR. *Radiat Eff* 1:213–227
82. Gordy W, Morehouse R (1966) Triplet-state electron spin resonance of an H-atom-methyl-radical complex in a solid matrix. *Phys Rev* 151:207–210
83. Gillbro T, Lund A (1974) Radical pair formation in n-decane and n-decane-d22 single crystals by γ -irradiation. Evidence by electron spin resonance for pairwise trapping at six different distances. *J Chem Phys* 61:1469–1474

84. Gillbro T, Lund A (1975) High-yield of radical pairs in deuterated normal-alkane single-crystals gamma-irradiated at 4.2 K. *Chem Phys Lett* 34:375–377
85. Gillbro T, Lund A (1976) Deposition of radiation energy in solids as visualized by distribution, structure and properties of alkyl radicals in gamma-irradiated normal-alkane single-crystals. *Int J Radiat Phys Chem* 8:625–641
86. Nilsson G, Lund A (1984) Radical pairs and trapped electrons in single-crystals of pentaerythritol—an electron-spin resonance and pulse-radiolysis kinetic-study. *J Phys Chem* 88:3292–3295
87. Nilsson G, Lund A, Samskog PO (1982) Radical pairs in single crystals of pentaerythritol—the formation of spatially correlated radicals in a hydrogen-bonded crystal. *J Phys Chem* 86:4144–4148
88. Baran NP, Maksimenko VM, Teslenko VV, Bugay AA (2008) EPR spectra of gamma-irradiated hydrated barium dithionate single crystals. *J Appl Spectroscopy* 75:15–20
89. Natarajan V, Seshagiri TK, Kadam RM, Sastry MD (2002) SO_4^- - SO_3^- radical pair formation in Ce doped and Ce, U co-doped $\text{K}_3\text{Na}(\text{SO}_4)_2$: EPR evidence and its role in TSL. *Radiat Meas* 35:361–368
90. Sagstuen E, Hole EO, Nelson WH, Close DM (1992) Radiation-induced free-radical formation in thymine derivatives. EPR/ENDOR of anhydrous thymine single crystals X-irradiated at 10 K. *J Phys Chem* 96:1121–1126
91. Sagstuen E, Hole EO, Nelson WH, Close DM (1998) Radiation damage to DNA base pairs. II. Paramagnetic resonance studies of 1-methyluracil-9-ethyladenine complex crystals X-irradiated at 10 K. *Radiat Res* 149:120–127
92. Peoples AR, Mercer KR, Bernhard WA (2010) What fraction of DNA double-strand breaks produced by the direct effect is accounted for by radical pairs? *J Phys Chem B* 114:9283–9288
93. Iwasaki M, Ichikawa T, Ohmori T (1969) Pairwise trapping of radicals in irradiated high polymers as studied by electron spin resonance. *J Chem Phys* 50:1984–1990
94. Iwasaki M, Ichikawa T (1967) ESR of radical pairs in irradiated polymers. The $\Delta M=2$ transitions. *J Chem Phys* 46:2851–2852
95. Toriyama K, Iwasaki M (1969) Change with temperature of the electron spin resonance spectra of $-\text{CF}_2\text{CF}_2$ -trapped in irradiated polytetrafluoroethylene. *J Phys Chem* 73:2919–2924
96. Gillbro T, Kinell PO (1973) Formation and decay of radical pairs in vinyl monomer single crystals. In: Kinell PO, Rånby B, Runnström-Reio V (eds) Nobel symposium 22, ESR applications to polymer research. Almquist and Wiksell, Uppsala, pp 83–93
97. Berclaz T, Bernardinelli G, Celalyan-Berthier A, Geoffroy M (1988) Radiation damage in organic phosphates. Crystal structure of 3-O-Diphenoxyphosphoryl-1,2-O-isopropylidene 5-O-Trityl- α -D-ribofuranose and an ESR study of the X-irradiated single crystal. *J Chem Soc Faraday Trans* 84:4105–4113
98. Komaguchi K, Nomura K, Shiotani M (2007) High-resolution ESR study of the $\text{H}\dots\text{CH}_3$, $\text{H}\dots\text{CHD}_2$, $\text{D}\dots\text{CH}_2\text{D}$, and $\text{D}\dots\text{CD}_3$ radical pairs in solid argon. *J Phys Chem A* 111:726–733
99. Itoh K, Hayashi H, Nagakura S (1969) Determination of the singlet-triplet separation of a weakly interacting radical pair from the E.S.R. spectrum. *Mol Phys* 17(6):561–577
100. Byberg JR, Bjerre N, Lund A, Samskog PO (1983) ESR effects of singlet-triplet mixing in radical pairs. Determination of the individual g tensors and the exchange coupling constant from spectral shifts due to off-diagonal Zeeman terms. *J Chem Phys* 78:5413–5419
101. Knight LBJr, Rice WE, Moore L, Davidson ER (1995) ESR observation of the $\text{H}\dots\text{H}$, $\text{H}\dots\text{D}$, and $\text{D}\dots\text{D}$ spin-pair radicals in rare gas matrices. *J Chem Phys* 103:5275–5278
102. Knight LBJr, Rice WE, Moore L, Davidson ER, Dailey RS (1998) Theoretical and electron spin resonance studies of the $\text{H}\dots\text{H}$, $\text{H}\dots\text{D}$, and $\text{D}\dots\text{D}$ spin-pair radicals in rare gas matrices: a case of extreme singlet-triplet mixing. *J Chem Phys* 109:1409–1424
103. Knight LBJr, Bell BA, Cobranchi DP, Davidson ER (1999) Electron spin resonance and theoretical studies of the $^{14}\text{N}\dots^{14}\text{N}$ and $^{15}\text{N}\dots^{15}\text{N}$ spin-pair radicals in neon matrices: the effects of mixing among the $^1\Sigma_g^+$, $^3\Sigma_u^+$, $^5\Sigma_g^+$, and $^7\Sigma_u^+$ electronic states. *J Chem Phys* 111:3145–3154

104. Kottis P, Lefebvre R (1963) Calculation of the electron spin resonance line shape of randomly oriented molecules in a triplet state. I. The $\Delta m = 2$ transition with a constant linewidth. *J Chem Phys* 39:393–403
105. Anderson RJM, Kohler BE (1975) Electron paramagnetic resonance of triplet diphenylmethylenes in single crystal benzophenone: evidence for a low temperature phase transition. *J Chem Phys* 63:5081–5086
106. Claesson O, Lund A (1980) Calculation of EPR spectra of triplet-state molecules with hyperfine and nuclear quadrupole interactions. *J Magn Reson* 41:106–111
107. Minakata K, Iwasaki M (1972) Hyperfine anomaly arising from the nuclear spin-forbidden transition, and absolute sign determination of the zero-field splitting constant. *Mol Phys* 23:1115–1131
108. Claesson O, Lund A, Gillbro T, Ichikawa T, Edlund O, Yoshida H (1980) A single crystal EPR study of ground state triplet trimethylenemethane. *J Chem Phys* 72:1463–1470
109. Yamaguchi T, Irie M, Yoshida H (1973) Electron paramagnetic resonance of trimethylenemethane formed by radiolysis of methylenecyclopropane. *Chemistry Letters* pp 975–978
110. Clarke RH (ed) (1982) Triplet state ODMR spectroscopy. Wiley, New York
111. Vrielinck H, Sabbe K, Callens F, Matthys P, Vandenbroucke D (2000) Magnetic resonance study of Rh complexes in AgCl microcrystals. *Spectrochim Acta Part A* 56:319–329
112. Shkrob IA, Marin TW, Chemerisov SD, Wishart JF (2011) Radiation induced redox reactions and fragmentation of constituent ions in ionic liquids. 1. Anions. *J Phys Chem B* 115:3872–3888
113. <http://www.epr.ethz.ch/software>. Accessed 30 Dec 2013
114. <http://www.epr.ethz.ch/links/index>. Accessed 30 Dec 2013
115. Hanson GR, Noble CJ, Benson S (2013) XSophe–Sophe–XeprView and molecular sophe: computer simulation software suites for the analysis of continuous wave and pulsed EPR and ENDOR spectra. In: Lund A, Shiotani M (eds) EPR of free radicals in solids I, trends in methods and applications. Springer, Dordrecht
116. Mombourquette MJ, Weil JA (1992) Simulation of magnetic resonance powder spectra. *J Magn Reson* 99:37–44
117. Kreiter A, Hüttermann J (1991) Simultaneous EPR and ENDOR powder spectra synthesis by direct Hamiltonian diagonalization. *J Magn Reson* 93:12–26
118. Schneider DJ, Freed JH (1989) Calculating slow-motional magnetic resonance spectra: a user's guide by spin labelling. Theory and applications. Vol. III. *Biol Magn Resonance* 8:1–76. (Plenum, NY)
119. Budil DE, Lee S, Saxena S, Freed JH (1996) Nonlinear least-squares analysis of slow-motional EPR spectra in one and two dimensions using a modified Levenberg-Marquardt algorithm. *J Magn Res A* 120:155–189
120. Earle KA, Budil DE (2006) Calculating slow-motion ESR spectra of spin-labeled polymers. In: Schlick S (ed) *Advanced ESR methods in polymer research*, Wiley, Hoboken
121. Shimada S, Hori Y, Kashiwabara H (1988) Molecular motion of the PMMA chain in poly(methylmethacrylate)/poly(vinylidene fluoride) blends by spin trapping labeling. *Macromolecules* 21:2107–2111
122. Kitahara T, Shimada S, Kashiwabara H (1980) Comparison of local molecular motions at chain end and inside of the polymer chain by use of spin trapping method. *Polymer* 21:1299–1303
123. Kevan L, Schlick S (1986) Peroxy spin probes as motional probes in polymers and on oxide surfaces. *J Phys Chem* 90:1998–2007
124. Shiotani M, Moro G, Freed JH (1981) ESR studies of O₂ adsorbed on titanium supported surfaces: analysis of motional dynamics. *J Chem Phys* 74:2616–2640
125. Benetis NP, Dmitriev Y (2013) Dynamical effects in CW and pulsed EPR. In: Lund A, Shiotani M (eds) EPR of free radicals in solids I, Trends in methods and applications. Springer, Dordrecht
126. Benetis NP, Dmitriev Y (2013) Anomalous EPR intensity distribution of the methyl radical quartet adsorbed on the surface of porous materials. Comparison with solid gas matrix isolation. *J Phys Chem A* 117:4233–4250

127. Benetis NP, Lindgren M, Lee HS, Lund A (1990) Intramolecular dynamics in small radicals with anisotropic magnetic interactions. 1. ESR lineshapes of carboxymethyl(1-) trapped in irradiated zinc acetate single crystal. *Appl Magn Reson* 1:267–281
128. Benetis NP, Mahgoub AS, Lund A, Nordh U (1994) Rotation of deuterated methylene groups in the diffusional regime. Isotope effect of anisotropic α -deuterons on ESR lineshapes of *CD_2 -COO- radical in irradiated ZnAC dihydrate single crystal. *Chem Phys Lett* 218:551–556
129. Brynda M, Berclaz T, Geoffroy M (2000) Intramolecular motion in dibenzobarrelene-phosphinyl radical: a single crystal EPR study at variable temperature. *Chem Phys Lett* 323:474–481
130. Brynda M, Dutan C, Berclaz T, Geoffroy M, Bernardinelli G (2003) Intramolecular motion in the triptycengermany radical: single crystal EPR study at variable temperature and DFT calculations. *J Phys Chem Solids* 64:939–946
131. Brynda M, Dutan C, Berclaz T, Geoffroy M (2002) Dynamic phenomena in barrelene-phosphinyl radicals: a complementary approach by density matrix analysis of EPR spectra and DFT calculations. *Current Topics in Biophysics* 26:35–42
132. Antzutkin ON, Benetis NP, Lindgren M, Lund A (1993) Molecular motion of the morpholin-1-yl radical in $CF_2ClCFCl_2$ as studied by ESR. Use of residual anisotropy of powder spectra to extract dynamics. *Chem Phys* 169:195–205
133. Sjöqvist L, Benetis NP, Lund A, Maruani J (1991) Intramolecular dynamics of the C_4H_8NH radical cation. An application of the anisotropic exchange theory for powder ESR lineshapes. *Chem Phys* 156:457–464
134. Benetis NP, Sjöqvist L, Lund A, Maruani J (1991) Theoretical comparison and experimental test of the secular and nonperturbative approaches on the ESR lineshapes of randomly oriented, anisotropic systems undergoing internal motion. *J Magn Reson* 95:523–535
135. Lloyd RV, Wood DE (1977) Electron paramagnetic resonance study of inversion barriers and conformations in substituted cyclopentyl radicals. *J Am Chem Soc* 99:8269–8273
136. Kubodera H, Shida T, Shimokoshi K (1981) ESR evidence for the cation radicals of tetrahydrofurans and dimethyl ether produced in a γ -irradiated frozen matrix of trichlorofluoromethane. *J Phys Chem* 85:2583–2588
137. Toriyama K (1991) ESR studies on cation radicals of saturated hydrocarbons. Structure, orbital degeneracy, dynamics and reactions. *Top Mol Organ Eng* 6:99–124
138. Sjöqvist L, Lund A, Maruani J (1988) An ESR investigation of the dynamical behavior of the cyclopentane cation in CF_3CCl_3 . *Chem Phys* 125:293–298
139. Sjöqvist L, Lindgren M, Lund A (1989) Internal motion of the cyclopentyl radical in $CF_2ClCFCl_2$: an ESR investigation. *Chem Phys Lett* 156:323–327
140. Sjöqvist L, Lindgren M, Shiotani M, Lund A (1990) Mirror inversion of the low-symmetry ground-state structures of the methylcyclohexane and 1,1-dimethylcyclohexane radical cations. An electron paramagnetic resonance study. *J Chem Soc Faraday Trans* 86:3377–3382
141. Shiotani M, Sjöqvist L, Lund A, Lunell S, Eriksson L, Huang MB (1990) An ESR and theoretical ab initio study of the structure and dynamics of the pyrrolidine radical cation and the neutral 1-pyrrolidinyl radical. *J Phys Chem* 94:8081–8090
142. Heinzer J (1971) Fast computation of exchange-broadened isotropic E.S.R. spectra. *Mol Phys* 22:167–177
143. Heinzer J (1971) ESREXN, QCPE program 209
144. Liu W, Wang P, Komaguchi K, Shiotani M, Michalik J, Lund A (2000) Structure and dynamics of $[(CH_3)_3N-CH_2]^{+\bullet}$ radical generated in γ -irradiated Al-offretite. *Phys Chem Chem Phys* 2:2515–2519
145. Liu W, Yamanaka S, Shiotani M, Michalik J, Lund A (2001) Structure and dynamics of triethylamine and tripropylamine radical cations generated in $AlPO_4$ by ionizing radiation: an EPR and MO study. *Phys Chem Chem Phys* 3:1611–1616
146. Liu W, Shiotani M, Michalik J, Lund A (2001) Cage effect on stability and molecular dynamics of $[(CH_3)_3N]^{+\bullet}$ and $[(CH_3)_3NCH_2]^{+\bullet}$ generated in γ -irradiated zeolites. *Phys Chem Chem Phys* 3:3532–3535
147. Portis AM (1953) Electronic structure of F centers: saturation of electron spin resonance. *Phys Rev* 91:1071–1079

148. Castner TGJr (1959) Saturation of the paramagnetic resonance of a V center. *Phys Rev* 115:1506–1515
149. Zhidkov OP, Lebedev YaS, Mikhailov AI, Provotorov BN (1967) Deduction of relaxation parameters from saturation in non-uniformly broadened lines. *Theoret Exp Chem* 3:135–139
150. Maruani J (1972) Continuous saturation of “dispersion” singularities and application to molecular triplet states. *J Magn Reson* 7:207–218
151. Zimbrick J, Kevan L (1967) Paramagnetic relaxation of trapped electrons in irradiated alkaline ices. *J Chem Phys* 47:2364–2371
152. Gillbro T, Lund A (1974) Relative concentrations and relaxation properties of isomeric alkyl radicals in γ -irradiated n-alkane single crystals. *Chem Phys* 5:283–290
153. Yordanov ND, Gancheva V, Karakirova Y (2013) Some recent developments of EPR dosimetry. In: Lund A, Shiotani M (eds) *EPR of free radicals in solids I, trends in methods and applications*. Springer, Dordrecht
154. Lund A, Liu W (2013) Continuous wave EPR of radicals in solids. In: Lund A, Shiotani M (eds) *EPR of free radicals in solids I, trends in methods and applications*. Springer, Dordrecht
155. Sagstuen E, Hole EO, Haugedal SR, Lund A, Eid OI, Erickson R (1997) EPR and ENDOR analysis of X-irradiated L-alanine and $\text{NaHC}_2\text{O}_4 \cdot \text{H}_2\text{O}$. Simulation of microwave power dependence of satellite lines. *Nukleonika* 42:353–372
156. Schneider F, Plato M (1971) *Elektronenspin-Resonanz*. Karl Thieme, München
157. Heydari MZ, Malinen E, Hole EO, Sagstuen E (2002) Alanine radicals. 2. The composite polycrystalline alanine EPR spectrum studied by ENDOR. Thermal annealing and spectrum simulations. *J Phys Chem A* 106:8971–8977
158. Gautschi NW (1969) Algorithm 363. Complex error function. *Comm ACM* 12:635
159. Gautschi NW (1970) Efficient computation of the complex error function. *SIAM J Num Anal* 7:187–198
160. Zamorano-Ulloa R, Flores-Llamas H, Yee-Madeira H (1992) Calculation of the relaxation times for an inhomogeneously broadened ESR line. *J Phys D Appl Phys* 25:1528–1532
161. Rist GH, Hyde JS (1970) Ligand ENDOR of metal complexes in powders. *J Chem Phys* 52:4633–4643
162. Erickson R, Lund A, Lindgren M (1995) Analysis of powder EPR and ENDOR spectra of the biphenyl radical cation on H-ZSM-5 zeolite, silica gel and in CFCl_3 matrix. *Chem Phys* 193:89–99
163. Erickson R, Benetis NP, Lund A, Lindgren M (1997) Radical cation of naphthalene on H-ZSM-5 zeolite and in CFCl_3 matrix. A theoretical and experimental EPR, ENDOR, and ESEEM study. *J Phys Chem A* 101:2390–2396
164. http://www.easyspin.org/documentation/userguide_salt.html Accessed 13 Jan 2014
165. Freed JH (1979) Theory of multiple resonance and ESR saturation in liquids and related media. In: Dorio MM, Freed JH (eds) *Multiple electron resonance spectroscopy*. Plenum, New York, pp 73–142
166. Clarkson RB, Belford RL, Rothenberger KS, Crookham HC (1987) ENDOR of perylene radicals adsorbed on alumina and silica-alumina powders. I. The ring protons. *J Catal* 106:500–511
167. Rothenberger KS, Crookham HC, Belford RL, Clarkson RB (1989) ENDOR of perylene radicals adsorbed on alumina and silica-alumina powders: II. The matrix effects. *J Catal* 115:430–440
168. Clarkson RB, Mattson K, Shi W, Wang W, Belford RL (1995) Electron magnetic resonance of aromatic radicals on metal oxide surfaces. In Lund A, Rhodes C (eds) *Radicals on surfaces*. Kluwer, Dordrecht, pp 89–117
169. Dalton LR, Kwiram AL (1972) ENDOR studies in molecular crystals. II. Computer analysis of the polycrystalline ENDOR spectra of low symmetry materials. *J Chem Phys* 57:1132–1145
170. Brustolon M, Cassol T, Micheletti L, Segre U (1987) ENDOR studies of methyl dynamics in molecular crystals. *Mol Phys* 61:249–255
171. Brustolon M, Maniero L, Segre U (1988) An ENDOR study of the slow intramolecular motion in the CH_2COO^- radical. *Mol Phys* 65:447–453

172. Erickson R (1996) Simulation of ENDOR spectra of radicals with anisotropic hyperfine and nuclear quadrupolar couplings in disordered solids. *Chem Phys* 202:263–275
173. Hoffman BM, Martinsen J, Venters RA (1984) General theory of polycrystalline ENDOR patterns. *g* and hyperfine tensors of arbitrary symmetry and relative orientation. *J Magn Reson* 59:110–123
174. Hoffman BM, Venters RA, Martinsen J (1985) General theory of polycrystalline ENDOR patterns. Effects of finite EPR and ENDOR component linewidths. *J Magn Reson* 62:537–542
175. Hoffman BM, Gurbiel RJ (1989) Polycrystalline ENDOR patterns from centers with axial EPR spectra. General formulas and simple analytic expressions for deriving geometric information from dipolar couplings. *J Magn Reson* 82:309–317
176. Hoffman BM, Gurbiel RJ, Werst MM, Sivaraja M (1989) Electron nuclear double resonance (ENDOR) of metalloenzymes. In: Hoff EJ (ed) *Advanced EPR: applications in biology and biochemistry*. Elsevier, Amsterdam, pp 541–591
177. Gurbiel RJ, Batie, CJ, Sivaraja M, True AE, Fee JA, Hoffman BM, Ballou DP (1989) Electron-nuclear double resonance spectroscopy of ^{15}N -enriched phthalate dioxygenase from *Pseudomonas cepacia* proves that two histidines are coordinated to the [2Fe-2S] Rieske-type clusters. *Biochemistry* 28:4861–4871
178. Hurst GC, Henderson TA, Kreilick RW (1985) Angle-selected ENDOR spectroscopy. 1. Theoretical interpretation of ENDOR shifts from randomly orientated transition-metal complexes. *J Am Chem Soc* 107:7294–7299
179. Henderson TA, Hurst GC, Kreilick RW (1985) Angle-selected ENDOR spectroscopy. 2. Determination of proton coordinates from a polycrystalline sample of bis(2,4-pentanedionato) copper(II). *J Am Chem Soc* 107:7299–7303
180. Gochev GP, Yordanov ND (1993) Polycrystalline “ENDOR Crystallography”, a new methodological approach. *J Magn Reson* 102:180–182
181. Möbius K, Lubitz W (1987) ENDOR spectroscopy in photobiology and biochemistry. In: Berliner LJ, Reuben J (eds) *Biological magnetic resonance*, vol 7. Plenum, New York
182. Toriyama K, Nunome K, Iwasaki M (1976) ENDOR studies of methyl radicals in irradiated single crystals of $\text{CH}_3\text{COOLi}\cdot 2\text{H}_2\text{O}$. *J Chem Phys* 64:2020–2026
183. Stoll S (2003) Spectral simulations in solid-state electron paramagnetic resonance, PhD thesis ETH 15059, Eidgenössische Technische Hochschule, Zürich
184. Stoll S, Schweiger A (2006) EasySpin, a comprehensive software package for spectral simulation and analysis in EPR. *J Magn Reson* 178:42–55
185. Schweiger A, Günthard HsH (1982) Transition probabilities in electron-nuclear double- and multiple-resonance spectroscopy with non-coherent and coherent radio-frequency fields. *Chem Phys* 70:1–22
186. Erickson R (1995) Electron magnetic resonance of free radicals. Theoretical and experimental EPR, ENDOR and ESEEM studies of radicals in single crystal and disordered solids, Linköping studies in science and technology, PhD Thesis No 391, ISBN 91-7871-582-2, Linköping, Sweden
187. Bender CJ, Sahlin M, Babcock GT, Barry BA, Chandrashekar TK, Salowe SP, Stubbe J, Lindström B, Petersson L, Ehrenberg A, Sjöberg B-M (1979) An ENDOR study of the tyrosyl free radical in ribonucleotide reductase from *Escherichia coli*. *J Am Chem Soc* 111:8076–8083
188. Fujimoto M, McDowell CA, Takui TJ (1979) Ligand ENDOR spectra of Cu(II) impurity complexes in α -glycine crystals. *Chem Phys* 70:3694–3701
189. Whiffen DH (1966) ENDOR transition moments. *Mol Phys* 10:595–596
190. LoBrutto R, Wei YH, Mascarenhas R, Scholes CP, King TE (1983) Electron nuclear double resonance and electron paramagnetic resonance study on the structure of the NO-ligated heme alpha 3 in cytochrome c oxidase. *J Biol Chem* 258:7437–7448
191. Chacko VP, McDowell CA, Singh BC (1980) ^{14}N and ^1H ENDOR studies of X-irradiated single crystals of hippuric acid. *J Chem Phys* 72:4111–4116
192. Erickson R, Lund A (1991) Analytical expressions of magnetic energies and wavefunctions of paramagnetic systems with $S=1/2$ and $I=1$ or $I=3/2$. *J Magn Reson* 92:146–151

General Appendices

Tables 1–5 and 7 below were adapted from the Appendix in [Anders Lund, Masaru Shiotani and Shigetaka Shimada: Principles and Applications of ESR Spectroscopy (Springer, 2011)] with permission from Springer.

Table 1 Fundamental constants^a

Quantity	Symbol	Value	SI unit
Speed of light	c	2.99792458×10^8	m s^{-1}
Elementary charge	e	1.602176×10^{-19}	C
Faraday constant	$F = N_A e$	9.648456×10^4	C mol^{-1}
Boltzmann constant	k	1.38065×10^{-23}	J K^{-1}
Gas constant	$R = N_A k$	8.31447	$\text{J K}^{-1} \text{mol}^{-1}$
Planck constant	h	6.626068×10^{-34}	J s
	$\hbar = h/2\pi$	1.054571×10^{-34}	J s
Avogadro constant	N_A	6.02214×10^{23}	mol^{-1}
Atomic mass unit	u	1.66054×10^{-27}	kg
Mass			
Electron	m_e	9.10938×10^{-31}	kg
Proton	m_p	1.67262×10^{-27}	kg
Neutron	m_n	1.67493×10^{-27}	kg
Vacuum permittivity	$\epsilon_0 = 1/c^2 \mu_0$	8.854188×10^{-12}	F m^{-1}

^a CODATA recommended values of the fundamental physical constants 2006, National Institute of Standards and Technology, Gaithersburg, Maryland 20899-8420, USA; <http://physics.nist.gov/cuu/Constants/>

Table 2 Magnetic constants in SI units^a

Quantity	Symbol	Numerical value	Unit
Magnetic constant	$\mu_0 = 4\pi \times 10^{-7}$	12.566370×10^{-7}	N A ⁻²
Bohr magneton	$\mu_B (\beta_e)$	$927.400915(23) \times 10^{-26}$	J T ⁻¹
Nuclear magneton	$\mu_N (\beta_N)$	$5.05078324(13) \times 10^{-27}$	J T ⁻¹
Electron <i>g</i> -factor	g_e	2.0023193043617(15)	
Electron gyromagnetic ratio	γ_e	$1.760859770(44) \times 10^{11}$	s ⁻¹ T ⁻¹
μ_B/h	μ_B/h	$13.9962464(35) \times 10^9$	Hz T ⁻¹
μ_B/hc	μ_B/hc	46.6864515(12)	m ⁻¹ T ⁻¹
μ_N/h	μ_N/h	7.62259384(19)	MHz T ⁻¹

^a CODATA recommended values of the fundamental physical constants 2006, National Institute of Standards and Technology, Gaithersburg, Maryland 20899-8420, USA; <http://physics.nist.gov/cuu/Constants/>

Table 3 Conversion factors for EPR (ESR) coupling constants

Unit	MHz	mT	cm ⁻¹
MHz	1	0.07144766/g	$0.333564095 \times 10^{-4}$
mT	13.99625 g	1	4.668645×10^{-4} g
cm ⁻¹	2.99792458×10^4	$0.2141949 \times 10^4/g$	1

A coupling given in a unit of the 1st column is calculated in other units by multiplication with the factor in the corresponding row.

Calculations of *g* from measured values of microwave frequency ν_e (GHz) and resonance field *B* (T), of resonance field, and of nuclear frequency ν_N (MHz):

$$g = \frac{h}{\mu_B} \cdot \frac{\nu_e}{B} = 0.071447656 \frac{\nu_e(\text{GHz})}{B(\text{T})}, \quad B(\text{T}) = \frac{h}{\mu_B} \cdot \frac{\nu_e}{g} = 0.071447656 \frac{\nu_e(\text{GHz})}{g}$$

$$\nu_N(\text{MHz}) = \frac{\mu_N}{h} \cdot g_N B = 7.622\,593\,84 \cdot g_N B(\text{T})$$

a The factors were obtained from CODATA recommended values of the constants in Table 1; <http://physics.nist.gov/cuu/Constants/>

b Mohr PJ, Taylor BN, Newell DB (2008) Rev Mod Phys 80:633; J Phys Chem Ref Data 37:1187

Table 4 Other useful conversion factors

1 eV	1.602 18 × 10 ⁻²³ J 96.485 kJ mol ⁻¹ 8065.5 cm ⁻¹
1 cal	4.184 J
1 atm	101.325 kPa
1 cm ⁻¹	1.9864 × 10 ⁻²³ J
1 D (Debye)	3.33564 × 10 ⁻³⁰ C m
1 Å	10 ⁻¹⁰ m
1 T	10 ⁴ G (or gauss)
1 L atm	= 101.325 J
θ/°C	= T/K - 273.15

Table 5 Symbols, variables and units in EPR (ESR)

Symbol	Name or description	Unit and/or value
<i>A, a</i>	Hyperfine coupling (splitting) constant	MHz, mT (milli-Tesla)
<i>D</i>	Zero-field splitting, fine structure	cm ⁻¹ , MHz, mT
<i>B (H)</i>	External magnetic field	T (Tesla)
<i>e</i>	Electron charge	1.602177 × 10 ⁻¹⁹ A s
<i>g</i>	g-factor	Dimensionless
<i>G</i>	Radiation yield	μmol J ⁻¹
<i>h</i>	Planck constant	6.626068 × 10 ⁻³⁴ J s
<i>I</i>	Nuclear spin angular momentum	J s
<i>I</i>	Nuclear spin quantum number	Dimensionless
<i>J</i>	Heisenberg exchange coupling	cm ⁻¹ , MHz, mT
<i>k</i>	Boltzmann constant	1.380658 × 10 ⁻²³ J K ⁻¹
<i>L</i>	Orbital angular momentum	J s
<i>l</i>	Orbital quantum number	Dimensionless
<i>m_e</i>	Electron mass	0.910939 × 10 ⁻³⁰ kg
<i>m_I</i>	Nuclear magnetic quantum number	Dimensionless
<i>m_S</i>	Electron magnetic quantum number	Dimensionless
<i>P</i>	Microwave power	J s ⁻¹
<i>Q</i>	Nuclear quadrupole coupling	cm ⁻¹ , MHz, mT
<i>S</i>	Electron spin angular momentum	J s
<i>S, s</i>	Electron spin quantum number	Dimensionless
<i>v</i>	Speed	m s ⁻¹
<i>λ</i>	Spin-orbit coupling constant	cm ⁻¹
<i>μ</i>	Magnetic moment	A s
<i>μ_B</i> (<i>β_e</i>)	Bohr magneton	9.274015 × 10 ⁻²⁴ J T ⁻¹
<i>μ_N</i> (<i>β_N</i>)	Nuclear magneton	5.050787 × 10 ⁻²⁷ J T ⁻¹
<i>ν</i>	Frequency	Hz

Table 6 Abbreviations

Abbreviation	Name or description	Chapter
Magnetic resonance		
CW	Continuous wave	16,19
DEER	Double electron-electron resonance	16
DQC	Double quantum coherence	16
EIE	ENDOR-induced EPR	6
ELDOR	Electron double resonance	16
EMR	Electron magnetic resonance	6,19
ENDOR	Electron nuclear double resonance	2, 6, 7, 11
EPR (ESR)	Electron paramagnetic resonance (Electron spin resonance)	1–12
EPRI	Electron paramagnetic resonance imaging	14
EQQ	Electric quadrupole-quadrupole	4
ESE	Electron spin echo	16
ESEEM	Electron spin echo envelope modulation	7, 15, 16
FDMR	Fluorescence detected magnetic resonance	17
FF ENDOR	Field frequency ENDOR	6
FID	Free induction decay	16
HF (hf)	Hyperfine	3, 6, 11
HFC(C) (hfc(c))	Hyperfine coupling (constant(s))	4, 8, 17, 19
HFS (hfs)	Hyperfine splitting	10
HYSCORE	Hyperfine sublevel correlation	6, 15
MW (mw)	Microwave	11, 16, 17
NQC (nqc)	Nuclear quadrupole coupling	19
OD EPR	Optically detected EPR	17
ODMR	Optically detected magnetic resonance	11, 19
P2P	Peak-to-peak	13
PC	Paramagnetic center	16
PDS	Pulsed dipolar spectroscopy	16
PEANUT	Phase-inverted echo-amplitude detected nutation	15
PELDOR	Pulsed electron double resonance	8, 16
Photo EPR	Photoexcitation EPR	11
RF	Radio frequency	19
SOPHE	(Simulation) Software nickname for EPR simulation programme (Sydney OPera HousE)	19
TCSPC	Time-correlated single photon counting	17
TR MFE	Time-resolved magnetic field effect	17
TRIPLE	Electron-nuclear-nuclear triple resonance	19
ZFS (zfs)	Zero-field splitting	19

Table 6 (continued)

Abbreviation	Name or description	Chapter
Radiation chemistry		
BNCT	Boron neutron capture therapy	14
CR	Charge resonance	1, 12
DEA	Dissociative electron attachment	8, 12
HRD	High dose rate	14
IMRT	Intensity modulated radiotherapy	14
IMTE	Inter-molecularly trapped electron	6
LDR	Low dose rate	14
LE	Local excitation	1
LET	Linear energy transfer	5, 8, 14, 16
Linac	Linear accelerator	1
MARY	Magnetically affected reaction yield	17
RA	Radical anion	17
RC	Radical cation	17
RIP	Radical ion pair	17
TLD	Thermoluminescence dosimetry	14
TNI	Transient negative ion	6
VMAT	Volumetric modulated arc therapy	14
Chemistry and biochemistry		
3'-AMP	Adenosine 3'-monophosphate	9
3'-CMP	Cytidine 3'-monophosphate	9
3'-GMP	Guanosine 3'-monophosphate	9
4-PyOBN	α -(1-oxy-4-Pyridyl)-N-tert-butyl nitron	9
5-BrU	5-Bromouracil	9
5-BrUrd	5-Bromouridine	9
5-BrdU	5-Bromodeoxyuridine	9
5-CU	5-Chlorouracil	9
5-CUrd	5-Chlorouridine	9
5-CdU	5-Chlorodeoxycytidine	9
5-FU	5-Fluorouracil	9
5-FUrd	5-Fluorouridine	9
5-FdU	5-Fluorodeoxyuridine	9
5'-AMP	Adenosine 5'-monophosphate	9
5'-CMP	Cytidine 5'-monophosphate	9
5'-GMP	Guanosine 5'-monophosphate	9
5'-dAMP	2'-Deoxyadenosine 5'-monophosphate	9
5'-dCMP	2'-Deoxycytidine 5'-monophosphate	9
5'-dGMP	2'-Deoxyguanosine 5'-monophosphate	9
AAc	Acrylic acid	10

Table 6 (continued)

Abbreviation	Name or description	Chapter
Ado	Adenosine	9
Alq ₃	Aluminum tris-8-oxyquinolate	17
BD	Butadiene	10
BOB	Bis(oxalato)borate (B[ox] ₂)	12
BuCl	Buthylchloride	1
CE	Crown ether(s)	12
CISS·	Chlorodisulfanyl radical	19
Cyd	Cytidine	9
Cyt c	Cytochrome c	1
DFOB	Difluorooxalatoborate	12
DMAD	1,3-Dimethyladamantane	17
DME	Dimethyl ether	3
DMPO	5,5-Dimethyl-1-pyrroline N-oxide	9
DNA	Deoxyribonucleic acid	1
DPPH	1,2-Diphenylpicrylhydrazyl	2
GLPC	Germanium lone pair center	7
Guo	Guanosine	9
H-ZSM-5	Zeolite Socony Mobil-5 with H ⁺ (proton)	19
HCAP	1,1,2,4,5,5-Hexacyano-3-azapentadienide	12
HFBD	Hexafluoro-1,3-butadiene	3
HME	Hexamethylethane	3, 19
IL	Ionic liquid	12
IOM	Insoluble organic matter	15
K2G1P	Dipotassium glucopyranose-1-phosphate	6
LH	Left-handed (quartz)	7
MMA	Methyl-methacrylate	10, 19
MMA-d	MMA deuterium (heavy hydrogen) substituted	19
MMA-h	MMA hydrogen (light hydrogen) substituted	19
MNP	2-Methyl-2-nitrosopropane	9
MTHF	(2-)Methyltetrahydrofuran	1
Mb	Myoglobin	1
NBOHC	Non bridging oxygen hole centre	7
NEP	Neopentane	3
PA	Polyamide	10
PAN	Polyacrylonitrile	10
PBN	α -Phenyl-N-tert-butylnitron	9
PCCP	1,2,3,4,5-Pentacyanocyclopentadienide	12

Table 6 (continued)

Abbreviation	Name or description	Chapter
PCP	1,1,2,3,3-Pentacyanopropenide	12
PCS	Polycarbosilane	10
PE	Polyethylene	10
PMMA	Poly(methyl methacrylate)	14
POR	Peroxy radical	7
PP	Polypropylene	10
PTFE	Polytetrafluoroethylene	10
PVC	Polyvinyl chloride	14
PVDF	Poly(vinylidene fluoride)	10
Ph ₂	Biphenyl	19
RH	Right-handed (quartz)	7
SAPO-42	Silicoaluminophosphate-42	19
SAR	Stable alanine radical	19
SiC	Silicon carbide	10
TBP	Trigonal bipyramid structure; tri(<i>n</i> -butylphosphate)	2, 12
TCAP	Tetracyano-2-azapropenide	12
TCPD	1,1,3,3-Tetracyanopropanediide	12
TDCP	1,2,3-Tris(dicyanomethylene) cyclopropanediide	12
TFB	Trifluorobenzene	17
TMM	Trimethylenemethane	19
TMP	Thymidine 5'-monophosphate	9
TMPD	N, N,N',N'-tetramethyl- <i>p</i> -phenylenediamine	3
TMPP	Tetramethylpiperidine	17
TMS	Tetramethylsilane	3, 19
TSIL	Task-specific IL	12
UHMWPE	Ultra-high molecular weight polyethylene	10
Urd	Uridine	9
dA	2'-deoxyAdenosine	9
dC	2'-deoxyCytidine	9
dG	2'-deoxyGuanosine	9
dT	Thymidine	9
dU	2'-deoxyUridine	9
ddTMP	2',3'-dideoxyThymidine 5'-monophosphate	9
dsb	Double strand break	8
o-H ₂	Ortho hydrogen	4
p-H ₂	Para hydrogen	4
<i>p</i> TP	<i>para</i> -Terphenyl	17
ssb	Single strand break	8

Table 6 (continued)

Abbreviation	Name or description	Chapter
Quantum chemistry		
B3LYP	Becke, three parameter, Lee-Yang-Parr	19
BFGS	Broyden-Fletcher-Goldfarb-Shanno	18
CNDO	Complete neglect of differential overlap	3
CPMD	Car-Parrinello Molecular Dynamics	6
DFT	Density functional theory	2, 3, 6, 7, 12, 18, 19
DFT-LDA	Density functional theory in the local density approximation	11
GAPW	Gaussian and augmented plane wave (method)	18
GPW	Gaussian and plane waves (dual basis set method)	18
HOMO	Highest occupied molecular orbital	3
INDO	Intermediate neglect of differential overlap	3,19
J-T	Jahn-Teller	3
LUMO	Lowest unoccupied molecular orbital	3
MD	Molecular dynamics	18
MO	Molecular orbital	3
MP	Møller-Plesset	4
NEB	Nudged elastic band method	18
NPLs	No-phonon lines	11
PES	Potential energy surface	17
SH	Spin Hamiltonian	6
SLE	Stochastic Liouville equation	19
SOMO	Singly occupied molecular orbital	2,3
TD DFT	Time-dependent DFT	3
UHF MO	Unrestricted Hartree-Fock MO	3
Others		
BIPM	Bureau international des poids et mesures	13
CT	Computer tomography	14
CVD	Chemical vapor deposition	11
DLTS	Deep level transient spectroscopy	11
ECL	Electrochemical luminescence	1
FCC (fcc)	Face centered cubic	4
FRET	Fluorescence resonance energy transfer	1
FTIR	Fourier transform IR	5
HCP (hcp)	Hexagonal close packed	4
HPSI	High-purity semi-insulating	11
HTCVD	High temperature chemical vapor deposition	11

Table 6 (continued)

Abbreviation	Name or description	Chapter
IP	Ionization potential	5
IR	Infrared	5
IT	Information technology	13
LHe	Liquid helium	4
LT	Low temperature	6
M2	Second moment	16
MLCFA	Maximum likelihood common factor analysis	6
MSDA	Magnetic circular dichroism of the absorption	11
NIST	National institute of standards and technology	13
NMI	National metrology institute	13
OA	Optical absorption	7
OLED	Organic light-emitting diode	17
PL	Photoluminescence	11
PMT	Photomultiplier tube	17
PVT	Physical vapor transport	11
RT	Room temperature	6
SI	Semi-insulating	11
UV	Ultraviolet	16

Table 7 Magnetic properties of stable and long-lived isotopes^{a,b,c}

Isotope	Atomic number (Z)	Natural abundance (%)	Nuclear spin (I)	Nuclear g-factor (g_N)
¹ H	1	99.985	0.5	5.58569
² H	1	0.0148	1	0.85744
³ He	2	0.00014	0.5	-4.25525
⁶ Li	3	7.5	1	0.82205
⁷ Li	3	92.5	1.5	2.17096
⁹ Be	4	100	1.5	-0.785
¹⁰ B	5	19.8	3	0.60022
¹¹ B	5	80.2	1.5	1.79242
¹³ C	6	1.11	0.5	1.40482
¹⁴ N	7	99.63	1	0.40376
¹⁵ N	7	0.366	0.5	-0.56638
¹⁷ O	8	0.038	2.5	-0.75752
¹⁹ F	9	100	0.5	5.25773
²¹ Ne	10	0.27	1.5	-0.4412
²³ Na	11	100	1.5	1.47839

Table 7 (continued)

²⁵ Mg	12	10	2.5	-0.34218
²⁷ Al	13	100	2.5	1.4566
²⁹ Si	14	4.67	0.5	-1.1106
³¹ P	15	100	0.5	2.2632
³³ S	16	0.75	1.5	0.42911
³⁵ Cl	17	75.77	1.5	0.54792
³⁷ Cl	17	24.23	1.5	0.45608
³⁹ K	19	93.26	1.5	0.26099
⁴⁰ K	19	0.0117	4	-0.32453
⁴¹ K	19	6.73	1.5	0.14325
⁴³ Ca	20	0.135	3.5	-0.37641
⁴⁵ Sc	21	100	3.5	1.35906
⁴⁷ Ti	22	7.4	2.5	-0.31539
⁴⁹ Ti	22	5.4	3.5	-0.31548
⁵⁰ V	23	0.25	6	0.55659
⁵¹ V	23	99.75	3.5	1.46836
⁵³ Cr	24	9.5	1.5	-0.3147
⁵⁵ Mn	25	100	2.5	1.3819
⁵⁷ Fe	26	2.15	0.5	0.1806
⁵⁹ Co	27	100	3.5	1.318
⁶¹ Ni	28	1.13	1.5	-0.50001
⁶³ Cu	29	69.2	1.5	1.484
⁶⁵ Cu	29	30.8	1.5	1.588
⁶⁷ Zn	30	4.1	2.5	0.35031
⁶⁹ Ga	31	60.1	1.5	1.34439
⁷¹ Ga	31	39.9	1.5	1.70818
⁷³ Ge	32	7.8	4.5	-0.19544
⁷⁵ As	33	100	1.5	0.95965
⁷⁷ Se	34	7.6	0.5	1.0693
⁷⁹ Br	35	50.69	1.5	1.40427
⁸¹ Br	35	49.31	1.5	1.51371
⁸³ Kr	36	11.5	4.5	-0.2157
⁸⁵ Rb	37	72.17	2.5	0.54125
⁸⁷ Rb	37	27.83	1.5	1.83427
⁸⁷ Sr	38	7	4.5	-0.24291
⁸⁹ Y	39	100	0.5	-0.27484
⁹¹ Zr	40	11.2	2.5	-0.52145
⁹³ Nb	41	100	4.5	1.3712
⁹⁵ Mo	42	15.9	2.5	-0.3656
⁹⁷ Mo	42	9.6	2.5	-0.3734
⁹⁹ Ru	44	12.7	2.5	-0.249
¹⁰¹ Ru	44	17	2.5	-0.279
¹⁰³ Rh	46	100	0.5	-0.1768
¹⁰⁵ Pd	46	22.2	2.5	-0.256
¹⁰⁷ Ag	47	51.83	0.5	-0.22725

Table 7 (continued)

¹⁰⁹ Ag	47	48.17	0.5	-0.26174
¹¹¹ Cd	48	12.8	0.5	-1.19043
¹¹³ Cd	48	12.2	0.5	-1.2454
¹¹³ In	49	4.3	4.5	1.22864
¹¹⁵ In	49	95.7	4.5	1.23129
¹¹⁵ Sn	50	0.38	0.5	-1.8377
¹¹⁷ Sn	50	7.75	0.5	-2.00208
¹¹⁹ Sn	50	8.6	0.5	-2.09456
¹²¹ Sb	51	57.3	2.5	1.3455
¹²³ Sb	51	42.7	3.5	0.72876
¹²³ Te	52	0.89	0.5	-1.4736
¹²⁵ Te	52	7	0.5	-1.7766
¹²⁷ I	53	100	2.5	1.1253
¹²⁹ Xe	54	26.4	0.5	-1.55595
¹³¹ Xe	54	21.2	1.5	0.46124
¹³³ Cs	55	100	3.5	0.73785
¹³⁵ Ba	56	6.59	1.5	0.55884
¹³⁷ Ba	56	11.2	1.5	0.62515
¹³⁸ La	57	0.089	5	0.74278
¹³⁹ La	57	99.911	3.5	0.7952
¹⁴¹ Pr	59	100	2.5	1.6
¹⁴³ Nd	60	12.2	3.5	-0.3076
¹⁴⁵ Nd	60	8.3	3.5	-0.19
¹⁴⁷ Sm	62	15.1	3.5	-0.2322
¹⁴⁹ Sm	62	13.9	3.5	0.1915
¹⁵¹ Eu	63	47.9	2.5	1.389
¹⁵³ Eu	63	52.1	2.5	0.6134
¹⁵⁵ Gd	64	14.8	1.5	-0.1723
¹⁵⁷ Gd	64	15.7	1.5	-0.2253
¹⁵⁹ Tb	65	100	1.5	1.342
¹⁶¹ Dy	66	19	2.5	-0.189
¹⁶³ Dy	66	24.9	2.5	0.266
¹⁶⁵ Ho	67	100	3.5	1.192
¹⁶⁷ Er	68	22.9	3.5	-0.1618
¹⁶⁹ Tm	69	100	0.5	-0.466
¹⁷¹ Yb	70	14.4	0.5	0.9885
¹⁷³ Yb	70	16.2	2.5	-0.27195
¹⁷⁵ Lu	71	97.39	3.5	0.63943
¹⁷⁶ Lu	71	2.61	7	0.452
¹⁷⁷ Hf	72	18.6	3.5	0.2267
¹⁷⁹ Hf	72	13.7	4.5	-0.1424
¹⁸¹ Ta	73	99.9877	3.5	0.67729
¹⁸³ W	74	14.3	0.5	0.23557
¹⁸⁵ Re	75	37.4	2.5	1.2748
¹⁸⁷ Re	75	62.6	2.5	1.2878
¹⁸⁷ Os	76	1.6	0.5	0.1311

Table 7 (continued)

¹⁸⁹ Os	76	16.1	1.5	0.488
¹⁹¹ Ir	77	37.3	1.5	0.097
¹⁹³ Ir	78	62.7	1.5	0.107
¹⁹⁵ Pt	78	33.8	0.5	1.219
¹⁹⁷ Au	79	100	1.5	0.09797
¹⁹⁹ Hg	80	16.8	0.5	1.01177
²⁰¹ Hg	80	13.2	1.5	-0.37348
²⁰³ Tl	81	29.5	0.5	3.24451
²⁰⁵ Tl	81	70.5	0.5	3.2754
²⁰⁷ Pb	82	22.1	0.5	1.1748
²⁰⁹ Bi	83	100	4.5	0.938
²³⁵ U	92	0.72	3.5	-0.1

^a Raghavan P (1989) *At Data Nucl. Data Tables* 42:189

^b <http://ie.lbl.gov/toipdf/mometbl.pdf>

^c Values for the isotropic and anisotropic hyperfine couplings of the isotopes are reported in Weil JA, Bolton JR (2007) *Electron paramagnetic resonance: elementary theory and practical applications*, 2nd edition. Wiley

Index

A

Ab initio
 calculations, 434
 supercell calculations, 435
Acetone radical anion, 180
Activation energies, 438, 722
Ag₃2⁺ in irradiated zeolite matrix, 713
[AlO₄]⁰ center, 259, 270
[AlO₄]⁺ center, 270
[AlO₄/Li]⁺, 270
Alanine, 512, 521, 675, 687
 agarose gel system, 517
 dosimeters, 515
 dosimetry, 489
 EPR
 dosimetry, 514, 516
 measurements, 527
 film dosimeters, 519
 strands, 521
Aldersson phantom, 521
Alkane radical cations, 647, 656
 in MARY, 656
Alkoxy, 692
 radical, 206–208
Alkyl, 207
 radical, 390
 type radical, 390
Allowed ($\Delta m_1 = 0$) hyperfine lines, 722
Alpha(α)-carbon radicals, 367
 α -type HF(hf) interactions, 197
Aluminum tris-8-oxyquinolate, 645
Amino acids, 668
Ammonium
 formate, 517
 tartrate, 615, 621
 dosimeters, 530
Amorphous, 389
Angular

 dependence, 191
 selection, 724
 selectivity, 724
Anisotropic, 70
 1H hf-splittings, 99
 HFCCs (hyperfine coupling constants),
 134
 powder spectrum, 97
Anisotropy (g and hf tensors), 189
Anthropomorphic phantom, 518, 519
Antioxidant, 473
Antisite, 417, 431, 435
 vacancy pairs, 431
Aqueous acrylic acid, 393
Archean, 544, 550, 551, 554–556, 562
Argon-like xenon, 156
Aryloxy, 473
A spins, 598, 600, 602

B

Back-transfer, 243
Base(s), 357
 moiety, 372
Beam profiles, 515
Benzene radical ions, 91
1-Benzyl-3-methylimidazolium, 462
1-Benzylpyridinium, 462, 473
Beta (β)-elimination, 692
 β -hydrogen splittings, 355
 β -hydroxyl proton coupling, 203
 β -proton, 197
Bio-Gel P-2 column, 370
Biosignature, 544, 547, 548
Biradical model, 264
Bis(ethylhexyl)phosphoric acid, 476
Bis(fluorosulfonyl)imide, 470
Bis(oxalato)borate, 469
Bistriflimide, 459

- Blended alanine dosimeters, 532
 Bloch equations, 596
 BLYP (Becke, Lee-Yang-Parr), 672
 Bond scissions, 242
 Boron neutron capture therapy (BNCT), 532
 Branched alkanes, 650
 Br atom, 461
 Br(CH₂)_nBr⁺, 80, 81
 Breit-Rabi equation, 707, 710
 Broken-ring radicals, 237
 5-BrU, 361
 B spins, 598, 600, 602, 606, 607, 617, 618
 Butadiene, 389
- C**
¹³C, 191
 enrichment, 237
 isotopic substitution, 207
 C₆F₆⁺ (cation), 93, 97
 C₆F₆⁻ (anion), 96, 97
 C₆H₅F⁺, 93
 (C₆H₅F)₂⁺, 99
 C₆H₆⁺, 91
 (C₆H₆)₂⁺, 99
 C₆HF₅⁺, 93
 1,2-C₆H₄F₂⁺, 93
 1,3-C₆H₄F₂⁺, 93
 1,4-C₆H₄F₂⁺, 93
 (1,4-C₆H₄F₂)₂⁺, 99
 1,2,4-C₆H₃F₃⁺, 93
 1,2,4,5-C₆H₃F₄⁺, 93
 1,2,4,6-C₆H₂F₄⁺, 93
 Carbohydrates, 668
 Carbon
 fiber, 399
 ion beams, 528
 5-Carbon aromatic cation, 471
 6-Carbon aromatic cations, 472
 Carbonate, 469
 Carbon-centered radicals, 201
 Carbonyl, 206
 Carrier compensation, 417
 Carrier lifetime, 425
 Cations of biphenyl, 734
 c-C₃F₆⁻, 70, 72
 c-C₃F₄⁻, 83
 c-C₄F₆⁻, 83
 c-C₄F₈⁻, 70, 72
 c-C₅F₁₀⁻, 70, 72
 c-C_nF_{2n}⁻ (n = 3–5), 72
 c-C_nF_{2n-2}⁻ (n = 3–5), 82
 Cd⁺ ions, 614
 Ceramic fiber, 400
 CF₂=CF₂⁻, 81
 CF₂=CFBr⁺, 85
 CF₂=CFCF₃⁺, 89
 CF₂=CFCl⁺, 85
 CF₂=CFH⁺, 89
 CF=CFX⁻ (X = Cl, Br, I), 84
 CF₂=CH₂⁺, 89
 CF₃CF=CFCF₃⁻, 83
 CF₃X⁻ (X = Cl, Br, I), 73
 CH₂NHCOC₆H₅, 732
 CH₂OH, 610-612, 615
 CH₃CH₂F⁺, 76
 CH₃F⁺, 76
 CH₃OCH₂Cl⁺, 100, 102
 CH₃OCH₂F⁺, 100
 CH₃OCH₃⁺, 100
 CH₄⁺, 76
 Chain
 reaction, 455
 scission, 388
 Charge resonance, 473
 Chemical exchange, 721, 741
 Chert, 542, 543, 545, 550, 551, 559, 562
 Chlorofluorocarbons, 69
 Choline chloride, 457
 Clarno chert *See also* Chert, 549, 554, 560
 Cl(CH₂)₂Cl⁺, 103
 Cl(CH₂)_nCl⁺, 79
 ClCH₂OCH₂Cl⁺, 102, 103
 Clinical electron beams, 510
 C_{loc} (local concentration), 592, 595
 Cluster
 calculations, 209
 model approach, 676
 Clustered damage, 300
 3'-CMP, 366
 5'-CMP, 366
 CNDO/2 calculations, 80
 Conduction band, 422, 425, 433, 441, 443, 444
 Convolution function, 726, 732, 733, 735
 Correlation tensor, 634
 Coulomb repulsion, 422
 CP2K (code), 670
 Cross
 recombination, 636
 relaxation, 601, 607, 616
 Crosslinking, 388
 Crown ethers, 478
 Cryostats, 163
 Crystalline, 389
 Crystallites, 394
 5-CU, 361

- CW ENDOR, 723
 CW-EPR, 586, 588, 593, 595, 596, 610, 704,
 737, 738
 spectra, 740
 Cyclic perfluoroalkane radical anions
 electron delocalization, 70
 Cyclohexadienyl radical, 175
 Cyclohexane RC (radical cation), 651, 652
 5',6-Cyclo-5,6-dihydro-2'- deoxyuridine, 374
 5',6-Cyclo-6-hydrocytidine C5 radical, 374
 Cyd (cytidine), 366
 Cylindrical phantom, 519
 Cytosine, 361
 related compounds, 373
- D**
 D_2^+
 in ground vibrational state, 120
 2'-dA, 372
 2'-dC, 359
 5'-dCMP, 366
 $D_2(H_2)D_2^+$, 130, 133
 D_2O , 191
 Dangling bonds, 423, 444
 Dating, 551
 Deadtime, 603
 Dealkylation, 475
 Decomposition, 223
 Deep level, 424
 DEER (double electron-electron resonance),
 582, 616–618, 620, 621
 Degenerate electron
 exchange, 648, 651
 transfer, 653
 Dehalogenation, 459
 Density matrix, 600, 633
 3'-Deoxyadenosine (cordycepin), 372
 Deoxyribose, 689
 Deprotonation, 179, 241, 465, 643
 Detector material, 511
 Deuterated, 191
 methane radical cations, 76
 Deuteration, 599
 Deuterium(D)-isotope effects, 100
 DFT (density functional theory), 71, 93, 99,
 262, 462
 calculations, 189
 computations, 73
 D-glucose, 362
 Diacetyl radical anion, 180
 Dialkylamidogen, 478
 Diamagnetic radiation products, 216
 Diatomic inorganic radicals, 173
 Dicyanamide, 466
 Dielectron, 612
 Dienyl radical, 395
 Diffusion equation, 391
 Difluorooxalatorborate, 469
 Diglycolamides, 478
 Dihedral angles, 207
 5,6-Dihydrothymidine-5-yl radical, 360
 Di-interstitial, 417
 Dimensions of the tracks, 612
 Dimer-monomer equilibrium, 356
 Dimer radical cations
 of fluorinated benzenes, 98
 Dimer radical ion, 462
 1,3-Dimethyladamantane, 654
 Dipolar coupling, 588
 Dipolar interaction, 582, 583, 585, 593,
 595,
 598, 599, 604, 606, 607
 Dipotassium glucose-1-phosphate, 189
 Diradical, 565, 570, 572
 Direction cosines, 198
 Direct(-type) effect(s), 300, 301
 Disaccharides, 216
 Disordered solid, 703, 704, 723
 Distonic complex, 655
 Di-*t*-butyl nitroxide, 355, 361
 Divacancy, 417, 432–436
 D-mannose, 362
 $\Delta m_I = 1$ transitions, 711, 723
 $\Delta m_I = \pm 1$ selection rule, 729
 $\Delta m_S = 1$ transitions, 718
 $\Delta m_S = 2$ line, 718
 DMPO, 367
 DNA, 354, 373, 378, 687
 helix, 190
 irradiated, 620
 DNase I, 378
 Dosimeter material, 512
 Dosimetry, 190
 codes, 514
 Double quantum coherence (DQC), 617, 620
 Dresser chert, 559, 561–563
 dT (thymidine), 359
 2'-dU, 359
 5'-dUMP, 366
- E**
 E'_1 center, 257, 258, 264, 265
 E'_2 center, 258, 262
 E'_3 center, 258, 264
 E'_5 centers, 258
 E'_7 center, 264
 E'_8 center, 264
 E'_9 center, 258, 264, 265

- E'_{10} center, 258
 e^-_{aq} , 300
 Easyspin, 715–717, 719, 720, 725, 726, 731, 734, 736, 737, 738, 740
 Echo decay, 613, 615
 Effective
 19F hfc, 717
 nuclear spin, 707
 E'_{Ge} (defect), 274, 281
 generation mechanisms of, 286
 Electrolyte, 469
 additives, 470
 Electron(s), 458, 612, 616
 affinity, 68
 arc treatment, 521
 attachment to fluorocarbons, 69
 beam, 400, 497
 bubbles, 141
 capture, 190
 delocalization, 463
 irradiation, 417, 418, 431, 443
 transfer, 653
 traps, 438
 Electron and hole transfer, 67
 Electron and photon irradiation, 512
 treatment, 524
 Electronegative, 431
 Electronic
 reorganization, 242
 structure, 68, 417
 Elimination reactions, 242
 Embedding, 209
 ENDOR (electron nuclear double resonance)
 96, 99, 255, 256, 704
 convolution function, 731
 powder lineshape, 726
 simulation method, 724
 spectra, 704, 723, 725, 726, 732
 with hfc due to $I = \frac{1}{2}$ nuclei, 737
 with hfc \approx nqc due to $I \geq 1$ nuclei, 737
 with hfc $>$ nqc due to $I \geq 1$ nuclei, 737
 in powders, 730
 transition
 frequencies, 724, 726
 probability, 726, 728
 ENDORF2, 727, 733, 734, 740, 741
 ENDOR-induced EPR (EIE), 195
 Energy
 minimization, 669
 Enzymatic digestion, 367
 EPR (electron paramagnetic resonance) 68, 151, 255
 analysis of motional effects, 721
 calculation, 673
 spectral simulation, 84
 EPR dosimetry, 509, 528, 533
 clinical applications of, 533
 in vivo, 523, 526
 EPR imaging (EPRI), 517
 Equivalent magnetic nuclei, 638
 Equivalent protons, 705, 727
 ESE (electron spin echo), 583, 588, 596
 envelope modulation (ESESME), 255, 256, 266
 ESR (electron spin resonance) *See also* EPR, 68, 299, 353
 1-Ethyluracil, 358
 Ethynyl radical, 171
 Exact
 simulation, 713
 treatments, 709
 Exchange
 interaction, 590, 601
 rate, 736
 Excitation, 239
 width, 731–733, 735, 737
 window, 726
 Excited state, 301, 424, 434
 External beam radiotherapy, 524
 Extraction agents, 475
 E'_α center, 272, 276
 E'_β center, 271
 $E'_\gamma(1)$ center, 275
 $E'_\gamma(2)$ center, 275
 E'_δ center, 271, 274
 E'_δ center, 272, 277, 279, 280
F
 Fast electron(s), 159
 Fast neutron radiotherapy, 532
 F-center, 461
 Fermi level, 437, 439, 442
 ^{19}F hf(c), 70, 716
 FID (free induction decay), 597, 598
 Field-frequency ENDOR (FF-ENDOR), 195
 Field-swept ENDOR, 708
 Fine-structure, 430
 parameter, 436
 splitting, 426
 First order
 ENDOR theory
 applications of, 730
 ENDOR transition
 probability of, 729
 $S = 1/2$ ENDOR spectra, 726
 simulation, 711
 spectrum, 706
 Five-membered ring, 80
 Fluorinated
 alkanes, 70

- benzene, 91, 644
 - radical anions, 96
 - radical cations, 92
- methane (CH₃F), 76
- pyridines, 96
- Fluorine-containing organic radicals, 69
- Fluorobenzenes, 643
- Fluorocarbons, 69
- Fluoroethylene related radical cations, 85
- Forbidden ($\Delta m_l = 1$) hyperfine lines, 722
- Formation energy, 420, 431
- Fourier deconvolution, 594, 595
- Four-membered ring, 80
- $f_{pc}(r)$ (radial distribution function), 591, 592, 595, 596, 603, 616, 620, 621
- Fraction of spin-correlated pairs, 636
- Free radicals in amorphous solid, 738
- Frenkel pair, 427, 428, 429, 441
- Freon matrix technique, 157
- Frequency
 - domain, 726
 - space, 710
- Fructose, 189, 675, 678
- 5-FU, 361
- Fuel cycle, 455
- 5-FUrd, 362
- G**
- Gamma (γ)-ray, 497
- γ -proton, 210
- Ge(1) (defect), 273, 274, 281–283
- Ge(2) (defect), 273, 274, 281–283
- Ge (germanium)
 - E₁' center, 260
 - E₂' center, 262
 - lone pair center (GLPC), 283
- Gel fraction, 402
- Gel permeation chromatography, 376
- Geminate
 - ion, 582
 - recombination, 642
 - radical ions, 656
 - recombination, 120, 142
 - RIP (radical ion pair), 632
- Generation mechanisms, 283
- [GeO₄]⁻_{I, II}, 270
- [GeO₄/Li]⁰_{A, C}, 270
- Geometry optimizations, 209
- Germoles, 643
- g(-)
 - factor, 194, 582, 594
 - tensor, 198
- Glucose, 191
- Glycine, 677, 681
- Glycosidic bond, 205
- Gordy-Bernhard, 206
- Graft polymerization, 388
- Gunflint chert, 560, 561, 567, 568
- H**
- H₂⁺, 120
 - in ground vibrational state, 120
 - core H₆⁺, 121, 122
 - core H₁₄⁺, 121
- H₃⁺, 120
 - core H₆⁺, 121
- H₆⁺ (ion), 120, 125
- H-abstraction, 205
- Halide, 460
- Halocarbon matrices, 69
- 5-Halodeoxyuridine, 361
- Halogenated
 - alkanes, 77
 - dimethyl ethers, 100
- Halogeno-trifluoroethylene radical anions
 - See also* CF₂=CFX⁻, 84
- H atom(s), 120
 - shifts, 242
- H(CH₂)_nH⁺, 75
- H(CH₂)_nX⁺ (X = Cl, Br; n = 1, 2), 76
- Hcp cage, 138
- HD⁺
 - in ground vibrational state, 120
- H₃D⁺, 125
- H₄D₂⁺, 125, 129
- H₂D₄⁺, 125
- H₂(D₂)D₂⁺, 130, 131, 133
- HD(H₂)HD⁺, 132, 133
- Heavy ions, 510
- Heinzer method, 722
- Heisenberg spin exchange, 719
- Heller-McConnell relation, 206, 671
- Heptamethylnonane, 650
- Heteroorganic compounds, 653
- Hexafluoro-1,3-butadiene radical cation (HFBD⁺), 89
 - photoisomerization of, 89
- Hexafluorocyclobutene *See also*
 - c-C₄F₆⁻, 83
- Hexamethylethane (HME), 70
- H₂(HD)H₂⁺, 133
- H₂(H₂)D₂⁺, 130, 133
- H₂(H₂)HD⁺, 132, 133
- H₂(H₂)H₂⁺, 133
- High density PE, 393
- High dose rate, 523
- Highest occupied molecular orbital (HOMO), 67, 93

- High field approximation, 706
 High-LET radiation, 512, 530
 High-level nuclear waste, 455
 High-performance liquid chromatography (HPLC), 354
 Histone H1, 379
 ^2H labeled, 191
 HLi_2O_4 , 271
 H_2O elimination, 205
 H_3O_4 , 271
 H_4O_4^+ , 271
 Hole, 458, 612, 614
 hopping diffusion, 141
 transfer, 301
 trapping, 471
 Hot radical cations, 178
 Hot reaction channels, 155
 1,2-H-shift, 691
 HXeCC , 176
 HXeO , 176
 Hydrated electrons, 356
 Hydrogen (H) atoms, 164, 596, 608, 614, 616
 Hydrogen-bound, 209
 5-Hydroxymethyluracil, 378
 Hyperfine (HF; Hf; hf), 68, 72, 74, 77, 82
 anisotropy, 594
 coupling (hfc), 354
 enhancement, 724, 734
 interaction, 427
 splitting, 395
 structure, 274, 276, 279, 281, 418, 420, 422, 426, 432, 436, 443
- I**
- Identification, 189
 Imidazolium, 470
 Imide, 467
 Imidyl, 470
 Implantation, 425
 IMRT (intensity modulated radiotherapy), 510, 526
 dose distributions, 522
 Indirect effects, 300, 301
 INDO calculations, 83
 Inequivalent nuclei, 705
 Inert-gas matrix, 69
 Influence quantities (dosimeter response), 495
 In situ X-irradiation, 193
 Insoluble organic matter, 543, 544
 Instantaneous diffusion, 599, 601–603, 613, 616, 619, 621
 Instrumental factors, 724
 Interactions with matrix, 76
 Inter-molecularly trapped electron (IMTE), 218
 Interstitial, 417, 422, 424, 426–428, 440
 sites, 166
 Intramolecular
 conversions, 242
 exchange, 645
 Intra-operative radiotherapy, 523
 Intrinsic defects, 438
 In vivo dosimetry, 522
 Ion
 exchange, 455
 irradiation, 513
 recombination, 630
 Ion-irradiated EPR dosimeter, 529
 Ionization, 190
 chamber measurements, 527
 density, 511, 512, 531
 energy (potential), 68
 Ionizing radiation, 68, 69, 77, 510
 Ionometry, 511, 527
 Ionophores, 475
 Irradiated solids, 711
 Irradiation, 429, 433, 435, 440, 444
 IR spectroscopy, 151
 Isochronal annealing, 439
 Isotope condensation, 139
 of H_6^+ , 141
 Isotropic, 70
 g_1 -tensor, 586
 hyperfine-coupling, 133
 PC (paramagnetic center), 588
- J**
- Jahn-Teller (J-T)
 distortion, 76, 420, 644
 effects, 76, 91
- K**
- Kerogen, 542, 544, 546–548
 Kolbe reaction, 459
- L**
- Lactose, 362
 L- α -alanine, 511
 Lanthanides, 475
 Large hfc constants, 714
 Large precessional motion, 133, 138
 Larmor frequency range, 195
 Left-handed (LH) quartz, 257, 258, 262
 LET, 607, 610, 612, 620
 dependence, 530
 Level crossing, 652

- Libration motion, 138
Lifetime
 control, 425
 of radical cations, 648, 653
Li-ion batteries, 469
6Li enriched lithium formate, 532
Linear alkane radical cations *See also*
 $\text{H}(\text{CH}_2)_n\text{H}^+$, 75
Liquid-liquid extraction, 455
 Lithiumdithionate, 532
Lithium formate, 520
 dosimeters, 530
 EPR
 dosimeters, 531
 dosimetry, 517, 522
 monohydrate, 513
Long-range charge-induced dipole and
 quadrupole interactions, 141
Low density PE, 393
Low dose rate (LDR), 523
Lowest unoccupied molecular orbital
 (LUMO), 67
Low field effect, 639
Low-LET
 photons, 530
 radiation, 512
Low-temperature stabilization, 153
Luminescence response, 630
Lysozyme, 366
- M**
Madelung correction, 421
Magnetic
 field effect, 638
 relaxation, 724
Magnetically
 diluted systems, 590
 equivalent nuclei, 636
 equivalent protons, 650
 non-equivalent nuclei, 635, 650
MARY spectra, 638, 640, 641, 645, 646, 656
Matrix
 catalysis, 179
 isolation, 68, 69, 153
 switching between reaction channels, 179
McConnell, 206
Metalorganic compounds, 652
Metastable, 215
 defects, 431
Meteorites, 544–546, 551, 556, 560–562, 564,
 565, 569, 572
Methane (CH_4), 76
Methanol, 609–612
Methyl-group rotation, 722
Methyl-methacrylate, 390
2-Methyl-2-nitrosopropane (MNP), 353
1-Methyluracil, 359
Microscopically tunable excess electron
 capture, 181
Microsolvation model, 181
Microwave field
 effect of, 631
Microwave
 power saturation, 529
 pulse, 598, 600, 604
Migration, 392
Mini-ALA dosimeters, 519
Minidosimeters, 515
Minimal energy path, 690
Minor actinides, 475
MNP-H adducts, 361
Model space, 675, 677
Molar absorbance coefficients, 356
Molecular dynamics (MD), 679
Molecular hosts, 157
Monosaccharides, 216
Monte Carlo
 algorithm, 675
 calculations, 519
 simulations, 511, 512, 533
Motional narrowing effect, 135
2-MTHF matrix., 98
Multi-component spectra, 708
Multi-composite EPR spectra, 197
Multimer radical anion, 463
Multistep formation mechanisms, 215
Murchison meteorite, 545, 547
- N**
N-alkane RC (radical cation), 649
Negative-U center, 421, 422, 424, 425
Ne matrices, 120
Neopentane (NEP), 70
Neutron
 absorption, 532
 dosimetry, 532
 irradiation, 418, 530
Nitroxide spin probes, 721
N, N, N', N'-tetramethyl-p-phenylenediamine
 (TMPD), 70
Noble gas(es), 153
 hydrides, 168
Non bridging oxygen hole centres
 (NBOHC), 272, 280
Nonequivalent HFCCs, 129
Nonequivalent magnetic nuclei, 637
Non-geminate RIPs (radical ion pairs), 632
Non-polar solution, 633

- Norbornane RC (radical cation), 654
 Normal alkanes, 648
 NOSYM, 677
 Nqc of the same order as the hfc, 727
 Nuclear spin diffusion, 609
 Nuclear Zeeman term, 736
 Nucleosides, 357
 Nucleotides, 357
- O**
 O, 83
 O⁻, 613
 O₂⁻, 259, 266, 267
 O₃⁻, 266
 O₂³⁻, 266, 269
 OD EPR spectra, 645
¹⁷O
 enriched crystal, 260, 270
 hyperfine, 259, 270, 320, 322
 OH radical (•OH), 300, 356
 Oligo(dC)10, 376
 Oligo(dT)10, 376
 Optical absorption (OA), 275, 281
 band, 272
 Optical bleaching, 219, 594
 Optimized geometries, 672
 Organic solids, 190
 Orgueil, 547
 meteorite, 559, 560, 562, 563, 567–570,
 572
 Origin of life, 542–544, 556
 Orthohydrogen, 118
 Oxidation, 241
 product, 221
 Oxidative, 692
 fragmentation, 459
 path, 300
 Oxygen
 radical ions, 612
 vacancy, 275, 278, 279
 model, 275, 276
 Oxyquinolate, 646
- P**
 Pake
 doublet, 588
 pattern, 588
 Parahydrogen, 118
 Paramagnetic relaxation, 636, 652
 Para-ortho
 conversion, 128
 ratio, 128
 Pascal triangle, 705, 707
 P-centered radicals, 230
 PCS (fiber), 400
 PELDOR (pulsed electron double resonance),
 194, 582, 588, 617
 Perfluoro-2-butene radical anion *See also*
 CF₃CF=CFCF₃⁻, 83
 Perfluoroalkene radical anions *See also*
 c-C_nF_{n-2}⁻
 structural distortion, 81
 Perfluorocycloalkane radical anion *See also*
 c-C_nF_{2n}⁻, 72
 Periodic, 677
 boundary conditions, 209
 Peroxy radical (POR), 272, 280, 393
 Peroxy spin probes, 721
 Phanerozoic, 550
 Phenyl radical, 172
 Phosphate ester bond, 244
 Photoelectric absorption, 159
 Photoinduced electron transfer
 reaction, 73
 Photolysis, 616
 Photoresist, 464
 Piperidine treatments, 377
 Pi(π)-sandwich dimer radical cation, 472
 π-systems, 470
 π* and σ* orbital mixing, 83
 PMMA phantom, 514, 516, 521
 Point-dipole approximation, 671
 Poly(A), 376
 Polyacrylamide gel electrophoresis (PAGE),
 377
 Polyacrylonitrile fiber, 399
 Polyamide, 388
 Polycarbosilane, 400
 Polyenyl radical, 395
 Polyethylene, 388
 Poly(I), 376
 Polymers, 388, 465
 Polynitrile anion, 467
 Polypropylene, 388
 Polytetrafluoroethylene, 388
 Poly(U), 376
 Poly(vinylidene fluoride), 394
 Positron annihilation spectroscopy, 443
 Potassium dithionate, 531
 Potential energy, 679
 Powder
 EPR, 197
 spectrum, 201
 Power saturation, 595
 Precessional motion, 135, 138
 Pre-irradiation, 393
 Primary radical
 cations, 647
 species, 193
 Principal directions, 198, 677

- Principal g values, 271
Processing of spent nuclear fuel, 455
Propargyl radical, 172
Protamine, 379
Proterozoic, 550, 551, 554, 555
Proton, 510
 HF (hf) tensors, 189
 shuffle, 241
 transfer, 656
Proton and heavy ion irradiation, 526
Pseudohalide, 460
Pseudorotation, 91, 644, 652
Pulse annealing, 217
Pulsed dipolar spectroscopy, 582, 617
Pure hydroxyalkyl radical, 206
Purine
 nucleosides, 375
 nucleotides, 375
Pyrolysis, 405
4-PyOBN, 360
- Q**
Q-band, 194
Quantum
 beats, 631, 633, 641, 643
 memory, 263
Quartz, 255, 256
 flat cell, 357
Quasi-classical approximation, 635
Quasi-direct effect, 300
Quaternary ammonium and phosphonium, 470
- R**
Radiation, 388
 chemical yield, 610, 611, 615
 chemistry, 458, 668
 curing, 400
 damage, 426
 doses, 190
 induced
 acidification, 459
 defects, 418, 430, 431, 439, 441
 effects, 285
 fragmentation, 457
 free radicals, 509
 radicals, 189
 quality, 512
 stability, 456, 475
Radical
 anion(s), 67, 180
 of perfluorocycloalkanes, 716
 pairs, 73
 cation, 67, 68, 154
 of hexamethylethane, 641
 diion, 458
 evolution, 216
 ion(s), 68, 614
 pairs (RIPs), 630, 632
 pair
 EPR spectra, 718, 736
Radioprotection, 475
Radiotherapy, 510, 522
 applications of, 533
 output factors, 515
Reaction
 pathway, 690
 rate constants, 356
Recombination, 594
 fluorescence, 632, 638, 643
Reduction, 240
 radiation products, 221
Reductive, 692
 path, 300
Regio-selective, 189
Regioselectivity, 689
Relative effectiveness, 512
Relative signs of the hfc and the zfs, 720, 721
Reverse micelles, 476
Reverse-phase HPLC, 355
Rhamnose, 220
Rhombicity, 201
RH (right-handed), 257
 crystals, 258
 quartz, 266
Ring formation, 79
Ring-opened species, 246
RNA, 690
Rotational state, 118
Ruby, 494
- S**
Schonland
 ambiguity, 189, 199
 conjugate, 199
Secondary
 electron, 239
 processes, 242
Second microwave pulse, 599
Second moment, 595
Second order
 hyperfine term, 122
 perturbation
 method, 712
 theory, 707, 715, 731, 734, 735, 736
 treatments, 712
 simulation, 712
Semi-empirical theory, 205
Sephadex G-25, 355, 379
SEP-PAK C18 cartridge, 355, 364
'2 + 1' Sequence, 617, 620

- ^{29}Si
 hyperfine, 259, 264
 nucleus, 271
 SiC micro tube, 410
 $\equiv\text{Si}-\text{O}-\text{O}\cdot$, 266
 Silicon carbide, 400
 Silicon nitride fibers, 412
 Siloles, 643
 Simfonia, 714
 Simulation
 methods, 735
 of ENDOR powder spectra, 723
 of isotropic EPR spectra, 708
 of microwave saturated EPR spectra, 722
 of $S = 1/2$ EPR powder spectra, 711
 Single crystal, 189
 EPR, 256
 Single molecule
 approach, 676
 calculations, 209
 Single-oxygen-vacancy model, 259
 Singlet spin state, 632
 Singlet state population, 632, 636
 Singlet-triplet (S-T)
 mixing, 719
 splitting, 718
 effects, 718
 transitions, 636, 648
 Singly occupied molecular orbital (SOMO),
 67, 72, 78, 84, 93
 SiO_2 , 255
 SO_4^- , 609
 ion radicals, 608
 Solar system, 542, 543, 551, 563, 564, 572,
 573
 Solid
 electrolyte interphase, 470
 hydrogen, 117
 parahydrogen, 117
 Solid state sugars, 189
 Solute cation–matrix chlorine interactions, 78
 Solvated electron, 458
 Solvent RC (radical cation), 643, 646, 648
 SOPHE, 740
 Sorbose, 189
 Spatial distributions, 591, 614
 Special perturbation methods, 736
 Spectral diffusion, 598, 599, 601, 604, 605
 kernel, 606
 Spectrum decomposition, 190, 228
 Statistical, 223
 Spin-adduct, 354
 Spin-correlated RIP, 639
 Spin
 correlation, 630, 631
 delocalization, 208
 density, 68, 421, 423, 428, 444, 445
 diffusion, 601
 echo, 597, 617
 Hamiltonian, 125
 labels, 582
 locking, 640
 packet, 597
 polarization, 206
 Spin-lattice relaxation, 263, 607, 640, 652,
 654
 Spin-spin interaction, 430
 Split interstitial(s), 430, 443
 Spur, 619
 Stable radical formation, 189
 Standards, 492
 Stick plot analysis, 705, 707
 Stimulated echo, 601
 Strand break, 190, 299
 Stretched Lorentzian, 551, 552, 554, 555, 565
 Strong nqc, 729
 interaction, 714
 Structural distortion, 83
 Structural relaxations, 215
 Structure manipulation, 669
 Styrene, 394
 Substitutional sites, 166
 Sucrose, 189, 670, 671, 681, 691
 Sugar moiety, 372
 Sugar-phosphate bonds, 230
 Sugar radical, 301
 Sulfonium, 473
 Supercell, 209
 calculations, 429, 432, 435
 Superexcited, 240
 Superhyperfine structure, 256, 461
 Symmetry-related
 ambiguities, 189, 205
 sites, 199
- T**
 T_1 samples, 604, 606, 609
 T_2 samples, 606
 Table sugar, 191
 Tagish Lake meteorite, 547, 548
 Task-specific ILs, 456
 TD (time-dependent)–DFT, 73, 84
 Tetrafluorocyclopropene radical anion
 See also $c\text{-C}_3\text{F}_4^-$, 83
 Tetrafluoroethylene radical anion
 See also $\text{CF}_2=\text{CF}_2^-$, 81
 Tetramethylpiperidine, 655
 Tetramethylsilane (TMS), 70
 Therapeutic proton beams, 527
 Thermal annealing, 189, 594

- bleaching, 219
 - electron attachment, 69
 - neutron dosimetry, 532
 - oxidation, 410, 425
 - treatments, 275
 - Thermostat, 683
 - Thiazolium, 472
 - Third order perturbation theory, 738
 - Thiyl radicals, 367
 - Thymine glycol, 378
 - Time-correlated single photon counting (TCSPC), 641
 - Time-resolved magnetic field effect (TRMFE), 633
 - TMP, 373
 - Tomotherapy, 514
 - Traceability, 490
 - Track, 619
 - effects, 610
 - radii, 610, 615
 - structure, 612, 631
 - Trajectory, 679
 - Transient nutation, 566, 567
 - Transition
 - metal, 443
 - probability formula, 734
 - state, 690
 - Transverse relaxation time T₂, 263
 - Trapped electron (e⁻_T), 140, 461, 596, 612, 613, 614
 - Trapping mechanism of free electrons, 140
 - Trehalose dihydrate, 189
 - Tricyanomethanide, 466
 - Triflate, 459
 - Trifluoromethyl, 460
 - halide radical anions, 73
 - 2,2,4-Trimethylpentane, 650
 - Tri(n-butylphosphate), 475
 - Triplet state EPR spectra, 719, 736
 - Triplet state model, 264
 - Trityl radical, 473
 - Tri-vacancy with an Al impurity model V(SiO₂)Al, 262
 - Two-center three-electron bond, 461
 - Tyrosyl free radical, 727
- U**
- UHF MO computations, 70
 - Ultracold helium nanodroplets, 143
 - Ultra-high molecular weight polyethylene, 394
 - 3'-UMP, 366, 373
 - Uncertainty (measurement), 501
 - Uniform distribution, 599, 601, 605, 609, 618, 620
 - Uniform spatial distribution, 611
 - 5'-UMP, 363
 - Unit cell, 677
 - Uracil, 358
 - Urd, 359, 369
 - U-tube, 357
 - UV, 611
 - absorbance spectrum, 370
- V**
- Vacancy, 417, 422, 426, 429, 430, 431, 434, 439, 441, 443, 444
 - donor pair, 441
 - interstitial pairs, 417
 - Valence band, 422
 - Vibrational spectra, 162
 - Vinyl radical, 174
 - VK center, 461
 - Voigt line shape, 723
- W**
- Water-equivalent phantom, 528
 - W-band spectra, 266
 - Weight function, 737
 - WinSim program, 708
 - Wurtzite, 419
- X**
- X-band, 193
 - X(CH₂)_nX⁺ (X = Cl, Br), 79
 - Xenon dihydride, 168
 - X-rays, 159, 191, 510, 513
- Y**
- Yeast RNA, 379
- Z**
- Zeeman interaction, 584
 - Zero-field
 - line, 639, 642
 - MARY line, 656
 - splitting, 426, 430, 434
 - Zero-point vibrational energy, 142
 - Zinc blende, 419
 - Zwitterion, 465